

Advances in Photosynthesis and Respiration
Volume 29

Photosynthesis *in silico*

Understanding Complexity from
Molecules to Ecosystems



Edited by
Agu Laisk, Ladislav Nedbal
and
Govindjee

 Springer

Photosynthesis *in silico*

Understanding Complexity from Molecules to Ecosystems

Advances in Photosynthesis and Respiration

VOLUME 29

Series Editor:

GOVINDJEE

University of Illinois, Urbana, Illinois, U.S.A.

Consulting Editors:

Julian EATON-RYE, *Dunedin, New Zealand*

Christine H. FOYER, *Harpenden, U.K.*

David B. KNAFF, *Lubbock, Texas, U.S.A.*

Anthony L. MOORE, *Brighton, U.K.*

Sabeeha MERCHANT, *Los Angeles, California, U.S.A.*

Krishna NIYOGI, *Berkeley, California, U.S.A.*

William PARSON, *Seattle, Washington, U.S.A.*

Agepati RAGHAVENDRA, *Hyderabad, India*

Gernot RENGGER, *Berlin, Germany*

The scope of our series, beginning with volume 11, reflects the concept that photosynthesis and respiration are intertwined with respect to both the protein complexes involved and to the entire bioenergetic machinery of all life. *Advances in Photosynthesis and Respiration* is a book series that provides a comprehensive and state-of-the-art account of research in photosynthesis and respiration. Photosynthesis is the process by which higher plants, algae, and certain species of bacteria transform and store solar energy in the form of energy-rich organic molecules. These compounds are in turn used as the energy source for all growth and reproduction in these and almost all other organisms. As such, virtually all life on the planet ultimately depends on photosynthetic energy conversion. Respiration, which occurs in mitochondrial and bacterial membranes, utilizes energy present in organic molecules to fuel a wide range of metabolic reactions critical for cell growth and development. In addition, many photosynthetic organisms engage in energetically wasteful photorespiration that begins in the chloroplast with an oxygenation reaction catalyzed by the same enzyme responsible for capturing carbon dioxide in photosynthesis. This series of books spans topics from physics to agronomy and medicine, from femtosecond processes to season long production, from the photophysics of reaction centers, through the electrochemistry of intermediate electron transfer, to the physiology of whole organisms, and from X-ray crystallography of proteins to the morphology of organelles and intact organisms. The goal of the series is to offer beginning researchers, advanced undergraduate students, graduate students, and even research specialists, a comprehensive, up-to-date picture of the remarkable advances across the full scope of research on photosynthesis, respiration and related processes.

For other titles published in this series, go to
www.springer.com/series/5599

Photosynthesis *in silico*

Understanding Complexity from Molecules
to Ecosystems

Edited by

Agu Laisk

*University of Tartu
Estonia*

Ladislav Nedbal

*Institute of Systems Biology and Ecology
Academy of Sciences of the Czech Republic
Nové Hradý
Czech Republic*

and

Govindjee

*University of Illinois at Urbana-Champaign
Urbana
Illinois
USA*



Springer

Library of Congress Control Number: 2009921443

ISBN 978-1-4020-9236-7 (HB)
ISBN 978-1-4020-9237-4 (e-book)

Published by Springer,
P.O. Box 17, 3300 AA Dordrecht, The Netherlands.

www.springer.com

Cover: Photosynthesis *in silico*. Photo by Eero Talts, University of Tartu

Printed on acid-free paper

All Rights Reserved

© 2009 Springer Science+Business Media B.V.

No part of this work may be reproduced, stored in a retrieval system, or transmitted in any form or by any means, electronic, mechanical, photocopying, microfilming, recording or otherwise, without written permission from the Publisher, with the exception of any material supplied specifically for the purpose of being entered and executed on a computer system, for exclusive use by the purchaser of the work.

From the Series Editor

I am highly obliged to each and everyone of the authors from fifteen countries (Australia, Austria, Brazil, Canada, China, Czech Republic, Estonia, France, Germany, Lithuania, Russia, Switzerland, The Netherlands, U.K., and U.S.A.) for their valuable contributions to the successful and timely production of this unique book, Volume 29 in *Advances in Photosynthesis and Respiration: 'Photosynthesis in silico—Understanding Complexity from Molecules to Ecosystems'*, edited by two of the pioneers in the field (Agu Laisk, of Estonia; and Ladislav Nedbal, of the Czech Republic).

The authors are: Niels P.R. Anten (The Netherlands; Chapter 16); Michael J. Behrenfeld (U.S.A.; Chapter 20); Carl J. Bernacchi (U.S.A.; Chapter 10); Joseph Berry (U.S.A.; Chapter 9); Jan Červený (Czech Republic; Chapter 2); Jan P. Dekker (The Netherlands; Chapter 3); Gerald Edwards (U.S.A.; Chapter 14); Hillar Eichelmann (Estonia; Chapter 13); Hadi Farazdaghi (Canada; Chapter 12); Graham Farquhar (Australia; Chapters 9 and 10); Arvi Freiberg (Estonia; Chapter 4); Andrew Friend (U.K.; Chapter 20); Richard J. Geider (U.K.; Chapter 20); Jeremy Harbinson (The Netherlands; Chapter 11); Hubert Hasenauer (Austria; Chapter 19); Michael Hucka (U.S.A.; Chapter 1); Manfred Küppers (Germany; Chapter 18); Agu Laisk (Estonia; Chapters 13 and 14); Jérôme Laverne (France; Chapter 8); Dušan Lazár (Czech Republic; Chapter 5); Stephen P. Long (U.S.A.; Chapters 10 and 17); Ladislav Nedbal (Czech Republic; Chapter 2); Ülo Niinemets (Estonia; Chapter 16); Vladimir I. Novoderezhkin (Russia; Chapter 3); Vello Oja (Estonia; Chapter 13); Michael Pfiz (Germany; Chapter 18); Stephen A. Pietsch (Austria; Chapter 19); Carlos Pimentel (Brazil; Chapter 10); Ondřej Prášil (Czech Republic; Chapter 6); Galina Riznichenko (Russia; Chapter 7); David M. Rosenthal (U.S.A.; Chapter 10); Andrew Rubin (Russia; Chapter 7); James Schaff (U.S.A.; Chapter 1); Gert Schansker (Switzerland; Chapter 5); Henning Schmidt (Germany; Chapter 2);

Christopher J. Still (U.S.A.; Chapter 20); Paul C. Struik (The Netherlands; Chapter 11); Gediminas Trinkunas (Lithuania; Chapter 4); Rienk van Grondelle (The Netherlands; Chapter 3); Susanne von Caemmerer (Australia; Chapter 9); Wim Vredenberg (The Netherlands; Chapter 6); Ian E. Woodrow (Australia; Chapter 15); Xinyou Yin (The Netherlands; Chapter 11), and Xin-Guang Zhu (China; Chapter 17).

I also thank Jacco Flipsen, Noeline Gibson and André Tournois of Springer (Dordrecht, The Netherlands) for their patience with me during the production of this book. I am particularly thankful to Albert André Joseph (of SPi Technologies India Private Limited) for his wonderful cooperation in efficiently taking care of the corrections in the proofs of this book. Finally, I am grateful to my wife, Rajni Govindjee, and the offices of the Department of Plant Biology (Feng Sheng Hu, Head) and of Information Technology, Life Sciences (Jeff Haas, Director), of the University of Illinois at Urbana-Champaign, for their constant support.

A list of books, published under the Series '*Advances in Photosynthesis and Respiration*' is available at the Springer web site: <<http://www.springer.com/series/5599>>. Members of the ISPR (International Society of Photosynthesis Research) receive 25 % discount. For the Table of Content of most of the earlier volumes, see my web site at: <<http://www.life.uiuc.edu/govindjee/Reference-Index.htm>>.

Govindjee

Founding Editor of *Advances in Photosynthesis and Respiration*
Departments of Biochemistry and Plant Biology
and Center of Biophysics & Computational
Biology
University of Illinois at Urbana-Champaign,
Illinois, USA
E-mail: gov@life.illinois.edu

Contents

From the Series Editor	v
Preface	xv
The Editors	xvii
Author Index	xxi
Color Plates	CP1

Part I: General Problems of Biological Modeling

1 Trends and Tools for Modeling in Modern Biology	3–15
<i>Michael Hucka and James Schaff</i>	
Summary	3
I. Introduction	4
II. Representing Model Structure and Mathematics	4
III. Augmenting Models with Semantic Annotations	6
IV. Connecting Models to Results	9
V. Future Directions for Systems Biology Markup Language (SBML)	13
VI. Conclusions	13
References	14
 2 Scaling and Integration of Kinetic Models of Photosynthesis: Towards Comprehensive E-Photosynthesis	 17–29
<i>Ladislav Nedbal, Jan Červený and Henning Schmidt</i>	
Summary	17
I. Introduction	18
II. Mapping Partial Photosynthesis Models into the Comprehensive Model Space (CMS): The Principles and Strategies	19
III. Mapping of Photosystem II Models into the Comprehensive Model Space (CMS)	21
IV. Concluding Remarks	27
Acknowledgments	28
References	28

Part II: Modeling of Light Harvesting and Primary Charge Separation

3 Modeling Light Harvesting and Primary Charge Separation in Photosystem I and Photosystem II 33–53

Rienk van Grondelle, Vladimir I. Novoderezhkin and Jan P. Dekker

Summary	34
I. Introduction	34
II. Physical Models of Energy Transfer	35
III. Exciton Spectra and Energy Transfer in Photosystem I (PS I) Core	40
IV. Excitation Dynamics in Major Light Harvesting Complex II (LHCII)	41
V. Energy Transfers and Primary Charge Separation in Photosystem II Reaction Center	44
VI. Concluding Remarks	50
Acknowledgments	50
References	50

4 Unraveling the Hidden Nature of Antenna Excitations 55–82

Arvi Freiberg and Gediminas Trinkunas

Summary	55
I. Introduction	56
II. Disordered Frenkel Exciton Model for Absorbing States of Circular Antenna Aggregates	59
III. Shortcomings of the Disordered Frenkel Exciton Model	63
IV. Excitonic Polaron Model of the Antenna Fluorescing States	64
V. Evaluation of the Model Parameters from the Experimental Spectra	70
VI. Conclusions and Outlook	76
Acknowledgments	77
References	77

Part III: Modeling Electron Transport and Chlorophyll Fluorescence

5 Models of Chlorophyll a Fluorescence Transients 85–123

Dušan Lazár and Gert Schansker

Summary	86
I. Fluorescence Induction	86
II. Approaches and Assumptions in the Modeling of the Fluorescence Rise	91
III. Particular Models for the Fluorescence Rise	100
IV. Modeling the Whole Fluorescence Induction	111
V. Conclusions and Future Perspectives	115
Acknowledgments	115
References	115

6	Modeling of Chlorophyll a Fluorescence Kinetics in Plant Cells: Derivation of a Descriptive Algorithm	125–149
	<i>Wim Vredenberg and Ondřej Prášil</i>	
	Summary	126
	I. Introduction	126
	II. Variable (Chlorophyll) Fluorescence – Some Basics	128
	III. Application of Single, Twin and Multiple Turnover Flashes	132
	IV. Distinguishable Phases of Fluorescence Response upon Multiturnover Excitation	135
	V. Fluorescence Induction Algorithm for Experimental Curves	137
	VI. Concluding Remarks	144
	Acknowledgments	146
	References	146
7	Modeling of the Primary Processes in a Photosynthetic Membrane	151–176
	<i>Andrew Rubin and Galina Riznichenko</i>	
	Summary	151
	I. Introduction	152
	II. Fluorescence as an Indicator of the Photosystem State	153
	III. General Kinetic Model of the Processes in Photosynthetic Thylakoid Membrane	154
	IV. Multiparticle Modeling of the Processes in the Photosynthetic Membrane	166
	V. Concluding Remarks and Future Perspectives	171
	Acknowledgments	171
	References	171
8	Clustering of Electron Transfer Components: Kinetic and Thermodynamic Consequences	177–205
	<i>Jérôme Lavergne</i>	
	Summary	177
	I. Introduction	178
	II. Thermodynamic Performance of Integrated and Diffusive Photosynthetic Models	179
	III. Integrated Versus Diffusive Electron Transfer Chain	183
	IV. The Small Apparent Equilibrium Constant in the Donor Chain of <i>Rhodobacter sphaeroides</i>	189
	V. Quinone Domains	195
	VI. Statistical and Non Statistical Heterogeneities	198
	VII. Pool Function Test at Steady State	199
	VIII. Kinetic Analysis: Playing with Inhibitors, Redox Potential and Flash Intensity	201
	IX. Concluding Remarks	203
	Acknowledgments	203
	References	203

Part IV: Integrated Modeling of Light and Dark Reactions of Photosynthesis

9	Biochemical Model of C₃ Photosynthesis	209–230
	<i>Susanne von Caemmerer, Graham Farquhar and Joseph Berry</i>	
	Summary	210
	I. Introduction	210
	II. The Rate Equations of CO ₂ Assimilation	211
	III. Parameters and their Temperature Dependencies	215
	IV. The Role of Rubisco Activation State	218
	V. Estimating Chloroplast <i>p</i> CO ₂	219
	VI. Predicting Photosynthesis from Chloroplast Biochemistry	220
	VII. Predicting Chloroplast Biochemistry from Leaf Gas Exchange	223
	VIII. Concluding Remarks	224
	References	225
10	Modeling the Temperature Dependence of C₃ Photosynthesis	231–246
	<i>Carl J. Bernacchi, David M. Rosenthal, Carlos Pimentel, Stephen P. Long and Graham D. Farquhar</i>	
	Summary	232
	I. Introduction	232
	II. Processes Limiting to C ₃ Photosynthesis	233
	III. Modeling Photosynthesis and the Supply of CO ₂	240
	IV. Concluding Remarks	242
	Acknowledgments	243
	References	243
11	A Model of the Generalized Stoichiometry of Electron Transport Limited C₃ Photosynthesis: Development and Applications	247–273
	<i>Xinyou Yin, Jeremy Harbinson and Paul C. Struik</i>	
	Summary	247
	I. Introduction	248
	II. Model Development	250
	III. Model Applications	255
	IV. Concluding Remarks	269
	Acknowledgments	269
	References	270
12	Modeling the Kinetics of Activation and Reaction of Rubisco from Gas Exchange	275–294
	<i>Hadi Farazdaghi</i>	
	Summary	275
	I. Introduction	276
	II. Fundamental Photosynthesis Models	276
	III. Rubisco and Its Sequentially Ordered Reaction	279

IV. Rubisco in Steady State: Biochemical Models	281
V. Experimental Evaluation of the Models	287
VI. Concluding Remarks	290
Acknowledgments	291
References	291
13 Leaf C₃ Photosynthesis <i>in silico</i>: Integrated Carbon/Nitrogen Metabolism	295–322
<i>Agu Laisk, Hillar Eichelmann and Vello Oja</i>	
Summary	295
I. Introduction	296
II. The Structure of the Model	297
III. Mathematics	302
IV. Simulations	312
V. Concluding Remarks	317
Acknowledgments	319
References	319
14 Leaf C₄ Photosynthesis <i>in silico</i>: The CO₂ Concentrating Mechanism	323–348
<i>Agu Laisk and Gerald Edwards</i>	
Summary	324
I. Introduction	324
II. Principles of NADP-ME Type C ₄ Photosynthesis	325
III. The C ₄ Model	329
IV. Simulations	334
V. Knowns and Unknowns in Photosynthesis	338
Acknowledgments	345
References	345
15 Flux Control Analysis of the Rate of Photosynthetic CO₂ Assimilation	349–360
<i>Ian E. Woodrow</i>	
Summary	349
I. Introduction	350
II. Flux Control Coefficients: Theory and Challenges	352
III. Reversible Reactions Can Be Flux Limiting	352
IV. Small Control Coefficients Are Hard to Detect	354
V. Enzymes with Higher Control Coefficients	356
VI. Photosynthetic Electron Transport	358
VII. Concluding Remarks	358
Acknowledgments	359
References	359

Part V: From Leaves to Canopies to the Globe

16	Packing the Photosynthetic Machinery: From Leaf to Canopy	363–399
	<i>Ülo Niinemets and Niels P.R. Anten</i>	
	Summary	364
	I. Introduction	364
	II. Inherent Differences in Microenvironment and Photosynthetic Potentials Within the Canopy	367
	III. Scaling Photosynthesis from Leaves to Canopy	379
	IV. Concluding Remarks	389
	Acknowledgments	389
	References	390
17	Can Increase in Rubisco Specificity Increase Carbon Gain by Whole Canopy? A Modeling Analysis	401–416
	<i>Xin-Guang Zhu and Stephen P. Long</i>	
	Summary	401
	I. Introduction	402
	II. Theory and Model Description	404
	III. The Impact of the Inverse Relationship on Leaf and Canopy Level Photosynthesis	407
	IV. Current Efforts of Engineering Rubisco for Higher Photosynthesis	410
	V. Why Has Evolution Failed to Select the Optimal Rubisco?	412
	VI. Concluding Remarks	413
	Acknowledgments	413
	References	413
18	Role of Photosynthetic Induction for Daily and Annual Carbon Gains of Leaves and Plant Canopies	417–440
	<i>Manfred Küppers and Michael Pfiz</i>	
	Summary	417
	I. Introduction	418
	II. Representation of Plant Architecture by Digital Reconstruction	418
	III. The Dynamic Light Environment	419
	IV. Models of Dynamic Photosynthesis	427
	V. Calculation of Crown Carbon Acquisition	429
	VI. Annual Carbon Gains from Steady-state and Dynamic Photosynthesis Simulations	431
	VII. Concluding Remarks	436
	Acknowledgments	436
	References	436

19	Photosynthesis Within Large-Scale Ecosystem Models	441–464
	<i>Stephan A. Pietsch and Hubert Hasenauer</i>	
	Summary	441
	I. Introduction	442
	II. Biogeochemical Cycles	443
	III. Models of Biogeochemical Cycles	446
	IV. Model Application	452
	V. Examples of Model Application	456
	VI. Concluding Remarks	461
	Acknowledgments	462
	References	462
20	Photosynthesis in Global-Scale Models	465–497
	<i>Andrew D. Friend, Richard J. Geider, Michael J. Behrenfeld and Christopher J. Still</i>	
	Summary	466
	I. Introduction	467
	II. Description of Model Approaches	469
	III. Global Simulation	480
	IV. Concluding Remarks	486
	Acknowledgments	488
	References	488
	Index	499

Preface

Scientific perception of nature relies on a process of transforming data to information, and then information into understanding. Data consist of observations and measurements and information is data organized according to some ontology, i.e. some set of assumptions about what entities exist and how they should be classified. Understanding is a model in the investigator's mind that describes how the entities relate to each other, a model created in the investigator's mind as a result of thinking. Thinking is thus a kind of self-programing of the brain, as a result of which understanding is achieved. When it "runs" in our brains, it allows us to predict the behavior of natural objects, e.g. in their temporal and spatial aspects. For communication within the scientific community, we first share new data, but then share the rigorous forms of the models, which may be verbal, graphic, or at their best, mathematical constructions, reflecting essential features of a natural system. The latter way of presentation of our understanding of photosynthesis is the subject of this book. In many chapters, the models are represented by differential equations that can reproduce the dynamics of the natural system, or in form of linear equations that define steady state fluxes or stoichiometries of such a system. A good model can not only reproduce already measured data about the behavior of the investigated system, but it can also predict results for future experiments.

By definition, models are approximations of nature that are by no means capable of capturing all aspects of the investigated system, no matter how powerful computers we may have used for it. In the early days of photosynthesis research, models were ingenious by their capacity to explain a prominent feature of the investigated process, such as, for example, the photochemical quenching of chlorophyll fluorescence. The early models were frequently relatively simple, not requiring a complex code or ontology. The closing of the reaction centers of Photosystem II during chlorophyll fluorescence induction was well described by Louis N. M. Duysens assuming a single component – the quencher Q. With increasing experimental accuracy and increasing complexity of the

experimental protocols, this simple model was, in terms of Karl Popper's logic of scientific discovery, falsified or, in other words, its validity limits were found. The simple 'Quencher 'Q' model' of Duysens fell short, for example, in explaining the periodicity of four that occurs in chlorophyll fluorescence emission with multiple single turnover flashes, or in explaining the sigmoidal shape of the chlorophyll fluorescence induction curve. This and other models are perpetually expanding to explain new data obtained with new experimental protocols.

Such an expectation of the linear expansion of the models is by itself a simplified model. Sometimes an established, "generally accepted", feature of the model is replaced by another modification, a novel mechanism that explains already known data as well as the previously assumed mechanism, but widens and deepens the predictive power of the model. Thus, different models can explain similar or related phenomena, but only those are accepted for wider use that are able to accommodate new experimental data and more sophisticated protocols. The 'falsified' older and simpler models are not necessarily rejected and forgotten. Much more often they continue to be used with reservation about their range of applicability. For example, one does not need to consider the participation of pheophytin for the understanding of simple chlorophyll fluorescence induction curve on the time scale of seconds. In the area of whole photosynthetic process that specifically includes carbon fixation, Graham Faquhar, Susanne von Caemmerer and Joseph Berry have elegantly approximated it with two enzymatic reactions only. These ontogenetically older (in the sense of model development) models are typically easier to solve and can be obtained from the newer models by mathematically rigorous or empirical dimensionality reduction.

Photosynthesis is a complex process spanning from femtoseconds to days to seasons to centuries in time domain and from atoms to the global biosphere in spatial domain. No single model can describe photosynthesis in its full complexity and even approaching such an elusive goal would not be practical because such a mathematical model

would not be solvable, being as complex in its structure as nature itself. Rather, the process can be described in a mosaic of models such as the ones offered in this book. With increasing complexity of the models, we suggest that the readers consult the first two chapters of this book for a standardization of the model description, so that models become more than abstractions of individual modelers that are hard to share, merge or even compare with each other. We expect this book to be a beginning for creating a comprehensive modeling space of photosynthetic processes that would facilitate an ongoing ‘falsification-upgrade’ modeling spiral and would allow mergers between related model lines. The individual model areas represented here begin with the absorption of a photon and include electron transport, carbon assimilation, and product synthesis. With all these molecular models at hand one can upscale to cell, organ, plant, canopy, and eventually to global biosphere. Chapters presented in this book show how different levels of biological hierarchy overlay and interact in the amazing process of photosynthesis.

Photosynthesis *in silico* is a unique book in its integrated approach to the understanding of photosynthesis processes from light absorption and excitation energy transfer to global aspects of photosynthetic productivity – all interconnected by the use of mathematical modeling. The book is written by 44 international authorities from 15 countries. Chapters in this book are presented in a review style with emphasis on the latest breakthroughs. Instead of providing mathematical details, only the key equations, the basis for the novel conclusions, are provided, with references to the original work at the end of each chapter. Thus, *de facto* this is not a mathematical book of equations, but dominantly verbal discussion showing why the quantitative logic of mathematics has been so efficient for understanding the subject. Yet, in order to exploit the full potential of the book, we hope the models will eventually be translated to the universal format of the *Systems Biology Mark-Up Language* and made accessible also in their full mathematical form on the internet. As argued in Chapter 1,

we stand here at the beginning of a qualitatively new scientific collaboration with its dynamics largely dependent on willingness of our research community to share resources to generate a free-access model database of photosynthesis. Such an endeavor is fully justified by an increasingly recognized role of photosynthesis in nature and lately also as an important alternative for technological solutions of currently surging energy needs of the humankind.

We thank our families and coworkers in our laboratories for their patience with us, and for their support during the preparation of this book. We also thank Noeline Gibson, Jacco Flipsen and André Tournois, of Springer, for their friendly and valuable guidance during the typesetting and printing of this book.

Agu Laisk

Institute of Molecular and Cell Biology
University of Tartu, Riia 23, Tartu 51010
Estonia

Telephone: 372 736 6021

Fax: 372 742 0286

e-mail: alaisk@ut.ee

Ladislav Nedbal

Department of Biological Dynamics
Institute of Systems Biology and Ecology CAS
Zámek 136, 37333 Nové Hradky
Czech Republic

Telephone/Fax: 420 386 361 231

e-mail: nedbal@greentech.cz

Govindjee

Department of Plant Biology
University of Illinois at Urbana-Champaign
265 Morrill Hall, 505 South Goodwin Avenue
Urbana, IL 61801-3707, USA

Telephone: 1 217 337 0627

Fax: 1 217 244 7246

e-mail: gov@illinois.edu

The Editors



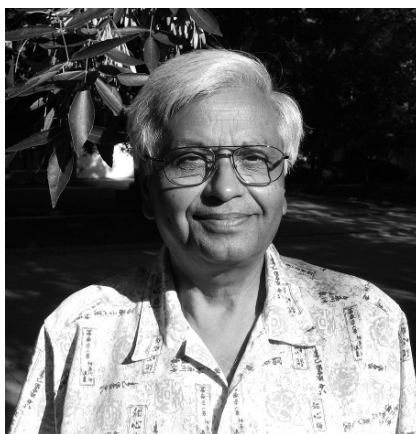
Agu Laisk, born in 1938, obtained BS and MS degrees in Physics at the University of Tartu (Estonia) in 1961. He then joined the research group of Juhan Ross to study the penetration of sunlight into plant canopies for the purpose of modeling of plant productivity. His “candidate of science” work (equivalent to Ph.D., in the former Soviet Union), on the ‘statistical distribution of light in the canopy’, was completed in 1966. Since then he became interested in mechanisms that determine the rate of photosynthesis of a leaf. Together with his former student Vello Oja, he observed that in photosynthesis O_2 competes with CO_2 for one and the same acceptor and in 1970 published a mathematical model of photosynthesis and photorespiration, based on the competition of CO_2 and O_2 for ribulosebisphosphate (RuBP). Then he observed that at high CO_2 concentrations, O_2 enhances photosynthesis, showing the importance of the Mehler reaction. Soon thereafter, sophisticated experiments on “flashing” a leaf with short pulses of CO_2 showed that photosynthesis is limited by Rubisco at low CO_2 , but by RuBP regeneration at high CO_2 levels. For these findings, the degree of Doctor of Science in Biology was awarded to him in 1976 by the Timiryazev Institute of Plant Physiology in Moscow (published as a monograph “*Kinetics of Photosynthesis and Photorespiration in C_3 Plants*” by “Nauka”, Moscow, 1977). The

specific approach of Laisk’s group is in using only intact leaves as objects for measurements. This requires original equipment to be built in the laboratory – now appreciated in several other laboratories and, in principle, described in a book (together with Vello Oja) “*Dynamics of Leaf Photosynthesis. Rapid-Response Measurements and their Interpretations*”, edited by Barry Osmond (CSIRO, Australia, 1998). A recent unexpected result from Laisk’s laboratory is that cyclic electron transport around Photosystem I is much faster than necessary to cover the possible deficit in ATP synthesis – indicating that cyclic electron flow may be largely uncoupled from proton translocation or there must be a controllable proton leak. The interpretation of such kinetic experiments is unthinkable without the application of mathematical modeling. Agu Laisk is a Fellow Member of Estonian Academy of Science, life-time corresponding member of The American Society of Plant Biologists (ASPB), a member of the editorial board of *Photosynthesis Research* and of *Photosynthetica*. He has received National Science Awards from the Estonian Government. His international collaborators, who have deeply influenced his views, include: Ulrich Heber (Germany), David Walker (UK), Barry Osmond (Australia), Gerry Edwards (USA) and Richard Peterson (USA). At Tartu University, he teaches Bioenergetics.



Ladislav Nedbal, born in 1955, studied Biophysics at the Faculty of Mathematics and Physics, Charles University in Praha, Czech Republic. He graduated in 1981 with a thesis on the ‘theory of the excitonic energy transfer in molecular crystals’. He learned about the fascinating process of photosynthesis from Ivan Šetlík, who is one of the founders of algal biotechnology. He moved over from doing modeling of energy transfer to research in experimental photosynthesis in the early years of his scientific career; this led to his present interest in modeling photosynthesis. Yet, preceding the present *déjà vu* with mathematical models were many more years of apprenticeship in experimental science that were marked with discreet advice from Govindjee. It was the present Series Editor of *Advances in Photosynthesis and Respiration*, who taught him the principles of technical writing in the late 1980s and introduced him, in 1990, to John Whitmarsh of the University of Illinois at Urbana-Champaign, USA. It was in John’s lab where Nedbal discovered the photoprotective role of cytochrome b559. His other important tutors were Tjeerd Schaafsma in Wageningen, The Netherlands, and Anne-Lise Etienne in France. A significant inspiration came from David Kramer during the postdoc years in Urbana-Champaign and in Paris, where they collaborated in constructing

a modulated light spectrophotometer and fluorometer. In that project he met Martin Trtilek, with whom he founded Photon Systems Instruments (PSI), a small company that has created a number of innovative instruments for photosynthesis research. The most important achievement was the development of the first commercial Pulse Amplitude Modulating (PAM) type imaging fluorometer – *FluorCam*. Recently, collaboration with Martin resulted in the construction of ‘intelligent’ photobioreactor for the cultivation of algae and cyanobacteria. The instrument collects, in real time, detailed information on the culture’s photochemical yields and on its growth dynamics. The combination of mathematical modeling with experimental research in photosynthesis and engineering approaches logically led to another *déjà vu* in his career, this time with algal biotechnology. In this area, mathematical models bring to light yet unexplored pathways towards commercially viable use of algae and cyanobacteria. Further stimulating his interest in models are the mysterious dynamic features that he and his co-workers, including both his co-Editors of the present volume Agu Laisk and Govindjee, recently discovered in harmonically modulated light. Understanding plant behavior in dynamic light remains a major challenge that will be tackled by the current book *Photosynthesis in silico*.



Govindjee, born in 1932, obtained his B.Sc. (Chemistry, Biology) and M.Sc. (Botany) in 1952 and 1954, from the University of Allahabad, India, and his Ph.D. (Biophysics) in 1960, from the University of Illinois at Urbana-Champaign (UIUC), IL, USA. His mentors were Robert Emerson and Eugene Rabinowitch. He is best known for his research on the excitation energy transfer, light emission, the primary photochemistry and the electron transfer in Photosystem II (PS II). His research, with many collaborators, has included the discovery of a short-wavelength form of chlorophyll (Chl) *a* functioning in the Chl *b*-containing system of PS II; of the two-light effects in Chl *a* fluorescence and in NADP reduction in chloroplasts (Emerson Enhancement); the basic relationships between Chl *a* fluorescence and photosynthetic reactions; the unique role of bicarbonate at the acceptor side of PS II. He provided the theory of thermoluminescence in plants, made the first picosecond measurement on the primary photochemistry of PS II and used Fluorescence Lifetime Imaging Microscopy (FLIM) of Chl *a* fluorescence in understanding photoprotection against excess light. His current focus is on the history of photosynthesis research, photosynthesis education, and possible existence of extraterrestrial life. He has served on the faculty of UIUC for about 40 years. Since 1999 he has been Professor Emeritus of Biochemistry, Biophysics and Plant Biology at the same institution. He is coauthor of '*Photosynthesis*' (with E. Rabinowitch; John Wiley, 1969), and editor of several books including *Bioenergetics of Photosynthesis* (Academic

Press, 1975); *Photosynthesis*, Volumes I and II (Academic Press, 1982); *Light Emission of Plants and Bacteria* (with J. Ames and D.C. Fork; Academic Press, 1986); *Chlorophyll *a* Fluorescence: A Signature of Photosynthesis* (with G.C. Papageorgiou, Springer, 2004); and *Discoveries in Photosynthesis* (with J.T. Beatty, H. Gest and J.F. Allen; Springer, 2005). His honors include: Fellow of the American Association of Advancement of Science; Distinguished Lecturer of the School of Life Sciences, UIUC; Fellow and Lifetime member of the National Academy of Sciences (India); President of the American Society for Photobiology (1980–1981); Fulbright Scholar and Fulbright Senior Lecturer; Honorary President of the 2004 International Photosynthesis Congress (Montréal, Canada); the 2006 Recipient of the Lifetime Achievement Award from the Rebeiz Foundation for Basic Biology; the 2007 Recipient of the Communication Award of the International Society of Photosynthesis Research (ISPR); and the 2008 Liberal Arts and Sciences Alumni Achievement Award of the University of Illinois. During 2007, *Photosynthesis Research* celebrated Govindjee's 50 years in Photosynthesis, and his 75th birthday through a two-Part special volume of the journal (Julian Eaton-Rye, editor). To celebrate his life-long achievement in Photosynthesis Research, Education, and its History, University of Indore, India, recently held a 3-day International Symposium (Nov. 27–29, 2008) on 'Photosynthesis in Global Perspective' (K.N. Guruprasad, Convener).

Govindjee has trained more than 20 Ph.D. students and about 10 postdoctoral associates.

Author Index

Anten, Niels P.R. 363–399

Behrenfeld, Michael J. 465–497

Bernacchi, Carl. J. 231–246

Berry, Joseph 209–230

Červený, Jan 17–29

Dekker, Jan P. 33–53

Edwards, Gerald 323–348

Eichelmann, Hillar 295–322

Farazdaghi, Hadi 275–294

Farquhar, Graham 209–230, 231–246

Freiberg, Arvi 55–82

Friend, Andrew D. 465–497

Geider, Richard J. 465–497

Harbinson, Jeremy 247–273

Hasenauer, Hubert 441–464

Hucka, Michael 3–15

Küppers, Manfred 417–440

Laisk, Agu 295–322, 323–348

Lavergne, Jérôme 177–205

Lazár, Dušan 85–123

Long, Stephen P. 231–246, 401–416

Nedbal, Ladislav 17–29

Niinemets, Ülo 363–399

Novoderezhkin, Vladimir I. 33–53

Oja, Vello 295–322

Pfiz, Michael 417–440

Pietsch, Stephan A. 441–464

Pimentel, Carlos 231–246

Prášil, Ondřej 125–149

Riznichenko, Galina 151–176

Rosenthal, David M. 231–246

Rubin, Andrew 151–176

Schaff, James 3–15

Schansker, Gert 85–123

Schmidt, Henning 17–29

Still, Chrisostopher J. 465–497

Struik, Paul C. 247–273

Trinkunas, Gediminas 55–82

Van Grondelle, Rienk 33–53

Von Caemmerer, Susanne 209–230

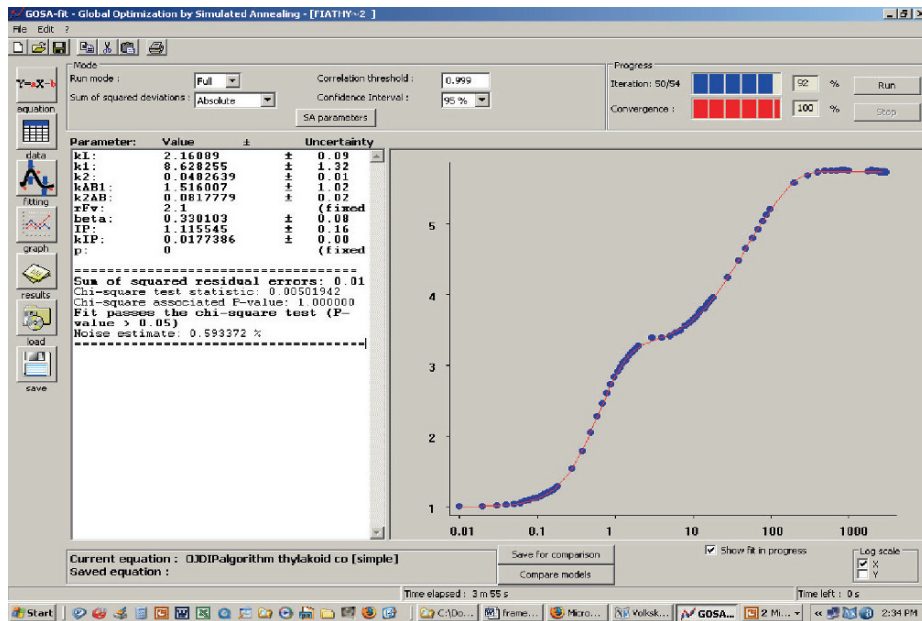
Vredenberg, Wim 125–149

Woodrow, Ian E. 349–360

Yin, Xinyou 247–273

Zhu, Xin-Guang 401–416

Color Plates



$$F(t)/F_0 = 1 + p + rFv \cdot (1 - k1 / (k1 - kL) \cdot \exp(-kL \cdot t) + kL / (k1 - kL) \cdot \exp(-k1 \cdot t)) \cdot ((1 - \beta) \cdot kL / (kL + kAB1) + \beta) \cdot (1 + (1 - k1 / (k1 - kL) \cdot \exp(-kL \cdot t) + kL / (k1 - kL) \cdot \exp(-k1 \cdot t)) \cdot \exp(-k2AB \cdot t))) + rFv \cdot (1 - \exp(-k2 \cdot t)) + IP \cdot (1 - \exp(-kIP \cdot t)) \cdot (1 + kIP \cdot t)) \quad [t \text{ in ms}]$$

Fig. 1. Display of the curve fitting procedure, using global optimization simulation annealing (GOSA) with equation derived after summation of Eqs. (6.9–6.11) (bottom line). Symbols are experimental points, line is the simulated curve. Note that the fit was obtained after an about 4 min iteration time. See Chapter 6, p. 139

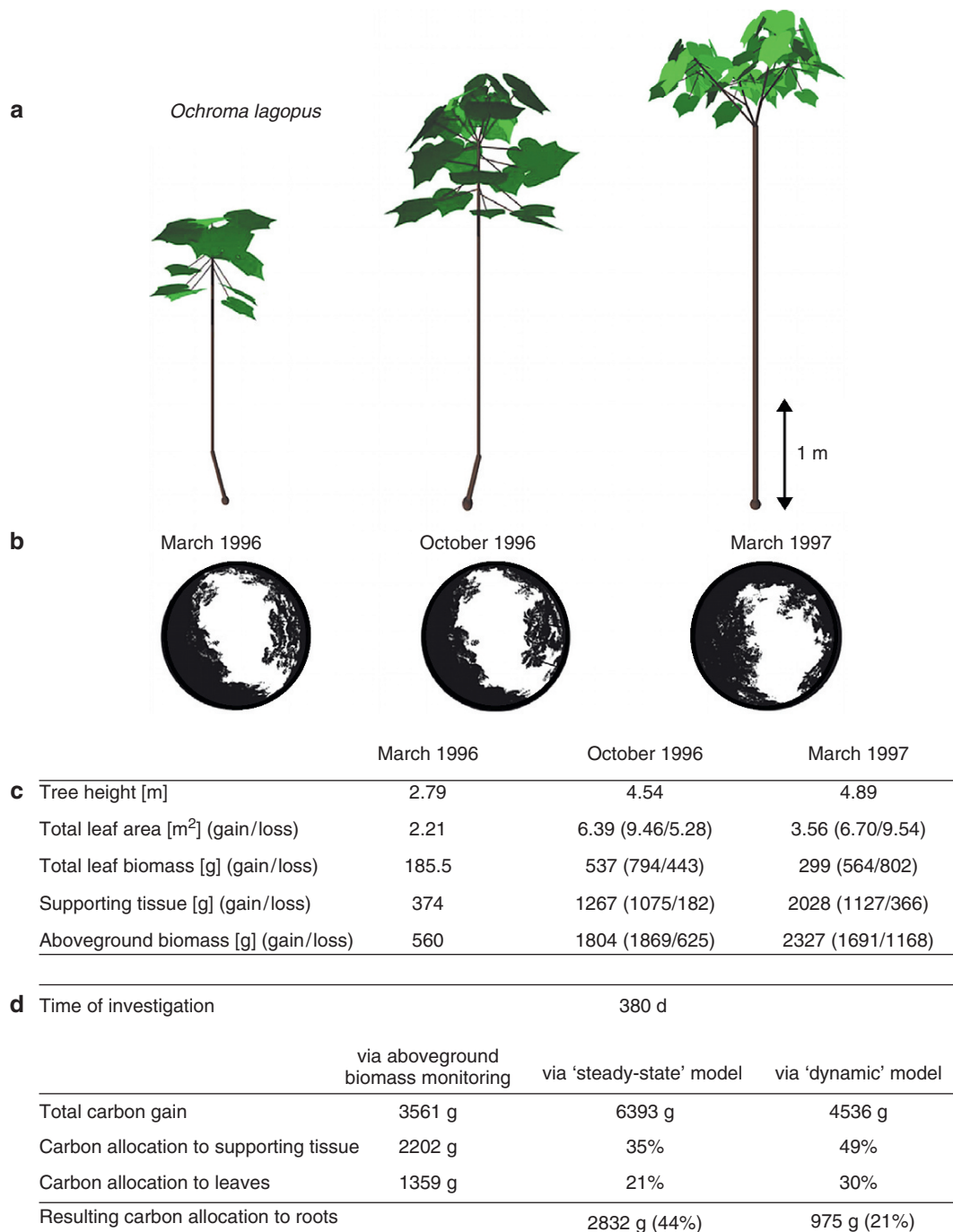


Fig. 2. Development of an individual of the shade-intolerant pioneer *Ochroma lagopus* from an open site and deduction of its annual carbon allocation. Light green leaf area: sun exposed, dark green: (self-)shaded (from Timm et al., 2004). **(a)** Above-ground architectural development as reconstructed via the method described in Fig. 18.1; **(b)** change in the individual's light environment as indicated by hemispherical photography immediately above its uppermost leaves; **(c)** growth and biomass parameters of the respective individual; **(d)** deduction of annual assimilate flux balances (carbon allocation) as percentage of total annual crown carbon gain, either via a steady-state or a dynamic photosynthesis model. Carbon gain and allocation of biomass are given in equivalents of dry matter (CH₂O)_n. See Chapter 18, p. 423

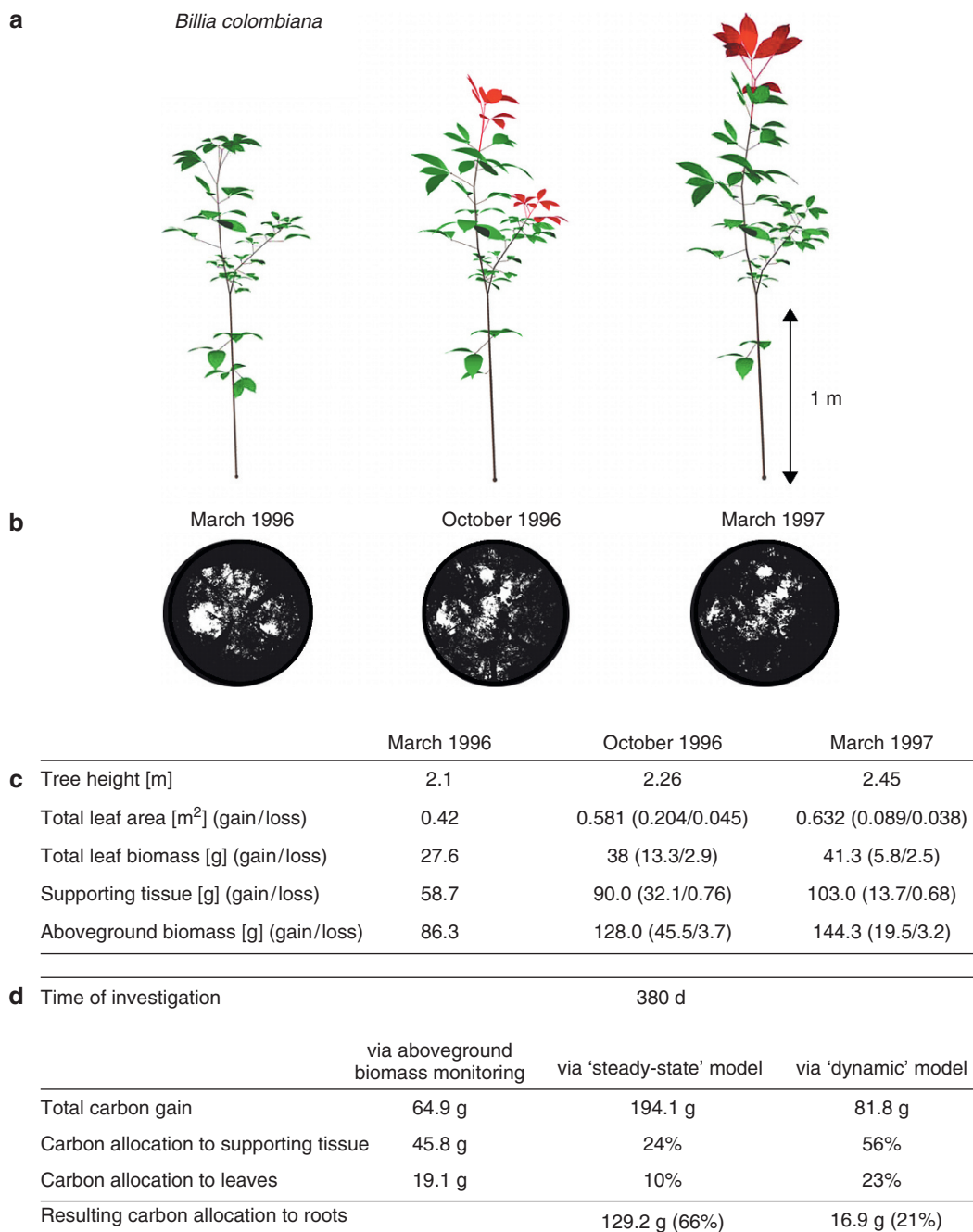


Fig. 3. The same as Fig. 18.4, but for an individual of the mid- to late-successional shade-tolerant *Billia colombiana* below a closed canopy. Red leaf area: newly developed (from Timm et al., 2004). See Chapter 18, p. 424

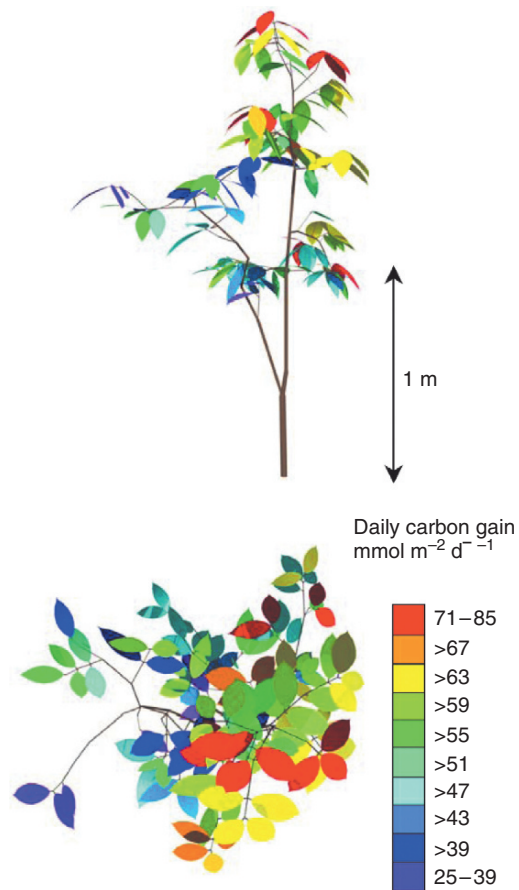


Fig. 4. Daily carbon balance of each individual leaf in the crown of a *Salacia petenensis* plant. Crown carbon gain was determined by summing up the individual balances. In the mean over 380 days carbon gain amounted to 426 mg day⁻¹ (from Timm et al., 2004). See Chapter 18, p. 432

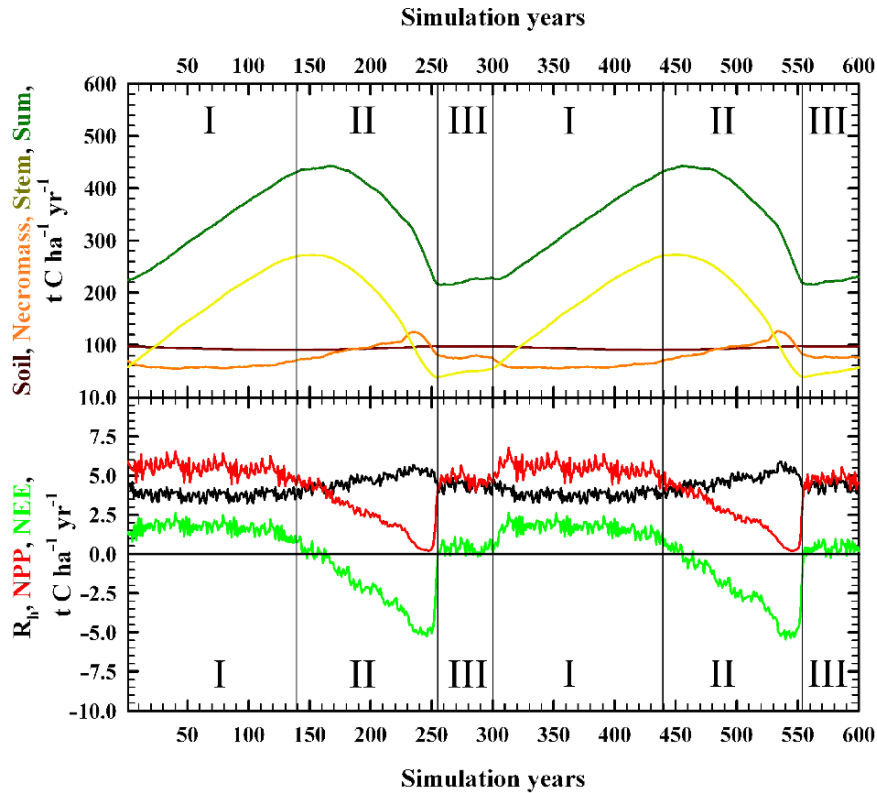


Fig. 5. Modeled pools and fluxes for the virgin forest reserve Rothwald using model parameters for Common beech forests. Upper graph: Comparison of the temporal development of modeled soil, necromass, stem and total ecosystem carbon content for 600 simulation years at landscape level steady state. Lower graph: Corresponding annual C fluxes from heterotrophic respiration (R_h), net primary production (NPP) and net ecosystem exchange (NEE). I – optimum phase; II – breakdown/regeneration phase; III – juvenescence (Pietsch and Hasenauer, 2006). See Chapter 19, p. 457

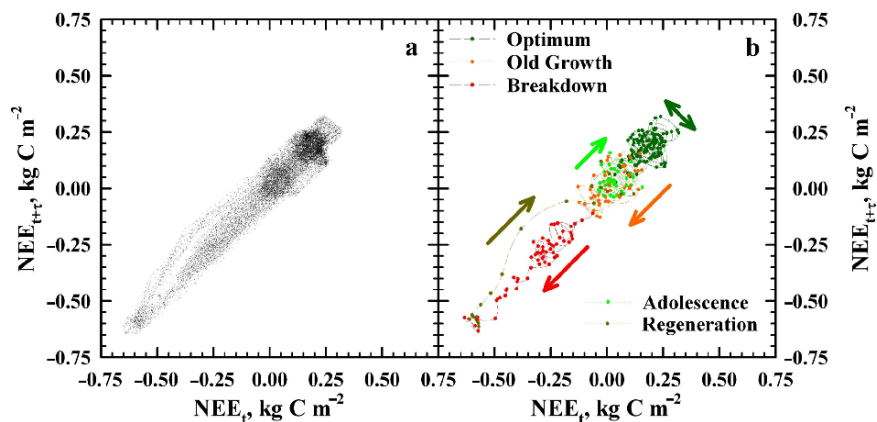


Fig. 6. Attractor of modeled NEE for the successional cycle evident within the virgin forest reserve Rothwald. a: NEE-Attractor for the virgin forest successional cycle reconstructed from model results using site and climate conditions of 18 research plots. b: Attractor reconstructed for one single plot and one successional cycle. Arrows indicate the trends of model behavior during different phases of the successional cycle. (S.A. Pietsch, unpublished) See Chapter 19, p. 460

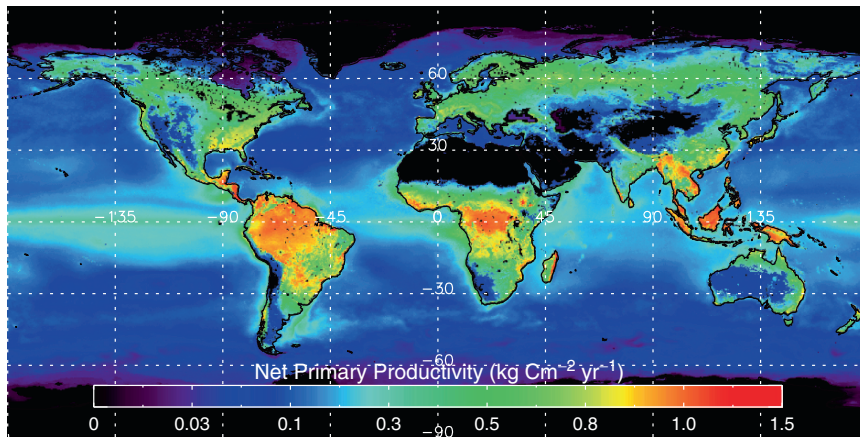


Fig. 7. Mean annual net primary productivity (NPP) simulated by Hybrid6.5 (land) and the CbPM (ocean) for the period 2000–2007. Total mean annual NPP is $107.3 \text{ Pg C year}^{-1}$, with 51.1% coming from land and 48.9% from the oceans. Land pixels simulated with $1/4^\circ$ resolution and ocean pixels with $1/12^\circ$ resolution. Land leaf area dynamics prescribed from MODIS satellite retrievals, ocean production calculated using data from the SeaWiFS instrument. Full simulation details are given in the text. See Chapter 20, p. 486

Chapter 1

Trends and Tools for Modeling in Modern Biology

Michael Hucka*

*Control and Dynamical Systems, California Institute of Technology, Pasadena, CA 91125,
USA*

James Schaff

*Richard D. Berlin Center for Cell Analysis and Modeling, University of Connecticut Health
Center, Farmington, CT 06030, USA*

Summary	3
I. Introduction.....	4
II. Representing Model Structure and Mathematics.....	4
III. Augmenting Models with Semantic Annotations	6
A. Systems Biology Ontology (SBO).....	6
B. Minimum Information Requested in the Annotation of Biochemical Models (MIRIAM).....	7
IV. Connecting Models to Results.....	9
A. Common Experimental and Modeling Activities.....	9
B. Supporting Modeling Activities Through Software Environments.....	10
V. Future Directions for Systems Biology Markup Language (SBML).....	13
VI. Conclusions.....	13
References.....	14

Summary

Computational modeling in biology requires sophisticated software tools. Precise communication and effective sharing of the models developed by researchers requires standard formats for storing, annotating, and exchanging models between software systems. Developing such standards is the driving vision behind the Systems Biology Markup Language (SBML) and several related efforts that we discuss in this chapter. At the same time, such standards are only enablers and ideally should be hidden “under the hood” of modeling environments that provide users with high-level, flexible facilities for working with computational models. As an example of the modern software systems available today, we discuss the Virtual Cell and illustrate its support for typical modeling activities in biology.

* Author for correspondence, e-mail: mhucka@caltech.edu

I. Introduction

Understanding the dynamic processes that are the essence of a living cell stands as one of the most important and most difficult challenges of twenty-first century biology. Today, it is widely appreciated that we can only hope to meet that challenge through the development and application of computational methods (Hartwell et al., 1999; Fraser and Harland, 2000; Arkin, 2001; Tyson et al., 2001; Noble, 2002; Alm and Arkin, 2003; Zerhouni, 2003), particularly the creation of mechanistic, explanatory models illuminating the functional implications of the data upon which they are built.

Models are not substitutes for experiments and data; rather, they are faithful teammates in the process of scientific discovery. A realistic computational model represents a modeler's dynamic understanding of the structure and function of part of a biological system. As the number of researchers constructing realistic models continues to grow, and as the models become ever more sophisticated, they collectively represent a significant accumulation of knowledge about the structural and functional organization of the system. Moreover, using them, the assimilation of new hypotheses and data can be done in a more systematic way because the additions must be fitted into a common, consistent framework. Once properly constructed, the models become a dynamic representation of our current state of understanding of a system in a form that can facilitate communication between researchers and help to direct further experimental investigations (Bower and Bolouri, 2001).

Today's models are large (and growing ever larger) and complex (and getting ever more complex). We are now long past the point of being able to communicate and exchange real-world models effectively by simply summariz-

ing them in written narratives featuring a few equations. The precise communication of computational models between humans and between software is critical to being able to realize modeling's promise. Achieving this requires standardizing the electronic format for representing computational models in a way independent of any particular software – after all, different research goals are often best served by different software tools, yet modelers still need to share their results with their colleagues. At the same time, today's researchers need powerful software environments that offer a range of capabilities to support the creation, analysis, storage and communication of models, all the while hiding the details of the model representation format and providing biological modelers with high-level user interfaces and capabilities matched to the tasks they need to do.

In this chapter, we discuss both standards and software for computational modeling in biology. We summarize the *de facto* standard format, the Systems Biology Markup Language (SBML), as well as ongoing related efforts to standardize the representation of model annotations through MIRIAM (the Minimum Information Requested In the Annotation of biochemical Models) and SBO (the Systems Biology Ontology). As critical as they are, however, such standards are in the end only *enablers*; they are (hopefully) not what users interact with directly. We therefore also discuss software systems, focusing on one in particular, the Virtual Cell, as a way to present typical modeling activities in the context of one of today's most full-featured, interactive modeling environments. The advanced capabilities of systems such as Virtual Cell also help drive further development of SBML and adjunct efforts, and so we close with a summary of present work to extend SBML as well as standardize other areas of modeling and simulation exchange, such as the description of simulations.

II. Representing Model Structure and Mathematics

Until the late 1980s, publication of a computational model almost universally involved publishing only the equations and parameter values, usually with some narrative descriptions of how

Abbreviations: DOI – digital object identifier; MIASE – minimum information about a simulation experiment; MIRIAM – minimum information requested in the annotation of biochemical models; SBGN – systems biology graphical notation; SBML – systems biology markup language; SBO – systems biology ontology; SSA – stochastic simulation algorithm; UML – unified modeling language; URN – uniform resource name; VCell – virtual cell; XML – eXtensible markup language

the model was coded in software and how it was simulated and analyzed. The systems of equations were, with few exceptions, directly implemented in software: in a very direct sense, the program *was* the model. Authors sometimes even wrote their own numerical integration code. This general approach was necessary because of the primitive state of computational platforms and electronic data exchange, and it was fraught with problems. The most significant problem is simply the opportunities for errors that arise when a model must be recapitulated by humans into and back out of natural language form. The degree to which this is a real problem is startling. Curators for databases of published models such as BioModels Database (Le Novère et al., 2006) and JWS Online (Snoep and Olivier, 2003; Olivier and Snoep, 2004), report by personal communication that when they first began operation in the 2000–2004 timeframe, over 95% of published models they encountered had something wrong with them, ranging from typographical errors to missing information (even today, the problem rate is greater than 60%). A second problem is that, when a model is inextricably intertwined with its software implementation, it is difficult to examine and understand the precise details of the actual model (rather than artifacts of its particular realization in software). A third problem is that having to reconstruct a model from a paper is an extremely tall hurdle to fast, efficient and error-free reuse of research results.

Some areas of biological modeling improved on this situation in the 1990s. The field of computational neuroscience was particularly advanced in this regard, having two freely-available simulation packages, GENESIS (Bower and Beeman, 1995; Bower et al., 2002) and NEURON (Hines and Carnevale, 1997), supported on a variety of operating systems. These simulation platforms made it possible for modelers to distribute abstract definitions of their models and simulation procedures in the form of scripts that could be interpreted automatically by the platform software. The approach vastly improved the reusability of models. However, there remained the limitation that the formats were specific to the simulation package in which they were developed. Whoever wanted to reuse the models had to run the same software in order to reuse the model (assuming they were able to get the nec-

essary files from the model's authors – electronic publishing of models as supplements to journal articles was still rare).

With the surge of interest in computational systems biology at the beginning of this century, software tools evolved one step further with the creation of *application-independent* model description formats such as CellML (Hedley et al., 2001) and SBML (Hucka et al., 2003, 2004). This form of representation is not an algorithm or a simulation script; it is a declarative description of the model structure that is then interpreted and translated by each individual software system into whatever internal format it actually uses. No longer tied to a particular software system, such software-independent formats permit a wider variety of experimentation in algorithms, user interfaces, services, and many other aspects of software tool development, by virtue of allowing multiple software authors to explore different facilities that all use the same input/output representation. In addition, and even more significantly, it enables practical publication of models in public databases.

The Systems Biology Markup Language (SBML; <http://sbml.org>) has become the de facto standard for this purpose, supported by over 120 software systems at the time of this writing. SBML is a machine-readable lingua franca defined neutrally with respect to software tools and programming languages. It is a model definition language intended for use by software – humans are not intended to read and write SBML directly. By supporting SBML as an input and output format, different software tools can all operate on the identical representation of a model, removing opportunities for errors in translation and assuring a common starting point for analyses and simulations. SBML is defined using a subset of UML, the Unified Modeling Language (Booch et al., 2000), and in turn, this is used to define how SBML is expressed in XML, the eXtensible Markup Language (Bray et al., 1998). Software developers can make use of a number of resources for incorporating SBML support in their applications (Bornstein et al., 2008).

SBML can encode models consisting of biochemical entities (species) linked by reactions to form biochemical networks. An important principle in SBML is that models are decomposed into explicitly-labeled constituent elements, the

set of which resembles a verbose rendition of chemical reaction equations; the representation deliberately does not cast the model directly into a set of differential equations or other specific interpretation of the model. This explicit, modeling-framework-agnostic decomposition makes it easier for a software tool to interpret the model and translate the SBML form into whatever internal form the tool actually uses. The main constructs provided in SBML include the following:

Compartment and *compartment type*: a compartment is a container for well-stirred substances where reactions take place, while a compartment type is an SBML construct allowing compartments with similar characteristics to be classified together.

Species and *species type*: a species in SBML is a pool of a chemical substance located in a specific compartment, while species types allow pools of identical kinds of species located in separate compartments to be classified together.

Reaction: a statement describing some transformation, transport or binding process that can change one or more species (each reaction is characterized by the stoichiometry of its products and reactants and optionally by a rate equation).

Parameter: a quantity that has a symbolic name.

Unit definition: a name for a unit used in the expression of quantities in a model.

Rule: a mathematical expression that is added to the model equations constructed from the set of reactions (rules can be used to set parameter values, establish constraints between quantities, etc.).

Function: a named mathematical function that can be used in place of repeated expressions in rate equations and other formulae.

Event: a set of mathematical formulae evaluated at a specified moment in the time evolution of the system.

The simple formalisms in SBML allow a wide range of biological phenomena to be modeled, including cell signaling, metabolism, gene regulation, and more. Significant flexibility and power comes from the ability to define arbitrary formulae for the rates of change of variables as well as the ability to express other constraints mathematically.

SBML is being developed in “levels”. Each higher level adds richness to the model defini-

tions that can be represented by the language. By delimiting sets of features at incremental stages, the SBML development process provides software authors with stable standards and the community can gain experience with the language definitions before new features are introduced. Two levels have been defined so far, named (appropriately enough) Level 1 and Level 2. The former is simpler (but less powerful) than Level 2. The separate levels are intended to coexist; SBML Level 2 does not render Level 1 obsolete. Software tools that do not need or cannot support higher levels can go on using lower levels; tools that can read higher levels are assured of also being able to interpret models defined in the lower levels. Open-source libraries such as libSBML (Bornstein et al., 2008) allow developers to support both Levels 1 and 2 in their software with a minimum amount of effort.

III. Augmenting Models with Semantic Annotations

The ability to have meaningful exchange of complex mathematical models of biological phenomena turns out to require a deeper level of semantic encoding and knowledge management than is embodied by a format such as SBML, which encompasses only syntax and a limited level of semantics. This realization came early in the context of CellML, whose developers added a standard scheme for metadata annotations soon after CellML was developed (Lloyd et al., 2004). CellML’s metadata scheme was adopted by SBML at the beginning of the development of SBML Level 2, but limitations with the scheme later led the SBML community to seek alternatives. These were found in the form of the Systems Biology Ontology (SBO; <http://www.ebi.ac.uk/SBO>; Le Novère et al., 2006), and the Minimum Information Requested in the Annotation of Biochemical Models (MIRIAM; Le Novère et al., 2005).

A. Systems Biology Ontology (SBO)

The rationale for SBO is to provide controlled vocabularies for terms that can be used to annotate components of a model in SBML (or indeed, any other formal model representation format).

It requires no change to the form of the basic model in SBML; rather, it provides the option to augment the basic model with machine-readable labels that can be used by software systems to recognize more of the semantics of the model. SBO provides terms for identifying common reaction rate expressions, common participant types and roles in reactions, common parameter types and their roles in rate expressions, common modeling frameworks (e.g., “continuous”, “discrete”, etc.), and common types of species and reactions. Recent versions of SBML Level 2 provide an optional attribute on every element where an SBO term may be attached. Table 1.1 lists the correspondences between major components of SBML and SBO vocabularies.

The relationship implied by the attribute value on an SBML model component is “is a”: the thing defined by that SBML component “is an” instance of the thing defined in SBO by indicated SBO term. By adding SBO term references on the components of a model, a software tool can provide additional details using independent, shared vocabularies that can enable other software tools to recognize precisely what the component is meant to be. Those tools can then act on that information. For example, if the SBO identifier SBO:0000049 is assigned to the concept of “first-order irreversible mass-action kinetics, continuous framework”, and a given reaction in a model has an SBO attribute with this value, then regardless of the identifier and name given to

the reaction itself, a software tool could use this to inform users that the reaction is a first-order irreversible mass-action reaction.

As a consequence of the structure of SBO, not only children are versions of the parents, but the mathematical expression associated with a child is a version of the mathematical expressions of the parents. This enables a software application to walk up and down the hierarchy and infer relationships that can be used to better interpret a model annotated with SBO terms. Simulation tools can check the consistency of a rate law in an SBML model, convert reactions from one modeling framework to another (e.g., continuous to discrete), or distinguish between identical mathematical expressions based on different assumptions (e.g., Henri-Michaelis-Menten vs. Briggs-Haldane). Other tools like SBMLmerge (Schulz et al., 2006) can use SBO annotations to integrate individual models into a larger one.

SBO adds a semantic layer to the formal representation of models, resulting in a more complete definition of the structure and meaning of a model. The presence of an SBO label on a compartment, species, or reaction, can also help map SBML elements to equivalents in other standards, such as (but not limited to) BioPAX (<http://www.biopax.org>) or the Systems Biology Graphical Notation (SBGN, <http://www.sbgn.org>). Such mappings can be used in conversion procedures, or to build interfaces, with SBO becoming a kind of “glue” between standards of representation.

Table 1.1. Correspondence between major SBML components and controlled vocabulary branches in the Systems Biology Ontology (SBO)

SBML component	SBO vocabulary
Model	Interaction
Function definition	Mathematical expression
Compartment type	Material entity
Species type	Material entity
Compartment	Material entity
Species	Material entity
Reaction	Interaction
Reaction’s kinetic law	Mathematical expression → Rate law
Parameter	Quantitative parameter
Initial assignment	Mathematical expression
Rule	Mathematical expression
Event	Interaction

B. Minimum Information Requested in the Annotation of Biochemical Models (MIRIAM)

While SBO annotations help add semantics, there remains a different kind of impediment to effective sharing and interpretation of computational models. Figure 1.1 illustrates the issue.

When a researcher develops a model, they often use simple identifiers for chemical substances, or at best, only one of a multitude of possible synonyms for the substance. The situation is even worse when it comes to the chemical reaction and other processes: these are often given names such as “R1”, “R2”, etc., or at best, generic

```

<sbml xmlns="http://www.sbml.org/sbml/level2/version2" level="2" version="2">
  <model id="model2">
    <listOfCompartments>
      <compartment id="cell" size="2.5"/>
    </listOfCompartments>
    <listOfSpecies>
      <species id="MTX5" compartment="cell" initialConcentration="0.1"/>
      <species id="MTX1b" compartment="cell" initialConcentration="0"/>
      <species id="MTX2b" compartment="cell" initialConcentration="0"/>
    </listOfSpecies>
    <listOfParameters>
      <parameter id="Keq" value="0.3"/>
    </listOfParameters>
    <listOfReactions>
      ...

```

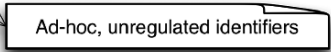


Fig. 1.1. An example fragment of an SBML file. The id fields in the lines above establish the identifiers of entities used in the model. This particular model contains a compartment identified only as “cell”; three biochemical species identified as “MTX5”, “MTX1b” and “MTX2b”; and a global parameter (constant) identified as “Keq”. These labels presumably have meaning to the creator of the model, but rarely to its readers, and even less so to software tools. Yet, such short identifiers are really what modelers often use in real-life models. It is not in the scope of SBML to regulate or restrict what the identifiers can or should be – a different approach is needed. The solution in use today is to provide a mechanism for augmenting (not replacing) the identifiers with annotations referring to regulated terms in “dictionaries”, controlled vocabularies, or entries in databases that provide detailed information about the biological entities to which the identifiers are meant to refer.

terms such as “mass-action” that do not reflect the role of the reaction as a process in the broader model. Searching for models based on useful criteria is next to impossible under these conditions. One could blame modelers for not being more thorough in naming and identifying the elements in their models; one could also blame software tools for not assisting modelers in this process. However, such criticisms would be both futile and misplaced. First, this situation is the reality for thousands of existing models and it is likely to persist into the foreseeable future. Second, different research subfields often have different names for the same chemical species, processes, and other concepts. Who would decide which is most appropriate to use?

The most practical solution found so far by the computational systems biology community is to augment models with annotations that provide links between the elements of a model and other (external) data resources and models. However, the potential and power of annotations is largely lost if the format of the annotations is not standardized to the point where different software systems can interpret them in the same way. This was one of the motivations for the development of MIRIAM, a set of guidelines for the Minimum Information Requested In the Annotation

of biochemical Models (Le Novère et al., 2005) encoded in a structured representation format such as SBML.

MIRIAM defines both (1) minimum consistency requirements for a model, and (2) a regular and simple annotation scheme for linking a model to its sources and linking model components to external data resources. The goal of the first aspect of MIRIAM is to ensure that a model is reliably attributed to a reference description (which is a document describing or referencing a description of the model, the model’s structure, numerical values necessary to instantiate a simulation, and the results to be expected from such a simulation) and is consistent with that description. The requirements apply to the model as a whole and are irrespective of any annotations placed in it. Table 1.2 summarizes these minimal requirements for reference correspondence.

The second broad aspect of the MIRIAM guidelines concerns the annotation content. The requirements for minimum attribution information are summarized in Table 1.3. They simply represent a basic level of information that is deemed to be necessary in order for a model’s readers to be able to associate the model with a reference description and a process used to encode the model in the structured format.

Table 1.2. MIRIAM guidelines for minimum consistency of a model

-
- The model must be encoded in a public, machine-readable format, either standardized (e.g., SBML) or supported by specific applications (e.g., MATLAB).
 - The encoded model must comply with the standard in which it is encoded, meaning that the syntax must be correct and the model must pass validation.
 - The model must be related to a single description that describes or references results that one can expect to reproduce using the model. If the model is derived from several sources (e.g., several publications), there must exist a single reference description associated with the combined model. Note that MIRIAM does not require the reference description to be published; it must merely be made available to consumers of the model.
 - The model's structure must reflect the biological processes listed in the reference description.
 - The encoded model must be instantiated in simulation, which implies that quantitative attributes, initial conditions, parameters, etc., must all be defined. (The actual values may be provided as a separate file from the model itself.)
 - When instantiated in a suitable environment, the model must be able to reproduce relevant and readily-simulated results given in the reference description, and the results must be quantitatively similar (with any differences being attributable to differences in algorithm roundup errors).
-

Table 1.3. MIRIAM guidelines for the minimum attribution information to be provided with a model

-
- A (preferred) name for the model.
 - A citation for the reference description. This can be bibliographic information, or a unique identifier (e.g., DOI), or even a URL pointing directly at the description – something to locate and identify the reference description and its authors.
 - Name and contact information for the model creator(s).
 - Date and time of creation.
 - Date and time of last modification.
 - A precise statement of the encoded model's terms of distribution. MIRIAM does not require freedom of distribution nor no-cost distribution, only a statement of what the distribution terms are.
-

As for the manner in which annotations are to be represented, the MIRIAM scheme is simple and does not require a particular format structured – in fact, the annotations can be recorded in something as simple as a separate text file,

though whatever method is used, the annotations must always be transferred with the model. Each annotation is a triplet consisting of a data type, an identifier, and an optional qualifier. The data type is a unique controlled description of the type of the data in annotation and should be recorded as a Uniform Resource Name (Jacobs and Walsh, 2004). The identifier refers/points to a specific datum in whatever source is identified by the data type. The qualifier serves to refine the nature of the relationship between the model component being annotated and the referred-to datum. Examples of common qualifiers include “is version of”, “has part”, etc. If the qualifier is absent, the assumed relationship is “is”.

IV. Connecting Models to Results

SBML, MIRIAM, and related technologies are all meant to be *under the hood*, so to speak, with software systems reading and writing models in SBML form (annotated in MIRIAM-compliant fashion), but ideally without exposing this level of detail to users. In this section, we examine how one particular modeling environment, the Virtual Cell, provides a wide range of modeling facilities while effectively hiding the details of interacting with models in SBML form. The Virtual Cell is an example of the modern trend towards providing powerful, general-purpose modeling environments supporting the whole gamut of tasks that biologist-modelers must do, from importing experimental data, to deriving a family of models from the data, to simulating and analyzing the models, and relating the results of the analyses back to the experimental data.

A. Common Experimental and Modeling Activities

To compare experimental results with the quantitative predictions generated from a biological model, the model must be exercised in a manner consistent with experimental protocols and apparatus. Experimental protocols are standardized procedures for experimental measurements and manipulations. Some protocols can be described simply as ideal processes that directly

perturb only the desired target or are perfect observers of some physiological states or anatomical structures. More realistic notions are routinely considered by the experimentalist who must parse unwanted behaviors and distortions to gain insight into a biological process. They design experiments to reduce the sensitivity of their results to those unwanted artifacts.

Before associating raw experimental data with model predictions, both the raw experimental data and the model predictions are often post-processed into quantities that can be more easily compared. This post-processing can suffice if we assume that measurements and manipulations are ideal and that the experimental intervention is separable from the biological processes. If these assumptions do not hold (e.g., when a fluorescent indicator functionally modifies or sequesters its ligand), changes to the model structure are required to properly represent the interaction of the protocols with the underlying biological system.

Validation of a quantitative model against multiple experiments typically requires the creation of a number of experiment-specific models that must retain a consistent core representing the physiological mechanisms and hypotheses. As new experimental evidence is considered, additional experiment specific models are created. The underlying mechanistic model evolves in a way that corresponds to the entire set of experimental data. During this process it is important to continually reassess the compatibility between the context of each experiment and the current model structure, parameters, and modeling assumptions.

A list of accumulated model assumptions should be maintained explicitly to identify contradictions and track applicability of experimental data. There are explicit modeling assumptions introduced by the physical approximations used within the model (e.g., preconditions for use of a particular kinetic law) as well as those imposed by the modeling framework (e.g., well-mixed compartments ignore spatial variation, deterministic population dynamics ignores stochastic variation). There are also implicit modeling assumptions when deciding which elements can be safely omitted from a model and when introducing functional dependencies. This growing list of assumptions and the collection of experimental data constrain the feasible space of consistent model structures and parameters.

This process of using new experimental data to refine models is important, but the reverse process is even more useful. Experimentalists and modelers working together can use interesting model predictions to suggest new experiments that can help discriminate between alternative model structures (alternative hypotheses) or help to define the boundaries of the model's domain of applicability.

B. Supporting Modeling Activities Through Software Environments

The Virtual Cell Modeling and Simulation framework (VCell; Slepchenko et al., 2003; Moraru et al.; 2008) will be used as an example architecture to describe how modeling tools can support these capabilities. VCell was developed by an interdisciplinary team of engineers, physicists, biologists and mathematicians who were also doing modeling in close collaboration with experimental biologists. Over time, interactions with the growing user community, especially at an intensive annual short course, have helped to keep VCell relevant and usable for modeling experimental biology.

The Virtual Cell supports modeling and simulating reaction networks, diffusive and advective transport, and electrophysiology. The system provides clear conceptual boundaries designed to maximize the reusability of a single mechanistic physiological model in multiple experimental contexts. A VCell "BioModel" is a biological model (as opposed to VCell's equation-based models) containing a single physiological model and multiple "Applications", each of which corresponds to or "applies" the model to an experimental context. Each VCell Application defines its modeling framework (i.e., spatial-deterministic, compartmental-deterministic, and compartmental-stochastic) and captures experimental data, cellular geometry, initial conditions, boundary conditions, knockouts, pseudo steady state approximations, and electrophysiological protocols sufficient for automatically generating an experiment-specific mathematical model.

VCell was developed with an emphasis on spatial modeling where reaction mechanisms have traditionally been described locally, that is, affecting local concentrations at a rate influenced only by local concentrations. When mapped spatially,

these local interactions are defined at each point in the appropriate domain; for example, membrane reactions are defined at each point on the membrane, and membrane/volumetric transport results in a spatially resolved flux density that is coupled to diffusive flux in the volume. When mapped non-spatially, these local interactions are integrated over the domains in which they are defined; for example, flux densities produced from membrane reactions are integrated over the membrane to produce a total flux. Support for spatial models is one of the areas of development for SBML Level 3.

VCell encourages modelers to represent a hypothesized indirect interaction between distant molecular species not as a single reaction, but as a series of local reactions and transport steps. In this way, each of these individual mechanisms must be physically realizable (e.g., reasonable kinetic parameters, concentrations, and transport rates) while combining to produce the desired behavior. While the absolute values of intermediate parameters may be underdetermined, the bounds on these parameters can introduce absolute physical limits on the time scale or sensitivity of an indirect functional relationship.

Modeling an indirect interaction between distant molecular species as a single reaction necessarily omits transport mechanisms or second messengers that act on an appropriately fast time scale. The advantage of these approximations is their simplicity and direct correspondence to some measured quantity without adding additional degrees of freedom; the disadvantage is that it introduces a phenomenological process that will not generalize well and will be insensitive to other parts of your model. Despite this, models containing indirect interactions are quite popular in many research domains. VCell has recently been extended to allow both local and non-local reaction mechanisms, where non-local reactions can only be mapped non-spatially or to molecular species that are constrained to be well-mixed.

For deterministic spatial modeling (partial differential equations), a spatial “Application” maps a user’s core physiological model to a three-dimensional cellular geometry (often derived from microscopy images) that supports heterogeneous distributions of processes and molecular species and allows definition of diffusive and

advective transport. In addition, all model parameters, initial conditions, boundary conditions and mechanisms can be explicit functions of time and space or derived from user supplied spatiotemporal data (e.g., experimental time series images). The experimental time series can be compared and visualized together with the spatiotemporal simulation results. For deterministic compartmental modeling (differential algebraic equations), the same core physiological model can be mapped to well-stirred compartments and associated with user defined time series datasets for parameter estimation. For stochastic compartmental modeling (Poisson processes) the core physiological model is mapped to jump processes with Poisson distributions and simulated with direct and hybrid solvers, but there is no corresponding experimental data handling at this time.

Electrophysiological modeling protocols are seamlessly integrated into the VCell “Application” as a Protocol Module. To simulate an electrophysiological experiment, the user selects where to place the patch-clamp electrodes and specifies a waveform for either a current-clamp or voltage-clamp protocol. Then, whenever the mathematical model for that Application is generated (preceding simulation or analysis), the appropriate electrical device (either a current source for current clamp or a voltage source for voltage clamp) is temporarily inserted across the appropriate membrane. This alters the “equivalent circuit” of the model so that the proper set of equations is generated. For either protocol, both the voltage and applied current (sum of capacitive and transmembrane currents) between the electrodes is computed so that the user can directly compare the simulated currents with an experimental recording.

A VCell “Application” adds crucial contextual information, such as initial conditions, reactions, boundary conditions, spatial domain (cellular geometry), the concentrations to hold fixed, and other characteristics, to a mechanistic model. The result completely specifies a mathematical model used to generate simulations. This approach allows several experiment-centric derived models – the Virtual Cell Applications – to be maintained as a single document. The original intent in VCell was to validate a single underlying biological model under several independent experimental conditions. However, some experimental measurements

and manipulations must be modeled by explicitly coupling the experimental processes and the biological processes (e.g., fluorescent calcium indicators also function as significant calcium buffers and so competes for free calcium and changes effective diffusion). Rather than require a modeler to manually incorporate the experimental process directly into a physiological model and thus destroy the model's reusability, it is more flexible to automatically generate the augmented experimentally-focused model as needed. The modeler can define which protocols to include and specify the required parameters (e.g. total fluorescent indicator added, affinity/kinetics with respect to each existing molecule, diffusion rate, bleaching characteristics). A "virtual experiment" will then be a comprehensive, experimentally-focused extension of a modeling application that will provide explicit representations for input data, protocols, measurement processes, and experimental reference data.

Note how this kind of separation between a model and its manipulations in a virtual experiment implies a need for a representation that is separate from SBML – which is precisely the reason why the MIASE project (Minimum Information About a Simulation Experiment; <http://www.ebi.ac.uk/compneur-srv/miase/>) was initiated. MIASE aims to represent in an application-independent way the common set of information that any modeler needs to provide in order to repeat a numerical simulation experiment derived from a given quantitative model.

Quantitative models should embody mechanistic hypotheses within a consistent theoretical

framework. A physics-based framework within a modeling tool provides a scaffold consisting of implicit conservation laws (e.g., mass conservation) that couple physical quantities and processes (e.g. biochemical reactions, patch-clamp electrodes, and measurement processes) to generate a mathematical model. In contrast, an equation-based framework (e.g. model explicitly defines entire system of differential-algebraic equations) requires that all relationships between data and model must be considered explicitly in the form of the model. However, the experimental conditions and apparatus often significantly change the mathematical form of the system (e.g. voltage-clamp electrodes, buffering effects of a fluorescent indicator, over-expression of a fluorescently labeled protein). SBML requires a physics-based framework for reactions with all other processes defined using ancillary equations added directly to the model. VCell extends the supported physical processes that can be described in models to include diffusive and advective transport in space and electrophysiology (e.g. Kirchhoff's Voltage and Current Laws are considered when constructing the equations for electric potential), and "Virtual Microscopy" extensions. These extensions support protocols incorporating fluorescent indicators, fluorescent labels, FRAP, photoactivation, focal stimuli while considering experimental optics.

Table 1.4 provides a summary of how many of the concepts in SBML map to concepts in VCell. Some of the areas of current development in SBML are discussed in the next section.

Table 1.4. SBML components versus their VCell counterparts

SBML component	Location in VCell component
Reactions	Reactions in model
Fast attribute for reaction	Fast reactions in application
Reaction kinetics	Lumped or local kinetics (in model)
Species	Species in model
Species initial conditions	Initial conditions in application
Compartment	Compartment in model
Compartment size	Spatial characteristics in application
Rate rules, algebraic rules, events	Expressions in application (<i>future version</i>)
Rate rules for membrane potential	Expressions in application
Spatial package (in development)	Diffusion/advection + geometry (Application)
SBML model	Model + 1 application
Multiple SBML models	BioModel (multiple applications)
MIASE	Simulation

V. Future Directions for Systems Biology Markup Language (SBML)

The needs of advanced modeling environments such as VCell are pushing forward the evolution of SBML and associated standards. The next generation of SBML, called SBML Level 3, will be a modular language based on a core and extension “packages” layered on top of the core. The core will be a minimally-modified Level 2 Version 4. One of the modifications will be a package mechanism that allows a model to declare which additional feature sets (packages) are used by the model. Software tools will be able to use this information to judge whether they can fully interpret a model that they encounter. Advanced software such as VCell will gain the ability to more fully represent classes of models that currently are not supported in SBML Level 2; on the other hand, software tools that do *not* support certain features used in a given model can inform users that only limited functionality can be provided – yet still be able to make *some* use of the SBML model by virtue of its use of core features. There are several SBML Level 3 packages in development today, but here we describe briefly just two, spatial geometry and hierarchical model composition. More information about these and other activities can be found online at the SBML website, <http://sbml.org/>.

The goal of supporting *spatial characteristics* in SBML Level 3 is to allow the representation of the geometric features of compartments and the spatial distribution of model quantities and processes. SBML models today are nonspatial: compartments are topological structures only, with dimensionality, size and containment being their only physical attributes. This was partly a conscious design decision, because even today, there are far more nonspatial modeling tools available, and so the SBML development priority reflected that. However, it is clearly insufficient for many potential modeling uses, including the problems described above. The focus for the spatial aspects of SBML will be on supporting at least the following characteristics: (1) the size and shape of physical entities whether compartments or reacting species; (2) the absolute or relative spatial location of reacting species in compartments, for instance in a volume, on membrane surfaces, or along microtubules; (3) the rates of diffusion

of species through compartments; and (4) the definition of rate equations and algebraic constraints describing phenomena either at specific locations, or distributed across compartments.

Model composition refers to the ability to include models as submodels inside other models. This requires defining the interfaces between the models and rules for connecting parts of models together. The motivation is to help contain model complexity by allowing decomposition. With this facility in place, users will be able to create reusable models, create libraries of components, etc., and combine them into larger models, much as is done in software development, electronics design, and other engineering fields.

VI. Conclusions

The use of computational modeling is clearly increasing in all areas of biology, from analyzing and extracting understanding from the vast quantities of data saturating researchers today, to designing biological circuits (Church, 2005). One of the most valuable features of computational models is their support of quantitative calculations, allowing researchers not only to test their understanding, but also to explore “what-if” scenarios and make testable predictions about the behavior of the system being studied. This is an essential requirement for being able to understand complicated systems that are replete with feedback mechanisms (the hallmark of biological systems), where the resulting behaviors are rarely predictable through intuitive reasoning alone. Even for the simplest components and systems, it can be impossible to predict such characteristics as sensitivity to exact parameter values without constructing and analyzing a model. Such analyses have shown that some systems are insensitive (e.g. Yi et al., 2000) whereas others are exquisitely sensitive (e.g. McAdams and Arkin, 1999). Computational modeling is thus an extension of the scientific method (Phair and Misteli, 2001; Fall et al., 2002; Slepchenko et al., 2002), providing the means to create precise, unambiguous, quantitative descriptions of biological phenomena that can be used to evaluate hypotheses systematically and to explore non-obvious dynamical

behavior of a biological system (Hartwell et al., 1999; Endy and Brent, 2001; Csete and Doyle, 2002).

The inescapable reality in systems biology is that models (that is to say, hypotheses cast in a computational form) will continue to grow in size, complexity and scope. New tools for gaining greater biological information ensure future revelations will continue to be uncovered at an ever increasing pace. Standardizing on common formats is essential for being able to move forward with increasingly larger-scale research endeavors. As discussed in this chapter, SBML in combination with other standards today permits representing computational models in a way that is independent of any particular software package, operating system, or simulation algorithms. Standardization of this kind removes an impediment to sharing results and permits other researchers to start with an unambiguous representation of their hypotheses and assumptions, thus able to examine it carefully, propose precise corrections and extensions, and apply new techniques and approaches – in short, to do better science.

In part because this standardization has encouraged attempts at collaboration and exchange like never before, limitations in the existing standards such as SBML are being recognized and being addressed. Modern software environments for modeling, such as the Virtual Cell described in this chapter, offer capabilities that exceed what can be represented in SBML Level 2 today. As a result of this and other inspirations, the SBML community is working on SBML Level 3, promising new capabilities for representing such things as spatial geometries and diffusion processes in models. This is one of the beneficial effects of increased collaboration enabled by standardized formats such as SBML: researchers and developers push the standards and encourage their continued evolution and expansion, which in turn encourages more collaboration and development. This feedback loop ensures that the future of computational modeling in biology looks brighter than ever.

References

- Alm E and Arkin AP (2003) Biological networks. *Curr Opin Struc Biol* 13: 193–202
- Arkin A (2001) Synthetic cell biology. *Curr Opin Biotech* 12: 638–644
- Booch G, Jacobson I and Rumbaugh J (2000) OMG Unified Modeling Language Specification. Object Management Group, Inc. Needham, MA, USA
- Bornstein BJ, Keating SM, Jouraku A and Hucka M (2008) LibSBML: An API library for SBML. *Bioinformatics* 24: 880–881
- Bower JM and Beeman D (1995) The Book of GENESIS: Exploring Realistic Neural Models with the GENeral NEural Simulation System. Springer, Santa Clara, California
- Bower JM and Bolouri H (2001) Computational Modeling of Genetic and Biochemical Networks. MIT Press, Cambridge, MA
- Bower JM, Beeman D and Hucka M (2002) The GENESIS simulation system. In: Arbib MA (ed) *The Handbook of Brain Theory and Neural Networks* pp. 475–478. MIT Press, Cambridge, MA
- Bray T, Paoli J and Sperberg-McQueen CM (1998) Extensible markup language (xml) 1.0 (w3c recommendation 10-february-1998). <http://www.w3.org/TR/>
- Church GM (2005) From systems biology to synthetic biology. *Mol Sys Biol* 1, p. 1, doi:10.1038/msb4100007
- Csete ME and Doyle JC (2002) Reverse engineering of biological complexity. *Science* 295: 1664–1669
- Endy D and Brent R (2001) Modelling cellular behaviour. *Nature* 409: 391–395
- Fall C, Marland ES, Wagner JM and Tyson JJ (2002) *Computational Cell Biology*. Springer, New York
- Fraser SE and Harland RM (2000) The molecular metamorphosis of experimental embryology. *Cell* 100: 41–55
- Hartwell LH, Hopfield JJ, Leibler S and Murray AW (1999) From molecular to modular cell biology. *Nature* 402: C47–C52
- Hedley WJ, Nelson MR, Bullivant DP and Nielson PF (2001) A short introduction to CellML. *Phil Trans R Soc A* 359: 1073–1089
- Hines ML and Carnevale NT (1997) The NEURON simulation environment. *Neural Comput* 9: 1179–1209
- Hucka M, Finney A, Sauro HM, Bolouri H, Doyle JC, Kitano H, Arkin AP, Bornstein BJ, Bray D, Cornish-Bowden A, Cuellar AA, Dronov S, Gilles ED, Ginkel M, Gor V, Goryanin II, Hedley WJ, Hodgman TC, Hofmeyr J-H, Hunter PJ, Juty NS, Kasberger JL, Kremling A, Kummer U, Le Novère N, Loew LM, Lucio D, Mendes P, Minch E, Mjolsness ED, Nakayama Y, Nelson MR, Nielsen PF, Sakurada T, Schaff JC, Shapiro BE, Shimizu TS, Spence HD, Stelling J, Takahashi K, Tomita M, Wagner J and Wang J (2003) The Systems Biology Markup Language (SBML): A medium for representation and exchange of biochemical network models. *Bioinformatics* 19: 524–531
- Hucka M, Finney A, Bornstein BJ, Keating SM, Shapiro BE, Matthews J, Kovitz BL, Schilstra MJ, Funahashi A, Doyle JC and Kitano H (2004) Evolving a lingua franca and associated software infrastructure for computational systems biology: The Systems Biology Markup Language (SBML) project. *Sys Biol* 1: 41–53

- Jacobs I and Walsh N (2004) Architecture of the world wide web, volume one: W3c recommendation 15 December 2004. W3C. <http://www.w3.org/TR/webarch/>
- Le Novère N, Finney A, Hucka M, Bhalla US, Campagne F, Collado-Vides J, Crampin EJ, Halstead M, Klipp E, Mendes P, Nielsen P, Sauro H, Shapiro BE, Snoep JL, Spence HD and Wanner BL (2005) Minimum Information Requested in the Annotation of biochemical Models (MIRIAM). *Nat Biotechnol* 23: 1509–1515
- Le Novère N, Bornstein BJ, Broicher A, Courtot M, Donizelli M, Dharuri H, Li L, Sauro HM, Schilstra MJ, Shapiro BE, Snoep JL and Hucka M (2006) Biomodels database: A free, centralized database of curated, published, quantitative kinetic models of biochemical and cellular systems. *Nucleic Acids Res* 34: D689–D691
- Lloyd CM, Halstead MD and Nielsen PF (2004) CellML: Its future, present and past. *Prog Biophys Mol Biol* 85: 433–450
- McAdams HH and Arkin A (1999) It's a noisy business! Genetic regulation at the nanomolar scale. *Trends Genet* 15: 65–69
- Moraru II, Schaff JC, Slepchenko BM, Blinov ML, Morgan F, Lakshminarayana A, Gao F, Li Y, Loew LM (2008) Virtual Cell modelling and simulation software environment. *IET Sys Biol* 2(5): 352–362
- Noble D (2002) The rise of computational biology. *Nat Rev Mol Cell Bio* 3: 460–463
- Olivier BG and Snoep JL (2004) Web-based kinetic modelling using JWS online. *Bioinformatics* 20: 2143–2144
- Phair RD and Misteli T (2001) Kinetic modelling approaches to *in vivo* imaging. *Nat Rev Mol Cell Bio* 2: 898–907
- Schulz M, Uhlenhof J, Klipp E and Liebermeister W (2006) SBMLmerge, a system for combining biochemical network models. *Genome Inform* 17: 62–71
- Slepchenko BM, Schaff JC, Carson JH and Loew LM (2002) Computational cell biology: Spatiotemporal simulation of cellular events. *Annu Rev Bioph Biom* 31: 423–441
- Slepchenko BM, Schaff JC, Macara I and Loew LM (2003) Quantitative cell biology with the virtual cell. *Trends Cell Biol* 13: 570–576
- Snoep JL and Olivier BG (2003) JWS online cellular systems modeling and microbiology. *Microbiology* 149: 3045–3047
- Tyson JJ, Chen K and Novak B (2001) Network dynamics and cell physiology. *Nat Rev Mol Cell Biol* 2: 908–916
- Yi T-M, Huang Y, Simon MI and Doyle J (2000) Robust perfect adaptation in bacterial chemotaxis through integral feedback control. *Proc Natl Acad Sci USA* 97: 4649–4653
- Zerhouni E (2003) The NIH roadmap. *Science* 302: 63–64

Chapter 2

Scaling and Integration of Kinetic Models of Photosynthesis: Towards Comprehensive E-Photosynthesis

Ladislav Nedbal

*Department of Biological Dynamics, Institute of Systems Biology and Ecology and Institute
of Physical Biology, Zámek 136, 37333 Nové Hradky, Czech Republic*

Jan Červený

*Department of Biological Dynamics, Institute of Systems Biology and Ecology Zámek 136,
37333 Nové Hradky, Czech Republic*

Henning Schmidt*

*Department of Computer Science, University of Rostock, Albert Einstein st. 21,
18051 Rostock, Germany*

Summary.....	17
I. Introduction.....	18
II. Mapping Partial Photosynthesis Models into the Comprehensive Model Space (CMS): The Principles and Strategies.....	19
III. Mapping of Photosystem II Models into the Comprehensive Model Space (CMS).....	21
A. Construction and Graphical Representation of the Photosystem II Comprehensive Model Space.....	21
B. Mathematically Rigorous Dimensionality Reduction.....	24
C. Translation to the Biology-Wide Formats and Model Solution.....	26
IV. Concluding Remarks.....	27
Acknowledgments.....	28
References.....	28

Summary

Mathematical models are essential to understand dynamic behavior of complex biological systems. Photosynthesis as it occurs in a natural environment reflects not only the primary biophysical and biochemical reactions but also a network of regulatory interactions that act across timescales and spatial boundaries. Modeling such a tightly regulated biosystem is feasible when the model is reduced to describe only a rather particular experimental situation such as fluorescence response to a single turnover light flash or the dynamics around the steady-state of Calvin–Benson cycle. Then, the external

* Author for correspondence, e-mail: henning@hschmidt.de

regulatory interactions can be considered negligible or not changing so that the investigated dynamics can be predicted by modeling the system with only few key components that are relevant for the given time and complexity scale. Such an empiric dimensionality reduction has been successfully applied in photosynthesis research, leading to a mosaic of partial models that map along the Z-scheme of light reactions as well as covering parts of carbon metabolism. The validity ranges of the partial models are frequently not overlapping, leaving gaps in the photosynthesis modeling space. Filling the gaps and, even more important, modeling of regulatory interactions between modeled entities are hampered by incompatibility of the partial models that focus on different time scales or that are restricted to particular experimental situations. This led us to propose the Comprehensive Modeling Space, CMS where the partial photosynthesis models would be shared by means of the Systems Biology Mark-Up Language, SBML, which is the de-facto standard for the formal representation of biochemical models. The model validity is defined by a customized extension of the biology-wide standard of Minimum Information Requested in the Annotation of Biochemical Models, MIRIAM. The hierarchy and connectivity of the partial models within the Comprehensive Modeling Space is determined by rigorous dimensionality reduction techniques. Here, we exemplify the principles of the comprehensive modeling approach based on partial models of the Photosystem II.

I. Introduction

Models are approximate abstractions representing particular dynamic, structural, stoichiometric, or other essential features of the underlying system. In oxygenic photosynthesis, the mod-

eled features often reflect a sub-network of photochemical, redox, and metabolic molecular reactions and relate them to CO₂ uptake, O₂ evolution or some of the variety of reporter signals, e.g. such as the chlorophyll fluorescence emission. The model parameters that represent the plant environment are temperature, CO₂ and O₂ concentration, humidity, and irradiance. In this chapter, we focus on irradiance that fluctuates or is modulated on timescales spanning from femtoseconds to minutes causing a significant perturbation of the steady state.¹ The photosynthetic apparatus is a highly complex and inherently nonlinear system. Due to its complexity and the vast amount of required dynamic state variables, its light driven dynamics can hardly be reflected by a single solvable mathematical model. Such a hyper-model that would be expected to simulate all potential dynamic features of photosynthesis is neither practical nor necessary. Instead, we propose to collect the existing partial kinetic models of C₃ photosynthesis into a consistent database of the Comprehensive Model Space (CMS). The CMS concept was recently introduced as “a framework in which the earlier small models, each focusing on a different time-scale of interest and/or behavior(s) of interest, are integrated and synchronized” (Nedbal et al., 2007).

Abbreviations: CheBI – chemical entities of biological interest is a freely available dictionary of molecular entities focused on ‘small’ chemical compounds (<http://www.ebi.ac.uk/chebi/>); Chl – chlorophyll; Chl_D – primary electron donor of photosystem II; CMS – comprehensive modeling space; Cyt b₆/f – cytochrome b₆/f complex; GO – gene ontology (<http://www.geneontology.org/>); Fd – ferredoxin; FNR – ferredoxin-NADP⁺ oxidoreductase; InterPro – database of protein families, domains and functional sites (<http://www.ebi.ac.uk/interpro/>); KEGG – kyoto encyclopedia of genes and genomes (<http://www.genome.jp/kegg/>); NEWT – taxonomy database maintained by the UniProt group (<http://www.ebi.ac.uk/newt/>); MIRIAM – minimum information requested in the annotation of biochemical models; P680 – special pair electron donor of photosystem II; P700 – primary electron donor of photosystem I; PC – plastocyanin; Pheo – pheophytin; PS I – photosystem I; PS II – photosystem II; Q_A – quinone electron acceptor of photosystem II; QSSA – quasi steady-state approximation; Rubisco – ribulose-1,5-bisphosphate carboxylase/oxygenase; SBML – systems biology mark-up language; SBO – systems biology ontology; S_n – oxidation states of manganese oxygen-evolving cluster; *t* – time; UniProt – universal protein resource, a comprehensive catalog of information on proteins (<http://www.expasy.uniprot.org/>); Y_Z – tyrosine Z, secondary electron donor of PS II

¹ The steady-state approaches such as metabolic pathway analysis are reviewed, e.g., in Rios-Esteva and Lange (2007).

The existing models of photosynthesis are conceptual, such as photosynthetic unit (Emerson and Arnold, 1932; Gaffron and Wohl, 1936), qualitative, such as Z-scheme (Hill and Bendall, 1960), or quantitative, such as models explaining kinetics of the fluorescence induction phenomena (reviewed in Part III in this volume or Lazár, 2006) or features of the Calvin–Benson cycle (reviewed in Part IV in this volume or Zhu et al., 2007).

For our purposes, the quantitative models are of the primary interest. These quantitative models do not only describe the involved molecular or cellular components and the interactions between these components. They also define the mathematics behind the interactions and the values of the involved kinetic parameters. Typically used mathematical frameworks for quantitative modeling are ordinary and partial differential equations. However, Section II in Chapter 1 of this volume provides strong arguments that a wide use of models is hindered by their presentation in form of sets of differential equations. Rather, its authors Michael Hucka and James Schaff advocate presentation of models in platform neutral formats combined with publically available solvers.

Similarly here, an issue of major importance regarding modeling of biochemical systems, such as photosynthesis, and the incorporation of models into the CMS, is a unified, flexible and neutral representation format for the partial models, the involved components, and their interactions. The Systems Biology Markup Language, SBML (Chapter 1 in this volume, Hucka et al., 2003) is such a format that is based on the Extensible Markup Language, XML. SBML has become a de-facto standard in the area of systems biology. It aims at facilitating the exchange of information between different researchers, eliminating the need for recoding models each time a different software tool is to be used for modeling, simulation, or analysis purposes. Apart from facilitating and accelerating the workflow, SBML also aims at ensuring the survival of models over the software tools they are represented in. A selection of tools that are able to import SBML models for subsequent analysis and simulation are the SBTOOLBOX2 for MATLAB (<http://www.sbtoolbox2.org>, Schmidt and Jirstrand, 2006), COPASI (<http://www.copasi.org>, Hoops et al., 2006) and MathSBML

for Mathematica (<http://sbml.org/software/mathsbml>, Shapiro et al., 2004). For a full list of SBML compliant tools and solvers see <http://sbml.org>

A complicating factor for the mathematical implementation of photosynthetic subsystems is the fact that particular experimental situations require particular model implementations. For instance, one mathematical model is used to simulate fluorescence emission kinetics in the Photosystem II following a femto-second flash (e.g. Holzwarth et al., 2006), while the slow Kautsky effect requires a completely different implementation for modeling the same photosystem.

When such different models are collected in the CMS it is important to be able to differentiate between models of the same subsystem in order to assess their range of validity, defined by properties, such as the considered experimental settings and their dynamic ranges. This can be achieved by complementing the models with additional information. For models of photosynthetic systems such additional information comprises information about organism or structure modeled, the model output to be compared with the experiment, the expected time resolution, or what irradiance or irradiance temporal modulation is applied. A proposed standard in systems biology for such an additional model-specific information is the Minimum Information Requested in the Annotation of Biochemical Models, MIRIAM (Le Novère et al., 2005). Our goal is to collect MIRIAM annotated models of photosynthetic subsystems in the CMS, creating a base to derive a wide range of new models to simulate desired experimental settings. In this chapter we will exemplify this approach for the Photosystem II.

II. Mapping Partial Photosynthesis Models into the Comprehensive Model Space (CMS): The Principles and Strategies

The Comprehensive Modeling Space (CMS) will enable the linking of partial models with overlapping validity ranges and filling the gaps between disjunctive partial models, always using unified, mutually compatible formats. Figure 2.1 maps some of the existing model classes as a discrete

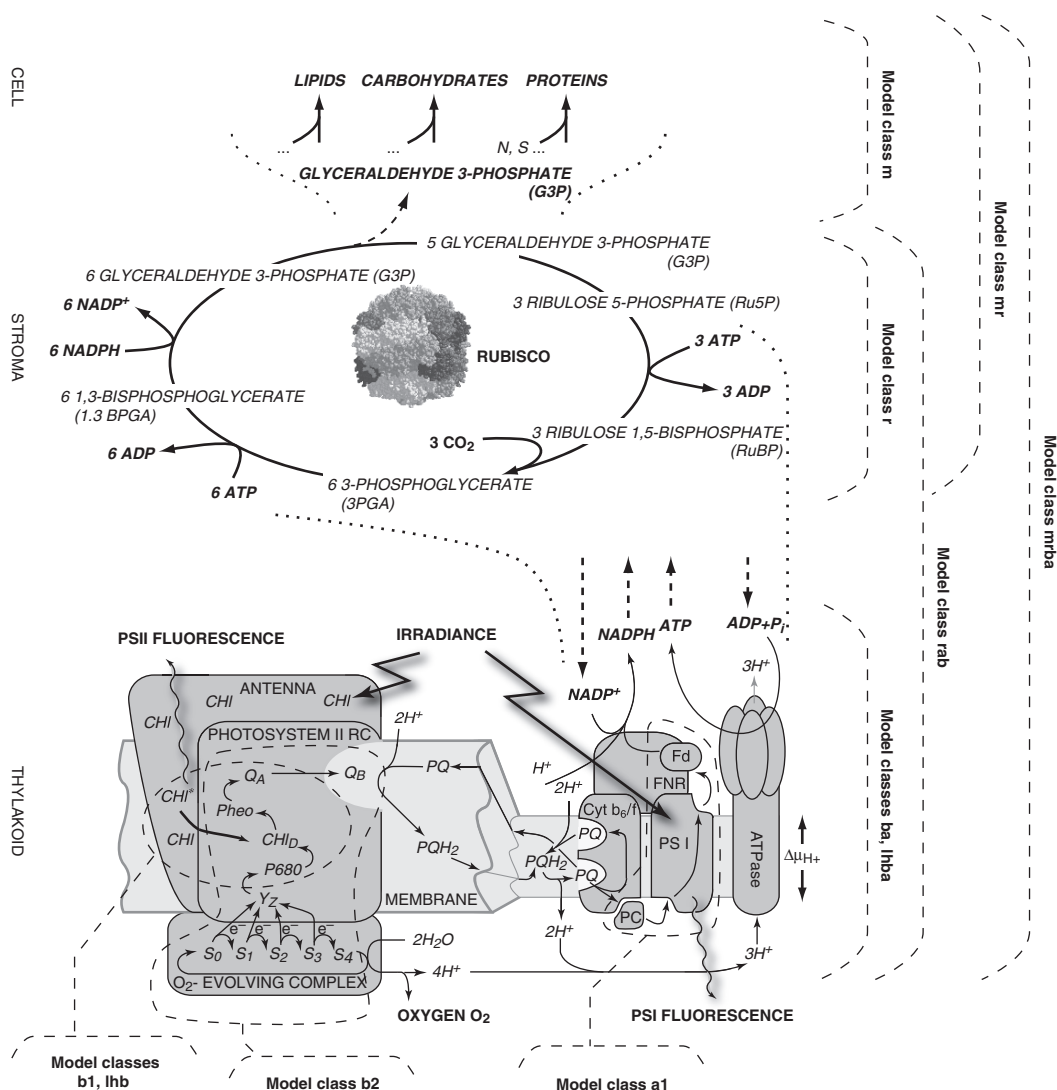


Fig. 2.1. A scheme mapping the model classes (dashed lines) in a graphical representation of the light reactions in the thylakoid (bottom), of the Calvin-Benson cycle (middle), and of some metabolic fluxes (top). The model classes are labeled by 'b' when focused to Photosystem II, 'a' to Photosystem I, 'lh' to light harvesting, 'r' to Rubisco, and 'm' to a broader metabolic network. The scheme itself is a model reflecting only selected aspects of C₃ photosynthesis with proportions that are dictated rather by the information on the model classes than by reality. In this sense, the scheme is a model of the comprehensive modeling space rather than a graphical model of photosynthesis. For example, Photosystem I (PS I) is drawn smaller relative to Photosystem II (PS II) to indicate a larger number of models and model classes that exist for PS II. The scheme also shows some of the typical model outputs such as CO₂ and O₂ fluxes and chlorophyll fluorescence

mosaic covering the spectrum of photosynthetic processes from Z-scheme to Calvin-Benson cycle and to growth. Note that some photosynthesis models already integrate reactions of all model classes outlined in Fig. 2.1 (e.g. Chapter 13 of this book by Agu Laisk, Hillar Eichelmann and Vello Oja). Complexity of such models is very high. Recent models of Calvin-Benson

cycle operate with 35 (Zhu et al., 2007) and 27 state variables (Poolman et al., 2004) and yield as model outputs CO₂ influx and ATP, NADPH and P_i levels. Laisk and Edwards (2000) couple the Calvin-Benson cycle with state variables that reflect the light reactions involving both Photosystems. The model in Chapter 13 of this volume by Laisk et al. includes 28 state variables.

Time constants of the processes that are represented in Fig. 2.1 range from femto-seconds to seconds. One can expect that modeling the subsystems with slow dynamics, such as the Calvin–Benson cycle, the fast photochemical reactions can be lumped together in quasi-steady state fluxes of ATP and NADPH that govern the dynamics of this subsystem. Conversely, considering the subsystems with fast dynamics, the slow reactions of the Calvin–Benson cycle will not respond to a rapid perturbation by, for example, a short intense flash of light that can produce information-rich transients in chlorophyll fluorescence emission, electrochromic shift, P700 signal, oxygen evolution, or in other experimentally relevant reporter signals. Thus, in this case it is a valid approximation to assume the slow reactions to be constant.

The models that focus on the slow dynamic limit of the Calvin–Benson cycle, and include wider metabolic networks, are crucial because they simulate the key features of the carbon metabolism. The fast dynamics models are, on the other hand, indispensable to decipher the network of the light reactions that drive the cellular machinery including the carbon metabolism. Empiric decoupling of the two dynamic realms into separate model spaces simplifies the mathematics and, thus, has often been highly productive. However, the decoupling hampers, for example, quantitative kinetic modeling of the regulation of the fast photochemical reactions that is dynamically controlled by the slow processes. We suggest that it is the separation of fast and slow dynamic domains that makes it difficult to understand molecular mechanism of the oscillatory phenomena in photosynthesis (Nedbal et al., 2003, 2005). An example of interaction acting across timescales and spatial boundaries is the regulation of the photosynthetic yields by non-photochemical quenching that depends strongly on lumenal pH, which, in turn, depends on the

photosynthetic light reactions, on the ATP-ase activity, as well as on the ATP and NADPH consumption in the Calvin–Benson cycle. This and other regulatory interactions couple the slow and fast reactions. Thus, it is important to include models from both dynamic extremes in a single Comprehensive Modeling Space.

The integration of models of the Calvin–Benson cycle is relatively straightforward, since newer models typically represent extensions of earlier models, and the values of the kinetic constants, involved in the networks, are reasonably well defined. In contrast, the modeling space of the light reactions is much more difficult to organize because the dynamic range is much wider, again roughly from femto-seconds to seconds. Furthermore, models of the same subsystems, but focusing on different dynamic features, can be disjunctive. We demonstrate here the integration of models of primary photochemistry using the model of the ultrafast reactions in Photosystem II (Holzwarth et al., 2006). The model is translated into SBML and MIRIAM annotated. The rigorous dimensionality reduction, in terms of lumping of ultrafast reactions, is demonstrated using the same model.

III. Mapping of Photosystem II Models into the Comprehensive Model Space (CMS)

A. Construction and Graphical Representation of the Photosystem II Comprehensive Model Space

The Comprehensive Model Space must accommodate all existing partial models of Photosystem II. The principal components and their states are listed in Table 2.1. The 25 states of the nine principal components that are listed in Table 2.1 can be combined in 4,800 combinatorial states.

Table 2.1. States of the principal components of Photosystem II

Antenna	<i>Peripheral Antenna</i>	Ground	Excited			
	<i>Core Antenna</i>	Ground	Excited			
Donors	<i>Mn Cluster</i>	S ₀	S ₁	S ₂	S ₃	S ₄
	<i>Y_Z</i>	Neutral	Oxidized			
	<i>P680</i>	Neutral	Oxidized			
	<i>Chl_D</i>	Ground	Excited	Oxidized		
Acceptors	<i>Pheo</i>	Neutral	Reduced			
	<i>Q_A</i>	Neutral	Reduced			
PQ	<i>Q_B</i>	Neutral	Reduced	2-Reduced	PQH ₂	Empty

The CMS-PS II complexity is further increased when external parameters such as plastoquinone pool redox state or non-photochemical quenching are introduced. Only some of the 4800 PS II combinatorial states are relevant under natural conditions. However, one must be careful not to eliminate states from the CMS-PS II that seem irrelevant under one experimental condition but are important in another. For example, simultaneous excitation of the core and peripheral antennae is very unlikely in natural solar irradiance and, yet, may play a decisive role in experiments with strong laser flashes.

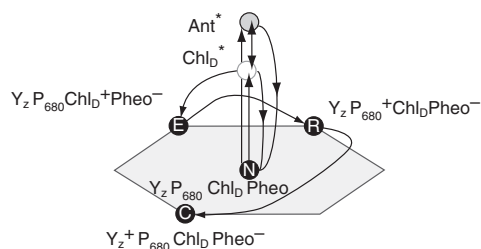
The 4800 PS II combinatorial states can be represented as nodes of a network that can be linked by millions of combinatorial internodal connections. Only a fraction of these internodal connections represent relevant photosynthetic reactions. Yet, some of the internodal connections that do not represent natural reactions can be needed for modeling. For instance, the direct internodal connection between $P680^+-Q_A$ and $P680-Q_A^-$ does not represent any single-step chemical reaction and yet is essential for representing the famous model of Duysens and Sweers (1963) as well as many other relevant models that do not include the intermediate radical pair states involving the primary monomer chlorophyll electron donor Chl_D and/or the pheophytin acceptor Pheo.

Here, we use a modeling space that is generated according to the rules that reflect most (but not all) natural processes:

1. Excitation transition from the ground state antenna and ground state Chl_D (N in Fig. 2.2A) to the excited antenna (Ant^* in Fig. 2.2A) or to the excited primary chlorophyll donor (Chl_D^* in Fig. 2.2A)²: $N \rightarrow Ant^*$ or $N \rightarrow Chl_D^*$ ³
2. Energy transfer $Chl_D Ant^* \leftrightarrow Chl_D^* Ant$
3. Non-radiative and fluorescence de-excitation: ($Ant^* \rightarrow N$) or ($Chl_D^* \rightarrow N$). Both mechanisms and processes of de-excitation are represented by a single arrow in Fig. 2.2A
4. Primary charge separation: Fig. 2.2 solid line $Chl_D^* \rightarrow E (Y_Z P_{680} Chl_D^+ Pheo^-)$

5. Stable radical-pair generation: Fig. 2.2 solid line $E (Y_Z P_{680} Chl_D^+ Pheo^-) \rightarrow R (Y_Z P_{680}^+ Chl_D Pheo^-)$
6. Quinone Q_A reduction preserving P_{680} oxidized: $R (Y_Z P_{680}^+ Chl_D Pheo^-)/Q_A \rightarrow A (Y_Z P_{680}^+ Chl_D Pheo^-)/Q_A^-$ (dashed line $R \rightarrow A$ in Fig. 2.2B)
7. Tyrosine oxidation: $A (Y_Z P_{680}^+ Chl_D Pheo^-)/Q_A^- \rightarrow B (Y_Z^+ P_{680} Chl_D Pheo^-)/Q_A^-$ (solid line $A \rightarrow B$ in Fig. 2.2B)
8. Tyrosine oxidation preserving Pheo reduced: $R (Y_Z P_{680}^+ Chl_D Pheo^-) \rightarrow C (Y_Z^+ P_{680} Chl_D Pheo^-)$ indicated by the solid line $R \rightarrow C$ in Fig. 2.2
9. Quinone Q_A reduction preserving Y_Z oxidized: $C (Y_Z^+ P_{680} Chl_D Pheo^-)/Q_A \rightarrow B (Y_Z^+ P_{680} Chl_D Pheo^-)/Q_A^-$ (dashed line $C \rightarrow B$ in Fig. 2.2B)
10. Quinone Q_A reduction: $D (Y_Z P_{680} Chl_D Pheo^-)/Q_A \rightarrow N (Y_Z P_{680} Chl_D Pheo^-)/Q_A^-$ (dashed line $D \rightarrow N$ in Fig. 2.2B)
11. S-state transition: $B (Y_Z^+ P_{680} Chl_D Pheo^-)/S_n \rightarrow N (Y_Z P_{680} Chl_D Pheo^-)/S_{n+1}$ (dashed line $B \rightarrow N$ in Fig. 2.2B)
12. S-state transition with Pheo reduced: $C (Y_Z^+ P_{680} Chl_D Pheo^-)/S_n \rightarrow D (Y_Z P_{680} Chl_D Pheo^-)/S_{n+1}$ (dashed line $C \rightarrow D$ in Fig. 2.2B)

a



b

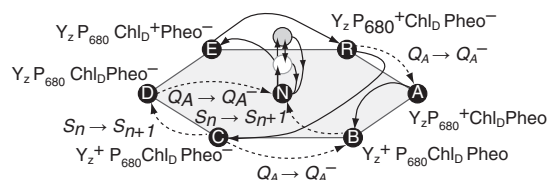


Fig. 2.2. Graphical representation of the core PS II model space motifs. *Top panel, (a)* The fast primary reactions that start with ground neutral state of PS II (N) and that involve neither S-states transition nor Q_A reduction. *Bottom panel, (b)* A more complete set that includes also S-states and Q_A

² Chl_D^* can be used to represent the core PS II antenna in some of the partial models.

³ Note that our model space does not include excitation of the PS II reaction centers that are partially oxidized or reduced.

13. The S-state transition $S_4 \rightarrow S_0$ is accompanied by the release of molecular oxygen: $2 \text{H}_2\text{O} - 4 \text{e}^- \rightarrow \text{O}_2 + 4 \text{H}^+$

Using these rules one can generate the core model motif shown in Fig. 2.2.

The redox reactions specified by these rules can be reversible (arrows in Fig. 2.2 indicate only the forward direction). The core model motif shown in Fig. 2.2A represents only the reactions that would occur in PS II particles without Q_A and without oxygen evolving complex; thus, it does not represent Q_A reduction and S-state transitions. The core motif is extended to Q_A and S-states in Fig. 2.2B (dashed arrows).

The graphical models of PS II in Fig. 2.2 are inadequate in describing natural systems because

Q_B states are not included and individual states of Q_A and S-states are not shown. This deficiency is removed in the more extended scheme shown in Fig. 2.3 that represents reactions occurring with the oxygen-evolving complex in S_1 state (solid rectangle in the center) and the reactions from S_0 to S_1 (lines from the dashed rectangle at the bottom to the central solid rectangle) and from S_1 to S_2 (lines from the central solid rectangle the dashed rectangle at the top).

Figure 2.4 shows the complete Comprehensive Model Space of PS II generated using the rules 1–13 listed above. To our best knowledge, the PS II models in present literature can all be represented in the network in Fig. 2.4.

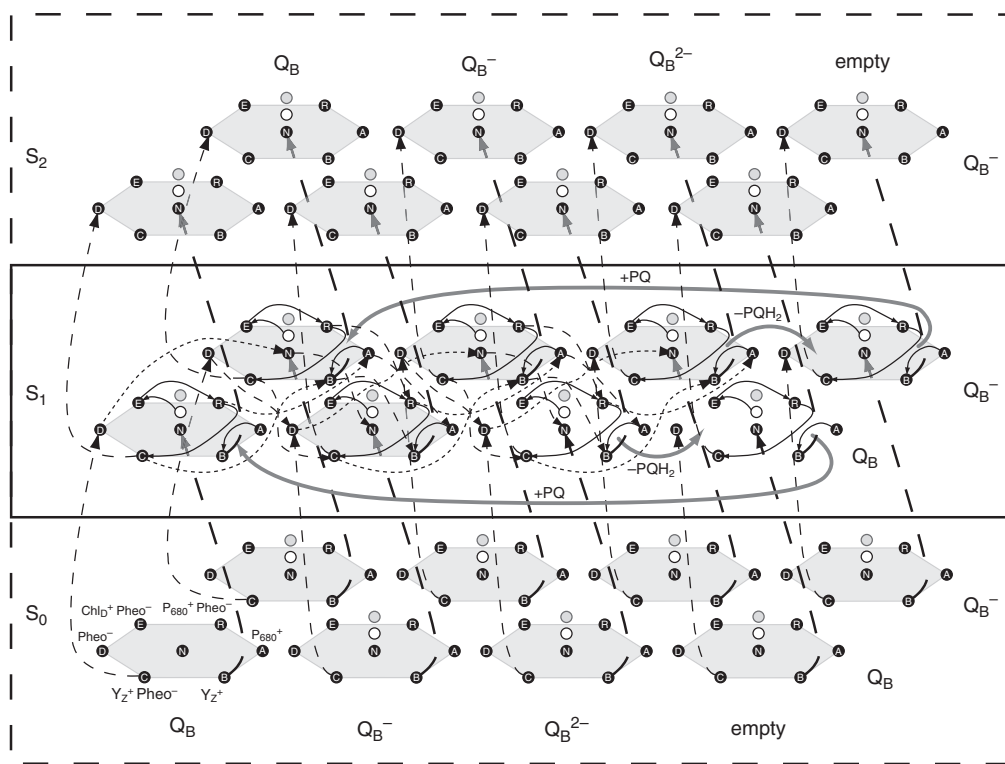


Fig. 2.3. Graphical representation of the S_1 -states in the PS II model space. The scheme shows also the reactions connecting the S_1 -states with S_0 and S_2 state layers. The hexagons (introduced and shown in detail in Fig. 2.2) represent here the processes including Y_Z P_{680} Chl_D $Pheo$ electron donors and acceptors. The front row of the hexagons represents the states with the Q_A quinone acceptor neutral. The back row represents the states with Q_A^- . The reactions resulting in the $Q_A \rightarrow Q_A^-$ reduction ($R \rightarrow A$, $C \rightarrow B$, $D \rightarrow N$) are shown by dotted arrows connecting the respective state nodes in the front and back rows of the S_1 layer (hidden in S_0 and S_2). The four columns represent the Q_B , Q_B^- , and Q_B^{2-} states, and the vacant Q_B pocket state of Photosystem II. The reduction of the Q_B acceptor, reactions $Q_A^- Q_B \rightarrow Q_A Q_B^-$, $Q_A^- Q_B^- \rightarrow Q_A Q_B^{2-}$ ($N \rightarrow N$, $R \rightarrow R$, $A \rightarrow A$, $B \rightarrow B$, $C \rightarrow C$, $D \rightarrow D$) are shown by dashed arrows. The protonation of Q_B^{2-} and PQH_2 release of the reduced from Photosystem II is indicated by thick solid arrows from Q_B^{2-} to empty column. The binding of oxidized PQ to Photosystem II is shown by the solid thick arrows from empty to Q_B column

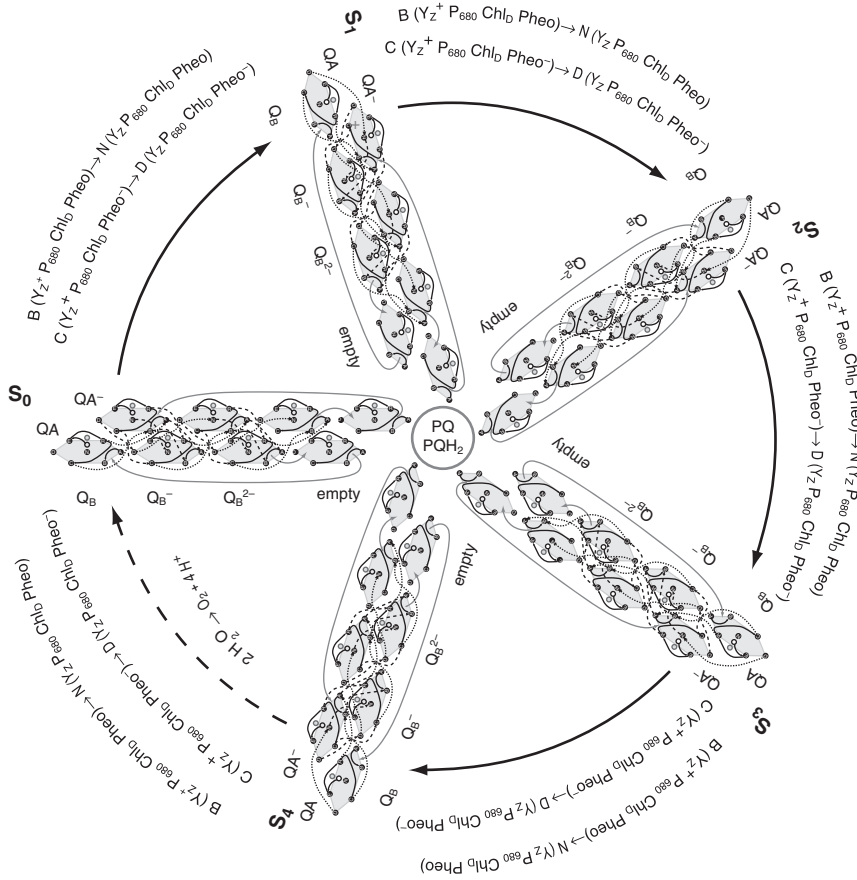


Fig. 2.4. Graphical representation of the PS II part of the Comprehensive Model Space generated by the rules 1–13 that are listed in the text

B. Mathematically Rigorous Dimensionality Reduction

For the reduction of the complexity of the PS II system, traditionally, semi-empiric and insight-based approaches have been employed. The photosynthetic models were reduced based on biochemical insight or observations that there are states of the model that cannot be reached by certain stimuli, are unlikely to occur in reality, or states that do not contribute to the output of interest.

In engineering sciences, several model reduction methods have been developed that are more systematic and mathematically thorough than insight-based approaches. However, the large

number of available model reduction methods reflects the fact that no single method is universally superior. Their appropriateness depends on the type of complexity in the original model, and on the purpose of its reduction.

A mathematical model reduction method that is based on a systems' controllability and observability⁴ (Rugh, 1996) is denoted *balanced truncation*, and it is frequently used in technical applications

⁴ Roughly, controllability reflects existence of input stimuli that could bring the system in a finite time from an initial state to a particular system state. If such a stimulus is not available, the particular state can be eliminated from the reduced model. Observability reflects influence that a particular state exerts on any of the model outputs.

(Skogestad and Postlethwaite, 1996). However, for biological systems this method is often less appropriate since the states of the reduced model do correspond to linear combinations of the states of the original models and thus may not be easy to interpret biochemically. Furthermore, the method is mainly applicable to linear (or at least linearized) systems, even if extensions to nonlinear systems have been developed (Condon and Ivanov, 2004). However, a possible use of this method in comprehensive photosynthesis modeling is to reduce only the parts of the system for which no mechanistic understanding is required. An example for this latter use is given by Liebermeister et al. (2005). Methods that lead to the exclusion of reactions are sensitivity analysis and term-based methods. Such methods remove the reactions or terms that have the least impact on the output variables of the model (Okino and Mavrovouniotis, 1998).

Other reduction methods make use of the fact that a systems dynamics span over a wide range of timescales. In reaction systems this means that fast reactions can be considered instantaneous in comparison to the slower reactions. This leads to the so called quasi steady-state approximation, QSSA. Two methods based on the QSSA are the computational singular perturbation and the algebraic approximation of the inertial manifold (Okino and Mavrovouniotis, 1998). Unfortunately, also with these methods the states of the reduced model are usually linear combinations of the states of the original model, complicating detailed molecular interpretation of the new state variables. *Lumping* is another model reduction method that is based on the presence of different timescales within the system. Lumping is commonly used in biochemical modeling based on insight into the system. Nevertheless, lumping may also be based on a systematic mathematical analysis of the system (Maertens et al., 2005). The resulting reduced model contains states and reactions that are lumps of the states and reactions in the original model.

In the following we will show the results of a novel, lumping based reduction method used to reduce a partial model of PS II that is exposed to a single sub-picosecond flash of light in an experiment in which only the fluorescence emission of the excited reaction center is measured. For the sake of the demonstration we chose

mathematically simple case study model of PS II (Holzwarth et al., 2006), depicted in Fig. 2.5A. The lumping procedure starts by defining the relevant dynamic window, e.g. by high and low frequency limits. For the sake of simplicity, we shall define the model reduction only by the high frequency limit. This corresponds, for example, to a light detector that cannot capture fluorescence emission earlier than τ following the flash. But it can also correspond to the limit to which fast dynamics are of relevance in the case that the reduced model is to be combined with a model of another subsystem that shows slower dynamics. In fact, this latter interpretation is the more interesting one for our comprehensive modeling approach. The model reduction algorithm yields new state variables, some of them being lumped state variables of the non-reduced model. Lumping obtained for a slow detector ($\tau = 1$ ns) is shown by Fig. 2.5D. Fluorescence kinetics predicted by such a reduced model are shown in the bottom of Fig. 2.5 by the kinetic trace D. The simulations by the original non-reduced model (trace A) and by the reduced model coincide for the time range 1 ns and longer whereas the reduced model, by construction, fails to simulate correctly the faster dynamics.

Modeling of experimental results obtained with a light detector that is of intermediate time response ($\tau = 100$ ps) is represented in Fig. 2.5C. The match between the simulations by the non-reduced model (trace A) and by the model limited to 100 ps response time (trace C) is poor in the fast domain $t < 100$ ps and it is not perfect in the slower time domain $t > 100$ ps. This partial failure of the intermediate reduced model is due to the fact that the chosen detector response time of 100 ps is not sufficiently distinct from the turnover times of the system.

The model reduction by lumping that corresponds to the short detector response time $\tau = 10$ ps is shown in Fig. 2.5 by trace B. Clearly, the fluorescence transient modeled by the reduced model $\tau = 10$ ps (trace B) is closely matching the transient simulated by the original, non-reduced model (trace A). Also, the back-translation from the lumped state of the reduced model to the original states of the non-reduced model yielded state dynamics nearly identical to the non-reduced model (data not shown).

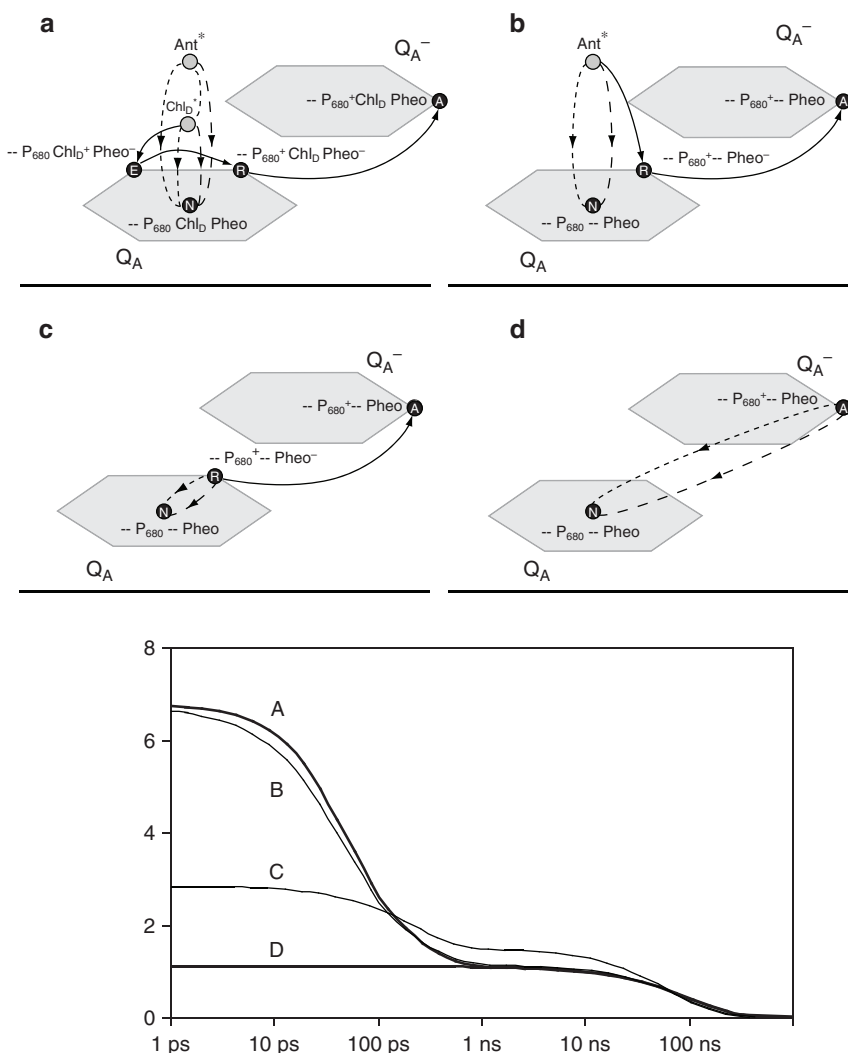


Fig. 2.5. Model of Photosystem II that is exposed to a sub-picosecond flash of light (a) and reduction by mathematically rigorous lumping (b–d). Four lumping levels are presented here: no lumping (a) corresponds to the model of Holzwarth et al. (2006). Fast detector lumping ($\tau = 10$ ps) is represented by (b), intermediate detector lumping ($\tau = 100$ ps) is shown by (c) and slow detector lumping ($\tau = 1$ ns) is represented by (d). The upper part of the figure shows the structure of the non-reduced and reduced models. The lower panel shows modeled fluorescence transients (Adapted from Nedbal et al., 2007)

C. Translation to the Biology-Wide Formats and Model Solution

We will now use the model of Fig. 2.5A to give a quick introduction on how to convert it to SBML and define its validity using extended MIRIAM annotations. One tool that can be used for this task is the SBML editor (<http://www.ebi.ac.uk/compneur-srv/SBMLEditor.html>, Rodriguez et al., 2007). The model editing process is guided in the following steps:

Start the editing process: File/New

Annotation1 (Add/creator): Names, addresses and affiliations of the persons who developed the model.

Annotation2 (Add/relation – literature): The literature reference to the model description is specified by adding a relation with the qualifier “isDescribedBy” and a hyperlink to the particular paper or to its doi number. In our example: 10.1073/pnas.0505371103 (Holzwarth et al., 2006). The qualifier “isVersionOf” can be used to

refer to a broader reference related to the model such as Nedbal et al. (2007).

Annotation3 (Add/relation – organism): The experimental data used to validate the model were obtained with spinach (T3562 in the NEWT taxonomy browser <http://www.ebi.ac.uk/newt/display?search=3562>) and *Synechococcus elongatus* (T32046).

Annotation4 (Add/relation – modeled system, process): In Gene Ontology (<http://www.geneontology.org/>), GO:0030095 and GO:0030096 represent chloroplast Photosystem II and plasma membrane Photosystem II. Photosystem II “isPartOf” GO:0015979 (photosynthesis).

Compartment specification (listOfCompartments/Add New compartment): Compartment Photosystem II is of dimension 0 having annotation GO:0030095 (chloroplast Photosystem II) or GO:0030096 (plasma membrane-derived thylakoid Photosystem II).

Species specification, initial conditions (listOfSpecies/Add New species): The state variables have always identical chemical nature which is the PS II core and differ by redox states or by excitation of its components. The SBML annotation tools are not yet prepared for such entities. Thus, the individual PS II states are represented only by the species unique number assigned automatically by the SBML editor and by its name such as for example $P680^+/\text{Chl}_D/\text{A}/\text{Pheo}^-/\text{Q}_A$. The initial conditions are entered to each individual species. The annotation of the Photosystem II core states is for all species identical specifying its parts by “hasPart” relation qualifier. The components of PS II core are annotated using relation qualifiers as follows:

The antenna A (“is” GO:0009655 in Gene Ontology <http://www.geneontology.org/>, “isPartOf” IPR000932 in the InterPro database <http://www.ebi.ac.uk/interpro/>)

The chlorophyll primary donor Chl_D (“is” C05306 in KEGG, and 18230 in ChEBI, that is bound to the D1 protein “isPartOf” IPR005867)

The P_{680} special pair (“is” C05306, CHEBI: 18230, bound to D1 “isPartOf” IPR005867, and to D2 “isPartOf” IPR005868)

The Pheo, pheophytin a (“is” CHEBI:44898), “isPartOf” IPR005867)

The Q_A , plastoquinone Q_A (“is” C02061, “isPartOf” IPR005867)

Parameters such as numeric values of the rate constants: These are entered preferably using the same nomenclature as in the original literature.

Reactions, reactants, products, kinetic law: The reactions can be annotated only partly:

$P680/\text{Chl}_D/\text{A}^*/\text{Pheo}/\text{Q}_A \rightarrow P680/\text{Chl}_D/\text{A}/\text{Pheo}/\text{Q}_A$ antenna de-excitation by either heat dissipation or by fluorescence emission can be described as a monoexponential decay (SBO:0000080) but the fluorescence and heat dissipation classes are not available in the present ontologies. The same is true for $P680/\text{Chl}_D^*/\text{A}/\text{Pheo}/\text{Q}_A \rightarrow P680/\text{Chl}_D/\text{A}/\text{Pheo}/\text{Q}_A$ de-excitation of the primary donor.

The primary charge separation $P680/\text{Chl}_D^*/\text{A}/\text{Pheo}/\text{Q}_A \leftrightarrow P680/\text{Chl}_D^+/\text{A}/\text{Pheo}^-/\text{Q}_A$ is annotated as GO:0009771.

The stabilization of separated charges $P680/\text{Chl}_D^+/\text{A}/\text{Pheo}^-/\text{Q}_A \leftrightarrow P680^+/\text{Chl}_D/\text{A}/\text{Pheo}^-/\text{Q}_A$ and $P680^+/\text{Chl}_D/\text{A}/\text{Pheo}^-/\text{Q}_A \leftrightarrow P680^+/\text{Chl}_D/\text{A}/\text{Pheo}/\text{Q}_A^-$ is annotated as version of oxido-reductase activity GO:0016491.

Once the model has been entered in the editor it can be validated and saved for inclusion in databases, simulation using SBML enabled simulators, and exchange of models between researchers.

IV. Concluding Remarks

In this chapter, we have discussed the important issue of the integration of quantitative models of photosynthetic subsystems to comprehensive models. We propose to collect existing partial kinetic models of photosynthesis into a consistent database, building up the Comprehensive Model Space, CMS. One important issue hereby is a flexible and formal representation of the models in terms of their components, interactions, and underlying mathematics, for which we propose the use of the Systems Biology Markup Language, SBML. Another important issue is the documentation of a models range of validity. As discussed above, existing models for the same subsystem can be different in many aspects.

The reason for this is that different experimental settings are modeled, or the application of a certain model required a different level of complexity. In order to add the information about the model validity we propose to complement models using Minimum Information Requested in the Annotation of Biochemical Models, MIRIAM.

The final goal of our effort is to collect and provide MIRIAM annotated models of photosynthetic subsystems in the CMS, creating a base to derive a wide range of new models to simulate desired experimental settings. These models will be integrated into the E-photosynthesis.org framework that will be publicly accessible at <http://www.e-photosynthesis.org>. Apart from the development and annotation of models, computational tools will also be required by the CMS. These tools need to support the integration of submodels to comprehensive models. Of major importance will be methods for the reduction of model complexity. In this chapter we have provided an example for such model reduction based on a model for Photosystem II and exemplified the MIRIAM annotation for the same model.

Acknowledgments

JČ and LN were supported in part by the AUTO-SCREEN project LSHG-CT-2007-037897, AV0Z60870520 (Czech Academy of Sciences), and MSM6007665808 (Czech Ministry of Education).

References

- Condon M and Ivanov R (2004) Empirical balanced truncation of nonlinear systems. *J Nonlinear Sci* 14: 405–414
- Duysens LNM and Sweers HE (1963) Mechanism of the two photochemical reactions in algae as studied by means of fluorescence. In: *Studies on Microalgae and Photosynthetic Bacteria*, pp. 353–372. University of Tokyo Press, Tokyo
- Emerson R and Arnold W (1932) A separation of the reactions in photosynthesis by means of intermittent light. *J Gen Physiol* 15: 391–420
- Gaffron H and Wohl K (1936) Zur Theorie der Assimilation. *Naturwissenschaften* 24: 103–107
- Hill R and Bendall F (1960) Function of the two cytochrome components in chloroplasts: a working hypothesis. *Nature* 186: 136–137
- Holzwarth AR, Müller MG, Reus M, Nowaczyk M, Sander J and Rögner M (2006) Kinetics and mechanism of electron transfer in intact photosystem II and in the isolated reaction center: pheophytin is the primary electron acceptor. *Proc Natl Acad Sci USA* 103: 6895–6900
- Hoops S, Sahle S, Gauges R, Lee C, Pahle J, Simus N, Singhal M, Xu L, Mendes P and Kummer U (2006) COPASI – a Complex Pathway Simulator. *Bioinformatics* 22: 3067–3074
- Hucka M, Finney A, Sauro H, Bolouri H, Doyle J, Kitano H, Arkin A, Bornstein B, Bray D, Cornish-Bowden A, Cuellar A, Dronov S, Gilles E, Ginkel M, Gor V, Goryanin I, Hedley W, Hodgman T, Hofmeyr J-H, Hunter P, Juty N, Kasberger J, Kremling A, Kummer U, Le Novère N, Loew L, Lucio D, Mendes P, Minch E, Mjolsness E, Nakayama Y, Nelson M, Nielsen P, Sakurada T, Schaff J, Shapiro B, Shimizu T, Spence H, Stelling J, Takahashi K, Tomita M, Wagner J and Wang J (2003) The systems biology markup language (SBML): a medium for representation and exchange of biochemical network models. *Bioinformatics* 19: 524–531
- Laisk A and Edwards G (2000) A mathematical model of C_4 photosynthesis: the mechanism of concentrating CO_2 in NADP-malic enzyme type species. *Photosynth Res* 66: 199–224
- Lazár D (2006) The polyphasic chlorophyll a fluorescence rise measured under high intensity of exciting light. *Funct Plant Biol* 33: 9–30
- Le Novère N, Finney A, Hucka M, Bhalla US, Campagne F, Collado-Vides J, Crampin EJ, Halstead M, Klipp E, Mendes P, Nielsen P, Sauro H, Shapiro B, Snoep JL, Spence HD, and Wanner BL (2005) Minimum information requested in the annotation of biochemical models (MIRIAM). *Nature Biotech* 23: 1509–1515
- Liebermeister W, Baur U and Klipp E (2005) Biochemical network models simplified by balanced truncation. *The FEBS J* 272: 4034–4043
- Maertens J, Donckels BMR, Lequeux G and Vanrolleghem PA (2005) Metabolic model reduction by metabolite pooling on the basis of dynamic phase planes and metabolite correlation analysis. In: *Proceedings of the Conference on Modeling and Simulation in Biology*, pp. 147–151. Linköping, Sweden
- Nedbal L, Březina V, Adamec F, Štys D, Oja V, Laisk A and Govindjee (2003) Negative feedback regulation is responsible for the non-linear modulation of photosynthetic activity in plants and cyanobacteria exposed to a dynamic light environment. *Biochim Biophys Acta* 1607: 5–17
- Nedbal L, Březina V, Červený J and Trtílek M (2005) Photosynthesis in dynamic light: Systems biology of unconventional chlorophyll fluorescence transients in *Synechocystis* sp. PCC6803. *Photosynth Res* 84: 99–106
- Nedbal L, Červený J, Rascher U and Schmidt H (2007) E-photosynthesis: a comprehensive modeling approach to understand chlorophyll fluorescence transients and other

- complex dynamic features of photosynthesis in fluctuating light. *Photosynth Res* 93: 223–234
- Okino MS and Mavrouniotis ML (1998) Simplification of mathematical models of chemical reaction systems. *Chem Rev* 98: 391–408
- Poolman M, Assmus H and Fell D (2004) Applications of metabolic modelling to plant metabolism. *J Exp Bot* 55: 1177–1186
- Rios-Esteva R and Lange BM (2007) Experimental and mathematical approaches to modeling plant metabolic networks. *Phytochemistry* 68: 2351–2374
- Rodriguez N, Donizelli M and Le Novère N (2007) SBML-Editor: effective creation of models in the Systems Biology Markup Language (SBML). *BMC Bioinformatics* 8: 79
- Rugh WJ (1996) *Linear System Theory*. Prentice-Hall, NJ, USA
- Shapiro BE, Hucka M, Finney A and Doyle J (2004) MathSBML: a package for manipulating SBML-based biological models. *Bioinformatics* 20: 2829–2831
- Schmidt H and Jirstrand M (2006) Systems biology toolbox for MATLAB: a computational platform for research in systems biology. *Bioinformatics* 22: 514–515
- Skogestad S and Postlethwaite I (1996) *Multivariable Feedback Control*. Wiley, Hoboken, NJ, USA
- Zhu X-G, de Sturler E and Long SP (2007) Optimizing the distribution of resources between enzymes of carbon metabolism can dramatically increase photosynthetic rate: a numerical simulation using an evolutionary algorithm. *Plant Physiol* 145: 513–526

Chapter 3

Modeling Light Harvesting and Primary Charge Separation in Photosystem I and Photosystem II

Rienk van Grondelle*

*Department of Biophysics, Faculty of Sciences, Vrije Universiteit, De Boelelaan 1081,
1081 HV Amsterdam, The Netherlands*

Vladimir I. Novoderezhkin

*A. N. Belozersky Institute of Physico-Chemical Biology, Moscow State University,
Leninskie Gory, 119992, Moscow, Russia*

Jan P. Dekker

*Department of Biophysics, Faculty of Sciences, Vrije Universiteit, De Boelelaan 1081,
1081 HV Amsterdam, The Netherlands*

Summary.....	34
I. Introduction.....	34
II. Physical Models of Energy Transfer.....	35
A. Collective Electronic Excitations.....	35
B. Exciton–Phonon Coupling and Spectral Line Shapes.....	36
C. Modified Redfield and Generalized Förster Theories.....	36
D. Mixing of the Excited and Charge Transfer States.....	39
III. Exciton Spectra and Energy Transfer in Photosystem I (PS I) Core.....	40
A. Extraction of the Site Energies Using Evolutionary-based Search for PS I Core.....	40
B. Assignment of the Red States and Identification of the Reaction Center (RC) Band.....	40
C. Time Scales of Energy Transfer.....	41
IV. Excitation Dynamics in Major Light Harvesting Complex II (LHCII).....	41
A. Simultaneous Fit of Linear Spectra and Nonlinear Transient Absorption Kinetics in LHCII.....	41
B. Visualization of Excitation Dynamics.....	42
C. Comparing the Exciton Model and Single Molecule Spectra.....	44
V. Energy Transfers and Primary Charge Separation in Photosystem II Reaction Center.....	44
A. Simultaneous Fitting of Linear Spectra for Normal and Modified RCs.....	44
B. Mixing with CT States: Multiple Charge Separation Pathways.....	47
C. Verification of the Model from the Fit of Time-dependent Kinetics.....	49
VI. Concluding Remarks.....	50
Acknowledgments.....	50
References.....	50

* Author for correspondence, e-mail: rienk@nat.vu.nl

Summary

We discuss how the light harvesting in photosystem I, photosystem II and in light-harvesting complex II can be modeled at a quantitative level by taking into account the exciton structure of the chromophores in the pigment-protein complexes, static (conformational) disorder, and coupling of electronic excitations and charge-transfer (CT) states to fast nuclear motion. We show examples of simultaneous fitting of linear and nonlinear (time-dependent) spectral responses based on the modified Redfield theory that resulted in a consistent physical picture of the energy and electron transfer reactions. This picture (including the time scales and pathways of energy and charge transfer) allows a visualization of the excitation dynamics, thus leading to a deeper understanding of how photosynthetic pigment-proteins perform their function in harvesting of solar energy.

I. Introduction

In the primary steps of photosynthesis, solar photons are absorbed by a complex system of membrane-associated pigment-proteins (light-harvesting antenna) and the electronically excited state is efficiently transferred to a reaction center (RC), where it is converted into the primary charge-separated state that initiates creating of a transmembrane electro-chemical potential difference (Van Grondelle et al., 1994; Van Amerongen et al., 2000). In plant photosynthesis, antenna complexes consist of chlorophylls (Chl) as main light-harvesting pigments, carotenoids with both light-harvesting and photoprotective functions and other cofactors bound to the proteins. Electron crystallography studies revealed intermediate- and high-resolution structures of the major light-harvesting complex LHCII (Kühlbrandt et al., 1994; Liu et al., 2004; Standfuss et al., 2005), the core complexes of cyanobacterial photosystem I (PS I) (Jordan et al., 2001) and photosystem II (PS II) (Zouni et al., 2001; Kamiya and Shen, 2003; Ferreira et al., 2004; Loll et al., 2005) and of a PSI-LHCI supercomplex from plants (Ben-Shem et al., 2003; Amunts et al., 2007). All these complexes

bind a large number of chlorophylls, from 36 in the PS II core to 168 in the PS I-LHCI supercomplex, more or less arranged in two parallel layers close to the stromal or the lumenal surface of the membrane. The distance between nearest-neighbour pigments can be as short as 9–10 Å, thus giving rise to strong pigment–pigment interactions. As a result, the whole antenna is generally characterized by a complicated manifold of excited states, including collective electronic excitations (excitons) with a high degree of delocalization in combination with more localized excitations of weakly coupled pigments.

Modulation of the electronic transition energies (generally different) by slow conformational motion of the protein matrix results in additional disorder of the site energies within a single complex (thus producing more localized exciton wavefunctions). Different disorder patterns determined by conformational changes are viewed in conventional bulk spectroscopy (with ensemble averaging) as inhomogeneous broadening. The conformational dynamics can be monitored directly using single-molecule techniques (Moerner, 2002; Barkai et al., 2004).

Coupling of excitations to fast nuclear motions (intra- and interpigment vibrations, phonons) results in: (i) homogeneous broadening of the electronic transition spectra, (ii) their red shift due to reorganization effects (associated with changes in equilibrium position of the nuclear modes after electronic excitation), (iii) a further decrease of the delocalization size due to polaron effects, and (iv) the transfer of electronic excitation within the excited state manifold, including fast (fs) relaxation between exciton states within strongly-coupled clusters and slower (ps) energy migration between clusters or monomeric sites. In native antenna complexes, excitations

Abbreviations: CD – circular dichroism; Chl – chlorophyll; Chlz – Chl bound at the periphery of the reaction center of photosystem II; CT – charge-transfer state; FL – fluorescence; FLN – fluorescence line-narrowing; LD – linear dichroism; LHCII – light-harvesting complex II; OD – optical density (also referred to as absorption); P – special pair of Chls in reaction center; Phe – pheophytin; PR – participation ratio; PS I – photosystem I; PS II – photosystem II; Q_y , Q_x – lowest electronic transitions of Chl and Phe; RC – reaction center; TA – transient absorption; ZPL – zero-phonon line

are coupled to a continuum of low-frequency phonons and to several dozens of high-frequency vibrational modes, allowing energy transfer between excited states belonging to the same or to different spectral bands. This energy transfer is the basic mechanism of photosynthetic light-harvesting, producing ultrafast cascading from higher- to lower-energy states, an effective energy migration in the antenna and the delivery of excitation energy to the RC. Since the biochemical isolation of antenna complexes and the discovery of their structure, the fast energy transfer and primary charge separation events have been studied using a variety of advanced laser spectroscopic methods, including time-resolved (sub-100 fs) nonlinear techniques together with theoretical modeling (see for a review Dekker and Van Grondelle, 2000; Van Amerongen et al., 2000; Gobets and Van Grondelle, 2001; Renger et al., 2001; Diner and Rappaport, 2002; Van Amerongen and Dekker, 2003; Van Grondelle and Gobets, 2004; Renger and Schlodder, 2006; Savikhin, 2006; Van Grondelle and Novoderezhkin, 2006).

In this chapter we show how the light harvesting in PS I, PS II and LHCI can be modeled at a quantitative level by taking into account the exciton structure of the antenna, static (conformational) disorder, and coupling of electronic excitations and charge-transfer (CT) states to fast nuclear motion in a pigment-protein complex. Modeling of spectra of the PS I core complex has led to an understanding of the exciton structure and time scales of energy transfer. Simultaneous fittings of linear and nonlinear (dependent on the excited state evolution) spectral responses for the LHCI complex and for the isolated RC complex of PS II have been performed at a quantitative level using modified Redfield theory. The consistent physical picture of energy and electron transfers emerging from these models allowed a visualization of the excitation dynamics.

II. Physical Models of Energy Transfer

A. Collective Electronic Excitations

The possibility of effective light harvesting in photosynthesis is connected with the existence of relatively long-lived (nanoseconds) excited states of Chls with high cross-section for light absorption. The elementary excitation of the antenna

is described by the wavefunction $|n\rangle$, which correspond to excitation of the n -th Chl. Quantum mechanics allows a superposition of such wavefunctions, i.e. $c_1|n_1\rangle + c_2|n_2\rangle + \dots$, where one elementary excitation is shared between a number of molecules. Such a collective excitation (denoted ‘exciton’) is different from independently excited molecules n_1, n_2, \dots due to correlation (‘coherences’) between them given by $c_1^*c_2$. Such coherences can be produced if the electronic Hamiltonian contains off-diagonal terms, i.e. $H \sim |n_2\rangle\langle n_1|$. In this coherent state one molecule ‘knows’ about the excitation of its neighbours. This dramatically changes the spectrum of a pigment aggregate as well as the energy transfer dynamics. In natural antenna complexes these features produce more efficient light absorption, faster conversion from short- to long-wavelength spectral bands, and increase the irreversible trapping of excitations by the RC.

The Hamiltonian of the antenna in the basis of the local excited-state wavefunctions $|n\rangle$ is:

$$H = \sum_{n=1}^N E_n |n\rangle\langle n| + \sum_{n \neq m}^N M_{nm} |n\rangle\langle m| \quad (3.1)$$

where N is the number of Chls in the antenna, E_n is the electronic transition energy of the n -th Chl molecule (for simplicity we only consider the lowest excited state of the chlorophyll, corresponding to the Q_y transition), M_{nm} is the interaction energy between the n -th and m -th molecules. The off-diagonal couplings M_{nm} produce new (collective) eigenstates delocalized over a number of Chls instead of excitations of individual pigments. The energies ω_k and wavefunctions $|k\rangle$ of the exciton eigenstates can be obtained by diagonalization of the Hamiltonian (Eq. 3.1):

$$H = \sum_{k=1}^N \omega_k |k\rangle\langle k|; \quad |k\rangle = \sum_{n=1}^N c_n^k |n\rangle \quad (3.2)$$

where the collective exciton states $|k\rangle$ contain a coherent superposition of the individual molecular excitations $|n\rangle$. The wavefunction amplitudes c_n^k reflect the participation of the n -th site in the k -th exciton state.

Generally the energies ω_k of the exciton states exhibit some shifts from the site energies E_n due to exciton splitting (determined by

couplings M_{nm}). The resulting exciton band is then given by a manifold of N discrete exciton transitions. Interaction with phonons induces a homogeneous broadening (in combination with additional shifting) of the corresponding spectral lines (as described in the next section).

B. Exciton-Phonon Coupling and Spectral Line Shapes

The line shape corresponding to excitation of the k -th exciton level (from the manifold of N one-exciton levels) is given by the coupling of this level to fast nuclear modes (low-frequency phonons determined by collective modes of the pigment-protein matrix and intramolecular high-frequency vibrations). Absorption (OD) and fluorescence (FL) spectra of the whole complex are then given by the sum of contributions from all exciton components:

$$\begin{aligned}
 OD(\omega) &= \omega \sum_k d_k^2 \operatorname{Re} \int_0^\infty A_k(t) dt \\
 FL(\omega) &= \omega \sum_k P_k d_k^2 \operatorname{Re} \int_0^\infty F_k(t) dt \quad (3.3) \\
 A_k(t) &= e^{i(\omega - \omega_k)t - g_{kkkk}(t)} \\
 F_k(t) &= e^{i(\omega - \omega_k)t + 2i\lambda_{kkkk}t - g_{kkkk}^*(t)}
 \end{aligned}$$

where P_k denotes the steady-state population and d_k represents the transition dipole moment of the k -th exciton state. The function $g_{kkkk}(t)$ determines the line-broadening of the k -th exciton state due to exciton-phonon coupling, λ_{kkkk} is the corresponding reorganization energy. These quantities are related to the exciton-phonon spectral density $C(\omega)$ (Mukamel, 1995; Meier et al., 1997; Zhang et al., 1998):

$$\begin{aligned}
 g_{kk'k''k'''}(t) &= - \int_{-\infty}^{\infty} \frac{d\omega}{2\pi\omega^2} C_{kk'k''k'''}(\omega) \\
 &\times \left[\coth \frac{\omega}{2k_B T} \times (\cos \omega t - 1) \right. \\
 &\quad \left. - i(\sin \omega t - \omega t) \right]
 \end{aligned}$$

$$\lambda_{kk'k''k'''} = \int_{-\infty}^{\infty} \frac{d\omega}{2\pi\omega} C_{kk'k''k'''}(\omega) \quad (3.4)$$

$$C_{kk'k''k'''}(\omega) = \sum_n c_n^k c_n^{k'} c_n^{k''} c_n^{k'''} C_n(\omega)$$

where T is temperature, k_B is the Boltzmann constant, $C_n(\omega)$ is the spectral density in the site representation corresponding to phonon-induced modulation of the transition energy of the n -th site (we suppose that modulations of different sites are uncorrelated and we do not include modulations of the pigment-pigment interaction energies).

Equation (3.3) yields the homogeneous line shape. In the presence of static disorder (disorder of the site energies E_n and couplings M_{nm}) the homogeneous FL profiles should be averaged over a random distribution of E_n and M_{nm} that will perturb energies and eigenfunctions of the exciton states. Nonlinear spectral responses can be expressed in terms of the line-broadening functions (Eq. 3.4) as well, for example pump-probe (Zhang et al., 1998; Renger and Marcus, 2002; Novoderezhkin et al., 2004a, 2005a, b; Raszewski et al., 2005) and Stark spectra (Novoderezhkin et al., 2007), photon echoes (Meier et al., 1997), and 2D echoes (Cho et al., 2005).

The spectral density needed to evaluate the spectral responses can be obtained from molecular dynamics simulations (Damjanović et al., 2002a) or can be extracted from experiments, for example from hole-burning (Pieper et al., 1999), or fluorescence line-narrowing (FLN) data (Peterman et al., 1997, 1998). In Fig. 3.1 we show the $C_n(\omega)$ function for the Chl *a* molecules in the LHCII complex obtained from FLN data (Peterman et al., 1997; Novoderezhkin et al., 2004a).

C. Modified Redfield and Generalized Förster Theories

When the spectral density $C_n(\omega)$ is specified, the functions (Eq. 3.4) provide a unified tool for calculating not only spectral shapes (Eq. 3.3) but also energy transfer rates. Thus, the rate of population transfer from the state k' to the state k expressed in terms of line-broadening functions (Eq. 3.4) is (Zhang et al., 1998; Yang and Fleming, 2002):

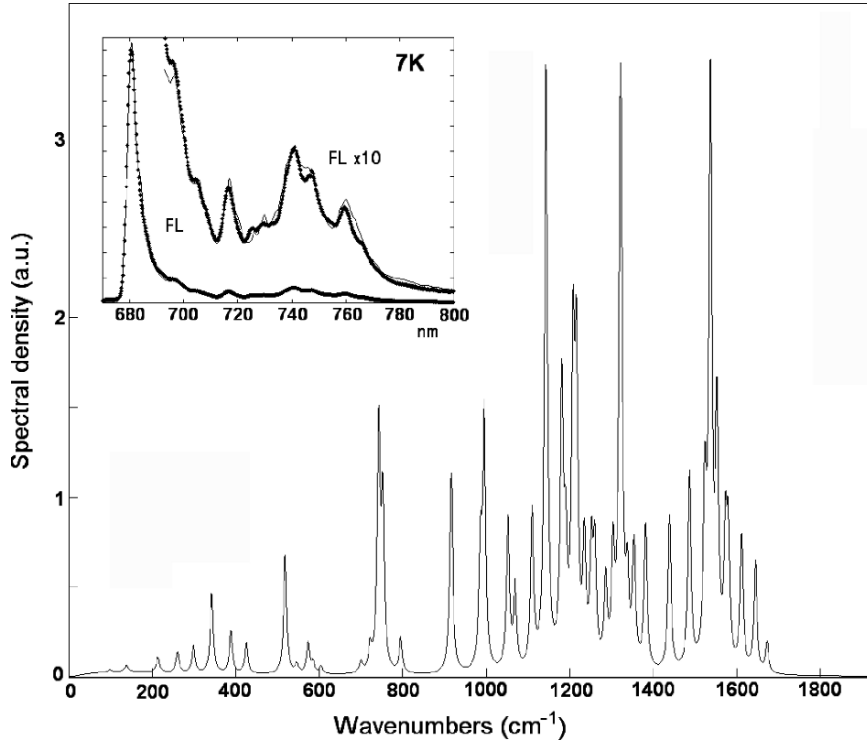


Fig. 3.1. Experimental exciton-phonon spectral density $C_n(\omega)$ for Chl *a* obtained using low-temperature FLN spectra of LHCII. The spectral density is modeled as a sum of an over-damped Brownian oscillator and 48 high-frequency modes with Huang-Rhys factors taken from the FLN experiment (Peterman et al., 1997) and adjusted from the fit of non-selective FL profiles (Novoderezhkin et al., 2004a). The insert shows the 7 K non-selective (inhomogeneously broadened) FL spectrum for LHCII calculated with this spectral density (thin line) together with the measured one (points)

$$R_{kk'k'} = 2 \operatorname{Re} \int_0^\infty dt A_k(t) F_{k'}^*(t) V_{kk'}(t)$$

$$V_{kk'}(t) = \exp(2g_{k'k'kk}(t) + 2i\lambda_{k'k'kk}t) \times [\ddot{g}_{kk'k'k}(t) - \{\dot{g}_{k'kk'k'}(t) - \dot{g}_{k'kkk}(t) + 2i\lambda_{k'kk'k'}\} \times \{\dot{g}_{k'k'kk'}(t) - \dot{g}_{kkkk}(t) + 2i\lambda_{k'k'kk'}\}] \quad (3.5)$$

where $F(t)$ and $A(t)$ are line-shape functions corresponding to fluorescence of the donor state and absorption of the acceptor, respectively, defined by Eq. (3.3), while V describes the electrostatic interaction between donor and acceptor. Note that Eq. (3.5) is valid for arbitrary delocalization of the donor and acceptor states and arbitrary strong coupling to phonons, but polaron effect are neglected (the polaron-induced localization

length is supposed to be larger than the disorder-induced localization size). This approach is usually denoted as modified Redfield (Yang and Fleming, 2002).

If the donor and acceptor states are localized at the m -th and n -th sites (i.e. $c_m^k = 1$ and $c_n^k = 1$) then V is given by

$$V_{kk'}(t) = |M_{nm}|^2 \quad (3.6)$$

where M_{nm} is the interaction energy corresponding to a weak coupling between the localized sites n and m . Switching to the Fourier-transforms of $F(t)$ and $A(t)$ we can rewrite the integral in a form of donor-acceptor spectral overlap (Yang and Fleming, 2002). Thus, we obtain the Förster formula (Förster, 1965).

The standard Förster formula can be generalized to the case of energy transfer between two weakly connected clusters (Novoderezhkin and Razjivin, 1994, 1996; Sumi, 1999; Scholes and

Fleming, 2000; Jang et al., 2004). The rate of energy transfer from the k' -th exciton state of one cluster to the k -th state of the other cluster is given by Eq. (3.5) with

$$V_{kk'}(t) = \left| \sum_{n,m} c_n^k M_{nm} c_m^{k'} \right|^2 \quad (3.7)$$

where n and m designate molecules belonging to different clusters. In this generalized Förster formula, the donor and acceptor states k' and k can have an arbitrary degree of delocalization (corresponding to arbitrarily strong excitonic interactions within each cluster), but the inter-cluster interactions M_{nm} are supposed to be weak, thus producing only a small spatial overlap between the k' and k wavefunctions.

In the case of significant spatial overlap of the wavefunctions $c_m^{k'}$ and c_n^k the transfer rate cannot be calculated by treating M_{nm} as a perturbation, as in Eqs. (3.6) and (3.7). In this case the energy transfer should be calculated on the basis of the exciton states of the whole system. The rates of relaxation between these states (with arbitrary wavefunction overlap) are given by the modified Redfield theory (Eq. 3.5).

In Fig. 3.2 we compare the transfer rates between two Chl molecules (as a function of the energy gap $E_1 - E_2$ between them) calculated using the Förster (Eq. 3.6) and modified Redfield (Eq. 3.5) expressions assuming a realistic spectral density (Fig. 3.1). The difference between the two rates is compared with the delocalization length (N_{del}) calculated as the inverse participation ratio that varies from 1 (in the localized limit) to 2 (uniform delocalization over two molecules).

In the case of strong coupling ($M_{12} = 255 \text{ cm}^{-1}$) Redfield rates are higher than predicted by the Förster theory. Deviation between the two rates is proportional to the deviation of delocalization length from the localized limit. For large energy gaps ($E_1 - E_2 > 5M_{12}$) corresponding to the localized limit ($1 < N_{\text{del}} < 1.1$) the Förster and Redfield theories give approximately the same rate.

For moderate coupling ($M_{12} = 55 \text{ cm}^{-1}$) the two theories give the same results everywhere, but for small gaps ($E_1 - E_2 < 5M_{12} = 275 \text{ cm}^{-1}$) excitations become delocalized and Redfield theory gives bigger rates.

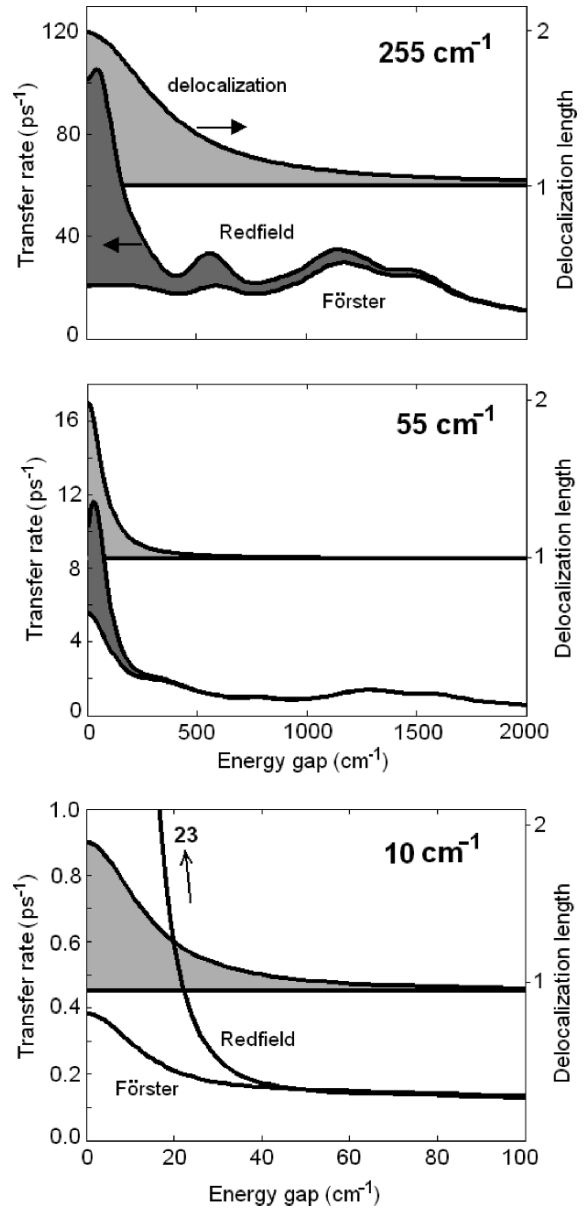


Fig. 3.2. The energy transfer rate as a function of the energy gap between two molecules calculated with the Förster and modified Redfield theories (only downhill rates are shown). The delocalization length N_{del} is calculated as the inverse participation ratio of the exciton wavefunctions. The $N_{\text{del}} = 1$ line is shown to highlight the deviations from the localized limit. The three frames correspond to strong, moderate and weak coupling, i.e. $M_{nm} = 255, 55$, and 10 cm^{-1} (the energy gaps range is $0-2,000 \text{ cm}^{-1}$ for strong and moderate coupling and $0-100 \text{ cm}^{-1}$ for weak coupling). We use the exciton-phonon spectral density shown in Fig. 3.1. The relaxation rates have been calculated for 77 K. The specific non-monotonous dependence of the rates on the energy gap is determined by the shape of the phonon wing

Both for strong and moderate coupling the Redfield theory predicts two to five times faster transfer in the isoenergetic case ($E_1 - E_2 = 0$) due to delocalization. But this deviation of the Redfield rates from the Förster limit become anomalously (and unrealistically) high in the weak coupling limit. Thus, for $M_{12} = 10 \text{ cm}^{-1}$ we got localized excitations and transfer rates of about $0.15 - 0.4 \text{ ps}^{-1}$ (time constants of 2.5–7 ps) predicted both by the Förster and Redfield theories (see lower frame in Fig. 3.2). On the other hand, for very small gaps ($E_1 - E_2 < 20\text{--}30 \text{ cm}^{-1}$) the Redfield theory predicts an abrupt increase in the transfer rate up to 23 ps^{-1} (time constant of 40 fs) in the $E_1 - E_2 = 0$ limit, i.e. we can have two to three orders of magnitude increase in transfer rate! Formally, such fast transfer is possible if the excitation is delocalized over two isoenergetic molecules (even if these molecules are well separated in space and weakly interacting). In reality such kind of delocalization will be destroyed by polaron effects (dynamic localization), a feature that is not included into the Redfield approach. Obviously, the Förster theory (where localization is assumed *a priori*) gives more correct results in this case.

To avoid the weak-coupling artifact of the Redfield theory a combined Redfield–Förster theory can be used (Yang et al., 2003). In this approach the relaxation dynamics within strongly coupled clusters (with intra-cluster interactions $M_{nm} > M_{cr}$) is calculated with the modified Redfield theory, whereas transfers between these clusters (with inter-clusters couplings $M_{nm} < M_{cr}$) are modeled by the generalized Förster theory. The coupling cutoff value M_{cr} is about $20\text{--}30 \text{ cm}^{-1}$ (Yang et al., 2003; Cho et al., 2005).

D. Mixing of the Excited and Charge Transfer States

In complexes containing RCs (and in Chl aggregates with small intermolecular distances) excited states can be mixed with CT states. Generally, CT states are characterized by stronger couplings to phonons and, consequently, larger displacements along nuclear coordinates as compared to the excited states. Thus, any pair of exci-

ton and CT states is represented by two potential surfaces with different displacements along effective nuclear coordinates. The mixing of the two surfaces near their crossing point will produce a redistribution of the dipole moments of the two states. This gives rise to some borrowing of the transition dipole strength from the exciton state (making the CT state weakly allowed), and borrowing of the static dipole from the CT state (increasing the amplitude of the Stark signal). This mixing will also induce the transfer from the exciton to the CT state (and the back transfer). Relaxation along the nuclear coordinates within the exciton and CT potentials causes a dynamic localization of the excitation/CT-state near the bottom of the corresponding surfaces.

The Förster theory allows a calculation of the exciton-CT transfer rates supposing a complete localization of the two states without taking into account the mixing of their wavefunctions (thus, excluding all spectral consequences of such mixing, like the shape of the red wing of the OD spectrum, the broadening of the FL profile, and the increase of the Stark amplitude).

In the opposite limit the coupling between the two states is supposed to be independent of the nuclear coordinates, giving rise to a uniform mixing of the two potential surfaces. Then the relaxation rates between the mixed eigenstates as well as the spectral features induced by such mixing can be calculated using the modified Redfield theory where CT is included as one more state, formally equivalent to the excited states in Eq. (3.1). This approach is valid if the reorganization energy associated with the relative displacements of the excited- and CT states is smaller than their coupling. Otherwise the degree of mixing will be overestimated, especially in the case of a small energy gap between the two states.

Extrapolation between these two limiting cases (localized and strongly mixed, described by the Förster and modified Redfield theories, respectively) is possible by including explicitly the dynamics along a limited number of effective nuclear coordinates. The relaxation in such a system can be described using the Redfield theory on the basis of electron-vibrational eigenstates (Jean and Fleming, 1995; Renger and May, 1997; Novoderezhkin et al., 2004b).

III. Exciton Spectra and Energy Transfer in Photosystem I (PS I) Core

A. Extraction of the Site Energies Using Evolutionary-based Search for PS I Core

Following the discovery of the structure of the PS I core from the cyanobacterium *T. elongatus* (Jordan et al., 2001) several attempts have been made to model the exciton spectra of the complex (Byrdin et al., 2002; Damjanović et al., 2002b; Sener et al., 2002; Yang et al., 2003; Brüggemann et al., 2004), where contributions from the 96 Chls are superimposed producing a single broad Q_y absorption band around 680 nm. Although the pigment–pigment coupling can be calculated from the high-resolution structure, the site energies reflecting the shifted transition energies of individual Chls, each in a different protein environment, are not known. They should be determined either by semiempirical quantum chemical calculations (Damjanović et al., 2002b) or by fitting linear spectra (Byrdin et al., 2002; Brüggemann et al., 2004; Schlodder et al., 2007). High-accuracy fitting of the linear spectra (absorption, circular dichroism, and linear dichroism) over a wide temperature range based on an evolutionary strategy allowed a rather precise determination of the site energies for a number of Chls (Brüggemann et al., 2004). In addition, there are Chls whose site energies cannot be unambiguously determined from

the fit. Thus, at the moment there does not exist a unique exciton model for the PS I core. Different theoretical approaches to model the spectra and excitation dynamics in PS I and their relation to experimental data have been reviewed by Renger and Schlodder (2006).

An evolutionary-based fit of low-temperature absorption (OD), linear dichroism (LD), and circular dichroism (CD) spectra of PS I is shown in Fig. 3.3. The evolutionary strategy includes generating of the site energies from initial sets by adding randomly chosen energy deviations followed by a fitness calculation to build up the next generation (Brüggemann et al., 2004). The line shapes were obtained using the standard Redfield theory (Redfield, 1965).

B. Assignment of the Red States and Identification of the Reaction Center (RC) Band

The structure of the PS I core of *T. elongatus* reveals the presence of closely spaced Chl clusters, i.e. dimers (A38–A39 and the special pair S1–S2 of the RC) and trimers (B31–B32–B33 and A31–A32–B7). CT states with enhanced electron–phonon coupling can be present within these clusters. Enhanced electron–phonon coupling of these CT states is accompanied by an increase in the reorganization energy, thus producing an additional red shift of the exciton transitions mixed with the CT states.

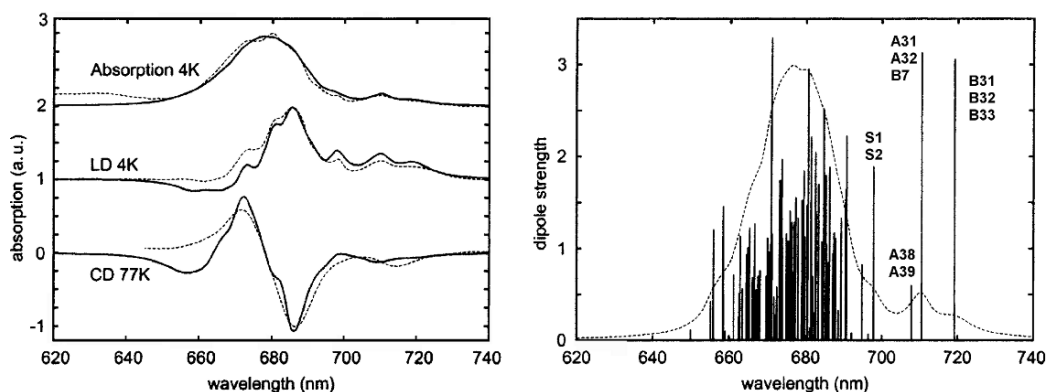


Fig. 3.3. *Left frame*: Fitting of the low-temperature Optical Density (OD; also referred to as 'Absorbance'), Liner Dichroism (LD) and Circular Dichroism (CD) spectra of the PS I core complex of *Thermosynechococcus elongatus* (Brüggemann et al., 2004). Measured spectra (dashed lines) are shown together with the calculated ones (solid lines) obtained by an evolutionary search of the site energies. *Right frame*: Wavelengths and dipole strengths of the exciton components (thin bars) that contribute to the calculated 4K OD (dashed line). The Chls which mainly contribute to the four lowest exciton states are indicated (Brüggemann et al., 2004)

Long-wavelength spectral forms found in PS I complexes are usually assigned to such exciton transitions within strongly coupled Chl clusters (Frese et al., 2002; Karapetyan et al., 2006).

Earlier hole-burning studies of PS I complexes from spinach suggested that there are, at least, two types of Chl *a* molecules in the PS I complex which are characterized by larger electron-phonon couplings (as compared to the bulk Chls *a*) because of the CT character in their electronic excited states (Gillie et al., 1989). Later, hole burning studies of PS I from *T. elongatus* (Zazubovich et al., 2002) showed increased exciton-phonon coupling (with respect to the bulk Chls) for the primary donor and for Chl states peaking at 708, 715, and 719 nm. To account for this type of heterogeneity, different types of spectral densities $C_n(\omega)$ must be used in the modeling: one for the primary electron donor (special pair), one for the Chl dimers and trimers with CT character, and one for the many (bulk) Chls without CT character (Yang et al., 2003; Brüggemann et al., 2004).

According to Gobets et al. (2003) and Brüggemann et al. (2004), the 719-nm absorption is determined by the B31–B32–B33 trimer, the 710 nm line(s) are due to the A38–A39 pair and the A31–A32–B7 trimer, and the 700 nm band corresponds to the lowest exciton level of the special pair S1–S2 (see Fig. 3.3). The higher exciton level of the special pair is moved into the main absorption band, thus improving the energy transfer from the bulk Chls to RC.

In a model based on quantum chemical calculations (Damjanović et al., 2002b; Yang et al., 2003) the two Chls of the special pair are suggested to be strongly asymmetric in energy, putting the lowest exciton state at 710 nm.

C. Time Scales of Energy Transfer

Computation of time-dependent spectra (based on the standard Redfield theory and using the exciton model shown in Fig. 3.3) yielded components of 0.4, 1.0, 3.4, and 10 ps upon short-wavelength excitation at 650 nm (Brüggemann et al., 2004). The fast components of 0.4 and 1.0 ps describe the equilibration within bulk Chls and some energy transfer to the red states due to local energy relaxation from the directly excited higher states to the lower exciton states of the

red Chls. The 3.4 and 10 ps components characterize the equilibration of the bulk Chls with the red Chls at 710 and 719 nm, respectively. It was also concluded that slower than 10 ps components correspond to the energy trapping by the RC. These calculated time constants and corresponding decay associated spectra are in good agreement with the measured ones (Brüggemann et al., 2004). Notice that modeling based on the site energies obtained from quantum chemical calculations (Yang et al., 2003) gave similar components but the 10 ps component was not reproduced.

In the case of red excitation at 710 nm there are 0.5 and 1.7 ps components reflecting transfers from the 710 nm Chl states to the main absorption band. This is followed by a slower equilibration from the 710 nm states to the 719 nm state with 10 ps. These calculated components are close to the measured 0.7 and 10 ps ones (Gobets et al., 2003; Brüggemann et al., 2004).

The modeling (Brüggemann et al., 2004) does not include energy trapping by RC, but the experimental data suggest that there is a competition between energy transfer to the 719 nm pool and energy trapping by the RC during the 10 ps process (Gobets et al., 2003; Van Grondelle and Gobets, 2004; Savikhin, 2006). The 38 ps component reflects slow trapping after quasi-equilibrium with the red 719 nm Chls is reached. The corresponding fluorescence decay spectrum is peaking near 719 nm (Gobets et al., 2003; Van Grondelle and Gobets, 2004).

IV. Excitation Dynamics in Major Light Harvesting Complex II (LHCII)

A. Simultaneous Fit of Linear Spectra and Nonlinear Transient Absorption Kinetics in LHCII

The structure of the LHCII complex has recently been obtained at 2.72 Å (Liu et al., 2004) later followed by a structure at 2.5 Å resolution (Standfuss et al., 2005). The 14 chlorophylls (Chl) present in each monomeric subunit of LHCII were unambiguously assigned to 8 Chls *a* and 6 Chls *b* and no indication for mixed binding sites was found. Also the orientations of the Chl molecules were determined allowing a quantitative calculation of the spectral and

dynamic properties of the complex. Only the site energies for Chls remain unspecified and therefore should be determined from the spectroscopic data. Following the discovery of the structure it was demonstrated that the unperturbed transition energies for 14 Chls of each monomeric subunit can be extracted from a simultaneous fit of the linear spectra and TA kinetics upon different excitation conditions using the modified Redfield approach (Novoderezhkin et al., 2005a).

The arrangement of the Chls within the LHCII trimer is shown in Fig. 3.4D. On the stromal side there are two tightly packed clusters of Chls *a*, i.e. the trimer *a*610–*a*611–*a*612 and the dimer *a*602–*a*603. They are closely connected with three Chls *b* on the stromal side, Chls *b*601, *b*608, and *b*609. The structure suggests significant coupling between *b*601 and *b*609 from adjacent monomeric subunits. So, one can consider the *b*601–*b*608–*b*609 group (encircled in Fig. 3.4D) as a *b*-cluster, which is expected to have a short excited-state lifetime due to excitation energy transfer to the *a*610–*a*611–*a*612 and *a*602–*a*603 clusters of the two subunits. In the Chl *a*-region one can expect fast exciton relaxation within the *a*610–*a*611–*a*612 and *a*602–*a*603 clusters as well as slower hopping between these clusters.

On the lumenal side there are two groups of pigments i.e. the *a*613–*a*614 dimer and the *b*605–*b*606–*b*607–*a*604 tetramer (encircled in Fig. 3.4D). The *b*605, *b*606, *b*607, and *a*604 sites of the tetramer are weakly connected to the remaining part of the complex. The excited-state dynamics within this cluster should be dominated by fast downhill transfer of excitations from the *b*-sites to the monomeric *a*604 pigment. The latter is weakly coupled to other Chls *a*, and therefore is the best candidate for a long-lived ‘bottleneck’ state in the Chl *b* → Chl *a* energy transfer that was suggested by analysis of experimental TA kinetics upon 660–670 nm excitation (Visser et al., 1996; Kleima et al., 1997; Gradinaru et al., 1998).

Extraction of the site energies from a simultaneous fit of the linear spectra (OD, LD, and FL) has been performed using an evolutionary-based search (Novoderezhkin et al., 2005a). An example of the fit is shown in Fig. 3.4A. The two main absorption peaks at 650 and 675 nm are determined by the Chls *b* and *a*, respectively. Although the number of free parameters is not so

big (i.e. 14 site energies, that are supposed to be the same for each of the three subunits of a trimer) the fit is not unique. About two–three dozens suitable models with different site energies have been found. These sets of site energies have been further verified by fitting of the TA spectra upon 650 and 662 nm excitation.

The kinetics upon 650 nm excitation reflects fast (sub-ps) energy transfer from initially populated *b*-band to the *a*-region around 670–680 nm (Fig. 3.4B). Checking out the models (that survived after the fit of the linear spectra) allowed ruling out those that gave the wrong spectral shape of the TA or failed to reproduce the time scales of energy transfer. But several models still allowed a satisfactory fit. However, most of them could be ruled out after also considering the kinetics upon 662 nm excitation. The 662 nm narrow-band excitation allows selective excitation of the intermediate blue-shifted *a*-states. Thus the kinetics are much more sensitive to the fine structure of the blue wing of the *a*-band. A simultaneous fit of the 650 and 662 nm TA was possible only with one model (shown in Fig. 3.4).

B. Visualization of Excitation Dynamics

Parameters of the model determined from the fit of the spectroscopic data give us the time scales and pathways of energy transfer, thus allowing a visualization of the whole excitation dynamics in the complex. The dynamics in the Chl *a* region is determined by fast (90–300 fs) exciton relaxation within the *a*-clusters: *a*610–*a*611–*a*612, *a*602–*a*603, and *a*613–*a*614. The coupling between these clusters produces slower (250–600 fs) inter-cluster transfers. The Chl *b* region is characterized by a fast relaxation within the stromal-side *b*601–*b*608–*b*609 cluster (100 fs) and sub-ps transfer from this cluster to the *a*-clusters at the stromal-side, i.e. *a*610–*a*611–*a*612 and *a*602–*a*603.

At the lumenal side there is fast population of the *b*605 and *a*604 pigments due to equilibration within the *b*606–*b*607–*b*605–*a*604 group. The *b*605 site is then slowly depopulated via ps transfer to *a*604 or to the *b*601–*b*608–*b*609 cluster at the stromal side. Thus, the *b*605 is a ‘bottleneck’ site responsible for slow (few ps) component in the *b* → *a* transfer. Another, even longer-lived

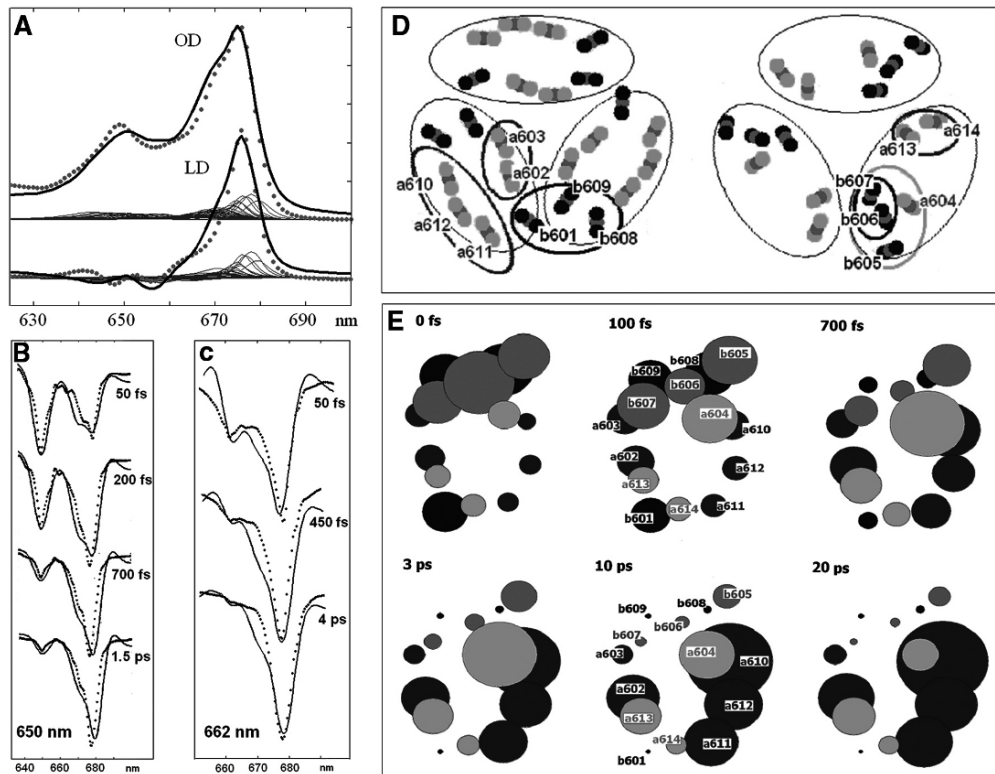


Fig. 3.4. Simultaneous fit of steady-state and time-dependent spectra for LHCII with modified Redfield theory and visualization of the excitation dynamics in the complex (Novoderezhkin et al., 2005a). Panel A: Experimental OD and LD spectra measured for the LHCII trimer at 77 K (points) and calculated ones (solid lines). Calculated spectra are shown together with individual exciton components (thin lines). Panel B: Evolution of the TA spectra upon excitation of Chls *b* (excitation wavelength 650 nm, pulse duration 90 fs, pump-probe delays 50, 200, 700, and 1,500 fs). Measured spectra (points) are shown together with the calculated ones (solid lines). Panel C: Dynamics of the TA upon selective excitation of the intermediate region (662 nm, 180 fs pulses, and 50, 450, and 4,000 fs delays). Experiment (points), and simulation (solid lines). Panel D: Arrangement of chlorophylls within the LHCII trimer at the stromal (*left*) and luminal (*right*) sides. Chlorophylls are represented by the central magnesium and two nitrogen atoms (according to Liu et al., 2004). Clusters of Chls *a*, Chls *b*, and a mixed group containing long-lived intermediate sites are encircled. Panel E: Dynamics of the site populations (averaged over disorder) during 0–20 ps upon 650 nm excitation at 77 K. The Chl sites within one monomeric subunit are shown by circles. Time-dependent area of the circle is proportional to a population of the corresponding site. The monomeric subunit is viewed from the luminal to the stromal side, i.e. Chls from luminal side (shown by grey) are on the top, and stromal-side Chls (shown by black) are behind them

‘bottleneck’ site is *a604*. This site is characterized by a very slow flow of energy to the remaining *a*-sites with time-constants of 40–50 ps.

Figure 3.4E provides a visualization of the site population dynamics related to the positions within a monomeric subunit. The first three frames (0–700 fs) show the excitation energy flow from the stromal-side Chls *b* (*b601*, *b608*, and *b609*) to the *a*-sites and the redistribution of energy within the *a*-clusters. Also redistribution within the luminal-side *b606*–*b607*–*b605*–*a604*

group is clearly seen (with transfer from *b606* to *b607* and *b605* and predominant population of the intermediate *a604* site). The next three frames (3–20 ps) show slow transfer from *a604* (and from the *b606*–*b607*–*b605* cluster) to the quasi-equilibrated *a*-sites. In equilibrium a predominant population of the *a610*–*a611*–*a612* cluster (mostly *a610*) is reached. The location of this cluster on the outer side of the LHCII trimer is likely to provide a good connection with the other subunits of PS II.

C. Comparing the Exciton Model and Single Molecule Spectra

Spectral responses and the dynamics simulated in Fig. 3.4 are averaged over many realizations of the static disorder. These realizations are associated with the passage of the antenna complex through a number of conformational sub-states that are characterized by various disorder patterns (distribution of the site energies) producing spectra with different peak positions and shapes. These spectral fluctuations on the microsecond to second time scale associated with conformational dynamics have for the first time been observed in bacterial antenna complexes (Bopp et al., 1999; Van Oijen et al., 1999; Tietz et al., 1999; Rutkauskas et al., 2004, 2005, 2006; Novoderezhkin et al., 2006). Recently similar data has been obtained for single trimeric LHCII complexes (Krüger et al., in preparation).

Figure 3.5 shows room-temperature FL spectra of single immobilized LHCII complexes. The peak position of the measured FL spectra is fluctuating around the FL maximum of the bulk spectrum. Moreover, a shift of the FL peak is accompanied by specific changes in line shape. Explanation of these features is a challenging problem that is one more test for the exciton model that emerged from the interpretation of the bulk spectra of the LHCII complex (Fig. 3.4).

Remarkably, the observed FL spectral fluctuations can be reproduced with the same model (i.e. with the same site energies, phonon couplings and same disorder value) as used for the calculation of the bulk spectra (Krüger et al., in preparation). In Fig. 3.5 we compare the measured FL profiles with different peak shifts with the calculated spectra. The latter are obtained from the ensemble of FL spectra calculated for different realizations of the disorder. Note that the calculated spectra have essentially the same characteristic line shape as the measured FL profiles with the same peak position.

From this modeling of the single molecule emission spectra of LHCII we concluded that the red shift of the spectrum corresponds to an increasingly more non-uniform distribution of the PR with predominant localization on the *a602* or *a610* pigments (see inserts in Fig. 3.5). The disorder-induced red shift of the *a602* or the *a610* sites breaks the delocalization within

the Chl *a* clusters in the stromal side (i.e. within the *a610*–*a611*–*a612* or the *a602*–*a603* clusters) thus increasing the reorganization shift accompanied by a further red-shifting of the lowest exciton states. As a result the emission on the red side is significantly increased. In realizations with strong disorder the FL spectrum appears to consist of two-components (one from the strongly red-shifted lowest exciton state and one from the next level).

Thus, we conclude that each single molecule spectrum is determined by a specific localization pattern controlled by a conformationally-induced disorder of the site energies.

V. Energy Transfers and Primary Charge Separation in Photosystem II Reaction Center

A. Simultaneous Fitting of Linear Spectra for Normal and Modified RCs

The D1/D2/Cytb₅₅₉ reaction center of Photosystem II (PS II-RC) performs the initial charge separation in oxygenic photosynthesis (Dekker and Van Grondelle, 2000; Diner and Rappaport, 2002; Yoder et al., 2002; Barber, 2003). According to the X-ray structure (Zouni et al., 2001; Kamiya and Shen, 2003; Ferreira et al., 2004; Loll et al., 2005) the PS II-RC comprises eight chlorins and two carotenes participating in excitation energy and electron transfer. Four chlorophyll (Chl) and two pheophytin (Phe) molecules are arranged in two branches associated to the D1 and D2 proteins, respectively, and are located in the central part of the complex. The D1 branch is known to be active in charge separation (Diner and Rappaport, 2002). Two additional Chls are bound at the periphery of the complex at distances of about 24 Å from the nearest core pigments.

The first attempt to explain the spectra and kinetics in the PS II-RC was performed using the so-called ‘multimer model’, based on the idea that, in contrast to the bacterial RC, spectroscopically there is no special pair in the PS II-RC (Durrant et al., 1995; Barter et al., 2003). In the multimer model the transition energies of the six core pigments (P_{D1} , P_{D2} , Chl_{D1} , Chl_{D2} , Phe_{D1} , and Phe_{D2}) were taken to be equal, giving rise to delocalized exciton states. The Redfield relaxation

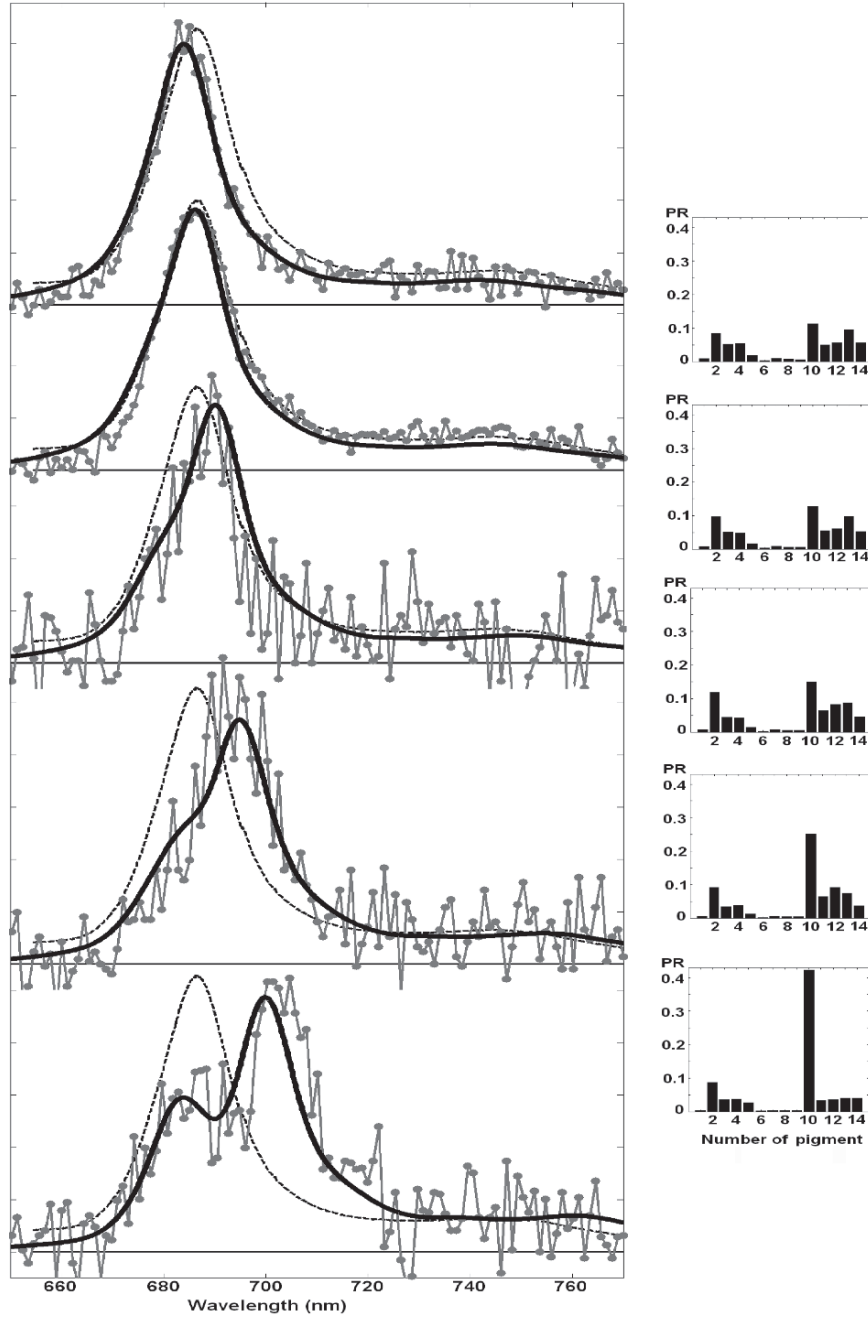


Fig. 3.5. Room-temperature FL spectra of single immobilized LHCII complex (Krüger et al., in preparation). FL profiles measured at different time moments (points connected by lines) are shown together with the averaged FL spectrum (dashed line). Measured profiles shown from top to bottom display different shifts from the bulk spectrum, i.e. from a small blue shift (top spectrum) to increasingly bigger red shifts (three lower spectra). The calculated spectra with the same peak positions are shown for comparison. These spectra are taken from the ensemble of FL spectra calculated for different realizations of the disorder using the same exciton model of LHCII as in Fig. 3.4. *Inserts on the right* show the participation ratio (PR) of the pigments corresponding to the same realizations as the calculated FL spectra. The PR values of the n -th pigment are defined as $PR_n = \sum_k p_k (c_n^k)^4$, where p_k is the steady-state population of the k -th exciton state, c_n^k is the wavefunction amplitude (Eq. 3.2). Numbers from $n = 1$ –14 correspond to pigments from 601 to 614 in the notation of Liu et al. (2004)

theory was then used to model the dynamics within the excited state manifold and its spectral signatures, such as pump-probe (Leegwater et al., 1997; Renger and Marcus, 2002) and photon echo responses (Prokhorenko and Holzwarth, 2000), but the multimer model (with equal site energies) used in this study did not give a good quantitative fit of the spectral shapes. Later the multimer model was replaced by a more realistic model where site energies were extracted from a simultaneous evolutionary-based fit of the linear spectra (OD, LD, CD, and FL) over a wide

temperature range using the modified Redfield approach (Raszewski et al., 2005; Novoderezhkin et al., 2005b, 2007). These site energies were further verified by modelling of the spectra for modified RCs, such as RCs with (i) modified Phe_{D2}, (ii) modified Phe_{D1} and Phe_{D2}, (iii) reduced Phe_{D1}, (iv) so-called 'RC5 complexes' that lack one of the peripheral Chls, and (v) triplet-minus-singlet (T - S) spectra.

An example of the fit is shown in Fig. 3.6. The line shapes have been calculated using the exciton-phonon spectral density taken from the

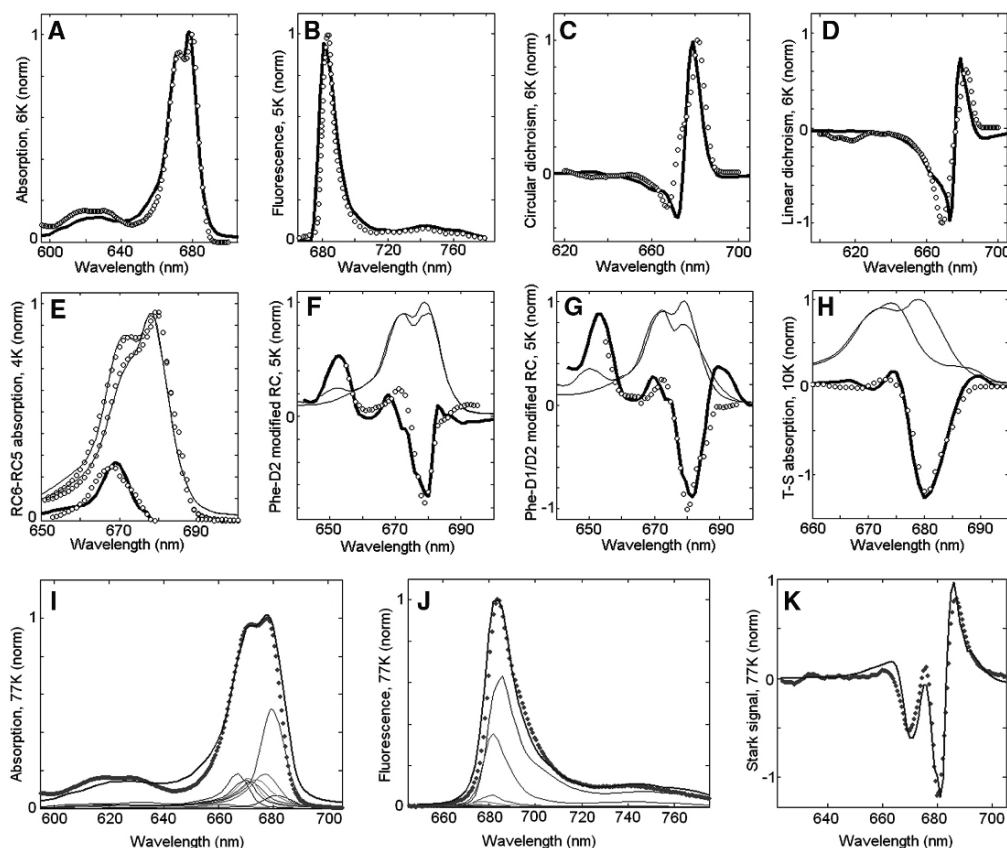


Fig. 3.6. Simultaneous fit of the low-temperature spectra of isolated PS II-RC (Novoderezhkin et al., 2007). Open circles show the experimental data, solid lines (including thick lines in panels A–H and thin lines in E–H) represent calculated spectra. Panels A,C,D: Modeling of the 6 K OD, CD, and LD spectra. Panel B: Modeling of the non-selective FL profile at 5 K. Panel E: Modeling of the 4 K absorption spectra for normal 6-chlorophyll RC (RC6) and for modified RC lacking one of the peripheral Chls (RC5). The calculated RC6, RC5, and difference RC6-RC5 spectra are shown together with the measured ones. Panels F,G: Modeling of absorption changes induced by modification of Phe_{D2} (F) or both Phe_{D2} and Phe_{D1} (G) at 5 K. Thin solid lines show absorption spectra calculated for normal and modified RCs. The latter display a bleaching near 680 nm and a new absorption peak near 650 nm due to the blue shift of the modified Phe. Panel H: Modeling of the triplet minus singlet (T - S) spectra measured at 10 K. The calculated T - S spectrum (thick line) is obtained as the difference between the ground-state absorption (thin line) and absorption without contribution of the Chl_{D1} (thin line), implying localization of the triplet state on Chl_{D1} at 10 K. Panels I,J,K: Simultaneous fit of the 77 K spectra including OD, FL, and Stark spectrum. The calculated OD (I) and FL (J) spectra are shown together with contributions from the individual exciton states (thin lines)

FLN data obtained for the PS II-RC (Peterman et al., 1998). The main absorption band in the 660–690 nm region is determined by the Q_y transitions of the eight pigments. The sub-bands at 670 and 680 nm appear due to different site energies of the pigments (in combination with the exciton splitting and phonon-induced reorganization shifts). The broad absorption at 620 nm is determined by coupling of the Q_y transitions to high-frequency vibrations. The low-temperature FL has its main peak at 680 nm and displays a broad vibrational wing with a maximum at 740 nm.

We notice that the fit of the linear spectra (OD, CD, LD, and FL) is not unique, i.e. there are several models with different site energies that allow a good simultaneous fit of these four spectra. To this end we have extended the fit by modelling also the spectra of modified RCs. This allows a precise determination of the energies of some particular pigments, thus making a determination of the other site energies easier. For example, the difference between RC6 and RC5 absorption (Fig. 3.6E) indicates that the monomeric peripheral Chl_{zs} must have an absorption peak near 670 nm. The spectra of Phe-modified RCs (Fig. 3.6F and D) suggest that both Phe_{D2} and Phe_{D1} contribute to the exciton states that determine the 680 nm absorption peak. The triplet-minus-singlet (T – S) spectrum depends on the energies of the sites which carry the triplet excitation. It is well established that the triplet state at low temperature is localized on the accessory Chl_{D1} (Van Mieghem et al., 1991; Noguchi et al., 1993; Kamlowski et al., 1996; Diner et al., 2001). Thus, the T – S bleaching at 680 nm (Fig. 3.6H) suggests that Chl_{D1} contributes to this spectral region. On the other hand, P_{D1} peaks most likely at about 672 nm (Diner et al., 2001).

The lowest state (with an absorption peak near 682 nm – see Fig. 3.6I, J) corresponds to a charge-transfer state. This state becomes weakly allowed borrowing some dipole strength due to mixing with the pure exciton states. Introduction of a coupling between the excited and the CT state produces relatively small changes in the absorption-type spectra (OD, CD, LD), but has a dramatic effect on the FL profile. The FL spectrum is mostly determined by contributions from the two lowest states, i.e. a mixed exciton-CT state (peaking at 682 nm) and a superradiant

‘multimeric’ exciton state (delocalized over D1 branch and peaking at 680 nm) which means that the FL profile will be extremely sensitive to the precise energy of the CT state. On the other hand, the presence of the CT state with a huge static dipole significantly affects the Stark spectrum (Fig. 3.6K).

B. Mixing with CT States: Multiple Charge Separation Pathways

The lowest excited state from which the charge separation is initiated consists of a coherent superposition of four pigments, i.e. Chl_{D1}, Phe_{D1}, P_{D1}, and P_{D2} (Fig. 3.7). Participation of these sites in the ‘multimeric’ exciton state is not uniform: on the average the excitation is predominantly localized at Chl_{D1}, the average population of Phe_{D1} is about two times less, the average population of the special pair is even smaller (see insert in the left frame of Fig. 3.7). On the other hand, there is a strong coherence between these four sites, which means that some CT state coupled with any of these four pigments will be effectively mixed with the whole set of exciton states (the amount of mixing depending on the size of the energy gap between the excitonic and CT state). Thus, the primary electron transfer toward Phe can in principle start from P_{D2}, Chl_{D1}, or P_{D1} producing the first charge-separated configuration $P_{D2}^+P_{D1}^-$, $Chl_{D1}^+Phe_{D1}^-$, or $P_{D1}^+Chl_{D1}^-$, respectively.

Including the Stark spectra into the fit allowed for a precise determination of the energy of the first CT state and the degree of its mixing with the excited states. Moreover, the Stark spectrum is also sensitive to the configuration of the CT state. Only the first two configurations yield a reasonable fit of the Stark spectrum (Fig. 3.7, right frame).

The predominant population of Chl_{D1} is a strong argument for considering this pigment as the primary electron donor producing the charge transfer state $Chl_{D1}^+Phe_{D1}^-$. On the other hand, the special pair is characterized by a bigger overlap of the electronic wavefunctions of the two pigments, thus creating a better coupling between the excited states of P_{D1} and P_{D2} and the $P_{D2}^+P_{D1}^-$ charge transfer state. It is clear that these two factors compete and this competition between them

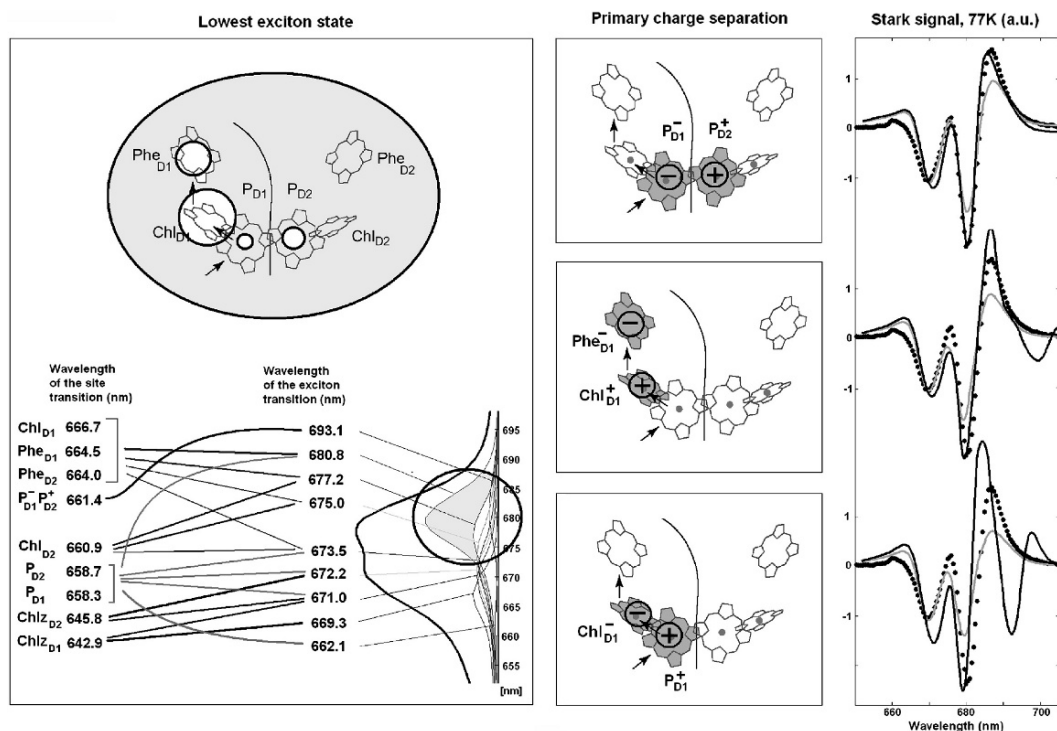


Fig. 3.7. *Left frame*: Exciton structure of PS II-RC (Novoderezhkin et al., 2007). Diagram in the bottom shows wavelengths corresponding to the unperturbed site energies of eight pigments and the first CT intermediate $P_{D2}^+P_{D1}^-$ (without including the reorganization shift), wavelengths of the zero-phonon lines (ZPL) of the exciton eigenstates averaged over disorder (lines indicate participation of the pigments in the exciton states), and the 77 K absorption with the individual exciton components. Insert on the top shows the structure of the lowest exciton state, where the circles show the pigments that on the average are coherently mixed in the lowest exciton state. The area under the circle is proportional to population of the corresponding site. *Middle frames*: Possible pathways for primary charge separation in the PS II-RC. Circles show the localization of the electron and hole in the CT states (i.e. $P_{D2}^+P_{D1}^-$, $Chl_{D1}^+Phe_{D1}^-$, and $P_{D1}^+Chl_{D1}^-$) that can be coupled to the lowest exciton state. *Right frame*: The Stark spectra calculated with the same CT states as shown in the middle frame. Points correspond to experimental data, the Stark signal is calculated with coupling to CT (black line) and without coupling to CT state (gray line)

will be strongly dependent on the realization of the disorder producing different participations of the pigments (P_{D2} , P_{D1} , and Chl_{D1}) in the lowest exciton state as well as different energy gaps between the lowest exciton state and the corresponding CT state. For instance, in some realizations the excitation can be strongly localized at Chl_{D1} ; moreover, this localized state can be even lower in energy than the $P_{D2}^+P_{D1}^-$ charge transfer state. Obviously, in such realizations even in the presence of mixing between the excited states and the $P_{D2}^+P_{D1}^-$ intermediate, the charge transfer will be started from Chl_{D1} with the formation of the $Chl_{D1}^+Phe_{D1}^-$ radical pair. On the other hand, in delocalized ‘multimeric’ realizations the $P_{D2}^+P_{D1}^-$ state is much better connected with the whole

excited-state manifold, and thus can play the role of the initial CT state.

Thus, probably the pathways of charge separation in PS II-RC are strongly disorder-controlled (Novoderezhkin et al., 2007). In the presence of the two alternative charge separation pathways a particular realization of the disorder can destroy one of them and create a good condition for the other. Consequently, the measured kinetics (averaged over disorder) will contain a superposition of components corresponding to different pathways. As a result, various experimental methods sensitive to different aspects of the electron transfer can produce a large spread of the estimated ‘time constants’ of primary charge separation.

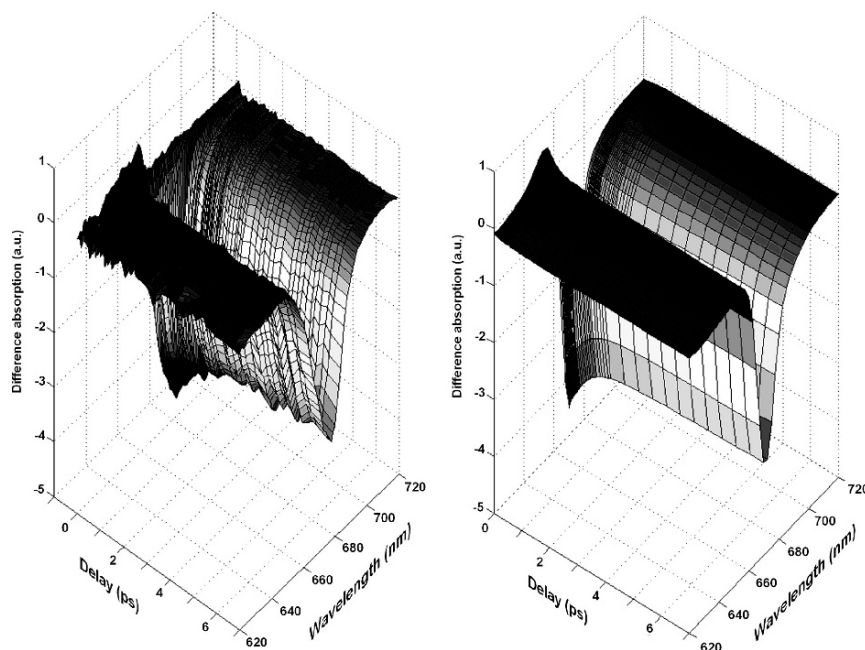


Fig. 3.8. Transient absorption of PS II-RC upon 662 nm excitation at room temperature (Novoderezhkin et al., 2005b). Experiment (*left*) and calculation (*right*)

C. Verification of the Model from the Fit of Time-dependent Kinetics

The dynamics of energy transfer and primary charge separation can be studied by modelling of the time-dependent spectral responses, including fs TA and ps FL kinetics (Novoderezhkin et al., 2005b). In Fig. 3.8 we show an example of the TA pump-probe spectra measured and calculated for the PS II-RC. The calculation is performed using the modified Redfield theory, where the relaxation rates are determined by the site energies extracted from the fit of the steady-state line shapes. Thus, modelling of the TA kinetics allow the verification (and further adjustment) of the exciton model.

At short (sub-ps) delays following short-wavelength excitation we obtain a typical excitonic TA spectrum with a negative bleach band and blue-shifted excited-state absorption. At longer delays this spectrum is evolving toward the difference absorption corresponding to radical pair formation, i.e. containing only a bleach of the pigments participating in the CT states. According to the modelling the first CT state (strongly mixed with the lowest exciton states) is populated within 500 fs with a fastest component of less

than 100 fs. The following electron transfer to the second and third radical pair is much slower and occurs on a ps time scale (Novoderezhkin et al., 2005b).

Note that interpretation of the data measured in the Q_y absorption band (660–690 nm) is greatly complicated because contributions from the excited and CT states are strongly superimposed in this region. Additional information about the charge transfer dynamics can be obtained from the TA kinetics in the Phe Q_x absorption band at 545 nm or Phe-anion absorption band at 460 nm (Greenfield et al., 1997) as well as from visible-pump-midIR probe kinetics (Groot et al., 2005) where contributions from pigments (or radical pairs) can be identified through their specific IR signatures.

The model where charge separation starts from $P_{D2}^+P_{D1}^-$ predicts slow ps kinetics with fastest components of about 7.5 ps at 460 nm and 12 ps at 545 nm (Novoderezhkin et al., 2005b). If on the other hand the initial CT state is $Chl_{D1}^+Phe_{D1}^-$, the kinetics at 460 and 545 nm will be fast, reflecting sub-ps dynamics of Phe_{D1}^- formation. Both slow and fast components are present in the measured kinetics, thus confirming the idea of mixing of the two charge separation pathways (Novoderezhkin

et al., 2007). Earlier, a similar co-existence of slow and fast dynamics was observed in visible-pump-midIR-probe studies (Groot et al., 2005).

VI. Concluding Remarks

We show that nonlinear spectroscopy in combination with the modelling based on the high-resolution structure have unveiled the pathways of energy transfer in PS I and PS II complexes and in the major plant light-harvesting complex LHCII. In these complexes a strong coupling within clusters of light-harvesting pigments is present together with weak coupling between clusters and separated monomeric sites, giving rise to complicated interplay of fast exciton relaxation and slow migration. Obviously, the traditional Förster theory for excitation energy transfer among weakly coupled chromophores does not work in this case. A self-consistent description of the dynamics and steady-state spectra can only be obtained using a unified physical model valid for an arbitrary degree of delocalization, like modified Redfield or modified Redfield–Förster theory. On the other hand, including the mixing of excitonic states with CT states requires even more sophisticated approaches, where dynamics along nuclear coordinates should be treated explicitly.

Combination of increasingly realistic physics with new experimental results provides the unique possibility to reveal the exact nature of elementary events and their interplay in all the excitation dynamics using a global systematic modelling. Simultaneous quantitative fittings of the steady-state spectra and nonlinear kinetics have been done successfully for the subunits of PS II, and LHCII complex. On the other hand, modelling of the whole core complexes of PS I and PS II still remains puzzling due to the complexity of the system.

Acknowledgments

V.N. was supported by visitor's grant from the Netherlands Organisation for Scientific Research (NWO), and by the Russian Foundation for Basic Research, Grant No. 06-04-48917. This work was also supported by the European Union via the

Intro2 Marie Curie Research Training Network, contract no. MRTN-CT-2003-505069.

References

- Amunts A, Drory O and Nelson N (2007) The structure of a plant photosystem I supercomplex at 3.4 Å resolution. *Nature* 447: 58–63
- Barber J (2003) Photosystem II: the engine of life. *Quart Rev Biophys* 36: 71–89
- Barkai E, Jung YJ and Silbey RJ (2004) Theory of single-molecule spectroscopy: Beyond the ensemble average. *Annu Rev Phys Chem* 55: 457–507
- Barter LMC, Durrant JR and Klug DR (2003) A quantitative structure-function relationship for the Photosystem II reaction center: Supermolecular behavior in natural photosynthesis. *Proc Natl Acad Sci USA* 100: 946–951
- Ben-Shem A, Frolow F and Nelson N (2003) Crystal structure of plant photosystem I. *Nature* 426: 630–635
- Bopp MA, Sytnik A, Howard TD, Cogdell RJ and Hochstrasser RM (1999) The dynamics of structural deformations of immobilized single light-harvesting complexes. *Proc Natl Acad Sci USA* 96: 11271–11276
- Brüggemann B, Sznee K, Novoderezhkin V, Van Grondelle R and May V (2004) From structure to dynamics: Modeling exciton dynamics in the photosynthetic antenna PS1, *J Phys Chem B* 108: 13536–13546
- Byrdin M, Jordan P, Krauss N, Fromme P, Stehlik D and Schlodder E (2002) Light harvesting in photosystem I: Modeling based on the 2.5-Å structure of photosystem I from *Synechococcus elongatus*. *Biophys J* 83: 433–457
- Cho M, Vaswani HM, Brixner T, Stenger J and Fleming GR (2005) Exciton analysis in 2D electronic spectroscopy. *J Phys Chem B* 109: 10542–10556
- Damjanović A, Kosztin I, Kleinekathoefer U and Schulten K (2002a) Excitons in a photosynthetic light-harvesting system: A combined molecular dynamics, quantum chemistry, and polaron model study. *Phys Rev E* 65: 031919-1–031919-24
- Damjanović A, Vaswani HM, Fromme P and Fleming GR (2002b) Chlorophyll excitations in photosystem I of *Synechococcus elongatus*. *J Phys Chem B* 106: 10251–10262
- Dekker JP and Van Grondelle R (2000) Primary charge separation in photosystem II. *Photosynth Res* 63: 195–208
- Diner BA and Rappaport F (2002) Structure, dynamics, and energetics of the primary photochemistry of photosystem II of oxygenic photosynthesis. *Annu Rev Plant Biol* 53: 551–580
- Diner BA, Schlodder E, Nixon JP, Coleman WJ, Rappaport F, Lavergne J, Vermaas WFJ and Chisholm DA (2001) Site-directed mutations at D1-His198 and D2-His197 of photosystem II in *Synechocystis* PCC 6803: Sites of primary charge separation and cation and triplet stabilization. *Biochemistry* 40: 9265–9281

- Durrant JR, Klug DR, Kwa SLS, Van Grondelle R, Porter G and Dekker JP (1995) A multimer model for P680, the primary electron donor of photosystem II. *Proc Natl Acad Sci USA* 92: 4798–4802
- Ferreira KN, Iverson TM, Maghlaoui K, Barber J and Iwata S (2004) Architecture of the photosynthetic oxygen-evolving center. *Science* 303: 1831–1838
- Förster T (1965) Delocalized excitation and excitation transfer. In: Sinanoğlu (ed) *Modern Quantum Chemistry, Part III. B. Action of Light and Organic Crystals*, pp. 93–137. Academic, New York
- Frese RN, Palacios MA, Azzizi A, Van Stokkum IHM, Kruij J, Roegner M, Karapetyan NV, Schlodder E, Van Grondelle R and Dekker JP (2002) Electric field effects on red chlorophylls, β -carotenes and P700 in cyanobacterial photosystem I complexes. *Biochim Biophys Acta* 1554: 180–191
- Gillie JK, Small GJ and Golbeck JH (1989) Nonphotochemical hole burning of the native antenna complex of photosystem I (PS I-200). *J Phys Chem* 93: 1620–1627
- Gobets B and Van Grondelle R (2001) Energy transfer and trapping in photosystem I. *Biochim Biophys Acta* 1507: 80–99
- Gobets B, Van Stokkum IHM, Van Mourik F, Dekker JP and Van Grondelle R (2003) Excitation wavelength dependence of the fluorescence kinetics in photosystem I particles from *Synechocystis* PCC 6803 and *Synechococcus elongatus*. *Biophys J* 85: 3883–3898
- Gradinaru CC, Özdemir S, Gülen D, Van Stokkum IHM, Van Grondelle R and Van Amerongen H (1998) The flow of excitation energy in LHCII monomers. Implications for the structural model of the major plant antenna. *Biophys J* 75: 3064–3077
- Greenfield SR, Seibert M, Govindjee and Wasielewski M (1997) Direct measurement of the effective rate constant for primary charge separation in isolated photosystem II reaction centers. *J Phys Chem B* 101: 2251–2255
- Groot M-L, Pawlowicz NP, Van Wilderen LJGW, Breton J, Van Stokkum IHM and Van Grondelle R (2005) Initial electron donor and acceptor in isolated photosystem II reaction centers identified with femtosecond mid-IR spectroscopy. *Proc Natl Acad Sci USA* 102: 13087–13092
- Jang S, Newton MD and Silbey RJ (2004) Multichromophoric Förster resonance energy transfer. *Phys Rev Lett* 92: 218301-1–218301-4
- Jean JM and Fleming GR (1995) Competition between energy and phase relaxation in electronic curve crossing processes. *J Chem Phys* 103: 2092–2101
- Jordan P, Fromme P, Witt HT, Klukas O, Saenger W and Krauß N (2001) Three-dimensional structure of cyanobacterial photosystem I at 2.5 Å resolution. *Nature* 411: 909–917
- Kamiya N and Shen J-R (2003) Crystal structure of oxygen-evolving photosystem II from *Thermosynechococcus vulcanus* at 3.7 Å resolution. *Proc Natl Acad Sci USA* 100: 98–103
- Kamlowski A, Frankemoller L, Van der Est A, Stehlik D and Holzwarth AR (1996) Evidence for delocalization of the triplet state $^3\text{P680}$ in the D1-D2cytb559-complex of photosystem II. *Ber Bunsenges Phys Chem* 100: 2045–2051
- Karapetyan N, Schlodder E, Van Grondelle R and Dekker JP (2006) The long wavelength chlorophylls of photosystem I. In: Golbeck JH (ed) *Photosystem I: The Light-Driven Plastocyanin:Ferredoxin Oxidoreductase*, pp. 177–192. Springer, The Netherlands
- Kleima FJ, Gradinaru CC, Calkoen F, Van Stokkum IHM, Van Grondelle R and Van Amerongen H (1997) Energy transfer in LHCII monomers at 77 K studied by sub-picosecond transient absorption spectroscopy. *Biochemistry* 36: 15262–15268
- Kühlbrandt W, Wang DN and Fujiyoshi Y (1994) Atomic model of plant light-harvesting complex by electron crystallography. *Nature* 367: 614–621
- Leegwater JA, Durrant JR and Klug DR (1997) Exciton equilibration induced by phonons: Theory and application to PS II reaction centers. *J Phys Chem B* 101: 7205–7210
- Liu Z, Yan H, Wang K, Kuang T, Zhang J, Gui L, An X and Chang W (2004) Crystal structure of spinach major light-harvesting complex at 2.72 Å resolution. *Nature* 428: 287–292
- Loll B, Kern J, Saenger W, Zouni A and Biesiadka J (2005) Towards complete cofactor arrangement in the 3.0 Å resolution structure of photosystem II. *Nature* 438: 1040–1044
- Meier T, Chernyak V and Mukamel S (1997) Femtosecond photon echoes in molecular aggregates. *J Chem Phys* 107: 8759–8774
- Moerner WE (2002) A dozen years of single-molecule spectroscopy in physics, chemistry, and biophysics. *J Phys Chem B* 106: 910–927
- Mukamel S (1995) *Principles of Nonlinear Optical Spectroscopy*. Oxford University Press, New York, Oxford
- Noguchi T, Inoue Y and Satoh K (1993) FT-IR studies on the triplet state of P680 in the photosystem II reaction center: Triplet equilibrium within a chlorophyll dimer. *Biochemistry* 32: 7186–7195
- Novoderezhkin VI and Razjivin AP (1994) Exciton states of the antenna and energy trapping by the reaction center. *Photosynth Res* 42: 9–15
- Novoderezhkin VI and Razjivin AP (1996) The theory of Förster-type migration between clusters of strongly interacting molecules: Application to light-harvesting complexes of purple bacteria. *Chem Phys* 211: 203–214
- Novoderezhkin VI, Palacios MA, Van Amerongen H and Van Grondelle R (2004a) Energy-transfer dynamics in the LHCII complex of higher plants: Modified Redfield approach. *J Phys Chem B* 108: 10363–10375
- Novoderezhkin VI, Yakovlev AG, Van Grondelle R and Shuvalov VA (2004b) Coherent nuclear and electronic dynamics in primary charge separation in photosynthetic reaction centers: A Redfield theory approach. *J Phys Chem B* 108: 7445–7457

- Novoderezhkin VI, Palacios MA, Van Amerongen H and Van Grondelle R (2005a) Excitation dynamics in the LHCII complex of higher plants: Modeling based on 2.72 Å crystal structure. *J Phys Chem B* 109: 10493–10504
- Novoderezhkin VI, Andrizhiyevskaya EG, Dekker JP and Van Grondelle R (2005b) Pathways and timescales of primary charge separation in the photosystem II reaction center as revealed by a simultaneous fit of time-resolved fluorescence and transient absorption. *Biophys J* 89: 1464–1481
- Novoderezhkin VI, Rutkauskas D and Van Grondelle R (2006) Dynamics of the emission spectrum from single LH2 complex: Interplay of slow and fast nuclear motions. *Biophys J* 90: 2890–2902
- Novoderezhkin VI, Dekker JP and Van Grondelle R (2007) Mixing of exciton and charge-transfer states in photosystem II reaction centers: Modeling of Stark spectra with modified Redfield theory. *Biophys J* 93: 1293–1311
- Peterman EJG, Pullerits T, Van Grondelle R and Van Amerongen H (1997) Electron-phonon coupling and vibronic fine structure of light-harvesting complex II of green plants: Temperature dependent absorption and high-resolution fluorescence spectroscopy. *J Phys Chem B* 101: 4448–4457
- Peterman EJG, Van Amerongen H, Van Grondelle R and Dekker JP (1998) The nature of the excited state of the reaction center of photosystem II of green plants: A high-resolution fluorescence spectroscopy study. *Proc Natl Acad Sci USA* 95: 6128–6133
- Pieper J, Voigt J and Small GJ (1999) Chlorophyll *a* Franck-Condon factors and excitation energy transfer. *J Phys Chem B* 103: 2319–2322
- Prokhorenko VI and Holzwarth AR (2000) Primary processes and structure of the photosystem II reaction center: A) Photon echo study. *J Phys Chem B* 104: 1563–11578
- Raszeski G, Saenger W and Renger Th (2005) Theory of optical spectra of photosystem II reaction centers: Location of the triplet state and the identity of the primary electron donor. *Biophys J* 88: 986–998
- Redfield AG (1965) The theory of relaxation processes. *Adv Mag Res* 1: 1–32
- Renger Th and Marcus R (2002) Photophysical properties of PS-2 reaction centers and a discrepancy in exciton relaxation times. *J Phys Chem B* 106: 1809–1819
- Renger Th and May V (1997) Theory of multiple exciton effects in the photosynthetic antenna complex LHC-II. *J Phys Chem B* 101: 7232–7240
- Renger Th and Schlodder E (2006). Modeling of optical spectra and light harvesting in photosystem I. In: Golbeck JH (ed) *Photosystem I: The Light-Driven Plastocyanin:Ferredoxin Oxidoreductase*, pp. 595–610. Springer, The Netherlands
- Renger Th, May V and Kühn O (2001) Ultrafast excitation energy transfer dynamics in photosynthetic pigment-protein complexes. *Phys Rep* 343: 137–254
- Rutkauskas D, Novoderezhkin V, Cogdell RJ and Van Grondelle R (2004) Fluorescence spectral fluctuations of single LH2 complexes from *Rhodospseudomonas acidophila* strain 10050. *Biochemistry* 43: 4431–4438
- Rutkauskas D, Novoderezhkin V, Cogdell RJ and Van Grondelle R (2005) Fluorescence spectroscopy of conformational changes of single LH2 complexes. *Biophys J* 88: 422–435
- Rutkauskas D, Novoderezhkin V, Gall A, Olsen J, Cogdell RJ, Hunter CN and Van Grondelle R (2006) Spectral trends in the fluorescence of single bacterial light-harvesting complexes: Experiments and modified Redfield simulations. *Biophys J* 90: 2475–2485
- Savikhin S (2006) Ultrafast optical spectroscopy of photosystem I. In: Golbeck JH (ed) *Photosystem I: The Light-Driven Plastocyanin:Ferredoxin Oxidoreductase*, pp 155–176. Springer, The Netherlands
- Schlodder E, Shubin VV, El Mohnsawy E, Roegner M and Karapetyan NV (2007) Steady-state and transient polarized absorption spectroscopy of photosystem I complexes from the cyanobacteria *Arthrospira platensis* and *Thermosynechococcus elongatus*. *Biochim Biophys Acta* 1767: 732–741
- Scholes GD and Fleming GR (2000) On the mechanism of light harvesting in purple bacteria: B800 to B850 energy transfer. *J Phys Chem B* 104: 1854–1868
- Sener MK, Lu DY, Ritz T, Park S, Fromme P and Schulten K (2002) Robustness and optimality of light harvesting in cyanobacterial photosystem I. *J Phys Chem B* 106: 7948–7960
- Standfuss J, Van Scheltinga1 ACT, Lamborghini M and Kühlbrandt W (2005) Mechanisms of photoprotection and nonphotochemical quenching in pea light harvesting complex at 2.5 Å resolution. *EMBO J* 24: 919–928
- Sumi H (1999) Theory on rates of excitation-energy transfer between molecular aggregates through distributed transition dipoles with application to the antenna system in bacterial photosynthesis. *J Phys Chem B* 103: 252–260
- Tietz C, Chekhlov O, Dräbenstedt A, Schuster J and Wrachtrup J (1999) Spectroscopy on single light-harvesting complexes at low temperature. *J Phys Chem B* 103: 6328–6333
- Van Amerongen H and Dekker JP (2003) Light-harvesting in photosystem II. In: Green BR and Parson WW (ed) *Light-Harvesting Antennas in Photosynthesis*. Kluwer, Dordrecht, pp. 219–251
- Van Amerongen H, Valkunas L and Van Grondelle R (2000) *Photosynthetic Excitons*. World Scientific Publishers, Singapore
- Van Grondelle R and Gobets B (2004) Transfer and trapping of excitations in plant photosystems. In: Papageorgiou GC and Govindjee (eds) *Chlorophyll *a* Fluorescence: A Signature of Photosynthesis*, pp. 107–132. Springer, The Netherlands

- Van Grondelle R and Novoderezhkin V (2006) Energy transfer in photosynthesis: Experimental insights and quantitative models. *Phys Chem Chem Phys* 8: 793–807
- Van Grondelle R, Dekker JP, Gilbro T and Sundstroem V (1994) Energy transfer and trapping in photosynthesis. *Biochim Biophys Acta* 1187: 1–65
- Van Mieghem FJE, Satoh K and Rutherford AW (1991) A chlorophyll tilted 30° relative to the membrane in the photosystem II reaction centre. *Biochim Biophys Acta* 1058: 379–385
- Van Oijen AM, Ketelaars M, Köhler J, Aartsma TJ and Schmidt J (1999) Unraveling the electronic structure of individual photosynthetic pigment-protein complexes. *Science* 285: 400–402
- Visser HM, Kleima FJ, Van Stokkum IHM, Van Grondelle R and Van Amerongen H (1996) Probing of many energy-transfer processes in the photosynthetic light-harvesting complex II at 77 K by energy-selective sub-picosecond transient absorption spectroscopy. *Chem Phys* 210: 297–312
- Yang M and Fleming GR (2002) Influence of phonons on exciton transfer dynamics: comparison of the Redfield, Förster, and modified Redfield equations. *Chem Phys* 275: 355–372
- Yang M, Damjanović A, Harsha M, Vaswani and Graham R, Fleming (2003) Energy transfer in photosystem I of cyanobacteria *Synechococcus elongatus*: Model study with structure-based semi-empirical hamiltonian and experimental spectral density. *Biophys J* 85: 140–158
- Yoder LM, Cole AG and Sension RJ (2002) Structure and function in the isolated reaction center complex of photosystem II: Energy and charge transfer dynamics and mechanism. *Photosynth Res* 72: 147–158
- Zazubovich V, Matsuzaki S, Johnson TW, Hayes JM, Chitnis PR and Small GJ (2002) Red antenna states of photosystem I from cyanobacterium *Synechococcus elongatus*: A spectral hole-burning study. *Chem Phys* 275: 47–59
- Zhang WM, Meier T, Chernyak V and Mukamel S (1998) Exciton-migration and three-pulse femtosecond optical spectroscopies of photosynthetic antenna complexes. *J Chem Phys* 108: 7763–7774
- Zouni A, Witt HT, Kern J, Fromme P, Krauß N, Saenger W and Orth P (2001) Crystal structure of photosystem II from *Synechococcus elongatus* at 3.8 Å resolution. *Nature* 409: 739–743

Chapter 4

Unraveling the Hidden Nature of Antenna Excitations

Arvi Freiberg*

Institute of Physics, University of Tartu, Riia 142, 51014 Tartu, Estonia and Institute of Molecular and Cell Biology, University of Tartu, Riia 23, 51010 Tartu, Estonia

Gediminas Trinkunas

Institute of Physics, Savanoriu 231, LT-02300 Vilnius, Lithuania

Summary.....	55
I. Introduction.....	56
A. Light Harvesting.....	56
B. Irregular Pigment Organization and the Energy Funneling Principle.....	56
C. Light Harvesting by Purple Photosynthetic Bacteria.....	58
II. Disordered Frenkel Exciton Model for Absorbing States of Circular Antenna Aggregates.....	59
III. Shortcomings of the Disordered Frenkel Exciton Model.....	63
IV. Excitonic Polaron Model of the Antenna Fluorescing States.....	64
A. Ground States of the Excitonic Polarons in Regular and Disordered Circular Aggregates.....	66
B. Ensemble-averaged Characteristics of the Antenna Excitonic Polarons.....	68
V. Evaluation of the Model Parameters from the Experimental Spectra.....	70
A. Resonant Coupling Energy, Inhomogeneous Spectral Broadening, and Reorganization Energy.....	70
B. The Wavelength-dependent Exciton–Phonon Coupling and the Weighted Density of the Phonon States.....	72
VI. Conclusions and Outlook.....	76
Acknowledgments.....	77
References.....	77

Summary

The three main parameters that determine the electronic structure and dynamics of the photosynthetic antenna excitations are the resonant (exciton) coupling energy, the inhomogeneous spectral broadening, and the exciton–lattice coupling energy. Generally, information about these factors can be obtained by optical spectroscopy. However, in conventional optical spectroscopy only ensemble-averaged data are accessible. Adequate theoretical modeling is, therefore, required to uncover various hidden parameters. Here, we focus on the peripheral LH2 and core LH1 antenna complexes from purple bacteria. These bacteriochlorophyll-containing antennas show quasi-linear optical spectra that allow detailed spectroscopic studies not only at cryogenic temperatures but at physiological temperatures as well. The strongly overlapping chlorophyll spectra in higher plant antennas are in that respect much less informative. Secondly, the bacterial antennas present wonderfully ordered quasi- one-dimensional structures of pigment molecules amenable for straightforward physical modeling. Complexity of the antennas and incomplete structural data render similar level of multi-parameter modeling in higher plants more challenging.

* Author for correspondence, e-mail: Arvi.Freiberg@ut.ee

We notice that the generally applied disordered Frenkel exciton model, while sufficient for describing steady-state absorption spectra, falls short in characterization of the fluorescence emission properties of the bacterial antennas. Therefore, an excitonic polaron model is introduced, much better suitable for description of the relaxed excited electronic states in the disordered one-dimensional bacteriochlorophyll aggregates representing the emitting antenna structures with relatively strong interaction between excitons and lattice vibrations. The static disorder considerably reduces critical exciton–lattice coupling energy required for initiation of the smooth exciton self-trapping transition. It also allows coexistence of multiple self-trapped excitons in the same lattice. Such a situation in regular structures is only possible at higher dimensions. The exciton self-trapping might promote energy transport and trapping processes in bacterial photosynthesis by broadening the LH2 and LH1 antenna spectra and by maximizing their fluorescence emission rate.

I. Introduction

A. Light Harvesting

Photosynthesis utilizes two coupled pigment systems, a light-harvesting (LH) antenna and a photochemical reaction center, cooperating in conversion of solar energy into chemically stable high-energy products sustaining life on Earth. Together, the antenna and the reaction center form an entity called photosynthetic unit, the concept first introduced in the beginning of 1930s (Emerson and Arnold, 1932) to explain efficiency of the photosynthetic solar energy conversion. L. N. M. Duysens and collaborators (Duysens, 1952; Vredenberg and Duysens, 1963) provided an early experimental proof of this concept by spectroscopic means. Subsequent biochemical studies revealed further complexity with different pigment-protein complexes performing the antenna and reaction center functions. Detailed research on molecular level vastly expanded our understanding of the photosynthetic apparatus and its functioning with new insights provided by the high-resolution crystallographic characterization of the bacterial photosynthetic reaction center (Michel and Deisenhofer, 1990) as well as of a number of LH units of both bacterial (Fenna and Matthews, 1975; McDermott et al., 1995; Koepke et al., 1996) and higher plant origin (Loll et al., 2005; Amunts et al., 2007). By now, it is firmly

established for all photosynthetic organisms that the LH antenna proteins are composed of a large number of pigment molecules. Their task is to collect sunlight and deliver energy to the reaction center protein. The latter, by contrast, comprise only a few pigment molecules, whose organization and interactions are optimized for unidirectional electron transfer across the photosynthetic membrane leading to a long-lived charge separation state. The turnover time of the reaction centers is much shorter than intervals between its photon capture. The additional light harvesting by antenna structures is increasing the photon capture frequency and, thus, increasing the efficiency of the photosynthetic unit by several orders of magnitude. Further enhancement is achieved by broadening spectral range of the light harvesting above that of the reaction center only.¹

B. Irregular Pigment Organization and the Energy Funneling Principle

The most abundant LH complexes are composed of different forms of chlorophyll or bacteriochlorophyll molecules that are non-covalently bound to the surrounding protein matrix. Structural studies give evidence for complex spatial pattern of the pigments. In all known antenna complexes, the densely packed pigment constellations (including dimers, trimers, and larger oligomers of up to thousand molecules) interlace with scarcely occupied regions. The spatial heterogeneity is not accidental. It was demonstrated in a series of modeling papers (Fetisova

Abbreviations: Bchl – bacteriochlorophyll *a*; DOS – density of states; FLN – fluorescence line narrowing; FWHM – full width at half maximum; LH – light-harvesting; PSB – phonon sideband; SDF – site/state distribution function; ZPL – zero phonon line; 1D, 2D, 3D – one-, two-, three-dimensional

¹ This unique principle of natural photosynthesis has lately been introduced into modern photovoltaic technology (see Markvart, 2000 for a review).

et al., 1985, 1989; Fetisova, 2004) that the clustered antenna structure increases efficiency of the delivery of excitations from the antenna to the reaction center compared with that of a system with uniform distribution of the pigments.

The spatial structure of the antenna complexes, especially the mutual orientation of the pigments, also determines to a large extent their spectroscopic properties and excited-state dynamics. High local concentration of the pigments, favoring extensive inter-pigment couplings, causes coherent de-localization of the excited states over at least a part of the cluster. Therefore, as first realized already 70 years ago (Franck and Teller, 1938), delocalized Frenkel excitons (Knox, 1963; Davydov, 1971) rather than excited states of individual molecules are relevant electronic excitations for the densely packed arrays of the antenna pigments. It, however, took hard work and determination of several generations of scientists (Robinson, 1967; Sauer and Austin, 1978; Pearlstein, 1982; Scherz and Parson, 1986; Novoderezhkin and Razjivin, 1993, 1995) until the exciton concept in photosynthesis has been generally accepted (Van Amerongen et al., 2000). The progress made in high-resolution structural studies of LH complexes of purple bacteria (Karrasch et al., 1995; McDermott et al., 1995; Koepke et al., 1996; Walz et al., 1998; McLuskey et al., 2001) has strongly stimulated these investigations (Jimenez et al., 1996; Sauer et al., 1996; Scholes et al., 1997, 1999; Wu et al., 1997b; Sumi, 1999a, b, 2000; Sundström et al., 1999; Van Oijen et al., 1999; Scholes and Fleming, 2000; Green and Parson, 2003; Hu et al., 2002; Van Grondelle and Novoderezhkin, 2006).

Excitons are scattered by various structural irregularities (generally called disorders) that exist in the assembly of molecules. Relative to the exciton lifetime or to the time-window of the measurement these irregularities are static or dynamic (time dependent). The static and dynamic disorders produce spectral line broadening called inhomogeneous and homogeneous broadening, respectively. Thermal fluctuations in the positions of atoms and molecules mediated by electron-phonon² coupling are the main cause of the homogeneous broadening of the exciton

spectra (Mukamel, 1995; Renger and Marcus, 2002; Heijs et al., 2005). In contrast to, for example, molecular crystals, the excitons in pigment-proteins are affected both in nature and dynamics by physical size and structure of these complexes (Sumi, 2000; Scholes and Rumbles, 2006). A very large inhomogeneous line-broadening characteristic for nano-particle type pigment-proteins may even obscure their exciton features. This certainly was one of the main factors slowing down the progress of recognizing excitons in the photo-synthetic antennas.

In the antenna pigment-protein complexes, it is worth distinguishing between spectral inhomogeneity and spectral heterogeneity (Pullerits et al., 1994). The heterogeneity is a result of large-scale systematic differences in the surroundings of the pigment molecules (e.g., due to binding to different polypeptides or to different parts of a polypeptide chain), while the inhomogeneity is caused by small, random fluctuations in the positions and orientations of the pigment molecules. The heterogeneity results in the absorption spectrum in more or less distinct lines or bands, which can be attributed to spatially distinct groups of the pigments in the antenna structure as shown in Fig. 4.1.

In the spectroscopy of organic impurity crystals such combination of the inhomogeneous

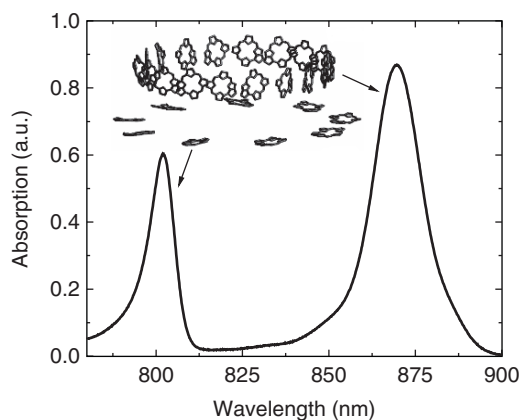


Fig. 4.1. Relationship between the structural arrangement of the Bchl molecules in the LH2 light-harvesting complex from the purple bacterium *Rps. acidophila* and their absorption spectra in the near-infrared region at 5 K. The Bchl molecules are represented by their bacteriochlorin cores. The B850 absorption band corresponding to the closely spaced upper-ring molecules (B850 is a conventional term, here the band is at 868 nm in *Rps. acidophila*) is the main focus of this work

² The term “phonon” in this text is loosely assigned to any vibrational motion, extended or localized, if not otherwise indicated.

and heterogenous broadenings is known as the Shpol'skii effect (Gooijer et al., 2000).

A spatially ordered arrangement of different spectral forms of the pigments in the heterogeneous antennas improves the photosynthetic unit efficiency if the groups of the antenna pigments are spatially organized with respect to the reaction center in a way that an energy gradient is created driving the excitation energy toward the reaction center (Duyens, 1986). The green photosynthetic bacteria as well as cyanobacteria, which contain extra-membranous accessory antenna complexes (chlorosomes and phycobilisomes, respectively), are the two archetypical representatives of such a funnel type antenna arrangement (Porter et al., 1978; Fetisova et al., 1988, 1995). The same principle facilitates effective exciton transfer also in the purple bacteria (Freiberg et al., 1987; Godik et al., 1988; Pullerits and Freiberg, 1991; Freiberg, 1995).

C. Light Harvesting by Purple Photosynthetic Bacteria

The photosynthetic membrane of many purple bacteria contains two types of LH complexes, the core LH1 and the peripheral LH2 complex. The LH1 complex directly surrounds the reaction center (Karrasch et al., 1995; Walz et al., 1998; Roszak et al., 2003; Bahatyrova et al., 2004), whereas LH2, usually not in straight contact with the reaction center, transfers its energy to the reaction center via the core complex (Sundström et al., 1999; Hu et al., 2002; Cogdell et al., 2006). Both LH1 and LH2 contain a remarkable circular assembly of the light-harvesting pigments in their protein matrix. The basic building block of these structures is a heterodimer of a α - and β -apoproteins. The whole LH2 complex consists of either nine (*Rhodospseudomonas* (*Rps.*) *acidophila*, *Rhodobacter* (*Rb.*) *sphaeroides*) (McDermott et al., 1995) or eight (*Rhodospirillum* (*Rs.*) *molischianum*) (Koepke et al., 1996) such $\alpha\beta$ -heterodimers, each non-covalently binding three bacteriochlorophyll *a* (Bchl) molecules and one carotenoid molecule. The LH1 complex from *Rb. sphaeroides* consists of 16 $\alpha\beta$ -heterodimers (Walz et al., 1998), each binding two Bchl molecules and one or two carotenoid molecules.

The arrangement of Bchl molecules in the LH2 complex from *Rps. acidophila* (McDermott et al., 1995) and the related absorption spectrum are shown in Fig. 4.1. A striking feature of the organization of the 27 Bchl molecules in this LH2 complex is their partition into two concentric rings. The upper ring consists of a group of 18 closely coupled (intermolecular separation <1 nm) Bchls with their bacteriochlorin planes oriented parallel to the vertical symmetry axis of the complex. These molecules give rise to absorption around 850–870 nm (different in different species) named as the B850 band. The nine loosely packed Bchls (intermolecular distance ≥ 2 nm) in the lower ring are responsible for the B800 absorption band. These molecules have their bacteriochlorin planes perpendicular to the symmetry axis.

A single-ring arrangement of the Bchls in LH1 reminds that in the upper circle of LH2. These strongly coupled pigments give rise to an absorption in the 875 nm region. All the three spectral bands (B800, B850, and B875) of the LH1 and LH2 antenna complexes originate in the lowest Q_y singlet electronic transition.

Upon excitation, the energy is funneled from B800 to B850 molecules in 1–2 ps (Sundström et al., 1986; Godik et al., 1987; Van Grondelle et al., 1987; Freiberg et al., 1989; Shreve et al., 1991). Subsequent electronic energy transfer from LH2 to LH1, i.e., between the B850 and B875 antenna rings, is less uniform (Nuijs et al., 1986; Sundström et al., 1986; Godik et al., 1987, 1988; Freiberg et al., 1989). In wild type membranes (chromatophores) of *Rb. sphaeroides*, for example, most ($\sim 70\%$) of the LH2 excitations carry their energy to LH1 very fast, in less than 10 ps, while the rest are much delayed, taking about 50 ps (Godik et al., 1987; Freiberg et al., 1988, 1989). It was proposed that those of the LH2 complexes that exhibit restrained transfer rate, must lie in a periphery of the antenna cluster (Godik et al., 1987; Freiberg et al., 1989; Zhang et al., 1992). The proposed antenna pattern, with some remote LH2 and some LH2 that are directly coupled to LH1, is remarkably similar to the antenna topology discovered more than a decade later by atomic force microscopy (Scheuring, 2006).

The overall (quasi-equilibrium) lifetime of excitations in intact membranes with the reac-

tion centers in the photoactive state is 50–70 ps (Borisov and Godik, 1972; Godik and Borisov, 1977; Sebban and Moya, 1983; Freiberg et al., 1984; Sebban et al., 1984; Borisov et al., 1985; Dobek et al., 1990). There is a general consensus that this lifetime is primarily limited by the slow rate of energy transfer from the core LH1 antenna to the reaction center trap (see Zhang et al., 1992; Timpmann et al., 1993; Beekman et al., 1994; Timpmann et al., 1995; Freiberg et al., 1996; Katiliene et al., 2004 for relevant discussions).

The experimentally confirmed ultrafast excitation energy funneling toward the reaction center assigns special role to the densely packed B850 and B875 rings of Bchls. Characterized with the lowest electronic transition energies in the respective LH2 and LH1 complexes, they govern the functionally important flow of the solar excitation energy in the photosynthetic membranes of purple bacteria. Our aim in this chapter is not only a better qualitative understanding of the origin of the lowest electronic excited states of the B850 and B875 pigment aggregates, but also a quantitative evaluation of the main physical parameters related to this origin. The study is based on theoretical analysis and numerical simulations of the steady-state conventional and selective spectroscopy data obtained on ensembles of disordered LH2 and LH1 complexes at low temperatures. As a convention, the term “selective” will be used to denote excitation of an electronic state within its inhomogeneously broadened origin band. Such excitation results in line-narrowed fluorescence (FLN) and absorption (hole burning) spectra. Since high-resolution structural information is available only for the peripheral LH2 antenna complex, the main discussion is based on the B850 aggregate. However, most of the results are applicable for the B875 aggregate as well.

II. Disordered Frenkel Exciton Model for Absorbing States of Circular Antenna Aggregates

The X-ray structure of *Rps. acidophila* refined to a resolution of 0.2 nm (Papiz et al., 2003) shows distances close to 0.87 nm between the central Mg atoms of the Bchls in the B850 basic unit and only slightly larger space of 0.97 nm

between the adjacent units. Close arrangement and large dipole strength of the Q_y electronic transition give rise to significant resonant interactions between the neighboring Bchls that readily distribute (delocalize) the excited states over at least part of the B850 molecules. Hence, a natural starting point to describe the excited states of the B850 assembly is by applying the Frenkel exciton model (Davydov, 1971). In its idealized form (without static and dynamic disorders taken into account), the key aspects of this model are as follows (Van Amerongen et al., 2000). The proper exciton eigenstates are characterized by a quantum number, k , which can take the values $0, \pm 1, \pm 2, \dots, \pm 8, 9$. Owing to the circular symmetry and tangential orientation of the transition dipoles of the Bchl molecules almost on the B850 ring plain, only the states $k = \pm 1$ carry an appreciable transition-dipole moment, making them easily accessible by ground-state absorption spectroscopy. The symmetric $k = \pm 8$ states at the upper-energy edge of the exciton state manifold are very weak, whereas the remaining 14 states are inaccessible from the ground state. These strict optical selection rules in regular aggregates are characteristic for the delocalized exciton states and result from the fact that the exciton wavefunctions are the Bloch states that span over the whole molecular structure. In addition, the exciton states of the B850 aggregate are influenced by a periodic dimeric organization of the Bchl molecules in the ring imposed by the supporting α - and β -apoproteins (Liuolia et al., 1997).³ Because of that, a site excitation energy difference for the neighboring Bchls appears together with two nearest-neighbor exciton coupling energies, V and V' . Their ratio estimated in the dipole–dipole coupling approximation from the X-ray structure (Papiz et al., 2003) is $V'/V \approx 0.76$. The exciton band that is $2(V + V')$ broad is split into two Davydov subbands, separated by a bandgap of $2(V - V')$. As can be seen in Fig. 4.2a (central bars), each Davydov subband comprises of four pair-wise degenerate exciton states and one non-degenerate state at either the low-energy or the high-energy edge.

³ Making connection with the solid-state physics terminology: there are two molecules per unit cell of the ring structure.

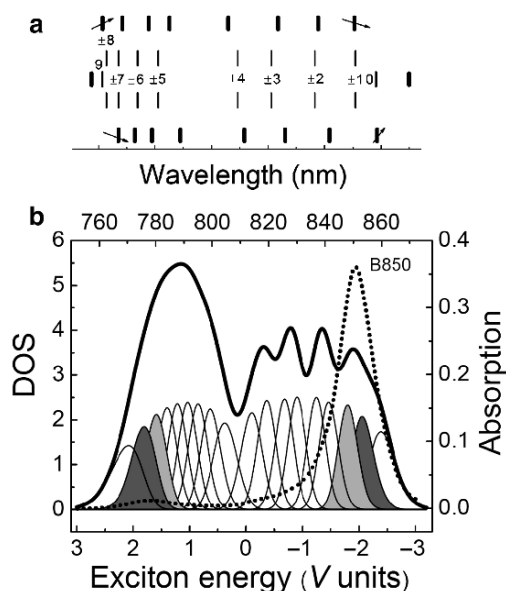


Fig. 4.2. Panel **a**: excitonic level diagrams for regular (central thin bars) and diagonally disordered (flank thick bars) B850 aggregates. The arrows indicate transition dipole moments for the disorder-split $k = \pm 1$ and $k = \pm 8$ exciton states. A single diagonal disorder realization of site energies from a Gaussian distribution (see Eq. 4.2) with $\sigma = 0.6V$ is represented. Panel **b**: the absorption spectrum (dotted curve) and the corresponding DOS (thick curve) for an ensemble of 2000 B850 aggregates. The shapes drawn with thin line represent ensemble distributions of 18 individual exciton states. The filled gray areas highlight the distributions for the split $k = \pm 1$ and $k = \pm 8$ states. The model parameters suitable for LH2 from *Rb. sphaeroides* have been used in these calculations

Certain amount of static structural disorder exists in all proteins. As already indicated, these fluctuations lead to heterogeneous and inhomogeneous spectral line broadening. The low-temperature persistent hole burning studies of Small and Völker (Van der Laan et al., 1990; Reddy et al., 1992) provided the first clear proof that the B800, B850, and B875 bands are inhomogeneously broadened. These data nicely corroborated the indirect evidence that was obtained previously from picosecond time-resolved measurements (Freiberg et al., 1987, 1989; Zhang et al., 1992). More recently, the large variability of the antenna spectra both at cryogenic and physiological temperatures was affirmed by single complex studies (Tietz et al.,

1999; Van Oijen et al., 1999). In hole burning spectroscopy, an intense, narrow bandwidth laser selects a sub-population of chromophores in the inhomogeneous absorption band. Photochemical and/or photophysical processes cause bleaching of the chromophores resonant with the laser frequency. While the photochemical mechanism acts directly on the chromophores, the photophysical mechanism is believed to modify only the environment of the chromophores. The missing absorption at excitation frequency appears as nearly homogeneously broadened inverted spectral profile, a hole, in the inhomogeneous absorption band. The narrow spectral holes burned in the low-energy region of the LH2 and LH1 absorption spectra failed to spot any significant phonon sidebands (Van der Laan et al., 1990; Reddy et al., 1992). This was taken (erroneously, as we shall see shortly) as a proof of a rather weak coupling between the pigment molecules and the surrounding protein matrix (below referred to as electron- or exciton-phonon coupling), promoting the disordered Frenkel exciton approach for the photosynthetic excitations.

As follows, a disordered Frenkel exciton model is introduced in relation with absorption spectra of the B850 aggregates. In this model, perturbations of the exciton states by static variances of the Q_y transition energies and coordinates of individual Bchl molecules are considered more significant than the dynamic disorder due to vibrating protein and pigment nuclei. Since the results of this theory are widely known (Jimenez et al., 1996; Wu et al., 1997a; Novoderezhkin et al., 1999), only those of its aspects will be discussed that are needed to understand the fluorescence emission anisotropy measurements of the LH2 complexes as a function of the excitation wavelength (Timpmann et al., 2004a). In these experiments, the edges of the exciton state manifold corresponding to the $k = \pm 1$ and $k = \pm 8$ states were probed. Hence, the width of the B850 exciton band and the corresponding exciton coupling energies could be first reliably estimated. Similar studies for the LH1 complex (i.e., the B875 aggregate) were performed in (Timpmann et al., 2005).

The rigid-lattice exciton Hamiltonian, which takes into account both diagonal (or energetic),

$\delta\varepsilon_n$, and off-diagonal (or structural), δt_{nm} , disorders reads⁴

$$H_0 = \sum_{n=1}^N (\varepsilon_0 + \delta\varepsilon_n) |n\rangle\langle n| + \sum_{n,m=1; n \neq m}^N (t_{nm} + \delta t_{nm}) |n\rangle\langle m|. \quad (4.1)$$

Here, $|n\rangle$ and $\langle n|$ represent the ket and bra vectors, respectively, for the excitation that is localized on the n -th Bchl molecule (shortly, on site n), N is the total number of the sites, and t_{nm} denotes the intermolecular coupling energy between the sites n and m ($n \neq m$). Physically, the first sum in Eq. (4.1) relates to the individual molecular excitations, while the second term accounts for the electronic couplings between the molecules. The latter couplings are mediated by the Coulomb interactions of the electrons and nuclei whose leading contribution is the transition dipole-dipole term. Due to the achieved resonance of the transition frequencies the molecular excitations start moving around, in principle covering the whole aggregate. The maximal absolute value of the coupling, $V = \max \{|t_{nm}|\}$ (corresponding to the $\alpha\beta$ intra-dimer coupling in the LH2 structure of *Rps. acidophila*), is in the following computations utilized as an energy unit.

The Q_y excited state energies, ε_n , of the Bchls are assumed to be random variables distributed according to the normal law, $P(\varepsilon_n)$, with the mean, ε_0 , and the standard deviation, σ ⁵:

$$P(\varepsilon_n) = \frac{1}{\sqrt{2\pi}\sigma^2} \exp\left(-\frac{(\varepsilon_n - \varepsilon_0)^2}{2\sigma^2}\right). \quad (4.2)$$

Equation (4.2) thus constitutes the diagonal disorder model, where $\varepsilon_n = \varepsilon_0 + \delta\varepsilon_n$. As for the off-diagonal model, there are many ways how the structural disorder can be implemented (Jang et al., 2001). For example, one could distribute the Bchl distances, R_n , from the symmetry center of the aggregate in conformity with the normal law (4.2). In this case, ε_0 should be replaced with

the mean radius R_0 , while σ , with the standard deviation from the mean, σ_R . It was, however, shown (Fidder et al., 1991) that as far as the steady-state properties of the excitons are considered, the effects of random diagonal and off-diagonal disorder are almost indistinguishable. This notion in relation to the B850 excitation was confirmed in (Wu and Small, 1998). Therefore, in most of our calculations just the diagonal disorder is applied.

The disordered Frenkel exciton wavefunctions

$$|k\rangle = \sum_{n=1}^N a_{nk} |n\rangle \quad (4.3)$$

and its energy spectrum, E_k , are found by solving the eigenvalue problem

$$\sum_{m=1}^N \langle n| H_0 |m\rangle a_{mk} = E_k a_{nk}. \quad (4.4)$$

The intensities and positions of the absorption bands are determined by the square of the transition dipole moments of the exciton states. The latter can be expressed as follows:

$$\mu_k = \sum_{n=1}^N a_{nk} \mathbf{e}_n, \quad (4.5)$$

where \mathbf{e}_n stands for the unit vector of the transition dipole moment representing a Bchl molecule on site n .

Shown with the flank bold bars on Fig. 4.2a are the exciton levels calculated for a model B850 circular aggregate subject to static diagonal disorder. The foremost influence of the disorder on the exciton level structure is via spreading the state manifold (the exciton band broadening) and lifting the pair-wise degeneracy of the states. In an ensemble representation of Fig. 4.2b the Davydov bandgap is, therefore, practically lost. The underlying mechanism of these changes is the disorder-induced mixing of the Frenkel exciton eigenstates. While in a perfect aggregate the exciton wavefunctions are Bloch states spread all over the structure, in disordered aggregates they shrink and the excitons localize on smaller parts of the aggregate.⁶ The mixing also relaxes

⁴ The division of the static disorder into two independent types is an approximation that originates from the matrix representation of Hamiltonian (4.1). In fact, the structural and site energy disorders are interrelated.

⁵ The full width at half maximum (FWHM) of the distribution function is defined as $FWHM = 2\sqrt{2\ln 2}\sigma$.

⁶ In the solid-state literature, such localization is known as Anderson localization.

the strict selection rules of the regular aggregate, resulting in redistribution of the $k = \pm 1$ (and $k = \pm 8$) states transition dipole strength among other states. Hence, the lowest $k = 0$ as well as the intermediate exciton states become optically available as shown in Fig. 4.2b. Since, however, the dipole strength is still concentrated on the low-energy edge of the density of the exciton states distribution (DOS), the coherent nature of the antenna excitons is largely preserved at the moderate disorder used ($\sigma = 0.6$ V). This justifies our usage of the same quantum number (k) entry for denoting both the delocalized excitons in regular antenna lattices as well as for the localized excitations in the disordered structures to underline their relationship.

A distribution of weak and narrow spectral holes on the low-energy side of the B850 absorption band was recorded (Reddy et al., 1992). This dispersion, conveniently named as B870, was assigned to the expected distribution of the disordered Frenkel exciton $k = 0$ states. Indeed, the individual $k = 0$ states, being the lowest excited states of the aggregate, must be spectrally very sharp. Their width at close to zero temperatures should approach $(2\pi T_1)^{-1}$, being only limited by the exciton lifetime T_1 of the order of 1–2 ns (Monshouwer et al., 1997; Timpmann et al., 2004a). The similar distribution found in LH1 was called B896 (Reddy et al., 1992). Inhomogeneous and relaxation broadening obstructs observation of the split $k = \pm 1$ (as well as of all other states) in steady-state ensemble conditions. Their presence was, however, confirmed by transient hole burning spectroscopy (Freiberg et al., 1998a, b) using spectrally narrow (transform-limited) subpicosecond laser pulses and, more directly, by single molecule fluorescence excitation spectroscopy (Van Oijen et al., 1998, 1999).

As demonstrated in Fig. 4.2b, disorder in principle opens up the whole antenna exciton band for observations by ground state absorption. The energy gap between the mean energies of the split $k = \pm 1$ and $k = \pm 8$ exciton state couples could then be operationally considered as a measure of the exciton bandwidth. In reality, however, the rather weak exciton band top (the $k = \pm 8$ states region) overlaps with broad absorbance of non-functional pigments present both in purified LH2 protein solutions as well as in intact membranes (Rätsep et al., 2005). Moreover, due to the

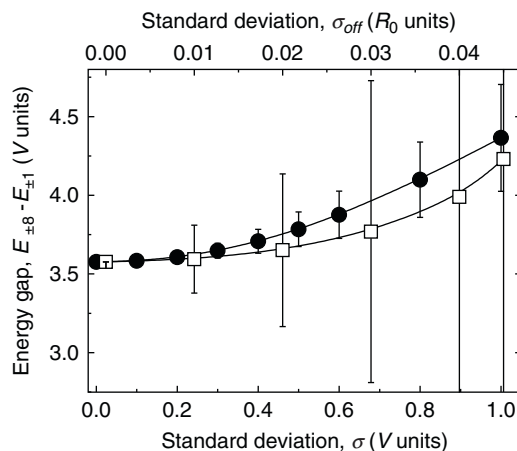


Fig. 4.3. Mean value of the energy gap between the $k = \pm 1$ and $k = \pm 8$ state couples as a function of the static disorder. The solid circles and open squares are for the diagonal and off-diagonal disorder respectively. The bars indicate standard deviation of the gap distribution functions. Off-diagonal disorder has been simulated according to reference (Jang et al., 2001) by randomly distributing the Bchl distances R_0 from the centre of the LH2 ring in accordance with normal distribution with standard deviation σ_{off}

disorder-induced band broadening (see Fig. 4.3), the very weak $k = \pm 8$ spectral structure is almost smeared out. These issues seriously complicate recording of the exciton band top using conventional absorption spectroscopy.

It turns out that boundaries of the exciton band in circular aggregates may still be accessed by taking advantage of their special polarization properties. In the regular aggregates the transition dipole moments of all degenerate state pairs are mutually perpendicular in the ring plane. We have checked that this perpendicularity is in average preserved also in the disordered aggregates with split state pairs. For each state pair then energy exists where the excitons with perpendicular polarizations will be excited at equal probability. Fluorescence anisotropy minima appear designating these excitation energies, unless the angle distribution is not too broad.

Figure 4.4 demonstrates a fairly sharp angle distribution close to the solid angle obtained for the $k = \pm 1$ states and the much broader one in case of the $k = \pm 8$ states. In agreement with experiment (Timpmann et al., 2004b, 2005), the sharp $k = \pm 1$ distribution results in deep and narrow low-energy anisotropy dip, while the broad distribution representing

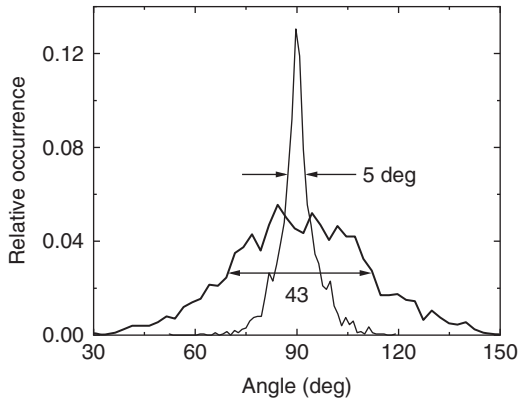


Fig. 4.4. Distributions of angles between the transition dipole moments of the $k = \pm 1$ (thin line) and $k = \pm 8$ (thick line) states calculated for an ensemble of 2000 diagonally disordered B850 aggregates with $\sigma/V = 0.6$. Model parameters suitable for the LH2 from *Rps. acidophila* have been used. Indicated are FWHMs of the distribution functions

the $k = \pm 8$ states produces but a shallow high-energy anisotropy depression. Since the remaining state pairs confirmed still larger average deviation from the solid angle than the $k = \pm 8$ states, the anisotropy minima are practically observable only for the $k = \pm 1$ and $k = \pm 8$ exciton band border states (see further details in Section V). Given that off-diagonal disorder creates more diffuse band edges than diagonal disorder (see Fig. 4.3), the latter model is better suited for description of the antenna fluorescence anisotropy data (Trinkunas and Freiberg, 2006).

III. Shortcomings of the Disordered Frenkel Exciton Model

We have already pointed out that the B870 zero-phonon hole distribution was interpreted as a distribution of the lowest ($k = 0$) states of the Frenkel excitons in disordered ensembles of the B850 aggregates. Yet, calculations have shown (Freiberg et al., 1999, 2003b) that if the exciton coupling energy and the standard deviation of the disorder are kept within the commonly accepted limits, it is impossible to reproduce the B870 band in terms of its width, relative peak position (with respect to the B850 absorption maximum, ΔE), and fractional intensity (relative

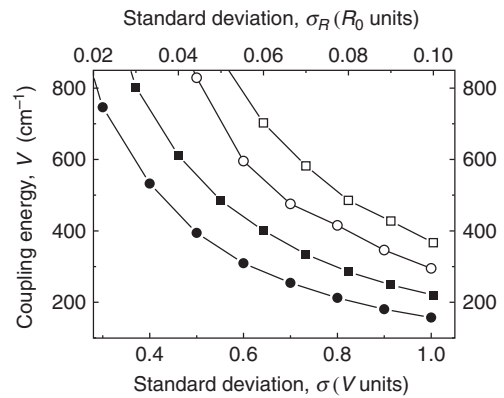


Fig. 4.5. Consistency plots for the diagonal (circles) and off-diagonal (squares) disorder models of the LH2 excitonic states. The open symbols correspond to the average gap between the $k = 0$ state energy and the midpoint of the $k = \pm 1$ state energies. Solid symbols represent the FWHM of the $k = 0$ state energy distribution

to the total B850 absorption intensity). Figure 4.5 highlights the same inconsistency from a different perspective.

The FWHM and ΔE both depend on disorder as well as on exciton coupling energy. Therefore, it is possible to build two separate curves (one for FWHM and the second for ΔE) that describe the relationship between the coupling energy and the disorder by fixing each parameter to its experimental value (FWHM = 147 cm^{-1} and $\Delta E = 204 \text{ cm}^{-1}$, as measured for the LH2 complexes from *Rb. sphaeroides* at 5 K (Freiberg et al., 2003b; Timpmann et al., 2004a)). A crossing of the curves would then provide consistent values of the coupling energy and disorder variables. As can be seen from Fig. 4.5, no crossing is observed within realistic limits of the coupling energy (V between 100 and $1,000 \text{ cm}^{-1}$) and relative disorder (σ/V between 0.2 and 1.0 or σ_R/R_0 between 0.02 and 0.1).

Listed below are a few other experimental observations for ensembles of LH2 complexes that cannot find satisfactory explanation within the disordered Frenkel exciton approach:

- (i) Due to weak exciton-phonon coupling suggested by the hole burning experiment (Reddy et al., 1992), the resonant fluorescence spectrum cannot be much broader than the B870 absorption band. However, the width of the respective ensemble emission spectrum exceeds this figure by more than a factor of two (Freiberg et al., 1999, 2003b).

- (ii) Evidence has been found from the FLN experiment that the broad emission spectrum is essentially homogeneously broadened suggesting that the exciton–phonon coupling for the transition from the relaxed excited state must be strong (Timpmann et al., 2001). This is in contrast with the red edge of the absorption spectrum, which appears mostly inhomogeneously broadened. For LH1 complexes, similar inconsistencies between the narrow hole burning absorption spectra (Reddy et al., 1992) and broad FLN spectra (Van Mourik et al., 1992; Monshouwer et al., 1995; Timpmann et al., 2004a) have been noticed and discussed (Pullerits et al., 1994; Timpmann et al., 2004a).
- (iii) Rising the temperature from cryogenic temperatures to room temperature should thermally populate the strongly allowed $k = \pm 1$ exciton states and result in a significant reduction of the fluorescence lifetime. Yet, the fluorescence lifetime is virtually independent on temperature up to ~ 170 K, while shortening thereafter only by about 20% (Freiberg et al., 2003b). On the basis of the exciton model this can only be explained by assuming static disorder that is much too large to be consistent with the absorption spectrum.
- (iv) To explain temperature dependences of the conjugate absorption and fluorescence spectra of LH2 complexes from three different bacterial species using the same dynamic theory model an extra red shift of the lowest exciton state by $\sim 90 \text{ cm}^{-1}$ was required (Urboniene et al., 2005, 2007).

It is thus quite clear that the genuine Frenkel exciton model, which includes only static disorder, misses some essential aspects of the reality. In solids the phonons scatter the excitons causing homogeneous line broadening (Mukamel, 1995). Strong scattering also leads to fast processes on time scales of the nuclear movements known as excitonic polaron formation and exciton self-trapping. The latter term refers to the fact that by coupling to the surroundings the exciton may induce a deformation of the lattice that lowers the exciton energy and causes its long-time trapping on a limited region of the material space (Lu and Mukamel, 1991; Meier et al., 1997; Tanaka, 2003). In bulk ionic and molecular crystals, where the exciton self-trapping is most thoroughly studied (Rashba, 1982; Ueta et al., 1986; Song and Williams, 1992), character-

istic multi-phonon self-trapped exciton emission bands are commonly observed. These broad and featureless spectra are much red shifted (Stokes shifted) relative to the typically more structured free exciton emission bands.

One could think of the B850 and B875 circles of resonantly coupled Bchl molecules as being electronically one-dimensional (1D). This concept is valid as long as the nearest-neighbor couplings much surpass those between the non-nearest-neighbors and also the symmetry-breaking electron-lattice couplings. Differently from regular two-dimensional (2D) and three-dimensional (3D) lattices, where self-trapping has an energetic threshold and happens abruptly, in 1D arrays the process is smooth taking place at any non-vanishing electron-lattice coupling energy (Rashba, 1982; Sumi, 1994; Cruzeiro-Hansson et al., 2000). Similar topological differences exist relative to the Anderson localization. Therefore, in contrast to the bulk solids, the spectra of the excitons self-trapped in 1D lattice may necessarily not be broad and a great deal Stokes shifted. Clear-cut spectra corresponding to shallow self-trapped excitons have been recorded in some low-symmetry molecular crystals such as β -perylene (Matsui et al., 1984). As follows, a polaronic model of excitons in the B850 and B875 antenna aggregates is introduced. The model is based on the adiabatic Holstein Hamiltonian (Holstein, 1959), being the simplest means to introduce polaronic effects into 1D molecular arrays. Alternative approaches, which, however, have not been applied for comparison with experiment, can also be found (Meier et al., 1997; Damjanovic et al., 2002).

IV. Excitonic Polaron Model of the Antenna Fluorescing States

The relevant excitonic polaron Hamiltonian reads:

$$H = H_0 + c \sum_n q_n |n\rangle \langle n| + \frac{1}{2} \sum_n q_n^2. \quad (4.6)$$

It is modified compared with the original Holstein equation by including static disorder in the rigid-lattice Hamiltonian, H_0 , as shown in Eq. (4.1). The second term in Eq. (4.6) stands for the exciton–phonon coupling energy and the

last term represents the lattice potential energy. The lattice kinetic energy is ignored because of the applied adiabatic approximation, $\nu_m/V \ll 1$, where ν_m is the vibrational frequency inducing the polaronic lattice distortion. Further variables in Eq. (4.6) are q_n , the local lattice distortion at site n and c , the coupling constant characterizing the short-range, on-site exciton–phonon coupling. It is worth noticing here that $c^2/2 = E_{LR}$ defines the site reorganization energy, i.e. an energy which is thermalized (absorbed by the surrounding lattice) as a result of optical excitation/excited state decay in a single antenna site.

By expressing the eigenstates of the exciton–lattice system in the basis of local state vectors

$$|v\rangle = \sum_n \varphi_{nv} |n\rangle \quad (4.7)$$

with amplitudes φ_{nv} , the expectation value of the Hamiltonian (4.6) can be derived as:

$$\begin{aligned} J_v(\{\varphi_{nv}\}, \{q_n\}) &= \langle v | H | v \rangle = \sum_n \varepsilon_n \varphi_{nv}^* \varphi_{nv} \\ &+ \sum_n \sum_{m(\neq n)} t_{nm} \varphi_{nv}^* \varphi_{mv} \\ &+ c \sum_n q_n \varphi_{nv}^* \varphi_{nv} \\ &+ \frac{1}{2} \sum_n q_n^2 \left(\sum_m \varphi_{mv}^* \varphi_{mv} \right). \end{aligned} \quad (4.8)$$

Population of the quantum states is defined by temperature. In case of sparse states and at sufficiently low temperatures, the conditions that are relevant to our subjects, only the lowest-energy or ground excitonic polaron state is populated. Normalization of the ground state (indicated by subscript 0) amplitudes of the excitonic polarons, φ_{n0} , is accomplished by adding a Lagrange multiplier E_0 :

$$J'_0 = J_0 - E_0 \left(\sum_i \varphi_{i0}^* \varphi_{i0} - 1 \right). \quad (4.9)$$

To determine the ground state properties, such as its energy, localization length, and reorganization energy, variations of the functional (4.9) with respect to parameters $\{\varphi_{n0}\}$, $\{q_n\}$, and E_0 are performed. By varying $\{\varphi_{n0}^*\}$, a system of coupled equations is obtained

$$\left[\varepsilon_n + c q_n + \frac{1}{2} \left(\sum_i q_i^2 \right) \right] \varphi_{n0} + \sum_{m(\neq n)} t_{nm} \varphi_{m0} = E_0 \varphi_{n0}, \quad (4.10)$$

where the optimal distortions,

$$q_n = - \frac{c \varphi_{n0}^* \varphi_{n0}}{\sum_i \varphi_{i0}^* \varphi_{i0}}, \quad (4.11)$$

have been found from the following condition:

$$\frac{\partial J'_0(\{\varphi_{n0}\}, \{q_n\})}{\partial q_n} = 0. \quad (4.12)$$

The optimal distortions obey a sum rule

$$\sum_n q_n = -c. \quad (4.13)$$

By substitution the distortions (4.11) into Eq. (4.10) a coupled system of discrete nonlinear Schrödinger equations is obtained for the optimal ground-state exciton amplitudes

$$\varepsilon_n \varphi_{n0} + \sum_{m(\neq n)} t_{nm} \varphi_{m0} - c^2 |\varphi_{n0}|^2 \varphi_{n0} = E_0 \varphi_{n0}. \quad (4.14)$$

These amplitudes determine the modified potential of the site energies due to dynamic lattice deformations:

$$\tilde{\varepsilon}_n = \varepsilon_n - \frac{c^2}{2} |\varphi_{n0}|^2. \quad (4.15)$$

Equations (4.14) are nonlinear with respect to the amplitudes φ_{n0} . The cubic term, proportional to c^2 , while introducing dependence of the ground state properties on initial excitation amplitudes, also excludes analytic solutions of Eq. (4.14), even for the simplest set of the coupling matrix elements. This problem was overcome by applying an iterative procedure described in (Noba and Kayanuma, 1998). In this method, the distortions (4.11) are first calculated for certain initial or seed (hence the superscript s) set of amplitudes, $\{a_{nk}^s\}$. Then, Eq. (4.10) are solved numerically using distortions as parameters. The obtained lowest state eigenvector is subsequently used as a seed for the next iteration. The procedure is repeated until convergent energy and amplitudes are obtained.

A. Ground States of the Excitonic Polarons in Regular and Disordered Circular Aggregates

The most important parameters characterizing excitonic polarons and/or self-trapped excitons in the ground state are their energy, E_0^s , localization length (or shortly size), L_0^s , and superradiance enhancement factor, F_0^s .

The eigenvalue E_0^s is obtained as an expectation value of Hamiltonian (4.6), $E_0^s = \min J_v(\{\varphi_{n0}^s\})$. In experimental spectra, it relates to sharp zero phonon lines (ZPL), representing the phononless energy of self-trapped excitons. The phonon sidebands (PSB) that accompany ZPLs in absorption/fluorescence spectra lay above/below the ZPL energy. Their maxima are shifted relative to the ZPL position by a potential energy of lattice distortion, λ_0^s , also called reorganization energy:

$$\lambda_0^s = \frac{c^2}{2} \sum_n |\varphi_{n0}|^4. \quad (4.16)$$

The localization length, L_0^s , may be defined as the inverse participation ratio (Leggett et al., 1987; Fidler et al., 1991; see Dahlbom et al., 2001 for other conventions) that represents the size in terms of the lattice sites shared by the excitonic polaron wavefunction:

$$L_0^s = \frac{1}{\sum_n |\varphi_{n0}|^4}. \quad (4.17)$$

From Eqs. (4.16) and (4.17) it then appears that the reorganization energy is inversely proportional to the excitonic polaron size:

$$\lambda_0^s = \frac{c^2}{2L_0^s}. \quad (4.18)$$

The superradiance enhancement factor, F_0^s , measures emission intensity of excitonic polarons relative to that of single solvated pigments:

$$F_0^s = \sum_{nm} (\mathbf{e}_n \mathbf{e}_m) \varphi_{n0}^* \varphi_{m0}. \quad (4.19)$$

Polaronic features of excitons depend most on the dimensionless coupling constant, g , being defined as a ratio, $g = E_{LR}/2V = c^2/4V$, of the site reorganization energy and half of the exciton bandwidth. When g exceeds a certain threshold

value, g_c , the excitons in 2D and 3D systems abruptly self-trap. At $g > g_c$, both delocalized (free) and localized (self-trapped) excitons may coexist, separated by a potential barrier in a configurational coordinate space. In ordered 1D systems, however, just a single ground state is present. Its properties change smoothly with g beginning from a totally delocalized exciton state at $g = 0$ towards progressively more localized (self-trapped) states (Rashba, 1982; Kabanov and Mashtakov, 1993; Sumi, 1994; Noba and Kayanuma, 1998; Romero et al., 1999).

Disorder breaks ideal periodicity of the circular antenna aggregates. Therefore, all their states are more or less Anderson-localized from the outset, i.e., already at $g = 0$. The concrete state properties are, however, determined by a combined effect of the resonant interaction, static disorder, and exciton–phonon coupling. In that the latter factor may be decisive. It has been shown (Trinkunas and Freiberg, 2005) that in disordered 1D aggregates the exciton–phonon coupling not only promotes further localization of excitons (beyond the margin set by competition of resonant interaction and static disorder) but, similar to the 2D and 3D lattices, it also introduces abrupt self-trapping type branching of the states at certain critical g value. These branched states can be obtained by solving Eq. (4.10) for two seed amplitude distributions, one that corresponds to a localized single-site excitation and the second, to a totally delocalized excitation creating equal amplitudes on all sites. Multiple stable self-trapped excitons with different size and reorganization energy may thus coexist in a disordered 1D array if exciton–phonon coupling is sufficiently strong.

Figure 4.6 presents the ground state characteristics (E_0^k , L_0^k , and F_0^k) of excitonic polarons in a single diagonally disordered B850 aggregate as a function of g . The simulations are performed for the initial amplitude distributions that correspond to the first three ($k = 0, \pm 1$) disordered Frenkel exciton eigenvectors (Eq. 4.3). The seed amplitude distributions with equal (delocalized) or single-site (localized) excitation probabilities referred to above have no practical reasoning because it is hard to produce such initial states. At the same time, it is in principle possible to selectively excite the disordered Frenkel exciton

states using narrowband lasers. The only limitation is that the energy gap between the adjacent exciton states in the rigid lattice should be larger than the characteristic phonon energy, $h\nu_m$, mixing these states. We shall revisit this issue in Section V.B.

As can be seen from Fig. 4.6, by exciting the $k = 0$ state all the three characteristics follow a smooth path with increasing g , typical for the regular 1D aggregate. Yet, the self-trapping transition that in this particular case is recognizable at $g \approx 0.55$ by contraction of the excitonic polaron size (panel b) as well as by strong increase of its emission strength (panel c) generally appears much earlier than in the ordered

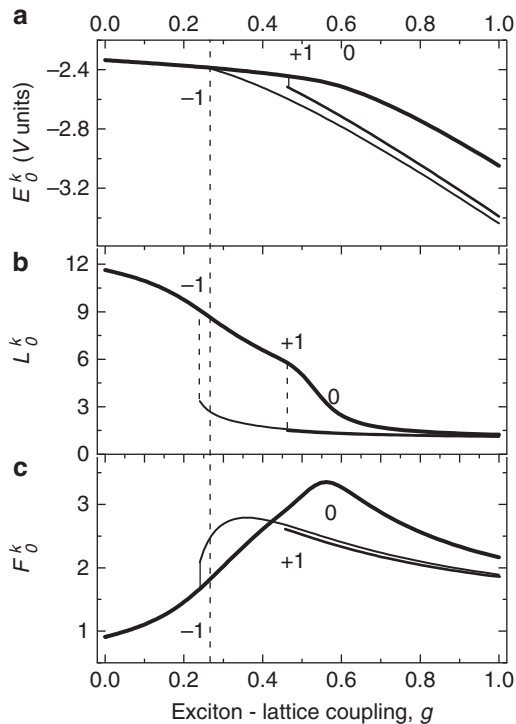


Fig. 4.6. Ground state properties – (a), the energy, (b), the localization length and (c), the superradiance enhancement factor – of the three excitonic polaron states distinguished by the initial amplitude distributions k in diagonally disordered circular aggregates as a function of the exciton-lattice coupling constant g . A single realization of diagonally disordered site energies as shown in Fig. 4.7b is applied to calculate the data. Dashed vertical lines indicate abrupt changes (bifurcations) of the state properties discussed in the text. The vertical dotted line at $g = 0.27$ crossing all panels points the coupling strength used when calculating the distributions of the lattice deformation energy in Fig. 4.7a

aggregate (see Fig. 4.8 below). The dependences for $k \neq 0$ seed distributions are even more intricate. They initially follow the same path as the $k = 0$ state but then new branches split off (at the g values indicated with vertical dashed lines). All the three initial conditions thus result in self-trapped excitons, which have distinct ground state energies as well as other characteristics. Different states on one and the same aggregate can be stable only if they are separated by energy barrier(s). Energy transfer along such a structure is enabled by incoherent hopping mechanism or by tunneling, the former mechanism being temperature-sensitive, while the latter not.

To visualize conformational distortions of large cyclic aggregates such as B850 caused by dynamic exciton–phonon coupling, it is helpful to stretch out the molecular subunits in a linear way and plot the deviations from the site energies according to Eq. (4.15) against the site number. Figure 4.7a presents such distributions for the two self-trapped exciton states of Fig. 4.6, simultaneously supported at $g = 0.27$. The respective static site energy distribution is shown in Fig. 4.7b. One can observe that the deformations corresponding to the two states are largely localized on separate areas of the aggregate. Also, excitons tend to self-trap around the sites with lowest energy, in agreement with (Emin and Bussac, 1994; Stoneham et al., 2007).

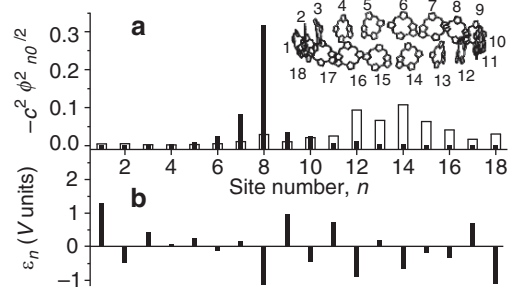


Fig. 4.7. Distributions of the lattice deformation energy due to dynamic exciton–phonon coupling (Eq. 4.15) (a) and the corresponding distribution of static site excitation energies (b). The linear string of the lattice sites numbered from 1 to 18 schematically represents the circular aggregate shown in the insert. The solid and empty bars in (a) correspond to the two self-trapped exciton states in Fig. 4.6 that are supported in the same disordered B850 aggregate at $g = 0.27$, labeled with $k = 0$ and $k = -1$, respectively

B. Ensemble-averaged Characteristics of the Antenna Excitonic Polarons

The data in Figs. 4.6 and 4.7 represent just a single diagonal disorder realization sampled out from the distribution (4.2) of molecular rings that are assumed to simulate the B850 antenna complexes. We are already aware that the onset of self-trapping and the number of coexisting states depend on excitation. In statistical ensembles of antenna rings the excitation conditions vary considerably from ring to ring due to fluctuating absorption spectra. Figure 4.8 provides ensemble characteristics of the excitonic polarons in the B850 antenna aggregates as a function of g , averaged over 5,000 diagonal disorder realizations.

As one can see, within the wide error bars the overall behavior of the curves in Fig. 4.8 is similar for those in Fig. 4.6. The large uncer-

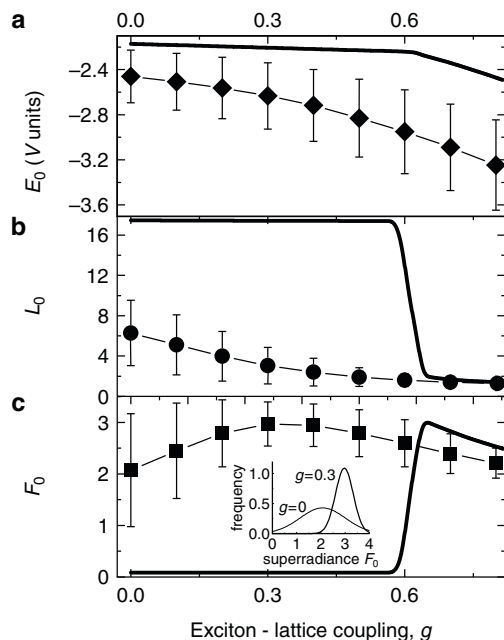


Fig. 4.8. Ensemble averaged characteristics of self-trapped excitons in the B850 aggregates as a function of the exciton-lattice coupling constant: (a) energy; (b) localization length and (c) superradiance enhancement factor. Average is taken over 5,000 samples from the Gaussian distribution (Eq. 4.2) with $\sigma = 0.6$ V and $\varepsilon_0 = 0$. The symbols and error bars designate the mean and the FWHM, respectively, of the corresponding distributions. The inset on panel c shows the normalized distribution of superradiance enhancement factors at $g = 0$ and at $g = 0.3$. Shown with thick solid line are the data for the regular (disorder free) B850 aggregate

tainty is due to disorder and varying excitation conditions as emphasized above. With growing exciton-phonon coupling the excitonic polaron energy and its localization length both smoothly decrease beginning from the respective average disordered Frenkel exciton values of -2.5 V and of 6.3 sites. At the selected relative static disorder $\sigma = 0.6$ V, which satisfies most of the experiments, see Section V), the Frenkel excitons are localized on about one third of the aggregate circle. Dynamic interactions further reduce this size. At $g \approx 0.3$, relevant for the LH2 complexes, the average number of occupied sites is just 3.1, more than twice less compared with the initial ($g = 0$) value. The behavior of F_0 is most fascinating (Fig. 4.8c). The relative emission power, being initially as high as 2.1 grows with g , achieves a maximum of ~ 3.0 at $g \approx 0.3$, and decreases thereafter. The efficiency of incoherent excitation energy transfer increases with emission rate of the donor molecules (Scholes, 2003). Any process that enhances the antenna ability to emit thus serves for optimization of photosynthetic energy transfer and trapping processes. The inset on Fig. 4.8c compares distributions of superradiance enhancement factors at $g = 0$ and 0.3. It is obvious that in the LH2 complexes the efficiency gain due to exciton self-trapping may be essential. Due to different geometry, however, the increase of F_0 in LH1 is rather minor (from five to less than six).

The large effects of disorder on the excitonic polaron characteristics may be best appreciated from comparison with the regular circular aggregate (bold curves in Fig. 4.8). As it was already noticed, disorder considerably reduces the exciton-lattice coupling strength required for the exciton self-trapping. While in the regular B850 aggregate the self-trapping transition is expected at $g = 0.6$, in qualitative agreement with previous works on linear aggregates (Kabanov and Mashtakov, 1993; Sumi, 1994; Noba and Kayanuma, 1998), it occurs at $g \approx 0.3$ in more realistic disordered conditions. Other effects of disorder apparent in Fig. 4.8 (lowering of the transition energy, shrinking of the exciton size, and redistribution of the dipole strength between the exciton states) have been discussed in Section II and do not require further comments.

A well-known qualitative relationship exists between the free exciton size and its transition

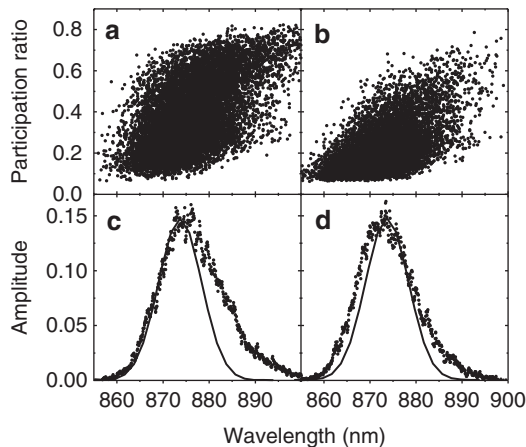


Fig. 4.9. (a) Relationship between the participation ratio L_0^{-1} and the ZPL position chE_0^{-1} for the ground state of self-trapped excitons at $g = 0.24$. (b) The same as in panel (a) for the lowest $k = 0$ Frenkel exciton states ($g = 0$). Panels (c) and (d), the distribution of zero-phonon holes (the B870 band) for the B850 aggregates in B800 deficient LH2 complexes from *Rb. sphaeroides* (solid lines) and the simulated distributions of the relative transition dipole strength for the two models (scattered points). A diagonally disordered ensemble of 10^4 aggregates emulating B800 deficient LH2 complexes has been used in the simulations

energy: the larger the exciton, the lower its energy (Scholes and Rumbles, 2006). Here, we are trying to establish whether similar correlation exists in disordered ensembles of self-trapped (Fig. 4.9a) and Frenkel (Fig. 4.9b) excitons. For convenience the data in Fig. 4.9 are plotted in the $L_0^{-1} - chE_0^{-1}$ (exciton participation ratio – wavelength of ZPL) axes scale. Here h and c have the usual meaning of the Planck's constant and of the speed of light, respectively. An ensemble of the B800 deficient LH2 complexes was assumed characterized with $g = 0.24$. At this exciton–lattice coupling constant the majority of the antenna rings host just a single self-trapped exciton state, while about 10% of them support two such states.

Figures 4.9a and b illustrate positive correlations that exist between the participation ratio and the ZPL position in the ensembles of self-trapped excitons and excitons, respectively. The excitons and self-trapped excitons that absorb/emit at longer wavelengths are generally more localized. However, the slope of an imaginary line through constellations of the data points is considerably

greater in the case of the self-trapped excitons than excitons. Furthermore, while the Frenkel exciton data points are densely flocking on the low left hand corner of the graph signifying delocalization, the data for the self-trapped excitons are widely spread toward more localized states.

Figures 4.9c and d compare the calculated according to Eq. (4.19) distributions of the relative transition dipole strength with the experimental distribution (Freiberg et al., 2003b; Rätsep et al., 2005) of zero-phonon holes (the B870 band). As seen, the excitonic polaron model (Fig. 4.9c) is able to reproduce the high-energy slope and the maximum of the experimental curve very well. The discrepancy observed at the low-energy side is explained by the fact that the simplified calculations do not take into account the actual spectral lineshapes. As it will be in more detail described below, the transition dipole strength in the excitonic polaron spectra is shared by narrow ZPL and broad PSB. Division of intensity between these components depends on size of the excitonic polarons. At blue side intense ZPLs dominate the spectrum, whereas at red side the spectral intensity is concentrated into PSBs. By virtue of the hole burning technique, the low-burn distribution of the zero phonon hole depths (the B870 band) emphasizes contribution of the ZPLs. In agreement with Fig. 4.9c, therefore, a decent fit could only be expected at high-energy side of the spectrum where most exciton-like excitonic polaron states donate. The match in the case of the Frenkel exciton model (Fig. 4.9d) is in almost every aspect much less satisfactory.

At any excitation wavelength the antenna rings corresponding to broad range of participation ratios and, according to Eq. (4.18), of reorganization energies are simultaneously excited. Since the reorganization energy is related to the shift and broadening of the spectra, the efficiency of selective spectroscopy methods (such as hole burning and FLN) is reduced when applied to ensembles of self-trapped excitons. Let us explain the situation once again using a configuration coordinate representation of Fig. 4.10.

The four excited state parabolas in this figure represent two free exciton states (with their potential energy minima unshifted relative to the ground state curve) and two self-trapped exciton

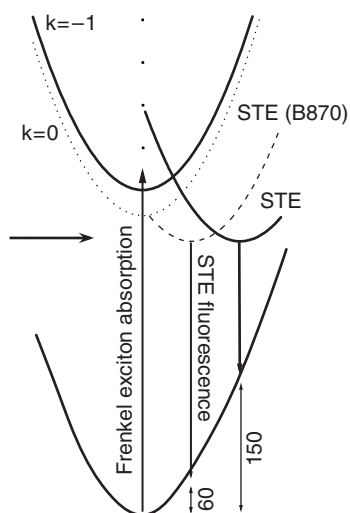


Fig. 4.10. A configuration coordinate diagram for excitations in B850 antenna aggregates. The shifted self-trapped exciton (STE) diabatic potential energy curves are for the two self-trapped exciton states (represented by dashed and thick solid lines) that belong to different or the same antenna rings. The numbers denote approximate reorganization energies in wave numbers estimated from the selective fluorescence data for the B850 aggregates from *Rb. sphaeroides*. The un-shifted excited states indicated with k -numbers represent average positions of the two lowest disordered exciton distributions in Fig. 4.2b

states (shifted curves).⁷ The self-trapped excitons selected out from an ensemble of the B850 rings have the same ZPL energy but different reorganization energies (small for dashed and large for thick solid line). Therefore, the fluorescence recorded upon resonant excitation with a narrowband laser (horizontal arrow) appears to be a sum of two (narrow for small and broad for large reorganization energy) overlapping spectra that are difficult to separate. No such broadening mechanism is available for the Frenkel excitons. At all excitation wavelengths nearly the same sharp lineshape is produced. Obviously, only the excitonic polaron model is compatible with the experiments on LH2 and LH1 antenna complexes where poor selectivity of the FLN spectra was observed (Van Mourik et al., 1992; Freiberg et al., 2003a, b; Monshouwer et al., 1995).

⁷ An energy difference between the $k = 0$ exciton state and the self-trapped exciton states is due to dynamic lattice deformation. Therefore, by analogy with regular lattices, it might be called the self-trapping binding energy.

V. Evaluation of the Model Parameters from the Experimental Spectra

A. Resonant Coupling Energy, Inhomogeneous Spectral Broadening, and Reorganization Energy

The excitonic polaron model identifies three main parameters that determine the true nature of the photosynthetic antenna excitations, those being the resonant (exciton) coupling energy, the inhomogeneous spectral broadening, and the reorganization energy. Large amount of heterogeneity usually prevents assessment of these parameters from the conventional optical spectra of aggregates. Non-conventional approaches are, therefore, required to obtain necessary information and to test the models. As follows, a method of evaluation of the interrelated exciton coupling energy, inhomogeneous spectral broadening, and reorganization energy from fluorescence anisotropy spectra is demonstrated (Timpmann et al., 2004a, 2005; Trinkunas and Freiberg, 2006).

Figure 4.11 shows fluorescence anisotropy as a function of the linearly polarized excitation light wavelength for the B800-deficient LH2 complexes from *Rb. sphaeroides*. This mutant sample was chosen for the illustration in order to display the B850 spectroscopy in its most basic form, having getting rid from the complications due to the quasi-monomeric B800 molecules.

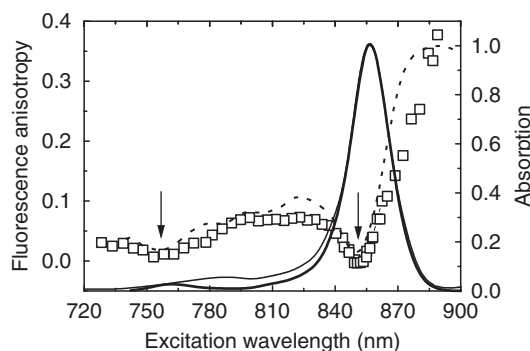


Fig. 4.11. Absorption (measured: thin solid curve; simulated: thick solid curve) and fluorescence anisotropy (see Eq. 4.23) excitation spectra (experimental: squares; simulated: dashed curve) of purified B800-deficient LH2 complexes from *Rb. sphaeroides* at 5 K. The polarized fluorescence was recorded broadband at the long-wavelength part of the emission spectrum where the anisotropy is constant

The fluorescence anisotropy, r , is related to the linearly polarized fluorescence emission intensities I_{vv} and I_{vh} as

$$r = \frac{I_{vv} - I_{vh}}{I_{vv} + 2I_{vh}}. \quad (4.20)$$

Here, the I_{vv} and I_{vh} are the emission intensities polarized, respectively, parallel and perpendicular to the orientation of the electric vector of the excitation light. In agreement with the previous measurements on wild type complexes (Kramer et al., 1984; Visschers et al., 1995; Timpmann et al., 2004b), the low anisotropy observed at shorter wavelengths rises steeply across the B850 absorption band closing a theoretical limit of 0.4 at its long-wavelength slope. In addition, however, there are two anisotropy drops pointed out with arrows, a shallow high-energy depression at 757 nm and a deeper and narrower low-energy dip at 851 nm. As discussed above, these minima could be related to the weakly ($k = \pm 8$) and strongly ($k = \pm 1$) absorbing exciton band edges, respectively.

The fluorescence spectrum (with emission frequency ν_e) of a single LH2 complex upon selective excitation at ν_a can be calculated as (Trinkunas and Freiberg, 2006):

$$I(\nu_e, \nu_a) = N_{pol}^{-1} \sum_k |\mu_k|^2 |\mu^k|^2 F^k(\nu_e) \times \int_{-\Delta/2}^{\Delta/2} A(E_k - \nu_a + \nu') d\nu'. \quad (4.21)$$

In Eq. (4.21), μ_k is the transition dipole moment vector of the absorbing Frenkel exciton states (Eq. 4.5), μ^k is the transition dipole moment vector of the emitting excitonic polaron states, $F^k(\nu_e)$ is the normalized emission profile of self-trapped excitons, $A(E_k - \nu_a)$ is the normalized homogeneously broadened absorption profile of Frenkel excitons centered at E_k , and N_{pol} is the number of different self-trapped exciton states per complex. At low temperatures when energy transfer is absent the fluorescence from all these states should be accounted for independently. The

sum in Eq. (4.21) counts the Frenkel exciton states that have energy between $\nu_a - \Delta/2$ and $\nu_a + \Delta/2$ and is required for comparison with experiment, because Δ limits the available excitation selectivity (Agarwal et al., 2002; Freiberg et al., 1999). $\Delta = \sqrt{8 \ln 2} \sigma_{ext}$, where σ_{ext} , the standard deviation of the external diagonal disorder, is determined by random variations of the mean transition energy in different complexes.

The emission profile, $F^k(\nu_e)$, is modeled by a function:

$$F^k(\nu_e) = l(E_0^k) \exp\left(-\frac{\lambda_0^k}{h\nu_m}\right) + f^k(\nu_e) \left[1 - \exp\left(-\frac{\lambda_0^k}{h\nu_m}\right)\right], \quad (4.22)$$

where $l(E_0^k)$ represents the ZPL centered at E_0^k and $f^k(\nu_e)$, the associated PSB. The dimensionless parameter $S = \lambda_0^k / h\nu_m$, commonly named as the Huang-Rhys factor, corresponds to an average number of phonons that accompany absorption or fluorescence emission transitions (see, e.g., Rebane, 1970). In actual computations that assumed extreme low temperatures, the shape of $l(E_0^k)$ was approximated by a Gaussian of experimentally limited FWHM ($\sim 1.5 \text{ cm}^{-1}$), while that of $f^k(\nu_e)$, by the following function:

$$f^k(\nu_e) = \begin{cases} \frac{E_0^k - h\nu_e}{(\lambda_0^k)^2} \exp\left(-\frac{|E_0^k - h\nu_e|}{\lambda_0^k}\right), & h\nu_e < E_0^k \\ 0, & h\nu_e \geq E_0^k \end{cases}. \quad (4.23)$$

The fluorescence anisotropy dependence for a single aggregate was computed using an equation $r_k = (3 \cos^2 \alpha_k - 1)/5$ (α_k is the angle between the transition dipole moment vectors of absorbing (μ_k) and emitting (μ^k) states). At low temperatures the emitting state is always the ground state of the self-trapped excitons. The parallel, I_{par} , and perpendicular, I_{per} , fluorescence emission components were obtained from Eq. (4.21) by multiplying each k -term under the sum with orientation factors $1 + 2r_k$ and $1 - r_k$, respectively. Ensembles averages $\langle I_{par} \rangle$ and $\langle I_{per} \rangle$ were then calculated, being directly related to the experimental intensities I_{vv} and I_{vh} , respectively.

The simulated data, averaged over an ensemble of 10,000 diagonal disorder realizations, are compared with the experiment in Fig. 4.11. The couplings between all pigment were calculated in transition dipole–dipole approximation using the crystallographic structure of LH2 of *Rps. acidophila* strain 10,050 (Papiz et al., 2003). Adjusted by fitting circular dichroism spectra, the site energy difference in the basic heterodimer unit was set to a value of 0.8 V. Similar figure was suggested by (Koolhaas et al., 1997). Simultaneous fine-tuning of this number of free parameters for large ensembles is computationally costly. To curtail the procedure, an iterative approach briefly described below was applied. We began with simulations of the absorption spectrum, from which rough estimates for the relative disorders, σ/V and σ_{ext}/V were obtained. Then a zero-order value of V was evaluated from simulations of the anisotropy curve. Finally, the fluorescence spectrum characteristics (peak position and FWHM) were fitted as a function of excitation wavelength. This comparison is sensitive to the site reorganization energy, E_{LR} , as well as to the mean vibrational frequency, ν_m . The emission bandshape is also susceptible to disorder. Adjustment of the disorder parameters for the emission spectrum launched next twist of the search. The iterative procedure was continued until satisfactory match with experimental data was achieved.

The fits in Fig. 4.11 seem very reasonable, considering the possibility that slight differences between real and used crystal structures may exist. Moreover, the calculated spectra understandably lack any contribution from the non-functional Bchls (see Rätsep et al., 2005). This in large explains the absorption spectrum discrep-

ancy observable at 787 nm. The anisotropy curve very well reproduces the positions of the two experimental minima. The deviations observed in the middle and upper exciton band regions with higher DOS (see Fig. 4.2b) may be explained by partial failure of the adiabatic criterion in this range. Comparison with the absorption spectrum proves that the two anisotropy minima are indeed well correlated with the $k = \pm 1$ and $k = \pm 8$ states at the exciton band boundaries. The best-fit parameters obtained from all these comparisons are gathered into Table 4.1. For overview, Table 4.1 also includes fitting parameters for all other bacterial antenna aggregates analyzed so far with similar approach. Due to space limits, however, we cannot comment on those other results in any length.

B. The Wavelength-dependent Exciton–Phonon Coupling and the Weighted Density of the Phonon States

Much of the controversy underscored in Section III between the absorbing and emitting properties of the LH2 and LH1 antennas is a result of the early estimates (Reddy et al., 1992; Wu et al., 1997a) of the Huang-Rhys factor and the effective phonon frequency: $S \approx 0.3$ and $V_m \approx 20 \text{ cm}^{-1}$, respectively. These numbers, obtained from the photophysical hole-burning experiments, suggest very small reorganization energy compatible with rather weak exciton–phonon coupling. It was only recently realized (Pieper et al., 1999; Rätsep and Freiberg, 2003) that the hole-burning spectra of the antenna complexes are strongly distorted due to limited inhomogeneous spread of the lowest

Table 4.1. Model parameters for the B820, B850, and B875 ring aggregates of bacterial antenna complexes^a

Sample	V/V' cm^{-1}	$\sigma_{\text{int}}/\sigma_{\text{ext}}$ cm^{-1}	$\langle \epsilon_0 \rangle_{\text{ext}}$ cm^{-1}	E_{LR} cm^{-1}	g	$\frac{\sigma_{\text{int}}}{V}$	Bandwidth ^b (sim/exp)
LH2 from <i>Rb. spaeroides</i>	315/245	220/60	12,390	160	0.25	0.70	1,280/1,250
B800-deficient mutant	370/290	240/60	12,400	190	0.26	0.65	1,450/1,500
LH2 from <i>Rb. spaeroides</i>							
LH2 from <i>Rps. acidophila</i>	350/270	180/40	12,160	200	0.28	0.51	1,480/1,450
LH3 from <i>Rps. acidophila</i>	320/250	200/50	12,800	180	0.28	0.64	1,300/1,290
LH1 from <i>Rb. spaeroides</i> ^c	420/330	230/50	12,130	185	0.22	0.55	1,950/1,950

^aThe estimated standard deviation of the parameters is typically 10%, except for the mean of the Bchl transition energies $\langle \epsilon_0 \rangle_{\text{ext}}$ where it is about 0.25%.

^bExciton bandwidth determined as an energy gap between the anisotropy dips (sim: from simulations, exp: from experiments).

^cApparent variances with the data in (Timpmann et al., 2004a) are explained with different static disorder models applied.

states. Moreover, since the photophysical bleaching mechanism just redistributes the hole burning products within the spectra range of the original absorption band, the hole burning spectra are obscured by the absorbance of the products. A thorough analysis made in (Rätsep and Freiberg, 2003, 2007) concluded that reliable characterization of the exciton–lattice coupling in antenna systems requires a more involved selective spectroscopy technique referred to as differential fluorescence line narrowing (Δ FLN).

Analogous to the hole-burning spectrum, which is obtained as a difference between the pre- and post-burn absorption spectra, the Δ FLN spectrum is a difference between the FLN spectra recorded before and after burning spectral holes. Thus, the Δ FLN spectrum corresponds to the emission of those chromophores that are selectively bleached out between two successive FLN measurements. The main advantage of the Δ FLN method is that it yields almost undistorted ZPLs together with the corresponding phonon structure (see Fig. 4.12), so that electron–phonon and/or exciton–phonon coupling strengths can be determined directly (Rätsep and Freiberg, 2003, 2007). Stabilized lasers and samples of very high optical

quality that almost do not scatter light are still required for successful measurements.

Within the basic model that includes adiabatic, harmonic, Condon, and linear electron-phonon coupling approximations, the single site/state fluorescence spectrum at zero temperature of chromophores embedded into an amorphous protein matrix may be written down as (Hayes et al., 1994):

$$L(\nu) = e^{-S} l_0(\nu - \Omega) + \sum_{R=1}^{\infty} S^R \frac{e^{-S}}{R!} l_R(\nu - \Omega + R\nu_m), \quad (4.24)$$

where S is the already defined Huang-Rhys factor. The first term in Eq. (4.24) describes ZPL, while the second one characterizes PSB. The ZPL of shape l_0 peaks at frequency Ω . The l_R -terms with $R = 1, 2, \dots$ correspond to the one-phonon and multi-phonon transitions. The area-normalized one-phonon spectral profile, $l_1(\nu)$, also called the weighted density of the phonon states, is an important characteristics of dynamical systems that interact with their surroundings. It is a product of two frequency-dependent terms, the density of vibrating states and the electron–phonon coupling strength (Rebane, 1970).

The Δ FLN spectrum in the short burn time limit may be represented as (Pieper et al., 1999):

$$\begin{aligned} \Delta FLN(\nu) \propto & \sum_{R,P=0}^{\infty} \left(S^R \frac{e^{-S}}{R!} \right) \left(S^P \frac{e^{-S}}{P!} \right) \\ & \times \int d\Omega N(\Omega - \nu_c) l_R(\nu - \Omega + R\nu_m) \\ & \times l_P(\nu_E - \Omega - P\nu_m). \end{aligned} \quad (4.25)$$

Here, $N(\Omega - \nu_c)$ is the Gaussian inhomogeneous site/state distribution function (SDF) centered at ν_c . The ZPL at the excitation frequency ν_E corresponds to the transitions with $R, P = 0$. All other transitions constitute the PSB.⁸ The Huang-Rhys factor S is calculated from Eq. (4.26)

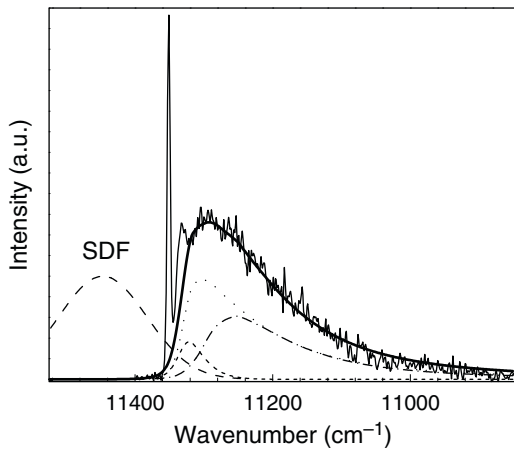


Fig. 4.12. Experimental (thin solid line with noise) Δ FLN spectrum of B800-deficient LH2 complexes from *Rh. sphaeroides* at 5 K. The narrow line at $11,351 \text{ cm}^{-1}$ (881 nm) is the ZPL. Its width is limited by the resolution of the experimental setup. The three contributions to the calculated PSB (thick solid line) are: real-PSB (dotted), pseudo-PSB (dash-dotted), and multi-PSB (short dashed). A Gaussian SDF with FWHM equal to 151 cm^{-1} and peak at $11,447 \text{ cm}^{-1}$ is represented with dashed line (See text for further details)

⁸ Only excitations within the inhomogeneously broadened fluorescence origin band that are resonant with ZPLs are spectrally selective, resulting in line-narrowed FLN spectra. The excitation is nonselective with respect to such sites/states whose fluorescence origin band lies at lower energy than the excitation wavelength, so that the fluorescing state is populated via relaxation. As a result, non-line-

$$e^{-S} = \frac{I_{ZPL}}{I_{ZPL} + I_{real-PSB}}, \quad (4.26)$$

where I_{ZPL} is the integral intensity of the ZPL and $I_{real-PSB}$, that of the real phonon sideband (real-PSB). The latter term requires an explanation. In selective spectra, including Δ FLN, the intensity of PSB with respect to ZPL is always larger than in the corresponding homogeneously broadened spectrum represented by Eq. (4.24). This is because of two additional contributions, the so-called pseudo-PSB and multi-PSB, which appear in inhomogeneously broadened spectra due to non-resonant excitation via the phonon sidebands⁹ (Kikas, 1978; Sapozhnikov and Alekseev, 1984; Pieper et al., 1999; Rätsep and Freiberg, 2003).

Figure 4.12 demonstrates a model analysis of the Δ FLN spectrum for the B800-deficient LH2 complexes at 881-nm excitation. As seen, the real-PSB that according to Eq. (4.26) reports about the exciton–phonon coupling strength constitutes only a bit more than half of the experimental PSB. If the observed PSB was used to calculate the Huang-Rhys factors, instead of the real-PSB much exaggerated value of S would have been obtained. Careful simulations of the experimental spectra are thus required to derive correct model parameters from the selective spectra. Notice that the simplified PSB fit presented in Fig. 4.12 ignores a sharp feature of the experimental sideband of pseudo-local phonon origin shifted by 18–20 cm^{-1} with respect to ZPL.

In relation with Figs. 4.9 and 4.10, reduced efficiency of the selective spectroscopy methods, when applied on the ensembles of LH antennas, was emphasized. Setting up just a single variable, e.g., excitation wavelength, does not guarantee top selectivity. At least two coordinates (excitation energy and the participating ratio/reorganization energy) should in the present model be simultaneously addressed for more complete selection. This is also the key for under-

narrowed (inhomogeneously broadened) fluorescence spectra are obtained.

⁹ The terms “resonant” and “nonresonant” are generally used to describe the two contributions to the line-narrowed optical spectra according to the mode of their excitation. Whereas ZPL and real-PSB correspond to the resonant excitation, the pseudo-PSB and multi-PSB constitute the nonresonant parts.

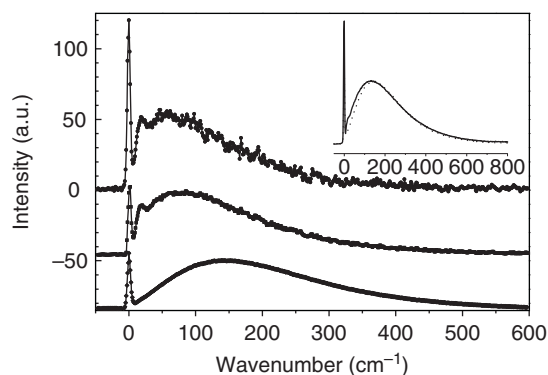


Fig. 4.13. The Δ FLN spectra (two top curves) of the B800-deficient LH2 complexes from *Rb. sphaeroides* at 5 K. The area-normalized spectra are measured at 881 nm with burn fluence of 0.4 J cm^{-2} (top) and 21.6 J cm^{-2} (middle). The bottom curve is the FLN spectrum recorded after hole burning with fluence of 21.6 J cm^{-2} . The spectra are arbitrarily shifted relative to each other for clarity. The latter FLN spectrum is redrawn with dotted line in the inset to compare with the initial FLN spectrum (black continuous line) before any deliberate hole burning. Notice that in the FLN spectrum the scattered laser line at zero frequency obscures the ZPL.

standing the fast broadening and loss of structure of the experimental Δ FLN spectra with increasing burn fluence shown in Fig. 4.13.

Initially, under low burn fluence, the exciton-like polarons with smallest participation ratio and strongest ZPLs will be burned out, resulting in narrow and structured Δ FLN spectrum. According the fluence buildup, the high-participation-ratio antenna forms, corresponding to self-trapped excitons, start gradually disappear that broadens the remaining spectrum. Because of this burn dependence, all the parameters evaluated from the selective spectra, such as S factors, should be extrapolated to the zero-burn limit. The inset of Fig. 4.13 shows that the FLN spectrum remaining after extensive burning still pretty much reminds the original FLN line shape, except the rather small low-frequency part that has been burned out. These observations suggest that in agreement with Fig. 4.9a the bulk of the excitations generated at the low-energy edge of the absorption spectrum (e.g., at 881 nm) correspond to the dynamically self-trapped excitons.

According to Fig. 4.9a, variations of the FLN spectra with excitation wavelength should appear, the spectra excited at longer wavelength being generally broader (stronger coupled) than those

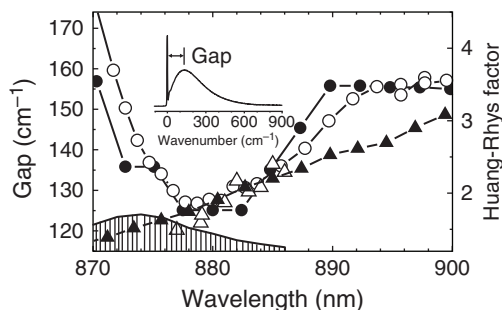


Fig. 4.14. Excitation wavelength dependence of the energy gap (open circles: experiment, filled circles: simulations) and of the Huang-Rhys factor (open triangles: experiment, filled triangles: simulations) in the FLN spectra of B800-deficient LH2 complexes from *Rb. sphaeroides* at 5 K. The energy gap definition is provided in the inset. Sketched with solid vertical lines is the B870 distribution of the spectral hole depths

measured at shorter wavelengths. Figure 4.14, where excitation wavelength dependence of the gap (as defined in the inset) and the Huang-Rhys factor is shown for the B800-deficient LH2 complexes, fully confirms these expectations. The gap, a measure of the reorganization energy, having a minimum value of $\sim 127 \text{ cm}^{-1}$ at 878 nm. It increases toward longer wavelengths until becoming saturated at $\sim 157 \text{ cm}^{-1}$ above 894 nm.¹⁰ Where comparison is available (experimental evaluation of the factors from the FLN spectra is technically limited by the ability to burn well-defined spectral holes), the experimental and model behaviors of the gap and are similar. The exciton-phonon coupling is strong because the Huang-Rhys factor is greater than 1 over the whole spectral range available to the measurements. As seen, the simulations predict that S may reach 3 or even greater values at the far-red edge of the spectrum. A reasonable fit was achieved with ν_m in the range of $40\text{--}50 \text{ cm}^{-1}$. In Section V. A mean frequencies around $30\text{--}40 \text{ cm}^{-1}$ were used. It is worth noticing that with all these frequencies the adiabatic approximation of the Holstein model is well obeyed, since $\nu_m/V \approx (40\text{--}50)/370 \ll 1$.

¹⁰ An increase of the gap below 878 nm is due to the excitation energy relaxation as explained above and has no relevance to the exciton-phonon coupling change, our main concern here.

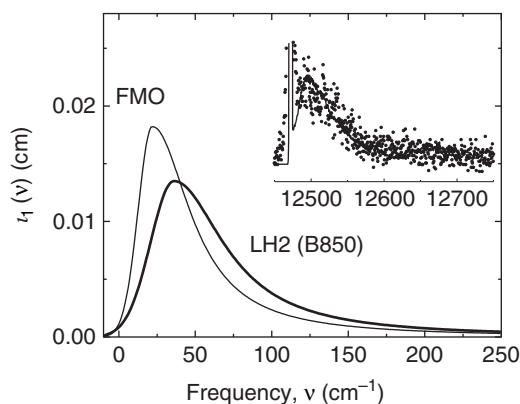


Fig. 4.15. One-phonon functions obtained for the B800-deficient LH2 complexes from *Rb. sphaeroides* (thick solid curve) and for the FMO complexes from *Chlorobium tepidum* (thin solid curve). The inset compares the low-temperature sidebands in the fluorescence excitation spectrum of a B800 molecule in a single LH2 complex from *Rs. molishianum* (scatter) (Hofmann et al., 2005) and in the Δ FLN spectrum of the FMO complexes (continuous line) (Rätsep and Freiberg, 2007). To achieve the overlap the ZPL at 827.1 nm in the FMO spectrum was shifted until it coincided with the origin of the single molecule spectrum and then its x-axis was reversed

The selective spectroscopy model described, in principle, allows the one-phonon profile, $I_1(\nu)$, to be recovered from experimental spectra. A solution of such inverse problem for the B800-deficient LH2 complexes is shown in Fig. 4.15.¹¹ Exposed also in this figure is the similarly computed profile for the FMO antenna complex. It is a generally believed that a single Bchl molecule is responsible for the fluorescence emission of the FMO complex. This indeed might be the case because, as demonstrated in the inset, the shape of the PSB in the FMO emission spectrum almost coincides with the PSB in the fluorescence excitation spectrum of quasi-monomeric B800 molecules in the LH2 complex from *Rs. molishianum*, measured in a single molecule experiment (Hofmann et al., 2005). The FMO spectrum thus provides a reference one-phonon spectrum of a single Bchl molecule locally coupled to protein environment.

¹¹ Let us notice again (see remark at Fig. 4.12) that for simplicity the pseudo-local phonon feature of the experimental spectrum has been ignored in these simulations.

As can be seen from Fig. 4.15, the two profiles differ considerably. The one-phonon spectrum of B850 is much broader than that of FMO (FWHM equal to 58 cm^{-1} and 41 cm^{-1} , respectively) with its peak at almost twice higher frequency (36 cm^{-1} and 22 cm^{-1} , respectively). To the extent that the FMO spectrum represents the true local response of the protein to the electronic transition in every single Bchl molecule, these differences could be associated with assembly of the Bchl molecules into the B850 aggregate. Let us notice that the peak phonon energy is generally smaller than the energy gap between the adjacent exciton states of the B850 aggregate at the lower Davydov subband region ($\sim 100\text{ cm}^{-1}$ (Wu et al., 1997b; Freiberg et al., 1999; Van Oijen et al., 1999)). This validates the selective excitation approximation discussed in Section IV.A.

The knowledge of the one-phonon profile and the Huang-Rhys factor (i.e., the spectral density function) provides a method for calculation of the reorganization energy of the excitonic polarons according to Eq. (4.27):

$$\lambda_0 = hS \int_0^\infty d\nu l_1(\nu) \nu. \quad (4.27)$$

Taking $S = 1.6$ for the B850 aggregate and $S = 0.4$ for the FMO complex (those are the Huang-Rhys factor values at half height of the corresponding SDFs (see Fig. 4.14 and reference Rätsep and Freiberg, 2007), the reorganization energies of 128 cm^{-1} and 25 cm^{-1} , respectively, were obtained by integration between 0 and 500 cm^{-1} . In the case of FMO, one is justified to write $\lambda_0^{FMO} \equiv E_{LR}^{FMO}$. In reference (Adolphs and Renger, 2006), the same feature was calculated equal to 40 cm^{-1} . The much bigger site reorganization energy of $E_{LR}^{B850} = 190\text{ cm}^{-1}$ found for the Bchls in the B850 complex of B800-deficient LH2 complexes from the anisotropy simulations (see Table 4.1) is qualitatively consistent with the basic idea followed in this work that excitons in the tightly packed antenna aggregates are rather strongly coupled to the environment. In this regard, it is worth noticing that the surroundings of the aggregated Bchls include both the protein subunits and the neighboring pigments, differently from the lone Bchl in the FMO complex hosted just by the protein. Since $L_0 = E_{LR}/\lambda_0$

(see Eq. 4.18), one gets $L_0 \approx 1.4$, the value which is within the standard deviation of calculated sizes of the excitonic polarons at $g = 0.3$ (Fig. 4.8b).

VI. Conclusions and Outlook

In this chapter, the origin of the electronic excited states in the ring-shaped bacteriochlorophyll aggregates has been studied by theoretical analysis and numerical evaluation of various spectroscopic parameters characterizing these states. Such aggregates govern the functionally important ultrafast funneling of the solar excitation energy in the photosynthetic membranes of purple bacteria. The optical spectroscopy data of LH1 and LH2 antenna complexes acquired at low temperatures when the quantum aspects of the material excitations dominate were investigated in terms of collective (exciton and excitonic polaron) quantum eigenstates. The limited size and the known spatial structure of the aggregates greatly support such detailed analysis. On broader molecular physics vista, these aggregates may be considered as unique model systems of a 1D topology having fixed (genetically predetermined) size with practically zero dispersion.

We have shown that the absorbing and the emitting electronic states of the antenna aggregates could not be adequately described within the common disordered Frenkel exciton approach. This is understandable since in 1D molecular arrays already infinitesimal couplings between the exciton and the bath of vibrational modes (that in the antenna pigment-protein complexes involve movements of both the protein and the pigment atoms) develop excitonic polarons and/or self-trapped excitons with non-uniform displacement of the nuclear coordinates. The Holstein Hamiltonian has been applied for characterization of steady-state eigenstates of the excitonic polarons in 1D systems. To analyze real situations, static disorder should be included. Despite apparent simplicity of such a model, its quantitative evaluation in the case of the B850 and B875 aggregates happened to be challenging. This is because the energetic parameters that govern the electronic structure and the dynamics of the antenna excitations

such as σ , V , E_{LR} are all of the same order of magnitude. Also, new effects distinct from those in the regular 1D systems appear. At exciton–phonon couplings above some critical strength, the disordered antenna aggregates may support multiple self-trapped excitons with different size, reorganization energy, and spatial location. In certain sense they become similar to the 2D and 3D ordered systems where free excitons coexist with the self-trapped excitons, separated by an energy barrier. Yet, the excitons in disordered 1D aggregates are always to some extent localized by static disorder. Attracted by the low energy sites of the lattice they can further dynamically localize by the self-trapping mechanism. The critical exciton–phonon coupling value for the coexistence depends on particular disorder realization.

Exciton self-trapping generally results in broadened and Stokes shifted fluorescence spectra, potentially improving efficiency of the incoherent energy transfer between the antenna complexes. Furthermore, at $g \approx 0.3$ and $\sigma \approx 0.6V$, appropriate numbers for the B850 aggregate, the emission rate is at the highest possible value, being a couple of times larger than that for disordered Frenkel excitons. This notable amplification of the emission rate might also have photosynthetic relevance by optimizing energy transport and trapping processes. It was recently proposed (Markvart and Greef, 2004) that the incoherent Förster energy transfer mechanism and the thermally activated transport of self-trapped excitonic polarons are closely related. Efforts are still required to explicitly demonstrate this idea on clusters of antenna complexes and on complete photosynthetic membranes.

The excitonic polaron model presented in this chapter for the first time allows a consistent description of the low-temperature absorption and emission spectra of bacterial antennas. The spectra measured at physiological temperatures generally require more sophisticated analysis based on density matrix methods (see e.g. Van Grondelle and Novoderezhkin, 2006; Urbaniene et al., 2007). However, recent studies (Schröder et al., 2006) of the LH2 complexes using non-Markovian as well as modified Redfield approaches have demonstrated that it is difficult to choose between the various dynamic models, as their differences are smeared out by ensemble average. Therefore, the energetic

parameters obtained at low temperatures are very valuable for the calibration of various dynamic theories.

Acknowledgments

This work was partially supported by the Estonian Science Foundation grant No. 7002. The authors are grateful to M. Rätsep, K. Timpmann, and L. Valkunas for useful comments. Rätsep and Timpmann also provided experimental data for Figs. 4.11–4.15. J. Köhler kindly made available the single molecule spectrum shown in the inset of Fig. 4.15.

References

- Adolphs J and Renger T (2006) How proteins trigger energy transfer in the FMO complex of green sulfur bacteria. *Biophys J* 91: 2778–2797
- Agarwal R, Rizvi AH, Prall BS, Olsen JD, Hunter CN and Fleming GR (2002) Nature of disorder and inter-complex energy transfer in LH2 at room temperature: A three photon echo peak shift study. *J Phys Chem A* 106: 7573–7578
- Amunts A, Drory O and Nelson N (2007) The structure of a plant photosystem I supercomplex at 3.4 Å resolution. *Nature* 447: 58–63
- Bahatyrva S, Frese RN, Van der Werf KO, Otto C, Hunter CN and Olsen JD (2004) Flexibility and size heterogeneity of the LH1 light harvesting complex revealed by atomic force microscopy. *J Biol Chem* 279: 21327–21333
- Beekman LMP, Van Mourik F, Jones MR, Visser HM, Hunter CN and Van Grondelle R (1994) Trapping in mutants of the photosynthetic purple bacterium *Rhodobacter sphaeroides*: Influence of the charge separation rate and consequences for the rate-limiting step in the light-harvesting process. *Biochemistry* 33: 3143–3147
- Borisov AY and Godik VI (1972) Energy transfer in bacterial photosynthesis. I. Light intensity dependences of fluorescence lifetimes. *J Bioenerg* 3: 211–220
- Borisov AY, Freiberg AM, Godik VI, Rebane K and Timpmann K (1985) Kinetics of picosecond bacteriochlorophyll luminescence in vivo as a function of the reaction center state. *Biochim Biophys Acta* 807: 221–229
- Cogdell RJ, Gall A and Köhler J (2006) The architecture and function of the light-harvesting apparatus of purple bacteria: From single molecules to in vivo membranes. *Quart Rev Biophys* 39: 227–324
- Cruzeiro-Hansson L, Eilbeck JC, Marin JL and Russell FM (2000) Interplay between dispersive and non-dispersive modes in the polaron problem. *Phys Lett A* 266: 160–166

- Dahlbom M, Pullerits T, Mukamel S and Sundstrom V (2001) Exciton delocalization in the B850 light-harvesting complex: Comparison of different measures. *J Phys Chem B* 105: 5515–5524
- Damjanovic A, Kosztin I, Kleinekathöfer U and Schulten K (2002) Excitons in a photosynthetic light-harvesting system: A combined molecular dynamics, quantum chemistry, and polaron model study. *Phys Rev E* 65: 031919–031943
- Davydov AS (1971) *Theory of Molecular Excitons*. Plenum Press, New York
- Dobek A, Deprez J, Paillotin G, Leibl W, Trissl HW and Breton J (1990) Excitation trapping efficiency and kinetics in *Rb. sphaeroides* R26.1 whole cells probed by photovoltage measurements on the picosecond time-scale. *Biochim Biophys Acta* 1015: 313–321
- Duysens LNM (1952) PhD Thesis: Transfer of Excitation Energy in Photosynthesis. State University, Utrecht
- Duysens LNM (1986) Introduction to (bacterio) chlorophyll emission: A historical perspective. In: Govindjee, Ames J and Fork DC (eds) *Light Emission by Plants and Bacteria*, pp 3–28. Academic, Orlando, FL
- Emerson R and Arnold WA (1932) The photochemical reaction in photosynthesis. *J Gen Physiol* 16: 191–205
- Emin D and Bussac M-N (1994) Disorder-induced small-polaron formation. *Phys Rev B* 49: 14290–14300
- Fenna RE and Matthews BW (1975) Chlorophyll arrangement in a bacteriochlorophyll protein from *Chlorobium limicola*. *Nature* 258: 573–577
- Fetisova ZG (2004) Survival strategy of photosynthetic organisms. 1. Variability of the extent of light-harvesting pigment aggregation as a structural factor optimizing the function of oligomeric photosynthetic antenna. Model calculations. *Mol Biol* 38: 434–440
- Fetisova ZG, Borisov AY and Fok MV (1985) Analysis of structure-function correlations in light-harvesting photosynthetic antenna: Structure optimization parameters. *J Theor Biol* 112: 41–75
- Fetisova ZG, Freiberg A and Timpmann K (1988) Long-range molecular order as an efficient strategy for light harvesting in photosynthesis. *Nature* 334: 633–634
- Fetisova ZG, Shibaeva LV and Fok MV (1989) Biological expedience of oligomerization of chlorophyllous pigments in natural photosynthetic systems. *J Theor Biol* 140: 167–184
- Fetisova ZG, Shibaeva LV and Taisova AS (1995) Oligomerization of light-harvesting pigments as a structural factor optimizing photosynthetic antenna function. I. Model calculations. *Mol Biol (Moscow)* 29: 1384–1390
- Fidder H, Knoester J and Wiersma DA (1991) Optical properties of disordered molecular aggregates: A numerical study. *J Chem Phys* 95: 7880–7890
- Franck J and Teller E (1938) Migration and photochemical action of excitation energy in crystals. *J Chem Phys* 6: 861–872
- Freiberg A (1995) Coupling of antennas to reaction centers. In: Blankenship RE, Madigan MT and Bauer CE (eds) *Anoxygenic Photosynthetic Bacteria*, pp 385–398. Kluwer, Dordrecht, The Netherlands
- Freiberg A, Godik VI and Timpmann K (1984) Excitation energy transfer in bacterial photosynthesis studied by picosecond laser spectrochronography. In: Sybesma C (ed) *Advances in Photosynthesis Research*, pp 45–48. Nijhoff, Hague, The Netherlands
- Freiberg A, Godik VI and Timpmann K (1987) Spectral dependence of the fluorescence lifetime of *Rhodospirillum rubrum*. Evidence for inhomogeneity of B880 absorption band. In: Biggins J (ed) *Progress in Photosynthesis Research*, pp 45–48. Nijhoff, Dordrecht, The Netherlands
- Freiberg A, Godik VI, Pullerits T and Timpmann KE (1988) Directed picosecond excitation transport in purple photosynthetic bacteria. *Chem Phys* 128: 227–235
- Freiberg A, Godik VI, Pullerits T and Timpman K (1989) Picosecond dynamics of directed excitation transfer in spectrally heterogeneous light-harvesting antenna of purple bacteria. *Biochim Biophys Acta* 973: 93–104
- Freiberg A, Allen JP, Williams J and Woodbury NW (1996) Energy trapping and detrapping by wild type and mutant reaction centers of purple non-sulfur bacteria. *Photosynth Res* 48: 309–319
- Freiberg A, Jackson JA, Lin S and Woodbury NW (1998a) Subpicosecond pump-supercontinuum probe spectroscopy of LH2 photosynthetic antenna proteins at low temperature. *J Phys Chem A* 102: 4372–4380
- Freiberg A, Timpmann K, Lin S and Woodbury NW (1998b) Exciton relaxation and transfer in the LH2 antenna network of photosynthetic bacteria. *J Phys Chem B* 102: 10974–10982
- Freiberg A, Timpmann K, Ruus R and Woodbury NW (1999) Disordered exciton analysis of linear and nonlinear absorption spectra of antenna bacteriochlorophyll aggregates: LH2-only mutant chromatophores of *Rhodobacter sphaeroides* at 8 K under spectrally selective excitation. *J Phys Chem B* 103: 10032–10041
- Freiberg A, Rätsep M, Timpmann K and Trinkunas G (2003a) Self-trapped excitons in circular bacteriochlorophyll antenna complexes. *J Luminescence* 102–103: 363–368
- Freiberg A, Rätsep M, Timpmann K, Trinkunas G and Woodbury NW (2003b) Self-trapped excitons in LH2 antenna complexes between 5 K and ambient temperature. *J Phys Chem B* 107: 11510–11519
- Godik VI and Borisov AY (1977) Excitation trapping by different states of photosynthetic reaction centers. *FEBS Lett* 82: 355–358
- Godik VI, Freiberg A, Timpmann K, Borisov AY and Rebane K (1987) Picosecond excitation energy transfer between different light-harvesting complexes and reaction centers in purple bacteria. In: Biggins J (ed) *Progress in Photosynthesis Research*, pp 41–44. Nijhoff, Dordrecht, The Netherlands

- Godik VI, Timpmann KE and Freiberg AF (1988) Spectral inhomogeneity of the bacteriochlorophyll absorption band of *Rhodospirillum rubrum* as studied by picosecond fluorescence spectroscopy. Dokl Akad Nauk SSSR 298: 1469–1473
- Gooijer C, Ariese F and Hofstraat JW (2000) Shpol'skii Spectroscopy and Other Site-Selective Methods. Wiley, New York, USA
- Green BR and Parson WW (eds) (2003) Light-Harvesting Antennas in Photosynthesis. Kluwer, Dordrecht/Boston, MA/ London
- Hayes JM, Lyle PA and Small GJ (1994) A theory for the temperature dependence of hole-burned spectra. J Phys Chem 98: 7337–7341
- Heijs DJ, Malyshev VA and Knoester J (2005) Decoherence of excitons in multichromophore systems: Thermal line broadening and destruction of superradiant emission. Phys Rev Lett 95: 177402
- Hofmann C, Michel H, Van Heel M and Köhler J (2005) Multivariate analysis of single-molecule spectra: Surpassing spectral diffusion. Phys Rev Lett 94: 195501
- Holstein T (1959) Studies of polaron motion. Part I. The molecular-crystal model. Ann Phys 8: 325–342
- Hu X, Ritz T, Damjanovic A, Autenrieth F and Schulten K (2002) Photosynthetic apparatus of purple bacteria. Quart Rev Biophys 35: 1–62
- Jang S, Dempster SE and Silbey RJ (2001) Characterization of the static disorder in the B850 of LH2. J Phys Chem B 2001: 6655–6665
- Jimenez R, Dikshit SN, Bradforth SE and Fleming GR (1996) Electronic excitation transfer in the LH2 complex of *Rhodobacter sphaeroides*. J Phys Chem 100: 6825–6834
- Kabanov VV and Mashtakov OY (1993) Electron localization with and without barrier formation. Phys Rev B 47: 6060–6064
- Karrasch S, Bullough PA and Ghosh R (1995) The 8.5 Å projection map of the light-harvesting complex I from *Rhodospirillum rubrum* reveals a ring composed of 16 subunits. EMBO J 14: 631–638
- Katiliene Z, Katilius E, Uyeda G, Williams J-AC and Woodbury NW (2004) Increasing the rate of energy transfer between the LH1 antenna and the reaction center in the photosynthetic bacterium *Rhodobacter sphaeroides*. J Phys Chem B 108: 3863–3870
- Kikas J (1978) Effects of inhomogeneity and site selective impurity-phonon coupling in solid solutions. Chem Phys Lett 57: 511–513
- Knox RS (1963) Theory of Excitons. Academic, New York
- Koepke J, Hu X, Muenke C, Schulten K and Michel H (1996) The crystal structure of the light-harvesting complex II (B800–850) from *Rhodospirillum rubrum*. Structure 4: 581–597
- Koolhaas MHC, Van der Zwan G, Frese RN and Van Grondelle R (1997) Red shift of the zero crossing in the CD spectra of the LH2 antenna complex of *Rhodospseudomonas acidophila*: A structure-based study. J Phys Chem B 101: 7262–7270
- Kramer HJM, Van Grondelle R, Hunter CN, Westerhuis WHJ and Amesz J (1984) Pigment organization of the B800–850 antenna complex of *Rhodospseudomonas sphaeroides*. Biochim Biophys Acta 765: 156–165
- Leggett AJ, Chakravarty S, Dorsey AT, Fischer MPA, Garg A and Zwerger W (1987) Dynamics of the dissipative two-state system. Rev Mod Phys 59: 1–85
- Liuolia V, Valkunas L and Van Grondelle R (1997) Excitons in dimerized chains. J Phys Chem B 101: 7343–7349
- Loll B, Kern J, Saenger W, Zouni A and Biesiadka J (2005) Towards complete cofactor arrangement in the 3.0 Å resolution structure of photosystem II. Nature 438: 1040–1044
- Lu N and Mukamel S (1991) Polaron and size effects in optical lineshapes of molecular aggregates. J Chem Phys B 95: 1588–1607
- Markvart T (2000) Light harvesting for quantum solar conversion. Prog Quant Electr 24: 107–186
- Markvart T and Greef R (2004) Polaron-exciton model of resonance energy transfer. J Chem Phys 121: 6401–6405
- Matsui A, Mizuno K and Nishimura H (1984) Zero-phonon lines associated with self-trapped exciton states and exciton dynamics in β -perylene. J Phys Soc Jpn 53: 2818–2827
- McDermott G, Prince SM, Freer AA, Hawthornthwaite-Lawless AM, Papiz MZ, Cogdell RJ and Isaacs NW (1995) Crystal structure of an integral membrane light-harvesting complex from photosynthetic bacteria. Nature 374: 517–521
- McLuskey K, Prince SM, Cogdell RJ and Isaacs NW (2001) The crystallographic structure of the B800–820 LH3 light-harvesting complex from the purple bacteria *Rhodospseudomonas acidophila* strain 7050. Biochemistry 40: 8783–8789
- Meier T, Zhao Y, Chernyak V and Mukamel S (1997) Polarons, localization, and excitonic coherence in superradiance of biological antenna complexes. J Chem Phys 107: 3876–3893
- Michel H and Deisenhofer J (1990) The photosynthetic reaction center from the purple bacterium *Rhodospseudomonas viridis*: aspects of membrane protein structure. Curr Top Membr Transp 36: 53–69
- Monshouwer R, Visschers RW, Van Mourik F, Freiberg A and Van Grondelle R (1995) Low-temperature absorption and site-selected fluorescence of the light-harvesting antenna of *Rhodospseudomonas viridis*. Evidence for heterogeneity. Biochim Biophys Acta 1229: 373–380
- Monshouwer R, Abrahamsson M, Van Mourik F and Van Grondelle R (1997) Superradiance and exciton delocalization in bacterial photosynthetic light-harvesting systems. J Phys Chem B 101: 7241–7248
- Mukamel S (1995) Principles of Nonlinear Optical Spectroscopy. Oxford/New York

- Noba K and Kayanuma Y (1998) Numerically rigorous results for the ground state of exciton-lattice systems. *J Phys Soc Jpn* 67: 3972–3975
- Novoderezhkin VI and Razjivin AP (1993) Excitonic interactions in the light-harvesting antenna of photosynthetic purple bacteria and their influence on picosecond absorbance difference spectra. *FEBS Lett* 330: 5–7
- Novoderezhkin VI and Razjivin AP (1995) Exciton dynamics in circular aggregates: application to antenna of photosynthetic purple bacteria. *Biophys J* 68: 1089–1100
- Novoderezhkin V, Monshouwer R and Van Grondelle R (1999) Disordered exciton model for the core light-harvesting antenna of *Rhodospseudomonas viridis*. *Biophys J* 77: 666–681
- Nuijs AM, Van Grondelle R, Joppe HLP, Cees Van Bochove A and Duysens LNM (1986) A picosecond-absorption study on bacteriochlorophyll excitation, trapping and primary-charge separation in chromatophores of *Rhodospirillum rubrum*. *Biochim Biophys Acta* 850: 286–293
- Papiz MZ, Prince SM, Howard T, Cogdell RJ and Isaacs NW (2003) The structure and thermal motion of the B800–850 LH2 complex from *Rps. acidophila* at 2.0 Å resolution at 100 K: New structural features and functionally relevant motions. *J Mol Biol* 326: 1523–1538
- Pearlstein RM (1982) Exciton migration and trapping in photosynthesis. *Photochem Photobiol* 35: 835–844
- Pieper J, Voigt J, Renger G and Small GJ (1999) Analysis of phonon structure in line-narrowed optical spectra. *Chem Phys Lett* 310: 296–302
- Porter G, Tredwell CJ, Searle GFW and Barber J (1978) Picosecond time-resolved energy transfer in *Porphyridium cruentum*. *Biochim Biophys Acta* 501: 232–245
- Pullerits T and Freiberg A (1991) Picosecond fluorescence of simple photosynthetic membranes: evidence of spectral inhomogeneity and directed energy transfer. *Chem Phys* 149: 409–418
- Pullerits T, Visscher KJ, Hees S, Sundstroem V, Freiberg A, Timpmann K and Van Grondelle R (1994) Energy transfer in the inhomogeneously broadened core antenna of purple bacteria: a simultaneous fit of low-intensity picosecond absorption and fluorescence kinetics. *Biophys J* 66: 236–248
- Rashba IE (1982) Self-trapping of excitons. In: Sturge MD (ed) *Excitons*, pp 543–602. North-Holland, Amsterdam
- Rätsep M and Freiberg A (2003) Resonant emission from the B870 exciton state and electron-phonon coupling in the LH2 antenna chromoprotein. *Chem Phys Lett* 377: 371–376
- Rätsep M and Freiberg A (2007) Electron-phonon and vibronic couplings in the FMO bacteriochlorophyll a antenna complex studied by difference fluorescence line narrowing. *J Luminescence* 127: 251–259
- Rätsep M, Hunter CN, Olsen JD and Freiberg A (2005) Band structure and local dynamics of excitons in bacterial light-harvesting complexes revealed by spectrally selective spectroscopy. *Photosynth Res* 86: 37–48
- Rebane KK (1970) *Impurity Spectra of Solids*. Plenum Press, New York
- Reddy NRS, Picorel R and Small GJ (1992) B896 and B870 components of the *Rhodobacter sphaeroides* antenna: A hole burning study. *J Phys Chem* 96: 6458–6464
- Renger T and Marcus RA (2002) On the relation of protein dynamics and exciton relaxation in pigment-protein complexes: An estimation of the spectral density and a theory for the calculation of optical spectra. *J Chem Phys* 116: 9997–10019
- Robinson GW (1967) Excitation transfer and trapping in photosynthesis. *Brookhaven Symp Biol* 19: 16–48
- Romero AH, Brown DW and Lindenberg K (1999) Effects of dimensionality and anisotropy on the Holstein polaron. *Phys Rev B* 60: 14080–14091
- Roszak AW, Howard TD, Southall J, Gardiner AT, Law CJ, Isaacs NW and Cogdell RJ (2003) Crystal structure of the RC-LH1 core complex from *Rhodospseudomonas palustris*. *Science* 302: 1969–1972
- Sapozhnikov MN and Alekseev VI (1984) Site selective luminescence spectroscopy of impurity centres in solids: Model calculations and experiment. *Chem Phys Lett* 107: 265–271
- Sauer K and Austin LA (1978) Bacteriochlorophyll-protein complexes from the light-harvesting antenna of photosynthetic bacteria. *Biochemistry* 17: 2011–2019
- Sauer K, Cogdell RJ, Prince SM, Freer A, Isaacs NW and Scheer H (1996) Structure-based calculations of the optical spectra of the LH2 bacteriochlorophyll-protein complex from *Rhodospseudomonas acidophila*. *Photochem Photobiol* 64: 564–576
- Scherz A and Parson WW (1986) Interactions of the bacteriochlorophylls in antenna bacteriochlorophyll-protein complexes of photosynthetic bacteria. *Photosynth Res* 9: 21–32
- Scheuring S (2006) AFM studies of the supramolecular assembly of bacterial photosynthetic core-complexes. *Curr Opin Chem Biol* 10: 387–393
- Scholes GD (2003) Long-range resonance energy transfer in molecular systems. *Annu Rev Phys Chem* 54: 57–87
- Scholes GD and Fleming GR (2000) On the mechanism of light harvesting in photosynthetic purple bacteria: B800 to B850 energy transfer. *J Phys Chem B* 104: 1854–1868
- Scholes GD and Rumbles G (2006) Excitons in nanoscale systems. *Nat Mater* 5: 683–693
- Scholes GD, Harcourt RD and Fleming GR (1997) Electronic interactions in photosynthetic light-harvesting complexes: The role of carotenoids. *J Phys Chem B* 101: 7302–7312
- Scholes GD, Gould IR, Cogdell RJ and Fleming GR (1999) Ab initio molecular orbital calculations of electronic couplings in the LH2 bacterial light-harvesting complex of *Rps. acidophila*. *J Phys Chem B* 103: 2543–2553

- Schröder M, Kleinekathöfer U and Schreiber M (2006) Calculation of absorption spectra for light-harvesting systems using non-Markovian approaches as well as modified Redfield theory. *J Chem Phys* 124: 084903
- Sebban P and Moya I (1983) Fluorescence lifetime spectra of in vivo bacteriochlorophyll at room temperature. *Biochim Biophys Acta* 722: 436–442
- Sebban P, Jolchine G and Moya I (1984) Spectra of fluorescence lifetime and intensity of *Rhodospseudomonas sphaeroides* at room and low temperature. Comparison between the wild type, the C 71 reaction center-less mutant and the B800–850 pigment-protein complex. *Photochem Photobiol* 39: 247–253
- Shreve AP, Trautman JK, Frank HA, Owens TG and Albrecht AC (1991) Femtosecond energy-transfer processes in the B800–850 light-harvesting complex of *Rhodobacter sphaeroides* 2.4.1. *Biochim Biophys Acta* 1058: 280–288
- Song KS and Williams RT (1992) *Self-Trapped Excitons*. Springer, Berlin/Heidelberg/New York
- Stoneham AM, Gavartin J, Shluger AL, Kimmel AV, Múnoz Ramo D, Rønnow HM, Aeppli G and Renner C (2007) Trapping, self-trapping and the polaron family. *J Phys: Condens Matter* 19: 255208
- Sumi H (1994) Two types of self-trapped states for excitons in one dimension. *J Phys Soc Jpn* 63: 4489–4498
- Sumi H (1999a) Theory of rapid excitation-energy transfer from B800 to optically-forbidden exciton states of B850 in the antenna system LH2 of photosynthetic purple bacteria. *J Phys Chem B* 103: 6096–6102
- Sumi H (1999b) Theory of rates of excitation-energy transfer between molecular aggregates through distributed transition dipoles with application to the antenna system in bacterial photosynthesis. *J Phys Chem B* 103: 252–260
- Sumi H (2000) Bacterial photosynthesis begins with quantum-mechanical coherence. *Chem Rec* 1: 480–493
- Sundström V, Van Grondelle R, Bergstroem H, Aakesson E and Gillbro T (1986) Excitation-energy transport in the bacteriochlorophyll antenna systems of *Rhodospirillum rubrum* and *Rhodobacter sphaeroides*, studied by low-intensity picosecond absorption spectroscopy. *Biochim Biophys Acta* 851: 431–446
- Sundström V, Pullerits T and Van Grondelle R (1999) Photosynthetic light-harvesting: Reconciling dynamics and structure of purple bacterial LH2 reveals function of photosynthetic unit. *J Phys Chem B* 103: 2327–2346
- Tanaka S (2003) Ultrafast relaxation dynamics of the one-dimensional molecular chain: The time-resolved spontaneous emission and exciton coherence. *J Chem Phys* 119: 4891–4904
- Tietz C, Chekhlov O, Dräbenstedt A, Schuster J and Wrachtrup J (1999) Spectroscopy on single light-harvesting complexes at low temperature. *J Phys Chem B* 103: 6328–6333
- Timpmann K, Zhang FG, Freiberg A and Sundström V (1993) Detrapping of excitation energy from the reaction center in the photosynthetic purple bacterium *Rhodospirillum rubrum*. *Biochim Biophys Acta* 1183: 185–193
- Timpmann K, Freiberg A and Sundström V (1995) Energy trapping and detrapping in the photosynthetic bacterium *Rhodopseudomonas viridis*: transfer-to-trap-limited dynamics. *Chem Phys* 194: 275–283
- Timpmann K, Katiliene Z, Woodbury NW and Freiberg A (2001) Exciton self-trapping in one-dimensional photosynthetic antennas. *J Phys Chem B* 105: 12223–12225
- Timpmann K, Rätsep M, Hunter CN and Freiberg A (2004a) Emitting excitonic polaron states in core LH1 and peripheral LH2 bacterial light-harvesting complexes. *J Phys Chem B* 108: 10581–10588
- Timpmann K, Trinkunas G, Olsen JD, Hunter CN and Freiberg A (2004b) Bandwidth of excitons in LH2 bacterial antenna chromoproteins. *Chem Phys Lett* 398: 384–388
- Timpmann K, Trinkunas G, Qian P, Hunter CN and Freiberg A (2005) Excitons in core LH1 antenna complexes of photosynthetic bacteria: Evidence for strong resonant coupling and off-diagonal disorder. *Chem Phys Lett* 414: 359–363
- Trinkunas G and Freiberg A (2005) Abrupt exciton self-trapping in finite and disordered one-dimensional aggregates. *J Luminescence* 112: 420–423
- Trinkunas G and Freiberg A (2006) A disordered polaron model for polarized fluorescence excitation spectra of LH1 and LH2 bacteriochlorophyll antenna aggregates. *J Luminescence* 119–120: 105–110
- Ueta M, Kanzaki H, Kobayashi K, Toyozawa Y and Hanamura E (1986) *Excitonic Processes in Solids*. Springer, Berlin
- Urboniene V, Vrublevskaja O, Gall A, Trinkunas G, Robert B and Valkunas L (2005) Temperature broadening of LH2 absorption in glycerol solution. *Photosynth Res* 86: 49–59
- Urboniene V, Vrublevskaja O, Trinkunas G, Gall A, Robert B and Valkunas L (2007) Solvation effect of bacteriochlorophyll excitons in light-harvesting complex LH2. *Biophys J* 93: 2188–2198
- Van Amerongen H, Valkunas L and Van Grondelle R (2000) *Photosynthetic Excitons*. World Scientific, Singapore
- Van der Laan H, Schmidt T, Visschers RW, Visscher KJ, Van Grondelle R and Volker S (1990) Energy transfer in the B800–850 antenna complex of purple bacteria *Rhodobacter sphaeroides*: a study by spectral hole-burning. *Chem Phys Lett* 170: 231–238
- Van Grondelle R and Novoderezhkin VI (2006) Energy transfer in photosynthesis: experimental insights and quantitative models. *Phys Chem Chem Phys* 8: 793–807
- Van Grondelle R, Bergström H, Sundström V and Gillbro T (1987) Energy transfer within the bacteriochlorophyll antenna of purple bacteria at 77 K, studied by picosecond absorption recovery. *Biochim Biophys Acta* 894: 313–326
- Van Mourik F, Visschers RW and Van Grondelle R (1992) Energy transfer and aggregate size effects in the

- inhomogeneously broadened core light-harvesting complex of *Rhodobacter sphaeroides*. Chem Phys Lett 193: 1–7
- Van Oijen AM, Ketelaars M, Köhler J, Aartsma TJ and Schmidt J (1998) Spectroscopy of single light-harvesting complexes from purple photosynthetic bacteria at 1.2 K. J Phys Chem B 102: 9363–9366
- Van Oijen AM, Ketelaars M, Köhler J, Aartsma TJ and Schmidt J (1999) Unraveling the electronic structure of individual photosynthetic pigment-protein complexes. Science 285: 400–402
- Vischers RW, Germeroth L, Michel H, Monshouwer R and Van Grondelle R (1995) Spectroscopic properties of the light-harvesting complexes from *Rhodospirillum rubrum*. Biochim Biophys Acta 1230: 147–154
- Vredenberg WJ and Duysens LMN (1963) Transfer of energy from bacteriochlorophyll to a reaction centre during bacterial photosynthesis. Nature 4865: 355–357
- Walz T, Jamieson SJ, Bowers CM, Bullough PA and Hunter CN (1998) Projection structures of three photosynthetic complexes from *Rhodobacter sphaeroides*: LH2 at 6 Å, LH1 and RC-LH1 at 25 Å. J Mol Biol 282: 833–845
- Wu H-M and Small GJ (1998) Symmetry-based analysis of the effects of random energy disorder on the excitonic level structure of cyclic arrays: Application to photosynthetic antenna complexes. J Phys Chem B 102: 888–898
- Wu H-M, Rätsep M, Jankowiak R, Cogdell RJ and Small GJ (1997a) Comparison of the LH2 antenna complexes of *Rhodopseudomonas acidophila* (strain 10050) and *Rhodobacter sphaeroides* by high-pressure absorption, high-pressure hole burning, and temperature-dependent absorption spectroscopies. J Phys Chem B 101: 7641–7653
- Wu H-M, Rätsep M, Lee I-J, Cogdell RJ and Small GJ (1997b) Exciton level structure and energy disorder of the B850 ring of the LH2 antenna complex. J Phys Chem B 101: 7654–7663
- Zhang FG, Van Grondelle R and Sundström V (1992) Pathways of energy flow through the light-harvesting antenna of the photosynthetic purple bacterium *Rhodobacter sphaeroides*. Biophys J 61: 911–920

Chapter 5

Models of Chlorophyll a Fluorescence Transients

Dušan Lazár*

*Laboratory of Biophysics, Faculty of Science, Palacký University, Třída Svobody 26, 771 46
Olomouc, Czech Republic*

Gert Schansker

*Laboratory of Bioenergetics, Department of Plant Biology, University of Geneva, Chemin des
Embouchis 10, 1254 Jussy, Geneva, Switzerland*

Summary.....	86
I. Fluorescence Induction.....	86
A. Relation Between Photosynthesis and Fluorescence.....	86
B. Summary of Used Fluorescence Techniques.....	87
C. Summary of Processes Reflected in the Fluorescence Rise.....	90
II. Approaches and Assumptions in the Modeling of the Fluorescence Rise.....	91
A. Why Model?.....	91
B. Why Measure and Simulate the Fluorescence Rise?.....	92
C. Relationship Between the Origin of Fluorescence and the Model Structure.....	92
D. Basic Types of Photosystem II Models.....	93
E. Kinetics and Rate Constants.....	95
F. Fluorescence and “Closed” Reaction Centers.....	97
G. Model Formulation and Simplification.....	99
III. Particular Models for the Fluorescence Rise.....	100
A. Modeling Fluorescence Rise in DCMU Inhibited Samples.....	100
1. Using Analytical Functions.....	100
2. The Application of Reversible Radical Pair Models.....	101
B. Modeling of the O–(J–)I–P Phases in Fluorescence Rise.....	102
1. Using Analytical Functions.....	102
2. Two-electron Gate Models.....	103
3. Extended Two-electron Gate Models.....	104
4. Combined Reversible Radical Pair and Two-electron Gate Models.....	104
5. Complex Models.....	107
IV. Modeling the Whole Fluorescence Induction.....	111
A. Experimental Observations and Models.....	111
B. Oscillations in the Fluorescence Intensity.....	114
V. Conclusions and Future Perspectives.....	115
Acknowledgments.....	115
References.....	115

* Author for correspondence, e-mail: lazard@seznam.cz

Summary

In this chapter we describe modeling efforts of fluorescence rise (FLR) transients over the last 20 years. During this period the complexity of the models has increased significantly. Nowadays, the more complex models consist of a combination of the Kok model for the reactions on the donor side of photosystem II (PS II), the reversible radical pair model for the primary PS II photochemistry, the two-electron gate model for electron transport on the acceptor side of PS II, reactions related to reduction and oxidation of plastoquinone (PQ) and, in some cases, of cytochrome b_6f , plastocyanin and photosystem I. In some models additional processes are considered like electric field effects and dark reactions of photosynthesis occurring in the stroma and cytosol.

The chapter begins with an introduction of topics important for the construction of a model: relevant fluorescence theories, measuring techniques, the physiology behind the FLR, the role of the integrity of the sample, enzyme kinetics and rate constants. Subsequently several published models are discussed. A major problem for many FLR models is that the fluorescence rises much faster (often by a factor 10) than experimentally observed. Possible reasons for this mismatch are discussed in the context of different models. The large majority of models is based on the postulate that the redox state of Q_A is the major determinant of the variable fluorescence yield. In several models $P680^+$ and quenching by the PQ pool are added, but this is still insufficient to correctly model the slowest rise phase. The question is raised whether additional assumptions are needed to correctly simulate the O–J–I–P transient.

At the end of the chapter the fluorescence decrease following the initial rise is discussed. Only a few models include this part of the fluorescence transient. A flaw of these models is that they ignore the experimentally observed transient block at the acceptor side of photosystem I, limiting both electron flow and proton transport during the FLR. As a consequence, activation of photosynthesis occurs in models with considerably faster kinetics than observed experimentally.

I. Fluorescence Induction

A short introduction to Chlorophyll (Chl) *a* fluorescence, its relation to the function of the photosynthetic apparatus, the techniques used to measure fluorescence and a summary of processes reflected in the fluorescence rise (FLR) is given below in this section. See Govindjee et al. (1986) and Papageorgiou and Govindjee (2004) for background and further details on all aspects of Chl *a* fluorescence.

A. Relation Between Photosynthesis and Fluorescence

When photosynthetic samples are illuminated, excited states (ES) of pigments are formed. The excitation energy can be transferred to the reaction center (RC) pigments where the energy is used for the transfer of an electron toward the other side of the membrane (a charge separation). The transferred electrons are then transported through and along the thylakoid membrane via a chain of electron carriers in order to reduce nicotinamide adenine dinucleotide phosphate ($NADP^+$). The electron transport through the membrane also drives the

Abbreviations: Chl – chlorophyll; cyt b_6f – cytochrome b_6f ; $\Delta\Psi$ – transmembrane electric potential; DBMIB – 2,5-dibromo-3-methyl-6-isopropyl-p-benzoquinone; DCMU (Diuron) – 3-(3', 4'-dichlorophenyl)-1,1-dimethylurea; ES – excited state; F_0 – minimal fluorescence; Fd – ferredoxin; FFI – flash fluorescence induction; FLD – fluorescence decrease; FLI – fluorescence induction; FLR – fluorescence rise; F_M – maximal fluorescence; FNR – ferredoxin-NADP⁺-reductase; F_{pl} – plateau in the FLR measured upon exposure to low intensity of exciting light; FR – far-red; FRR – fast repetition rate; F_V – variable fluorescence; LHC II – light harvesting antenna of PS II; O, K, J (I_1), I (I_1), D, P (M , F_P), S (S_1 , S_2), M (M_1 , M_2), T – particular steps of the FLI; OEC – oxygen evolving complex; MV – methylviologen (1,1'-dimethyl-4,4'-bipyridinium-dichloride); p – parameter of energetic connectivity; P680 – PS II electron donor; P700 – PS I electron donor; PAP – pump and probe; PC – plastocyanin; PDP – pump during probe; Pheo – pheophytin, the primary PS II electron acceptor; PQ – plastoquinone; PQH₂ – plastoquinol (reduced and protonated plastoquinone); PS I – photosystem I; PS II – photosystem II; Q_A – the primary quinone PS II electron acceptor; Q_B – the secondary quinone PS II electron acceptor; qE – energy dependent non-photochemical fluorescence quenching; RC – reaction center; RRP – reversible radical pair; SFK – structure, function and kinetics; S_i -states – redox states of OEC ($i = 0, 1, 2, 3$); TEG – two-electron gate; TST – three state trapping; $V(t)$ – relative variable fluorescence; Y_Z – tyrosine 161

formation of a transmembrane proton gradient (difference in proton concentrations). The proton gradient in turn drives the formation of adenosine triphosphate (ATP). The formation of ES does not always lead to a stable charge separation and subsequent electron transport. Even if the primary quinone electron acceptor of photosystem II (PS II), Q_A , is in the oxidized state there is a small probability that the ES can be deactivated as fluorescence or heat emission. If Q_A is in the reduced state this probability increases due to a longer lifetime of the ES. Fluorescence is a radiative conversion of the (usually) first singlet ES of a molecule to its ground state. In addition to fluorescence emission, the excited singlet state can be deactivated within a molecule by inter-system crossing to the triplet state or by radiationless internal conversion to the ground state by means of heat dissipation. The quantum yield of Chl fluorescence in solution is about 20–35% (Förster and Livingston, 1952; Latimer et al., 1956), but in actively photosynthesizing samples it is only about 2% (Trissl et al., 1993), mainly because of competitive quenching by photochemistry. For overviews see Ke (2001) and Papageorgiou and Govindjee (2004).

B. Summary of Used Fluorescence Techniques

Since many techniques have been used to measure Chl *a* fluorescence transients, a summary of the techniques and the used nomenclature is provided here first. The Chl *a* fluorescence transient (induction, FLI) represents the time course of the fluorescence intensity emitted by a photosynthetic sample on a sudden transition from darkness to (usually) continuous illumination. FLI consists of a fast FLR followed by a slower fluorescence decrease (FLD). The rise and subsequent decline of the fluorescence intensity on a dark to light transition were first observed by Kautsky and Hirsch (1931). As a reference to this initial observation, the FLI is often called the Kautsky effect. In one form or another, the FLI is used in almost every laboratory dealing with photosynthesis research. The measurement of Chl *a* fluorescence is attractive because it is non-invasive, fast and easy, and above all it provides access to a range of processes that play a role in photosynthetic energy conversion (Govindjee, 1995).

In a dark-adapted photosynthetic sample, the acceptor side of PS II is normally predominantly in the oxidized state. In this state, all RCs are called open. This state is associated with a low fluorescence intensity called minimal fluorescence, F_0 , and denoted as O (for origin; see Fig. 5.1). On illumination, electrons are pumped by PS II into the electron transport chain and the acceptor side of PS II becomes more reduced. As a consequence the efficiency of photochemistry declines, the lifetime of the ES increases and the fluorescence intensity goes up. After a few hundreds of milliseconds of illumination the fluorescence intensity reaches a maximal level, F_M , denoted as P (for peak), or M (for maximum) on the transient curve (see Fig. 5.1). At this level all the RCs are closed (photochemistry is zero). When the intensity is not saturating, the use of the term P (or F_P) for the maximum of the FLI curve is more appropriate. The difference between F_M (F_P) and F_0 is called variable fluorescence, F_V .

The intensity of the exciting light does not only determine whether the F_M is reached or not, but it also determines the overall shape of the FLR. If FLRs are measured using low intensities of exciting light ($50\text{--}100\mu\text{mol photons m}^{-2}\text{ s}^{-1}$) the FLR lasts for several seconds and only one step can be distinguished between O and P, called plateau (denoted as F_{pl} ; Forbush and Kok, 1968). As discussed by Lavergne and Braintais (1996), the fluorescence rise to F_{pl} is determined by a mixture of contributing processes: closure of Q_B non-reducing centers, changes in the fluorescence intensity due to S-state transitions of the oxygen evolving complex (OEC), equilibration between Q_A and the secondary quinone electron acceptor, Q_B , in Q_B reducing (active) RCs and, finally, a slight “actinic effect” (some Q_A^- accumulation in active RCs in excess of the equilibrium; Hsu, 1993; Tomek et al., 2003; Schansker and Strasser, 2005).

At low light intensities in this type of experiments the excitation rate is low enough to detect the whole FLR with a fluorometer equipped with a mechanical shutter that fully opens in about 1–2 ms. At somewhat higher excitation intensities, the fluorescence transient begins to show its multi-step kinetics although this was initially obscured by the limited time resolution of the shuttered systems that were used for the early

measurements. For such transients, Munday and Govindjee (1969) introduced the steps I (inflection) and D (dip). The dip observed in the published transients (e.g. Kautsky et al., 1960) is probably due to the partial reduction of the plastoquinone (PQ) pool at the start of the measurement reducing, initially, electron flow through PS II without much of an effect on PS I activity. The presence of the dip allows the observation of what is now called the J step (see below) even with a shuttered system. The inflection point of the J-step in a continuously rising transient is difficult to discern in a shuttered system. However, if the PQ pool is initially (partially) reduced then the J step is followed by a decreasing phase (see e.g. Fig. 1 in Tóth et al., 2007b) and this can also be easily recognized in a shuttered system. In our opinion, by overlaying fluorescence transients

from fully dark-adapted leaf samples on transients from samples with partially reduced PQ, it can be shown that what Munday and Govindjee (1969) called I and D equate in our present day terminology the J and I steps, respectively, when measured in high intensity exciting light.

With the introduction of faster shutters or (e.g. LED-based) shutterless systems with high intensity light sources with short response times, it became possible to measure the FLR at high (saturating) intensities of exciting light ($3,000 \mu\text{mol photons m}^{-2} \text{s}^{-1}$ and more). In this case the FLR reaches its maximum level within about 200 ms and two steps appear between F_0 and F_M , which were first denoted as I_1 and I_2 (measured with a pulse-amplitude modulation PAM fluorometer, Neubauer and Schreiber, 1987; Schreiber and Neubauer, 1987; Fig. 5.1C) and later as J and I, respectively (measured with a PEA fluorometer, Strasser and Govindjee, 1991, 1992; Fig. 5.1A). The equivalence between the J

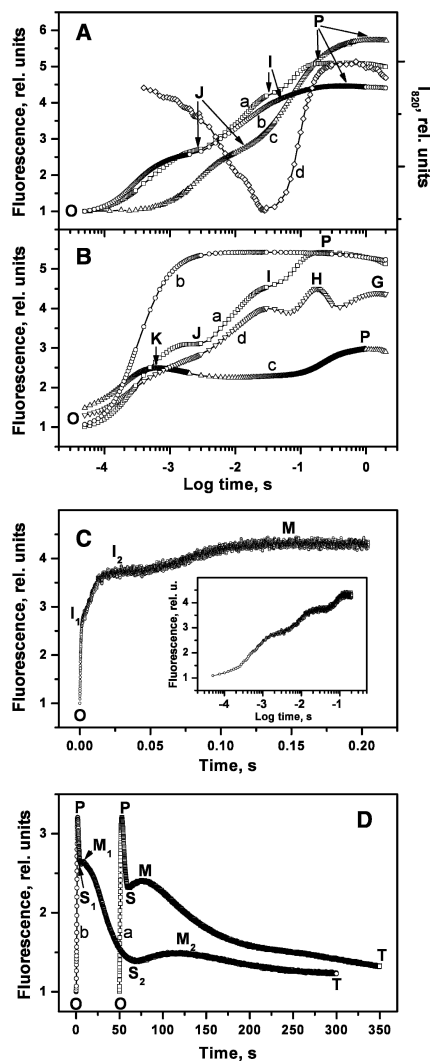


Fig. 5.1. Measured Chl *a* fluorescence transients and transmission changes at 820 nm (I_{820}) beginning from a dark-adapted state. Panel A – FLR measured with a pea leaf (curve a), spinach thylakoids (curve b) and PS II membranes (curve c) and simultaneously measured I_{820} signal with the pea leaf (curve d). Minimal fluorescence (O level) of all the curves was normalized to 1. Panel B – FLRs measured with a control pea leaf (curve a), DCMU-treated pea leaf (200 μM , 14 h; curve b), high temperature treated barley leaf (47 °C, 5 min; curve c) and lichen thalli of *Umbilicaria hirsuta* (curve d). Minimal fluorescence (O level) of curve a was normalized to unity. Measurements were made with a PEA fluorometer upon illumination with red light of 1, 800 $\mu\text{mol photons m}^{-2} \text{s}^{-1}$ (panel A, curves a and d and panel B, curve d), 3,000 $\mu\text{mol photons m}^{-2} \text{s}^{-1}$ (panel A, curve b and panel B, curves a and b) and 3,400 $\mu\text{mol photons m}^{-2} \text{s}^{-1}$ (panel B, curve c) and with a laboratory-built fluorometer upon illumination with 3,500 $\mu\text{mol photons m}^{-2} \text{s}^{-1}$ of red light (panel A, curve c). All curves are shown on a logarithmic time-axis. For description of H and G steps, see text. Panel C – FLR measured with a tobacco leaf using a PAM fluorometer upon illumination with 9,000 $\mu\text{mol photons m}^{-2} \text{s}^{-1}$ of white light. The same curve is presented on a logarithmic time-axis in the inset. Minimal fluorescence (O level) was normalized to unity. The nomenclature used here is that of U. Schreiber (see text). Panel D – FLI measured with two different pea leaves using a PAM fluorometer upon illumination with 40 $\mu\text{mol photons m}^{-2} \text{s}^{-1}$ of red light. Curve a is shifted to the right by 50 s. Minimal fluorescence (O level) of both the curves was normalized to unity. Data were taken from Lazár (1999) – both curves of panel D, Pospíšil and Dau (2000) – curve c of panel A, Tóth et al. (2005) – curves a and b of panel B, Boisvert et al. (2006) – curve b of panel A, Ilik et al. (2006) – curves a and d of panel A and curve d of panel B, Lazár (2006) – curve c of panel B and the curve of panel C.

and I_1 steps and the I and I_2 steps was later established by Strasser et al. (1995). As the O–J–I–P notation is more commonly used in the literature, we shall use it in this chapter. The J and I steps measured using high intensity exciting light usually appear at about 2–3 and 20–30 ms, respectively (Fig. 5.1A). The shape of the FLR depends on the intactness of the system. During isolation of thylakoid membranes, ferredoxin (Fd) is lost from the acceptor side of PS I (Sato, 1981) and fluorescence transients with a less pronounced I step are detected (Pospíšil and Dau, 2002; Joly et al., 2005; Boisvert et al., 2006; Fig. 5.1A). The FLR measured using PS II membranes does not contain an I step at all (Pospíšil and Dau, 2000, 2002; Heredia and De Las Rivas, 2003; Beauchemin et al., 2007; Fig. 5.1A) since such membranes only consist of PS II and a small PQ pool. In addition, in some organisms (foraminifers, zooxanthellae, lichens and some algae) an additional peak is observed beyond the P step even under standard conditions (Tsimilli-Michael et al., 1998; Ilík et al., 2006; Fig. 5.1B). However, Tsimilli-Michael et al. (1998) introduced a new nomenclature for these organisms calling P and the additional peak: H and G , respectively. In these organisms the fast fluorescence decline following P is due to a fast activation of electron transport at the acceptor side of PS I (Ilík et al., 2006). Further, high temperature stress of photosynthetic samples unveils a new step, K , occurring after 300–400 μ s of illumination in the FLR (Guissé et al., 1995; Lazár and Ilík, 1997; Fig. 5.1B).

As the relative amplitude of the O–J phase and its initial slope are strongly dependent on the intensity of exciting light, the O–J phase is called the photochemical phase of the FLR (Delosme, 1967; Neubauer and Schreiber, 1987; Strasser et al., 1995). The J–I–P phase of the FLR on the other hand is called the thermal phase of the FLR (Delosme, 1967; Neubauer and Schreiber, 1987) because its kinetics is more sensitive to the temperature of the sample (within physiological range).

Once the maximum of the FLR curve is reached, fluorescence slowly decreases through the S and M (note: the same notation is used here as for a maximum M of the FLR) steps to the steady-state or terminal level T (Papa-georgiou and Govindjee, 1968; Fig. 5.1D), which

is reached after several minutes of illumination. Additional local maxima can be present in the FLR and then the steps are denoted as P – S_1 – M_1 – S_2 – M_2 – T (Yamagishi et al., 1978; Govindjee and Satoh, 1986; Fig. 5.1D) and under some conditions complex damped oscillations can be measured (Walker et al., 1983; Sivak and Walker, 1985).

The FLI transients mentioned thus far were all measured upon continuous illumination where PS II turns over many times and a large number of electrons are transported along the electron transport chain. To simplify the FLR, 3-(3', 4'-dichlorophenyl)-1,1-dimethylurea (DCMU, also referred to as "Diuron") is often used. As DCMU binds to the Q_B pocket of the D1 protein of PS II (Oettmeier and Soll, 1983; Trebst and Draber, 1986; Shigematsu et al., 1989) and thus blocks electron transport beyond Q_A , only a single stable charge separation can occur. As a consequence, the FLR consists of a single rise phase that strongly depends on the light intensity and at moderate to high light intensities the maximum fluorescence level is reached at about the same time as the J step in uninhibited samples (Fig. 5.1B).

A complete reduction of Q_A can be obtained not only by application of DCMU but also by application of a short (about 50 μ s) but very intense flash of light during which the fluorescence is detected. This technique is referred to as "pump during probe" technique (PDP, Olson et al., 1996) or "flash fluorescence induction" (FFI, Nedbal et al., 1999). The shape of the PDP (FFI) transients is the same as DCMU–FLR but the rise kinetics is complete within a much shorter time. Due to the very high light intensities used, the reduction of all Q_A molecules is much faster than the rate of forward electron transport towards Q_B .

All techniques mentioned above are based on the detection of fluorescence during continuous excitation (either single or multiple turnover) of different durations. However, techniques that are based on light flashes have also been developed. In the "fast repetition rate" (FRR) technique (Kolber et al., 1998), up to 120 short (0.6–0.8 μ s), sub-saturating flashes, called flashlets, are applied with a given time interval (1–2 μ s) between the flashlets to produce a saturating single-turnover flash. When about 3,000

flashlets of 0.8 μ s duration are applied, a multiple turnover of RCs takes place, and O–J–I–P-like FLRs are generated (Kolber et al., 1998). By changing the interval between flashlets, the effective light intensity can be modulated. Comparing the FRR transients of Kolber et al. (1998) and continuous light induced O–J–I–P transients, differences in the form are observed. Especially the slower rise phases of the FLRs (J–I and I–P) are strongly limited by dark reactions. At high intensities of light the excitation rate is much higher than the exchange of doubly reduced Q_B for an oxidized molecule from the PQ pool and the re-oxidation of reduced PQH₂ (plastoquinol) by the cytochrome b_6f (cyt b_6f) complex. In addition, these reactions continue in darkness. Therefore, using intense short flashes with a dark interval between the flashes is not the same as using continuous light, because there is a different relationship between excitation and the dark reactions for these two cases. The strongly diminished thermal phase observed for the FLRs measured with the FRR method could therefore be due to this kinetic difference between flash and continuous light. The FFI approach also utilizes a large number of flashes to realize multiple turnover illumination (Koblížek et al., 2001). A technique based on a slightly different principle is the “pump and probe” technique (PAP; Mauzerall, 1976; Valkunas et al., 1991; France et al., 1992) where strong flashes of different duration (the pump flashes, from hundreds of picoseconds to milliseconds)

are applied, and the generated state is probed at certain times after the pump flash by measuring the fluorescence emission induced by weak flashes, the probe flashes.

The above illustrates that many techniques have been developed to modulate the redox state of the photosynthetic electron transport chain and to obtain different “types” of Chl *a* fluorescence transients. However, by far the most popular method remains the study of the fluorescence transient induced by continuous, multiple-turnover excitation. This is also reflected in the published models that are dominated by simulations of the FLR as measured upon continuous excitation (either in the presence or absence of DCMU). For this reason we will concentrate in the present chapter on the modeling of the FLR (O–J–I–P) and FLD (P–S–M–T) transients obtained using continuous, multiple-turnover, light.

C. Summary of Processes Reflected in the Fluorescence Rise

Many researchers have attempted to characterize the mechanisms underlying the different phases of the FLR. This has resulted in a large number of proposals for the processes involved. In Table 5.1, a summary of the processes suggested to define each of the rise phases is given. For a more detailed description of the proposed mechanisms

Table 5.1. Processes suggested in the literature to be involved in the O–J–I–P FLR. The table lists processes revealed from experiments with whole leaves, thylakoids and PS II membranes and by using different chemicals. Processes denoted in italics were considered in modeling of the FLR in particular studies (see also Lazár, 2006).

Photochemical phase (O–J)	Thermal phase (J–I–P)
<i>Accumulation of only Q_A^- from the Q_B reducing PS IIs and the Q_B non-reducing PS IIs</i>	<i>Accumulation of $Q_B^{-(2-)}$ in addition to Q_A^-</i>
<i>The donor side of PS II</i>	<i>Protonation of Q_B^{2-}</i>
<i>Excitation energy transfer</i>	<i>The donor side of PS II</i>
<i>Transmembrane electric potential</i>	<i>Transmembrane electric potential</i>
<i>Recombination between PS II electron acceptors and donors</i>	<i>Heterogeneity in the rate of PQ pool reduction</i>
<i>Electron transport through the inactive branch in PS II</i>	<i>Fluorescence quenching by oxidized PQ</i>
	<i>Electron transport reactions beyond PS II</i>
	<i>Light gradient within a sample</i>
	<i>Cyt b_{559}</i>
	<i>Fluorescence quenching in CP43</i>
	<i>Fluorescence coming from PS I</i>
	<i>Reduction of the Q_2 component</i>
	<i>Changes in yield of recombination fluorescence</i>

see Lazár (2006). Note that the processes written in italics were considered in the modeling of the FLR in particular published studies. Readers who are interested in further experimental studies on the physiology and kinetics of the FLI may consult reviews related to various aspects of the FLI: general aspects of variable fluorescence (Krause and Weis, 1991; Dau, 1994; Govindjee, 1995), the complete fluorescence transient (Papageorgiou, 1975; Briantais et al., 1986; Govindjee and Satoh, 1986; Papageorgiou et al., 2007), the O–J–I–P-transient (Lazár, 1999, 2006; Schreiber, 2004; Strasser et al., 2004) and PS II heterogeneity (Black et al., 1986; Govindjee, 1990; Laverne and Briantais, 1996; Samson et al., 1999). References to additional papers, not covered in these reviews, are included in this chapter.

II. Approaches and Assumptions in the Modeling of the Fluorescence Rise

Many models of the FLR have been published, different in their structures, approaches and assumptions. This section summarizes these aspects of the modeling of the FLR.

A. Why Model?

On a dark-to-light transition, the kinetics of the FLR first follows the reduction of the PS II acceptor side, subsequently the reduction of the PQ pool and finally the reduction of the acceptor side of PS I. In addition, the FLR is affected by PS II heterogeneity and modulation of the fluorescence intensity by other effects, e.g. S-state transitions of OEC, connectivity between PS II antennae, and electric field effects, among others. A model that would allow a perfect fit of the FLR, obtained in a single 1-s measurement, would generate an enormous amount of information on the stoichiometry and functionality of the photosynthetic apparatus. However, the complexity of the system that has to be simulated and the disagreements with respect to the interpretation of the different kinetic phases of the fluorescence transient has kept us far from a perfect model. In the absence of a model that can simulate all known experimental observations, simulations can fulfill another role. *In silico*, parameters can be varied that are difficult to change in leaves. By showing how

the form of the transient changes in response to changes in certain parameters may help experimentalists to interpret their measurements, suggesting which parameters may be important and which can probably be ignored.

In this respect, it is important to keep in mind that already a qualitative agreement between experiment and theory is a useful goal in the case of modeling of the FLR. The FLI (FLR) is a manifestation of a very complex biological system and therefore hard to describe correctly and comprehensively – this is quite different from the modeling of technical systems that can be described correctly and where a quantitative agreement between experiments and theory is strictly required.

Modeling can be approached in two ways: fitting or simulation. In the case of a fit, a mathematical routine searches for values of model parameters to obtain the best agreement between theoretical and experimental curves. The routine automatically fits the model parameters for the best agreement, hiding the fitting procedure from the modeler's attention. A problem with such fitting is, however, that there is often more than one theoretical solution for the same transient, because a change in the value of one parameter can be compensated by a change in another parameter (Baake and Schlöder, 1992). Thus, the question of the uniqueness of obtained model parameters is of concern. In order to find the best fit, characterized by a global minimum of a so-called criterion function, not by a local minimum, very sophisticated mathematical routines must be used (so-called genetic algorithms). However, even if the best fit is found, the obtained values of parameters need not agree with values known from other sources (e.g. Strasser and Stirbet, 2001). Therefore, the researcher still has to judge if the obtained results are really meaningful.

Simulations, on the other hand, use fixed or pre-set values for the parameters, e.g. those from literature. The generated simulated curve is subsequently compared with experimental data obtained under the same conditions. Normally no absolute agreement between experimental and simulated transient is obtained. Instead, changes in the form of the simulated transient are studied as a function of the value of a model parameter. This way the simulation procedure approaches the non-automatic, manual fitting procedure. An

advantage of simulations is that it is possible to quantify how much model parameters affect a selected property of the simulated curve (e.g. the F_M -value) by means of an additional, so-called control analysis (e.g. Lazár et al., 2005a; see also Chapter 15 by Ian E. Woodrow in this book).

For modeling, one can use either simpler analytical functions or more complex mathematics based on known structures, functions and kinetics (SFK). In the first case, the FLR is described by a sum of usually exponential and sigmoidal functions, which simulate or fit the experimental FLR. For the case of e.g. the DCMU-FLR this approach enables the determination of the PS II $\alpha/\beta(\gamma/\delta)$ heterogeneity related to the antenna size and the energetic connectivity (Lazár et al., 2001). For the case of the non-DCMU-FLR, the analytical functions can be used for a quantitative description of the FLR and parameters derived from it (Pospíšil and Dau, 2002), but partially also for the determination of some rate constants having molecular meaning (Vredenberg, 2008a; see Chapter 6 by Wim Vredenberg and Ondřej Prášil in this book). However, even if the sum of the analytical expressions can describe the FLR very well, the functions generally do not say too much about the molecular basis of the FLR. This is in contrast to the second case when models based on known SFK to model the FLR are used. Using this approach, it is possible to determine contributions of particular reactions to particular features of the FLR. Both these approaches are described and discussed in Section III.

B. Why Measure and Simulate the Fluorescence Rise?

Rappaport et al. (2007) recently wrote that it is better to measure fluorescence transients at a low intensity of excitation light, because low light intensities are more physiological. The authors could have taken this argument one step further, if they had written that it would have been better not to measure induction transients at all, since pure dark-to-light transitions are extremely rare in nature. Why do we then invest so much energy in the study of fluorescence transients obtained under such non-physiological conditions? The advantage of dark-to-light transitions is the well-defined dark-adapted state. We know quite well what the redox-state of the manganese cluster of the OEC, Q_A and the PQ pool are in the dark.

The use of the high-intensity excitation light of about $3,000 \mu\text{mol photons m}^{-2} \text{ s}^{-1}$ also has clear advantages: an excitation rate of about once per 200–300 μs makes it possible to detect the reduction of the acceptor side of PS II, the reduction of the PQ pool and the reduction of the acceptor side of PS I (Lazár and Pospíšil, 1999). At more physiological, lower intensities of light, the excitation rate of PS II is so low that only the reduction of the acceptor side of PS I can still be detected, as noted also by Rappaport et al. (2007). Pospíšil and Dau (2002) and Boisvert et al. (2006) demonstrated that the FLR can be approximated by three exponentials. We do not believe that the complete O–J–I–P FLR can be well simulated using only three exponentials, but it shows that the different phases of the transient measured with high light intensities are kinetically well separated. As noted by Tóth et al. (2007b) the kinetic separation between the reduction of the PQ pool and the reduction of the PS I acceptor side disappears if the PQ pool was already partially reduced at the start of the measurement. Up to the re-oxidation of reduced PQH_2 by the $\text{cyt } b_6\text{f}$ complex each subsequent step is slower than its predecessor. As a consequence, a lot of stoichiometric information on the whole photosynthetic electron transport chain can be obtained. Also from a simulation point of view, measurements at high light intensities have clear advantages. Since more reactions taking place in the electron transport chain have an effect on the form of the transient, there is less uncertainty with respect to the correctness of the simulation.

C. Relationship Between the Origin of Fluorescence and the Model Structure

According to our current understanding, at room temperature and under physiological conditions variable fluorescence originates from PS II (for reviews see Krause and Weis, 1991; Dau, 1994; Govindjee, 1995). Therefore, most models of the FLR describe electron transport reactions occurring in PS II and the PQ pool (Stirbet et al., 1998; Lazár, 2003; Zhu et al., 2005). However, fluorescence measurements on intact systems show a clear effect on the FLR of electron transport through PS I (Kautsky et al., 1960; Munday and Govindjee, 1969; Satoh and Katoh, 1981; Hansen et al., 1991; Schansker et al., 2003, 2005). Therefore, some models consider also electron

on thylakoid membranes illuminated by a low intensity of exciting light characterized by the O–I–P steps (see Section III.B.2). However, extended versions of the TEG model were also used for modeling of the O–J–I–P transient (see Section III.B.3). When the TEG model is used for the modeling of the FLR, the fluorescence signal is assumed to be proportional to the amount of reduced Q_A (see Section II.F).

The second basic model is the reversible radical pair (RRP) model (Breton, 1983; Van Grondelle, 1985; Schatz et al., 1987, 1988; Leibl et al., 1989; Roelofs et al., 1992; Fig. 5.3; Table 5.2), which describes the formation of ES and primary photochemistry (charge separation, recombination, and stabilization) in “open” (Q_A) and “closed” (Q_A^-) PS II, i.e., it describes electron transport from a PS II electron donor, P680, via the primary electron acceptor pheophytin (Pheo) to Q_A . The original RRP model was suggested for interpretation of pico- and nanosecond-scale transients following excitation by a very short laser flash and, therefore, this original RRP model does not include the much slower reduction of $P680^+$ by the PS II donor side. In order to use the RRP model for the modeling of the FLR, the model must be extended involving the $P680^+$ reduction processes (see Section III.A.2). The original RRP model also assumed that all the pigments of the adjacent light harvesting antennae are in ultra-fast kinetic equilibrium with pigments

of RC II and with the donor pigment, an assumption of the so-called monopartite model (see Dau, 1994). In addition, the original RRP model assumed that P680 is the primary PS II electron donor. However, later findings suggested that an accessory chlorophyll, Chl_{acc} D1, that is located between P680 and Pheo, is the primary PS II electron donor (see e.g. Groot et al., 2005; Holzwarth et al., 2006). Therefore, the RRP model was extended to include also these facts (for more details see Chapter 3 by Rienk van Grondelle, Vladimir I. Novoderezhkin and Jan P. Dekker in this book). When the RRP model is used for the modeling of the FLR, the fluorescence signal can be assumed to be proportional to the amount of reduced Pheo and/or Q_A or to the deactivation of the ES (see Section II.F). As the RRP model describes only electron transport up to Q_A , the RRP model alone can only be used for modeling of the DCMU–FLR (see Section III.A.2).

Neither TEG nor the RRP model includes an explicit description of PS II with respect to the electron transport properties on the PS II donor side, i.e. electron transport from tyrosine 161 (Y_Z) to P680 and electron transport from OEC to Y_Z . Therefore, to have a complete description of PS II, Y_Z and OEC should also be considered. During PS II turnover, the Mn cluster of the OEC, together with Y_Z , cycles through five redox-states, the S-states, as described by the Kok model (Kok et al., 1970; Fig. 5.4; Table 5.2).

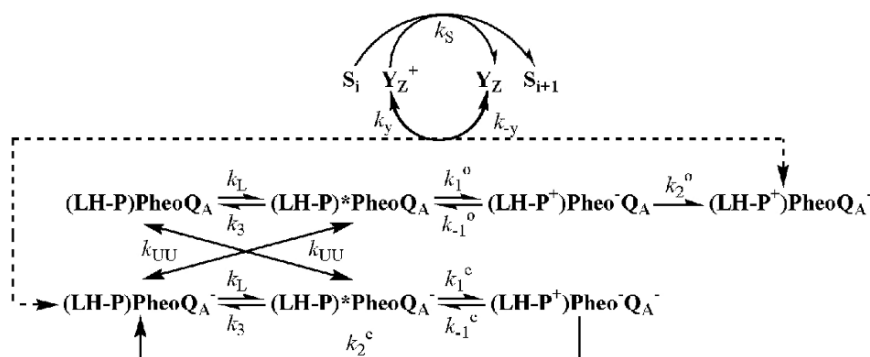


Fig. 5.3. A scheme of the RRP model. The original RRP model is represented by the two lower lines of reactions, where the upper line represents reactions occurring in an open RC II (Q_A is initially oxidized) and the lower line represents reactions occurring in a closed RC II (Q_A is initially reduced). The reaction marked by a dashed arrow above the dashed arrow describe a reversible reduction of $P680^+$ by Y_Z and a reduction of Y_Z^+ by OEC. S_i and k_S represent particular S-state and the related value of the rate constant, respectively, according to the Kok model (see Fig. 5.4). LH–P means all Chls of the adjacent light harvesting antennae of PS II (LH), which are in ultrafast kinetic equilibrium with P680 (P). For rate constants see Table 5.2.

Table 5.2. A summary of approximate values of the rate constants of a control sample (room temperature, no chemicals) considered in the TEG (Fig. 5.2), RRP (Fig. 5.3) and Kok's S-state (Fig. 5.4) models. Rate constants are first order or are considered to be pseudo-first order (for the second order reactions) and all have dimensions of s^{-1} . Open and closed states of RC II mean states with Q_A initially oxidized and reduced, respectively. For more details on known ranges of rate constants and related references see e.g. Lazár (2003) and Zhu et al. (2005).

Rate constant	Value, s^{-1}	Description
k_L	4,000	For $3,000 \mu\text{mol photons m}^{-2} \text{ s}^{-1}$; rate of ES formation
k_1^o	3×10^9	Charge separation in open RC II
k_{-1}^o	3×10^8	Radiative charge recombination in open RC II
k_2^o	2.3×10^9	Charge stabilization in open RC II
k_1^c	4.8×10^8	Charge separation in closed RC II
k_{-1}^c	3.4×10^8	Radiative charge recombination in closed RC II
k_2^c	1×10^9	Nonradiative charge recombination in closed RC II
k_3	5×10^8	Deactivation of ES (includes heat dissipation and fluorescence emission)
k_{UU}	1×10^9	Energy transfer between open and closed RC IIs
k_y	$4\text{--}40 \times 10^6$	Reduction of $P680^+$ by Y_Z ; S-state dependent
k_{-y}	$1\text{--}7 \times 10^6$	Backward electron transport from $P680$ to Y_Z^+ ; S-state dependent
k_{01}	20,000	S_0 – S_1 transition of OEC
k_{12}	10,000	S_1 – S_2 transition of OEC
k_{23}	3,330	S_2 – S_3 transition of OEC
k_{30}	1,000	S_3 – S_0 transition of OEC
k_{AB1}	3,500	Electron transport from Q_A^- to Q_B
k_{BA1}	175	Backward electron transport from Q_B^- to Q_A
k_{AB2}	1,750	Electron transport from Q_A^- to Q_B^-
k_{BA2}	35	Backward electron transport from Q_B^{2-} to Q_A
$k_{(B/PQ)\text{ex}}$	70–800	Exchange of Q_B^{2-} (includes its protonation) with oxidized PQ molecule from PQ pool
$k_{(PQ/B)\text{ex}}$	70–800	Backward exchange of reduced PQ molecule (includes its deprotonation) from PQ pool with Q_B
$k_{PQ\text{ox}}$	10–500	Oxidation of reduced PQ pool
$k_{PQ\text{red}}$	10–500	Backward reduction of oxidized PQ pool

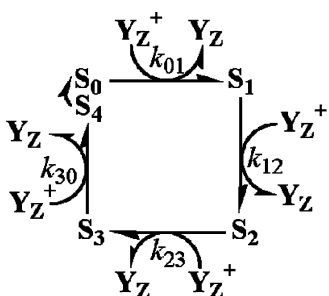


Fig. 5.4. A simplified scheme of the Kok's S-state model. S_i ($i = 0, 1, 2, 3, 4$) represents the particular S-states of the manganese cluster of OEC. The S_4 -state is assumed to be kinetically indistinguishable from the S_0 -state. Y_Z is the electron donor to $P680$. For rate constants see Table 5.2.

The models of e.g. Lazár (2003) and Zhu et al. (2005) consist of a combination of the TEG, RRP and Kok models to simulate the FLR (see Section III.B.4).

E. Kinetics and Rate Constants

Mass action theory is routinely used in modeling of the FLR. However, a proper choice between first and second order reactions has to be made. For example, if we assume that electron transport from Q_A^- to Q_B in a model is irreversible, this reaction can be described as: (i) $[Q_A^-] + [Q_B] \rightarrow [Q_A] + [Q_B^-]$ or as (ii) $[Q_A^- Q_B] \rightarrow [Q_A Q_B^-]$, where (i) is a second order reaction with a rate of product formation $d[Q_A]/dt = d[Q_B^-]/dt = \text{rate constant} \times [Q_A^-](t) \times [Q_B](t)$ and (ii) is a

first order reaction with a rate of product formation $d[Q_A Q_B^-]/dt = \text{rate constant} \times [Q_A^- Q_B](t)$.

From the point of view of chemical reaction kinetics, second order kinetics can be used when two components can freely move and react together in a free volume that can be used for the interaction of e.g. PQ with the Q_B pocket, PQ with cyt b_6f , PC with cyt b_6f , PC with P700, etc., but not for reactions occurring inside a protein (e.g. electron transport from Q_A^- to $Q_B^{(-)}$), where the components are fixed in their positions. In this case first order kinetics should be used. From a “physiological” point of view, second order kinetics in fact means that Q_A^- from one PS II can react with Q_B from any other PS II, which is of course not the case (see also Chapter 7 by Andrew Rubin and Galina Riznichenko in this book). The different kinetics also leads to different simulations of the FLR as shown by Stirbet and Strasser (1995, 1996).

Another point of which a researcher must be aware is related to the values of rate constants used in the model. The published values of rate constants present several potential problems to the modeler. In the first place, the experimental conditions used to determine the rate constant do not necessarily match the conditions found e.g. in a leaf. To give an example of this, the equilibrium constant for electron transport between Q_A and Q_B depends on the pH of the stroma (Robinson and Crofts, 1984). If the rate constant used in the model was determined at pH 7, but the stroma of a dark-adapted leaf is approximately at pH 7.5 (Hauser et al., 1995; Schansker and Strasser, 2005), there will be a mismatch. Also the intactness of the system used to determine the rate constants may affect their values. Rate constants based on measurements with PS II core particles may deviate from the values found in leaves. An additional problem occurs if the technique used to determine a rate constant was not precise enough and the obtained value is in reality only a rough estimate. An example of the differences between experimental material and technical limitations is presented by the list of very different values for the halftimes of the particular S-state transitions collected by Razeghi-fard et al. (1997). Further, almost every model is a simplification and a reaction in a model may in fact consist of several partial reactions. Therefore, it is important to know which partial reaction is rate limiting for

the model reaction, in order to use the appropriate value.

According to the Marcus theory of electron tunneling in biological systems (Marcus and Sutin, 1985) and its empirical simplification (Page et al., 1999, 2003), the rate constant of an electron transport reaction in a protein (k_{et}) depends (i) on the edge-to-edge distance (R) between electron donor and acceptor, (ii) on the reorganization energy (λ), and (iii) on the driving force of the reaction (difference in standard free energy, ΔG^0):

$$\log k_{et} = 15 - 0.6R - 3.1(\Delta G^0 + \lambda)^2/\lambda. \quad (5.1)$$

For the origin of the numeric terms in Eq. (5.1) see Page et al. (1999, 2003). However, in RC IIs (or in thylakoid membranes in general) several processes take place that can affect this simple equation. Light-induced electron transport causes structural changes in the protein (Christophorov et al., 2000; Goushcha et al., 2000). Simultaneously, a light-induced electric field is evolving. The formation of the electric field effect can be divided into three components: (i) formation of the electric field inside PS II due to charge separation, (ii) transmembrane electric potential ($\Delta\Psi$) caused by the transport of protons during the initial formation of a pH gradient between the stroma and the lumen and (iii) changes in $\Delta\Psi$, caused by the subsequent movement of accompanying secondary ions across the thylakoid membrane. These processes affect the values of the rate constant for particular electron transport reactions. In the absence of experimental data giving insight in the precise effects of these processes on electron transport rates and, in addition, the complicated mathematics involved, these processes have seldom been considered in modeling of the FLR. Usually the rate constants are assumed to be constant in time or, in some cases, the effect of electric field has been considered (see Sections III.B.4 and III.B.5).

According to the RRP model, the above process (i) is manifested as a decrease of the rate constant for charge separation and an increase of the rate constant for charge recombination when Q_A is already (initially) reduced (Schatz et al., 1987, 1988). Similarly, a decrease of the rate constant of charge separation and an increase of the

rate constant of charge recombination was documented for process (iii) (Dau and Sauer, 1991, 1992). The changes in the above-mentioned rate constants increase the concentration of the ES and therefore lead to an increased fluorescence yield (Dau and Sauer, 1991, 1992). But process (iii) does not affect the fluorescence yield in initially closed (Q_A^-) RC II (Bulychev et al., 1986; Dau and Sauer, 1991), probably because the ion-related transmembrane electric field is too weak compared to the local field induced by the electron stored on Q_A . However, the theory of Wim Vredenberg and Alexander Bulychev (the so-called photo-electrochemical fluorescence stimulation) predicts a fluorescence increase caused by process (iii) even if all the RC IIs are closed (Bulychev and Niyazova, 1989; Vredenberg and Bulychev, 2002; Vredenberg et al., 2006; see Chapter 6 by Wim Vredenberg and Ondřej Prášil in this book). Graan and Ort (1983) showed that during the first 200 ms of illumination valinomycin (ionophore known to short-circuit the flow of K^+ ions) was able to accelerate the rate of plastoquinol oxidation, whereas nigericin (supposed to act as protonophore) was ineffective. These authors therefore concluded that process (iii) and not process (ii) dominates the decrease of the rate of plastoquinol oxidation. On the other hand, process (ii) begins to dominate changes in the rate of plastoquinol oxidation after longer periods of illumination. The additive effect of $\Delta\Psi$ and pH changes agrees with the work of David Kramer and coworkers (Cruz et al., 2001; Kramer et al., 2003). It is important that process (ii) not only affects plastoquinol oxidation, but also affects electron transport from Q_A^- to Q_B : an alkalization of stroma causes a decrease in the apparent equilibrium constant of the electron transport reaction (Robinson and Crofts, 1984), i.e., the probability to find an electron on Q_A increases (see also Belyaeva et al., 2006 and Sections III.B.4 and III.B.5). The biophysical mechanism behind all the electric field induced changes of the rate constants – direct and reverse – is a change in the ΔG^0 of a given reaction.

For the proper use of rate constants in the modeling of the FLR, attention should also be paid to their units, which are either s^{-1} or $M^{-1} s^{-1}$, for the first and second order reactions, respectively. The first order rate constants range for PS II from about $10^{11} s^{-1}$ (primary charge separation) to

about $10^3 s^{-1}$ (electron transport from Q_A to Q_B) and the value of the second order rate constant related to PS II is about $10^6 M^{-1} s^{-1}$ (binding of a PQ molecule to the Q_B pocket of PS II). To simplify and speed up calculations, a normalization is used. For the basic TEG model, the initial concentration of $Q_A Q_B$ (in the dark-adapted state) is set to 1 (instead of about $0.05 \mu M$, typical for a thylakoid suspension of $20 \mu g \text{ Chl ml}^{-1}$). After rescaling of the rate constants, the first order rate constants have the same values and units (s^{-1}) as the original values, but the second order rate constants, having much smaller values than before the normalization, now have the unit s^{-1} (since PS II concentration was assumed to be unity).

F. Fluorescence and “Closed” Reaction Centers

To model the FLR, one must know which processes determine the change in the fluorescence yield between O and P. Usually, it is assumed that fluorescence is proportional to the fraction of “closed” RC II. However, what characterizes a closed RC II?

Duysens and Sweers (1963) defined as closed a RC II with Q_A^- . Using this approach, fluorescence is directly proportional to the amount of Q_A^- , but on the assumption that PS II units are energetically disconnected. This assumption leads to an exponential fluorescence rise when the sample is inhibited by DCMU (see Section III.A.1). If PS II units are energetically connected, then fluorescence is expressed by Eq. (5.5) (Lazár, 1999; see also Section III.A.1). In the case of energetically connected PS II units, the fluorescence rise measured on samples inhibited by DCMU is sigmoidal. However, an alternative explanation for the sigmoidal fluorescence rise has been suggested, based on the assumption that Y_Z^+ quenches fluorescence (Vredenberg, 2008b; Section III.A.1; see also Chapter 6).

A few years after the publication of the study of Duysens and Sweers (1963), René Delosme introduced the terms photochemical phase and thermal phase, referring to the fast and the slower rise phases of the FLR (Delosme, 1967; see Section I.B). In that paper, he assumed that most Q_A was already reduced at the end of the photochemical phase (J step) and therefore the J–I–P rise had to be something else. Over the years

more observations were made that suggested that Q_A was not the only determinant of the variable fluorescence. Joliot and Joliot (1979) working with DCMU-inhibited samples introduced a second quinone Q_2 (a putative electron acceptor which needs more than one flash to be reduced in the presence of DCMU; not identical with Q_B) that together with $Q_1 (= Q_A)$ would explain the data. Another observation that is difficult to explain in the context of the hypothesis of Duysens and Sweers (1963) is that in the presence of DCMU, 2 ms of illumination is enough to reach F_M , whereas in its absence only about 60% of the maximum fluorescence yield can be reached in 2 ms even if intensities of excitation light of $15,000 \mu\text{mol photons m}^{-2} \text{ s}^{-1}$ are used (e.g. Neubauer and Schreiber, 1987; Schansker et al., 2006). The same is true for a single turnover flash with which only about 60% of the F_M , caused by continuous excitation, can be induced (Samson and Bruce, 1996). Samson et al. (1999) tentatively suggested that the occupation state of the Q_B site also plays a role in determining fluorescence yield; Schansker et al. (2006) have provided some experimental evidence that seems to support this interpretation. There may indeed be a second determinant of the fluorescence yield, but in the absence of credible experimental evidence we can only guess what it is and what its underlying molecular mechanism may be. Suggestions found in the literature are: recombination fluorescence (Schreiber and Krieger, 1996), the redox state of Pheo (Vredenberg, 2000), electron flow along the inactive branch of PS II (Schreiber, 2002), fluorescence quenching caused by $P680^+$ (Butler, 1972; Bruce et al., 1997) and by oxidized PQ molecules (Vernotte et al., 1979; Kurreck et al., 2000), the quenching by the oxidized PS II donor side (Hsu, 1993; Lavergne and Leci, 1993), and Y_Z^+ (Vredenberg, 2008b) and, perhaps, a conformational change, all of which would affect the fluorescence yield.

Few modelers have explored the possibility that there is a second determinant of the fluorescence yield. The main exception, in this respect, is the so-called three state trapping (TST) model put forward by Wim Vredenberg (2000; also see Chapter 6 in this book). In the TST model, closed RC IIs are defined as having either oxidized P680 or reduced Pheo. It is a state in which ES cannot be used for photochemistry. This approach was

adopted from the definition of closed RCs that was originally proposed for bacteria (Vredenberg and Duysens, 1963). Because the rate constant of excitation (related to the applied intensity of actinic light) used in the FLR experiments is much lower than the rate constants of both $P680^+$ reduction by Y_Z and Pheo $^-$ oxidation by Q_A , a closed RC II is in fact in the $P680\text{Pheo}^-Q_A^-$ state. Assuming that the redox state of Pheo is a co-determinant of the variable fluorescence yield, two electrons are necessary to close a single RC II. In this model, the $P680\text{Pheo}Q_A^-$ state is called semi-open (also called semi-closed) state, having a fluorescence yield that is half the maximal value of the $P680\text{Pheo}^-Q_A^-$ state. Strasser and Stirbet (2001) and Stirbet and Strasser (2001) have explored the approaches of Duysens and Sweers (1963) and that of Vredenberg (2000), mentioned above, and have added, as a third approach, the idea that only the redox state of Pheo determines whether an RC II is open or closed. In this case the fluorescence at time t is directly proportional to the amount of Pheo $^-$.

Independent of the number of determinants of the fluorescence yield, the best approach would be to define the fluorescence intensity as radiative deactivation of ES, i.e. as $k_F \times [\text{ES}](t)$ where k_F is the rate constant of fluorescence emission and ES can be formed either in RC II or in the light harvesting antennae (Baake and Schlöder, 1992; Lebedeva et al., 2002; Lazár, 2003; Zhu et al., 2005). This approach takes into account the physical origin of fluorescence as presented by the well-known Jablonski diagram (see Lakowicz, 1999).

All the above approaches assume that changes in fluorescence yield are caused only by changes in the efficiency of photochemistry via changes in the amount of closed RC IIs, whatever the “closed” means. However, in principle, changes in the fluorescence yield reflect changes in the efficiency of any processes utilizing excitation energy: in addition to photochemistry also the dissipation of ES to heat. These changes are then reflected in changes of measured fluorescence lifetime(s) (e.g. Holub et al., 2000, 2007; Moise and Moya, 2004a,b). Energy-dependent non-photochemical fluorescence quenching (qE) is e.g. interpreted to be due to a change in the rate constant for heat dissipation (Gilmore et al., 1995; Vasil'ev et al., 1998). Only in the models

of Goltsev and Yordanov (1997) and Laisk et al. (2006a) it is assumed that excitation dissipation also changes during the transient, in parallel with changes in the efficiency of photochemistry.

G. Model Formulation and Simplification

In formulating a model to simulate experimental data one always has to find a balance between the correctness of the model (it should include all “important” reactions) and the simplicity of the model (simplifying both the calculations and the interpretation of the simulated curves). There are also procedures – so-called model reductions – for the simplification of complicated models (see e.g. Riznichenko et al., 1999, 2000; Lebedeva et al., 2000; Nedbal et al., 2007; Chapter 2 by Ladislav Nedbal, Jan Červený and Henning Schmidt in this book).

The implications of different approaches to model reduction can be discussed in the context of a PS II model. We could take a model that only consists of the S_i -states of the OEC, P680, Q_A , Q_B and the PQ pool, assuming a homogeneous population of PS II. Depending on model simplifications, it contains different numbers of state variables (also called model forms). If all electron carriers are separate state variables, there are four S_i -states (S_1 , S_2 , S_3 , S_0), two states of P680 (P680 and P680⁺), two states of Q_A (Q_A , Q_A^-), three states of Q_B (Q_B , Q_B^- , Q_B^{2-}), and two states of the PQ pool (reduced, oxidized), that is, $4 + 2 + 2 + 3 + 2 = 13$ state variables (differential equations) describing all possible redox states in this model. However, as already discussed in Section II.E, it is not correct to consider electron carriers inside PS II as separate entities (state variables).

To make a more correct model consisting of the above-mentioned electron carriers, it is possible to define a state variable, a PS II with a particular combination of redox states of P680, Q_A , and Q_B (e.g. P680⁺ $Q_A^-Q_B$), but still leaving the S_i -states of the OEC as separate state variables. This would mean OEC is considered separated from PS II. Also, if one considers the exchange of doubly reduced Q_B for an oxidized PQ molecule a second order reaction (e.g., P680⁺ $Q_A^-Q_B^{2-} + PQ^{oxidized} \leftrightarrow P680^+Q_A^-Q_B + PQ^{reduced}$), then there are $2 \times 2 \times 3 = 12$ state variables describing all possible

redox states of PS II plus four variables describing the four S_i -states plus two variables describing the redox states of the PQ pool, that is 18 state variables (differential equations) describing all possible redox states in this model.

It is however well known that OEC forms an integral part of PS II and that the Q_B^{2-}/PQ exchange occurs via two subsequent reactions ($S_1P680^+Q_A^-Q_B^{2-} \leftrightarrow S_1P680^+Q_A^-E + PQ^{reduced}$ followed by $S_1P680^+Q_A^-E + PQ^{oxidized} \leftrightarrow S_1P680^+Q_A^-Q_B$, where E stands for an empty Q_B pocket). In this case there are $4 \times 2 \times 2 \times 4$ (there are now four instead of three Q_B states, because the empty Q_B pocket is considered a separate case) = 64 state variables describing all possible redox states of electron carriers inside PS II and the OEC plus two variables describing the redox states of the PQ pool. In other words, there would be 66 variables (differential equations) that describe all possible redox states in this model.

The above discussion illustrates that models with different levels of complexity can be obtained depending on the approach (simplifications) used in formulation of these models. It is also clear that even if simplifications result in “easier” models, such models do not exactly reflect the SFK properties of PS II. Moreover, as shown in Fig. 5.5 (see Lazár and Jablonský,

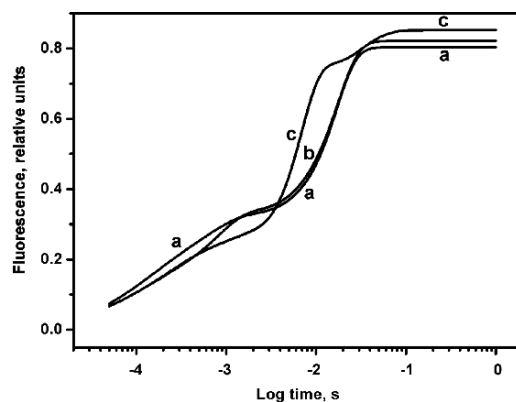


Fig. 5.5. Simulations of Chl *a* FRL on the basis of the model approaches described in the second (curve a), third (curve b) and fourth (curve c) paragraph of Section II.G (see Lazár and Jablonský, 2009). A homogeneous population of PS II was assumed and values of rate constants and initial conditions in all the models were the same. The FRL curves were calculated according to Eq. (5.5) with $p = 0.55$ and using time courses of the closed RC II (with Q_A^-). The FRL curves are shown on a logarithmic time-axis.

2009), the three models described above lead to the simulation of different FLRs (keeping the values of rate constants and initial conditions in all the models the same). The transients shown in Fig. 5.5 illustrate that the chosen approach can significantly affect the shape of simulated FLR.

III. Particular Models for the Fluorescence Rise

This section summarizes particular models and their results, used for modeling FLR with and without DCMU.

A. Modeling Fluorescence Rise in DCMU Inhibited Samples

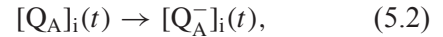
As mentioned in Section I.B, in the presence of DCMU (Diuron) electron transport beyond Q_A is inhibited. This results in a steep rise of the fluorescence intensity, reaching the maximum level after about 2 ms when measured with an intensity of excitation light of $3,400 \mu\text{mol photons m}^{-2} \text{s}^{-1}$ (Fig. 5.1B). Reducing the intensity of excitation will increase the time needed to reach the maximum level. The description of the electron transport reactions occurring in the presence of DCMU, needed for SFK-based models, is considerably simpler than the description in its absence, and can be done using analytical functions only.

1. Using Analytical Functions

Analytical functions have been used to explore PS II heterogeneity (Lazár et al., 2001). The method allows an analysis of PS II antenna size heterogeneity, characterized by differences in k_i and heterogeneity in energetic connectivity between PS II units characterized by differences in p_i (see below). This heterogeneous behavior of PS IIs was first recognized and analyzed by Melis and Homann (1975, 1976); they based their interpretation on the observation of heterogeneity in the time course of the complementary area (area between FLR curve and a horizontal line representing the F_M level). Melis and Homann (1975, 1976) distinguished two phases that were ascribed to two types of PS II reaction centers: PS II α and PS II β that differed in their antenna size and energetic connectivity (see e.g. Black et al.,

1986 and Laverne and Braintais, 1996 for a discussion of the literature). This analysis method was further elaborated by Sinclair and Spence (1988, 1990) and Hsu et al. (1989; see also Hsu and Lee, 1991). Sinclair and Spence (1988, 1990) identified two additional kinetic phases: γ and δ . The γ -phase was also identified by Hsu et al. (1989). However, we note that the nomenclature used for PS II types by different authors need not really refer to the same types of PS II (Lazár et al., 2001). The γ -phase has been suggested to be the same as the Q_B non-reducing RC IIs, just determined by other means based on their relative contributions (Schansker and Strasser, 2005) and we cannot exclude that the δ -phase reflects RC IIs that were not inhibited by DCMU. For a discussion of the DCMU-leak hypothesis, see e.g. Laverne and Braintais (1996).

It is assumed in this approach that closed RC IIs are those with Q_A^- (see Section II.F). Closure of RC IIs can then be described as:



where, i indicates the type of RC II (PS II α , β , γ or δ) and the closure of each RC II $_i$ proceeds with a separate rate constant k_i . This can be mathematically written as:

$$[Q_A^-]_i(t) = [Q_A]_i(0)[1 - \exp(-k_i t)], \quad (5.3)$$

where, t is time and $[Q_A]_i(0)$ is the fraction of a particular type of PS II ($\sum [Q_A]_i(0) = 1$).

If there is no energetic connectivity between RC IIs of a given type then the relative variable fluorescence $V_i(t) = (F_i(t) - F_{0,i})/(F_{M,i} - F_{0,i})$ is proportional to the amount of $[Q_A^-]_i(t)$ and there is an exponential rise of fluorescence as described by Eq. (5.3). On the other hand, if RC IIs of a given type are energetically connected, the closure of the RC IIs with time causes an increase in the effective antenna size of the remaining open RC IIs, leading thus to an increase of the rate of the Q_A reduction in the remaining open RC IIs. Therefore, k_i is a function of time:

$$k_i(t) = k_i^0 / (1 - p_i[Q_A^-]_i(t)), \quad (5.4)$$

where k_i^0 is the initial rate constant (at $t = 0$) for the closure of a particular type of RC II (i.e., for Q_A reduction) and p_i is the connectivity parameter according to Joliot and Joliot (1964). A formula for $k_i(t)$ similar to Eq. (5.4) was also derived for a situation in which energetic con-

nectivity between all RC IIs is unlimited (RC IIs behave according to the so-called lake model; for a review see Lazár, 1999). $V_i(t)$ of the energetically connected RC IIs is described as:

$$V_i(t) = ((1-p_i)[Q_A^-]_i(t)) / (1-p_i[Q_A^-]_i(t)), \quad (5.5)$$

which leads to a sigmoidal rise of fluorescence. Equations similar to Eq. (5.5) were derived by several authors (for a review see Lazár, 1999). An alternative explanation has been suggested by Vredenberg (2008b); in this interpretation, the sigmoidicity is caused by comparable rates of formation of the charge-stabilized state and of the release of fluorescence quenching by Y_Z^+ without any consideration of energetic connectivity between PS II units (see Chapter 6).

It is important to note that the approach described above is generally valid and is also used for simulations of the FLR measured without DCMU using models where fluorescence is assumed to reflect the amount of Q_A^- (see sections below).

2. The Application of Reversible Radical Pair Models

At first sight, the DCMU–FLR contains a feature that is sometimes misleading. At an intensity of excitation light of about $3,400 \mu\text{mol photons m}^{-2} \text{ s}^{-1}$ the maximum fluorescence intensity is reached after 2–3 ms (Fig. 5.1B). For the used light intensity, one excitation occurs per 200–300 μs (Lazár and Pospíšil, 1999) that equates to about ten excitations (in theory ten charge separations) during the 2–3 ms interval. However, when DCMU is present, a maximum of two excitations is used for photochemistry leading to storage of only two electrons, one on Pheo and one on Q_A . This discrepancy is explained on the basis of the RRP model (Fig. 5.3) if reduction of $P680^+$ by the PS II donor side is included in the model: only following a reduction of $P680^+$ by Y_Z and a re-reduction of Y_Z by the manganese cluster of OEC the recombination reactions are prevented and it takes, therefore, some time to reach the maximum value (Lavergne and Rappaport, 1998).

Trissl et al. (1993) were the first to apply the RRP approach to the modeling and analysis of the DCMU–FLR. However, they used the original

RRP model (see Section II.D), which does not explicitly include the $P680^+$ reduction by the PS II donor side. To bypass this problem, Trissl and coworkers calculated the amount of the respective state variables using a backward (recursive) way (that is also the reason why the FLRs are shown in this study on a pseudo time base). Some numerical errors in this paper (for a discussion of these errors see Falkowski et al., 1994; Trissl, 1994) allowed Holzwarth (1993) to suggest that no useful information could be obtained on the basis of the DCMU–FLR. The RRP model was further used to explore the relationship between the fluorescence transient and energetic connectivity (Lavergne and Trissl, 1995) and PS II antenna heterogeneity (Trissl and Lavergne, 1995). Trissl and Lavergne (1995) concluded on the basis of their analysis that energetic connectivity due purely to a PS II α dimer organization was less likely, but that a PS II α dimer organization with limited energetic connectivity between the individual dimers would explain the results well. Vavilin et al. (1998) used the model of Lavergne and Trissl (1995) to analyze photoinhibition; they assumed that photoinhibited PS IIs do not trap ESs for photochemistry but efficiently dissipate the absorbed light energy.

All studies mentioned above used the original RRP model and therefore did not take into account the influence of the PS II donor side on the results. Heat stress destroys the manganese cluster of OEC and thereby changes the properties of the donor side of PS II (Cheniae and Martin, 1970; Kimimura and Katoh, 1972; Enami et al., 1994; Tóth et al., 2007a). To analyze the effects of a high temperature treatment on the DCMU–FLR, the original RRP model was extended adding a description of the donor side reactions (Lazár and Pospíšil, 1999). Using this model, a fit of the experimental DCMU–FLR could be obtained without the assumption of PS II heterogeneity.

Lazár et al. (2005a) observed a nearly linear relationship between the amount of initially reduced cyt b_{559} and the F_M level in DCMU-inhibited thylakoid membranes. To explain this relationship the RRP model was extended to include also cyt b_{559} , which was assumed to accept electrons from Pheo $^-$ and donate electrons to $P680^+$ thereby enabling a well-known cyclic electron transport around PS II (Heber et al., 1979; Falkowski et al., 1986; Miyake and Yokota,

2001; Laisk et al., 2006). In the crystal structure of RC II (Kamiya and Shen, 2003; Ferreira et al., 2004; Loll et al., 2005) cyt b_{559} was found to be located on the Q_B side of the RC. Therefore, the Pheo donating electrons to cyt b_{559} in the model of Lazár et al. (2005a) is possibly the Pheo localized in the D2 protein, which is part of the inactive branch of PS II. The inactive branch has been suggested earlier to play a role in the FLR (Schreiber, 2002).

B. Modeling of the O–(J–)I–P Phases in Fluorescence Rise

This section summarizes particular approaches used for modeling of the FLR measured when dark-adapted samples are exposed to low (O–I–P curve) or high (O–J–I–P curve) intensity of exciting light.

1. Using Analytical Functions

Pospíšil and Dau (2000, 2002) and Boisvert et al. (2006) used a very simple approach to fit the Chl a fluorescence transients measured on PS II and thylakoid membranes. In all cases, these authors assumed that the transients could be fitted with two to three exponentials. For PS II-membranes Pospíšil and Dau (2002) argued that the O–J phase represented the reduction of Q_A whereas the rest of the rise (the J–P phase) was due to the reduction of the PQ pool and a concomitant loss of quenching by PQ. These two processes were assumed, for all practical purposes, to be kinetically independent. Pospíšil and Dau (2002) assumed that the third phase (the J–I phase) that occurs in thylakoid membranes was due to $\Delta\Psi$. Support for this interpretation was found in the effect of the ionophore valinomycin: it caused the reduction of the amplitude of the J–I phase¹.

¹ Vredenberg and Bulychiev (2003) have pointed out that valinomycin accelerates the re-oxidation kinetics of PQH_2 (Graan and Ort, 1983). Further, Vredenberg and Bulychiev (2003) have observed, in leaves, an effect of valinomycin on the I–P phase. We, however, believe that this is probably not a direct electric field effect because it is accompanied by an incomplete re-reduction of $P700^+$ and PC^+ suggesting an effect on the properties of the acceptor side of PS I (S.Z. Tóth and G. Schansker, 2003, unpublished).

Boisvert et al. (2006) used the same three-exponential approach in combination with an analysis of Arrhenius plots for their analysis of the FLR, and noted complementarity between O–J and J–I amplitudes. This complementarity is a logical consequence of the fact that the FLR reflects the kinetics of a series of sequential reactions. It means that the amplitudes of the different phases of the FLR are interdependent. Therefore, in our opinion, the three-exponential analysis does not necessarily yield useful quantitative information. Rather, the fact that the three-exponential analysis works at all makes it clear that the three phases of the FLR are kinetically well separated.

Pospíšil and Dau (2002) and Boisvert et al. (2006) used the following formula to fit the FLR:

$$F(t) = F_0 + A_{O-J}[1 - \exp(-k_{O-J}t)] + A_{J-I}[1 - \exp(-k_{J-I}t)] + A_{I-P}[1 - \exp(-k_{I-P}t)], \quad (5.6)$$

where, A 's and k 's are amplitudes and rate constants, respectively, of the particular phases of the FLR. Similarly, Pospíšil and Dau (2002) fitted the FLR of PS II membranes using Eq. (5.6) but without the central product because PS II membranes do not show the J–I phase of the FLR. We note that Eq. (5.6) is a sum of pure exponentials and therefore it does not take into account the energetic connectivity between PS II units (see Section III.A.1).

Antal and Rubin (2008) have used Eq. (5.6) without the F_0 term for fitting not of raw curves $F(t)$ as was done previously (Pospíšil and Dau, 2000, 2002; Boisvert et al., 2006), but of a transformed curve, $F_{\text{transformed}}(t)$, according to the following formula:

$$F_{\text{transformed}}(t) = [1 - F_0 / F(t)](F_V / F_M)^{-1}. \quad (5.7)$$

Antal and Rubin (2008) derived that $F_{\text{transformed}}(t)$ should reflect the relative amount of closed PS IIs (relative amount of Q_A^-). However, experimental data confirming the relationship between the transformation and the amount of closed PS IIs will be needed to make this a viable approach.

Vredenberg (2008a; Chapter 6) also uses a sum of exponentials to fit the FLR. However, the functions used by Vredenberg (2008a) partly represent the different electron transport reactions that

play a role in his TST model (Vredenberg, 2000; see Sections II.F and III.B.3) and therefore do not represent the type of extreme simplification that dominated the approach discussed above. The Vredenberg model of the FLR is for that reason more likely to yield meaningful information on the molecular basis of the FLR.

2. Two-electron Gate Models

The basic TEG model, as shown in Fig. 5.2, was used for the modeling of the O–I–P FLR measured in low intensity of exciting light. Renger and Schulze (1985) demonstrated for thylakoid membranes that it is only possible to fit the experimental FLR when there is an exponential decrease in the rate of exchange of doubly reduced Q_B with PQ as a function of the time of illumination. Renger and Schulze (1985) suggested that the changes in the exchange rate might be due to conformational changes. A 3:1 ratio between PS II α and PS II β centers, a connectivity parameter p of 0.5 for PS II α centers, and 5.5 and 1.5 PQ molecule per PS II α and PS II β -center, respectively, were needed to obtain a satisfactory fit (Renger and Schulze, 1985). Hsu (1992) criticized this study by noting that the initial PQH₂ exchange rate of 10 s^{-1} used by Renger and Schulze (1985) was much slower than the rate of 100 s^{-1} known from the literature and used by Hsu (1992). Further, Hsu (1992) studied FLRs induced by approximately $2\text{--}5\text{ }\mu\text{mol photons m}^{-2}\text{ s}^{-1}$ assuming for simplicity that there were only PS II α centers; he concluded that under these conditions a match between measured and simulated curves was only possible if he assumed that the PS II α centers fed electrons to PQ pools with a heterogeneous distribution of PQ pool sizes, with an average PQ pool size of 4.7 PQ molecule per PS II. Simulating samples partially inhibited with DCMU broadened the distribution and increased the effective PQ pool size per PS II. Goltsev and Yordanov (1997) slightly extended the TEG model considering also electron transport from PQH₂ to PS I and from PQH₂ and PS I to exogenous acceptors. They also considered the light-induced accumulation of protons in the lumen, which led in their model to a decrease of the rate constant for the re-oxidation of PQH₂ (see Section II.E) and to an effect on fluorescence signal through changes of rate constant of heat

dissipation. Hsu (1992) and Tomek et al. (2003) concluded on the basis of their TEG-model simulations that Q_B reducing (=active) PS II centers contribute to the F_{pl} level of the FLR. As noted by Hsu (1993), this contribution is due to the equilibrium between Q_A and Q_B . These studies confirmed the original observation of Forbush and Kok (1968) that the dark-adaptation kinetics of the F_{pl} level was biphasic and therefore presented two processes. As noted among others by Lavergne and Braintais (1996) and Tomek et al. (2003) the $F_0 - F_{pl}$ rise overestimates the amount of the Q_B non-reducing PS II centers. However, as shown by Schansker and Strasser (2005), using a far-red (FR) light pre-pulse, it is possible to reduce the problem to these two components (Q_B non-reducing PS II and the equilibrium between Q_A and Q_B) of which the relative amplitudes can be determined by a kinetic analysis.

The basic TEG model was also used for modeling of the O–J–I–P FLR measured upon a high intensity of exciting light. The first of these studies was published by Stirbet and Strasser (1995) followed by other papers (Stirbet and Strasser, 1996; Strasser and Stirbet, 1998). In these studies, Alexandrina Stirbet and Reto Strasser showed how parameters like the PQ pool size, the rate constant for the re-oxidation of PQH₂ and the excitation rate k_L (Stirbet and Strasser, 1995, 1996) and PS II heterogeneity (Strasser and Stirbet, 1998) affect the simulated FLR. Lazár et al. (1997), Tomek et al. (2001), and Sušila et al. (2004) used a model similar to the one of Strasser and coworkers. In the three studies mentioned, this model was extended by a more detailed description of the exchange of $Q_B^{2-}(H^+)_2$ for an oxidized PQ molecule from the pool; further, the effect of the rates of the S-state transitions of the OEC on the rate of Q_A reduction was implicitly taken into account. This extended model was subsequently used for a detailed analysis of the effect of PS II herbicides on the FLR in leaves (Lazár et al., 1997), the dependence of the shape of the FLR on intensity of exciting light in leaves (Tomek et al., 2001), and the effect of the light gradient within thylakoid membrane samples on the shape of the FLR (Sušila et al., 2004).

We note that all studies mentioned above, with the exception of the work by Strasser and Stirbet (1998), assumed the presence of an unknown component X, which accepts electrons from

Q_B^- with a high rate. Without this assumption, no typical O–J–I–P FLR could be simulated (the I step would appear below 10 ms and it would be too high; data not shown in these studies).

3. Extended Two-electron Gate Models

The TEG model was further extended to include a more detailed description of the electron transport reactions occurring at the donor and the acceptor sides of PS II reaction centers. These extended TEG models were used for modeling of the O–J–I–P FLR: Stirbet et al. (1998) extended the TEG model, including the S-state transitions of the OEC. However, simulations based on this model rise too fast, showing particular steps of the FLR at times considerably shorter than the experimentally observed times. This model was subsequently used to fit the experimental FLR (Stirbet and Strasser, 2001). The fits confirmed the problems with the earlier simulations: to obtain a good fit, the model electron transport reactions on the acceptor side of PS II had to be much slower than observed experimentally. Even consideration of Q_B non-reducing centers and the exponential law for the exchange of a molecule $Q_B^{2-}(H^+)_2$ with a PQ molecule from the pool – similarly to the one used by Renger and Schulze (1985) – did not lead to a better result (Stirbet et al., 2001). In follow-up studies, the TEG model was adapted considering the role of Pheo (Strasser and Stirbet, 2001) and Pheo and P680 (Stirbet and Strasser, 2001). The goal of these studies was to explore and discuss alternative definitions of variable Chl *a* fluorescence and closed RCs (see Section II.F for a description of these different definitions). But for all the explored definitions the fitted values of some of the model parameters (rate constants) were far from the values found in the literature.

Although the basis of the TST model was originally formulated considering redox states of only P680, Pheo and Q_A (Vredenberg, 2000; see Section II.F), the TST model was later extended by inclusion of Q_B , Y_Z and S-states of OEC (Vredenberg et al., 2001). The extended TST model can therefore be considered as an extended TEG model. A special feature of the extended TST model is that it assumes that Y_Z^+ is a quencher of fluorescence (Vredenberg et al., 2001; Vredenberg, 2004, 2008a, b). The extended TST model

is able to simulate a FLR curve, which reaches its maximum at the position of the I step and only one step (J step) appears between the F_0 and F_M levels. But when the I–P phase is ascribed to the effect of $\Delta\Psi$ and implicitly included in the model (Vredenberg et al., 2006), a typical O–J–I–P FLR can be obtained. For more details on Vredenberg's models see Chapter 6.

4. Combined Reversible Radical Pair and Two-electron Gate Models

Particular models of PS II, consisting of a combination of the RRP and TEG models are described below and the energy/electron carriers and processes considered in each particular model are summarized in Table 5.3 to allow an easier comparison of the various approaches.

Baake and Schlöder (1992) used a TEG model in combination with a quasi-steady-state solution of the RRP model to fit FLRs measured at three low intensities of exciting light (O–I–P transient). Despite the fact that they obtained a good fit, a systematic deviation between theory and experiments was detected around the position of the I step. Therefore, Baake and Schlöder (1992) extended their model to take into account the Q_B non-reducing RC IIs or electron outflow from reduced PQ to PS I and Fd, but none of these extensions led to a better fit.

The models of Andrei Rubin and coworkers (Riznichenko et al., 1999, 2000; Lebedeva et al., 2000, 2002; Belyaeva et al., 2006; see Chapter 7 by Andrew Rubin and Galina Riznichenko in this book) differ from the other models, because more emphasis is placed on processes that are only indirectly related to electron transport. In all these studies, the pH of stroma and lumen affected the rates of Q_B^{2-} protonation and Q_B^{2-}/PQ exchange (see Section II.E) and rate of P680⁺ reduction, respectively. Further, in all the studies mentioned above, $\Delta\Psi$ affected rates of electron transport reactions directed perpendicularly to membrane surface. A general concept of description of electron transport through all carriers and protein complexes in thylakoid membrane was introduced by Riznichenko et al. (1999, 2000) and later elaborated by Lebedeva et al. (2002) (see Section III.B.5), but Lebedeva et al. (2000) and Belyaeva et al. (2006) used a PS II model

Table 5.3. Summary of energy/electron carriers and processes considered in the PS II models, consisting of a combination of the RRP and TEG models, used for simulations of the FLR. The carriers are as follows: Chl, Chl_p and Chl_c – all chlorophylls of whole, peripheral and core, respectively, LHC II; S-states – the S-states of OEC; Y_Z – tyrosine Z; P680 – a PS II electron donor (chlorophyll); Pheo – the primary PS II electron acceptor (pheophytin); Q_A – the primary quinone PS II electron acceptor; Q_B – the secondary quinone PS II electron acceptor; PQ – plastoquinone. Energy/electron carriers connected by a hyphen were considered to be in kinetic equilibrium (for more details, see the text and the particular studies mentioned).

	Baake and Schlöder (1992)	Lebedeva et al. (2000)	Belyaeva et al. (2006)	Lazár (2003)	Zhu et al. (2005)
Electron carriers in PS II model	Chl-P680, Pheo, Q _A , Q _B , PQ pool	Chl-P680, Pheo, Q _A , Q _B , PQ pool; reduced PS II model	Chl-P680, Pheo, Q _A , Q _B , PQ pool	S-states, Y _Z , Chl-P680, Pheo, Q _A , Q _B , PQ pool	S-states, Chl _p , Chl _c -P680, Pheo, Q _A , Q _B , PQ pool
PS II heterogeneity	Q _B reducing, Q _B non-reducing PS IIs	–	–	Q _B reducing, Q _B non-reducing PS IIs; PS II α , PS II β ; heterogeneity in the size of the PQ pool and rate of its reduction	Q _B reducing, Q _B non-reducing PS IIs
Fluorescence during FLR	Deactivation of ES	Deactivation of ES	Deactivation of ES	Deactivation of ES	Deactivation of ES
Other processes that were considered	Energetic connectivity	Concentration of H ⁺ in stroma and lumen are constant in time and pH of stroma and lumen affects rates of protonation of Q _B ²⁻ and Q _B ²⁻ /PQ exchange and of P680 ⁺ reduction, respectively; transmembrane electric potential is constant in time and affects rates of reactions directed perpendicularly to membrane surface		Energetic connectivity; quenching by P680 ⁺ and by the oxidized PQ pool	

alone. Models of PS II considered in all the above research, originating in the group of Andrei Rubin, consist of a combination of RRP and TEG models, further treating the PS II model in different ways.

Based on time hierarchy of energy and electron transport reactions occurring in PS II, a model consisting of 28 redox states of PS II, was reduced (see Section II.G) by Lebedeva et al. (2000) to a PS II model consisting of ten redox states. Time courses of the ten redox states of PS II were calculated first. On the basis of these ten time courses the time courses of all the 28 redox states of PS II were calculated using a set of equations “connecting” the redox states of the reduced PS II model with the redox states of the original PS II model. The model used by Lebedeva et al. (2000) considered only H⁺ ions, whose concentrations in stroma and lumen were constant in time. $\Delta\Psi$, as well as concentrations of PQ and PQH₂, were also considered constant in time. As noted by

Lebedeva et al. (2000), the constancy of $\Delta\Psi$ and of concentrations of H⁺ ions used in their model are reasons why fluorescence only monotonously increases and no typical O–I–D–P/O–J–I–P transients were simulated. We note that the model reduction used by Lebedeva et al. (2000) might as well be a reason for the unsuccessful simulation, because the model reduction procedure always causes a loss of information.

Belyaeva et al. (2006) considered the PS II model (with 28 redox states) mentioned above, with time-dependent concentrations of oxidized and reduced PQ, but they did not apply any reduction of the model. The original PS II model did not consider Y_Z (an intermediate between Mn complex and P680) and cycling of S-states and described reduction of P680⁺ by a single rate constant. Also, fluorescence quenching by P680⁺ and oxidized PQ pool was not considered. On the other hand, because the main goal of Belyaeva et al. (2006) was to simulate the fluorescence sig-

nal after the application of a strong and short laser flash (see Steffen et al., 2005), other processes were included in this model: nonradiative charge recombination between $P680^+$ and $Pheo^-$ as well as between Q_A^- and a positive charge stored on the donor side of PS II. With respect to the considered ions and $\Delta\Psi$, the same “constraints” were used by Belyaeva et al. (2006) as mentioned above for the paper by Lebedeva et al. (2000). The O–J–I–P-transients, simulated on the basis of this model (Belyaeva et al., 2006), were characterized by an O–J rise that was dominant (on the order of 90% of the total FLR) and the J and I steps occurred sooner than observed experimentally (e.g. Strasser et al., 1995; Fig. 5.1A): J was below 1 ms and I after a few ms. The dominance of the O–J rise could be due to the use of a high value for the rate constant of ES formation ($k_L = 6,000\text{ s}^{-1}$) and also to the fact that quenching by neither $P680^+$ nor PQ pool was considered. As the shape of the fluorescence transient simulated in Belyaeva et al. (2006) resembles the shape of the transients simulated in Lebedeva et al. (2000), the time independence of $\Delta\Psi$ and of amount of H^+ ions assumed in Belyaeva et al. (2006) may also be the reason for the dominant J step in the simulations presented by Belyaeva et al. (2006).

Lazár (2003) and Zhu et al. (2005) used very similar models. In both cases, a combination of TEG, RRP and Kok models was used to model the FLR measured upon high intensity of exciting light (O–J–I–P transient). In both models, the existence of quenching by $P680^+$ (Butler, 1972; Bruce et al., 1997) and PQ (Vernotte et al., 1979; Kurreck et al., 2000) was assumed. There are, however, some differences. Lazár (2003) takes the S-state dependence of the reduction of $P680^+$ by Y_Z into account, whereas Zhu et al. (2005) use a single rate constant, but they split the light harvesting antenna of PS II (LHC II) into its peripheral and core parts – a detail that is missing in the model of Lazár (2003). With respect to the model of Xinguang Zhu and his coworkers, Laisk et al. (2006) remarked that this model had ignored that the reactions within PS II electron transport should have been restricted to acceptors and donors within the same complex (i.e. first order kinetics should have been used instead of second order kinetics; see Section II.E for a discussion of this point). Lazár (2003) had also used second order kinetics for a description of some reactions

(on the PS II donor side) but in an improved web-based version of this model (Lazár, 2005) it was modified. Belyaeva et al. (2006) wrote that the description of the exchange of PQH_2 at the Q_B site in the model of Lazár (2003) is insufficient in the sense that it does not take into account changes in the stromal pH (see Section II.E). The model of Lazár (2003) has now been modified in several respects (Jablonsky and Lazar, 2008), the main modification being the introduction of the so-called intermediate S-states. This enabled the simulation of oscillations in oxygen evolution and fluorescence signal under a train of single-turnover flashes without consideration of the miss and double-hit parameters defined by Kok et al. (1970). This modification however only leads to a slightly higher and less pronounced J step in the FLR (data not shown in that study). As a consequence the shape of the FLR remains qualitatively unchanged compared to the FLRs simulated on the basis of the original model of Lazár (2003).

Both the simulations of Lazár (2003) and Zhu et al. (2005) reach a maximum after 30–40 ms. However, the interpretation of this level is quite different. Lazár (2003) concluded that it was not possible to simulate the I–P phase with his own model, whereas Zhu et al. (2005) concluded that their 40 ms point represented P. Looking at the kinetics of transients simulated by Zhu et al. (2005), two steps between the F_0 and F_M levels are observed. However, the steps occur sooner (J at about 600 μs , I at about 3 ms and P at about 40 ms) than observed experimentally (see e.g., Strasser et al., 1995; Fig. 5.1A). The incorrect time dependence may, however, also be due to an incorrect assignment of the phases. The different steps would come very close to an O–K–J–I transient. An argument that can be made against this reasoning is that according to the model of Zhu et al. (2005), all Q_A was reduced after 40 ms and therefore it was by definition P. See discussion below for this point. Laisk et al. (2006) criticized the Zhu et al. (2005) model also for ignoring the kinetic role of PS I. In the Laisk et al. (2006) model (see below) the I–P phase is assigned to the slow-down of electron transport due to the reduction of PS I acceptors. A further comparison between models of Lazár (2003) and Zhu et al. (2005) shows that there is an important difference in the behavior of $P680^+$

as a function of the initial S-state distribution. In the model of Zhu et al. (2005), P680⁺ quenching has no effect on the FLR if the starting condition consisted of mostly S₁ (S₁/S₀ = 0.8/0.2), but a huge effect was observed if there was initially mostly S₀ (S₁/S₀ = 0.1/0.9). The S₀-effect was due to the choice of k_{01} (rate constant for the S₀ to S₁ transition) of 50 s⁻¹ compared to 20,000 s⁻¹ in the model of Lazár (2003) (see Razeghifard et al., 1997 for a discussion of these values). Far-red light is a very inefficient excitation source for PS II (Pettai et al., 2005; Schansker and Strasser, 2005). As argued by Schansker and Strasser (2005) this means that leaves that were pre-illuminated with FR light for 10 s will start out with a mixture of S-states. In such samples, the O–J rise is much slower in a way that is quite similar to transients simulated by the model of Lazár (2003) for high initial concentrations of S₂ and S₃ (cf. Schansker and Strasser, 2005, and Fig. 5.6 in Lazár, 2003). If the J step of Zhu et al. (2005) would be K, then the break in the kinetics of the transient at approximately 300 μs simulated for the case that there is 100% Q_B⁻ in the starting state (trace 0:1 in Fig. 5.5d of Zhu et al., 2005) does not agree with what is observed experimentally, since experimental curves of control samples (no treatments) have quite smooth kinetics between 20 μs and 2 ms (see curves a and c in Fig. 5.1B). However, if there is no or very little Q_B⁻ initially, the break disappears and the O–J–I rise of Zhu et al. (2005; Fig. 5.5d, trace 1:0 therein) starts to look like the O–J rise observed experimentally. In this respect it may be noted that the study of Schansker and Strasser (2005) implies that in well dark-adapted leaves the initially Q_B⁻ concentration is low.

The studies discussed above show that it is difficult to simulate a complete O–J–I–P transient on the basis of models which solely describe PS II reactions. Lazár (2003) concluded that he was only able to simulate the O–J–I transient on that basis. And the same was probably true for Zhu et al. (2005). As noted above, even for the simulation of the O–J–I transient it is necessary to assume that there is quenching by P680⁺ (Butler, 1972; Bruce et al., 1997) and PQ (Vernotte et al., 1979; Kurreck et al., 2000). But as shown experimentally by Tóth et al. (2005), quenching by PQ probably does not occur in leaves, though it can be observed in thylakoid preparations of

different integrity. The inability to simulate the whole transient does not seem to be due to a lack of understanding of the kinetics of the system. As discussed above, the slow-down of the O–J rise modeled by Lazár (2003) agrees quite well with the O–J rise following a FR pre-illumination that creates similar conditions. One solution to this problem is to introduce some tricky assumptions. As noted in Section III.B.2, in several older models a fast outflow of electrons from Q_B⁻ towards a component X was introduced in order to slow down the FLR. Lazár (2003) demonstrated that by introducing slowly reducing PQ pool, and special (slow) properties of PS II_B, Q_B non-reducing centers, simulated FLR transients approach the experimentally measured transients. However, the dark-adaptation kinetics of the O–J–I–P transient (Schansker et al., 2005) provides very little support for such innovations. Another approach would be to admit that the redox state of Q_A is perhaps the dominant but not the only important determinant of the fluorescence yield and that the type of heterogeneity introduced by Delosme (1967) – whatever its underlying mechanism – provides us with the tool to simulate the whole O–J–I–P transient. Certain experimental observations (see Section II.F), as well as the above-discussed simulations, point in this same direction.

5. Complex Models

The results described in the previous sections indicate that even very complicated models describing the reactions occurring in PS II are not able to simulate the correct O–J–I–P FLR curve. It shows that consideration of only the reactions occurring in PS II is not enough, and that more reactions in the electron transport chain must be considered. Several complex models are described below and the components and processes considered in each particular model are summarized in Table 5.4 for easier comparison.

Riznichenko et al. (1999, 2000) considered PS II and the following electron transport carriers/systems: PQ, cyt b₆f, PC, PS I, and Fd in their FLR model. They also considered cyclic electron transport around PS I (from Fd to cyt b₆f), formation of the transmembrane proton gradient, Δμ_{H⁺}, and its role in ATP synthesis, passive leakage of H⁺, K⁺, and Cl⁻ ions across

Table 5.4. Summary of model components and processes considered in the complex models used for simulations of the FLR. Particular energy/electron carriers (in parentheses) used for a description of the given electron transport system are as follows: Chl – all chlorophylls of whole LHC II; OEC – oxygen evolving complex; S-states – the S-states of OEC; P680 – PS II electron donor (chlorophyll); Pheo – primary PS II electron acceptor (pheophytin); Q_A – primary quinone PS II electron acceptor; Q_B – secondary quinone PS II electron acceptor; PQ – plastoquinone; FeS_{cyt} – iron–sulfur center of cyt b₆f; f – cytochrome f; b_L – low potential form of cyt b; b_H – high potential form of cyt b; Q_o – lumenal site of cyt b₆f where plastoquinol is oxidized; Q_i – stromal site of cyt b₆f where plastoquinone is reduced; PC – plastocyanin; P700 – PS I electron donor (chlorophyll); A₀ – primary PS I electron acceptor (chlorophyll); A₁ – secondary PS I electron acceptor (phyloquinone); F_X – PS I electron acceptor (iron–sulfur center); F_A – PS I electron acceptor (iron–sulfur center); F_B – PS I electron acceptor (iron–sulfur center); FeS_{ps I} – iron–sulfur center of PS I generally; Fd – ferredoxin; NADPH – reduced nicotinamide adenine dinucleotide phosphate. Energy/electron carriers connected by a hyphen were considered to be in kinetic equilibrium (for more details, see the text and the particular studies mentioned).

	Riznichenko et al. (1999, 2000)	Lebedeva et al. (2002)	Kroon and Thoms (2006)	Laisk et al. (2006)	D. Lazár (2007, unpublished)
Model components	Reduced PS II model (Chl-P680, Pheo, Q _A , Q _B)	PS II (Chl-P680, Pheo, Q _A , Q _B)	PS II (Q _A , Q _B)	PS II (OEC-Chl-PS II)	PS II (S-states, P680, Q _A , Q _B)
PS I cyclic electron transport	PQ pool	PQ pool	PQ pool	PQ pool	PQ pool
	Cyt b ₆ f (FeS _{cyt-f} , b _L , b _H)	Cyt b ₆ f (FeS _{cyt-f} , b _L , b _H)	Cyt b ₆ f (Q _o , FeS-f, b _L , b _H , Q _i)	Cyt b/f (cyt b ₆ f-PC)	Cyt b ₆ f (f, b _L , b _H)
	PC	PC	PC	PC (PC-P700)	PC
	PS I (P700, FeS _{ps I})	PS I (P700, FeS _{ps I})	PS I (P700, A ₀ , A ₁ , F _X , F _A -F _B)	PS I (PC-P700)	PS I (P700, F _X)
	Fd, NADPH	Fd	Fd	Fd-NADPH	Fd, NADPH
Fluorescence during FLR	From Fd to cyt b ₆ /f	From Fd to cyt b ₆ f	From Fd to cyt b ₆ f	From Fd to PQ pool	From Fd to cyt b ₆ f
Other processes that were considered	Deactivation of ES	Deactivation of ES	Proportional to amount of Q _A ⁻	Proportional to amount of reduced PS II	Proportional to amount of Q _A ⁻
	Concentrations of H ⁺ , K ⁺ and Cl ⁻ in stroma and lumen are variable and pH of stroma and lumen affects rates of protonation of Q _B ²⁻ and Q _B ²⁻ /PQ exchange and of P680 ⁺ reduction, respectively; transmembrane electric potential is variable in time and affects rates of reactions directed perpendicularly to membrane surface		–	Reactions occurring in the stroma (Calvin–Benson cycle and starch synthesis) and in the cytosol (sucrose synthesis)	–

the membrane, and the dependence of rate constants on stromal and lumenal pH and on $\Delta\Psi$ (see Section III.B.4 and Chapter 7). Their original PS II model consisting of 21 redox states (those with vacant Q_B pocket were not considered, in comparison with the PS II model with 28 redox states mentioned above) was reduced in Riznichenko et al. (1999, 2000) to one consisting of only four redox states (Lebedeva et al., 2000, see Section III.B.4). In the model of Galina Riznichenko, Andrei Rubin and coworkers, it is assumed that PQ and PC in dark-adapted samples are in the oxidized state. In our opinion, these assumptions are incorrect. In general, PC is considered to be reduced after dark adaptation (see e.g. Oja et al., 2003; Schansker et al., 2003) and the O–I–D–P transients are characteristic of samples with an initially partially reduced PQ pool (e.g. Kautsky et al., 1960). Riznichenko et al. (1999) assumed that the O–I rise is due to a $\Delta\Psi$ -induced slow-down of several electron transport reactions (appearance of the I step corresponds with the maximum rate of $\Delta\Psi$ increase) and that the subsequent I–D decline is due to a decline in the rate of $\Delta\Psi$ increase due to K^+ and Cl^- fluxes. The following D–P FLR is caused by electron back-pressure caused by the accumulation of electrons on the PS II acceptor side.

Lebedeva et al. (2002) considered PS II and the following electron transport reactions, as well as all other properties of the model of Riznichenko et al. (1999, 2000), except that all the 28 redox states (without any reduction) were used by Lebedeva et al. (2002). A typical feature of the transient modeled by Lebedeva et al. (2002) is the slow rise of the I–P phase. In leaves, the I–P rise is much steeper, because ferredoxin-NADP⁺-reductase (FNR) is inactive in darkness, transiently blocking electron transport beyond Fd (Sato and Katoh, 1980; Carrillo and Vallejos, 1987; Foyer et al., 1992). If this had been taken into account, a much better correspondence between model and experiment could have been obtained (see next section). By ignoring inactive FNR, the Lebedeva et al. (2002) model had much more electron transport and, therefore, a much greater release of protons into the lumen during the I–P phase than would occur under *in vivo* conditions. However, this effect may be canceled in part if the activation of ATP synthase was slower than instantaneous as assumed in that study. A

curiosity of the form of the simulated transient is that it looks as if it was pre-illuminated with FR (cf. Schansker and Strasser, 2005). Thus, even this complex model was not able to simulate the positions and heights of the particular steps of the experimental O–J–I–P FLR.

A model including PS II, PQ, cyt b_6f , PC, PS I, Fd and cyclic electron flow, but not the processes on the donor side of PS II, was used by Kroon and Thoms (2006) for phytoplankton photosynthesis. It used second order instead of first order kinetics (see Section II.E) for some reactions occurring in PS I. For simulation of the FLR, the stoichiometry between the components of the photosynthetic electron transport chain was considered to be $C_{PS\ II}:C_{b_6f}:C_{PS\ I}:C_{PQ}:C_{PC}:C_{Fd} = 1:1:1:4:1:1$. We note that in higher plants there is more than one molecule of PC and Fd per PS I (Terashima and Inoue, 1985; Haehnel et al., 1990; Klughammer and Schreiber, 1991; Holtgreffe et al., 2003) and this may also be the case for phytoplankton. Kroon and Thoms (2006) simulated the FLR measured using the FRR technique (see Section I.B). Quite a few differences were observed comparing the simulations with the experimental transients of Kolber et al. (1998). A problem with the transients of Kolber et al. (1998) is that for the highest excitation pressure (4,000 quanta $RC\ II^{-1}\ s^{-1}$) incomplete O–J–I–P transients were obtained (only O–J–I). Assuming that the simulated transients were complete, they had either a very broad J-step and no I–P phase or no J–I rise and an I–P phase that rose too fast. Taking into account that the number of electron acceptors that Kroon and Thoms (2006) assumed to exist beyond the cyt b_6f complex is too low, a fast I–P rise may not be an unexpected result. The re-oxidation of the electron transport chain following P (decline of the fluorescence intensity) for the lower light intensities is also far too limited compared to the curves measured by Kolber et al. (1998). The calculated cyclic electron transport rates around PS I as a function of the light intensity seem to underestimate the influence of the strong reduction of the available substrate (oxidized PQ) at the higher light intensities.

The most complex model (as for the number of considered reactions) employed so far for the FLR was used by Laisk et al. (2006; see also Section IV.A). Their model consists not only of

the light reactions occurring in thylakoid membranes but also of reactions occurring in the stroma and the cytosol (see Chapter 13 by Agu Laisk, Hillar Eichelmann and Vello Oja in this book). Laisk et al. (2006) used a rather simplified description of the light reactions, nevertheless, cyclic electron transport around PS I (from NADPH to the PQ pool) was considered. In the model, many electron-transport components were considered to be in a kinetic equilibrium (see Table 5.4) and redox state of PS II was described only by one state variable, which could be reduced or oxidized. On the other hand, Calvin–Benson cycle and starch synthesis occurring in the stroma, as well as sucrose synthesis occurring in the cytosol, were described in detail, including the activation of several enzymes that are under the control of the thioredoxin system. Reducing the acceptor side of PS II to a single state variable possibly explains why Laisk et al. (2006) were able to simulate the whole electron transport chain with their model. However, due to the fact that they ignored the presence of inactive FNR, the I–P rise is much slower than in comparable experimental transients. Another discrepancy between their model and the experimental transient is that the I step in the model is reached after almost 200 ms, whereas in experimental transients it is almost independent of the intensity of excitation light (cf. e.g. Tomek et al., 2001; Schansker et al., 2005). Lowering the light intensity lowers the relative amplitude of the I step but it is still observed around 30 ms. On the other hand, as also noted by Laisk et al. (2006), the rate of CO₂ uptake increases much faster in the model than in the experimental measurements. As will be discussed in the next section this may also be related to the absence of inactive FNR in the model of Laisk et al. (2006). With respect to the I₈₂₀ signal (the authors measured it at 810 nm), Laisk et al. (2006) model the FR-induced oxidation of the electron transport chain, and the dark recovery kinetics of the I₈₂₀ signal of samples darkened after reaching steady-state conditions. However, the I₈₂₀ kinetics paralleling the FLR was not modeled. As noted above there are major discrepancies between model and experiment and it remains to be seen if e.g. the introduction of inactive FNR in the model will produce a better simulation.

To test whether reactions occurring in and around PS I affect the FLR as suggested before (Kautsky et al., 1960; Munday and Govindjee, 1969; Satoh and Katoh, 1981; Hansen et al., 1991; Schansker et al., 2003, 2005), D. Lazár (2007, unpublished) used a model which consisted of PS II (considering S-states, P680, Q_A, and Q_B), PQ pool, cyt b₆f, PC, PS I (considering P700 and F_X), Fd and FNR, where Fd dependent cyclic electron transport around PS I was also considered. The goal was to simulate the FLR and light-induced changes in the I₈₂₀ signal paralleling the FLR. Results of simulations of the FLR and I₈₂₀ signal, as well as time courses of state variables responsible for these quantities, are shown in Fig. 5.6A. Although the

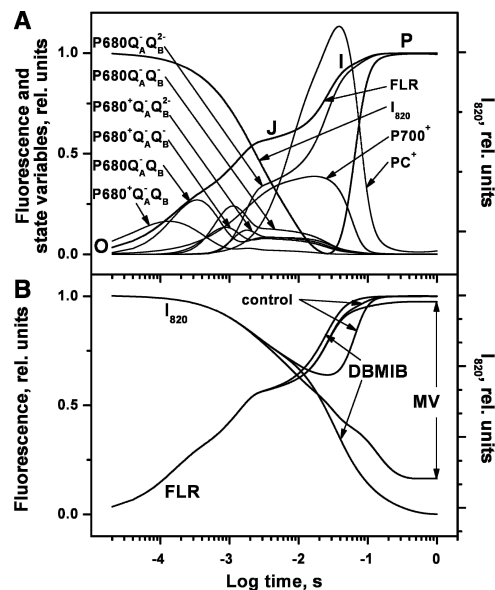


Fig. 5.6. Simulations of the Chl *a* FLR and changes in I₈₂₀ signal as well as time courses of model state variables responsible for these quantities (Panel A) and changes in the FLR and I₈₂₀ caused by DBMIB and MV (Panel B) based on the model of homogeneous PS II of D. Lazár (2007, unpublished). The FLR curve was calculated according to Eq. (5.5) with $p = 0.55$ and using time courses of the closed RC II (with Q_A⁻; time courses shown in the figure) and the I₈₂₀ curve was calculated according to the Lambert–Beer law assuming a contribution of both PC⁺ and P700⁺ (time courses shown in the figure) to the overall absorbance ($d = 0.01$ cm, $c_{RC\ II} = 5.24 \times 10^{-8}$ M, $\epsilon_{PC^+ (P700^+)} = 1,600$ (8,000) M⁻¹ cm⁻¹). All curves are shown on a logarithmic time-axis. The effect of DBMIB was modeled as prevention of the oxidation and reduction of reduced and oxidized PQ, respectively, at the luminal side of cyt b₆/f. The effect of MV was modeled allowing electron flow from reduced F_X to MV.

modeled FLR better simulates the one measured with thylakoid membranes than that with leaves (Fig. 5.1A), the model was also able to qualitatively simulate changes in the FLR and I_{820} signal (data not shown) as measured with different intensities of exciting light (Ilík et al., 2006) as well as that caused by the application of DBMIB and 1, 1'-dimethyl-4, 4'-bipyridinium-dichloride (methylviologen, MV) (c.f. Fig. 5.6B and Schansker et al., 2005).

The results described in this section show that even if very complex models are used for simulations of the FLRs, it is still difficult to get a perfect match with experimentally obtained transients. We also note that the description of PS II gets worse as the models become more complex (e.g. by introducing a single state variable to describe the acceptor side of PS II, which can be oxidized or reduced as Laisk et al. (2006) did in their model; see Table 5.4). This can also be the reason why some of these complex models were not very successful in simulating the form of the FLR.

IV. Modeling the Whole Fluorescence Induction

Few models simulate the FLD after the P step. Therefore, a discussion of processes which could be important for simulation of the whole FLI is provided in this section together with a description of models simulating fluorescence oscillations which sometimes occur in the FLI.

A. Experimental Observations and Models

As mentioned in Section I.2, the FLI consists both of a fast FLR and a subsequent slower FLD. So far, only modeling of the FLR was discussed. In the older literature a considerable effort was devoted to the characterization of the FLD (reviewed by Papageorgiou, 1975; Briantais et al., 1986; Govindjee and Satoh, 1986). However, a full experimental description of processes involved was never achieved and the studies of the processes occurring on this time scale took a completely different direction with the introduction of the saturating pulse method (reviewed by Roháček 2002; Schreiber, 2004;

Baker, 2008). On the other hand there exist very successful models of the Calvin–Benson cycle reactions (Farquhar et al., 1980; Von Caemmerer, 2000; Bernacchi et al., 2001; Ethier and Livingston, 2004; Chapter 9 by Susanne von Caemmerer, Graham D. Farquhar and Joseph Berry and Chapter 10 by Carl J. Bernacchi, David Rosenthal, Carlos Pimentel, Stephen P. Long and Graham D. Farquhar in this book).

For a model of the FLD it is very important to define the starting point, in other words, what is the state of the photosynthetic apparatus at the P step. Kautsky et al. (1960) were probably the first to describe a transient block of electron transport in dark-adapted samples. This observation was confirmed by Munday and Govindjee (1969) and about 10 years later Satoh and Katoh (1980) and Satoh (1981, 1982) localized this block between Fd and NADP^+ . The properties of FNR were studied in more details by N. Carrillo and coworkers (reviewed by Carrillo and Vallejos, 1987). The presence of this transient block of electron transport also plays an important role in the studies of the O–J–I–P-transient of Schansker et al. (2005, 2006). Despite extensive experimental support for the presence of inactive FNR in dark-adapted leaves and algae, it is often neglected. Both the model studies of Lebedeva et al. (2002) and Laisk et al. (2006) (see Section III.B.5 and Chapter 13) assume that there is a free outflow of electrons at the acceptor side of PS I. This has of course a quite drastic effect on the validity of the obtained simulations. In their models many more electrons flow through the electron transport chain and many more protons are transferred from stroma to lumen by the time the P step is reached. For inactive FNR, the number of electrons that have to flow through the electron transport chain (essentially to reduce $\text{Q}_\text{A} + \text{PQ} + \text{Fd}$) to reach P step can be estimated and that would also allow an estimate of the number of protons that are transferred to the lumen during this time interval. However, to determine the built-up of a proton gradient, the activation time of ATP synthase also has to be known. The activation kinetics of ATP synthase is quite complex (Groth and Strotmann, 1999; He et al., 2000). An electrochemical proton gradient is needed to activate ATP synthase, but the necessary gradient is smaller once a sulfur bridge in the protein is reduced by thioredoxin. Therefore, we raise the

question: how realistic is the quasi-instantaneous activation assumed by Lebedeva et al. (2002) and Laisk et al. (2006)?

There is much more heterogeneity in the kinetics of the FLD between species (see Papageorgiou et al., 2007) and an important factor for this is the time needed to activate FNR. FNR is activated in a few hundreds of milliseconds in *Trebouxia* possessing lichens (Ilík et al., 2006), *Ginkgo biloba* (G. Schansker, 2005, 2008, unpublished) and many conifers (Schansker et al., 2008). In angiosperms, however, the activation of FNR is quite slow. The secondary fluorescence kinetics observed in lichens, *Ginkgo biloba* and conifers is completely missing in angiosperms. This phenomenon may explain the differences in complexity of the various measured FLI transients (cf. Papageorgiou and Govindjee, 1968 with Yamagishi et al., 1978). In an angiosperm like pea, swings in the fluorescence intensity beyond the P step can be created by a partial activation of FNR induced by a short pre-illumination (G. Schansker, 2002, unpublished). Accompanying swings in the I_{820} signal seem to point to additional transient “traffic jams” in response to reduction of the NADP^+ and perhaps thioredoxin pools before the Calvin–Benson cycle is activated. From a simulation point of view the challenge will be to get good experimental data on the various processes involved.

Limitation on the acceptor side of PS I (activation state of FNR). As noted above, the activation of FNR in angiosperms is rather slow. Foyer et al. (1992) observed for pea plants that the $\text{NADPH}/\text{NADP}^+$ -ratio did not change much during the first 10 s of illumination ($750 \mu\text{mol photons m}^{-2} \text{s}^{-1}$) indicating that FNR was essentially inactive during this period of time. This phenomenon is also observed in the fluorescence and I_{820} measurements where both signals remain high during the first few seconds of illumination. For a simulation, this means that there is nearly no electron transport during this time interval. This is something that none of the existing models take into account. Schansker et al. (2006) demonstrated that the inactivation of FNR in pea leaves is observed as the recovery of the I–P phase. Probing pea leaves 200 s after pre-illumination by red light ($350 \mu\text{mol photons m}^{-2} \text{s}^{-1}$), it was observed that pre-illumination of at least 200 s are needed to obtain a maximum suppression of the

I–P phase and therefore a maximum activation of FNR (Schansker et al., 2008).

Transient reduction of the pool of NADP^+ (and thioredoxin). As noted above, Foyer et al. (1992) observed that the $\text{NADPH}/\text{NADP}^+$ -ratio during a dark-to-light transition did not change during the first 10 s. Subsequently, NADPH -levels were high between approximately 20 and 100 s of illumination. A limited availability of NADP as substrate for FNR will prolong the limitation on the outflow of electrons on the acceptor side of PS I and thereby electron flow through the photosynthetic electron transport chain. Partially pre-activating FNR by short pre-illuminations allows the visualization of small swings in the fluorescence signal and quite large swings in the I_{820} signal (G. Schansker, 2002, unpublished) probably related to changes in substrate availability. The absence of such swings in well dark-adapted angiosperms should simplify the task of the modeler considerably.

Cyclic electron transport around PS I. Under certain conditions, a swing in the fluorescence intensity beyond the P step can be observed that is not accompanied by a change in the I_{820} signal. An example of this can be found in Ilík et al. (2006) for a *Trebouxia*-possessing lichen and also in *Pinus halepensis* (Schansker et al., 2008). Ilík et al. (2006) did not observe an effect of the addition of inhibitors of cyclic electron transport around PS I on this fluorescence property. However, cyclic electron transport around PS I remains a good explanation for this phenomenon in the absence of more conclusive experimental evidence. For cyclic electron transport around PS I to occur a (partial) re-oxidation of the PQ pool is necessary and this condition is only met following a considerable activation of FNR. This means again that this process may be of limited relevance to the kinetic changes in the FLD of angiosperm plants.

Energy dependent non-photochemical fluorescence quenching (qE). In Fig. 5.7 FLR-transients are shown that have been measured 10 s after a 10–600 s long pre-illumination by red light ($350 \mu\text{mol photons m}^{-2} \text{s}^{-1}$). The high values of J steps demonstrate that the PQ pool was highly reduced under these measuring conditions and represent therefore a good alternative measure of the maximum fluorescence intensity. The figure also shows small swings in the transients in the

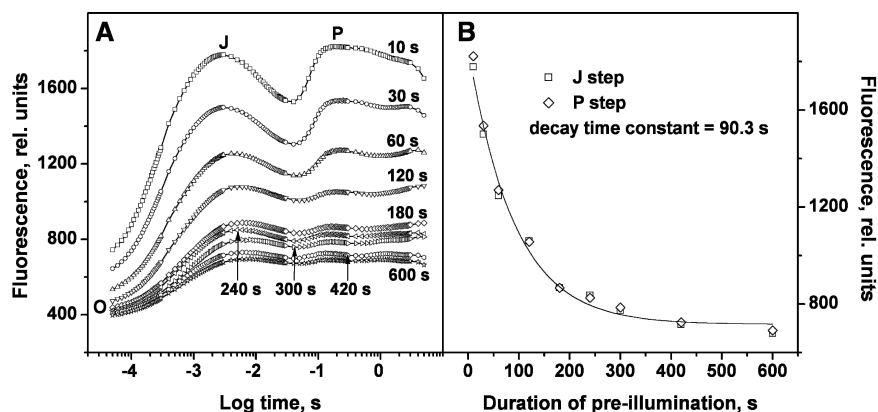


Fig. 5.7. Measured Chl *a* FLIs (Panel A) and related changes of fluorescence at the J (the maximum between 2 and 10 ms) and P steps (the maximum between 100 and 400 ms) (Panel B). Chl *a* FLI was measured by PEA Senior fluorometer upon illumination with $1,800 \mu\text{mol photons m}^{-2} \text{s}^{-1}$ of red light with pea leaves 10 s after 10–600 s pre-illumination by red light ($350 \mu\text{mol photons m}^{-2} \text{s}^{-1}$). Curves in panel A are shown on a logarithmic time-axis, pre-illumination times are indicated.

presence of a more or less activated FNR. In panel B of Fig. 5.7 fluorescence at the J and P steps are plotted as a function of the length of the pre-illumination. Both parameters change in parallel indicating that this change is dominated by changes in qE. The data can be described quite well by a single exponential with a time constant of approximately 90 s. During the first 10 s of illumination, no effect on the F_P -value was observed, which agrees with the slow activation of FNR noted above, but raises questions with respect to the role of the luminal pH during this part of the FLI. The development of qE is closely related to the luminal pH, which in turn depends both on the activity of ATP synthase and the electron transport activity. A description of the development of the qE will therefore also take care of the pH-related changes in the lumen. A considerably more sophisticated approach to the development of qE during the P to S decline would be to study changes in the fluorescence lifetime. An example of such a study on the alga *Chlamydomonas reinhardtii* can be found in Holub et al. (2007). The fact that the development of qE can be described by a single exponential indicates that it may be relatively simple to simulate this parameter. Using mutants, whose development of qE is slowed down (e.g. the one described by Govindjee and Spilotro, 2002), it is possible to obtain modified FLDs.

As noted above, qE has a major impact on the fluorescence emission of closed RCs. It is less clear if the qE reduces the excitation pressure of open RCs and if this leads to a qE-dependent reduction of linear electron transport. Schansker et al. (2006) observed that in pea leaves even at relatively high intensities of excitation light ($400\text{--}500 \mu\text{mol photons m}^{-2} \text{s}^{-1}$) the PQ pool remains quite oxidized. Further, G. Schansker (2006, unpublished) observed that in the STN7 mutant of *Arabidopsis thaliana*, the absence of the kinase responsible for the phosphorylation of LHC II only causes a slightly more reduced PQ pool at lower intensities of excitation light (about $70 \mu\text{mol photons m}^{-2} \text{s}^{-1}$) but not at higher intensities ($300\text{--}400 \mu\text{mol photons m}^{-2} \text{s}^{-1}$). It is another indication that qE may reduce the electron transport rate. However, this is a point that deserves further experimentation.

State I to state II transitions. Phosphorylation of LHC II may affect the fluorescence transient in several ways. A reduction of the antenna size reduces not only the excitation cross-section, it also reduces the maximum fluorescence intensity. However, the effect of state transitions on the electron transport rate is not so well defined. It is thought that, in higher plants, only a part of the RC IIs is affected by state transitions (Vallon et al., 1991; Bellaafiore et al., 2005) – possibly mainly those near the margins of the grana stacks. In these regions state transitions may have, as an

additional effect, that they reduce the extent of stacking (Vallon et al., 1991; Trissl and Wilhelm, 1993; Pesaresi et al., 2002). This may increase the extent of spillover between PS II and PS I antennae. Further, it has been shown that the kinase that phosphorylates LHC II is inhibited at high light (Rintamäki et al., 1997). At the same time it is possible that qE dominates anyway at higher light intensities. As noted above, in the kinaseless mutant of *Arabidopsis thaliana* an effect of this mutation on the redox state of the PQ pool is only observed at lower light intensities. All these complications could mean that for a given plant species, the light intensity dependence of state transitions has to be determined to determine the influence of this process on the FLD.

An additional problem in this respect is due to the absence of clear fluorescence parameters that can help to define the development of a state transition during photosynthetic induction. Schreiber et al. (1995) have suggested for *Chlamydomonas reinhardtii* and *Synechocystis* PCC 6803 that a reduction of the J–I amplitude could be an indicator for state transitions. However, proof for this suggestion in higher plants is at the moment missing. Nevertheless, a model which includes an effect of the state transitions was constructed and used for simulation of the FLI by Gordienko and Karavayev (2003). These authors calculated response curves for P700 on switching between FR and white light. Following the switch the calculated curves pass through a minimum before reaching a steady-state level. The steady-state level in the model of Gordienko and Karavaev (2003) depends also on the parameter related to the LHC II kinase, which leads to a redistribution of excitation light between PS II and PS I. In addition, the calculations by the authors show that, in their model, changes in the phosphorylation level of LHC II (leading to changes in the light distribution between both photosystems) have a strong effect on the fluorescence kinetics beyond the P level.

As noted in Section II.B, it makes sense for the simulation of the O–J–I–P FLR to work with transients induced by high light intensities. However, for the kinetics beyond the P step – that is dominated by biochemical processes – such an approach makes less sense. As discussed above, the P-level is a well-defined situation due to the presence of inactive FNR. In this respect,

a light intensity that is just saturating for the P step would probably create a very similar starting state for the FLD compared to the one obtained with high light intensities. Given the limited kinetic information that can be derived from an angiosperm FLD, an alternative approach would be to simulate probe pulses that can be given at various times following a pre-illumination representing a partial to full fluorescence transient (Fig. 5.7; Schansker et al., 2008).

B. Oscillations in the Fluorescence Intensity

As mentioned in Section I.B, upon certain conditions complex damped oscillations can be induced and measured in the FLD kinetics (Walker et al., 1983; Sivak and Walker, 1985). The oscillations can be detected not only in the fluorescence signal, but also in other parameters related to photosynthetic activity. Several hypotheses have been put forward to explain these oscillations (Lazár et al., 2005b and references therein). The oscillations in the FLD were theoretically simulated based on models, which described electron transport within thylakoid membrane, leading to the formation of ATP and its subsequent use in the Calvin–Benson cycle (Karavaev and Kukushkin, 1993; Khuznetsova and Kukushkin, 1999). A similar model, but then extended by cyclic electron transport around PS II, was published by Kukushkin (1997). Rovers and Giersch (1995) used a very simple model to describe the oscillations, describing the formation of ATP coupled to the formation of NADPH, which are both subsequently used in the Calvin–Benson cycle. The Calvin–Benson cycle in this model was described by the action of its two kinases (3-phosphoglycerate kinase and ribulose-5-phosphate kinase). A slightly extended version of the previous model was used by Lazár et al. (2005b). In this model the Calvin–Benson cycle was described in more detail by inclusion of the activation of ribulose-1,5-bisphosphate carboxylase/oxygenase by its activase.

The experimental conditions by which the oscillations are usually induced and measured (a re-illumination of the sample or a perturbation of the steady state by a change in the gas phase) differ from standard measurements of the whole FLI. Even so, the interpretation and modeling of

the oscillations performed so far might be helpful in understanding and modeling of the whole FLI.

V. Conclusions and Future Perspectives

Despite the extensive work that has been done in the field of mathematical modeling of the FLR it has, so far, only been possible to obtain a qualitative simulation. In those cases where a quantitative agreement was achieved (by means of fitting of model parameters), the parameters had values different from the ones known from the literature or the model structure was incomplete (e.g. some PS II components and/or reactions were missing). Nevertheless, even a qualitative agreement between theory and experiment is a big step forward for a system as complex as the FLR.

How to proceed from here? We expect future progress from several approaches. In the first place, it is possible to work with a larger number of well-defined FLRs. So far, most work has concentrated on two situations: uninhibited, dark-adapted samples and DCMU-treated samples. An alternative possibility would be to simulate DBMIB-treated samples. As shown by Schansker et al. (2005), DBMIB has two major effects on the FLR: it blocks electron flow at the cyt b_6f complex, reducing the transient to two steps, and DBMIB molecules affect electron flow at the Q_B site. The J-level goes up as the DBMIB concentration in the thylakoid membrane increases. Another possibility would be to work with samples that are partially anaerobic. A recent study by Tóth et al. (2007b) has shown that such FLRs can be well understood and described assuming that anaerobiosis mainly affects the redox state of the PQ pool (Kautsky et al., 1960; Schreiber and Vidaver, 1974). For models including a description of the FLD, as noted above, a better definition of the P-level is needed. None of the few existing models (see Section IV.A) have taken all the experimental knowledge of the state of the photosynthetic system at P into account. As a consequence, they have overestimated both electron flow and transfer of protons into the lumen during the first second of induction.

Progress may also be expected from the further increase of our knowledge of the physiology of the chloroplast. As shown above, several heterogeneities (PS II α/β , PQ pool size, light gradient)

have been explored in simulations. However, more quantitative data, especially for the *in vivo* situation, on these processes, together with the effects of the compartmentalization of the various forms of the electron transport components inside the chloroplast on activity would help to restrain future models. From a modeling point of view, the application of a control analysis (Fell, 1992; Visser and Heijnen, 2002) may be useful, allowing a more precise quantification of the extent by which a reaction or mechanism affects or drives a given property of the FLR/FLI (e.g. Lazár et al., 2005a, b).

A last point would be conceptual. In the majority of cases modeling is based on the principle that the redox state of Q_A is the major determinant of variable fluorescence. As noted above, there are several experimental observations that are at odds with this concept. At the same time, such a model makes it also difficult to take PS I reactions into account, since the impact of the light-induced changes in the redox state of PS I on Q_A -redox state are much smaller than the amplitude of such changes observed experimentally. Writing these words 40 years after the introduction of the photochemical and thermal phases by Delosme (1967) it is, perhaps, time to explore different versions of models considering two determinants of the fluorescence yield more seriously.

Acknowledgments

This work was financially supported by the Ministry of Education of the Czech Republic by a grant number MSM 6198959215 (DL) and by the Swiss National Foundation by a grant number 200021-116765/1 (GS). The authors thank N.E. Belyaeva, X.-G. Zhu and S. Thoms for suggestions related to the description of their models and P. Pospíšil and S. Boisvert for providing experimental data for Fig. 5.1.

References

- Antal T and Rubin A (2008) In vivo analysis of chlorophyll *a* fluorescence induction. *Photosynth Res* 96: 217–226
- Baake E and Schlöder JP (1992) Modelling the fast fluorescence rise of photosynthesis. *Bull Math Biol* 54: 999–1021
- Baker NR (2008) Chlorophyll fluorescence: a probe of photosynthesis in vivo. *Annu Rev Plant Biol* 59: 89–113

- Beauchemin R, Gauthier A, Harnois J, Boisvert S, Govindachary S and Carpentier R (2007) Spermine and spermidine inhibition of photosystem II: Disassembly of the oxygen evolving complex and consequent perturbation in electron donation from TyrZ to P680⁺ and the quinone acceptors Q_A⁻ to Q_B. *Biochim Biophys Acta* 1767: 905–912
- Bellafiore S, Barneche F, Peltier G and Rochaix J-D (2005) State transitions and light adaptation require chloroplast thylakoid protein kinase STN7. *Nature* 433: 892–895
- Belyaeva NE, Pashchenko VZ, Renger G, Riznichenko GY and Rubin AB (2006) Application of a photosystem II model for analysis of fluorescence induction curves in the 100 ns to 10 s time domain after excitation with a saturating light pulse. *Biofizika* 51: 860–872
- Bernacchi CJ, Singas EL, Pimentel C, Portis AR and Long S (2001) Improved temperature response functions for models of Rubisco-limited photosynthesis. *Plant Cell Environ* 24: 253–259
- Black MT, Brearley TH and Horton P (1986) Heterogeneity in chloroplast photosystem II. *Photosynth Res* 8: 193–207
- Boisvert S, Joly D and Carpentier R (2006) Quantitative analysis of the experimental O-J-I-P chlorophyll fluorescence induction kinetics. Apparent activation energy and origin of each kinetic step. *FEBS J* 273: 4770–4777
- Bouges-Bocquet B (1973) Electron transfer between the two photosystems in spinach chloroplasts. *Biochim Biophys Acta* 314: 250–256
- Breton J (1983) The emission of chlorophyll in vivo. Antenna fluorescence or ultrafast luminescence from reaction center pigments. *FEBS* 159: 1–5
- Briantais J-M, Verotte C, Krause GH and Weis E (1986) Chlorophyll *a* fluorescence of higher plants: chloroplasts and leaves. In: Govindjee, Ames J and Fork DC (eds) *Light Emission by Plants and Bacteria*, pp. 539–583. Academic, New York
- Bruce D, Samson G and Carpenter C (1997) The origins of nonphotochemical quenching of chlorophyll fluorescence in photosynthesis. Direct quenching by P680⁺ in photosystem II enriched membranes at low pH. *Biochemistry* 36: 749–755
- Bulychev AA and Niyazova MM (1989) Modelling of potential-depending changes of chlorophyll fluorescence in the photosystem 2. *Biofizika* 34: 63–67 (in Russian)
- Bulychev AA, Niyazova MM and Turovsky VB (1986) Electro-induced changes of chlorophyll fluorescence in individual intact chloroplasts. *Biochim Biophys Acta* 850: 218–225
- Butler WL (1972) On the primary nature of fluorescence yield changes associated with photosynthesis. *Proc Natl Acad Sci USA* 69: 3420–3422
- Butler WL and Kitajama M (1974) A tripartite model for chloroplast fluorescence. In: Avron M (ed) *Proceedings of the Third International Congress on Photosynthesis*, pp. 13–24. Elsevier, Amsterdam
- Carrillo N and Vallejos RH (1987) Ferredoxin-NADP + oxidoreductase. In: Barber J (ed), *The Light Reactions*, pp. 527–560. Elsevier, Amsterdam
- Cheniae GM and Martin IF (1970) Sites of function of manganese within photosystem II. Roles in O₂ evolution and system II. *Biochim Biophys Acta* 197: 219–239
- Christophorov LN, Holzwarth AR, Kharkyanen VN and Van Mourik F (2000) Structure-function self-organization in nonequilibrium macromolecular systems. *Chem Phys* 256: 45–60
- Crofts AR and Wraight CA (1983) The electrochemical domain of photosynthesis. *Biochim Biophys Acta* 726: 149–185
- Cruz JA, Sacksteder CA, Kanazawa A and Kamer DM (2001) Contribution of electric field ($\Delta\psi$) to steady-state transthylakoid proton motive force (*pmf*) *in vitro* and *in vivo*. Control of *pmf* parsing into $\Delta\psi$ and ΔpH by ionic strength. *Biochemistry* 40: 1226–1237
- Dau H (1994) Molecular mechanism and quantitative models of variable photosystem II fluorescence. *Photochem Photobiol* 60: 1–23
- Dau H and Sauer K (1991) Electric field effect on chlorophyll fluorescence and its relation to photosystem II charge separation reactions studied by a salt-jump technique. *Biochim Biophys Acta* 1098: 49–60
- Dau H and Sauer K (1992) Electric field effect on the picosecond fluorescence of photosystem II and its relation to the energetics and kinetics of primary charge separation. *Biochim Biophys Acta* 1102: 91–106
- Delosme R (1967) Étude de l'induction de fluorescence des algues vertes et des chloroplastes au début d'une illumination intense. *Biochim Biophys Acta* 143: 108–128 (in French)
- Duysens LNM and Sweers HE (1963) Mechanism of the two photochemical reactions in algae as studied by means of fluorescence. In: Japanese Society of Plant Physiologists (ed) *Studies on Microalgae and Photosynthetic Bacteria*, pp. 353–372. University of Tokyo Press, Tokyo
- Enami I, Kitamura M, Tomo T, Isokawa Y, Ohta H and Katoh S (1994) Is the primary cause of thermal inactivation of oxygen evolution in spinach PS II membranes release of the extrinsic 33 kDa protein or of Mn? *Biochim Biophys Acta* 1186: 52–58
- Ethier GJ and Livingston NJ (2004) On the need to incorporate sensitivity to CO₂ transfer conductance into the Farquhar-Von Caemmerer-Berry leaf photosynthesis model. *Plant Cell Environ* 27: 137–153
- Falkowski PG, Fujita Y, Ley A and Mauzerall D (1986) Evidence for cyclic electron flow around photosystem II in *Chlorella pyrenoidosa*. *Plant Physiol* 81: 310–312
- Falkowski PG, Kolber Z and Mauzerall D (1994) A comment on the call to throw away your fluorescence induction apparatus. *Biophys J* 66: 923–926

- Farquhar GD, Von Caemmerer S and Berry JA (1980) A biochemical model of photosynthetic CO₂ assimilation in leaves of C₃ species. *Planta* 149: 78–90
- Fell DA (1992) Metabolic control analysis: A survey of its theoretical and experimental development. *Biochem J* 286: 313–330
- Ferreira KN, Iverson TM, Maghlaoui K, Barber J and Iwata S (2004) Architecture of the photosynthetic oxygen-evolving center. *Science* 303: 1831–1838
- Forbush B and Kok B (1968) Reaction between primary and secondary electron acceptors of photosystem II of photosynthesis. *Biochim Biophys Acta* 162: 243–253
- Förster LS and Livingston R (1952) The absolute quantum yields of the fluorescence of chlorophyll in solutions. *J Chem Phys* 20: 1315–1320
- Foyer CH, Lelandais M and Harbinson J (1992) Control of the quantum efficiencies of photosystems I and II, electron flow, and enzyme activation following dark-to-light transitions in pea leaves. *Plant Physiol* 99: 979–986
- France LL, Geacintov NE, Breton J and Valkunas L. (1992) The dependence of the degrees of sigmoidicities of fluorescence induction curves in spinach-chloroplasts on the duration of actinic pulses in pump-probe experiments. *Biochim Biophys Acta* 1101: 105–119
- Franck F, Juneau P and Popovic R (2002) Resolution of the photosystem I and photosystem II contributions to chlorophyll fluorescence of intact leaves at room temperature. *Biochim Biophys Acta* 1556: 239–246
- Genty B, Wonders J and Baker NR (1990) Non-photochemical quenching of F₀ in leaves is emission wavelength dependent: Consequences for quenching analysis and its interpretation. *Photosynth Res* 26: 133–139
- Gilmore AM, Hazlett TL and Govindjee (1995) Xanthophyll cycle-dependent quenching of photosystem II chlorophyll *a* fluorescence: Formation of a quenching complex with a short fluorescence lifetime. *Proc Natl Acad Sci USA* 92: 2273–2277
- Gilmore AM, Itoh S and Govindjee (2000) Global spectral-kinetic analysis of room temperature chlorophyll *a* fluorescence from light-harvesting antenna mutants of barley. *Phil Trans R Soc Lond B* 355: 1371–1384
- Goltsev V and Yordanov I (1997) Mathematical model of prompt and delayed chlorophyll fluorescence induction kinetics. *Photosynthetica* 33: 571–586
- Gordienko TV and Karavayev VA (2003) Theoretical analysis of inductive effects in higher plant photosynthesis. *Biol Bull* 30: 34–39
- Goushcha AO, Kharkyanen VN, Scott GW and Holzwarth AR (2000) Self-regulation phenomena in bacterial reaction centers. I. General theory. *Biophys J* 79: 1237–1252
- Govindjee (1990) Photosystem II heterogeneity: Electron acceptor side. *Photosynth Res* 25: 151–160
- Govindjee (1995) Sixty-three years since Kautsky: Chlorophyll *a* fluorescence. *Aust J Plant Physiol* 22: 131–160
- Govindjee and Satoh K (1986) Fluorescence properties of chlorophyll b- and chlorophyll c-containing algae. In: Govindjee, Ames J and Fork DC (eds) *Light Emission by Plants and Bacteria*, pp. 497–537. Academic, New York
- Govindjee and Spillito P (2002) An *Arabidopsis thaliana* mutant, altered in the γ -subunit of ATP synthase, has a different pattern of intensity-dependent changes in non-photochemical quenching and kinetics of the *P*-to-*S* fluorescence decay. *Funct Plant Biol* 29: 425–434
- Govindjee, Ames J and Fork DC (eds) (1986) *Light Emission by Plants and Bacteria*. Academic, New York
- Graan T and Ort DR (1983) Initial events in the regulation of electron transfer in chloroplasts. The role of the membrane potential. *J Biol Chem* 258: 2831–2836
- Groot ML, Pawlowicz NP, Van Wilderen LJGW, Breton J, Van Stokkum IHM and Van Grondelle R (2005) Initial electron donor and acceptor in isolated photosystem II reaction centers identified with femtosecond mid-IR spectroscopy. *Proc Natl Acad Sci USA* 102: 13087–13092
- Groth G and Strotmann H (1999) New results about structure, function and regulation of the chloroplast ATP synthase (CF₀CF₁). *Physiol Plant* 106: 142–148
- Guisé B, Srivastava A and Strasser RJ (1995) The polyphasic rise of the chlorophyll *a* fluorescence (O-K-J-I-P) in heat-stressed leaves. *Archs Sci Genève* 48: 147–160
- Haehnel W, Mitchell R, Ratajczak R, Spillmann A and Robenek H (1990) Lateral diffusion of plastocyanin and plastoquinol in thylakoid membranes. In: Baltscheffsky M (ed) *Current Research in Photosynthesis*, Vol II, pp 739–746. Kluwer, Dordrecht
- Hansen U-P, Dau H, Brüning B, Fritsch T and Moldaenke C (1991) Linear analysis applied to the comparative study of the I-D-P phase of chlorophyll fluorescence as induced by actinic PS-II light, PS-I light and changes in CO₂-concentration. *Photosynth Res* 28: 119–130
- Hauser M, Eichelmann H, Oja V, Heber U and Laisk A (1995) Stimulation by light of rapid pH regulation in the chloroplast stroma in vivo as indicated by CO₂ solubilization in leaves. *Plant Physiol* 108: 1059–1066
- He X, Miginiac-Maslow M, Sigalat C, Keryer E and Haraux F (2000) Mechanism of Activation of the Chloroplast ATP Synthase; A kinetic study of the thiol modulation of isolated ATPase and membrane-bound ATP synthase from spinach by *Escherichia coli* thioredoxin. *J Biol Chem* 275: 13250–13258
- Heber U, Kirk MR and Boardman NK (1979) Photoreactions of cytochrome *b*-559 and cyclic electron flow in photosystem II of intact chloroplasts. *Biochim Biophys Acta* 546: 292–306
- Heredia P and De Las Rivas J (2003) Fluorescence induction of photosystem II membranes shows the steps till reduction and protonation of the quinone pool. *J Plant Physiol* 160: 1499–1506
- Holtgrete S, Bader KP, Horton P, Scheibe R, Von Schaewen A and Backhausen JE (2003) Decreased content of leaf

- ferredoxin changes electron distribution and limits photosynthesis in transgenic potato plants. *Plant Physiol* 133: 1768–1778
- Holub O, Seufferheld MJ, Gohlke C, Govindjee and Clegg RM (2000) Fluorescence lifetime imaging (FLI) in real-time – a new technique in photosynthesis research. *Photosynthetica* 38: 581–599
- Holub O, Seufferheld MJ, Gohlke C, Govindjee, Heiss GJ and Clegg RM (2007) Fluorescence lifetime imaging microscopy of *Chlamydomonas reinhardtii*: Non-photochemical quenching mutants and the effect of photosynthetic inhibitors on the slow chlorophyll fluorescence transient. *J Microsc* 226: 90–120
- Holzwarth AR (1993) Is it time to throw away your apparatus for chlorophyll fluorescence induction? *Biophys J* 64: 1280–1281
- Holzwarth AR, Müller GM, Niklas J and Lubitz W (2006) Ultrafast transient absorption studies on photosystem I reaction centers from *Chlamydomonas reinhardtii*. 2: Mutations near the P700 reaction center chlorophylls provide new insight into the nature of the primary electron donor. *Biophys J* 90: 552–565
- Hsu B-D (1992) A theoretical study on the fluorescence induction curve of spinach thylakoids in the absence of DCMU. *Biochim Biophys Acta* 1140: 30–36
- Hsu B-D (1993) Evidence for the contribution of the S-state transitions of oxygen evolution to the initial phase of fluorescence induction. *Photosynth Res* 36: 81–88
- Hsu B-D and Lee J-Y (1991) A study on the fluorescence induction curve from DCMU-poisoned chloroplasts. *Biochim Biophys Acta* 1056: 285–292
- Hsu B-D, Lee Y-S and Jang Y-R (1989) A method for analysis of fluorescence induction curve from DCMU-poisoned chloroplasts. *Biochim Biophys Acta* 975: 44–49
- Ilik P, Schansker G, Kotabová E, Vácz P, Strasser RJ and Barták M (2006) A dip in the chlorophyll fluorescence induction at 0.2–2 s in *Trebouxia*-possessing lichens reflects a fast reoxidation of photosystem I. A comparison with higher plants. *Biochim Biophys Acta* 1757: 12–20
- Jablonsky J and Lazar D (2008) Evidence for intermediate S-states as initial phase in the process of oxygen-evolving complex oxidation. *Biophys J* 94: 2725–2736
- Joliot A and Joliot P (1964) Étude cinétique de la réaction photochimique libérant l'oxygène au cours de la photosynthèse. *C R Acad Sc Paris* 258: 4622–4625 (in French)
- Joliot P and Joliot A (1979) Comparative study of the fluorescence yield and of the C550 absorption change at room temperature. *Biochim Biophys Acta* 546: 93–105
- Joly D, Bigras C, Harnois J, Govindachary S and Carpentier R (2005) Kinetic analyses of the OJIP chlorophyll fluorescence rise in thylakoid membranes. *Photosynth Res* 84: 107–112
- Kamiya N and Shen J-R (2003) Crystal structure of oxygen-evolving photosystem II from *Thermosynechococcus vulcanus* at 3.8-Å resolution. *Proc Natl Acad Sci USA* 100: 98–1003
- Karavaev VA and Kukushkin AK (1993) A theoretical model of light and dark processes of photosynthesis: The problem of regulation. *Biofizika* 38: 958–975 (in Russian)
- Kautsky H and Hirsch A (1931) Neue Versuche zur Kohlensäureassimilation. *Naturwissenschaften* 19: 964 (in German)
- Kautsky H, Appel W and Amann H (1960) Chlorophyllfluoreszenz und Kohlensäureassimilation: XIII. Die fluoreszenzkurve und die Photochemie der Pflanze. *Biochem Z* 332: 277–292 (in German)
- Ke B (2001) *Photosynthesis: Photobiochemistry and Photobiophysics*. Kluwer (now Springer), Dordrecht
- Khuznetsova SA and Kukushkin AK (1999) A new theoretical approach to the study of regulatory links in photosynthesis. *Biofizika* 44: 448–454 (in Russian)
- Kimimura M and Katoh S (1972) Functional site of manganese in photosynthetic electron-transport system. *Plant Cell Physiol* 13: 287–296
- Klughammer C and Schreiber U (1991) Analysis of light-induced absorbance changes in the near-infrared spectral region. I. Characterization of various components in isolated chloroplasts. *Z Naturforsch* 46c: 233–244
- Koblížek M, Kaftan D and Nedbal L (2001) On the relationship between the non-photochemical quenching of the chlorophyll fluorescence and the photosystem II light harvesting efficiency. A repetitive flash fluorescence induction study. *Photosynth Res* 68: 141–152
- Kok B, Forbush B and McGloin M (1970) Cooperation of charges in photosynthetic O₂ evolution – I. A linear four step mechanism. *Photochem Photobiol* 11: 457–475
- Kolber ZS, Prášil O and Falkowski PG (1998) Measurements of variable chlorophyll fluorescence using fast repetition rate techniques: Defining methodology and experimental protocols. *Biochim Biophys Acta* 1367: 88–106
- Kramer DM, Cruz JA and Kanazawa A (2003) Balancing the central roles of the thylakoid proton gradient. *Trends Plant Sci* 8: 27–32
- Krause GH and Weis E (1991) Chlorophyll fluorescence and photosynthesis: The basis. *Annu Rev Plant Physiol Plant Mol Biol* 42: 313–349
- Kroon BMA and Thoms S (2006) From electron to biomass: A mechanistic model to describe phytoplankton photosynthesis and steady-state growth. *Mates. J Phycol* 42: 593–609
- Kukushkin AK (1997) The influence of cyclic electron transport around photosystem II on the dampening oscillations in photosynthesis. *Biofizika* 42: 1224–1234 (in Russian)
- Kurreck J, Schödel R and Renger G (2000) Investigation of the plastoquinone pool size and fluorescence quenching in thylakoid membranes and Photosystem II (PS II) membrane fragments. *Photosynth Res* 63: 171–182
- Laik A, Eichelmann H and Oja V (2006a) C₃ photosynthesis *in silico*. *Photosynth Res* 90: 45–66

- Laisk A, Eichelmann H, Oja V, Rasulov B and Rämme H (2006b) Photosystem II cycle and alternative electron flow in leaves. *Plant Cell Physiol* 47: 972–983
- Lakowicz JR (1999) Principles of Fluorescence Spectroscopy, 2nd Edition. Kluwer/Plenum Publishers, New York
- Latimer P, Bannister TT and Rabinowitch E (1956) Quantum yields of fluorescence of plant pigments. *Science* 124: 585–586
- Lavergne J and Braintais J-M (1996) Photosystem II heterogeneity. In: Ort DR and Yocum CF (eds) *Oxygenic Photosynthesis: The Light Reactions*, pp 265–287. Kluwer, Dordrecht
- Lavergne J and Leci E (1993) Properties of inactive photosystem II centers. *Photosynth Res* 35: 323–343
- Lavergne J and Rappaport F (1998) Stabilization of charge separation and photochemical misses in photosystem II. *Biochemistry* 37: 7899–7906
- Lavergne J and Trissl H-W (1995) Theory of fluorescence induction of photosystem II: Derivation of analytical expressions in a model including exciton-radical-pair equilibrium and restricted energy transfer between photosynthetic units. *Biophys J* 68: 2474–2492
- Lazár D (1999) Chlorophyll *a* fluorescence induction. *Biochim Biophys Acta* 1412: 1–28
- Lazár D (2003) Chlorophyll *a* fluorescence rise induced by high light illumination of dark-adapted plant tissue studied by means of a model of photosystem II and considering photosystem II heterogeneity. *J Theor Biol* 220: 469–503
- Lazár D (2005) Systems biology of photosynthesis in dynamic light environment. <http://www.e-photosynthesis.org> (September 1, 2008)
- Lazár D (2006) The polyphasic chlorophyll *a* fluorescence rise measured under high intensity of exciting light. *Funct Plant Biol* 33: 9–30
- Lazár D and Ilík P (1997) High-temperature induced chlorophyll fluorescence changes in barley leaves. Comparison of the critical temperatures determined from fluorescence induction and from fluorescence temperature curve. *Plant Sci* 124: 159–164
- Lazár D and Jablonský J (2009) On the approaches applied in formulation of a kinetic model of photosystem II: Different approaches lead to different simulations of chlorophyll *a* fluorescence transients. *J Theor Biol* 257: 260–269
- Lazár D and Pospíšil P (1999) Mathematical simulation of chlorophyll *a* fluorescence rise measured with 3-(3', 4'-dichlorophenyl)-1,1-dimethylurea-treated barley leaves at room and high temperatures. *Eur Biophys J* 28: 468–477
- Lazár D, Nauš J, Matoušková M and Flašarová M (1997) Mathematical modeling of changes in chlorophyll fluorescence induction caused by herbicides. *Pestic Biochem Physiol* 57: 200–210
- Lazár D, Tomek P, Ilík P and Nauš J (2001) Determination of the antenna heterogeneity of photosystem II by direct simultaneous fitting of several fluorescence rise curves measured with DCMU at different light intensities. *Photosynth Res* 68: 247–257
- Lazár D, Ilík P, Kruk J, Strzałka K and Nauš J (2005a) A theoretical study on effect of the initial redox state of cytochrome *b*₅₅₉ on maximal chlorophyll fluorescence level (*F*_M): implications for photoinhibition of photosystem II. *J Theor Biol* 233: 287–300
- Lazár D, Kaňa R, Klinkovský T and Nauš J (2005b) Experimental and theoretical study on high temperature induced changes in chlorophyll *a* fluorescence oscillations in barley leaves upon 2% CO₂. *Photosynthetica* 43: 13–27
- Lebedeva GV, Belyaeva NE, Riznichenko GY, Rubin AB and Demin OV (2000) Kinetic model of photosystem II of higher green plants. *Russ J Phys Chem* 74: 1702–1710
- Lebedeva GV, Belyaeva NE, Demin OV, Riznichenko GY and Rubin AB (2002) Kinetic model of primary photosynthetic processes in chloroplasts. Description of the fast phase of chlorophyll fluorescence induction under different light intensities. *Biofizika* 47: 968–980
- Leibl W, Breton J, Deprez J and Trissl H-W (1989) Photoelectric study on the kinetics of trapping and charge stabilization in oriented PS II membranes. *Photosynth Res* 22: 257–275
- Loll B, Kern J, Saenger W, Zouni A and Biesiadka J (2005) Towards complete cofactor arrangement in the 3.0 Å resolution structure of photosystem II. *Nature* 438: 1040–1044
- Marcus RA and Sutin N (1985) Electron transfers in chemistry and biology. *Biochim Biophys Acta* 811: 265–322
- Mauzerall D (1976) Multiple excitations in photosynthetic systems. *Biophys J* 16: 87–91
- Melis A and Homann PH (1975) Kinetic analysis of the fluorescence induction in 3-(3,4-dichlorophenyl)-1,1-dimethylurea poisoned chloroplasts. *Photochem Photobiol* 21: 431–437
- Melis A and Homann PH (1976) Heterogeneity of the photochemical centers in system II of chloroplasts. *Photochem Photobiol* 23: 343–350
- Miyake C and Yokota A (2001) Photosystem II cycle and alternative electron flow in leaves. *Plant Cell Physiol* 42: 508–515
- Moise N and Moya I (2004a) Correlation between lifetime heterogeneity and kinetics heterogeneity during chlorophyll fluorescence induction in leaves: 1. Mono-frequency phase and modulation analysis reveals a conformational change of a PSII pigment complex during the IP thermal phase. *Biochim Biophys Acta* 1657: 33–46
- Moise N and Moya I (2004b) Correlation between lifetime heterogeneity and kinetics heterogeneity during chlorophyll fluorescence induction in leaves: 2. Multi-frequency phase and modulation analysis evidences a loosely connected PSII pigment-protein complex. *Biochim Biophys Acta* 1657: 47–60
- Munday JC Jr and Govindjee (1969) Light-induced changes in the fluorescence yield of chlorophyll *a* *in vivo*. III. The dip and the peak in the fluorescence transient of *Chlorella pyrenoidosa*. *Biophys J* 9: 1–21

- Nedbal L, Trtilek M and Kaftan D (1999) Flash fluorescence induction: A novel method to study regulation of Photosystem II. *J Photochem Photobiol B: Biol* 48: 154–157
- Nedbal L, Červený J, Rascher U and Schmidt H (2007) E-photosynthesis: A comprehensive modeling approach to understand chlorophyll fluorescence transients and other complex dynamic features of photosynthesis in fluctuating light. *Photosynth Res* 93: 223–234
- Neubauer C and Schreiber U (1987) The polyphasic rise of chlorophyll fluorescence upon onset of strong continuous illumination: I. Saturation characteristics and partial control by the photosystem II acceptor side. *Z Naturforsch C* 42: 1246–1254
- Oettmeier W and Soll HJ (1983) Competition between plastoquinone and 3-(3,4-dichlorophenyl)-1,1-dimethylurea at the acceptor side of photosystem II. *Biochim Biophys Acta* 724: 287–297
- Oja V, Eichelmann H, Peterson RB, Rasulov B and Laisk A (2003) Deciphering the 820 nm signal: Redox state of donor side and quantum yield of photosystem I in leaves. *Photosynth Res* 78: 1–15
- Olson RJ, Chekalyuk AM and Sosik HM (1996) Phytoplankton photosynthetic characteristics from fluorescence induction assays of individual cells. *Limnol Oceanogr* 41: 1253–1263
- Page CC, Moser CC, Chen X and Dutton PL (1999) Natural engineering principles of electron tunnelling in biological oxidation-reduction. *Nature* 402: 47–52
- Page CC, Moser CC and Dutton PL (2003) Mechanism for electron transfer within and between proteins. *Curr Opin Chem Biol* 7: 551–556
- Papageorgiou G (1975) Chlorophyll fluorescence: An intrinsic probe of photosynthesis. In: Govindjee (ed) *Bioenergetics of Photosynthesis*, pp 319–371. Academic, New York
- Papageorgiou G and Govindjee (1968) Light-induced changes in the fluorescence yield of chlorophyll *a* in vivo. II. *Chlorella pyrenoidosa*. *Biophys J* 8: 1316–1328
- Papageorgiou G and Govindjee (eds) (2004) *Chlorophyll a Fluorescence: A Signature of Photosynthesis*. *Advances in Photosynthesis and Respiration*, Volume 19, Springer, Dordrecht
- Papageorgiou G, Tsimilli-Michael M and Stamatakis K (2007) The fast and slow kinetics of chlorophyll *a* fluorescence induction in plants, algae and cyanobacteria: A viewpoint. *Photosynth Res* 94: 275–290
- Pesaresi P, Lunde C, Jahns P, Tarantino D, Meurer J, Varotto C, Hirtz R-D, Soave C, Scheller HV, Salamini F and Leister D (2002) A stable LHCII-PSI aggregate and suppression of photosynthetic state transitions in the *psae1-1* mutant of *Arabidopsis thaliana*. *Planta* 215: 940–948
- Pettai H, Oja V, Freiberg A and Laisk A (2005) Photosynthetic activity of far-red light in green plants. *Biochim Biophys Acta* 1708: 311–321
- Pfündel E (1998) Estimating the contribution of photosystem I to total leaf chlorophyll fluorescence. *Photosynth Res* 56: 185–195
- Pospíšil P and Dau H (2000) Chlorophyll fluorescence transients of photosystem II membrane particles as a tool for studying photosynthetic oxygen evolution. *Photosynth Res* 65: 41–52
- Pospíšil P and Dau H (2002) Valinomycin sensitivity proves that light-induced thylakoid voltages result in millisecond phase of chlorophyll fluorescence transients. *Biochim Biophys Acta* 1554: 94–100
- Rappaport F, Béal D, Joliot A and Joliot P (2007) On the advantages of using green light to study fluorescence yield changes in leaves. *Biochim Biophys Acta* 1767: 56–65
- Razeghifard MR, Klughammer C and Pace RJ (1997) Electron paramagnetic resonance kinetic studies of the S states in spinach thylakoids. *Biochemistry* 36: 86–92
- Renger G and Schulze A (1985) Quantitative analysis of fluorescence induction curves in isolated spinach chloroplasts. *Photobiochem Photobiophys* 9: 79–87
- Rintamäki E, Salonen M, Suoranta UM, Carlberg I, Andersson B and Aro E-M (1997) Phosphorylation of light-harvesting complex II and photosystem II core proteins shows different irradiance-dependent regulation *in vivo* – Application of phosphothreonine antibodies to analysis of thylakoid phosphoproteins. *J Biol Chem* 272: 30476–30482
- Riznichenko G, Lebedeva G, Demin O and Rubin A (1999) Kinetic mechanisms of biological regulation in photosynthetic organisms. *J Biol Phys* 25: 177–192
- Riznichenko G, Lebedeva G, Demin O, Belyaeva NE and Rubin A (2000) Levels of regulation of photosynthetic processes. *Biofizika* 45: 440–448
- Robinson HH and Crofts AR (1984). Kinetics of proton uptake and the oxidation-reduction reactions of the quinone acceptor complex of photosystem II from pea chloroplasts. In: Sybesma C (ed) *Advances in Photosynthesis Research*, Vol 1, pp. 477–480. Martinus Nijhoff/Dr. W. Junk Publishers, The Hague
- Roelofs TA, Lee C-H and Holzwarth AR (1992) Global target analysis of picosecond chlorophyll fluorescence kinetics from pea chloroplasts. A new approach to the characterization of the primary processes in photosystem II α - and β -units. *Biophys J* 61: 1147–1163
- Roháček K (2002) Chlorophyll fluorescence parameters: The definitions, photosynthetic meaning, and mutual relationships. *Photosynthetica* 40: 13–29
- Rovers W and Giersch C (1995) Photosynthetic oscillations and the interdependence of photophosphorylation and electron transport as studied by a mathematical model. *Biosystems* 35: 63–73
- Samson G and Bruce D (1996) Origins of the low yield of chlorophyll *a* fluorescence induced by single turnover flash in spinach thylakoids. *Biochim Biophys Acta* 1276: 147–153

- Samson G, Prášil O and Yaakoubd B (1999) Photochemical and thermal phases of chlorophyll *a* fluorescence. *Photosynthetica* 37: 163–182
- Satoh Ka (1981) Fluorescence induction and activity of ferredoxin-NADP⁺ reductase in *Bryopsis* chloroplasts. *Biochim Biophys Acta* 638: 327–333
- Satoh Ka (1982) Mechanism of photoactivation of electron-transport in intact *Bryopsis* chloroplasts. *Plant Physiol* 70: 1413–1416
- Satoh K and Katoh S (1980) Light-induced changes in chlorophyll *a* fluorescence and cytochrome *f* in intact spinach chloroplasts: The site of light-dependent regulation of electron transport. *Plant Cell Physiol* 21: 907–916
- Satoh K and Katoh S (1981) Fluorescence induction in chloroplasts isolated from the green alga *Bryopsis maxima* IV. The I-D dip. *Plant Cell Physiol* 22: 11–21
- Schansker G and Strasser RJ (2005) Quantification of non-Q_B-reducing centers in leaves using a far-red pre-illumination. *Photosynth Res* 84: 145–151
- Schansker G, Srivastava A, Govindjee and Strasser RJ (2003) Characterization of the 820-nm transmission signal paralleling the chlorophyll *a* fluorescence rise (OJIP) in pea leaves. *Funct Plant Biol* 30: 785–796
- Schansker G, Tóth SZ and Strasser RJ (2005) Methylviologen and dibromorhymoquinone treatments of pea leaves reveal the role of photosystem I in the Chl *a* fluorescence rise OJIP. *Biochim Biophys Acta* 1706: 250–261
- Schansker G, Tóth SZ and Strasser RJ (2006) Dark recovery of the Chl *a* fluorescence transient (OJIP) after light adaptation: The qT-component of non-photochemical quenching is related to an activated photosystem I acceptor side. *Biochim Biophys Acta* 1754: 787–797
- Schansker G, Yuan Y and Strasser RJ (2008) Chl *a* fluorescence and 820 nm transmission changes occurring during a dark-to-light transition in pine needles and pea leaves: A comparison. In: Allen JF, Osmond B, Golbeck JH and Gantt E (eds) *Energy from the Sun*, pp 951–955. Springer, Dordrecht
- Schatz GH, Brock H and Holzwarth AR (1987) Picosecond kinetics of fluorescence and absorbance changes in photosystem II particles excited at low photon density. *Proc Natl Acad Sci USA* 84: 8414–8418
- Schatz GH, Brock H and Holzwarth AR (1988) Kinetic and energetic model for the primary processes in photosystem II. *Biophys J* 54: 397–405
- Schreiber U (2002) Assessment of maximal fluorescence yield: Donor-side dependent quenching and Q_B-quenching. In: Van Kooten O and Snel JFH (eds) *Plant Spectrofluorometry: Applications and Basic Research*, pp 23–47. Rozenberg Publishers, Amsterdam
- Schreiber U (2004) Pulse-amplitude-modulation (PAM) fluorometry and saturation pulse method: An overview. In: Papageorgiou GC and Govindjee (eds) *Chlorophyll *a* Fluorescence: A Signature of Photosynthesis*, pp 279–319. Springer, Dordrecht
- Schreiber U and Krieger A (1996) Two fundamentally different types of variable chlorophyll fluorescence in vivo. *FEBS Lett* 397: 131–135
- Schreiber U and Neubauer C (1987) The polyphasic rise of chlorophyll fluorescence upon onset of strong continuous illumination: II. Partial control by the photosystem II donor side and possible ways of interpretation. *Z Naturforsch C* 42: 1255–1264
- Schreiber U and Vidaver W (1974) Chlorophyll fluorescence induction in anaerobic *Scenedesmus obliquus*. *Biochim Biophys Acta* 368: 97–112
- Schreiber U, Neubauer C and Klughammer C (1989) Devices and methods for room-temperature fluorescence analysis. *Phil Trans R Soc Lond B* 323: 241–251
- Schreiber U, Hormann H, Neubauer C and Klughammer C (1995) Assessment of photosystem II photochemical quantum yield by chlorophyll fluorescence quenching analysis. *Aust J Plant Physiol* 22: 209–220
- Shigematsu Y, Satoh F and Yamada Y (1989) A binding model for phenylurea herbicides based on analysis of a Thr 264 mutation in D-1 protein of tobacco. *Pestic Biochem Physiol* 35: 33–41
- Sinclair J and Spence SM (1988) The analysis of fluorescence induction transients from dichlorophenyl dimethylurea-poisoned chloroplasts. *Biochim Biophys Acta* 935: 184–194
- Sinclair J and Spence SM (1990) Heterogeneous photosystem 2 activity in isolated spinach chloroplasts. *Photosynth Res* 24: 209–220
- Sivak MN and Walker DA (1985) Chlorophyll *a* fluorescence: Can it shed light on fundamental questions in photosynthetic carbon dioxide fixation? *Plant Cell Environ* 8: 439–448
- Stahl U, Tusov VB, Paschenko VZ and Voigt J (1989) Spectroscopic investigations of fluorescence behavior, role and function of the long-wavelength pigment of photosystem I. *Biochim Biophys Acta* 973: 198–204
- Steffen R, Eckert HJ, Kelly AA, Dormann P and Renger G (2005) Investigations on the reaction pattern of photosystem II in leaves from *Arabidopsis thaliana* by time-resolved fluorometric analysis. *Biochemistry* 44: 3123–3133
- Stirbet A and Strasser RJ (1995) Numerical simulation of the fluorescence induction in plants. *Archs Sci Genève* 48: 41–60
- Stirbet AD and Strasser RJ (1996) Numerical simulation of the in vivo fluorescence in plants. *Math Comp Sim* 42: 245–253
- Stirbet A and Strasser RJ (2001) The possible role of pheophytine in the fast fluorescence rise OKJIP. In: *Proceedings of the 12th International Congress on Photosynthesis (CD-ROM)*, S11–027. CSIRO Publishing, Collingwood
- Stirbet A, Govindjee, Strasser BJ and Strasser RJ (1998) Chlorophyll *a* fluorescence induction in higher plants:

- Modelling and numerical simulation. *J Theor Biol* 193: 131–151
- Stirbet AD, Rosenau P, Ströder AC and Strasser RJ (2001) Parameter optimisation of fast chlorophyll fluorescence induction model. *Math Comput Simulat* 56: 443–450
- Strasser RJ and Govindjee (1991) The F_0 and the O-J-I-P fluorescence rise in higher plants and algae. In: Argyroudi-Akoyunoglou JH (ed) *Regulation of Chloroplast Biogenesis*, pp 423–426. Plenum Press, New York
- Strasser RJ and Govindjee (1992) On the O-J-I-P fluorescence transient in leaves and D1 mutants of *Chlamydomonas reinhardtii*. In: Murata N (ed) *Research in Photosynthesis*, Vol 2, pp 29–32. Kluwer, Dordrecht
- Strasser RJ and Stirbet AD (1998) Heterogeneity of photosystem II probed by the numerically simulated chlorophyll *a* fluorescence rise (O-J-I-P) *Math Comput Simulat* 48: 3–9
- Strasser RJ and Stirbet AD (2001) Estimation of the energetic connectivity of PS II centres in plants using the fluorescence rise O-J-I-P. Fitting of experimental data to three different PS II models. *Math Comput Simulat* 56: 451–461
- Strasser RJ, Srivastava A and Govindjee (1995) Polyphasic chlorophyll *a* fluorescence transient in plants and cyanobacteria. *Photochem Photobiol* 61: 32–42
- Strasser RJ, Tsimilli-Michael M and Srivastava A (2004) Analysis of the chlorophyll *a* fluorescence transient. In: Papageorgiou GC and Govindjee (eds) *Chlorophyll *a* Fluorescence: A Signature of Photosynthesis*, pp 321–362. Springer, Dordrecht
- Sušila P, Lazár D, Ilík P, Tomek P and Nauš J (2004) The gradient of exciting radiation within a sample affects relative heights of steps in the fast chlorophyll *a* fluorescence rise. *Photosynthetica* 42: 161–172
- Terashima I and Inoue Y (1985) Palisade tissue chloroplasts and spongy tissue chloroplasts in spinach; Biochemical and ultrastructural differences. *Plant Cell Physiol* 26: 63–75
- Tomek P, Lazár D, Ilík P and Nauš J (2001) On the intermediate steps between the O and P steps in chlorophyll *a* fluorescence rise measured at different intensities of exciting light. *Aust J Plant Physiol* 28: 1151–1160
- Tomek P, Ilík P, Lazár D, Štroch M and Nauš J (2003) On the determination of Q_B -non-reducing photosystem II centers from chlorophyll *a* fluorescence induction. *Plant Sci* 164: 665–670
- Tóth SZ, Schansker G and Strasser RJ (2005) In intact leaves, the maximum fluorescence level (F_M) is independent of the redox state of the plastoquinone pool: A DCMU-inhibition study. *Biochim Biophys Acta* 1708: 275–282
- Tóth SZ, Schansker G, Garab G and Strasser RJ (2007a) Photosynthetic electron transport activity in heat-treated barley leaves: The role of internal alternative electron donors to photosystem II. *Biochim Biophys Acta* 1767: 295–305
- Tóth SZ, Schansker G and Strasser RJ (2007b) A non-invasive assay of the plastoquinone pool redox state based on the OJIP-transient. *Photosynth Res* 93: 193–203
- Trebst A and Draber W (1986) Inhibitors of photosystem II and the topology of the herbicide and Q_B binding polypeptide in the thylakoid membrane. *Photosynth Res* 10: 381–392
- Trissl H-W (1994) Response to Falkowski et al. *Biophys J* 66: 925–926
- Trissl H-W and Lavergne J (1995) Fluorescence induction from photosystem II: Analytical equations for the yields of photochemistry and fluorescence derived from analysis of a model including exciton-radical pair equilibrium and restricted energy transfer between photosynthetic units. *Aust J Plant Physiol* 22: 183–193
- Trissl H-W and Wilhelm C (1993) Why do thylakoid membranes from higher plants form grana stacks? *Trends Biochem Sci* 18: 415–419
- Trissl H-W, Gao Y and Wulf K (1993) Theoretical fluorescence induction curves derived from coupled differential equations describing the primary photochemistry of photosystem II by an exciton-radical pair equilibrium. *Biophys J* 64: 974–988
- Tsimilli-Michael M, Pêcheux M and Strasser RJ (1998) Vitality and stress adaptation of the symbionts of coral reef and temperature foraminifers probed *in hospite* by the fluorescence kinetics OJIP. *Archs Sci Genève* 51: 205–240
- Valkunas L, Geacintov NE, France L and Breton J (1991) The dependence of the shapes of fluorescence induction curves in chloroplasts on the duration of illumination pulses. *Biophys J* 59: 397–408
- Vallon O, Bulté L, Dainese P, Olive J, Bassi R and Wollman F-A (1991) Lateral redistribution of cytochrome b_6/f complexes along thylakoid membranes upon state transitions. *Proc Natl Acad Sci USA* 88: 8262–8266
- Vasil'ev S, Wiebe S and Bruce D (1998) Non-photochemical quenching of chlorophyll fluorescence in photosynthesis. 5-hydroxy-1,4-naphthoquinone in spinach thylakoids as a model for antenna based quenching mechanisms. *Biochim Biophys Acta* 1363: 147–156
- Van Grondelle R (1985) Excitation energy transfer, trapping and annihilation in photosynthetic systems. *Biochim Biophys Acta* 811: 147–195
- Vavilin DV, Tyystjärvi E and Aro E-M (1998) Model for the fluorescence induction curve of photoinhibited thylakoids. *Biophys J* 75: 503–512
- Velthuys BR and Ames J (1974) Charge accumulation at the reducing side of system 2 of photosynthesis. *Biochim Biophys Acta* 333: 85–94
- Vernotte C, Etienne A-L and Briantais L-M (1979) Quenching of the system II chlorophyll fluorescence by the plastoquinone pool. *Biochim Biophys Acta* 545: 519–527
- Visser D and Heijnen J (2002) The mathematics of metabolic control analysis revisited. *Metab Eng* 4: 114–123
- Von Caemmerer S (2000) *Biochemical models of leaf photosynthesis*. CSIRO Publishing, Collingwood

- Vredenberg WJ (2000) A three-state model for energy trapping and chlorophyll fluorescence in photosystem II incorporating radical pair recombination. *Biophys J* 79: 26–38
- Vredenberg WJ (2004) System analysis and photoelectrochemical control of chlorophyll fluorescence in terms of trapping models of photosystem II: A challenging view. In: Papageorgiou GC and Govindjee (eds) *Chlorophyll *a* Fluorescence: A Signature of Photosynthesis*, pp 133–172. Springer, Dordrecht
- Vredenberg WJ (2008a) Algorithm for analysis of OJIP fluorescence induction curves in terms of photo- and electrochemical events in photosystems of plant cells: Derivation and application. *J Photochem Photobiol B: Biol* 91: 58–65
- Vredenberg WJ (2008b) Analysis of initial chlorophyll fluorescence induction kinetics in chloroplasts in terms of rate constants of donor side quenching release and electron trapping in photosystem II. *Photosynth Res* 96: 83–97
- Vredenberg WJ and Bulychev AA (2002) Photoelectrochemical control of photosystem II chlorophyll fluorescence in vivo. *Bioelectrochem* 57: 123–128
- Vredenberg WJ and Bulychev AA (2003) Photoelectric effects on chlorophyll fluorescence of photosystem II in vivo. Kinetics in the absence and presence of valinomycin. *Bioelectrochem* 60: 87–95
- Vredenberg WJ and Duysens LNM (1963) Transfer of energy from bacteriochlorophyll to a reaction centre during bacterial photosynthesis. *Nature* 197: 355–357
- Vredenberg WJ, Rodriguez GC and Van Rensen JJC (2001) A quantitative analysis of the chlorophyll fluorescence induction in terms of electron transfer rates at donor and acceptor sides of photosystem II. In: *Proceedings of the 12th International Congress on Photosynthesis (CD-ROM)*, S14–10. CSIRO Publishing, Collingwood
- Vredenberg WJ, Van Rensen JJS and Rodriguez GC (2006) On the sub-maximal yield and photo-electric stimulation of chlorophyll *a* fluorescence in single turnover excitations in plant cells. *Bioelectrochemistry* 68: 81–88
- Walker DA, Sivak MN, Prinsley RT and Cheesbrough JK (1983) Simultaneous measurement of oscillations in oxygen evolution in chlorophyll *a* fluorescence in leaf pieces. *Plant Physiol* 73: 542–549
- Yamagishi A, Satoh Ka and Katoh S (1978) Fluorescence induction in chloroplasts isolated from the green alga *Bryopsis maxima*. III. A fluorescence transient indicating proton gradient across the thylakoid membrane. *Plant Cell Physiol* 19: 17–25
- Zhu X-G, Govindjee, Baker NR, deSturler E, Ort DR and Long SP (2005) Chlorophyll *a* fluorescence induction kinetics in leaves predicted from a model describing each discrete step of excitation energy and electron transfer associated with Photosystem II. *Planta* 223: 114–133

Chapter 6

Modeling of Chlorophyll a Fluorescence Kinetics in Plant Cells: Derivation of a Descriptive Algorithm

Wim Vredenberg*

*Department of Plant Physiology, Wageningen University and Research Centre,
Arboretumlaan 4, 6703 BD Wageningen, The Netherlands*

Ondřej Prášil

*Laboratory of Photosynthesis, Institute of Microbiology, Academy of Sciences Czech
Republic, Opatovický mlyn, 37981 Třeboň, Czech Republic*

Summary.....	126
I. Introduction.....	126
II. Variable (Chlorophyll) Fluorescence – Some Basics.....	128
A. Transfer of Reaction Center States and Variable Fluorescence; Q_B Nonreducing Centers.....	128
B. Maximal Variable Fluorescence	130
C. Kinetics of Variable Fluorescence; Donor Side Quenching	130
D. Rate Equations for Reaction Center Transfers and Variable Fluorescence	130
E. Analytical Functions of Variable Fluorescence Kinetics.....	131
III. Application of Single, Twin and Multiple Turnover Flashes.....	132
A. Fluorescence Kinetics upon Single and Twin Turnover Excitation.....	133
B. Excitation with Single Turnover Flash Train	134
IV. Distinguishable Phases of Fluorescence Response upon Multiturnover Excitation	135
A. Photochemical OJD Phase in the 0–2.5 ms Time Range.....	135
1. Single Hit Excitation in β -(S_0) and (1- β)-(S_1) Fraction	135
2. Double Hit Excitation in β -(S_0) Fraction	136
B. Photo-electrochemical (J)DI Phase in the 2–50 ms Time Range	136
C. Phase IP in the 50–200 ms Time Range	137
V. Fluorescence Induction Algorithm for Experimental Curves.....	137
A. Dark-adapted Thylakoids	137
B. STF Pre-excited Thylakoids	138
C. Dark-adapted Thylakoids in the Presence of Diuron	139
D. Leaf at High and Low Excitation Rates.....	140
E. Leaf at Variable Excitation Rates.....	141
F. Leaf under Laser Flash Excitation.....	142
VI. Concluding Remarks	144
Acknowledgments.....	146
References.....	146

* Author for correspondence, e-mail: Wim.Vredenberg@wur.nl

Summary

In this chapter, we present the model and simulation of light-driven chlorophyll fluorescence induction in 10–20 min dark-adapted intact leaves and thylakoids. The algorithm for it has been derived from analyses of fluorescence kinetics upon excitation with single- (STF), twin- (TTF) and repetitive STF excitations. These analyses have led to definition and formulation of rate equations that describe the sequence of electron transfer steps associated with the oxidation of the oxygen evolving complex (OEC) and the reduction of the primary plastoquinone acceptor Q_A of photosystem II (PS II) in multi turnover excitation (MTF). The model considers heterogeneity in reaction centers (RCs) associated with the S-states of the OEC and incorporates the presence of a 20–35% fraction of Q_B nonreducing RCs that probably is identical with the S_0 fraction. The fluorescence induction algorithm (FIA) considers a photochemical O–J–D, a photo-electrochemical J–I and an I–P component (phase), which probably is associated with a photo-electric interaction between PS I and PS II. The photochemical phase incorporates the kinetics associated with the double reduction of the acceptor pair of pheophytin (Phe) and plastoquinone Q_A [$PheQ_A$] in Q_B nonreducing RCs and the associated doubling of the variable fluorescence, in agreement with the three-state trapping model (TSTM) of PS II. Application of and results with the algorithm are illustrated for a variety of MTF-induced OJDIP curves, measured in dark-adapted leaves and thylakoids under various light and dark conditions.

I. Introduction

Photosynthetic light reactions of plants, algae and cyanobacteria transform photon (light) energy into several forms of (electro-) chemically convertible energy. Their machinery is embedded in protein complexes that are oriented in the closed and partially folded membrane system (thylakoid) in the chloroplast. The transverse and lateral orientation and organization of this apparatus in the membrane serve several purposes. (i) The planar separation of two photochemical systems PS I and PS II, laterally connected by cytochrome b_6f complex that interacts with plastoquinone pool, allows the uphill electron transfer from water on the donor side of PS II to an intermediate at the acceptor side of PS I. (ii) The vectorial orientation of the reaction centers (RCs) of both photosystems in the membrane guarantees that exciton trapping, and subsequent charge separation, results in an electrogenic event associated with the generation of a trans-membrane electric potential. Its associated electromotive force acts as a driving force for the generation of electrochemical gradients of ions, in particular protons. (iii) The anchoring and proper orientation of active proton pumps, such as the RCs, the cytochrome b_6f complex and the ATP synthase which allow the system to function properly (Ke, 2001).

Chlorophyll *a* (Chl) fluorescence, for the major part emitted by PS II antenna chlorophylls, is a de-excitation pathway in the photosynthetic units (PSUs) and competes with photochemical energy trapping (conversion) in RCs resulting in fluorescence quenching when trapping in the RC is effective (Govindjee, 2004). Whenever we use the word fluorescence in this chapter, we mean Chl fluorescence. The complementary relation between fluorescence and photochemical yield has made fluorescence monitoring a sensitive non-invasive tool for probing the ongoing electron transport in PS II (Papageorgiou and Govindjee, 2004). Several models have been presented with the goal of quantitatively relating changes in fluorescence yield to the photochemical yield of electron transport to and from PS II (Vredenberg and Duysens, 1963; Joliot and Joliot, 1977; Dau, 1994; Lavergne and Trissl, 1995; Trissl and Lavergne, 1995; Schreiber and Krieger, 1996; Stirbet et al., 1998; Bernhardt and Trissl, 1999; Zhu et al., 2005; Lazar, 2006). The light-dependent Chl fluorescence yield in chloroplasts and intact leaves is variable between a lowest, intrinsic level F_0 (the “O” level) at full photochemical quenching under dark-adapted conditions and a maximal level F_m (the “P” level) at saturating light intensities at which all quenching is released. Variable fluorescence is defined as $F_v = F_m - F_0$. The primary quinone

acceptor of PS II, Q_A , has since long been known as the major and principal quencher; the quenching is released upon its photoreduction (Duysens and Sweers, 1963). F_m is associated with full reduction of Q_A and with a trapping-incompetent closed RC. Other additional quenchers have been proposed (Butler, 1972; Joliot and Joliot, 1977; Klimov and Krasnovskii, 1981; Kramer et al., 1995; Vasilév and Bruce, 1998; Kurreck et al., 2000; Koblízek et al., 2001; Vredenberg, 2004; Zhu et al., 2005; for a survey see Samson et al., 1999 and Papageorgiou et al., 2007) to account for the seeming paradox that the normalized variable fluorescence in a 300 ms multi-turnover pulse (nF_V^{MTF}) is about twice that

in a single turnover flash (nF_V^{STF}) (Samson and Bruce, 1996; Vasilév and Bruce, 1998; Kolber et al., 1998; Schreiber, 2002; Vredenberg et al., 2005, 2006). The fast fluorescence induction curve $F(t)$ in multi-turnover light pulses (MTF excitation) has become known as the so called OJDIP curve, where “O” is the minimal fluorescence, J is an intermediary maximum, D is the dip that follows, I is another intermediate plateau or inflection and P is the peak at the final maximal fluorescence F_m (see Govindjee, 1995, 2004). The OJD, JDI and IP parts of the curve cover the 0–2.5, 0.3–20 and 20–300 ms time range, respectively and can be identified as distinguishable phases of the induction (Strasser et al., 1995).

Abbreviations: β – fraction (S_0) of Q_B nonreducing RCs; DCMU – 3(3,4-Dichlorophenyl)-1,1-dimethylurea; DSQ – donor side quenching; FCCP – carbonyl cyanide p-trifluoromethoxyphenylhydrazone; $F_m^{S(M)TF}$ – fluorescence level of system with 100% closed PSUs after S(M)TF excitation in dark-adapted state; F_0 – fluorescence level of system with 100% open PSUs in dark-adapted state; FIA – fluorescence induction algorithm; GOSA – global optimization simulation annealing; k_1 (k_{dsq}) – rate constant of donor side quenching release; k_{-1} – rate constant of radical pair recombination; k_{AB} – rate constant of Q_A oxidation; k_{2AB} – rate constant of oxidation of $[PheQ_A]^{2-}$ in Q_B nonreducing RCs; k_d – rate constant of non-radiative radical pair transfer; k_{dsq} – see k_1 ; k_e – rate constant of Q_A photoreduction (charge stabilization at acceptor side); k_{IP} – rate constant of (unknown) transfer step associated with IP rise; k_L – excitation rate of photosystem in light pulse; k_{-nqb} – rate constant of quenching recovery in Q_B nonreducing RCs; k_{qbf} – rate constant associated with accumulation and reduction of Q_B nonreducing RCs; k_t – rate constant of photochemical trapping (charge separation) in PS II; k_w – rate constant of non-photochemical energy losses; k_{y_i, S_i} – rate constant of P^+ - and Y_z^+ -reduction, respectively, for OEC in $S = S_i$ state ($i = 0 \dots 3$); nF_V – normalized variable fluorescence $(F - F_0)/F_0$; rF_V – relative variable fluorescence $(F - F_0)/(F_m - F_0)$; q – fraction of RCs with Q_A^- ; q^{dsq} – fraction of RCs in which acceptor- and donor side quenching is released; MTF – multi-turnover flash (light pulse); OEC – oxygen evolving complex; ODE – ordinary linear differential equation; Φ_{tr}^0 – electron trapping efficiency of open RCs; P_{680} (or P) – mainstream electron donor of PS II; Phe (or Ph) – pheophytin, primary electron acceptor of PS II; PS II – photosystem II; PSU – photosynthetic unit; Q_A – primary quinone acceptor of PS II; Q_B – secondary quinone acceptor of PS II; RCII – reaction center of PS II; STF – single turnover flash (excitation); TTF – twin turnover flash; TSTM – three-state trapping model; Y_z – secondary electron donor of PS II

The normalized variable fluorescence $nF_V (= F_m/F_0 - 1)$ in dark adapted isolated chloroplasts, upon a saturating single (STF) and a twin (TTF) turnover excitation, has been found to be in the range between 1.7 and 2.3, with as an average $nF_V^{TTF} \sim 1.3 nF_V^{STF}$. The dark recovery of these STF- and TTF-induced fluorescence show a F(ast) (0.01–10 ms) and a S(low) phase extending into the 100 s time range. The S-phase is attributed to the (slow) reoxidation of the reduced $Q_A(Q_A^-)$ in the fraction with Q_B nonreducing RCs (Vredenberg et al., 2006; 2007). This fraction has been argued (Hiraki et al., 2004; Vredenberg, 2004) to be identical with the fraction in which the OEC is in the uncharged S_0 state (S_0 fraction). The OEC is known to run through subsequent states S_1 , S_2 , S_3 and $S_4 (=S_0)$ in an STF train (see Ke, 2001). Vermaas et al. (1984) showed that a system that is dark adapted for 5–30 min is heterogeneous with respect to the S-states, with $S_0/S_1 \sim 0.25/0.75$.

The F-phase of the fluorescence decay after STF excitation is composed of a major and a minor exponential component. The major component which is invariable in a STF and TTF excitation occurs with an average decay constant $k_{AB} (= 1/\tau_1 \sim 1/[0.25 \text{ ms}] \sim 4 \text{ ms}^{-1})$. It is associated with reoxidation of Q_A^- in the S_1 fraction with Q_B reducing RCs. The minor component, which is substantially higher in the TTF response, decays with a rate constant $k_{2AB} = 1/\tau_2 \sim 1/[2 \text{ ms}] \sim 0.5 \text{ ms}^{-1}$ and is attributed to reoxidation of the double-reduced acceptor pair $[PheQ_A]^{2-}$ in Q_B nonreducing RCs. The increment in the response that is caused by the TTF

shows single exponential decay with rate constant k_{2AB} . TTF (double) excitation causes double reduction of acceptor pair in Q_B nonreducing RCs. Vredenberg et al. (2007) proposed that these RCs are predominantly, if not exclusively, present in the S_0 fraction of dark-adapted thylakoids.

$F(t)$ curves in high frequency (1–4 kHz) STF trains in the 0–2.5 ms time range show a rise in the first STF towards $F^{STF1} \sim 3F_0$. This response is followed by a 20–30% transient rise in the next 2–3 STFs with partial recovery of the rise in the 2–3 ms time range during subsequent STFs (see Fig. 6.5 in Vredenberg et al., 2007). This pattern shows close resemblance to the $F(t)$ response in high intensity MTF excitation (Schansker et al., 2006).

The single turnover induced fluorescence responses and the $F(t)$ pattern in the 0–2.5 ms time domain induced by a train of single turnover excitations, have been interpreted to be caused by (i) a single hit induced photoreduction of the electron acceptor Q_A in the heterogeneous system with S_1 and S_0 RCs, followed by (ii) reduction of the reduced acceptor pair $[PheQ_A]^-$ in the S_0 fraction with Q_B nonreducing RCs and single reduction of the acceptor (pair) in the recovered part of the S_1 fraction with Q_B reducing RCs in second and subsequent excitations (Vredenberg et al., 2007).

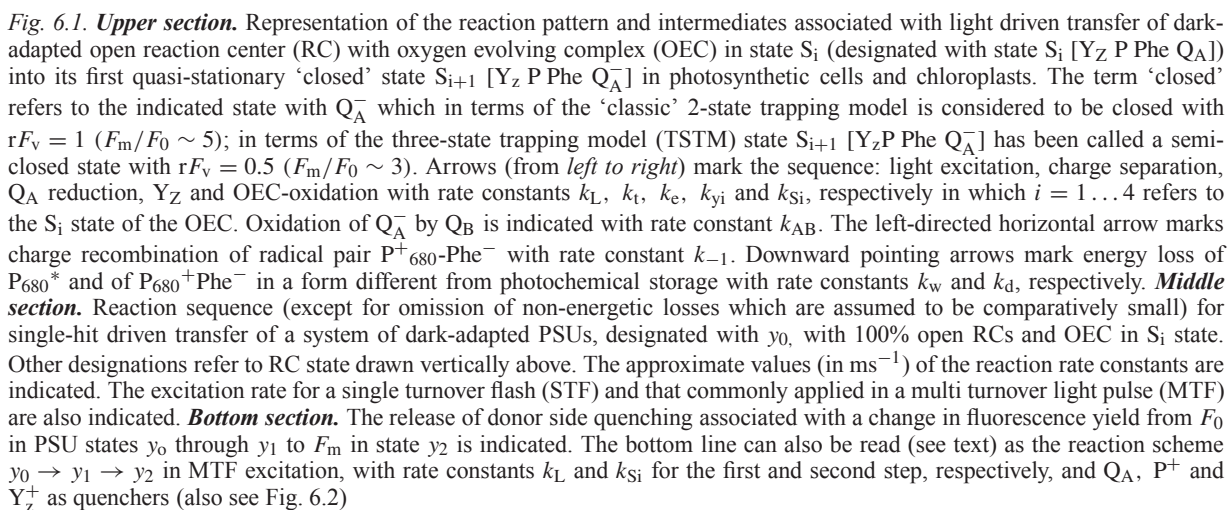
$F(t)$ responses upon saturating single turnover excitation at various repetition rates have given evidence for hitherto unrecognized properties and photochemical role of Q_B nonreducing RCs in PS II electron transport (Vredenberg et al., 2006, 2007; Vredenberg, 2008b, c). In contrast to what commonly has been assumed about inactivity of Q_B nonreducing RCs in PS II electron transport (Melis, 1985; Chylla et al., 1987; Lavergne and Leci, 1993), repetitive excitation data have shown that these centers are able to reduce Q_B after a second hit. The new fact that reduced Q_B nonreducing RCs (with Q_A^-) are electron trapping-competent, giving rise to a dark reversible variable fluorescence, suggests that the double reduced acceptor pair $[PheQ_A]^{2-}$ can reduce Q_B . It follows that the term ' Q_B nonreducing RCs' in fact only refers to OPEN centers of this type. A better nomenclature therefore would be ' Q_B nonreducing open RCs'. Here we have used the 'traditional' definition and nomenclature of Q_B nonreducing RCs as followed till now in the literature.

This chapter describes the fluorescence induction algorithm (FIA) which allows analysis and simulation of OJDIP fluorescence induction curves in intact leaves and thylakoids in relation to the primary photochemical and photo-electrochemical events in the photosynthetic membrane. The algorithm is based on a model for which concept, elements and assumptions are outlined in Sections II–IV. Briefly, the concept incorporates or assumes, in contrast to other similar models (Stirbet et al., 1998; Lazar, 2006; Zhu et al., 2005; Belyaeva et al., 2006; Jablonsky and Lazar, 2008; see also Chapter 5 of this book by Dušan Lazár and Gert Schansker): (i) donor side quenching by the oxidized intermediate between the Mn complex and the P_{680} , Y_z^+ (Vredenberg, 2004, 2008a), (ii) non-zero electron trapping efficiency of RCs with single-reduced acceptor pair $[PheQ_A]$ (i.e. semi-closed and with Q_A^-), (iii) accumulation of Q_B nonreducing RCs in association with and photo-electrochemically coupled to transthylakoid proton transport and (iv) time-independent rate constants of fluorescence quenching release, which implicitly means non-cooperativity (connectivity) between PSUs of PS II. Algorithm and model are validated and illustrated for various conditions of the photosynthetic materials in Section V and evaluated to some extent in Section VI.

II. Variable (Chlorophyll) Fluorescence – Some Basics

A. Transfer of Reaction Center States and Variable Fluorescence; Q_B Nonreducing Centers

The chain of reactions up to Q_A^- in a homogeneous system of separate PSUs of PS II centers with initially 100% open reaction centers (RCs) following a single picosecond (ps) excitation is given in the upper row of Fig. 6.1. The state of the RC in a PS II unit is identifiable and characterized by the redox state of the acceptor and donor pairs $[PheQ_A]$ and $[Y_ZP]$, respectively, and by the number (i) of charges accumulated in the oxygen evolving complex (OEC), designated with S_i ($i = 0 \dots 3$). When dark adapted for 10–30 min the PSUs have been found to be heterogeneous



The reaction scheme for the transfer of the RC upon a single turnover (STF) excitation is given in the second row of Fig. 6.1. The scheme is simplified by omitting the comparatively small dissipative and non-photochemical losses in antenna (k_w) and RC (k_d). Excitation (with rate constant k_L) causes the transfer of the dark-adapted ‘open’ state (y_0) via the excited (y_0^*) and ‘radical pair’ state (y_0^{RP}) to the electron-trapped (-stabilized) states $y_0^{\text{P}+}$, y_1 and y_2 . With picosecond laser STFs the excitation rate k_L ($\sim 10^9 \text{ ms}^{-1}$) exceeds the rate constant of photochemical trapping

(charge separation) $k_t (\sim 10^7 \text{ ms}^{-1})$. In that case the excited state y_0^* can be considered to be identical with y_0 . The transfer from y_0^{RP} to the state y_2 occurs via the intermediate states $y_0^{\text{P}+}$ and y_1 . The electron trapping efficiency $\Phi_{\text{tr}}^{\text{O}}$ in an excited open RC (y_0^{RP}) is $\Phi_{\text{tr}}^{\text{O}} = k_e / (k_e + k_{-1} + k_d) \sim k_e / (k_e + k_{-1})$ in which k_e , k_{-1} and k_d ($\ll k_e + k_{-1}$) are rate constants for Q_A photoreduction, radical pair recombination and non-radiative radical pair transfer, respectively (Fig. 6.1, second row). With appropriate values of the rate constants, given in Fig. 6.1, $\Phi_{\text{tr}}^{\text{O}} \sim 90\%$, i.e. close to 1. One should keep in mind that an attenuation of the primary rate constant of Q_A reduction

(k_e) or a stimulation of those of radical pair recombination (k_{-1}) or non-radiative recombination (k_d) results in a decrease in the usually high electron trapping efficiency of open centers (Φ_{tr}^0). Conversely, a temporary decrease in k_{-1} with unaltered k_e will cause a transient increase in Φ_{tr}^0 .

B. Maximal Variable Fluorescence

The time pattern of generation and decay of each of the intermediate RC states in the photochemical reaction chain follows from the solution of a system of ordinary linear differential equations (ODE) associated with the reaction scheme (for details see Vredenberg, 2004). Analytical solution of these equations yields expressions for y_0 , y_0^* , y_0^{RP} , y_0^{P+} , y_1 and y_2 as a function of time (see also Trissl, 2002 for a basic mathematical description). The transient state y_1 and the final photochemical product (y_2), under conditions at which Q_A^- oxidation is blocked, are formed within tens of nanoseconds and microseconds, respectively (see Vredenberg, 2004).

The concept of PSU closure by a single photon hit requires additional assumptions to confirm the kinetics of the variable fluorescence associated with the theoretical predictions. The single turnover induced transfer of an open reaction center into states with Q_A^- (Fig. 6.1) is accompanied by an approximately threefold increase in fluorescence yield from the minimal dark level F_0 to F_m (Vredenberg et al., 2006, 2007, and references therein) which is equivalent to a normalized variable fluorescence $nF_v = \frac{F_m - F_0}{F_0} = \frac{F_m}{F_0} - 1 \approx 2$. This variable fluorescence has been ascribed to the release of photochemical quenching by Q_A due to its reduction to Q_A^- (Duysens and Sweers, 1963).

C. Kinetics of Variable Fluorescence; Donor Side Quenching

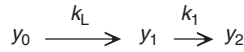
The kinetics of the STF-induced fluorescence increase have been shown to be bi-phasic (Mauzerall, 1972; Steffen et al., 2001; Steffen, 2003; Belyaeva et al., 2006, 2008) with the major rise occurring within tens of microseconds. The substantial attenuation of the rate (constant) of the STF-induced rise with respect to excitation rate has been ascribed to fluorescence

quenching by reaction intermediates at the donor side, e.g., by P^+ (Butler, 1972; Reifarth et al., 1997), Y_z^+ (Vredenberg et al., 2002) and others (Steffen, 2003). Fluorescence quenching by intermediates at the donor side is called donor side quenching (DSQ). The fact that the retarded fluorescence rise in STF excitation occurs in the same time range as of that reported for the $y_1 \rightarrow y_2$ state transfer (see Fig. 6.1, second row) has been interpreted as evidence that this rise is the reflection of the release of DSQ by Y_z^+ (Vredenberg et al., 2002). The components Q_A , P^+ and Y_z^+ , responsible for quenching in the single hit reaction sequence, are indicated in the fourth row of Fig. 6.1.

D. Rate Equations for Reaction Center Transfers and Variable Fluorescence

Continuous illumination with a 1 s multi-turnover light pulse (MTF excitation) of a dark-adapted homogeneous system of PS II centers with open RCs and equal antenna size will cause an inductive transfer of the system into one with reduced (Q_A^-) centers. The events caused by the first excitation of the MTF can be described *a priori* by the same set of rate equations as given for RC transfer in an individual PSU (Fig. 6.1), if inter-system exciton transfer (Joliot and Joliot, 1964; Strasser, 1978; Trissl and Lavergne, 1995), is assumed to be zero. The identification of the RC states y_j ($j = 0 \dots 2$) in the initial stage of a multi-turnover excitation then refers to the fraction of PSUs in which the RCs are in the y_j state (see Fig. 6.1). The average excitation rate (frequency) k_L of trapping competent (open) RCs during a multi-turnover light pulse is determined by antenna size, intensity of the pulse, density of the sample, i.e. Chl concentration, and the optical path length. Under usual experimental conditions, the excitation rate in commonly used commercial instruments is in the range between 1 and 10 ms⁻¹. A high intensity modification of a Hansatech fluorometer is available in which $k_L \sim 20$ ms⁻¹ at maximal power (Schansker et al., 2006). With the excitation rate in this range, k_L is of the same order of magnitude as the rate constant k_1 of the release of donor side fluorescence quenching (DSQ), probably coinciding with that of Y_z^+ reduction (OEC oxidation), in state S_1 . It is several orders of magnitude lower

Y_z^+ (and P^+) - donor side quenching [DSQ-model]



$$\frac{F(t)}{F_0} = 1 + \left(\frac{F_m}{F_0} - 1\right) * \left(1 + \frac{k_1}{k_L - k_1} e^{-k_L^* t} - \frac{k_L}{k_L - k_1} e^{-k_1^* t}\right) = 1 + \left(\frac{F_m}{F_0} - 1\right) * q^{dsq}(t)$$

With ps laser excitation
 $k_L (\sim 10^9 \text{ ms}^{-1}) \gg k_1$ and
 $F_m/F_0 \sim 3$

$$\frac{F(t)}{F_0} = 1 + 2^* (1 - e^{-k_1^* t})$$

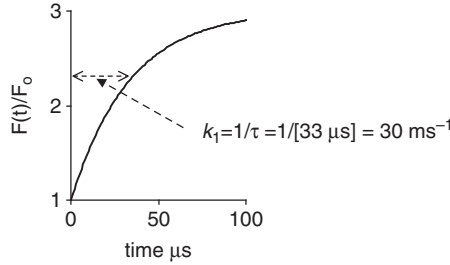


Fig. 6.2. **Upper section.** Reaction scheme of transfer of open RC via donor side quenched state y_1 [$Y_z^+ P$ Phe Q_A^-] to semi closed de-quenched state y_2 [$Y_z P$ Phe Q_A^-] under conditions at which Q_A^- reoxidation is negligible. **Middle section.** Analytical solution for variable fluorescence $F(t)$ dictated by solution of ODEs of $y_0 \rightarrow y_1 \rightarrow y_2$ reaction pattern and with F_m equal to the F level (amplitude) in an STF. **Graph.** $F(t)$ response calculated with equation for ultra short STF excitation with $k_L = 10^9 \text{ ms}^{-1}$ and $F_m/F_0 \sim 3$

than the rate constants of the primary electron transfer reactions (for survey see Dau, 1994; Vredenberg, 2004; Zhu et al., 2005). With k_L in the range between 1 and 5 ms^{-1} , each turnover excitation will take about 0.2–1 ms. This means that for these conditions with $k_L \ll k_e < k_t$ and with $\Phi_{tr}^o (=k_e/(k_e + k_{-1}) \sim 1$, and assuming that the major fraction of RCs is in S_1 state, the reaction pattern $y_0 \rightarrow y_0^* \rightarrow y_0^{RP} \rightarrow y_0^{P+} \rightarrow y_1 \rightarrow y_2$ (see Fig. 6.1) can be represented by a scheme $y_0 \rightarrow y_1 \rightarrow y_2$ with rate constants k_L and k_{s1} for the first and second step, respectively (Fig. 6.2). The three ODEs for each of the reaction partners in the scheme are: $\frac{dy_0}{dt} = -k_L y_0$, $\frac{dy_1}{dt} = k_L y_0 - k_{s1} y_1$, and $\frac{dy_2}{dt} = k_{s1} y_1$.

E. Analytical Functions of Variable Fluorescence Kinetics

The rate equations of variable fluorescence (Section II.D) give the following analytical solution (for an extensive derivation see Trissl (2002) and Vredenberg (2004)):

$$y_0(t) = e^{-k_L t}, \quad (6.1)$$

$$y_1(t) = \frac{k_L}{k_{s1} - k_L} (e^{-k_L t} - e^{-k_{s1} t}), \quad (6.2)$$

$$y_2(t) = 1 - \frac{k_{s1}}{k_{s1} - k_L} e^{-k_L t} + \frac{k_L}{k_{s1} - k_L} e^{-k_{s1} t}. \quad (6.3)$$

The same scheme and set of equations hold if the electron trapping efficiency $\Phi_{tr}^o < 1$. In that case, the $y_0 \rightarrow y_1$ transition occurs with an attenuated rate constant $k_L^* = \Phi_{tr}^o k_L$.

The $y_0 \rightarrow y_1 \rightarrow y_2$ reaction scheme (Fig. 6.2) represents the transfer of the fraction of open RCs at $t=0$ ($y_0 = 1$) to the combined fractions ($y_1 + y_2 = 1 - y_0$) of RCs in which acceptor side (Q_A) quenching is released and finally to the fraction y_2 in which acceptor and donor side (Q_A , P^+ and Y_z^+) quenching is released.

The fraction q^{dsq} of RCs in which the acceptor- and donor side quenching is released is equal to

$$q^{dsq}(t) = \frac{y_2}{y_0 + y_1 + y_2} = y_2(t) \text{ (see Eq. 6.3).} \quad (6.4)$$

This is different from the fraction q of ‘closed’ RCs in which only the acceptor side quenching is released, i.e. with Q_A^-

$$q(t) = \frac{y_1 + y_2}{y_0 + y_1 + y_2} = 1 - y_0(t) \\ = 1 - e^{-k_L t} \text{ (see Eq. 6.1).} \quad (6.5)$$

If it is assumed, based on evidence discussed earlier, that the fluorescence yield in $y_1 (= [Y^+_Z \text{ P Phe } Q_A^-])$ remains equal to that of y_0 due to effective DSQ, we can express the fluorescence induction curve as the sum of the contributions of the fractions $y_0(t) + y_1(t) [= 1 - q^{\text{dsq}}(t)]$ and $y_2(t) [= q^{\text{dsq}}(t)]$. One obtains for the normalized fluorescence induction curve $F(t)/F_0$, after substituting $F(t) = [1 - q^{\text{dsq}}(t)] \cdot F_0 + q^{\text{dsq}}(t) \cdot F_m$.

$$\frac{F(t)}{F_0} = 1 + \left(\frac{F_m}{F_0} - 1 \right) \cdot q^{\text{dsq}}(t) \\ = 1 + nF_v \cdot q^{\text{dsq}}(t), \quad (6.6)$$

in which $nF_v (= \frac{F_m}{F_0} - 1)$ is the normalized variable fluorescence.

Incorporation of donor side quenching thus leads to the conclusion that the relative variable fluorescence $rF_v (= y_2)$, in contrast to being linear to the fraction q^{dsq} of RCs in which quenching is released (Eq. 6.4), is non-linearly related to the fraction $q (= y_1 + y_2)$ of closed (Q_A^- -containing) RCs. A non-linear relation between rF_v and the fraction q of closed (Q_A^- -containing) RCs, which is commonly found for experimental $F(t)$ curves measured in the presence of the PS II acceptor side inhibitor DCMU, is routinely interpreted as an indicator and illustration of intersystem energy transfer (connectivity) between PS II units (e.g. Strasser, 1978; Lavergne and Trissl, 1995). Vredenberg (2008b) has presented a different and alternate analysis of these two fundamentally different rF_v versus q relationships and the likelihood that the contribution of connectivity between PSUs to the apparent non-linearity between normalized variable fluorescence and the fraction of closed RCs is small, if not negligible.

III. Application of Single, Twin and Multiple Turnover Flashes

We have applied and studied the fluorescence response upon what we call ‘twin’ single turnover flashes ($T_{\Delta t}\text{TF}$). A $T_{\Delta t}\text{TF}$, or in shorthand notation TTF (twin), is composed of two identical STFs (STF_1 and STF_2) which are separated by a dark time interval Δt (in microsecond) in the range between 10 and 500 μs . The idea behind application of TTFs is the following. STF_1 (i.e. the first partner of the twin) causes single reduction of the acceptor pair [$\text{Phe}Q_A$] associated with a change in fluorescence with amplitude $F_m^{\text{STF}} (\sim 3F_0)$. The second twin partner STF_2 is meant to reach the RC when its acceptor pair is still partly reduced, i.e. with a fraction in state [$\text{Phe}Q_A^-$]. As the reoxidation of Q_A^- is known to occur in the range of $\sim 250\text{--}500 \mu\text{s}$, nearly 100% Q_A^- is present if STF_2 is fired within 10–50 μs after STF_1 . STF_2 of $T_{10}\text{TF}$ (or $T_{20}\text{TF}$) then might cause a double reduction of the acceptor pair, resulting in [$\text{Phe}^-Q_A^-$] or [$\text{Phe}Q_A$] $^{2-}$. Depending on its actual life time, the double reduction by $T_{\Delta t}\text{TF}$ is expected to be associated with a further increase in F_m with $\Delta F_m = F_m^{\text{TTF}} - F_m^{\text{STF}} (= F_m^{\text{STF}_2} - F_m^{\text{STF}_1})$. An increase of this kind has been shown for a second STF in the presence of DCMU (Vredenberg et al., 2006; Fig. 6.3). The term ‘twin’ ($T_{\Delta t}\text{TF}$) is restricted here, unless indicated otherwise, for two subsequent STFs

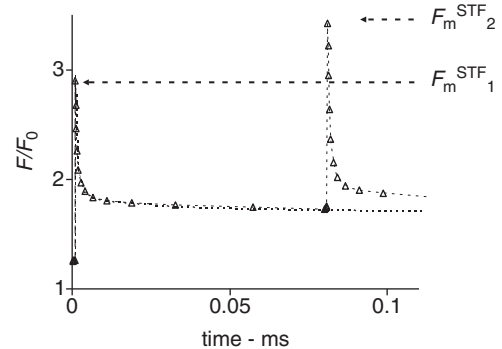


Fig. 6.3. Chlorophyll a fluorescence response, $F(t)$, of 10 min dark adapted pea chloroplasts in the 30 μs to 110 ms linear time range to a 12.5 Hz train of one and two single turnover flashes, STFs (35 μs duration) plotted relative to the fluorescence $F_0 (=1)$ at the onset of the first flash. F_m^{STF} is the maximum F level after each STF

with $\Delta t < 500 \mu\text{s}$. In the other cases they form elements of a train of STFs. Exponential decomposition and quadratic least square fitting of the fluorescence decay have been done (see Vredenberg et al., 2006) with standard routines provided by appropriate software (MathCad 13, MathSoft Inc. Cambridge, MA).

A. Fluorescence Kinetics upon Single and Twin Turnover Excitation

Figures 6.3 and 6.4 show, for a dark adapted thylakoid preparation isolated from fresh pea leaves, the release (upward moving trace) and dark recovery of chlorophyll fluorescence quenching in the first 2 STFs (Fig. 6.3) of a 12.5 Hz train (i.e., with dark interval 80 ms) and in addition (Fig. 6.4) upon a solitary twin-single turnover flash ($T_{50}\text{TF}$). The first STF in the train (STF_1), and identical to the first partner of the twin, causes a fluorescence increase with maximum $F_m^{\text{STF}_1} \sim 2.9$ (relative to $F_0 = 1$). This value agrees with single turnover F_m values reported for a variety of plant chloroplasts and algae (Samson and Bruce, 1996; Koblizek et al., 2001; Vredenberg et al., 2005). The second STF (STF_2) causes an increase towards $F_m^{\text{STF}_2} \sim 3.4$. Both

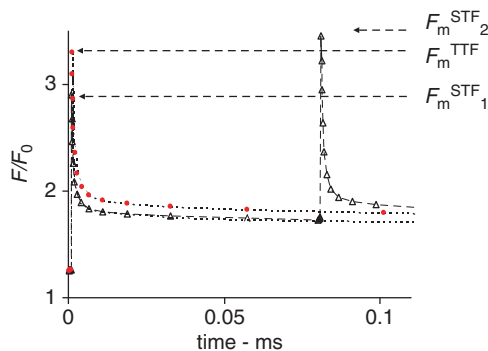


Fig. 6.4. Chlorophyll *a* fluorescence response, $F(t)$, of dark-adapted pea chloroplasts to a 12.5 Hz train of one and two STFs ($35 \mu\text{s}$ duration, open triangles) and to a twin turnover flash ($T_{50}\text{TF}$, small solid circles and dashes), plotted relative to the fluorescence $F_0 (=1)$ at the onset of the first flash. F_m^{TTF} is the maximum F level after twin turnover flash (TTF) excitation. The first partner (STF_1) of the $T_{50}\text{TF}$ (twin) is identical to the first STF in the train, the second partner (STF_2) is fired $50 \mu\text{s}$ after STF_1

STFs induce a variable fluorescence F_v^{STF} of comparable and nearly identical size.

The $T_{50}\text{TF}$ (twin), as shown in Fig. 6.4, induces a fluorescence increase with, for the present experiment, a maximum $F_m^{\text{T}_{50}\text{TF}} \sim 3.3 F_0$, which is $\sim 15\%$ above $F_m^{\text{STF}_1}$, but a little lower than $F_m^{\text{T}_{50}\text{TF}}$. The difference between the maximal fluorescence in $T_{\Delta t}\text{TF}$ – and STF-excitation is defined as the increase in variable fluorescence $\Delta F_v = \Delta F_m = F_m^{\text{T}_{\Delta t}\text{TF}} - F_v^{\text{STF}}$; it is caused by a TTF in dark adapted chloroplasts ($\sim 3.3 F_0$). Further, different chloroplast preparations show that $F_m^{\text{STF}_2}$ (in a train) is greater than $F_m^{\text{T}_{\Delta t}\text{TF}}$. This suggests that the response of the fraction of Q_B -reducing (‘normal’) RCs is higher in the second of the first two subsequent STFs in a train. This is in agreement with the documented binary oscillation of fluorescence associated with the two-electron gate mechanism at the acceptor side of PS II (Bowes and Crofts, 1980; Shinkarev and Govindjee, 1993; Shinkarev, 2004).

The dark recovery of the quenching after an STF has been shown to be multiphasic with a F(aster) and a S(lower) phase in the time domain before and after about 10 ms, respectively. The recovery period, as shown by many others, extends over more than 4 decades (Urban et al., 1999; Roberts et al., 2003; Steffen et al., 2005; Belyaeva et al., 2006, 2008; Vredenberg et al., 2006). A S(lower) phase which proceeds far in the minute range has been attributed to the recovery (re-oxidation) of single reduced (Q_A^- -containing) RCs in the variable β -fraction with Q_B nonreducing RCs (Vredenberg et al., 2007). The bi-exponential quenching recovery pattern after STF- and TTF-excitation during the so-called F phase in the $10 \mu\text{s}$ to 5 ms range is shown in Figs 6.5 and 6.6. A major part of the STF-induced variable fluorescence, as shown in Fig. 6.5, recovers with a rate constant $k_{AB} \sim 4 \text{ ms}^{-1}$ and has been attributed to reoxidation of single reduced ‘normal’ RCs in the so-called (1- β)-fraction. The increment in response, caused by TTF-excitation, recovers with a rate constant $k_{2AB} \sim 0.5 \text{ ms}^{-1}$ (Fig. 6.6) and has been attributed to generation and reoxidation of double reduced (with $[\text{PheQ}_A]^{2-}$) Q_B nonreducing RCs (Vredenberg et al., 2006, 2007) which populate the complementary β -fraction.

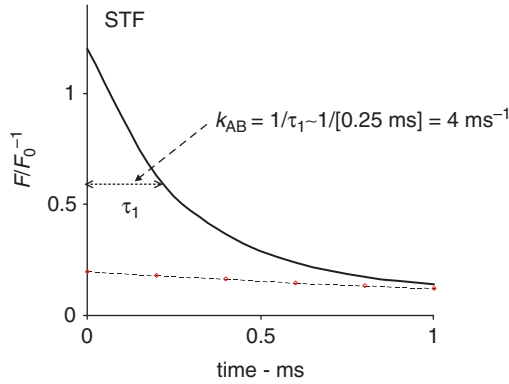


Fig. 6.5. Exponential recovery (decay) of the major component of the F(aster)-phase of the STF induced release of chlorophyll fluorescence quenching in dark adapted pea thylakoids, with a relaxation time τ_1 of $\sim 250 \mu\text{s}$

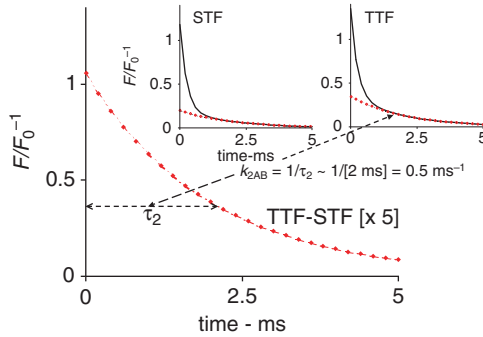


Fig. 6.6. Exponential recovery (decay) of the TTF-induced increment in fluorescence quenching in dark adapted pea thylakoids, with a relaxation time τ_2 of $\sim 2 \text{ ms}$. Inserts show the F phase of the STF- and TTF-induced $F(t)$ responses

B. Excitation with Single Turnover Flash Train

Figure 6.7 illustrates, in the 0.01–500 ms logarithmic range, the $F(t)$ response of a 5 min dark adapted chloroplast preparation in a 12.5 Hz (small open diamonds) and a 4 kHz (closed diamonds) train of 5 and 20 STF's, respectively. The curve in the 4 kHz train shows for the first flash $F_m^{\text{STF}_1} \sim 3F_0$, i.e. a normalized variable fluorescence $nF_v \sim 2$. F_m is increased in the first flashes with a maximum reached at the third flash (STF₃) of the train with, for this preparation, $F_m^{\text{STF}_3} \sim 3.6F_0$. The $\sim 20\%$ increase in F_m above $F_m^{\text{STF}_1}$ is transient and declines in the next 2 ms of 6–8 STF excitations in a 4 kHz flash train,

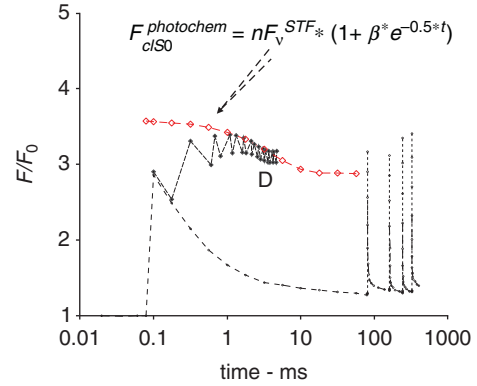


Fig. 6.7. Chlorophyll *a* fluorescence response to the first STF's in a 12.5 Hz (small open diamonds) and a 4 kHz (closed diamonds) flash train on a logarithmic time scale. The curve $F_{\text{cISO}}^{\text{photochem}}(t) = nF_v^{\text{STF}} \cdot (1 + \beta \cdot e^{-0.5t})$ (see Section III.B) with open diamonds is the fit of decay of the $F(t)$ transient in the 0–2 ms time range, with $nF_v^{\text{STF}} \sim 2$

reaching a dip D about 3 ms after the onset of the flash train. The response in the 12.5 Hz train shows part of the amply documented periodicities (Shinkarev, 2004; Vredenberg et al., 2007). The increase in F_m^{STF} in the high frequency train is, like we have shown for TTF excitation (Figs. 6.3–6.6), caused by electron trapping in a β -fraction populated with Q_B non reducing RCs. The transient decline in F_m^{STF} is likely to be caused by reoxidation of the double reduced acceptor pair in the Q_B nonreducing RCs of the β -fraction. We have seen (Vredenberg et al., 2006, 2007) that this reduction occurs with a rate constant in the range between $0.4\text{--}0.2 \text{ ms}^{-1}$, i.e. in the 2.5–5 ms time range (Fig. 6.7). The curve with open diamonds (Fig. 6.7) designated with

$$F_{\text{cISO}}^{\text{photochem}} = nF_v^{\text{STF}} (1 + \beta e^{-k_{2AB}t})$$

is the one simulated for the re-oxidation, with $k_{2AB} = 0.5 \text{ ms}^{-1}$, of double reduced RCs in a 30% β -fraction with $nF_v = 2$. Figure 6.8 shows the $F(t)$ response to a 4 kHz flash train in the 0–15 ms range. It shows, after the transient response during the initial 3 ms STF-excitation period, a gradual rise in F_m with, for a 1 kHz train (not shown, but see Figs. 5 and 6 in Vredenberg et al., 2007), a saturation level $F_m^{\text{STF}_{60}} \sim 5F_0$. The rise in the 3–60 ms time range (Vredenberg et al., 2007) has been found to be independent of the frequency of STF trains in the 1–4 kHz

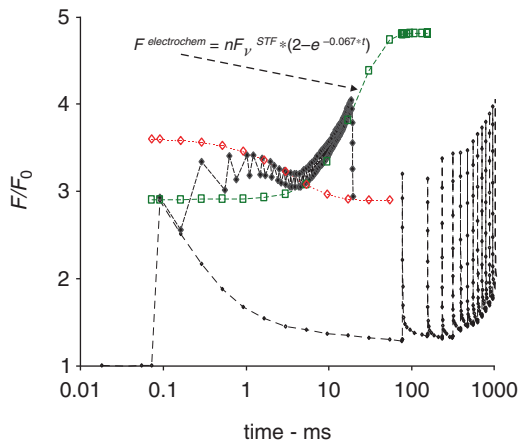


Fig. 6.8. See the legend of Fig. 6.7 for description, but here it is for 4 kHz train with a larger number of STFs extending into the 15 ms time range. The curve $F^{\text{electrochem}}(t) = nF_v^{\text{STF}} \cdot (2 - \beta \cdot e^{-0.067t})$ (see Section III.B) with open squares is the fit of increase in the $F(t)$ towards $F_m \sim 5F_0$, with $nF_v^{\text{STF}} \sim 2$, and attributed to accumulation of Q_B non-reducing RCs (Vredenberg et al., 2006)

range. Vredenberg et al. (2006) have shown that the STF-induced rise in the 3–60 ms time range is due to quenching release associated with double reduction of accumulating single reduced Q_B non-reducing RCs. It can be simulated (Fig. 6.8, curve with open squares) with an exponential function

$$\frac{F(t)}{F_0} = nF_v^{\text{STF}} \cdot (2 - e^{-k_{\text{qbf}}t}),$$

with $nF_v^{\text{STF}} \sim 2$ and $k_{\text{qbf}} \sim 0.067 \text{ ms}^{-1}$. This suggests that, in coarse approximation, the triggering reaction occurs with a turnover relaxation time of $\sim 15 \text{ ms}$ and leads, in agreement with earlier conclusion, to an approximate doubling of the variable fluorescence.

IV. Distinguishable Phases of Fluorescence Response upon Multiturnover Excitation

A. Photochemical OJD Phase in the 0–2.5 ms Time Range

The outcome of analyses of the STF and TTF induced responses and of the $F(t)$ pattern in high frequency STF trains in the 0–2.5 ms time range

allows the derivation of the equations for the components of the $F(t)$ response in this time range during MTF excitation caused by electron trapping events upon single and double hits in the S_1 and S_0 fraction.

1. Single Hit Excitation in β -(S_0) and $(1-\beta)$ -(S_1) Fraction

The reaction pattern in MTF excitation can be represented by a scheme $y_0 \rightarrow y_1 \rightarrow y_2$ and its reverse $y_2 \rightarrow y_0$ with rate constants k_L , k_1 and k_{AB} for the first, second and reverse step, respectively. k_L , k_1 and k_{AB} are rate constants of excitation, release of donor side quenching, and the average rate constant of Q_A^- reoxidation by Q_B or Q_B^- , respectively. The use of k_L as a time-independent rate constant implies that the PSUs operate independently from each other (separate units without connectivity); y_0 , y_1 and y_2 refer to the dark-adapted ‘open’-, the donor-side quenched- (with Y_Z^+ and Q_A^-), and the ‘de-quenched’ (semi-closed) state with Y_Z and Q_A^- , respectively (see Fig. 6.1, except for the reverse reaction). We assume, for simplicity, that the rate constant of the donor side quenching release is independent of the actual S-state during the progressing MTF excitation. Equation (6.1), which is the analytical solution of the rate equations for $k_L < k_1$, gives in approximation the variable fluorescence $F_v(t)$ associated with the reaction above

$$F_{\text{vs1}}^{\text{sc}}(t) = (1 - \beta) \cdot nF_v \cdot q^{\text{dsq}}(t) \cdot \frac{k_L}{k_L + k_{AB}}, \quad (6.7)$$

in which

$$q^{\text{dsq}} = 1 - \frac{k_1}{k_1 - k_L} e^{-k_L t} + \frac{k_L}{k_1 - k_L} e^{-k_1 t}$$

is the fraction of RCs wherein, at time t , acceptor (Q_A) and donor side quenching (Y_Z^+) has been released (Vredenberg, 2008a; see also Fig. 6.2).

As the β fraction (S_0) is populated with Q_B nonreducing RCs, the equation of its $nF_v(t)$ response is identical to Eq. (6.7) except for the substitution $k_{AB} = 0$ and the size of the fraction which gives Eq. (6.7a):

$$F_{\text{vs0}}^{\text{sc}}(t) = \beta \cdot nF_v \cdot q^{\text{dsq}}(t). \quad (6.7a)$$

2. Double Hit Excitation in β -(S_0) Fraction

The β fraction, because of being populated with Q_B nonreducing RCs, is susceptible to a trapping-competent double excitation. The reduction of this (single reduced) fraction will occur with reduced efficiency Φ because of rate limitation by the low rate of P^+ reduction when the OEC is in state S_0 (for explanation, see Vredenberg, 2004, p. 160, Fig. 14). The fraction q^c of single reduced (semi-closed) RCs in which quenching becomes released after double reduction of the acceptor pair [Ph Q_A] (closure) is

$$q^c(t) = 1 - \frac{k_1}{k_1 + \phi k_L} e^{-\phi k_L t} + \frac{\phi k_L}{k_1 + \phi k_L} e^{-k_1 t}, \quad (6.7b)$$

which, with $\phi k_L \ll k_1$, can be approximated with $q^c(t) = 1 - e^{-\phi k_L t}$. Thus the reduction of a $\beta q^{\text{dsq}}(t)$ fraction of single reduced S_0 RCs will yield a fraction $q^{2\text{dsq}}(t) = \beta q^{\text{dsq}}(t) q^c(t)$ of RCs with a double reduced acceptor pair. The recovery of this fraction (i.e. the re-oxidation of the double reduced acceptor pair) occurs (Figs. 6.5 and 6.6) with rate constant k_{2AB} (Vredenberg et al., 2007). The normalized variable fluorescence associated with the second excitation is

$$F_{\text{vs}0}^{\text{cl}}(t) = \beta \cdot nF_v \cdot q^{\text{dsq}}(t) \cdot (1 - e^{-\phi k_L t}) \cdot e^{-k_{2AB} t}. \quad (6.8)$$

The photochemical component of the $F(t)$ curve in the 0–2.5 ms time range defined as $F^{\text{photochem}}(t)$ is obtained by summation of Eqs. (6.7), (6.7a) and (6.8) which, after appropriate substitution, gives Eq. (6.9).

$$F^{\text{photochem}}(t) = 1 + nF_v \cdot q^{\text{dsq}}(t) \cdot \left[(1 - \beta) \cdot \frac{k_L}{k_L + k_{AB}} + \beta \cdot (1 + q^{\text{dsq}}(t)) \cdot (1 - e^{-\phi k_L t}) \cdot e^{-k_{2AB} t} \right]. \quad (6.9)$$

The graphs of $F^{\text{photochem}}(t)$ and its components (Eqs. 6.7, 6.7a and 6.8) in the 0–1 s time range are shown in Fig. 6.9. The individual curves are labeled with the equation numbers. $F^{\text{photochem}}(t)$ appears to give a nice coverage of the initial stage of the experimental OJD phase of the

fluorescence induction curve, in the 0–0.5 ms time range.

B. Photo-electrochemical (J)DI Phase in the 2–50 ms Time Range

$F(t)$ responses of thylakoids to low (10 Hz) and high frequency (1–4 kHz) STF trains have shown that the transient OJD response in the 0–3 ms time range is followed by an exponential rise towards a saturation level corresponding to an approximate doubling of the normalized variable fluorescence (Vredenberg et al., 2006, 2007). This rise was found to be sensitive to membrane modifying agents as it was fully inhibited by the protonophore carbonyl cyanide p-trifluoromethoxyphenylhydrazone (FCCP) (Vredenberg et al., 2006). Because of its protonophoretic sensitivity, the fluorescence rise has been attributed to photo-electrochemically-driven accumulation and double reduction of the

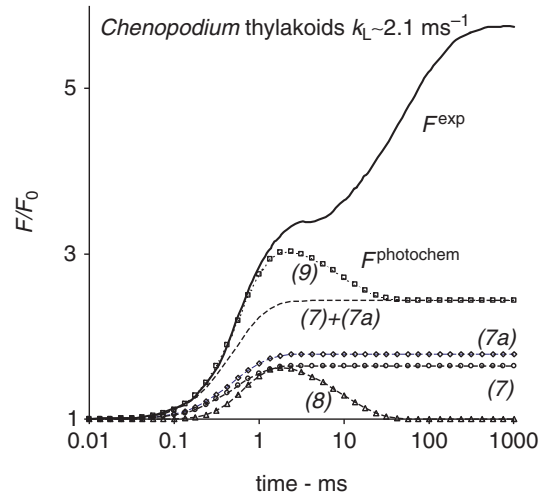


Fig. 6.9. Chlorophyll *a* fluorescence induction curve of 10 min dark-adapted thylakoids isolated from *Chenopodium album* upon 1 s multi-turnover flashes, MTF, excitation plotted on a log time scale (solid line). Graphs of the photochemical (OJD) phase $F^{\text{photochem}}$ and its constituting components calculated with elements of the fluorescence induction algorithm FIA (Eqs. 6.7–6.9) for matching F^{exp} in the 0–0.5 ms time range are shown; matching parameters are given in the third column of Table 6.1 (symbols). Constituting components are labeled with number of their corresponding equation (see text). The dotted curve [(7) + (7a)] represents $F^{\text{photochem}}$ in the absence of double reduction in the S_0 (β) fraction

acceptor pair in Q_B nonreducing RCs. The rate constant of the rise which is designated with k_{qbf} was found to be invariable in the 1–4 kHz frequency range with $k_{qbf} \sim 0.07 \text{ ms}^{-1}$. The normalized variable fluorescence associated with the electrochemical events in the 2–50 ms time range is approximated with

$$F^{\text{photoelectrochem}} = nF_v \cdot \left[1 - e^{-k_{qbf}t} \cdot \sum_{m=0}^N \frac{(k_{qbf}t)^m}{m!} \right] \cdot (1 - \beta). \quad (6.10)$$

Here N is an integer with $0 \leq N \leq 2$. Usually $N=0$ but under some conditions $1 \leq N \leq 2$ offers a better fit for the delay in and steepness of the J(D)I rise in the experimental curve. N cannot as yet be given a physiological meaning, but presumably, it is connected with the number of precursors in the onset of the Q-cycle proton pump (Vredenberg et al., 1998) and consequently with their effect on the kinetics (see below and Eq. (6.11), and for a perspective on Q-cycle, see Crofts, 2005).

C. Phase IP in the 50–200 ms Time Range

The maximal fluorescence level in the OJDIP induction curve upon MTF excitation is reached at the end of the IP phase in the 50–200 ms range. This phase is seen, in particular in intact leaves (Vredenberg, 2000; Schansker et al., 2006), as the final fluorescence rise starting from a stationary I-level at the end of the photo-electrochemical JDI phase in the OJDIP fluorescence transient. In thylakoids, the IP phase is in continuum with the JDI phase, except in the presence of some electron donors of PS I (Bukhov et al., 2003; Joly and Carpentier, 2007). For a variety of taxonomic different plant species (leaves) it appears that the experimental IP phase can be fitted with an analytical function $F_{IP}(t)$ with

$$F^{IP}(t) = A^{IP} \cdot \left[1 - e^{-k_{IP}t} \cdot \sum_{m=0}^{NN} \frac{(k_{IP}t)^m}{m!} \right], \quad (6.11)$$

in which A^{IP} and k_{IP} are amplitude and rate constant of $F^{IP}(t)$ (i.e. IP phase) and NN is an integer with $NN \leq 1$ for thylakoids and $5 \leq NN \leq 10$ for intact leaves. Equation (6.11) is derived from the analytical solution of a set of ODEs which describes the response of each state (z_j)

in a hypothetical chain of NN identical transfer steps (with rate constant k_{IP} and amplitude A^{IP}) $z_{j-1} \rightarrow z_j$ with $1 \leq j \leq NN$ (Walas, 1991, p. 387). This gives $z_N(t) = F^{IP}(t)$ of Eq. (6.11). This ‘best’ mathematical description of the IP phase, given by Eq. (6.11), hints to a mechanism in which a signal is propagated via a number (NN) of approximately identical transfer steps from a distantly located generation site to a responsive target. Equation (6.11) points to and describes quantitatively the delay and steepness of the IP phase. The difference in NN -value in intact leaf (cells) and thylakoids then would point to structural differences in the respective propagation pathways of the signal leading to the response. It can easily be seen from graphical representations of Eq. (6.11) that the delay time and steepness of this function increases with NN (not shown).

V. Fluorescence Induction Algorithm for Experimental Curves

The algorithm for the *in silico* $F^{FIA}(t)$ simulation of OJDIP fluorescence induction curves in MTF excitation in the 0–1 s time range is obtained after summation of Eqs. (6.9), (6.10) and (6.11). This gives $F^{FIA}(t) = F^{\text{photochem}}(t) + F^{\text{electrochem}}(t) + F^{IP}(t)$.

A. Dark-adapted Thylakoids

Figure 6.10 shows the $F^{FIA}(t)$ curve and its components obtained after application of a dedicated software routine in Mathcad (Mathcad13) which calculates the parameter values (vector) for which the least mean square function $\left[\sum_{n=1}^{NN} \{OJDIP_n - F^{FIA}(t_n)\}^2 \right]^{1/2}$ is minimal, where $OJDIP_n$ refers to the experimental data point at $t = t_n$, and NN is the number of data points (in our experiments $NN = 85$). The function in our cases gave a minimum value of less than 0.1. The fit parameters are given in the third column of Table 6.1.

Similarly, we can use the downloadable GOSA package (Global Optimization Simulation Annealing, (<http://www.bio-log.biz>; see the GOSA library Biophysics- Photosynthesis- Fluorescence- OJDIPAlgorithm). An example of the GOSA-fit for the experiment of Fig. 6.10 is

Table 6.1. Kinetics parameters (rate constants, amplitudes and fractions; see Abbreviations on p. 127) for the closest fit $F^{\text{FIA}}(t)$, using the fluorescence induction algorithm (FIA, Eq. 6.6), with the experimental OJDIP fluorescence induction curve $F(t)$ for the same thylakoid preparation (*Chenopodium*) under particular conditions (n.r. = not reported)

		Control	After 1 or 2 STFs	Control + DCMU
Rate constants (ms^{-1})				
Light excitation	k_L	2.1	2.6	3.3
Quenching release	k_1 (or k_{dsq})	8.3	13	16
Q_A^- reoxidation	k_{AB}	1.1	2.8	0
$[\text{Phe } Q_A]^{2-}$ reoxidation	k_{2AB}	0.1	n.r.	$<10^{-5}$
J(D)I rise	k_{nqb}	0.05	0.07	n.r.
IP rise	k_{IP}	0.02	0.02	n.r.
Amplitudes				
Normalized variable fluorescence	nF_v	2.1	2.2	2.1
IP rise	A^{IP}	1.1	1.4	n.r.
F_0 -offset	$F(0) - F_0$	0	0.15	0.6
Fractions				
S_0 fraction	β	0.31	0	0.3

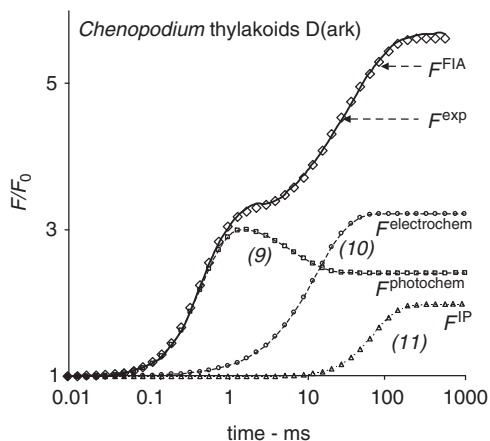


Fig. 6.10. Chlorophyll *a* fluorescence induction curve F^{exp} (solid line, same as Fig. 6.9) of *Chenopodium album* (Latin in italics) thylakoids and the graphs of the curve F^{FIA} (diamonds) calculated with the algorithm for matching with F^{exp} in the 0–1 s time range. The labels refer to the number of their corresponding equation (see text). Fit parameters are given in the third column of Table 6.1 and were calculated using GOSA (www.bio-log.biz)

shown in Fig. 6.11. There is a good fit between the experimental OJDIP and the $F^{\text{FIA}}(t)$ curve. Moreover the fit parameters, in particular those of $F^{\text{photochem}}(t)$, are in the range in which they usually are found. This adds to arguments that the $F^{\text{FIA}}(t)$ curve, with its determinant parameters, is a close representation and quantitative description of the events that give rise to the fluorescence induction curve upon MTF excitation under the given conditions.

B. STF Pre-excited Thylakoids

Figure 6.12 shows the complete $F^{\text{FIA}}(t)$ curve for the MTF-induced $F(t)$ response (solid curve) measured shortly after pre-excitation with two STFs. Table 6.1 (fourth column) shows the parameters. These data show and confirm similar experiments with intact leaves and thylakoids of other origin (Vredenberg, 2000, 2004) that pre-excitation with one or two STFs causes a drastic change in the $F(t)$ kinetic pattern in the 0–20 ms time range. Comparison of Figs. 6.10 and 6.12, and third and fourth columns of Table 6.1 illustrate that the major effect of STF pre-excitation is on the photochemical component $F^{\text{photochem}}(t)$ of the experimental OJDIP fluorescence curve and that this is nearly exclusively due to disappearance (absence) of the double-reducible β -fraction (S_0) with Q_B nonreducible RCs, reflected by $\beta = 0$. This is what we expected. Pre-excitation with one STF will shift, ignoring double- and miss hits, the original S_0/S_1 heterogeneity to an S_1/S_2 heterogeneity. Furthermore, it confirms an earlier conclusion, introduced here as an assumption, that the electron trapping efficiency in single reduced Q_B reducible RCs with the donor side in states S_1 , S_2 , or S_3 is negligible (Vredenberg et al., 2007). The small offset $F(0)$ ($> F_0 = 1$) in the curve after STF pre-excitation points to the presence of a small residual fraction of (semi-closed) RCs with Q_A^- .

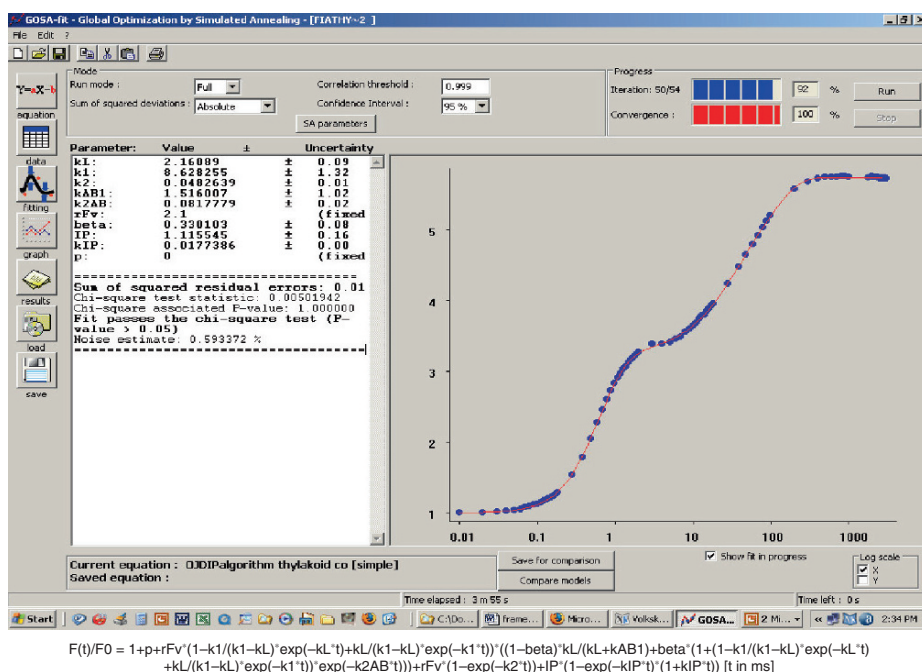


Fig. 6.11. Display of the curve fitting procedure, using global optimization simulation annealing (GOSA) with equation derived after summation of Eqs. (6.9–6.11) (bottom line). Symbols are experimental points, line is the simulated curve. Note that the fit was obtained after an about 4 min iteration time. See also Color Plates, Fig. 1

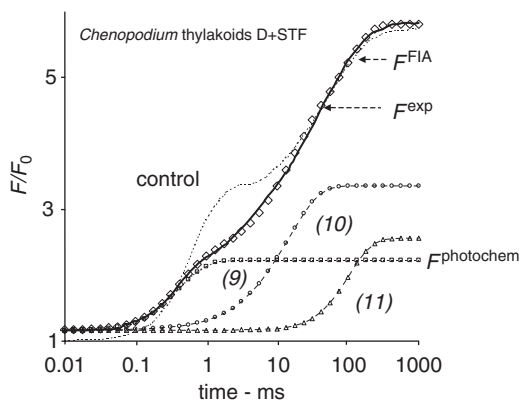


Fig. 6.12. Chlorophyll *a* fluorescence induction curve of the same preparation of *Chenopodium album* (Latin in italics) thylakoids as used in Figs. 6.10 and 6.11, but measured in MTF excitation shortly (<30 s) after pre-excitation with two STFs of 10 min dark-adapted thylakoids (solid line). The dotted curve is the experimental curve measured in the dark-adapted control (see Figs. 6.10 and 6.11). Graphs of F^{FIA} (diamonds) calculated with the algorithm for matching with F^{exp} in the 0–1 s time range, and its constituting components $F^{photochem}$ (Eq. 6.9), $F^{electrochem}$ (Eq. 6.10) and F^{IP} (Eq. 6.11); matching parameters are given in the fourth column of Table 6.1. Note the substantial difference in the kinetic profile of $F^{photochem}$ as compared to that in Fig. 6.10

C. Dark-adapted Thylakoids in the Presence of Diuron

Figure 6.13 (solid line) shows the $F(t)$ curve, of the same thylakoid preparation as in Figs. 6.10 and 6.12, in the presence of 20 μ M DCMU (known as Diuron). Ample evidence has been given (Hiraki et al., 2003) that DCMU addition in the dark to 5–30 min dark-adapted thylakoids causes (i) inhibition of Q_A^- reoxidation after excitation ($k_{AB} = 0$); (ii) inhibition of IP phase; (iii) shift (decrease) in equilibrium constant of reaction $Q_A^-/Q_B \leftrightarrow Q_{A/Q_B}^-$ in $S_0(\beta)$ fraction with associated rise of initial $F(t)$ level $F(0)$. This means that in relation to the algorithm, in the presence of DCMU, we have: (1) $F_{dcmu}^{electrochem}(t) = F_{dcmu}^{IP}(t) = 0$; (2) the $(1 - \beta)$ (or S_1) fraction is transferred into one with Q_B nonreducing RCs, and consequently it has become susceptible to double reduction of the acceptor pair [PhQ_A]; (3) the double reducible β fraction (S_0) is converted into the reduced (semi-closed) state; and (4) a shift of $F(0)$ has occurred towards $F_{dcmu}(0)$ with $F_{dcmu}(0) - F_0 = \beta \cdot nF_V$.

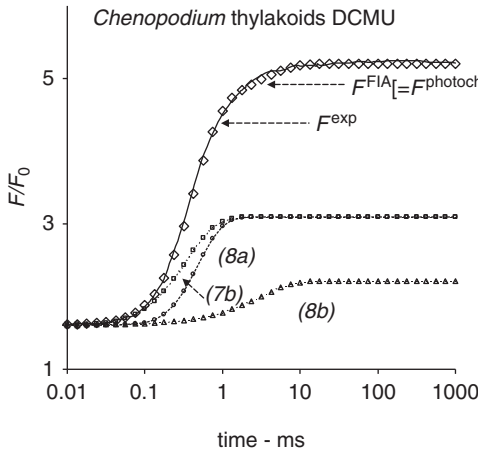


Fig. 6.13. Chlorophyll *a* fluorescence induction curve of the same preparation as used in Fig. 6.10 but measured now in MTF excitation shortly (<30 s) after addition, in the dark, of 20 μ M DCMU to 10 min dark-adapted thylakoids at a final concentration of 20 μ M (solid line). Graphs of F^{FIA} (diamonds) calculated with the algorithm for matching with F^{exp} in the 0–1 s time range, and the constituting components of $F^{photochem}$ (Eqs. 6.7b, 6.8a, 6.8b); matching parameters are given in the fifth column of Table 6.1. Note the relatively slow reduction (closure) of the reduced (semi-closed) $S_0(\beta)$ fraction

This results in modifications of Eqs. (6.7), (6.7a) and (6.8) into (6.7b), (6.8a) and (6.8b), respectively, as follows:

$$F_{vs1dcmu}^{sc}(t) = (1 - \beta) \cdot nF_v \cdot q^{dsq}(t), \quad (6.7b)$$

$$F_{vs1dcmu}^{cl}(t) = (1 - \beta) \cdot nF_v \cdot [q^{dsq}(t)]^2 \cdot e^{-k_{2AB}t}, \quad (6.8a)$$

$$F_{vs0dcmu}^{cl}(t) = \beta \cdot nF_v \cdot (1 - e^{-\phi k_L t}) \cdot e^{-k_{2AB}t}, \quad (6.8b)$$

in which ϕ is the electron trapping efficiency in the S_0 fraction with Q_B nonreducing RCs. $F_{dcmu}^{photochem}(t)$ is obtained after summation of Eqs. (6.7b), (6.8a) and (6.8b), and with $F_{dcmu}^{FIA}(t) = F_{dcmu}^{photochem}(t)$, one gets

$$F_{dcmu}^{FIA}(t) = 1 + nF_v \cdot [(1 - \beta) \cdot q^{dsq} \cdot (1 + q^{dsq} \cdot e^{-k_{2AB}t}) + \beta \cdot \{1 + (1 - e^{-\phi k_L t}) \cdot e^{-k_{2AB}t}\}]. \quad (6.9a)$$

$F_{dcmu}^{FIA}(t)$ (Fig. 6.13, symbols) shows a close fit with the $F(t)$ curve; the fit parameters are given

in the fourth column of Table 6.1. The result is in fair agreement with those reported before for DCMU-inhibited thylakoids (Vredenberg, 2000; Hiraki et al., 2004), in particular with respect to a higher excitation rate in the presence of inhibitor. This is not surprising because FIA in this case is identical with the equations applied for the TSTM model in the presence of DCMU (Hiraki et al., 2004). It confirms the low electron trapping efficiency $\Phi_{tr}^{sc} \sim 0.1$ in reduced (semi closed) S_0 RCs giving rise to the slow component in the $F(t)$ curve in the 1–10 ms time domain. It is also noteworthy that the F_0 -offset with $F_{dcmu}(0) - F_0 = \beta \cdot nF_v$ gives nearly the same β and nF_v values as calculated with FIA for the control (Table 6.1, third and fifth columns). It indicates and confirms that the β -fraction (S_0) for the major part is populated with Q_B nonreducing RCs in which Q_B is reduced.

D. Leaf at High and Low Excitation Rates

Figures 6.10, 6.12 and 6.13 that deal with FIA-analysis of $F(t)$ curves, in thylakoids after a particular treatment, can be supplemented with those measured at varying intensities (excitation rate k_L) in thylakoids and intact leaves. Figure 6.14 (also see Table 6.2, third column) shows the experimental OJDIP fluorescence curve (solid line) and the FIA curve (or GOSA-fit) and components thereof (symbols and fit parameters

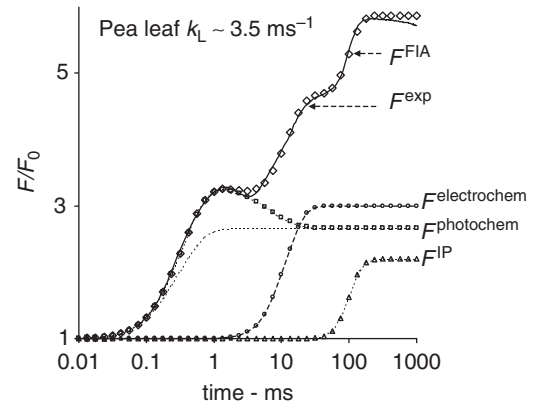


Fig. 6.14. Chlorophyll *a* fluorescence induction curve F^{exp} of 10 min dark-adapted pea leaf upon 1 s MTF excitation at maximum intensity plotted on a log time scale (solid line). Graphs of the total fit F^{FIA} , $F^{photochem}$, $F^{electrochem}$ and F^{IP} , calculated with FIA (Eqs. 6.7–6.9) for matching F^{exp} in the 0–1 s time range (symbols) are shown; matching parameters are given in the third column of Table 6.2

of a 10 min dark-adapted pea leaf measured at maximal light intensity by a Handy PEA fluorometer (Hansatech, UK), associated with $k_L = 3.6 \text{ ms}^{-1}$. The $F^{\text{electrochem}}$ and F^{FIA} are much steeper in an intact leaf than in thylakoids (compare Figs. 6.10 and 6.14). This causes, as mentioned before, the commonly found visual separation of the two phases in intact leaves. Figure 6.15 and Table 6.2 (fourth column) illustrate, for the same leaf, the curves and analyses measured at about 5% of the maximal light

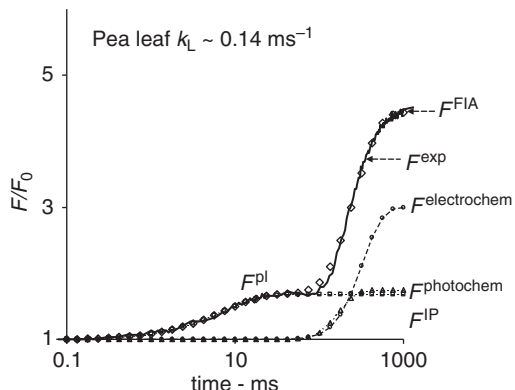


Fig. 6.15. See the legend of Fig. 6.14 for details, except that we used here 1 s MTF excitation for the same pea leaf at $\sim 4\%$ of maximal light intensity

Table 6.2. Parameters (rate constants, amplitudes and fractions) for the closest fit $F^{\text{FIA}}(t)$, using the algorithm (FIA, Eq. 6.6), with the experimental OJDIP fluorescence induction curve $F(t)$ for the same pea leaf exposed to a 1 s multi-turnover pulse of high and low intensity (n.r., not reported)

		High	Low
Rate constants (ms^{-1})			
Light excitation	k_L	3.6	0.15
Quenching release	k_1 (or k_{dsq})	20	15
Q_A^- reoxidation	k_{AB}	1.3	n.r.
$[\text{Phe } Q_A]^{2-}$ reoxidation	k_{2AB}	0.15	n.r.
J(D)I rise	k_{nqb}	0.26	0.005
IP rise	k_{IP}	0.06	0.03
Amplitudes			
Normalized variable fluorescence	nF_v	2	1.8
IP rise	A^{IP}	1.2	1.2
F_0 -offset	$F(0) - F_0$	0	0
Fractions			
S_0 fraction	β	0.37	0.35

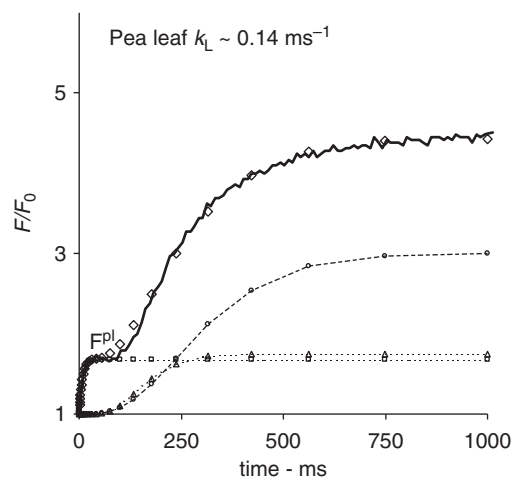


Fig. 6.16. Data of Fig. 6.15 are plotted on a linear time scale to show the plateau (F^{pl}) in $F(t)$ after 20 ms and the exponential character of the initial rise

intensity. They show and confirm, when plotted on a linear time scale (Fig. 6.16), that the photochemical component of the characteristic fluorescence curve measured at very low intensities, for instance corresponding with $k_L \sim 0.2 \text{ ms}^{-1}$, occurs with an exponential rise and a small amplitude originally denoted with F^{pl} (Forbush and Kok, 1968), and ascribed to quenching release in Q_B nonreducing RCs (Melis, 1985; Chylla et al., 1987; Lavergne and Leci, 1993). One can easily see that in this case $F^{\text{photochem}}$ (Eq. 6.9) is only determined by Eq. (7a), because the other components (Eqs. 6.7 and 6.8) vanish. This gives $F^{\text{photochem}}(t) = 1 + F_{\text{vs0}}^{\text{sc}}(t) = 1 + \beta \cdot nF_v \cdot (1 - e^{-k_L t})$, which confirms that $F^{\text{pl}} = 1 + \beta nF_v$ is associated with the de-quenching response of the β (or S_0) fraction with Q_B nonreducing RCs. The algorithm would in addition suggest that the secondary rise in the $F(t)$ at low intensities is of non-photochemical origin, and associated with either $F^{\text{electrochem}}$ or F^{IP} , or with both.

E. Leaf at Variable Excitation Rates

Figure 6.17 (left hand panel) shows fluorescence induction curves of 1 h dark-adapted pea leaves in the $3,000\text{--}15,000 \mu\text{mol photons m}^{-2} \text{ s}^{-1}$ intensity range (slightly modified from Schansker et al., 2006). The right hand panel shows FIA-simulations with all fit parameters kept constant except a variable light excitation rate k_L in the $3.5\text{--}20 \text{ ms}^{-1}$ range. There is, qualitatively, a nice

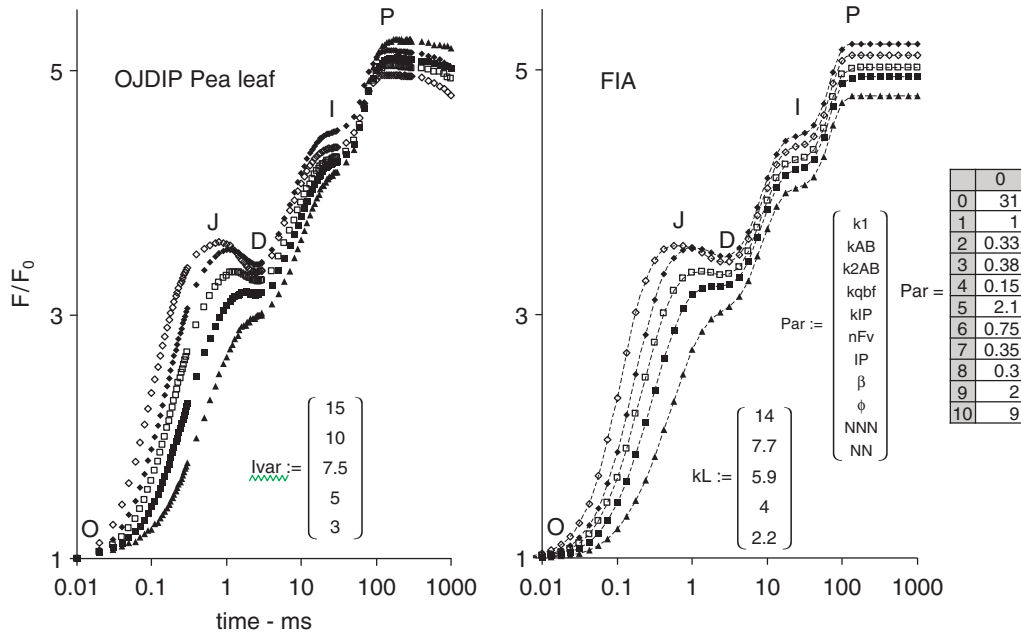


Fig. 6.17. **Left panel:** Chlorophyll *a* fluorescence induction curves (modified reproduction from Fig. 5 in Schansker et al. (2006), with original data provided by Gert Schansker) of 1 h dark-adapted pea leaves in MTFs of variable intensity, I_{var} , in the range from 15–3 mmol photons $\text{m}^{-2} \text{s}^{-1}$ for curves from *top to bottom*. **Right panel:** FIA-simulations with light excitation rate k_L in the 14–2.2 ms^{-1} range (from *top to bottom* curves). The FIA-fit parameters given in the right panel are for the middle curves at $I_{\text{var}} = 7.5 \text{ mmol photons m}^{-2} \text{s}^{-1}$ and $k_L = 5.9 \text{ ms}^{-1}$.

agreement between the experimental and simulated fit in the intensity range considered. This adds to our view that the algorithm (FIA) is a useful starting tool for analyzing the kinetics of MTF induced fluorescence induction curves in the 0–1 s time range in terms of primary photochemical and electrochemical events.

F. Leaf Under Laser Flash Excitation

Formation of a non-quenching state with Q_A^- and life time ($1/k_{AB}$) in the range 150–500 μs upon picosecond or nanosecond flash excitation occurs with rate constant (k_e) of the order of 10^6 ms^{-1} (Fig. 6.1). The rate of quenching release which we call k_{dsq} is substantially attenuated with respect to k_e and is determined by the rate constant of DSQ. The normalized fluorescence response $F(t)/F_0$ in a simplified concept with 100% Q_B reducing RCs follows the relation

$$\frac{F(t)}{F_0} = 1 + nF_v^{\text{STF}} \cdot (1 - e^{-k_{\text{dsq}}t}) \cdot e^{-k_{AB}t}, \quad (6.12)$$

with $nF_v^{\text{STF}} \sim 2$ in leaves and thylakoids.

For Q_B nonreducing RCs, k_{AB} in Eq. (6.12) is replaced by $k_{\text{-nqb}}$ where $k_{\text{-nqb}} \ll k_{AB}$ is the approximate rate constant of the slow reappearance of quenching associated with recovery of these RCs. For a heterogeneous system with a β -fraction (S_0) of Q_B nonreducing RCs, Eq. (6.12) can be rewritten as

$$F^{\text{DSQ}}(t) = \frac{F(t)}{F_0} = 1 + nF_v^{\text{STF}} \cdot \left\{ (1 - e^{-k_{\text{dsq}}t}) \cdot [(1 - \beta) \cdot e^{-k_{AB}t} + \beta \cdot e^{-k_{\text{-nqb}}t}] \right\}. \quad (6.12a)$$

Under conditions at which $k_{AB} \ll 0.1 \text{ ms}^{-1}$, which is true for Q_B nonreducing RCs or in the presence of DCMU, the graph of Eq. (6.12a) will show an exponential rise with reaction time $1/k_{\text{dsq}}$ towards a maximum with $F(t)/F_0 = 1 + nF_v^{\text{STF}} \sim 3$. This level will also be reached under conditions at which $k_{\text{dsq}} \gg k_{AB}$. It is noteworthy that the maximum $F(t)/F_0$ values after nanosecond flash excitation have been reported to be around 1.9 (Steffen et al., 2001, 2005; Belyaeva

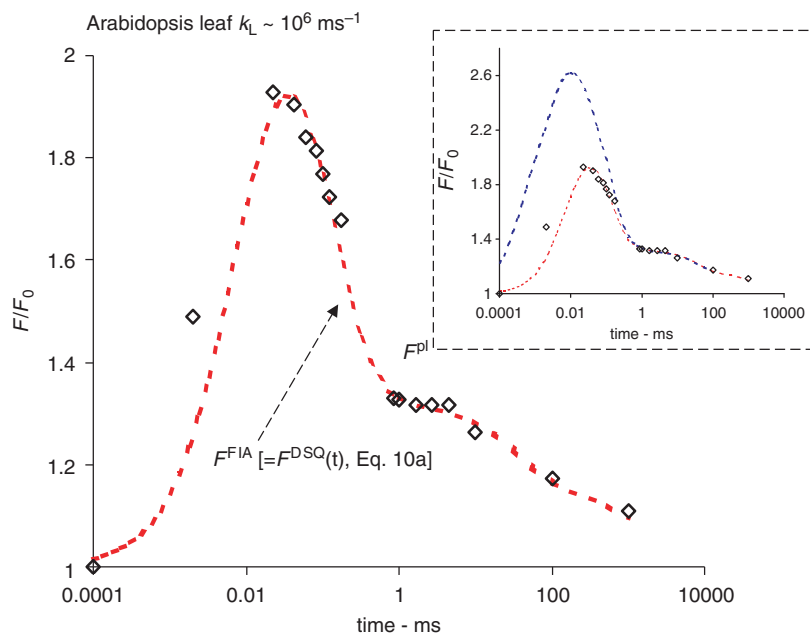


Fig. 6.18. Relative chlorophyll *a* fluorescence change (symbols) $F(t)/F_0$ of 1 h dark-adapted *Arabidopsis thaliana* leaf in 100 ns to 10 s time range (logarithmic) upon excitation with a saturating laser flash (6.2×10^{15} photons cm^{-2} /flash), reproduced from Fig. 2 in Steffen et al. (2005). Dashed curve is the FIA-simulated response $F^{\text{DSQ}}(t)$ using a modification of Eq. (6.12a). The modification accounts for a $S_0(\beta):S_1:S_2$ heterogeneity of 0.2:0.4:0.4 with corresponding rate constants of donor side quenching $k_{\text{dsq}} = 300, 60$ and 7 ms^{-1} , $k_{\text{AB}} \sim 9 \text{ ms}^{-1}$ and a biphasic decay of Q_B nonreducing RCs with rate constants $k_{\text{-nqb}} \sim 25$ and 0.5 s^{-1} and $nF_v = 1.8$. Note that F^{pl} is from (reduced) Q_B nonreducing RCs at the fractional size $\beta = 0.3/1.8 \sim 18\%$. The upper curve in the insert shows the $F^{\text{DSQ}}(t)$ response when k_{dsq} is increased 50 fold. It illustrates the effect of interference between k_{dsq} and k_{AB} on the maximum of $F(t)/F_0$

et al., 2006, 2008). The significantly reduced level of maximal variable fluorescence after laser flash excitation could be due to (i) either a poor quality of the sample preparations or (ii) to the lowered rate constant k_{dsq} of DSQ release when it is less than two orders of magnitude smaller than that of Q_A^- re-oxidation (k_{AB}). Evidence for the second interpretation is obtained from a closer analysis of Eqs. (6.12) and (6.12a), as will be illustrated in Fig. 6.18.

Figure 6.18, reproduced from Steffen et al. (2005), helps us in a quantitative understanding of the release and recovery of DSQ upon laser excitation. It shows for $F^{\text{DSQ}}(t) = F(t)/F_0$ that (i) a rise from 1 (at 100 ns) to ~ 1.9 reached at $t \sim 20 \mu\text{s}$; (ii) the well documented biphasic decay with fast (F) phase in the 0.02–1 ms time range towards an intermediate plateau level F^{pl} at $F^{\text{DSQ}}(t) \sim 1.3$ followed by the slow (S) phase far into the tens of seconds time range. The simulated time responses of $F^{\text{DSQ}}(t)$ is obtained after

substitution in Eq. (6.12a) the parameter values, listed in the legend of Fig. 6.18. The rough simulation (Fig. 6.18), based on the simplified reaction scheme, shows (1) a reasonable correspondence of the simulation with experimental curve; (2) that DSQ release occurs with rate constant $k_{\text{dsq}} \sim 35 \text{ ms}^{-1}$, and indicates (not shown), (3) that the low $F(t)/F_0$ maximum in the experimental curve is due to the interference of the rate constants of DSQ release and of Q_A^- reoxidation (regeneration of quenching).

It follows from Eq. (6.12a) that the kinetic profile of the experimental $F(t)/F_0$ curve in the 0.1–50 μs range, in contrast to what has been concluded by others (Reifarth et al., 1997; Steffen et al., 2001) cannot be considered to coincide proportionally with that of the P_{680}^+ -reduction. Proportionality would apply only to the nanosecond phase. For this phase $k_{\text{dsq}} > (100 \text{ ns})^{-1} \sim 10^5 \text{ ms}^{-1}$ and $F(t)/F_0$ then is proportional to nF_v^{STF} (Eq. 6.12a). For example, if the 100 ns

phase of the $F(t)/F_0$ response would be a reflection of DSQ release by fast P_{680}^+ -reduction and $nF_v^{STF} \sim 2$, then the size of this phase (~ 0.4) in the experiments with *Chlorella* (see Fig. 1 in Belyaeva et al., 2006) would indicate that the size of the fast nanosecond component of the P_{680}^+ reduction is $\sim 20\%$ (i.e. $100 \cdot 0.4/2$) of the total response, and that the complementary 80% of the reduction occurs in the tens of microseconds range. This is a rare ratio for the fast and slow components of P_{680}^+ reduction in a laser flash after dark adaptation (Christen et al., 1998; Steffen et al., 2005). Moreover in *Arabidopsis* the experimental $F(t)/F_0$ does not show a 100 ns component, whereas it is shown that $\sim 80\%$ of P_{680}^+ is reduced by Y_z via nanosecond-kinetics. The 100 ns component of the experimental $F(t)/F_0$ curve after laser flash excitation has been reported to be variable. Its relation with P_{680}^+ -reduction is doubtful.

In summary, the data reported in Reifarh et al. (1997), Christen et al. (1998), Steffen et al. (2001, 2005) and Belyaeva et al. (2006, 2008), in our opinion, are consistent with the hypothesis that release of donor side quenching, which occurs with a rate constant in the range of tens of millisecond, is associated with reoxidation of Y_z by the OEC. The evidence for association with P_{680}^+ reduction becomes weak when one considers the low value of the $F(t)/F_0$ maximum in the response curve and the strong interference between the rate of DSQ release at the donor side and of quenching regeneration at the acceptor side.

VI. Concluding Remarks

In Sections II–V of this chapter, we have illustrated the principles, applicability and usefulness of a fluorescence induction algorithm – FIA – with which experimental OJDIP fluorescence induction curves in thylakoids, chloroplasts and intact leaves can be analyzed and simulated. The model-based algorithm allows calculation, comparison, optimization and simulation of experimental curves under a variety of external conditions. Experimental chlorophyll fluorescence data, obtained during and after light pulses, thus, can be analyzed in terms of variables that are related or can be attributed to identifiable bio-

physical, biochemical and physiological parameters, associated with photochemical reactions of photosystem II.

The biophysical and physiological model on which the algorithm is based forms the central framework of the simulation approach that is aimed at a resolution of the complex OJDIP fluorescence light response in terms of rate constants and quantities associated with the photochemical and photo-electro-chemical events in the photosynthetic machinery. The framework of the model is obtained after assembling, identifying, characterizing and integrating the building blocks (reactions) of the process, in this case chlorophyll fluorescence induction in plant cells, chloroplasts and sub-chloroplasts fragments. Finally the *model* and its *algorithm*, like each model and algorithm, require *validation*. Validation refers to determining and comparing the fits of the model simulation with experimental results upon variation of a set of variables (parameters) in a defined dynamic range.

We have summarized and listed the *concept*, *elements*, and *assumptions* of the model and algorithm in Table 6.3. It has evolved from an earlier version (Vredenberg, 2000, 2004) which is named here TSTMvs00, to the present modified version TSTMvs05 (Vredenberg et al., 2005, 2006) and its associated algorithm FIA. Table 6.3 allows us to mark the conceptual difference of our model (FIA) with the other models (Stirbet et al., 1998; Lazar, 1999, 2006; Zhu et al., 2005; Belyaeva et al., 2006; Jablonsky and Lazar, 2008), which mutually show relatively small differences (see Chapter 5 of this book by Dušan Lazár and Gert Schansker). The differences with FIA are in particular on (i) donor side quenching by Y_z^+ , (ii) photo-electro-chemical accumulation and double reduction of Q_B nonreducing RCs, and (implicitly) (iii) on a serious over-estimation of the effect of the intersystem energy transfer (connectivity) in other models. These lead to fundamental discrepancies in interpretation and conclusions derived, for example, from changes in the OJDIP kinetics profile upon biotic and abiotic stressors. Some of these have been discussed in Vredenberg (2004).

A major difference of FIA with other models shows up in the photochemical OJD phase of the fluorescence induction curve in the 0–2.5 ms time range. For example, it has been proposed

Table 6.3. Overview of the concept, elements and assumptions of the three state trapping model (TSTM) and fluorescence induction algorithm (FIA) in relation to simulation and analysis of the OJDIP fluorescence induction in leaves and chloroplasts (thylakoids)

CONCEPT Elements	TSTM vs00	TSTM vs05	FIA
Double hit trapping mechanism;			
• RCs act as two electron traps	+	+	+
• Single hit causes semi-closure RCs with $[\text{PheQ}_A]^{1-}$	+	+	+
• Double hit causes closure RCs with $[\text{PheQ}_A]^{2-}$	+	+	+
Additive quenching release by $[\text{PheQ}_A]^{1-}$ and $[\text{PheQ}_A]^{2-}$ at acceptor side			
• Normalized variable fluorescence per trapped electron $nF_v \sim 2$	+	+	+
• Binary oscillation associated with two-gate mechanism			+
Donor side quenching (DSQ)			
• Quenching by P^+ and Y_z^+	+	+	+
• Period-of-four modulation (Kok cycle)		+	+
Electron trapping competitive with radical pair recombination			
• Low to negligible (S-state dependent) electron trapping efficiency in semi-closed RCs in $S_i \neq S_0$		+	+
RC-transfers from open \rightarrow semi-closed \rightarrow closed states are described by set of ODEs			
• Solution of ODEs gives time-dependent fraction q^{dsq} of RCs in which donor- and acceptor side quenching has been released	+	+	+
RC heterogeneity in dark adapted system only in:			
• S-state	+	+	+
• Q_B reducing/ Q_B nonreducing		+	+
• Absence of inactive centers		+	+
Q_B nonreducing RCs			
• Susceptible to double excitation (double reduction of acceptor pair) in TTFs		+	+
• Reoxidation of $[\text{PheQ}_A]^{2-}$ with rate constant $k_{2AB} \sim 0.5 \text{ ms}^{-1}$		+	+
• Short (sub- μs) lifetime of $[\text{PheQ}_A]^{2-}$ in Q_B reducing RCs		+	+
Doubling of variable fluorescence in low and high frequency STF trains			
• Accumulation of Q_B reducing RCs		+	+
• Rate of accumulation (doubling of yield) sensitive to membrane-modifying agents		+	+
• Similarities with ‘thermal’ phase in MTF excitation		+	+
Fluorescence yield sensitive to changes in electrical and electrochemical potentials	+	+	+
Assumptions			
Time independent light excitation rate k_L , implicitly synonymous with absence of inter-system energy transfer		+	+
S-state heterogeneity in 5–30 min dark-adapted preparations			
• $S_0/S_1 = \beta/(1 - \beta)$ with $\beta \sim 0.15\text{--}0.35$		+	+
• S_0 (β) fraction populated with Q_B nonreducing RCs		+	+
MODEL			
Assemblage of elements			
Photochemical phase; derivation of $F^{\text{photochem}}(t)$ composed of			
• F_v associated with semiclosure of all RCs	+	+	+
• F_v associated with closure of β -fraction (S_0) with Q_B nonreducing RCs		+	+
Photoelectrochemical phase; approximation of $F^{\text{electrochem}}(t)$			
• ‘Best fit’ mathematical function of accumulation phase			+
IP phase; approximation $F^{\text{IP}}(t)$			
• ‘Best fit’ mathematical function of IP phase			
– For thylakoids			+
– for intact leaves			+
ALGORITHM			
Definition of simulation function			
$F^{\text{FIA}}(t) = F^{\text{photochem}}(t) + F^{\text{electrochem}}(t) + F^{\text{IP}}(t)$			+
VALIDATION			
MTF excitation rate in $0.15\text{--}20 \text{ ms}^{-1}$ range		+	+
STF laser excitation			+
STF pre-excitation		+	+
Effect PS II herbicides	+	+	+

that the OJIP induction curve can be simulated satisfactorily by fitting it with the sum of three first order exponentials (Pospišil and Dau, 2002; Boisvert et al., 2006; Antal and Rubin, 2008). The experiments with high frequency STF trains (Section III.B, Figs. 6.7 and 6.8) and with MTF excitations at various excitation rates (Section V, Figs. 6.9 and 6.17) have clearly shown that a single exponential fit will fail to simulate the experimental curves. Inaccurate fitting with a single exponential in the 0–0.5 ms time range indeed has been illustrated in some of the aforementioned papers (Boisvert et al., 2006; Antal and Rubin, 2008; see also Chapter 7 of this book by Andrew Rubin and Galina Riznichenko). A major cause for the inadequacy of ‘mathematical’ fitting with one exponential of the experimental curves comes from the ignorance of presence and photochemical activity of Q_B nonreducing RCs. Kinetic modeling of PS II should incorporate a functional role of these centers (Vredenberg, 2008c). The model (we will call it here the JIP model) which forms the basis of the so called JIP test (Strasser B and Strasser R, 1995; Strasser et al., 2004) also is at strong variance with FIA. The JIP model and the JIP test, in our opinion, are based on disputable assumptions, for instance on the monomolecular character of the OJ rise (Q_A reduction) and quantified by the size of relative variable fluorescence at 0.3 and 2 ms. These assumptions are in serious conflict with the kinetics at various excitation rates (intensity) and with our FIA simulations (Section V, Fig. 6.17). The JIP model strongly suffers from incompleteness with respect to a correct analysis of the initial kinetics and, like the other models, from the ignorance of specific photochemical properties of Q_B nonreducing RCs in double hits (Section IV.A.2).

The $F^{\text{electrochem}}$ and F^{IP} components of F^{FIA} require further validation. F^{IP} in our opinion is of particular interest and will deserve special attention. The difference between its kinetic pattern of intact leaves and isolated chloroplasts comes into expression in Eq. (6.11): in chloroplasts $N \leq 1$ whereas in leaves N is between 5 and 10, reflected by a pronounced delay in and steeper rise of this phase in the latter. Future research must aim at obtaining evidence for the hypothesis that the IP fluorescence rise (F^{IP}) is connected with and a reflection of an electrical interaction between PS I and PS II. It seems promising to

follow a proposal (Bulychev and Vredenberg, 2001; Vredenberg et al., 2005) that the electrical field generated at excited PS I sites and distantly located from PS II is transversally propagated through the conducting lumen towards the PS II sites. This propagation through a non-linear planar conductor sheet can be thought of as requiring a sequence of identical activation steps.

The present simplified form of FIA is a promising and accurate means to analyze MTF-induced fluorescence induction curves in terms of primary photochemical, electrochemical and electrical events in PS II and PS I. Further refinements would be required to increase its applicability. The availability of FIA will offer a useful tool to study the effects of stressors on the photosynthetic performance of plants and algae via fluorescence measurements. It would allow us to come closer to an identification of the target sites of the stressors and possibly to a quantification of their primary effects. We hope that it would give an answer to whether or not the effects are on a structural (antenna size, lumen thickness, membrane conductance) or a functional level (photo- and electrochemical activity, donor and acceptor side inhibition).

Acknowledgments

We thank Jack van Rensen for discussions and Milan Dürchan, HenkJan Venema and Gustavo Rodrigues for doing (part of) the experiments. O.P. has been supported by grant of the Czech Grant Agency GACR 206/05/0335, project 1QS500200570 of AVCR and the institutional research concepts AV0Z50200510.

References

- Antal T and Rubin A (2008) In vivo analysis of chlorophyll a fluorescence induction. *Photosynth Res* 96: 217–226
- Belyaeva NT, Paschenko VZ, Renger G, Riznichenko G Yu and Rubin AB (2006) Application of photosystem II model for analysis of fluorescence induction curves in the 100 ns to 10 s time domain after excitation with a saturating light pulse. *Biophysics* (translated from *Biofizika*) 51 (6): 976–990
- Belyaeva NE, Schmitt F-J, Steffen, R, Paschenko VZ, Riznichenko G Yu, Chemeris YuK, Renger G, and Rubin AB (2008) PS II model-based simulations of single

- turnover flash-induced transients of fluorescence yield monitored within the time domain of 100 ns–10 s on dark-adapted *Chlorella pyrenoidosa* cells *Photosynth Res* 98: 105–119
- Bernhardt K and Trissl H-W (1999) Theories for kinetics and yields of fluorescence and photochemistry: how, if at all, can different models of antenna organization be distinguished experimentally? *Biochim Biophys Acta* 1409: 125–142
- Boisvert S, Joly D and Carpentier R (2006) Quantitative analysis of the experimental O-J-I-P chlorophyll induction kinetics. Apparent activation energy and origin of each kinetic step. *FEBS Lett* 273: 4770–4777
- Bowes JM and Crofts AR (1980) Binary oscillations in the rate of reoxidation of the primary acceptor of photosystem II. *Biochim Biophys Acta* 590: 373–384
- Bukhov NG, Govindachary S, Egorova EA, Joly D and Carpentier R (2003) N, N, N', N'-tetramethyl-p-phenylenediamine initiates the appearance of a well resolved I-peak in the kinetics of chlorophyll fluorescence rise in isolated thylakoids. *Biochim Biophys Acta* 1607: 91–96
- Bulychev AA and Vredenberg WJ (2001) Modulation of photosystem II chlorophyll fluorescence by electrogenic events generated by photosystem I. *Bioelectrochem* 54: 157–168
- Butler WL (1972) On the primary nature of fluorescence yield changes associated with photosynthesis. *Proc Natl Acad Sci USA* 69: 3420–3422
- Christen G, Reifarth F and Renger G (1998) On the origin of the '35- μ s kinetics' of P_{680}^{+} reduction in photosystem II with an intact water oxidizing complex. *FEBS Lett* 419: 49–52
- Chylla RA, Garab G and Whitmarsh J (1987) Evidence for slow turnover in a fraction of photosystem II complexes in thylakoid membranes. *Biochim Biophys Acta* 894: 562–571
- Crofts AR (2005) The Q-cycle—a personal perspective. In: Govindjee, J.T. Beatty, H. Gest and J.F. Allen (eds), *Discoveries in Photosynthesis*. *Advances in Photosynthesis and Respiration*, pp 47–499, Vol. 20, Springer, Dordrecht
- Dau H (1994) Molecular mechanisms and quantitative models of variable photosystem II fluorescence. *Photochem Photobiol* 60: 1–23
- Duysens LNM and Sweers HE (1963) Mechanisms of the two photochemical reactions in algae as studied by means of fluorescence. In: *Japanese Society of Plant Physiologists. Studies on Microalgae and Photosynthetic Bacteria*, pp 353–372. University of Tokyo Press, Tokyo
- Forbush B and Kok B (1968) Reaction between primary and secondary electron acceptors of photosystem II of photosynthesis. *Biochim Biophys Acta*, 162: 243–253
- Govindjee (1995) Sixty-three years since Kautsky: chlorophyll *a* fluorescence. *Aust J Plant Physiol* 22: 131–160
- Govindjee (2004) Chlorophyll *a* fluorescence: a bit of basics and history. In: Papageorgiou, GC, Govindjee (eds) *Chlorophyll *a* fluorescence: A signature of photosynthesis*. *Advances in Photosynthesis and Respiration*, Vol. 19, pp 1–42, Springer, Dordrecht
- Hiraki M, Van Rensen JJS, Vredenberg WJ and Wakabayashi K (2003) Characterization of the alterations of the chlorophyll *a* fluorescence induction curve after addition of photosystem II inhibiting herbicides. *Photosynth Res* 78: 35–46
- Hiraki M, Vredenberg WJ, Van Rensen JJS and Wakabayashi K (2004) A modified fluorometric method to quantify the concentration effect (pI_{50}) of photosystem II-inhibiting herbicides. *Pesticide Biochem Physiol* 80: 183–191
- Jablonsky J and Lazar D (2008) Evidence for intermediate S-states as initial phase in the process of oxygen-evolving complex oxidation. *Biophys J* 94: 2725–2736
- Joliot P and Joliot A (1964) Etude cinétique de la réaction photochimique libérant l'oxygène au cours de la photosynthèse *CR Acad Sci Paris* 258: 4622–4625
- Joliot P and Joliot A (1977) Evidence for a double hit process in photosystem II based on fluorescence studies. *Biochim Biophys Acta* 462: 559–574
- Joly D and Carpentier R (2007) The oxidation/reduction kinetics in the plastoquinone pool controls the appearance of the I-peak in the O-J-I-P chlorophyll fluorescence rise: Effects of various electron acceptors. *J Photochem Photobiol B* 88: 43–50
- Ke B (2001) Photosynthesis photobiochemistry and photobiophysics. In: Govindjee (ed), *Advances in Photosynthesis (and Respiration)*, Vol. 10, Kluwer (now Springer), Dordrecht
- Klimov VV and Krasnovskii AA (1981) Participation of pheophytin in the primary processes of electron transfer at the reaction centers of photosystem II. *Biophysics* 27: 186–198
- Koblizek M, Kaftan D and Nedbal L (2001) On the relationship between the non-photochemical quenching of the chlorophyll fluorescence and the photosystem II light harvesting efficiency. A repetitive flash fluorescence study. *Photosynth Res* 68: 141–152
- Kolber Z, Prášil O and Falkowski P (1998) Measurements of variable chlorophyll fluorescence using fast repetition rate technique. I. Defining methodology and experimental protocols. *Biochim Biophys Acta* 1367: 88–106
- Kramer DM, DiMarco G and Loreto F (1995) Contribution of plastoquinone quenching to saturation pulse-induced rise of chlorophyll fluorescence in leaves. In: Mathis P (ed), *Photosynthesis: From Light to Biosphere*, Vol. I, pp 147–150, Kluwer, Dordrecht, The Netherlands
- Kurreck J, Schödel R and Renger G (2000) Investigation of the plastoquinone pool size and fluorescence quenching in thylakoid membranes and Photosystem II (PSII) membrane fragments. *Photosynth Res* 63: 171–182
- Lavergne J and Leci E (1993) Properties of inactive photosystem II centers. *Photosynth Res* 35: 323–343
- Lavergne J, Trissl H-W (1995) Theory of fluorescence induction in photosystem II: Derivation of analytical

- expressions in a model including exciton-radical-pair equilibrium and restricted energy transfer between photosynthetic units. *Biophys J* 68: 2474–2492
- Lazár D (1999) Chlorophyll *a* fluorescence induction. *Biochim Biophys Acta* 1412: 1–28
- Lazár D (2006) The polyphasic chlorophyll *a* fluorescence rise measured under high intensity of exciting light. *Funct Plant Biol* 33: 9–30
- Mauzerall D (1972) Light induced fluorescence changes in *Chlorella*, and the primary photoreactions for the production of oxygen. *Proc Natl Acad Sci USA* 69: 1358–1362
- Melis A (1985) Functional properties of Photosystem II β in spinach chloroplasts. *Biochim Biophys Acta* 808: 334–342
- Papageorgiou GC and Govindjee (eds) (2004) Chlorophyll *a* fluorescence: A signature of photosynthesis. *Advances in Photosynthesis and Respiration*, Vol. 19, Springer, Dordrecht
- Papageorgiou GC, Tsimilli-Michael M and Stamatakis K (2007) The fast and slow kinetics of chlorophyll *a* fluorescence induction in plants, algae and cyanobacteria: a viewpoint. *Photosynth Res* 94: 275–290
- Pospišil P and Dau H (2002) Valinomycin sensitivity proves that light-induced thylakoid voltages result in millisecond phase of chlorophyll fluorescence transients. *Biochim Biophys Acta* 1554: 94–100
- Reifarth F, Christen G and Renger G (1997) Fluorimetric equipment for monitoring P_{680}^+ reduction in PSII preparations and green plants. *Photosynth Res* 51: 231–242
- Roberts AG, Gregor W, Britt RD and Kramer DM (2003) Acceptor and donor-side interactions of phenolic inhibitors of Photosystem II. *Biochim Biophys Acta* 1604: 23–32
- Samson G and Bruce D (1996) Origin of the low yield of chlorophyll fluorescence induced by single turnover flash in spinach thylakoids. *Biochim Biophys Acta* 1276: 147–153
- Samson G, Prášil O and Yaakoubd B (1999) Photochemical and thermal phases of chlorophyll *a* fluorescence. *Photosynthetica* 37: 163–182
- Schansker G, Toth SZ and Strasser RJ (2006) Dark recovery of the Chl *a* fluorescence transient (OJIP) after light adaptation: The qT-component of non-photochemical quenching is related to an activated photosystem I acceptor side. *Biochim Biophys Acta* 1757: 787–797
- Schreiber U (2002) Assessment of maximal fluorescence yield: Donor-side dependent quenching and Q_B -quenching. In: Van Kooten O and J Snel (eds) *Plant Spectrofluorometry: Applications and Basic Research*, pp 23–47. Rozenberg, Amsterdam
- Schreiber U and Krieger A (1996) Hypothesis: Two fundamentally different types of variable chlorophyll fluorescence in vivo. *FEBS Lett* 397: 131–135
- Shinkarev VP (2004) Photosystem II: Oxygen evolution and chlorophyll *a* fluorescence induced by multiple flashes. In: Papageorgiou GC and Govindjee (eds) *Chlorophyll *a* fluorescence: A signature of photosynthesis. Advances in Photosynthesis and Respiration*, Vol. 19, pp 197–229. Springer, Dordrecht
- Shinkarev VP and Govindjee (1993) Insight into the relationship of chlorophyll fluorescence yield to the concentration of its natural quenchers in oxygenic photosynthesis. *Proc Natl Acad Sci USA* 90: 7466–7469
- Steffen R (2003) Time-resolved spectroscopic investigation of photosystem II. Ph.D. thesis. Technical University, Berlin
- Steffen R, Christen G and Renger G (2001) Time-resolved monitoring of flash-induced changes of fluorescence quantum yield and decay of delayed light emission in oxygen-evolving photosynthetic organisms. *Biochemistry* 40: 173–180
- Steffen R, Eckert H-J, Kelly AA, Dörmann PG and Renger G (2005) Investigations on the reaction pattern of photosystem II in leaves from *Arabidopsis thaliana* by time-resolved fluorometric analysis. *Biochemistry* 44: 3123–3132
- Stirbet AD, Govindjee, Strasser BJ and Strasser, RJ (1998) Chlorophyll *a* fluorescence induction in higher plants: Modeling and numerical simulation. *J Theor Biol* 193: 131–151
- Strasser BJ and Strasser RJ. (1995) Measurement of fast fluorescence transients to address environmental questions; the JIP test. In: Mathis P (ed) *Photosynthesis: From Light to Biosphere*, pp 977–980, Kluwer, Dordrecht
- Strasser RJ (1978) The grouping model of plant photosynthesis. In: Akoyunoglou G (ed) *Chloroplast Development*, pp 513–524. Elsevier/North Holland, Amsterdam
- Strasser RJ, Srivastava A and Govindjee (1995) Polyphasic chlorophyll *a* fluorescence transient in plants and cyanobacteria. *Photochem Photobiol* 61: 32–42
- Strasser RJ, Tsimilli-Michael M and Srivastava, A (2004) Analysis of the fluorescence transient. In: Papageorgiou, G.C., Govindjee (eds) *Chlorophyll *a* fluorescence: a signature of photosynthesis. Advances in Photosynthesis and Respiration*, Vol. 19, pp 321–362. Springer, Dordrecht
- Trissl H-W (2002) Theory of fluorescence induction: an introduction. <http://www.biologie.uni-osnabrueck.de/biophysik/Trissl/teaching/teaching.html>
- Trissl H-W and Lavergne J (1995) Fluorescence induction from photosystem II: analytical equations for the yields of photochemistry and fluorescence derived from analysis of a model including exciton-radical pair equilibrium and restricted energy transfer between photosynthetic units. *Aust J Plant Physiol* 22: 183–193
- Urban O, Trtílek M, Feild T and Nedbal L (1999) Single-turnover flashes to saturate the Q_A reduction in a leaf were generated by the light-emitting diodes of a double

- modulation kinetic fluorometer. *Photosynthetica* 37: 201–207
- Vasilév S and Bruce D (1998) Nonphotochemical quenching of excitation energy in photosystem II. A picosecond time-resolved study of the low yield of chlorophyll a fluorescence induced by single-turnover flash in isolated spinach thylakoids. *Biochemistry* 37: 11046–11054
- Vermaas WFJ, Renger G and Dohnt G (1984) The reduction of the oxygen-evolving system in chloroplasts by thylakoid components. *Biochim Biophys Acta* 764: 194–202
- Vredenberg WJ (2000) A three-state model for energy trapping and chlorophyll fluorescence in photosystem II incorporating radical pair recombination. *Biophys J* 79: 25–38
- Vredenberg WJ (2004) System analysis of photoelectrochemical control of chlorophyll fluorescence in terms of trapping models of Photosystem II: a challenging view. In: Papageorgiou GC and Govindjee (eds) *Chlorophyll a fluorescence: a signature of photosynthesis*, *Advances in Photosynthesis and Respiration*, Vol. 19, pp 133–172. Springer, Dordrecht
- Vredenberg WJ (2008a) Analysis of initial chlorophyll fluorescence induction kinetics in chloroplasts in terms of rate constants of donor side quenching release and electron trapping in photosystem II. *Photosynth Res* 96: 83–97
- Vredenberg WJ (2008b) Algorithm for analysis of OJDIPI fluorescence induction curves in terms of photo- and electrochemical events in photosystems of plant cells. Derivation and application. *J Photochem Photobiol B* 91: 58–65
- Vredenberg WJ (2008c) Kinetic Models of Photosystem II should incorporate a Role for Q_B -nonreducing Reaction Centers. *Biophys J* 95: 3113–3114
- Vredenberg WJ and Duysens LNM (1963) Transfer and trapping of excitation energy from bacteriochlorophyll to a reaction center during bacterial photosynthesis. *Nature* 197: 355–357
- Vredenberg WJ, Snel JFH and Dassen JHA (1998) A sizeable increase in the electric conductance of the thylakoid lumen as an early event during reaction center and Q cycle turnover *Photosynth Res* 58: 111–121
- Vredenberg WJ, Rodrigues GC and Van Rensen JJS (2002) A quantitative analysis of the chlorophyll fluorescence induction in terms of electron transfer rates at donor and acceptor sides of photosystem II. In: *Proceedings of the 12th International Congress Photosynthesis*, Brisbane, 18–23 August, 2001 S14–10 (on CD)
- Vredenberg WJ, Van Rensen JJS and Rodrigues GC (2005) On the sub-maximal yield and photo-electric stimulation of chlorophyll a fluorescence in single turnover excitations in plant cells. *Bioelectrochemistry* 68: 83–90
- Vredenberg WJ, Kasalicky V, Durchan M and Prášil O (2006) The chlorophyll a fluorescence induction pattern in chloroplasts upon repetitive single turnover excitations: Accumulation and function of Q_B -nonreducing centers. *Biochim Biophys Acta* 1757: 173–181
- Vredenberg WJ, Durchan M and Prášil O (2007) On the chlorophyll fluorescence yield in chloroplasts upon excitation with twin turnover flashes (TTF) and high frequency flash trains. *Photosynth Res* 93:183–192
- Walas SM (1991) *Modeling with differential equations in chemical engineering*, Butterworth-Heinemann, Boston, MA
- Zhu X-G, Govindjee, Baker NR, deSturler E, Ort D and Long SP (2005) Chlorophyll a fluorescence induction kinetics in leaves predicted from a model describing each discrete step of excitation energy and electron transfer associated with photosystem II. *Planta* 23: 114–133

Chapter 7

Modeling of the Primary Processes in a Photosynthetic Membrane

Andrew Rubin and Galina Riznichenko*

*Biophysical Department, Biological Faculty, Moscow State Lomonosov University,
Leninskie Gory 1-12, 119992, Moscow, Russia*

Summary.....	151
I. Introduction.....	152
II. Fluorescence as an Indicator of the Photosystem State.....	153
III. General Kinetic Model of the Processes in Photosynthetic Thylakoid Membrane.....	154
A. The Structure of the Model.....	154
1. Principles of Electron Transfer in Multi-enzyme Complexes.....	154
2. Photosystem II Complex.....	156
3. Cytochrome b_6f Complex.....	159
4. Photosystem I Complex.....	160
5. Mobile Carriers in the Kinetic Model.....	161
6. The Role of Transmembrane Electrical Potential.....	161
7. Transmembrane Ion Transfer and $\Delta\mu H$ Generation.....	161
8. Buffer Properties of Lumen and Stroma.....	162
9. Parameter Values.....	162
B. Results of Simulation.....	163
1. Simulation of Fluorescence Transients at Different Light Intensities.....	163
2. The Role of Different States of Photosystem II in Fluorescence Induction.....	163
3. Simulation of $\Delta\Psi$ Kinetics.....	165
IV. Multiparticle Modeling of the Processes in the Photosynthetic Membrane.....	166
A. Restricted Diffusion of Mobile Electron Carriers.....	166
B. Direct Model Scene.....	167
C. Brownian Dynamics of Mobile Carriers.....	167
D. Simulation of Cyclic Electron Transport Around Photosystem I.....	168
V. Concluding Remarks and Future Perspectives.....	171
Acknowledgments.....	171
References.....	171

Summary

In this chapter general kinetic and “direct” simulatory multiparticle computer models of processes occurring in a photosynthetic membrane are described. The general kinetic model of the primary photosynthetic processes in a thylakoid membrane is based on the system of ordinary differential equations, describing the processes in multi-enzyme complexes of Photosystem I, Photosystem II and Cytochrome b_6f complex, coupled to transmembrane proton and other ion transport and generation of

* Author for correspondence, e-mail: riznich @biophys.msu.ru

transmembrane electrochemical potential. This model allows us to follow simultaneous kinetic changes of different variables, including concentrations of electron carriers at different redox states, electrical and electrochemical potential values; it adequately describes a set of fluorescence induction curves experimentally recorded at different light intensities under continuous illumination and after a short laser flash.

The direct multiparticle computer model, presented in this chapter, describes processes proceeding in the simulated membrane “scene”, which includes stroma, lumen and intramembrane compartments constructed according to structural data. Motions of mobile electron carriers are described using the formalism of Brownian dynamics. The simulatory model allows us to follow not only the kinetics, but it also mimics the visual image of the behavior of electron carriers. Such a model reveals the role of heterogeneous distribution of photoreaction centers and other elements of geometric membrane structure and of the spatial organization of the photosynthetic membrane.

I. Introduction

Mathematical and computer models make it possible to develop an integrated view of interactions of separate elements within a network of a complex system. In the last 2 decades detailed mathematical models of electron transport inside the reaction center complexes of photosystem I (Riznichenko et al., 1986, 1990) and photosystem II (Bukhov et al., 1988; Trissl et al., 1993; Trissl and Lavergne, 1994; Lavergne and Trissl, 1995; Stirbet and Strasser, 1995, 1996; Shinkarev, 1998; Stirbet et al., 1998; Lebedeva et al., 2000; Vredenberg, 2000; Strasser and Stirbet, 2001; Lazar, 2003; Strasser et al., 2004; Vredenberg et al., 2004, 2005, 2006; Zhu et al., 2005; Belyaeva et al., 2006) were developed. These models contain several dozens of differential equations and simulate experimental curves at initial stages of fluorescence induction in Photosystem II (PS II).

However, the processes occurring in a photosynthetic reaction center present only the initial step in the long chain of events, including light energy transformation into the energy of electrochemical transmembrane potential and then into the energy of ATP and reduced pyridine-nucleotide molecules; these are consumed later in dark metabolic pathways. To describe the relationship between primary photosynthetic processes in reaction centers and subsequent dark metabolic processes, it is necessary to construct a model (or rather, a series of models of different complexity), including the processes of electron transport and energy transformation at different levels – from light absorption and charge separation in a photosynthetic reaction center to the reduction of metabolites which take part in photosynthetic electron transport as well as in dark metabolism. These metabolites include plastoquinone (PQ), ferredoxin (Fd), NADPH, ATP, O_2 , H^+ and other ions. For a summary of these primary events see Ke (2001) and Renger (2007).

To describe the chemical kinetics of redox reactions scientists traditionally use mass action equations. The mass action approach assumes electron pathways to be in principle free for any reduced donor to react with any oxidized acceptor in the reaction medium. This approach is based on the statistical physics and is sufficient when the oxidized and reduced molecules collide in a solution. However, photosynthetic redox reactions are rather specific. Most of them occur in protein complexes embedded in a photosynthetic membrane. In these complexes the particular components of redox reactions (donors and acceptors) are situated in a fixed sequence, so that

Abbreviations : BD – brownian dynamics; Chl – chlorophyll; Cyt – cytochrome; DCMU – 3-(3', 4' – dichlorophenyl) - 1,1 – dimethylurea (diuron); EPR – electron paramagnetic resonance; F_0 – minimal Chl fluorescence; F_m – maximal Chl fluorescence; Fd – ferredoxin; FeSR – rieske iron-sulfur center; FL – fluorescence; FQR – ferredoxin-quinone reductase; LHC – light harvesting complex; O, J, I, P – steps in FL rise under exciting light; OEC – oxygen evolving complex; P680 – primary electron donor in PS II; P700 – primary electron donor in PS I; PAM – pulse amplitude modulation; Pc – plastocyanin; PEA – plant efficiency analyzer; PQ – plastoquinone; PS I – photosystem I; PS II – photosystem II; RC – reaction center; Q_A – primary quinone acceptor of PS II; Q_B – secondary quinone acceptor of PS II

an electron transport through each of the individual complex proceeds along a definite “electron pathway”. For example, from a reduced donor an electron can pass to the oxidized acceptor only if the latter is located in the same complex, such as PS II, PS I and Cytochrome (Cyt) b_6f . For the adequate description of such processes the master equation approach can be used, which considers electron movements to be limited inside the complexes.

On the basis of master equation approach we developed the models of electron transport in isolated complexes of PS I (Riznichenko et al., 1986, 1988, 1990), PS II (Bukhov et al., 1988) and bacterial reaction centers (Vorobjeva et al., 1986; Chamorovsky et al., 1990). The results have been summarized by Riznichenko (1991). During the last decade, we have constructed a general kinetic model to simulate the integrated system of regulatory processes proceeding simultaneously in a photosynthetic membrane (Riznichenko et al., 1999; Lebedeva et al., 2002; Riznichenko and Rubin, 2007). We have described the processes proceeding inside the complexes PS II, PS I and Cyt b_6f by means of the master-equation approach, whereas interactions between the complexes facilitated by mobile carriers plastoquinone (PQ), plastocyanin (Pc) and ferredoxin (Fd) were best described by the mass action approach. Section II of this chapter describes the fluorescence parameters as indicators of photosynthetic energy transduction. In Section III we will describe the general kinetic model simulating electron transport in the “Z-scheme” coupled to processes of electrochemical potential generation.

Kinetic models do not include information about the structure, where the reactions of electron transport occur. Nevertheless, the location and arrangement of the reaction compartments must play an important role in regulating the rate and directions of metabolic processes. Obviously, the traditional kinetic approach is not sufficient to properly simulate heterogeneous systems such as a photosynthetic cell. Therefore it is necessary to develop computer models, which can take into account complex geometry of the space, where interactions occur, especially when linear dimensions of the interacting molecules are comparable with those of reaction compartments. As to the mechanisms and efficiency of kinetic interactions

between bio-macromolecules, it is also important to consider charge distribution on their surfaces.

A series of direct computer multiparticle models, which describe the behavior and interactions of separate electron carriers and allow us to visualize the processes in a photosynthetic membrane have also been developed (Kovalenko et al., 2003, 2006, 2007). In these models we consider the ensembles of mobile carrier molecules which move chaotically according to the Brownian dynamics (BD) laws inside the compartments of the photosynthetic membrane. We describe them in Section IV. Direct multi-particle models give the possibility to follow the routes of individual mobile molecule movements as well as to determine kinetic and statistical parameters of the system and to visualize directly the whole scene of the involved processes.

II. Fluorescence as an Indicator of the Photosystem State

The intensity of PS II chlorophyll fluorescence is determined by a network of processes proceeding in the photosynthetic membrane. Thus, by analyzing the kinetics of the fluorescence induction under various conditions, we can obtain information about the processes occurring at different stages of the energy transduction in a photosynthetic membrane (Govindjee et al., 1986; Krause and Weis, 1991; Papageorgiou and Govindjee, 2004; Papageorgiou et al., 2007).

A fluorescence induction curve has two main phases. The “fast phase” is the increase in fluorescence intensity from the initial level F_0 up to the maximal level P during the period of about 1–2 s (depending on the exciting light intensity) with intermediate steps at 2 ms (J) and about 30 ms (I) – the so called OJIP-shape (Strasser et al., 1995, 2004). The “slow phase” is the following fluorescence intensity relaxation to the steady state level within a period of several tens of seconds. The complicated shape of the fluorescence transients, including several maxima and quasi-steady states (J and I), is usually attributed to different components of the photosynthetic apparatus; thus, the measured shape of the fluorescence induction curve reveals information about these components (Edwards and Baker, 1993; Schreiber and Bilger, 1993; Govindjee, 1995,

2004; Bernhardt and Trissl, 1999; Lazar, 1999, 2006; Bukhov et al., 2004; Strasser et al., 2004).

Several models have been presented for the fast initial phases of photosynthesis. Some of these (Renger and Schulze, 1985; Baake and Strasser, 1990; Baake and Schloder, 1992; Hsu, 1992, 1993) are limited to processes occurring in PS II at low light intensities. Others (Stirbet and Strasser, 1995, 1996; Stirbet et al., 1998; Lazar, 2003, 2005; Strasser et al., 2004; Zhu et al., 2005; Belyaeva et al., 2006) successfully simulated the characteristic features of the initial fast phase of fluorescence induction curves at high illumination intensities – specifically the intermediate maximum and the points of inflections (typical OJIP-shape). But such models of isolated PS II do not describe correctly the kinetics of the fluorescence induction curve at moderate and low light intensities nor they describe the slow phase of the induction curve. To analyze the slow phase it is necessary to consider processes responsible for the outflow of electrons from PS II, as well as processes affecting electron movements inside the PS II. These processes include electron transfer by PQ molecules from PS II to Cyt b_6f complex, coupled to proton transport, electron transport from Cyt b_6f to PS I, and, finally, electron flow to the CO_2 fixation cycle through ferredoxin (Fd) and ferredoxin-NADP reductase (FNR).

In these processes the influence of electrochemical transmembrane potential is important. However, until recently only experimental situations where the transmembrane potential can be neglected were simulated in models. In this work we extend the model to describe the regulation of the photosynthetic electron transport by the transmembrane electrochemical potential.

III. General Kinetic Model of the Processes in Photosynthetic Thylakoid Membrane

The model, presented in this chapter, describes the photosynthetic processes according to the classical Z-scheme, where PS II and PS I operate in series (Hall and Rao, 1994; Hauska and Arnold, 2000; Ke, 2001; Nelson and Yocum, 2006). The model was developed on the basis of the simulation of the electron transport processes in isolated fragments of PS I, PS II, and bacterial

reaction centers (Riznichenko et al., 1986, 1988, 1990; Vorobjeva et al., 1986; Bukhov et al., 1988; Chamarovsky et al., 1990). The distinctive feature of the present model is that it simulates the processes inside the photoreaction center complexes, taking into account also the roles of electrical and electrochemical potential.

A. The Structure of the Model

The processes simulated by the model are presented in Fig. 7.1. The general model includes the sub-models of separate parts of the electron transport chain: Photosystem II complex (Lebedeva et al., 2000; Belyaeva et al., 2006), cytochrome b_6f complex (Kamali et al., 2004) and (more schematically) photosystem I. Along with the processes proceeding in the photosynthetic reaction centers of PS I and PS II and in the Cyt b_6f complex the model describes also transmembrane proton fluxes directed into the intra-thylakoid lumenal space, the oxygen evolving complex (OEC), the build-up of electrical and electrochemical potential, ion fluxes across the membrane, ATP-synthase activity, the role of buffer groups in lumenal and stromal compartments of the thylakoid.

The model described below simulates the kinetics of the concentration changes of definite redox states of electron carriers as well as changes of electrical and electrochemical potential values in a photosynthetic membrane.

1. Principles of Electron Transfer in Multi-enzyme Complexes

Simulation of electron transfer inside PS II, Cyt b_6f and PS I complexes is based on the concept that the catalytic cycle for each of such complexes can be described as a sequence (or network) of states, the number of which is determined by the number of considered electron carriers and the number of redox states of each of the carriers (excited, oxidized, reduced, and protonized). Malkin (1971) and Sorokin (1973) were the first to raise the question of the application of the master-equation approach for the description of the electron transfer inside the complex, contrary to the description of this process by means of the mass action law (Holzapfel and Bauer, 1975; Kukushkin et al., 1975). The mathematical

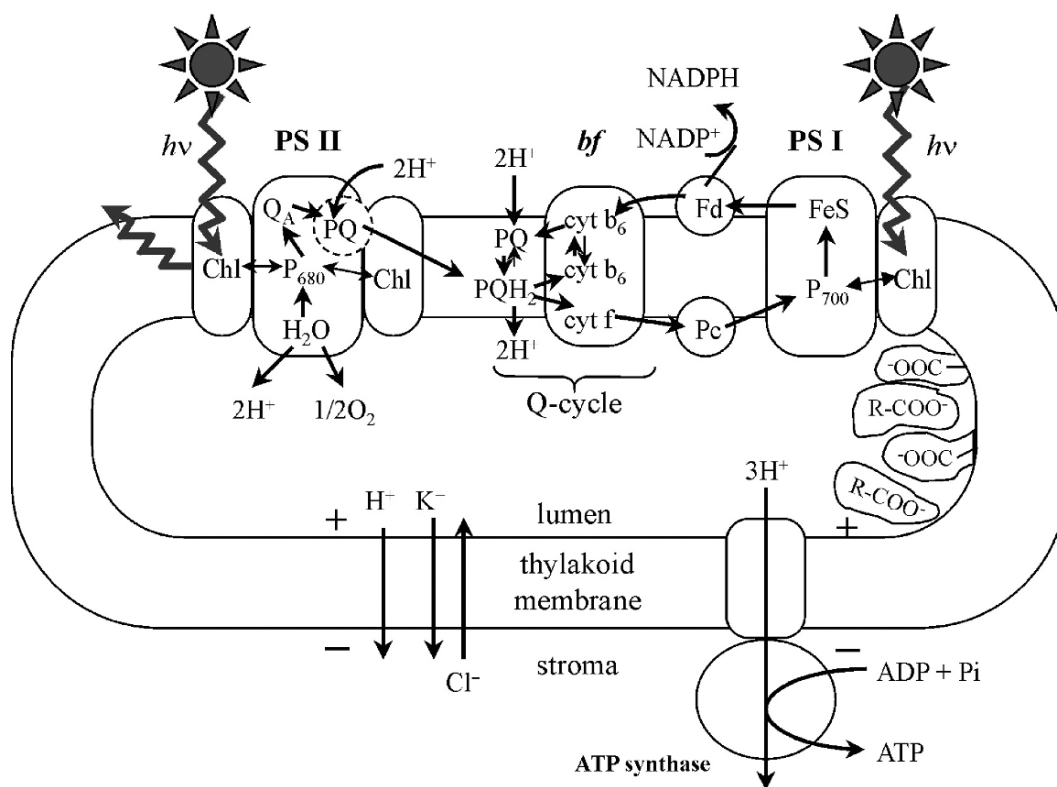


Fig. 7.1. Flow chart for the generalized model of primary photosynthetic processes. PS I, PS II – photosystems I and II; Chl – antenna chlorophyll; P680 and P700 – pigments of the PS II and PS I reaction centers; Q_A – primary quinone acceptor of PS II; FeS – acceptor complex of PS I; Fd – ferredoxin; Pc – plastocyanin; b_6f – cytochrome b_6f complex; PQ – plastoquinone, PQH_2 – plastoquinol; R – COO^- designate buffer groups. Signs (+) and (–) on the membrane indicate that the thylakoid lumen is charged positively and the chloroplast stroma is charged negatively in the course of photosynthetic processes. Zigzag arrows denote quanta of incident light and fluorescence. Common arrows indicate the direction of electron transfer along the chain and the ion fluxes across the thylakoid membrane upon the onset of the illumination (modified from Lebedeva et al., 2002)

description was developed by Shinkarev and Venedictov (1977) and by Rubin and Shinkarev (1984). The method was applied to describe electron transport processes in reaction centers of photosynthetic bacteria and in isolated PS I and PS II particles (Riznichenko et al., 1980, 1986, 1988, 1990, 1991; Malik et al., 1990).

According to the master-equation approach, the state of a complex consisting of n components C_1, C_2, \dots, C_n (depicted in square brackets)

$$\rightarrow [C_1 C_2 \dots C_n] \rightarrow \quad (7.1)$$

is considered as a consecutive order of different states of electron carriers C_i , included in the complex. Transitions between the states are described

by ordinary differential equations, which are linear in probabilities of the corresponding states:

$$\frac{dp_i}{dt} = \sum_{j=1}^l (p_j k_{ji} - p_i k_{ij}). \quad (7.2)$$

Here p_i is the probability to find the complex in the i -th state; k_{ij} – the rate constant of the transition from the i -th to the j -th state. Under the sum there is a difference between the probabilities of transitions to the i -th state from other states (positive term) and the probability of the transitions from i -th state to all other states (negative term). The initial probabilities are

$$p_i(0) = b, \quad i = 1, \dots, l.$$

In vectorial form, Eq. (7.2) can be written as

$$\frac{dP}{dt} = K^T P, \quad P(0) = B. \quad (7.3)$$

Here P is a vector of probabilities of all states of the complex under consideration, B – a vector of the initial states, K^T – transposed matrix of the rate constants of transitions between the states.

The probability to find the carrier number q in the certain state G is presented as

$$P_q(G) = \sum_{S_q \in G} p(S_q, t). \quad (7.4)$$

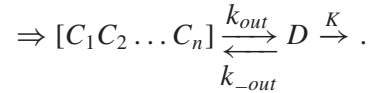
Here we sum over all states S_q , where the q -th component is presented in the state G .

Thus, p_i corresponds to the fraction of the complexes in the i -th state. To obtain the concentration of complexes in the i -th state, it is necessary to multiply p_i by the total concentration of all complexes $[C_1, C_2 \dots, C_n]$. To find the probability of the carrier to be in the certain state (oxidized, or reduced) it is necessary to sum probabilities to find the complex in all states, where the carrier is in this certain state. The resulting sum will be equal to the fraction of that carrier found in this particular state. To find the concentration of a definite carrier in a definite state, we multiply the value of the resulting probability by the total concentration of the complex.

Rate constants k_{ij} of the transitions between the states may not have constant values, but may depend on the state of the whole complex (for example, localized in the stromal or in the granal part of a thylakoid) as well as on other variables or parameters of the system, e.g., temperature, transmembrane potential, and external electric field. Thus the system of differential equations, describing the transitions between the states in a real photosynthetic complex is usually non-linear.

In Figs. 7.2 and 7.3 we consider the processes in PS II and Cyt b_6f complexes. A photosynthetic complex contains several components, each of which can be present in the oxidized or reduced form. Some carriers exist in more than two forms, e.g., chlorophyll (Chl) can be present in oxidized, reduced and excited form, Q_B – in double reduced form. Thus the scheme of the states and their transitions for photosynthetic complex usually includes dozens of states. The complexity of the scheme, that we want to use, depends on the goal of the modeling process.

The whole electron transport chain (Fig. 7.1) contains PS II, Cyt b_6f and PS I complexes with fixed structure. The interactions of these complexes among each other and with the environment proceed via mobile carriers PQ, Pc, Fd (Fig. 7.1). The step controlled by diffusion, of electron transfer between the complex $[C_1 C_2 \dots C_n]$ and the mobile carrier D can be presented in a simple scheme:



The changes of concentration of the mobile carrier D in the reduced form can be described by the mass action law equation

$$\begin{aligned} \frac{d[D^-]}{dt} &= k_{out}[C_n^-][D^+] \\ &\quad - k_{-out}[C_n^+][D^-] - K[D^-]. \end{aligned} \quad (7.5)$$

Here $[D^+]$ and $[D^-]$ are concentrations of the mobile carrier in the oxidized and the reduced forms. $[D^+] + [D^-] = [D_0]$, where $[D_0]$ is the total concentration of the mobile carrier; $[C_n^+]$ and $[C_n^-]$ are concentrations of the components of the complex, interacting with the mobile carrier in the oxidized and reduced forms, calculated according to Eq. (7.4); k_{out} and k_{-out} are bimolecular rate constants of the redox reaction between the complex $[C_1 C_2 \dots C_n]$ and the mobile carrier D ; K is the rate constant of the further metabolism of the mobile carrier D .

2. Photosystem II Complex

There are models describing O-J-I-P fluorescence transients, which consider detailed schemes of electron transport and energy transformation in PS II, especially the donor side of PS II (oxygen evolving complex), and the interaction of the PS II complex with Chl antenna molecules (Stirbet and Strasser, 1995, 1996; Stirbet et al., 1998; Strasser and Stirbet, 1998, 2001; Vredenberg, 2000, 2004; Vredenberg et al., 2004, 2006, 2007; Lazar, 2003; Zhu et al., 2005). The comparative study concerning the different nature of possible

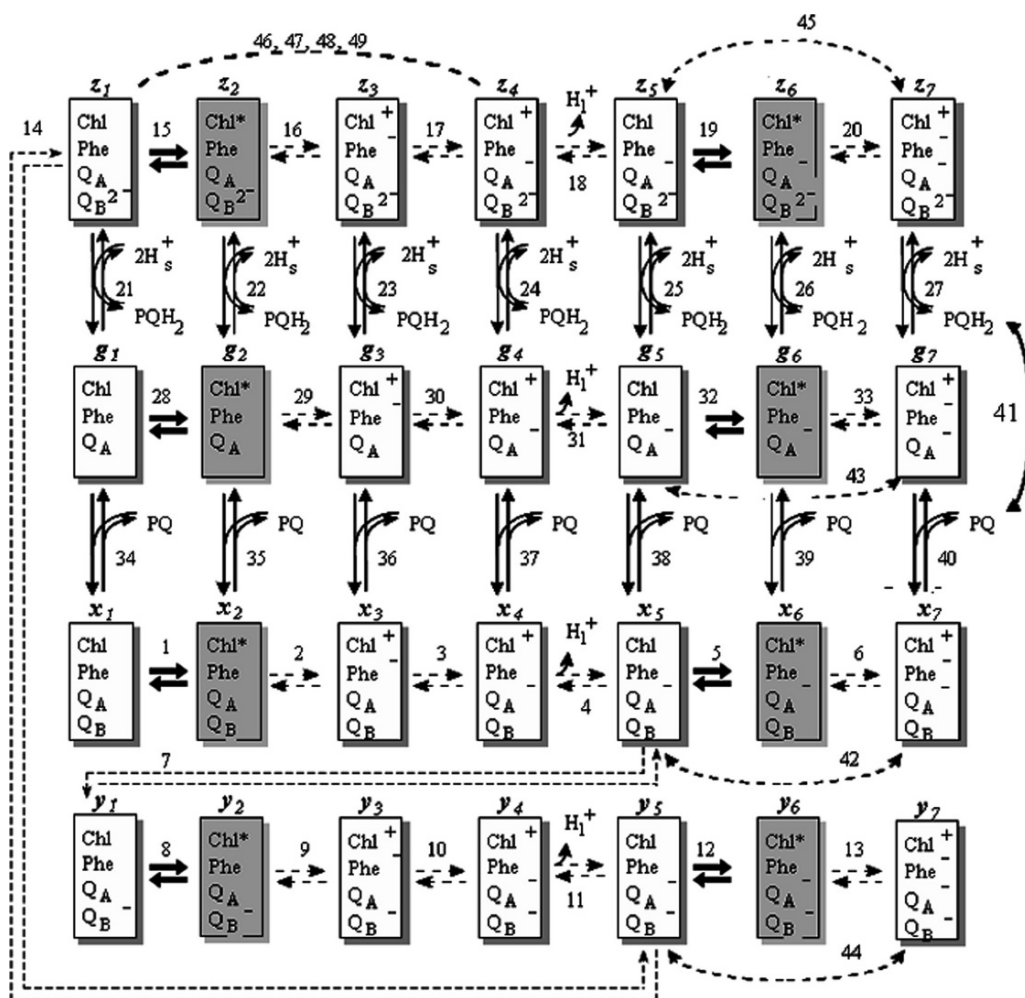


Fig. 7.2. The scheme of the catalytic cycle of photosystem II. Each rectangle refers to one of the states of the photosystem II complex, which is determined by redox states of carriers, included in the complex. Chl – the total PS II chlorophyll including the antenna and the P680 pigments; Phe – primary electron acceptor pheophytin; Q_A and Q_B – primary and secondary quinone acceptors. The letters above rectangles (x_i , y_i , z_i , g_i , $i = 1 \dots 7$) correspond to the model variables. Shaded are the excited states capable of emitting fluorescence quanta. Dotted arrows designate fast steps (characteristic time < 0.1 ms), continuous arrows denote slow steps (characteristic time > 1 ms). Bold arrows mark the light steps. Numbers at the arrows correspond to the step numbers. PQ – plastoquinone; PQH_2 – plastoquinol; H_L^+ – protons, which are released into lumen; H_S^+ – protons, absorbed from stroma. Dotted arcs designate two types of irreversible reactions of the processes of non-radiative recombination: Phe^- with $P680^+$ (42–45), Q_A^- with $P680^+$ (46–49) (adapted from Belyaeva et al., 2006)

FL quenchers was carried out by Strasser and Stirbet (2001) for three approaches describing FL yield as a function of the reduction state of carriers, either of $[Q_A^-]$ or $[Phe^-]$ or both of them. Since the simulations for these three models were equally satisfactory in fitting experimental data with an accuracy of about 2% over the time span of 20 μ s to 2 s, it was not possible to indicate the proper model corresponding to reality (see discussion in Strasser et al., 2004).

We used another scheme (Fig. 7.2), where we assume the intensity (yield) of FL to be proportional to the concentration of the PS II complexes with excited Chl*, which is the source of FL emission. The scheme, presented here, proved to contain the necessary details to simulate a set of experimental data.

In the model of PS II complex, we consider four constituent electron carriers: Chl, pheophytin (Phe), the primary one-electron quinone

acceptor Q_A , and the binding site for the secondary quinone acceptor Q_B . We assume that the excitation energy, initially localized on one of the antenna pigments, is rapidly equilibrated (within picoseconds) over the entire pool of PS II antenna pigments, including the P680 reaction center pigment. Thus, the designation Chl covers the whole complex of these pigments. The kinetic states x_i, y_i, z_i, g_i ($i = 1, 2, \dots, 7$) differ in the state of the Q_B binding site: in g_i the site is vacant, in x_i the site contains non-reduced Q_B , in y_i and z_i , the PQ in the site carries one (Q_B^-) and two electrons (Q_B^{2-}), respectively.

When the light is switched on, Chl goes into the excited state (steps 1 and 28), which may be accompanied by primary (steps 2 and 29) and secondary (steps 3 and 30) charge separation. In the dark (dark adaptation), the PS II complex acquires states x_1 , and g_1 , which come to equilibrium (step 34). The oxygen evolving complex (OEC) reduces the oxidized reaction center

pigment (steps 4 and 31). We do not consider the molecular mechanism of the OEC operation, but assume that for every electron transferred from OEC to the oxidized P680 one proton is released into the intra-thylakoid space. Thus, the sequence of steps 1–4 or 28–31 results in formation of the “closed” reaction center with reduced Q_A (states x_5 and g_5).

Further illumination of the closed RC may result in repeated excitation of the pigment (steps 5 and 32) and in primary charge separation (steps 6 and 33). Thereby, the states with oxidized pigment and reduced Phe and Q_A (states x_7 and g_7) appear in the PS II. In any state g_i ($i = 1, 2, \dots, 7$) PQ can bind at the Q_B site (steps 34–40) to give the corresponding states x_i ($i = 1, \dots, 7$). The bound Q_B is a two-electron carrier and can consequently accept two electrons from Q_A^- . Steps 7 and 14 (dashed lines in Fig. 7.3) describe the transfer of the first and the second electron to Q_B with the formation of states y_1 (Chl

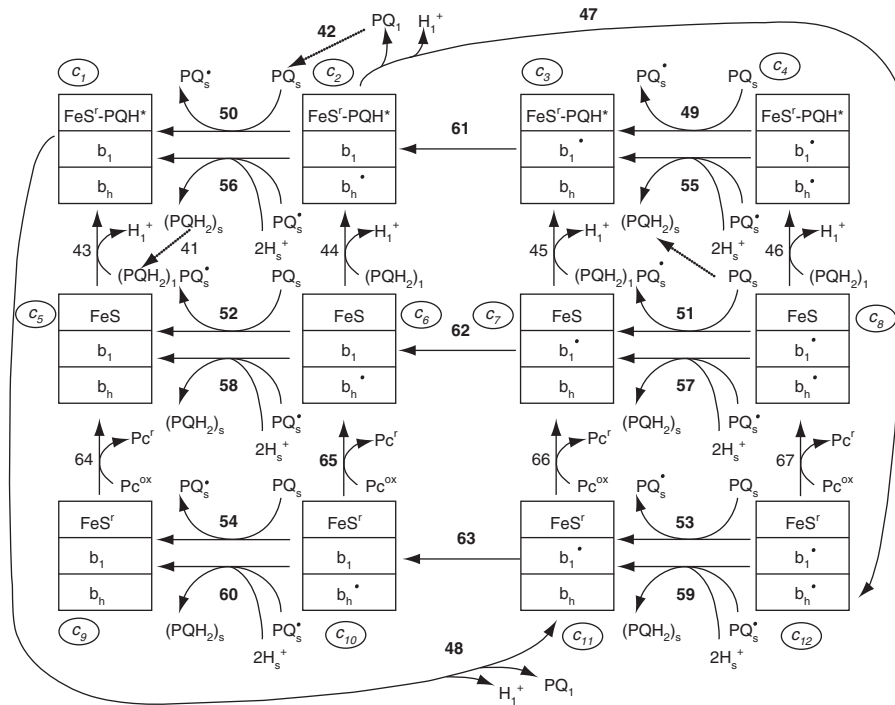


Fig. 7.3. The scheme of the catalytic cycle of cytochrome b_6f complex. Each rectangle represents one of the possible kinetic states of the complex, determined by the states of its components. b_h and b_l – high and low potential hemes; FeS , FeS^* – Rieske iron-sulfur center in neutral and reduced form; Pc^r and Pc^{ox} – reduced and oxidized plastocyanin, correspondingly. Letters c_i ($i = 1 \dots 12$) designate the variables in the model. H_1^+ – protons released into inter-thylakoid space, H_s^+ protons, absorbed from stroma; PQ – plastoquinone; PQH_2 – plastoquinol. Subscripts (l), (s) indicate the lumenal and stromal sites of the cytochrome complex; (•) indicates the presence of electron on the corresponding molecule (after Kamali et al., 2004)

Phe Q_A Q_B⁻) and g_1 (Chl Phe Q_A). Under illumination, these states can undergo the sequence of conversion described for x_1 and g_1 , including pigment excitation (steps 8 and 15), primary (steps 9 and 16) and secondary (steps 10 and 17) charge separation, reduction of oxidized P680 by OEC (steps 11 and 18) and excitation of closed RC (steps 12 and 19) attended by primary charge separation (steps 13 and 20).

In any state z_i ($i = 1 \dots 7$), plastoquinol (PQH₂) may be released (after the uptake of two protons H_s⁺ from the chloroplast stroma), giving states g_i ($i = 1 \dots 7$) with vacant Q_B site (steps 21–27). Steps 1, 5, 8, 12, 15, 19, 28 and 32 marked with bold arrows in the scheme are the “light-activated steps” describing the transition of Chl into the excited state Chl*, and the reverse process resulting in FL emission.

Excitation of Chl and generation of the state Chl* is given in the model by the corresponding “light” rate constants $k_L = k_i$, $i = 1, 5, 8, 12, 15, 19, 28, 32$, which are proportional to the light intensity. FL emission is determined by the rate constant $k_F = k_{-i}$. The FL yield (F) is calculated as the product of the sum of the excited states and the ratio between the rate constants k_F and k_L :

$$F = \frac{k_F}{k_L} \cdot (x_2 + y_2 + z_2 + g_2 + x_6 + y_6 + z_6 + g_6). \quad (7.6)$$

We use FL yield $F = FL/k_L$ (instead of FL intensity) to compare the energetic efficiency of photosynthetic processes in different conditions.

3. Cytochrome $b_6 f$ Complex

Cytochrome $b_6 f$ complex is one of the major photosynthetic protein units of the thylakoid membrane, positioned between the two photosystems, PS II and PS I, in the electron transport chain. This hetero-oligomeric dimeric complex mediates electron transfer between the PS II and PS I reaction center complexes by oxidizing the lipophilic plastoquinol and reducing the soluble plastocyanin (for reviews see O’Keefe, 1988; Cramer et al., 2004, 2005, 2006; for the structure of the Cyt $b_6 f$ complex see Kurisu et al., 2003; Yan et al., 2006; Yamashita et al., 2007).

The essential function of the Cyt $b_6 f$ complex is to couple an electron transport with electrochemical proton potential $\Delta\mu_H$ across the thy-

lakoid membrane, the dissipation of the latter leads to ATP synthesis. The main elements of the Cyt $b_6 f$ complex are the Rieske iron-sulfur center (FeS_R), cytochrome f , two hemes of cytochrome b (high-potential b_H and low-potential b_L) and two binding sites denoted here as l , luminal and s , stromal for plastoquinol oxidation and plastoquinone reduction. Recently, a novel heme c_n has been described that is supposed to play a special role on the cyclic electron transport around PS I (Yamashita et al., 2007).

In our model (Fig. 7.3) we used one of the most popular schemes of the Q-cycle, where the second electron from plastoquinol reduces b_L (Hope et al., 1992; Hauska et al., 1996; Hope, 2000). Electrons are fed into the Q-cycle at the luminal (l) side of the membrane (step 41, dotted arrow in the left-hand part of Fig. 7.3). Upon binding with the (l) center of the Cyt $b_6 f$ complex, the plastoquinol passes one electron to the Rieske iron-sulfur center (FeS) and releases one proton into the thylakoid lumen; this makes a complex of protonated PQ with reduced FeS (steps 43–46 depending on the redox states of FeS and cyt b hemes). If the low-potential heme b_L is reduced, the semiquinone remains bound at the Rieske center until b_L is oxidized (in steps 49, 55 and 61). Then the second proton is released, and the semiquinone of the FeS⁺-QH[•] complex gives the electron to the b_L heme, thus converting into free PQ (steps 47 and 48), and it, then, diffuses back to the stromal side (step 42, dotted arrow in the upper part of the scheme in Fig. 7.3). Further, the electron is transferred across the membrane from the low-potential to the high-potential heme (steps 61–63). Thereupon the reduced b_H heme reduces the PQ in the (s) center to produce semiquinone PQ_s[•] (steps 49–54). This semiquinone takes the second electron from b_H to become a plastoquinol consuming two protons from the stroma (steps 55–60). Simultaneously, the electron accepted by the FeS center is transferred to Cyt f and then to Pc (steps 64–67). The scheme does not show the step corresponding to the electron transfer between FeS and Cyt f , but these carriers are in fast equilibrium (both rate constants $> 10^5 \text{ s}^{-1}$, and the equilibrium constant is about 3, Hope, 1993). That is why we combine Cyt f – the compound actually interacting with Pc – with FeS_R in one component.

Kamali et al. (2004) developed the sub-model of Cyt b_6f complex assuming Q-cycling and considering the dependence of electron transfer rates on electrical potential. The model parameters were fitted with experimental data on redox conversions of Cyt b and Pc, as well as on the proton pumping into the thylakoid lumen upon a saturating light flash (Hope et al., 1992). The 20 ms kinetics was considered, whereas only the first 7 ms were used for fitting in the original work. We assumed that the Q-cycle has four electrogenic steps: the first one corresponds to the transmembrane electron transport from Cyt b_L to Cyt b_H (steps 61–63), while the three others correspond to the proton transport coupled with plastoquinone reduction (steps 55–60) and plastoquinol oxidation (steps 43–48). The interheme electron transport was assumed to be responsible for 80% of the overall electrogenesis, and the remaining 20% were shared equally between the proton-transport steps, which is in agreement with the data of Drachev et al. (1990), obtained for cytochrome bc_1 complex in purple bacteria.

4. Photosystem I Complex

The version of the model we discuss here is focused on the simulation of Chl a fluorescence

transients. There is a general agreement that at room temperatures, Chl fluorescence in plants, algae and cyanobacteria, in the 680–740 nm spectral region is emitted mainly by PS II (Dau, 1994; Strasser et al., 2004; Wydrzynski and Satoh, 2005; Golbeck, 2006). For this reason, we consider PS I complex in a rather simplified scheme (Fig. 7.4), though PS I may rather significantly effect the shape of fluorescence induction by regulating the electron outflow from PS II.

The PS I submodel (Fig. 7.4) includes five kinetic states which are determined by the state of the P700 reaction center pigment and the acceptor FeS complex. Note that FeS here designates the entire complex of acceptors: primary and secondary A_0 and A_1 as well as the iron-clusters F_x , F_A and F_B . We do not discuss the details of electron transport within the acceptor complex FeS, but assume that it can exist in an oxidized or a reduced state, as a “whole” carrier. This simplification appears reasonable, because the electron transfer along the $A_0 \rightarrow A_1 \rightarrow F_x$ chain is very rapid (10^{-12} to 10^{-9} s, Malkin and Niyogi, 2000).

Under illumination, P700 becomes excited ($P700^*$, step 68) with the subsequent charge separation (step 69) and formation of the state $P700^+ FeS_r$. This state can further be “utilized” in two ways. Oxidized $P700^+$ may first accept

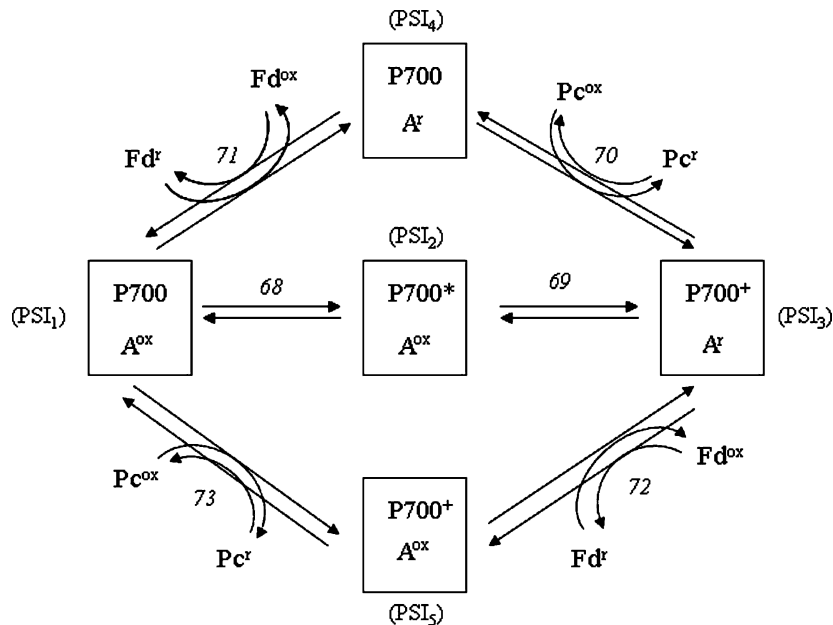


Fig. 7.4. Simplified scheme of electron transfer in PS I. P700 is the reaction center chlorophyll, FeS the entire acceptor complex; Fd – ferredoxin; Pc – plastocyanin; superscripts mark the reduced (r) and oxidized (ox) states. Designations (PSI)_i ($i = 1 \dots 5$) correspond to the model variables

an electron from Pc (step 70), after which the acceptor complex will reduce Fd (step 71) or vice versa; first the FeS_r complex may give its electron to Fd (step 72) and after that Pc reduces the oxidized P700 (step 73). Most of the equilibrium and rate constants were taken from Brettel (1997). At the same time, some parameters were optimized so as to attain satisfactory theoretical results fitting the experimental data.

5. Mobile Carriers in the Kinetic Model

Electron transport between complexes is carried out by mobile carriers (Fig. 7.1). Molecules of the protein plastocyanin (Pc) move in the inner lumenal part of a thylakoid. Molecules of ferredoxin (Fd) diffuse in the external stromal space, and molecules of plastoquinone in oxidized and double-reduced protonized form (PQ, PQH₂) move inside the lipid bilayer of the membrane. In the general kinetic model we assume interactions between the mobile carriers and the multienzyme complexes by means of the mass action law.

6. The Role of Transmembrane Electrical Potential

A photosynthetic membrane can be considered as a special capacitor. Transmembrane electron and ion transitions are accompanied by the formation of transmembrane electrical potential, $\Delta\Psi$, which in turn affects electron and ion fluxes. Numerous experiments on the influence of external electric field suggested that the rates of electron transfer inside the PS I, PS II and Cyt b₆f complexes depend on the thylakoid transmembrane potential (Dau and Sauer, 1992; Zheng et al., 1990).

We assume that $\Delta\Psi$ is a variable in the model, which is determined by the overall changes of the electrical charge in lumen and stroma resulting from transmembrane transfer of electrons and ions (Krab et al., 1985):

$$\frac{c_m}{F} \times \frac{d(\Delta\Psi)}{dt} = v(q_{lumen}) - v(q_{stroma}).$$

Here, the symbols are c_m , specific capacity; F , Faraday constant; $v(q_{lumen})$, $v(q_{stroma})$, volume charge density in lumen and stroma q_{lumen} , q_{stroma} , functions of the concentrations of

H⁺, K⁺ and Cl⁻ ions in appropriate thylakoid compartments. Concentrations of the H⁺, other positive ions (K⁺, Mg²⁺) and negative ions (Cl⁻) in lumen and stroma are the model variables.

In the model we assume that the rates of electron transport at the transfer steps directed normally to the membrane surface depend on $\Delta\Psi$. According to one formalism (Reynolds et al., 1985) our model takes into account the dependence of the rate constants on transmembrane electric potential $\Delta\Psi$ as follows:

$$\tilde{k}_+(\Delta\Psi) = \exp(-\delta \cdot \alpha \cdot \Delta\Psi \cdot (F/RT)) \cdot k_+,$$

$$\tilde{k}_-(\Delta\Psi) = \exp(-\delta \cdot \alpha \cdot \Delta\Psi \cdot (F/RT)) \cdot k_-.$$

Here α is the portion of $\Delta\Psi$ that is generated at the particular step by charge transfer across the membrane that affects the rate of the reaction; δ , the portion of the membrane potential $\alpha \cdot \Delta\Psi$ that affects the rate constant of the direct reaction; k_+ , k_- , the corresponding direct and reverse rate constants, respectively, at $\Delta\Psi = 0$; F , Faraday constant; R , gas constant and T is temperature.

We emphasize that the dependence of the reaction rate constants on transmembrane electrical potential is an important characteristic of the model which allows us to simulate experimental data when $\Delta\Psi$ varies (Belyaeva et al., 2003).

7. Transmembrane Ion Transfer and $\Delta\mu H$ Generation

Transmembrane proton gradient ΔpH is a model variable; at any moment of time, it is determined by the proton concentration difference in stroma [H_n] and lumen [H_p]: $\Delta pH = \lg[H_p] - \lg[H_n]$.

Transmembrane proton transfer in the direction opposite to the concentration gradient is coupled to electron transport and occurs at several steps of the photosynthetic chain. The main contribution is brought about by PQ reduction/oxidation and the Q-cycle. A mobile PQ molecule in the membrane binds to the acceptor side of PS II, accepts subsequently two electrons and takes up 2H⁺ from the stromal space. A double-protonized neutral molecule of PQH₂ detaches from the PS II complex and diffuses inside the membrane until it contacts the lumenal binding site of Cyt b₆f. As a result of this contact two electrons in series enter the chain of the Cyt b₆f complex, and two protons are released into the lumenal space, taking part in

the generation of the electrochemical membrane potential. Protons are liberated into the luminal space also as a result of water splitting at the donor side of PS II. These processes are considered in the scheme of transitions between the PS II states (Fig. 7.2), which takes into account the formation of the transmembrane proton gradient. Proton transport inside the thylakoid can occur also during cyclic electron transport around PS I.

$\Delta\mu\text{H}$ is consumed in the ATP-synthase reaction (Junge, 1999). The formation of ATP from the ADP and P_i is accompanied by proton transfer from the lumen to stroma. The proton gradient may decrease also due to passive proton leakage. The capture and release of protons at the stromal and luminal sites of PS II and Cyt b_6f coupled to the photoinduced electron transport lead to the redistribution of the charges in the stroma and lumen. The generated electrical potential $\Delta\Psi$ induces passive ion fluxes across the thylakoid membrane.

We used the model of ion transport through a three-barrier channel (Nicholls, 1974; Brown and Brand, 1986; Kholodenko, 1988; Tester and Blatt, 1989; Potossin and Schönknecht, 1996) for the description of the transmembrane movement of protons, positive (K^+ , Mg^{2+}) and negative ions (Cl^-). The rate equation for the ATP synthase reaction was based on the minimal kinetic scheme of ATP synthesis/hydrolysis (Boork and Wennerström, 1984).

8. Buffer Properties of Lumen and Stroma

The chloroplast stroma and the thylakoid lumen are known to exhibit buffer properties due to the presence of various proton-binding groups in their volume. In our model, we approximate the buffering in the compartments by three proton-binding groups (B_1 , B_2 , B_3), their pKs for protons varying from 4 to 8. The dissociation constants and the concentrations of buffering groups were chosen so as to fit the experimental data on the buffer capacity of the thylakoid lumen (Van Kooten et al., 1986).

9. Parameter Values

An estimation of the parameters is a special problem. Some values can be determined accurately, e.g. the rate constants for charge separation in PS

II and PS I (Schatz et al., 1988; Laisk and Walker, 1989; Renger, 2001, 2007; Strasser et al., 2004; Wydrzynski and Satoh, 2005; Golbeck, 2006). Other processes are less studied. This is particularly true for the slower processes such as PQ diffusion in a photosynthetic membrane as well as transmembrane ion transport and the buffer properties of lumen and stroma. The wide dispersion of these rate values is connected with the variability of geometry, pH, ionic strength and other parameters in different cells under different environmental conditions. We shall discuss this problem when we shall formulate the direct multiparticle model of photosynthetic electron transport in Section IV.

In our model most of the equilibrium and rate constants for the reactions were taken from the literature (Crofts and Wraight, 1983; Brettel et al., 1984; Renger and Schulze, 1985; Eckert and Renger, 1988; Schatz et al., 1988; Baake and Schloder, 1992; Roelofs et al., 1992; Bernarding et al., 1994; Vasil'ev et al., 1996; Stirbet et al., 1998; Schodel et al., 1999; Bulychev and Vredenberg, 2001; Renger, 2001; Lazar, 2003; Steffen et al., 2005; Zhu et al., 2005). For each reaction (n – the number of reaction) we take into account the relation between the rate constant of the forward k_n and reverse k_{-n} reactions through the equilibrium constant $K_{n,eq}$:

$$k_n = k_{-n} \cdot K_{n,eq}$$

where k_n , k_{-n} are the rate constants for reactions which are shown in schemes in Figs. 7.2–7.4.

The equilibrium constants of redox reactions were determined from the experimental data on midpoint redox potential,

$$K_{eq} = \exp\left(-\frac{\Delta E_m}{RT/n \cdot F}\right), \quad (7.7)$$

where ΔE_m – is the difference of midpoint redox potentials of the electron carriers, measured relative to a standard hydrogen electrode and n is the number of electrons transferred in the course of the redox reaction. The ΔE_m , k_n , k_{-n} values were taken from literature (e.g. Schatz et al., 1988; Laisk and Walker, 1989; Renger, 2001; Roelofs et al., 1992) and used as preliminary estimates. These values were changed to improve the fit with the experimental data. The detailed tables for model parameter values are available in

the original papers (Lebedeva et al., 2000, 2002; Kamali et al., 2004; Belyaeva et al., 2006).

B. Results of Simulation

Classical experimental fluorescence induction curves at different light intensities (Strasser et al., 1995) are presented in Fig. 7.5a. Our model, including the description of the whole electron transport chain, allows us to simulate the shape of fluorescence induction curve at low, intermediate and high light intensities. The low, middle and high intensities correspond to 15, 150 and 1,500 quanta s^{-1} per PS I and PS II. The light intensities were set with the appropriate values of the light-dependent rate constants k_i ($i = 1, 5, 8, 12, 15, 19, 28, 32, 68$) (schemes of PS II and PS I complexes, Figs. 7.2 and 7.4). The time-dependent relative fluorescence yield after

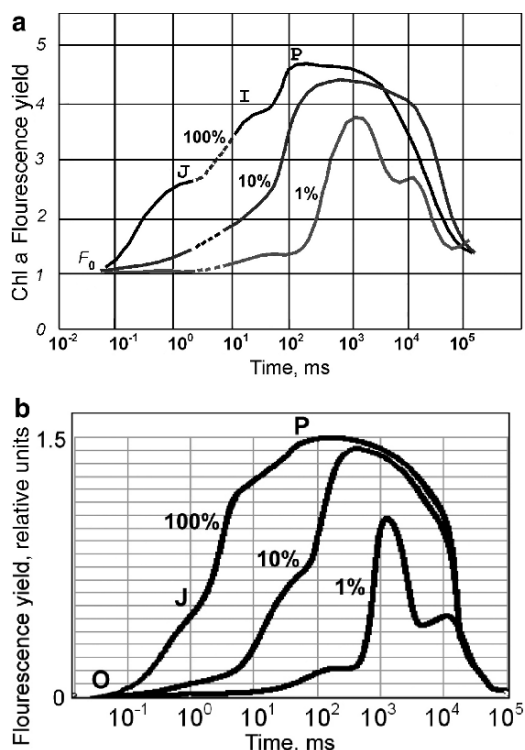


Fig. 7.5. Chlorophyll fluorescence yield induction curves at different light intensities. (a) Experimental data obtained on *Pisum sativum* leaves illuminated with red light at the intensity 600 (100%), 60 (10%) and 6 (1%) $W m^{-2}$ (Strasser et al., 1995). (b) Corresponding fluorescence induction curves, simulated by Lebedeva et al. (2002)

the onset of illumination (Fig. 7.5b) was calculated according to Eq. (7.6).

To simulate changes in the state of the photosynthetic system after switching on the light, we had to establish the initial values of the variables that would correspond to the “dark” state of the system. The stationary solution was obtained in the case when all the light-dependent rate constants were zero. We took this solution for the average chloroplast volume of $40 \mu m^3$; P700 content of 2 mmol per 1 mol chlorophyll; chloroplast stroma, thylakoid lumen, and thylakoid membrane volume ratio of 10:1:1. The stoichiometry of PS II, Cyt b_6f , PS I, PQ and Pc in the thylakoid membrane was taken to be 1:1:1:6:2.

1. Simulation of Fluorescence Transients at Different Light Intensities

For simulation we used the general model, including the processes presented in Fig. 7.1. The schemes of submodels of individual photosynthetic complexes are presented in Figs. 7.2–7.4 and are described above.

The model provides a rather good fit (Fig. 7.5) of simulations and experimental fluorescence transients, not only for high light intensities as published earlier (Stirbet et al., 1998; Strasser et al., 2004; Zhu et al., 2005; Lazar, 2003; Lazar et al., 2005), but also for low and middle light intensities. At low values of the light-dependent constants corresponding to low illumination (1% or $6 W m^{-2}$), fluorescence approaches the maximum in about 1–2 s, and the induction curve exhibits one intermediate phase (200 ms). A ten-fold increase in the light constants corresponding to medium illumination (10%, $60 W m^{-2}$) causes a rise in the signal and shortens the time for reaching the maximum (about 50 ms), while the intermediate phase becomes less pronounced. At the high light intensity (100%, $600 W m^{-2}$) fluorescence transient takes its classical OJIP-shape, reaching the peak in 100–200 ms, with two intermediate phases (J at about 2 ms and I at about 20 ms).

2. The Role of Different States of Photosystem II in Fluorescence Induction

The analysis of the model showed that to simulate the fluorescence induction curve at the low

light intensity and over time intervals longer than 1 s (the “slow phase” of fluorescence induction) it is necessary to consider the electrical and electrochemical potential, as well as the processes in Cyt b_6f and in PS I.

In Fig. 7.6 the system component transformations in response to illumination are presented. Chlorophyll fluorescence yield transients (curve F) and electrical potential (curve $\Delta\Psi$) are presented in Fig. 7.6a. In Fig. 7.6b, we have plotted the time dependence of the concentrations of PS II states capable of emitting fluorescence (shaded in Fig. 7.2). Simulation experiments revealed that at any given light intensity the contribution of the states with oxidized Q_A to the fluorescence is at least one order of magnitude lower than the contribution of the states with reduced Q_A . This is in accord with the existing notion that the variable fluorescence is approximately proportional to the concentration

of closed (Q_A^- -containing) reaction centers of PS II (Stirbet et al., 1998; Strasser et al., 2004). For this reason in Fig. 7.6b only PS II fluorescing states z_6 ($\text{Chl}^*\text{PheQ}_A^-\text{Q}_B^{2-}$), g_6 ($\text{Chl}^*\text{PheQ}_A^-$), x_6 ($\text{Chl}^*\text{PheQ}_A^-\text{Q}_B$), y_6 ($\text{Chl}^*\text{PheQ}_A^-\text{Q}_B^-$) with reduced Q_A are presented.

The relative concentration of each fluorescing form depends on the light intensity. Under low intensity, fluorescence is mostly emitted by states g_6 ($\text{Chl}^*\text{PheQ}_A^-$, the quinone acceptor with reduced Q_A and vacant Q_B) and z_6 ($\text{Chl}^*\text{PheQ}_A^-\text{Q}_B^{2-}$). Indeed, these states are generated by light absorption from g_5 (Chl PheQ_A^-) and z_5 ($\text{Chl PheQ}_A^-\text{Q}_B^{2-}$) which do not allow the electron transfer to proceed from Q_A (the secondary acceptor either absent or fully reduced). Since PQ attachment to the Q_B site and PQH_2 dissociation are relatively slow processes, states g_5 (Chl PheQ_A^-) and z_5 ($\text{Chl PheQ}_A^-\text{Q}_B^{2-}$) and

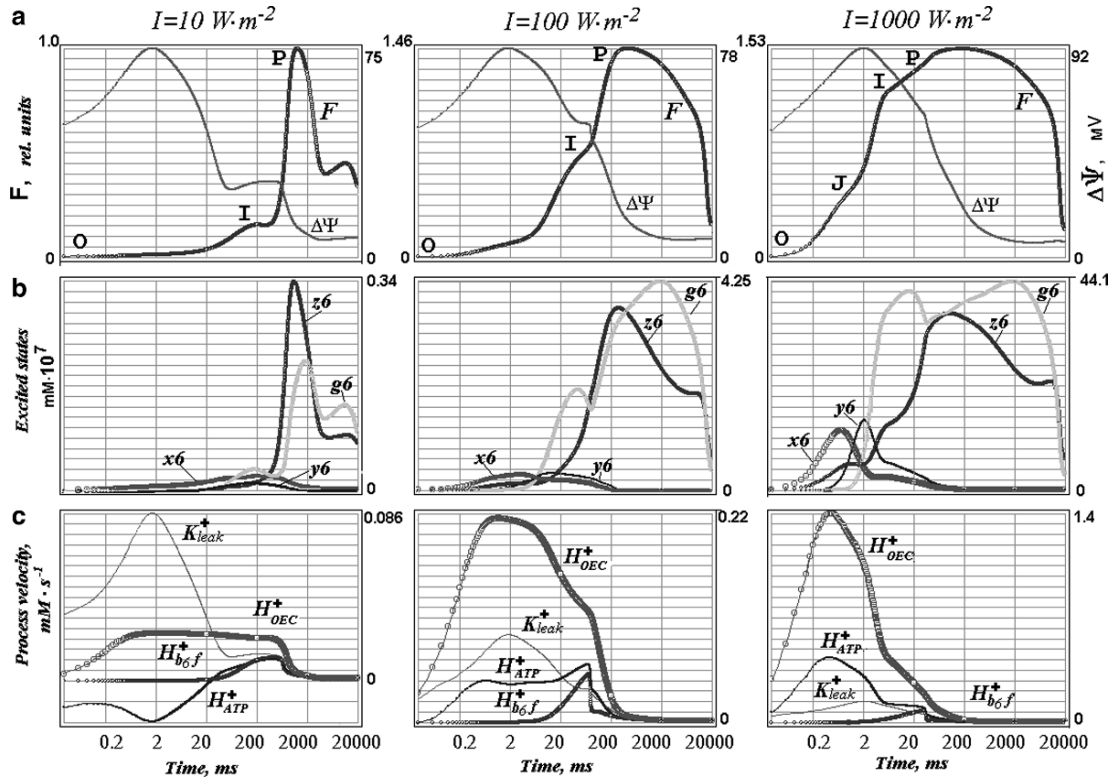


Fig. 7.6. Simulated induction curves for three different intensities of illumination: 1,000 (100%) 100 (10%) and 10 (1%) W m^{-2} . Results are presented on a logarithmic time scale. (a) Fluorescence yield (F) and transmembrane electrical potential ($\Delta\Psi$); (b) concentration of different excited states of photosystem II; (c) rates of the processes, generating and consuming electric charge in the thylakoid lumen. H_{bf}^+ – proton flux directed into the lumen by plastoquinol oxidation at the luminal site of Cyt b_6f complex; H_{oec}^+ – proton flux directed into the lumen from oxygen evolving complex; H_{atp}^+ – the rate of proton consumption in the ATP-synthase reaction; H_{leak}^+ – the rate of the leakage of H^+ ions from the lumen of thylakoid (Lebedeva et al., 2002)

hence g_6 ($\text{Chl}^*\text{PheQ}_\text{A}^-$) and z_6 ($\text{Chl}^*\text{PheQ}_\text{A}^-\text{Q}_\text{B}^{2-}$) can accumulate at greater concentrations than the corresponding x and y , in which the secondary acceptor is not fully reduced and the Q_A^- electron can be transferred to Q_B to yield respectively y_1 ($\text{ChlPhe Q}_\text{A}\text{Q}_\text{B}^-$) and z_1 ($\text{ChlPheQ}_\text{A}\text{Q}_\text{B}^{2-}$). At low light intensities the rate of this process exceeds the rate of formation of the excited states, so that fluorescing forms x_6 ($\text{Chl}^*\text{PheQ}_\text{A}^-\text{Q}_\text{B}$) and y_6 ($\text{Chl}^*\text{PheQ}_\text{A}^-\text{Q}_\text{B}^-$) are minor. Under moderate illumination, the fluorescence of the system is also largely determined by the sum of g_6 and z_6 , though the fractions of x_6 ($\text{Chl}^*\text{PheQ}_\text{A}^-\text{Q}_\text{B}$) and y_6 ($\text{Chl}^*\text{PheQ}_\text{A}^-\text{Q}_\text{B}^-$) somewhat also increase.

Under intense illumination, the contribution of x_6 ($\text{Chl}^*\text{PheQ}_\text{A}^-\text{Q}_\text{B}$) and y_6 ($\text{Chl}^*\text{PheQ}_\text{A}^-\text{Q}_\text{B}^-$) to the fluorescence is comparable to that of g_6 ($\text{Chl}^*\text{PheQ}_\text{A}^-$), and z_6 ($\text{Chl}^*\text{PheQ}_\text{A}^-\text{Q}_\text{B}^{2-}$), because the time between the photon hits becomes close to the time of electron transfer from reduced Q_A to Q_B . The fluorescence induction curve (Fig. 7.6, upper row) exhibits two distinct intermediate phases J and I, the J-phase is determined by x_6 and y_6 and the I-phase is determined largely by z_6 , while g_6 contributes to both.

From Fig. 7.6a, b we can draw some conclusions concerning the origins of the phases J, I, and P at different light intensities. The peak P corresponds to attaining the maximum sum of concentration of PS II fluorescing states with “closed” quinone acceptor complexes g_6 ($\text{Chl}^*\text{PheQ}_\text{A}^-$) and z_6 ($\text{Chl}^*\text{PheQ}_\text{A}^-\text{Q}_\text{B}^{2-}$). Phase I is quite distinct at any illumination intensity, and the time of this phase shortens with increasing light intensity. The onset of this phase roughly corresponds to the appearance of an intermediate maximum on the curve for the z_6 content. Phase J is clearly discerned only under sufficient intense light, and is associated with the accumulation of fluorescing states in which the acceptor is not fully reduced (not more than one electron on Q_B).

In this chapter we do not consider the role of non-photochemical FL quenching, known to contribute to the FL decay after reaching the maximum in the time domain after 1–2 s. Our results (Figs. 7.5 and 7.6) demonstrate the role of the electron fluxes between the two photosystems as being responsible for the FL decay in the time range 1–10 s.

3. Simulation of $\Delta\Psi$ Kinetics

The modeling analysis of Fig. 7.6 reveals explicitly the kinetic curves referring to $\Delta\Psi$ generation, different redox states taking part in fluorescence and ion fluxes, accompanying FL changes in time. In terms of our model, at any time moment $\Delta\Psi$ is determined by the electric charge difference between lumen and stroma. Figure 7.6c depicts the time changes in the rates of processes involved in the generation and the utilization of electric charge difference in the lumen. In the left-hand panel one can see that the emergence of the $\Delta\Psi$ “slow phase” coincides with the establishment of the quasi-steady phase I on the FL induction curves. It means that over the period from 50 to 300 ms, processes opposite in direction largely counterbalance one another. From 50 to 200 ms, the proton influx to the lumen increases due to plastoquinol oxidation at the lumenal side of the Cyt b_6f complex (Fig. 7.6c, $\text{H}_{\text{b}/\text{f}}^+$). The system accumulates states with Q_B^{2-} which upon protonation dissociate from PS II. The presence of plastoquinol at the stromal side of the thylakoid membrane triggers the Cyt b_6f complex operation. Proton influx from the oxygen evolving complex (H_{OEC}^+) is balanced by the K^+ and Mg^{2+} outflow and proton consumption in the ATP-synthase reaction (H_{ATP}^+). Besides, a fraction of protons is bound by the buffer. As a result, the evolving slow phase in the transmembrane potential kinetics leads to the inhibition of the electron transfer in potential-dependent reactions of PS II: electron transfer at the donor side from OEC to P680^+ and the electron transfers $\text{Phe} \rightarrow \text{Q}_\text{A}$ and $\text{Q}_\text{A} \rightarrow \text{Q}_\text{B}$ (at the acceptor side). Such inhibition, in its turn, hinders the rise in the z_6 ($\text{Chl}^*\text{PheQ}_\text{A}^-\text{Q}_\text{B}^{2-}$) population and produces the intermediate minimum (Fig. 7.6b), resulting in the appearance of the I-phase on the FL induction curve (Fig. 7.6a).

The break-down of the above-described quasi-steady state over 300–600 ms (Fig. 7.6c) is caused by the activation of PS I processes, with the enhancement of the cyclic electron transfer resulting in competition for PQ between PS II and the Cyt b_6f complex. As a consequence, elevated concentrations of the fluorescing forms g_6 ($\text{Chl}^*\text{PheQ}_\text{A}^-$) and z_6 ($\text{Chl}^*\text{PheQ}_\text{A}^-\text{Q}_\text{B}^{2-}$) result in enhanced fluorescence (Fig. 7.6b).

Thus, this analysis shows the dynamics of the separate states of the PS II complex; further, ion fluxes and electrical potential generation kinetics explain quite well the distinctive features of the fluorescence induction curve. The model allows us to extract information about $\Delta\Psi$ generation under different experimental conditions (Belyaeva et al., 2003). In some special experiments, e.g. fluorescence transients in the time domain from 100 ns to 10 s after excitation with a saturating 10 ns flash, we can use only the PS II submodel to describe the recorded events (Belyaeva et al., 2006). The analysis showed that under these conditions particular attention must be given to flash-induced recombination processes, including nonradiative recombination in PS II. For these experiments the PS II model was extended considering the sites blocked by diuron, which allowed simulation of fluorescence induction curves observed in the presence of this inhibitor.

IV. Multiparticle Modeling of the Processes in the Photosynthetic Membrane

A. Restricted Diffusion of Mobile Electron Carriers

The above-described kinetic models, based on ordinary differential equations, assume homogeneous distribution of the interacting components in space. However, some data have suggested that the multi-enzyme complexes are distributed heterogeneously in the membrane. For example, PS I complexes are concentrated in stroma-exposed, while PS II in granal (appressed) parts of the thylakoid membrane (Albertsson, 2000, 2001; Nelson and Yocum, 2006). Electron microscopy data show that in some membrane areas the multi-enzyme complexes may concentrate to such an extent that they prevent free diffusion of PQ in the membrane, forming small local microdomains (Joliot et al., 1992; Kirchhoff et al., 2000, 2002). Within each domain PQ diffuses rapidly, but long distance migration of PQ is restricted. As a result, Pc is assumed to play the main role in electron transport over long distances (Kirchhoff et al., 2000).

The small copper protein Pc diffuses in lumen and transfers electrons from Cyt f – a subunit of the Cyt b_6f complex – to P700, the reaction center of PS I (Hope, 2000; Nelson and Yocum, 2006). The difference in the Pc concentration in granal and stromal areas of the membrane during the light-dark transition was interpreted as evidence for the long-distance transport between these compartments (Haehnel et al., 1989). The mobility of Pc molecules is restricted by the membrane complexes protruding from the membrane into the lumen space. The mechanism of Pc mobility in the lumen is of special interest. In native chloroplasts, the luminal space is narrow (40–100 Å), and contains proteins protruding through the thylakoid membrane. Since the size of Pc molecule (40 × 28 × 30 Å) is about the thickness of the lumen, the diffusion of Pc in lumen is obviously hindered by the membrane protein complexes (Hope, 2000; Kirchhoff et al., 2000; Dekker and Boekema, 2005; Shimoni et al., 2005). It is not clear how Pc can rapidly diffuse over a distance of hundreds of nanometers between grana stacks and stroma lamellae. The 30–50 μs lag phase of Cyt f oxidation, after a saturating pulse of light, shows that it takes some time for the oxidized Pc to diffuse from P700 to the nearest Cyt b_6f complex (Haehnel et al., 1980). This lag is followed by multi-component relaxation kinetics that may correspond to different Pc diffusion distances. By the way, it is not obvious *a priori* whether the diffusion of Fd is free in the stromal space as well.

Electron fluxes at the diffusional stages are strongly regulated by cellular factors, such as pH, temperature, endogenous inhibitors, and metabolites. Changes of geometry of the system can even block the electron transport, as is the case under hyperosmotic stress (Cruz et al., 2001); further, illumination, as an external factor, influences the geometry of the system (Kruger et al., 1997).

Thus the basic assumption of the kinetic modeling by differential equations – free diffusion of mobile carriers and homogenous structure of the reaction system – is far from reality. The Brownian dynamics (BD) approach (Pearson et al., 1996; Pearson and Gross, 1998; Ullman et al., 1997; Gross and Pearson, 2003; Gross, 2004; Haddadian and Gross, 2005, 2006; Gross and Rosenberg, 2006) is used to simulate the interaction of two individual

protein molecules. The BD models are used to investigate the process of complex formation, to predict the structure of the complex and to estimate the rate constants of protein association. In this approach the proteins are treated as rigid or semi-rigid bodies, their geometric shape is considered at atomic resolution and electrostatic interactions are presented in great detail. However, the BD approach does not consider the interaction of ensembles of the molecules like those in the interior of photosynthetic membranes.

B. Direct Model Scene

The structural peculiarities of heterogeneous photosynthetic membranes can be described by direct multiparticle computer models (Kovalenko et al., 2003, 2006, 2007; Riznichenko and Rubin, 2007). Such modeling allows us to design the 3D visual dynamic image of processes proceeding simultaneously and to trace the individual behavior of separate components.

The direct multiparticle 3D model is presented by the three-dimensional scene including the thylakoid membrane, lumenal and stromal spaces. Visualization of the 3D stage for the model of cyclic electron transport around PS I (we

will describe this model below) is presented in Fig. 7.7. The inside volume of the thylakoid is restricted by two membrane planes. The membrane is penetrated by PS I, Cyt b_6f complexes and the hypothetical complexes of Fd-PQ-reductase (FQR), designated as R. The question if FQR is a separate complex, or a sub-unit of PS I, or of Cyt b_6f , is still a subject of discussion (Chow and Hope, 2004; Yamashita et al., 2007). In the version presented in Fig. 7.7, these complexes are fixed in the membrane. Concentrations and sizes of complexes were selected according to data presented in literature (Albertsson, 2000, 2001; Dekker and Boekema, 2005; Nelson and Yocum, 2006; Shimoni et al., 2005). Inside the thylakoid lumen mobile molecules of Pc can carry charges; similarly, mobile molecules of Fd can carry charges in the stroma. PQ (PQH_2) molecules move inside the membranes.

C. Brownian Dynamics of Mobile Carriers

To simulate the movement of Pc, PQ and Fd in their compartments, we use the formalism of Brownian dynamics taking into account the geometrical restrictions of the created model scene.

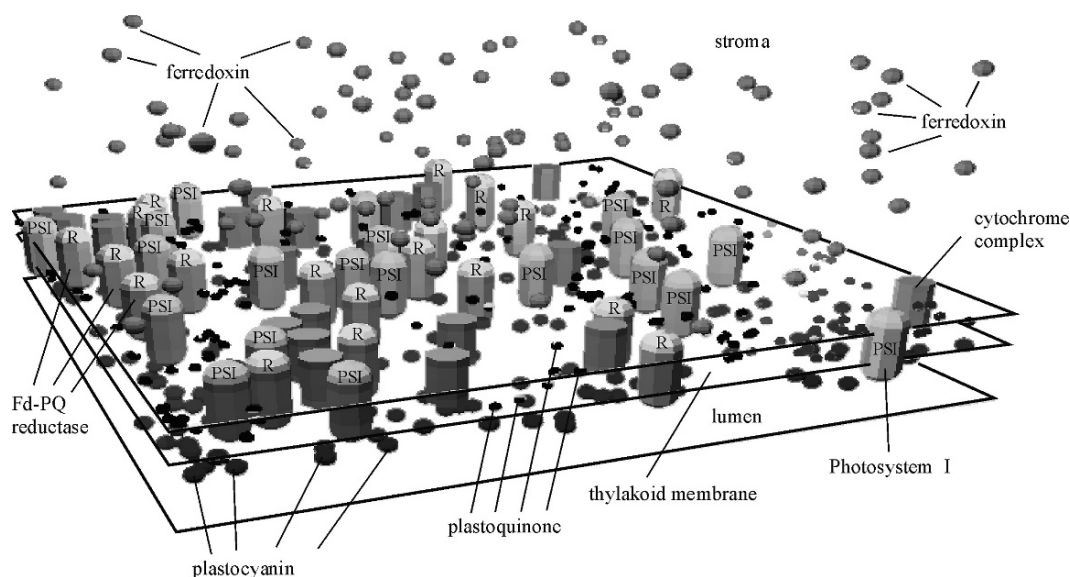


Fig. 7.7. Visualization of the three-dimensional stage for the direct multiparticle 3D model of cyclic electron transport around PS I. Segments of the thylakoid membrane, lumenal space, and stromal space are shown (Kovalenko et al., 2003)

We assume that the particle is moving in viscous medium under the influence of random forces:

$$\xi \frac{dx}{dt} = f(t). \quad (7.8)$$

According to the fluctuation-dissipation theorem (Kubo, 1966), $f(t)$, the random force, is normally distributed with zero mean value and the mean value of deviation of $2kT\xi$ (k is the Boltzmann constant and T , temperature). The friction coefficient for a spherical particle is $\xi = 6\pi\eta a$, where η is the viscosity of the medium and a is the radius of the particle.

The mechanism of electron transfer is considered as follows. If a mobile carrier moving by Brownian diffusion (chaotically) approaches a protein complex at a distance shorter than the effective radius of their interaction, the carrier docks to the complex with some probability. The docking probability and effective radius of interaction are parameters of the model (different for different types of complexes and mobile carriers). To estimate the effective radii and probabilities of the interactions of participants of photosynthetic electron transport, we analyzed the kinetic data for the interactions of proteins in solution (Kovalenko et al., 2006, 2007). The results of direct computer experiments show that the observed rate constant of interaction between two proteins in solution strongly depends on the shape of the space volume where these interactions occur. Thus the rate of interaction between Pc and Cyt f molecules is much lower in the narrow lumen space than in a large volume, provided that concentrations are equal (Kovalenko et al., 2007).

Equation (7.8) was solved numerically for the movement of every electron carrier. The states of the complexes, mechanisms of their interactions with mobile carriers, and physical laws of carrier movements were determined by rules described elsewhere (Kovalenko et al., 2003, 2006, 2007).

In Fig. 7.8, the model trajectory of a PQ molecule in the membrane protruded with PS I, PS II and Cyt b_6f complexes is presented. The concentrations and sizes of protein complexes were taken from the literature (Staehelin and Van der Staay, 1996; Albertsson, 2001). PS I particle density in a membrane was taken to be $8.47 \cdot 10^{-4}$, Cyt b_6f $3.5 \cdot 10^{-4}$ and PS II $2.2 \cdot 10^{-4}$ particles nm^{-2} (Albertsson, 2001). The number of

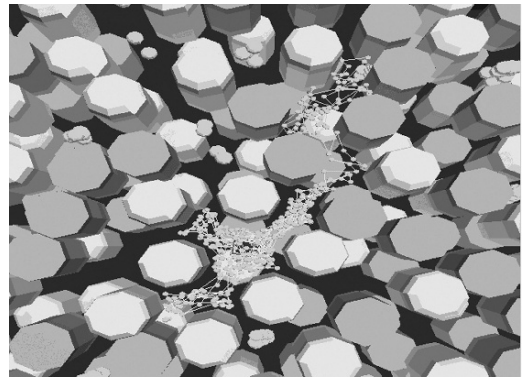


Fig. 7.8. A model trajectory of a PQ molecule in a membrane with PS I and Cyt b_6f complexes. We can see that the close-packed complexes limit the diffusion of PQ molecules (Kovalenko et al., 2007)

FQR complexes was assumed to be equal to the number of PS I complexes. The size of PS I in lateral plane was taken to be 13 nm (with LHC I), Cyt b_6f of 9 nm and PS II 13 nm (Staehelin and Van der Staay, 1996). Although there are places in Fig. 7.8 where PS II complexes should be located, the latter are not included for the sake of simplicity of the picture.

D. Simulation of Cyclic Electron Transport Around Photosystem I

The method of direct simulation was applied to the description of cyclic electron transport around PS I (Kovalenko et al., 2003, 2007). Computer simulations adequately describe the experimental kinetics of the EPR signal I, measured in thylakoids from pea (*Pisum sativum*) leaves of seedlings, growing under anaerobic conditions (Krendeleva et al., 2001; Kovalenko et al., 2003; in these experiments DCMU was added to the reaction mixture to block electron transport from PS II). Similar kinetics of P700 redox transformations, due to cyclic electron flow around PS I, in spinach leaves were published recently by Fan et al. (2007).

Figure 7.9 shows a scheme (Joliot and Joliot, 2002, 2005) for cyclic electron flow. It includes the processes of docking of the molecules of the mobile carrier Fd on the acceptor side of PS I and participation of the Cyt b_6f complex in redox transformations of PQ. We assume that electron transfer from Fd to PQ occurs through

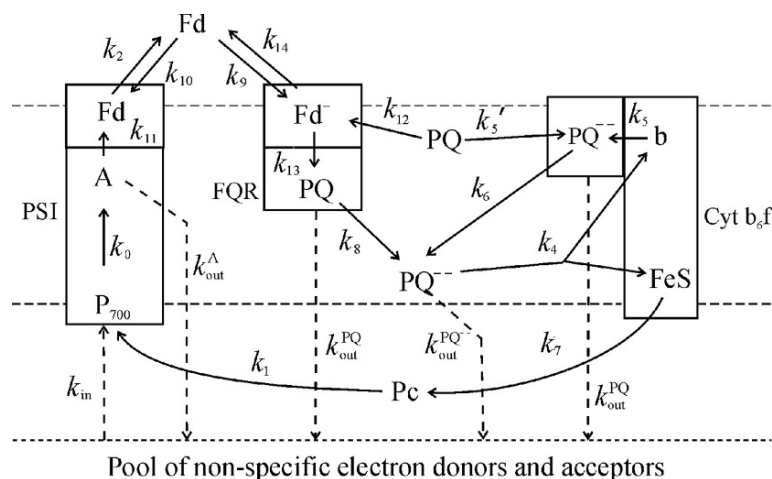


Fig. 7.9. Scheme of the kinetic model of cyclic electron transport around PS I. Boxes stand for PS I, FQR, and cytochrome b₆f complexes; P700 – pigment of PS I reaction center; A – acceptor complex; FeS – Rieske iron-sulfur center; b – high potential cytochrome b_h; Fd – ferredoxin; Pc – plastocyanin; PQ – plastoquinone; PQ^{••} – plastoquinol. Arrows indicate electron transport pathways; k_{in} , k_{out} , k_1, \dots, k_{14} – the rate constants for the respective reactions of electron transfer. Dashed lines depict the thylakoid membrane and the hypothetical pool of nonspecific electron donors and acceptors (Kovalenko et al., 2003)

the hypothetical complex of ferredoxin-quinone-reductase (FQR), which has the Fd docking site exposed into the stromal area and the PQ docking site exposed inside the membrane (Bendall and Manasse, 1995).

The kinetic model simulates the experimental data on the P700 reduction kinetics with fast and slow components at different Fd concentrations (Krendeleva et al., 2001; Kovalenko et al., 2003). As in the experiments, the amplitude and the contribution of the fast phase of the P700 reduction increases with Fd concentration, while its characteristic time changes very little, being determined by the rate of PQ interactions with Cyt b₆f. However, to correctly simulate the slow phase of P700 kinetics, we needed to introduce space heterogeneity of the system (Cleland and Bendall, 1992; Bendall and Manasse, 1995; Scheller, 1996), which probably is the real reason of the existence of the slow phase in P700 reduction. As assumed by Albertsson (2001), cyclic transport takes place in the inter-granular stromal lamellae, whereas linear transport occurs in granular terminal areas of thylakoid membranes. Accordingly, the 3D-scene of the direct model (Fig. 7.10) has two different adjoining areas – granal and stromal.

In the computer simulation experiment, the system was illuminated for 1.5 min similar to

real experiments. During this time, the PQH₂ molecules, reduced by Fd via FQR, are uniformly distributed in granal and stromal areas. After switching off the light, electrons from the PQH₂-pool still continue to be transferred to Pc via the Cyt b₆f complex. This process occurs in the granal as well as in the stromal area, because Cyt b₆f complexes are distributed uniformly in the membrane. In the stromal area, the reduced Pc molecules quickly transfer electrons to PS I reaction centers with the characteristic time of 200 ms. This process corresponds to the fast phase of P700⁺ reduction. As in experiments, the fast reduction of P700⁺ is not complete, but a fraction of P700⁺ still remains in the oxidized form (Fig. 7.11). The direct model demonstrates that this effect is due to the fact that a certain number of electrons are still bound to the molecules of PQ and Pc in the granal parts of the membrane, where PS I is absent.

Later the diffusion of PQ inside the membrane and the diffusion of Pc in the luminal space occur: electrons gradually return to the stromal area, where the additional P700⁺ reduction takes place. The characteristic time of this reduction phase is about 10 s and is determined by the size of the whole system. This result explains why the time course of the reduction of photo-oxidized P700⁺ can be approximated by the sum of two

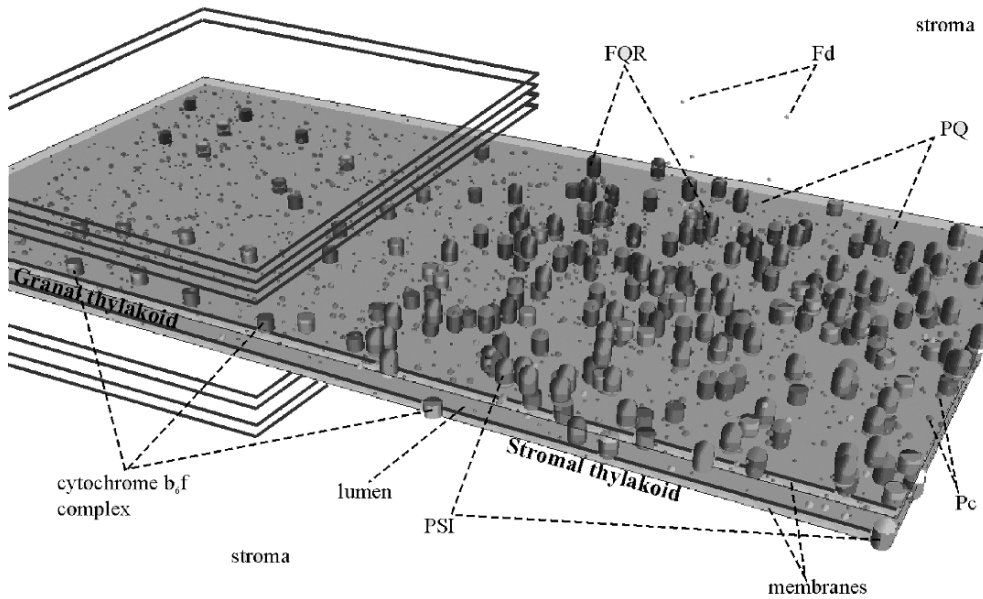


Fig. 7.10. Visualization of the 3D scene of the multiparticle model of cyclic electron transport. PS II complexes are not shown, although they were simulated. Note granal and stromal parts of the thylakoid membrane (Kovalenko et al., 2007)

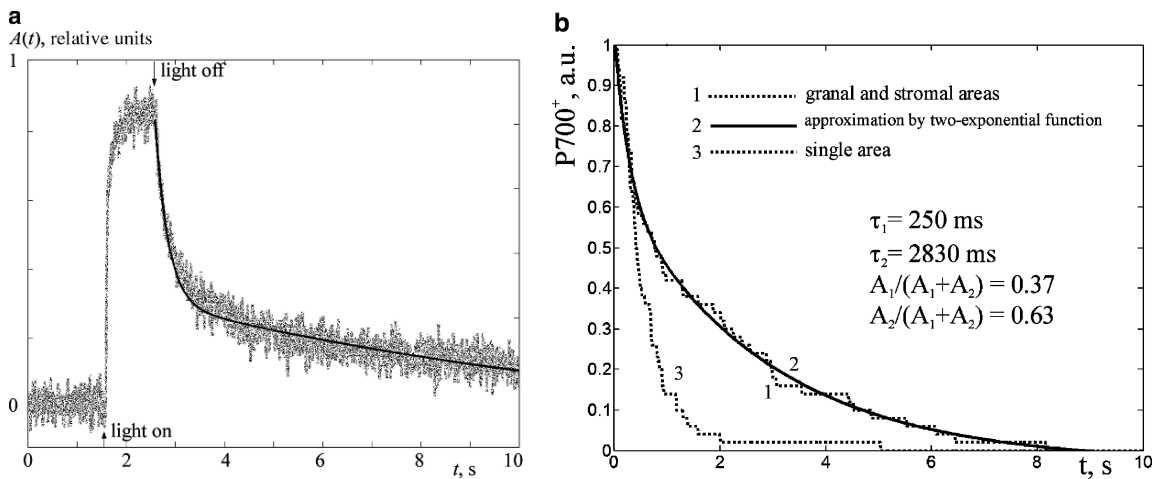


Fig. 7.11. Kinetics of redox transformations of the PS I photoactive pigment P700. (a) Experimental EPR-signal $A(t)$; (b) kinetics of $P700^+$ reduction obtained by the “direct” model simulation (Kovalenko et al., 2007). τ_1 , τ_2 , A_1 , A_2 – characteristic times and amplitudes of fast and slow phase

exponents (Fig. 7.11a). Thus the direct multiparticle model naturally explains the existence of two phases of the dark reduction in heterogeneous system without additional artificial assumptions about the existence of the pool of non-specific donors and acceptors.

The direct multiparticle modeling of the cyclic electron transport around PS I demonstrates that

the experimentally observed redox kinetics of electron carriers are determined not only by the concentrations, redox states of the reagents and conformation states of the complexes, but also by the spatial distribution of the mobile carriers and configuration of the reaction volume (lumen, stroma). It is known that changes of the physiological state of the cell under different pH and

salt concentrations lead to changes of the distances between thylakoid grana as well as in the geometry of the system. The multiparticle model approach allows us to see how these changes affect the kinetic characteristics of photosynthesis, providing new mechanisms of its regulation.

V. Concluding Remarks and Future Perspectives

The general kinetic model, described in this chapter, can accurately simulate the main features of fluorescence induction curves. Such modeling can be used as a tool for the investigation of different specific features of the photosynthetic machinery between species, ecological niches, and growth conditions. Different stress effects (inhibitors, starvation) modify the patterns of fluorescence induction curves showing sharp differences after 1–2 s from the onset of illumination. These distinctions are often related to the oxygen stress effects, damages in protein synthesis system, and other processes, the mechanisms of which we do not know in any details, but we need to include them in our models if we wish the model to be an instrument of the quantitative analysis in biotechnological and ecological monitoring.

The classical kinetic approach proved to be productive in evaluating the rate constants of individual reactions of electron transport and the ratios of energy fluxes at different steps of the electron transport chain, but using only differential equations it is difficult to take into account the spatial heterogeneity and complex geometry of the interacting macromolecules, as well as the interior of the photosynthetic membrane, where these interactions occur. To solve this problem, we have developed the “direct” multiparticle models, mimicking the processes on the molecular level. In these models the molecules are assumed to be moving in accordance with the Brownian dynamics, interacting in a spatial “scene” mimicking the photosynthetic membrane. The future development of such modeling may include processes of chlororespiration, interactions of primary photosynthetic processes with Calvin-Benson cycle, nitrogen cycle, and other metabolic ways influencing the state of the PQ pool, the efficiency of PS I operation,

relationships of linear and cyclic electron fluxes around PS I. Using the Protein Data Base we can calculate the electrical potential distribution around each of the interacting molecules and evaluate the role of electrostatic interactions in the processes of molecule orientation and super-complex formation in redox reactions. The direct modeling approach is promising in demonstrating how physical mechanisms of molecular interaction (diffusion, electrostatic interactions) determine the overall dynamics in a cell. However, as the models become larger, in more general models it probably will not be necessary to include many details of the sub-models of individual photosystems, but using their reduced versions may appear sufficient. However, the adequacy of such reduced modeling requires evidence that the main characteristics of the detailed model are still retained.

Acknowledgments

We thank all our colleagues and Ph.D. students of the Department of Biophysics, Biological Faculty of the Moscow State University, taking part in this work: A. Abaturova, N. Beljaeva, O. Demin, M. Kamali, G. Lebedeva, I. Kovalenko and D. Ustinin. We also thank M. Patrin for technical assistance. We are especially grateful to Dr. E. Grachev, Department of Computer Methods in Physics, Physical Faculty of the Moscow State University, for collaboration in the development of direct computer models.

We are grateful to Govindjee and Agu Laisk, editors of this book, for their valuable comments which greatly helped us in preparing this chapter for publication.

The work was supported by grants of the Russian Foundation of Basic Research, 1999–2007 (now grant # N 07-04-00375).

References

- Albertsson PA (2000) The domain structure and function of the thylakoid membrane. *Recent Res Dev Bioener* 1: 143–171
- Albertsson PA (2001) A quantitative model of the domain structure of the photosynthetic membrane. *Trends Plant Sci* 6: 349–354

- Baake E and Schloder JP (1992) Modeling the fast fluorescence rise of photosynthesis. *Bull Math Biol* 54: 999–1021
- Baake E and Strasser RJ (1990) A differential equation model for the description of the fast fluorescence rise (O-I-D-P transient) in leaves. In: Baltscheffsky M (ed) *Current Research in Photosynthesis*, Vol 1, pp 567–570. Kluwer, Dordrecht
- Belyaeva NE, Lebedeva GV and Riznichenko GYu (2003) Kinetic model of primary photosynthetic processes in chloroplasts. Modeling of electron potential on thylakoid membrane. In: Riznichenko GYu (ed) *Mathematics. Computer. Education*, Vol 10, pp 263–276. RCD, Moscow
- Belyaeva NE, Paschenko VZ, Renger G, Riznichenko GYu and Rubin AB (2006) Application of a Photosystem II model for analysis of fluorescence induction curves in the 100 ns to 10 s time domain after excitation with a saturating light pulse. *Biophysics* 51: 860–872
- Bendall DS and Manasse RS (1995) Cyclic photophosphorylation and electron transport. *Biochim Biophys Acta* 1229: 23–38
- Bernarding J, Eckert H-J, Eichler HJ, Napiwotzki A and Renger G (1994) Kinetic studies on the stabilization of the primary radical pair $P680^+Pheo^-$ in different photosystem II preparations from higher plants. *Photochem Photobiol* 59: 566–573
- Bernhardt K and Trissl H-W (1999) Theories for kinetics and yield of fluorescence and photochemistry: how, if at all, can different models of antenna organization be distinguished experimentally? *Biochim Biophys Acta* 1409: 125–142
- Boork J and Wennerström H (1984) The influence of membrane potentials on reaction rates. Control in free-energy-transducing systems. *Biochim Biophys Acta* 767(2): 314–320
- Brettel K (1997) Electron transfer and arrangement of the redox cofactors in photosystem I. *Biochim Biophys Acta* 1318(3): 322–373
- Brettel K (1998) Electron transfer and arrangement of the redox cofactors in photosystem I. *Biochim Biophys Acta* 1318(3): 322–373
- Brettel K, Schloder E and Witt HT (1984) Nanosecond reduction kinetics of photooxidized chlorophyll-a (P-680) in single flashes as a probe for the electron pathway, H^+ -release and charge accumulation in the O_2 -evolving complex. *Biochim Biophys Acta* 766: 403–415
- Brown GC and Brand MD (1986) Changes in permeability to protons and other cations at high proton motive force in rat liver mitochondria. *Biochem J* 234: 75–81
- Bukhov NG, Damirov HG, Dzhibladze HB, Karapetjan NV, Riznichenko GYu and Rubin AB (1988) Kinetic analysis of variable and delayed fluorescence induction transitions in the presence of diuron and carbonylcyanidephenylhydrosone. *Biological Sciences (Rus)* 4: 28–37
- Bukhov NG, Egorova EA, Govindachary S and Carpentier R (2004) Changes in polyphasic chlorophyll a fluorescence induction curve upon inhibition of donor or acceptor side of photosystem II in isolated thylakoids. *Biochim Biophys Acta* 1657: 121–130
- Bulychev AA and Vredenberg WJ (2001) Modulation of photosystem II chlorophyll fluorescence by electrogenic events generated by photosystem I. *Bioelectrochemistry* 54: 157–168
- Chamorovsky SK, Chrabrova EN and Riznichenko GY (1990) Parameter identification of the model of electron transport in multihaem cytochromes c, connected with photosynthetic electron center. *Biophysics (Rus)* 36: 16–21
- Chow WS and Hope AB (2004) Electron fluxes through Photosystem I in cucumber leaf discs probed by far-red light. *Photosynth Res* 81: 77–89
- Cleland RE and Bendall DS (1992) Photosystem I cyclic electron transport: measurement of ferredoxin-plastoquinone reductase activity. *Photosynth Res* 34: 409–418
- Cramer WA, Zhang H, Yan J, Kurisu G and Smith JL (2004) Evolution of photosynthesis: time-independent structure of the cytochrome b_6f complex. *Biochemistry* 43: 5921–5929
- Cramer WA, Yan J, Zhang H, Kurisu J and Smith GL (2005) Structure of the cytochrome b_6f complex: new prosthetic groups, Q-space, and the ‘hors d’oeuvres hypothesis’ for assembly of the complex. *Photosynth Res* 85: 133–144
- Cramer WA, Zhang H, Yan J, Kurisu G and Smith JL (2006) Trans-membrane traffic in the cytochrome b_6f complex. *Annu Rev Biochem* 75: 769–790
- Crofts AR and Wraight CA (1983) The electrochemical domain of photosynthesis. *Biochim Biophys Acta* 726: 149–185
- Cruz JA, Salbilla BA, Kanazava A and Kramer DM (2001) Inhibition of plastocyanin to $P700^+$ electron transfer in *Chlamydomonas reinhardtii* by hyperosmotic stress. *Plant Physiol* 127: 1167–1179
- Dau H (1994) Molecular mechanisms and quantitative models of variable photosystem II fluorescence. *Photochem Photobiol* 60: 1–23
- Dau H and Sauer K (1992) Electric field effect on the primary picosecond fluorescence of photosystem II and its relation to the energetics and kinetics of primary charge separation. *Biochim Biophys Acta* 1102: 91–106
- Dekker JP and Boekema EJ (2005) Supramolecular organization of thylakoid membrane proteins in green plants. *Biochim Biophys Acta* 1706: 12–39
- Drachev LA, Mamedov MD and Semenov AY (1990) Electrogenesis associated with proton transfer in the reaction center protein of purple bacteria *Rhodospirillum rubrum*. *FEBS Lett* 259: 324–326
- Eckert H-J and Renger G (1988) Temperature dependence of $P680^+$ reduction in O_2 -evolving PS II membrane frag-

- ments at different redox states Si of the water oxidizing system. *FEBS Lett* 236: 425–431
- Edwards GE and Baker NR (1993) Can CO₂ assimilation be predicted accurately from chlorophyll fluorescence analysis? *Photosynth Res* 37: 89–102
- Fan D-Y, Nie Q, Hope AB, Hillier W, Pogson BJ and Chow WS (2007) Quantification of cyclic electron flow around Photosystem I in spinach leaves during photosynthetic induction. *Photosynth Res* 94: 347–357
- Foyer C, Furbank R, Harbinson J and Horton P (1990) The mechanisms contributing to photosynthetic control of electron transport by carbon assimilation in leaves. *Photosynth Res* 25: 83–100
- Golbeck JH (ed) (2006) Photosystem I. The light-driven plastocyanin: ferredoxin oxidoreductase. Series: *Advances in Photosynthesis and Respiration* (Series ed, Govindjee), Vol 24. Springer, Dordrecht
- Govindjee (1995) Sixty-three years since Kautsky: chlorophyll a fluorescence. *Aust J Plant Physiol* (now *Functional Plant Biol*) 22: 131–160
- Govindjee (2004) Chlorophyll a fluorescence: a bit of basics and history. In: Pageorgieou G and Govindjee (eds) *Chlorophyll Fluorescence: A Signature of Photosynthesis*, Vol 19, pp 1–42. Springer, Dordrecht
- Govindjee, Ames J and Fork DC (eds) (1986) *Light Emission by Plants and Bacteria*. Academic, New York
- Gross EL (2004) A Brownian dynamics study of the interaction of *Phormidium laminosum* plastocyanin with *Phormidium laminosum* cytochrome f. *Biophys J* 87: 2043–2059
- Gross EL and Pearson DC Jr (2003) Brownian dynamics simulations of the interaction of *Chlamydomonas* cytochrome f with plastocyanin and cytochrome c₆. *Biophys J* 85: 2055–2068
- Gross EL and Rosenberg I (2006) A Brownian dynamics study of the interaction of *Phormidium* cytochrome f with various cyanobacterial plastocyanins. *Biophys J* 90: 366–380
- Haddadian EJ and Gross EL (2005) Brownian dynamics study of cytochrome f interactions with cytochrome c₆ and plastocyanin in *Chlamydomonas reinhardtii* plastocyanin, and cytochrome c₆ mutants. *Biophys J* 88: 2323–2339
- Haddadian EJ and Gross EL (2006) A brownian dynamics study of the interactions of the luminal domains of the cytochrome b₆f complex with plastocyanin and cytochrome c₆: the effects of the Rieske FeS protein on the interactions. *Biophys J* 91: 2589–2600
- Haehnel W, Pröpper A and Krause H (1980) Evidence for complexed plastocyanin as the immediate electron donor of P-700. *Biochim Biophys Acta* 593: 384–399
- Haehnel W, Ratajczak R and Robenek H (1989) Lateral distribution and diffusion of plastocyanin in chloroplast thylakoids. *J Cell Biol* 108: 1397–1405
- Hall DO and Rao KK (1994) *Photosynthesis*. Cambridge University Press, Cambridge
- Hauska G and Arnold M (2000) Energy transduction in the Z-scheme. In: Yunus M, Pathre U and Mohanty P (eds) *Probing Photosynthesis*, pp 109–126. Taylor & Francis, London
- Hauska GA, Schutz M and Butter M (1996) The cytochrome b₆-f complex – composition, structure and function. In: Ort DR and Yocum CD (eds) *Oxygenic Photosynthesis: The Light Reaction Advances in Photosynthesis*, Vol 4, pp 377–398. Kluwer, Dordrecht
- Holzappel C and Bauer R (1975) Computer simulation of primary photosynthetic reactions compared with experimental results on O₂ – exchange and chlorophyll fluorescence of green plants. *Z Naturforsch* 30: 489–498
- Hope AB (1993) The chloroplast cytochrome b₆f complex: a critical focus on function. *Biochim Biophys Acta* 1143: 1–22
- Hope AB (2000) Electron transfers amongst cytochrome f, plastocyanin and photosystem I: kinetics and mechanisms. *Biochim Biophys Acta* 1456: 5–26
- Hope AB, Huilgol RR, Panizza M, Thomson M and Matthews DB (1992) The flash-induced turnover of cytochrome b-563, cytochrome f and plastocyanin in chloroplasts. Models and estimation of kinetic parameters. *Biochim Biophys Acta* 1100: 15–26
- Hsu B-D (1992) A theoretical study on the fluorescence induction curve of spinach thylakoids in the absence of DCMU. *Biochim Biophys Acta* 1140: 30–36
- Hsu B-D (1993) Evidence for the contribution of the S-state transitions of oxygen evolution to the initial phase of fluorescence induction. *Photosynth Res* 36: 81–88
- Joliot P and Joliot A (2002) Cyclic electron transfer in plant leaf. *Proc Natl Acad Sci USA* 99: 10209–10214
- Joliot P and Joliot A (2005) Quantification of cyclic and linear electron flows in plants. *Proc Natl Acad Sci USA* 102: 4913–4918
- Joliot P, Lavergne J and Beal D (1992) Plastoquinone compartmentation in chloroplasts. I. Evidence for domains with different rates of photo-reduction. *Biochim Biophys Acta* 1101: 1–12
- Junge W (1999) ATP synthase and other motor proteins. *Proc Natl Acad Sci USA* 96: 4735–4737
- Kamali MJ, Lebedeva GV, Demin OV, Belyaeva NE, Riznichenko GYu and Rubin AB (2004) A kinetic model of the cytochrome b₆f complex with fitted parameters. *Biophysics* 49: 1061–1068
- Ke B (2001) *Photosynthesis: Photobiochemistry and Photo-biophysics*, *Advances in Photosynthesis and Respiration*, Vol 10. Springer, Dordrecht
- Kholodenko BN (1988) *Stabilizing regulation on multienzyme systems: modeling of bioenergetic processes*. Doktoral (Phys.-Math) Dissertation, Belozersky Institute of Physico-Chemical Biology, Moscow State University, Moscow

- Kirchhoff H, Horstmann S and Weis E (2000) Control of the photosynthetic electron transport by PQ diffusion microdomains in thylakoids of higher plants. *Biochim Biophys Acta* 1459: 148–168
- Kirchhoff H, Mukherjee U and Galla HJ (2002) Molecular architecture of the thylakoid membrane: lipid diffusion space for plastoquinone. *Biochemistry* 41: 4872–4882
- Kovalenko IB, Ustinin DM, Grachev NG, Kredeleva TE, Kukharskikh GP, Timofeev KN, Riznichenko GYu, Grachev EA and Rubin AB (2003) Cyclic electron transport around photosystem I: an experimental and theoretical study. *Biophysics* 48: 614–623
- Kovalenko IB, Abaturova AM, Gromov PA, Ustinin DM, Grachev NG, Riznichenko GYu, Grachev EA and Rubin AB (2006) Direct simulation of plastocyanin and cytochrome *f* interactions in solution. *Phys Biol* 3: 121–129
- Kovalenko IB, Abaturova AM, Gromov PA, Ustinin DM, Grachev NG, Riznichenko GYu, Grachev EA and Rubin AB (2007) Multiparticle computer simulation of photosynthetic transport in a thylakoid membrane. *Biophysics* 52: 492–502
- Krab K, Van Walraven HS, Schoolts MJS and Krayenhoff R (1985) Measurement of diffusion potential in liposomes. *Biochim Biophys Acta* 809: 236–244
- Krause GH and Weis E (1991) Chlorophyll fluorescence and photosynthesis; the basics. *Annu Rev Plant Physiol Plant Mol Biol* 42: 313–349
- Kredeleva TE, Kukharskikh GP, Timofeev KN, Ivanov VN and Rubin AB (2001) Ferredoxin-dependent cyclic electron transport in isolated thylakoids occurs with the participation of ferredoxin-NADP-reductase (Rus). *Dokl Ross Akad Nauk* 379: 1–4
- Kruger GHJ, Tsimilli-Michael M and Strasser RJ (1997) Light stress provokes plastic and elastic modification in structure and function of Photosystem II in camellia leaves. *Physiol Plantarum* 101: 265–287
- Kubo R (1966) The fluctuation-dissipation theorem. *Rep Prog Phys* 29: 255–285
- Kukushkin AK, Tikhonov AN, Blumenfeld LA and Ruuge EK (1975) Theoretical aspects of the primary photosynthetic processes kinetics of algae and green plants. *Sov Plant Physiol (Rus)* 22: 241–250
- Kurisu G, Zhang H, Smith JL and Cramer WA (2003) Structure of the cytochrome *b₆f* complex of oxygenic photosynthesis: tuning the cavity. *Science* 302: 1009–1014
- Laisk A and Walker DA (1989) A mathematical model of electron transport. Thermodynamic necessity for photosystem II regulation. *Proc R Soc Lond B* 237: 417–444
- Lavergne J and H-W Trissl (1995) Theory of fluorescence induction in photosystem II: derivation of analytical expressions in a model including exciton-radical-pair equilibrium and restricted energy transfer between photosynthetic units. *Biophys J* 68: 2474–2492
- Lazar D (1999) Chlorophyll *a* fluorescence induction. *Biochim Biophys Acta* 1412: 1–28
- Lazar D (2003) Chlorophyll *a* fluorescence rise induced by high light illumination of dark-adapted plant tissue studied by means of a model of photosystem II and considering photosystem II heterogeneity. *J Theor Biol* 220: 469–503
- Lazar D (2006) The polyphasic chlorophyll *a* fluorescence rise measured under high intensity of exciting light. *Funct Plant Biol* 33: 9–30
- Lazar D, Ilik P, Kruk J, Strzalka K and Naus J (2005) A theoretical study on effect of the initial redox state of cytochrome *b*-559 on maximal chlorophyll fluorescence level F_{m0} . Implications for photoinhibition of photosystem II. *J Theor Biol* 233: 287–300
- Lebedeva GV, Belyaeva NE, Riznichenko GYu, Rubin AB and Demin OV (2000). Kinetic model of photosystem II of higher plants. *Biophys Chem* 74: 1874–1883
- Lebedeva GV, Belyaeva NE, Demin OV, Riznichenko GYu and Rubin AB (2002) Kinetic model of primary photosynthetic processes in chloroplasts. Description of the fast phase of chlorophyll fluorescence induction under different light intensities. *Biophysics* 47: 968–980
- Malik M, Riznichenko GYu, Rubin AB (1990) Biological Electron Transport Processes. Their Mathematical Modeling and Computer Simulation. Academia, Praha, Horwood, London
- Malkin S (1971) Fluorescence induction studies in isolated chloroplast. On the electron-transfer equilibrium in the pool of electron acceptors of photosystem II. *Biochim Biophys Acta* 234: 425–427
- Malkin R and Niyogi K (2000) Photosynthesis ages. In: Buchanan B, Gruissem W and Jones R (eds) *Biochemistry & Molecular Biology of Plants*, pp 413–429. Kluwer, Dordrecht
- Nelson N and Yocum CF (2006) Structure and function of photosystems I and II. *Annu Rev Plant Biol* 57: 521–565
- Nicholls DG (1974) The influence of respiration and ATP hydrolysis on the proton-electrochemical gradient across the inner membrane of rat-liver mitochondria as determined by ion distribution. *Eur J Biochem* 50: 305–315
- O'Keefe DP (1988) Structure and function of the chloroplast cytochrome *b₆f*-complex. *Photosynth Res* 17: 189–216
- Papageorgiou G and Govindjee (eds) (2004) Chlorophyll *a* Fluorescence: A Signature of Photosynthesis. *Advances in Photosynthesis and Respiration*, Vol 19. Springer, Dordrecht
- Papageorgiou GC, Tsimilli-Michael M and Stamatakis K (2007) The fast and slow kinetics of chlorophyll *a* fluorescence induction in plants, algae and cyanobacteria: a viewpoint. *Photosynth Res* 94: 275–290
- Pearson DC and Gross EL (1998) Brownian dynamics study of the interaction between plastocyanin and cytochrome *f*. *Biophys J* 75: 2698–2711

- Pearson DC, Gross EL and David ES (1996) Electrostatic properties of cytochrome f: implications for docking with plastocyanin. *Biophys J* 71: 64–76
- Potossin II and Schönknecht G (1996) Ion channel permeable for divalent and monovalent cations in native spinach thylakoid membranes. *J Membr Biol* 152: 223–233
- Renger G (2001) Photosynthetic water oxidation to molecular oxygen: apparatus and mechanism. *Biochim Biophys Acta* 1503: 210–228
- Renger G (ed) (2007) *Primary Processes of Photosynthesis: Principles and Apparatus*, 2 Parts. Royal Society of Chemistry Publishers, Cambridge
- Renger G and Schulze A (1985) Quantitative analysis of fluorescence induction curves in isolated spinach chloroplasts. *Photochem Photobiol* 9: 79–87
- Reynolds IA, Johnson EA and Tanford (1985) Incorporation of membrane potential into theoretical analysis of electrogenic ion pumps. *Proc Natl Acad Sci USA* 82: 6869–6873
- Riznichenko GYu (1991) *Advances in Science and Techniques. Mathematical Models of Primary Photosynthetic Processes (Rus)*. Biophysics, V. 31. Publishing House of VINITI, Moscow
- Riznichenko GYu, Kiljachkov AA, Pyt'eva NF and Rubin AB (1980) Possible mechanism of regulation of electron transport flows in bacterial photosynthesis. *Photosynthetica* 14: 161–170
- Riznichenko GYu, Vorobjeva TN, Chrabrova EN and Rubin AB (1986) Comparative analysis of kinetic and conformational characteristics of solubilized and embedded in liposomes Photosystem 1 complexes of higher plants. *Biophysics* 31: 793–799
- Riznichenko GYu, Chrabrova EN and Rubin AB (1988) Identification of the parameters of photosynthetic electron transport system. *Stud Biophys* 126: 51–59
- Riznichenko GYu, Vorobjeva TN, Chrabrova EN and Rubin AB (1990) Identification of kinetic parameters of plastocyanin and P-700 interactions in chloroplasts and pigment-protein complexes of photosystem 1. *Photosynthetica* 24: 37–51
- Riznichenko GYu, Lebedeva GV, Demin OV, Belyaeva NE and Rubin AB (1999) Kinetic mechanisms of biological regulation in photosynthetic organisms. *J Biol Phys* 25: 177–192
- Riznichenko GYu and Rubin AB (2007) Models of regulation of photosynthetic electron transport. In: Rubin AB (ed) *Problems of Regulation in Biological Systems (Rus)*, pp 165–194. Institute of Computer Research, Moscow
- Roelofs TA, Lee C-H and Holzwarth AR (1992) Global target analysis of picosecond chlorophyll fluorescence kinetic from pea chloroplasts. *Biophys J* 61: 1147–1163
- Rubin AB and Shinkarev VP (1984) *Electron Transport in Biological Systems (Rus)*. Nauka Publishing, Moscow
- Schatz GH, Brock H and Holzwarth AR (1988) Kinetic and energetic model for the primary processes in photosystem II. *Biophys J* 54: 397–405
- Scheller HV (1996) In vitro cyclic electron transport in barley thylakoids follows two independent pathways. *Plant Physiol* 110: 187–194
- Schreiber U and Bilger W (1993) Progress in chlorophyll fluorescence research: major developments during the past years in retrospect. *Prog Bot* 54: 151–173
- Schodel R, Irrgang KD, Voigt J and Renger G (1999) Quenching of chlorophyll fluorescence by triplets in solubilized light-harvesting complex II (LHCII). *Biophys J* 76: 2238–2248
- Shimoni EO, Rav-Hon O, Ohad I, Brumfeld V and Reich Z (2005) Three-dimensional organization of higher-plant chloroplast thylakoid membranes revealed by electron tomography. *Plant Cell* 17: 2580–2586
- Shinkarev VP (1998) The general kinetic model of electron transfer in photosynthetic reaction centers activated by multiple flashes. *Photochem Photobiol* 67: 683–699
- Shinkarev VP and Venedictov PS (1977) Probability description of the processes of electron transport in multi molecular complexes. *Biophysics (Rus)* 22: 413–418
- Sorokin EM (1973) Non-cyclic electron transport and connected processes. *Sov Plant Physiol (Rus)* 20: 389–399
- Staehelin LA and Van der Staay GWM (1996) Structure, composition, functional organization and dynamic properties of thylakoid membranes. In: Ort DR and Yocum CF (eds) *Oxygenic Photosynthesis: The Light Reactions*, pp 11–30. Kluwer, Dordrecht
- Steffen R, Eckert H-J, Kelly AA, Dormann P and Renger G (2005) Investigations on the reaction pattern of photosystem II in leaves from *Arabidopsis thaliana* by time-resolved fluorometric analysis. *Biochemistry* 44: 3123–3133
- Stirbet AD and Strasser RJ (1995) Numerical simulation of the fluorescence induction in plants. *Arch Sci* 48: 41–59
- Stirbet AD and Strasser RJ (1996) Numerical simulation of the in vivo fluorescence induction in plants. *Math Comput Simulat* 42: 245–253
- Stirbet AD, Govindjee, Strasser BJ and Strasser RJ (1998) Chlorophyll a fluorescence induction in higher plants: modelling and numerical simulation. *J Theor Biol* 193: 131–151
- Strasser RJ and Govindjee (1992) On the O-J-I-P fluorescence transient in leaves and D1 mutants of *Chlamydomonas reinhardtii*. In: Murata N (ed) *Research in Photosynthesis*, Vol 4, pp 29–32. Kluwer, Dordrecht
- Strasser RJ and Stirbet AD (1998) Heterogeneity of Photosystem II probed by the numerically simulated chlorophyll a fluorescence rise (OJIP). *Math Comput Simulat* 48: 3–9
- Strasser RJ and Stirbet AD (2001) Estimation of the energetic connectivity of PS II centers in plants using the fluorescence rise (O-J-I-P) - fitting of experimental data to three different PS II models. *Math Comput Simulat* 56: 451–461

- Strasser RJ, Srivastava A and Govindjee (1995) Polyphasic chlorophyll *a* fluorescence transient in plants and cyanobacteria. *Photochem Photobiol* 61: 2–42
- Strasser RJ, Tsimilli-Michael M and Srivastava A (2004) Analysis of the chlorophyll *a* fluorescence transients. In: Papageorgiou G and Govindjee (eds) *Chlorophyll Fluorescence: A Signature of Photosynthesis*, Vol 19, pp 321–362. Springer, Dordrecht
- Tester M and Blatt MR (1989) Direct measurement of K^+ channels in thylakoid membranes by incorporation of vesicles into planar lipid bilayers. *Plant Physiol* 91: 249–252
- Trissl H-W and Lavergne J (1994) Fluorescence induction from photosystem II: analytical equations for the yields of photochemistry and fluorescence derived from analysis of a model including exciton-radical pair equilibrium and restricted energy transfer between photosynthetic units. *Aust J Plant Physiol* 22: 183–193
- Trissl H-W, Gao Y and Wulf K (1993) Theoretical fluorescence induction curves derived from coupled differential equations describing the primary photochemistry of photosystem II by an exciton-radical pair equilibrium. *Biophys J* 64: 974–988
- Ullmann GM, Knapp E-W and Kostic NM (1997) Computational simulation and analysis of dynamic association between plastocyanin and cytochrome *f*. Consequences for the electron-transfer reaction. *J Am Chem Soc* 119: 42–52
- Van Kooten O, Snel JFH and Vredenberg WJ (1986) Photosynthetic free energy transduction to the electric potential changes across the thylakoid membrane. *Photosynth Res* 9: 211–227
- Vasil'ev S, Bergmann A, Redlin H, Eichler H-J and Renger G (1996) On the role of exchangeable hydrogen bonds for the kinetics of $P680^+Q_A^-$ formation and $P680^+Pheo^-$ recombination in photosystem II. *Biochim Biophys Acta* 1276: 35–44
- Vorobjeva TN, Riznichenko GY and Shaitan KV (1986) Physical mechanisms of the electron transfer between primary quinone and pigment in reaction centers of photosynthetic bacteria *Rh. sphaeroides* during transition from the illumination to the darkness. *Mol Biol (Rus)* 20: 1203–1213
- Vredenberg WJ (2000) A 3-state model for energy trapping and fluorescence in PS II incorporating radical pair recombination. *Biophys J* 79: 26–38
- Vredenberg WJ (2004) System analysis and photoelectrochemical control of chlorophyll fluorescence in terms of trapping models of photosystem II: a challenging view. In: Papageorgiou G and Govindjee (eds) *Advances in Photosynthesis and Respiration*, Vol 19. *Chlorophyll a Fluorescence: A Signature of Photosynthesis*, pp 133–172. Springer, Dordrecht
- Vredenberg WJ, Kasalicky V, Bina D and Prášil O (2004) System analysis of chlorophyll fluorescence kinetics in chloroplasts: submaximal yield in single turnover excitations and electrical interactions. In: Van der Est A, Bruce D (eds) *PS2004 Proceedings: 13th International Congress on Photosynthesis: From Fundamental Aspects to Global Aspects*, Vol 1, pp 190–192. Allen Press, Montreal, Canada
- Vredenberg WJ, Van Rensen JJS and Rodrigues GC (2005) On the submaximal yield and photo-electric stimulation of chlorophyll *a* fluorescence in single turnover excitations in plant cells. *Bioelectrochemistry* 68: 81–88
- Vredenberg WJ, Kasalicky V, Dürchan M and Prášil O (2006) The chlorophyll *a* fluorescence induction pattern in chloroplasts upon repetitive single turnover excitations: accumulation and function of QB-nonreducing centers. *Biochim Biophys Acta* 1757: 173–181
- Vredenberg WJ, Dürchan M and Prášil O (2007) On the chlorophyll *a* fluorescence yield in chloroplasts upon excitation with twin turnover flashes (TTF) and high frequency flash trains. *Photosynth Res* 93: 183–192
- Wydrzynski TJ and Satoh K (eds) (2005) *Photosystem II. The Light-Driven Water: Plastoquinone Oxidoreductase*. *Advances in Photosynthesis and Respiration* (Series ed, Govindjee), Vol 22. Springer, Dordrecht
- Yamashita E, Zhang H and Cramer WA (2007) Structure of the cytochrome b_6f complex: quinone analogue inhibitors as ligands of heme c_H . *J Mol Biol* 370: 39–52
- Yan J, Kurisu G and Cramer WA (2006) Structure of the cytochrome b_6f complex: binding site and intraprotein transfer of the quinone analogue inhibitor 2,5-dibromo-3-methyl-6-isopropyl-p-benzoquinone. *Proc Natl Acad Sci USA* 103: 67–74
- Zheng C, Davis ME and McCammon JA (1990) Electrofield distribution inside the bacterial photosynthetic reaction center of *Rhodospseudomonas viridis*. *Chem Phys Lett* 173: 246–252
- Zhu X-G, Govindjee, Baker NR, deSturler E, Ort DR and Long SP (2005) Chlorophyll *a* fluorescence induction kinetics in leaves predicted from a model describing each discrete step of excitation energy and electron transfer associated with Photosystem II. *Planta* 223: 114–133

Chapter 8

Clustering of Electron Transfer Components: Kinetic and Thermodynamic Consequences

Jérôme Lavergne*

*Laboratoire de Bioénergétique Cellulaire, Unité Mixte de Recherche 6191
CNRS/CEA/Université Aix-Marseille, CEA Cadarache
Saint-Paul-lez-Durance, F-13108, France*

Summary.....	177
I. Introduction.....	178
II. Thermodynamic Performance of Integrated and Diffusive Photosynthetic Models.....	179
A. The Thermodynamic Potential Available from Light.....	179
B. Coupling the Reaction Center with the Proton Pumping Complex.....	180
III. Integrated Versus Diffusive Electron Transfer Chain.....	183
A. Quasi-equilibrium Steady State in a Diffusing Three One-electron Carrier (ABC) Chain.....	183
B. Quasi-equilibrium Steady State in a Solid State ABC Chain.....	184
IV. The Small Apparent Equilibrium Constant in the Donor Chain of <i>Rhodobacter sphaeroides</i>	189
A. The Supercomplex Model.....	189
B. Distributed Stoichiometry: Crofts' Chromatophore Model.....	192
V. Quinone Domains.....	195
A. Quinone Domains in vivo.....	195
B. Purified Core Complexes RC-LH1 as Model Quinone Domains.....	196
VI. Statistical and Non Statistical Heterogeneities.....	198
VII. Pool Function Test at Steady State.....	199
VIII. Kinetic Analysis: Playing with Inhibitors, Redox Potential and Flash Intensity.....	201
IX. Concluding Remarks.....	203
Acknowledgments.....	203
References.....	203

Summary

This chapter is devoted to the effects of the organization of electron transfer chains, discussing issues related to compartmentalization at various scales as opposed to homogeneous, solution-like behavior. Mobile carriers (like quinones, cytochrome c_2 , plastocyanin) are required as shuttles between the reaction center complexes and the cytochrome bc_1 or b_6f complexes; the question under focus is whether these mobile carriers diffuse freely, or remain attached to particular (super-) complexes or to particular structural regions. The effects of clustering are first examined from a theoretical point of view, characterizing some thermodynamic and kinetic consequences of integrated (first-order reactions) or collisional (second order reactions) organization. It is shown that an ideal integrated photosynthetic system (a supercomplex associating a reaction center and a proton pump) is able to deliver more free energy power than its diffusive counterpart. The comparison is pursued by examining the case of a multi-carrier electron transfer chain, showing that here, the integrated system is less favorable than the

* Author for correspondence, e-mail: jerome.lavergne@cea.fr

diffusive one. This is due to the statistical distribution of the number of electrons present in the system, which causes over-reduction of the low potential carriers and over-oxidation of the high potential ones. This anomalously low “apparent equilibrium constant” results in decreased kinetic efficiency. The rest of the chapter analyzes various cases where restricted diffusion of the mobile carriers has been reported. The low apparent equilibrium constant found in *Rhodobacter sphaeroides* between the reaction center and its secondary electron donors has been one of the arguments leading to the supercomplex model, associating two reaction centers, one cytochrome bc_1 complex and one cytochrome c_2 . An alternative explanation has been proposed, based on a distribution of the stoichiometric ratio between the electron transfer components within the small chromatophore vesicle. Evidence for restricted diffusion of quinones, on the acceptor side of Photosystem II or in *Rhodobacter sphaeroides* has also been reported: the diffusion domain contains a small number (≈ 3 – 4) of reaction centers. These and some other cases are described together with the mathematical treatments that allow simulating the behavior of these models in various circumstances.

I. Introduction

When describing a bioenergetic chain, we often place electron carriers along a redox potential scale in a representation that is indifferent to structural constraints. X transfers an electron to Y, but does this mean that each X is transferring to a particular Y or can any X react with any Y? Are the two possibilities equivalent in principle? Are there functional tests that can allow one to distinguish between them? This chapter is aimed at discussing these two questions, partly from a theoretical point of view and partly by reviewing specific cases.

Photosynthetic electron transfer chains – bioenergetic chains in general – involve a sequence of prosthetic groups associated with integral protein complexes (reaction centers, cytochrome bc_1 or cytochrome b_6f complex) and mobile carriers (cytochrome c_2 , plastocyanin, ferredoxin, quinones). This raises the question of the extent to which the mobile carriers are mobile. Their role is to shuttle between different protein complexes, but this could occur in different ways. Two extreme views have been denoted by Rich (1984) as the liquid and solid state models. The liquid state model is the realm of second order

kinetics, while the solid state model is that of first order kinetics. The liquid model implies free diffusion of the carriers that randomly collide with their protein partners. This has been for long the predominant view in photosynthesis (Crofts and Wraight, 1983) as well as in respiration (Rich, 1984; Hackenbrock et al., 1986). On the other hand, the solid state model implies association between different protein complexes (supercomplexes) and confinement (channeling) of the mobile carriers. Intermediate models are obviously possible where associations and channeling may occur in a somewhat flexible way. There has been growing evidence suggesting some confinement of the mobile carriers in bacterial and oxygenic photosynthesis. Functional supercomplexes associating the whole photosynthetic chain of *Rhodobacter (Rb.) sphaeroides* (reaction centers and bc_1 complexes, cytochrome c_2 and quinones) have been proposed. A similar trend appears in the mitochondrial literature. A discussion and references on these topics can be found in a review chapter by Lavergne et al. (2008).

Besides the question of the degree of confinement of the mobile carriers, one may focus on the protein complexes themselves – indisputably a solid state domain – and wonder what the implications are for setting the boundary between mobile and fixed redox centers at some particular place. To give some examples, there are three redox centers in the acceptor chain of type II RCs while there are five (or more if one takes into account bifurcated paths between the two quasi-symmetrical chains) in type I RCs. On the donor side of bacterial type II RCs, some species have a tetraheme subunit serving as an

Abbreviations: AFM – atomic force microscopy; b_6f – cytochrome b_6f complex; bc_1 – cytochrome bc_1 complex; DCMU – dichlorophenyl dimethylurea; EM – electron microscopy; Fd – Ferredoxin; P – photochemical primary electron donor; PC – plastocyanin; PQ – plastoquinone; PQ – (*in italics*) photochemical donor acceptor pair; not to be confused with plastoquinone; PS I, II – photosystem I, II; Q – quinone; *Rb* – *Rhodobacter*; RC – reaction center; UQ – ubiquinone

intermediate between the primary donor P and the mobile periplasmic carrier, while in other species cytochrome c_2 interacts directly with P . It is of interest to examine whether these integrated multi-carrier segments have any kinetic and thermodynamic specificity, to what extent their response to external constraints is equivalent to that of the diffusing pathways.

The purpose of this chapter is to discuss some issues related to the kinetic and thermodynamic consequences of various organization patterns of the electron carriers, ranging from free diffusion to solid-state ordered arrangement and, in between, confinement within large or small domains. Much of the emphasis will be on experimental tests and the mathematical tool box for discriminating between these various situations. The game of guessing structural organization from functional responses has always been a favorite in the bioenergetics field, but it is becoming still more exciting (and risky) now that we have detailed, if not complete, knowledge of the pathways and mechanisms and that structural techniques, in particular crystallography and Atomic Force Microscopy (AFM) at different scales, are providing a wealth of valuable information.

II. Thermodynamic Performance of Integrated and Diffusive Photosynthetic Models

The mission of a photosynthetic system, if it chooses to accept it, is to convert the energy of light into biochemically usable free energy. In the present perspective, one may wonder whether, *in principle*, a solid state photosynthetic apparatus presents any advantage or disadvantage as regards the free energy conversion mission. Efficient photochemical charge separation requires a solid state arrangement of cofactors, since very fast electron transfer is required in order to prevent recombination reactions. But what about the complete system? Considering, for instance, a cyclic electron transfer chain as in bacteria (or in chloroplasts, for a fraction of Photosystem I), would it be better to arrange all the components as a single autonomous unit associating a reaction center and a bc_1 complex (or b_6f) or is the mediation of diffusive carriers between separate complexes advantageous, or neutral? One motivation

for raising this question is that, as shown in subsequent sections of this chapter, solid-state arrangement prevents equilibration between homologous carriers in separate chains, maintaining local correlations in the electron distribution and hence a lower entropic content. Introducing “lateral” equilibration between electron transfer chains implies a relaxation, hence a dissipation of free energy. Thus, it may be interesting to examine whether there are thermodynamic implications of a fundamental nature in the mode of coupling the solid-state photochemical reaction center and the electron-driven proton pump which completes the cyclic transfer. Before addressing this issue, I would like to give an outline of the boundary condition at the photochemical interface, common to both models.

A. The Thermodynamic Potential Available from Light

From the thermodynamic point of view, light can be considered as a source of free energy at a potential which depends on its spectrum and intensity (see Lavergne, 2006 and references therein). For simplicity, let us consider the interaction of monochromatic light at frequency ν_0 tuned with an absorber’s transition at energy $h\nu_0$. The beam intensity is denoted as $I(\nu_0)$. As pointed out by Duysens (1959), photochemical conversion works like a heat engine subject to the efficiency limit expressed by the Carnot yield:

$$\Delta\mu \leq h\nu_0 \left(1 - \frac{T}{T_r}\right), \quad (8.1)$$

where T is the temperature at which the converter works (the “cold reservoir” temperature) and T_r (r for “radiation”), is that of a black body (the “hot reservoir”) that would radiate the intensity $I(\nu_0)$. If the intensity $I(\nu_0)$ is chosen in the range of daylight illumination, the corresponding temperature T_r is not, contrary to a popular error, close to the temperature of the Sun’s surface (5,780 K), but much lower ($T_r \approx 1,180$ K). This is because, fortunately enough, the light intensity reaching the Earth is much attenuated (there is a geometrical effect depending on the square of the distance) with respect to its value on the Sun. Thus, while the spectral shape is roughly that of a 5,780 K source, the intensity (e.g. in the red region), which determines the rate of

photochemical excitation, corresponds to a cooler source (see the discussion in Lavergne, 2006). The quantity $\Delta\mu$ in Eq. (8.1) is the maximum amount of work that can be extracted from an amount of heat $h\nu_0$ (i.e. one photon) taken from the hot reservoir. It is thus a free energy per photon absorbed, or per Einstein (mol of photons) if one adopts, as in the following, the molar scale.

From the viewpoint of the light-absorbing pigment (P) involved in the transduction process, the energetic issues can be described as follows. The free energy (or chemical potential) that can be derived from the excited pigment (P^*) is

$$\Delta\mu = \Delta\mu_0 + RT \ln \left(\frac{[P^*]}{[P]} \right). \quad (8.2)$$

The standard free energy difference $\Delta\mu_0$ is $h\nu_0$, the energy involved in the $P \rightarrow P^*$ transition. The steady-state ratio of the excited and ground states featuring in the $\ln(\dots)$ term depends on the absorption and deactivation rates, i.e.

$$\Delta\mu \leq h\nu_0 + RT \ln \left(\frac{AI(\nu_0)}{B} \right), \quad (8.3)$$

where, A and B are absorption and emission coefficients. The \leq sign is used because B stands for the spontaneous emission rate of the pigment, ignoring additional deactivation processes that would cause a depletion of P^* . Stimulated emission is neglected since in the relevant intensity range, $[P^*]$ is quite small. Now, there is a deep physical relation, entangling the A , B coefficients and the black body radiation law, which ensures the equivalence of Eqs. (8.1) and (8.3):

$$\ln \left(\frac{AI(\nu_0)}{B} \right) = \frac{h\nu_0}{RT_r}. \quad (8.4)$$

One can summarize the above points in the following way. Given an illumination of intensity $I(\nu_0)$, the maximum chemical potential that can be derived is given by Eq. (8.1), where T_r is related to $I(\nu_0)$ through the black body law. The free energy that can be extracted from one photon depends on the density of photons in the illumination beam. The photon is not a ‘‘grain of free energy’’, which is an oxymoron, because concepts such as free energy or work imply collective, macroscopically averaged phenomena. For strong daylight, the Carnot yield is typically $\approx 70\%$.

Thus, the potential of the chlorophyll-based solar battery is about $1.8 \times 0.7 = 1.26$ eV.

The quantity that really matters, however, is not the potential as such, but the effective free energy power that can be derived from a given illumination. Drawing energy will deplete the steady-state amount of P^* and hence the potential, in a similar way as drawing current from a battery decreases its voltage (the effect of the ‘‘internal resistance’’). When calculating this effect, it turns out that the internal resistance is very low, i.e. the optimum regime corresponds to a high quantum yield ($\approx 95\%$) of photoelectron tapping: this is due to the fact that $h\nu_0 \gg RT$. This implies that efficient solar energy conversion is primarily a matter of quantum yield, i.e. maximizing trapping efficiency and preventing back reactions. The architecture of biological photosynthetic systems is such that large standard potential drops occur upon secondary electron transfer, particularly on the acceptor side. Whereas this stabilization policy is apt to prevent back reaction, it may become disadvantageous, if pushed too far, as regards quantum efficiency. For instance in type II bacterial reaction centers, there is a ~ 840 meV standard free energy difference between the P^+/P^* and Q_A/Q_A^- couples; in PS II the gap is ~ 540 meV (Rappaport et al., 2002). This means huge equilibrium constants, minimizing back reactions. On the other hand, this implies a significant population of Q_A^- under steady-state load conditions, meaning degraded quantum efficiency (Lavergne and Joliot, 1996). This is an indication (among others) that selection pressure has not been solely focused on pure energetic aspects, but that other parameters (e.g. prevention of toxic species formation) have imposed delicate trade-offs.

B. Coupling the Reaction Center with the Proton Pumping Complex

A solid state integrated model of the bacterial chain could for instance associate a reaction center to a bc_1 complex as a single supercomplex, sequestering somehow the intermediate carriers (quinone and c_2), or one could think of placing these components at a 1:1 ratio within small individual vesicles. The simplest integrated photosynthetic supercomplex can be imagined as a two state system, PQ (ground

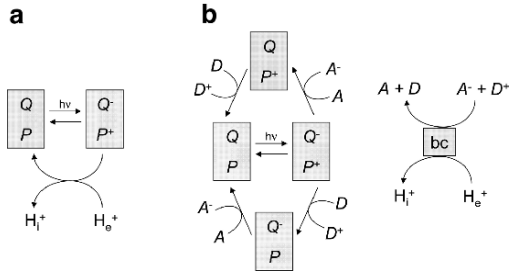


Fig. 8.1. Two versions of a minimal photosynthetic system. (a) Integrated model, with direct utilization of the charge-separated state for driving proton pumping from an “external” into an “internal” compartment. (b) Model implying diffusion of mobile carriers. The proton-pumping moiety “bc” is distinct from the photochemical complex

state, photochemically active) and P^+Q^- (energized, photochemically closed; PQ is meant here as a photochemical donor acceptor pair and should not be confused with plastoquinone). The productive return of P^+Q^- to PQ is coupled to electrogenic proton pumping. In the diffusing counterpart of this system one has separate RC and proton pump interacting through mobile intermediates that we denote A (Acceptor) and D (Donor). The schemes under discussion are shown in Fig. 8.1. The integrated model may look as a theorist’s craze, but there is a real biological system which is almost its exact incarnation, namely bacteriorhodopsin. The only, unimportant, difference is that the bacteriorhodopsin cycle does not involve a charge-separated state.

Denoting as I the light absorption rate, as $J < I$ the net flux of electrons directed to the utilization pathway (directly into the proton pump in a or through the mobile carriers in b; in the latter case, J lumps together the reactions of P^+Q^- with A and D) and as k_{rec} the rate constant for intrinsic recombination, steady-state is expressed by:

$$\frac{d[P^+Q^-]}{dt} = I[PQ] - k_{\text{rec}}[P^+Q^-] - J = 0. \quad (8.5)$$

In the case of model a, one has $[P^+Q^-] + [PQ] = 1$ and from Eq. (8.5), one obtains for Z_a , the ratio of the excited over ground states:

$$Z_a(I, J) \equiv \frac{[P^+Q^-]}{[PQ]} = \frac{I - J}{k_{\text{rec}} + J}. \quad (8.6)$$

For model B, there are additional states (PQ^- and P^+Q) and the expression for $Z_B(I, J)$ will be derived later. In both models, the potential available from the photochemical converter is:

$$\begin{aligned} \Delta\mu^{PQ} &= \Delta\mu_0^{PQ} + RT \ln \left(\frac{[P^+Q^-]}{[PQ]} \right) \\ &= \Delta\mu_0^{PQ} + RT \ln Z(I, J). \end{aligned} \quad (8.7)$$

The standard term, $\Delta\mu_0^{PQ}$, is the difference of the standard potentials of P and Q . If the rate constants of the reactions leading from P^* to the charge separated state P^+Q^- are fast enough, there is no free energy dissipation on these steps and $\Delta\mu^{PQ}$ is equal to the photochemical $\Delta\mu$ as featured in Eq. (8.2). Notice that this photochemical $\Delta\mu$ would also apply to a photochemical converter based on conformational changes rather than charge separation, as bacteriorhodopsin.

In model a, the potential $\Delta\mu^{PQ}$ is directly utilized, so that the power output is:

$$\begin{aligned} P_a(I, J) &= J \Delta\mu^{PQ} \\ &= J \left(\Delta\mu_0^{PQ} + RT \ln Z_a(I, J) \right). \end{aligned} \quad (8.8)$$

In model b, the potential available for driving the proton pump is:

$$\begin{aligned} \Delta\mu^{DA} &= E(D) - E(A) \\ &= \Delta\mu_0^{DA} + RT \ln \left(\frac{[D^+][A^-]}{[D][A]} \right). \end{aligned} \quad (8.9)$$

$\Delta\mu_0^{DA}$ is the difference of the standard (midpoint) potentials of D and A . The most favorable situation for the diffusing system b is obtained when (i) there are quasi-equilibria between P and D , and Q and A (so that the free energy drop at these stages is negligible); (ii) the fraction of RCs with P^+ is equal to the fraction of RCs with Q^- : let us denote as x this fraction. The equilibrium assumption implies:

$$\begin{aligned} \Delta\mu^{DA} &= E(P) - E(Q) \\ &= \Delta\mu_0^{PQ} + RT \ln \left(\frac{\sum P^+ \sum Q^-}{\sum P \sum Q} \right). \end{aligned} \quad (8.10)$$

The Σ notation is meant as the sum of states with P^+ , etc. For instance:

$$\begin{aligned}\sum P^+ &= [P^+Q^-] + [P^+Q] = x = \sum Q^- \\ \sum P &= [PQ^-] + [PQ] = 1 - x = \sum Q.\end{aligned}\quad (8.11)$$

The equalities with ΣQ^- and ΣQ derive from assumption (ii) above. Thus,

$$\Delta\mu^{DA} = \Delta\mu_0^{PQ} + RT \ln \left(\frac{x}{1-x} \right)^2. \quad (8.12)$$

Under quasi-equilibrium conditions, the distribution of P^+ and Q^- are independent, so that the concentration of state $P^+ Q^-$ is the joint probability of having P^+ and Q^- . Therefore:

$$\begin{aligned}[P^+Q^-] &= x^2 [PQ] = (1-x)^2 \\ [P^+Q] &= [PQ^-] = x(1-x).\end{aligned}\quad (8.13)$$

Hence:

$$\frac{[P^+Q^-]}{[PQ]} = \left(\frac{x}{1-x} \right)^2. \quad (8.14)$$

This shows that expressions (8.7) and (8.12) are equivalent, as expected from the equilibrium condition. Inserting the values from Eq. (8.13) into Eq. (8.5), one obtains a quadratic equation whose solution ($0 < x < 1$) allows us to express x as a function of I and J . To keep the equations simple we just denote it as $x(I, J)$. The expression for Z_b is then:

$$Z_b(I, J) = \left(\frac{x(I, J)}{1-x(I, J)} \right)^2. \quad (8.15)$$

We can now write the power output in model b as:

$$P_b(I, J) = J \left(\Delta\mu_0^{PQ} + RT \ln Z_b(I, J) \right). \quad (8.16)$$

Figure 8.2c illustrates the behavior of $P(I, J)$ in both models, adopting for $\Delta\mu_0^{PQ}$ and k_{rec} values inspired from the RC of *Rb. sphaeroides* (see legend of Fig. 8.2). As could be expected, the integrated model delivers more power than the diffusive one. However, the handicap is moderate ($\approx 20\%$) and the diffusive organization remains a viable option. In both models, the maximum

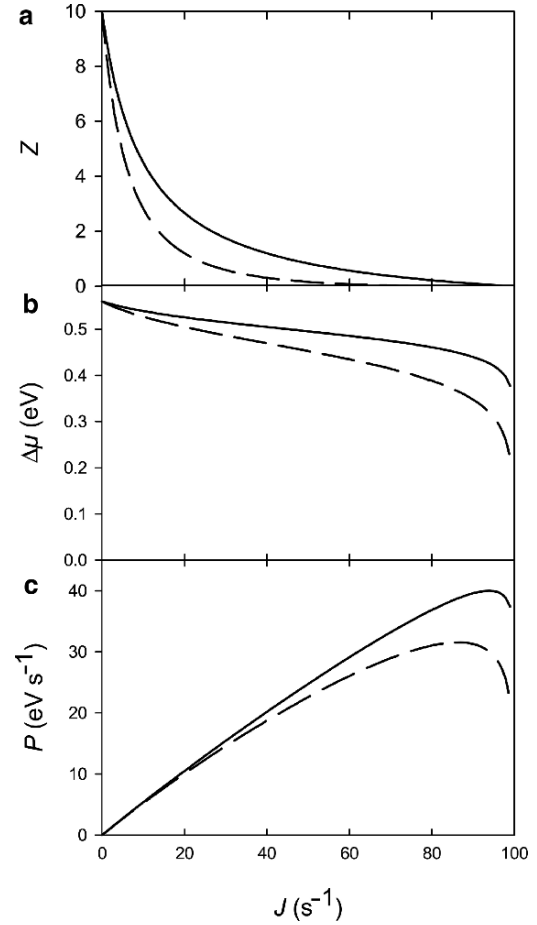


Fig. 8.2. A comparison of the performances of the models depicted in Fig. 8.1 (integrated model, solid line; diffusive model, dashed line). The parameters used were $I = 100 \text{ s}^{-1}$, $k_{\text{rec}} = 10 \text{ s}^{-1}$ and $\Delta\mu_0^{PQ} = 0.5 \text{ eV}$. The horizontal scale in the three plots is $J(< I)$, the electron flux taken into the utilization (proton pumping) pathway. The vertical scales are: (a) the ratio $Z = [P^+Q^-]/[PQ]$ computed from Eqs. (8.6) and (8.15); (b) the potential $\Delta\mu$ available for driving the proton pump; (c) the power delivered ($\Delta\mu \times J$)

power is obtained for high yields of electron utilization (J/I), about 0.94 for model a and 0.86 for model b (Fig. 8.1), which has thus a larger “internal resistance”. The poorer performance of the diffusive system is due to the fact that lateral equilibration causes a dilution into additional states (PQ^- and P^+Q), which are inactive both for photochemical charge separation and as a driving force for conversion into work (proton pumping). For a given potential (or Z), this implies a lower J , or, for a given J , a lower output potential (see panels a and b of Fig. 8.2).

III. Integrated Versus Diffusive Electron Transfer Chain

In this section we consider a chain of three one-electron carriers, A, B, C, where rapid electron transfer can occur between A and B or B and C, but not directly between A and C. The choice of a three carrier chain is arbitrary: it allows a more general presentation than when dealing with two carriers and, on the other hand, the effects under scrutiny become less pronounced when the number of redox centers increases. One assumes that electrons are fed into the chain from an upstream source X that interacts with A, and they are delivered to a downstream sink Y that interacts with C. The issue under scrutiny here is: what are the thermodynamic and kinetic consequences – if any – of an integrated ABC arrangement, compared with a diffusing system? Clearly, there is an obvious answer to this question, noting that the arrangement of ABC as fixed cofactors in a protein matrix can allow very high electron transfer rate constants, eliminating the delay inherent in diffusion limited reactions. This is true, of course, but I will show that besides such effects, there are quite significant and less obvious differences between both situations.

Although an integrated electron transfer chain may look simpler than its diffusive counterpart (all reactions are first order) the kinetic equations are in fact more complex, even at steady state. This is due to the fact that the number of species that must be taken into account is much (exponentially) larger, because one has to deal with all possible electron distributions in the complex. Techniques for writing explicitly the steady-state expressions corresponding to a network of first order reactions have been developed by enzymologists (King and Altman, 1956; Hill, 1989; Cornish-Bowden, 2004). The present discussion is restricted to the case where quasi-equilibrium is achieved in the ABC chain (the internal electron transfer reactions are assumed to be fast compared with the upstream and/or downstream reactions involving X and Y). By comparing quasi-equilibrium behavior in the integrated and diffusive chains, we exclude the trivial effects due to the possibly smaller rate constants involved in the diffusing system.

A. Quasi-equilibrium Steady State in a Diffusing Three One-electron Carrier (ABC) Chain

Let us first describe the diffusive model. We denote as E_A , E_B , E_C the midpoint (standard) potentials of the carriers. Hereafter, we use bold type to specify that potentials are expressed in units of RT/F (or $2.3 RT/F \approx 60$ meV if base 10 is preferred). The equilibrium condition writes:

$$E(A) = E(B) = E(C) = E, \quad (8.17)$$

with:

$$\begin{aligned} E(A) &\equiv E_A + \ln \frac{[A]}{[A^-]} \\ E(B) &\equiv E_B + \ln \frac{[B]}{[B^-]} \\ E(C) &\equiv E_C + \ln \frac{[C]}{[C^-]} \end{aligned} \quad (8.18)$$

where $E(A)$, $E(B)$ and $E(C)$ are the effective potentials of the carriers and E the common equilibrium value. A nice visual representation consists in depicting the carriers as vials whose filling level represents both the fraction of the reduced state and the potential $E(V)$ of vial V. The vial must then have the shape of a symmetrical *amphora* with tapered ends, and its midplane location corresponds to the midpoint potential of the carrier. (This design would also apply to the description of proton binding on acid groups, replacing electrons by protons, redox potential by $-\text{pH}$ and midpoint potential by $-\text{pK}_a$.) Figure 8.3 shows this representation applied to the XABCY electron transfer chain.

The common filling level at E in the A, B, C amphoras expresses the assumption of equilibrium in this part of the chain. Some potential drop occurs between X at potential $E(X)$ and the ABC group at potential E , and also downstream between ABC and Y at potential $E(Y)$. The extent of these drops depends on the rate constants for the electron transfer reaction between X and A (denoted as k_{XA} and k_{AX}) on the one hand, and between C and Y (k_{CY} and k_{YC}) on the other hand. E lies between the imposed values of $E(X)$ and $E(Y)$, with a smaller potential drop on whichever

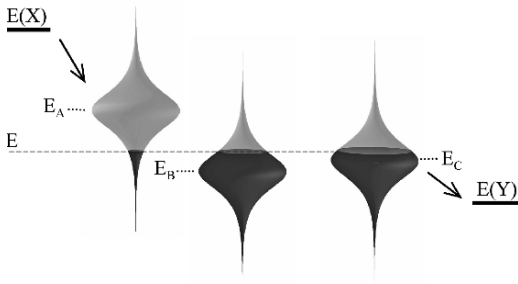


Fig. 8.3. A scheme illustrating the energetics of electron transfer across a chain of diffusive carriers. The vertical scale refers to redox potential (positive downward). Each of the A, B, C carriers is represented as a vial whose midplane is located at the midpoint potential. The filled volume indicates the reduced fraction. The three vials are filled at the same level E, indicating that quasi-equilibrium is achieved. The potentials of the source E(X) and sink E(Y) are featured

step is faster. The steady-state electronic current through the chain is:

$$J = k_{XA}[X^-][A] - k_{AX}[X][A^-] \\ = k_{CY}[C^-][Y] - k_{YC}[C][Y^-]. \quad (8.19)$$

Rearranging the first equation yields:

$$J = J_X[A] \left(1 - \frac{k_{AX}[X][A^-]}{k_{XA}[X^-][A]} \right). \quad (8.20)$$

In the latter expression, $J_X = k_{XA}[X^-]$ is the maximum current that can be delivered by the upstream source. Similarly, we denote as $J_Y = k_{CY}[Y]$ the maximum current that can be delivered to the downstream sink. The use of these parameters, together with the imposed E(X) and E(Y) potentials, exempts us from specifying the midpoint potentials of X and Y. Assuming that the species A, B, C are all at unit concentration (i.e. $[A] + [A^-] = 1$, etc.) and using Eq. (8.18), one obtains e.g.:

$$[A] = \frac{1}{1 + e^{E_A - E}}. \quad (8.21)$$

The ratio appearing in Eq. (8.20) is that of the forward and backward one-way fluxes, which is simply expressed as a function of the free energy drop, $E(X) - E$ (Hill, 1989):

$$\frac{k_{AX}[X][A^-]}{k_{XA}[X^-][A]} = e^{E(X) - E}. \quad (8.22)$$

The above equation is derived from expressions such as Eq. (8.18), using the fact that

$\ln(k_{AX}/k_{XA})$ is equal to the difference of the standard potentials, $E_X - E_A$.

Using Eqs. (8.21) and (8.22), expression (8.20) becomes:

$$J = J_X \frac{1 - e^{E(X) - E}}{1 + e^{E_A - E}}. \quad (8.23)$$

Applying the same procedure to the rightmost member of Eq. (8.19), we obtain:

$$J = J_Y \frac{1 - e^{E - E(Y)}}{1 + e^{E - E_C}}. \quad (8.24)$$

Now, given the ratio J_X/J_Y , the boundary potentials E(X), E(Y) and the midpoint potentials of A and C, we can obtain E (and J) by solving numerically the equation whose sides are given by Eqs. (8.23) and (8.24). In the diffusive model, the presence of one or more intermediates between the end carriers A and C has no consequence (insofar as equilibrium is assumed) and the midpoint potential E_B does not feature in the equations. Accordingly, the problem is fully determined by specifying four parameters (one may adopt for instance E(Y) as an origin for the potentials; the parameters are then E(X), E_A, E_C and the ratio J_X/J_Y).

B. Quasi-equilibrium Steady State in a Solid State ABC Chain

We shall now deal with the steady-state behavior of the integrated ABC chain. To keep things simple and allow a direct comparison with the diffusive system, we ignore until further notice the mutual interactions between the carriers (i.e. the midpoint potential of each carrier is assumed to be independent of the redox state of its neighbors). One has to consider the four macrostates $S(n)$ corresponding to $n = 0$ to 3 electrons present in the chain. While states $S(0)$ and $S(3)$ are non-degenerate, there are several (three) substates specifying the location of the electrons in states $S(1)$ and $S(2)$. But, due to the equilibrium condition, each substate is in a fixed proportion, determined by the midpoint potentials of the carriers. The general expression for the fraction of a particular substate k can be written:

$$P_k = \frac{e^{E_k}}{\sum_j e^{E_j}}. \quad (8.25)$$

The index j runs over the various substates within a given $S(n)$ state. For example, within $S(2)$, one may number the states AB^-C^- , A^-BC^- , A^-B^-C as $j = 1-3$, respectively. The E_j exponent is obtained by summing the midpoint potentials of the reduced carriers in the j state and dividing by RT/F . Thus, for instance, the fraction of substate A^-BC^- within the macro-state $S(2)$ is:

$$P_2 = \frac{e^{E_A+E_C}}{e^{E_A+E_B} + e^{E_A+E_C} + e^{E_B+E_C}}. \quad (8.26)$$

In order to calculate the steady-state distribution of the $S(n)$ states, one needs quantities like $A_{\text{red}}(n)$ or $C_{\text{red}}(n)$, i.e. the fractions of reduced A or C in the macro-state n . This is readily obtained from Eq. (8.26) by summing over the relevant micro-states. For instance:

$$A_{\text{red}}(2) = \frac{e^{E_A+E_B} + e^{E_A+E_C}}{e^{E_A+E_B} + e^{E_A+E_C} + e^{E_B+E_C}},$$

$$C_{\text{red}}(2) = \frac{e^{E_A+E_C} + e^{E_B+E_C}}{e^{E_A+E_B} + e^{E_A+E_C} + e^{E_B+E_C}}. \quad (8.27)$$

The electron input rate into state $S(n)$ (i.e. the rate constant for forming the $S(n+1)$ state) is:

$$k_{n,n+1} = J_X (1 - A_{\text{red}}(n)) + J_Y^- (1 - C_{\text{red}}(n)), \quad (8.28)$$

where J_Y^- denotes the maximum rate $k_{YC}[Y^-]$ of the reverse electron flow from Y to C; it is related to J_Y by:

$$\frac{J_Y^-}{J_Y} = \frac{k_{YC}[Y^-]}{k_{CY}[Y]} = e^{E_C-E(Y)}. \quad (8.29)$$

The rate constant for forming $S(n)$ from $S(n+1)$ (losing one electron) is:

$$k_{n+1,n} = J_X^- A_{\text{red}}(n+1) + J_Y C_{\text{red}}(n+1), \quad (8.30)$$

where, again, the reverse rate J_X^- is related to J_X by:

$$\frac{J_X^-}{J_X} = \frac{k_{AX}[X]}{k_{XA}[X^-]} = e^{E(X)-E_A}. \quad (8.31)$$

Using Eqs. (8.28) and (8.30), the “equilibrium constant” between the two states is:

$$K_{n+1,n} = \frac{S(n+1)}{S(n)} = \frac{k_{n,n+1}}{k_{n+1,n}} = \frac{J_X (1 - A_{\text{red}}(n)) + J_Y e^{E_C-E(Y)} (1 - C_{\text{red}}(n))}{J_X e^{E(X)-E_A} A_{\text{red}}(n+1) + J_Y C_{\text{red}}(n+1)}. \quad (8.32)$$

The quotes are meant as a caveat that we are dealing with steady-state rather than equilibrium; however, since the kinetic scheme is linear (no cycle) there is no steady-state flux between the $S(n)$ and Eq. (8.32) is valid. Then, using the fact that $S(0) + S(1) + S(2) + S(3) = 1$, one obtains:

$$S(0) = \frac{1}{1 + K_{10} + K_{21} + K_{32}}. \quad (8.33)$$

And, the other state fractions follow, e.g. $S(1) = K_{10}S(0)$, etc. The problem is thus fully solved in terms of five parameters, i.e. the ratio J_X/J_Y and (locating at $E(Y)$ the origin of potentials) $E(X)$, E_A , E_B (which must be specified here, at variance with the diffusive model) and E_C . Using Eq. (8.27), the reduced fractions of each carrier can be computed, i.e.:

$$A_{\text{red}}^{\text{tot}} = \sum_{n=0}^3 A_{\text{red}}(n)S(n). \quad (8.34)$$

One can also compute the “apparent potential” of each carrier, e.g.:

$$E'(A) \equiv E_A + \ln \left(\frac{1 - A_{\text{red}}^{\text{tot}}}{A_{\text{red}}^{\text{tot}}} \right). \quad (8.35)$$

The derivation of J in Eqs. (8.19)–(8.23) remains valid provided that E be replaced by $E'(A)$. Thus:

$$J = J_X \frac{1 - e^{E(X)-E'(A)}}{1 + e^{E_A-E'(A)}}. \quad (8.36)$$

Results computed with the above equations are displayed in Fig. 8.4. The chosen midpoint potentials are arranged in tiers, with $E(X)$ and $E(Y)$ set equal to E_A and E_C , respectively. Panel a shows the apparent potentials of each carrier, as a function of J_X/J_Y . As expected, the potentials are close to $E(X)$ when the $C \rightarrow Y$ reaction is

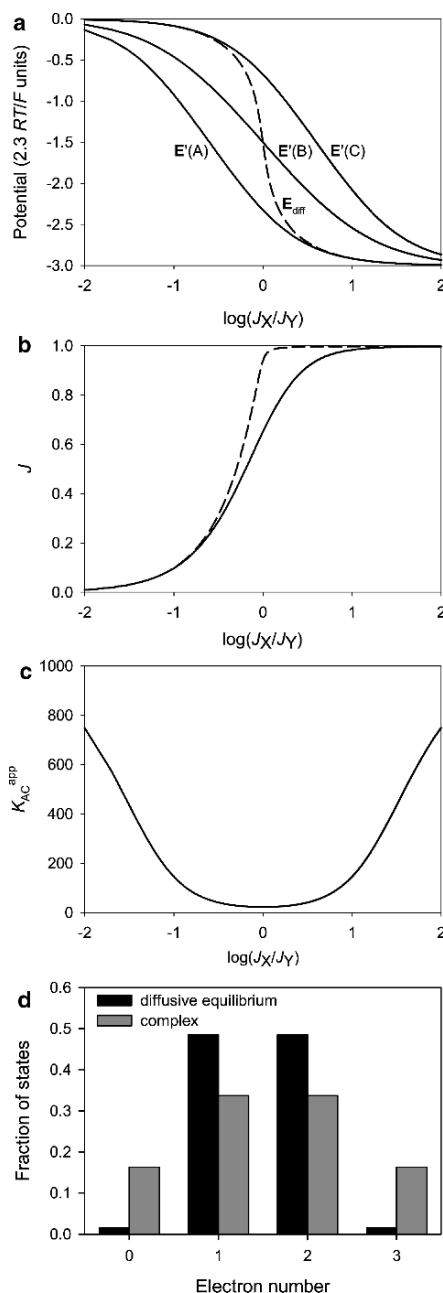


Fig. 8.4. Thermodynamic and kinetic behavior of an integrated electron transfer chain ABC under steady-state conditions. The limiting steps are located upstream and/or downstream of the chain, and intracomplex equilibrium is assumed. The parameters chosen were (locating at $E(Y)$ the origin of potentials), $E(X) = -3$, $E_A = -3$, $E_B = -1.5$, $E_C = 0$ (in units of $2.3RT/F \approx 60$ mV) and $J_Y = 1$. The horizontal scale is the log of the ratio of the maximum input (J_X) and output fluxes (J_Y). For large negative values of this quantity, the upstream step is entirely responsible for the rate limitation and the chain equilibrates at the potential of the sink; conversely, for large positive values, the downstream step is rate-limiting and the chain equilibrates at the potential of the source. (a) A plot of the apparent potentials of the three carriers and of E_{diff} (dashed line), which is the effective quasi-equilibrium potential in the diffusing model with otherwise identical conditions. (b) The steady-state electron flux through the integrated system (solid line) and in the diffusing model (dashed line). (c) The apparent equilibrium constant between carriers A and C (the true equilibrium constant is 1,000). (d) Distribution of the macro-states with 0, 1, 2, 3 electrons in the complex for $J_X = J_Y$. The gray bars refer to the integrated chain; the black bars indicate the distribution attained when lateral equilibration is allowed

limiting (large J_X/J_Y ratio) and close to $E(Y)$ when the upstream reaction is limiting (small J_X/J_Y ratio). A remarkable feature is observed in the intermediate region, where the apparent potentials split, despite the fact that equilibrium is maintained in the ABC chain. For comparison, the (unique) potential achieved in the diffusive ABC system with the same parameters is also shown (dashed line). The effect observed with the clustered carriers consists in an over-oxidation of the high potential carrier (C) and over-reduction of the low potential carrier (A), with respect to the levels that would be observed if the components were equilibrated at a common ambient potential. The equilibration would occur if “lateral” interaction between the individual ABC chains were allowed, e.g. through an efficient redox mediator, or through direct collisions between the chains. The X and Y partners of the chain do allow a lateral interaction, but not in a sufficiently reversible manner – except when one of the rates (J_X or J_Y) is much larger than the other one.

The phenomenon illustrated by Fig. 8.4a, i.e. the average over-reduction of the low potential carrier and under-reduction of the high potential carrier is clearly unfavorable as regards kinetic efficiency; the effect is illustrated in Fig. 8.4b, showing a plot of J as a function of J_X/J_Y for the complex (Eq. 8.36) and the diffusing system (Eqs. 8.23 and 8.24).

An observer measuring the steady-state reduction levels in the integrated ABC system and assuming full equilibrium would infer that the gaps between the midpoint potentials are smaller than is actually the case: the apparent equilibrium constants are smaller than the real ones, which can be estimated from equilibrium redox titrations. The apparent equilibrium constant between A and C, for instance is (using the quantities defined in Eq. 8.34):

$$K_{AC}^{app} \equiv \frac{(1 - A_{red}^{tot})}{A_{red}^{tot}} \frac{C_{red}^{tot}}{(1 - C_{red}^{tot})}. \quad (8.37)$$

As shown in panel c this “apparent constant” is far from being constant: it tends towards the thermodynamic value (1,000) for large J_X or J_Y and decreases dramatically in the intermediate region. It may then seem paradoxical that when looking at particular macro-states of the system, i.e. ABC complexes with one electron, or with

two electrons, the equilibrium constants prevailing within these subsystems are *larger* than in the solution equilibrium, i.e. the opposite of the effect globally observed in the steady-state system (Lavergne and Joliot, 1991). Let us consider for example the equilibrium between A and C, when only one electron is present in the ABC complex. Using Eq. (8.27), one has:

$$\begin{aligned} A_{red}(1) &= \frac{e^{E_A}}{e^{E_A} + e^{E_B} + e^{E_C}} \\ C_{red}(1) &= \frac{e^{E_C}}{e^{E_A} + e^{E_B} + e^{E_C}} \end{aligned} \quad (8.38)$$

and the equilibrium constant in this subsystem is:

$$K_{AC}(1) = \frac{(1 - A_{red}(1)) C_{red}(1)}{A_{red}(1) (1 - C_{red}(1))} = \frac{(e^{E_B} + e^{E_C}) e^{E_C}}{e^{E_A} (e^{E_A} + e^{E_B})}. \quad (8.39)$$

With the parameters adopted in Fig. 8.4, one has $K_{AC}(1) = K_{AC}(2) \approx 32,000$, while the equilibrium constant for the fully equilibrated system is $e^{E_C - E_A} = 1,000$. The effect is even more marked in a two partner complex, where the apparent equilibrium constant in the S(1) state is the *square* of the solution equilibrium constant:

$$\begin{aligned} K_{AB}(1) &= \frac{[A_{ox}][B_{red}]}{[A_{red}][B_{ox}]} \\ &= \frac{[AB^-][AB^-]}{[A^-B][A^-B]} = (e^{E_B - E_A})^2. \end{aligned} \quad (8.40)$$

On practical grounds, it is obviously difficult or impossible to monitor the electron distribution within individual macro-states such as S(1) or S(2), when the system is subjected to a steady-state electron flow. But – this is typically a case when photosynthesists may feel entitled to look down on mitochondrialists – things are different in the context of experiments using single turnover flashes, i.e. promoting one photochemical charge separation on all the RCs. For example, the S(1) state is commonly observed following one flash in the $Q_A Q_B$ quinone acceptor system of type II RCs, or in the tetraheme of RCs from, e.g., *Blastochloris viridis* (ignoring the low potential hemes).

The reason for the small global apparent equilibrium constant in the steady-state

regime, despite the opposite effect in individual macro-states discussed above, is that the macro-states $S(1)$ and $S(2)$ are less populated while the fully oxidized and fully reduced macro-states, $S(0)$ and $S(3)$, are more populated than when lateral equilibration is achieved. This is illustrated in Fig. 8.4d, showing the two distributions for $J_X = J_Y$. The distribution in the case of lateral equilibration corresponds to the statistics for picking three objects with probabilities R_A , R_B and R_C that each object is in the reduced state. These are the fractions of A^- , B^- and C^- at redox equilibrium with a potential $E = -1.5$ (the solution potential when $J_X = J_Y$), i.e., from Eq. (8.21):

$$\begin{aligned} R_A &= \frac{1}{1 + e^{E-E_A}} \\ R_B &= \frac{1}{1 + e^{E-E_B}} \\ R_C &= \frac{1}{1 + e^{E-E_C}}. \end{aligned} \quad (8.41)$$

As alluded above, the discrepancy between the complex and solution behavior is more or less pronounced depending on the number of partners involved. A chain with many carriers behaves more like a solution. One may notice that pushing the midpoint potential of one carrier far away from the others amounts to effectively removing this carrier from the chain within a certain range of working regimes. For example, under most circumstances, a tetraheme with two high potential and two low potential hemes, may be viewed as a two carrier chain, with the low potential hemes fixed in the oxidized state (the uphill steps implied by the low potential hemes affect the rate constants, though; see below). The physical reason for the “low apparent equilibrium constant effect” is that in the absence of lateral equilibration, the distribution of the $S(n)$ macro-states is not, or not only, governed by thermodynamic parameters, but also, loosely speaking, by the statistical input and output of electrons, which are Poisson processes. This is the origin of the relative over-population of the fully reduced and fully oxidized macro-states. If lateral interaction is allowed, a “dismutation” reaction can

take place [i.e., for a two-carrier chain $A^-B^- + AB \leftrightarrow 2(AB)^-$] that restores the narrower thermodynamic distribution of macro-states.

In previous work (Lavergne et al., 1989; Lavergne and Joliot, 1991), the occurrence of a low apparent equilibrium constant in a complex was characterized (in the context described in the next section) during a kinetic transient, e.g. the photo-oxidation under weak light of an initially reduced chain. We believed that the experimental procedure where a complex was filled irreversibly with oxidized (or reduced) equivalents was a requirement for observing this behavior and that a steady-state regime implying two-way interactions with the electron source and sink would cause sufficient lateral interaction to restore the solution-like equilibrium distribution. The present analysis shows that this is not true. The distortion with respect to homogeneous equilibrium does occur at steady-state, whenever the rate-limitation does not bear entirely on the upstream or downstream step.

The analysis developed in this section shows that, all other things being equal, the clustering of electron transfer carriers within an integrated complex is unfavorable with respect to kinetic and thermodynamic efficiency. Compared with the “equivalent” diffusive system, the complex is more resistive, it tends to waste free energy and (if fed by a reaction center) to decrease the quantum yield. Things are made still worse if one takes into account the mutual interactions between the carriers. For instance, in the ABC chain, if the midpoint potential of B is shifted to a more negative value when an electron is present on C, this tends to favor state A^-BC^- over state AB^-C^- , resulting in a still lower apparent equilibrium constant. In PS II for instance, the presence of one electron on Q_A^- shifts the potential of the pheophytin (its upstream partner) by almost -90 mV, affecting dramatically the photochemical and recombination properties of the RC (Gibasiewicz et al., 2001), which accounts for the fact that RCs in the Q_A^- state are “closed”. Similar effects were found for PS I (Polm and Brettel, 1998). In defense for the integrated system, one may first point out that “all things being equal” may not be achievable, e.g. if the slower rate constants in the diffusing system offset its potential advantage. This

applies typically to the RC cofactors involved in the early steps of charge separation and stabilization. Furthermore, the drawbacks of the integrated system can be remedied by implementing a sufficient number of redox centers. On the other hand, the problem raised by mutual interactions can be remedied as well, by inserting redox centers with midpoint potential much below or above the working potential range (i.e. out of the $E(X) - E(Y)$ range in the models treated above). With a proper design as regards distances and midpoint potential arrangements, the uphill steps remain compatible with high kinetic rates and the inserted carriers act as spacers, preventing too strong interactions between the “normal potential” carriers (such a suggestion was put forward by Nitschke and Dracheva, 1995; see Alric et al., 2006, for a detailed study of interactions and kinetic issues). These considerations may help to understand two features frequently encountered in electron transfer proteins: the presence of many more redox centers than would seem necessary, and the “roller coaster” arrangement of the midpoint potentials, alternating high and low potential carriers.

To conclude the part of this chapter devoted to purely theoretical considerations, it appears that the solid state option for the photosynthetic system as a whole is advantageous (Section II), while the opposite is true for multi-carrier electron transfer chains (this section). In rather loose terms, this may be rationalized as follows. The constraint of keeping systems isolated from one another implies incomplete equilibration and higher free energy (lower entropy) content. In the photosynthetic system discussed in Section II, the interfaces with the environment consist in processes that create (RC) or consume (proton pump) a charge-separated pair: the correlated presence of both the + and – charges is a requirement at these interfaces. Thus, the passage through the de-correlated realm of second order processes means a decreased efficiency. On the other hand, in the case of the XABCY chain, the interfaces with X and Y are already of a second order nature; the passage through the constrained ABC complex requires a sort of “uphill step” (there is less entropy in the integrated chain than in a diffusive chain), which is responsible for the decreased efficiency.

IV. The Small Apparent Equilibrium Constant in the Donor Chain of *Rhodobacter sphaeroides*

Whereas the finding of an anomalously low apparent equilibrium constant is a sure diagnostic of hampered equilibration, there may be quite different structural organizations responsible for such situation. A first case, as considered above, is that of a complex associating a small number of redox centers in a fixed stoichiometry. Another case is that of a diffusing system confined to a small compartment with a statistically distributed stoichiometry of the components. Interestingly, both interpretations have been proposed as alternative explanations for the low apparent equilibrium on the donor side chain of *Rb. sphaeroides*. This gives us an opportunity to discuss the treatment of both models in the same context.

A. The Supercomplex Model

Joliot et al. (1989) studied the photo-oxidation under continuous illumination of the donor chain in whole cells of *Rb. sphaeroides* treated with myxothiazol in order to block the injection of electrons from quinol into the bc_1 complex. One can then monitor the oxidation of the chain comprising the reaction center's special pair (P), the soluble cytochrome c_2 and the high potential redox centers of the bc_1 complex (heme c_1 and the iron-sulfur center denoted as FeS). The average stoichiometry RC: c_2 : bc_1 is, roughly, 2:1:1. Typically, the cells were poised at an ambient potential where these components were reduced in the dark, while the quinone pool on the acceptor side was oxidized. The illumination intensity was rate-limiting, i.e. the photochemical turnover rate was low with respect to the rate of the electron transfer reactions. Roughly, the midpoint potentials (E_m) of the secondary donors (c_2 , c_1 , FeS) lie around 300 mV, while that of P is ≈ 450 mV. There is thus a large E_m gap between P and its partners and one expects a large equilibrium constant, meaning that the oxidation of P will not be observed until the other carriers are almost fully oxidized (i.e. the photo-oxidation kinetics of P should have a sigmoidal shape with a pronounced lag). At variance with this prediction, Joliot et al. (1989) showed a

much earlier appearance of P^+ , i.e. a case where the apparent equilibrium constant is much lower than expected from the E_m values. Based on this result and an analysis of the flash-induced kinetics, Joliot et al. (1989) proposed a supercomplex model, associating two RCs, one bc_1 and one c_2 (the model also postulated the presence of 30% incomplete supercomplexes, devoid of bc_1 ; this will be ignored in the treatment below).

To simulate the photo-oxidation of the supercomplex, one can proceed as follows. Since the process under study is slow with respect to intra-complex equilibration, the state of the system at any time is fully specified by the distribution of the macro-states $S(n)$, where n is the number of oxidized equivalents (more convenient than electrons in the present case) contained in the complex ($S(n, t)$ refers to the fraction of complexes present in the macro-state with oxidation number n at time t). The kinetic scheme is thus: $S(0) \xrightarrow{k_0} S(1) \xrightarrow{k_1} S(2) \xrightarrow{k_2} \dots$, implying a system of differential equations:

$$\frac{d}{dt}S(n, t) = k_{n-1}S(n-1, t) - k_nS(n, t). \quad (8.42)$$

This is easily integrated with standard methods and one obtains:

$$\begin{aligned} S(0, t) &= e^{-k_0 t}, \\ S(1, t) &= k_0 \left(\frac{e^{-k_0 t}}{k_1 - k_0} + \frac{e^{-k_1 t}}{k_0 - k_1} \right), \\ S(n, t) &= \left(\prod_{j=0}^{n-1} k_j \right) \sum_{p=0}^n \frac{e^{-k_p t}}{\prod_{\substack{q \leq n \\ q \neq p}} (k_q - k_p)}, \end{aligned} \quad (8.43)$$

which takes into account the initial conditions $S(0, 0) = 1$, $S(n > 0, 0) = 0$. The rate constants k_n express the probabilities per unit time of an additional photo-oxidation of $S(n)$, which depends on the fraction of open RCs. Denoting as $P1(n)$ and $P2(n)$ the fractions of complexes with oxidation number n that have, respectively, one or both reduced P 's (i.e. the competent state for photochemistry), one expects that

$$k_n = 2IP2(n) + IP1(n), \quad (8.44)$$

where I (the probability of one charge separation per RC per unit time) is a photochemical rate constant depending on the illumination intensity and on the antenna absorption. As the equilibrium constant between P and the secondary donors is large, one has $k_0 \approx k_1 \approx k_2$, so that most of the denominators in Eq. (8.43) approach zero. When all k_n are equal, the solution of Eq. (8.42) takes on a different form, which is simply a Poisson distribution. The fraction of states with n oxidized equivalents at time t is $\text{Pois}(n, 2It)$, the probability to have received n "photons", when the complexes have received an average of $2It$ photons. In practice, to avoid numerical inaccuracies due to small values of the denominators in Eq. (8.43), numerical integration of Eq. (8.42) is easily implemented, e.g. using a Runge-Kutta method.

Equation (8.44) is generally not accurate, however, because several RCs share a common antenna array, so that the light-harvesting cross section of an open RC increases when its neighbors are closed. To account for this effect one may consider two possibilities. First, one may assume that the domain for excitation connectivity is essentially the supercomplex itself, i.e. the S-shaped LH1 antenna associating the two RCs (for EM and AFM images of the RC-LH1 dimer, see Jungas et al., 1999; Bahatyrova et al., 2004; Siebert et al., 2004). Then, the photochemical rate of an open RC is increased by a factor $(1 + J_{\text{dim}})$, with $J_{\text{dim}} \leq 1$, when its partner in the dimer is oxidized (Comayras et al., 2005a) and one can replace Eq. (8.44) by:

$$k_n = 2IP2(n) + I(1 + J_{\text{dim}})P1(n). \quad (8.45)$$

Another possibility is to assume a more delocalized connectivity so that an open RC is not exclusively sensitive to the state of its companion, but rather "feels" the time-dependent average population of closed/open RCs. The dependence on the average fraction $\langle P_{\text{red}}(t) \rangle$ of reduced P can be described as (Lavergne and Trissl, 1995; Comayras et al., 2005a):

$$k_n = \frac{I(1 + J_{\text{av}})}{1 + J_{\text{av}} \langle P_{\text{red}}(t) \rangle} (2P2(n) + P1(n)). \quad (8.46)$$

The parameter J_{av} quantifies the effect of antenna connectivity. This is a more complicated situation

because the k_n 's are not time-independent any more and one cannot obtain an analytical solution of the kinetic expressions as above: one has to resort to numerical integration. In *Rb. sphaeroides*, the connectivity parameter (J_{dim} or J_{av} , depending on the assumed model) is about 0.7. The correct model for excitonic connectivity is probably intermediate between local (intra-dimer) and fully delocalized, but does seem however closer to the former (Comayras et al., 2005a).

The final ingredients we need are the expressions for $P1(n)$, $P2(n)$ and for the reduced fractions of the other components in the macro-state n . The recipe for obtaining these expressions was given above (Eqs. 8.25–8.27); transposition from the three-partner ABC complex to the five-partner supercomplex is straightforward. Let us write a general form of the equation giving the fraction of each substate, for a complex including m types of redox centers, with standard potentials $\mathbf{E}_1, \dots, \mathbf{E}_i \dots \mathbf{E}_m$ and with each center present as $N_1, \dots, N_i, \dots, N_m$ copies. This is a bit out-sized in the present case as one has just $m = 4$ and $N_1 = 2$, $N_2 = N_3 = N_4 = 1$, but in the next section larger N numbers will be used and the general expression will be required. Within the macro-state $S(N_{\text{tot}}-p)$ containing p electrons ($N_{\text{tot}} \equiv \sum N_i$ is the total electron capacity), the fraction of a substate with the electron distribution $n_1, \dots, n_i, \dots, n_m$ (with $\sum n_i = p$ and $n_i \leq N_i$) is:

$$P(p, n_i) = \frac{\binom{N_1}{n_1} \cdots \binom{N_i}{n_i} \cdots \binom{N_m}{n_m}}{Z(p)} \times \exp(n_1 \mathbf{E}_1 + \dots + n_i \mathbf{E}_i + \dots + n_m \mathbf{E}_m) \quad (8.47)$$

The pre-exponential factors in the numerator are combination numbers; $Z(p)$ is the sum of terms similar to the numerator, for all possible combinations of the n_i constrained by $\sum n_i = p$.

For instance, the fraction of supercomplexes with three oxidized components (hence containing two electrons) that have one reduced P is:

$$P1(2) = \frac{2e^a}{2e^a + e^b + e^c},$$

with

$$\begin{aligned} a &= \mathbf{E}_1 + \mathbf{E}_2 + \mathbf{E}_3 \\ b &= 2\mathbf{E}_1 + \mathbf{E}_2 \\ c &= 2\mathbf{E}_1 + \mathbf{E}_3. \end{aligned} \quad (8.48)$$

Figure 8.5a shows the computed kinetics for the photo-oxidation of P (curves 1 and 2) and of the cytochromes ($c_1 + c_2$) (curves 1' and 2'). Curves 1 and 1' were computed with Eq. (8.44), neglecting the effect of antenna connectivity. This effect was taken into account for curves 2 and 2', using Eq. (8.45). The result is an acceleration of the final part of the P^+ kinetics, while the cytochrome kinetics are almost not affected. Panel b shows the square plot of the reduced fractions of P and cytochrome, illustrating the low apparent equilibrium constant. Curve 2 is the plot obtained when the antenna connectivity is implemented, showing that this causes a further lowering of the apparent equilibrium constant. The effect is relatively small, however: for simplicity it will not be considered further.

Curves 3 and 3' were computed assuming lateral equilibration over a large number of chains (diffusive model). This model was treated by writing the reduced fractions of each carriers $n_i(\mathbf{E})$ as a function of an "equilibrium" potential \mathbf{E} , as in Eqs. (8.18), (8.21). One can then obtain the function $\mathbf{E}(p)$, which gives the potential corresponding to p electrons in the system, by solving numerically the equation:

$$p - \sum n_i(\mathbf{E}) = 0. \quad (8.49)$$

The time course is then obtained by iterating the sequence:

$$\begin{aligned} \delta p &= -2In_1(\mathbf{E}(p)) \delta t \\ p &\leftarrow p + \delta p \end{aligned} \quad (8.50)$$

The first equation expresses the number of electrons taken from the system during a small time interval δt : this is proportional to $n_1(\mathbf{E})$, the

fraction of reduced P (when the effect of antenna connectivity is ignored); p is then updated in the second expression.

The low apparent equilibrium constant in the supercomplex model is due to the distribution of photons according to a Poisson process. It is thus specific of the continuous illumination mode and will not be observed when the photo-oxidation is driven by a series of single turnover flashes. The evolution of the supercomplex under a train of single turnover flashes is a simple Markovian process where, upon each flash, the oxidation number is increased by one or two units for complexes that have one or two reduced P 's. Denoting as $S(n, f)$ the fraction of supercomplexes with oxidation number n after flash number f , one has:

$$\begin{aligned} S(0, 0) &= 1 \\ S(n > 0, 0) &= 0 \\ S(n, f) &= P0(n) S(n, f-1) \\ &+ P1(n-1) S(n-1, f-1) \\ &+ P2(n) S(n-2, f-1). \end{aligned} \quad (8.51)$$

The first line expresses the initial condition of an entirely reduced supercomplex. The

second line is the recurrence relation, where $P0(n) = 1 - P1(n) - P2(n)$ is the fraction of the n -oxidized complexes with both P oxidized. Results simulated from Eq. (8.51) appear later in Fig. 8.7.

B. Distributed Stoichiometry: Crofts' Chromatophore Model

The supercomplex model is not the only possible explanation for the low equilibrium constant between P and its secondary donors during photo-oxidation under continuous illumination. Crofts et al. (1998) pointed out that this effect could also arise in a model allowing lateral equilibration through the diffusion of cytochrome c_2 , but presenting a distribution of the stoichiometric ratios between the components (as previously proposed for the PS II acceptor chain, see next section). Specifically, the idea is that the diffusion of c_2 is restricted to the chromatophore vesicles (which is obvious when dealing with isolated chromatophores; however, experiments of Joliot et al. (1989) were carried out *in vivo*, where chromatophores are invaginations open to the periplasmic space, rather than closed vesicles).

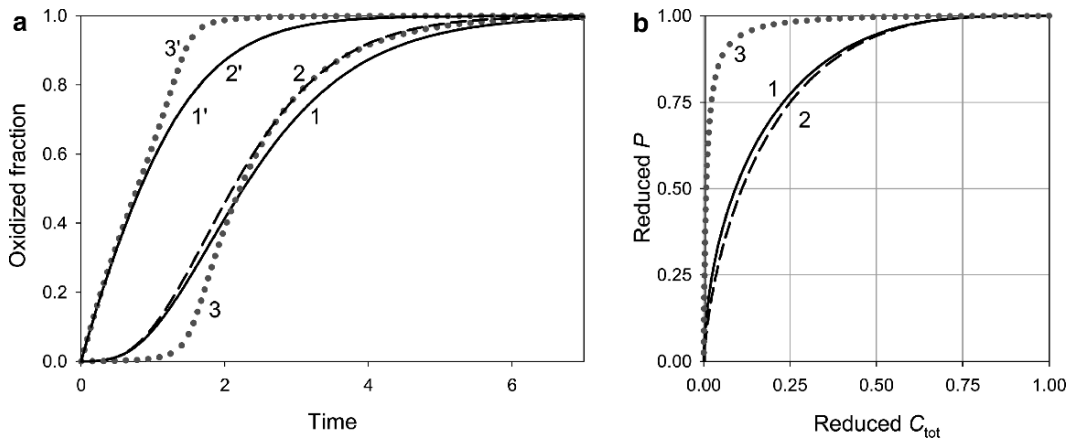


Fig. 8.5. (a) Simulated photo-oxidation kinetics in the supercomplex, showing the accumulation of P^+ (curve 1) and $C_{\text{tot}}^+ = c_1^+ + c_2^+$ (curve 1'). The midpoint potentials used here and in the two following figures were 450, 340, 270, and 300 mV for P , c_2 , c_1 and FeS, respectively. The effect of antenna connectivity was ignored when computing curves 1 and 1', but taken into account for curves 2 and 2' (the latter is superimposed on 1'), assuming $J_{\text{dim}} = 0.7$ (Eq. 8.45). The dotted curves (3 and 3') show the kinetics expected in a diffusive model, where c_2 can react with many RC and bc_1 complexes. In the kinetic equations used here and for Fig. 8.6a, the photochemical rate I was given a value of 1 (time unit) $^{-1}$. (b) The plots of P^{red} vs. $C_{\text{tot}}^{\text{red}}$ in the various cases: 1 and 2, supercomplex without or with antenna connectivity, respectively; 3, diffusive model

Due to their small size, the chromatophores contain small average number of the electron transfer components (i.e. reaction center, bc_1 complex and cytochrome c_2) and one may expect a statistical distribution of these components and thus of their relative ratios. Crofts and coworkers assumed that on average, there were 16 RCs, 8 cytochromes c_2 and 4 dimers of the bc_1 complex per chromatophore. It is now clear that the RCs are dimeric in *Rb. sphaeroides*, so that 16 RCs means 8 dimers. Now, if one assumes a Poisson distribution of these proteins, the fraction of chromatophores with p RC dimers, c cytochromes c_2 and b bc_1 dimers is:

$$F(p, c, b) = \text{Pois}(p, 8) \text{Pois}(c, 8) \text{Pois}(b, 4). \quad (8.52)$$

A problem with this modeling is that it treats the complexes as dots that can be allocated randomly to chromatophores, without any steric hindrance or interaction. Given the dense packing of protein complexes observed in chromatophores as in other bioenergetic membranes and given the size of the RC-LH1 dimeric complexes, this treatment is clearly not satisfactory. This should be kept in mind while using the Poisson distribution – for want of a more elaborate statistical description.

For chromatophores with given p , c , b numbers, the time evolution for the accumulation of oxidized species under illumination is that of a big supercomplex with $2p$ reaction centers, c cytochromes c_2 and $2b$ cytochromes c_1 and FeS. This can be computed by adapting the techniques described in the preceding section; the computation time required is much longer because of the number of configurations that must be taken into account in expressions like that in Eq. (8.47), but remains quite acceptable (≈ 30 min on a personal computer). Figure 8.6 shows the photo-oxidation kinetics computed in this manner and averaged according to Eq. (8.52). The outcome is strikingly similar to the simulation of the supercomplex model.

In the present model, there are two statistical effects contributing to the lowering of the apparent equilibrium constant. The first one is of the same nature as in the supercomplex, i.e. the Poisson distribution of “photons” (or photochemical hits) over complexes comprising small num-

bers of redox centers (so that some complexes will be fully oxidized while others are still at an earlier stage of the photo-oxidation process). This effect is not as pronounced as in the supercomplex, because we are dealing with larger numbers, but it is still significant: one may compare in this respect curves 3 and 4 in Fig. 8.6b, which illustrate the difference between the “average chromatophore” (with $p = 8$, $b = 8$ and $c = 4$) and the fully diffusive model. The discrepancy is of course more important for chromatophores that have less redox centers than the average chromatophore. The second effect is the distribution of the stoichiometric ratio R of P to its electron donors that results from the random, Poisson distribution of each component. The shape of the distribution of R is shown in the inset of panel a. The effect on the kinetics and apparent equilibrium constant can be estimated by comparing the curves for the “average” and “distributed” chromatophore (curves 3 and 2, respectively in panel b and their counterparts in panel a), which shows that the stoichiometric distribution has the largest effect with respect to the lowering of the apparent equilibrium constant.

The result of Fig. 8.6, showing very close curves for the supercomplex and distributed chromatophore models disagrees with the conclusion reported in previous work (Lavergne et al., 2008). We had claimed that the figures for the average values of p , c and b retained by Crofts and coworkers, although about twofold smaller than generally believed (Saphon et al., 1975; Crofts et al., 1983; Drews and Golecki, 1995) were still not sufficiently small to account for the actually observed low equilibrium constant and that the figures required to do so were unlikely. The discrepancy with the present results arises from two factors. First, the previous calculations assumed that the electronic distribution could be approximated by equilibrium expressions, neglecting the effect of the Poisson distribution of photons (as highlighted by comparing curves 3 and 4 in Fig. 8.6b). The second and major factor was that the RCs were treated as monomers rather than dimers (in line with Crofts’ original view, but at variance with the current knowledge). The broader stoichiometric distribution implied by allocating an average of 8 RC dimers rather than 16 RC monomers has significant consequences as regards the present issue.

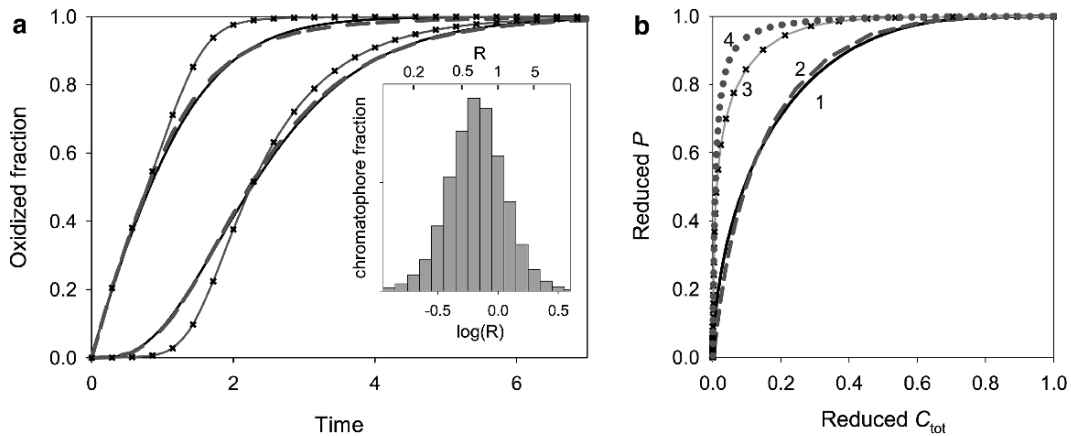


Fig. 8.6. (a) Photo-oxidation kinetics for the supercomplex model (solid black lines, same as curves 1, 1' in Fig. 8.5), for the distributed chromatophore model (thick gray dashed lines) and for the “average chromatophore” with $p = p_{av} = 8$ dimers of RC, $c = c_{av} = 8 c_2$ and $b = b_{av} = 4$ dimers of bc_1 (thin lines with \times symbol). For the averaging in the distributed model, the configurations taken into account were $1 \leq p \leq 16$, $1 \leq c \leq 10$ and $0 \leq b \leq 10$; this included 98.9% of the distribution given by Eq. (8.52). The inset shows the distribution of the ratio $R = [P]/[\text{secondary donors}] = 2p/(c + 4b)$. The histogram is plotted on a log scale (bottom); the corresponding values of R are indicated on the top scale. (b) The plot of P^{red} vs $C_{\text{tot}}^{\text{red}}$ for the supercomplex (curve 1), the distributed chromatophore (curve 2), the average chromatophore (curve 3) and the fully equilibrated (diffusive) model (curve 4, same as curve 3 in Fig. 8.5)

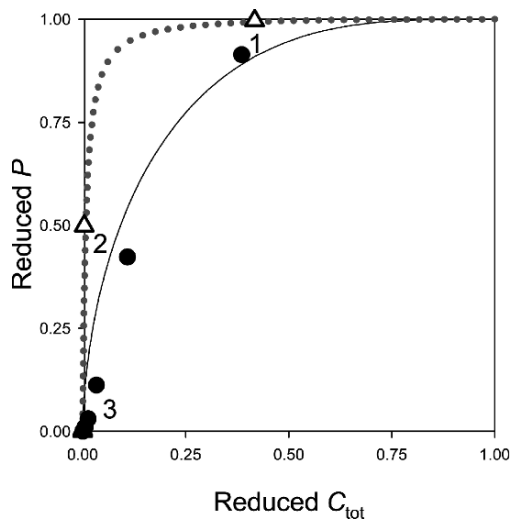


Fig. 8.7. The plot of P^{red} vs $C_{\text{tot}}^{\text{red}}$ during a series of single turnover flashes. The open triangles show the successive data points (flash numbers as indicated) predicted for the supercomplex model, using Eq. (8.51). The solid circles show the results for Crofts' chromatophore model. The solid line is the plot predicted in the supercomplex model for continuous illumination (same as curve 1 in Figs. 8.5 and 8.6). The dotted curve is the equilibrium relation (same as curve 3 in Fig. 8.5 or curve 4 in Fig. 8.6)

Interestingly, while the two models give almost identical predictions for photo-oxidation under continuous illumination, they diverge when con-

sidering flash-induced patterns. When using single turnover flashes, the effect of the Poisson distribution of photons is completely abolished, so that the supercomplex does not present a low apparent equilibrium constant any more (but rather the opposite, as noted earlier). Hence we observe the behavior shown by the open triangles in Fig. 8.7. For the distributed chromatophore model, things are quite different (circles), because the effect of the distributed stoichiometry remains as efficient as under continuous light. Thus, in principle, this experimental procedure could be used to discriminate between the two interpretations; the Joliot-Verméglio model, however, involves a 30% fraction of incomplete supercomplexes (lacking the bc_1), which complicates the interpretation of the data (see Fig. 8.6 in Joliot et al., 1989). Nevertheless, this track may be worth further efforts.

Detailed account of the current status of these models is provided in Lavergne et al. (2008) and references therein. Both models make rather bold and falsifiable predictions concerning the organization of the photosynthetic apparatus in *Rb. sphaeroides*. Since the bc_1 complex is clearly dimeric, the supercomplex hypothesis must be recast into a “super-supercomplex”, an edifice comprising four (two dimers) RC-LH1 complexes, two cytochromes c_2 and one dimer of bc_1

(Joliot et al., 2005). As opposed to this extreme order, Anthony Crofts' model requires a high dose of disorder. The suspense is maintained by the intriguing failure of imaging techniques (EM or AFM) to locate the bc_1 complex.

V. Quinone Domains

We now focus on the other side of the reaction center and discuss the behavior of the electron acceptor pool. Type 2 reaction centers reduce quinone molecules Q to the quinol form QH_2 at a specialized site of the RC, the Q_B pocket, which manages the two electron and proton transfer steps involved in the overall process. Besides the hydrophobic character of the quinone head group, the quinones found in our systems (PQ-9 in chloroplasts, mostly UQ-10 in bacteria) are equipped with an isoprenoid tail 9 or 10 units long, which prohibits any "temptation" of escaping the membrane. The quinol reoxidation is handled by the bc_1 complex that injects the two quinol protons together with two additional protons pumped from the other side of the membrane into the luminal (thylakoids) or periplasmic (bacteria) space. Thus, the Q/QH_2 couple acts as a mobile electron and proton carrying shuttle between the RC and the bc_1 (or b_6f) complex.

A. Quinone Domains in vivo

The quinones are present in stoichiometric excess with respect to reaction centers or bc_1/b_6f complexes: there are about 6 PQ per PS II in chloroplasts, or 20–25 UQ per RC in *Rb. sphaeroides*. This whole amount of quinones is readily photoreduced when the electron flow through the bc_1/b_6f is blocked, showing that the pool is not on a side path. One can then design experiments in the same spirit as those described above, monitoring the states of Q_A (the primary quinone on the RC) and of the quinone pool during a photoreduction process carried out under quasi-equilibrium conditions. The gap between the standard potentials of Q_A and of the pool quinones is ≥ 110 mV in both the oxygenic and bacterial systems, so that the "true" equilibrium constant between these carriers is about 100 or larger. A much lower apparent constant is observed experimentally (Joliot

et al., 1992; Lavergne et al., 1992; Comayras et al., 2005a, b), suggesting that, in this case also, statistical distortions are present, revealing restricted thermodynamic equilibration.

The issue of a possible restriction to quinone diffusion can be addressed independently by examining the effect of a partial inhibition of the RCs on the kinetics of photoreduction of the pool of quinones. If quinones are freely diffusing over large regions of the membrane comprising many RCs, the inhibition of a fraction f of the RCs should slow down the photoreduction process by a factor f , but it should not affect the final, total amount of the reduced quinones. Another extreme case would be a confinement of the quinones around each RC: then, the rate of the kinetics should not be affected, but the extent of reducible quinones would be decreased in proportion to f . More generally, if we define a quinone "domain size" n as the average number of RCs interacting with the same pool, one sees that the decrease in the amount of photoreducible quinones corresponds to domains where *all* RCs are inhibited, thus with a probability f^n . This experiment was carried out in thylakoids, using dichlorophenyl-dimethylurea (DCMU) as an inhibitor (Joliot et al., 1992), and in chromatophores of *Rb. sphaeroides*, using stigmatellin (Comayras et al., 2005a, b). The outcome, $n \approx 3$ –4, was strikingly similar in both the materials. The experimental analysis was more detailed in the case of chromatophores, showing that the plot of the photoreducible pool vs. f was more complex than the $(1 - f^n)$ dependence predicted by this crude model, suggesting a marked heterogeneity in the distribution of quinone domain size. Interestingly, a more homogeneous curve (together with a smaller $n \approx 1.7$) was obtained in a mutant lacking the PufX subunit, where the RC-LH1 complexes are monomeric instead of dimeric.

Returning to the issue of the low equilibrium constant between Q_A and its acceptor pool, the size of the "isolated" domains found (about 4 RCs and 4×25 UQs in chromatophores or 4×6 PQs in thylakoids, thus electron capacities of 50–200) precludes large effects arising from fluctuations of the "number of photochemical hits", as in the supercomplex model. The major effect arises from the distribution of the stoichiometric ratio (number of pool quinones per Q_A). The shape of

this distribution was experimentally determined in thylakoids (Joliot et al., 1992). In bacterial chromatophores it could not be determined as precisely because the apparent equilibrium constant is not as low as in thylakoids, in line with the three- to fourfold larger overall pool/RC ratio, leading to smaller relative fluctuations (as further discussed below).

One important issue is, of course, to understand the physical constraint that limits quinone diffusion to relatively small regions. In the work of Joliot et al. (1992) on thylakoids, the proposed interpretation was that the crowding of the membrane by proteins was above the threshold allowing percolation of the quinones. One would thus have closed quinone-containing lipidic cells, of irregular size and shape, with membrane protein borders presenting variable amounts of RC (and, for that matter, b_6f) sites. A problem with this model is that Brownian wiggling is expected to modify incessantly this pattern, eventually allowing effective long-range diffusion of the quinones (Drepper et al., 1993). This may be questioned, however, because there are interactions between the complexes, which are responsible for some large scale organization of the system, as analyzed in a series of papers by Kirchhoff et al. (2000, 2002, 2004a) and Tremmel et al. (2003). Depending on the strength of these interactions, the percolation properties of the network, i.e., the effective range for quinone diffusion, could greatly vary. Nevertheless, the results that we have obtained (Comayras et al., 2005b), when studying quinone traffic in the PufX⁻ mutant of *Rb. sphaeroides*, cast serious doubt on the possibility of sequestering the quinones within more or less random protein barriers. In this mutant, the LH1 antenna associated with the RC adopts a closed structure surrounding the center (Francia et al., 1999; Siebert et al., 2004), at variance with the wild type organization, where the RC-LH1 complexes adopt a dimeric configuration with an open, S-shaped structure of the LH1. Despite the presence of a closed LH1 “wall” around the RC, the turnover (on a sustained regime) of the quinones on the RC was only moderately slowed down as compared to the wild type (we estimated a time penalty of ~ 1 ms for crossing the LH1 barrier), as well as the diffusion time of QH₂ from the RC to the bc_1 complex. This implies that even a relatively tight structure as the $(\alpha\beta)_{16}$

oligomeric LH1 ring is far from constituting an impenetrable obstacle for quinones. This finding is in line with the fact that in many purple bacteria, the native structure of the RC-LH1 complexes is the closed ring type, implying that this does not prevent efficient enough quinone shuttling. We thus proposed an alternative explanation for quinone domains, where the proteins do not act mostly as barriers, but as attractors. In this model, the quinones would tend to form clusters around “quinone-friendly” proteins (such as the RC-LH1 and bc_1 complexes).

The distribution of the pool/RC ratio, determined in thylakoids, was found to be consistent with the percolation model, then favored by Lavergne et al. (1992). As regards the compatibility with the quinone aggregation model, described above, it should be noted that the distribution is much broader than would be predicted by a Poisson function for the association of e.g., an average of 12 quinones per dimer of RCs and even more so for an average of 24 quinones per cluster of two RC dimers. This implies that purely random association is not the final word. Additional geometric heterogeneities involved in the percolation model may be required. Another possibility is described below: a broadening of the distribution is expected if the quinone clustering is a cooperative phenomenon, which is actually a corollary of the aggregation model.

B. Purified Core Complexes RC-LH1 as Model Quinone Domains

The RC-LH1 core complexes from *Rb. sphaeroides* and other purple bacteria can be easily solubilized and purified using mild detergents. One can in this manner prepare isolated dimers (or monomers; monomers and dimers appear as separate bands on a sucrose gradient) of these complexes. These preparations retain a significant fraction of the endogenous pool, in agreement with the view that quinones tend to aggregate around these proteins. Francia et al. (2004) obtained about 10–15 quinones per RC in their preparations of dimeric core complexes from *Rb. sphaeroides*, i.e. 40–60% of the pool present in the original membrane. Our own preparations (Comayras et al., 2005a) contained somewhat less ubiquinone (~ 7

UQ/RC). This local quinone pool is readily photoreducible, and the techniques described above can be applied to this system. In particular, one can run the domain size assay, monitoring the extent of the pool that can be photoreduced as a function of the fraction of stigmatellin-inhibited RCs. Not surprisingly – but reassuringly – the domain size found for the dimeric preparation was close to 2, and close to 1 for the monomer (similar results were obtained for tests concerning the excitonic connectivity). Another type of experiment was to monitor the reduction kinetics of the acceptor pool and of Q_A during a series of flashes or under continuous illumination. The approach is quite the same as described above in the case of thylakoids or chromatophores – except that the system under test is much simpler. If the complexes had a fixed UQ/RC stoichiometry, the reduction of Q_A would not be observed until the secondary pool is almost completely reduced, because of the large equilibrium constant between Q_A and the “free” quinones. Conversely, one will observe a more progressive accumulation of Q_A^- (a low apparent equilibrium constant) if the number of quinones per complex is not fixed, but obeys some statistical distribution. The analysis of the data can thus give an insight into the distribution function for the number of quinones per complex.

For simplicity, we just treat here the case of monomers, making the justified approximation that in a given complex, Q_A remains oxidized until its acceptor pool is fully reduced. We also ignore the detailed functioning of the two electron Q_B gate. For a given duration of the illumination, t , an open RC has transferred a mean number of electrons It . The fraction of (open) RCs that have transferred n electrons is given by the Poisson distribution:

$$Pois(n, It) = (It)^n \exp(-It)/n!. \quad (8.53)$$

Denoting as q the average amount of pool quinones per complex, we assume that the fraction of complexes with m quinones is given by some distribution function $P(m, q)$. At a given time, among the complexes that have m quinones, those which have transferred (strictly) more than $2m$ electrons have Q_A^- , while those which have transferred $2m$ electrons or less still have Q_A .

Thus, the fraction of Q_A^- accumulated at time t is:

$$C(t) = \sum_{m=0}^{\infty} \left[P(m, q) \left(1 - \sum_{j=0}^{2m} Pois(j, It) \right) \right]. \quad (8.54)$$

The amount of photo-electrons injected into the system (pool + Q_A) during the time interval dt is the product of Idt by the amount of oxidized Q_A , i.e. $(1 - C)$. The fraction of reduced pool at time t is then:

$$N(t) = \frac{I \int_0^t [1 - C(x)] dx - C(t)}{2q}. \quad (8.55)$$

Figure 8.8 shows a square plot from data recorded during the photoreduction kinetics of monomeric core complexes from *Rb. sphaeroides* with $q = 7$. The dotted line is the simulation obtained with Eqs. (8.54) and (8.55), taking for $P(m, q)$ a Poisson distribution. Although the simulated curve is not far from the data, it presents a systematic deviation, which was found in a number of experiments. The deviation (smaller

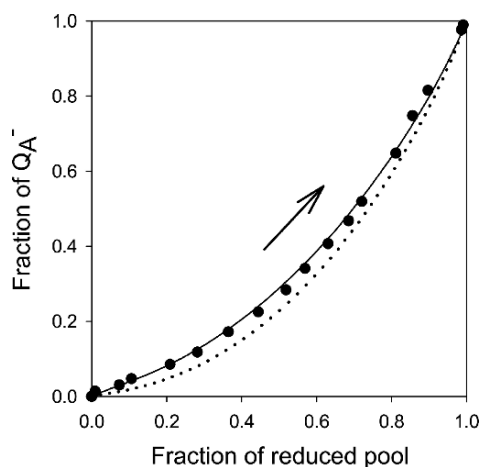


Fig. 8.8. A plot of the fraction of reduced primary acceptor Q_A^- as a function of reduced UQ pool in monomeric RC-LH1 core complexes from *Rb. sphaeroides*. This was obtained during continuous illumination (the arrow indicates the direction of the time evolution). The dotted line is the plot predicted using Eqs. (8.54) and (8.55), using for the distribution $P(m, q)$ of the number of quinones per complex a Poisson distribution with the experimentally determined average value $q = 7$. The solid line is the plot predicted with a broader (cooperative) distribution, as described in the text (Redrawn from Comayras et al., 2005a)

apparent equilibrium constant) suggests that the distribution is broader than predicted by the purely random Poisson distribution. In physico-chemical terms, this is indicative of a cooperative binding of quinones to the core complexes (conversely, anti-cooperativity, like that observed for the length of queues in supermarkets, tends to make distributions narrower). One can introduce cooperativity in a Poisson-like distribution by decreasing the number of independent objects to be distributed, as would be the case if quinones did not bind individually, but as lumps of $k > 1$ molecules (“ k -mers”); k has a meaning close to that of the Hill number in enzymology. The solid line in Fig. 8.8 is a simulation obtained in this manner, with $k = 1.5$. This suggests that quinones tend to cluster together, in line with the interpretation proposed above for quinone domains in photosynthetic membranes.

VI. Statistical and Non Statistical Heterogeneities

In the foregoing, I have discussed different phenomena that have all tended to lower the apparent equilibrium constant. A multi-center electron carrier chain, with a fixed arrangement of its components, will present statistical fluctuations in the number of electrons present on the complex. This occurs when the system is progressively filled with reducing or oxidizing equivalents as the result of illumination. But it also occurs under steady-state conditions and the nature of the source (photochemical or purely chemical) is unimportant in this respect. A quite different case is that of a distribution of the stoichiometric ratio between mobile components. This applies to quinone domains, where the pool/RC ratio appears broadly distributed around its mean value, in thylakoids, bacteria, or, more trivially, in isolated core complexes. The proposed interpretation is again statistical: the quinone domains probably do not arise from a well-defined, fixed arrangement, but from some flexible organization pattern. Then, statistical fluctuations are expected that are believed to be the origin of the stoichiometry distribution. In the case of Anthony Crofts’ “small chromatophore” model, or for the acceptor pool in isolated core complexes, the two types of fluctuations contribute to the lowering of the apparent equilibrium constant.

The precise shape of the statistical distributions involved in these different cases depends on the specific models. But generally, the rule of thumb holds: if the statistics concerns N objects, the relative order of magnitude of the fluctuation will be $\sim 1/\sqrt{N}$. In the supercomplex model, the electron capacity of the donor chain (P , P , c_2 , c_1 , FeS) is $N = 5$, so that $1/\sqrt{5} = 0.45$. Indeed, when the system contains a mean value of 5 oxidized equivalents, which in a big equilibrated system would imply $\approx 100\%$ of P oxidized, one has in fact only about 64% of P^+ . In bacterial core complexes with seven pool quinones, the relative size for the fluctuations of the quinone number (affecting the stoichiometric distribution effect) is $1/\sqrt{7} = 0.38$, while the electron capacity is 15 ($1 + 2 \times 7$), predicting a relative width of about $1/\sqrt{15} = 0.26$ for the distribution of the number of electrons under continuous light; accordingly, both effects are significant, but the stoichiometric effect predominates. In thylakoids, with a domain size including a mean of three to four centers and about 20 quinones, the stoichiometric fluctuations are significant (as discussed above, they are actually broader than predicted by our “rule of thumb”), but those affecting the number of electrons can be neglected.

The above reasoning suggests that when an anomalously low equilibrium constant is observed, this should be indicative of some kind of confinement isolating a relatively small number of objects. This is not necessarily true, however: one may encounter heterogeneities that are not due to fluctuations and concern large numbers. This is likely to be the case in thylakoids, whose complex architecture (Mustardy, 1996; Albertsson, 2001) generates large membrane regions with specific membrane protein contents. This observation was a central element in the interpretations put forward by Kirchhoff et al. (2004b) and by Joliot and Joliot (2005) for explaining the low apparent equilibrium constants found under various circumstances on the donor side of PS I. Photosystem I is excluded from the appressed membrane regions in the grana stacks. Thus, it is found in the stroma lamellae (largely devoid of PS II), in the margin regions (i.e. the edges of the grana stacks) and in the end membranes capping the grana (Albertsson, 1995, 2001). This predicts three regions with different PS II/PS

I ratios: an excess of PS II should be found in core grana stacks, where PS I is only present in the margins; in the external discs (with an end membrane and an appressed membrane), one expects a moderate excess of PS I; in the stroma lamellae, there is a large excess of PS I. The b_6f complex and plastocyanin (PC, a small soluble protein sequestered in the lumen) are probably roughly evenly distributed.

Kirchhoff et al. (2004b) studied the reduction of cyt f , PC and P_{700} immediately after switching off a strong illumination, using thylakoids or leaves. The rate-limiting step during the illumination is the quinol oxidation by the b_6f , so that the downstream carriers are oxidized while the quinone pool is reduced. When the illumination stops, electrons from the PQ pool keep flowing into the PS I donor chain and accumulate there. Due to the large equilibrium constant (≥ 100 ; but only ≈ 10 for PC bound to PS I), the reduction of P_{700}^+ should precede markedly that of PC^+ and cyt f^+ . The experimental results show much more overlap between these events than expected in this manner, i.e. the apparent equilibrium constant is much smaller than the thermodynamic constant. When using destacked thylakoids the apparent equilibrium constant was closer to the thermodynamic one. A low equilibrium constant between P_{700} and PC was also found in the experiments of Joliot and Joliot (2005), who studied the oxidation of this chain in leaves, upon a weak 720 nm beam exciting essentially PS I.

Kirchhoff et al. (2004b) interpreted their result as arising from a kinetic heterogeneity due to different times required for PC diffusion between the b_6f complex and P_{700} . This process would be fast for the PS I located in the grana end membranes, but slow for PS I located in the stroma lamellae and grana margin. A difficulty in this interpretation is that it implies that P_{700}^+ reduction is rate-limited, at least partly, by the diffusion of PC and not or not only by the b_6f reactions. But if such were the case, one should not be able to fully oxidize PC and cyt f during the light pulse. The interpretation proposed by Joliot and Joliot (2005) assumes that PC diffusion is locally rapid within the grana discs and that there is no efficient long-range PC diffusion (e.g. the “frets” inter-connecting the lumen from different grana discs and from lamellae do not allow the passage of PC). This is consistent with Albertsson’s

view that there is no long-range diffusion between grana and stroma lamellae of the mobile carriers, PQ and PC. In this model, the $\sim 30\%$ P_{700} present in stroma lamellae would be essentially devoted to cyclic transfer. One has then three types of lumenal compartments (core grana disc, end disc, stroma lamellae), where the PC/ P_{700} stoichiometric ratio may be different. Redox equilibration is achieved in each of these compartments, but the stoichiometric distribution causes a spread of the photo-oxidation (or reduction) kinetics that can account for the low apparent equilibrium constant.

As pointed out by Joliot and Joliot (2005), this functional compartmentation, implying a distribution of the stoichiometric PS II/PS I ratio, could well be the origin for the overall low apparent equilibrium constant between Q_A (PS II) and P_{700} (PS I) (Joliot et al., 1968). Under steady-state weak illumination, one observes a coexistence of oxidized P_{700} and reduced Q_A , which is easily understood if this represents mixed contributions from compartments with an excess of either PS II or PS I.

A possible difficulty with the experiments based on kinetics under continuous illumination (photo-reduction or photo-oxidation transients) is that a low apparent equilibrium constant may arise from antenna or illumination heterogeneity, resulting in a mixture of slow and fast transients and this may be misinterpreted in terms of electron transfer compartmentation. Cross-checks using single turnover flashes or subjecting the system to steady-state flux may then help sort things out.

VII. Pool Function Test at Steady State

The techniques based on kinetic transients are popular among photosynthesists, using dark-light transitions or flashes. Such approaches are more difficult when studying mitochondrial respiration and most investigations are carried under steady-state conditions. The issue of the pool function of ubiquinone or cytochrome c in the respiratory chain has been under focus for long, with new developments. The tests are based on the effect on the rate of electron flow of a partial inhibition of one or the other respiratory complex. This book is not about mitochondria *in silico*, but the scientific

concerns are very much the same and it is worth taking a glance. A semantic clarification may be useful. The term “pool” may have a stoichiometric meaning (implying that several quinones interact with the electron transfer complexes) or it may have a structural meaning (quinones diffuse all over and can interact with many partners). The view developed above was that in photosynthetic chains, the quinones constitute clearly a pool in the stoichiometric sense (they are in excess with respect to the protein complexes and this whole pool can be readily reduced by the RC or oxidized by the bc_1/b_6f complex); on the other hand, we argued that quinones were not freely diffusing, but were confined to domains including a small number of RCs (e.g. 3–4) and bc_1/b_6f complexes. It has often been assumed in the mitochondrial literature that the two meanings could be lumped together, implying that if two protein complexes (e.g. a quinone reductase such as complex I and the bc_1) were associated as a supercomplex forming a functional unit, this implied that one specialized sequestered quinone was shuttling between its partners, leaving most of the pool as a passive reserve (Lenaz, 2001). But in the model proposed by Comayras et al. (2005a, b), the quinones are confined within a coating around protein clusters (e.g. a super-supercomplex including 2 RC-LH1 dimers and a dimer of bc_1). Local mobility within a domain does not necessarily mean unrestricted diffusion.

Kröger and Klingenberg (1973a, b) developed an experimental and theoretical investigation, measuring the steady-state electron flow J in submitochondrial particles while inhibiting a variable fraction f of the bc_1 complex. The expected relation is linear in the case of separate chains (with a qualification discussed below) and hyperbolic insofar as several bc_1 complexes share a common pool. The “pool equation” derived by Kröger and Klingenberg (1973a, b) for the case of an “infinite” quinone domain size is constrained by a single parameter, the ratio $\rho = V_r/V_o$ of the maximum rates for the pool reduction and oxidation, obtained with a fully oxidized or reduced pool, respectively:

$$v(f) = \frac{1 + \rho}{1 + \rho/(1 - f)}. \quad (8.56)$$

In this expression, $v(f)$ is the electron flux normalized to its value at $f = 0$. This expression is derived by assuming that the pool reduction level depends linearly on the electron input and output rates (with coefficients of opposite signs), which was experimentally verified by Kröger and Klingenberg (1973a, b).

To discuss the significance of this equation in the context of quinone domains, one may first notice that for a model comprising several bc_1 complexes immersed in a quinone patch, Eq. (8.56) remains “locally” valid. For example, if there are two complexes (one dimer) the throughput of domains where (only) one complex is blocked is obtained from Eq. (8.56) with $f = 0.5$. The average behavior is a sum on Eq. (8.56) weighted by the fractions of domains with 0, 1, 2, inhibited complexes. The hyperbolicity of the $v(f)$ curve thus obtained increases with the number of complexes per domain and a quantitative agreement with Eq. (8.56) is in support of a large or infinite domain size. The qualification mentioned above concerns the inhibitor turnover. Considering the case of a domain with one complex, one may imagine two extreme behaviors depending on the dwell time of the inhibitor. If the dwell time is long, one observes a mixture of permanently blocked and active domains, yielding a linear $v(f)$. Conversely, if the dwell time is brief, each complex is inhibited for a fraction f of the time and one has a hyperbolic dependence verifying Eq. (8.56). The critical time to decide which case applies is the duration required to fill the pool with electrons. For instance, if the input rate is 20 electrons per second for a pool of ten quinones, the filling time is 1 s. The dwell time is the reciprocal of the inhibitor’s $k_{\text{off}} = k_{\text{on}} K_d$. Thus, for instance, one has a dwell time of 1 s for an inhibitor with a dissociation constant of 100 nM and binding rate constant $k_{\text{on}} = 10^7 \text{ M}^{-1} \text{ s}^{-1}$ (thus about two orders of magnitude slower than diffusion limitation). The message here is that due attention should be paid to the inhibitor turnover rate for an unambiguous interpretation of such experiments.

The experimental results of Kröger and Klingenberg (1973a, b), using submitochondrial particles with inhibition by antimycin, were in good quantitative agreement with Eq. (8.56) supporting (with the qualification expressed above)

a large delocalization of the quinones under their conditions. More recently, Boumans et al. (1998) reported antimycin titrations of the respiration rate in yeast mitochondria. A fast (NADH) or slow (succinate) quinone reducing substrate was used in order to test the “pool function” of either cytochrome *c* or UQ, respectively. In both cases, the observed dependence was either linear or hyperbolic, depending on the medium used. Boumans et al. (1998) concluded that under physiological conditions, the whole yeast respiratory chain behaves as a single functional unit. In mammalian mitochondria, another study (Bianchi et al., 2004) concluded that complexes I and III (*bc*₁) were functionally associated as autonomous supercomplexes, while lateral diffusion was involved for quinone between complexes II and III and for cytochrome *c* between complexes III and IV (cytochrome *c* oxidase). Considering these results and similar indications for photosynthetic membranes, it appears likely that supercomplex associations are labile, depending on preparation types, medium, membrane shape; one may then speculate that this lability could facilitate regulatory rearrangements.

VIII. Kinetic Analysis: Playing with Inhibitors, Redox Potential and Flash Intensity

A simple way, in principle, to decide whether a mobile carrier has access to a large or small number of partners is to examine what happens with regards to the time course and amplitude of the kinetics when the stoichiometric ratio of both reactants is varied. The technique described above for estimating the quinone domain size (average number of RCs sharing a common pool) is an example where the relative amount of RCs was varied by using subsaturating concentrations of Q_B pocket inhibitors. Some other examples are described below.

Prince et al. (1978) analyzed the case of cytochrome *c*₂ in chromatophores of *Rb. sphaeroides*. One experiment was designed to test the interaction between the RC and the cytochrome, using chromatophores where the cytochrome *c*₂ content was particularly low. A light flash of variable intensity was fired, forming

P⁺ in a fraction of the RCs and the amount of oxidized *c*₂ (actually *c*₂ + *c*₁, see below) formed by reducing *P*⁺ was measured. In a model where *c*₂ diffuses rapidly, one expects that all the *c*₂ will be oxidized in a few milliseconds, as long as the amount of *P*⁺ formed by the flash exceeds the amount of *c*₂ (the E_m difference between *P* and *c*₂ is about 110 mV, hence an equilibrium constant of ~70; furthermore, the dwell time of the cytochrome on the RC is known to be a few hundreds microseconds). At variance with this prediction, the amount of oxidized cytochrome decreased linearly with the amount of *P*⁺ formed initially. This suggests an association between the cytochrome and the RC so that the cytochromes associated with RCs that were not hit by the flash remained reduced even though some *P*⁺ was present on RCs devoid of cytochrome. In the same work, the kinetics of cytochrome reduction were also studied, again varying the initial amount of oxidized cytochrome by attenuating the flash and varying the amount of the reducing partner by changing the redox poise. In contrast with the solid-state type response obtained in the first experiment, this test was consistent with a second order reaction between diffusing partners. The functioning of the *bc*₁ complex was not understood at that time and cytochrome *c*₁ had not been identified so that cytochromes *c*₂ and *c*₁ were lumped together. Thus, the data would need to be reinterpreted in the light of present knowledge (in particular, one must take into account that depending on the conditions, one or several turnovers of the *bc*₁ can be required for completing the cytochrome reduction). One aspect which is clearly evidenced by these experiments (and others: Crofts et al., 1977, 1983) is that the reduction rate depends almost linearly on the amount of reduced quinones, showing that the *bc*₁ complex reacts with a pool of many quinones rather than with a single partner – but this does not imply that this pool is shared by many *bc*₁ complexes.

A similar question was investigated by Drachev et al. (1989), who studied the reduction kinetics of the high potential *b* heme (*b*_H) of the *bc*₁, either through photovoltage or absorption change measurements. The experiments were done at an ambient potential ≈300 mV, with an oxidized quinone pool, so that the *bc*₁ reactions are triggered (and kinetically limited) by the capture of the quinol released by the RC

(this occurs on the second flash given to a dark adapted sample, because of the two-electron gate mechanism). Antimycin A was added in order to block the reduction of quinone by reduced b_H at the Q_i site: in this manner one is assured of dealing with the first turnover of the complex. Drachev et al. (1989) found that the reaction rate was independent of the amount of quinol formed (varying the flash intensity) and also (using the inhibitor myxothiazol) of the amount of active bc_1 complexes. This pattern was thus indicative of a first order, “monomolecular” process. The authors’ interpretation was that quinone exchange between the RC and bc_1 complex occurs via a local quinone pool, thus a model similar to that proposed later by Comayras et al. (2005a, b). It should be mentioned, however, that the kinetic discrimination between first and second order processes is not as marked as was assumed by Drachev et al. (1989). As pointed out by Prince et al. (1978) the half-time of a second order reaction shows a maximum when the ratio of the two reactants is unity. This is illustrated in Fig. 8.9, also showing the hyperbolic

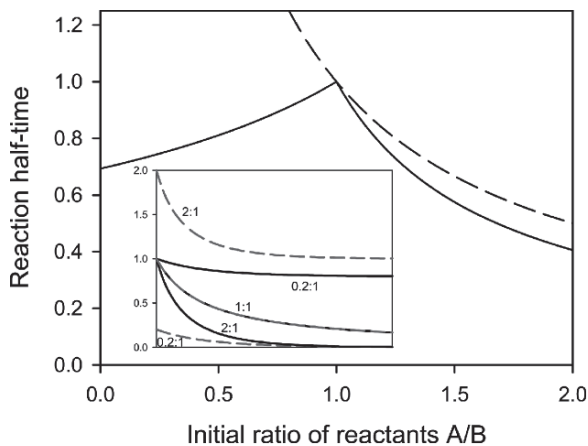


Fig. 8.9. A plot of the half-time of a second-order reaction as a fraction of the initial ratio (A/B) of the two reactants. Expressions for the half-time are $\frac{1}{k(A-B)} \ln\left(\frac{2A-B}{A}\right)$ when $A > B$ and $\frac{1}{k(A-B)} \ln\left(\frac{B}{2B-A}\right)$ when $A < B$ (see Prince et al., 1978). A value of 1 (time unit \times concentration unit) $^{-1}$ was assumed for the bimolecular rate constant k . The dashed line is the hyperbolic dependence assumed by Drachev et al. (1989). The inset shows examples of kinetics assuming initially $B = 1$ (the traces for this species are the solid black lines) and $A = 0.2, 1, 2$ as indicated (the traces for this species are the dashed gray lines)

dependence (incorrectly) expected by Drachev et al. (1989). Nevertheless, the point made by the authors, i.e. that the observed kinetics are more consistent with a first rather than second order process, remains valid.

The study of Joliot et al. (1996) on chromatophores of *Rb. sphaeroides* also made use of the electrogenic phase (“phase III”, measured from the carotenoid electrochromic shift) taking place in the bc_1 complex, but the ambient potential was more reducing, implying the presence of a reduced quinone pool. The mobile carrier under test in these experiments is cytochrome c_2 . Another difference with the experiments of Drachev et al. (1989) was the absence of antimycin, so that phase III (after appropriate correction of the distortion due to the decay of the membrane potential) reflects the integral of the multi-turnover electron transfer passing through the low potential chain of the bc_1 complex. When decreasing the amount of active complexes by using myxothiazol, Joliot et al. (1996) found that the amplitude of the change decreased, at variance with a diffusion model where the amplitude would remain constant, with slower kinetics. The relation between the overall amplitude measured at 100 ms and the fraction of inhibited complexes was consistent with a model of the domain type, with a domain including about two bc_1 complexes. However, in these partially inhibited chromatophores, the time course of phase III was in fact multiphasic. The fast component, completed at 10 ms, presented a “first order” behavior (unchanged kinetics and amplitude directly proportional to the amount of active bc_1). Thus, Joliot et al. (2005) proposed a model involving a dimer of bc_1 complexes, two dimers of RCs and two cytochromes c_2 : a dimer of their previous supercomplex model. Over a rapid time scale (≤ 10 ms) each cytochrome c_2 reacts with a definite bc_1 partner, but on a longer time scale it may interact with both members of the dimer.

The conclusions of Joliot et al. (1996) disagree with a previous study by Fernandez-Velasco et al. (1991) who studied the reduction kinetics of cytochromes $c_2 + c_1$ in chromatophores where the bc_1 complex was partially inhibited by stigmatellin (an inhibitor blocking electron transfer between the FeS center and c_1 ; notice that stigmatellin is also an inhibitor of the Q_B pocket on the RC). The

results were consistent with a diffusion domain for cytochrome c_2 with a size approaching that of the chromatophore. The reason for the discrepancy between the two research groups is still unclear.

IX. Concluding Remarks

When investigating the function of photosynthetic material, cells or membranes, we generally obtain an average response over Avogadro size numbers of systems and we often ignore the disturbing thought that heterogeneities may be present and affect the responses to a large extent so as to make the “average” view rather inaccurate. The scope is evolving, however, with the development of techniques which focus on mesoscopic scale information (EM and AFM) or even on individual objects (AFM and single molecule spectroscopies). On the other hand, properly devised functional approaches using classical techniques can also, in certain cases, detect and characterize such heterogeneities, thus getting beyond coarse-grained global averages. One may then obtain richer information that can reveal unsuspected molecular interactions or structural organization. Photosynthesis researchers are fortunate because the photochemical triggering of the electron transfer reactions offers particular opportunities for such approaches. While the term “heterogeneity” is rather vague, it may be useful to consider the antonym – homogeneity. A homogeneous system is what one gets after some mechanical or chemical treatment that destroys particular structures, solubilizes all reactants so that random collisional interactions occur with the same probability everywhere. In such a system, it makes no difference whether electrons for example, are introduced by using single turnover flashes or continuous illumination. As shown in this chapter, the association of redox centers forming an electron transfer complex has already markedly departed from the homogeneous paradigm. In this case, it does make a difference to bring in electrons with flashes or continuous light; and the steady-state behavior of the system is quite different from that of homogeneous reactants. Departure from homogeneity is relatively easy to detect through thermodynamic and kinetic effects. The problem is that very dif-

ferent organizations can have similar effects and multiple tests are generally necessary to obtain a less ambiguous picture. As illustrated above, the “low apparent equilibrium constant” appearance is a good diagnostic for non-homogeneity, but it does not suffice to distinguish between a “crystalline”, ordered arrangement (e.g. the supercomplex model), a distributed stoichiometry due to small size confinement (as proposed in Anthony Crofts’ chromatophore model, or for quinone domains), or large scale stoichiometric heterogeneity (as probably occurs in thylakoids). Tests based on comparing the effects of continuous light and single turnover flashes can in principle distinguish between ordered systems and distributed stoichiometry – but in the latter case, they do not tell whether the distributed stoichiometry occurs on a small scale (suggesting a statistical origin) or large scale (suggesting structural heterogeneity). In turn, this issue can be addressed by experiments based on partial inhibition. Eventually, progress in this field will depend on a “dialog” between functional and structural techniques. Much is to be done in this respect. For instance, with slight caricaturing, structural information alone would have tended to predict that quinones cannot pass the LH1 ring around RCs in *Blastochloris viridis* or *Rhodospirillum rubrum*; and structural data still fail to locate the bc_1 complexes that seem to mischievously flee away from the AFM tips.

Acknowledgments

My interest for the topics discussed in this chapter originates largely from ideas put forward by Pierre Joliot. I am glad to express my gratitude for many years of a highly stimulating interaction.

References

- Albertsson P-Å (1995) The structure and function of the chloroplast photosynthetic membrane – a model for the domain organization. *Photosynth Res* 46: 141–149
- Albertsson P-Å (2001) A quantitative model of the domain structure of the photosynthetic membrane. *Trends Plant Sci* 6: 349–354
- Alric J, Lavergne J, Rappaport F, Verméglio A, Matsuura K, Shimada K and Nagashima KVP (2006) Kinetic performance and energy profile in a roller coaster electron

- transfer chain: a study of modified tetraheme-reaction center constructs. *J Am Chem Soc* 128: 4136–4145
- Bahatyrova S, Frese RN, Siebert CA, Olsen JD, Van Der Werf KO, Van Grondelle R, Niederman RA, Bullough PA, Otto C and Hunter CN (2004) The native architecture of a photosynthetic membrane. *Nature* 430: 1058–1062
- Bianchi C, Genova ML, Parenti CG and Lenaz G (2004) The mitochondrial respiratory chain is partially organized in a supercomplex assembly: kinetic evidence using flux control analysis. *J Biol Chem* 279: 36562–36569
- Boumans H, Grivell LA and Berden JA (1998) The respiratory chain in yeast behaves as a single functional unit. *J Biol Chem* 273: 4872–4877
- Comayras F, Jungas C and Lavergne J (2005a) Functional consequences of the organization of the photosynthetic apparatus in *Rhodobacter sphaeroides*. I. Quinone domains and excitation transfer in chromatophores and reaction center antenna complexes. *J Biol Chem* 280: 11203–11213
- Comayras F, Jungas C and Lavergne J (2005b) Functional consequences of the organization of the photosynthetic apparatus in *Rhodobacter sphaeroides*: II. A study of PufX[−] membranes. *J Biol Chem* 280: 11214–11223
- Cornish-Bowden A (2004) *Fundamentals of Enzyme Kinetics*. Portland Press, London
- Crofts AR and Wraight CA (1983) The electrochemical domain of photosynthesis. *Biochim Biophys Acta* 726: 149–185
- Crofts AR, Crowther D, Bowyer J and Tierney GV (1977) Electron transport through the antimycin sensitive site in *Rhodospseudomonas capsulata*. In: Van Dam K and Van Gelder BF (eds) *Structure and Function of Energy Transducing Membranes*, pp. 133–155. Elsevier, Amsterdam
- Crofts AR, Meinhardt SW, Jones KR and Snozzi M (1983) The role of the quinone pool in the cyclic electron-transfer chain of *Rhodospseudomonas sphaeroides*. A modified Q-cycle mechanism. *Biochim Biophys Acta* 723: 202–218
- Crofts AR, Guergova-Kuras M and Hong S (1998) Chromatophore heterogeneity explains phenomena seen in *Rhodobacter sphaeroides* previously attributed to supercomplexes. *Photosynth Res* 55: 357–362
- Drachev LA, Mamedov MD, Mulikidjanian AY, Semenov AY, Shinkarev VP and Verkhovsky MI (1989) Transfer of ubiquinol from the reaction center to the bc₁ complex in *Rhodobacter sphaeroides* chromatophores under oxidizing conditions. *FEBS Lett* 245: 43–46
- Drepper F, Carlberg I, Andersson B and Haehnel W (1993) Lateral diffusion of an integral membrane protein: Monte Carlo analysis of the migration of phosphorylated light-harvesting complex II in the thylakoid membrane. *Biochemistry* 32: 11915–11922
- Drews G and Golecki JR (1995) Structure, molecular organization, and biosynthesis of membranes of purple bacteria. In: Blankenship RE, Madigan MT and Bauer CE (eds) *Anoxygenic Photosynthetic Bacteria*, pp 231–257. Kluwer, Dordrecht
- Duysens LNM (1959) The path of light in photosynthesis. In: *The Photosynthetic Apparatus: Its Structure and Function*. Brookhaven Symposia in Biology, Vol 11, pp 10–25. Brookhaven National Laboratory, Upton, NY
- Fernandez-Velasco J and Crofts AR (1991) Complexes or super complexes: inhibitor titrations show that electron transfer in chromatophores from *Rhodobacter sphaeroides* involves a dimeric UQH₂: cytochrome c₂ oxidoreductase, and is delocalized. *Biochem Soc Trans* 19: 588–593
- Francia F, Wang J, Venturoli G, Melandri BA, Barz WP and Oesterhelt D (1999) The reaction center-LHI antenna complex of *Rhodobacter sphaeroides* contains one PufX molecule which is involved in dimerization of this complex. *Biochemistry* 38: 6834–6845
- Francia F, Dezi M, Rebecchi A, Mallardi A, Palazzo G, Melandri BA and Venturoli G (2004) Light-harvesting complex 1 stabilizes P⁺Q_B[−] charge separation in reaction centers of *Rhodobacter sphaeroides*. *Biochemistry* 43: 14199–14210
- Gibasiewicz K, Dobek A, Breton J and Leibl W (2001) Modulation of primary radical pair kinetics and energetics in photosystem II by the redox state of the quinone electron acceptor Q_A. *Biophys J* 80: 1617–1630
- Hackenbrock CR, Chazotte B and Gupte SS (1986) The random collision model and a critical assessment of diffusion and collision in mitochondrial electron transport. *J Bioenerg Biomembr* 18: 331–368
- Hill TL (1989) *Free Energy Transduction and Biochemical Cycle Kinetics*. Dover, Mineola, NY
- Joliot P and Joliot A (2005) Quantification of cyclic and linear flows in plants. *Proc Natl Acad Sci USA* 102: 4913–4918
- Joliot P, Joliot A and Kok B (1968) Analysis of the interactions between the two photosystems in isolated chloroplasts. *Biochim Biophys Acta* 153: 635–652
- Joliot P, Verméglio A and Joliot A (1989) Evidence for supercomplexes between reaction centers, cytochrome c₂ and cytochrome bc₁ complex in *Rhodobacter sphaeroides* whole cells. *Biochim Biophys Acta* 975: 336–345
- Joliot P, Lavergne J and Béal D (1992) Plastoquinone compartmentation in chloroplasts. 1. Evidence for domains with different rates of photo-reduction. *Biochim Biophys Acta* 1101: 1–12
- Joliot P, Verméglio A and Joliot A (1996) Supramolecular organization of the photosynthetic chain in chromatophores and cells of *Rhodobacter sphaeroides*. *Photosynth Res* 48: 291–299
- Joliot P, Joliot A and Verméglio A (2005) Fast oxidation of the primary electron acceptor under anaerobic conditions requires the organization of the photosynthetic chain of *Rhodobacter sphaeroides* in supercomplexes. *Biochim Biophys Acta* 1706: 204–214

- Jungas C, Ranck JL, Rigaud JL, Joliot P and Verméglio A (1999) Supramolecular organization of the photosynthetic apparatus of *Rhodobacter sphaeroides*. *EMBO J* 18: 534–542
- King EL and Altman C (1956) A schematic method of deriving the rate laws for enzyme-catalyzed reactions. *J Phys Chem* 60: 1375–1378
- Kirchhoff H, Horstmann S and Weis E (2000) Control of the photosynthetic electron transport by PQ diffusion microdomains in thylakoids of higher plants. *Biochim Biophys Acta* 1459: 148–168
- Kirchhoff H, Mukherjee U and Galla HJ (2002) Molecular architecture of the thylakoid membrane: lipid diffusion space for plastoquinone. *Biochemistry* 41: 4872–4882
- Kirchhoff H, Tremmel I, Haase W and Kubitschek U (2004a) Supramolecular photosystem II organization in grana thylakoid membranes: evidence for a structured arrangement. *Biochemistry* 43: 9204–9213
- Kirchhoff H, Schöttler MA, Maurer J and Weis E (2004b) Plastocyanin redox kinetics in spinach chloroplasts: evidence for disequilibrium in the high potential chain. *Biochim Biophys Acta* 1659: 63–72
- Kröger A and Klingenberg M (1973a) The kinetics of the redox reactions of ubiquinone related to electron-transport activity in the respiratory chain. *Eur J Biochem* 34: 358–368
- Kröger A and Klingenberg M (1973b) Further evidence for the pool function of ubiquinone as derived from the inhibition of the electron transport by antimycin. *Eur J Biochem* 39: 313–323
- Lavergne J (2006) Commentary on: “photosynthesis and negative entropy production” by Jennings and coworkers. *Biochim Biophys Acta* 1757: 1453–1459
- Lavergne J and Joliot P (1991) Restricted diffusion in photosynthetic membranes. *Trends Biochem Sci* 16: 129–134
- Lavergne J and Joliot P (1996) Dissipation in bioenergetic electron transport chains. *Photosynth Res* 48: 127–138
- Lavergne J and Trissl H-W (1995) Theory of fluorescence induction in Photosystem II: derivation of analytical expressions in a model including exciton-radical pair equilibrium and restricted energy transfer between photosynthetic units. *Biophys J* 68: 2474–2492
- Lavergne J, Joliot P and Verméglio A (1989) Partial equilibration of photosynthetic electron carriers under weak illumination: a theoretical and experimental study. *Biochim Biophys Acta* 975: 346–354
- Lavergne J, Bouchaud JP and Joliot P (1992) Plastoquinone compartmentation in chloroplasts. 2. Theoretical aspects. *Biochim Biophys Acta* 1101: 13–22
- Lavergne J, Verméglio A and Joliot P (2008) Functional coupling between reaction centers and cytochrome *bc*₁ complexes. In: Hunter CN, Daldal F, Thurnauer MC and Beatty JT (eds) *The Purple Phototrophic Bacteria*, pp 509–536. Springer, Dordrecht
- Lenaz G (2001) A critical appraisal of the mitochondrial coenzyme Q pool. *FEBS Lett* 509: 151–155
- Mustardy L (1996) Development of thylakoid membrane stacking. In: Ort DR and Yocum CF (eds) *Oxygenic Photosynthesis: The Light Reactions*, pp 59–68. Kluwer, Dordrecht, The Netherlands
- Nitschke W and Dracheva SM (1995) Reaction centers associated cytochromes. In: Blankenship RE, Madigan MT and Bauer CE (eds) *Anoxygenic Photosynthetic Bacteria*, pp 775–805. Kluwer, Dordrecht, The Netherlands
- Polm M and Brettel K (1998) Secondary pair charge recombination in photosystem I under strongly reducing conditions: temperature dependence and suggested mechanism. *Biophys J* 74: 3173–3181
- Prince RC, Bashford LC, Takamiya K, Van den Berg WH and Dutton PL (1978) Second order kinetics of the reduction of cytochrome *c*₂ by the ubiquinone cytochrome *b-c*₂ oxidoreductase of *Rhodopseudomonas sphaeroides*. *J Biol Chem* 253: 4137–4142
- Rappaport F, Guergova-Kuras M, Nixon PJ, Diner BA and Lavergne J (2002) Kinetics and pathways of charge recombination in photosystem II. *Biochemistry* 41: 8518–8527
- Rich PR (1984) Electron and proton transfers through quinones and cytochrome *bc* complexes. *Biochim Biophys Acta* 768: 53–79
- Saphon S, Jackson JB, Lerbs V and Witt HT (1975) The functional unit of electrical events and phosphorylation in chromatophores from *Rhodopseudomonas sphaeroides*. *Biochim Biophys Acta* 408: 58–66
- Siebert CA, Qian P, Fotiadis D, Engel A, Hunter CN and Boulough PA (2004) Molecular architecture of photosynthetic membranes in *Rhodobacter sphaeroides*: the role of PufX. *EMBO J* 23: 690–700
- Tremmel IG, Kirchhoff H, Weis E and Farquhar GD (2003) Dependence of plastoquinol diffusion on the shape, size, and density of integral thylakoid proteins. *Biochim Biophys Acta* 1607: 97–109

Chapter 9

Biochemical Model of C₃ Photosynthesis

Susanne von Caemmerer*

Molecular Plant Physiology Group, Research School of Biological Sciences, Australian National University, Box 475 Canberra ACT 2601, Australia

Graham Farquhar

Environmental Biology Group, Research School of Biological Sciences, Australian National University, Box 475 Canberra ACT 2601, Australia

Joseph Berry

*Department of Global Ecology, Carnegie Institution of Washington
260 Panama st. Stanford, CA 94305, USA*

Summary.....	210
I. Introduction.....	210
II. The Rate Equations of CO ₂ Assimilation.....	211
A. RuBP Saturated (or Rubisco Limited) CO ₂ Assimilation Rate.....	213
B. RuBP Regeneration Limited (or Electron Transport Limited) CO ₂ Assimilation Rate.....	213
C. Light Intensity Dependence of Electron Transport Rate.....	214
D. Export Limited CO ₂ Assimilation Rate.....	215
E. Summary of Rate Equations.....	215
III. Parameters and their Temperature Dependencies.....	215
A. Rubisco Kinetic Constants.....	216
B. Parameterization of Chloroplast Electron Transport Rate.....	217
IV. The Role of Rubisco Activation State.....	218
A. Variation of Rubisco Activation with Light and <i>p</i> CO ₂	218
B. Variation of Rubisco Activation with Temperature.....	219
V. Estimating Chloroplast <i>p</i> CO ₂	219
VI. Predicting Photosynthesis from Chloroplast Biochemistry.....	220
A. Environmental Responses.....	220
B. Photosynthesis for Photosynthetic Mutants.....	221
C. Integration of the Leaf Photosynthesis Model with Stomatal Models.....	221
D. Canopy Photosynthesis.....	223
VII. Predicting Chloroplast Biochemistry from Leaf Gas Exchange.....	223
VIII. Concluding Remarks.....	224
References.....	225

* Author for correspondence, e-mail: susanne.caemmerer@anu.edu.au

Summary

A brief overview of the C_3 photosynthesis model described by Graham Farquhar, Susanne von Caemmerer and Joseph Berry is provided. The model was designed to help interpret gas exchange measurements of CO_2 assimilation of leaves and to represent C_3 photosynthesis in other systems such as stomatal control and the CO_2 concentrating function of C_4 photosynthesis. It can predict steady state CO_2 assimilation rates under different environmental conditions of light intensity, temperature, CO_2 and O_2 concentrations. The model is based on Rubisco's kinetic properties and the rate of CO_2 assimilation is given as the minimum of either a Rubisco limited rate, where the substrate ribulose biphosphate (RuBP) is saturating, or a chloroplast electron transport (or RuBP regeneration) limited rate. The model can be used to estimate in vivo Rubisco activity and chloroplast electron transport capacity. This however requires information on the partial pressure of CO_2 in the chloroplast which has been shown to be less than that in the intercellular airspaces. The temperature dependence of Rubisco kinetic constants is based on both in vitro and in vivo measurements of these parameters. The temperature dependence of the maximum chloroplast electron transport has also been parameterized from both in vivo and in vitro measurements; however the fact that thermal acclimation changes thylakoid properties and the temperature dependence of chloroplast electron transport prevents a unique parameterization. Further studies are required to investigate whether CO_2 assimilation rate at temperature extremes is limited by Rubisco and its activation state or by electron transport capacity in order to improve the model's accuracy under these conditions.

I. Introduction

In this chapter we discuss key attributes of the C_3 photosynthesis model first described by G. Farquhar, S. Von Caemmerer and J. Berry (Berry and Farquhar, 1978; Farquhar et al., 1980; Von Caemmerer and Farquhar, 1981; Farquhar and Von Caemmerer, 1982). This model was designed to help interpret gas exchange measurements of CO_2 assimilation of leaves. It is used to predict steady state CO_2 assimilation rates under different environmental conditions of light intensity, temperature, CO_2 and O_2 partial pressures (pCO_2 and pO_2) and can be embedded in larger models of the global carbon cycle and of land surface feedbacks on climate. It is also frequently used in reverse to predict underlying biochemical properties of leaves from gas exchange measurements (Long and Bernacchi, 2003).

Simplicity is the key to making this type of model useful. This requires careful consideration of the detail that needs to be incorporated and what can safely be left out. It is important to keep the number of parameters that have to be assigned to a minimum. This has been the guiding principle of the design of the model discussed in this chapter and sets it apart from other models that seek to incorporate a larger

number of biochemical steps involved in CO_2 assimilation with the purpose of studying regulation of metabolism (Laisk and Oja, 1998; Laisk et al., 2006; Zhu et al., 2007). The model is generally most useful in describing steady state CO_2 assimilation rates, although it has also been incorporated into models describing CO_2 uptake transients during sun flecks (Percy et al., 1997).

The model is based on the kinetic properties of ribulose 1,5-bisphosphate carboxylase/oxygenase (Rubisco, EC 4.1.1.39) and an interesting historical perspective of Rubisco research and discoveries is given by Portis and Parry (2007). The importance of Rubisco in determining the rate of photosynthesis had been inferred early on from correlations between photosynthetic rate and the amount of Rubisco protein in leaves (Björkman, 1968; Wareing et al., 1968; Bowes et al., 1971; Bowes and Ogren, 1972). But perhaps the pivotal event was the discovery that O_2 was a competitive inhibitor of CO_2 fixation, an alternative substrate leading to the side reactions that fuel photorespiration (Bowes et al., 1971; Bowes and Ogren, 1972). This led to the development of photosynthetic models based on Rubisco kinetic properties (Laisk, 1970, 1977; Laing et al., 1974; Peisker, 1974, 1976; Hall and Björkman, 1975). For example, Laing et al.

(1974) and Peisker (1974) showed that a linear dependence of the CO₂ compensation point could be explained from Rubisco's kinetic properties. The impact of Rubisco kinetic properties on C₃ photosynthesis has been elegantly highlighted in recent studies where the C₃-model has been used to characterize Rubisco kinetic properties in transgenic plants expressing mutated Rubisco (Whitney et al., 1999; Whitney and Andrews, 2001; Sharwood et al., 2008).

The model continues to be used almost unchanged from when it was conceived in the late 1970s and early 1980s and it has served as a template for development of other models (Collatz et al., 1991, 1992; Sellers et al., 1996a). The key innovation of this model stemmed from the recognition that losses in coupling between the light dependent reactions and the carbon reactions are minimal. Therefore, the overall rate of photosynthesis could be approximated as the minimum of the potential rates of these processes taken separately (Eq. 9.20). The basis for this efficient coupling is still not well understood (Woodrow and Berry, 1988). Perhaps most surprisingly the equations relating chloroplast electron transport rate to light intensity are still treated empirically in whole leaf models and several different equations are in use (Farquhar et al., 1980; Farquhar and Von Caemmerer, 1982; Farquhar and Wong, 1984; Collatz et al., 1990, 1991, 1992; Long and Bernacchi, 2003). Equations relating ATP production to chloroplast electron transport rate continue to change according to new understanding of the proton requirements of ATP production. Sharkey and co-workers drew attention to a third limitation that may come into play by the rate of triose phosphate export (Sharkey, 1985a; Harley and Sharkey, 1991). There are however several questions that deserve further attention. For example, it is important to know what the CO₂ partial pressure ($p\text{CO}_2$) is at the site of Rubisco carboxylation and what defines the conductance of CO₂ diffusion from intercellular airspace to the chloroplast stroma. This research area is currently receiving considerable attention (Evans and Von Caemmerer, 1996; Terashima et al., 2006; Flexas et al., 2007a, b; Warren, 2007). This question is of particular importance in biotechnological research attempting to redirect photorespiratory CO₂ release to the chloroplast (Kebeish et al., 2007) and to attempts at

introducing a C₄ type CO₂ concentrating mechanism into C₃ cells where one would like to be able to manipulate CO₂ diffusion properties of membranes (Matsuoka et al., 2001; Von Caemmerer, 2003; Mitchell and Sheehy, 2006). Understanding what limits CO₂ fixation at extreme temperatures has also become an important question in the endeavor to predict CO₂ assimilation rates in these environments. There is at present considerable debate on whether the capacity of chloroplast electron transport to regenerate RuBP or the activation state of Rubisco provide the primary limitation and it is clear that we need a better understanding how Rubisco activation state is modulated by environmental variables (Weis and Berry, 1988; Crafts-Brandner and Salvucci, 2000; Wise et al., 2004; Cen and Sage, 2005; Yamori et al., 2005, 2006b, 2008).

The photosynthesis model described here provides a set of hypotheses brought together in a quantitative form that can be used as a research tool to design and interpret both field and laboratory based experiments. Both the current availability of transgenic plants with biochemical impairments and the range of Arabidopsis knockout mutants and the interest in improving CO₂ assimilation rates through genetic manipulation are providing interesting new tests and applications for modeling photosynthesis (Von Caemmerer, 2000, 2003; Raines, 2003, 2006). Newer portable gas exchange systems have opened up opportunities for ecophysiological studies (Björkman et al., 1972; Ellsworth et al., 2004; Wright et al., 2004).

II. The Rate Equations of CO₂ Assimilation

Farquhar et al. (1980) showed that CO₂ assimilation rate A was given by

$$A = V_c - 0.5V_o - R_d, \quad (9.1)$$

where A denotes net CO₂ assimilation rate, V_c and V_o are the carboxylase and oxygenase rates of Rubisco and R_d denotes day respiration, which comprises mitochondrial CO₂ release occurring in the light other than that of photorespiration. Equation (9.1) can be rewritten in a simpler

form as:

$$A = V_c (1 - 0.5\phi) - R_d, \quad (9.2)$$

where ϕ is the ratio of oxygenation to carboxylation rates, V_o/V_c . Rubisco, located in the chloroplast stroma, catalyses the competing reactions of the carboxylation and the oxygenation of ribulose biphosphate (Andrews and Lorimer, 1987). The carboxylation of RuBP is the first step of the photosynthetic carbon reduction (PCR) cycle and the carboxylation of 1 mol of RuBP leads to the formation of 2 mols of phosphoglycerate (PGA). The oxygenation of 1 mol of RuBP on the other hand leads to the formation of 1 mol of PGA and 1 mol of phosphoglycolate (PGly). We assume that the recycling of 1 mol of PGly in the photorespiratory carbon oxidation (PCO) cycle results in the release of 0.5 mol of CO_2 in the mitochondria (Fig. 9.1). It has been suggested that the release may be less than 0.5 and there continue to be reports of complete oxidation of glycolate as proposed by Israel Zelitch (Hanson and Peterson, 1986; Zelitch, 1989; Harley and Sharkey, 1991).

The ratio of oxygenation to carboxylation rate, ϕ , is determined solely by the kinetic constants of Rubisco:

$$\phi = \frac{V_o}{V_c} = \left(\frac{1}{S_{c/o}} \right) \frac{O}{C} = \left(\frac{V_{o\max}}{K_o} \frac{K_c}{V_{c\max}} \right) \frac{O}{C}, \quad (9.3)$$

where $S_{c/o}$ is the relative specificity of Rubisco and C and O are the chloroplastic $p\text{CO}_2$ and $p\text{O}_2$; $V_{c\max}$, $V_{o\max}$, K_c and K_o are the maximal

rates and the Michaelis–Menten constants of carboxylation and oxygenation, respectively.

Inspection of Eq. (9.2) shows that when $R_d = 0$, $A = 0$ when $\phi = 2$. The chloroplast $p\text{CO}_2$ at which this occurs has been named Γ^* (Laisk, 1977; Laisk and Oja, 1998) and from the above equation it follows that

$$\Gamma^* = \frac{0.5O}{S_{c/o}} = \gamma^* O \quad (9.4)$$

and

$$\phi = \frac{2\Gamma^*}{C}. \quad (9.5)$$

Substituting this into Eq. (9.2) one can show that

$$A = (1 - \Gamma^*/C) V_c - R_d. \quad (9.6)$$

It is assumed that some mitochondrial respiration (R_d) continues in the light although not necessarily at the rate that occurs in the dark (Brooks and Farquhar, 1985; Atkin et al., 1998; Hoefnagel et al., 1998). It has also been suggested that the rate of day respiration may depend on the rate of photorespiration (Bykova et al., 2005; Tcherkez et al., 2008). If this were indeed the case and the two were related in a predictable way then Eqs. (9.1), (9.2), (9.6) would need to be modified to reflect this.

The rate of photorespiration (V_{phr}) is half the rate of oxygenation and is given by $(\Gamma^*/C)V_c$ and can be calculated from gas exchange measurements by the following equation:

$$V_{\text{phr}} = \frac{\Gamma^*}{C - \Gamma^*} (A + R_d). \quad (9.7)$$

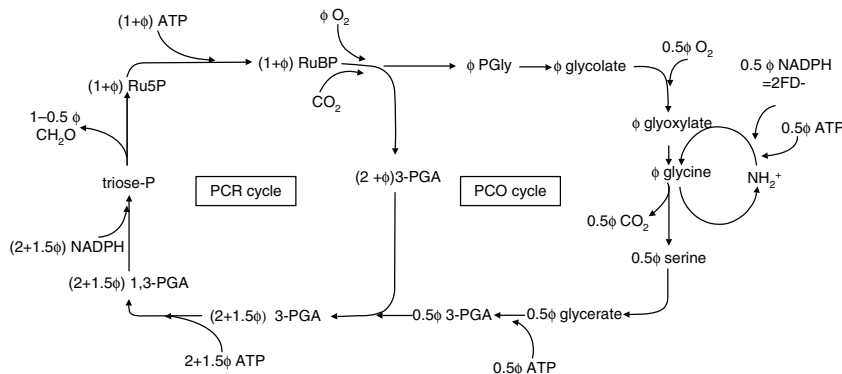


Fig. 9.1. Stoichiometry of the photosynthetic carbon reduction (PCR) cycle and photorespiratory carbon oxidation (PCO) cycle (ϕ denotes the ratio of Rubisco oxygenation to carboxylation)

The basis of the Rubisco limited part of the model is given by Eqs. (9.1)–(9.3). To complete this part of the model the dependencies of Rubisco velocity on $p\text{CO}_2$, $p\text{O}_2$, irradiance and temperature need to be added. Rubisco occurs at high concentration in the chloroplast stroma relative to the Michaelis–Menten constant for its substrate RuBP and it was the special kinetics that apply under these conditions that allowed the simple binary formulation of CO_2 assimilation rate as being either RuBP saturated, or limited by the rate of RuBP regeneration (Berry and Farquhar, 1978; Collatz, 1978; Farquhar, 1979; Farquhar et al., 1980; Farquhar and Von Caemmerer, 1982; Collatz et al., 1990).

A. RuBP Saturated (or Rubisco Limited) CO_2 Assimilation Rate

Since O_2 inhibits RuBP carboxylation competitively with respect to CO_2 , the RuBP saturated carboxylation rate is given by

$$W_c = \frac{C V_{c \max}}{C + K_c (1 + O/K_o)} \quad (9.8)$$

(Bowes and Ogren, 1972; Badger and Andrews, 1974). Using Eq. (9.8) to substitute for V_c in Eq. (9.6) yields an expression for the RuBP saturated rate of CO_2 assimilation,

$$A_c = \frac{(C - \Gamma^*) V_{c \max}}{C + K_c (1 + O/K_o)} - R_d. \quad (9.9)$$

Because of its dependence on the maximum Rubisco activity ($V_{c \max}$), A_c is also often called the Rubisco limited rate of CO_2 assimilation.

The Rubisco limited rate of CO_2 assimilation suggests that the dependence of CO_2 assimilation on $p\text{CO}_2$ should have a Michaelis–Menten form. However as noted by several researchers (Laik and Oja, 1974; Lilley and Walker, 1975; Ku and Edwards, 1977) CO_2 assimilation rate saturates more quickly than can be predicted from the RuBP saturated CO_2 assimilation rate alone. This can be seen in the example of a CO_2 response curve for CO_2 assimilation rate of a tobacco leaf (Fig. 9.2). In the leaf of a transgenic tobacco with an antisense construct to the small subunit of Rubisco the amount of Rubisco per leaf area has been reduced with little alteration to other chloroplast components. In this case the rate of

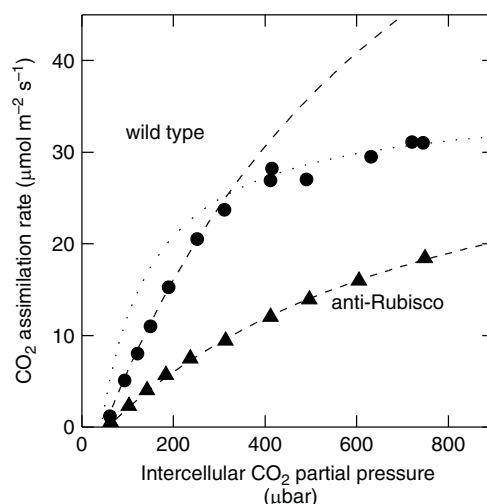


Fig. 9.2. CO_2 assimilation rate, A , as a function of intercellular $p\text{CO}_2$ for a leaf of a wild type (●) and transgenic tobacco with reduced amount of Rubisco (▲). Measurements were made at an irradiance of $1,000 \mu\text{mol quanta m}^{-2} \text{s}^{-1}$ and a leaf temperature of 25°C . The dashed lines are A predicted from the Rubisco limited rate (Eq. 9.9). The dotted line is A predicted from the RuBP regeneration (electron transport) limited rate (adapted from Von Caemmerer et al., 1994)

CO_2 assimilation can be modeled solely by the Rubisco limited rate.

B. RuBP Regeneration Limited (or Electron Transport Limited) CO_2 Assimilation Rate

The synthesis of RuBP requires energy in the form of NADPH and ATP and the rate of the Rubisco reaction may become limited by the supply of RuBP. Farquhar (1979) showed that the partitioning of RuBP to carboxylation and oxygenation follows the same kinetics (Eq. 9.3) under limiting RuBP supply. The consumption rates of ATP and NADPH required to regenerate RuBP at the rate of $(1 + \phi)V_c$ were derived from the stoichiometries given in Fig. 9.1. Summing the requirements,

$$\text{the rate of NADPH consumption} = (2 + 2\phi)V_c \quad (9.10)$$

and

$$\text{the rate of ATP consumption} = (3 + 3.5\phi)V_c \quad (9.11)$$

(Berry and Farquhar, 1978; Farquhar et al., 1980; Farquhar and Von Caemmerer, 1982; Von Caemmerer, 2000).

The reduction of NADP^+ to $\text{NADPH} + \text{H}^+$ requires the transfer of two electrons through the whole electron transport chain. The rate of whole chain electron transport, required to regenerate RuBP can be calculated from the rate of NADPH consumption (Eq. 9.10) as:

$$(4 + 4\phi)V_c = (4 + 8\Gamma^*/C)V_c \quad (9.12)$$

and the electron transport limited rate of RuBP regeneration is given by

$$W_j = \frac{J}{(4 + 8\Gamma^*/C)}, \quad (9.13)$$

where J is the potential electron transport rate, which depends on irradiance.

Light driven electron transport is coupled to the transfer of protons across the thylakoid membrane into the lumen, but neither the stoichiometry of the H^+/e^- ratio or the number of protons required to generate one ATP are known with certainty and may well be flexible. We therefore use the NADPH limited expressions in this chapter. For a more detailed discussion on the formulation for an ATP limited rate of electron transport see Von Caemmerer (2000) or Yin et al. (2004) and Chapter 11 by Xinyou Yin, Jeremy Harbinson and Paul Struik of this book.

Substituting W_j for V_c in Eq. (9.6) yields an expression for the RuBP regeneration (or electron transport) limited rate of CO_2 assimilation:

$$A_j = \frac{(C - \Gamma^*)J}{4C + 8\Gamma^*} - R_d. \quad (9.14)$$

The CO_2 dependence of A_j is shown in Fig. 9.2 by the dotted line. Here the assumption is made that chloroplast electron transport rate is limiting the rate of RuBP regeneration rather than the enzymes involved in the regeneration of RuBP such as FBPase or SBPase. Studies with transgenic tobacco plants with antisense reductions in the content of chloroplast cytochrome b_6f complex show a close linear relationship between the cytochrome b_6f content and CO_2 assimilation rate, in support of this hypothesis (Price et al., 1995, 1998; Ruuska et al., 2000a; Baroli et al., 2008) and an example is shown in Fig. 9.3. Studies with

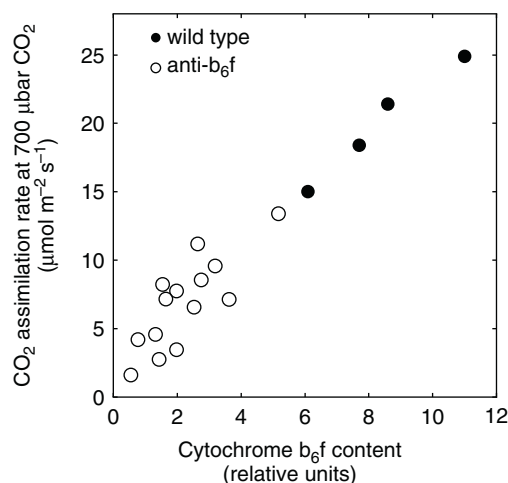


Fig. 9.3. CO_2 assimilation rate versus chloroplast cytochrome b_6f content in wild type and transgenic tobacco with an antisense construct against the Rieske FeS protein of the chloroplast cytochrome b_6f complex. Gas exchange measurements were made at $1,000 \mu\text{mol quanta m}^{-2} \text{s}^{-1}$, $700 \mu\text{bar CO}_2$ and a leaf temperature of 25°C (data from Ruuska et al., 2000a)

transgenic plants with reductions in GAPDH, FBPase, SBPase, and phosphoribulokinase have also confirmed that assuming an electron transport limitation is a reasonable assumption under most circumstances (Stitt and Sonnewald, 1995; Raines, 2003). However there are also some studies that show enhanced CO_2 assimilation rates in transgenic plants overexpressing SBPase (Miyagawa et al., 2001; Lefebvre et al., 2005; Feng et al., 2007; Chapter 15 of this book by Ian E. Woodrow). It is possible to write expressions for limitations of CO_2 assimilation rate by any of the enzymes involved in RuBP regeneration following the stoichiometries given by Farquhar and Von Caemmerer (1982), Brooks and Farquhar (1985) and Von Caemmerer (2000). It is important to note that if these reactions were limiting CO_2 assimilation rate the CO_2 dependence would be different to that if electron transport limited the rate.

C. Light Intensity Dependence of Electron Transport Rate

At present the following empirical equation (Farquhar and Wong, 1984) is used to link potential electron transport rate, J , to irradiance:

$$\theta J^2 - J(I_2 + J_{\max}) + I_2 J_{\max} = 0, \quad (9.15)$$

where I_2 is the useful light absorbed by PS II and J_{\max} is the maximum electron transport rate and θ is an empirical curvature factor (0.7 is a good average value, Evans, 1989). I_2 is related to incident irradiance I by

$$I_2 = I \cdot \text{abs} \cdot (1 - f)/2. \quad (9.16)$$

In sunlight the absorptance (*abs*) of leaves is commonly about 0.85 and f is to correct for spectral quality of the light ($f \sim 0.15$, Evans, 1987). Ögren and Evans (1993) give a detailed discussion of the parameters of Eq. (9.16). The denominator 2 is because we assume half the light absorbed needs to reach each photosystem. The equation can be solved for J as follows

$$J = \frac{I_2 + J_{\max} - \sqrt{(I_2 + J_{\max})^2 - 4\theta I_2 J_{\max}}}{2\theta}. \quad (9.17)$$

This equation is a non-rectangular hyperbola with a smooth transition from light limitation ($J = I_2$) to light saturation ($J = J_{\max}$), where J_{\max} is an upper limit to potential chloroplast electron transport determined by the components of the chloroplast electron transport chain. Support for this hypothesis of a limitation on the maximum capacity for RuBP regeneration is shown in Fig. 9.3 where CO₂ assimilation rate measured at high $p\text{CO}_2$ and high irradiance is correlated with the amount of cytochrome *b₆f* content in tobacco plants where cytochrome *b₆f* content has been reduced via antisense techniques (Price et al., 1998; Ruuska et al., 2000a; Baroli et al., 2008).

D. Export Limited CO₂ Assimilation Rate

At high CO₂ partial pressure, particularly in combination with high irradiance, or low O₂ partial pressure or at low temperatures, the rate of CO₂ assimilation can sometimes be limited by the rate at which triose phosphates are utilized in the synthesis of starch and sucrose. Then

$$W_p = 3T_p / (1 - \Gamma^* / C) \quad (9.18)$$

and CO₂ assimilation rate is given by

$$A_p = 3T_p - R_d, \quad (9.19)$$

where T_p is the rate of inorganic phosphate supply to the chloroplast, and equal to the triose phosphate export from the chloroplast (Farquhar and Von Caemmerer, 1982; Sharkey, 1985b; Harley and Sharkey, 1991). Under these conditions A is insensitive to changes in CO₂ and O₂ partial pressure. For a detailed discussion see Harley and Sharkey (1991).

E. Summary of Rate Equations

Equations (9.8), (9.13), (9.18) describe the basic C₃ model with

$$A = (1 - \Gamma^* / C) \cdot \min \{ W_c, W_j, W_p \} - R_d, \quad (9.20)$$

or using Eqs. (9.9), (9.14), (9.19)

$$A = \min \{ A_c, A_j, A_p \}, \quad (9.21)$$

when $C > \Gamma^*$. This is illustrated in Fig. 9.2 for wild type tobacco where the solid line shows the actual rate of CO₂ assimilation and the dashed line is the Rubisco limited rate A_c , and the dotted line is the electron transport limited rate A_j . A phosphate limitation rate for A_p is not shown in this example (but see Von Caemmerer, 2000; Long and Bernacchi, 2003; Chapter 10 of this book by Carl J. Bernacchi, David Rosenthal, Carlos Pimentel, Stephen P. Long and Graham D. Farquhar).

In this form the model has discontinuities at the transitions between the different limitations. This can provide mathematical problems when the model is used as a submodel in other applications. The discontinuities can be smoothed using quadratic expressions (Kirschbaum and Farquhar, 1984; Collatz et al., 1991).

III. Parameters and their Temperature Dependencies

Depending on the application of the model most of the parameter values can be assigned a priori leaving only V_{\max} and J_{\max} and g_i (the conductance to CO₂ diffusion from intercellular airspace to the chloroplast, discussed in the next section) to be assigned anew.

A. Rubisco Kinetic Constants

Kinetic constants of Rubisco are similar amongst C_3 species and it is common to use the same K_c , K_o , and $S_{c/o}$ for all higher plant C_3 species. There are however reports of variation of Rubisco kinetic parameters which may need to be considered in some applications of the model, although very few complete data sets exist at present (Sage, 2002; Galmes et al., 2005; Tcherkez et al., 2006; Kubien et al., 2008). Farquhar et al. (1980) used constants derived from in vitro measurements by Badger and co-workers. Von Caemmerer et al. (1994) used transgenic tobacco with reduced amounts of Rubisco to determine Rubisco kinetic constants in vivo at 25°C (Table 9.1). These values were in good agreement with in vitro measurements made in tobacco (Whitney et al., 1999). Brooks and Farquhar (1985) measured Γ^* as a function of temperature and found that spinach had a slightly higher value than wheat, a result borne out by subsequent specificity measurements in vitro (Kane et al., 1994). It is important to note that $S_{c/o}$, K_c and K_o are linked (Eq. 9.3) to assure consistency when assigning values.

The maximum rate V_{cmax} is dependent on the amount and the activation state of Rubisco protein present in the leaf and will vary from leaf to leaf. Rubisco has a molecular weight of 550 kDa and eight catalytic sites per molecule. To be catalytically competent Rubisco's sites must be acti-

vated. This requires the carbamylation of a lysine residue within the catalytic site to allow the binding of a Mg^{2+} (rev. Andrews and Lorimer, 1987). In C_3 species Rubisco has a catalytic turnover rate of approximately 3.5 s^{-1} per site and thus 1 g m^{-2} of Rubisco has a V_{cmax} of $51 \mu\text{mol m}^{-2} \text{ s}^{-1}$ when all sites are carbamylated.

It was shown early on with the first gas exchange measurements that the temperature dependencies of Rubisco's carboxylation and oxygenation rates are reflected in the temperature dependency of the CO_2 assimilation rates of leaves (Björkman and Pearcy, 1971; Björkman et al., 1980). The need for accurate estimates of the temperature dependencies of Rubisco kinetic parameters has become more urgent as mathematical modelers try to predict the impact of increasing global CO_2 concentrations and temperatures (Bowes, 1991; Long, 1991; McMurtrie and Wang, 1993; Whitehead et al., 2001; Medlyn et al., 2002; Lloyd and Farquhar, 2008). The temperature dependence of the kinetic constants can be described by an Arrhenius function of the form

$$\text{Parameter}(T) = \text{Parameter}(25^\circ\text{C}) \times \exp \left[(t - 25) E / (298R (273 + t)) \right], \quad (9.22)$$

where R ($8.31 \text{ J K}^{-1} \text{ mol}^{-1}$) is the universal gas constant and t is temperature in °C (Badger and Collatz, 1977). Using the Arrhenius function to describe temperature dependencies of the photosynthetic processes is a semi empirical approach, but allows for easy comparison between studies. The Q_{10} function has also been used to approximate the temperature dependence of these kinetic constants (Woodrow and Berry, 1988). Table 2.2 in Von Caemmerer (2000) provides a comparison of experimental measurements of the in vitro temperature dependencies of Rubisco kinetic constants. Temperature dependencies were also reviewed by (Medlyn et al., 2002). Bernacchi and co workers using a similar approach to Von Caemmerer et al. (1994) determined the temperature dependence of Γ^* , K_c and K_o in vivo in transgenic tobacco with reduced amounts of Rubisco (Bernacchi et al., 2001, 2002; Chapter 10) and these are shown in Table 9.1. They are surprisingly similar to the initial temperature dependencies used by Farquhar et al. (1980), except that K_c has a greater apparent activation energy.

Table 9.1. Photosynthetic parameters at 25°C and their activation energies E

Parameter	Value	E (kJ mol^{-1})
K_c (μbar)	260 ^a (267) ^b	59.36 ^c (80.99) ^b
K_o (mbar)	179 ^a (164)	35.94 (23.72)
$S_{c/o}$ (mol/mol)	97.5 ^a	
$S_{c/o}$ (bar/bar)	2,585	
γ^* (bar/bar) ($0.5/S_{c/o}$)	0.0001935	23.4
Γ^* ($\mu\text{bar CO}_2$, 200 mbar O_2)	38.6 ^a (36.9)	23.4 (24.6)
V_{cmax} ($\mu\text{mol m}^{-2} \text{ s}^{-1}$)	80 ^d	58.52
R_d ($\mu\text{mol m}^{-2} \text{ s}^{-1}$)	1 ^d	66.4
J_{max} ($\mu\text{mol m}^{-2} \text{ s}^{-1}$)	160 ^d	37
H (kJ mol^{-1})	220	
S ($\text{J K}^{-1} \text{ mol}^{-1}$)	710	

^a (Von Caemmerer et al., 1994)

^b Numbers in brackets are taken from Bernacchi et al. (2002) assuming an average atmospheric pressure of 987 mbar in Urbana Illinois

^c Activation energies used by Farquhar et al. (1980)

^d Varies dependent on photosynthetic capacity of the leaf

Throughout this chapter, the values of chloroplastic CO₂ and O₂, K_c and K_o are given in units of partial pressure. The chemical activity of a dissolved gas is proportional to its gas phase (vapor) pressure and thus the partial pressure of a gas existing in equilibrium with that in solution is a better measure of its chemical activity than dissolved concentrations (Badger and Collatz, 1977). The main difference between the use of gas phase units of partial pressure and that of dissolved concentrations (μM) arises when temperature dependencies are considered. If dissolved concentrations are used the temperature dependencies of the solubility of the dissolved gas need to be considered.

B. Parameterization of Chloroplast Electron Transport Rate

To parameterize the RuBP regeneration limited rate of CO₂ assimilation, Γ^* and the light dependence of potential electron transport rate need to be considered (Eq. 9.15). Values of absorbance and the curvature factor θ have only a very small temperature dependence and can be assigned a priori with the values given in Eqs. (9.15), (9.16) (Bernacchi et al., 2003). The only parameter that needs to be newly assigned is the maximum electron transport rate J_{\max} . We assume that J_{\max} depends on the amount of thylakoid components such as the cytochrome b₆f complex for example and is dependent on the amount of thylakoid protein present (Fig. 9.3). J_{\max} is given in $\mu\text{mol e}^- \text{m}^{-2} \text{s}^{-1}$ and the ratio of J_{\max} to V_{cmax} is usually between 1.5–2 at 25 °C (Wullschlegel, 1993; de Pury and Farquhar, 1997).

The dependence of J_{\max} on temperature has been estimated in vitro with isolated thylakoids (Armond et al., 1978; Björkman et al., 1980; Sage et al., 1995; Cen and Sage, 2005; Yamori et al., 2008). Farquhar et al. (1980) used the data of Nolan and Smillie (1976) to determine the parameters E , S , H in the following empirical expression:

$$J_{\max} = J_{\max}(25^\circ\text{C}) \exp\left(\frac{(T - 298)E}{298RT}\right) \cdot \frac{\left[1 + \exp\left(\frac{298S-H}{298R}\right)\right]}{\left[1 + \exp\left(\frac{ST-H}{RT}\right)\right]}, \quad (9.23)$$

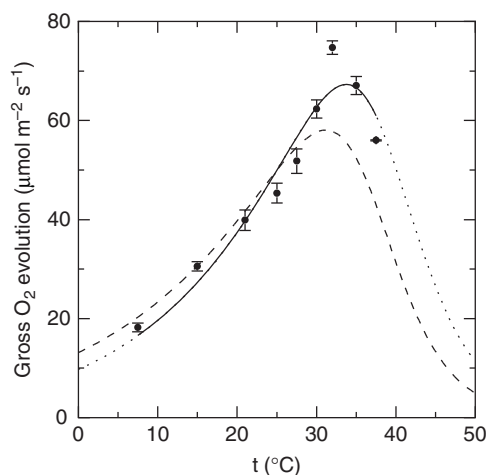


Fig. 9.4. Gross O₂ evolution as a function leaf temperature measured on leaf discs of tobacco as ¹⁶O₂ evolution at 1,700 $\mu\text{mol quanta m}^{-2} \text{s}^{-1}$, 1.5% CO₂. Measurements were made as described by Ruuska et al. (2000b) and data are redrawn from Badger et al. (2000). The data were fitted with Eqs. (9.23) and (9.24) and $E = 44.72 \text{ kJ mol}^{-1}$, $H = 210 \text{ kJ mol}^{-1}$, $S = 673 \text{ J K}^{-1} \text{mol}^{-1}$ and gross O₂ evolution of $50 \mu\text{mol m}^{-2} \text{s}^{-1}$ at 25 °C. These measurements and the fit are compared with the temperature dependence of J_{\max} (Eq. 9.23) used by Farquhar et al. (1980), expressed here as gross O₂ evolution normalized to the value at 25 °C. Parameters are given in Table 9.1

where T is in °K. This equation is shown in Fig. 9.4 with parameters listed in Table 9.1. The parameters S and H are the entropy and enthalpy of a hypothetical equilibrium between an active and inactive form of the limiting component of electron transport, E is the apparent activation energy for low temperature limited electron transport. Discussions on the origins of Eq. (9.23) can be found in several publications (Tenhunen et al., 1976; Hall, 1979; Farquhar et al., 1980; Von Caemmerer, 2000; Medlyn et al., 2002). Acclimation of the thylakoid membrane can occur when plants are grown at different temperatures, shifting the temperature optimum (Berry and Björkman, 1980; Björkman et al., 1980; Sage et al., 1995; Yamori et al., 2008). It is therefore useful to have an equation for the temperature optimum:

$$T_{\text{opt}} = H [S + R \ln (H/E - 1)]. \quad (9.24)$$

Equations (9.23) and (9.24) can be used together to fit temperature response curves of in vivo or in vitro measurements of electron transport rate.

An example of measurements of actual electron transport rate is shown in Fig. 9.4. In this case the actual electron transport rate was measured as $^{16}\text{O}_2$ evolution at high $p\text{CO}_2$ and high light intensity in tobacco leaf discs (Badger et al., 2000; Ruuska et al., 2000b). Other temperature dependencies have been given using empirical fitting functions (Kirschbaum and Farquhar, 1984; Bernacchi et al., 2003; June et al., 2004; Yamori et al., 2008). It needs to be borne in mind that many of the temperature dependencies derived for J_{max} in vitro may not represent true temperature dependencies of maximal electron transport rate in vivo as downstream reactions in carbon metabolism can exert feedback inhibition on electron transport (Woodrow and Berry, 1988). There is concern that the steep decline in J_{max} at high temperature may be an artifact of the in vitro measuring system. However, Yamori et al. (2008) compared the temperature dependence of J_{max} estimated in vivo from measurements of CO_2 assimilation rate at high CO_2 with in vitro measurements and found close agreement over a wide temperature range except at the lowest and highest temperatures. Bernacchi et al. (2003) found that J estimated from gas exchange could be fitted with a simple exponential function and did not saturate in high temperature grown tobacco. A simpler empirical form was introduced by June et al. (2004):

$$J(t_L) = J(t_0)e^{-\left(\frac{t_L - t_0}{\Omega}\right)^2}, \quad (9.25)$$

where t_L is the leaf temperature ($^{\circ}\text{C}$), $J(t_0)$ is the rate of electron transport at the optimum temperature t_0 , and Ω is the difference in temperature from t_0 at which J falls to e^{-1} (0.37) of its value at t_0 .

IV. The Role of Rubisco Activation State

One of the concerns in modeling Rubisco limited CO_2 assimilation rate is if and how to incorporate a function for the variation of Rubisco activation state. To function, Rubisco's catalytic sites must be activated through the reversible carbamylation of a lysine residue within the site, followed by the rapid binding of an essential Mg^{2+} (Andrews and Lorimer, 1987). It is possible to measure both Rubisco activity and the

carbamylation state of Rubisco in leaf extracts (Butz and Sharkey, 1989). In vitro studies of Rubisco activation kinetics suggest that the equilibrium carbamylation in the absence of RuBP would be less than 25% at the pH, Mg^{2+} , and CO_2 concentrations thought to occur in the chloroplast (Lorimer et al., 1976). Furthermore, when RuBP was present in vitro assays, it appeared to block carbamylation by binding tightly to non-carbamylated sites (Jordan and Chollet, 1983). These in vitro difficulties in Rubisco carbamylation are eliminated in vivo by the presence of a second protein, Rubisco activase (Portis, 2003). Activase requires ATP hydrolysis to function and removes sugar phosphates from carbamylated and uncarbamylated Rubisco sites, thereby promoting carbamylation (Andrews et al., 1995; Portis, 2003). In vivo Rubisco activation state has been shown to vary with irradiance, temperature and $p\text{CO}_2$ (Von Caemmerer and Quick, 2000; Weis and Berry, 1988; Salvucci and Crafts-Brandner, 2004a). Although Rubisco is frequently observed to be fully active at high irradiance, ambient $p\text{CO}_2$ and moderate temperatures (Von Caemmerer and Edmondson, 1986) its activation state can decline steeply at high temperature (Weis and Berry, 1988; Crafts-Brandner and Salvucci, 2000; Cen and Sage, 2005; Yamori et al., 2006b).

A. Variation of Rubisco Activation with Light and $p\text{CO}_2$

Von Caemmerer (2000) reviewed the role Rubisco activation state may play in modeling C_3 photosynthesis with variation in irradiance and $p\text{CO}_2$. At low $p\text{CO}_2$ Rubisco can be almost fully carbamylated even at low light whereas it declines at high $p\text{CO}_2$ (Sage et al., 1990; Von Caemmerer and Quick, 2000). Sage (1990) therefore suggested that Rubisco's activation state was lowered only under conditions where RuBP regeneration rate was limiting CO_2 assimilation rate. If this is the case Rubisco activation state would not need to be introduced as a separate variable into the model equations. There is some support for this hypothesis in gas exchange measurements which show that the initial slope of the CO_2 response curve is frequently independent of irradiance down to quite low irradiance levels (Brooks and Farquhar, 1985; Evans, 1986; Sage et al., 1990). At low $p\text{CO}_2$ the capacity for RuBP

regeneration exceeds the carboxylation capacity and presumably the transthylakoid ΔpH as well as the ATP/ADP ratio are likely to be high, which in turn may translate into a greater activase activity. In the same vein, the carbamylation state was found to be high at low irradiance and ambient pCO_2 in transgenic tobacco plants with reduced amount of Rubisco compared to wild type plants (Quick et al., 1991), whereas transgenic tobacco with reduced cytochrome b₆f content had reduced carbamylation levels compared to wild type (Price et al., 1998; Ruuska et al., 2000a). The complex dependence of activation on pCO_2 and irradiance illustrates that Rubisco carbamylation is no simple function of irradiance. The results with transgenic plants suggest some interaction between Rubisco activation state and the balance between potential electron transport rate and Rubisco carboxylation rate as had been suggested by Sage (1990).

B. Variation of Rubisco Activation with Temperature

Experiments with a variety of species have established that Rubisco activation state declines with increasing temperature at ambient pCO_2 (Weis, 1981; Weis and Berry, 1988; Feller et al., 1998; Crafts-Brandner and Salvucci, 2000; Haldimann and Feller, 2004, 2005; Salvucci and Crafts-Brandner, 2004a; Yamori et al., 2006b). It is thought that Rubisco is inactivated at high temperature due to heat induced inactivation of Rubisco activase which regulates Rubisco activation state (Salvucci and Crafts-Brandner, 2004a, b). Cen and Sage (2005), who examined the interaction of pCO_2 and temperature on Rubisco activation in sweet potato, found Rubisco activation states to be greater at low compared to high pCO_2 at all temperature. There is at the moment no complete information on how temperature, pCO_2 and irradiance interact to modulate Rubisco activation and clearly more research is required to establish the underlying mechanisms. If both Rubisco activation and electron transport are reduced as was suggested by the study of Yamori et al. (2006b) then Rubisco activation state may need to be introduced as an extra variable in Eqs. (9.8) and (9.9). Sellers et al. (1996a) introduced the following

equation for Rubisco activation as a function of leaf temperature:

$$a_R = 1 / (1 + e^{0.3(T_1 - S_2)}), \quad (9.26)$$

where a_R is the fraction of Rubisco that is active and S_2 is a temperature at which half of the Rubisco is inactive. S_2 varies from 303 K for needle leaf conifers to 313 K for tropical evergreen trees (Table 5 in Sellers et al., 1996b). This equation has similar properties to Eq. (9.23) and can be applied equally well to J_{max} . There is little empirical difference between assuming that J_{max} or Rubisco activation limits photosynthesis at high temperature and ambient pCO_2 since both activities have similar sensitivity to temperature, but there may be subtle differences in the simulated response under low or high pCO_2 conditions. The models of Collatz et al. (1991) and Sellers et al. (1996a) assume that Rubisco activation is most limiting.

V. Estimating Chloroplast pCO_2

To examine the biochemistry of photosynthesis in leaves ideally one would like to measure CO_2 assimilation rate in relation to chloroplast CO_2 partial pressures, as this is the CO_2 pressure determining the Rubisco carboxylation. It is common practice to calculate the CO_2 partial pressure in the sub-stomatal cavities (referred to as intercellular CO_2 partial pressure) from water vapor exchange measurements. This eliminates an important variability, as stomatal conductance varies as stomata themselves respond to CO_2 and irradiance and this has become a standard reference CO_2 (Von Caemmerer and Farquhar, 1981). However measurements of carbon isotope discrimination concurrently with gas exchange measurements have shown that there is a substantial drop in pCO_2 from intercellular airspace to the chloroplast which needs to be considered (Evans et al., 1986; Evans and Von Caemmerer, 1996). Evans and Von Caemmerer (1991) assumed that the CO_2 transfer conductance from the sub-stomatal cavities to the sites of carboxylation in the chloroplast, g_i , would be constant for a leaf since it is to a large degree related to the anatomy of the leaf such as the chloroplast surface area appressing intercellular airspace. The explicit

inclusion of a constant CO_2 transfer conductance, g_i , from the sub stomatal cavities to the carboxylation sites leads to a quadratic relationship between CO_2 assimilation rate, A and the intercellular CO_2 partial pressure, C_i . The relationship between A and g_i is given by

$$A = g_i (C_i - C_c), \quad (9.27)$$

and solving for C_c and combining with Eq. (9.9) or Eq. (9.14) one obtains the following two quadratic equations:

$$A_c^2 - A_c \{ g_i (C_i + K_c (1 + O/K_o)) + V_{c\max} + R_d \} + g_i \{ V_{c\max} (C_i - \Gamma^*) - R_d (C_i + K_c (1 + O/K_o)) \} = 0 \quad (9.28)$$

and

$$A_j^2 - A_j \{ g_i (C_i + 2\Gamma^*) + J/4 + R_d \} + g_i \{ (C_i - \Gamma^*) J/4 - R_d (C_i + 2\Gamma^*) \} = 0. \quad (9.29)$$

The presence of a significant internal diffusion resistance to CO_2 affects both the quantitative relationship between CO_2 assimilation rate and maximal Rubisco activity and the shape of the CO_2 response curve. The internal conductance to CO_2 has been estimated in various ways: by concurrent measurements of carbon isotope discrimination (Evans et al., 1986; Von Caemmerer and Evans, 1991; Evans and Von Caemmerer, 1996; Hanba et al., 2004; Yamori et al., 2006a), by combined measurements of chlorophyll fluorescence and gas exchange (Evans and Von Caemmerer, 1996; Bernacchi et al., 2002; Flexas et al., 2006, 2007a; Warren and Dreyer, 2006; Warren, 2007) or by fitting Eqs. (9.27) and (9.28) to CO_2 response curves (Ethier and Livingston, 2004; Ethier et al., 2006; Sharkey et al., 2007). There is active research in examining the temperature response of g_i and it appears that g_i increases with temperature but there is species to species variation in this response (Bernacchi et al., 2002; Warren and Dreyer, 2006; Yamori et al., 2006a). A review of temperature dependencies was given by Warren (2008). There has been a recent report that suggests that g_i may vary with both $p\text{CO}_2$ and irradiance, which would make the approach of deriving g_i from a fit of Eqs. (9.28) and (9.29) invalid (Flexas et al., 2007a).

VI. Predicting Photosynthesis from Chloroplast Biochemistry

A. Environmental Responses

The model provides predictions on how the CO_2 assimilation rate varies with $p\text{CO}_2$, $p\text{O}_2$, irradiance and temperature. Many of these predictions were discussed by Farquhar et al. (1980) and one such example is given in Fig. 9.5, which shows the predicted CO_2 assimilation rate at different irradiances and $p\text{CO}_2$. The model predicts that CO_2 assimilation rate is independent of

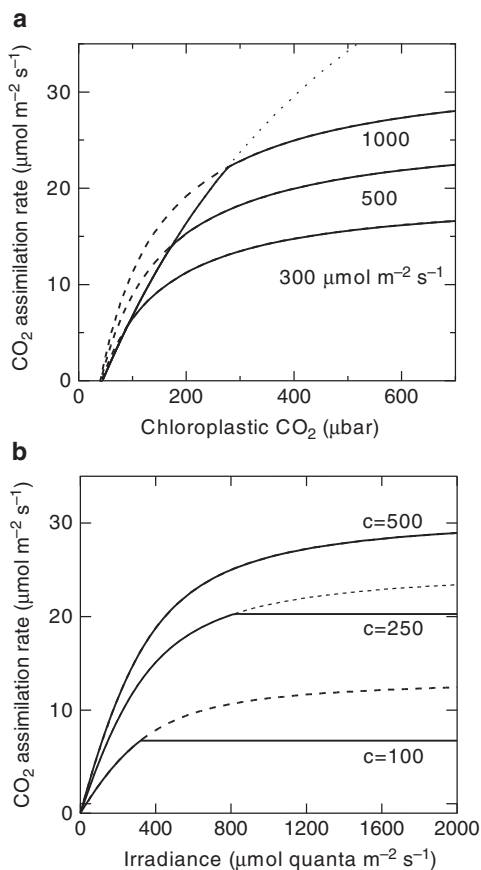


Fig. 9.5. (a) Modeled CO_2 assimilation rate (solid lines) as a function of chloroplast $p\text{CO}_2$ at three different irradiances. The extensions of the Rubisco limited rate A_c (dotted line) and the electron transport limited rate A_j (dashed lines) are also shown. Parameters used are given in Table 9.1. Leaf temperature was assumed to be 25°C and $p\text{O}_2 = 200$ mbar. (b) Modeled CO_2 assimilation rate (solid lines) as a function of irradiance at three different chloroplast $p\text{CO}_2$. The electron transport limited rates A_j (dashed lines) are also shown. Other details are as in (a)

irradiance (except at very low irradiance) at low pCO_2 where CO_2 assimilation rate is limited by (in this case) fully active Rubisco, whereas at high pCO_2 it is determined by the electron transport limited rate. This suggested that the initial slope of the CO_2 assimilation rate vs. pCO_2 curve can be quantitatively related to V_{cmax} as was done by Von Caemmerer and Farquhar (1981). The modeled irradiance response curves predict that the light saturation of CO_2 assimilation rate depends on pCO_2 , a fact which is often ignored. Model predictions can be tested by gas exchange measurements and are useful in planning experiments (Von Caemmerer and Farquhar, 1981). The model also predicted the measured changes in quantum yield with pCO_2 and temperature (Ehleringer and Björkman, 1977), the linear dependence of the CO_2 compensation point on O_2 partial pressure (Laing et al., 1974) and its dependence on respiration rate (Farquhar and Von Caemmerer, 1982). The ability of the model to accurately predict variation of CO_2 assimilation rate with temperature will depend on gaining a better understanding of the modulation of Rubisco activation state with temperature (see Section V.B.)

B. Photosynthesis for Photosynthetic Mutants

Recent advances in chloroplast transformation have made it possible to engineer tobacco expressing mutant Rubiscos (Whitney et al., 1999; Whitney and Andrews, 2003). Using the in vitro kinetic constants of those Rubiscos it was possible to use the model to predict the characteristics of the expected CO_2 assimilation rate of these plants (Fig. 9.6). Whitney et al. (1999) also used the model in the reverse direction and predicted Rubisco kinetic properties from gas exchange measurements. This example highlights the predictive power of the model. An elegant application of the model to the question of how will canopy photosynthesis be affected if we could engineer plants with different Rubiscos was given by Zhu et al. (2004), exemplifying the use of the model to answer a “what if” question.

C. Integration of the Leaf Photosynthesis Model with Stomatal Models

Photosynthesis and transpiration by leaves in nature is determined by the photosynthetic activity of the mesophyll cells within the leaf and by

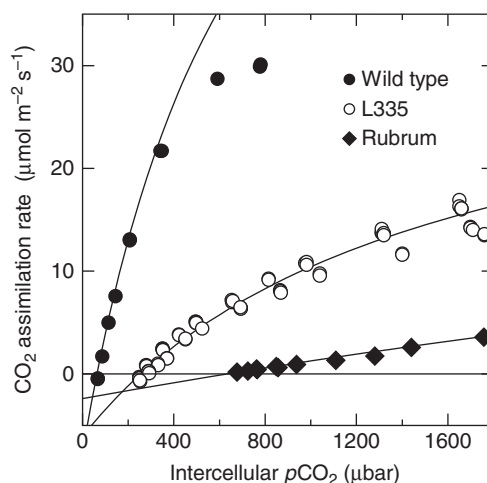


Fig. 9.6. CO_2 assimilation rate, A , as a function of intercellular pCO_2 for a leaf of a wild type (\bullet), transgenic tobacco with a mutant Rubisco where the Leu335 was changed to a Val (\circ), transgenic tobacco where native Rubisco was replaced by Rubisco from *Rhodospirillum rubrum* (\blacklozenge). Measurements were made at an irradiance of $1,000 \mu mol \text{ quanta m}^{-2} \text{ s}^{-1}$ and a leaf temperature of $25^\circ C$ at $pO_2 = 200 \text{ mbar}$. The lines are A predicted from the Rubisco limited rate (Eq. 9.9). For the L335 mutant tobacco $V_{cmax} = 37 \mu mol \text{ m}^{-2} \text{ s}^{-1}$, $K_c = 318 \mu bar$, $K_o = 55.6 \text{ mbar}$, $\Gamma^* = 140 \mu bar$ and $R_d = 2.5 \mu mol \text{ m}^{-2} \text{ s}^{-1}$. For the *R. rubrum* tobacco mutant $V_{cmax} = 42 \mu mol \text{ m}^{-2} \text{ s}^{-1}$, $K_c = 4,461 \mu bar$, $K_o = 126 \text{ mbar}$, $\Gamma^* = 415 \mu bar$ and $R_d = 1 \mu mol \text{ m}^{-2} \text{ s}^{-1}$ (Whitney et al., 1999; Whitney and Andrews, 2001; Mueller-Cajar et al., 2007)

the diffusive conductance of the epidermis that separates the intercellular air space from the surrounding atmosphere. Diffusion may be thought of as the supply function and biochemical processes as the demand function for CO_2 and the pCO_2 within the intercellular air spaces of the leaf is determined by the interaction of supply and demand. Figure 9.7 shows a graphical solution for the intercellular pCO_2 at which the rate of diffusion of CO_2 into the leaf exactly matches the rate of CO_2 uptake by the leaf cells. Given a value for conductance, the ambient pCO_2 , and the inputs required for the biochemical model, one can develop an analytical solution or use a computer program to seek the intercellular pCO_2 that satisfies both the supply and demand functions.

The biochemical model has been widely used in this way to examine physiological responses of leaves in natural environments (e.g. Tenhunen et al., 1994). However, a major limitation of this

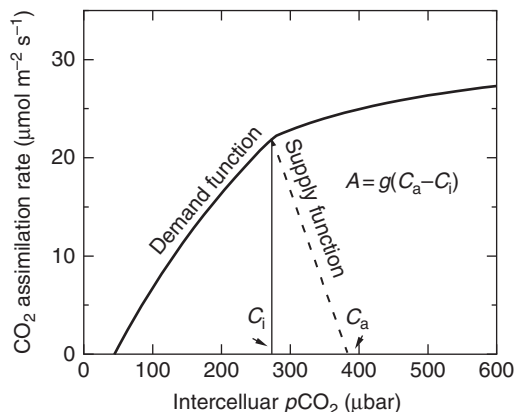


Fig. 9.7. CO_2 assimilation rate, A , versus intercellular $p\text{CO}_2$. The solid line indicates the “demand function” the dependence of A on intercellular $p\text{CO}_2$. The dashed line indicates the “supply function”, the equation describing the gaseous diffusion of CO_2 from the atmosphere to the intercellular spaces. In this diagram the $p\text{CO}_2$ at the site of carboxylation is assumed to be equal to the $p\text{CO}_2$ in the intercellular space

approach is that conductance itself is a dynamic and regulated property of the leaf. Variation of conductance can have very profound effects on energy and water exchange by leaves in nature, modifying not only the intercellular $p\text{CO}_2$, but also the physical environment (principally temperature and water potential) of the mesophyll cells. Therefore, an understanding of the full extent of physiological control of photosynthesis and transpiration of leaves in nature requires a second model capable of predicting stomatal conductance that could be coupled to the photosynthesis model.

Models of stomatal response to environmental variables had long been available (e.g. Jarvis, 1976; see also Collatz et al., 1991), but these considered conductance as separate from photosynthesis and proved difficult to integrate with a photosynthesis model. Systematic measurements of stomatal conductance and photosynthesis to changes in light, $p\text{CO}_2$, leaf temperature and atmospheric humidity were used by Ball et al. (1987) to develop an empirical relationship for stomatal conductance as a function of CO_2 assimilation rate:

$$g = m \cdot A \cdot h_s / C_s + b, \quad (9.30)$$

where m and b are regression coefficients, A is the rate of net CO_2 assimilation, and h_s and C_s

are the partial pressure of water vapor and CO_2 at the surface of the leaf – inside the laminar boundary layer. It is of interest that without some independent means of predicting the rate of photosynthesis, the Ball et al. model would have no predictive value. On the other-hand, when used together with a photosynthesis model the terms for the response to temperature, light intensity and leaf to leaf variation in humidity deficit and water potential used in other models of stomatal conductance (e.g. Jarvis, 1976) are subsumed in the response of A to these variables, making it easier to combine these models. This linkage of stomatal conductance to A was indicated by Wong et al. (1979, 1985), who showed that stomatal conductance of leaves during steady-state photosynthesis is strongly correlated with the rate of CO_2 assimilation, and it is consistent with the theoretical arguments on optimal control of stomatal conductance proposed by Cowan and Farquhar (1977).

Ball (1988), Tenhunen et al. (1990), Leuning (1990), Collatz et al. (1991, 1992) and Harley et al. (1992) developed coupled models of photosynthesis, transpiration and the leaf energy budget using the Ball et al. (1987) stomatal model and the Farquhar et al. (1980) photosynthesis model. Lloyd and Farquhar (1994) and Leuning et al. (1995) have developed alternative stomatal models for use in coupled model systems. These coupled models are now widely used to simulate carbon, water and energy exchange at the scale of fields (de Pury and Farquhar, 1997) ecosystems (Colello et al., 1998) and the globe (Randall et al., 1996).

Baldocchi (1994) proposed an analytical solution to a coupled system of models arguing that iterative solutions were unreliable. One factor contributing to this problem is that the approach of taking the minimum of the rates of the potential biochemical processes leads to discontinuities or “breaks” in the response curve at the transitions from one factor to the next (Fig. 9.1). Collatz et al. (1991) addressed this problem by using quadratic equations of the form

$$\theta J^2 - J(J_1 + J_2) + J_1 J_2 = 0, \quad (9.31)$$

where the value of J obtained from the root is the minimum of J_1 and J_2 with a smooth transition between these with a curvature in the transition

defined by the parameter, θ ($1 < \theta > 0$). Two quadratic equations can be used in sequence to select among three potential limitations. The C₃ and C₄ models presented by Collatz et al. (1991, 1992) are structured such that expressions for the potential limiting processes unique to each pathway are processed by identical quadratic expressions making it possible to easily switch between pathways in the same subroutine. This approach yields very similar answers to the original Farquhar et al. implementation with continuous functions of net CO₂ assimilation leading to robust iterative solutions.

D. Canopy Photosynthesis

Leaf models are now commonly used as a basis for simulating the water, carbon and energy exchange of plant canopies consisting of millions of leaves. Calibration of these models is largely based on leaf scale measurements with only limited constraint from measurements such as eddy correlation at the scale of application. The accuracy of such models is therefore highly dependent on the assumptions used in integrating from the leaf to the canopy scale. Heterogeneity in the thermal, aerodynamic and light climates within the canopy is important as is the corresponding heterogeneity in the property of leaves that develop in different positions within the canopy. This is a complex area that is beyond the scope of this review. The reader is referred to papers by de Pury and Farquhar (1999), Wang and Leuning (1999), Baldocchi et al. (2002) and to Chapter 16 by Ülo Niinemets and Niels P. R. Anten and Chapter 18 by Manfred Küppers and Michael Pfiz. Interestingly, this has become an important approach for simulating the conductance of vegetated land surfaces to water vapor. This is a critical parameter controlling the partitioning of absorbed radiation to sensible heat or evaporation of water – an important driver of the physical climate system. The reader is referred to Sellers et al. (1997) for a review of this topic.

VII. Predicting Chloroplast Biochemistry from Leaf Gas Exchange

The C₃ model is most often used to infer chloroplast biochemistry from gas exchange measurements (Ainsworth et al., 2002; Leuning, 2002;

Medlyn et al., 2002; Long and Bernacchi, 2003; Ethier and Livingston, 2004; Sharkey et al., 2007). Von Caemmerer and Farquhar (1981, 1984) compared in vitro measurements of Rubisco activity and chloroplast electron transport with gas exchange measurements and showed that they could be quantitatively related to gas exchange measurements made in *Phaseolus vulgaris* grown under different environmental conditions. It is often easier to infer leaf biochemistry from gas exchange measurements than make the required in vitro measurements especially since it is difficult to extract functional enzymes from many species. Long and Bernacchi (2003) provide an excellent review and discussion of how to best make these measurements. A routine that facilitates the fitting of gas exchange data has been provided by Sharkey et al. (2007).

It is possible to determine whether RuBP regeneration capacity (including electron transport capacity) limits CO₂ assimilation rate from measurements of CO₂ responses and calculations of the RuBP regeneration rate, as well as other fluxes, such as of FBP formation and consumption and electron transport rate required to support measured CO₂ assimilation rates (Farquhar and Von Caemmerer, 1982; Brooks and Farquhar, 1985; Von Caemmerer and Quick, 2000). An example is solving for the actual electron transport rate J_a using Eq. (9.14) as was done by Von Caemmerer and Farquhar (1981). It can be seen (Fig. 9.8) that J_a calculated from A increases with increasing intercellular $p\text{CO}_2$ and then becomes constant at higher C_i . A constant J_a can be taken as an indication of an electron transport limitation (although some caution is needed, especially at high irradiance, as other components of RuBP regeneration have the same relative dependencies on $p\text{CO}_2$ and $p\text{O}_2$). Triose phosphate limitation may also occur at high $p\text{CO}_2$, but should cause J_a to decrease with increasing $p\text{CO}_2$. Note that CO₂ assimilation rate continues to increase with increasing C_i as energy consumption is diverted from photorespiration to carboxylation. The calculated electron transport rate was confirmed with concomitant measurements of the quantum yield of PS II (ϕ_{PSII}) from chlorophyll fluorescence, which is proportional to chloroplast electron transport rate at a given irradiance (Genty et al., 1989).

Combined measurements of gas exchange and chlorophyll fluorescence have become a popular

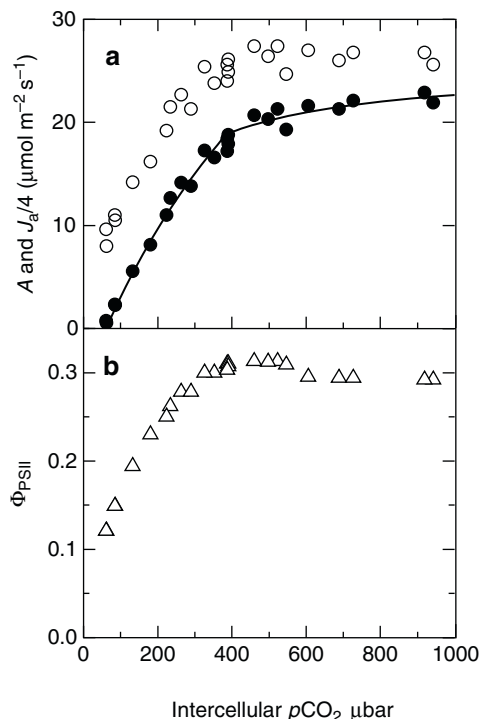


Fig. 9.8. (a) CO₂ assimilation rate, A , and calculated actual chloroplast electron transport rate, $J_a/4$, as functions of intercellular $p\text{CO}_2$ for a tobacco leaf. Measurements were made at an irradiance of $1,000 \mu\text{mol quanta m}^{-2} \text{s}^{-1}$, leaf temperature of 25°C and $p\text{O}_2 = 200 \text{ mbar}$. $J_a/4$ was calculated from CO₂ assimilation rate by estimating chloroplast $p\text{CO}_2$ from Eq. (9.26) with an internal conductance $g_i = 0.3 \text{ mol m}^{-2} \text{s}^{-1} \text{bar}^{-1}$ (data from Hudson et al., 1992). (b) The quantum yield of PS II (Φ_{PSII}) estimated from chlorophyll fluorescence measured concurrently with gas exchange. Chlorophyll fluorescence was measured on the adaxial surface and Φ_{PSII} was calculated according to Genty et al. (1989)

tool to assess chloroplast biochemistry (Long and Bernacchi, 2003). The chlorophyll fluorescence provides an excellent way to distinguish RuBP regeneration limited CO₂ assimilation rate from Rubisco limited rate, because chloroplast electron transport calculated from fluorescence becomes independent of $p\text{CO}_2$ when RuBP regeneration limits CO₂ assimilation rate (Fig. 9.8). We believe that this is a useful tool at low light or temperature extremes where it may be difficult to distinguish an RuBP regeneration limitation from a Rubisco limitation. The

quantitative comparison between CO₂ assimilation rate measurements and chlorophyll fluorescence measurements can however be more problematic as the two measurements average different chloroplast populations of the leaf.

If estimates of V_{cmax} and J are to be related to other leaf measurements such as nitrogen or chlorophyll content, it is important to also estimate the conductance to internal CO₂ diffusion as otherwise these parameters will be underestimated (Long and Bernacchi, 2003; Ethier and Livingston, 2004; Ethier et al., 2006; Warren, 2007). Careful measurements of CO₂ and light response curves over a range of temperature have been valuable in providing *in vivo* temperature responses for both Rubisco and electron transport parameters and provide a means for species comparisons (Kirschbaum and Farquhar, 1984; Von Caemmerer et al., 1994; Walcroft et al., 1997; Bernacchi et al., 2001, 2002, 2003).

VIII. Concluding Remarks

The photosynthesis model described here provides a quantitative framework that can be used as a research tool to design and interpret both field and laboratory based experiments. The papers cited here represent only a small fraction of studies that have used the model to interpret results. Both *in vivo* and *in vitro* studies have provided us with parameterization of the Rubisco limited CO₂ assimilation rate and studies with transgenic plants with mutant Rubiscos have highlighted the predictive power of the model in this regard. An elegant application of the model to the question of how will canopy photosynthesis be affected if we could engineer plants with different Rubiscos was given by Zhu et al. (2004), exemplifying the use of the model to answer “what if” questions. However there are three main areas where further research is needed. We need to learn more about what governs Rubisco activation *in vivo*, work towards a more mechanistic understanding of what determines chloroplast electron transport rate and the conductance to CO₂ diffusion from intercellular airspace to the chloroplast.

References

- Ainsworth EA, Davey PA, Hymus GJ, Drake BG and Long SP (2002) Long-term response of photosynthesis to elevated carbon dioxide in a Florida scrub-oak ecosystem. *Ecol Appl* 12: 1267–1275
- Andrews TJ and Lorimer GH (1987) Rubisco: structure, mechanisms, and prospects for improvement. In: Hatch MD and Boardman NK (eds) *The Biochemistry of Plants: A Comprehensive Treatise*, Vol 10, Photosynthesis, pp 131–218. Academic Press, New York
- Andrews TJ, Von Caemmerer S, Mate CJ, Hudson GS and Evans JR (1995) The regulation of Rubisco catalysis by Rubisco activase. In: Mathis P (ed) *Photosynthesis: from Light to Biosphere*, pp 17–22. Kluwer, Dordrecht
- Armond PA, Schreiber U and Björkman O (1978) Photosynthetic acclimation to temperature in the desert shrub *Larrea divaricata* II. Light-harvesting efficiency and electron transport. *Plant Physiol* 61: 411–415
- Atkin OK, Evans JR and Siebke K (1998) Relationship between the inhibition of leaf respiration by light and enhancement of leaf dark respiration following light treatment. *Aust J Plant Physiol* 25: 437–443
- Badger MR and Andrews TJ (1974) Effects of CO₂, O₂ and temperature on a high-affinity form of ribulose diphosphate carboxylase-oxygenase from spinach. *Biochem Biophys Res Commun* 60: 204–210
- Badger MR and Collatz GJ (1977) Studies on the kinetic mechanism of RuBP carboxylase and oxygenase reactions, with particular reference to the effect of temperature on kinetic parameters. *Carnegie Inst Wash Yearbook* 76: 355–361
- Badger MR, Von Caemmerer S, Ruuska S and Nakano H (2000) Electron flow to oxygen in higher plants and algae: rates and control of direct photoreduction (Mehler reaction) and rubisco oxygenase. *Phil Trans R Soc Lond - Ser B: Biol Sci* 355: 1433–1445
- Baldocchi D (1994) An analytical solution for coupled leaf photosynthesis and stomatal conductance models. *Tree Physiol* 14: 1069–1079
- Baldocchi DD, Wilson KB and Gu LH (2002) How the environment, canopy structure and canopy physiological functioning influence carbon, water and energy fluxes of a temperate broad-leaved deciduous forest—an assessment with the biophysical model CANOAK. *Tree Physiol* 22: 1065–1077
- Ball JT (1988) An analysis of stomatal conductance. Ph.D. thesis. Stanford University, Stanford, CA
- Ball TJ, Woodrow IE and Berry JA (1987) A model predicting stomatal conductance and its contribution to the control of photosynthesis under different environmental conditions. In: Biggins J (ed) *Progress in Photosynthesis Research*, pp 221–224. Martinus-Nijhoff, Dordrecht, The Netherlands
- Baroli I, Price GD, Badger MR and Von Caemmerer S (2008) The contribution of photosynthesis to the red light response of stomatal conductance. *Plant Physiol* 146: 737–747
- Bernacchi CJ, Singsaas EL, Pimentel C, Portis AR and Long SP (2001) Improved temperature response functions for models of Rubisco-limited photosynthesis. *Plant Cell Environ* 24: 253–259
- Bernacchi CJ, Portis AR, Nakano H, Von Caemmerer S and Long SP (2002) Temperature response of mesophyll conductance. Implications for the determination of Rubisco enzyme kinetics and for limitations to photosynthesis in vivo. *Plant Physiol* 130: 1992–1998
- Bernacchi CJ, Pimentel C and Long SP (2003) In vivo temperature response functions of parameters required to model RuBP-limited photosynthesis. *Plant Cell Environ* 26: 1419–1430
- Berry JA and Björkman O (1980) Photosynthetic response and adaptation to temperature in higher-plants. *Annu Rev Plant Physiol Plant Mol Biol* 31: 491–543
- Berry JA and Farquhar GD (1978) The CO₂ concentrating function of C₄ photosynthesis: a biochemical model. In: Hall D, Coombs J and Goodwin T (eds) *The Proceedings of the Fourth International Congress on Photosynthesis*, pp 119–131. Biochemical Society of London, London
- Björkman O (1968) Carboxydismutase activity in shade and sun adapted species of higher plants. *Physiol Plantarum* 21: 1–10
- Björkman O and Pearcy RW (1971) The effect of growth temperature on the temperature dependence of photosynthesis in vivo and on CO₂ fixation by carboxydismutase in vitro in C₃ and C₄ species. *Carnegie Inst Wash Yearbook* 70: 520–526
- Björkman O, Pearcy RW, Harrison AT and Mooney HA (1972) Photosynthetic adaptation to high temperatures: a field study in Death Valley, California. *Science* 175: 786–789
- Björkman O, Badger MR and Armond PA (1980) Response and adaptation of photosynthesis to high temperatures. In: Turner NC and Kramer PJ (eds) *Adaptation of Plants to Water and High Temperature Stress*, pp 233–249. Wiley, New York
- Bowes G (1991) Growth at elevated CO₂: photosynthetic responses mediated through Rubisco. *Plant Cell Environ* 14: 795–806
- Bowes G and Ogren WL (1972) Oxygen inhibition and other properties of soybean RuDP carboxylase. *J Biol Chem* 247: 2171–2176
- Bowes G, Ogren WL and Hageman RH (1971) Phosphoglycolate production catalyzed by ribulose diphosphate carboxylase. *Biochem Biophys Res Commun* 45: 716–722
- Brooks A and Farquhar GD (1985) Effect of temperature on the CO₂/O₂ specificity of ribulose-1,5-bisphosphate

- carboxylase oxygenase and the rate of respiration in the light—estimates from gas-exchange measurements on spinach. *Planta* 165: 397–406
- Butz ND and Sharkey TD (1989) Activity ratios of ribulose-1,5-bisphosphate carboxylase accurately reflect carbamylation ratios. *Plant Physiol* 89: 735–739
- Bykova NV, Keerberg O, Pärnik T, Bauwe H and Gardeström P (2005) Interaction between photorespiration and respiration in transgenic potato plants with antisense reduction in glycine decarboxylase. *Planta* 222: 130–140
- Cen YP and Sage RF (2005) The regulation of rubisco activity in response to variation in temperature and atmospheric CO₂ partial pressure in sweet potato. *Plant Physiol* 139: 979–990
- Colello GD, Grivet C, Sellers PJ and Berry JA (1998) Modeling of energy, water, and CO₂ flux in a temperate grassland ecosystem with SiB2: May–October 1987. *J Atmos Sci* 55: 1141–1169
- Collatz GJ (1978) The interaction between photosynthesis and ribulose-P₂ concentration – effects of light, CO₂, and O₂. *Carnegie Inst Wash Yearbook* 77: 248–251
- Collatz GJ, Berry JA, Farquhar GD and Pierce J (1990) The relationship between the Rubisco reaction mechanism and models of photosynthesis. *Plant Cell Environ* 13: 219–225
- Collatz GJ, Ball JT, Grivet C and Berry JA (1991) Physiological and environmental regulation of stomatal conductance, photosynthesis and transpiration – a model that includes a laminar boundary-layer. *Agric Forest Meteorol* 54: 107–136
- Collatz GJ, Ribas-Carbo M and Berry JA (1992) Coupled photosynthesis-stomatal model for leaves of C₄ plants. *Aust J Plant Physiol* 19: 519–538
- Cowan IR and Farquhar GD (1977) Stomatal function in relation to leaf metabolism and environment. *Symp Soc Exp Biol* 31: 317–345
- Crafts-Brandner SJ and Salvucci ME (2000) Rubisco activase constrains the photosynthetic potential of leaves at high temperature and CO₂. *Proc Natl Acad Sci USA* 97: 13430–13435
- de Pury DG and Farquhar GD (1997) Simple scaling of photosynthesis from leaves to canopies without the errors of big-leaf models. *Plant Cell Environ* 20: 537–557
- de Pury DG and Farquhar GD (1999) A commentary on the use of a sun/shade model to scale from the leaf to a canopy. *Agric Forest Meteorol* 95: 257–260
- Ehleringer J and Björkman O (1977) Quantum yields for CO₂ uptake in C₃ and C₄ plants. Dependence on temperature, CO₂ and O₂ concentration. *Plant Physiol* 59: 86–90
- Ellsworth DS, Reich PB, Naumburg ES, Koch GW, Kubiske ME and Smith SD (2004) Photosynthesis, carboxylation and leaf nitrogen responses of 16 species to elevated pCO₂ across four free-air CO₂ enrichment experiments in forest, grassland and desert. *Global Change Biol* 10: 2121–2138
- Ethier GJ and Livingston NJ (2004) On the need to incorporate sensitivity to CO₂ transfer conductance into the Farquhar-Von Caemmerer-Berry leaf photosynthesis model. *Plant Cell Environ* 27: 137–153
- Ethier GJ, Livingston NJ, Harrison DL, Black TA and Moran JA (2006) Low stomatal and internal conductance to CO₂ versus Rubisco deactivation as determinants of the photosynthetic decline of ageing evergreen leaves. *Plant Cell Environ* 29: 2168–2184
- Evans JR (1986) The relationship between carbon-dioxide-limited photosynthetic rate and ribulose-1,5-bisphosphate-carboxylase content in two nuclear-cytoplasm substitution lines of wheat, and the coordination of ribulose-bisphosphate-carboxylation and electron-transport capacities. *Planta* 167: 351–358
- Evans JR (1987) The dependence of quantum yield on wavelength and growth irradiance. *Aust J Plant Physiol* 14: 69–79
- Evans JR (1989) Photosynthesis and nitrogen relationships in leaves of C₃ plants. *Oecologia* 78: 9–19
- Evans JR and Von Caemmerer S (1996) Carbon dioxide diffusion inside leaves. *Plant Physiol* 110: 339–346
- Evans JR, Sharkey TD, Berry JA and Farquhar GD (1986) Carbon isotope discrimination measured concurrently with gas-exchange to investigate CO₂ diffusion in leaves of higher plants. *Aust J Plant Physiol* 13: 281–292
- Farquhar GD (1979) Models describing the kinetics of RuBP carboxylase-oxygenase. *Arch Biochem Biophys* 193: 456–468
- Farquhar GD and Von Caemmerer S (1982) Modelling of photosynthetic response to environmental conditions. In: Lange OL, Nobel PS, Osmond CB and Ziegler H (eds) *Physiological Plant Ecology II. Encyclopedia of Plant Physiology, New Series, Vol. 12 B*, pp 550–587. Springer, Berlin/Heidelberg
- Farquhar GD and Wong CS (1984) An empirical model of stomatal conductance. *Aust J Plant Physiol* 11: 191–210
- Farquhar GD, Von Caemmerer S and Berry JA (1980) A biochemical-model of photosynthetic CO₂ assimilation in leaves of C₃ species. *Planta* 149: 78–90
- Feller U, Craftsbrandner SJ and Salvucci ME (1998) Moderately high temperatures inhibit ribulose-1,5-bisphosphate carboxylase/oxygenase (Rubisco) activase-mediated activation of Rubisco. *Plant Physiol* 116: 539–546
- Feng L, Wang K, Li Y, Tan Y, Kong J, Li H and Zhu Y (2007) Overexpression of SBPase enhances photosynthesis against high temperature stress in transgenic rice plants. *Plant Cell Rep* 26: 1635–1646
- Flexas J, Ribas-Carbo M, Hanson DT, Bota J, Otto B, Cifre J, McDowell N, Medrano H and Kaldenhoff R (2006) Tobacco aquaporin NtAQP1 is involved in mesophyll conductance to CO₂ in vivo. *Plant J* 48: 427–439
- Flexas J, Diaz-Espejo A, Galmes J, Kaldenhoff R, Medrano H and Ribas-Carbo M (2007a) Rapid variations of mesophyll conductance in response to changes in CO₂

- concentration around leaves. *Plant Cell Environ* 30: 1284–1298
- Flexas J, Ribas-Carbo M, Diaz-Espejo A, Galmes J and Medrano H (2007b) Mesophyll conductance to CO₂: current knowledge and future prospects. *Plant Cell Environ* 31: 602–621
- Galmes J, Flexas J, Keys AJ, Cifre J, Mitchell RAC, Madgwick PJ, Haslam RP, Medrano H and Parry MAJ (2005) Rubisco specificity factor tends to be larger in plant species from drier habitats and in species with persistent leaves. *Plant Cell Environ* 28: 571–579
- Genty B, Briantais J-M and Baker N (1989) The relationship between the quantum yield of photosynthetic electron transport and quenching of chlorophyll fluorescence. *Biochim Biophys Acta* 990: 87–92
- Haldimann P and Feller U (2004) Inhibition of photosynthesis by high temperature in oak (*Quercus pubescens* L.) leaves grown under natural conditions closely correlates with a reversible heat-dependent reduction of the activation state of ribulose-1,5-bisphosphate carboxylase/oxygenase. *Plant Cell Environ* 27: 1169–1183
- Haldimann P and Feller U (2005) Growth at moderately elevated temperature alters the physiological response of the photosynthetic apparatus to heat stress in pea (*Pisum sativum* L.) leaves. *Plant Cell Environ* 28: 302–317
- Hall AE (1979) A model of leaf photosynthesis and respiration for predicting carbon dioxide assimilation in different environments. *Oecologia* 143: 299–316
- Hall AE and Björkman O (1975) A model of leaf photosynthesis and respiration. In: Gates DM and Schmerl R (eds) *Perspectives of biophysical ecology*, pp 55–72. Springer, Berlin
- Hanba YT, Shibasaka M, Hayashi Y, Hayakawa T, Kasamo K, Terashima I and Katsuhara M (2004) Overexpression of the barley aquaporin HvPIP2;1 increases internal CO₂ conductance and CO₂ assimilation in the leaves of transgenic rice plants. *Plant Cell Physiol* 45: 521–529
- Hanson KR and Peterson RB (1986) Regulation of photorespiration in leaves: evidence that the fraction of ribulose biphosphate oxygenated is conserved and stoichiometry fluctuates. *Arch Biochem Biophys* 246: 332–346
- Harley PC and Sharkey TD (1991) An improved model of C₃ photosynthesis at high CO₂: reversed O₂ sensitivity explained by lack of glycerate reentry into the chloroplast. *Photosynth Res* 27: 169–178
- Harley PC, Thomas RB, Reynolds JF and Strain BR (1992) Modelling photosynthesis of cotton grown in elevated CO₂. *Plant Cell Environ* 15: 271–282
- Hoefnagel MHN, Atkin OK and Wiskich JT (1998) Interdependence between chloroplasts and mitochondria in the light and the dark. *Biochim Biophys Acta Bioenergetics* 1366: 235–255
- Hudson GS, Evans JR, Von Caemmerer S, Arvidsson YBC and Andrews TJ (1992) Reduction of ribulose-1,5-bisphosphate carboxylase/oxygenase content by antisense RNA reduces photosynthesis in transgenic tobacco plants. *Plant Physiol* 98: 294–302
- Jarvis PG (1976) The interpretation of the variation in leaf water potential and stomatal conductance found in canopies in the field. *Phil Trans R Soc B-Biol Sci* 273: 593–610
- Jordan DB and Chollet R (1983) Inhibition of ribulose bisphosphate carboxylase by substrate ribulose 1,5-bisphosphate. *J Biol Chem* 258: 13752–13758
- June T, Evans JR and Farquhar GD (2004) A simple new equation for the reversible temperature dependence of photosynthetic electron transport: a study on soybean leaf. *Funct Plant Biol* 31: 275–283
- Kebeish R, Niessen M, Thiruveedhi, K, Bari, R, Hirsch HJ, Rosenkranz R, Stabler N, Schonfeld B, Kreuzaler F and Peterhansel C (2007) Chloroplastic photorespiratory bypass increases photosynthesis and biomass production in *Arabidopsis thaliana*. *Nat Biotechnol* 25: 593–599
- Kirschbaum MUF and Farquhar GD (1984) Temperature dependence of whole-leaf photosynthesis in *Eucalyptus pauciflora*. *Aust J Plant Physiol* 11: 519–538
- Ku SB and Edwards GE (1977) Oxygen inhibition of photosynthesis II. Kinetic characteristics affected by temperature. *Plant Physiol* 59: 991–999
- Kubien DS, Whitney SM, Moore PV and Jesson LK (2008) The biochemistry of Rubisco in *Flaveria*. *J Exp Bot* 59: 1767–1777
- Laing WA, Ogren WL and Hageman RH (1974) Regulation of soybean net photosynthetic CO₂ fixation by the interaction of CO₂, O₂, and ribulose 1,5-bisphosphate carboxylase. *Plant Physiol* 54: 678–685
- Laik A (1970) A model of leaf photosynthesis and photorespiration. In: Setlik I (ed) *Prediction and Measurement of Photosynthetic Productivity*, pp 295–306. Centre for Agricultural Publishing and Documentation (PUDOC), Wageningen
- Laik A (1977) Kinetics of Photosynthesis and Photorespiration in C₃ Plants. Nauka Publishing, Moscow (in Russian)
- Laik A and Oja V (1974) Leaf photosynthesis under short pulses of CO₂: the carboxylation reaction in vivo. *Fiziologija Rastenij (Soviet Plant Physiology)* 21: 1123–1131 (in Russian)
- Laik A and Oja V (1998) Dynamics of Leaf Photosynthesis: Rapid-Response Measurements and Their Interpretation. CSIRO Publishing, Collingwood, Australia
- Laik A, Eichelmann H and Oja V (2006) C₃ photosynthesis in silico. *Photosynth Res* 90: 45–66
- Lefebvre S, Lawson T, Zakhleniuk OV, Lloyd JC and Raines CA (2005) Increased sedoheptulose-1,7-bisphosphatase activity in transgenic tobacco plants stimulates photosynthesis and growth from an early stage in development. *Plant Physiol* 138: 451–460
- Leuning R (1990) Modelling stomatal behavior and photosynthesis of *Eucalyptus grandis*. *Aust J Plant Physiol* 17: 159–175

- Leuning R (1995) A critical appraisal of a combined stomatal-photosynthesis model for C_3 plants. *Plant Cell Environ* 18: 339–355
- Leuning R (2002) Temperature dependence of two parameters in a photosynthesis model. *Plant Cell Environ* 25: 1205–1210
- Lilley RM and Walker DA (1975) Carbon dioxide assimilation by leaves, isolated chloroplasts, and RuDP carboxylase from spinach. *Plant Physiol* 55: 1087–1092
- Lloyd J and Farquhar GD (1994) C^{13} Discrimination during CO_2 assimilation by the terrestrial biosphere. *Oecologia* 99: 201–215
- Lloyd J and Farquhar GD (2008) Effects of rising temperatures and $[CO_2]$ on the physiology of tropical forest trees. *Phil Trans R Soc Lond - Ser B: Biol Sci* 363: 1811–1817
- Long SP (1991) Modification of the response of photosynthetic productivity to rising temperature by atmospheric CO_2 concentrations: Has its importance been underestimated? *Plant Cell Environ* 14: 729–739
- Long SP and Bernacchi CJ (2003) Gas exchange measurements, what can they tell us about the underlying limitations to photosynthesis? Procedures and sources of error. *J Exp Bot* 54: 2393–2401
- Lorimer GH, Badger MR and Andrews TJ (1976) The activation of ribulose-1,5-bisphosphate carboxylase by carbon dioxide and magnesium ions. Equilibria, kinetics, a suggested mechanism and physiological implications. *Biochemistry* 15: 529–536
- Matsuoka M, Furbank RT, Fukayama H and Miyao M (2001) Molecular engineering of C_4 photosynthesis. *Annu Rev Plant Physiol Plant Mol Biol* 52: 297–314
- McMurtrie RE and Wang YP (1993) Mathematical models of the photosynthetic response of tree stands to rising CO_2 concentrations and temperatures. *Plant Cell Environ* 16: 1–14
- Medlyn BE, Dreyer E, Ellsworth, D, Forstreuter, M, Harley PC, Kirschbaum MUF, Le Roux X, Montpied P, Strassmeyer J, Walcroft A, Wang, K and Loustau D (2002) Temperature response of parameters of a biochemically based model of photosynthesis. II. A review of experimental data. *Plant Cell Environ* 25: 1167–1179
- Mitchell PL and Sheehy JE (2006) Supercharging rice photosynthesis to increase yield. *New Phytol* 171: 688–693
- Miyagawa Y, Tamoi M and Shigeoka S (2001) Overexpression of a cyanobacterial fructose-1,6-/sedoheptulose-1,7-bisphosphatase in tobacco enhances photosynthesis and growth. *Nat Biotechnol* 19: 965–969
- Mueller-Cajar O, Morell M and Whitney SM (2007) Directed evolution of Rubisco in *Escherichia coli* reveals a specificity-determining hydrogen bond in the form II enzyme. *Biochemistry* 46: 14067–14074
- Ögren E and Evans JR (1993) Photosynthetic light response curves. I. The influence of CO_2 partial pressure and leaf inversion. *Planta* 189: 182–190
- Pearcy RW, Gross LJ and He D (1997) An improved dynamic model of photosynthesis for estimation of carbon gain in sunfleck light regimes. *Plant Cell Environ* 20: 411–424
- Peisker M (1974) A model describing the influence of oxygen on photosynthetic carboxylation. *Photosynthetica* 8: 47–50
- Peisker M (1976) Ein Modell der Sauerstoffabhängigkeit des Photosynthetischen CO_2 -Gaswechsels von C_3 Pflanzen. *Kulturpflanze XXIV*: 221–235
- Portis AR (2003) Rubisco activase – Rubisco's catalytic chaperone. *Photosynth Res* 75: 11–27
- Portis AR and Parry MAJ (2007) Discoveries in Rubisco (Ribulose 1,5-bisphosphate carboxylase/oxygenase): a historical perspective. *Photosynth Res* 94: 121–143
- Price GD, Yu J-W, Von Caemmerer S, Evans JR, Chow WS, Anderson JM, Hurry V and Badger MR (1995) Chloroplast cytochrome *b6/f* and ATP synthase complexes in tobacco: transformation with antisense RNA against nuclear-encoded transcripts for the Rieske FeS and ATPd polypeptides. *Aust J Plant Physiol* 22: 285–297
- Price GD, Von Caemmerer S, Evans JR, Siebke K, Anderson JM and Badger MR (1998) Photosynthesis is strongly reduced by antisense suppression of chloroplastic cytochrome *b6/f* complex in transgenic tobacco. *Aust J Plant Physiol* 25: 445–452
- Quick WP, Schurr U, Scheibe R, Schulze E-D, Rodermeier SR, Bogorad L and Stitt M (1991) Decreased ribulose-1,5-bisphosphate carboxylase-oxygenase in transgenic tobacco transformed with “antisense” *rbcS*. I. Impact on photosynthesis in ambient growth conditions. *Planta* 183: 542–554
- Raines CA (2003) The Calvin cycle revisited. *Photosynth Res* 75: 1–10
- Raines CA (2006) Transgenic approaches to manipulate the environmental responses of the C_3 carbon fixation cycle. *Plant Cell Environ* 29: 331–339
- Randall DA, Dazlich DA, Zhang, C, Denning, AS, Sellers PJ, Tucker CJ, Bounoua, L, Los SO, Justice CO and Fung I (1996) A revised land surface parameterization (Sib2) for Gcms.3. The greening of the Colorado State University General Circulation Model. *J Climate* 9: 738–763
- Ruuska SA, Andrews TJ, Badger MR, Price GD and Von Caemmerer S (2000a) The role of chloroplast electron transport and metabolites in modulating rubisco activity in tobacco. Insights from transgenic plants with reduced amounts of cytochrome *b6/f* complex or glyceraldehyde 3-phosphate dehydrogenase. *Plant Physiol* 122: 491–504
- Ruuska SA, Badger MR, Andrews TJ and Von Caemmerer S (2000b) Photosynthetic electron sinks in transgenic tobacco with reduced amounts of Rubisco: little evidence for significant Mehler reaction. *J Exp Bot* 51: 357–368
- Sage RF (1990) A model describing the regulation of ribulose-1,5-bisphosphate carboxylase, electron transport, and triose phosphate use in response to light intensity and CO_2 in C_3 plants. *Plant Physiol* 94: 1728–1734
- Sage RF (2002) Variation in the k_{cat} of Rubisco in C_3 and C_4 plants and some implications for photosynthetic performance at high and low temperature. *J Exp Bot* 53: 609–620

- Sage RF, Sharkey TD and Seemann JR (1990) Regulation of ribulose-1,5-bisphosphate carboxylase activity in response to light intensity and CO₂ in the C₃ annuals *Chenopodium album* L. and *Phaseolus vulgaris* L. *Plant Physiol* 94: 1735–1742
- Sage RF, Santrucek J and Grise DJ (1995) Temperature effects on the photosynthetic response of C₃ plants to long-term CO₂ enrichment. *Vegetatio* 121: 67–77
- Salvucci ME and Crafts-Brandner SJ (2004a) Inhibition of photosynthesis by heat stress: the activation state of Rubisco as a limiting factor in photosynthesis. *Physiol Plantarum* 120: 179–186
- Salvucci ME and Crafts-Brandner SJ (2004b) Relationship between the heat tolerance of photosynthesis and the thermal stability of rubisco activase in plants from contrasting thermal environments. *Plant Physiol* 134: 1460–1470
- Sellers PJ, Randall DA, Collatz GJ, Berry JA, Field CB, Dazlich DA, Zhang C, Collelo GD and Bounoua L (1996a) A revised land surface parameterization (SiB2) for atmospheric GCMs. Part 1: Model formulation. *J Climate* 9: 676–705
- Sellers PJ, Los SO, Tucker CJ, Justice CO, Dazlich DA, Collatz GJ and Randall DL (1996b) A revised land surface parameterization (SiB2) for atmospheric GCMs. Part II: The generation of global fields of terrestrial biophysical parameters from satellite data. *J Climate* 9: 706–737
- Sellers PJ, Dickinson RE, Randall DA, Betts AK, Hall FG, Berry JA, Collatz GJ, Denning AS, Mooney HA, Nobre CA, Sato N, Field CB and Henderson-Sellers A (1997) Modeling the exchanges of energy, water, and carbon between continents and the atmosphere. *Science* 275: 502–509
- Sharkey TD (1985a) O₂-insensitive photosynthesis in C₃ plants - its occurrence and a possible explanation. *Plant Physiol* 78: 71–75
- Sharkey TD (1985b) Photosynthesis in intact leaves of C₃ plants: physics, physiology, and rate limitations. *Bot Rev* 51: 53–105
- Sharkey TD, Bernacchi CJ, Farquhar GD and Singsaas EL (2007) Fitting photosynthetic carbon dioxide response curves for C₃ leaves. *Plant Cell Environ* 30: 1035–1040
- Sharwood RE, Von Caemmerer S, Maliga P and Whitney SM (2008) The catalytic properties of hybrid Rubisco comprising tobacco small and sunflower large subunits mirror the kinetically equivalent source Rubiscos and can support tobacco growth. *Plant Physiol* 146: 83–96
- Stitt M and Sonnewald U (1995) Regulation of metabolism in transgenic plants. *Annu Rev Plant Physiol Plant Mol Biol* 46: 341–368
- Tcherkez G, Farquhar GD and Andrews TJ (2006) Despite slow catalysis and confused substrate specificity, all ribulose bisphosphate carboxylases may be nearly perfectly optimized. *Proc Natl Acad Sci USA* 103: 7246–7251
- Tcherkez G, Bligny R, Gout E, Mahe A, Hodges M and Cornic G (2008) Respiratory metabolism of illuminated leaves depends on CO₂ and O₂ conditions. *Proc Natl Acad Sci USA* 105: 797–802
- Tenhunen JD, Yocum CS and Gates DM (1976) Development of a photosynthesis model with an emphasis on ecological applications 1. Theory. *Oecologia* 26: 89–100
- Tenhunen JD, Sala Serra A, Harley PC, Dougherty RL and Reynolds JF (1990) Factors influencing carbon fixation and water use by mediterranean sclerophyll shrubs during summer drought. *Oecologia* 82: 381–393
- Tenhunen JD, Hanano R, Abril M, Weiler EW and Hartung W (1994) Above- and below-ground environmental influences on leaf conductance of *Ceanothus Thyrsiflorus* growing in a chaparral environment – drought response and the role of abscisic acid. *Oecologia* 99: 306–314
- Terashima I, Hanba YT, Tazoe Y, Vyas P and Yano S (2006) Irradiance and phenotype: comparative eco-development of sun and shade leaves in relation to photosynthetic CO₂ diffusion. *J Exp Bot* 57: 343–354
- Von Caemmerer S (2000) *Biochemical Models of Leaf Photosynthesis*. CSIRO Publishing, Collingwood, Australia
- Von Caemmerer S (2003) C₄ photosynthesis in a single C₃ cell is theoretically inefficient but may ameliorate internal CO₂ diffusion limitations of C₃ leaves. *Plant Cell Environ* 26: 1191–1197
- Von Caemmerer S and Edmondson DL (1986) Relationship between steady-state gas exchange, *in vivo* ribulose bisphosphate carboxylase activity and some carbon-reduction cycle intermediates in *Raphanus sativus*. *Aust J Plant Physiol* 13: 669–688
- Von Caemmerer S and Evans JR (1991) Determination of the average partial-pressure of CO₂ in chloroplasts from leaves of several C₃ plants. *Aust J Plant Physiol* 18: 287–305
- Von Caemmerer S and Farquhar GD (1981) Some relationships between the biochemistry of photosynthesis and the gas exchange of leaves. *Planta* 153: 376–387
- Von Caemmerer S and Farquhar GD (1984) Effects of partial defoliation, changes in irradiance during growth, short-term water stress and growth at enhanced p(CO₂) on the photosynthetic capacity of leaves of *Phaseolus vulgaris* L. *Planta* 160: 320–329
- Von Caemmerer S and Quick WP (2000) Rubisco: Physiology *in vivo*. In: Leegood RC, Sharkey TD and Von Caemmerer S (eds) *Photosynthesis: Physiology and Metabolism*, pp 85–113. Kluwer, Dordrecht, The Netherlands
- Von Caemmerer S, Evans JR, Hudson GS and Andrews TJ (1994) The kinetics of ribulose-1,5-bisphosphate carboxylase/oxygenase *in vivo* inferred from measurements of photosynthesis in leaves of transgenic tobacco. *Planta* 195: 88–97
- Walcroft AS, Whitehead D, Silvester WB and Kelliher FM (1997) The response of photosynthetic model parameters to temperature and nitrogen concentration in *Pinus radiata* D. Don. *Plant Cell Environ* 20: 1338–1348

- Wang YP and Leuning R (1999) Reply to a commentary on the use of a sun/shade model to scale from the leaf to canopy by D.G.G. de Pury and G.D. Farquhar. *Agric Forest Meteorol* 95: 261–265
- Wareing PF, Khalifa MM and Treharne KJ (1968) Rate-limiting processes in photosynthesis at saturating light intensities. *Nature* 220: 453–457
- Warren C (2007) Estimating the internal conductance to CO₂ movement. *Funct Plant Biol* 34: 82–114
- Warren CR (2008) Stand aside stomata, another actor deserves centre stage: the forgotten role of the internal conductance to CO₂ transfer. *J Exp Bot* 59: 1475–1487
- Warren CR and Dreyer E (2006) Temperature response of photosynthesis and internal conductance to CO₂: results from two independent approaches. *J Exp Bot* 57: 3057–3067
- Weis E (1981) The temperature-sensitivity of dark-inactivation and light-activation of the ribulose-1,5-bisphosphate carboxylase in spinach-chloroplasts. *FEBS Lett* 129: 197–200
- Weis E and Berry JA (1988) Plants and high temperature stress. *Symp Soc Exp Biol* 42: 329–346
- Whitehead D, Leathwick JR and Walcroft AS (2001) Modeling annual carbon uptake for the indigenous forests of New Zealand. *Forest Sci* 47: 9–20
- Whitney SM and Andrews TJ (2001) Plastome-encoded bacterial ribulose-1,5-bisphosphate carboxylase/oxygenase (RubisCO) supports photosynthesis and growth in tobacco. *Proc Natl Acad Sci USA* 98: 14738–14743
- Whitney SM and Andrews TJ (2003) Photosynthesis and growth of tobacco with a substituted bacterial rubisco mirror the properties of the introduced enzyme. *Plant Physiol* 133: 287–294
- Whitney SM, Von Caemmerer S, Hudson GS and Andrews TJ (1999) Directed mutation of the Rubisco large subunit of tobacco influences photorespiration and growth. *Plant Physiol* 121: 579–588
- Wise RR, Olson AJ, Schrader SM and Sharkey TD (2004) Electron transport is the functional limitation of photosynthesis in field-grown Pima cotton plants at high temperature. *Plant Cell Environ* 27: 717–724
- Wong SC, Cowan IR and Farquhar GD (1979) Stomatal conductance correlates with photosynthetic capacity. *Nature* 282: 424–426
- Wong SC, Cowan IR and Farquhar GD (1985) Leaf conductance in relation to rate of CO₂ assimilation. I Influence of nitrogen nutrition, phosphorus nutrition, photon flux density, and ambient partial pressure of CO₂ during ontogeny. *Plant Physiol* 78: 821–825
- Woodrow IE and Berry JA (1988) Enzymatic regulation of photosynthetic CO₂ fixation in C₃ plants. *Annu Rev Plant Physiol Plant Mol Biol* 39: 533–594
- Wright IJ, Reich PB, Westoby M, Ackerly DD, Baruch Z, Bongers F, Cavender-Bares J, Chapin T, Cornelissen JHC, Diemer M, Flexas J, Garnier E, Groom PK, Gulias J, Hikosaka K, Lamont BB, Lee T, Lee W, Lusk C, Midgley JJ, Navas ML, Niinemets U, Oleksyn J, Osada N, Poorter H, Poot P, Pyankov VI, Ronnet C, Thomas SC, Tjoelker MG, Veneklaas EJ and Villar R (2004) The worldwide leaf economics spectrum. *Nature* 428: 821–827
- Wullschlegel SD (1993) Biochemical limitations to carbon assimilation in C₃ plants - a retrospective analysis of the A/C_i curves from 109 species. *J Exp Bot* 44: 907–920
- Yamori W, Noguchi K and Terashima I (2005) Temperature acclimation of photosynthesis in spinach leaves: analyses of photosynthetic components and temperature dependencies of photosynthetic partial reactions. *Plant Cell Environ* 28: 536–547
- Yamori W, Noguchi K, Hanba YT and Terashima I (2006a) Effects of internal conductance on the temperature dependence of the photosynthetic rate in spinach leaves from contrasting growth temperatures. *Plant Cell Physiol* 47: 1069–1080
- Yamori W, Suzuki K, Noguchi K, Nakai M and Terashima I (2006b) Effects of Rubisco kinetics and Rubisco activation state on the temperature dependence of the photosynthetic rate in spinach leaves from contrasting growth temperatures. *Plant Cell Environ* 29: 1659–1670
- Yamori W, Noguchi K, Kashino Y and Terashima I (2008) The role of electron transport in determining the temperature dependence of the photosynthetic rate in spinach leaves grown at contrasting temperatures. *Plant Cell Physiol* 49: 583–591
- Yin X, Van Oijen M and Schapendonk A (2004) Extension of a biochemical model for the generalized stoichiometry of electron transport limited C₃ photosynthesis. *Plant Cell Environ* 27: 1211–1222
- Zelitch I (1989) Selection and characterization of tobacco plants with novel O₂-resistant photosynthesis. *Plant Physiol* 90: 1457–1464
- Zhu XG, Portis AR and Long SP (2004) Would transformation of C₃ crop plants with foreign Rubisco increase productivity? A computational analysis extrapolating from kinetic properties to canopy photosynthesis. *Plant Cell Environ* 27: 155–165
- Zhu XG, de Sturler E and Long SP (2007) Optimizing the distribution of resources between enzymes of carbon metabolism can dramatically increase photosynthetic rate: a numerical simulation using an evolutionary algorithm. *Plant Physiol* 145: 513–526

Chapter 10

Modeling the Temperature Dependence of C₃ Photosynthesis

Carl J. Bernacchi*

Photosynthesis Research Unit, USDA-ARS, Champaign, IL 61801, USA

David M. Rosenthal

Department of Plant Biology, University of Illinois, Champaign, IL 61801, USA; USDA-ARS, Photosynthesis Research Unit, Urbana, IL 61801, USA

Carlos Pimentel

Departamento de Fitotecnia, Universidade Federal Rural do Rio de Janeiro, Seropédica, 23851-970, Brazil

Stephen P. Long

Department of Plant Biology, University of Illinois, Urbana, IL 61801, USA

Graham D. Farquhar

Environmental Biology Group, Research School of Biological Sciences, Australian National University, Canberra City, Australian Capital Territory 2601, Australia

Summary.....	232
I. Introduction.....	232
II. Processes Limiting to C ₃ Photosynthesis.....	233
A. Rubisco-limited Photosynthesis.....	234
1. The Loss of Rubisco Activity at Higher Temperatures.....	235
2. Temperature Functions Associated with Rubisco-limited Photosynthesis.....	237
B. Ribulose 1,5-Bisphosphate (RuBP)-limited Photosynthesis.....	237
1. Temperature Acclimation of RuBP-limited Photosynthesis.....	239
2. Temperature Functions Associated with RuBP-limited Model.....	239
C. Triose Phosphate Utilization (TPU)-limited Photosynthesis.....	240
III. Modeling Photosynthesis and the Supply of CO ₂	240
A. Mitochondrial Respiration.....	241
B. Temperature Parameterizations for the Leaf Photosynthesis Model.....	242
IV. Concluding Remarks.....	242
Acknowledgments.....	243
References.....	243

* Author for correspondence, e-mail: bernacch@illinois.edu

Summary

The steady-state C_3 model of photosynthesis originally developed by Graham Farquhar et al. (1980) and subsequently modified by others describes responses of leaf carbon assimilation to environmental variation. This mechanistic model states that photosynthesis will be limited by the slowest of three biochemical processes: (1) the maximum rate of Rubisco-catalyzed carboxylation, (2) the rate of ribulose 1,5-bisphosphate (RuBP) regeneration via electron transport (J), or (3) the rate of RuBP regeneration via triose phosphate utilization (TPU). Each of these processes is modeled with parameters that have different responses to temperature; therefore accurate temperature functions are vital to model photosynthetic responses accurately, and they are critical to predict plant ecosystem responses to future predicted increases in temperature and CO_2 . Temperature functions used for modeling are frequently derived from Arrhenius equations, which describe changes in rate constants with temperature. Rubisco-limited photosynthesis is modeled using five parameters: two describe enzyme kinetics of carboxylation (V_{cmax} and K_c), one accounts for photorespiration (K_o), one for Rubisco specificity for CO_2 vs. O_2 (Γ^*) and one for mitochondrial respiration (R_d). At light saturation and current atmospheric CO_2 concentration, photosynthesis is usually carboxylation-limited. Two of the above parameters, Γ^* and R_d , are also used to model the rate of RuBP regeneration and follow the same temperature functions. The maximum rate of electron transport (J_{max}) is needed to model RuBP regeneration, which is particularly important at sub-saturating irradiance, higher temperatures, or supra ambient CO_2 concentrations, and is estimated by fitting the response of potential electron transport to light. Unlike the parameters that are dependent on the relatively conserved kinetic properties of Rubisco enzyme, electron transport is sensitive to environmental variation and can vary widely even within species. Triose phosphate limitation can occur at high CO_2 , low O_2 , high irradiance, or low temperature and is generally difficult to anticipate in field based experiments. Finally, consideration should be given to the supply of CO_2 to the site of carboxylation mediated by mesophyll conductance (g_m) when modeling photosynthetic responses to temperature, as g_m has been shown to vary with temperature, among species and growth conditions.

I. Introduction

The steady-state mechanistic model of C_3 photosynthetic carbon assimilation of Farquhar et al. (1980) is fundamental for predicting leaf responses to environmental variation (Long, 1991). This model provides the basis for scaling carbon uptake from leaves to canopies (Wang and Jarvis, 1990; Amthor, 1995; Lloyd and Farquhar, 1996; dePury and Farquhar, 1997; Wittig et al., 2005), ecosystems (Field and Avissar, 1998) and landscapes (Sellers et al., 1996, 1997). The leaf-level photosynthesis model is also a key component of earth system models (Cramer et al., 2001). Photosynthesis provides the ultimate source of energy for all organisms within terrestrial ecosystems, and models are currently available to predict how photosynthesis is altered by change

Abbreviations: A – net CO_2 uptake rate ($\mu\text{mol m}^{-2} \text{s}^{-1}$); c – scaling constant (unitless); C – CO_2 concentration ($\mu\text{mol mol}^{-1}$); C_c – CO_2 concentration in the chloroplast ($\mu\text{mol mol}^{-1}$); C_i – CO_2 concentration in the leaf intercellular airspaces ($\mu\text{mol mol}^{-1}$); g_{bl} – boundary layer conductance ($\text{mol m}^{-2} \text{s}^{-1}$); g_m – mesophyll diffusion conductance ($\text{mol m}^{-2} \text{s}^{-1} \text{bar}^{-1}$); g_s – stomatal conductance ($\text{mol m}^{-2} \text{s}^{-1}$); J_{max} – maximum light saturated rate of electron transport ($\mu\text{mol m}^{-2} \text{s}^{-1}$); K_c – Michaelis constant for carboxylation ($\mu\text{mol mol}^{-1}$); K_o – Michaelis constant for oxygenation (mmol mol^{-1}); O – oxygen concentration (mmol mol^{-1}); Q – photon flux density ($\mu\text{mol m}^{-2} \text{s}^{-1}$); R – universal gas constant ($\text{J K}^{-1} \text{mol}^{-1}$); R_d – respiratory CO_2 released via mitochondrial respiration in the light ($\mu\text{mol m}^{-2} \text{s}^{-1}$); $V_{c,max}$ – maximum rate of carboxylation of Rubisco ($\mu\text{mol m}^{-2} \text{s}^{-1}$); $V_{o,max}$ – maximum rate of oxygenation ($\mu\text{mol m}^{-2} \text{s}^{-1}$); ΔH_a – energy of activation (kJ mol^{-1}); ΔH_d – energy of deactivation (kJ mol^{-1}); Γ^* – photosynthetic CO_2 compensation point ($\mu\text{mol mol}^{-1}$); Φ_{PSII} – the maximum quantum yield of electron transport (unitless); Θ – the convexity of the transition between the initial slope and the plateau of the

hyperbola (unitless); Ω – the range of temperature in which J falls to $e^{-1} = 0.36$ from its optimum value ($^{\circ}\text{C}$); τ – Rubisco specificity factor (unitless).

in the environment. Given the importance of these models, its accuracy over a wide range of environmental conditions is important for predictions of carbon uptake over numerous scales from leaves to the globe. It is particularly critical that models make accurate predictions over a wide temperature range, as temperature is known to influence many aspects of the biochemical and biophysical reactions that determine rates of photosynthesis (Bernacchi et al., 2001). Accurate modeling is particularly important considering the impact anthropogenically-induced atmospheric and climate change is predicted to have on ecosystems around the globe (Solomon et al., 2007).

Both mean temperature and atmospheric CO₂ concentration are expected to continue increasing during the twenty-first century; therefore predicting photosynthetic changes in response to the interactive effects of rising CO₂ concentration and temperature is critical for understanding how best to manage ecosystems and maximize productivity in the future (Brennan et al., 2007). Growing C₃ plants at high temperature generally leads to a temperature acclimation which increases the thermal optimum for photosynthesis (Berry and Björkman, 1980). It is also well known that elevated CO₂ concentration stimulates photosynthesis by increasing the substrate for carboxylation and by competitively inhibiting oxygenation leading to photorespiration. Therefore the predicted increases in CO₂ and temperature over the next century (Solomon et al., 2007) are expected to have a synergistic effect on photosynthesis (Long, 1991).

Despite the extensive validation of the C₃ photosynthesis model, estimates of the biochemical parameters in the model became more limiting as temperatures deviated from 25 °C and, as originally parameterized, model accuracy decreased at higher and lower temperatures (Bernacchi et al., 2001, 2003). A number of studies have been published providing temperature responses for the parameters used in the photosynthesis model (McMurtrie and Wang, 1993; Harley and Baldocchi, 1995; Bernacchi et al., 2001, 2002, 2003), each with their specific strengths and weaknesses. The focus of this chapter is to provide a discussion of how in the photosynthesis model of Farquhar et al. (1980) CO₂ assimilation rate

responds to changes in temperature, with emphases on the temperature dependent parameters and the impact temperature has on the supply of CO₂ into the mesophyll. A complete description of the steady-state photosynthesis model was presented previously (Farquhar et al., 1980; Von Caemmerer, 2000), and an excellent review discussing a mechanistic understanding of the temperature responses of photosynthesis already exists (Sage and Kubien, 2007). Further, numerous modeling studies utilizing the photosynthesis models at multiple scales are available (Long, 1991; Harley and Baldocchi, 1995; Sellers et al., 1997; Wittig et al., 2005).

II. Processes Limiting to C₃ Photosynthesis

The C₃ steady-state photosynthesis model of Farquhar et al. (1980), building upon earlier work (Berry and Farquhar, 1978), reasons that photosynthesis will be limited by the slowest of two biochemical processes: (1) the maximum rate of ribulose 1,5-bisphosphate (RuBP) carboxylase/oxygenase (Rubisco) catalyzed carboxylation (Rubisco-limited) and (2) the regeneration of RuBP controlled by electron transport rate (RuBP-limited). The model presented by Farquhar et al. (1980) reasoned that the rate of carboxylation could not exceed the minimum of either of these two limitations, although the actual rate would be lower than either of these. Both ADP and NADP⁺, availability of which is dependent on the dark reactions, are required by the light reactions for the regeneration of ATP and NADPH. As ATP/ADP and NADPH/NADP⁺ provide a direct linkage between the ‘dark’ and ‘light’ reactions, the potential limitation imposed by the Calvin–Benson–Bassham cycle would likely impact both Rubisco- and RuBP-limited photosynthesis equally (e.g. Farquhar and Von Caemmerer, 1982). Therefore, for the purpose of modeling, it is assumed that photosynthesis is limited by only Rubisco or RuBP regeneration (Berry and Farquhar, 1978; Farquhar and Von Caemmerer, 1982; Chapter 9 of this book by Susanne von Caemmerer, Graham Farquhar and Josph Berry). A third limitation to leaf CO₂ uptake rate is the rate of inorganic phosphate release from the utilization of triose

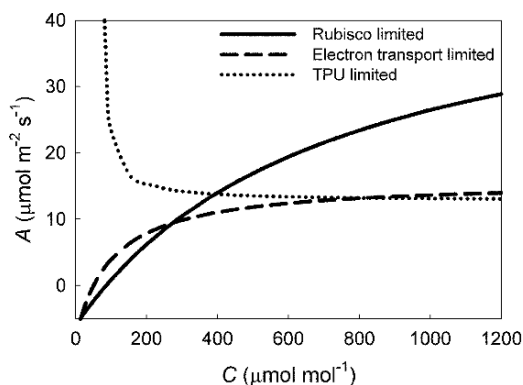


Fig. 10.1. Schematic representation of a photosynthesis (A) vs. CO_2 concentration (C) response curve at saturating light, demonstrating the three potential biochemical/biophysical limitations. Photosynthesis is assumed to operate at whichever limitation gives the lowest rate. At low CO_2 concentrations, the rate is limited by Rubisco, then by electron transport, and at very high CO_2 concentrations by triose phosphate utilization (TPU, dotted line)

phosphates, termed TPU- or P_i -limited photosynthesis (Sharkey, 1985).

The rate of carbon assimilation at any point in time equals the lowest potential rate of the three potential limitations under prevailing environmental conditions, as typically visualized using a photosynthetic CO_2 response curve (Fig. 10.1). We note that when chloroplastic CO_2 concentration is at or below the photosynthetic CO_2 compensation point (Γ^*), this assumption no longer holds. A complexity in modeling photosynthesis is that both CO_2 and O_2 compete for the same active site on Rubisco. Carboxylation of RuBP results in the assimilation of one molecule of CO_2 , resulting in two molecules of phosphoglycerate (PGA), which is a precursor to stored or transported carbohydrates. Oxygenation of RuBP, on the other hand, forms one PGA and one phosphoglycolate (PGly) (Bowes et al., 1971; Zelitch, 1971). The formation of PGly initiates photorespiration, where after oxygenation, one CO_2 is eventually released as a by-product (Berry and Farquhar, 1978; Ogren, 1984). Because CO_2 and O_2 compete for the same active site, the mechanistic model of photosynthesis relies on the kinetics of Rubisco regardless of which process limits photosynthesis (Portis, 1992). The complexity associated with the assimilation of CO_2 from photosynthesis and the release of CO_2 from photorespiration is further complicated by simul-

taneous CO_2 release from mitochondrial respiration in the light (Amthor, 1995). Each of the three processes has parameters that follow different temperature responses, which has traditionally made modeling photosynthesis with temperature difficult (Von Caemmerer, 2000). In the following sections, we will discuss the limiting processes of steady-state leaf photosynthesis with an emphasis on the parameters that are temperature dependent. We will also discuss the temperature functions commonly employed for each of the parameters associated with each limiting process.

A. Rubisco-limited Photosynthesis

The equation describing Rubisco-limited photosynthesis (Farquhar et al., 1980) is:

$$A = (1 - \Gamma^*/C) \left(\frac{C \cdot V_{c,\max}}{C + K_c(1 + O/K_o)} \right) - R_d, \quad (10.1)$$

where Γ^* is the photosynthetic CO_2 compensation point in the absence of mitochondrial respiration ($\mu\text{mol mol}^{-1}$), C is CO_2 concentration ($\mu\text{mol mol}^{-1}$), $V_{c,\max}$ is the maximum rate of carboxylation of Rubisco ($\mu\text{mol m}^{-2} \text{s}^{-1}$), K_c is the Michaelis constant for carboxylation ($\mu\text{mol mol}^{-1}$), O is the oxygen concentration (mmol mol^{-1}), and K_o is the Michaelis constant for oxygenation (mmol mol^{-1}). The equation represents Michaelis–Menten kinetics for an enzyme-catalyzed reaction between a substrate, CO_2 , and a competitive inhibitor, O_2 (Farquhar et al., 1980) with the term $(1 - \Gamma^*/C)$ representing the proportion of CO_2 that is assimilated relative to the amount of CO_2 that is originally fixed catalytically by Rubisco. Respiratory CO_2 released via mitochondrial respiration in the light is denoted R_d ($\mu\text{mol m}^{-2} \text{s}^{-1}$). Five parameters used in the Rubisco-limited photosynthesis model which represent Rubisco kinetics and mitochondrial respiration (Γ^* , $V_{c,\max}$, K_c , K_o , R_d) are temperature dependent, and thus the temperature responses incorporated into the model are critical for model accuracy (Von Caemmerer, 2000).

The terms K_c , K_o and $V_{c,\max}$ represent Rubisco enzyme kinetics, and Γ^* is derived from these terms and from the maximum rate of oxygenation ($V_{o,\max}$). Kinetic parameters have often

been derived from fits to *in vitro* data, but in *in vitro* conditions seldom represent those experienced *in vivo*. For example, changes in temperature have numerous implications for the internal conditions of the leaf, including pH, which can alter the activity of numerous enzymes including Rubisco (Bernacchi et al., 2001). A major challenge associated with *in vivo* determination of the Rubisco kinetics stems from the limited range of CO_2 in which photosynthesis is Rubisco-limited (Fig. 10.1). The initial portion of the *A* vs. *C* response curve corresponds with Rubisco-limited photosynthesis and consists of a range of CO_2 concentrations below the values of K_c and the rates below $0.5V_{c,\max}$. When fitting parameters characteristic to the range outside the CO_2 limited one (e.g. $V_{c,\max}$), small measurement errors can result in large errors in the derived kinetic parameters (Long and Bernacchi, 2003). This results in statistical challenges, further confounded by the large number of parameters that need to be solved (K_c , K_o , Γ^* , $V_{c,\max}$ and R_d).

Despite the complexities associated with solving for the values of the five parameters from the Rubisco-limited photosynthesis, the results have suggested that the Rubisco kinetic parameters (but not V_{\max}) are highly conserved among higher plants (Von Caemmerer, 2000; although this may not apply for all C_3 species and for all growth conditions, e.g., Galmés et al., 2005). The term $V_{c,\max}$ will vary among leaves within a plant, between plants and among species, even at a standard temperature (Wullschlegel, 1993), not speaking about its temperature-dependence. Values will depend on the total number of Rubisco sites active at a given temperature. The number of Rubisco sites is parameterized by the imposition of a particular value of $V_{c,\max}$ at a standard reference temperature. A function normalized to unity at the reference temperature will allow for $V_{c,\max}$ values to be determined over a wide temperature range from a value measured at a given temperature (Farquhar et al., 1980).

1. The Loss of Rubisco Activity at Higher Temperatures

An idealized curve showing how Rubisco-limited photosynthesis changes with temperature is provided in Fig. 10.2. The mechanism responsible for the observed decline in assimilation above

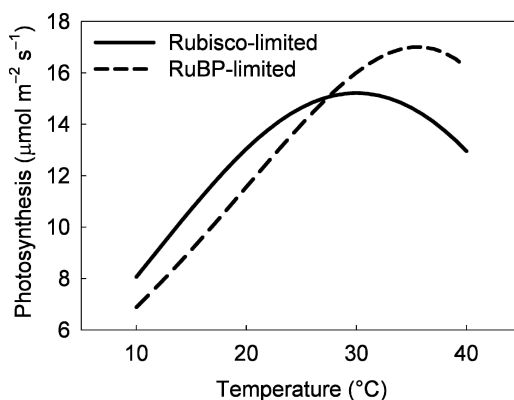


Fig. 10.2. Modeled photosynthetic carbon assimilation plotted as a function of temperature using the Rubisco-limited and the RuBP regeneration-limited photosynthesis model. The curves demonstrate that the rate-limiting process will vary with temperature at constant CO_2 concentration and light intensity. The temperature at which the transition of the rate-limiting process occurs varies (adapted from Kirschbaum and Farquhar, 1984; Cen and Sage, 2005)

the thermal optimum is dual. The first reason is the rapidly increasing affinity for O_2 relative to CO_2 binding to RuBP enediol form in the Rubisco active site (Farquhar et al., 1980). The higher affinity for O_2 results in relatively higher frequencies of oxygenation events at higher temperatures. The second reason is the loss of Rubisco activity due to the deactivation of Rubisco activase at temperatures above the thermal optimum, but below the temperature of enzyme denaturation (Weis, 1981; Kobza and Edwards, 1987; Crafts-Brandner and Salvucci, 2000, 2004; Portis, 2003; Salvucci and Crafts-Brandner, 2004a–c). Whether Rubisco deactivation occurs is currently the focus of debate (Crafts-Brandner and Salvucci, 2000; Salvucci and Crafts-Brandner, 2004a–c; Cen and Sage, 2005; Sage and Kubien, 2007; Sage et al., 2008); however, the implications of this process for modeling photosynthesis at higher temperatures are considered in this chapter.

Most parameters in the Rubisco-limited photosynthesis model (K_c , K_o , Γ^*) are not influenced by changes in the amount or activation state of Rubisco. However, $V_{c,\max}$ is linked directly to the number of active Rubisco sites. Thus conditions where Rubisco activity is predicted to decrease, such as supra-optimal temperatures, are critical to model accuracy. Many published datasets provide temperature responses of $V_{c,\max}$ using a

variety of techniques (Kirschbaum and Farquhar, 1984; McMurtrie and Wang, 1993; Medlyn et al., 1999; Bernacchi et al., 2001, 2003; Medlyn et al., 2002). If Rubisco is becoming progressively more limiting at temperatures above the thermal optimum as a result of a loss in Rubisco activase stabilization (Eckardt and Portis, 1997), then $V_{c,max}$ will begin to decrease at these temperatures. Of the published datasets, examples exist where $V_{c,max}$ begins to taper off or decrease, although most data suggests that the optimum temperature is reached above 37°C, if at all (Farquhar, 1979; Harley and Tenhunen, 1991; Harley et al., 1992b; Bernacchi et al., 2001, 2003; Medlyn et al., 2002; Pimentel et al., 2007). A lack of an apparent decrease in Rubisco activity in the *in vivo* temperature responses provided by Bernacchi et al. (2001, 2002) might

be attributed to the antisense construct in the transformant tobacco, which depressed Rubisco content to about 10% of wild-type concentrations without affecting Rubisco activase. In these plants, a 90% loss in the activity of Rubisco activase could therefore occur without affecting the Rubisco activation state. Other published temperature functions of $V_{c,max}$ listed above, as well as the temperature response of $V_{c,max}$ from *Citrus limon* (Fig. 10.3), indicate no decline at temperatures below the temperature at which denaturation of Rubisco occurs.

Although $V_{o,max}$ is shown to increase with temperature, the ratio of $V_{o,max}/V_{c,max}$ declines with temperature, showing that higher temperatures favor an increase in the velocity of carboxylation over oxygenation (Fig. 10.3; Bernacchi et al., 2001). However, the increase with temperature

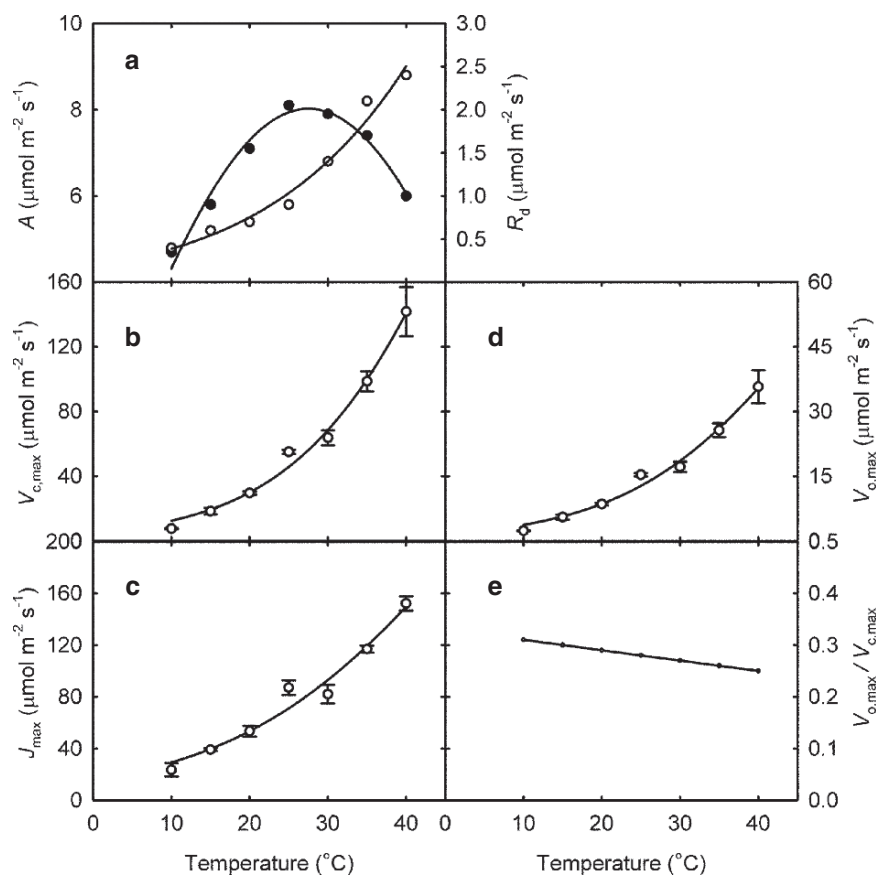


Fig. 10.3. Panel (a) shows representative temperature responses of photosynthesis and mitochondrial respiration in the light measured with *Citrus limon*. As a result of photorespiration, the temperature optimum of A is between 25°C and 30°C, whereas R_d continues to increase beyond 40°C. Panels (b–e) show the measured temperature responses of $V_{c,max}$ (b), $V_{o,max}$ (c), J_{max} (d), and the ratio of $V_{c,max}$ to J_{max} (e). A second order polynomial is fitted to A and Eq. (10.2) is fitted to the other parameters

in maximum rate of carboxylation is offset by changes in affinities of Rubisco for CO₂ and for O₂ (Long, 1991). The Michaelis constant for CO₂ (K_c) increases at a greater rate relative to the Michaelis constant for O₂ (K_o). This results in the affinity for CO₂ increasing slower with temperature than for O₂. The change in the relative enzyme affinities are substantial enough to more than compensate for the increase in $V_{c,max}$ with temperature.

2. Temperature Functions Associated with Rubisco-limited Photosynthesis

The temperature responses of the various model parameters have been described using temperature functions, most commonly Q_{10} (Farquhar et al., 1980), polynomial (Kirschbaum and Farquhar, 1984; McMurtrie and Wang, 1993), exponential (Badger and Collatz, 1977; Harley and Tenhunen, 1991; Bernacchi et al., 2001, 2002, 2003; Medlyn et al., 2002), and the normal distribution (June et al., 2004). Temperature functions for parameters that are based on Rubisco kinetic properties and do not have an optimum are expected to be similar among C₃ species and follow a temperature function which includes only a unitless scaling constant (c) and an energy of activation (ΔH_a , kJ mol⁻¹; Harley and Tenhunen, 1991):

$$Parameter = \exp[c - \Delta H_a / RT_k], \quad (10.2)$$

where R is the universal gas constant (8.314 J K⁻¹ mol⁻¹) and T_k is the leaf temperature (K). This approach simplifies Michaelis constants by assuming that the chemical reactions involved are completely dominated by one rate-limiting step. Equation (10.2) is also standardized to include only ΔH_a (Farquhar et al., 1980; Harley and Baldocchi, 1995):

$$Parameter = Parameter_{25} \exp\left[\frac{(T_k - 298)\Delta H_a}{RT_k 298}\right]. \quad (10.3)$$

Thus, the parameter at 25 °C represents a scaling constant similar to c in Eq. (10.2) and the term $Parameter_{25}$ has associated biological meaning (Harley and Baldocchi, 1995). The significance of ΔH_a in the context of these equations must also be carefully considered. The Michaelis con-

stant is a ratio of the combination of true kinetic constants. The use of an activation energy for it assumes that the 'off' reactions are dominated by a single rate step, which in this case is the formation of product. In situations where a single 'off' step is not dominating the rate, this approach will no longer be strictly applicable. The reverse carboxylation reaction is often thought to be very slow, allowing the temperature expression to be used with confidence. Nevertheless, the approximation probably works reasonably well even when there is significant reverse reaction.

The above Eqs. (10.2 and 10.3) predict that a given model parameter continues to increase exponentially with temperature and that thermal deactivation does not occur. Parameters are often decreasing at higher temperatures and require that the above equations be modified to include energy of deactivation (ΔH_d ; kJ mol⁻¹) and an entropy term (ΔS ; kJ K⁻¹ mol⁻¹) as suggested by Harley and Tenhunen (1991):

Parameter =

$$parameter_{25} \frac{\exp[c - \Delta H_a / RT_k]}{1 + \exp[(\Delta ST_k - \Delta H_d) / RT_k]}, \quad (10.4)$$

which again has been further modified to remove the scaling constant, c , as:

Parameter = $parameter_{opt}$

$$\times \frac{H_d \exp\{(\Delta H_a / R)[(1/T_{opt}) - (1/T_k)]\}}{H_d - H_a [1 - \exp\{(H_a / R)[(1/T_{opt}) - (1/T_k)]\}]}. \quad (10.5)$$

In this latter example, the $parameter_{opt}$ is the value of the parameter at its optimum temperature, (T_{opt}), in which the peak value is achieved. The above examples of temperature functions are not the only functions that have been utilized in determining temperature responses of the model parameters. Unlike polynomials, the functions above are derived from the Arrhenius equations which are based on activation energies.

B. Ribulose 1,5-Bisphosphate (RuBP)-limited Photosynthesis

Light saturation and current ambient CO₂ conditions surrounding the leaf commonly result in photosynthesis being Rubisco-limited. However,

in the natural environment, some leaves are not light-saturated for at least part of the day. For these leaves, the regeneration of RuBP will limit photosynthesis. Temperature is also shown to alter the control of photosynthesis from one limitation to another, and the point of transition varies substantially due to numerous factors (e.g. Fig. 10.2; Cen and Sage, 2005). Additionally, rising atmospheric CO₂ concentration promotes a shift from Rubisco-limited to RuBP-limited photosynthesis, even in saturating light (Fig. 10.1). For these reasons it is equally important to model this limiting process accurately.

It is widely accepted that the regeneration of RuBP is highly dependent on the capacity for electron flow on the chloroplast thylakoid (Evans, 1987; Ögren and Evans, 1993). The RuBP-limited photosynthetic condition of the model of Farquhar et al. (1980) couples RuBP-regeneration to the electron requirements of NADPH and ATP formation, as given by the equation:

$$A = (1 - \Gamma^*/C) \left(\frac{C \cdot J}{4C + 8\Gamma^*} \right) - R_d. \quad (10.6)$$

The potential of whole chain electron transport (J) is predicted as an empirical hyperbolic function of absorbed photon flux (Q) and the efficiency of photon use (Farquhar and Wong, 1984; Ögren and Evans, 1993). The relationship of J to Q is expressed using a non-rectangular hyperbolic response determined by three parameters: (1) J_{\max} , the maximum rate of electron transport, (2) Φ_{PSII} , the maximum quantum yield of electron transport, and (3) Θ , the convexity of the transition between the initial slope and the plateau of the hyperbola (Fig. 10.4). As visualized from Fig. 10.4, the relative importance of these parameters varies with Q : RuBP-limited photosynthesis is more dependent on Φ_{PSII} at lower Q , on Θ at moderate Q , and on J_{\max} at higher Q . While the temperature responses of these parameters are critical to modeling accurately RuBP-limited photosynthesis, Φ_{PSII} , and to a lesser extent Θ , is more critical at lower Q where photosynthetic rates are low. Thus, the model is generally less sensitive to errors in these two parameters than those in J_{\max} , associated with high photosynthetic rates.

In vitro measurements from isolated thylakoids have been used to estimate J_{\max} (Armond

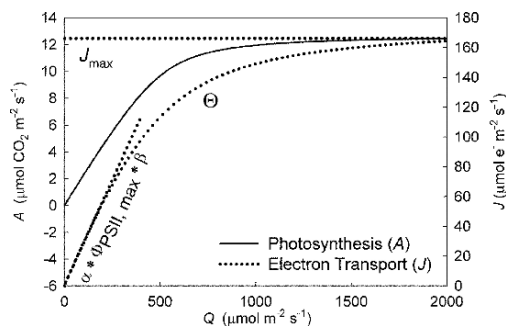


Fig. 10.4. Representation of the parameters required for modeling RuBP regeneration-limited photosynthesis, based on the response of electron transport (J) to incident photon flux (Q). As α and $\Phi_{\text{PSII}, \max}$ are dominant parameters at low light (thus low rates of photosynthesis), the model is less sensitive to errors associated with these than with J_{\max} .

et al., 1978; Sage et al., 1995); this technique assumes that the chemical environment of the assay reflects that of the thylakoid, yet large changes occur in vivo that may not be mimicked in vitro. Temperature responses of J_{\max} have been determined in vivo from gas-exchange measurements of photosynthesis A vs. leaf intercellular CO₂ concentration C_i (Harley and Tenhunen, 1991; McMurtrie and Wang, 1993; Harley and Baldocchi, 1995; Dreyer et al., 2001; Bernacchi et al., 2003). This method relies on fitting data measured at higher CO₂ concentrations to the RuBP-limited equation for photosynthesis from the Farquhar et al. (1980) model. Estimation of J_{\max} from A vs. C_i curves, however, may introduce errors since these curves are often measured at saturating light whereas the photosynthesis model should, in practice, mimic a wide range of conditions, including low light intensities. Model parameterization should also include the possibility that other parameters of the J vs. Q relationship may change with temperature. Changes in these parameters would be especially important when modeling light-limited photosynthesis. Most parameterizations assume Φ_{PSII} to remain constant at 0.85 and the convexity of the transition of J from low to high Q (Θ) to remain constant at 0.7 over a range of temperatures (Farquhar et al., 1980). Advances in gas exchange and fluorescence measurement techniques provided the opportunity to directly measure temperature responses of the parameters required to model RuBP-limited photosynthesis (Bernacchi et al., 2003). These methods provide

simultaneous yet independent measurements of carbon assimilation and electron transport through the thylakoid. Since the RuBP-limited model of photosynthesis predicts the rate of regeneration of RuBP based on the electron requirements for converting NADP to NADPH and ADP to ATP, the temperature responses of Φ_{PSII} and of Θ should be based on the relationship of J to Q (Bernacchi et al., 2003) rather than being derived from A vs. Q response curves (but see Cen and Sage, 2005).

1. Temperature Acclimation of RuBP-limited Photosynthesis

Unlike the parameters associated with the Rubisco-limited photosynthesis model, which are highly dependent on enzyme kinetics and generally conserved among C_3 plants, the parameters associated with the RuBP-limited photosynthesis model, particularly J_{max} , can be highly variable for different C_3 species (Wullschlegel, 1993) and for growth conditions, particularly temperature (Sage et al., 1995; Kitao et al., 2000; Von Caemmerer, 2000; Bernacchi et al., 2003; June et al., 2004). The mechanisms behind temperature acclimation of RuBP-limited photosynthesis likely involve changes in thermostability of thylakoid reactions (Berry and Björkman, 1980; Haldimann and Feller, 2005) driven by changes in membrane lipid composition (Raison et al., 1982; Mikami and Murata, 2003) and the possibility that certain Calvin–Benson–Bassham cycle enzymes (e.g. fructose 1,6-bisphosphatase) become limiting under certain circumstances (Badger et al., 1982; Hikosaka et al., 2006). While the mechanisms of acclimation of photosynthesis to temperature (Sage and Kubien, 2007), nutrients (June et al., 2004), and growth irradiance (Von Caemmerer and Farquhar, 1981) are discussed in detail elsewhere, it is critical to consider the variability these factors might induce on the temperature response of the parameters used to model RuBP-limited photosynthesis.

2. Temperature Functions Associated with RuBP-limited Model

Two parameters, Γ^* and R_d , are associated with Rubisco- as well as with RuBP-limited photosynthesis, and as such, their temperature responses

are identical whether they are used to model Rubisco- or RuBP-limited photosynthesis. The maximum potential electron transport rate at a particular irradiance (“potential” because it may exceed the actual electron transport rate when the assimilation rate is Rubisco-limited) is critically important for modeling RuBP-limited photosynthesis. As stated above, it is dependent on Φ_{PSII} and to some extent on J_{max} and Θ . Of these three parameters, J_{max} is the most critical for accurate modeling of high rates of photosynthesis, while errors in Φ_{PSII} and Θ can influence model predictions at relatively low light-limited rates of photosynthesis, having little impact on model output. Despite that, temperature responses have been published for both Φ_{PSII} and Θ in tobacco (Bernacchi et al., 2003). The results from this study show that Φ_{PSII} changes only with temperatures below 25 °C and is not altered by growth temperature, whereas Θ is temperature dependent over larger temperature ranges, also acclimating to growth temperature.

Many studies have provided temperature responses of J_{max} using a variety of different methods. While the number of equations used to describe the temperature response of J_{max} under varying growth conditions are many (Harley and Tenhunen, 1991; McMurtrie and Wang, 1993; Ögren and Evans, 1993; Von Caemmerer, 2000; Dreyer et al., 2001; Ziska, 2001; Bernacchi et al., 2003), a simple equation has been presented, accounting for the variation imposed by altered growth conditions (June et al., 2004). The equation expresses the rate of electron transport at a given temperature, $J(T_L)$, as:

$$J(T_L) = J(T_{\text{opt}})e^{-\left(\frac{T_L - T_{\text{opt}}}{\Omega}\right)^2}, \quad (10.7)$$

where $J(T_{\text{opt}})$ is the rate of electron transport at the optimum temperature, T_{opt} , and Ω is the range of temperature in which J falls to e^{-1} from its optimum value (June et al., 2004). While this temperature function has been shown to fit numerous published datasets, varying the parameters $J(T_{\text{opt}})$, T_{opt} and Ω within species and individual leaves provides the temperature response of J at high irradiance, but not of J_{max} . Simple equations have been employed to estimate J_{max} from J derived from Eq. (10.7) at a given irradiance (Farquhar and Wong, 1984; Ögren and Evans, 1993; Von Caemmerer, 2000; Bernacchi

et al., 2003). More experiments are needed to see whether Eq. (10.7) would also apply to J_{\max} directly.

C. Triose Phosphate Utilization (TPU)-limited Photosynthesis

Certain conditions result in photosynthesis being limited by the export and utilization of triose phosphate from the Calvin–Benson–Bassham cycle (Sharkey, 1985; Harley and Sharkey, 1991). This limiting process, termed triose phosphate utilization limited (TPU-limited) photosynthesis, most commonly occurs at high CO_2 , low O_2 , high irradiance, and/or low temperatures. Triose phosphates created during photosynthesis are mainly converted into starch in the chloroplast or exported into the cytosol and metabolized to sucrose (Leegood, 1996). As triose phosphates are utilized in the chloroplast, inorganic phosphate molecules are released and reused in photophosphorylation. Similarly, when triose phosphates are exported from the chloroplast, they are exchanged 1:1 with inorganic phosphate (Flügge et al., 2003). In cases where sugar phosphates are produced at rates higher than they are consumed, the pool of inorganic phosphate within the chloroplast becomes depleted to the level limiting photophosphorylation (Sharkey, 1985; Sharkey et al., 1986; Leegood and Furbank, 1986; Von Caemmerer, 2000). TPU-limited photosynthesis may result in much lower rates of RuBP regeneration than predicted from rates of electron transport using the RuBP-limited model.

The presence of TPU-limited photosynthesis is difficult to detect even under laboratory conditions. As demonstrated in the A vs. C_i response curves for *Citrus limon* (Fig. 10.5), the presence of TPU-limited photosynthesis is apparent at some measurement temperatures, but not at others. Despite similar laboratory conditions other than measurement temperature, TPU-limited photosynthesis is apparent at lower CO_2 for the measurements at 35°C than for any other measurement temperature. Despite the evidence of TPU-limited photosynthesis in experimental situations, there is little evidence for this limitation in field-based measurements (Reid and Fiscus, 1998; Adam et al., 2000). Since the TPU-limitation usually occurs in conditions that

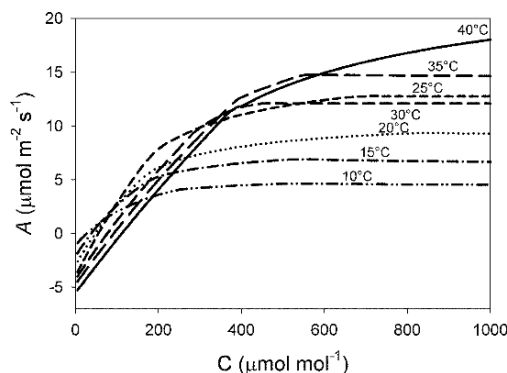


Fig. 10.5. Relationship between photosynthesis (A) and intercellular CO_2 concentration (C_i) for *Citrus limon* measured at temperatures ranging from 10°C to 40°C . This dataset demonstrates the influence of rising temperatures on Rubisco-limited (initial slopes), RuBP regeneration-limited (mid to high C_i), and TPU-limited (the highest C_i) photosynthesis. The latter indicates an unpredictable local minimum at 30°C .

are also typical of RuBP-limited photosynthesis (Sharkey, 1985; Harley and Sharkey, 1991), it is often difficult to differentiate between RuBP- and TPU-limited photosynthesis (e.g. Figs. 10.1 and 10.5).

III. Modeling Photosynthesis and the Supply of CO_2

In addition to the biochemical limitations discussed above, carbon supply is also physically limited at the leaf surface (boundary layer conductance g_{bl}), through the stomatal pore (stomatal conductance, g_s), across intercellular air spaces (Nobel, 2005), and from the surface of the mesophyll cells to the chloroplasts. Together, the two latter components are usually termed the ‘mesophyll diffusion conductance’, g_m . The stomatal conductance, g_s , may increase or remain unchanged in response to temperature changes (Sage and Kubien, 2007), and these responses appear to be independent of photosynthetic biochemistry (Kubien and Sage, 2008). Generally, in the absence of drought and at low leaf-to-air vapor pressure differences, stomatal limitations are largely unchanged at moderately high temperatures (Berry and Björkman, 1980). Modeling photosynthesis without accounting for g_s will overestimate rates of CO_2 uptake to a degree which will vary with environmental conditions.

Another important consideration for modeling photosynthesis is whether to base the model on CO_2 concentration in the leaf intercellular airspaces (C_i) or in the chloroplast (C_c). The importance of using C_i has long been known since g_s responds rapidly to changes in the environment surrounding the leaf (Farquhar and Sharkey, 1982). Historically, it was assumed that the differences between C_i and C_c were sufficiently small and could be ignored (Farquhar and Sharkey, 1982). However, as techniques were developed to address g_m , the conductance associated with the movement of CO_2 from the intercellular airspaces into the chloroplast (Evans et al., 1986; Harley et al., 1992a), it became apparent that g_m could represent a significant limitation to photosynthesis (Evans et al., 1986; Harley et al., 1992a; Loreto et al., 1992; Bernacchi et al., 2002).

Temperature affects various properties associated with cell walls, cytosol, chloroplast membrane, and the stroma, which together constitute g_m (Evans et al., 2004; Loreto et al., 2004; Nobel, 2005). Temperature can also influence the dissolution of CO_2 and its subsequent movement across plasma membranes, which is likely to be influenced by carbonic anhydrase and/or aquaporins (Price et al., 1994; Bernacchi et al., 2002; Terashima and Ono, 2002; Uehlein et al., 2003; Hanba et al., 2004). While the hydration of CO_2 and the following transport of bicarbonate can limit carbon uptake (Price et al., 1994), it appears that membrane transport is the main factor affecting the temperature response of g_m (Uehlein et al., 2003; Hanba et al., 2004).

Measured and estimated values of g_m demonstrate that it varies widely across species and with environmental conditions, but usually it is of sufficient magnitude to significantly affect calculated rates of photosynthesis (Ethier and Livingston, 2004; Warren, 2008). The temperature response of g_m varies across species and growth environments (Bernacchi et al., 2002; Pons and Welschen, 2003; Warren and Dreyer, 2006; Yamori et al., 2006; Diaz-Espejo et al., 2007; Warren et al., 2007). The temperature coefficient (Q_{10}) of g_m is approximately 2.2 for tobacco (Bernacchi et al., 2002), which is consistent with an enzyme-mediated process. Warren and Dreyer (2006) have measured the temperature response of g_m in *Quercus*

canariensis: while g_m increased at lower temperatures (from 10 °C to 20 °C), it was stable at higher temperatures (20–35 °C). Similarly, Yamori et al. (2006) showed that g_m increased almost twofold from 10 °C to 20 °C, but changed little at higher temperatures. The range of observed natural variation in g_m indicates that we should be cognizant of its effects when modeling photosynthetic carbon exchange.

Despite the increase in g_m with temperature, the limitation imposed on photosynthesis is shown to increase at higher temperatures (Bernacchi et al., 2002), which suggests the need to incorporate g_m into photosynthesis models. However, this necessity will depend on the objectives for using the model, as parameterizations based either on C_i or on C_c can be employed under different circumstances. Parameterizations based on C_i (e.g. Bernacchi et al., 2001) have changes in g_m confounded with changes in kinetics. It has been shown that photosynthetic capacity and g_m are coupled (Evans and Von Caemmerer, 1996), suggesting that model parameterization based on C_i may be appropriate under conditions where the coupling between g_m and photosynthesis is not expected to change (however the conditions where this assumption applies have not yet been fully elucidated). Modeling exercises where photosynthesis is scaled up from the leaf level may not require incorporation of g_m . However, if the model is employed for determination of V_{cmax} and/or J_{max} , observed differences between treatments may actually be caused by changes in g_m (Ethier and Livingston, 2004).

A. Mitochondrial Respiration

The three processes that limit photosynthesis each dominate under different conditions; however, mitochondrial respiration in the light (R_d) occurs under all conditions and is also shown to be highly temperature dependent (Farquhar et al., 1980; Von Caemmerer, 2000; Bernacchi et al., 2001; Atkin et al., 2005). Whereas the temperature optimum of photosynthesis is generally between 25 °C and 30 °C (as specified above), the temperature optimum of R_d over short timescales (minutes to hours) occurs just below the temperature at which thermal deactivation of enzymes occurs (generally above 42 °C,

e.g. Fig. 10.1). Therefore, modeling photosynthesis at any scale higher than the chloroplast requires that R_d be modeled independently. Traditionally, R_d is considered to follow a temperature function similar to that proposed for many of the photosynthesis parameters, namely that a value at a reference temperature is considered and an exponential function similar to Eq. (10.2) is applied (e.g. Bernacchi et al., 2001). Acclimation of R_d to temperature is shown to occur, and with the acclimation, it has been demonstrated that a generic exponential function normalized to a reference temperature may not represent both the pre- and post-acclimated temperature functions (Atkin et al., 2005). The impact of temperature acclimation of R_d is further complicated by the suppression of mitochondrial respiration in the light, and evidence also exists that changes in CO_2 and O_2 concentrations influence respiratory metabolism (Tcherkez et al., 2008). Despite the need to account for both temperature acclimation and impacts of changes in the environment surrounding the leaf on R_d , a mechanistic understanding – and thus a general model of R_d – is lacking. Therefore, at present, the above-described method in which a relative temperature response is scaled to a value at a reference temperature is utilized.

B. Temperature Parameterizations for the Leaf Photosynthesis Model

There exist a number of datasets providing temperature response functions for models of Rubisco-limited photosynthesis. The original parameterization of the model (Farquhar et al., 1980) incorporated values for the activation energy of $V_{c,\max}$, K_c , and K_o based on in vitro Rubisco enzyme activity (Badger and Collatz, 1977). From these values, the temperature response of Rubisco specificity between carboxylation and oxygenation (τ) and of the photosynthetic CO_2 compensation point (Γ^*) were calculated using the relationships:

$$\tau = \frac{V_{c,\max} K_o}{K_c V_{o,\max}} \quad (10.8)$$

and

$$\Gamma^* = \frac{0.5O}{\tau}. \quad (10.9)$$

The temperature responses provided by Badger and Collatz (1977) and a number of additional temperature responses (see Von Caemmerer, 2000) are based purely on in vitro measurements and thus do not accurately mimic the in vivo changes in the leaf which occur over a range of temperatures. Temperature response functions were compiled in the form of a review (McMurtrie and Wang, 1993), although the studies included in the review were also dominated by in vitro measurements.

In vivo kinetics using transgenic tobacco with reduced amounts of Rubisco have been used to determine kinetic constants at 25°C (Von Caemmerer et al., 1994) and over a biologically significant temperature range (Bernacchi et al., 2001). The benefit of using transgenic tobacco plants for parameterization is that photosynthesis is always limited by Rubisco, allowing for measurements at CO_2 concentrations above those of K_c , approaching $V_{c,\max}$. Since the kinetic parameters K_c , K_o and Γ^* are not influenced by the amount of enzyme present, values obtained from these transgenic species are applicable to wild-type plants. The absolute values of $V_{c,\max}$ are substantially lower in these transgenic plants; however, the relative temperature response of this parameter is, for the sake of modeling, generally assumed to be similar among higher C_3 species, allowing for these plants to provide more accurate temperature responses for the parameters needed to model Rubisco-limited photosynthesis. The temperature responses derived from these transgenic tobacco plants (Bernacchi et al., 2001) have been validated for a wide range of species.

IV. Concluding Remarks

The response of the net CO_2 uptake rate (A) to temperature is parabolic, and yet the temperature optimum is very plastic and can vary with species, ecotype, site and time of year (Baldocchi and Amthor, 2001). Depending on a wide range of conditions, including temperature, A can be limited by very different processes. The amount and activation state of photosynthetic enzymes, each representing a different limiting process to overall CO_2 assimilation, are integral for determining the temperature optimum of photosynthesis. Each of these limitations needs to be accurately modeled, and thus the temperature

functions accurately represented to provide realistic model output. The C_3 model of photosynthesis (Farquhar et al., 1980) has been used extensively for a variety of purposes, including predicting leaf, canopy, ecosystem, regional and global photosynthesis. The accuracy of the model is dependent on proper parameterization, which includes accurate representation of the parameters over a wide range of temperatures. The parameters incorporated into the model include a range of variables representing enzyme kinetics of Rubisco for both carboxylation and oxygenation as well as variables representing the rate of electron transport for regeneration of RuBP. The supply of CO_2 into the chloroplast, which is frequently temperature dependent, needs to be considered when parameterizing the photosynthesis model. Many parameterizations have been derived from both in vitro and in vivo techniques, with in vivo parameterizations preferred, as it is impossible to mimic the internal environment of the chloroplast in vitro, particularly over a wide range of temperatures.

Acknowledgments

The authors would like to thank George Hickman and Christina E. Burke for helpful comments on the manuscript and support from Integrative Photosynthesis Research training grant to CJB (NSF DBI96-02, 240).

References

- Adam NR, Wall GW, Kimball BA, Pinter PJ Jr, LaMorte RL, Hunsaker DJ, Adamsen FJ, Thompson T, Matthias AD, Leavitt SW and Webber AN (2000) Acclimation response of spring wheat in a free-air CO_2 enrichment (FACE) atmosphere with variable soil nitrogen regimes. 1. Leaf position and phenology determine acclimation response. *Photosynth Res* 66: 65–77
- Amthor JS (1995) Terrestrial higher-plant response to increasing atmospheric $[CO_2]$ in relation to the global carbon cycle. *Glob Change Biol* 1: 243–274
- Armond PA, Schreiber U and Bjorkman O (1978) Photosynthetic acclimation to temperature in the desert shrub *Larrea divericata*: light harvesting and electron transport. *Plant Physiol* 61: 411–415
- Atkin OK, Bruhn D, Hurry VM and Tjoelker MG (2005) The hot and the cold: unraveling the variable response of plant respiration to temperature. *Funct Plant Biol* 32: 87–105
- Badger MR and Collatz GJ (1977) Studies on the kinetic mechanism of Ribulose-1,5-bisphosphate carboxylase and oxygenase reactions, with particular reference to the effect of temperature on kinetic parameters. *Carnegie Inst Ann Report Dept Pl Bio* 76: 355–361
- Badger MR, Björkman O and Armond PA (1982) An analysis of photosynthetic response and adaptation to temperature in higher plants: temperature acclimation in the desert evergreen *Nerium oleander* L. *Plant Cell Environ* 5: 85–99
- Baldocchi DD and Amthor JS (2001) Canopy photosynthesis: history, measurements and models. In: Roy J, Saugier B and Mooney HA (eds) *Terrestrial Global Productivity*, pp 9–31. Academic, San Diego, CA
- Bernacchi CJ, Singaas EL, Pimentel C, Portis AR Jr and Long SP (2001) Improved temperature response functions for models of Rubisco-limited photosynthesis. *Plant Cell Environ* 24: 253–259
- Bernacchi CJ, Portis AR Jr, Nakano H, Von Caemmerer S and Long SP (2002) Temperature response of mesophyll conductance. Implications for the determination of Rubisco enzyme kinetics and for limitations to photosynthesis *in vivo*. *Plant Physiol* 130: 1992–1998
- Bernacchi CJ, Pimentel C and Long SP (2003) In vivo temperature response functions of parameters required to model RuBP-limited photosynthesis. *Plant Cell Environ* 26: 1419–1430
- Berry J and Björkman O (1980) Photosynthetic response and adaptation to temperature in higher plants. *Annu Rev Plant Physiol* 31: 491–543
- Berry JA and Farquhar GD (1978) The CO_2 concentrating function of C_4 photosynthesis. A biochemical model. In: Hall D, Coombs J and Goodwin T (eds) *Proceedings of 4th International Congress on Photosynthesis*, Reading, England, 1977, pp 119–131. The Biochemical Society, London
- Bowes G, Ogren WL, and Hageman RH (1971) Phosphoglycolate production catalyzed by ribulose diphosphate carboxylase. *Biochem Biophys Res Commun* 45: 716–722
- Brennan WJ, Kaye J, Leinen M, Dearry A, Elwood J, Glackin M, Gruber P, Hohenstein W, Lawson L, Leahy P, Neale P, Schafer J, Scherega J and Watson H (eds) (2007) *Our Changing Planet. The U.S. Climate Change Science Program for Fiscal year 2007. U.S. Global Change Research Program*, Washington, DC
- Cen Y-P and Sage RF (2005) The regulation of Rubisco activity in response to variation in temperature and atmospheric CO_2 partial pressure in sweet potato. *Plant Physiol* 139: 979–990
- Crafts-Brandner SJ and Salvucci ME (2000) Rubisco activase constrains the photosynthetic potential of leaves at high temperature and CO_2 . *Proc Natl Acad Sci USA* 97: 13430–13435
- Crafts-Brandner SJ and Salvucci ME (2004) Analyzing the impact of high temperature and CO_2 on net photosynthesis: biochemical mechanisms, models and genomics. *Field Crops Res* 90: 75–85

- Cramer W, Bondeau A, Woodward FI, Prentice IC, Betts RA, Brovkin V, Cox PM, Fisher V, Foley JA, Friend AD, Kucharik C, Lomas MR, Ramankutty N, Sitch S, Smith B, White A and Young-Molling C (2001) Global response of terrestrial ecosystem structure and function to CO₂ and climate change: results from six dynamic global vegetation models. *Glob Change Biol* 7: 357–373
- de Pury DGG and Farquhar GD (1997) Simple scaling of photosynthesis from leaves to simple canopies without the errors of big-leaf models. *Plant Cell Environ* 20: 537–557
- Diaz-Espejo A, Nicolas E and Fernandez JE (2007) Seasonal evolution of diffusional limitations and photosynthetic capacity in olive under drought. *Plant Cell Environ* 30: 922–933
- Dreyer E, Le Roux X, Montpied P, Daudet FA and Masson F (2001) Temperature response of leaf photosynthetic capacity in seedlings from seven temperate tree species. *Tree Physiol* 21: 223–232
- Eckardt NA and Portis AR Jr (1997) Heat denaturation profiles of ribulose-1,5-bisphosphate carboxylase/oxygenase (Rubisco) and Rubisco activase and the inability of Rubisco activase to restore activity of heat-denatured Rubisco. *Plant Physiol* 113: 243–248
- Ethier GJ and Livingston NJ (2004) On the need to incorporate sensitivity to CO₂ transfer conductance into the Farquhar-Von Caemmerer-Berry leaf photosynthesis model. *Plant Cell Environ* 27: 137–153
- Evans JR (1987) The Dependence of quantum yield on wavelength and growth irradiance. *Funct Plant Biol* 14: 69–79
- Evans JR and Von Caemmerer S (1996) Carbon dioxide diffusion inside leaves. *Plant Physiol* 110: 339–346
- Evans JR, Sharkey TD, Berry JA and Farquhar GD (1986) Carbon isotope discrimination measured concurrently with gas exchange to investigate CO₂ diffusion in leaves of higher plants. *Aust J Plant Physiol* 13: 281–292
- Evans JR, Terashima I, Hanba YT and Loreto F (2004) Chloroplast to leaf. In: Smith WK, Vogelmann TC and Critchley C (eds) *Photosynthetic Adaptation: Chloroplast to Landscape*, pp 107–132. Springer, New York
- Farquhar GD (1979) Models describing the kinetics of ribulose biphosphate carboxylase-oxygenase. *Arch Biochem Biophys* 193: 456–468
- Farquhar GD and Sharkey TD (1982) Stomatal conductance and photosynthesis. *Annu Rev Plant Physiol* 33: 317–345
- Farquhar GD and Von Caemmerer S (1982) Modeling of photosynthetic responses to environmental conditions. In: Lange OL, Nobel PS, Osmond CB and Zeigler H (eds) *Physiological Plant Ecology II. Encyclopedia of Plant Physiology, New Series*, pp 550–587. Springer, Heidelberg
- Farquhar GD and Wong SC (1984) An empirical model of stomatal conductance. *Aust J Plant Physiol* 11: 191–210
- Farquhar GD, Von Caemmerer S and Berry JA (1980) A biochemical model of photosynthetic CO₂ assimilation in leaves of C₃ species. *Planta* 149: 78–90
- Field CB and Avissar R (1998) Bidirectional interactions between the biosphere and the atmosphere- introduction. *Glob Change Biol* 4: 459–460
- Flügge UI, Häusler RE, Ludewig F and Fischer K (2003) Functional genomics of phosphate antiport systems of plastids. *Physiol Plantarum* 118: 475–482
- Galmés J, Flexas J, Keys AJ, Cifre J, Mitchell RAC, Madgwick PJ, Haslam RP, Medrano H and Parry MAJ (2005) Rubisco specificity factor tends to be larger in plant species from drier habitats and in species with persistent leaves. *Plant Cell Environ* 28: 571–579
- Haldimann P and Feller U (2005) Growth at moderately elevated temperature alters the physiological response of the photosynthetic apparatus to heat stress in pea (*Pisum sativum* L.) leaves. *Plant Cell Environ* 28: 302–317
- Hanba YT, Shibasaki M, Hayashi Y, Hayakawa T, Kasamo K, Terashima I and Katsuhara M (2004) Overexpression of the barley aquaporin HvPIP2;1 increases internal CO₂ conductance and CO₂ assimilation in the leaves of transgenic rice plants. *Plant Cell Physiol* 45: 521–529
- Harley PC and Baldocchi DD (1995) Scaling carbon dioxide and water vapour exchange from leaf to canopy in a deciduous forest. I. Leaf model parametrization. *Plant Cell Environ* 18: 1146–1156
- Harley PC and Sharkey TD (1991) An improved model of C₃ photosynthesis at high CO₂: reversed O₂ sensitivity explained by lack of glycerate reentry into the chloroplast. *Photosynth Res* 27: 169–178
- Harley PC and Tenhunen JD (1991) Modeling the photosynthetic response of C₃ leaves to environmental factors. In: Boote KJ and Loomis RS (eds) *Modeling Crop Photosynthesis: from Biochemistry to Canopy*, Special Publication No. 19, pp 17–39. Crop Science Society of America, Madison, WI
- Harley PC, Loreto F, Marco GD and Sharkey TD (1992a) Theoretical considerations when estimating the mesophyll conductance to CO₂ flux by analysis of the response of photosynthesis to CO₂. *Plant Physiol* 98: 1429–1436
- Harley PC, Thomas RB, Reynolds JF and Strain BR (1992b) Modelling photosynthesis of cotton grown in elevated CO₂. *Plant Cell Environ* 15: 271–282
- Hikosaka K, Ishikawa K, Borjigidai A, Muller O and Onoda Y (2006) Temperature acclimation of photosynthesis: mechanisms involved in the changes in temperature dependence of photosynthetic rate. *J Exp Bot* 57: 291–302
- June T, Evans JR and Farquhar GD (2004) A simple new equation for the reversible temperature dependence of photosynthetic electron transport: a study on soybean leaf. *Funct Plant Biol* 31: 275–283
- Kirschbaum MUF and Farquhar GD (1984) Temperature dependence of whole-leaf photosynthesis in *Eucalyptus pauciflora* Sieb. Ex Spreng. *Funct Plant Biol* 11: 519–538
- Kitao M, Lei TT, Koike T, Tobita H, Maruyama Y, Matsumoto Y and Ang L-H (2000) Temperature response

- and photoinhibition investigated by chlorophyll fluorescence measurements for four distinct species of dipterocarp trees. *Physiol Plantarum* 109: 284–290
- Kobza J and Edwards GE (1987) Influence of leaf temperature on photosynthetic carbon metabolism in wheat. *Plant Physiol* 83: 69–74
- Leegood RC (1996) Primary photosynthate production: physiology and metabolism. In: Zamski E and Schaffer AA (eds) *Photoassimilate Distribution in Plants and Crops. Source–Sink Relationships*, pp 21–42. Marcel Dekker, New York
- Leegood RC and Furbank RT (1986) Stimulation of photosynthesis by 2 percent oxygen at low temperature is restored by phosphate. *Planta* 168: 84–93
- Lloyd J and Farquhar GD (1996) The CO₂ dependence of photosynthesis, plant growth responses to elevated CO₂: concentrations and their interaction with soil nutrient status. 1. General principles and forest ecosystems. *Funct Ecol* 10: 4–32
- Long SP (1991) Modification of the response of photosynthetic productivity to rising temperature by atmospheric CO₂ concentrations: Has its importance been underestimated? *Plant Cell Environ* 14: 729–739
- Long SP and Bernacchi CJ (2003) Gas exchange measurements, what can they tell us about the underlying limitations to photosynthesis? Procedures and sources of errors. *J Exp Bot* 54: 2393–2401
- Loreto F, Harley PC, DiMarco G and Sharkey TD (1992) Estimation of mesophyll conductance to CO₂ flux by three different methods. *Plant Physiol* 98: 1437–1443
- Loreto F, Baker NR and Ort DR (2004) Chloroplast to Leaf. In: Smith WK, Vogelmann TC and Critchley C (eds) *Photosynthetic Adaptation: Chloroplast to Landscape*, pp 231–261. Springer, New York
- McMurtrie RE and Wang YP (1993) Mathematical models of the photosynthetic response of tree stands to rising CO₂ concentrations and temperature. *Plant Cell Environ* 16: 1–13
- Medlyn BE, Badeck FW, DePury DGG, Barton CVM, Broadmeadow M, Ceulemans R, DeAngelis P, Forstreuter M, Jach ME, Kellomaki S, Laitat E, Marek M, Philippot S, Rey A, Strassemeier J, Laitinen K, Liozon R, Portier B, Roberntz P, Wang K and Jarvis PG (1999) Effects of elevated [CO₂] on photosynthesis in European forest species: a meta-analysis of model parameters. *Plant Cell Environ* 22: 1475–1495
- Medlyn BE, Dreyer E, Ellsworth D, Forstreuter M, Harley PC, Kirschbaum MUF, Le Roux X, Montpied P, Strassemeier J, Walcroft A, Wang K and Loustau D (2002) Temperature response of parameters of a biochemically based model of photosynthesis. II. A review of experimental data. *Plant Cell Environ* 25: 1167–1179
- Mikami K and Murata N (2003) Membrane fluidity and the perception of environmental signals in cyanobacteria and plants. *Prog Lipid Res* 42: 527–543
- Nobel PS (2005) *Physicochemical and Environmental Plant Physiology*, 3rd Edition. Elsevier, Amsterdam
- Ögren E and Evans JR (1993) Photosynthetic light-response curves. *Planta* 189: 182–190
- Ogren WL (1984) Photorespiration: pathways, regulation, and modification. *Annu Rev Plant Physiol Plant Mol Biol* 35: 415–442
- Pimentel C, Bernacchi CJ and Long SP (2007) Limitations to photosynthesis at different temperatures in the leaves of *Citrus limon*. *Brazilian J Plant Physiol* 19: 141–147
- Pons TL and Welschen RAM (2003) Midday depression of net photosynthesis in the tropical rainforest tree *Eperua grandiflora*: contributions of stomatal and internal conductances, respiration and Rubisco functioning. *Tree Physiol* 23: 937–947
- Portis AR Jr (1992) Regulation of Ribulose-1,5-bisphosphate carboxylase/oxygenase activity. *Annu Rev Plant Physiol Plant Mol Biol* 43: 415–437
- Portis AR Jr (2003) Rubisco activase - Rubisco's catalytic chaperone. *Photosynth Res* 75: 11–27
- Price GD, Von Caemmerer S, Evans JR, Yu JW, Lloyd J, Oja V, Kell P, Harrison K, Gallagher A and Badger MR (1994) Specific reduction of chloroplast carbonic anhydrase activity by antisense RNA in transgenic tobacco plants has a minor effect on photosynthetic CO₂ assimilation. *Planta* 193: 331–340
- Raison JK, Pike CS and Berry JA (1982) Growth temperature-induced alterations in the thermotropic properties of *nerium-oleander* membrane lipids. *Plant Physiol* 70: 215–218
- Reid C and Fiscus E (1998) Effects of elevated [CO₂] and/or ozone on limitations to CO₂ assimilation in soybean (*Glycine max*). *J Exp Bot* 49: 885–895
- Sage RF and Kubien DS (2007) The temperature response of C₃ and C₄ photosynthesis. *Plant Cell Environ* 30: 1086–1106
- Sage RF, Santrucek J and Grise DJ (1995) Temperature effects on the photosynthetic response of C₃ plants to long-term CO₂ enrichment. *Vegetatio* 121: 67–77
- Sage RF, Way DA and Kubien DS (2008) Rubisco, Rubisco activase, and global climate change. *J Exp Bot* 59: 1581–1595
- Salvucci ME and Crafts-Brandner SJ (2004a) Inhibition of photosynthesis by heat stress: the activation state of Rubisco as a limiting factor in photosynthesis. *Physiol Plantarum* 120: 179–186
- Salvucci ME and Crafts-Brandner SJ (2004b) Mechanism for deactivation of Rubisco under moderate heat stress. *Physiol Plantarum* 122: 513–519
- Salvucci ME and Crafts-Brandner SJ (2004c) Relationship between the heat tolerance of photosynthesis and the thermal stability of Rubisco activase in plants from contrasting thermal environments. *Plant Physiol* 134: 1460–1470
- Sellers PJ, Bounoua L, Collatz GJ, Randall DA, Dazlich DA, Los SO, Berry JA, Fung I, Tucker CJ, Field CB and

- Jensen TG (1996) Comparison of radiative and physiological effects of doubled atmospheric CO₂ on climate. *Science* 271: 1402–1406
- Sellers PJ, Dickinson RE, Randall DA, Betts AK, Hall FG, Berry JA, Collatz GJ, Denning AS, Mooney HA, Nobre CA, Sato N, Field CB and Henderson-Sellers A (1997) Modeling the exchanges of energy, water, and carbon between continents and the atmosphere. *Science* 275: 502–509
- Sharkey TD (1985) O₂-insensitive photosynthesis in C₃ plants - its occurrence and a possible explanation. *Plant Physiol* 78: 71–75
- Sharkey TD, Stitt M, Heineke D, Gerhardt R, Raschke K and Heldt HW (1986) Limitation of photosynthesis by carbon metabolism. 2. O₂-insensitive CO₂ uptake results from limitation of triose phosphate utilization. *Plant Physiol* 81: 1123–1129
- Solomon S, Qin D, Manning M, Marquis M, Averyt K, Tignor MMB, Miller HL Jr and Chen Z (eds) (2007) *Climate Change 2007, The Physical Science Basis*. Cambridge University Press, Cambridge
- Tcherkez G, Bligny R, Gout E, Mahe A, Hodges M and Cornic G (2008). Respiratory metabolism of illuminated leaves depends on CO₂ and O₂ conditions. *Proc Natl Acad Sci USA* 105: 797–802
- Terashima I and Ono K (2002) Effects of HgCl₂ on CO₂ dependence of leaf photosynthesis: evidence indicating involvement of aquaporins in CO₂ diffusion across the plasma membrane. *Plant Cell Physiol* 43: 70–78
- Uehlein N, Lovisolo C, Siefritz F and Kaldenhoff R (2003) The tobacco aquaporin NtAQP1 is a membrane CO₂ pore with physiological functions. *Nature* 425: 734–737
- Von Caemmerer S (2000) *Biochemical Models of Leaf Photosynthesis*. Techniques in Plant Science, No 2. CSIRO Publishing, Collingwood, Victoria
- Von Caemmerer S and Farquhar GD (1981) Some relationships between the biochemistry of photosynthesis and the gas-exchange of leaves. *Planta* 153: 376–387
- Von Caemmerer S, Evans JR, Hudson GS and Andrews JT (1994) The kinetics of ribulose-1,5-bisphosphate carboxylase/oxygenase in vivo inferred from measurements of photosynthesis in leaves of transgenic tobacco. *Planta* 195: 88–97
- Wang YP and Jarvis PG (1990) Description and validation of an array model: MAESTRO. *Agric Forest Meteorol* 51: 257–280
- Warren CR (2008) Stand aside stomata, another actor deserves center stage: the forgotten role of the internal conductance to CO₂ transfer. *J Exp Bot* 59: 1475–1487
- Warren CR and Dreyer E (2006) Temperature response of photosynthesis and internal conductance to CO₂: results from two independent approaches. *J Exp Bot* 57: 3057–3067
- Warren CR, Low M, Matyssek R and Tausz M (2007) Internal conductance to CO₂ transfer of adult *Fagus sylvatica*: variation between sun and shade leaves and due to free-air ozone fumigation. *Environ Exp Bot* 59: 130–138
- Weis E (1981) The temperature sensitivity of dark-inactivation and light-activation of the Ribulose-1,5-Bisphosphate Carboxylase in spinach chloroplasts. *FEBS Lett* 129: 197–200
- Wittig VE, Bernacchi CJ, Zhu X-G, Calfapietra C, Ceulemans R, DeAngelis P, Gielen B, Miglietta F, Morgan PB and Long SP (2005) Gross primary production is stimulated for three *Populus* species grown under free-air CO₂ enrichment from planting through canopy closure. *Glob Change Biol* 11: 644–656
- Wullschleger SD (1993) Biochemical limitations to carbon assimilation in C₃ plants – a retrospective analysis of the A-C_i curves from 109 species. *J Exp Bot* 44: 907–920
- Yamori W, Noguchi K, Hanba YT and Terashima I (2006) Effects of internal conductance on the temperature dependence of the photosynthetic rate in spinach leaves from contrasting growth temperatures. *Plant Cell Physiol* 47: 1069–1080
- Zelitch I (1971) *Photosynthesis, Photorespiration, and Plant Productivity*. Academic, New York
- Ziska LH (2001) Growth temperature can alter the temperature dependent stimulation of photosynthesis by elevated carbon dioxide in *Albutilon theophrasti*. *Physiol Plantarum* 111: 322–328

Chapter 11

A Model of the Generalized Stoichiometry of Electron Transport Limited C₃ Photosynthesis: Development and Applications

Xinyou Yin*, Jeremy Harbinson and Paul C. Struik

Department of Plant Sciences, Wageningen University, The Netherlands

Summary.....	247
I. Introduction.....	248
II. Model Development.....	250
A. Stoichiometry of Electron Transport in the Farquhar-Von Caemmerer-Berry Model.....	250
B. A Contemporary View of Electron Transport in Thylakoids.....	251
C. The Generalized Stoichiometry of Electron Transport.....	252
D. Farquhar-Von Caemmerer-Berry Model as Special Cases of the Generalized Model.....	253
III. Model Applications.....	255
A. Potential Pitfalls of Existing Approaches.....	256
B. Unraveling Insights into Photosynthesis Physiology.....	257
1. On Conversion Efficiency of Incident Light into Linear Electron Transport.....	257
2. On Alternative Electron Transport Under Limiting Light.....	258
3. On Cyclic Electron Transport and Excitation Partitioning.....	260
4. On Cyclic as a Brake for Linear Electron Transport.....	262
5. On the Effect of Light Wavelength on Quantum Yield.....	263
C. An Integrated Approach to Estimating Photosynthesis Parameters.....	264
1. Quantum Yield of Photosystem II.....	265
2. Cyclic Electron Transport and Excitation Partitioning.....	265
3. Maximum Electron Transport Rate of Photosystem II.....	266
4. Mesophyll Diffusion Conductance and Rubisco Parameters.....	266
5. Additional Alternative Electron Flow.....	267
6. Partial Involvement of the Q-cycle.....	268
IV. Concluding Remarks.....	269
Acknowledgments.....	269
References.....	270

Summary

We describe an extended Farquhar, Von Caemmerer and Berry (FvCB) model for the RuBP regeneration-limited or electron transport-limited steady-state C₃ photosynthesis. Analytical algorithms are presented to account for (i) the effects of Photosystem (PS) I and II photochemical efficiencies and of cyclic electron transport around PS I (CET) on the photosynthetic quantum yields and related interphotosystem excitation partitioning, and (ii) CET and pseudocyclic electron transport (PET) that may act in concert with linear electron transport (LET, with or without the Q-cycle) to permit flexibility in the ratio of NADPH and ATP synthesis to meet the variable demands of the carbon reduction cycle and photorespiration. The two widely used forms of the original FvCB model represent the most and least

* Author for correspondence, e-mail: Xinyou.Yin@wur.nl

efficient electron transport stoichiometry, respectively, of special cases covered by the extended model. The generalized model integrates most basic elements of C_3 photosynthesis. The model implies that even within the electron transport-limited range the relationship between quantum yields of CO_2 assimilation and PS II photochemical efficiency is linear only if the latter varies in proportion with PS I photochemical efficiency. The model can be used (i) to assess any occurrence of alternative electron transport and to answer 'what-if' questions with respect to uncertain or unmeasured parameters, and (ii) to estimate photosynthetic parameters by curve-fitting to combined gas exchange and biophysical measurements (e.g. chlorophyll fluorescence) under various irradiance and CO_2 levels. As long as current biophysical measurements were accurate, our analyses support (i) the possible *in vivo* occurrence of CET and basal PET even under limiting irradiance, (ii) CET as a 'brake' for LET to accommodate the balance between quantum yields of electron transport and CO_2 assimilation, and (iii) the mode of a variable Q-cycle to obtain a correct NADPH/ATP ratio with varying light and CO_2 levels if no ATP from chloroplast is used for processes other than carbon reduction and photorespiration. Our model provides a tool to facilitate understanding the stoichiometries, bioenergetics and regulation of photosynthesis under different environmental conditions.

I. Introduction

Nearly 3 decades ago Farquhar et al. (1980) and Farquhar and Von Caemmerer (1982) published a biochemical model for steady-state C_3 photosynthetic rates (Chapter 9 of this book by Susanne von Caemmerer, Graham Farquhar and Joseph Berry). This model, referred to in this chapter as the FvCB model, predicts net photosynthesis A (see Table 11.1 for a full list of model variables and their units) as the minimum of the ribulose 1,5-bisphosphate (RuBP)-saturated, A_c , and the RuBP regeneration-limited, A_j , rate of CO_2 assimilation:

$$A = \min(A_c, A_j). \quad (11.1)$$

The value of A_c is calculated as a function of the maximum carboxylation capacity of Rubisco V_{cmax} by:

$$A_c = \frac{(C_c - \Gamma^*)V_{cmax}}{C_c + K_{mC}(1 + O/K_{mO})} - R_d, \quad (11.2)$$

Abbreviations: Chl – chlorophyll; CET – cyclic electron transport around PS I; e^- – electron; H^+ – proton; J_a – alternative electron transport rate of PS II; J_c – electron transport rate of PS II based on CO_2 uptake measurement; J_f – electron transport rate of PS II based on chlorophyll fluorescence measurement; LET – linear electron transport; N – nitrogen; PET – pseudocyclic electron transport; PETa – additional PET as occurred when the rubisco activity limits photosynthetic rate; PETb – basal PET; PS I – photosystem I; PS II – photosystem II; RuBP – Ribulose-1,5-bisphosphate; WWC – water-water cycle

where Γ^* is the CO_2 compensation point in the absence of R_d (the chloroplast CO_2 partial pressure at which photorespiratory CO_2 evolution equals carboxylation rate), which depends on the O_2 concentration O and the Rubisco CO_2/O_2 specificity factor $S_{c/o}$ as follows: $\Gamma^* = 0.5O/S_{c/o}$.

In the calculation of A_j the FvCB model assumes 100% noncyclic e^- transport, thus excluding cyclic e^- transport around PS I (CET). There are two widely used forms of the equation for RuBP regeneration-limited rate of photosynthesis:

$$A_j = \frac{(C_c - \Gamma^*)J}{4C_c + 8\Gamma^*} - R_d, \quad (11.3a)$$

$$A_j = \frac{(C_c - \Gamma^*)J}{4.5C_c + 10.5\Gamma^*} - R_d. \quad (11.3b)$$

Based on an analysis of Farquhar and Von Caemmerer (1981), the relationship between e^- transport rate J in Eqs. (11.3a, b) and irradiance was described as a rectangular hyperbola (Farquhar and Von Caemmerer, 1982) using the quantum yield of e^- transport under limiting light $\alpha_{(LL)}$ and the maximum capacity of e^- transport J_{max} . Following Farquhar and Wong (1984), however, most applications of the FvCB model describe J typically as a non-rectangular hyperbolic function of irradiance by

$$J = (\alpha_{(LL)}I_{abs} + J_{max}) - \sqrt{(\alpha_{(LL)}I_{abs} + J_{max})^2 - 4\theta J_{max}\alpha_{(LL)}I_{abs}} / (2\theta). \quad (11.4)$$

Table 11.1. Variables and units used in equations

Variable	Definition	Unit
a	Absorptance by leaf photosynthetic pigments	—
A	Net photosynthesis rate	$\mu\text{mol CO}_2 \text{ m}^{-2} \text{ s}^{-1}$
A_c	Rubisco activity limited net photosynthesis rate	$\mu\text{mol CO}_2 \text{ m}^{-2} \text{ s}^{-1}$
A_j	Electron transport limited net photosynthesis rate	$\mu\text{mol CO}_2 \text{ m}^{-2} \text{ s}^{-1}$
C_c	Chloroplast CO_2 partial pressure	μbar
C_i	Intercellular CO_2 partial pressure	μbar
f_{cyc}	Fraction of electrons at PS I that follow cyclic transport around PS I	—
f_{pseudo}	Fraction of electrons at PS I that follow pseudocyclic transport	—
$f_{\text{pseudo(a)}}$	Fraction of electrons at PS I that follow the additional pseudocyclic electron (e^-) transport if photosynthesis is limited by Rubisco activity	—
$f_{\text{pseudo(b)}}$	Fraction of electrons at PS I that follow the basal pseudocyclic e^- flow	—
$f_{\text{pseudo(wwc)}}$	Fraction of electrons at PS I that follow the pseudocyclic e^- flow in support of the water-water cycle	—
f_Q	Fraction of electrons at reduced plastoquinone that follow the Q-cycle	—
g_m	Mesophyll diffusion conductance	$\text{mol m}^{-2} \text{ s}^{-1} \text{ bar}^{-1}$
H	Number of protons required to produce one ATP	mol mol^{-1}
I_2	Photon flux density absorbed by Photosystem II	$\mu\text{mol photon m}^{-2} \text{ s}^{-1}$
I_{abs}	Photon flux density absorbed by leaf photosynthetic pigments	$\mu\text{mol photon m}^{-2} \text{ s}^{-1}$
I_{inc}	Photon flux density incident to leaves	$\mu\text{mol photon m}^{-2} \text{ s}^{-1}$
J	Linear plus additional pseudocyclic e^- transport rate through PS II	$\mu\text{mol e}^- \text{ m}^{-2} \text{ s}^{-1}$
J_2	Rate of e^- transport through PS II	$\mu\text{mol e}^- \text{ m}^{-2} \text{ s}^{-1}$
J_{max}	Maximum value of J under saturated light	$\mu\text{mol e}^- \text{ m}^{-2} \text{ s}^{-1}$
$J_{2\text{max}}$	Maximum value of J_2 under saturated light	$\mu\text{mol e}^- \text{ m}^{-2} \text{ s}^{-1}$
J_{NADP^+}	Linear e^- transport rate (i.e. rate with NADP^+ as end acceptor)	$\mu\text{mol e}^- \text{ m}^{-2} \text{ s}^{-1}$
K_{mC}	Michaelis–Menten constant for CO_2	μbar
K_{mO}	Michaelis–Menten constant for O_2	mbar
N	Leaf nitrogen content	g N m^{-2}
O	Oxygen partial pressure	mbar
R_d	Day respiration or mitochondrial respiration in the light	$\mu\text{mol CO}_2 \text{ m}^{-2} \text{ s}^{-1}$
s	A lumped parameter, see Eq. (11.12)	—
$S_{\text{c/o}}$	Relative CO_2/O_2 specificity factor for Rubisco	$\text{mbar } (\mu\text{bar})^{-1}$
v_{H^+}	Flux of protons across the thylakoid membrane	$\mu\text{mol proton m}^{-2} \text{ s}^{-1}$
V_{cmax}	Maximum rate of Rubisco activity-limited carboxylation	$\mu\text{mol CO}_2 \text{ m}^{-2} \text{ s}^{-1}$
$\alpha_{\text{(LL)}}$	Quantum efficiency of J under strictly limiting light, on the combined PS I- and PS II-absorbed light basis	$\text{mol e}^- (\text{mol photon})^{-1}$
α_2	Quantum efficiency of J_2 , on both PS I- and PS II-absorbed light basis	$\text{mol e}^- (\text{mol photon})^{-1}$
$\alpha_{2\text{(LL)}}$	Quantum efficiency of J_2 under strictly limiting light, on the combined PS I- and PS II-absorbed light basis	$\text{mol e}^- (\text{mol photon})^{-1}$
κ_2	Conversion efficiency of incident light into J	$\text{mol e}^- (\text{mol photon})^{-1}$
$\kappa_{2\text{(LL)}}$	Value of κ_2 at the strictly limiting light	$\text{mol e}^- (\text{mol photon})^{-1}$
θ	Convexity factor for response of J to absorbed light	—
θ_2	Convexity factor for response of J_2 to absorbed light	—
ρ_2	Proportion of absorbed light partitioned to PS II	—
Φ_1	Quantum efficiency of PS I e^- flow on PS I-absorbed light basis	$\text{mol e}^- (\text{mol photon})^{-1}$
$\Phi_{1\text{(LL)}}$	Value of Φ_1 at the strictly limiting light level	$\text{mol e}^- (\text{mol photon})^{-1}$
Φ_2	Quantum efficiency of PS II e^- flow on PS II-absorbed light basis	$\text{mol e}^- (\text{mol photon})^{-1}$
$\Phi_{2\text{(LL)}}$	Value of Φ_2 at the strictly limiting light level	$\text{mol e}^- (\text{mol photon})^{-1}$
Φ_{CO_2}	Quantum efficiency of CO_2 assimilation on the I_{abs} basis	$\text{mol CO}_2 (\text{mol photon})^{-1}$
$\Phi_{\text{CO}_2\text{(LL)}}$	Value of Φ_{CO_2} at strictly limiting light	$\text{mol CO}_2 (\text{mol photon})^{-1}$
Φ_{O_2}	Quantum efficiency of O_2 evolution on the I_{abs} basis	$\text{mol O}_2 (\text{mol photon})^{-1}$
$\Phi_{\text{O}_2\text{(LL)}}$	Value of Φ_{O_2} at strictly limiting light	$\text{mol O}_2 (\text{mol photon})^{-1}$
Γ_*	Chloroplast CO_2 compensation point in the absence of R_d	μbar

The FvCB model makes no attempt to model all the processes of photosynthesis from light harvesting to metabolism; rather it focuses on a small number of key processes that dominate photosynthesis. Because of its high performance/complexity ratio, the FvCB model has been widely used in diverse roles, from analyzing underlying leaf biochemistry to predicting photosynthetic fluxes of ecosystems in response to global warming.

There is, however, an ambiguity in the calculation of A_j , as shown by the use of Eqs. (11.3a, b). In applying the FvCB model, some (e.g. Ethier et al., 2006) used Eq. (11.3a), whereas others (e.g. Wong and Woo, 1986) used Eq. (11.3b), with little explanation why one form was preferred to the other. Equations (11.3a, b) were derived by assuming that noncyclic e^- transport was the only photosynthetic e^- transport process active in leaves. This assumption results in two possible outcomes: either the NADPH or the ATP supply will limit overall photosynthesis, applying to Eqs. (11.3a, b), respectively. Furthermore, Eq. (11.3a) assumes 100% LET – the noncyclic e^- flux used for carbon reduction and photorespiration. Equation (11.3b) implies that in addition to LET there is some pseudocyclic e^- transport PET, which is defined for use in the models presented here as the noncyclic e^- flux not used for carbon reduction and photorespiration. The difference between Eqs. (11.3a, b) implies that ATP production is more limiting than NADPH supply. So, in Eq. (11.3b) PET was assumed to occur in vivo with the result that NADPH and ATP supplies co-limit metabolism.

In chloroplasts, alternative e^- transport pathways other than PET may also occur to contribute to the balanced synthesis of NADPH and ATP. For example, Farquhar and Von Caemmerer (1981) discussed how much CET might be needed to provide additional required ATP. Recent insights into the interplay of LET, CET and PET in the thylakoid reactions have shown how they can meet a flexible requirement for the correct ATP/NADPH ratio while maintaining the regulation of e^- transport and the non-photochemical quenching of PS II (Allen, 2003; Avenson et al., 2005a, b; Cruz et al., 2005).

A steady-state model for the description of e^- transport has been developed, allowing for co-limitation by NADPH and ATP (Yin et al., 2004). Here we will discuss the development of this model as an extension of the FvCB model for the RuBP regeneration- or e^- transport-limited CO_2 assimilation rate. Equations (11.3a, b) of the FvCB model become special cases of the extended model. We will also apply this generalized model to gain more insight into the relevance of alternative e^- transport pathways and will present an integrated approach to estimate a number of C_3 photosynthesis parameters.

II. Model Development

A. Stoichiometry of Electron Transport in the Farquhar-Von Caemmerer-Berry Model

In C_3 metabolic reactions, each carboxylation or oxygenation requires 2 NADPH. Given that the ratio of oxygenation to carboxylation is $2\Gamma^*/C_c$ (Farquhar and Von Caemmerer, 1982), the rate of NADPH consumption can be expressed as $(2 + 4\Gamma^*/C_c)V$, where V is the rate of carboxylation. Since the reduction of one $NADP^+$ to NADPH requires two e^- (Fig. 11.1), the rate of e^- transport that will meet the NADPH requirement is $(4 + 8\Gamma^*/C_c)V$. This gives rise to Eq. (11.3a) of the FvCB model for calculating A_j in terms of NADPH requirement, considering the fraction of CO_2 released by photorespiration can be expressed by Γ^*/C_c .

Both carboxylation and oxygenation require ATP: each carboxylation requires 3 ATP, and each oxygenation requires 3.5 ATP. The rate of ATP consumption in C_3 reactions is therefore expressed as $(3 + 7\Gamma^*/C_c)V$. The movement of one e^- through the whole chain through both photosystems II and I, if the Q-cycle is not operating (at the time the FvCB model was developed the existence of a Q-cycle in photosynthetic e^- transport was not widely supported – see below), results in the translocation of two H^+ through the membrane, one from the splitting of water in PS II and one from the shuttle of reduced plastoquinone across the membrane (Fig. 11.1).

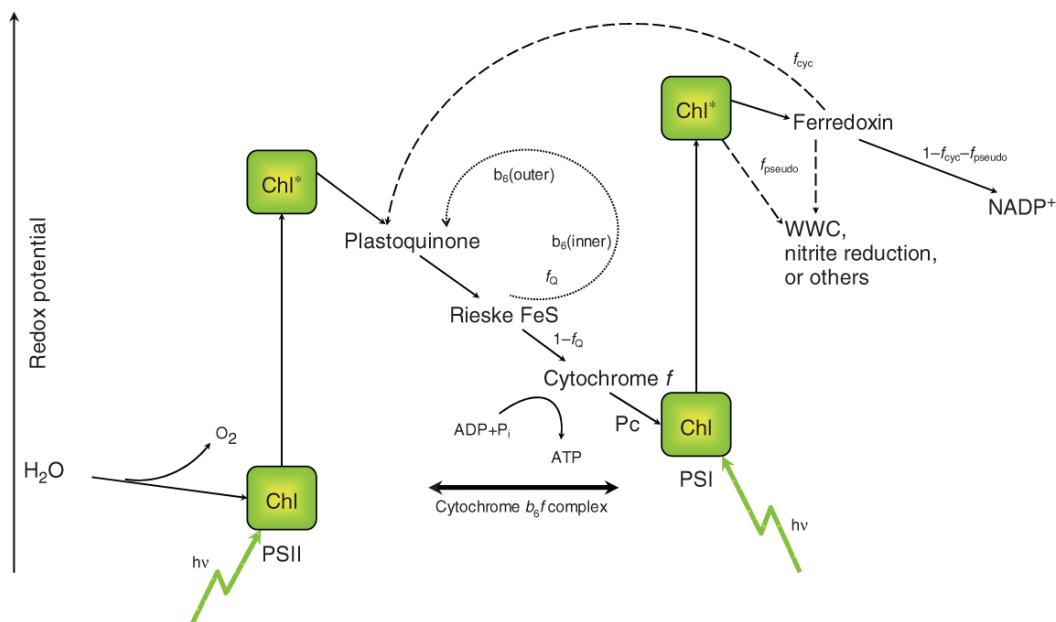


Fig. 11.1. The Z scheme for photosynthetic thylakoid reactions showing linear (solid arrows), cyclic and pseudocyclic (dashed arrows) electron transport routes. From reduced ferredoxin, a fraction f_{cyc} of electrons follows the cyclic mode around PS I. Another fraction f_{pseudo} of electrons that have passed PS I follows the pseudocyclic mode for supporting the water–water cycle WWC, or nitrite reduction, or other minor metabolic processes (see text). The remaining fraction $1 - f_{cyc} - f_{pseudo}$ is transferred to $NADP^+$ – the terminal acceptor of the linear electron transport. A fraction f_Q of electrons passes through the Q-cycle (dotted arrow), the fraction $1 - f_Q$ is transferred directly to cytochrome f and plastocyanin Pc. Chl, chlorophyll; hv, photons absorbed either by PS I or by PS II (adapted from Allen, 2003; Yin et al., 2006)

The FvCB model assumes that 3 H^+ are required for the photophosphorylation of 1 ADP to ATP, reflecting the belief at the time the model was developed that the thylakoid ATPase required 3 H^+ per ATP. Therefore, the flow of one e^- through the whole chain only produces 2/3 ATP. If the whole-chain non-cyclic e^- flow is the only H^+ translocating process then the required rate of e^- flow is $(4.5 + 10.5\Gamma^*/C_c)V$. This gives rise to Eq. (11.3b) for calculating A_j in terms of ATP requirement.

B. A Contemporary View of Electron Transport in Thylakoids

From the stoichiometry assumed in the FvCB model, we see that there is a conflict in the rates of e^- transport required to produce sufficient ATP and NADPH to match the combined demands of carboxylation and photorespiratory metabolism,

and overall, the rate of ATP synthesis would limit metabolism. There are various mechanisms (Fig. 11.1), by which this apparent imbalance or disparity could be resolved (Farquhar and Von Caemmerer, 1982; Heber, 2002; Allen, 2003).

First, more ATP would be synthesized if a portion of the e^- transport through the cytochrome b_6f complex followed the Q-cycle, rather than going directly from the Rieske FeS towards plastocyanin. The Q-cycle (Mitchell, 1975; Cape et al., 2006) is a mechanism which, operating in parallel with cytochrome f reduction, efficiently doubles the H^+/e^- translocation ratio at the cytochrome b_6f complex from 1 to 2 (Furbank et al., 1990; Allen, 2003), although the exact sequence and timing for its ‘roadmap’ are not yet fully elucidated (Osyczka et al., 2005; Cape et al., 2006). It has also been debated whether this more efficient energy conservation mechanism is operative under all conditions (Hauska

et al., 1996); one of the problems is how the various ‘short-circuits’ or bypass reactions that would prevent the operation of the Q-cycle are avoided. It seems that the rate of these bypass reactions increases as the rate of the Q-cycle decreases (Cape et al., 2006), implying that as e^- transport slows the yield of the Q-cycle decreases. So, although the full participation of the Q-cycle under unstressed conditions may be normal (Sacksteder et al., 2000), the possibility that the Q-cycle is only facultative under some (stress) conditions remains.

Secondly, the disparity could be removed if a portion of the e^- transport through PS I followed the cyclic path. Like the noncyclic e^- flow, CET also passes through the ‘coupling site’ of ATP synthesis (Allen, 2003) – it generates a trans-thylakoid H^+ potential and can thus drive ATP synthesis, but as it is a cyclic flux there is no net generation of reduced (or oxidized) products (e.g. NADPH). This cycle contributes one (Farquhar and Von Caemmerer, 1982) or two (Allen, 2003) H^+ per e^- involved, depending on whether or not the Q-cycle is operating (Von Caemmerer, 2000).

The third likely mechanism that is considered to be a viable means for balancing rates of ATP and reductant synthesis is PET. PET is conventionally defined as the reaction in which O_2 is reduced by the e^- transport chain on the acceptor of PS I; as O_2 is generated by the e^- transport chain at the donor side of PS II there is no net formation of reduced or oxidized products and a trans-thylakoid H^+ potential is generated. Ultimately for every O_2^- produced another electron is required by the detoxification pathway in which one H_2O_2 is reduced to two water molecules – giving rise to another name for this process, the water-water cycle WWC (Asada, 1999). In addition to direct O_2 reduction, other reducing processes located in the stroma such as nitrite reduction, or cytosolic or mitochondrial processes such as nitrate reduction, can be driven by reducing power, either NADPH or reduced ferredoxin generated from the chloroplast e^- transport chain (Bakhausen et al., 1998, 2000). All these e^- fluxes are included as PET in our model, because these fluxes all generate a trans-thylakoid H^+ gradient permitting the synthesis of ATP, whereas

the reductive process to which they are associated needs either no or only small amounts of ATP. Therefore the ATP generating potential of these fluxes can play a part in balancing the supply of ATP and NADPH with the demands of carboxylation and photorespiration.

There are some other, minor e^- transport pathways in the chloroplast, such as the PS II cycle and the chlororespiration based pathway. These pathways are, however, only occasionally observed and typically account for only a negligible fraction of the total e^- flux, so for the time being we will not include them in our model.

C. The Generalized Stoichiometry of Electron Transport

Within our model, three modes of e^- transport (LET, CET and PET) are considered to be involved (Fig. 11.1), thus permitting flexibility in the ATP/NADPH ratio according to metabolic demands (Allen, 2003). The fraction of the total e^- transport through PS I that is cyclic around PS I f_{cyc} , or pseudocyclic f_{pseudo} , and the fraction of the total e^- fluxes through the Reiske FeS that is involved in the Q-cycle f_Q , can be derived as (see Appendix B of Yin et al., 2004)

$$1 - f_{cyc} - f_{pseudo} = \frac{(4C_c + 8\Gamma^*)(2 + f_Q - f_{cyc})}{h(3C_c + 7\Gamma^*)} \quad (11.5)$$

The term h in Eq. (11.5) – the number of H^+ required to produce 1 ATP – is an additional parameter, because of the uncertainty in the stoichiometry for ATP synthesis from H^+ transport. The accepted value of parameter h has changed with time. At the time the original FvCB model was developed it was considered to be 3, then it increased to 4 (Von Caemmerer, 2000). More recently, many (e.g. Allen, 2003; Avenson et al., 2005b) have suggested that h probably has a value of 14/3, based on the observation of Seelert et al. 2000) that the H^+ turbine of spinach chloroplast ATP synthase has 14 subunits instead of the expected 12. The value of h may even depend on species (Junge et al., 2001; Avenson et al., 2005b; Baker et al., 2007). Note that these estimates

are based upon observations of the subunit stoichiometry of the ATP synthase and take no account of slippage in the coupling between H^+ efflux and ATP synthesis, even though slippage is both observed and theoretically expected (Juretić and Westerhoff, 1987; Groth and Junge, 1993; Nelson et al., 2002).

The derivation of Eq. (11.5) required the following assumptions: (i) CET, regardless of its pathways (see review by Cruz et al., 2005), contributes one or two H^+ per e^- , depending on whether the Q-cycle runs (Von Caemmerer, 2000), (ii) the Q-cycle, once active, works equally for noncyclic e^- transport and CET, (iii) there is no ATP export from chloroplasts to support processes other than the carbon reduction cycle and photorespiration, (iv) there is no H^+ uncoupling or 'slip' in the ATP synthase reaction (Groth and Junge, 1993), (v) there is no chlororespiration (Field et al., 1998), and (vi) there is no PS II cycle, although such a cycle has been reported under saturating light conditions (Miyake and Yokota, 2001; Laisk et al., 2006).

The equation for A_j can be expressed by analogy to Eq. (11.3a) but as a function of the rate of e^- transport to $NADP^+$, J_{NADP^+} : $A_j = J_{NADP^+}(C_c - \Gamma^*)/(4C_c + 8\Gamma^*) - R_d$. The value of J_{NADP^+} is $(1 - f_{cyc} - f_{pseudo})J_1$, where J_1 is the total rate of e^- transport through PS I (Fig. 11.1). Electrons transported by PS II only account for a fraction of those transported by PS I if CET is engaged, i.e. $J_2 = (1 - f_{cyc})J_1$, where J_2 is the rate of e^- transport through PS II (see Appendix B of Yin et al., 2004). Combining these algorithms results in a model for A_j as

$$A_j = J_2 \left(1 - \frac{f_{pseudo}}{1 - f_{cyc}} \right) \frac{C_c - \Gamma^*}{4C_c + 8\Gamma^*} - R_d. \quad (11.6)$$

The relation between J_2 and photon flux absorbed by chloroplast photosynthetic pigments I_{abs} can be expressed in a form similar to Eq. (11.4):

$$J_2 = \left(\alpha_{2(LL)} I_{abs} + J_{2max} - \sqrt{(\alpha_{2(LL)} I_{abs} + J_{2max})^2 - 4\theta_2 J_{2max} \alpha_{2(LL)} I_{abs}} \right) / (2\theta_2), \quad (11.7)$$

with

$$\alpha_{2(LL)} = \frac{\Phi_{2(LL)}(1 - f_{cyc})}{\Phi_{2(LL)}/\Phi_{1(LL)} + (1 - f_{cyc})}. \quad (11.8)$$

Here J_{2max} is the upper limit to J_2 , equivalent to the maximum rate of whole chain e^- transport with the simultaneous activity of CET; $\alpha_{2(LL)}$ is the e^- transport efficiency of PS II under strictly limiting light condition on the basis of irradiance absorbed by both photosystems, $\Phi_{1(LL)}$ and $\Phi_{2(LL)}$ are the absolute e^- transport efficiencies of PS I and PS II, respectively, under limiting light condition on the basis of irradiance absorbed by each photosystem alone.

Equation (11.8), which expresses the dependence of $\alpha_{2(LL)}$ on f_{cyc} , $\Phi_{1(LL)}$ and $\Phi_{2(LL)}$, has a threefold rationale. First, if CET does not run, the less efficient photosystem (usually assumed to be PS II) would need to receive more photons than the other photosystem to ensure an equal e^- flux passing the two photosystems. Second, if CET is engaged, electrons transported by PS II only account for the part $1 - f_{cyc}$ of those transported by PS I. Third, in order to carry more electrons to run CET, PS I must either have a higher radiation absorbance or $\Phi_{1(LL)}$ must be higher than $\Phi_{2(LL)}$. The derivation of Eq. (11.8) was given in Appendix C of Yin et al. (2004), in which $\Phi_{1(LL)}$ was assumed to be 1, given that the absolute yield of PS I e^- transport is 0.95 or greater (Trissl and Wilhelm, 1993). As will be discussed later, Eq. (11.8) results in a model for estimating the required excitation partitioning between PS I and PS II, given the simultaneous running of cyclic and non-cyclic e^- transports and the difference between $\Phi_{1(LL)}$ and $\Phi_{2(LL)}$.

D. Farquhar-Von Caemmerer-Berry Model as Special Cases of the Generalized Model

Equations (11.5–11.8) represent the extended model for the RuBP regeneration-limited CO_2 assimilation rate. Our model differs from the original FvCB model in (i) incorporation of CET,

and (ii) co-limitation of e^- transport by NADPH and ATP, so both CET and PET are considered in the extended model as complementary e^- fluxes to LET. We call this a generalized model as the two forms of A_j equations of the original FvCB model are special cases of it. This may best be shown in the equation for calculating the quantum yield of CO_2 assimilation under limiting light condition:

$$\begin{aligned}\Phi_{CO_2(LL)} &= \lim_{I_{abs} \rightarrow 0} \frac{A_j + R_d}{I_{abs}} \\ &= \frac{(C_c - \Gamma^*)\Phi_{2(LL)}(1 - f_{cyc} - f_{pseudo(b)})}{(4C_c + 8\Gamma^*)[\Phi_{2(LL)}/\Phi_{1(LL)} + (1 - f_{cyc})]}\end{aligned}\quad (11.9)$$

The e^- flow assumption of Eqs. (11.3a) or (11.3b) in the original FvCB model yields

$$\Phi_{CO_2(LL)} = \frac{\alpha_{(LL)}(C_c - \Gamma^*)}{4C_c + 8\Gamma^*} \quad (11.10a)$$

or

$$\Phi_{CO_2(LL)} = \frac{\alpha_{(LL)}(C_c - \Gamma^*)}{4.5C_c + 10.5\Gamma^*}. \quad (11.10b)$$

In the absence of CET, the theoretical maximum value for $\alpha_{(LL)}$ is 0.5, because one quantum must be absorbed by each of the two photosystems to move an electron from H_2O to $NADP^+$. This upper value will be found if both PS I and PS II have an absolute e^- transport quantum efficiency of 1. Farquhar and Von Caemmerer (1981, 1982) set the $\alpha_{(LL)}$ value in Eqs. (11.10a, b) for their rectangular hyperbola for the response of e^- transport to irradiance as $1/2.1$ ($= 0.476$), rather than 0.5, to account for what they called a 'biological miss' of PS II (i.e. relative to PS I, PS II is believed to have a lower absolute quantum efficiency). In many later applications of the FvCB model, $\alpha_{(LL)}$ was often adjusted empirically to match the measured $\Phi_{CO_2(LL)}$ (e.g. Harley, 1992; Wullschlegel, 1993). Parameter $\alpha_{(LL)}$ in Eqs. (11.10a, b) may be calculated as $\Phi_{2(LL)}/(1 + \Phi_{2(LL)}/\Phi_{1(LL)})$, derived from Eq. (11.8) for the case in the absence of CET. This allows $\alpha_{(LL)}$ in the FvCB model to be calculated from biophysical measurements for a difference in e^- transport efficiency between PS I and PS II. Biophysical

measurements imply that the absolute yield of maximum PS I e^- transport is 0.95 or greater (Trissl and Wilhelm, 1993). Setting $\Phi_{1(LL)} = 1$ and then solving $\Phi_{2(LL)}/(1 + \Phi_{2(LL)}/\Phi_{1(LL)}) = 1/2.1$ for $\Phi_{2(LL)}$ requires that $\Phi_{2(LL)} = 0.9091$. So the value of $\Phi_{2(LL)}$ initially assumed by Farquhar and Von Caemmerer (1981, 1982) was somewhat higher than 0.83, the maximum PS II photochemical efficiency assessed from the chlorophyll (Chl) fluorescence parameter F_v/F_m (Björkman and Demmig, 1987). Note, however, that in practice, neither photosystem will have a quantum efficiency for charge separation of 1; in the case of PS II the F_v/F_m fluorescence parameter is frequently assumed to be a good estimate of $\Phi_{2(LL)}$, but this is unlikely to be the case (see below).

It can be seen that Eqs. (11.10a, b) are special cases of Eq. (11.9) which lack CET ($f_{cyc} = 0$), as assumed in the original FvCB model. In addition, Eq. (11.10a) presumes that no PET occurs ($f_{pseudo} = 0$), and that a Q-cycle is required if the chloroplast e^- transport chain provides the NADPH/ATP ratio to meet the requirements for carboxylation and oxygenation. Solving Eq. (11.5) for the required f_Q for such a condition gives: $f_Q = h(3C_c + 7\Gamma^*)/(4C_c + 8\Gamma^*) - 2$. Equation (11.10b) results from the additional condition that the Q-cycle does not run ($f_Q = 0$), but that PET operates to provide the additional ATP. Solving Eq. (11.5) for the required f_{pseudo} gives: $f_{pseudo} = 1 - 2(4C_c + 8\Gamma^*)/[h(3C_c + 7\Gamma^*)]$; substituting this f_{pseudo} into Eq. (11.9) with $h = 3$ (the value used in the original FvCB model) results in Eq. (11.10b). From this analysis, we now know that the biological meaning of parameter $\alpha_{(LL)}$ in Eq. (11.10a) differs from that in Eq. (11.10b): the definition in Table 11.1 suits $\alpha_{(LL)}$ in Eq. (11.10a), whereas $\alpha_{(LL)}$ in Eq. (11.10b), strictly speaking, represents the noncyclic e^- transport (LET plus all PET) efficiency on the basis of light absorbed by the two photosystems. Similarly, variable J and parameter J_{max} in Eq. (11.3) when applied to Eq. (11.3b) represent the actual and maximum rate of the noncyclic e^- transport, respectively.

A third distinct special case is when CET is the sole mechanism for balancing production of ATP and NADPH. Solving Eq. (11.5) for the required $f_{cyc} = 1 - (4C_c + 8\Gamma^*)/[h(3C_c +$

$7\Gamma^*) - (4C_c + 8\Gamma^*)]$ and substituting this into Eq. (11.9) results in

$$\Phi_{\text{CO}_2(\text{LL})} = \frac{(C_c - \Gamma^*)\Phi_{2(\text{LL})}}{[(4C_c + 8\Gamma^*)(1 - \Phi_{2(\text{LL})}/\Phi_{1(\text{LL})}) + h(3C_c + 7\Gamma^*)\Phi_{2(\text{LL})}/\Phi_{1(\text{LL})}]}. \quad (11.10c)$$

Setting $\Phi_{1(\text{LL})} = 1$, $\Phi_{2(\text{LL})} = 0.9091$ and $h = 3$ (the values used in the original FvCB model), Eq. (11.10c) yields $\Phi_{\text{CO}_2(\text{LL})} = (C_c - \Gamma^*)/(9.364C_c + 21.727\Gamma^*)$. This is compatible with an equation, introduced by Farquhar and Von Caemmerer (1981, 1982; see Eq. (16.63b) in their 1982 paper) but which was subsequently not widely used, for quantum yield when CET is the only means for adjusting the NADPH/ATP ratio.

Clearly, the quantum yield for CO_2 assimilation $\Phi_{\text{CO}_2(\text{LL})}$ depends on which e^- transport mechanisms are used to balance the NADPH/ATP ratio. It is most evident that of the three special cases given by Eqs. (11.10a–c), the highest $\Phi_{\text{CO}_2(\text{LL})}$ is given by Eq. (11.10a), resulting from an NADPH-limited mechanism in the FvCB model. It is less evident, but mathematically provable, that as long as $\Phi_{1(\text{LL})} > \Phi_{2(\text{LL})}$, the lowest $\Phi_{\text{CO}_2(\text{LL})}$ results from the operation of PET alone, i.e. the ATP-limited mechanism in the FvCB model, although relative to Eq. (11.10c), the ATP-limited mechanism predicts a lower $\Phi_{\text{CO}_2(\text{LL})}$ by a very small margin for a given h (Yin et al., 2004). Therefore, the two widely used forms of the FvCB model, which assume a limitation of CO_2 assimilation by e^- transport due to a deficiency of either NADPH or ATP, predict the highest and the lowest photosynthetic quantum yields, respectively, of the distinct special cases given by the generalized equation. This conclusion holds so long as $h \geq 2(4C_c + 8\Gamma^*)/(3C_c + 7\Gamma^*)$ which can be obtained if the above required f_Q , or f_{pseudo} or f_{cyc} is > 0 . This threshold h value varies within a narrow range from 2.40 to 2.67 for a wide range of C_c from Γ^* to infinity (Yin et al., 2004). For any h value close to or lower than this threshold value (e.g. 2.0–2.5 as indicated in some early literature, Trebst, 1974), the quantum yield for CO_2 assimilation given by Eq. (11.10a) becomes valid because ATP is no longer limiting. In addition to the lower

threshold h , Yin et al. (2004) also discussed another threshold for parameter h . If only the Q-cycle is operated to balance the NADPH/ATP ratio, then an upper limit for h also exists. Setting the condition that $f_Q \leq 1$ in the equation for f_Q yields $h \leq 3(4C_c + 8\Gamma^*)/(3C_c + 7\Gamma^*)$. For a wide range of C_c from Γ^* to infinity, this h limit ranges from 3.6 to 4.0. Any higher h value, e.g. 14/3 as indicated by the contemporary literature (Seelert et al., 2000), requires that the full engagement of the Q-cycle should be supplemented by extra H^+ translocating capacity (either CET or PET, or both), to produce sufficient ATP as required by the Rubisco-catalyzed metabolism. The calculation also supports the proposition that in the absence of photorespiration and with $h = 4$, then LET alone combined with the full operation of the Q-cycle generates the exact NADPH/ATP ratio of 2/3 required by the carbon reduction cycle. With this perfect matching under non-photorespiring conditions, Von Caemmerer (2000) preferred to use (see her Eq. 2.22)

$$A_j = \frac{(C_c - \Gamma^*)J}{4C_c + 9.3\Gamma^*} - R_d \quad (11.11)$$

to replace Eq. (11.3b) as the ATP-limited version of the model. Again, Eq. (11.11) can be derived from the generalized model by substituting $(1 - f_{\text{cyc}} - f_{\text{pseudo}})$ from Eq. (11.4) into Eq. (11.5) and then fixing $h = 4$, $f_Q = 1$ and $f_{\text{cyc}} = 0$.

III. Model Applications

The light-dependent production of ATP and reductants by the photosynthetic apparatus *in vivo* involves a series of e^- and H^+ transfers. Regulation of these e^- and H^+ transfers is required for the thylakoids to meet the fluctuating metabolic demands of the photosynthetic cell. Our model integrates most mechanisms that chloroplasts exhibit to flexibly regulate e^- and H^+ fluxes in order to match the light use for ATP and reductant production with the down-stream metabolic requirements, assuming that e^- transport either limits or, along with metabolism, co-limits photosynthesis. Combined with non-invasive gas exchange data and biophysical measurements of e^- transport

efficiencies through PS I and PS II, our model can provide insights into the operation of such regulatory processes in vivo. Together with measurements of leaf absorbance, CO₂ exchange, O₂ evolution, PS I e⁻ transport efficiency, and PS II e⁻ transport efficiency, our model can be used to estimate a number of important parameters. The model can also be used to answer 'what-if' questions in case of uncertainties in measurements or our understanding of physiological processes. In this section, we will discuss these potential applications of the model. First of all, however, we will discuss the potential pitfalls of existing approaches.

A. Potential Pitfalls of Existing Approaches

Assessing photosynthesis parameters is important for predicting the rates of, and analyzing physiological limitations to, C₃ photosynthesis under various environmental conditions. The FvCB model has been frequently used to evaluate and predict CO₂ assimilation rates, initially based on in vitro enzyme properties and using the intercellular CO₂ partial pressure C_i as a proxy for C_c . Attempts have been made to estimate the kinetics of Rubisco in vivo from measurements of photosynthesis in leaves (Von Caemmerer et al., 1994; Bernacchi et al., 2002). Many studies (e.g. Epron et al., 1995; Ethier and Livingston, 2004) have emphasized the importance of incorporating mesophyll diffusion conductance g_m into FvCB-type models since there is a significant drawdown of C_c in comparison with C_i .

As early as 1986 Wong and Woo reported an analysis of photosynthetic physiology using measurements of steady-state Chl fluorescence together with net CO₂ uptake rates. Genty et al. (1989) demonstrated that the quantum efficiency of PS II e⁻ transport can be estimated from Chl fluorescence signals by $\Delta F/F'_m = (F'_m - F_s)/F'_m$, where F_s is the steady-state fluorescence emission and F'_m is the maximum fluorescence emission induced by a saturating light pulse. Similarly, signals F_0 (the minimum fluorescence when all PS II reaction centers are open) and F_m (the maximum fluorescence reached in a saturating light pulse that closes all PS II reaction centers) measured on dark-adapted leaves (when non-photochemical quenching is absent) can be used to derive

an estimate of the maximum PS II quantum efficiency: $F_v/F_m = (F_m - F_0)/F_m$. Techniques using light induced absorbance changes, usually around 820 nm, were developed to measure the efficiency of PS I photochemistry Φ_1 in vivo (Harbinson and Woodward, 1987). More recently, light induced electrochromic shifts ECS using absorption spectroscopy were used to analyze the light-driven proton flux v_{H^+} across the thylakoid membranes (Sacksteder and Kramer, 2000; Sacksteder et al., 2000; Avenson et al., 2005a). These biophysical techniques are described in a recent review (Baker et al., 2007). It should be emphasized that Φ_1 measured by the 820-nm technique and v_{H^+} indicated by the ECS technique are not absolute but relative values. It is also unlikely that $\Delta F/F'_m$ represents exactly the real PS II e⁻ transport efficiency Φ_2 , and Laverne and Trissl (1995) pointed out that $\Delta F/F'_m$ tends to underestimate Φ_2 . The error is probably 10% or less, which for most applications of the technique will be insignificant. Unfortunately in the more quantitative analyses of e⁻ transport this likely error can create serious problems. Furthermore, F_v/F_m is often not the same as $\Phi_{2(LL)}$, not only because the errors associated with the use of $\Delta F/F'_m$ also apply to F_v/F_m (which means that F_v/F_m is not exactly $\Phi_{2(DK)}$ – the real PS II e⁻ transport efficiency of dark adapted leaves), but also because some net loss of q_Q (the probability that an exciton in PS II will encounter a PS II reaction centre with an oxidized primary e⁻ acceptor to PS II) is often observed at low lights, which means that $\Phi_{2(LL)}$ is not exactly equal to $\Phi_{2(DK)}$.

Of these biophysical techniques, Chl fluorescence has been most commonly exploited. The use of gas exchange data combined with Chl fluorescence measurements has become a popular method for determining, for example, g_m (Harley et al., 1992a; Evans and Von Caemmerer, 1996; Bernacchi et al., 2002), alternative e⁻ flows (Makino et al., 2002), and the Rubisco CO₂/O₂ specificity factor $S_{c/o}$ (Peterson, 1989). Typically, these previous studies focused one single parameter, requiring assumptions about other parameters. For example, studies in which Chl fluorescence based methods were used to estimate g_m often assume the lack of alternative e⁻ transport, so all e⁻ flows are assumed to be LET supporting only Rubisco-catalyzed CO₂ fixation

and photorespiration. In these methods, $\Delta F/F'_m$ is converted into the flux of PS II e^- transport (denoted as J_f) using either measured or assumed leaf absorbance and a factor for excitation partitioning to PS II ρ_2 , which is often empirically assumed to be 0.5. Then J_f is compared with J_c – the e^- transport rate based on CO_2 uptake measurements. The difference between J_f and J_c is interpreted as being due to mesophyll diffusion resistance – the reciprocal of g_m .

Several assumptions underlying this analysis are debatable (Yin et al., 2006). For example, as mentioned above, the $(\Delta F/F'_m)/\Phi_2$ ratio is not unity exactly (e.g. Genty et al., 1990; Lavergne and Trissl, 1995; Pfündel et al., 1998), and parameter ρ_2 may not be exactly 0.5. Other uncertainties include light absorbance by non-photosynthetic pigments, different chloroplast populations sampled by gas exchange and Chl fluorescence measurements, nonlinearity between $\Delta F/F'_m$ and quantum efficiency of CO_2 fixation Φ_{CO_2} at low irradiance (Seaton and Walker, 1990; Öquist and Chow, 1992), and influences of the choice of actinic spectrum on photosynthetic efficiency (Evans, 1987). Furthermore, this approach based upon Chl fluorescence-based estimates of Φ_2 as a means of calculating LET often overlooks the possible occurrence of PET. As discussed in the earlier section, PET supporting basal rates of the WWC and metabolic demands such as nitrogen assimilation and other (minor) processes (sulfate assimilation, light-stimulated synthesis of fatty acids, oxaloacetate reduction to malate used for e.g. nitrate reduction), which we denote as the basal PETb, could account for an appreciable fraction of the total e^- flux (Noctor and Foyer, 1998; Fridlyand and Scheibe, 1999; Backhausen et al., 2000). When photosynthesis is limited by Rubisco, extra e^- may follow PET in support of the WWC (Asada, 1999; Ort and Baker, 2002) and other processes (Backhausen et al., 2000). This component of PET, which we referred to as the additional PETa, might be another source of error for the Chl fluorescence based method to estimate g_m using data in the low C_i range. To correct for any operation of alternative e^- transport, other studies have used the relationship between J_f and J_c , or between Φ_2 and Φ_{CO_2} (both measured under non-photorespiratory conditions), as a calibration curve (e.g. Cornic and Ghashghaie, 1991; Long and Bernacchi, 2003; Warren, 2006). However,

although this allows J_f measurements to be more accurately converted into J_c equivalents, it must be borne in mind that alternative e^- transport is unlikely to be constant across different CO_2 or irradiance levels used to generate the calibration curve (Von Caemmerer, 2000). Some of these problems were overcome by the comprehensive, step-wise measurement and model procedure, first described by Laisk and Loreto (1996) and further elaborated by Laisk et al. (2002, 2006; hereafter, the L-method), in which a large number of photosynthetic parameters can be estimated. The L-method is very thorough, but it depends largely on a circular or iterative logic to determine g_m , J_c and J_a .

B. Unraveling Insights into Photosynthesis Physiology

1. On Conversion Efficiency of Incident Light into Linear Electron Transport

In most studies the calibration curve used to translate Chl fluorescence based estimates of e^- transport into a rate of e^- transport relevant to metabolism uses data from the entire light or/and C_i response curves measured under a low O_2 condition that eliminates photorespiration. We propose a method in which only the data of the e^- transport-limited range of the light or/and C_i response curves are used. This method can easily be linked with most applications of the FvCB model, in which e^- transport rate J is modelled using a constant incident-light based quantum yield of e^- transport under limiting light $\kappa_{2(LL)}$. However, the underlying meaning of parameter $\kappa_{2(LL)}$ has not been clearly defined, so its value is usually corrected empirically for the observed quantum efficiency of CO_2 assimilation under limiting light conditions $\Phi_{CO_2(LL)}$ (e.g. Harley et al., 1992b; Wullschlegel, 1993; Warren and Adams, 2006). In fact, the photosynthetic quantum yield will depend upon the balance of excitation between the two photosystems and the maximum efficiency of charge separation of each photosystem. Furthermore, any involvement of CET or PET will diminish the observed $\Phi_{CO_2(LL)}$.

From Eq. (11.6) a relation for calculating e^- transport-limited A under the non-photorespiratory condition can be derived as

$$\begin{aligned}
A_j &= J_2 \left(1 - \frac{f_{\text{pseudo(b)}}}{1 - f_{\text{cyc}}} \right) / 4 - R_d \\
&= \rho_2 a I_{\text{inc}} \Phi_2 \left(1 - \frac{f_{\text{pseudo(b)}}}{1 - f_{\text{cyc}}} \right) / 4 - R_d \\
&= s (I_{\text{inc}} \Phi_2 / 4) - R_d \quad (11.12)
\end{aligned}$$

where $s = \rho_2 a [1 - f_{\text{pseudo(b)}} / (1 - f_{\text{cyc}})]$. The slope factor s and R_d can be estimated by regressing A against $(I_{\text{inc}} \Phi_2 / 4)$ within the e^- transport-limited range, in which Φ_2 is measured in practice by $\Delta F / F'_m$. This also suggests a method to estimate R_d based on both gas exchange and Chl fluorescence (Yin et al., 2009). The assumptions underlying Eq. (11.12) are: (i) R_d does not vary significantly with light level, (ii) the photosynthetic limitation set by triose phosphate utilization (Sharkey, 1985) either does not occur to a significant extent, or its occurrence is quantitatively mirrored by a down-regulation of e^- transport and thus Φ_2 via feedback regulation, and (iii) a , ρ_2 , f_{cyc} and $f_{\text{pseudo(b)}}$ do not vary significantly with changes in C_i or light levels. These assumptions have also been employed (e.g. Cornic and Ghashghaie, 1991) when constructing a calibration curve, assuming that a constant proportion of the reductants resulting from noncyclic e^- flux is utilized for CO_2 fixation.

By comparing Eq. (11.3a) with Eq. (11.6), the following can be written, considering parameter s described in Eq. (11.12):

$$\begin{aligned}
J &= J_2 \left(1 - \frac{f_{\text{pseudo(b)}}}{1 - f_{\text{cyc}}} \right) \\
&= \rho_2 a I_{\text{inc}} \Phi_2 \left(1 - \frac{f_{\text{pseudo(b)}}}{1 - f_{\text{cyc}}} \right) \\
&= s I_{\text{inc}} \Phi_2. \quad (11.13a)
\end{aligned}$$

So, the efficiency of converting incident light into J (κ_2) is given by

$$\kappa_2 = J / I_{\text{inc}} = s \Phi_2. \quad (11.13b)$$

The value of κ_2 for the strictly limiting light condition is therefore given by

$$\kappa_{2(\text{LL})} = s \Phi_{2(\text{LL})}. \quad (11.13c)$$

Equations (11.12) and (11.13c) indicate that parameter $\kappa_{2(\text{LL})}$ depends on (i) light absorbance by leaf photosynthetic pigments (a), (ii) the fraction of the absorbed light partitioned to PS II (ρ_2), (iii) the impact of alternative e^- path-

ways, in the form of $[1 - f_{\text{pseudo(b)}} / (-f_{\text{cyc}})]$, and (iv) PS II photochemical efficiency under limiting light $\Phi_{2(\text{LL})}$. Points (i) and (ii) are well recognized. Point (iii) has been recognized occasionally (e.g. Warren, 2006), but its quantitative form $[1 - f_{\text{pseudo(b)}} / (1 - f_{\text{cyc}})]$ can only be elucidated by the generalized model. Finally, the parameter s and, as a result, $\kappa_{2(\text{LL})}$ may also correct for other factors such as possible differences between $\Delta F / F'_m$ and Φ_2 or errors due to different chloroplast populations being sampled by gas exchange and Chl fluorescence.

In some C_3 photosynthesis modelling studies, the parameter $\kappa_{2(\text{LL})}$ was empirically treated as a constant, e.g. as 0.24 across all stages of growth and CO_2 levels during growth (Harley et al., 1992b), 0.24 across N treatments (Warren, 2004), or 0.18 across species (Wullschleger, 1993). From measurements on flag leaves of wheat plants (*Triticum aestivum* L.), we calculated $\kappa_{2(\text{LL})}$ using a procedure based on Eqs. (11.12) and (11.13c). The calculated value of $\kappa_{2(\text{LL})}$ ranged from 0.24 to 0.30, depending on flag-leaf stage and nitrogen (N) treatments (Yin et al., 2009). This dependence is not surprising because one of the components of $\kappa_{2(\text{LL})}$, the parameter a , depends on leaf Chl content (Evans 1993) – which is strongly related to leaf N, although $\Phi_{2(\text{LL})}$ does, and other underlying parameters f_{cyc} and $f_{\text{pseudo(b)}}$ may, vary with leaf N content as well. Therefore, $\kappa_{2(\text{LL})}$ should not be considered as constant.

2. On Alternative Electron Transport Under Limiting Light

Yin et al. (2006) have shown that the generalized model can be used to assess any occurrence of alternative e^- transport by analyzing concurrent measurements of gas exchange and Chl fluorescence (using F_v / F_m) under steady-state, limiting light, non-photorespiratory conditions. The data under these conditions were obtained from the measurements of Björkman and Demmig (1987) for 37 C_3 species and Long et al. (1993) for 11 C_3 species. Measurements in the two studies were made with a quartz-iodide light source (a broad-band ‘white’ light source), so the possible influence of differing spectral distributions on the quantum yield of CO_2 fixation (Evans, 1987) can be discounted. The mean quantum yield

of O_2 evolution $\Phi_{O2(LL)}$ measured for the 37 species tested by Björkman and Demmig (1987) was $0.106 \text{ mol } O_2 (\text{mol photon})^{-1}$, about 12% higher ($P < 0.01$) than the mean quantum yield of CO_2 uptake $\Phi_{CO2(LL)}$, of $0.093 \text{ mol } CO_2 (\text{mol photon})^{-1}$ for the 11 species tested by Long et al. (1993). Since the two studies used different species, the possibility of taxonomic differences cannot be ruled out, but this seems unlikely given the broad diversity of taxa used in the two studies. A higher $\Phi_{O2(LL)}$ than $\Phi_{CO2(LL)}$ suggests the occurrence of PET fluxes in support of processes other than WWC, as both LET and non-WWC mediated PET lead to O_2 evolution. Assuming a negligible WWC under limiting irradiance, the equation for $\Phi_{O2(LL)}$ can be derived, by analogy to Eq. (11.9) for $\Phi_{CO2(LL)}$:

$$\Phi_{O2(LL)} = \frac{(C_c - \Gamma^*)\Phi_{2(LL)}(1 - f_{cyc})}{(4C_c + 8\Gamma^*)[\Phi_{2(LL)}/\Phi_{1(LL)} + (1 - f_{cyc})]} \quad (11.14a)$$

Equation (11.14a) for $\Phi_{O2(LL)}$ or Eq. (11.9) for $\Phi_{CO2(LL)}$ can be extended to the non-limiting light situation if $\Phi_{O2(LL)}$, $\Phi_{CO2(LL)}$, $\Phi_{1(LL)}$ and $\Phi_{2(LL)}$ are replaced with Φ_{O2} , Φ_{CO2} , Φ_1 and Φ_2 , respectively, as long as they are obtained within the range in which A is limited by e^- transport. An important outcome of the equations is that the relationship between Φ_{O2} (or Φ_{CO2}) and Φ_2 in the absence of alternative e^- transport will not be entirely linear if Φ_1 and Φ_2 did not vary in proportion to each other.

The value for f_{cyc} can be solved from Eq. (11.14a):

$$f_{cyc} = \frac{[(C_c - \Gamma^*) - \Phi_{O2(LL)}(4C_c + 8\Gamma^*)](1/\Phi_{1(LL)} + 1/\Phi_{2(LL)})}{(C_c - \Gamma^*) - \Phi_{O2(LL)}(4C_c + 8\Gamma^*)/\Phi_{2(LL)}} \quad (11.14b)$$

The measured mean F_v/F_m for the 37 species tested by Björkman and Demmig (1987) was 0.832, very similar to 0.838 – the mean value for the 11 species tested by Long et al. (1993), reflecting a fundamental similarity between different species in the basic organization and operation of the PS II primary processes. The

photochemical efficiency of PS I was not measured, but the efficiency of charge separation by PS I is very high, and thus $\Phi_{1(LL)}$ is believed to be at least 0.95 (Trissl and Wilhelm, 1993). In the analysis of Yin et al. (2006) $\Phi_{1(LL)}$ was provisionally set to 1. With this $\Phi_{1(LL)}$ and assuming that $\Phi_{2(LL)}$ can be well represented by F_v/F_m , Eq. (11.14a) predicts that the $\Phi_{O2(LL)}$ in the absence of CET is $0.832/[4*(0.832/1 + 1)] = 0.1135$ under non-photorespiratory conditions. It is not surprising that this value is lower than 0.125 – the theoretical upper limit in the absence of any alternative e^- flow if both PS I and PS II had an absolute efficiency of 1. Note, however, that it is likely that $\Phi_{2(DK)} > F_v/F_m$ and $\Phi_{2(LL)} < \Phi_{2(DK)}$. The calculation using Eq. (11.14b) showed that among the 37 species, 4 had a small negative f_{cyc} (Fig. 11.2). A negative f_{cyc} is physiologically impossible; its occurrence as a mathematical solution indicates that the measured $\Phi_{O2(LL)}$ was higher than what can be expected from the measured $\Phi_{2(LL)}$ in the presence of only LET for these four species, possibly reflecting that F_v/F_m underestimates $\Phi_{2(DK)}$. The data for these four species, on the other hand, indicate that $\Phi_{1(LL)}$ is indeed extremely close to 1, because f_{cyc} predicted by Eq. (11.14b) would be even lower if $\Phi_{1(LL)}$ is significantly lower than 1. For the other 33 species, the estimated f_{cyc} ranged evenly from

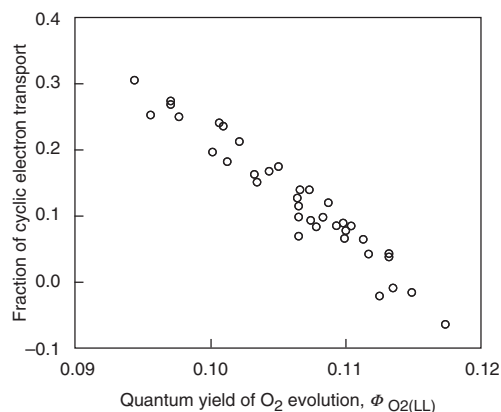


Fig. 11.2. Fraction of cyclic electron transport f_{cyc} calculated by Eq. (11.14b), plotted against quantum efficiency of O_2 evolution $\Phi_{O2(LL)}$ in 37 C_3 species tested by Björkman and Demmig (1987). The calculation presumed that $\Phi_{2(LL)} = F_v/F_m$ and $\Phi_{1(LL)} = 1$. Because F_v/F_m was conservative across the species, points for the calculated f_{cyc} were almost exclusively dependent on the value of $\Phi_{O2(LL)}$.

0.04 to 0.31 (Fig. 11.2). The mean f_{cyc} for all 37 species was 0.131, although the measured mean $\Phi_{\text{O}_2(\text{LL})}$ (0.106) is only about 7% lower than the theoretical value (0.1135). In other words, the model at this stage estimates that about 13.1% of total e^- fluxes via PS I are calculated to be CET as a brake for LET, so that the theoretical $\Phi_{\text{O}_2(\text{LL})}$ expected from e^- transport stoichiometry is exactly equal to the measured $\Phi_{\text{O}_2(\text{LL})}$ (0.106). However, the model is not at this point taking into account the need to balance ATP and NADPH synthesis, nor is it allowing for the possibility that not all light absorbed by the leaf will be used for photosynthesis. It also does not allow for any WWC. The conclusion that 13.1% of PS I e^- transport is CET depends strongly on these assumptions, which will be dealt with later.

Concurrent measurements of CO_2 exchange, O_2 evolution and Chl fluorescence on the same leaves would provide a solid data set to determine both f_{cyc} and $f_{\text{pseudo(b)}}$ if WWC is negligible under limiting light. A usually slightly higher net O_2 evolution than CO_2 uptake, measured simultaneously (e.g. Ruuska et al., 2000; Laisk et al., 2006), suggests some 'basal' PET. Assuming that this mechanism accounts for the slightly higher $\Phi_{\text{O}_2(\text{LL})}$ of Björkman and Demmig (1987) than $\Phi_{\text{CO}_2(\text{LL})}$ of Long et al. (1993), $f_{\text{pseudo(b)}}$ can be calculated by dividing Eq. (11.9) by Eq. (11.14a):

$$f_{\text{pseudo(b)}} = (1 - \Phi_{\text{CO}_2(\text{LL})}/\Phi_{\text{O}_2(\text{LL})})(1 - f_{\text{cyc}}) \quad (11.15)$$

Using the mean value of $\Phi_{\text{CO}_2(\text{LL})}$ from data of Long et al. (1993), the mean value of $\Phi_{\text{O}_2(\text{LL})}$ from data of Björkman and Demmig (1987), and the mean f_{cyc} estimated above, Eq. (11.15) gives 0.107 for the mean $f_{\text{pseudo(b)}}$. Interestingly, this value is very close to a theoretical value 0.11 predicted by a required fraction of PET, $1 - (4C_c + 8\Gamma^*)/(4.5C_c + 10.5\Gamma^*)$ (see Section 'FvCB Model as Special Cases of the Generalized Model') under the non-photorespiratory condition for the ATP-limited version of the FvCB model.

Our analysis supports the existence of CET and PET. To this end, neither Eq. (11.3a) nor Eq. (11.3b) of the FvCB model is accurate as they both ignore CET. However, of the two forms of the FvCB model, Eq. (11.3b) is closer to reality for photosynthetic rates in leaves in

which PETb is active in support of the processes – notably nitrate reduction (Noctor and Foyer, 1998) – that consume reductants generated by chloroplast e^- transport chain. Some reports have shown little difference between $\Phi_{\text{O}_2(\text{LL})}$ and $\Phi_{\text{CO}_2(\text{LL})}$ (Evans, 1987; Laisk et al., 2007), probably because nitrate reduction occurs mainly in roots in some species or under certain conditions. For such species or conditions, $f_{\text{pseudo(b)}}$ should be much smaller, for which our model using CET as the mechanism to balance the rates of NADPH and ATP synthesis (Eq. 11.10c), might be more appropriate.

3. On Cyclic Electron Transport and Excitation Partitioning

The detection of CET in vivo is difficult. Most strategies are based upon the comparison of measurements of Φ_1 to Φ_2 (or J_1 and J_2), or measurements of photosynthetic H^+ fluxes with e^- transport. If the ratio of these measurements changes this is attributed to a change in CET; for example if Φ_2 decreases more than Φ_1 then this is taken as evidence of an increase in CET (Harbinson and Foyer, 1991; Sacksteder et al., 2000; Makino et al., 2002; Holtgreffe et al., 2003; Miyake et al., 2005). Using this approach, some studies (Laisk et al., 2005; Miyake et al., 2005) have inferred that the CET flux as a proportion of the total noncyclic flux must vary over a wide range of irradiances, whereas in other cases it has been predicted that the fraction of CET, if occurred, should be constant over a wide range of conditions (Sacksteder et al., 2000; Kramer et al., 2004; Johnson, 2005; Avenson et al., 2005a). Hence, if CET remains constant as a proportion of total e^- transport, it could not be detected in this way. Also, this approach bypasses the estimation of interphotosystem excitation partitioning of light absorbed by photosynthetic pigments, but implies a fixed factor for it (typically 0.5), which is, in any case, hard to measure in a working system (Baker et al., 2007). A possible source of error with this strategy is that changes in the absorbance of either PS I or PS II could produce changes in the Φ_1/Φ_2 ratio or the rate constant for e^- transport that could mimic those produced by CET. Note that combining measurements of rate constants for P700^+ reduction with Φ_1 measurements should make it

possible to separate state transitions from CET, although at the time of writing of this chapter and to the best of our knowledge this has not yet been done. Using gas exchange data as additional information, our approach, as shown by Yin et al. (2006), can theoretically estimate the factor of energy partitioning between PS I and PS II, at least for the light-limited situation and when no non-photosynthetic pigments are absorbing light, in a mathematically and biologically consistent manner.

Let ρ_2 be the fraction of the absorbed light partitioned to PS II. Assuming a negligible quantum absorption by non-photosynthetic pigments (an assumption which is certainly not valid in some cases, Inada, 1976), ρ_2 can be defined as:

$$\rho_2 = I_2/I_{\text{abs}} = (J_2/\Phi_2)/(J_2/\alpha_2) = \alpha_2/\Phi_2, \quad (11.16)$$

where I_2 is the absorbed light partitioned to PS II and α_2 is the efficiency of PS II e^- transport on the basis of light absorbed by both photosystems. The partitioning fraction for PS I can then be simply set at $1 - \rho_2$. Equation (11.16) is the mathematical expression equivalent to the graphical procedure of Laisk et al. (2002) that estimates the relative optical cross-section of PS II antenna for the case where LET functions alone. From Eqs. (11.13a, b), (11.16), we can easily see a relation between parameters α_2 and κ_2 , that is: $\kappa_2 = a[1 - f_{\text{pseudo(b)}}/(1 - f_{\text{cyc}})]\alpha_2$.

For limiting light conditions, substituting Eq. (11.8) into Eq. (11.16) gives an expression for ρ_2 in the presence of CET:

$$\rho_2 = \frac{1 - f_{\text{cyc}}}{\Phi_{2(\text{LL})}/\Phi_{1(\text{LL})} + (1 - f_{\text{cyc}})}. \quad (11.17)$$

Equation (11.17) is in line with a qualitative statement of Albertsson (2001) that additional quanta for carrying out CET are required to be distributed to PS I. If, for example, $\Phi_{2(\text{LL})} = F_v/F_m$ (0.83) and $\Phi_{1(\text{LL})} = 1$, Eq. (11.17) predicts that in the absence of CET, the required ρ_2 to keep equal velocity in photochemistry of PS I and PS II would be about 0.55 (instead of the intuitively assumed 0.5). If CET is active, a lower ρ_2 is required. With the earlier estimated f_{cyc} , the calculated ρ_2 using Eq. (11.17) varies from 0.480 to 0.521, with a mean of 0.503 for the 11 species of Long et al. (1993), and from 0.457 to 0.559, with

a mean of 0.511 for the 37 species of Björkman and Demmig (1987). It thus appears that the need for a higher partitioning to the less efficient PS II is roughly cancelled out by the need for a higher partitioning to PS I to meet the requirement for extra quanta by PS I to run CET, so the theoretical ρ_2 is close to the intuitively assumed 0.5. In other words, if the commonly used value 0.5 for ρ_2 is true, there has to be some CET, given the general consensus that the photochemical efficiency of non-oxidized PS I reaction centers is higher than that of open PS II centers.

In principle, Eq. (11.17) can be extended for the non-limiting light situation:

$$\rho_2 = \frac{1 - f_{\text{cyc}}}{\Phi_2/\Phi_1 + (1 - f_{\text{cyc}})}. \quad (11.18)$$

Equation (11.18) says that when excitation partitioning varies (e.g. due to state transition, Haldrup et al., 2001) there will be no guarantee that a change in the Φ_2/Φ_1 ratio results from a change in the operation of CET – the assumption used by some studies to detect CET (see above). A plot of Φ_2/Φ_1 against irradiance using data of Genty and Harbinson (1996) shows a general decrease of the ratio with increasing irradiance (Fig. 11.3). Also, differences in the ratio of Φ_2/Φ_1 between different leaves could be due to the differing penetration into the leaves of the measuring wavelengths used for determining Φ_2 and Φ_1 , which highlights

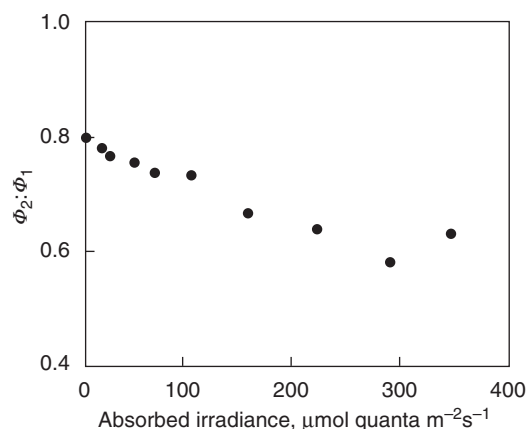


Fig. 11.3. The ratio of quantum efficiencies of electron transport of PS II Φ_2 to that of PS I Φ_1 under various irradiance levels. Ambient partial pressure of CO_2 350 μ bar, of O_2 210 mbar, assumed leaf absorptance 0.85. Original data from Genty and Harbinson (1996) for the tropical epiphyte *Juanulloa aurantiaca*

an important caveat about all model based analyses. However, even when this last point is considered, Eq. (11.18) predicts that a decrease in the Φ_2/Φ_1 ratio results in an increase either in ρ_2 if f_{cyc} stays constant or an increase in f_{cyc} if ρ_2 stays constant – a dilemma created by the model for non-limiting light conditions.

It is perhaps worth noting that similarly, any active CET also has implications for the Q-cycle activity. It has been concluded that an H^+ -pumping Q-cycle is continuously engaged, drawn from the observed proportional relationship between relative J_2 and relative v_{H^+} under low to saturating illumination (Sacksteder et al., 2000; Avenson et al., 2005a). Note, however, that a constant v_{H^+}/J_2 ratio is comparable with complementary changes in CET and Q-cycle activation (see Eq. B8b of Yin et al., 2004) as

$$v_{H^+}/J_2 = (2 + f_Q - f_{cyc})/(1 - f_{cyc}), \quad (11.19)$$

so, whether f_Q is constant depends on if f_{cyc} is constant even when the v_{H^+}/J_2 ratio is constant.

Many studies paid little attention to the ‘chicken-egg’ type interrelationship between f_{cyc} and ρ_2 as shown in Eq. (11.18). A best way to solve the dilemma would be to conduct combined gas exchange and biophysical measurements (e.g. Laisk et al., 2007), preferably under non-photorespiratory conditions, of Φ_{O_2} , Φ_2 and Φ_1 at various irradiance or CO_2 levels yet within the e^- transport-limited range. The version of Eq. (11.14a, b) for the non-limiting light situation and Eq. (11.18) can be applied to quantify f_{cyc} and ρ_2 at each light or CO_2 level. If Φ_{CO_2} and v_{H^+} are also measured, $f_{pseudo(b)}$ and f_Q can then be assessed by Eqs. (11.15) and (11.19), respectively. To cope with such a subtle research question, advanced gas exchange and biophysical measurements need to be very accurate.

4. On Cyclic as a Brake for Linear Electron Transport

Our analysis summarized above using data of Björkman and Demmig (1987) and Long

et al. (1993) has made use of assumptions, some of which have already been alluded to. First, it is assumed that the quantum absorption by non-photosynthetic pigments is negligible. Secondly, as stated earlier, $\Delta F/F'_m$ is not an exact measure of Φ_2 , and F_v/F_m is not an exact measure of $\Phi_{2(LL)}$. Thirdly, our analysis assumes that the WWC does not take place under strictly limiting light.

Due to the significance of these uncertainties, we attempted to show what the consequences would be if some of the assumptions were incorrect. We examined the extent to which the estimated electron transport fractions vary if light absorbance by non-photosynthetic pigments exists (Fig. 11.4a) or if the $\Phi_{2(LL)}/(F_v/F_m)$ ratio is not equal to 1 (Fig. 11.4b). The occurrence of a negative f_{cyc} in Fig. 11.4a means that absorbance by non-photosynthetic pigments cannot be higher than approximately 7% if other parameters are measured with sufficient accuracy. In other words, a prediction of 0.131 for f_{cyc} is equivalent to 7% non-photosynthetic absorbance in reducing quantum yield of photosynthesis.

Whether or not the WWC runs under limiting light is an uncertainty. If the WWC does function, the required absolute value for f_{cyc} would be lower, which can be seen from an equation for f_{cyc} derived from Eq. (11.9), where $\Phi_{CO_2(LL)}$ is replaced by $\Phi_{O_2(LL)}$ and $f_{pseudo(b)}$ refers to the fraction of PET in support of WWC ($f_{pseudo(wwc)}$):

$$f_{cyc} = \frac{\left\{ (C_c - \Gamma^*)(1 - f_{pseudo(wwc)}) - \Phi_{O_2(LL)}(4C_c + 8\Gamma^*) \left(\frac{1}{\Phi_{1(LL)}} + \frac{1}{\Phi_{2(LL)}} \right) \right\}}{(C_c - \Gamma^*) - \Phi_{O_2(LL)}(4C_c + 8\Gamma^*)/\Phi_{2(LL)}}. \quad (11.20)$$

The fraction of the basal PET supporting the non-WWC processes can then still be calculated by Eq. (11.15). Using the default values as set in Fig. 11.4, Eq. (11.20) predicts that the maximum $f_{pseudo(wwc)}$ is 0.068, at which point $f_{cyc} = 0$. Figure 11.4c shows the calculated f_{cyc} and $f_{pseudo(b)}$ for non-WWC processes under various hypothetical $f_{pseudo(wwc)}$ values, as a function of the $\Phi_{2(LL)}/(F_v/F_m)$ ratio. The occurrence of negative f_{cyc} indicates that WWC can never

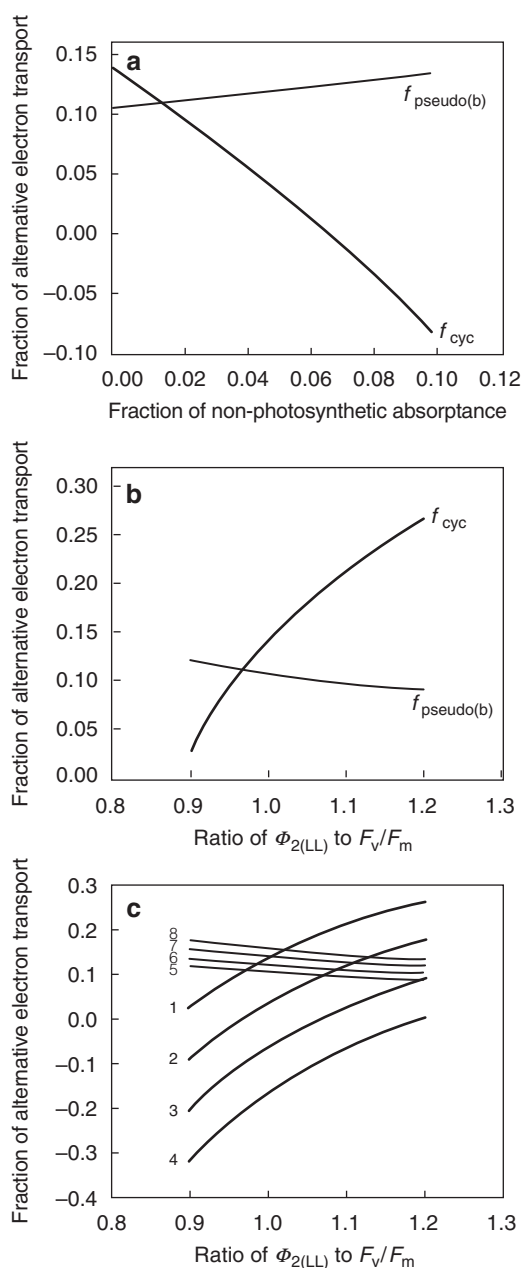


Fig. 11.4. Estimated fraction of cyclic electron transport f_{cyc} and fraction of basal pseudocyclic electron flow $f_{\text{pseudo(b)}}$ in response to the fraction of non-photosynthetic quantum absorption in the leaves (panel a), in response to the ratio of real PS II efficiency $\Phi_{2(\text{LL})}$ to the value given by F_v/F_m (b), and in response to the same ratio but at different values for $f_{\text{pseudo(wwc)}}$ (c). In calculations the values of parameters were 1.0 for $\Phi_{1(\text{LL})}$, 0.835 for F_v/F_m , 0.093 and 0.106 for $\Phi_{\text{CO}_2(\text{LL})}$ and $\Phi_{\text{O}_2(\text{LL})}$, respectively. In (c) f_{cyc} is shown by curves 1–4, and $f_{\text{pseudo(b)}}$ is shown by curves 5–8, with $f_{\text{pseudo(wwc)}} = 0.0$ for curves 1 and 5, 0.05 for curves 2 and 6, 0.10 for curves 3 and 7, and 0.15 for curves 4 and 8 (reproduced from Yin et al., 2006)

consume more than 15% of total PS I e^- fluxes under limiting light. This is compatible with the estimate of Cruz et al. (2005) for the WWC (about 12% of the total non-cyclic flux) to fill the ATP deficit between the light reactions and downstream metabolism.

Figure 11.4 shows that the estimate of f_{cyc} is always more responsive than the estimate of $f_{\text{pseudo(b)}}$ to a change in either light absorption by non-photosynthetic pigments or the error introduced by the use of Chl fluorescence-based parameters as measures of PS II efficiency. The sensitivity of f_{cyc} is similar to that shown in Fig. 11.2. The sensitivity of $f_{\text{pseudo(b)}}$ can become higher only if $\Phi_{\text{CO}_2(\text{LL})}$ is substantially lower than $\Phi_{\text{O}_2(\text{LL})}$ (results not shown), which is not expected from reported simultaneous measurements of CO_2 uptake and O_2 evolution (Ruuska et al., 2000; Laisk et al., 2006). CET was easily detected in isolated chloroplasts (Arnon, 1959), or in vivo during the induction period, when dark-adapted leaves are first illuminated (Holtgreffe et al., 2003; Joliot and Joliot, 2005). The participation of CET in ATP synthesis in green algae, cyanobacteria, and in C_4 bundle sheath chloroplasts is well recognized. For C_3 vascular plants, CET (if any) has been supposed to play a role under stress or at high light intensities (Cornic et al., 2000; Johnson, 2005; Miyake et al., 2005). The higher sensitivity of f_{cyc} than $f_{\text{pseudo(b)}}$ to the accuracy of fluorescence estimates or light-absorption, as shown in Fig. 11.4, indicates that the estimate of CET will be more prone to uncertainties in the inputs than will be the estimate of PET. This also suggests that if CET and PET run in concert, CET probably acts as a more active brake for LET to avoid or minimise any mismatch between Φ_{CO_2} and Φ_2 , even under the limiting light condition. As the model assumes that CET is coupled with ATP synthesis, the suggested role of CET has implications on the estimation of the required f_Q (Yin et al., 2006), and this will also be shown later.

5. On the Effect of Light Wavelength on Quantum Yield

One tricky, but not trivial, uncertainty in relation to the calculation of Φ_{O_2} or Φ_{CO_2} is the non-photosynthetic quantum absorption in leaves of many plants that have a high blue-light

absorptance due to non-photosynthetic pigments, which are often in the epidermal cells (McCree, 1972; Inada, 1976), and the wavelength dependency of either Φ_{O_2} or Φ_{CO_2} (Evans, 1987). These reports indicated that maximum quantum efficiency was achieved at about 600 nm. The effect of light wavelength on quantum yield is a complex issue and not fully understood, and may reflect an adaptation strategy (Chow et al., 1990). Nonetheless, Von Caemmerer (2000) updated the parameter $\alpha_{(LL)}$ in Eq. (11.4) of the FvCB model as $0.5(1 - f)$, see her Eq. (2.14), where 0.5 reflects that each photosystem ideally absorbs half the available light and f ($=0.15$) corrects for spectral quality of the light based on the result of Evans (1987) that quantum yields obtained in white light are about 85% of those in the 600-nm light. These factors predict $\alpha_{(LL)}$ being 0.425, and if applied to Eq. (11.10a), predict that the quantum yield is 0.106 under the non-photorespiratory condition, the same as the mean $\Phi_{O_2(LL)}$ for 37 species examined by Björkman and Demmig (1987). Since each of the two photosystems contains distinct pigment-protein complexes that harvest light from different regions of the visible spectra, Evans (1987) explained the variability of the quantum efficiency in terms of wavelength dependent changes in the partitioning of excitation energy between the photosystems. An unbalanced excitation of the photosystems would result in a loss of quantum efficiency of one photosystem relative to the other and an increase in energy loss via thermal dissipation from PS I or PS II (also see Genty and Harbinson, 1996).

Earlier, Farquhar et al. (1980) also used $0.5(1 - f)$ to describe the parameter $\alpha_{(LL)}$ in Eq. (11.4) but in this case f was the fraction of light lost by absorption other than by the chloroplast lamellae (see their Eq. 8). Later, Farquhar and Wong (1984) used the same expression (see their Eq. A3), but they then used f as the fraction of absorbed photon irradiance unavailable for carbon reduction and photorespiration, e.g. the fraction of absorbed irradiance used for driving alternative e^- sinks. Interestingly, f was specified as 0.23 in both the Farquhar et al. (1980) and Farquhar and Wong (1984) papers. The value 0.23 appears to be too high to be solely due to the non-photosynthetic absorption of light (Fig. 11.4a), and probably also reflects the loss of quantum yield due to the activity of CET or PET.

It is clear, therefore, that within the model there are links between non-photosynthetic absorption, wavelength effects, excitation partitioning, and alternative e^- transport. Non-photosynthetic absorption may explain a part of the decline for the blue light regions relative to the 600-nm lights. To what extent our analysis described above on the CET and excitation partitioning reconciles or disagrees with Evans' (1987) hypothesis merits a further quantitative study. Evans's explanation seemed to call for an increasing partitioning to PS II ($\rho_2 > 0.5$) for wavelengths other than around the 600-nm region. It follows, according to our model, that a decreased Φ_2 (an increased thermal dissipation from PS II), relative to Φ_1 , is required for these wavelengths. State transition, in principle, is the physiological mechanism by which excitation imbalances are corrected. However, as a regulatory mechanism, state transition has one problem – the contradictory evidence for its effect in vivo. Again, it seems that more research is needed to reconcile the contradictions.

C. An Integrated Approach to Estimating Photosynthesis Parameters

Using the generalized model, we will now describe an approach using curve-fitting to measurements of A and Φ_2 at various levels of irradiance and intercellular CO_2 partial pressure (C_i). The method consists of the following six steps, in which we provisionally bypass the currently unsolved ρ_2 vs. f_{cyc} dilemma by assuming that neither ρ_2 (as in the L-method) nor f_{cyc} change with light or CO_2 levels. The method will be demonstrated using the experimental data of Cheng et al. (2001) for leaves of 'Fuji' apple (*Malus domestica* Borkh). The apple trees had been grown under one of six N-nutrition regimes (hereafter, N1 to N6). The N contents of the leaves used for the irradiance response measurements were 4.0, 3.2, 2.4, 1.8, 1.6, and 1.0 g m⁻², and those for the C_i response measurements were 3.8, 3.2, 2.3, 2.0, 1.5, and 1.1 g m⁻², respectively for the N1 to N6 treatments. The photosynthetic responses were measured at 25°C, and the light response curves of A and $\Delta F/F'_m$ were obtained under a non-photorespiratory condition (20 mmol mol⁻¹ O₂ and 1,300 μ mol mol⁻¹ CO₂). The C_i response curves of A and $\Delta F/F'_m$ were

obtained at 210 mmol mol⁻¹ O₂ and an incident irradiance of 1,000 μmol quanta m⁻² s⁻¹. For this analysis, we will assume that the non-photosynthetic quantum absorption is negligible and $\Delta F/F'_m$ equals Φ_2 . All non-linear regression was performed using the Gauss–Newton method in the PROC NLIN of the SAS software (SAS Institute Inc., Cary, NC, USA).

1. Quantum Yield of Photosystem II

Although in our earlier analysis for the limiting light situation we set $\Phi_{2(LL)} = F_v/F_m$, $\Phi_{2(LL)}$ may be better estimated by extrapolating light response curves of Φ_2 to the zero irradiance. From measurements of Φ_2 , J_2 can be expressed as $J_2 = \Phi_2 \rho_2 I_{abs}$. Substituting this equation into Eq. (11.7) and solving for Φ_2 give

$$\Phi_2 = \left(\frac{\alpha_{2(LL)} I_{abs} + J_{2max}}{-\sqrt{(\alpha_{2(LL)} I_{abs} + J_{2max})^2 - 4\theta_2 J_{2max} \alpha_{2(LL)} I_{abs}}} \right) / (2\theta_2 \rho_2 I_{abs}), \quad (11.21)$$

where $\alpha_{2(LL)}$ is given by Eq. (11.8), and ρ_2 is calculated as $\alpha_{2(LL)}/\Phi_{2(LL)}$ (see Eq. 11.16 and Yin et al., 2006). It is clear from Eq. (11.8) that f_{cyc} and $\Phi_{1(LL)}$ should be known a priori. However, using a range of trial values for f_{cyc} and $\Phi_{1(LL)}$ it was shown that unlike J_{2max} , the estimates of θ_2 , $\Phi_{2(LL)}$ and goodness of fit are hardly affected by changes in f_{cyc} or $\Phi_{1(LL)}$. Thus, $\Phi_{2(LL)}$ can be obtained using arbitrary values of f_{cyc} and $\Phi_{1(LL)}$, provided they are within a physiologically reasonable range. The estimated values of $\Phi_{2(LL)}$ were 0.749(standard error 0.005), 0.726(0.011), 0.722(0.012), 0.730(0.005), 0.727(0.011), and 0.651(0.010) from N1 to N6, respectively. These values are apparently lower than 0.83 revealed as F_v/F_m by Björkman and Demmig (1987) or Long et al. (1993), but not unreasonable when compared to Φ_2 values measured under limiting irradiances, which are normally lower than the corresponding dark-adapted measurements of F_v/F_m (e.g. Genty et al., 1990).

2. Cyclic Electron Transport and Excitation Partitioning

Parameters f_{cyc} and ρ_2 may be estimated by linear regression of A against $(I_{inc}\Phi_2/4)$, based on Eq. (11.12), using data within the low light range. Owing to the limited number of data points within the low light range in the data set of Cheng et al. (2001), we estimated them, using the measured a and R_d (assumed by Cheng et al. the same as in the dark) as inputs, by a nonlinear regression of A against I_{abs} using a non-rectangular hyperbolic equation in which the $\Phi_{CO2(LL)}$ values calculated by Eq. (11.9) are combined. This procedure requires $\Phi_{1(LL)}$ and $f_{pseudo(b)}$ to be known a priori in order to fit f_{cyc} and ρ_2 . As outlined earlier, an estimation of $f_{pseudo(b)}$ would need combined data of CO₂ exchange and O₂ evolution (Eq. 11.15). Without this type of data, $f_{pseudo(b)}$ was assumed to be conservative for mature leaves, and a value of 0.1, as identified earlier, is provisionally used. This value is similar to that predicted theoretically by Fridlyand and Scheibe (1999). If nitrogen assimilation is the major sink of PETb, this value predicts that the ratio of nitrogen- to carbon-assimilation is about 0.05–0.10 (Yin et al., 2006), similar to the ratio that is widely reported (reviewed by Noctor and Foyer, 1998). Again, $\Phi_{1(LL)}$ was provisionally assumed to be 1.

The estimated f_{cyc} was 0.201(0.011), 0.224(0.022), 0.193(0.041), 0.193(0.037), 0.293(0.081) and 0.275(0.193) from N1 to N6, respectively. Apart from the value for N6, all estimated values for f_{cyc} differed significantly from zero. Using a fixed value for $\Phi_{1(LL)}$ and estimated values for f_{cyc} and $\Phi_{2(LL)}$, ρ_2 can be calculated using Eq. (11.17). But to obtain standard errors for the estimates, we derived its value using the non-linear fitting routine. The estimates of ρ_2 were 0.516(0.003), 0.517(0.007), 0.528(0.013), 0.525(0.011), 0.493(0.029) and 0.527(0.067) from N1 to N6, respectively.

To test the possibility that $\Phi_{1(LL)} < 1$, we estimated $\Phi_{1(LL)}$, with $f_{cyc} = 0$ as an input. The obtained average $\Phi_{1(LL)}$ was 0.72, similar to the estimated $\Phi_{2(LL)}$. Given the general recognition that photochemical efficiency of non-oxidized PS

I reaction centers is higher than that of open PS II centers, we consider a non-zero f_{cyc} as a more likely scenario than a $\Phi_{1(\text{LL})}$ as low as $\Phi_{2(\text{LL})}$. In the event that $\Phi_{1(\text{LL})}$ is indeed lower than 1, the estimated f_{cyc} would reflect both the real CET and the loss of PS I efficiency under limiting light. The uncertainty in $\Phi_{1(\text{LL})}$ has a strong impact on estimation of f_{cyc} but little impact on ρ_2 . For example, if $\Phi_{1(\text{LL})}$ was allowed to vary from 1.0 to 0.7, the estimated f_{cyc} for N6 decreased monotonically from 0.275 to 0.043 whereas ρ_2 only decreased from 0.527 to 0.507.

3. Maximum Electron Transport Rate of Photosystem II

Using the measurements of Φ_2 at various light levels, Eq. (11.21), when combined with Eq. (11.8) and using the estimated $\Phi_{2(\text{LL})}$ and f_{cyc} as inputs, can be used to fit θ_2 and $J_{2\text{max}}$. The estimated θ_2 varied from 0.68 to 0.91, tending to be higher than the commonly used value of 0.7 (Von Caemmerer, 2000). The estimated $J_{2\text{max}}$ scaled linearly with leaf nitrogen (N , g m^{-2}), with $J_{2\text{max}} = 146.61(N - 0.657)$, $r^2 = 0.99$. The uncertainty in $\Phi_{1(\text{LL})}$ had no impact on the fitted θ_2 and $J_{2\text{max}}$, as long as the input f_{cyc} was allowed to vary accordingly with $\Phi_{1(\text{LL})}$ for a given $\Phi_{\text{CO2}(\text{LL})}$.

It is worth noting that as in the FvCB model, our model formulae take no consideration of limitation by triose phosphate utilization (Sharkey, 1985) nor any other source of metabolic limitation of electron transport. However, this limitation, if it occurred, would have been implicitly accounted for in the estimated $J_{2\text{max}}$ and θ_2 , as the limitation would have a feedback effect on e^- transport rate which can be reflected by Chl fluorescence signals (Sharkey et al., 1988; Yin et al., 2009).

4. Mesophyll Diffusion Conductance and Rubisco Parameters

Replacing C_c in Eqs. (11.2) and (11.6) with $(C_i - A_c/g_m)$ and $(C_i - A_j/g_m)$ respectively, and

then solving for A_c and A_j gives (Von Caemmerer et al., 1991; Von Caemmerer, 2000):

$$\begin{aligned}
 & A_c \text{ or } A_j \\
 & = \left\{ \begin{array}{l} x_1 - R_d + g_m(C_i + x_2) \\ - \sqrt{[x_1 - R_d + g_m(C_i + x_2)]^2 - 4g_m[(C_i - \Gamma^*)x_1 - R_d(C_i + x_2)]} \end{array} \right\} / 2 \\
 & \text{with } x_1 = \begin{cases} V_{\text{c max}} & \text{for } A_c \\ [1 - f_{\text{pseudo(b)}}/(1 - f_{\text{cyc}})]J_2/4 & \text{for } A_j \end{cases} \\
 & x_2 = \begin{cases} K_{\text{mC}}(1 + O/K_{\text{mO}}) & \text{for } A_c \\ 2\Gamma^* & \text{for } A_j \end{cases} \quad (11.22)
 \end{aligned}$$

Equation (11.22), combined with Eqs. (11.1), (11.7) and (11.8), provides a simultaneous model with which to solve g_m , $S_{\text{c/o}}$, and $V_{\text{c max}}$ in a single curve-fitting procedure, using a least squares regression that minimizes the difference between the measured and estimated values of A . Equation (11.22) is similar to that of Ethier and Livingston (2004), known as the curvature method, to estimate g_m (Warren, 2006). Their method to estimate g_m is based entirely on $A - C_i$ curves (Ethier et al., 2006) and has not used $\Delta F/F'_m$ measurements.

Curve-fitting with Eq. (11.22) requires measurements of A at various C_i levels under photorespiratory conditions at certain light level(s). Measurements under photorespiratory conditions are required because the estimation of g_m using the A_j part of the model works only in the presence of photorespiration since it is based on the re-assimilation of photorespiratory CO_2 (Laisk and Loreto, 1996; Laisk et al., 2002). This is similar to the Chl fluorescence based methods (Harley et al., 1992a; Evans and Von Caemmerer, 1996). However differences are evident. First, in our method not all of the e^- flux through PS I is used for carbon reduction and photorespiration: some of the flux is used to reduce the PETb acceptors (as allowed by Laisk et al., 2006), some is the PETa flux (if any), and some is the CET flux (if any). Secondly, since $S_{\text{c/o}}$ is simultaneously estimated in our method, the inclusion of measurements made at various O_2 levels is preferred,

as this avoids the problem that afflicts existing Chl fluorescence based methods due to strong sensitivity of the estimate of g_m on the chosen value of $S_{c/o}$. Finally, our parameter-solving method using Eq. (11.22) to fit data points over the whole C_i range in a single curve-fitting procedure, which itself identifies the cut-off point between A_c and A_j limitations, ensures that the estimated g_m value applies for both A_c - and A_j -limited ranges. The use of a combined curve-fitting procedure allows the simultaneous estimation of $S_{c/o}$ and V_{cmax} that yield the best fit to the combined data of both A_c - and A_j -limited ranges. By this statistical fitting method the iterative logic in the L-method for estimating g_m , $S_{c/o}$ and PETa is avoided. In our model PETa is assumed to occur only over the A_c -limited range (see Model step 5 below).

In the experiment of Cheng et al. (2001) $A - C_i$ curves are obtained from plants of the same genotype grown at six N levels. While $S_{c/o}$ varies with plant species (Jordan and Ogren, 1981; Delgado et al., 1995; Galmés et al., 2005) and probably within a species (Pettigrew and Turley, 1998), $S_{c/o}$ is expected to be constant for a specific genotype. As shown for the J_{max} estimates we forced V_{cmax} and g_m to scale with leaf N in order to obtain a common estimate for $S_{c/o}$ across the range of N levels. The required input parameters at this step are K_{mC} and K_{mO} , in addition to the parameters estimated in the above steps. Values for K_{mC} (287 μ bar) and K_{mO} (204 mbar) at 25°C were taken from the comprehensive data of Von Caemmerer et al. (1994). A first curve-fitting result showed that g_m was not entirely correlated with the N level in the data set of Cheng et al. (2001), because the fit became worse if g_m was allowed to scale with leaf N in the curve-fitting (as was V_{cmax}), so g_m was set to a single value across the N levels; the overall fit was thus improved ($R^2 = 0.992$). The estimated slope for the linear relationship between V_{cmax} and $(N - 0.486)$ is $75.7(5.2) \mu\text{mol s}^{-1} \text{g}^{-1}$. The estimated $S_{c/o}$ is $3.12(0.22) \text{ mbar } (\mu\text{bar})^{-1}$. The estimated overall g_m is $0.277 \text{ mol m}^{-2} \text{ s}^{-1} \text{ bar}^{-1}$.

Unlike stomatal conductance, the value of g_m has been considered to represent a physiolog-

ical property of a leaf, being relatively stable across certain environmental conditions (Evans and Von Caemmerer, 1996). This is an assumption, upon which existing approaches to estimate g_m (including ours) are based. Recently, Flexas et al. (2007) reported rapid variation of g_m in response to changes in both CO_2 and irradiance (resembling the response of stomatal conductance) in several species. If this response turns out to be general, our estimated g_m should be considered as an overall mean value across the range of C_i and irradiances used, and could be lower than g_m estimated using data of low C_i ranges only.

5. Additional Alternative Electron Flow

At high irradiance or low CO_2 partial pressure, the calculated A_j is likely to be higher than A_c , implying that there are more non-cyclic electrons than required for the carbon reduction cycle, photorespiration, and processes supported by PETb. These additional electrons (PETa), may be dissipated by the WWC in the chloroplast (Asada, 1999), or exported to the cytosol via the malate-oxaloacetate shuttle where they could be used for nitrate reduction or possibly used to reduce O_2 in the mitochondria (Backhausen et al., 2000). The fraction of J_1 that serves as the PETa ($f_{\text{pseudo(a)}}$) is derived from Eq. (11.6):

$$f_{\text{pseudo(a)}} = (1 - f_{\text{cyc}}) \left\{ 1 - \frac{4(A + R_d)[(C_i + 2\Gamma^*)g_m - A]}{J_2[(C_i - \Gamma^*)g_m - A]} \right\} - f_{\text{pseudo(b)}}, \quad (11.23)$$

where A is the value calculated from Eq. (11.1). To estimate any $f_{\text{pseudo(a)}}$ under high light, J_2 in Eq. (11.23) can be calculated by Eq. (11.7) using the estimates of $J_{2\text{max}}$, $\Phi_{2(\text{LL})}$, f_{cyc} and θ_2 as described above. In the current model J_2 is only related to irradiance and not to C_i (Eq. 11.7); so, to estimate any $f_{\text{pseudo(a)}}$ at low C_i , J_2 is estimated as $J_2 = \Phi_2 \rho_2 I_{\text{abs}}$ using measured Φ_2 values so as to reflect the possible feedback regulation of low C_i on Φ_2 . Random noise in measured Φ_2 can affect the estimated $f_{\text{pseudo(a)}}$ at low C_i , as

measured data for Φ_2 were not smoothed by curve-fitting.

Non-zero $f_{\text{pseudo(a)}}$ values were found when irradiance became higher than a threshold. The threshold light level was higher in high N than low N leaves. The average $f_{\text{pseudo(a)}}$ across 11 light levels decreased with leaf N, from 0.14 for N6 to 0.07 for N1. $f_{\text{pseudo(a)}}$ was also often above the detection level at low C_i , with a maximum of about 0.19.

6. Partial Involvement of the Q-cycle

The total fraction of PET (f_{pseudo}) is the sum of $f_{\text{pseudo(b)}}$ and $f_{\text{pseudo(a)}}$. After f_{cyc} and f_{pseudo} are estimated, the value of f_Q – the required fraction of electrons from plastoquinol that follow the Q-cycle – can be calculated by solving Eq. (11.5) for f_Q . This calculation assumes that (i) all e^- are H^+ coupled, e.g. there is no e^- cycle within PS II, (ii) all H^+ efflux from the thylakoid lumen is coupled to ATP synthesis, e.g. no H^+ slip or leak, (iii) any ATP requirement by processes other than the Benson-Calvin cycle and photorespiration is met by non-photosynthetic processes (e.g. oxidative phosphorylation). The model could be extended to include the small ATP consumption of nitrate reduction (Noctor and Foyer, 1998) if the exact ratio for carbon to nitrogen assimilation were known. Similarly the model could potentially account for other (minor) processes (e.g. starch synthesis) if our understanding or procedural solutions allow the quantification of these minor fluxes in relation to their ATP requirements. However, the ATP cost for nitrate reduction and other minor processes are usually attributed to mitochondrial respiration (Cannell and Thornley, 2000). In the event that these processes indeed use ATP generated by the chloroplast e^- transport chain, it, together with their consumption of reductants (in the form of PET), may partly explain why the mitochondrial respiration can be inhibited by light, as frequently reported (e.g. Brooks et al., 1985; Laisk and Loreto, 1996).

Three H^+ /ATP ratios ($h = 3$, or 4, or $14/3$) were used in the calculation. Because $f_{\text{pseudo(a)}}$ varies with irradiance, CO_2 and N levels, it is expected that f_Q required for the Benson-Calvin cycle and photorespiration will also vary. An example is shown in Fig. 11.5 for the dependence

of f_Q on light and C_i for the N1 treatment. In response to changing irradiance, the estimates of f_Q first stayed constant and then decreased with increasing light (Fig. 11.5a). Increasing C_i provoked decreases in f_Q (Fig. 11.5b), because $f_{\text{pseudo(a)}}$ was virtually zero for N1. The small decrease of f_Q with increasing C_i may be due to the slightly higher requirement for ATP by oxygenation than carboxylation and the decrease of the oxygenation/carboxylation ratio with increasing C_i . Figure 11.5 shows that if $h = 3$ (an obsolete value included solely because of its use in the original FvCB model), the estimated values of f_Q were all negative, indicating no need for the Q-cycle but an excess H^+ pumping capacity by the e^- transport chain relative to the demands

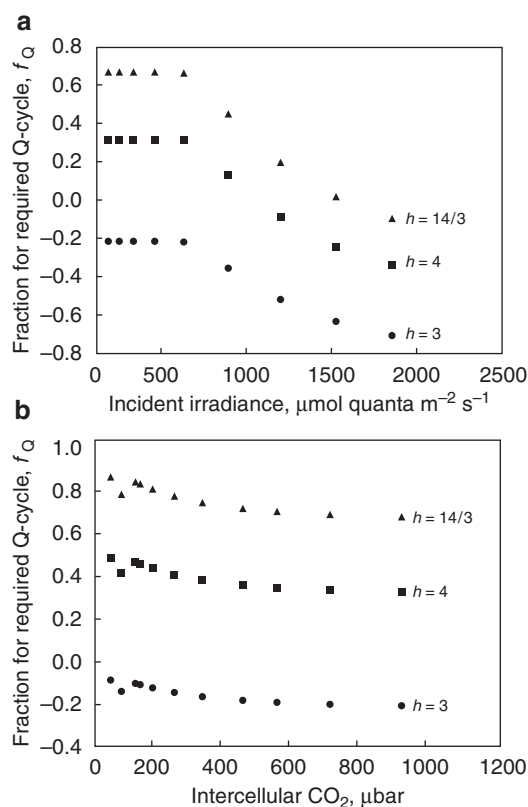


Fig. 11.5. Estimated fraction of electrons that are required to follow the Q-cycle (f_Q) in support of carbon reduction and photorespiration, in apple leaf (N1, the highest nitrogen level) measured at various irradiances under the non-photorespiratory condition (panel a) or at various intercellular CO_2 partial pressure with constant incident irradiance ($1,000 \mu\text{mol m}^{-2} \text{s}^{-1}$, panel b), assuming parameter h (the number of protons required to synthesize 1 ATP) is 3 (circles) or 4 (squares) or $14/3$ (triangles)

of carboxylation and photorespiration. This contrasts with the FvCB model that implies a deficiency of ATP relative to NADPH supply. If $h = 4$ or $h = 14/3$, a higher degree of involvement of the Q-cycle to supply ATP for photosynthetic metabolism is required, but an obligate Q-cycle ($f_Q = 1$) was never required (Fig. 11.5).

The calculated f_Q should not be considered as definite as there are uncertainties: we assumed that $\Phi_{1(LL)} = 1$, and that there was a zero non-photosynthetic quantum absorption. This will tend to result in an overestimation of f_{cyc} ; a high CET will generate some ATP that otherwise would require a higher f_Q to achieve. Nevertheless, the pattern for the calculated f_Q in relation to light and C_i levels seems to support a variable H^+ -pumping Q-cycle mode, as has been suggested (e.g. Cornic et al., 2000). Whether the Q-cycle is obligatory or variable is still under debate. If obligatory (e.g. Sacksteder et al., 2000), parameter h has to be high, e.g. $14/3$. Our calculation for the N1 level using the earlier estimated $\Phi_{CO2(LL)}$ and $\Phi_{2(LL)}$ showed that if $f_Q = 1$ and $h = 14/3$, f_{cyc} would be about -0.4 and $f_{pseudo(b)}$ would be about 0.43 . Again a negative f_{cyc} is impossible but implies an overcapacity of H^+ pumping. So, if the Q-cycle is obligatory, some of the following must be true: that some ATP are used for processes other than carbon reduction and photorespiration, that some e^- flows are uncoupled from the H^+ transport, e.g. a basal H^+ leakage through the thylakoid membrane (Groth and Junge, 1993), or an e^- transport cycle within PS II (Miyake and Yokota, 2001; Laisk et al., 2006).

IV. Concluding Remarks

Linear whole-chain e^- transport plays a dominant role in generating NADPH and ATP required for carbon fixation in chloroplasts. However, as suggested by many reviews (e.g. Allen, 2003; Cruz et al., 2005; Avenson et al., 2005b), other e^- pathways may be present to contribute to the flexibility of e^- transport in meeting demands by various down-stream metabolic processes. Quantification of the plasticity of the light reactions of photosynthesis and photosynthetic regulation in response to environmental changes requires

a model that incorporates various e^- transport pathways. Within this context, our generalized model was developed. Although there are some uncertainties in the model, e.g. the number of H^+ transported by CET and how CET is coupled with the Q-cycle, the model can be easily refined to accommodate future revelations. The heuristic role for the model has been illustrated, and the model can also be used to better frame new research questions. Our model can quantify the range of variation for uncertain or non-measured parameters and answer ‘what-if’ questions with respect to these uncertainties; some of these analyses were shown in this chapter. Further uncertainty analysis may be conducted with respect to variation of dark respiration with light levels, maximum PS I efficiency, the required Q-cycle if ATP export, or a PS II cycle, or H^+ leakage occurs, and the required reductant export to cytosol if the malate valve precedes activation of CET and the WWC. If combined with sufficient, advanced measurements which could be very accurate by future equipment design, the approach can quantify a large number of parameters that can be used to analyze physiological limitation to steady-state C_3 photosynthesis under various environmental conditions. This is important for understanding photosynthesis under sub-optimal conditions when abiotic stresses like low temperature, drought or mineral deficiency prevail. The operation of the alternative e^- pathways is especially relevant under these conditions, because non-assimilatory e^- flow may replace assimilatory e^- flow in order to act as a protective mechanism against photoinhibition (Ort and Baker, 2002). Our model, combined with accurate gas exchange and biophysical measurements, will facilitate understanding bioenergetics and regulations of photosynthesis induced by these stress events.

Acknowledgments

We thank Drs. M. Van Oijen and A.H.C.M. Schapendonk for their early contribution to the development of the model and anonymous reviewers of our related papers for their enlightening comments at various stages of the work described in this chapter.

References

- Albertsson P-Å (2001) A quantitative model of the domain structure of the photosynthetic membrane. *Trends Plant Sci* 6: 349–354
- Allen JF (2003) Cyclic, pseudocyclic and noncyclic photophosphorylation: new links in the chain. *Trends Plant Sci* 8: 15–19
- Arnon DI (1959) Conversion of light into chemical energy in photosynthesis. *Nature* 184: 10–21
- Asada K (1999) The water-water cycle in chloroplasts: Scavenging of active oxygens and dissipation of excess photons. *Annu Rev Plant Physiol Plant Mol Biol* 50: 601–639
- Avenson TJ, Cruz JA, Kanazawa A and Kramer DM (2005a) Regulating the proton budget of higher plant photosynthesis. *Proc Natl Acad Sci USA* 102: 9709–9713
- Avenson TJ, Kanazawa A, Cruz JA, Takizawa K, Ettinger WE and Kramer DM (2005b) Integrating the proton circuit into photosynthesis: progress and challenges. *Plant Cell Environ* 28: 97–109
- Backhausen JE, Emmerlich A, Holtgreffe S, Horton P, Nast G, Rogers JJM, Müller-Röber B and Scheibe R (1998) Transgenic potato plants with altered expression levels of chloroplast NADP-malate dehydrogenase: interactions between photosynthetic electron transport and malate metabolism in leaves and in isolated intact chloroplasts. *Planta* 207: 105–114
- Backhausen JE, Kitzmann C, Horton P and Scheibe R (2000) Electron acceptors in isolated intact spinach chloroplasts act hierarchically to prevent over-reduction and competition for electrons. *Photosynth Res* 64: 1–13
- Baker NR, Harbinson J and Kramer DM (2007) Determining the limitations and regulation of photosynthetic energy transduction in leaves. *Plant Cell Environ* 30: 1107–1125
- Bernacchi CJ, Portis AR, Nakano H, Von Caemmerer S and Long SP (2002) Temperature response of mesophyll conductance. Implication for the determination of Rubisco enzyme kinetics and for limitations to photosynthesis *in vivo*. *Plant Physiol* 130: 1992–1998
- Björkman O and Demmig B (1987) Photon yield of O₂ evolution and chlorophyll fluorescence characteristics at 77 K among vascular plants of diverse origins. *Planta* 170: 489–504
- Brooks A and Farquhar GD (1985) Effect of temperature on the CO₂/O₂ specificity of ribulose-1,5-bisphosphate carboxylase/oxygenase and the rate of respiration in the light. *Planta* 165: 397–406
- Cannell MGR and Thornley JHM (2000) Modelling the components of plant respiration: Some guiding principles. *Ann Bot* 85: 45–54
- Cape JL, Bowman MK and Kramer DM (2006) Understanding the cytochrome *bc* complexes by what they don't do. The Q-cycle at 30. *Trends Plant Sci* 11: 46–55
- Cheng L, Fuchigami LH and Breen PJ (2001) The relationship between photosystem II efficiency and quantum yield for CO₂ assimilation is not affected by nitrogen content in apple leaves. *J Exp Bot* 52: 1865–1872
- Chow WS, Melis A and Anderson JM (1990) Adjustments of photosystem stoichiometry in chloroplasts improve the quantum efficiency of photosynthesis. *Proc Natl Acad Sci USA* 87: 7502–7506
- Cornic G and Briantais J-M (1991) Partitioning of photosynthetic electron flow between CO₂ and O₂ reduction in a C₃ leaf (*Phaseolus vulgaris* L.) at different CO₂ concentrations and during drought stress. *Planta* 183: 178–184
- Cornic G and Ghashghaie J (1991) Effect of temperature on net CO₂ assimilation and photosystem II quantum yield of electron transport of French bean (*Phaseolus vulgaris* L.) leaves during drought stress. *Planta* 185: 255–260
- Cornic G, Bukhov NG, Wiese C, Bligny R and Heber U (2000) Flexible coupling between light-dependent electron and vectorial proton transport in illuminated leaves of C₃ plants. Role of photosystem I-dependent proton pumping. *Planta* 210: 468–477
- Cruz JA, Avenson TJ, Kanazawa A, Takizawa K, Edwards GE and Kramer DM (2005) Plasticity in light reactions of photosynthesis for energy production and photoprotection. *J Exp Bot* 56: 395–406
- Delgado E, Medrano H, Keys AJ and Parry MAJ (1995) Species variation in Rubisco specificity factor. *J Exp Bot* 46: 1775–1777
- Epron D, Godard G, Cornic G and Genty B (1995) Limitation of net CO₂ assimilation rate by internal resistances to CO₂ transfer in leaves of two tree species (*Fagus sylvatica* L. and *Castanea sativa* Mill.). *Plant Cell Environ* 18: 43–51
- Ethier GJ and Livingston NJ (2004) On the need to incorporate sensitivity to CO₂ transfer conductance into the Farquhar-Von Caemmerer-Berry leaf photosynthesis model. *Plant Cell Environ* 27: 137–153
- Ethier GJ, Livingston NJ, Harrison DL, Black TA and Moran JA (2006) Low stomatal and internal conductance to CO₂ versus Rubisco deactivation as determinants of the photosynthetic decline of ageing evergreen leaves. *Plant Cell Environ* 29: 2168–2184
- Evans JR (1987) The dependence of quantum yield on wavelength and growth irradiance. *Aust J Plant Physiol* 14: 69–79
- Evans JR (1993) Photosynthetic acclimation and nitrogen partitioning within a lucerne canopy. II. Stability through time and comparison with a theoretical optimum. *Aust J Plant Physiol* 20: 69–82
- Evans JR and Von Caemmerer S (1996) Carbon dioxide diffusion inside leaves. *Plant Physiol* 110: 339–346
- Farquhar GD and Von Caemmerer S (1981) Electron transport limitations in the CO₂ assimilation rate of leaves: A model and some observations in *Phaseolus vulgaris* L. In: Akoyunoglou G (ed) *Photosynthesis*, Vol. IV: Regulation of Carbon Metabolism, pp 163–175. Balaban International Science Services, Philadelphia, PA

- Farquhar GD and Von Caemmerer S (1982) Modelling of photosynthetic response to environmental conditions. In: Lange OL, Nobel PS, Osmond CB and Ziegler H (eds) *Physiological Plant Ecology II, Water Relations and Carbon Assimilation*. Encyclopedia of Plant Physiology, New Series, Vol. 12 B, pp 549–588. Springer, Berlin
- Farquhar GD and Wong SC (1984) An empirical model of stomatal conductance. *Aust J Plant Physiol* 11: 191–210
- Farquhar GD, Von Caemmerer S and Berry JA (1980) A biochemical model of photosynthetic CO₂ assimilation in leaves of C₃ species. *Planta* 149: 78–90
- Field TS, Nedbal L and Ort DR (1998) Nonphotochemical reduction of the plastoquinone pool in sunflower leaves originates from chlororespiration. *Plant Physiol* 116: 1209–1218
- Flexas J, Diaz-Espejo A, Galmes J, Kaldenhoff R, Medrano H and Ribas-Carbó M (2007) Rapid variation of mesophyll conductance in response to changes in CO₂ concentration around leaves. *Plant Cell Environ* 30: 1284–1298
- Fridlyand LE and Scheibe R (1999) Controlled distribution of electrons between acceptors in chloroplasts: a theoretical consideration. *Biochim Biophys Acta* 1413: 31–42
- Furbank RT, Jenkins CLD and Hatch MD (1990) C₄ photosynthesis: Quantum requirement, C₄ acid overcycling and Q-cycle involvement. *Aust J Plant Physiol* 17: 1–7
- Galmés J, Flexas J, Keys AJ, Cifre J, Mitchell RAC, Madgwick PJ, Haslam RP, Medrano H and Parry MAJ (2005) Rubisco specificity factor tends to be larger in plant species from drier habitats and in species with persistent leaves. *Plant Cell Environ* 28: 571–579
- Genty B and Harbinson J (1996) Regulation of light utilization for photosynthetic electron transport. In: Baker NR (ed) *Advances in Photosynthesis, Vol 5, Photosynthesis and the Environment*, pp 66–99. Kluwer, Dordrecht
- Genty B, Briantais J and Baker N (1989) The relationship between the quantum yield of photosynthetic electron transport and quenching of chlorophyll fluorescence. *Biochim Biophys Acta* 990: 87–92
- Genty B, Wonders J and Baker NR (1990) Non-photochemical quenching of F₀ in leaves is emission wavelength dependent consequences for quenching analysis and its interpretation. *Photosynth Res* 26: 133–139
- Groth G and Junge W (1993) Proton slip of the chloroplast ATPase: its nucleotide dependence, energetic threshold, and relation to an alternating site mechanism of catalysis. *Biochemistry* 32: 8103–8111
- Haldrup A, Jensen PE, Lunde C and Scheller HV (2001) Balance of power: a view of the mechanism of photosynthetic state transitions. *Trends Plant Sci* 6: 301–305
- Harbinson J and Foyer CH (1991) Relationships between the efficiencies of photosystems I and II and stromal redox state in CO₂-free air: Evidence for cyclic electron flow *in vivo*. *Plant Physiol* 97: 41–49
- Harbinson J and Woodward FI (1987) The use of light induced absorbance change at 820 nm to monitor the oxidation state of P700 in leaves. *Plant Cell Environ* 10: 131–140
- Harley PC, Loreto F, Di Marco G and Sharkey TD (1992a) Theoretical considerations when estimating the mesophyll conductance to CO₂ flux by analysis of the response of photosynthesis to CO₂. *Plant Physiol* 98: 1429–1436
- Harley PC, Thomas RB, Reynolds JF and Strain BR (1992b) Modelling photosynthesis of cotton grown in elevated CO₂. *Plant Cell Environ* 15: 271–282
- Hauska G, Schütz M and Büttner M (1996) The cytochrome *b₆f* complex – composition, structure and function. In: Ort DR and Yocum CF (eds) *Oxygenic Photosynthesis: The Light Reactions*. *Advances in Photosynthesis Vol 4*, pp 377–398. Kluwer, Dordrecht
- Heber U (2002) Irrungen, Wirrungen? The Mehler reaction in relation to cyclic electron transport in C₃ plants. *Photosynth Res* 73: 223–231
- Holtgreve S, Bader KP, Horton P, Scheibe R, Von Schaewen A and Backhausen JE (2003) Decreased content of leaf ferredoxin changes electron distribution and limits photosynthesis in transgenic potato plants. *Plant Physiol* 133: 1768–1778
- Inada K (1976) Action spectra for photosynthesis in higher plants. *Plant Cell Physiol* 17: 355–365
- Johnson GN (2005) Cyclic electron transport in C₃ plants: facts or artefacts? *J Exp Bot* 56: 407–416
- Joliot P and Joliot A (2005) Quantification of cyclic and linear flows in plants. *Proc Natl Acad Sci USA* 102: 4913–4918
- Jordan DB and Ogren WL (1981) Species variation in the specificity of ribulose biphosphate carboxylase/oxygenase. *Nature* 291: 513–515
- Junge W, Panke O, Cherepanov DA, Gumbiowski K, Muller M and Engelbrecht S (2001) Inter-subunit rotation and elastic power transmission in F₀F₁-ATPase. *FEBS Lett* 504: 152–160
- Juretić D and Westerhoff HV (1987) Variation of efficiency with free-energy dissipation in models of biological energy transduction. *Biophys Chem* 28: 21–34
- Kramer DM, Avenson TJ and Edwards GE (2004) Dynamic flexibility in the light reactions of photosynthesis governed by both electron and proton transfer reactions. *Trends Plant Sci* 9: 349–357
- Laisk A and Loreto F (1996) Determining photosynthetic parameters from leaf CO₂ exchange and chlorophyll fluorescence. Ribulose-1,5-bisphosphate carboxylase/oxygenase specificity factor, dark respiration in the light, excitation distribution between photosystems, alternative electron transport rate, and mesophyll diffusion resistance. *Plant Physiol* 110: 903–912
- Laisk A, Oja V, Rasulov B, Rämama H, Eichelmann H, Kasparova I, Pettai H, Padu E and Vapaavuori E (2002) A computer-operated routine of gas exchange and optical measurements to diagnose photosynthetic apparatus in leaves. *Plant Cell Environ* 25: 923–943

- Laisk A, Eichelmann H, Oja V and Peterson RB (2005) Control of cytochrome *b₆f* at low and high light intensity and cyclic electron transport in leaves. *Biochim Biophys Acta* 1708: 79–90
- Laisk A, Eichelmann H, Oja V, Rasulov B and Rämme H (2006) Photosystem II cycle and alternative electron flow in leaves. *Plant Cell Physiol* 47: 972–983
- Laisk A, Eichelmann H, Oja V, Talts E and Scheibe R (2007) Rates and roles of cyclic and alternative electron flow in potato leaves. *Plant Cell Physiol* 48: 1575–1588
- Lavergne J and Trissl HW (1995) Theory of fluorescence induction in photosystem II: derivation of analytical expressions in a model including exciton-radical-pair equilibrium and restricted energy transfer between photosynthetic units. *Biophys J* 68: 2474–2492
- Long SP and Bernacchi CJ (2003) Gas exchange measurements, what can they tell us about the underlying limitations to photosynthesis? Procedures and sources of error. *J Exp Bot* 54: 2393–2401
- Long SP, Postl WF and Bolhár-Nordenkampf HR (1993) Quantum yields for uptake of carbon dioxide in *C₃* vascular plants of contrasting habitats and taxonomic groupings. *Planta* 189: 226–234
- McCree KJ (1972) The action spectrum, absorptance and quantum yield of photosynthesis in crop plants. *Agric Meteorol* 9: 191–216
- Makino A, Miyake C and Yokota A (2002) Physiological functions of the water-water cycle (Mehler reactions) and the cyclic electron flow around PS I in rice leaves. *Plant Cell Physiol* 43: 1017–1026
- Mitchell P (1975) The proton motive Q-cycle: a general formulation. *FEBS Lett* 59: 137–139
- Miyake C and Yokota A (2001) Cyclic flow of electrons within PS II in thylakoid membranes. *Plant Cell Physiol* 42: 508–515
- Miyake C, Miyata M, Shinzaki Y and Tomizawa K (2005) CO₂ response of cyclic electron flow around PS I (CEF-PS I) in tobacco leaves – Relative electron fluxes through PS I and PS II determine the magnitude of non-photochemical quenching (NPQ) of Chl fluorescence. *Plant Cell Physiol* 46: 629–637
- Nelson N, Sacher A and Nelson H (2002) The significance of molecular slips in transport systems. *Nat Rev Mol Cell Biol* 3: 876–881
- Noctor G and Foyer CH (1998) A re-evaluation of the ATP:NADPH budget during *C₃* photosynthesis: a contribution from nitrate assimilation and its associated respiratory activity? *J Exp Bot* 49: 1895–1908
- Öquist G and Chow WS (1992) On the relationship between the quantum yield of Photosystem II electron transport, as determined by chlorophyll fluorescence and the quantum yield of CO₂-dependent O₂ evolution. *Photosynth Res* 33: 51–62
- Ort DR and Baker NR (2002) A photoprotective role for O₂ as an alternative electron sink in photosynthesis? *Curr Opin Plant Biol* 5: 193–198
- Osyczka A, Moser CC and Dutton PL (2005) Fixing the Q cycle. *Trends Biochem Sci* 30: 176–182
- Peterson RB (1989) Partitioning of noncyclic photosynthetic electron transport to O₂-dependent dissipative processes as probed by fluorescence and CO₂ exchange. *Plant Physiol* 90: 1322–1328
- Pettigrew WT and Turley RB (1998) Variation in photosynthetic components among photosynthetically diverse cotton genotypes. *Photosynth Res* 56: 15–25
- Pföndel E (1998) Estimating the contribution of photosystem I to total leaf chlorophyll fluorescence. *Photosynth Res* 56: 185–195
- Ruuska SA, Badger MR, Andrews TJ and Von Caemmerer S (2000) Photosynthetic electron sinks in transgenic tobacco with reduced amounts of Rubisco: little evidence for significant Mehler reaction. *J Exp Bot* 51: 357–368
- Sacksteder CA and Kramer DM (2000) Dark interval relaxation kinetics of absorbance changes as a quantitative probe of steady-state electron transfer. *Photosynth Res* 66: 145–158
- Sacksteder CA, Kanazawa A, Jacoby ME and Kramer DM (2000) The proton to electron stoichiometry of steady-state photosynthesis in living plants: A proton-pumping Q cycle is continuously engaged. *Proc Natl Acad Sci USA* 97: 14283–14288
- Seaton GGR and Walker DA (1990) Chlorophyll fluorescence as a measure of photosynthetic carbon assimilation. *Proc R Soc Lond Ser B Biol Sci* 242: 29–35
- Seelert H, Poetsch A, Dencher NA, Engel A, Stahlberg H and Müller DJ (2000) Proton powered turbine of a plant motor. *Nature* 405: 418–419
- Sharkey TD (1985) Photosynthesis in intact leaves of *C₃* plants: physics, physiology and rate limitations. *Bot Rev* 51: 53–105
- Sharkey TD, Berry JA and Sage RF (1988) Regulation of photosynthetic electron-transport in *Phaseolus vulgaris* L., as determined by room-temperature chlorophyll a fluorescence. *Planta* 176: 415–424
- Trebst A (1974) Energy conservation in photosynthetic electron transport of chloroplasts. *Annu Rev Plant Physiol* 25: 423–458
- Trissl H-W and Wilhelm C (1993) Why do thylakoid membranes from higher plants form grana stacks? *Trends Biochem Sci* 18: 415–419
- Von Caemmerer S (2000) Biochemical models of leaf photosynthesis. *Techniques in Plant Sciences* No. 2. CSIRO Publishing, Collingwood, Victoria
- Von Caemmerer S and Evans JR (1991) Determination of the average partial pressure of CO₂ in chloroplasts from leaves of several *C₃* plants. *Aust J Plant Physiol* 18: 287–305
- Von Caemmerer S, Evans JR, Hudson GS and Andrews TJ (1994) The kinetics of ribulose-1,5-bisphosphate carboxylase/oxygenase in vivo inferred from measurements of photosynthesis in leaves of transgenic tobacco. *Planta* 195: 88–97

- Warren CR (2004) The photosynthetic limitation posed by internal conductance to CO_2 movement is increased by nutrient supply. *J Exp Bot* 55: 2313–2321
- Warren CR (2006) Estimating the internal conductance to CO_2 movement. *Funct Plant Biol* 33: 431–442
- Warren CR and Adams MA (2006) Internal conductance does not scale with photosynthetic capacity: implications for carbon isotope discrimination and the economics of water and nitrogen use in photosynthesis. *Plant Cell Environ* 29: 192–201
- Wong S-C and Woo KC (1986) Simultaneous measurements of steady-state chlorophyll a fluorescence and CO_2 assimilation in leaves. The relationship between fluorescence and photosynthesis in C_3 and C_4 plants. *Plant Physiol* 80: 877–883
- Wullschlegel SD (1993) Biochemical limitations to carbon assimilation in C_3 plants – A retrospective analysis of the A/C_i curves from 109 species. *J Exp Bot* 44: 907–920
- Yin X, Van Oijen M and Schapendonk AHCM (2004) Extension of a biochemical model for the generalized stoichiometry of electron transport limited C_3 photosynthesis. *Plant Cell Environ* 27: 1211–1222
- Yin X, Harbinson J and Struik PC (2006) Mathematical review of literature to assess alternative electron transports and interphotosystem excitation partitioning of steady-state C_3 photosynthesis under limiting light. *Plant Cell Environ* 29: 1771–1782 (with corrigendum in *Plant Cell Environ* 29: 2252)
- Yin X, Struik PC, Romero P, Harbinson J, Evers JB, Van der Putten PEL and Vos J (2009) Using combined measurements of gas exchange and chlorophyll fluorescence to estimate parameters of a biochemical C_3 photosynthesis model: A critical appraisal and a new integrated approach applied to leaves in a wheat (*Triticum aestivum*) canopy. *Plant Cell Environ* 32: 448–464

Chapter 12

Modeling the Kinetics of Activation and Reaction of Rubisco from Gas Exchange

Hadi Farazdaghi*

89 Willcocks st., Toronto, ON M5S1C9 Canada

Summary.....	275
I. Introduction.....	276
II. Fundamental Photosynthesis Models.....	276
A. The Blackman Theory.....	277
B. The Michaelis–Menten Theory.....	277
C. The Basic Equations: Blackman and Rectangular Hyperbola.....	277
D. Limitations of the Blackman Type Models and the Convexity Factor.....	278
E. Application and Extension of the Foundational Models.....	278
III. Rubisco and Its Sequentially Ordered Reaction.....	279
A. The First Step: Rubisco Activation and Enediol Synthesis.....	280
1. Rubisco Activation.....	280
2. Enediol Synthesis.....	281
B. The Second Step: Carboxylation/Oxygenation and Enzyme Release.....	281
IV. Rubisco in Steady State: Biochemical Models.....	281
A. Single Process Models.....	282
1. Single-step Michaelis–Menten Type Models.....	282
2. Two-step Kinetics.....	282
B. The Two-process Limiting Theory.....	285
1. The Independence of the Two Processes.....	285
2. Limits and Parameters of the Model.....	286
V. Experimental Evaluation of the Models.....	287
A. Integrated Datasets.....	287
B. The Two-process Single Response Line Modeling Versus Curve Fitting?.....	289
VI. Concluding Remarks.....	290
Acknowledgments.....	291
References.....	291

Summary

Oxygenic life begins with photosynthesis. This process controls natural CO₂ sequestration and is responsible for terrestrial and marine life on the planet. An increase in the global CO₂/O₂ concentration ratio creates positive feedback cycles, which in the atmosphere, lead to increases in temperature and water holding capacity. In the oceans, the holding capacities of CO₂ and other gases are decreased, leading to their release into the atmosphere and accelerated climate change.

Rubisco kinetic models are used as core modules for simulations of agricultural and natural productivity, environmental and ecological management, and climate change. Thus, a scientific theory that can be

* Author for correspondence, e-mail: hadi@farazdaghi.com

used reliably as the core module of such interactive processes is essential for maintaining the vitality of the planet. This chapter provides a comparison of the kinetic theories for Rubisco activation and reaction and their mathematical models. The two dominant schools of thought in the theory of Rubisco reaction are (1) the single-process or co-limitation theory and (2) the two-process theory. In the single-process theory, Rubisco is the gatekeeper and thus the paramount controller of CO₂ fixation under any condition.

The most widely used two-process theory assumes that carboxylation is limited by one of the two independent processes: (a) fully-activated RuBP-saturated capacity of Rubisco at low CO₂, and (b) RuBP regeneration capacity at high CO₂. The single-process model is consistent with a biochemically correct understanding of Rubisco reaction.

I. Introduction

Global oxygenic life is dependent on Rubisco (Ribulose 1,5-bisphosphate carboxylase/oxygenase), an old and the most abundant enzyme on the planet (Ellis, 1979). Rubisco controls and mediates the entry of CO₂ into the tissue of green plants and algae through photosynthesis. Consequently, the photosynthetic O₂ production and net CO₂ absorption facilitated by Rubisco constitute almost all of the terrestrial and marine life. In addition to photosynthesis, oceans and other large bodies of water, with large potential storage capacities for CO₂, have significant interactive effect on global CO₂ levels. For example, the greenhouse effect of CO₂ increases water surface temperatures, thus decreasing the CO₂ holding capacity of the water, releasing CO₂ to the atmosphere, causing an ensuing positive feedback cycle (Torn and Harte, 2006; Scheffer et al., 2006). Conversely, rising atmospheric temperature increases the water holding capacity of the atmosphere, leading to severe storms (Karl

and Trenberth, 2003). The observed carbon-cycle feedbacks may occur faster than expected by our current understanding of the processes driving the sinks (Canadell et al., 2007; Cox et al., 2000).

Rubisco is responsible for the enzymatic process of CO₂ fixation through photosynthesis in an ordered reaction with RuBP first and CO₂ next (Spreitzer and Salvucci, 2002). Rubisco consists of eight large (L) and eight small (S) subunits in an L₈S₈ arrangement (type I) in higher plants, algae and other photosynthetic organisms. There are also Rubisco's of type II and type III. Type II is from purple bacteria, while type III – the archaeal form (Finn and Tabita, 2004) – operates in anaerobic organisms and may have research promise in thermal tolerance and specificity due to its unusually high optimal reaction temperature at 90°C (Ashida et al., 2005, 2008; Spreitzer et al., 2005). Photosynthesis models, largely based on the submodels of Rubisco, are now forming the basis of subsequent models for biome responses to global change, global warming, climate change, genetic manipulations for designing a better plant etc. (Baldocchi and Wilson, 2001; Cramer et al., 2001, 2004; Medlyn et al., 2002; Spreitzer and Salvucci, 2002).

Abbreviations: A – gross photosynthesis minus photorespiration; C – CO₂ concentration; CA1P – 2-carboxyarabinitol1-phosphate; CRC – carbon reduction-oxidation cycle; e_i – the fraction of incident radiation that is absorbed by plant; E – free enzyme; E-enediol – Rubisco-enediol complex; E_t – total enzyme; ES – enzyme-substrate complex; GAPDH – glyceraldehyde 3-phosphate dehydrogenase; k – $V_{0\max}/V_{C\max}$; K_C – Michaelis constant for CO₂; M – Mg⁺⁺; PGA – 3-phosphoglyceric acid; PS I – photosystem I; PS II – photosystem II; S – substrate; V – reaction velocity; $V_{C\max}$ – maximum capacity of Rubisco transitional reaction; V_{\max} – maximum capacity of Rubisco steady-state reaction; XuBP – xylulose biphosphate; Φ – quantum efficiency of photosynthesis; Γ – CO₂ concentration at compensation point; Θ – convexity factor; τ – relative specificity of CO₂/O₂; Ψ – carboxylation efficiency

II. Fundamental Photosynthesis Models

Photosynthesis modeling has been used widely since 1960s. Early in this period, it was used to estimate the extent of variations in agricultural and natural productivity for short and long-term agricultural production management (de Wit, 1965; Monteith, 1965). Since the very beginning, two platforms were attractive for mechanistic modeling of photosynthesis: the Blackman and Michaelis–Menten theories.

A. The Blackman Theory

The Blackman (1905) Law is an application, to plant CO_2 assimilation, of the Liebig Law of the Minimum, which has been in use for application of fertilizer to agricultural crops since the eighteenth century. Blackman theory is based on the principle that the maximum reaction velocity cannot exceed the minimum of either enzyme capacity or its substrate supply. In these reasonings the rates of substrate supply and the capacity (amount) of free enzyme, on which the rate of reaction is dependent, are assumed independent of one another.

B. The Michaelis–Menten Theory

This theory, on the other hand, addresses enzyme reactions in which free enzyme $[E]$, reacts with substrate $[S]$, and produces an enzyme-substrate complex $[ES]$. The rate of formation of $[ES]$ is proportional to $[E]$ and $[S]$, while the reaction rate, V , is also proportional to the rate of conversion of $[ES]$ to the product(s). Since the total enzyme concentration $[E_t]$ is fixed, then $[E] = [E_t] - [ES]$. Therefore, the Michaelis–Menten model can be viewed as a special case of the

Liebig–Blackman law, in which the velocity of reaction is determined by $[ES]$, which in turn is dependent on the free enzyme $[E]$ or the substrate $[S]$ times the rate constant. But unlike the Blackman model, here $[E]$ and $[S]$ are not independent variables, because as $[S]$ increases, $[ES]$ increases too, and as a result of this $[E]$ decreases progressively and approaches zero at substrate saturation, when $[ES] = [E_t]$. Therefore, the curvature in the Michaelis–Menten curve is due to the co-limitation by the free enzyme $[E]$ and the enzyme-substrate complex, $[ES]$, for the use of a limited resource $[E_t]$ (Fig. 12.1).

C. The Basic Equations: Blackman and Rectangular Hyperbola

The two simplest equations used in modeling chemical/biochemical reactions are the Blackman model – equivalent to a broken line with a horizontal segment – and the Michaelis–Menten model – equivalent to a rectangular hyperbola. In Blackman models the independence of the factors involved in the reaction is essential, while because of the formation of enzyme-substrate complex, Michaelis–Menten models exhibit co-limitation of substrate and enzyme.

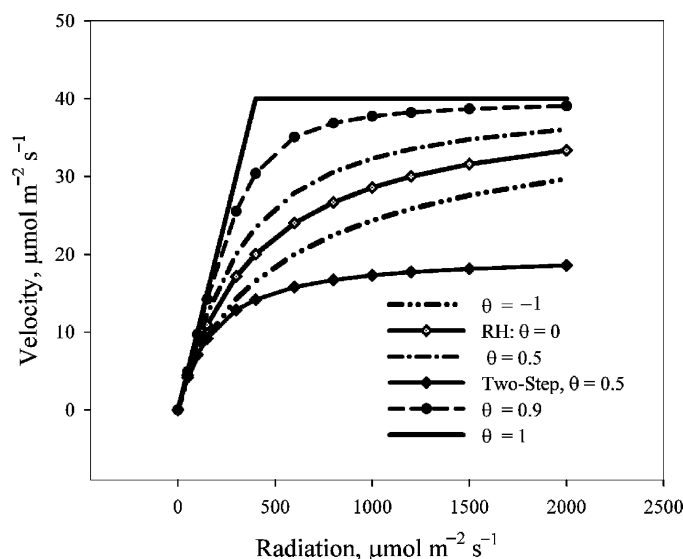


Fig. 12.1. A generic example of carboxylation initial velocity (A/I curve) with maximum velocity $V_{\text{Cmax}} = 40 \mu\text{mol CO}_2 \text{ m}^{-2} \text{ s}^{-1}$ and maximum quantum efficiency of $\Phi_{\text{C}} = 0.08$. The graphs are represented by their values of the convexity factor (θ), with rectangular hyperbola (RH) having a $\theta = 0$ value. An additional curve $\theta = -1$ that has been used by Buckley and Farquhar (2004) is also included. The two-step reaction with the parameter β , equivalent to $\theta = 0.5$ (that is a special case of Farazdaghi, 2004), is also shown. All curves start from zero radiation and velocity with the same initial slope or maximum efficiency, and eventually end up with V_{Cmax} (or V_{max} in the case of the two-step model) at the top of the curves

However, in complex reactions the response curves follow neither Blackman nor Michaelis–Menten curves, but something in between the two. Often an empirical coefficient – the convexity factor Θ – has been used to produce some arbitrary curvature in the Blackman equation in these cases. These are generally called “Blackman type” models. Some modelers have considered Θ as a measure of co-limitation (Collatz et al., 1990; Buckley and Farquhar, 2004). It is important to note that in these cases, as mentioned in Section B, the independence of the limiting factors will be lost due to co-limitation.

The mathematical models describing these rate equations with respect to CO_2 as the substrate are:

$$V_C^2 - V_C(\Psi_C C + V_{C\max}) + \Psi_C C V_{C\max}, \quad (12.1)$$

$$V_C = V_{C\max} \frac{C}{C + K_C}, \quad (12.2)$$

$$V_C = V_{C\max} \Psi_C \frac{C}{V_{C\max} + \Psi_C C}, \quad (12.3)$$

$$\Theta V_C^2 - V_C(\Psi_C C + V_{C\max}) + \Psi_C C V_{C\max} = 0. \quad (12.4)$$

In Eqs. (12.1), (12.3) and (12.4) the initial slope of the kinetic curve, $\Psi = V_{C\max}/K_m$ has been used instead of the half-saturation concentration K_m . The effect of oxygenation can be introduced in Eq. (12.2) by replacing K_C with K_a , as:

$$K_a = K_C (1 + O/K_O). \quad (12.5)$$

After this replacement, Eq. (12.2) will be equivalent to the equation of Laing et al. (1974). Then for Eqs. (12.1), (12.3) and (12.4) Ψ_C should be replaced with Ψ_a according to Eq. (12.6) as shown by Farazdaghi and Edwards (1988a):

$$\Psi_a = \frac{\Psi_C}{1 + O/K_O}. \quad (12.6)$$

In earlier models radiation was treated like a substrate for an enzymatic reaction. A rectangular hyperbola for the rate of assimilation with respect to radiation, I , (Rabinowitch, 1951) is given by Eq. (12.7):

$$V_I = V_{C\max} \frac{\Phi I}{V_{C\max} + \Phi I}, \quad (12.7)$$

where Φ is the initial slope or, in the given case, the maximum quantum efficiency.

Mathematically, the Blackman model (Eq. 12.1) is equivalent to the Blackman type model of Eq. (12.4) with $\Theta = 1$. Likewise, the rectangular hyperbola of Eq. (12.3) is equivalent to Eq. (12.4) with $\Theta = 0$. The rectangular hyperbola of Eq. (12.3) is simply a different way of writing the Michaelis–Menten formula of Eq. (12.2) with

$$K_C = \frac{V_{C\max}}{\Psi_C}, \quad (12.8)$$

as shown by Farazdaghi and Edwards (1988b). A Blackman type model similar to Eq. (12.4) can also be written for radiation by replacing $\Psi_C C$ with ΦI as follows:

$$\Theta A_I^2 - A_I(\Phi I + A_{\max}) + \Phi I A_{\max} = 0. \quad (12.9)$$

D. Limitations of the Blackman Type Models and the Convexity Factor

While Blackman (1905) outlined the laws of limitations, he did not give any quantitative equation, nor did he envisage a convexity factor in his theory. The introduction of an empirical coefficient allows the equation to be adjusted to fit experimental data. Naturally, models based on empirical coefficients lose their ability to predict experimental results in advance. Convexity factors of $0 < \Theta < 1$ have mainly been used for light response (A/I) curves (Thornley, 1976; Chartier and Prioul, 1976), but beyond its empirical use for curve fitting, the biochemical significance of Θ has not been explained.

E. Application and Extension of the Foundational Models

In early studies of photosynthesis, the rectangular hyperbola has been considered the most appropriate function for modeling A/I curves, while the similar Michaelis–Menten equation has been favored for modeling A/C_i responses (Rabinowitch, 1951; Van Bavel, 1975; Farazdaghi and Edwards, 1988b). In some cases, these models did not provide a good fit to experimental data, causing some researchers to abandon the conventional approach based on the kinetics of a single enzyme, Rubisco (Farquhar et al., 1980; Collatz et al., 1990), and seek alternative models.

Others (Terry, 1980, 1983; Taylor and Terry, 1984; Arulanantham et al., 1990; Farazdaghi and Edwards, 1988a, b, 1992; Farazdaghi, 2004, 2005, 2007) continued research into single enzyme kinetics in order to find new solutions that do not conflict with the basic Blackman and Michaelis–Menten principles.

III. Rubisco and Its Sequentially Ordered Reaction

The abundance of Rubisco is, to a large extent, to compensate for its low efficiency, Ψ_C , and slow maximum velocity, V_{Cmax} , (Spreitzer and Salvucci, 2002). In darkness Rubisco is combined with its substrate, RuBP, into a non-reactive dead-end storage site (RuBP-inhibited state). The reaction requires, first, separation of RuBP from Rubisco, then activation (carbamylation and binding Mg^{++}), then binding RuBP to produce the E-enediol (Rubisco–RuBP complex) form of RuBP. The scheme of Fig. 12.2 is consistent with the reaction schemes of Taylor and Andersson (1996), Farazdaghi (2004) and Andersson (2008).

If RuBP is not limiting, the sequential chain of reactions that initially leads to transitional reaction of carboxylation (Ruuska et al., 1998) is described by the Michaelis–Menten equation (Fig. 12.3). At the extreme, when the enzyme is saturated with both substrates, the rate approaches $V = V_{Cmax}$ (Laisk, 1985; Farazdaghi and Edwards, 1988b, 1992; Ruuska et al., 1998).

In vitro the rate of a two-substrate ordered reaction, such as reported by Jamin et al. (1991) and Mullis et al. (1991), gradually declines from the fast transitional velocity toward its steady-state lower value. The lower steady-state value is the result of a dynamic equilibrium between the two steps of the reaction: one is the production of enediol before carboxylation and the other is carboxylation of enediol, product formation and separation and release of enzyme. The carboxylation of enediol is irreversible as shown by Mizioroko and Lorimer (1983) and Andrews and Lorimer (1978). The steady state kinetics deviate sharply from Michaelis–Menten curve (Laisk, 1985; Ruuska et al., 1988; Laisk and Oja, 1998). In the initial transitional phase total enzyme is available to all steps of the reaction that react sequentially, therefore the reaction contains one enzyme-substrate complex, and constitutes only one large step. Therefore, the rate of reaction is determined by the enzyme-substrate complex up to the capacity of total enzyme. The same principle applies to steady-state reaction, but with a difference that under steady state conditions two enzyme-substrate complexes (E-enediol and E-enediol-C) must exist concurrently, each of which constitutes one step. The rate of reaction is determined by the slower step, and the enzyme-substrate of the faster step is included in the free enzyme. But as both substrates approach saturation, the enzyme-substrate complexes of the faster step and the slower step that are sequentially ordered are added together and make a larger step. As a result the capacity of

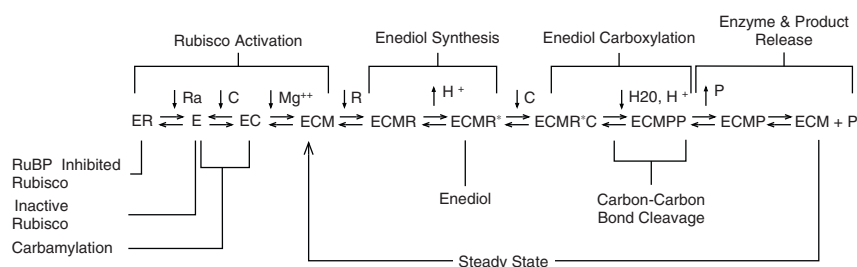


Fig. 12.2. Biochemical steps in enzyme activation and reaction of Rubisco, including the effect of Rubisco activase (RA) in separation of RuBP (R) from inactive enzyme (E), carbamylation of enzyme (EC) and its stabilization by Mg^{2+} (ECM). This step is followed by the reaction with RuBP, abstraction of proton to produce enediol, and then the capture of CO_2 that is followed by the formation of 3-keto-2-carboxyarabinitol biphosphate, hydration, carbon–carbon cleavage, absorption of proton, and production of two moles of PGA that should be released in order for the resumption of the next round of reaction. The first round of reaction that allows participation of total enzyme in the reaction is transitional. The carboxylation of enediol is irreversible and when the reaction reaches steady state or quick equilibrium, the active enzyme is subdivided into two main steps: (i) the synthesis of enediol with ECM and R, and (ii) carboxylation of enediol and the release of ECM

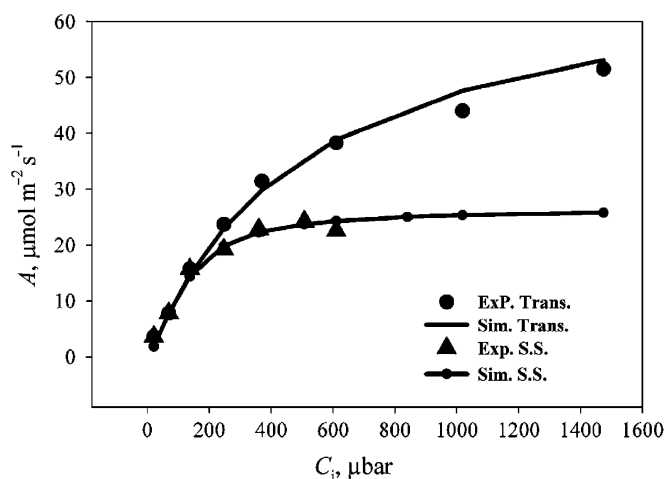


Fig. 12.3. The relationship between the transitional (●) and the steady state (▲) carboxylation rates. Experimental data are approximate values, extracted from Ruuska et al. (1998). The experiments have been performed at 2% O_2 and $I = 1,000 \mu\text{mol quanta m}^{-2} \text{s}^{-1}$. The transitional reaction is described by a Michaelis–Menten equation (top curve), where $V_C = (A + R_d)$, $V_{C\max} = 72.5$ and $R_d = 1$, both in $\mu\text{mol m}^{-2} \text{s}^{-1}$, and $K_C = 500 \mu\text{bar}$. The value of steady-state V_{\max} was considered $27.7 \mu\text{mol m}^{-2} \text{s}^{-1}$. The transitional reaction rate follows the Michaelis–Menten model (Eq. 12.3), but the steady state rate (observed ▲, simulated ●) stops at $V = V_{\max}$, about 40% of $V_{C\max}$ (modeled after Farazdaghi, 2004)

free enzyme is limited only to the enzyme that can return after the removal of PGA. This cumulative limitation causes severe co-limitation and the rate of reaction deviates from the Michaelis–Menten curve (Farazdaghi, 2004). The two sequential steps of the reaction are described below.

A. The First Step: Rubisco Activation and Enediol Synthesis

1. Rubisco Activation

Although carboxylation is considered a dark reaction, it cannot function in darkness. In darkness, Rubisco is at least partially bound with RuBP (Brooks and Portis, 1988), or in some plants with carboxyarabinitol 1-phosphate (CA1P) (Andralojc et al., 1994; Khan et al., 1999). The inhibition of Rubisco by RuBP, like its inhibition by CA1P, was suggested as protection for Rubisco from hydrolysis and, additionally, the conservation of RuBP for use in the initial synthesis of enediol at the onset of light (Farazdaghi, 2007). Thus Rubisco and RuBP have a role of reciprocal and mutual protection.

In the light, Rubisco activase is activated and maintained active with the help of PS I (Campbell and Ogren, 1990), and it requires light-increased

ATP/ADP ratio and reduced thioredoxin f in some plants (Zhang and Portis, 1999). By changing the dissociation rate of RuBP from its Rubisco site, Rubisco activase increases the competitiveness of CO_2 for binding to the regulatory site, leading to carbamylation, followed by stabilization by Mg^{2+} (Portis et al., 1995). At this stage Rubisco is active (ECM in Fig. 12.2) and its activity is positively related to the content of Rubisco activase (Mott and Woodrow, 1993). However, the activation power of Rubisco activase is sensitive to temperature and dependent on ATP/ADP ratio (Parry et al., 1999; Hammond et al., 1998; Mott and Woodrow, 2000; Jensen, 2000; Salvucci and Crafts-Brandner, 2004).

As shown in the biochemical relationship of Fig. 12.2, the activation of Rubisco to form ECM and the reaction of ECM with RuBP are sequentially ordered, therefore they are integral parts of the initial transitional reaction. However, in the steady-state reaction, the active enzyme, ECM, is returned after product release and Rubisco activase plays the role of maintenance of ECM. In the case of transitional reaction the CO_2 that is used in carbamylation is regulatory and the energy that is used by Rubisco activase is very small relative to the energy content of RuBP, thus neither could be distinguishable in gas exchange measurements.

2. Enediol Synthesis

The active Rubisco (ECM) binds with RuBP to produce ECMR, which, after deprotonation, produces E-enediol (ECMR*). The described mathematical model includes reactions from this step on. The biochemical model in Fig. 12.2 is similar to that of Taylor et al. (2001), without the effects of oxygenation and inhibitors, such as xylulose 1,5-bisphosphate (XuBP) and carboxyarabinitol 1-phosphate (CA1P).

B. The Second Step: Carboxylation/Oxygenation and Enzyme Release

The second step is the carboxylation/oxygenation of E-enediol, including the reaction steps that lead to the release of ECM. Factors in the carbon reduction cycle (CRC) that either directly or indirectly affect the concentration of PGA influence the rate of release of ECM by feedback inhibition.

Carboxylation is the process of adding one carbon to the five-carbon skeleton of enediol and production of 3-keto, 2-carboxyarabinitol bisphosphate (ECMR*C), which, after hydration, re-protonation and carbon-carbon bond cleavage, produces two molecules of PGA (Taylor et al., 2001; Andersson, 2008). E-enediol also combines with O_2 in oxygenation (ECMR*O) and produces one molecule of PGA and one molecule of phosphoglycolate, PG (Bowes et al., 1971; Ku and Edwards, 1978). Two molecules of PG are finally metabolized into one molecule of PGA and one molecule of CO_2 . This process is conducted through a chain of energetically wasteful reactions of photorespiration (Farazdaghi and Edwards, 1988b). Oxygenation is a significant substitution for the reaction of carboxylation and attains two main goals. First, energy is consumed in oxygenation, to help for the survival of plants in excess radiation and, second, the release of CO_2 from photorespiration maintains the turnover of CRC when external CO_2 supply is restricted due to stomatal closure. Thus, attempts in removing oxygenation through genetic manipulation may not necessarily produce a better plant (see Chapter 17 of this book by Xin-Guang Zhu and Stephen Long). Under CO_2 limitation and high light photorespiration plays a crucial role in protecting plant from excess

radiation by recycling of CO_2 and consuming the reducing power and ATP (Farazdaghi, 2004). In C_4 plants this problem is avoided by the CO_2 concentrating mechanism that can maintain high CO_2 levels, outcompeting the oxygenation of RuBP.

The removal of PGA from the enzyme is essential for the release of active Rubisco (ECM), as well as for the fast steady-state turnover of CRC (Farazdaghi, 2004). The PGA that is produced in carboxylation is reduced in CRC by NADPH from the light reactions. Steady-state photosynthesis requires the concurrent existence of all of the enzyme forms in the pathway of Fig. 12.2. The consequence of the concurrent distribution of enzyme between the two steps of reaction is that, based on Liebig–Blackman law of limitations, the rate of reaction will be limited by the rate of the slower, rate-limiting step. Therefore, under steady-state conditions, the rate of carboxylation will be limited by the rate of supply of either CO_2 or E-enediol up to the limit of the capacity of active Rubisco (ECM) when both substrates are saturating according to Eq. (12.10):

$$A = \min \{V_i, V_C\}_0^{V_{\max}} - R_d, \quad (12.10)$$

where V_i is the velocity of carboxylation when radiation (RuBP supply) is limiting and V_C is the velocity of carboxylation when CO_2 is limiting. However, as the substrates RuBP and CO_2 approach saturation, the enzyme-substrate complexes of the two steps co-limit and cause a sharper deviation from the Michaelis–Menten curve (Farazdaghi, 2004, 2005). The relationships of both, transitional and steady state reactions, are shown in Fig. 12.3.

IV. Rubisco in Steady State: Biochemical Models

At present there are two distinct approaches to mathematically describe the assimilation of CO_2 . One considers that – since Rubisco controls the entry of CO_2 into CRC – the kinetics of Rubisco, as dependent on its inputs and outputs, must control the rate of CO_2 assimilation. This single process (or single enzyme) approach considers Rubisco as the ultimate controller of CO_2 assimilation (Rabinowitch, 1951; Bowes et al., 1971; Van Bavel, 1975; Jordan and Ogren, 1984;

Laisk, 1985; Farazdaghi and Edwards, 1988a, b, 1992; Eichelmann and Laisk, 1999; Farazdaghi, 2004, 2007), but other processes and reactions participate as they control the levels of Rubisco substrates and products. The other, two-process approach, assumes that steady-state CO_2 assimilation is controlled by two *independent* processes: the fully activated and RuBP-saturated Rubisco capacity is limiting at low, strictly limiting CO_2 , and RuBP regeneration rate is limiting at high, saturating CO_2 , as well as when RuBP regeneration is limited by low light intensities (Farquhar et al., 1980, 2001; Collatz et al., 1990; Von Caemmerer 2000; Sage and Sharkey, 1987; Sharkey et al., 2007).

A. Single Process Models

Haldane (1930) extended the single substrate Michaelis–Menten models to both random and ordered two-substrate reactions. The pioneering attempt at modeling photosynthesis, based on the biochemistry and biophysics of the subject, comes from Rabinowitch (1951) with the use of rectangular hyperbola and Michaelis–Menten equations. Further models were developed by Charles-Edwards and Ludwig (1974), Van Bavel (1975), Chartier and Prioul (1977), and Farazdaghi and Edwards (1988b) to simulate photosynthesis as a two-substrate biochemical reaction. Here the models of photosynthesis developed on the basis of the biochemical Rubisco reaction are referred to as the single-process (or single-enzyme) models. The single-process photosynthesis models that include both RuBP and CO_2 can be divided into two groups: single-step Michaelis–Menten models and two-step kinetic models.

1. Single-step Michaelis–Menten Type Models

The model of Farazdaghi and Edwards (1988b) was based on the co-limiting principles of Michaelis–Menten that were extended by Haldane (1930) for two-substrate reactions. Co-limitation in the context of Michaelis–Menten theory means that photosynthesis is limited by the levels of both enzyme-substrate complexes (E-enediol and from E-enediol-C to E-PGA) up to the maximum capacity of Rubisco. The application of carboxylation efficiency for CO_2

or relative CO_2/O_2 specificity, τ , had been used before (Chartier and Prioul, 1976; Jordan and Ogren, 1984). However, because of the potential differences in responses of V_{Cmax} , Ψ_{C} and Ψ_{O} to environmental factors Farazdaghi and Edwards (1988a, b) were the first to emphasize the advantages of carboxylation efficiency (Ψ_{C}) as the second enzyme parameter over the Michaelis–Menten constant, K_{C} (Eqs. 12.2 and 12.3). In addition, for steady-state reactions, they considered that due to the order of reactions and the irreversibility of carboxylation, interaction between the two enzyme-substrate complexes, with RuBP and with RuBP plus CO_2 , are minimized. Johnson (1992) confirmed this view and stated that the two independent kinetic constants of a reaction are its maximum rate (V_{Cmax}) and the maximum reaction efficiency (or initial slope, Ψ).

Farazdaghi and Edwards presented their model in terms of maximum reaction efficiency (Ψ). Furthermore, they substituted the RuBP term, which was the dominant energy-rich input component of the reaction, with the apparent quantum efficiency (Φ) multiplied by the absorbed radiation, $e_i I$, (Eq. 12.11):

$$A = \frac{V_{\text{Cmax}} I (C - \Gamma^*)}{\left(I + \frac{V_{\text{Cmax}}}{e_i \Phi_{\text{C}}}\right) \left(C + \frac{2\Gamma^*}{k}\right) + \frac{V_{\text{Cmax}} I}{\Psi}} - R_{\text{d}}. \quad (12.11)$$

Equation (12.11) provided good results, particularly with varying radiation, but produced less agreement with data sets that had abrupt changes around saturation. This was noted and critiqued by Collatz et al. (1990) that simulations with Eq. (12.11) predicted the rates of photosynthesis of 30–50% of the RuBP saturated capacity of Rubisco. But the results were consistent with experimental observations of Ruuska et al. (1998).

2. Two-step Kinetics

The biochemical model of Fig. 12.2 is an extension of the model of Laing and Christeller (1976) and Farazdaghi (2004) without the oxygenation component. Farazdaghi (2004) presented a more comprehensive account of the kinetics of two-substrate ordered reaction of Rubisco by using

two steps, as described above. Farazdaghi (2007) also included the activation process of Rubisco into the model, considering that the E-enediol production rate is limited, first, by activation of Rubisco activase (by radiation) and purification of Rubisco from the inhibitors (Fig. 12.2) and, second, by activation of Rubisco by carbamylation and addition of Mg^{2+} . The Rubisco activation is limited either by the availability of CO_2 and Mg^{2+} , or by radiation via the activation of Rubisco activase with energy from PS I that is dependent on ATP/ADP ratio (Campbell and Ogren, 1990). However, it was noted that, because of the sequential order of reactions up to including the enediol step, the preceding slower steps of the activation reaction collapse into one larger step with the RuBP binding step. Thus, the model of Farazdaghi (2004) did not change.

Under steady state the two reaction steps are separated at the carboxylation node which is irreversible and committed to product (PGA) formation (Fig. 12.2). When there is no limitation of either the CO_2 or RuBP supply, then separation of PGA from ECM will limit regeneration of the free enzyme. Of course, other inhibitory factors such as CA1P, tightly bound RuBP, XuBP, rebinding of PGA or P_i , can be contributory factors to the limitation of Rubisco.

In step 1 of Fig. 12.2 the RuBP substrate is replaced with its energy requirements, i.e. the fraction of visible radiation ($\Phi_{\max} e_i I$) that is used in photosynthesis, excluding the radiation lost in sensible heat, albedo and other ways ($1 - e_i$). Also, considering $e_i \Phi_{\max} = \Phi_m$, the apparent quantum efficiency of assimilation can be calculated from Eq. (12.12):

$$\begin{aligned}\Phi &= \Phi_m \frac{V_C}{V_C + V_O} = \Phi_m \frac{\Psi_C C}{\Psi_C C + \Psi_O O} \\ &= \Phi_m \frac{C}{C + 2\Gamma^*}. \quad (12.12)\end{aligned}$$

The energy used by Rubisco activase for separation of Rubisco from RuBP, CA1P or XuBP is mainly supplied from electron transport reactions

around PS I (Campbell and Ogren, 1990). Also, the energy used by CRC mainly for the removal of PGA and the return of ECM is supplied from the light reactions supported by PS II and PS I.

a. The Two-step Kinetic Model

The biochemical model of Fig. 12.2 with competition between CO_2 and O_2 is used to derive the general model of Eq. (12.13):

$$\begin{aligned}\left(\frac{V}{V_{C\max}}\right)^2 &\left[\frac{\alpha_1 K_R}{R} + \frac{(1 + \alpha_2) K_{Ca}}{C}\right] \\ &- \frac{V}{V_{C\max}} \left[1 + \alpha_1 + \alpha_2 + \frac{K_R}{R} + \frac{K_{Ca}}{C}\right. \\ &\left. + \frac{K_R (k_2 k_4 + k_{11} O)}{k_5 R C}\right] + 1 = 0. \quad (12.13)\end{aligned}$$

Equation (12.13) represents the kinetics of a two-substrate two-step reaction. The first part of the equation represents the rate limiting steps for each substrate, α_1 for RuBP (R) in Step 1, and $(1 + \alpha_2)$ for C in Step 2, while the remainder is a two-substrate Michaelis–Menten type equation. The values of α_1 and α_2 are related according to Eq. (12.15). When one of the substrates, C or R , is not limiting, the term that contains that substrate will be removed from the equation. When C is limiting, Eq. (12.13) is reduced to

$$\begin{aligned}(1 + \alpha_2) (A_C + R_d)^2 - (A_C + R_d) \\ \times [(1 + \alpha_1 + \alpha_2) \Psi_{Ca} C + V_{C\max}] \\ + V_{C\max} \Psi_{Ca} C = 0, \quad (12.14)\end{aligned}$$

where A_C is the steady-state rate of reaction with a maximum of $A_{\max} = V_{\max} - R_d$, $\Psi_{Ca} = \Psi_C / (1 + O/K_O)$, and the relationship between V_{\max} and $V_{C\max}$ is determined by Eq. (12.15):

$$\frac{V_{C\max}}{V_{\max}} = 1 + \alpha = 1 + \alpha_1 + \alpha_2, \quad (12.15)$$

where the minimum values of α_1 and α_2 are 1 and 0 respectively. In Step 1, radiation controls Rubisco activase and through that carbamylation maintenance. Also, radiation is a major component of the regeneration of RuBP for the synthesis of enediol. In Step 2, radiation controls the removal of PGA by CRC, which results in the release of active enzyme. This is the reason why the relationship of assimilation with radiation can have two distinct forms, depending on which step of reaction is limiting (compare Eqs. 12.16 and 12.18). When the first step of reaction is limiting, the equation can be written as:

$$\begin{aligned} & \alpha_1 (A_I + R_d)^2 - (A_I + R_d) \\ & \times [(1 + \alpha_1 + \alpha_2) \Phi_a (I - I_C) + V_{C_{\max}}] \\ & + \Phi_a (I - I_C) V_{C_{\max}} = 0, \end{aligned} \quad (12.16)$$

where

$$\Phi_a = \Phi \left[1 - \frac{V_O}{V_C + V_O} \right] = \Phi_m \frac{C - \Gamma^*}{C + 2\Gamma^*}. \quad (12.17)$$

However, when Step 1 is limiting, the value of α_1 must be larger than $(1 + \alpha_2)$ or $\alpha_1 > 1$. By considering a minimum value of $\alpha_1 = 1$ in Eqs. (12.14 or 12.16), we note that the steady state maximum rate of assimilation at saturation of both substrates cannot exceed 50% of $V_{C_{\max}}$. This is consistent with and in support of the experimental findings of Laisk (1985), Laisk and Oja (1998) and Ruuska et al., (1998) and the experimental and theoretical findings of Farazdaghi and Edwards (1992) and Farazdaghi (2004).

b. Limitation of Rubisco

Farazdaghi (2004, 2005) presented a third equation (Eq. 12.18) for the conditions of enediol limitation due to limited RuBP regeneration rate, when RuBP-enediol is limiting, but it does not respond to increases in radiation:

$$\begin{aligned} & (1 + \alpha_2) (A_I + R_d)^2 - (A_I + R_d) \\ & \times [(1 + \alpha_1 + \alpha_2) \Phi_a I + V_{C_{\max}}] \\ & + \Phi_a I V_{C_{\max}} = 0. \end{aligned} \quad (12.18)$$

This is the condition that some researchers have attributed to a limitation of orthophosphate (Harley and Sharkey, 1991), or glyceraldehyde-3-phosphate dehydrogenase (Price et al., 1995). This case is applicable to both A/C_i and A/I response curves when a sharper departure from Michaelis–Menten curve is observed. Since such effects delay the separation of PGA from Rubisco, they can cause product inhibition and their feedback is shown through modification of the values of α_2 in Eqs. (12.14, 12.18).

c. A Special Blackman Type Case

A special case of Eq. (12.16) is when $\alpha_1 = 1$ and $\alpha_2 = 0$. Then the equation will be reduced to

$$\begin{aligned} & 0.5 (A_I + R_d)^2 - (A_I + R_d) [\Phi_a I + A_{\max}] \\ & + \Phi_a I A_{\max} = 0. \end{aligned} \quad (12.19)$$

This equation mimics Blackman type models with a convexity factor of $\Theta = 0.5$, and this can help to understand why Blackman type models sometimes provide very good fit to the data and why sometimes there are interactions between the value of Φ_a and A_{\max} . If both sides of Eqs. (12.14), (12.16) and (12.18) are divided by $(1 + \alpha_1 + \alpha_2)$, and considering Eq. (12.15), we get equations similar to Eq. (12.17) with a coefficient, for example λ in place of 0.5. It is evident that this coefficient is different for A/C_i and A/I curves, but it is important to note that λ , although a constant, is a hybrid parameter and remains constant as long α_1 and α_2 remain constant. Therefore, if Rubisco is fully activated, then variations of λ may be more controlled by V_{\max} and its value will be variable if both substrates have not attained saturation, or if there are other metabolic interactions. Actually Eq. (12.19) loses its usefulness because of the loss of the interaction factor between λ and V_{\max} , however, the relationships expressed here and the similarities with Blackman type models can help translate some of the vast empirical results of the last decades into the two-step model, which has more explanatory power and expansion capacity.

B. The Two-process Limiting Theory

This approach (Farquhar et al., 1980; Von Caemmerer and Farquhar, 1981) assumes that assimilation rate is the minimum of two independent processes: (i) limitation of RuBP saturated Rubisco at high light and/or low CO₂, and (ii) limitation of RuBP regeneration at low light and/or high CO₂. A third limiting factor (P_i release from triosephosphate, TPU), was added by T. Sharkey (Sharkey, 1985; Sharkey et al., 2007).

The Farquhar et al. (1980) theory provided an account of the biochemistry of CRC in C₃ photosynthesis, presenting a widely used two-process model. The authors proposed a separate model for each of the two processes:

$$W_C = V_{C_{\max}} \frac{C - \Gamma^*}{C + K_C \left(1 + \frac{\theta}{K_O}\right)} \quad (12.20)$$

and

$$W_e = J_{\max} \frac{I (C - \Gamma^*)}{(4.5C + 7\frac{\Gamma^*}{3}) (I + 2.1J_{\max})}. \quad (12.21)$$

Equation (12.20) is a Michaelis–Menten equation for the response to CO₂ with O₂ inhibition for RuBP-saturated but Rubisco-limited photosynthesis (at high light and low CO₂ concentrations), while Eq. (12.21) accounts for light limitation, where linearly light-dependent electron transport function, J , with an empirical ximum J_{\max} , is shared between RuBP carboxylation and oxygenation. Subsequently an empirical convexity factor, θ , was used by Collatz et al. (1990) to describe the intrinsic light-saturation of J :

$$\theta J_C^2 - J_C (W_C + W_e) + W_C W_e = 0. \quad (12.22)$$

The purpose of θ was to provide a smooth shift from one limitation to the other.

The Farquhar et al. (1980) model has attracted many researchers and modelers who applied the model to areas from global carbon cycle to environmental and production studies (Farquhar et al., 2001). The version of Sharkey et al. (2007) is even more attractive in terms of curve fitting. However, in an analysis of different versions of the model, Farazdaghi (2005, 2007) emphasized some drawbacks that may challenge validity of this two-process approach.

1. The Independence of the Two Processes

a. Carboxylation Under Low Light and CO₂ Influences RuBP Regeneration

The first signs of disagreement with the theory came from Terry and associates (Terry, 1980, 1983; Taylor and Terry, 1984; Arulanantham et al., 1990) who demonstrated that the supply of RuBP limits photosynthesis at low photochemical capacity, and disagreed with the views of Farquhar et al. (1980) that Rubisco is always fully activated and RuBP-saturated at low CO₂. They showed positive effects of light on RuBP regeneration under low light and CO₂ levels. This was also consistent with the findings of Quick et al. (1991) who found the dependency of Rubisco activation state on radiation. Portis et al. (1995) demonstrated that there is coordination between enzyme activity and the minimum levels of either CO₂ or RuBP. These results are consistent with the model of Farazdaghi and Edwards (1988b, 1992) for co-limitation of RuBP and CO₂, and the two-step reaction theory of Farazdaghi (2004).

This system of dependency questions the independence of the two processes of Farquhar et al. (1980) and confirms the control of Rubisco over one process with two steps that are RuBP conversion to E-enediol and its carboxylation.

b. Electron Transport Is Dependent on Carboxylation

Farquhar et al. (1980) assumed that electron transport (J) is dependent on absorbed irradiance (I) but independent of Rubisco carboxylation. Von Caemmerer and Farquhar (1981) used Eq. (12.23) to describe this dependence:

$$J = J_{\max} \frac{I}{I + 2.1J_{\max}}. \quad (12.23)$$

The latter authors calculated the rate of electron transport as a function of carboxylation as given in Eq. (12.24)

$$\text{“electron transport rate”} = 4(1 + 2\Gamma^*/C)V_c. \quad (12.24)$$

Equation (12.24) makes J directly dependent on Rubisco carboxylation (V_c). In absence of oxygen:

$$J = 4V_c = 4A. \quad (12.25)$$

This is contrary to the basic assumption of independence of the two processes. Sharkey et al. (2007) used Eq. (12.24) in the form of Eq. (12.26) and transferred a part of the curvature of Rubisco reaction that is due to competition between CO_2 and O_2 to electron transport J :

$$A = J \frac{C_c - \Gamma^*}{4C_c + 8\Gamma^*}. \quad (12.26)$$

In addition to the built-in interdependence between the rates of Rubisco reaction and RuBP regeneration, the experimental value of assimilation rate A is used in Eq. (12.26) to calculate J , and then in a circular way J is used to “predict” A . Furthermore, in the example given by Sharkey et al. (2007), A is used to calculate C_c , and then C_c is used circularly to calculate A .

According to Sharkey et al. (2007), ‘TPU-limited’ means a limitation of TPU at the plateau of the A/C_i curve, with no increase in the rate of reaction beyond that limit (Fig. 12.6A). A limitation of this type is theoretically possible because the reaction rate is not sensitive to the variable factor that is CO_2 . But, considering that Price et al. (1995) consider a limitation of GAPDH as a limitation of RuBP regeneration rate, it is not clear how the limitations by TPU and RuBP regeneration can be differentiated without elaborate experimentation in addition to gas exchange measurements. In a departure from the two-process theory, Sharkey et al. (2007) stated that Rubisco-limited means limitation due to “low $[\text{CO}_2]$ rather than V_{max} of the enzyme”. However, the authors did not elaborate on how this conclusion, which is not consistent with the Blackman law, has been reached.

2. Limits and Parameters of the Model

a. J_{max} as a Limit for RuBP Regeneration

Wullschlegel (1993) demonstrated that V_{Cmax} and J_{max} were inter-related for over 100 species of plants, rendering the interdependence of the two processes. Leuning (1997) reexamined the data of Wullschlegel (1993) with corrections for

temperature differences and validated the results with higher degrees of statistical confidence. Some model users have used this proportionality ($J_{\text{max}}/V_{\text{Cmax}}$) as a means of calculating J_{max} of RuBP regeneration from estimates of V_{Cmax} for the Farquhar et al. model (Bernacchi et al., 2002; Ainsworth et al., 2003). It is consistent with the theory of Farazdaghi (2004, 2005) that the ratio of $V_{\text{Cmax}}/V_{\text{max}}$ reflects the distribution of enzyme between the two steps of reaction and determines the extent of co-limitation. Farazdaghi and Edwards (1992) stated that because of the distribution of enzyme between the two steps the maximum velocity of steady state reaction V_{max} cannot exceed one half of the value of V_{Cmax} . V_{max} , which is equal to $A_{\text{max}} + R_d$, is the value of steady state RuBP and CO_2 saturated photosynthesis at the plateau of response curve, usually considered RuBP regeneration-limited rate of assimilation.

b. The Convexity Factor

The convexity factor, Θ , as discussed before, is an empirical coefficient that, if used with Blackman equation, as in Eq. (12.22), it can produce an arbitrary adjustment to the curvature at the intersection of two lines. Farquhar et al. (1980) state that the equation of $V_c = \min\{W_c, W_e\}$ “will emerge as a limiting case of perfect coupling of photochemical cycle with the other two” (PCR and PCO cycles). Collatz et al. (1990) recommended the use of the convexity or curvature factor in anticipation that further research in the way would make the nature of this empirical coefficient. According to Farazdaghi (2004), in fact, the convexity factor can conceal the interacting factor(s) that consistently and systematically are reflected in experimental results. This parameter was later found to have a much wider spectrum of variation (Evans and Farquhar, 1991; Ögren and Evans, 1993; Von Caemmerer 2000) than those reported by Collatz et al. (1990). The latter work indicated that since the Michaelis–Menten equation can be viewed as a Blackman type equation with $\Theta = 0$, therefore, Θ can be considered as a measure of co-limitation ranging between the single-limiting factor of Blackman model (with $\Theta = 1$) and the co-limiting model of Michaelis–Menten. Interestingly, Buckley and

Farquhar (2004) used a lower limit of $\Theta = -1$, but they did not include any experimental data or theoretical explanations on the biological or biochemical meaning, and the significance and usefulness of this extension to allow negative values. Sharkey et al. (2007) advanced the new version of the three-limiting processes in which the co-limiting curvature of Michaelis–Menten CO_2 response curve was totally placed on the competition between CO_2 and O_2 . Obviously this does not reflect the co-limitation of the two steps of reaction, one of which is carboxylation and oxygenation of the RuBP enediol complex.

c. Problems of Interpretation of Genetic Evidence

In response to Collatz et al. (1990), Farazdaghi and Edwards (1992) challenged the Rubisco-limited theory of Farquhar et al. (1980) and showed that Rubisco limitation occurs only at double saturation of both RuBP and CO_2 , and the maximum rate of steady state reaction is less than one half of the maximum transitional velocity of Rubisco. However, by using antisense technology for genetic manipulation of C_3 plants, it was shown that when Rubisco was greatly reduced, plant response to CO_2 followed Michaelis–Menten equation, while the response of control (wild type) plants deviated from Michaelis–Menten model (Von Caemmerer et al., 1994; Price et al., 1995; Ruuska et al., 1998; Von Caemmerer, 2000). The authors considered this observation as unequivocal evidence that in wild type plants at high CO_2 partial pressures and high light the CO_2 assimilation rates are limited by the supply of RuBP (Von Caemmerer, 2000). Further indirect evidence was presented by Price et al. (1995) from experiments with reduced GAPDH (one of the two enzymes that control the reduction of PGA into triose-phosphate). The authors demonstrated that at low levels of this enzyme (10% of wild-type plants, Fig. 6B in Price et al., 1995), the response curve of photosynthesis to CO_2 deviates faster from the Michaelis–Menten curve than in the wild type plants. A similar result was obtained with respect to radiation. However, Farazdaghi (2004) interpreted the evidence from Price et al. (1995) only showing that when CO_2 was saturating, the maximum rate of photosyn-

thesis of tobacco leaves was almost triple that of photosynthesis at ambient CO_2 . Therefore, this genetic information is equivocally supporting either the Rubisco-limited or RuBP regeneration-limited theories.

V. Experimental Evaluation of the Models

Experimental evaluation of the two-process model has been made by Farazdaghi (2004, 2007), who noted that the model of Farquhar et al. (1980) provided a systematic deviation from the experimental values for datasets with more than two response curves. Since the goal of any predictive model is to provide information for more than one line of data, both the two-process and the single-process model were tested with different data sets, including the Sharkey et al. (2007) version that has only a single CO_2 response line crossing the areas of three rate-limiting processes.

A. Integrated Datasets

The validation of the two-process theory was performed by Von Caemmerer and Farquhar (1981). Their data were extracted and re-evaluated by Farazdaghi (2004). Figure 12.4 shows a comparison of the two models. The two-process model (Fig. 12.4A) was calculated according to the authors' instruction, but Fig. 12.4B was modeled according to the two-step single-enzyme (or single-process) model using Eq. (12.14). Evidently, the two simulation lines of Von Caemmerer and Farquhar (1981) can hardly describe the observed experimental data, while the single-enzyme model provides a close fit to the data.

An additional test of the two-step single-enzyme model is provided in Fig. 12.5. The details of physiological parameters have been deducted from the experimental data. The close fit of the integrated model in Fig. 12.5A verifies the validity of the model (Eqs. 12.14, 12.16). Figure 12.5B shows application of the model to experimental data with the limiting factor in step 1 (Eq. 12.19). The data requirement of this special case is minimal and is the same as that of a rectangular hyperbola. The structure of Eq. (12.19) provides an interesting key to the interpretation of the relationship of present model with Blackman type models and

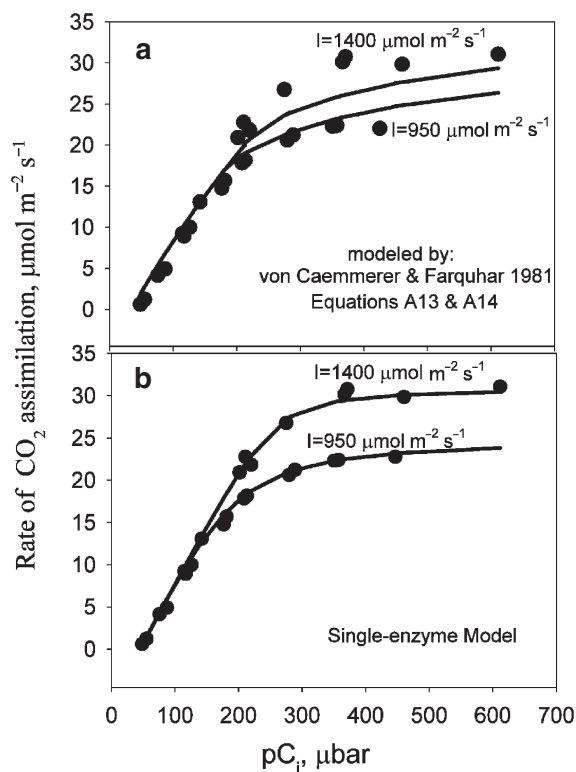


Fig. 12.4. A comparison of the CO_2 responses of assimilation; data of bean leaves under high and low light intensities (shown at the curves) for the models of (panel A) Farquhar et al. (1980) and (panel B) Farazdaghi (2004), with the data of Von Caemmerer and Farquhar (1981). Kinetic data in A were $V_{\text{Cmax}} = 115 \mu\text{mol m}^{-2} \text{s}^{-1}$, $\Gamma^* = 34 \mu\text{bar}$, $R_d = 0 \mu\text{mol m}^{-2} \text{s}^{-1}$, $K_C = 533 \mu\text{bar}$, $\text{O}_2 = 200 \text{mbar}$, $K_O = 381 \text{mbar}$, $J_{\text{max}} = 210 \mu\text{mol m}^{-2} \text{s}^{-1}$, $\theta = 1$, smaller values of θ did not improve the data fit. In B: $V_{\text{Cmax}} = 180$, $R_d = 2$, $A_{\text{maxH}} = 31$, $A_{\text{maxL}} = 24$, all in $\mu\text{mol m}^{-2} \text{s}^{-1}$, $\Gamma^* = 34 \mu\text{bar}$, $\Psi_a = 0.14 \mu\text{mol m}^{-2} \text{s}^{-1} \mu\text{bar}^{-1}$, $\alpha_{\text{IH}} = 0.05$ and $\alpha_{\text{IL}} = 0.3$

shows why they can often provide satisfactory fit to the A/I curves. It further demonstrates the nature of co-limitation and the observed interactions (Evans and Farquhar, 1991) between the convexity factor and A_{max} (Farazdaghi, 2007). An important factor in successful modeling of the two-step reaction is the establishment of the parameters of the Michaelis–Menten (rectangular) hyperbola of the transitional reaction first. Without accurate measurements of these parameters, the authenticity of the predicted parameters cannot be guaranteed, although curve fitting may produce satisfactory results.

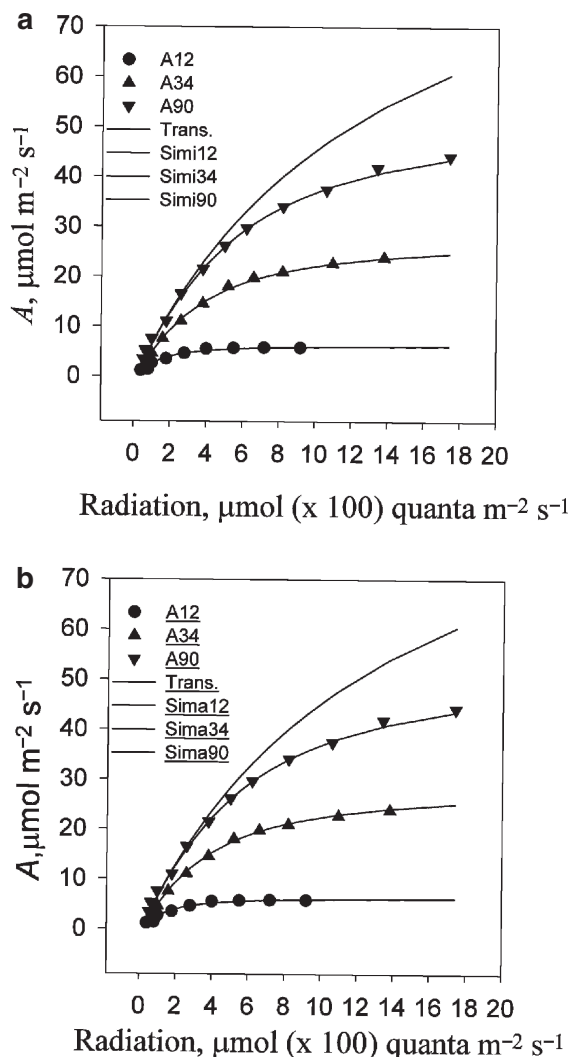


Fig. 12.5. Simulation of A/I response of *Salix* sp. (data of Ögren, 1993) leaves grown under light intensity of $1,400 \mu\text{mol quanta m}^{-2} \text{s}^{-1}$. The three different internal partial pressures of CO_2 were 12, 34 and 90 Pa. Experimental values of A are shown by symbols, simulated data by lines. The top panel (A) is integrated solution. This method produces a double saturation curve with respect to both radiation and CO_2 using a rectangular hyperbola for transitional state that covers the lower part of the curve. Equation (12.17) was used with a $V_{\text{Cmax}} = 110 \mu\text{mol m}^{-2} \text{s}^{-1}$; $\Phi_m = 0.080 \text{mol/mol quanta}$; Eq. (12.19) was used with $\Psi_a = 0.88 \mu\text{mol m}^{-2} \text{s}^{-1} \text{Pa}^{-1}$ and the same V_{Cmax} for the light saturated A/C_i response. The values of Φ were calculated from Eq. (12.9). The bottom panel is single-set approximate solution. The data of the top panel were used with a common value of $R_d = 1$ and only two parameters, Φ (0.05, 0.065, and 0.08 mol mol^{-1}) and A_{max} (7.5, 30 and $55 \mu\text{mol m}^{-2} \text{s}^{-1}$) in Eq. (12.20)

B. The Two-process Single Response Line Modeling Versus Curve Fitting?

Sharkey (1989) defines regulation as “adjustment for proper functioning or according to a rule”. He states that “limitation is what establishes the maximum”. Here the two rules are used to evaluate the model of Sharkey et al. (2007) with the example data and computer package of the authors.

In terms of fitting a single response line, the model of Sharkey et al. (2007) provides a good fit to the data of A versus C_i , though it does not provide any relationship with radiation. Figure 12.6 shows the response of CO_2 assimilation rate to leaf intercellular CO_2 concentration and the three limits proposed by Sharkey et al. (2007). Contrary to the criteria of Sharkey (1989), limitations of neither Rubisco nor RuBP regeneration produce a maximum, and the rate of reaction

gains positive increments as the supply of CO_2 increases. It may also be of interest to note that the RuBP regeneration-limited curve of Sharkey et al. (2007) crosses the Rubisco-limited curve of the modelers twice. No mention has been made by the authors as to whether this is a flaw or they would attach some biological significance to this double visitation.

Also, the significant difference between the single substrate response curves of Sharkey et al. (2007) and Farazdaghi (2004) is that in the former model the curvature is controlled only by the competition between of CO_2 and O_2 , while in the latter one it is partly affected by the competition, which changes the apparent Michaelis constant, and partly by the co-limitation of enzyme-substrate complexes. While the model is sensitive to the kinetic constants of Rubisco (such as K_C) the curve fitting software provided rather

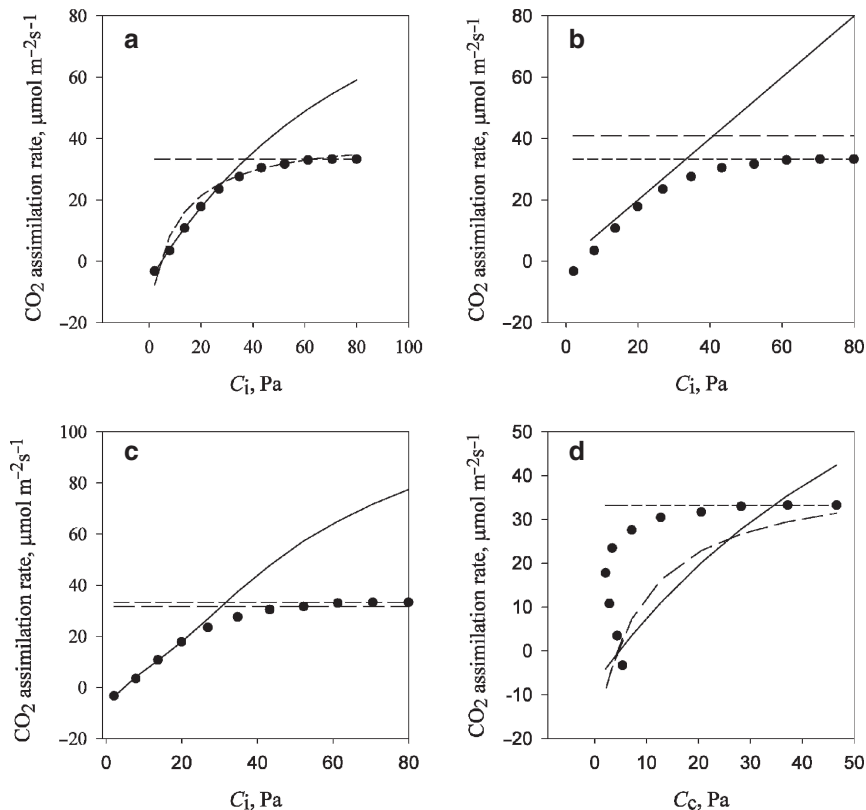


Fig. 12.6. (Panel A) The example and data of Sharkey et al. (2007) with ambient air and with respect to C_i , using the model and the solver for curve fitting. Symbols: ●, observed values; solid lines, Michaelis–Menten estimates; broken lines, A_j estimates; small dash lines, TPU limitation. (Panel B) As in A, but with zero oxygen, using only the model without the curve fitting solver. (Panel C) As in B, but with the curve fitting solver. (Panel D) As in (A), but with respect to C_c and with $g_m = 1$. The result shows the effect of circular calculations of C_c and g_m in the model with respect to observed A

good fit to the data even when K_C was varied from 10 to 10,000 Pa. Therefore, judging the validity of the model from the curve fitting output may not always provide reliable evaluations of enzymic parameters. In addition to the various problems mentioned previously, the effect of the circular nature of calculations for J and g_m from A can be observed from Fig. 12.6D, where assimilation is plotted against C_C , but the latter was circularly calculated from the assimilation rate.

VI. Concluding Remarks

Rubisco is the gate to CO_2 fixation and oxygenic life. No other enzyme has played such significant role in evolution of the planet, from the composition of its atmosphere, its propagation and support of life, to its ecological diversity and environmental quality. Thus, a biochemically correct model of understanding the behavior of this enzyme is essential to our management of natural resources and environment. A biochemical analysis of Rubisco and comparison of quantitative models has been performed in this chapter.

The two-step single-enzyme model is consistent with the biochemical principles of Michaelis and Menten (1913) that have been extended to two-substrate ordered reactions under steady state conditions. Though not explicit in the model, the role of Rubisco Activase is paramount in the activation of Rubisco. It facilitates the separation of dark-bound RuBP, as well as XuBP and CA1P from Rubisco, giving a competing advantage to CO_2 for carbamylation. The irreversible carboxylation of E-enediol (RuBP enediol) starts the second step of reaction leading to product (PGA). The competitive binding of PGA to the enzyme is an important regulatory process. It appears that there is an inverse relationship between the concentrations of RuBP and PGA (Price et al., 1995). As the activity of PCR cycle increases, the concentration of RuBP per Rubisco site increases to 4.5 mol mol^{-1} and that of PGA decreases until the molar ratio of RuBP/PGA stabilizes at around $0.8\text{--}1 \text{ mol mol}^{-1}$. This suggests that, although two moles of PGA are produced in carboxylation of one mole of RuBP, only one mole of PGA is required to inhibit one mole of Rubisco. This provides strong regulatory power to the PCR cycle over the Rubisco activity by controlling PGA.

As a result, under steady state conditions, the kinetics of the two-step Rubisco reaction change considerably and both K_C and V_{\max} lose their defined values. Then a good alternative is to use the kinetic values determined by the transient reaction (Laik, 1985; Laik and Oja, 1998; Farazdaghi 2004). Nevertheless, the initial slope (or efficiency Ψ) always remains a reliable and viable parameter of Rubisco kinetics (Farazdaghi and Edwards, 1988b; Johnson, 1992). Its measurement can often help to verify K_C and $V_{C\max}$ using Eq. (12.8).

In a test of limitations it is essential to observe the hierarchy of reactions. It is incorrect to suggest that either Rubisco or RuBP is limiting before confirming that CO_2 is not limiting, and always enzyme should be the last limiting factor considered. The two-process model of Farquhar et al. (1980) has been through significant changes with time. Farquhar et al. (1980) assumed that CO_2 assimilation rate was determined by the minimum of two independent processes: fully activated and RuBP-saturated Rubisco at high light and low CO_2 and RuBP regeneration at low light and/or high light and high CO_2 . The model received wide acceptance because of its apparent clarity and lack of ambiguity. However, Farazdaghi and Edwards (1992) presented a single-enzyme model, suggesting that the deviation of the Rubisco reaction velocity from the Michaelis–Menten curve is due to the distribution of enzyme between the two reaction steps and establishment of a steady-state condition. It was pointed out that the plateau of the assimilation curve is the steady-state rate of carboxylation (A_{\max}) that is controlled by Rubisco. Tcherkez et al. (2006) presented a theory, which, in contrast to the assumption of Rubisco limitation at low CO_2 , considered that “all ribulose biphosphate carboxylases may be nearly perfectly optimized”. The clear understanding from this theory is that due to optimized Rubisco, carboxylation is not Rubisco-limited, and even more, it is “nearly optimized”. This is consistent with the single enzyme (or single-process) theory. Sharkey et al. (2007) presented a new version of the model of Farquhar et al. (1980). This article was designed along the lines of the model modifications of Collatz et al. (1990), Von Caemmerer et al. (1994), Price et al. (1995), Ruuska et al. (1998) and Von Caemmerer (2000). The model,

however, considers a limitation of RuBP regeneration while carboxylation still responds to CO₂, which is inconsistent with the expectation of a maximum according to Sharkey (1989).

With global climate change, and its variability in time, location and intensity, the need for better planning and management tools is ever increasing. Expandable models should embody the correct structure of the process concerned. This would help to find the exact location and function of inputs, internal interactions, competitions and inhibitions, as well as outputs and the effects of feedbacks and environmental interactions. If the model is correct, then experimental simulation can open new frontiers by reducing time and the number of physical experiments to a minimum, for achieving and maximizing the positive results.

Acknowledgments

The author wishes to thank the editor, Agu Laisk, for his in-depth discussion of the manuscript and his constructive comments. Thanks also to the countless number of scientists and researchers for their discussions and emails about the theory and the model.

References

- Ainsworth EA, Rogers A, Blum H, Nösberger J and Long SP (2003) Variation in acclimation of photosynthesis in *Trifolium repens* after eight years of exposure to Free Air CO₂ Enrichment (FACE). *J Exp Bot* 54: 2769–2774
- Andersson I (2008) Catalysis and regulation in Rubisco. *J Exp Bot* 59(7): 1555–1568
- Andralojc PJ, Dawson GW, Parry MA and Keys AJ (1994) Incorporation of carbon from photosynthetic products into 2-carboxyarabinitol-1-phosphate and 2-carboxyarabinitol. *Biochemistry* 304: 781–786
- Andrews TJ and Lorimer GH (1978) Photorespiration still unavoidable? *FEBS Lett* 90: 1–9
- Arulanantham A, Raviraj L, Madhusudana R and Terry N (1990) Limiting factors in photosynthesis VI: Regeneration of ribulose 1,5-bisphosphate limits photosynthesis at low photochemical capacity. *Plant Physiol* 93: 1466–1475
- Ashida H, Danchin A and Yokota A (2005) Was photosynthetic RuBisCO recruited by acquisitive evolution from RuBisCO-like proteins involved in sulfur metabolism? *Research in Microbiology* 156: 611–618
- Ashida H, Saito Y, Nakano T, Tandeau de Marsac N, Sekowska A, Danchin A and Yokota A (2008) RuBisCO-like proteins as the enolase enzyme in the methionine salvage pathway: functional and evolutionary relationships between RuBisCO-like proteins and photosynthetic RuBisCO. *J Exp Bot* 59: 1543–1554
- Baldocchi DD and Wilson KB (2001) Modeling CO₂ and water vapor exchange of a temperate broadleaved forest across hourly to decadal time scales. *Ecol Modell* 142: 155–184
- Bernacchi CJ, Portis AR, Nakano H, Von Caemmerer S and Long SP (2002) Temperature response of mesophyll conductance. Implications for the determination of Rubisco enzyme kinetics and for limitations to photosynthesis in vivo. *Plant Physiol* 130: 1992–1998
- Blackman FF (1905) Optima and limiting factors. *Ann Bot* 19: 281–295
- Bowes G, Ogren WL and Hageman R (1971) Phosphoglycolate production catalysed by ribulose diphosphate carboxylase. *Biochem Biophys Res Commun* 45: 716–722
- Brooks A and Portis AR Jr (1988) Protein-bound Ribulose bisphosphate correlates with deactivation of ribulose bisphosphate carboxylase in leaves. *Plant Physiol* 87: 244–249
- Buckley TN and Farquhar GD (2004) A new analytical model for whole-leaf potential electron transport rate. *Plant Cell Environ* 27: 1487–1502
- Campbell WJ and Ogren WL (1990) Glyoxylate inhibition of ribulose bisphosphate carboxylase/oxygenase activation in intact, lysed, and reconstituted chloroplasts. *Photosynth Res* 23: 257–268
- Canadell JG, Corinne B, Le Quéré CD, Raupacha MR, Fielde CB, Buitenhuis ET, Ciais P, Conway TJ, Gillette NP, Houghton RA and Marland G (2007) Contributions to accelerating atmospheric CO₂ growth from economic activity, carbon intensity, and efficiency of natural sinks. *Proc Natl Acad Sci USA* 104: 18866–18870
- Charles-Edwards DA and Ludwig LJ (1974) A model for leaf photosynthesis by C₃ plant species. *Ann Bot* 38: 921–930
- Chartier P and Prioul JL (1976) The effects of irradiance, carbon dioxide and oxygen on the net photosynthetic rate of the leaf: a mechanistic model. *Photosynthetica* 10: 20–24
- Collatz GJ, Berry JA, Farquhar GD and Pierce J (1990) The relationship between the Rubisco reaction mechanism and models of photosynthesis. *Plant Cell Environ* 13: 219–225
- Cox PM, Betts RA, Jones CD, Spall SA and Totterdell IJ (2000) Acceleration of global warming due to carbon-cycle feedbacks in a coupled climate model. *Nature* 408: 184–187
- Cramer W, Bondeau A, Woodward FI, Prentice IC, Betts RA, Brovkin V, Cox PM, Fisher V, Foley J, Friend AD, Kucharik C, Lomas MR, Ramankutty N, Sitch S, Smith B, White A and Young-Molling C (2001) Global response of terrestrial ecosystem structure and function to CO₂ and climate change: Results from six dynamic global vegetation models. *Global Change Biol* 7: 357–373

- Cramer W, Bondeau A, Schaphoff S, Lucht W, Smith B and Sitch S (2004) Tropical forests and the global carbon cycle: Impacts of atmospheric CO₂, climate change and rate of deforestation. *Phil Trans R Soc Lond B* 359: 331–343
- de Wit CT (1965) Photosynthesis of leaf canopies. Verslag Landbouwkundig Onderzoek (Agr. Research Rep.) nr. 663, PUDOC, Wageningen
- Eichelman H and Laisk A (1999) Ribulose-1,5-bisphosphate carboxylase/oxygenase content, assimilatory charge, and mesophyll conductance in leaves. *Plant Physiol* 119: 179–189
- Ellis RJ (1979) The most abundant protein in the world. *Trends Biochem Sci* 4: 241–244
- Evans JR and Farquhar GD (1991) Canopy photosynthesis from the biochemistry of the C₃ chloroplast. In: Boote KJ and Loomis RS (eds) *Modeling Crop Photosynthesis – From Biochemistry to Canopy*, p 140. ASA, Madison, WI
- Farazdaghi H (2004) A theory and model for the kinetics of the two-substrate ordered reaction of Rubisco with rate-determining steps, and the effects of RuBP regeneration on the hierarchy of limitations. <http://www.farazdaghi.com/papers/html/photosynthesis.htm>
- Farazdaghi H (2005) Modeling of C₃ photosynthesis. Comments: <http://www.farazdaghi.com/index.php?itemid=5>
- Farazdaghi H (2007) Modeling Rubisco reaction with a new two-substrate ordered model with a rate-limiting step. Solar Energy and Artificial Photosynthesis conference, The Royal Society, London, 17–19 July 2007. <http://www.farazdaghi.com/papers/pdf/FarazdaghiRoyalSociety.pdf>
- Farazdaghi H and Edwards GE (1988a) A mechanistic model for photosynthesis based on the multisubstrate ordered reaction of ribulose-1,5-bisphosphate carboxylase. *Plant Cell Environ* 11: 789–798
- Farazdaghi H and Edwards GE (1988b) A model for photosynthesis and photorespiration in C₃ plants based on the biochemistry and stoichiometry of the pathways. *Plant Cell Environ* 11: 799–809
- Farazdaghi H and Edwards GE (1992) The co-limiting and mono-limiting theories of photosynthesis and photorespiration in C₃ plants. *Plant Physiol* 99: Special Issue-P 9. Abst. 49
- Farquhar GD, Von Caemmerer S and Berry JA (1980) A biochemical model of photosynthetic CO₂ assimilation in leaves of C₃ plants. *Planta* 149: 78–90
- Farquhar GD, Von Caemmerer S and Berry JA (2001) Models of photosynthesis. *Plant Physiol* 125: 42–45
- Finn MW and Tabita FR (2004) Modified pathway to synthesize ribulose 1,5-bisphosphate in methanogenic archaea. *J Bacteriol* 185: 3049–3059
- Haldane JBS (1930) *Enzymes*. Longmans Green and Co, London
- Hammond ET, Andrews TJ and Woodrow IE (1998) Regulation of ribulose-1,5-bisphosphate Carboxylase/Oxygenase by carbamylation and 2-carboxyarabinitol 1-phosphate in tobacco: insights from studies of antisense plants containing reduced amounts of rubisco activase. *Plant Physiol* 118: 1463–1471
- Harley P and Sharkey TD (1991) An improved model of C₃ photosynthesis at high CO₂: Reversed O₂ sensitivity explained by lack of glycerate reentry into the chloroplast. *Photosynth Res* 27: 169–178
- Jamin M, Adam M, Damblon C, Christiaens L and Frere J (1991) Accumulation of acyl-enzyme in DD-peptidase-catalyzed reactions with analogues of peptide substrates. *Biochem J* 280: 499–506
- Jensen RG (2000) From the cover: Activation of Rubisco regulates photosynthesis at high temperature and CO₂. *Proc Natl Acad Sci USA* 97: 12937–12938
- Johnson, KA (1992) Transient state kinetic analysis of enzyme reaction pathways. In: Sigman DS (ed) *The Enzymes*, 3rd ed, vol 20, pp 1–61. Academic Press, New York
- Jordan DB and Ogren WL (1984) The CO₂/O₂ specificity of ribulose 1,5-bisphosphate carboxylase oxygenase. Dependence on ribulose bisphosphate concentration, pH and temperature. *Planta* 161: 308–313
- Karl TR and Trenberth KE (2003) Modern global climate change. *Science* 302: 1719–1723
- Khan S, Andralojc PJ, Lea PJ and Parry MA (1999) 2'-carboxy-D-arabinitol 1-phosphate protects ribulose 1, 5-bisphosphate carboxylase/oxygenase against proteolytic breakdown. *Eur J Biochem* 266: 840–847
- Ku SG and Edwards GE (1978) Photosynthetic efficiency of *Panicum hiatts* and *Panicum milioides* in relation to C₃ and C₄ plants. *Plant Cell Physiol* 19: 665–675
- Laing WA and Christeller JT (1976) A model for the kinetics of activation and catalysis of ribulose 1,5-bisphosphate carboxylase. *Biochem J* 159: 563–570
- Laing WA, Ogren WL and Hageman RH (1974) Regulation of soybean net photosynthetic CO₂ fixation by the interaction of CO₂, O₂, and ribulose-1,5-diphosphate-carboxylase. *Plant Physiol* 54: 678–685
- Laisk A (1985) Kinetics of photosynthetic CO₂ uptake in C₃ plants. In: Viil J, Grishina G and Laisk A (eds) *Kinetics of Photosynthetic Carbon Metabolism in C₃ Plants*, pp 21–34. Valgus Publishing, Tallinn, Estonia
- Laisk A and Oja V (1998) Dynamics of leaf photosynthesis: Rapid response measurements and their interpretations. CSIRO Publishing, Collingwood, Australia
- Leuning R (1997) Scaling to a common temperature improves the correlation between photosynthesis parameters J_{max} and V_{cmax} . *J Exp Bot* 48: 345–347
- Medlyn BE, Dreyer E, Ellsworth D, Forstreuter M, Harley PC, Kirschbaum MUF, Le Roux X, Montpied P, Strassmeyer J, Walcroft A, Wang K and Loustau D (2002) Temperature response of parameters of a biochemically based model of photosynthesis. II. A review of experimental data. *Plant Cell Environ* 25: 1167–1179
- Michaelis L and Menten M (1913) Die Kinetik der Invertinwirkung. *Biochem Z* 49: 333–369

- Miziorko HM and Lorimer GH (1983) Ribulose-1,5-bisphosphate carboxylase oxygenase. *Annu Rev Biochem* 52: 507–553
- Monteith JL (1965) Light distribution and photosynthesis in field crops. *Ann Bot* 29: 17–37
- Mott KA and Woodrow IE (1993) Effects of O₂ and CO₂ on non-steady-state photosynthesis. Further evidence for ribulose-1,5-bisphosphate carboxylase/oxygenase limitation. *Plant Physiol* 102: 859–866
- Mott KA and Woodrow IE (2000) Modelling the role of Rubisco activase in limiting non-steady-state photosynthesis. *J Exp Bot* 51: 399–406
- Mullis J, Holmquist B and Vallee BL (1991) Hydrophobic anion activation of human liver xx alcohol dehydrogenase. *Biochemistry* 30: 5743–5749
- Ogren WL and Bowes G (1971) Ribulose diphosphate carboxylase regulates soybean photorespiration. *Nature New Biol* 230: 159–160
- Ögren E (1993) Convexity of the photosynthetic light response curve in relation to intensity and direction of light during growth. *Plant Physiol* 101: 1013–1019
- Ögren E and Evans JR (1993) Photosynthetic light-response curves. I. The influence of CO₂ partial pressure and leaf inversion. *Planta* 189: 182–190
- Parry MAJ, Loveland JE and Andralojc PJ (1999) Regulation of Rubisco. In: Bryant JA, Burrell MM and Kruger NJ (eds) *Plant Carbohydrate Biochemistry*, pp 127–145. Bios Scientific Publishers, Oxford
- Portis AR Jr, Lilley RM and Andrews TJ (1995) Subsaturating ribulose-1,5-bisphosphate concentration promotes inactivation of ribulose-1,5-bisphosphate carboxylase/oxygenase (Rubisco). Studies using continuous substrate addition in the presence and absence of Rubisco Activase. *Plant Physiol* 109: 1441–1451
- Price GD, Evans JR, Von Caemmerer S, Yu JW and Badger MR (1995) Specific reduction of chloroplast glyceraldehyde-3-phosphate dehydrogenase activity in ribulose bisphosphate regeneration in transgenic tobacco plants. *Planta* 195: 369–378
- Quick WP, Schurr U, Scheibe R, Schulze ED, Rodermel SR, Bogorad L and Stitt M (1991) Decreased ribulose-1,5-bisphosphate carboxylase-oxygenase in transgenic tobacco transformed with antisense rbcS. 1. Impact on photosynthesis in ambient growth-conditions. *Planta* 183: 542–554
- Rabinowitch E (1951) *Photosynthesis and Related Processes*. Interscience Publishers, New York
- Ruuska SA, Andrews TJ, Badger MR, Hudson GS, Laisk A, Price GD and Von Caemmerer S (1998) The interplay between limiting processes in C₃ photosynthesis studied by rapid response gas exchange using transgenic tobacco impaired in photosynthesis. *Funct Plant Biol* 25: 859–870
- Sage RF and Sharkey TD (1987) The effect of temperature on the occurrence of O₂ and CO₂ insensitive photosynthesis in field-grown plants. *Plant Physiol* 84: 658–664
- Salvucci ME and Crafts-Brandner SJ (2004) Mechanism for deactivation of Rubisco under moderate heat stress. *Physiol Plantarum* 122: 513–519
- Scheffer M, Brovkin V and Cox P (2006) Positive feedback between global warming and atmospheric CO₂ concentration inferred from past climate change. *Geophys Res Lett* 33: L10702
- Sharkey TD (1985) O₂-insensitive photosynthesis in C₃ plants. Its occurrence and a possible explanation. *Plant Physiol* 78: 71–75
- Sharkey TD (1989) Evaluating the role of Rubisco regulation in photosynthesis of C₃ plants. *Phil Trans R Soc Lond B* 323(121) 435–448
- Sharkey TD, Bernacchi CJ, Farquhar GD and Singsaas EL (2007) Fitting photosynthetic carbon dioxide response curves for C₃ leaves. *Plant Cell Environ* 30: 1035–1040
- Spreitzer RJ and Salvucci ME (2002) RUBISCO: Structure, regulatory interactions, and possibilities for a better enzyme. *Annu Rev Plant Biol* 53: 449–475
- Spreitzer RJ, Peddi SR and Satagopan S (2005) Phylogenetic engineering at an interface between large and small subunits imparts land-plant kinetic properties to algal Rubisco. *Proc Natl Acad Sci USA* 102: 17225–17230
- Taylor TC and Andersson I (1996) Structural transitions during activation and ligand binding in hexadecameric Rubisco inferred from the crystal structure of the activated unliganded spinach enzyme. *Nat Struct Biol* 3: 95–101
- Taylor SE and Terry N (1984) Limiting factors in photosynthesis. V: Photochemical energy supply co-limits photosynthesis at low values of intercellular CO₂ concentration. *Plant Physiol* 75: 82–86.
- Taylor TC, Backlund A, Bjorhall K, Spreitzer RJ and Andersson I (2001) First crystal structure of Rubisco from a green alga, *Chlamydomonas reinhardtii*. *J Biol Chem* 276: 48159–48164
- Tcherkez GGB, Farquhar GD and Andrews TJ (2006) Despite slow catalysis and confused substrate specificity, all ribulose bisphosphate carboxylases may be nearly perfectly optimized. *Proc Natl Acad Sci USA* 103: 7246–7251
- Terry N (1980) Limiting factors in photosynthesis. I. Use of iron stress to control photochemical capacity in vivo. *Plant Physiol* 65: 114–120
- Terry N (1983) Limiting factors in photosynthesis. IV. Iron stress mediated changes on light-harvesting and electron transport capacity and its effects on photosynthesis in vivo. *Plant Physiol* 71: 855–860
- Thornley JHM (1976) *Mathematical Models in Plant Physiology*. Academic Press, London
- Torn MS and Harte J (2006) Missing feedbacks, asymmetric uncertainties, and the underestimation of future warming. *Geophys Res Lett* 33: 1–56
- Van Bavel CHM (1975) A behavioral equation for leaf carbon dioxide assimilation and a test of its validity. *Photosynthetica* 9: 165–76

- Von Caemmerer S (2000) Biochemical Models of Photosynthesis. Techniques in Plant Sciences, No.2. CSIRO Publishing, Collingwood, Australia
- Von Caemmerer S and Farquhar GD (1981) Some relationships between the biochemistry of photosynthesis and the gas exchange of leaves. *Planta* 53: 376–387
- Von Caemmerer S, Evans JR, Hudson GS and Andrews TJ (1994) The kinetics of ribulose-1,5-bisphosphate carboxylase/oxygenase in vivo inferred from measurements of photosynthesis in leaves of transgenic tobacco. *Planta* 195: 88–97
- Wullschlegel SD (1993) Biochemical limitations to carbon assimilation in C₃ plants - a retrospective analysis of the A/Ci curves from 109 species. *J Exp Bot* 44: 907–920
- Zhang N and Portis AR (1999) Mechanism of light regulation of Rubisco: a specific role for the larger Rubisco activase isoform involving reductive activation by thioredoxin-f. *Proc Natl Acad Sci USA* 96: 9438–9444

Chapter 13

Leaf C₃ Photosynthesis *in silico*: Integrated Carbon/Nitrogen Metabolism

Agu Laisk*, Hillar Eichelmann and Vello Oja

Institute of Molecular and Cell Biology, Tartu University, Riia 23, Tartu 51010, Estonia

Summary.....	295
I. Introduction.....	296
II. The Structure of the Model.....	297
A. Basics of C ₃ Photosynthesis in the Model.....	297
B. Hypothetical Mechanism of Integrated C/N Metabolism.....	301
III. Mathematics.....	302
A. Rate Equations.....	302
1. Compartmentation.....	302
2. Photosystems.....	303
3. Photosystem II and Chlorophyll Fluorescence.....	303
4. Photosystem I and Optical Transmittance Signals.....	305
5. Electron/Proton Transport Reactions.....	306
6. RuBP Carboxylase/Oxygenase (Rubisco).....	307
7. Carbon Reduction Cycle.....	308
8. Photorespiratory Carbon Oxidation Cycle.....	310
9. Organic and Amino Acid Synthesis.....	310
B. Budget Equations.....	310
1. Electron-Proton Transport and ATP Synthesis.....	310
2. Carbon Reduction Cycle.....	311
3. Organic and Amino Acid Synthesis.....	312
4. Sucrose Synthesis.....	312
5. Non-photochemical Excitation Quenching.....	312
IV. Simulations.....	312
A. Light Responses.....	312
B. CO ₂ Responses.....	313
C. Induction Transients.....	314
D. "To Understand Oscillations Is to Understand Photosynthesis".....	314
E. Modeling the O ₂ /CO ₂ Exchange Ratio.....	316
V. Concluding Remarks.....	317
Acknowledgments.....	319
References.....	319

Summary

A computer model of C₃ photosynthesis comprising light reactions, electron-proton transport, enzymatic reactions and regulatory functions is presented as a system of differential budget equations for intermediate compounds. Carbon and nitrite reduction systems are linked assuming that nitrite reduction is the

* Author for correspondence, e-mail: alaisk@ut.ee

dominant proton-coupled alternative electron transport pathway compensating for ATP consumption by starch synthesis and other non-photosynthetic processes. The principal theoretical hypothesis is that the carbon skeletons for the freshly synthesized amino acids are partitioned from the pool of phosphoglyceric acid (PGA) before its reduction in photosynthesis. Consequently, the rate of nitrite reduction is controlled by ferredoxin reduction and PGA levels. The latter simultaneously controls the rate of starch synthesis – the major alternative ATP consumer linking nitrite reduction with starch synthesis. The model reproduces light and CO₂ response curves of photosynthesis, chlorophyll fluorescence and 810 nm transmittance signals during steady state, as well as during induction and oscillations. The model explains the integral Nitrogen/Carbon (N/C) ratios of plant tissues and predicts that the availability of nitrogen may limit the photosynthetic rate in natural communities.

I. Introduction

Photosynthesis research is digging deeper and deeper towards molecules, but for the understanding of the whole process the bits and pieces, verbally described e.g. in the previous volumes of this series, must be put together again. The recombined, integrated information forms a mathematical model of photosynthesis. The structure of a well-done mathematical model of photosynthesis is as complicated as the natural process itself, and its behavior is as difficult to understand as that of real photosynthesis due to the enormous number of combinations of parameter values. Only the development of models that are continuously confronted with new experiments allows one to identify realistic parameters, sometimes even to suggest (i.e., theoretically predict) novel structural connections and regulatory loops. In this chapter we describe such novel models for C₃ leaf photosynthesis.

In the first mathematical models the whole photosynthetic process was simplified to the level

of a single biochemical process, either with the Blackman type kinetics or with Michaelis–Menten type kinetics (see Chapter 12 of this book by Hadi Farazdaghi). However, the importance of the mass transfer processes was immediately understood, modifying the single-enzyme model by the inclusion of the diffusion resistance for CO₂ transport (Brown and Escombe, 1900; Rabinowitch, 1951, 1953; Chartier, 1966). The resulting non-rectangularly hyperbolic curves are used in models up to the present day as convenient, flexible mathematical formulations (Chapter 11 of this book by Xinyou Yin, Jeremy Harbinson and Paul C. Struik). Significant progress was made by modeling the interaction of photosynthesis and photorespiration in C₃ plants on the basis of Rubisco kinetics (Laisk, 1970; Farquhar et al., 1980). This single-enzyme approach was epitomized in the popular model of G. Farquhar, S. Von Caemmerer and J. Berry (Farquhar and Von Caemmerer, 1982; Chapter 9 of this book by Susanne von Caemmerer, Graham Farquhar, and Joseph Berry). In this approach the light-saturated, but Rubisco- and CO₂-limited photosynthesis was modeled considering Rubisco kinetics with respect to CO₂ and O₂ as substrates and photosynthetic CO₂ fixation and simultaneous photorespiratory CO₂ evolution as the components of net CO₂ uptake (Von Caemmerer, 2000). By assuming constant Rubisco activation state and RuBP-saturation of the reaction, the model predicts well the CO₂ response of leaf net photosynthesis, provided that the kinetic parameters of Rubisco are known for the particular leaf. The problem still is in the relation of Rubisco activity to its content in the leaf. For example, the *in vivo* average k_{cat} of an active site varies from 1.5 to 4 s⁻¹ or faster depending

Abbreviations: CRC – carbon reduction/oxidation cycle; Cyt b₆f – cytochrome b₆f complex; Cyt f – cytochrome f; ETR – electron transport rate; FNR – ferredoxin/NADP reductase; FRL – far-red light; GAPDH – glyceraldehyde phosphate dehydrogenase; GOGAT – glutamine synthetase/glutamate synthase; MDH – chloroplast malate dehydrogenase; NDH – chloroplast NADPH dehydrogenase; NPQ – nonphotochemical quenching; PFD, PAD – photon flux densities, incident and absorbed; P_i – inorganic phosphate in text (OP in equations); *pmf* – proton motive force; PRK – phosphoribulokinase; PS II, PS I – photosystem II, photosystem I; P680 – PS II donor pigment; Q_A – PS II primary quinone acceptor; Q_B – PS II secondary quinone acceptor; T₈₁₀, T₉₅₀ – leaf transmittance at 810 and 950 nm; Other denotations in the legend to Fig. 13.1.

on the Rubisco active site density and other as yet unknown factors (Eichelmann and Laisk, 1999; Eichelmann et al., 2008). Nevertheless, thanks to the high performance/complexity ratio, this model has been intensely exploited in large-scale modeling of plant communities (Chapter 16 by Ülo Niinemets and Niels P. R. Anten; Chapter 19 by Stephan A. Pietsch and Hubert Hasenauer). Further development of this model aims at processes determining the maximum quantum yield of photosynthesis (Yin et al., 2004). By considering excitation partitioning between the two photosystems, as well as quantum losses for alternative and cyclic pathways of electron transport, a tool for the determination of these rates from the measured quantum yield of photosynthesis has been created (Yin et al., 2006; Chapter 11 of this book by Xinyou Yin, Jeremy Harbinson and Paul C. Struik).

Complex models involving an extensive network of biochemical reactions of photosynthesis were aimed at more complete understanding of interactions between electron transport and carbon assimilation during light and CO₂ limitation as well as during light and CO₂ saturation. From these computer models, it soon became clear that reversible reactions (Pettersson and Ryde-Pettersson, 1988), rather than simplified irreversible reactions (Hahn, 1987) must be considered for the sake of stabilization of the complex biochemical system. Moreover, the metabolic network could be stabilized only after the control of sucrose and starch synthesis was included (Laisk, 1977b; Laisk and Laarin, 1983; Laisk and Walker, 1986; Laisk et al., 1989). These mathematical models reflected the metabolic network involving reactions having large free energy change, forcing the fluxes to rapidly flow downhill towards the end products. For a stable operation, the rate of carbon outflow to sucrose and starch must be regulated equal to the rate of inflow through RuBP carboxylation. Since the CO₂ acceptor RuBP is re-synthesized from the intermediates of the same metabolic system, it would be fatal if the rates of sucrose and starch synthesis are allowed to increase to the extent that they out-compete the synthesis of RuBP, because then the cycle would become depleted of metabolites and photosynthesis would cease. The stable balance between carbon outflow and inflow was established in models

after sucrose synthesis was modeled as controlled by cytosolic fructose biphosphatase (activated by triosephosphates and inactivated by inorganic phosphate) and starch synthesis as controlled by ADP glucose pyrophosphorylase, activated by PGA, and inactivated by inorganic phosphate (Laisk and Eichelmann, 1989; Laisk et al., 1989).

II. The Structure of the Model

A. Basics of C₃ Photosynthesis in the Model

In the latest C₃ photosynthesis model (Laisk et al., 2006a) the photosynthetic metabolism is assumed to take place in four compartments – thylakoid membranes, thylakoid lumen, chloroplast stroma and cytosol (Fig. 13.1). Photoreactions and electron carriers are embedded in the membrane, while protons accumulate in the lumen. Carbon reduction and starch synthesis pathways are located in the stroma with sucrose synthesis in the cytosol. The phosphate translocator transports metabolites through the chloroplast membrane. Molar concentrations of metabolites required in the kinetic equations are the state variables. If necessary, the total amount of a specific compound per unit leaf area is expressed multiplying its concentration by the volume of the compartment per unit leaf area.

In the thylakoid membranes, photosystems II and I (abbreviated as PS II and PS I in the text, but denoted PS2 and PS1 as model variables) convert light energy into chemical energy. Our model assumes that quanta are absorbed in the homogeneous Chl antenna by each photosystem. Excitation rates of the reaction centers are calculated considering incident Photon Flux Density (PFD), absorption by Chl, and the number of Chl in the antenna. Excitation is equilibrated between the antenna and the reaction center of each PS II. The transfer of excitation between PS IIs by antenna connectivity is not included, neither is the spillover from PS II to PS I. Losses caused by fluorescence and non-photochemical quenching of excitation are considered in the antenna of PS II, but not in the antenna of PS I. In PS II, an oxygen-evolving complex (OEC) as well as a primary acceptor Q_A are attached to each photosystem. Neighboring PS IIs share the PQ

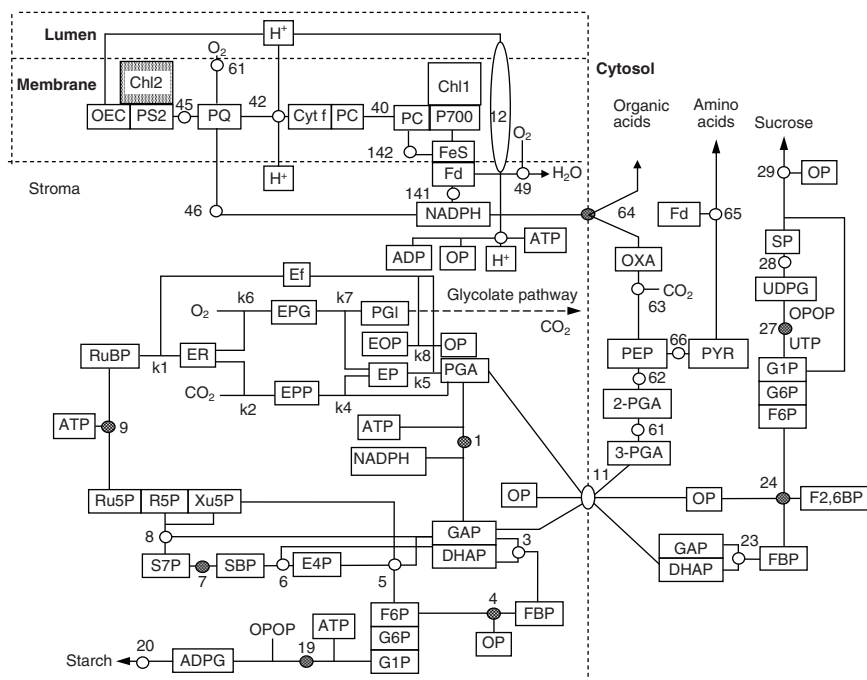


Fig. 13.1. The structure of the model of C_3 photosynthesis. State variables are boxed, boxes joined together denote one state variable containing equilibrated compounds. Numbers denote enzymes, shading indicates regulated enzymes and non-photochemical quenching in PS2 antenna. Dotted lines separate compartments. Glycolate pathway is integrated, neglecting the intermediates. Acronyms and denotations used in Fig. 13.1 and in the text: ADPGlu – ADP-glucose; Cyt f – cytochrome f; DHAP – dihydroxyacetone phosphate; E4P – erythrose 4-phosphate; FBP – fructose 1,6-bisphosphate; F2,6BP – fructose 2,6-bisphosphate; Fd – ferredoxin; F6P – fructose 6-phosphate; GAP – glyceraldehyde phosphate; G6P – glucose 6-phosphate; G1P – glucose 1-phosphate; MDH – malate dehydrogenase; NPQ – non-photochemical quenching; OEC – oxygen evolving complex; OP – inorganic phosphate; OPOP – pyrophosphate; OXA – oxaloacetate; PC – plastocyanin; PGI – phosphoglycerate; PFD – photon flux density; PAD – photon absorption density; PGA – phosphoglycerate; PEP – phosphoenol pyruvate; PQ – plastoquinone; PS2 – photosystem II; PYR – pyruvate; P700 – donor pigment of photosystem I; R5P – ribose 5-phosphate; Ru5P – ribulose 5-phosphate; RuBP – ribulose 1,5-bisphosphate; SBP – seduheptulose 1,7-bisphosphate; S7P – seduheptulose phosphate; SP – sucrose phosphate; P5P – pentose 5-phosphates; T3P – triose 3-phosphates; UDPG – UDP-glucose. Rubisco (ribulose 1,5-bisphosphate carboxylase-oxygenase) intermediate complexes: ER – with RuBP; EPP – with two PGA; EPG – with PGA and phosphoglycerate; EP – with one PGA; EOP – with phosphate; Ef – free enzyme

pool. Electron transport is possible only if P680 is reduced and Q_A is oxidized inside a single PS II, but not allowed from a PS II with reduced P680 to a different PS II with oxidized Q_A . The secondary acceptor Q_B is assumed to equilibrate rapidly with the free PQ pool, neglecting effects caused by two-electron gating at Q_B . Other details like S-states of the water-splitting Mn complex, structural heterogeneity of the antenna system, and pheophytin as an intermediate step in electron transfer are neglected in our model (but see the more extensive recent PS II models by Zhu et al., 2005; Porcar-Castell et al., 2006 and Chapter 7 of this book by Andrew Rubin and Galina Riznichenko).

Electrons are transported from Q_A (denoted PS2A in the model) to plastoquinone (PQ, includes also Q_B) and further to cytochrome b_6f , plastocyanin (PC) and P700, the latter being the donor pigment of PS I. Diffusion of PQ is not rate-limiting, but the partial limitation of electron transport by diffusion of plastocyanin, PC (Kirchhoff et al., 2004) is considered. The total PC pool is divided into two parts, one in redox equilibrium with Cyt f (Cyt fPC), and the other in redox equilibrium with P700 (PCP700). Electrons are exchanged between these pools by diffusion of reduced and oxidized PC. This somewhat simplified structure helps to evaluate the characteristic behavior of the 810 and 950 nm

optical signals by simulating the partial limitation of electron transport by PC diffusion.

The diffusion in proximity of PS I is different from that around PS II, leading to different mathematical description of the photosystems. PC cross-diffuses rapidly enough to ensure that the donor-side electron pool is redox-equilibrated among all PS I units. If P700 becomes oxidized in a particular PS I the electron vacancy can rapidly delocalize to other PS Is in the neighborhood, so that, in principle, the reduction states of P700 become equilibrated. On the acceptor side of PS I, ferredoxin (Fd) is the first rapidly diffusing electron acceptor after the bound FeS carriers. We assume that Fd is redox-equilibrated with preceding low-potential carriers (although the whole sequence of the primary electron carriers is modeled as one, denoted FeS) that can block electron flow through PS I when reduced. According to this scheme, the redox-equilibrated donor side carriers PC and P700 can be mathematically treated as a single pool and, likewise, so can the acceptor side carriers Fd and FeS. In view of redox equilibration of $PC \leftrightarrow P700$ and $Fd \leftrightarrow FeS$, we assume that the rate of PS I electron transport is determined by the rate of PS I antenna excitation times the fraction of reduced P700 times the fraction of oxidized FeS, thereby avoiding necessity that the reduced P700 and oxidized FeS be present in one and the same PS I. These different mathematical treatments of PS II and PS I evidently are idealizations approximating reality from different extremes.

Electron branching at Fd (and NADPH) is crucial in photosynthesis. The main linear pathway goes from Fd to NADP via Fd-NADP reductase (FNR) and the other pathways which branch off from Fd lead to nitrite and oxygen reduction. The principal importance of the nitrite and oxygen pathways is in regulation of ATP/NADP stoichiometry, because electrons entering these “alternative” pathways have co-translocated protons supporting ATP synthesis, but this extra ATP is not consumed by these same metabolic pathways. Another alternative electron pathway branches off from NADPH: the latter can be used for reduction of oxaloacetate (OXA) by chloroplast malate-dehydrogenase (MDH) (Scheibe, 1987).

When considered in the context of the alternative pathways, cyclic electron transport around PS I has caused confusion and controversy. There are two cyclic pathways. One transports electrons from NADPH to plastoquinone via chloroplast NDH – a chloroplast analog of Complex I of the mitochondrial electron transport chain (Sazanov et al., 1995; Peltier and Cournac, 2002; Lascano et al., 2003). There is no doubt that this pathway is proton-coupled, but its observed rate is very slow raising doubts about its importance in photosynthesis. Another cyclic pathway is assumed to begin from reduced Fd, donating electrons to PQ either via a still undiscovered Fd/PQ reductase (Bendall and Manasse, 1995) or via the PQ-reducing site of the Cyt b₆f complex. A recent experimental analysis was not able to confirm that PS I cyclic electron flow is H⁺-coupled, but a fast, probably H⁺-uncoupled pathway was observed at light saturation of photosynthesis (Laik et al., 2007). This pathway is tentatively included in the model as donating electrons from Fd⁻ to Cyt f via a hypothetical pathway that bypasses the Q-cycle.

Linear electron transport is coupled to transmembrane proton translocation. For every e⁻, one H⁺ is released in the lumen from the Oxygen Evolving Complex (OEC) and two protons are transported at Cyt b₆f with the help of the Q-cycle (Rich, 1991). Though the molecular mechanism of the Q-cycle is complex (Cramer et al., 2006), in our model the internal complexity of the Cyt b₆f complex is approximated by a single enzyme with hyperbolic kinetics. The mechanism of “photosynthetic control” of electron transport through Cyt b₆f (regulation of Cyt b₆f turnover) has been an enigma. The common assumption is that the proton backpressure shifts the equilibrium constant of the reaction, counteracting the large ΔE between the substrate PQH₂ and the product PC. The mathematical modeling helps us to understand whether the shift of the reaction equilibrium is sufficient to control the rate of the reaction in accordance with observations.

In the current model, the proton motive force (*pmf*) is based on H⁺ concentration gradient, but its electrical component is neglected. From the measurements of electrochromic shift, it has been shown that the transport of Mg²⁺ counter-ions

through the thylakoid membrane neutralizes the electric field rather slowly (Cruz et al., 2001). Thus, the field-based driving force for ATP synthesis is generated immediately after light is turned on, but luminal pH decreases more slowly. This may be the actual mechanism for the slow onset of non-photochemical excitation quenching NPQ, the temporal kinetics of which are based on the actually slow adjustment of the luminal pH, but are now modeled by assuming a formal slow intermediate step between the thylakoid pH and NPQ.

The most amazing molecular machine, ATP synthase, is also modeled as an ordinary enzyme-catalyzed reaction, neglecting fine mechanistic details. Nevertheless, the basic property of the reaction – the reversible equilibrium between the opposing chemical potentials of ATP hydrolysis and transmembrane *pmf* – is considered by calculating the actual, “dynamic” equilibrium constant of the reaction at each integration step. The proton requirement of the chloroplast ATP synthase is of primary importance, determining the mechanistic necessity for alternative and cyclic electron flows. The requirement of $12\text{H}^+/3\text{ATP}$ (Rumberg et al., 1990) satisfies the ATP requirement for sucrose synthesis, leaving only a small proton deficiency caused by the consumption of ATP for starch and protein synthesis and some proton ‘slip’ in the ATP synthase (Feniouk et al., 2005). If the requirement is $14\text{H}^+/3\text{ATP}$ as suggested from the atomic force micrographs of the spinach chloroplast ATP synthase (Seelert et al., 2000), the necessity for significant alternative and/or cyclic electron flow to balance the H^+/e^- ratio is evident. However, such fast alternative cyclic electron flow as predicted by the model for the requirement of $14\text{H}^+/\text{ATP}$ was not observed experimentally (Laisk et al., 2007).

The carbon reduction cycle (CRC) is described considering the reaction kinetics for all enzymes except hexosephosphate-, pentosephosphate-, and triosephosphate isomerases-epimerases that are assumed to be in equilibrium (Pettersson and Ryde-Pettersson, 1988; Laisk et al., 1989). Possible differences in the reaction mechanism of enzymes, e.g. the sequence of substrate binding, are neglected, but the random binding of substrates is assumed for all reactions (Cleland, 1963). The rate equation is expressed in the format containing the equilibrium

constant, considering that the standard free energy difference is usually known. The K_m values are recalculated for the ionized forms of the substrates, known to be the actual reacting species (Laisk et al., 1989). Rubisco reaction kinetics are modeled in more detail, considering reaction intermediates competing in the carboxylase and oxygenase reactions. Competition between RuBP, PGA and P_i for the free enzyme is also considered (we use the acronym P_i to denote inorganic phosphate in text, but denote it OP in equations).

The correct balancing of carbon input and output for the CRC is crucial for stabilizing the intermediate pools of the cycle (Pettersson and Ryde-Pettersson, 1988; Laisk et al., 1989). The activity of ADP-glucose pyrophosphorylase in the starch synthesis pathway is allosterically controlled by the PGA/ P_i ratio (Heldt et al., 1977; Tetlow et al., 2004). Likewise, the activity of sucrose phosphate synthase is controlled by F6P and P_i in the cytosol (Huber, 1989). The concentration of pyrophosphate (PP_i , but denoted OPOP in equations) is assumed to be low and constant. The fine control of sucrose synthesis is exerted by fructose 2,6-bisphosphate (F2,6BP), an inhibitor of the cytosolic FBPase. The synthesis and degradation reactions of F2,6BP are regulated by triosephosphate (T3P), PGA and P_i levels in such a way that the cytosolic FBPase is activated when T3P is high and P_i is low and inactivated when T3P is low and P_i is high (Stitt, 1987; reactions of the synthesis and degradation of F2,6BP are not shown in Fig. 13.1). Redox-controlled enzymes [glyceraldehyde phosphate dehydrogenase, GAPDH (1), fructose-bisphosphatase, FBPase (4), seduheptulose-bisphosphatase, SBPase (7) and phosphoribulokinase, PRK (9)] are activated by the reversible transfer of reducing equivalents from Fd^- via thioredoxin f to thiol groups.

The total pools of phosphate (we use an acronym P_{IT} for it in text, but denote OP_{T} in equations) are constant in cytosol and stroma (denotations are in italics for model variables in formulae, but regular fonts are used to denote acronyms for chemical compounds in text). The level of free P_i is calculated at each step as the difference between P_{IT} and the sum of phosphate bound in all phosphate esters. Phosphate is liberated during sucrose and starch synthesis, as well

as from bisphosphatase and phosphoglycolate phosphatase reactions. ATP synthase binds the free P_i and reactions coupled with ATP hydrolysis transfer it back into the phospho-esters of the CRC. In the calculations of Laisk et al. (2006a) phosphate turnover was tuned to be predominantly rate-limiting at saturating light and CO₂; however, in the present model the capacity for nitrite reduction is the dominant rate-limiter. The phosphate translocator in the chloroplast membrane keeps the phosphate pools separated in stroma and cytosol by interchanging T3P²⁻, PGA²⁻ and P_i²⁻ between stroma and cytosol (Flügge, 1991). The level of ionized substrates dependent on pH is calculated not only for the phosphate translocator but for all enzymes that are known to react with ionized substrates (Laisk et al., 1989); however, the stromal pH is still set constant.

Processes closely related to photosynthesis are modeled schematically, considering the essential budget relationships. The photorespiratory glycolate pathway is described in an integrated way, considering its overall carbon, ATP and NADPH budget, but not the pools of individual intermediates. As a result of this simplification, the steady-state rate of photorespiration is calculated correctly, but in transients only RuBP and other CRC pools are considered, neglecting kinetic effects caused by the accumulation of glycolate pathway intermediates. In the light in absence of external CO₂, the photorespiratory CO₂ evolution is continuing, indicating that the products of glycolysis enter CRC via the phosphate translocator, serving as substrates for photorespiration. Such an “internal feeding” of CRC ensures that its pools are not completely depleted in the dark or in the absence of CO₂ (Pärnik and Keerberg, 1995).

Chloroplast dark metabolism is represented by the chlororespiratory pathway (Peltier and Cournac, 2002). The reversal of the reductive part of the CRC generates NADPH and ATP necessary for the dark metabolism in the chloroplast. NADPH-plastoquinone oxidoreductase (NDH, reaction 46) reduces PQ at the expense of NADPH, coupled to translocation of 2H⁺/e⁻. The chlororespiratory terminal oxidase uses PQH₂ as the substrate at the luminal side of the membrane. However, chloroplast dark metabolism is not well understood and is correspondingly poorly represented in the model lead-

ing to spurious results when running the model with PFD set to zero.

In accordance with experimental data used to test the model (CO₂ and O₂ gas exchange, Chl fluorescence and 810 nm signal transients) the fastest temporal resolution of calculations is about 1 ms. This sets the limit for the modeling of faster transients, e.g. those related to excitation energy transfer and electron transport through the photosystems. The faster processes are assumed to be in quasi-steady state during the integration step (variable during the calculations dependent on the speed of the transient, from about 10⁻⁵ to 10⁻² s). According to this principle, processes of excitation and electron transfer in and around PS II and PS I are solved as a system of algebraic equations at each integration step. Similarly, several enzymic reactions, as well as electron transfer at the donor and acceptor side of PS I, are considered to be so fast that they do not shift far from the chemical (redox) equilibrium. Such groups of chemically equilibrated compounds are considered one state variable in the system of differential equations, but their internal structure – the distribution of equilibrated compounds – is solved as a system of algebraic equations at each integration step.

B. Hypothetical Mechanism of Integrated C/N Metabolism

In recent experiments on potato leaves, under low O₂ concentrations to eliminate the Mehler reaction and photorespiration, Laisk et al. (2007) observed exactly equal photosynthetic CO₂ uptake and O₂ evolution rates independent of light intensity and CO₂ concentration. Measurements of PS I electron transport showed no cyclic electron flow at limiting light intensities. The results suggested the extra ATP for starch and protein synthesis is supported by alternative electron transport to acceptors initially having lower reduction level than carbohydrates. Only after reduction by the alternative electron flow do these acceptors reach a reduction level comparable to carbohydrates. The strict O₂/CO₂ equality suggested that the compound participating in the alternative electron flow is partitioned from photosynthetic intermediates before reduction – which could only be 3-phosphoglyceric acid (PGA).

In the previous model (Laisk et al., 2006a) we considered the alternative electron transport pathway mediated by the “malate valve”, but neglected the question of origin of the substrate OXA. The calculated O_2/CO_2 ratio exceeded unity on the assumption that nitrite reduction was the dominant alternative pathway and that the carbon skeletons for the amino acids formed were partitioned from the Krebs cycle. In the present version of the model we suggest a new control loop of the alternative electron transport by assuming it is related to the PGA level.

With allowance for protein and other secondary syntheses, starch synthesis is the main alternative consumer of photosynthetic ATP. In order to ensure stability, alternative electron transport must be regulated in parallel with the rate of starch synthesis. Considering that starch synthesis is strongly activated by PGA (Heldt et al., 1977; Tetlow et al., 2004), we suggest the alternative electron acceptors are the derivatives of this metabolite. In the present version of the model, before being reduced to triosephosphates, chloroplast PGA is exported to the cytosol via the phosphate translocator exchanging PGA^{2-} for P_i^{2-} . In the cytosol, PEP is formed from 3-PGA via 2-PGA (Fig. 13.1). PEP is the central branching point between the pathways of organic acid (malate) and amino acid (alanine) synthesis. Synthesis of C_4 amino acids by transamination of oxaloacetate is not yet considered in the model.

We assume that for the N reduction pathway the terminal acceptor of the amino group is pyruvate (PYR), produced by dephosphorylation of PEP and converted to alanine (ALA) by transamination. It has been shown experimentally that ALA is an end product of photosynthetic CO_2 fixation and the pathway is regulated by light intensity as well as by CO_2 and O_2 concentrations (Keerberg et al., 1983; Ivanova et al., 1993). Our current approach assumes that the alternative electron transport pathway of N reduction is co-rate-limited by both the availability of reducing power and carbon skeletons for amino acid formation. The resulting O_2/CO_2 exchange ratio is a complex function: decreased by the export of PGA before its reduction and by additional CO_2 fixation due to PEP carboxylation and increased by the reduction of OXA (1 NADPH/OXA) and much more by the reduction of nitrite. As a result, the observed O_2/CO_2 ratio of unity is possible if

PGA is exported from the CRC and its derivative is transaminated about proportionally with the rate of starch synthesis. This scheme requires a well regulated balance between starch synthesis and nitrite reduction that can be analyzed only mathematically.

At present, details of the N reduction chemistry are not included in the model, but the aim of modeling the O_2/CO_2 ratio by regulating alternative electron flow is still achieved. A sequence of reactions leading from 3-PGA via 2-PGA to PEP and further branching to PYR and OXA is described by standard kinetic equations. The reduction of OXA by chloroplast MDH is described assuming shuttling of OXA and MAL between stroma and cytosol by non-rate-limiting translocators. The reduction of nitrite by Fd^- and the subsequent transaminations, including the GOGAT cycle, up to the formation of ALA are integrated in one single kinetic step, co-limited by the levels of Fd^- and PYR.

The experiments of Laisk et al. (2007) suggested other modifications to the earlier model (Laisk et al., 2006a). These include proton-uncoupled cyclic electron transport around PS I and PS II and the strong control of Fd -NADP reductase by NADPH. In the latter case, the NADPH/NADP ratio maintains the FNR reaction in a state of disequilibrium (Carrillo and Ceccarelli, 2003).

III. Mathematics

A. Rate Equations

1. Compartmentation

Leaf volume is divided into chloroplast thylakoid membrane (V_{me}), chloroplast thylakoid lumen (V_{lu}), chloroplast stroma (V_{st}), and cytosol (V_{cy}) calculated considering leaf anatomy and compartment volume measurements (Winter et al., 1993, 1994):

$$V_{me} = C_{vme} \cdot Chl, \quad (13.1)$$

$$V_{lu} = C_{lu} \cdot V_{me}, \quad (13.2)$$

$$V_{st} = C_{st} \cdot V_{me}, \quad (13.3)$$

$$V_{cy} = C_{cy} \cdot V_{me}. \quad (13.4)$$

With a chlorophyll (*Chl*) content of $550 \times 10^{-6} \text{ mol m}^{-2}$ and $C_{\text{vme}} = 4.01 (\text{mol Chl})^{-1}$, thylakoid membranes occupy a volume of 0.00221 m^{-2} . We assume that lumen and the membrane volumes are equal, stromal volume is eight times the volume of thylakoids (0.01761 m^{-2}), and that cytosol and stromal volumes are equal. In all compartments the concentrations of metabolites are calculated in moles per liter and reaction rates are calculated in moles per liter per second. Where reactions in different compartments are linked mass and charge are conserved, i.e. a decrease of mass (charge) in one compartment is balanced by an increase of mass (charge) in the other compartment. For convenience, total concentrations of orthophosphate P_{IT} , pyridine nucleotides NADP_{T} , adenylates AD_{T} , plastoquinone PQ_{T} , as well as V_{m} values for enzymes are initially entered per square meter of leaf but converted into molar units prior to calculations.

2. Photosystems

Chlorophyll is partitioned between PS II and PS I according to partitioning constants (C),

$$\text{Chl}_2 = \text{Chl} \cdot C_{\text{Chl2}}, \quad (13.5)$$

$$\text{Chl}_1 = \text{Chl} \cdot C_{\text{Chl1}}. \quad (13.6)$$

Excitation partitioning constants of $C_{\text{Chl2}} = 0.47$ and $C_{\text{Chl1}} = 0.5$ were determined from simultaneous measurements of CO₂ uptake, chlorophyll fluorescence, and 800 nm absorbance (denoted as a_{II} and a_{I} , respectively, in Eichelmann and Laisk, 2000 and Laisk et al., 2006b).

The concentration of PS II centers per square meter of leaf ($\text{PS2}_{\text{T}} = 2.01 \mu\text{mol m}^{-2}$) was based on single-turnover flash O₂ evolution measurements (Oja and Laisk, 2000). The densities of PS I ($\text{PS1}_{\text{T}} = 1.55 \mu\text{mol m}^{-2}$) and plastocyanin ($\text{PC}_{\text{T}} = 3.57 \mu\text{mol m}^{-2}$) were obtained from oxidative and reductive PS I titrations (Oja et al., 2003, 2004). The photosystem antenna sizes (photosynthetic units $\text{PSU}_2 = 129$ and $\text{PSU}_1 = 177$) were calculated as

$$\text{PSU}_2 = \text{Chl}_2 / \text{PS2}_{\text{T}} \quad (13.7)$$

and

$$\text{PSU}_1 = \text{Chl}_1 / \text{PS1}_{\text{T}}. \quad (13.8)$$

The excitation rate of Chl is

$$\text{ER}_{\text{Chl2}} = \frac{\text{PFD} \cdot L_{\text{abs}}}{\text{Chl}} + 0.06 \cdot \frac{\text{FRL}}{\text{Chl}_2} \quad (13.9)$$

$$\text{ER}_{\text{Chl1}} = \frac{\text{PFD} \cdot L_{\text{abs}}}{\text{Chl}} + 0.94 \cdot \frac{\text{FRL}}{\text{Chl}_1}, \quad (13.10)$$

where L_{abs} is leaf absorption coefficient for incident white light. The model allows for preferential excitation of PS I if far-red light (FRL) is applied or understorey conditions are modeled. Equations (13.9) and (13.10) consider that laboratory FRL (720 nm) excites 94% of PS I and 6% of PS II Chls (Pettai et al., 2005). Based on the above, we calculate the excitation rate of a PS II reaction center (s^{-1}):

$$\text{ER}_{\text{PS2}} = \frac{\text{PSU}_2 \cdot \text{ER}_{\text{Chl2}}}{1 + k_{\text{f}} + N_{\text{q}} \cdot k_{\text{N}} + k_{\text{i}}}. \quad (13.11)$$

Equation (13.11) considers that PS II excitation is competitively de-activated by photochemistry (relative rate constant = 1), fluorescence (rate constant k_{f}), and thermal processes (rate constants k_{N} and k_{i}). “Energy-dependent” non-photochemical quenching (k_{N}) is dependent on the quenching factor $0 < N_{\text{q}} < 1$ which varies with luminal proton concentration. Other (less dynamic) types of non-photochemical quenching are joined under the rate-constant k_{i} (“inhibitory” quenching). Non-photochemical quenching and fluorescence are neglected in PS I:

$$\text{ER}_{\text{PS1}} = \text{PSU}_1 \cdot \text{ER}_{\text{Chl1}}, \quad (13.12)$$

where ER_{Chl1} is given by Eq. (13.10).

3. Photosystem II and Chlorophyll Fluorescence

Photosystem II is described as an electron-transporting complex that may have reduced or oxidized donor and acceptor sides. First-order rate constants describe the movement of electrons. An individual PS II may exist in four different states depending on the reduction state of its donor (D) and acceptor (A) sides (denotations italic): State *A* = D⁻A⁻; State *B* = D⁻A⁺; State *C* = D⁺A⁻; State *D* = D⁺A⁺. Differential

equations describe the rates of mutual conversion of these states (Laisk et al., 1997; see also

Chapter 7 of this book by Andrew Rubin and Galina Riznichenko):

$$dA_2/dt = j_{2d} \cdot C_2 - (j_{2r} + k_{2d}) \cdot A_2 + k_{2r} \cdot B_2 = 0 \quad (13.13)$$

$$dB_2/dt = j_{2d} \cdot D_2 + k_{2d} \cdot A_2 + n_{2r} \cdot C_2 - (j_{2r} + k_{2r} + n_{2d}) \cdot B_2 = 0 \quad (13.14)$$

$$dC_2/dt = j_{2r} \cdot A_2 + k_{2r} \cdot D_2 + n_{2d} \cdot B_2 - (k_{2d} + j_{2d} + n_{2r}) \cdot C_2 = 0 \quad (13.15)$$

$$dD_2/dt = j_{2r} \cdot B_2 + k_{2d} \cdot C_2 - (j_{2d} + k_{2r}) \cdot D_2 = 0 \quad (13.16)$$

$$A_2 + B_2 + C_2 + D_2 = PS2_T \quad (13.17)$$

where subscript 2 indicates that the system is written for PS II and d indicates that the rate constant is for the forward and r for the reverse reaction. Rate constants are j for D^+ re-reduction; n for e^- transfer from the reduced donor, D^- , to the oxidized acceptor, A^+ ; and k for e^- transfer away from the reduced acceptor side, A^- . These mathematics neglect the bound Q_B , but assume the bound and free PQ form one equilibrated pool. The forward rate constant n_{2d} equals to the PS II excitation rate

$$n_{2d} = ER_{PS2}, \quad (13.18)$$

where ER_{PS2} is given by Eq. (13.11). On the donor side of PS II the rate constant of e^- arrival from the OEC was assumed to be $j_{2d} = (250 \mu s)^{-1}$ averaged over all S-states (Laisk and Oja, 2000a) and the reaction was assumed to be irreversible ($j_{2r} = 0$). The rate constant for PS II e^- transport to oxidized PQ was set to $(600 \mu s)^{-1}$ at complete oxidation of PQ (Laisk and Oja, 2000b). However, it can vary depending on the oxidation state of PQ and the reverse reaction is allowed:

$$k_{2d} = RC_{45} \cdot PQ \quad (13.19)$$

and

$$k_{2r} = RC_{45} \cdot PQ^- / k_{E45}, \quad (13.20)$$

where PQ^- indicates plastoquinol (this system of denotation of the reduced state is used throughout the model, except for NADPH; reactions are numbered as in Fig. 13.1). With this mathematics we shift the slowest step from Q_B release to the $Q_A \rightarrow Q_B$ electron transfer. The cycle around PS II is described as charge recombination from Q_A^- (denoted $PS2A^-$). A pre-set value of the rate constant for charge recombination, $n_{2r} = 700 s^{-1}$ best fitted the increasing PS II cycle at light saturation of photosynthesis (Laisk et al., 2006b, 2007).

Since photoreactions occur faster than on a pico- to microsecond time scale, the system (Eqs. 13.13–13.17) is analytically solved for quasi-stationary conditions at each integration step (this leads to errors in transients faster than 1 ms). The fractions $A = D^-A^-$, $B = D^-A^+$, $C = D^+A^-$ and $D = D^+A^+$ are obtained from the solution and the pools of $PS2A^-$ (PS II with reduced acceptor side) and $PS2A$ (with oxidized acceptor side) are calculated as follows:

$$PS2A^- = A_2 + C_2 \quad (13.21)$$

and

$$PS2A = PS2_T - PS2A^-. \quad (13.22)$$

Fluorescence from PS II with an oxidized acceptor side is the minimum fluorescence F_0 ,

$$F_0 = FIA = \frac{k_f}{1 + k_f + N_q k_N + k_i}. \quad (13.23)$$

Likewise, fluorescence from PS II with a reduced acceptor side is the maximum fluorescence F_m ,

$$F_m = FIA^- = \frac{k_f}{k_f + N_q k_N + k_i}. \quad (13.24)$$

Finally, the steady state fluorescence yield is weighted with the fractions of PS II emitting at F_0 and F_m levels

$$F = \frac{FIA \cdot PS2A + FIA^- \cdot PS2A^-}{PS2_T}. \quad (13.25)$$

We emphasize that the values of the rate constants k (Eqs. 13.23 and 13.24) are expressed relative to the rate constant for charge separation/stabilization $k_p = 1$ (Laisk et al., 1997). For example, in calculations below $k_f = 0.19$ and $k_N = 0.63$. Fluorescence yield is scaled between 0 and 1, the latter value corresponding to the completely unquenched ‘predawn’ F_{md} . The constant

k_i stands for ‘photoinhibitory quenching’ to account for dark-stabilized fluorescence quenching when $N_q = 0$.

The ‘energy-dependent’ non-photochemical quenching is controlled by the parameter $0 \leq N_q \leq 1$ which depends, in turn, on the luminal pH via an inertial link, since non-photochemical quenching has slower kinetics compared to changes in luminal pH (we assume that pmf is mainly caused by the concentration gradient, see Section II.A.). First, a parameter QH is calculated as follows:

$$QH = \frac{\left(\frac{HI_{ft}}{k_{E50}}\right)^2}{1 + \left(\frac{HI_{ft}}{k_{E50}}\right)^2}. \quad (13.26)$$

Equation (13.26) assumes the parameter $0 \leq QH \leq 1$ is in fast two-proton equilibrium with free protons in the lumen HI_{ft} (a linear term in the denominator is neglected). The equilibrium constant k_{E50} corresponds to a pK of 5.65 in the calculations. A differential equation (Eq. 13.84) ensures that N_q follows QH slowly, with a rate constant $RC_{50} = 0.03 \text{ s}^{-1}$. Relative rate constants for PS II excitation quenching are determined from measured fluorescence values as follows (Laisk et al., 1997):

$$k_f = \frac{F_0}{F_{md} (1 - F_0/F_{md})}; \quad k_N = k_f \cdot \left(\frac{F_{md}}{F_m}\right), \quad (13.27, 13.28)$$

where F_0 and F_{md} are the dark-adapted (predawn) values and F_m (Eq. 13.28) is measured at the maximum PFD, to ensure fully induced NPQ (Eq. 13.28 is valid at full quenching when $N_q = 1$, corresponding to light saturation). The photoinhibitory rate constant k_i is adjusted to fit the F_m value measured after the light response curve (Fig. 13.2).

4. Photosystem I and Optical Transmittance Signals

Electron transport through PS I is calculated differently from that through PS II, considering the fast cross-diffusion of plastocyanin (PC) between different PS I complexes on the donor side and of free ferredoxin (Fd) on the acceptor side. The series of low-potential carriers at the PS I acceptor side is combined and denoted FeS (FeS⁻ if

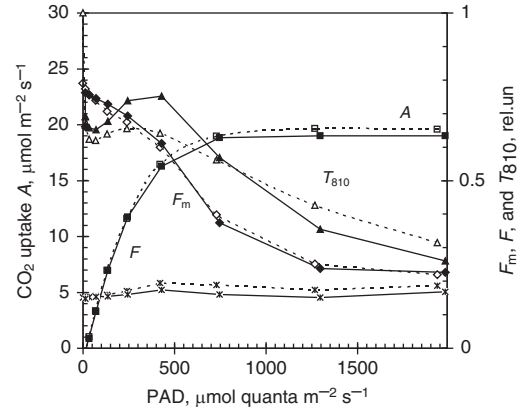


Fig. 13.2. Calculated (filled symbols and solid lines) and measured (empty symbols and dashed lines) steady-state light response curves of net CO₂ assimilation rate A , steady-state F and pulse-saturated fluorescence yield F_m , and 810 nm transmittance signal T_{810} in a potato leaf at the atmospheric conditions, CO₂ concentration 360 ppm and O₂ concentration 21%, leaf temperature 22–23°C

reduced to the extent that causes acceptor side closure). Redox equilibrium is assumed between ferredoxin and the low-potential acceptor $Fd \leftrightarrow FeS$. This redox pair is considered to be a single electron pool (state variable) in the differential equations for electron transport (denoted PS1A⁻). A similar redox pair $PC_P \leftrightarrow P700$ is assumed on the donor side, where PC_P is a subpool of PC in close vicinity to P700. The redox states of equilibrated components of both redox pairs, $Fd \leftrightarrow FeS$ and $PC_P \leftrightarrow P700$ are calculated from a second order equation (not shown) at each step of numeric integration, considering the total number of electrons in the pair. PS I is considered to be capable of electron transport after excitation when P700 is reduced and FeS is oxidized. Thus, the electron transport rate through PS I is

$$ETR_{PSI} = ER_{PSI} \cdot P700^- \cdot FeS/PSI_T, \quad (13.29)$$

where PS I excitation rate ER_{PSI} (s⁻¹), is given by Eq. (13.12). In contrast to PS II electron transport, Eq. (13.29) assumes that, thanks to fast cross-diffusion of PC, electrons can move from any PS I with reduced P700 to any PS I with oxidized FeS.

In order to analyze the possible limitation of electron transport by PC diffusion, the PC_T (total) pool is divided into two parts, one equilibrated with P700 (PC_P) and the other equilibrated with Cyt f (PC_F). The latter redox pair, $Cytf \leftrightarrow PC_F$,

forms another numerically integrated pool of the PS I high-potential donors (Fig. 13.1). Electron transfer between the two pools is diffusion limited (rate constant RC_{40}):

$$V_{40} = RC_{40} (PC_F^- - PC_P^-). \quad (13.30)$$

Optical transmittance signals from reduced FeS, PC and P700 are calculated as follows:

$$T_{810} = \frac{0.33 (PC_F^- + PC_P^-) + P700^- + 0.2 Fd^-}{0.33 PC_T + PSI_T}, \quad (13.31)$$

$$T_{950} = \frac{0.11 (PC_F^- + PC_P^-) + 0.077 \cdot P700^-}{0.11 \cdot PC_T + 0.077 \cdot PSI_T}. \quad (13.32)$$

The signals are normalized to $T_{810} = 0$ and $T_{950} = 0$ for completely oxidized and unity for completely reduced PC and P700, respectively. The additional signal from Fd^- may push T_{810} beyond the dark reference line, as observed during experiments. Equations (13.31, 13.32) consider the actual relative magnitude of the optical signal from a single molecule: 1.0 from $P700^-$ at 810 nm and 0.077 at 950 nm; 0.33 from PC^- at 810 nm and 0.11 at 950 nm; 0.2 from Fd^- at 810 nm and zero at 950 nm (Kirchhoff et al., 2004; V. Oja, 2008, unpublished data).

5. Electron/Proton Transport Reactions

Plastoquinone reduction by PS II is calculated as a reversible second order reaction between reduced Q_A and oxidized plastoquinone, with the following rate equation:

$$V_{45} = RC_{45} \cdot (PS2A^- \cdot PQ - PS2A \cdot PQ^- / k_{E45}), \quad (13.33)$$

where $PS2A^-$ and $PS2A$ are represented by Eqs. (13.21–13.22). The capture of H^+ by PQ^- is assumed to be fast (we remind that denotation PQ^- is equivalent to PQH_2).

Reduced plastoquinone (PQ^-) is oxidized by the Cyt b_6f complex. Reversible electron transport from PQ^- to the $Cyt f \leftrightarrow PC_F$ redox pair is 'photosynthetically controlled' by the

energization of the thylakoid membrane. The corresponding rate equation is the following:

$$V_{42} = \frac{V_{m42} \cdot (PQ^- \cdot Cyt f - Cyt f^- \cdot PQ / k_{E42d})}{Cyt f_T \cdot (K_{m42PQ^-} + PQ^-)}, \quad (13.34)$$

$$\text{where } k_{E42d} = k_{E42} \cdot \left(\frac{HI_{fs}}{HI_{ft}} \right)^{HER}. \quad (13.35)$$

Equation (13.34) is written for one-electron transfer and the kinetics of the Q-cycle inside the Cyt b_6f complex are approximated as a single-enzyme reaction. The reaction is saturated with respect to PQ^- at low concentrations and the equilibrium constant k_{E42d} is dynamically calculated at every integration step dependent on the ratio of free proton concentrations in the stroma (HI_{fs}) and in the lumen (HI_{ft}). A high proton gradient tends to decrease the otherwise very high k_{E42} value, increasing the reversibility of electron transfer through the Cyt b_6f complex. 'Hydrogen per electron ratio' ($HER = 2$) is a constant of the Q-cycle, reflecting the increased back-pressure by the two H^+ transported per every electron.

On the acceptor side of PS I, Fd -NADP reductase carries out the reaction $Fd^- + NADP \leftrightarrow Fd + NADPH$ (reaction 141, Fig. 13.1). The kinetics of the reaction are described as a two-substrate and two-product reaction (Eq. 13.44). The strong inhibition of the reaction by NADPH (Carrillo and Ceccarelli, 2003) is modeled by setting a lower value for $K_{m141}(NADPH) = 500 \mu M$ compared to $K_{m141}(NADP^+) = 1 mM$, so that accumulating NADPH would significantly block the reaction.

Pseudocyclic Mehler type e^- flow is assumed to be a simple second order reaction between dissolved oxygen and reduced Fd^- :

$$V_{49} = RC_{49} \cdot Fd^- \cdot O_{wc}, \quad (13.36)$$

where O_{wc} is the O_2 concentration in chloroplast. Reactions forming the water–water cycle (Asada, 2000) are not modeled.

Proton-coupled PS I cyclic electron flow is modeled as PQ reduction via the NADP-dehydrogenase at the stromal side (NDH, reaction 46), the chlororespiratory terminal oxidase (reaction 61) is oxidizing PQH_2 at the luminal side, supporting some proton translocation inside the NDH complex. Both reactions are very slow,

important only for maintaining a slow rate of ATP synthesis in the dark, necessary for the stabilization of the model when PFD = 0.

Protons accumulate in the lumenal space due to H⁺-coupled electron transport through PS II and Cyt b₆f. Altogether 3H⁺/e⁻ accumulate in the lumen, one during water splitting at PS II and two during electron transfer through the Q-cycle in the Cyt b₆f complex. The lumen space (membrane surface) has a high buffering capacity so the total amount of protons is much greater than the amount of free protons in the lumen. In our earlier models a single-pK buffer equation was used (Laisk and Eichelmann, 1989), but its buffering range appeared to be too narrow. Here we apply a simple proportional relationship

$$HI_{ft} = HI_t/1000, \quad (13.37)$$

where HI_{ft} is the free and HI_t is the total proton concentration in the lumen volume (the buffering capacity of 1,000 is probably overestimated, but the high value decreases the stiffness of the budget equation, Eq. 13.59). Proton leakage is also allowed, the rate of which is proportional to the difference of free H⁺ concentrations between lumen and stroma, but the rate was set to zero in calculations.

ATP synthase catalyses the reaction $ADP + P_i \leftrightarrow ATP$ (12/3 H⁺ transported from the lumen to the stroma). This reaction is modeled as an ordinary enzyme-catalyzed reaction (Eq. 13.44), except that the 'dynamic' equilibrium constant k_{E12d} depends on the proton gradient:

$$V_{12} = V_{m12} \cdot \frac{(ADP \cdot OP - ATP/k_{E12d})}{K_{m12ADP} \cdot K_{m12OP} \cdot Den}, \quad (13.38)$$

where

$$Den = 1 + \frac{ADP}{K_{m12ADP}} + \frac{OP}{K_{m12OP}} + \frac{ATP}{K_{m12ATP}} + \frac{ADP}{K_{m12ADP}} \cdot \frac{OP}{K_{m12OP}},$$

where k_{E12d} is calculated at every integration step as

$$k_{E12d} = k_{E12} \cdot \left(\frac{HI_{ft}}{HI_{fs}} \right)^{HPR}, \quad (13.39)$$

and HPR is the number of H⁺ transported per ATP synthesized, i.e. 12/3 (Rumberg et al., 1990).

We have also assumed that the proton 'slip' through ATP synthase increases when ADP or P_i levels drop close to their K_m :

$$SLP = 1 + \frac{0.05 \cdot K_{m12ADP}}{ADP} + \frac{0.05 \cdot K_{m12OP}}{OP}. \quad (13.40)$$

The slip factor SLP is considered in the budget equation for protons in the thylakoid lumen (Eq. 13.59). In practice, ADP decreases at strictly limiting CO₂ and O₂ concentrations and P_i decreases at saturating CO₂ and light levels, when end product synthesis becomes rate-limiting.

6. RuBP Carboxylase/Oxygenase (Rubisco)

RuBP carboxylase-oxygenase is the major rate-limiting enzyme at naturally occurring CO₂ concentrations. Therefore, the model describes Rubisco in greater detail than other CRC enzymes by considering oxygenase reaction and competitive binding of RuBP, P_i and PGA to the enzyme. The reaction is modeled based on the following sequence of events. First, RuBP binds to free enzyme (E_f), to form an enzyme-RuBP complex (ER, Fig. 13.1). The latter can react either with CO₂ to form a complex of the enzyme with an intermediate compound equivalent to two PGA (EPP) or, competitively, with O₂ to form an enzyme complex with an intermediate compound equivalent to phosphoglycolate and PGA (EPG). These complexes dissociate, leaving enzyme complexed with one PGA (EP). The last step of the reaction is dissociation of PGA from the enzyme, leaving free enzyme ready for the next catalytic cycle. PGA and P_i have relatively high affinity for the active site, and thus may compete with RuBP for binding to the free enzyme. This accounts for competitive inhibition of Rubisco by PGA and free phosphate, shown to occur *in vitro* (Badger and Lorimer, 1981; Jordan et al., 1983). These partial reactions in Rubisco are described with rate constants and differential equations describing the system have been presented (Laisk and Edwards, 2000). The rates of

RuBP carboxylation (V_C) and oxygenation (V_O) in moles per liter per second in the stroma are expressed as:

$$V_C = k_2 \cdot ER \cdot C_{wc}, \quad (13.41)$$

$$V_O = k_6 \cdot ER \cdot O_{wc}, \quad (13.42)$$

where ER is the concentration of the enzyme-RuBP complex and C_{wc} and O_{wc} denote the dissolved CO_2 and O_2 concentrations at the reaction site. The net CO_2 uptake rate is calculated as

$$A_C = V_{st} \cdot (V_C - V_O/2) + R_{mit}, \quad (13.43)$$

where V_{st} is the specific stromal volume ($l\ m^{-2}$) that converts the reaction rate from moles per liter per second into moles per square meter per second, R_{mit} is the constant mitochondrial respiration rate.

Due to the high concentration of active sites and relatively slow turnover, the system of Rubisco partial reactions is computer-integrated on the same time-scale as other reactions. The molar CO_2 and O_2 concentrations dissolved in water at the carboxylation-oxygenation site, C_{wc} and O_{wc} , are calculated as in our experimental data-processing programs (Laisk and Oja, 1998; Laisk et al., 2002) considering diffusion resistance in the gaseous and liquid phase of the leaf and photosynthetic CO_2 uptake and photorespiratory CO_2 evolution rate generated by the model. The chloroplast O_2 concentration is assumed to be the same as external gas phase (considering O_2 solubility). As a result of these transformations, the input parameters of the model are mole fractions of CO_2 and O_2 in the gas phase, leaf temperature (considered only in solubility calculations), and diffusion resistances in the gas phase (stomatal and boundary layer) and in the liquid phase (mesophyll diffusion resistance).

7. Carbon Reduction Cycle

The model for the C_3 carbon reduction cycle is that of Laisk et al. (1989). It contains all the reactions of the Calvin cycle, starch and sucrose synthesis, and the major regulatory mechanisms known to stabilize this cycle. The rates of individual enzymatic reactions are described by the general kinetic equation for the random binding of

ligands (Cleland, 1963), converted into the form containing the equilibrium constant k_E :

$$V = V_m \frac{(A \cdot B - C \cdot D/k_E)}{K_{mA} \cdot K_{mB} \cdot Den}, \quad (13.44)$$

where

$$Den = 1 + \frac{A}{K_{mA}} + \frac{B}{K_{mB}} + \frac{C}{K_{mC}} + \frac{D}{K_{mD}} + \frac{A}{K_{mA}} \cdot \frac{B}{K_{mB}} + \frac{C}{K_{mC}} \cdot \frac{D}{K_{mD}}.$$

In the case of one substrate or product, the second order term is omitted in the denominator. Equilibrium constants and ionic forms of the substrates (the actual reactants), are calculated from free energy (or redox potential) differences and from pK values of the dissociating groups (Laisk et al., 1989). Below we describe how enzyme activities are controlled.

Starch synthesis is one pathway of outflow from the CRC, fine-controlled for balancing the carbon budget of the cycle. An important feature of starch synthesis is that it consumes additional ATP, synthesized at the expense of alternative electron transport to acceptors other than BPGA (an intermediate product of reaction 1, not explicit in differential equations). Therefore, starch synthesis and alternative electron flows are tightly coupled and regulated similarly. The rate of starch synthesis is regulated by ADP-glucose pyrophosphorylase, the V_m of which is assumed to be increased by PGA and decreased by P_i levels to the second power (Heldt et al., 1977; Preiss et al., 1985; Tetlow et al., 2004):

$$V_{m19a} = V_{m19} \left(\frac{PGA}{OP} \right)^2. \quad (13.45)$$

The mathematical formulation of the activation kinetics of this enzyme is important for the realistic behavior of the model over widely ranging CO_2 and O_2 concentrations and light intensities. This simple approach may not be optimal, but it qualitatively simulates regulation of starch synthesis well.

Ferredoxin-thioredoxin system of enzyme activation. The maximum turnover rates (V_m) of GAP-dehydrogenase, FBPase, SBPase, and Ru5P kinase are modeled as proportionally activated by the reduction state of thiol groups on the corresponding proteins. The kinetics of activation are modeled in two steps. First, thioredoxin f is reduced by Fd^- and, second, the enzyme protein is reduced by the thioredoxin:

$$\frac{dTRf^-}{dt} = RC_{52} \cdot (Fd^- \cdot TRf - TRf^- \cdot Fd/k_{E52}), \quad (13.46)$$

$$\frac{dENf^-}{dt} = RC_{53} \cdot (TRf^- \cdot ENf - ENf^- \cdot TRf/k_{E53}). \quad (13.47)$$

At any point in time the relative activation state ($ACTf$) of an enzyme is determined by the fraction of reduced protein

$$ACTf = ENf^- / ENf_T, \quad (13.48)$$

where ENf_T is the total amount of enzyme activatable by the thioredoxin f system. A similar sequence of equations is written for the thioredoxin m activated enzyme MDH, differing only by the values of the standard redox potentials (the equilibrium constant k_E is calculated from the difference of the midpoint redox potentials). This modeling assumes that the enzyme thiol groups are reversibly equilibrated with the reduction state of ferredoxin.

Chloroplast phosphate translocator is described as an enzyme reversibly transporting P_i^{2-} , $T3P^{2-}$ and PGA^{2-} between the stromal and cytosolic pools. The kinetics are described as for Eq. (13.44), but the presence of the three competitive substrates and products complicates the mathematical expressions which contain three K_m values (Laik et al., 1989). In calculations, however, the phosphate translocator was set as only slightly rate-limiting, which ensured that the products of concentrations of P_i^{2-} , $T3P^{2-}$ and PGA^{2-} were about equal in the stroma and in the cytosol. The preset stromal and cytosolic pH values are considered only for the calculations of the ionic forms of the substrates.

Sucrose synthesis occurs in the cytosol and is controlled first by cytosolic fructosebisphosphatase (FBPase, reaction 24) and secondly

by sucrose phosphate synthase (SPS, reaction 28). Cytosolic FBPase is regulated by the 'false key' fructose-2,6 bisphosphate, modifying $K_{m24}(FBP)$:

$$K_{m24FBP} = K_{m024FBP} \cdot \left[1 + \left(\frac{F26BP}{K_{i24F26BP}} \right)^2 \right]. \quad (13.49)$$

Here we have increased the sensitivity of the control compared with Laik et al. (1989) by applying the square function. *In vitro* studies have shown that the kinetics of the cytosolic FBPase with respect to FBP are sigmoidal (Herzog et al., 1984), mandating a second order term in the kinetic equation:

$$V_{24} = V_{m24} \frac{FBP \cdot (FBP_c - F6P_c \cdot OP_c / k_{E24})}{K_{m24FBP}^2 \cdot Den}, \quad (13.50)$$

where

$$Den = 1 + \frac{FBP_c^2}{K_{m24FBP}^2} + \frac{F6P_c}{K_{m24F6P}} + \frac{F6P_c \cdot OP_c}{K_{m24F6P} \cdot K_{m24OP}} + \frac{OP_c}{K_{m24OP}}.$$

The rates of F2,6BP synthesis and degradation are strictly controlled by triosephosphate and P_i . The rate of F2,6BP kinase is assumed to be saturated with respect to F6P:

$$V_{31} = V_{m31} \cdot \frac{1 + \frac{OP_c^2}{K_{a31OP}^2}}{1 + \frac{(T3P_c + PGA_c)^2}{K_{i31T3P}}}. \quad (13.51)$$

The F2,6BPase rate is assumed to have first order kinetics with respect to F2,6BP, is activated by triosephosphates and PGA, and inhibited by P_i and hexosephosphates:

$$V_{32} = V_{m32} \cdot \frac{F26BP_c}{K_{m32F26BP}} \cdot \frac{1 + \frac{(T3P_c + PGA_c)^2}{K_{m32T3P}^2}}{1 + \frac{OP_c^2}{K_{i32OP}^2} + \frac{HeP_c}{K_{i32HeP}}}. \quad (13.52)$$

The kinetics of SPS are also sigmoidal with the $K_m(\text{F6P})$ being modulated by P_i :

$$K_{m28\text{F6P}} = K_{m028\text{F6P}} \cdot \left(1 + \frac{OP_c}{K_{x28OP}}\right); \quad (13.53)$$

$$V_{28} = V_{m28} \cdot \frac{F6P_c}{K_{m28\text{F6P}}} \cdot \frac{F6P_c \cdot \text{UDPGlu}_c - \text{UDP}_c \cdot \text{SUCP}_c \cdot HI_{rc}/k_{E28}}{K_{m28\text{F6P}} \cdot K_{m28\text{UDPGlu}} \cdot \text{Den}}, \quad (13.54)$$

where

$$\begin{aligned} \text{Den} = 1 + & \frac{F6P_c^2}{K_{m28\text{F6P}}^2} + \frac{\text{UDPGlu}_c}{K_{m28\text{UDPGlu}}} + \frac{\text{SUCP}_c}{K_{m28\text{SUCP}}} \\ & + \frac{\text{UDP}_c}{K_{m28\text{UDP}}} + \frac{F6P_c^2}{K_{m28\text{F6P}}^2} \cdot \frac{\text{UDPGlu}_c}{K_{m28\text{UDPGlu}}} \\ & + \frac{\text{SUCP}_c}{K_{m28\text{SUCP}}} \cdot \frac{\text{UDP}_c}{K_{m28\text{UDP}}} + \frac{OP_c}{K_{i28OP}} \end{aligned}$$

Other reactions in the sucrose synthesis pathway are described by Eq. (13.44).

8. Photorespiratory Carbon Oxidation Cycle

This metabolic pathway is described in an integrated way, considering its overall ATP, NADP, P_i , CO_2 and carbon budget (Laik and Edwards, 2000). Since the rate of photorespiration and its energy requirement are considered in the corresponding budget equations, steady state net CO_2 exchange rates and transients in photorespiration related to pool changes in CRC are calculated correctly, but transients in photorespiratory CO_2 evolution related to accumulation of glycolate pathway intermediates are neglected. In order to reproduce the phenomenon of photorespiratory CO_2 evolution in the light into CO_2 -free air, a reverse flow of carbon into the cytosolic triosephosphate pools, A_{rev} , was postulated – an integrated presentation of glycolysis occurring in the light.

9. Organic and Amino Acid Synthesis

The inclusion of this pathway is novel and based on the necessity for co-regulation of starch synthesis and the production of alternative electron

acceptors. We assume that the carbon precursors of oxaloacetate (the acceptor of electrons from MDH, reaction 64) and pyruvate (the major terminal acceptor of amino groups newly reduced from nitrite in the chloroplast) arise from PGA exported from the stroma to the cytosol. Metabolic conversions are described by Eq. (13.44). We suggest that reduction of OXA is a possible pathway of alternative electron transport under conditions where nitrite reduction is impossible. But, the dominant alternative pathway is nitrite reduction which implies sequential transaminations leading to formation of alanine by transamination of PYR formed from PEP. This complex pathway is presently modeled integrally, simply as an irreversible second order reaction between reduced Fd and PYR:

$$V_{65} = V_{m65} \cdot \frac{Fd^- \cdot \text{PYR}_c}{K_{m65\text{Fd}^-} \cdot K_{m65\text{PYR}} \cdot \text{Den}}, \quad (13.55)$$

where

$$\begin{aligned} \text{Den} = 1 + & \frac{Fd^-}{K_{m65\text{Fd}^-}} + \frac{\text{PYR}_c}{K_{m65\text{PYR}}} \\ & + \frac{Fd^-}{K_{m65\text{Fd}^-}} \cdot \frac{\text{PYR}_c}{K_{m65\text{PYR}}}. \end{aligned}$$

B. Budget Equations

Differential budget equations describe the movement of metabolites through the chain of reactions, the rates of which are given by the concentration-dependent expressions. One differential equation applies for each metabolite (or pool for those metabolites considered to be in equilibrium). Since correct budgeting of carbon, adenylates and reducing equivalents is the primary prerequisite of such metabolic modeling, we list the complete set of equations here with comments (reaction numbering as in Fig. 13.1).

1. Electron-Proton Transport and ATP Synthesis

$$dPQ^-/dt = (V_{45} - V_{42})/2 + V_{46} \cdot V_{st}/V_{me} - V_{61}; \quad (13.56)$$

here rates (V) are in moles per electron per liter per second in the membrane volume; V_{46} is NDH,

its rate converted from the stromal to the membrane volume, V_{61} is the chlororespiratory terminal oxidase, a very slow rate important only in the dark.

$$dCytPCf^-/dt = V_{42} - V_{40}; \quad (13.57)$$

electron budget for the redox-equilibrated Cyt f^- ↔ PC redox pair;

$$dPCpP700^-/dt = V_{40} - ETR_{PSI} + V_{142}; \quad (13.58)$$

electron budget for the redox-equilibrated PC ↔ P700 redox pair; the last term is proton-uncoupled cyclic flow assumed to enter this complex.

$$\begin{aligned} dHI_t/dt = & (V_{45} + HER \cdot V_{42}) \cdot V_{me}/V_{lu} \\ & - SLP \cdot HPR \cdot V_{12} \cdot V_{st}/V_{lu} \\ & - V_{44} + 4 \cdot V_{46} \cdot V_{st}/V_{lu} \\ & - 2 \cdot V_{61} \cdot V_{me}/V_{lu} \end{aligned} \quad (13.59)$$

The proton budget is an example of how compartment volumes are considered when substances are transported through compartment boundaries. V_{45} considers H^+ release during water-splitting, V_{42} is from the Q-cycle, $HER (= 2)$ is the corresponding gain factor, $HPR (= 4)$ is the H^+ requirement of ATP synthase, SLP is the 'slip' factor (Eq. 13.40). $V_{44} (= 0)$ is the H^+ leak, V_{46} assumes that $2H^+/e^-$ are translocated by chloroplast NDH similar to mitochondrial Complex 1, the terminal oxidase V_{61} rebinds H^+/e^- into water in the luminal space. The last terms are very slow, assumed to be important only during dark metabolism.

$$\begin{aligned} dPSIA^-/dt = & (ETR_{PSI} - V_{142}) \cdot V_{me} \\ & - (V_{141} + V_{49}) \cdot V_{st} \\ & - V_{65} \cdot V_{cy}; \end{aligned} \quad (13.60)$$

this redox-equilibrated complex is shared between the membrane and the stromal volumes, because of this the budget is written per leaf area unit.

$$dNADPH/dt = V_{141}/2 - V_{64} - V_1 - V_O/2; \quad (13.61)$$

the last term considers the consumption of reducing power in the glycolate pathway.

$$dATP/dt = V_{12} - V_1 - V_9 - V_{19} - V_O/2 - V_O/2; \quad (13.62)$$

V_{19} is ATP consumption for starch synthesis, the last two terms consider ATP consumption in the photorespiratory pathway for glycerate phosphorylation and for the photorespiratory ammonia re-assimilation. The consumption of ATP for the amination of newly formed amino acids, not explicitly included in the budget, is assumed to be covered by dephosphorylation of PEP during the same process.

2. Carbon Reduction Cycle

$$dRuBP/dt = V_9 - k_1 \cdot E_f \cdot RuBP + k_{-1} \cdot ER; \quad (13.63)$$

$$\begin{aligned} dPGA/dt = & k_4 \cdot EPP + k_5 \cdot EP \\ & - (k_{-4} \cdot EP + k_{-5} \cdot E_f) \cdot PGA \\ & + V_O/2 - V_1 - V_{PGAout}; \end{aligned} \quad (13.64)$$

the first two terms account for the production of PGA from the Rubisco reaction (Eq. 13.63), the terms in the brackets account for the rebinding of PGA to the free and PGA-containing enzyme, $V_O/2$ accounts for the phosphorylated glycerate returning from the glycolate pathway, and V_{PGAout} is the flux of PGA through the phosphate translocator.

$$\begin{aligned} dT3P/dt = & V_1 - 2 \cdot V_3 - V_5 - V_6 - V_8 \\ & - V_{T3Pout}; \end{aligned} \quad (13.65)$$

V_3 and V_6 are aldolase, V_5 and V_8 are transketolase rates; the last term is the phosphate translocator.

$$dFBP/dt = V_3 - V_4; \quad (13.66)$$

$$dHeP/dt = V_4 - V_5 - V_{19}; \quad (13.67)$$

V_{19} is the starch synthesis pathway.

$$dE4P/dt = V_5 - V_6; \quad (13.68)$$

$$dSBP/dt = V_6 - V_7; \quad (13.69)$$

$$dS7P/dt = V_7 - V_8; \quad (13.70)$$

$$dP5P/dt = 2 \cdot V_8 + V_5 - V_9; \quad (13.71)$$

$$dADPglu/dt = V_{19} - V_{20}; \quad (13.72)$$

3. Organic and Amino Acid Synthesis

$$dPGA_c/dt = V_{PGAout} \cdot V_{st}/V_{cy} - V_{61}; \quad (13.73)$$

the last term considers 3-PGA conversion into 2-PGA; subscript c indicates cytosolic pools.

$$dP2GA_c/dt = V_{61} - V_{62}; \quad (13.74)$$

$$dPEP_c/dt = V_{62} - V_{63} - V_{66}; \quad (13.75)$$

$$dOXA_c/dt = V_{63} - V_{64}; \quad (13.76)$$

$$dPYR_c/dt = V_{66} - V_{65}/6 \cdot V_{st}/V_{cy}; \quad (13.77)$$

the rate equation V_{65} is written for the consumption of Fd^- for nitrite reduction in the stroma; six electrons are consumed to produce an amino group that combines with one PYR in the cytosol.

4. Sucrose Synthesis

$$dT3P_c/dt = V_{T3Pout} \cdot V_{st}/V_{cy} - 2 \cdot V_{23} + A_{rev}/V_{cy}; \quad (13.78)$$

A_{rev} denotes the rate (mol m^{-2}) of 'internal' carbon feeding into the triosephosphate pool, probably from the glycolytic pathway.

$$dFBP_c/dt = V_{23} - V_{24}; \quad (13.79)$$

$$dF26BP_c/dt = V_{31} - V_{32}; \quad (13.80)$$

For the budget of F2,6BP see (Laisk et al., 1989).

$$dHeP_c/dt = V_{24} - V_{27} - V_{28}; \quad (13.81)$$

$$dUDPglu_c/dt = V_{27} - V_{28}; \quad (13.82)$$

$$dSUCP_c/dt = V_{28} - V_{29}. \quad (13.83)$$

5. Non-photochemical Excitation Quenching

$$d/N_q dt = RC_{50} \cdot (QH - N_q); \quad (13.84)$$

QH is a protonated quenching site, while N_q slowly follows the protonation state. Equation (13.84) sets the time kinetics of non-photochemical quenching.

The system is computer-integrated using Euler's method and programmed in Turbo Pascal 7.0. The integration step DT is variable between 0 and 20 ms, calculated from the condition that

during one step the most dynamic pool could change by no more than 0.1%. This guarantees stability of the system under practically all fluctuations (although under unusual conditions the integration may virtually stop due to a very short time step, run-time errors are avoided).

IV. Simulations

Contrary to models aimed at simulation of a single process (e.g., fluorescence induction) the present model was tuned using different experimental data obtained on a single potato leaf (dataset of Laisk et al., 2007). The heuristic aim of such modeling is to check how well the model reproduces the wide range of interacting internal relationships with a single set of parameters.

A. Light Responses

First, parameters determining steady-state responses (calculated until the results stabilized, Fig. 13.2) were fitted using experimental values measured on intact leaves (techniques see Laisk et al., 2002; Oja et al., 2003, 2004; results from Laisk et al., 2007). For example, Rubisco parameters K_{sp} , V_m , and $K_m(\text{CO}_2)$, as well as the diffusion resistances of stomata and the mesophyll liquid phase determine the light-saturated net CO_2 uptake rate under CO_2 -limiting conditions. The light-limited rate (quantum yield) requires measurements of leaf absorption coefficient and partitioning of excitation to PS II and PS I (for this specific leaf $C_{\text{Chl2}} = 0.47$ and $C_{\text{Chl1}} = 0.50$, 3% of quanta were absorbed by photosynthetically inactive chromophores). Fluorescence-indicated losses at PS II are accounted for by considering the actual dark values of F_m and F_0 and allowing for some photoinhibition induced by the measurements of the light responses (the 'predawn' F_{md} in the complete absence of NPQ is scaled to 1). From this data the relative rate constants k_f and k_i are calculated. The rate constant of non-photochemical quenching k_N requires the minimum F_m value at the strongest NPQ. These parameters fix the boundary values of F_m at low and high light, but its actual change with increasing PFD depends on pK of the protonation of the quenching substance (Eq. 13.26). For this

potato leaf the best fit is obtained with a pK of 5.65, in accordance with Horton and Ruban (1992) and Rees et al. (1992).

The 810 nm transmittance signal is calculated considering the oxidation of PC and P700 and the reduction of Fd (Eq. 13.31). The signal is scaled to 1 when PC and P700 are reduced (Fd oxidized) and 0 when PC and P700 are completely oxidized. In this experiment PC remained partially oxidized even at very low PFDs and became fully reduced only in complete darkness. This behavior is reproduced by setting the antenna cross-sections of PS II and PS I as above. Since fluorescence-induced losses are present in PS II but not in PS I, the latter is more efficient at low PFDs, causing partial oxidation of the PS I high potential donors. PS II efficiency decreases at medium PFDs due to the developing NPQ, while PS I efficiency decreases due to acceptor side reduction. In our present model the latter process seems to be overestimated at intermediate light, causing a more pronounced maximum of the 810 nm transmittance than was observed at 200–300 $\mu\text{mol quanta m}^{-2} \text{s}^{-1}$. At high PFDs the calculated 810 nm signal shows more oxidation than measured, an indication of overestimated PS I activity. However, the latter difference may be caused by underestimated cyclic electron transport also.

Such mechanistic modeling helps to reveal some relatively unexpected regulatory relationships in NPQ. For example, development of NPQ with increasing PFD depends on the total pool of phosphate in the stroma (Fig. 13.3). The reason is that with higher P_i concentration the ΔpH supporting the ATP level required for photosynthesis is lower, consequently the luminal pH is higher for the associated photosynthetic rate (Fig. 13.3a). Similarly, a lower stromal pH shifts the luminal pH downwards, because a certain ΔpH is required to support the observed photosynthetic rate (Fig. 13.3b). Considerable NPQ may be generated at very low light if stromal pH is low. The stromal pH of 8.05 gives the best fit for this leaf, in accordance with measurements based on CO₂ solubilisation in leaves (Oja, 1985).

Another important notion is related to the Kok effect in the CO₂ uptake and to the problem of inhibition of dark respiration in the light. According to the present model, PEP carboxylation is tightly related to the photosynthetic rate. Accord-

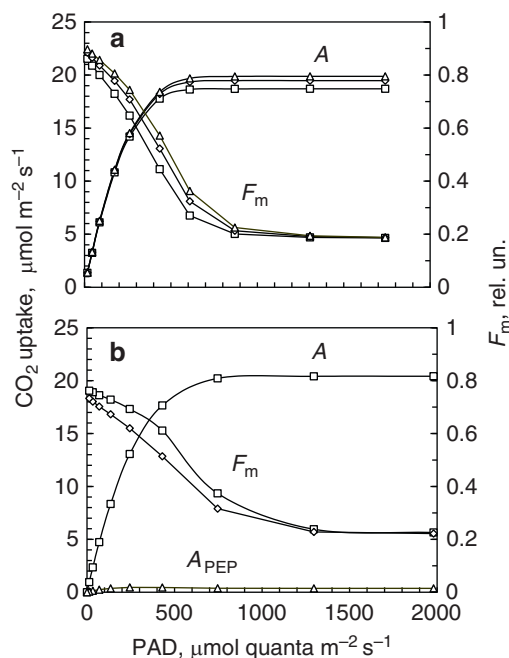


Fig. 13.3. Calculated light responses of CO₂ uptake A and pulse-saturated fluorescence yield F_m dependent on (panel a) the stromal phosphate pool of 300 (squares), 400 (diamonds) and 500 $\mu\text{mol m}^{-2}$ (triangles) and (panel b) stroma pH of 7.8 (diamonds) and 8.15 (squares). Calculated CO₂ uptake does not depend on the stroma pH. A_{PEP} – the rate of PEP carboxylation

ingly, any measured decrease in the net respiratory CO₂ evolution in the light should not be a priori interpreted as inhibition of dark respiration (e.g. Laisk, 1977a; Brooks and Farquhar, 1985), but rather as additional CO₂ uptake by PEP carboxylation (Fig. 13.3b).

B. CO₂ Responses

At limiting CO₂ concentrations, in 21% and 2% O₂, the model satisfactorily matches the responses of photosynthesis to varying CO₂ and O₂ concentrations (see also Laisk et al., 2006a). The inhibition of Rubisco by oxygen, causing a decrease in the carboxylation conductance (the initial slope of the A vs. C_c curve) at 21% versus 2% O₂, is reproduced as the result of competition between CO₂, O₂ and PGA for the free enzyme (Fig. 13.4). At CO₂ concentrations below the compensation point the calculated steady-state curves become s-shaped because of carbon depletion of the CRC (the linear experimental data points in Fig. 13.4a were measured with

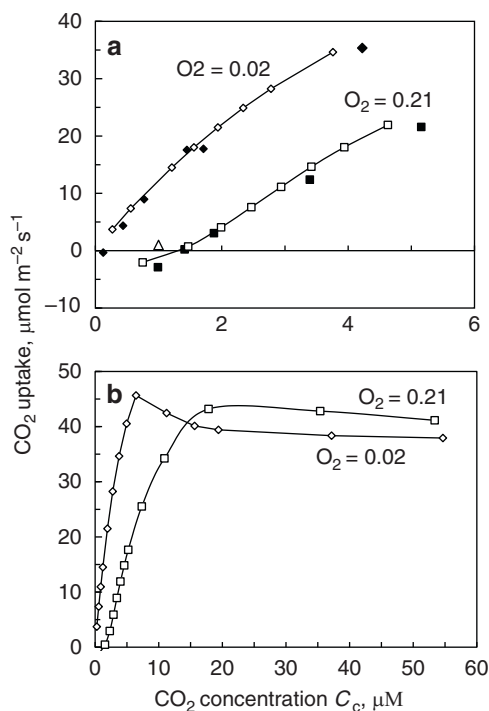


Fig. 13.4. Calculated (empty symbols and solid lines) and measured (filled symbols) CO₂ responses of potato leaf photosynthesis at PFD of 2,000 μmol quanta m⁻² s⁻¹ and O₂ concentration as indicated at the curves, mol mol⁻¹. Panel a is expanded at low CO₂ concentrations, panel b shows the full CO₂ range

a rapid-response gas exchange system before the CRC became depleted of carbon). Depletion of the cycle is less pronounced when internal feeding of the cycle (A_{rev}) is set to about 1 μmol triosephosphates m⁻² s⁻¹ (not shown).

The modeled CO₂ saturated region exhibits sharp bending to the saturation level, followed by a slight decrease in rate in the absence of O₂ (Fig. 13.4b). Hence, the curve calculated for 21% O₂ crosses the 0% O₂ curve, indicative of enhancement of photosynthesis by oxygen at saturating CO₂ concentrations – a phenomenon discovered decades ago (Viil et al., 1972). This effect is caused by alleviation of PS I acceptor side reduction by the Mehler reaction, as suggested by Viil et al. (1977).

C. Induction Transients

The model reproduces rather well transients in Chl fluorescence. In the Kautsky type fluorescence induction curve the fast and slow compo-

nents in the onset of NPQ are reproduced while the initial part of the induction reproduces a typical OJIP transient (see Laisk et al., 2006a). Fluorescence yield generally follows PS II acceptor side reduction. The O–J jump is caused by initial partial reduction of the acceptor side quinones, creating an initial driving force for electron transfer from the bound to the free PQ. The I phase is adjusted as an equilibrium between light input and maximum PQH₂ oxidation rate through the Cyt b₆f complex. The following I–P increase in fluorescence is caused by the final slow-down of electron transport due to the limiting electron sinks at the PS I acceptor side; however, rapidly induced NPQ simultaneously begins to decrease fluorescence. Contrary to the fluorescence induction, the dark-light induction of CO₂ uptake was considerably faster in the Laisk et al. (2006a) model than in the experiment. We suggest that the dark-light induction of CO₂ uptake does not reflect only enzyme activation and build-up of CRC pools; rather an additional important component is the build-up of the ATP pool, critically limited by the capacity for alternative electron transport.

The present model was stabilized at a low PFD of 20 μmol quanta m⁻² s⁻¹ for 200 s followed by an increase in PFD to 1,500 μmol quanta m⁻² s⁻¹ (the model does not yet realistically reproduce chloroplast metabolism in the dark). The calculated transients exhibited a characteristic initial fast phase, followed by a slower induction (Fig. 13.5a). At saturating CO₂ the induction was oscillatory. In the absence of oxygen the oscillations were more pronounced than in the presence of 21% O₂. These features are also present in the experimentally recorded induction curves corresponding to the dark time of 3 min (Fig. 13.5b), however, in experiments the influence of oxygen is greater than predicted by the model. The significant slow-down of induction after long dark exposures of up to 15 min is not reproduced, presumably because the PGA pool – the substrate for alternative electron transport – is not depleted by dark respiration in the model.

D. “To Understand Oscillations Is to Understand Photosynthesis”

The title of this section is borrowed from Walker (1992). Oscillations in photosynthesis

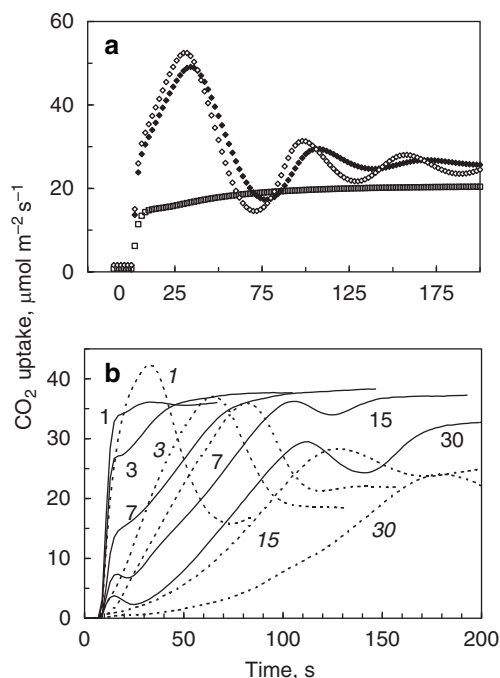


Fig. 13.5. Calculated (a) and measured (b) induction of photosynthesis. In panel (a) low PFD of 20 was increased to 1,500 $\mu\text{mol quanta m}^{-2} \text{s}^{-1}$ at time zero under 360 ppm CO₂ and 21% O₂ (squares), under 2,000 ppm CO₂ and 21% O₂ (filled diamonds) and under 2,000 ppm CO₂ and 0% O₂ (empty diamonds). In panel (b) a sunflower leaf was pre-adapted in the dark as indicated at the curves (min) and then PFD of 1,500 $\mu\text{mol quanta m}^{-2} \text{s}^{-1}$ was turned on. During the induction ambient CO₂ concentration was 2,000 ppm, O₂ concentration 21% (solid lines) or 0% in N₂ (panel b from Laisk and Oja 1998)

observed at CO₂ and light saturation (Laisk and Oja, 1972; Laisk, 1977a) were the initial catalyst for mathematical modeling of the complete mechanism of photosynthesis (Laisk and Walker, 1986). Importantly, oscillations similar to those experimentally observed have not been reproduced by any of the mathematical models developed so far, because no phase shift (delay) of necessary length could be generated in the intermediates of the electron transport and carbon reduction pathways due to their rapid turnover. The present model reproduces these oscillations, because a feedback delay causing overshoot is built into the pathway of alternative electron flow, where rates are about 50 times slower than the main streams of electron and carbon flows.

Oscillations induced by a transition from a limiting to a saturating CO₂ concentration begin with

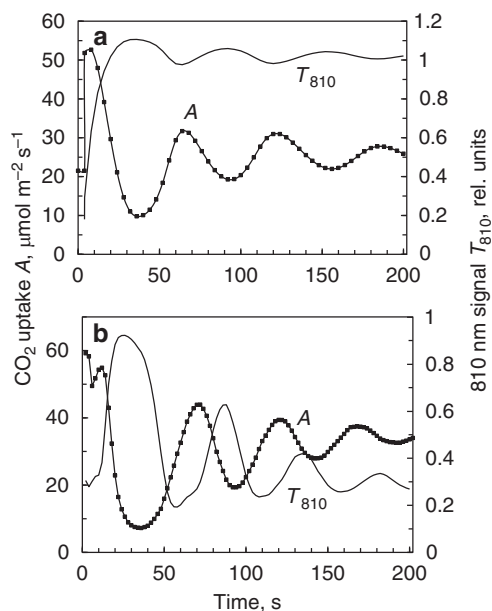


Fig. 13.6. Calculated (a) and measured (b) oscillations in photosynthesis. In panel (a) at the time of 4 s CO₂ concentration was increased from 300 to 2,000 ppm, PFD 2,000 $\mu\text{mol quanta m}^{-2} \text{s}^{-1}$, in panel (b) CO₂ concentration was increased from 340 to 2,000 ppm, PFD 1,600 $\mu\text{mol quanta m}^{-2} \text{s}^{-1}$, sunflower leaf (panel b from Laisk et al., 1992)

a peak of CO₂ uptake, followed by a deep collapse dropping considerably below the prior rate at the initial low CO₂ concentration (Fig. 13.6). This is the most important characteristic feature of such oscillations that in principle cannot be reproduced by models that postulate a phase shift in the main carbon stream (Ryde-Pettersson, 1991; Giersch et al., 1991; Giersch, 1994). Recovery from the collapse proceeds via damped oscillations of about 60-s period. The calculated period, which quite exactly matches the experimental value, was not adjusted in these calculations, but is a natural consequence of realistic pool sizes and rates. However, although the measured oscillations in CO₂ uptake are relatively well reproduced by the model, the calculated 810 nm signal still differs from that measured. The characteristic counterphase feature – T₈₁₀ going up when CO₂ uptake is going down – is reproduced, but the calculated absolute T₈₁₀ value indicates much more PS I acceptor side reduction than is observed (Fig. 13.6b). The principle difference between the measurements and the model is even more visible from the phase portraits (Fig. 13.7), where CO₂

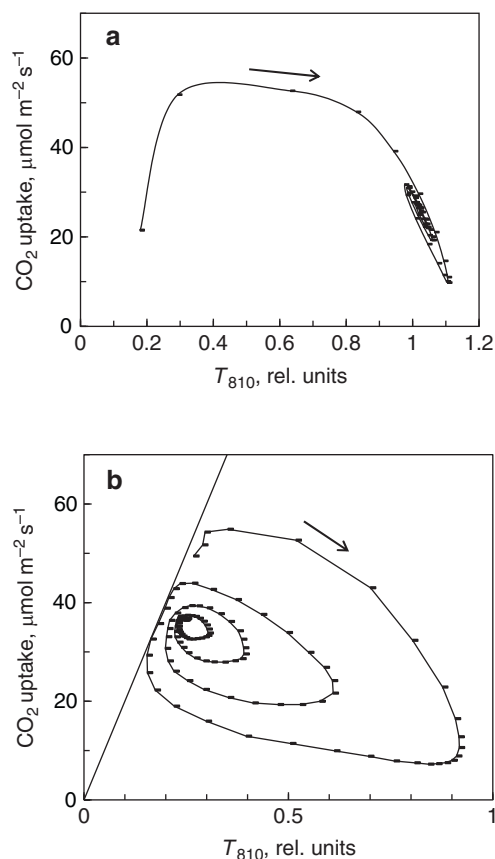


Fig. 13.7. Phase portraits of oscillations of Fig. 13.6: the calculated (a) and measured (b) CO_2 uptake rate is plotted against T_{810} synchronously (arrow indicates the direction of time). The straight line in panel b corresponds to complete donor side limitation of PS I electron transport

uptake is plotted against T_{810} synchronously during oscillations. Despite the fact that the initial parts of both diagrams are rather similar, showing the drop of photosynthesis accompanying the reduction of the PS I acceptor side, the following recovery is completely different; in fact, there is no recovery from acceptor side over-reduction in the model.

In experiments an unknown process drives the PS I donor side back toward oxidation directly and rapidly during the minima (troughs) of the CO_2 oscillations. In the model there is a nascent but unsuccessful attempt to return to the oxidized state along the same trajectory established during the reduction phase. This shows that although oscillations were not understood before, they are better understood now, yet incompletely. Clearly, a critical unknown process controlling electron

donation to PS I is yet to be included in the model. The model analysis predicts that photosynthetic control of Cyt b_6f turnover is directly regulated – in addition to proton backpressure – by acceptor side reduction of PS I, e.g. as suggested by Johnson (2003).

E. Modeling the O_2/CO_2 Exchange Ratio

Recent measurements carried out on potato leaves with overexpressed, unaltered, and under-expressed chloroplast MDH levels, showed the O_2/CO_2 exchange ratio was very close to 1.0 independent of MDH expression level (Laisk et al., 2007). Since oxaloacetate and nitrite reduction would be expected to add extra O_2 evolution of up to 10% raising the O_2/CO_2 exchange ratio to 1:1 (Noctor and Foyer, 1998), this experimental result seemingly indicated the complete absence of nitrite reduction as well as MDH-catalyzed oxaloacetate reduction. In order to address this discrepancy we introduced important changes into the model compared with the earlier version of Laisk et al. (2006a). In the present dynamic model of integrated C/N metabolism the proposed mechanism assumes that carbon skeletons for the alternative electron acceptors originate from PGA exported from the CRC. Exporting PGA to form an end product of photosynthesis would decrease the resulting O_2/CO_2 exchange ratio below unity. The reduction of OXA derived from PGA coupled to PEP carboxylation would decrease the O_2/CO_2 ratio even further because the reduction by $2e^-$ ($= 0.5\text{O}_2$ evolved) is accompanied by the uptake of one additional CO_2 . On the other hand, the transfer of an amino group to PYR to form ALA significantly increases the O_2/CO_2 ratio, because six electrons are consumed ($= 1.5\text{O}_2$ evolved) during reduction of nitrite. Similarly, if OXA is not reduced but transaminated to form aspartate, the net gain will be 0.5O_2 . Partitioning between the nitrite-reducing (ALA-directed) and oxaloacetate-reducing (MAL-directed) pathways occurs at the level of PEP.

PEP is the branch point for several secondary metabolic processes; e.g. shikimate and isoprene synthesis pathways, amino acid synthesis, C_4 organic acid synthesis, and anaplerotic support of mitochondrial respiration. Presently we do not know the mechanisms governing partitioning of

PEP between the carboxylation and dephosphorylation pathways, but the photosynthetic O₂/CO₂ ratio depends on this partitioning. We calculated the resulting O₂/CO₂ ratios by presetting several OXA/PYR partitioning ratios on PEP. The data of Fig. 13.8, which agree well with the experimen-

tal result of Laisk et al. (2007), were calculated using a ratio of about 2:1 between electron transport rates for nitrite and oxaloacetate reduction, respectively.

Table 13.1 compares the modeled rates of carbon partitioning into alanine and starch with experimental values based on the kinetics of newly assimilated ¹⁴C incorporation (Keerberg et al., 1983; Ivanova et al., 1993). Without special fitting of parameters the model reproduces the partitioning of 30–40% of carbon to starch, as measured in tobacco leaves. The calculated carbon partitioning to alanine of 2–4% also is not far from the values measured at limiting CO₂ concentrations. However, the distinct increase in ALA synthesis at saturating CO₂ concentration observed in bean is not yet reproduced by the model.

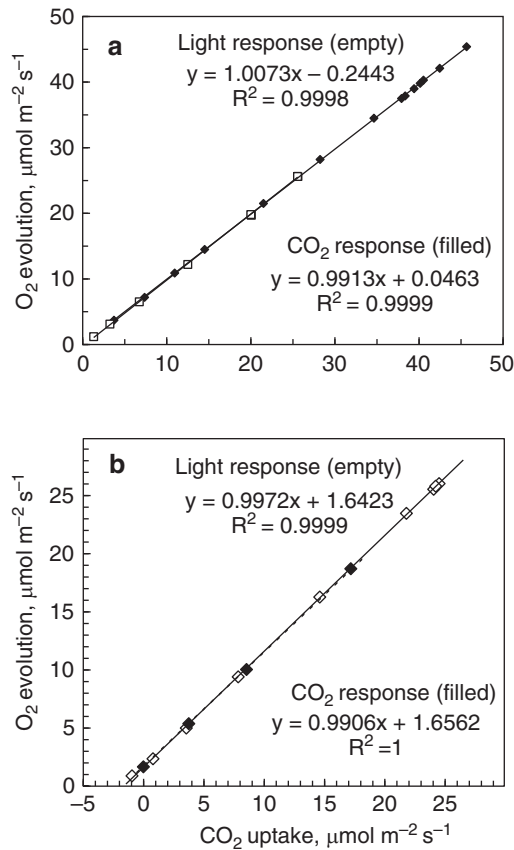


Fig. 13.8. Calculated (a) and measured (b) O₂ evolution rate is plotted against CO₂ uptake rate during photosynthesis of a potato leaf. Empty symbols – light response curve, filled symbols – CO₂ response curve (extended to saturation in a); O₂ concentration was about 50 ppm in N₂ (panel b from Laisk et al., 2007)

V. Concluding Remarks

The major result of this modeling is progress towards understanding how the integral protein/carbohydrate ratio is formed in plants. Although in the model amino acids are presented as the primary product ALA only, the term should be understood as the total of newly synthesized amino acids formed by the transfer of amino groups from glutamate. The predicted C partitioning of 3% to ALA is equivalent to the molar N/C assimilation ratio of 1%, considering the 1N/3C ratio in ALA. Over a longer period, about 50% of assimilated C is evolved via growth and maintenance respiration (Penning de Vries, 1974), which increases the molar N/C ratio of compounds remaining in plants to 2%. As most of the carbon is deposited in carbohydrates, the dry mass is 30 times the molar C content, but N mass is 14 times its molar content. As a result, the relative content of N amounts to 1% on a dry

Table 13.1. Modeled and measured fractional deposition of freshly assimilated carbon into starch and alanine

Gas concentrations		Relative deposition of carbon					
CO ₂	O ₂	Modeled		Measured ^a		Measured ^b	
		Starch	Alanine	Starch	Alanine	Starch	Alanine
Atmospheric	Atmospheric	0.37	0.03	0.45	0.02	0.15	0.01
	Low	0.39	0.04	0.38	0.03		
Saturating	Atmospheric	0.32	0.02			0.25	0.06

^aData for tobacco from Keerberg et al., 1983

^bData for beans from Ivanova et al., 1993

mass basis (gg^{-1}). This value is somewhat lower than is typical for leaves of plants growing under N deficit in natural communities. For example, in birch leaves in a natural habitat the N content was about 2% on a mass basis (Eichelmann et al., 2005). In the nutrient-replete potato leaf of Fig. 13.2 there was an even higher 7.4% N in the dry mass.

The latter result needs explanation, in particular since the high N content corresponded to high protein content and, therefore, most N was indeed reduced to the ammonium level. In principle, faster N reduction must be accompanied by correspondingly faster alternative ATP consumption, exceeding what can be accounted for by starch synthesis. Some extra ATP is consumed for protein synthesis in chloroplasts. Due to this, the N/C assimilation ratio is not determined only by starch synthesis considered in the model, but protein synthesis is “self-supporting” additional N assimilation by the alternative ATP consumption. However, no less important than protein synthesis during photosynthesis is the fact that leaves export most of the produced carbohydrates, yet the proportion of N/C in the phloem flow is lower than the same ratio during photosynthesis which facilitates accumulation of protein in leaves. Thus, not just the N/C ratio of leaves, but the average of the whole plant must be considered for evaluating the integrated C/N assimilation model. A complete dataset of N/C ratios in trees growing in central European forests has been collected by Pietsch et al. (2005). The average mass-based N/C ratio is reported to be 4% in leaves of deciduous broad-leaf forest trees and 2.4% in evergreen needle-leaf trees. In other living parts of the trees the ratio is about 2%, but only 0.1–0.2% in the dead wood. Thus, the average N/C ratio of whole trees is less than 2%, not far above the value predicted by the model.

The integrated C/N photosynthesis model described here was developed from an earlier model of carbon metabolism (Laisk et al., 2006a) by adding a rather schematic description of nitrite reduction metabolism and neglecting details of the glutamine synthetase/glutamate synthase (GOGAT) cycle, translocators and transaminases. The present level of detail of the N-reduction part of our model is far below that of the scheme of Noctor and Foyer (1998). However, our principal progress in this direction is

not the modeling of N reduction according to the textbook metabolic pathways. Based on the metabolic scheme that oxoglutarate is the primary acceptor of the amino group, the photosynthetic C/N metabolism has been tightly linked with the mitochondrial metabolism of oxoglutarate synthesis (Foyer et al., 2003; Dutilleul et al., 2003, 2005). In contrast, our O_2/CO_2 exchange measurements carried out in almost complete absence of oxygen did not indicate drastic disturbances in photosynthesis (Laisk et al., 2007), in spite of the fact that mitochondrial metabolism was unbalanced even more than in the *Nicotiana sylvestris* CMS mutant lacking the functional Complex I (Dutilleul et al., 2005). Hence we hypothesized that photosynthetic N reduction is not critically dependent on synthesis of oxoglutarate in mitochondria, but rather is dependent on the export from CRC of carbon skeletons for amino acids newly synthesized by amino group transfer from glutamate. This hypothesis was supported by an observation that alanine is an end product of photosynthesis, accommodating a few per cent of freshly assimilated carbon (Ivanova et al., 1993; Pärnik and Keerberg, 1995). Combining this observation with our own evidence that the photosynthetic O_2/CO_2 exchange ratio is unity independent of CO_2 concentration and light intensity (Laisk et al., 2007) suggested that PGA is exported from the chloroplast before reduction, converted to PYR via PEP, and the former is transaminated forming ALA. According to this scheme oxoglutarate is just a recycling, temporary carrier of amino groups; its net synthesis is not required for new amino acid synthesis.

The scheme once again confirms the role of PEP as an important metabolic branch point, partitioning carbon for C_3 amino acid synthesis, for C_4 dicarboxylic and amino acids (yet insufficiently analyzed in the model), for the shikimate pathway and for isoprene synthesis, as well as for feeding mitochondrial respiration via the anaplerotic pathway. In Fig. 13.1 the whole chain of ALA formation is indicated in the cytosol, but actually a part of it may operate in chloroplasts considering the presence of a PEP translocator in the chloroplast envelope (Eicks et al., 2002). This possibility is actually considered in the ATP budget (Eq. 13.62) by the assumption that ATP formed from PEP is used to facilitate the amination of PYR (actually of

glutamate, but transamination is non-explicitly involved in the model). The model also suggests a more dynamic role for starch, predicting that a higher proportion of starch synthesis is expected to be accompanied by higher protein content. This prediction was not confirmed, for example, in the *Nicotiana sylvestris* CMS mutant, where starch was low though amino acids accumulated (Dutilleul et al., 2005); however, in these experiments the handicapped oxidative phosphorylation could have inhibited protein synthesis instead of activating N incorporation into amino acids.

Evidently, our theory of integrated C/N assimilation is not yet able to solve many special cases (e.g. plants where starch is not synthesized or N is supplied as ammonium will be objects for experimental investigation in our laboratory). Nevertheless, it emphasizes the basic principle that nitrogen is being reduced in stoichiometry with ATP consumption for alternative syntheses in chloroplasts. This theoretically predicted link between N and C metabolisms in photosynthesizing cells sets the stage for understanding the formation of the N/C ratio in plants. It is basically similar to, yet quantitatively different from, the approach of Noctor and Foyer (1998) which significantly overestimated the N/C ratio. Another important realization from this modeling is that low availability of nitrogen can limit the rate of photosynthesis, explaining how low nitrate levels control carbon assimilation by photosynthesis in natural plant communities. Thus, nitrate is mechanistically included in the list of factors which in natural plant communities limit photosynthetic rate, even more strictly than sucrose and starch synthesis (Sharkey et al., 1986) or CO₂ diffusion. This explains why N/C ratios of plants are relatively similar independent of the widely variable N content in the soil, and why the global increase of CO₂ concentration may not be accompanied by a proportional increase in photosynthetic primary production.

Acknowledgments

This work was supported by Targeted Financing Theme SF0180045s08 from Estonian Ministry of Education and Science and Grants 6607 and 6611 from Estonian Science Foundation.

We appreciate the help and discussions by Dr. R. B. Peterson (The Connecticut Agricultural Experiment Station).

References

- Asada K (2000) The water-water cycle as alternative photon and electron sinks. *Phil Trans R Soc Lond B* 355: 1419–1431
- Badger MR and Lorimer GH (1981) Interaction of sugar phosphates with the catalytic site of ribulose-1,5-bisphosphate carboxylase. *Biochemistry* 20 (8): 2219–2225
- Bendall DS and Manasse R (1995) Cyclic phosphorylation and electron transport. *Biochim Biophys Acta* 1229: 23–38
- Brooks A and Farquhar GD (1985) Effect of temperature on the CO₂/O₂ specificity of ribulose-1,5- bisphosphate carboxylase/oxygenase and the rate of respiration in the light. *Planta* 165: 397–406
- Brown HT and Escombe ELS (1900) Static diffusion of gases and liquids in relation to the assimilation of carbon and translocation in plants. *Phil Trans R Soc Lond B* 193: 223–291
- Carrillo N and Ceccarelli EA (2003) Open questions in ferredoxin-NADP⁺ reductase catalytic mechanism. *Eur J Biochem* 270: 1900–1915
- Chartier P (1966) Etude theorique de l'assimilation brute de la feuille. *Ann Physiol Veg* 8: 167–195
- Cleland WW (1963) The kinetic of enzyme-catalyzed reactions with two or more substrates or products. I. Nomenclature and rate equations. *Biochim Biophys Acta* 767: 432–443
- Cramer WA, Zhang H, Yan J, Kurisu G and Smith JL (2006) Transmembrane traffic in the cytochrome *b₆f* complex. *Annu Rev Biochem* 75: 769–790
- Cruz JA, Sacksteder CA, Kanazawa A and Kramer DM (2001) Contribution of electric field ($\Delta\psi$) to steady-state transthylakoid proton motive force (*pmf*) in vitro and in vivo. Control of *pmf* parsing into $\Delta\psi$ and Δ pH by ionic strength. *Biochemistry* 40: 1226–1237
- Dutilleul C, Garmier M, Noctor G, Mathieu C, Chetrit P, Foyer C and De Paepe R (2003) Leaf mitochondria modulate whole cell homeostasis, set antioxidant capacity, and determine stress resistance through altered signaling and diurnal regulation. *Plant Cell* 15: 1212–1226
- Dutilleul C, Lelarge C, Prioul J-L, De Paepe R and Foyer CH (2005) Mitochondria-driven changes in leaf NAD status exert a crucial influence on the control of nitrate assimilation and the integration of carbon and nitrogen metabolism. *Plant Physiol* 139: 64–78
- Eichelmann H and Laisk A (1999) Ribulose-1,5-bisphosphate carboxylase/oxygenase content, assimilatory charge and mesophyll conductance in leaves. *Plant Physiol* 119: 179–189

- Eichelmann H and Laisk A (2000) Cooperation of photosystems II and I in leaves as analysed by simultaneous measurements of chlorophyll fluorescence and transmittance at 800 nm. *Plant Cell Physiol* 41: 138–147
- Eichelmann H, Oja V, Rasulov B, Padu E, Bichele I, Pettai H, Mänd P, Kull O and Laisk A (2005) Adjustment of leaf photosynthesis to shade in a natural canopy: Reallocation of nitrogen. *Plant Cell Environ* 28: 389–401
- Eichelmann H, Talts E, Oja V, Rasulov B, Padu E and Laisk A (2008) Rubisco activity is related to photosystem I in leaves. In: Allen JF, Gantt E, Golbeck JH and Osmond B (eds) *Photosynthesis. Energy from the Sun: 14th International Congress on Photosynthesis*, pp 853–856. Springer, Dordrecht, The Netherlands
- Eicks M, Maurino VKS, Flügge U-I and Fischer K (2002) The plastidic pentose phosphate translocator represents a link between the cytosolic and plastidic pentose phosphate pathways in plants. *Plant Physiol* 128: 512–522
- Farquhar GD and Von Caemmerer S (1982) Modelling of photosynthetic response to environmental conditions. In: Lange OL, Nobel PS, Osmond CB and Ziegler H (eds) *Physiological Plant Ecology. Encyclopedia of Plant Physiology, New Series Vol. 12B*, pp 549–588. Springer, Berlin
- Farquhar GD, Von Caemmerer S and Berry JA (1980) A biochemical model of photosynthetic CO₂ assimilation in leaves of C₃ species. *Planta* 149: 78–90
- Feniouk BA, Mulikidjanian AY and Junge W (2005) Proton slip in the ATP synthase of *Rhodospirillum rubrum*: Induction, proton conduction, and nucleotide dependence. *Biochim Biophys Acta* 1706: 184–194
- Flügge U-I (1991) Metabolite translocators of the chloroplast envelope. *Annu Rev Plant Physiol Plant Mol Biol* 42: 129–144
- Foyer CH, Parry M and Noctor G (2003) Markers and signals associated with nitrogen assimilation in higher plants. *J Exp Bot* 54: 585–593
- Giersch C (1994) Photosynthetic Oscillations: Observations and Models. *Comments on Theoretical Biology*, pp 339–364. Overseas Publishers Association, Amsterdam
- Giersch C, Sivak MN and Walker DA (1991) A mathematical skeleton model of photosynthetic oscillations. *Proc R Soc Lond B* 245: 77–83
- Hahn BD (1987) A mathematical model of photorespiration and photosynthesis. *Ann Bot* 60: 157–169
- Heldt HW, Chon CJ, Maronde D, Herold A, Stankovic ZS, Walker DA, Kraminer A, Kirk MR and Heber U (1977) Role of orthophosphate and other factors in the regulation of starch formation in leaves and isolated chloroplasts. *Plant Physiol* 59: 1146–1155
- Herzog B, Stitt M and Heldt HW (1984) Properties of the cytosolic fructose 1,6-bisphosphatase. *Plant Physiol* 75: 561–565
- Horton P and Ruban AV (1992) Regulation of photosystem II. *Photosynth Res* 34: 375–385
- Huber SC (1989) Biochemical mechanism for regulation of sucrose accumulation in leaves during photosynthesis. *Plant Physiol* 91: 656–662
- Ivanova H, Keerberg O and Pärnik T (1993) Influence of oxygen concentration on the rates of carbon fluxes in the biochemical system of CO₂ assimilation. *Proc Estonian Acad Sci Chem* 42: 185–197
- Johnson G (2003) Thiol regulation of the thylakoid electron transport chain – a missing link in the regulation of photosynthesis. *Biochemistry* 42: 3040–3044
- Jordan DB, Chollet R and Ogren WL (1983) Binding of phosphorylated effectors by active and inactive forms of ribulose-1,5-bisphosphate carboxylase. *Biochemistry* 22: 3410–3418
- Keerberg O, Keerberg H, Pärnik T, Viil J and Vark E (1983) The metabolism of photosynthetically assimilated ¹⁴CO₂ under different concentrations of carbon dioxide. *Int J Appl Radiat Isot* 34 (5): 861–864
- Kirchhoff H, Schöttler MA, Maurer J and Weis E (2004) Plastocyanin redox kinetics in spinach chloroplasts: Evidence for disequilibrium in the high potential chain. *Biochim Biophys Acta* 1659: 63–72
- Laisk A (1970) A model of leaf photosynthesis and photorespiration. In: Shetlik I (ed) *Prediction and Measurement of Photosynthetic Productivity*, pp 295–306. Centre for Agricultural Publishing and Documentation, Wageningen
- Laisk A (1977a) Kinetics of Photosynthesis and Photorespiration in C₃ Plants. Publishing House Nauka, Moscow
- Laisk A (1977b) Modelling of the closed Calvin cycle. In: Unger K (ed) *Biophysikalische Analyse pflanzlicher Systeme*, pp 175–182. VEB Fischer Verlag, Jena, DDR
- Laisk A and Edwards GE (2000) A mathematical model of C₄ photosynthesis: The mechanism of concentrating CO₂ in NADP-malic enzyme type species. *Photosynth Res* 66: 199–224
- Laisk A and Eichelmann H (1989) Towards understanding oscillations: A mathematical model of the biochemistry of photosynthesis. *Phil Trans R Soc Lond* 323: 369–384
- Laisk A and Laarin P (1983) Feedback regulation of the potential rate of photosynthesis. In: Margna U (ed) *Regulation of Plant Growth and Metabolism*, pp 135–150 (in Russian). Publishing House Valgus, Tallinn
- Laisk A and Oja V (1972) Positive Feedback and Rhythmic Phenomena in the Pentosephosphate Cycle of Photosynthesis. Abstracts of the IV International Biophysical Congress, Sections XVI–XXV. Publishing House Nauka, Moscow
- Laisk A and Oja V (1998) *Dynamic Gas Exchange of Leaf Photosynthesis. Measurement and Interpretation*. CSIRO Publishing, Canberra
- Laisk A and Oja V (2000a) Alteration of PSII properties with non-photochemical excitation quenching. *Phil Trans R Soc Lond B* 355: 1405–1418

- Laisk A and Oja V (2000b) Electron transport through photosystem II in leaves during light pulses: Acceptor resistance increases with nonphotochemical excitation quenching. *Biochim Biophys Acta* 1460: 255–267
- Laisk A and Walker DA (1986) Control of phosphate turnover as a rate-limiting factor and possible cause of oscillations in photosynthesis: A mathematical model. *Proc R Soc Lond B* 227: 281–302
- Laisk A, Eichelmann H, Oja V, Eatherall A and Walker DA (1989) A mathematical model of the carbon metabolism in photosynthesis. Difficulties in explaining oscillations by fructose 2,6-bisphosphatase. *Proc R Soc Lond B* 237: 389–415
- Laisk A, Oja V, Walker D and Heber U (1992) Oscillations in photosynthesis and reduction of Photosystem I acceptor side in sunflower leaves. Functional Cyt b/f-PSI-FNR complexes. *Photosynthetica* 27 (4): 465–479
- Laisk A, Oja V, Rasulov B, Eichelmann H and Sumberg A (1997) Quantum yields and rate constants of photochemical and nonphotochemical excitation quenching. Experiment and model. *Plant Physiol* 115: 803–815
- Laisk A, Oja V, Rasulov B, Rämme H, Eichelmann H, Kasparova I, Pettai H, Padu E and Vapaavuori E (2002) A computer-operated routine of gas exchange and optical measurements to diagnose photosynthetic apparatus in leaves. *Plant Cell Environ* 25: 923–943
- Laisk A, Eichelmann H and Oja V (2006a) C₃ photosynthesis *in silico*. *Photosynth Res* 90: 45–66
- Laisk A, Eichelmann H, Oja V, Rasulov B and Rämme H (2006b) Photosystem II cycle and alternative electron flow in leaves. *Plant Cell Physiol* 47: 972–983
- Laisk A, Eichelmann H, Oja V, Talts E and Scheibe R (2007) Rates and roles of cyclic and alternative electron flow in potato leaves. *Plant Cell Physiol* 48: 1575–1588
- Lascano HR, Casano LM, Martin M and Sabater B (2003) The activity of the chloroplastic Ndh Complex is regulated by phosphorylation of the NDH-F subunit. *Plant Physiol* 132: 256–262
- Noctor G and Foyer CH (1998) A re-evaluation of the ATP:NADPH budget during C₃ photosynthesis: A contribution from nitrate assimilation and its associated respiratory activity? *J Exp Bot* 49: 1895–1908
- Oja V (1985) Estimation of pH and carbonic anhydrase activity in intact leaves on the basis of the kinetics of CO₂ dissolution. In: Viil J, Grishina GS and Laisk A (eds) *Kinetics of Photosynthetic Carbon Metabolism in C₃ Plants*, pp 104–108. Publishing House Valgus, Tallinn
- Oja V and Laisk A (2000) Oxygen yield from single turnover flashes in leaves: Non-photochemical excitation quenching and the number of active PSII. *Biochim Biophys Acta* 1460: 291–301
- Oja V, Eichelmann H, Peterson RB, Rasulov B and Laisk A (2003) Decyphering the 820 nm signal: Redox state of donor side and quantum yield of photosystem I in leaves. *Photosynth Res* 78: 1–15
- Oja V, Bichele I, Hüve K, Rasulov B and Laisk A (2004) Reductive titration of photosystem I and differential extinction coefficient of P700⁺ at 810–950 nm in leaves. *Biochim Biophys Acta* 1658: 225–234
- Pärnik T and Keerberg O (1995) Decarboxylation of primary and end products of photosynthesis at different oxygen concentrations. *J Exp Bot* 46: 1439–1447
- Peltier G and Cournac L (2002) Chlororespiration. *Annu Rev Plant Biol* 53: 523–550
- Penning de Vries FWT, Brunsting AHM and Van Laar HH (1974) Products, requirements and efficiency of biosynthesis. A quantitative approach. *J Theor Biol* 45: 339–377
- Pettai H, Oja V, Freiberg A and Laisk A (2005) Photosynthetic activity of far-red light in green plants. *Biochim Biophys Acta* 1708: 311–321
- Pettersson G and Ryde-Pettersson U (1988) A mathematical model of the Calvin photosynthesis cycle. *Eur J Biochem* 175: 661–672
- Pietsch S, Hasenauer H and Thornton PE (2005) BGC-model parameters for tree species growing in central European forests. *Forest Ecol Manag* 211: 264–295
- Porcar-Castell A, Bäck J, Juurola E and Hari P (2006) Dynamics of the energy flow through photosystem II under changing light conditions: A model approach. *Funct Plant Biol* 33: 229–239
- Preiss J, Robinson S, Spilatro S and McNamara K (1985) Starch synthesis and its regulation. In: Heath RL, Preiss J (eds) *Regulation of Carbon Partitioning in Photosynthetic Tissue*, pp 1–26. University of California Press, Riverside, CA
- Rabinowitch E (1951) *Photosynthesis and Related Processes*, Vol. II, Part I. Interscience Publishers, New York
- Rabinowitch E (1953) *Photosynthesis II*. Publishing House of Foreign Liter, Moscow (in Russian)
- Rees D, Noctor G, Ruban AV, Crofts J, Young A and Horton P (1992) pH dependent chlorophyll fluorescence quenching in spinach thylakoids from light treated or dark adapted leaves. *Photosynth Res* 31: 11–19
- Rich, PR (1991) The osmochemistry of electron-transfer complexes. *Biosci Rep* 11: 539–571
- Rumberg B, Schubert K, Strelow F and Tran-Anh T (1990) The H⁺/ATP coupling ratio at the H⁺-ATP-synthase of spinach chloroplasts is four. In: Baltscheffsky M (ed) *Current Research in Photosynthesis*, Vol. III, pp 125–128. Kluwer, Dordrecht, The Netherlands
- Ryde-Pettersson U (1991) A theoretical treatment of damped oscillations in biochemical reaction systems with application to the photosynthetic oscillations. Dissertation, University of Lund, Department of Biochemistry
- Sazanov LA, Burrows P and Nixon PJ (1995) Presence of a large protein complex containing the ndhK gene product and possessing NADH-specific dehydrogenase activity in thylakoid membranes of higher plant chloroplasts. In: Mathis P (ed) *Photosynthesis. From Light to Biosphere*, Vol. 2., pp 705–708. Kluwer, Dordrecht, The Netherlands

- Scheibe R (1987) NADP⁺-malate dehydrogenase in C₃-plants: Regulation and role of a light-activated enzyme. *Physiol Plantarum* 71: 393–400
- Seelert H, Poetsch A, Dencher NA, Engel A, Stahlberg H and Müller DJ (2000) Proton powered turbine of a plant motor. *Nature* 405: 418–419
- Sharkey TD, Stitt M, Heineke D, Gerhardt R, Raschke K and Heldt HW (1986) Limitation of photosynthesis by carbon metabolism. II. O₂-intensive CO₂ uptake results from limitation of triose phosphate utilization. *Plant Physiol* 81: 1123–1129
- Stitt M (1987) Fructose 2,6-bisphosphate and plant carbohydrate metabolism. *Plant Physiol* 84: 201–204
- Tetlow IJ, Morell MK and Emes MJ (2004) Recent developments in understanding the regulation of starch metabolism in higher plants. *J Exp Bot* 55: 2131–2145
- Viil J, Laisk A, Oja V and Pärnik T (1972) Positive influence of oxygen on photosynthesis. *Doklady AN SSSR (Proc Acad Sci USSR)* 204 (5): 1269–1271 (in Russian)
- Viil J, Laisk A, Oja V and Pärnik T (1977) Enhancement of photosynthesis caused by oxygen under saturating irradiance and high CO₂ concentrations. *Photosynthetica* 11 (3): 251–259
- Von Caemmerer S (2000) *Biochemical Models of Leaf Photosynthesis*. CSIRO Publishing, Australia
- Walker DA (1992) Concerning oscillations. *Photosynth Res* 34: 387–395
- Winter H, Robinson DG and Heldt HW (1993) Subcellular volumes and metabolite concentrations in barley leaves. *Planta* 191: 180–190
- Winter H, Robinson DG and Heldt HW (1994) Subcellular volumes and metabolite concentrations in spinach leaves. *Planta* 193: 530–535
- Yin X, Van Oijen M and Schapendonk AHCM (2004) Extension of a biochemical model for the generalized stoichiometry of electron transport limited C₃ photosynthesis. *Plant Cell Environ* 27: 1211–1222
- Yin X, Harbinson J and Struik PC (2006) Mathematical review of literature to assess alternative electron transports and interphotosystem excitation partitioning of steady-state C₃ photosynthesis under limiting light. *Plant Cell Environ* 29: 1771–1782
- Zhu X-G, Govindjee, Baker NR, deSturler E, Ort DR and Long SP (2005) Chlorophyll a fluorescence induction kinetics in leaves predicted from a model describing each discrete step of excitation energy and electron transfer associated with photosystem II. *Planta* 223: 114–133

Chapter 14

Leaf C₄ Photosynthesis *in silico*: The CO₂ Concentrating Mechanism

Agu Laisk

Institute of Molecular and Cell Biology, Tartu University, Riia 23, Tartu 51010, Estonia

Gerald Edwards*

School of Biological Sciences, Washington State University, Pullman, WA 99164-4236 U.S.A.

Summary.....	324
I. Introduction.....	324
II. Principles of NADP-ME Type C ₄ Photosynthesis.....	325
A. Reducing Power Requirement During C ₄ Photosynthesis.....	325
B. Assimilatory Power Requirement During C ₄ Photosynthesis.....	326
C. Causes and Mechanism for CO ₂ Overcycling.....	327
1. Photorespiration and Overcycling.....	327
2. ATP/NADPH Stoichiometry and Overcycling in NADP-ME Type C ₄ Species.....	327
III. The C ₄ Model.....	329
A. Photoreactions in Mesophyll Chloroplasts.....	329
B. Electron Transport in Bundle Sheath Chloroplasts.....	329
C. Dark Reactions: The C ₄ Cycle.....	330
D. Dark Reactions: The C ₃ Cycle.....	331
E. Compartmentalization and Metabolite Diffusion.....	331
IV. Simulations.....	334
A. Fitting Rates and Pool Sizes to Experimental Data.....	334
B. The Ratio of ATP/NADPH in Bundle Sheath Chloroplasts.....	334
C. Role of Oxygen in C ₄ Photosynthesis.....	335
D. CO ₂ and Light Responses: Connection of C ₄ and C ₃ Cycles.....	337
V. Knowns and Unknowns in Photosynthesis.....	338
A. Photosystem II.....	338
B. Cytochrome b ₆ f and Interphotosystem Electron Transport.....	339
C. ATP Synthase.....	340
D. Photosystem I.....	341
E. Cyclic Electron Flow.....	342
F. The C ₃ Cycle of Carbon Assimilation.....	343
G. C ₄ plant CO ₂ Concentrating Mechanisms.....	344
Acknowledgments.....	345
References.....	345

* Author for correspondence, e-mail: edwardsg@wsu.edu

Summary

A computer model comprised of light reactions in PS II and PS I, electron–proton transport reactions in mesophyll and bundle sheath (BS) chloroplasts, all enzymatic reactions, and most of the known regulatory functions of NADP-malic enzyme type C_4 photosynthesis, has been developed as a system of differential budget equations for intermediate compounds. Rate-equations were designed on principles of multisubstrate-multiproduct enzyme kinetics. The model provided good simulations for rates of photosynthesis and pool sizes of intermediates under varying light, CO_2 and O_2 . A principle novelty of the model for NADP-ME type species is the hypothesis that electrons transported into the BS chloroplasts via the malate shuttle enter the electron transport chain with the help of NAD(P)H-plastoquinone oxyreductase (NDH, or an enzyme of similar function). In the model, the electrons from reduced plastoquinone pass through the Q-cycle and photosystem I (PS I) only once, without cycling around PS I, as commonly assumed. With this the ratio of 2 ATP/NADPH, satisfying the energy requirements process, is fixed, provided that $2 H^+ / e^-$ are transported by the Q-cycle and $2 H^+ / e^-$ by NDH, and 4 H^+ are utilized per ATP generated. The hypothesis is based on modeling results showing that there must be fine control of the ATP/NADPH ratio in BS chloroplasts for optimum function of C_4 photosynthesis. The CO_2 concentrating function of NADP-ME type C_4 photosynthesis, which occurs as the rate of the C_4 cycle exceeds the rate of CO_2 assimilation in BS cells (overcycling), can be explained on the basis of two processes. First, alternative consumption of some ATP in BS chloroplasts to support other processes (e.g. starch and protein synthesis) reduces the ATP/NADPH ratio available in BS. As a result, some CO_2 imported into BS remains unassimilated and accumulates, resulting in overcycling back to the mesophyll. Second, the residual photorespiratory activity alternatively consumes some ribulose 1,5-bisphosphate for oxygenation; as with the alternative consumption of ATP, some CO_2 imported into BS remains unassimilated and accumulates, causing overcycling. The CO_2 evolved from photorespiration in BS also contributes to the CO_2 pump in C_4 plants.

I. Introduction

C_4 photosynthesis is a more complex process than C_3 photosynthesis, involving also a C_4 cycle pumping CO_2 from its capture in the mesophyll cells and release in the bundle sheath (BS) cells, where the C_3 cycle operates. The metabolic pathways of both cycles have been thoroughly

described (Edwards and Walker, 1983; Hatch, 1987; Kanai and Edwards, 1999), but despite knowing the network of biochemical reactions, their cooperation is not well understood. For example, it is not clear how the rates of the two cycles are synchronized so that the C_4 cycle transports just enough CO_2 to cover the needs of the C_3 cycle, plus some excess to support the elevated levels around Rubisco, and the leakage of CO_2 from BS back to mesophyll.

A dominant view is that enzyme activities of the two cycles (mainly of the PEP and RuBP carboxylases, PEPC and Rubisco) are adjusted so that the C_4 cycle is supplying CO_2 faster than the C_3 cycle can fix it. This results in a rise of CO_2 in BS cells, which represses photorespiration, but also results in some leakage of CO_2 back to mesophyll cells at a rate dependent on the CO_2 concentration gradient and the diffusive resistance. Several models of C_4 photosynthesis have been developed using these principles to describe steady-state situations (Berry and Farquhar, 1978; Peisker, 1979) and for environmental modeling (Collatz et al., 1992). These simplified treatments

Abbreviations: A_m , A_b – CO_2 fixation rates in mesophyll and bundle sheath; BPGA – bisphosphoglycerate; BS – bundle sheath; CET – cyclic electron transport; C_m , C_b – CO_2 concentrations in mesophyll and bundle sheath; CRC – the C_3 carbon reduction/oxidation cycle; Cyt b_6f – cytochrome b_6f complex; ETR – electron transport rate; Fd – ferredoxin; FNR – ferredoxin-NADP reductase; GAP – glyceraldehyde phosphate; MAL – malate; MC – mesophyll cells; NADP-ME – NADP-malic enzyme; NDH – chloroplast NADP-plastoquinone oxyreductase; OAA – oxaloacetate; PC – plastocyanin; PEPC – phosphoenolpyruvate carboxylase; PFD – photon flux density; PGA – 3-phosphoglyceric acid; PQ – plastoquinone; PS II, PS I – photosystems II and I; PYR – pyruvate; Rubisco – RuBP carboxylase/oxygenase; RuBP – ribulose 1,5-bisphosphate; T3P – triose 3-phosphate; T_{810} – leaf 810 nm transmittance

resulted in analytical solutions, e.g. in quadratic equations (Von Caemmerer and Furbank, 1999). Basically, they combined the properties of two enzymes, PEPC in mesophyll cells having a higher affinity for atmospheric CO_2 (utilizing bicarbonate as substrate with catalysis insensitive to O_2) and Rubisco in BS cells having a lower affinity for atmospheric CO_2 (utilizing CO_2 as substrate with O_2 as a competitive inhibitor), to simulate rates of photosynthesis in response to varying atmospheric levels of CO_2 . Analyses were made with variable input for diffusive resistance of CO_2 from sites of decarboxylation in BS cells to the mesophyll cells. They showed with equal rates of flux through both enzymes the CO_2 concentration at Rubisco (C_b) is higher than at PEPC (C_m) by a factor of $(V_m/K_m)_{PEPC}/(V_m/K_m)_{Rubisco}$, which is equal to the ratio of the initial slopes of the kinetic curves of the enzymes (Von Caemmerer, 2000). However, due to leakiness of the BS cells for CO_2 , the rate through Rubisco is always less than through PEPC, which correspondingly decreases the C_b/C_m ratio compared to that defined by the above ratio of affinities. Analyses by isotope discrimination methods estimate leakage of 20–40% depending on species and environmental conditions (Henderson et al., 1992; Kubasek et al., 2007).

The above approach to modeling produced a low CO_2 compensation point and high carboxylation efficiency, characteristic of C_4 plants. During conditions of strictly CO_2 -limited C_4 photosynthesis, both cycles are operating under CO_2 limitation, with a predicted substantial flux through photorespiration, and allowing for an increase of the rates of both cycles with increasing CO_2 concentration. The rate of photorespiration under limiting CO_2 was dependent on the value for bundle sheath diffusive resistance: higher diffusive resistance causes higher BS CO_2 concentration, and correspondingly lower photorespiration. However, the principle of simultaneous CO_2 limitation in both cycles remains critical in these models. This discrepancy was avoided in the model by Laisk and Edwards (2000), which involves incorporating all enzymes of the C_4 and C_3 cycles, control of the ATP/NADPH ratio, and a novel hypothesis about the mechanism of ATP synthesis in BS cells.

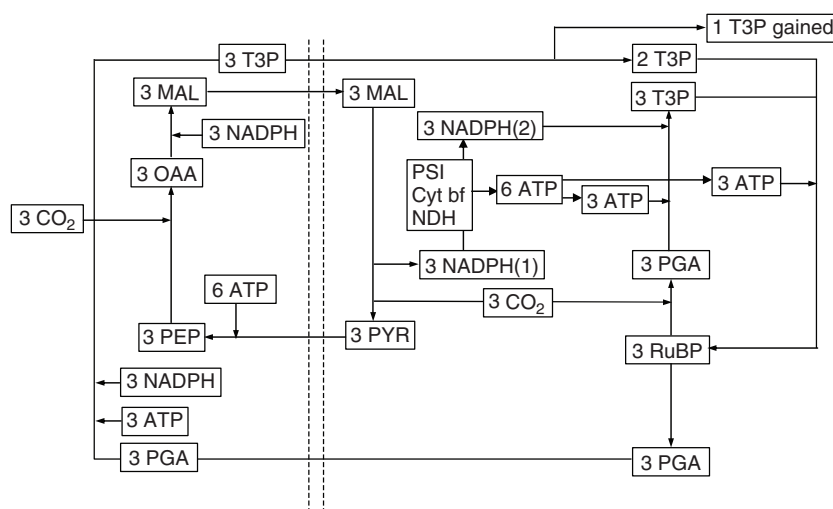
Experimental evidence with C_4 plants showing photorespiration is restricted under low CO_2 compared to C_3 plants is important in considering

modeling C_4 photosynthesis and the linkage between the C_4 cycle pump and the process of photorespiration. This was shown in early work combining measures of the net rates of photosynthesis by CO_2 exchange and gross and net rates of O_2 evolution (Furbank and Badger, 1982). An important piece of evidence for this metabolic modeling came from the parallel measurements of CO_2 fixation and Chl fluorescence, showing that at rate-limiting CO_2 concentrations in the NADP-ME type C_4 plant sorghum, electron transport supporting photorespiration is much slower than in the C_3 plant sunflower (Laisk and Edwards, 1998). The conclusion was that even when external CO_2 was rate-limiting for PEPC, the CO_2 concentration in the bundle-sheath was near saturating for Rubisco, strongly suppressing the oxygenation reaction. Knowing that, in the C_3 cycle under CO_2 saturation, the rate-limiting process is RuBP regeneration, we concluded that the RuBP regeneration rate was directly dependent on the rate of NADPH import into the BS. Another experiment reinforced the above conclusion: C_4 photosynthesis slowly responds to increasing CO_2 concentration (Laisk and Edwards, 1997), indicating that CO_2 is not the kinetically rate-limiting substrate. These important experimental facts and ideas were accounted for in the structure of a biochemical model of NADP-ME type C_4 photosynthesis (Laisk and Edwards, 2000) involving a novel assumption – in fact, an important theoretical prediction about the metabolism of C_4 photosynthesis. The result of this modeling was a new understanding of the mechanism of concentrating CO_2 in the BS cells of NADP-ME malic enzyme type C_4 plants, based on the need to maintain a strict ATP/NADPH stoichiometry in generation of assimilatory power in BS cells.

II. Principles of NADP-ME Type C_4 Photosynthesis

A. Reducing Power Requirement During C_4 Photosynthesis

Figure 14.1 shows key reactions in the NADP-ME type C_4 and C_3 cycles per 3 CO_2 fixed in the C_4 and C_3 pathways, as predicted in the absence of photorespiration, without overcycling,



Balance per 3 CO₂ fixed in mesophyll and 3 CO₂ fixed in bundle sheath
 Mesophyll: 6 NADPH generated + 9 ATP; Bundle sheath: 3 NADPH imported + 6 ATP
 Total: 6 NADPH + 15 ATP

Fig. 14.1. Compartmentation of energy-consuming reactions for C₄ photosynthesis in NADP-ME type species. Shown is the balance per 3 CO₂ fixed, when the rate of the C₄ cycle equals the rate of the C₃ cycle

and without additional losses of ATP for starch and protein synthesis. The energy budget for use of reducing power is as follows.

In NADP-ME type species like sorghum, 6 NADPH are produced photochemically in mesophyll chloroplasts per every 3 CO₂ fixed. There are two reactions where reductive power is needed in NADP-ME type C₄ photosynthesis, one in the reduction of OAA to MAL, and the other in the reduction of PGA to triose phosphates (T3P). In the fixation of 3 CO₂ in the C₄ cycle, 3 NADPH are needed to reduce 3 OAA to 3 MAL. The 3 MAL move into the BS and are decarboxylated via malic enzyme, which is coupled with the formation of 3 NADPH in the BS. The 3 CO₂ released are captured by RuBP carboxylase to form 6 PGA. Since NADP-ME type C₄ plants like sorghum and sugarcane lack PS II activity in the BS chloroplasts, the 3 NADPH derived from MAL decarboxylation are the only reducing power which is directly available to the C₃ cycle per 3 CO₂. Thus, only 3 PGA can be reduced to T3P in the BS, while the other 3 PGA diffuse to the mesophyll, where the remaining 3 NADPH are used for their reduction. This results in synthesis of 3 T3P, at least two of which must be transported back to the BS, where they combine with the 3 T3P formed there, to regenerate 3 RuBP. This results in carbon gain

of one T3P per 3 CO₂ fixed, which is utilized mainly for carbohydrate synthesis, i.e. sucrose synthesis in mesophyll cells, or starch biosynthesis in BS chloroplasts (Furbank et al., 1985; Edwards, 1986).

B. Assimilatory Power Requirement During C₄ Photosynthesis

In the above process, 9 ATP per 6 NADPH are generated during linear electron transport in the mesophyll chloroplasts (see later discussion of stoichiometry). The assimilation of 3 CO₂ in the mesophyll chloroplast requires exactly 9 ATP, with 6 ATP used for the regeneration of 3 PEP from 3 PYR, and 3 ATP to facilitate the reduction of the 3 PGA arriving from the BS. However, an additional 6 ATP are required in BS to complete the C₃ cycle (3 ATP for the reduction of 3 PGA and 3 ATP for the regeneration of 3 RuBP). It is generally believed that in BS cells the ATP is generated by PS I-mediated cyclic photophosphorylation as required for any stoichiometric relationship. However, such a simple concept is inadequate, e.g. it does not explain what determines the available pool of cycling electrons. While the mechanism of ATP synthesis in BS cells is not resolved, Laisk and Edwards (2000)

hypothesized that the ATP production is stoichiometrically related to the transport of reductive power into the BS. Their model assumes that the imported NADPH(1) via the malate shuttle, is compartmentalized in a way that it can only feed electrons into the PQ pool of the BS chloroplasts. This is accomplished by coupling NADPH produced by decarboxylation of malate with the NADPH dehydrogenase (NDH) in BS chloroplasts; e.g. if malic enzyme were complexed with the chloroplast NADPH dehydrogenase (NDH), the electrons could pass via NDH through the electron transport chain to PS I only once – without cycling. Then, the terminal acceptor NADP(2) pool (see Fig. 14.1) is compartmentalized in a way that it can reduce BPGA, but not PQ (or it may be a free pool provided that the malic enzyme is complexed with NDH). The transport of every electron through the chain is coupled with the transmembrane translocation of 4 H⁺, from which 2 H⁺ in the Q-cycle and 2 H⁺ in the NDH complex. As a result of passing six electrons (3 NADPH), 24 H⁺ are translocated, which is sufficient to generate 6 ATP (assuming 4H⁺/ATP). According to this hypothesis, there is not cyclic phosphorylation around PS I, but rather linear electron flow of reductive power from MAL to NDH to PS I to BPGA in BS chloroplasts generating 2 ATP per MAL, which essentially accounts for the energy cost of running the C₃ cycle.

This means of controlling ATP production in BS chloroplasts, with half of the PGA reduced in the mesophyll chloroplasts, fits well the energy budget of Fig. 14.1 showing the energy requirement per 3 CO₂ fixed, which corresponds to the theoretical minimum requirement of 5 ATP and 2 NADPH per CO₂ fixed in C₄ photosynthesis. However, this maximum energetic efficiency does not support any CO₂ overcycling and, thus, no CO₂ concentrating function. In practice the C₄ cycle runs faster than carbon fixation by Rubisco – as previously noted, overcycling is from 20% to 40%, based on carbon isotope fractionation analyses (Henderson et al., 1992; Kubasek et al., 2007). Contrary to previous models, the hypothesis of Laisk and Edwards (2000) explains and predicts why, and to what extent, the C₄ cycle turns faster than the C₃ cycle in NADP-ME type species, pumping up the CO₂ concentration in the BS.

C. Causes and Mechanism for CO₂ Overcycling

1. Photorespiration and Overcycling

The first step in evolution of C₄ plants from C₃ plants is proposed to be the partitioning of the photorespiratory release of CO₂ and its refixation to the BS cells (by selective expression of glycine decarboxylase in BS cell mitochondria), with the mesophyll chloroplasts carrying out normal C₃ photosynthesis (Monson, 1984; Edwards and Ku, 1987; Sage, 2004). This contributes to the CO₂ concentrating mechanism in BS cells by generating and refixing photorespired CO₂ which results in increased CO₂ fixation under limited CO₂ and lower CO₂ compensation points.

Subsequent specialization of chloroplasts in mesophyll and BS cells occurred with development of the C₄ cycle, and selective compartmentation of the C₃ cycle with Rubisco in BS chloroplasts. Thus, a common feature of all C₄ plants (NADP-ME, NAD-ME and PEP-CK type C₄ cycles) is the specific location of glycine decarboxylase in BS cell mitochondria and function of Rubisco in BS cells, with the relative carboxylase and oxygenase activities depending on the availability of CO₂ and O₂. The competing reaction by O₂ results in consumption of RuBP which will lead to overcycling and some concentrating of CO₂ in the BS compartment. The rate of overcycling is dependent on the rate of delivery of CO₂ to the BS by the C₄ cycle, minus the net rate of CO₂ fixation by Rubisco which is equal to velocity of carboxylase minus generation of CO₂ by photorespiration (0.5 times velocity of oxygenase). The C₄ cycle drives the CO₂ concentrating mechanism, while release of CO₂ in the BS compartment by photorespiration contributes to sustaining the CO₂ pool, and limiting oxygenase activity.

2. ATP/NADPH Stoichiometry and Overcycling in NADP-ME Type C₄ Species

In addition to overcycling due to consequences of RuBP oxygenase activity in the BS cells, in NADP-ME type C₄ species control of the ratio of available ATP/NADPH is critical. This mechanism is based on the assumption of a controlled stoichiometry between the number of electrons (in the form of NADPH) arriving at the BS

the synthesis of 3 RuBP. Thus, partitioning of ATP for non-photosynthetic processes requires increased import of NADPH to produce the extra ATP. However, half of the extra ATP is consumed to support other processes, while the other half facilitates the increased reduction of PGA. These re-arrangements in energetics result in fixation of 3 CO₂ in BS cells (as without leakage), while the additional 0.3 CO₂ which is imported to the BS diffuses back to the mesophyll, forming the over-cycling. As emphasized, this mechanism predicts the rate of CO₂ overcycling, not the concentration of CO₂ in BS cells. The CO₂ concentration in BS will rise to a level sufficient to ensure its diffusion back to the mesophyll. The higher the diffusional resistance between the BS and the mesophyll, the higher will be the CO₂ concentration in the BS. In the mesophyll, CO₂ fixation by PEP carboxylase is increased due to overcycling: while 3 CO₂ are taken from outside (as without leakage), 0.3 CO₂ which leaks from the BS cells is refixed in the mesophyll. Due to overcycling the ATP requirement for regenerating PEP from PYR increases from 6 to 6.6. Another 2.7 ATP are required in mesophyll cells to facilitate the reduction of PGA imported from the BS, thus, 9.3 ATP are now needed in the mesophyll. The requirement for reductive power for assimilating three external CO₂ is still 6 NADPH, the same with or without overcycling, but – assuming that the additional 0.3 ATP are synthesized at the expense of alternative electron transport in the mesophyll – electrons equivalent to 0.2 NADPH must be partitioned for nitrite or O₂ reduction or other electron acceptors. As one can see, the extra (alternative) consumption of ATP in BS will be finally covered by increased alternative electron flow in mesophyll. This example illustrates how the available ATP/NADPH ratio in the BS can drive the CO₂ concentrating mechanism independent of RuBP oxygenase activity.

In C₃ photosynthesis, CO₂ saturation of the rate is characterized as a limitation of RuBP regeneration by the availability of NADPH and ATP. In the NADP-ME type C₄ system, the same condition exists in the BS at any external CO₂ concentration: NADPH and ATP are imported into BS always proportionally with CO₂, never being over-saturating. Accordingly, photorespiration is strongly suppressed at any external CO₂ concentration in the NADP-ME type C₄ plants.

III. The C₄ Model

The reaction circuit of Fig. 14.2 was mathematically modeled as a system of differential equations (Laisk and Edwards, 2000). Reactions which are kinetically similar in C₃ and C₄ photosynthesis were modeled as described in Chapter 13 of this book by Agu Laisk, Hillar Eichelmann and Vello Oja. The distinguishing features of the C₄ model are emphasized below.

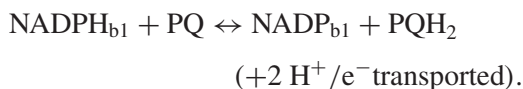
A. Photoreactions in Mesophyll Chloroplasts

The excitation rate of Chl by white light was determined by Eqs. (13.9) and (13.10) of Chapter 13 (since the mathematical treatment of photoreactions in the C₄ mesophyll cells is similar to photoreactions of C₃ photosynthesis, below we refer to equations of Chapter 13), considering non-photochemical quenching of excitation at PS II (Eq. 13.11), but not in PS I. For mesophyll chloroplasts, the transport of electrons through both photosystems was described by the system of equations considering that transport is possible when the donor is reduced and the acceptor is oxidized in the same photosystem (Eqs. 13.13–13.17). For PS I, the donor side resistance was related to the turnover rate of Cyt b₆ and considered variable with dependence on the PQH₂ pool and the proton gradient. Acceptor side rate constants for PS I were described by the rate equation of the Fd-NADP reductase. In mesophyll chloroplasts, a Mehler type e[−] flow to O₂ was allowed from PS I to cover any additional demands for ATP beyond that provided from linear e[−] flow to NADP (or, equivalent e[−] flow could be considered for nitrite reduction, Eq. 13.36). The rate constant for e[−] transport from the donor to the acceptor side was considered to be equal to the excitation rate of the photosystem, without assuming any charge recombination is occurring.

B. Electron Transport in Bundle Sheath Chloroplasts

We proposed that the pool of NADPH generated in BS chloroplasts of NADP-ME type species needs to interact with photochemistry in some way to control the stoichiometry of ATP production. In order to mechanistically describe the

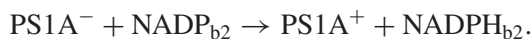
H^+/e^- stoichiometry in the model, the NADPH generated by NADP-ME is linked to an enzyme complex, similar to NADPH dehydrogenase, which reduces PQ coupled to translocation of $2H^+/e^-$, in BS of NADP-ME type C_4 plants. The NAD(P)H dehydrogenase (NDH) carries out the reaction



The $NADPH_{b1}$ pool is assumed to be compartmentalized with NDH resulting in channeled electron transport. Nevertheless, the rate is described according to principles of general enzyme kinetics (Eq. 13.44), with the equilibrium constant dependent on proton back-pressure. K_m values for NADPH and PQ were chosen so that the reaction would saturate within the limits of maximum possible concentrations of the substrates; redox potentials of e^- carriers were taken from (Edwards and Walker, 1983).

The reaction describing electron flow through the Cyt b_6f complex is described on similar principles (Eqs. 13.34, 13.35). The proton budget in the thylakoid lumen is calculated separately for mesophyll and BS chloroplasts.

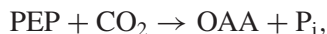
Ferredoxin-NADPH reductase carries out the reaction



The reduced PS I acceptor side, denoted $PSIA^-$ (the equilibrium complex containing Fd^- and FeS^-) is the immediate e^- donor to $NADP_{b2}$. The pool $NADP(H)_{b2}$ is assumed to be complexed with GAP dehydrogenase, so that the rate of PGA reduction is directly linked (equalized) to the speed of the Fd -NADP reductase reaction – an attempt to model the possible electron channeling.

C. Dark Reactions: The C_4 Cycle

PEP carboxylase catalyzes the reaction



where P_i is free phosphate (denoted OP in kinetic equations). The kinetics are described with the standard equation (Eq. 13.44), using estimated affinity of PEPC for CO_2 from analysis of CO_2 fixation in the gas phase, although the actual substrate for the enzyme is bicarbonate. The K_m

for PEP was adjusted to a lower value considering the increased affinity caused by some metabolites (Doncaster and Leegood, 1987; Jiao and Chollet, 1988; Gao and Woo, 1996).

NADP-malate dehydrogenase catalyzes the reaction



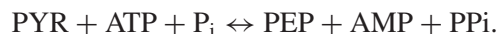
This reaction is also described according to Eq. (13.44). Thioredoxin activation of NADP-MDH is not considered.

Malic enzyme (NADP-ME) catalyzes the following reaction:



Although NADP-ME has a high affinity for NADP, probably reflecting electron channeling (Kanai and Edwards, 1999), a $K_m(NADP)$ of 0.5 mM was used in order to reduce the “stiffness” in running of the model; using the actual micromolar K_m values has little effect on the rate, but the calculated pool of NADP is lower. Thus, artificially increasing some K_m values results in over-estimation of the steady state pool size of the related metabolite, but the reaction rate does not change. Feedback inhibition of the reaction is considered by using a $K_m(CO_2)$ of 1.1 mM. CO_2 is the product of the decarboxylase, and simultaneously, the substrate for Rubisco – resulting in a very small pool if only the dissolved gas is considered. Again, in order to prevent “stiffness” in the model, CO_2 is assumed to be equilibrated with bicarbonate in BS chloroplasts assuming a stromal pH giving a bicarbonate/ CO_2 ratio of 50/1 (although CO_2 equilibration to bicarbonate in the BS cells may be limited by lack of carbonic anhydrase, Ku and Edwards, 1975). This assumption does not influence the steady-state values, because flux rates are dependent on free CO_2 , not bicarbonate. The rate of change in BS CO_2 concentration in transients is only slightly slowed down by this assumption.

Pyruvate P_i dikinase catalyzes the following reaction:



Because P_i is taken as a constant in mesophyll and AMP is not explicitly considered, this reaction is actually modeled, using Eq. (13.44), as



assuming adenylate kinase activity is very high.

PGA enolase and mutase catalyze the following sequence:



which is a means of linking the C₄ and C₃ cycles. Parallel changes in PGA and PEP pools in leaves, and *in vitro* analysis of PGA-PEP interconversions, indicate that these pools are equilibrated via the enolase–mutase reactions (Edwards and Walker, 1983; Leegood and Von Caemmerer, 1989). In the model, these reactions are compartmentalized in BS cells, where the PGA level is high due to synthesis there by Rubisco. When this reaction was assumed to be compartmentalized in mesophyll cells, the predicted accumulation of PEP concentration became very low, limiting photosynthesis due to the low PGA concentration in the mesophyll ($\Delta G'$ values were taken from Mahler and Cordes, 1966).

D. Dark Reactions: The C₃ Cycle

The model for the C₃ carbon reduction cycle in BS cells is similar to that described in Chapter 13, except the adjustment of Rubisco activity is considered, and the amino acid synthesis pathway – the novelty of the present C₃ model in Chapter 13 – is omitted. Initially, simulations were carried out assuming that the Rubisco activation state was constant over the range of CO₂ concentrations and light intensities, with the result that the calculated RuBP pools significantly decreased at low CO₂ concentrations and light intensities, which is not in accordance with experimental data. In order to account for this difference, Rubisco activity is modeled as a decreasing function with decreasing CO₂ or decreasing light, as shown in the corresponding panels of Figs. 14.3 and 14.4. Mechanistically, we assume that the activation state of Rubisco is governed by the flux of reductive power to the BS chloroplasts via the C₄ cycle, linking the Rubisco activation state to electron transport through PS I in BS chloroplasts (Campbell and Ogren, 1990, 1992).

The enzymes PGA-kinase and GAP-dehydrogenase are assumed to function as a complex:



Due to the very low concentration of BPGA and extremely low $K_m(\text{NADPH})$ values (Edwards and Walker, 1983), mathematical treatment of the intermediate BPGA pool is difficult, causing “stiffness” of equations. Therefore, in mesophyll cells the kinase-dehydrogenase reactions are combined and the NADPH/NADP ratio is included in the equilibrium constant (see Chapter 13). In BS, the rates of PGA kinase and GAP dehydrogenase are assumed to be subordinated (equalized) to the rate of electron arrival from PS I, allowing for channeling of electrons directly from PS I to GAP dehydrogenase. This channeling prevents NDH and FNR from forming a futile cycle.

The photorespiratory glycolate pathway is included in an integrated way, considering its overall ATP, NADP, P_i, CO₂, and carbon budget, but not every individual reaction is included, as described also in Chapter 13.

E. Compartmentalization and Metabolite Diffusion

Leaf volume is divided into the following compartments in mesophyll and in BS: cytosol, V_{cym} ; chloroplast stroma, V_{stm} ; chloroplast envelope, V_{mem} ; and chloroplast thylakoid lumen, V_{lum} . The same compartments in BS are V_{cyb} , V_{stb} , V_{meb} and V_{lub} . Thylakoid membrane volume is related to chlorophyll content; the lumen, stroma and cytosol volumes are then related to the thylakoid membrane volume, considering general leaf anatomy and compartment volume measurements (Winter et al., 1993 1994). The rate-equation for diffusion is used to describe metabolite transport between the compartments

$$V = \frac{C_{M1} - C_{M2}}{R_M},$$

where C_{M1} and C_{M2} are the concentrations of a given metabolite M in compartments 1 and 2, respectively, and R_M is the diffusion resistance for this metabolite. The resistance is expressed in units of s mm^{-1} , C in mol l^{-1} , and the rate V in $\text{mol m}^{-2} \text{s}^{-1}$ per leaf area ($1 \text{ s mm}^{-1} = 25 \text{ m}^2 \text{ s mol}^{-1}$). The measured diffusion resistances of BS cells for metabolites are up to an order of magnitude higher than that for CO₂, which may be due to CO₂ having a higher diffusion coefficient than metabolites,

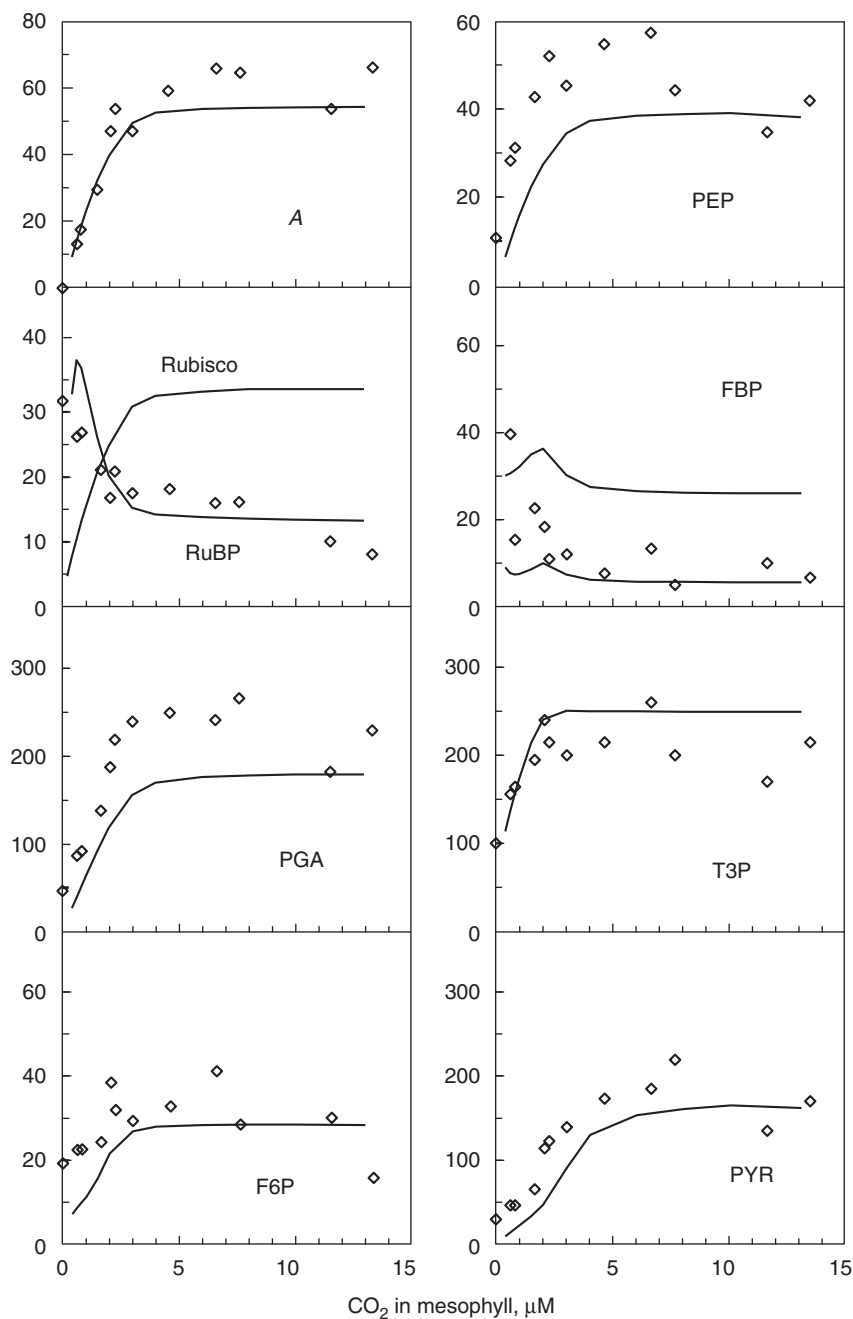


Fig. 14.3. Changes in the rate of CO₂ assimilation *A*, μmol CO₂ m⁻² s⁻¹, and contents of photosynthetic intermediate pools, μmol m⁻² in leaves of *Z. mays* in relation to CO₂ concentration in mesophyll cells (data points from Leegood and Von Caemmerer, 1989) and the same variables (solid lines) calculated from the model at PFD = 1,600 μmol quanta m⁻² s⁻¹, O₂ = 270 μM. The pool size of the active form of Rubisco, micromole active sites per square meter, is shown together with RuBP. The pool of FBP in bundle sheath chloroplasts is shown separately (lower line). (Adapted from Laisk and Edwards, 2000)

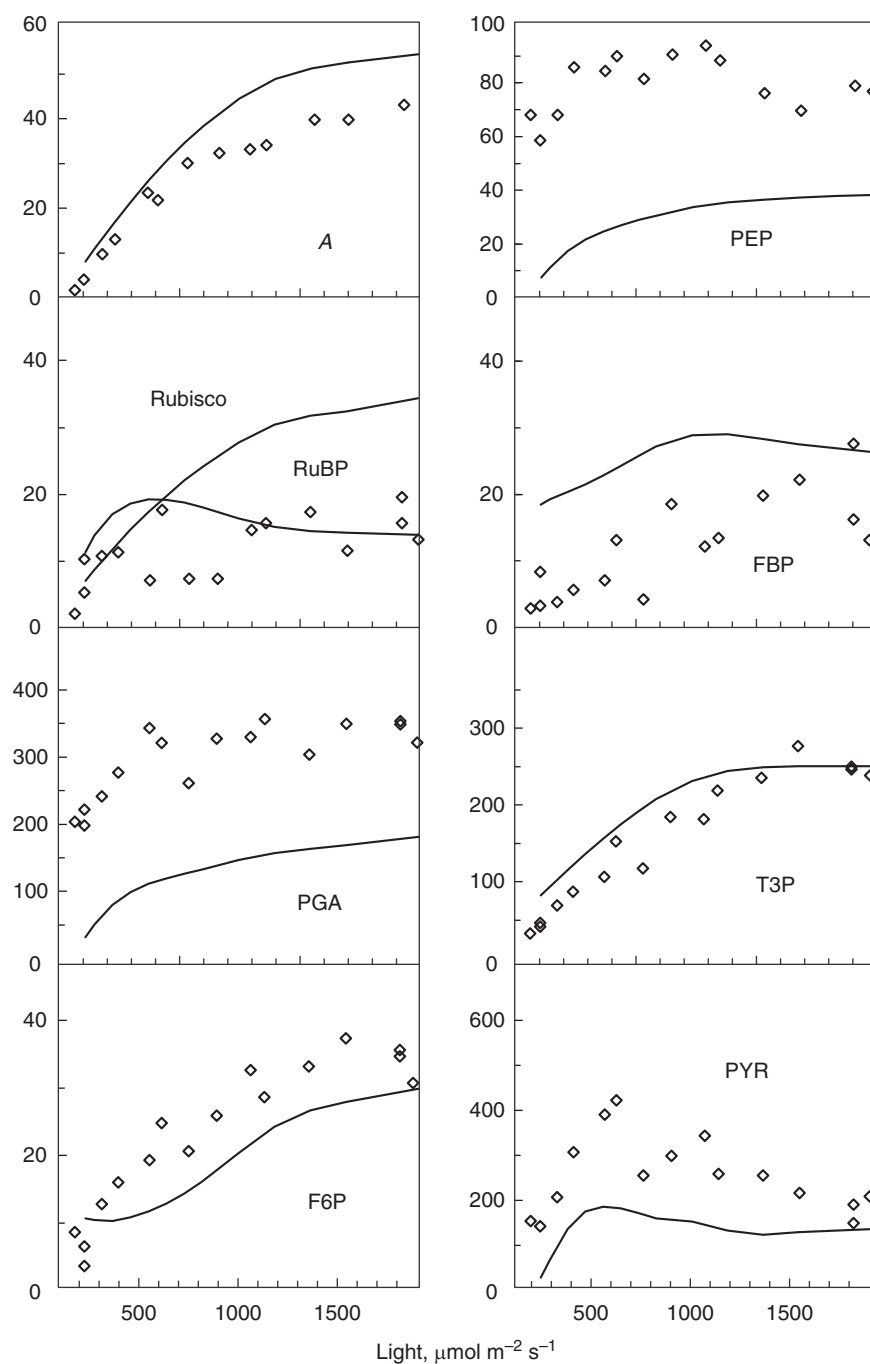


Fig. 14.4. Changes in the rate of CO₂ assimilation A , $\mu\text{mol CO}_2 \text{ m}^{-2} \text{s}^{-1}$, and contents of photosynthetic intermediate pools, $\mu\text{mol m}^{-2}$, in leaves of *Z. mays* in relation to irradiance (Data points from Leegood and Von Caemmerer, 1989), and the same variables (solid lines) calculated from the model. CO₂ concentration in mesophyll cells $C_m = 4 \mu\text{M}$, O₂ = 270 μM . The pool of Rubisco active form, $\mu\text{mol active sites m}^{-2}$, is shown together with RuBP. (Adapted from Laisk and Edwards, 2000)

and to metabolites diffusing only through plasmodesmata, versus CO_2 diffusing about equally through plasmodesmata and cell walls (Weiner et al., 1988; Furbank et al., 1989). In the model, the resistances R_{MAL} , R_{PYR} , R_{PEP} , R_{PGA} and R_{T3P} are assumed to be equal (100 s mm^{-1}), the value was chosen to adjust concentration gradients for transported metabolites (MAL, PYR, PGA, T3P) to no less than 5 mM under saturating light and CO_2 (Stitt and Heldt, 1985) and allowing a maximum rate of photosynthesis of at least $50 \mu\text{mol CO}_2 \text{ m}^{-2} \text{ s}^{-1}$. An intermediate value from literature of 10 s mm^{-1} (He and Edwards, 1996) was used for R_{CO_2} in most calculations below.

IV. Simulations

A. Fitting Rates and Pool Sizes to Experimental Data

Although there are some quantitative differences in model output and experimental values, the model reproduces very well the trends in changes of metabolite pools in response to varying light and CO_2 . Figures 14.3 and 14.4 show the results of model output for pool size data, compared to experimental data for the C_4 plant maize from (Leegood and Von Caemmerer, 1989). Initially, when Rubisco activity was assumed to be constant, the modeled RuBP pool decreased at low CO_2 . This happened because the C_3 cycle remains CO_2 -saturated at externally limiting CO_2 concentrations in the mesophyll cell and, under this condition, the low carboxylation rates are possible only with low RuBP concentrations. Since the experimental results showed increasing RuBP with decreasing CO_2 (Usuda, 1987; Leegood and Von Caemmerer, 1989), the discrepancy was alleviated assuming Rubisco activity decreased at lower CO_2 concentrations, as suggested from early studies (Canvin et al., 1980). If Rubisco activity is assumed to vary as shown in Figs. 14.3 and 14.4, the characteristic behaviour of the RuBP pool is reproduced.

The initial slope of the light response curve for CO_2 fixation (the maximum quantum yield, Fig. 14.3) is reproduced well by partitioning of light harvesting chlorophyll, 45% to PS II, 30.5% to PS I in the mesophyll and 15% to PS I in

the BS, leaving 9.5% for non-photosynthetic light absorption (Cseh et al., 2005). Simulation of the pattern of change in the PYR pool at low irradiation required a fine adjustment of chlorophyll distribution to PS I in mesophyll to 30.5% and increasing the rate constant for alternative electron flow, which increased the capacity for ATP synthesis and PYR utilization. This shows that employing a simple proportionality of the alternative electron flow relative to the level of reduced Fd is insufficient, and that more complex kinetics are required, e.g. the involvement of PGA as hypothesized in the C_3 model (Chapter 13).

There is generally a good fit between modeled and experimental responses of metabolite pools to varying levels of CO_2 and light. The most apparent deviation is in the RuBP pool under limiting CO_2 , fitting the model to data required assuming that Rubisco activity drops in concert with the flux through the C_4 cycle. The proportional changes between PEP and PGA are well-reproduced by inclusion of the PGA enolase-mutase reactions in the BS cytosol. As the rate of photosynthesis increases by increasing CO_2 or light, the rate of PGA production increases and feeds more carbon into PEP which, in turn, increases the capacity of the C_4 cycle.

B. The Ratio of ATP/NADPH in Bundle Sheath Chloroplasts

A critically novel assumption of this modeling of NADP-ME type C_4 photosynthesis is that the photochemical production of ATP in BS chloroplasts is in stoichiometry with the import of reducing power through MAL. By coupling this to chloroplastic NDH, we assume that 2 ATP are produced by photophosphorylation in BS cells per NADPH generated via NADP-ME, as described above. The amount of ATP which is actually available to the C_3 cycle per NADPH produced will be slightly lower due to some utilization of ATP for starch and/or protein synthesis in BS chloroplasts. A numeric experiment was performed to investigate the possible range in which C_4 photosynthesis can function if the ATP/NADPH ratio in BS chloroplasts is variable, e.g. if there were flexible engagement of cyclic photophosphorylation. In this experiment, an allowance was made for use of 5% of the available ATP in BS chloroplasts out-

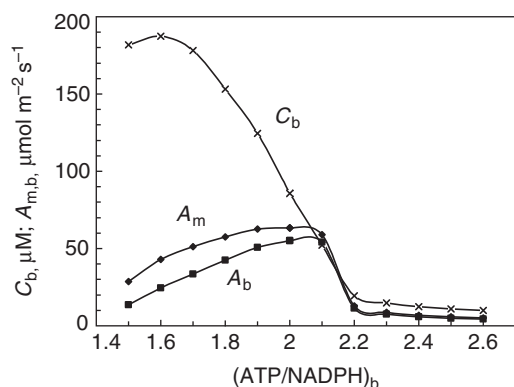


Fig. 14.5. Calculated CO_2 concentration in the bundle sheath, C_b , net CO_2 assimilation rate in bundle sheath, A_b , and CO_2 fixation rate in mesophyll, A_m , and their dependence on the variably preset ATP/NADPH stoichiometry which is available to support CO_2 fixation in bundle sheath chloroplasts. $\text{PFD} = 2,000 \mu\text{mol quanta m}^{-2} \text{s}^{-1}$, $C_m = 4 \mu\text{M}$, an allowance was made for use of 5% of the available ATP in BS chloroplasts outside the C_3 cycle (Laisk and Edwards, 2000)

side the C_3 cycle (e.g. for starch synthesis). The highest rates of photosynthesis occur around ATP/NADPH of 2.0. The system is stable down to ATP/NADPH ratio = 1.5 (Fig. 14.5), at which point all the PGA is reduced in the BS chloroplasts, and there is 50% overcycling. While the rate of CO_2 fixation falls when the ATP/NADPH ratio decreases, the CO_2 concentration in BS, C_b , increases dramatically, with a high level of overcycling which, consequently, decreases the quantum yield of CO_2 fixation. Overcycling is minimal when the BS ATP/NADPH stoichiometric ratio is around 2. With decreasing ATP/NADPH, overcycling increases until a ratio of 1.5 is obtained where one of every two transported CO_2 leaks back to mesophyll. This is accompanied by the extreme high CO_2 concentration C_b of $190 \mu\text{M}$, which compared to no leakage doubles the energy requirements in the C_4 cycle.

At the other extreme, the ATP production can be increased to 2.1 ATP/NADPH, but beyond that, the CO_2 concentrating function collapses. In these calculations, the critical value of 2.1 instead of 2.0 is caused by use of extra ATP (5%) for starch synthesis, but above that, ATP is in excess. This result indicates that the ratio of ATP/NADPH in BS must be strictly controlled in order for the C_4 cycle to function with reasonable overcycling. Overproduction of ATP, e.g. with

uncontrolled cyclic photophosphorylation, would cause the CO_2 concentrating function to collapse. The available ATP/NADPH ratio to support CO_2 fixation in the C_3 cycle in BS chloroplasts needs to be controlled at about 2.0, to adequately concentrate CO_2 and support maximum rates of photosynthesis.

C. Role of Oxygen in C_4 Photosynthesis

Figure 14.6 illustrates the proposed energetics and fluxes associated with photorespiration at the CO_2 compensation point in C_4 plants (shown without alternative ATP consumptions). Then, as determined by the stoichiometries, the rate of CO_2 re-fixation in mesophyll is three times faster than in bundle sheath. The CO_2 (photo-)compensation concentration in bundle sheath cells must be the same as that of C_3 plants, about $1.5 \mu\text{M}$ at room temperature and 21% O_2 (Sumberg and Laisk, 1995), while in mesophyll it is very close to zero. Thus, the concentration difference driving the CO_2 overcycling at the CO_2 compensation point cannot be more than $1.5 \mu\text{M}$. This concentration difference and the CO_2 diffusion resistance (R_{CO_2} of 10 s mm^{-1} in model calculations) allow for a rate of $0.15 \mu\text{mol CO}_2 \text{ m}^{-2} \text{s}^{-1}$, which is the turnover rate of the C_4 cycle at the CO_2 compensation point, while that of the C_3 cycle can only be one third of it, i.e. of $0.05 \mu\text{mol m}^{-2} \text{s}^{-1}$. By comparison, in the C_3 plant sunflower the CO_2 re-fixation rate can be as fast as $10 \mu\text{mol m}^{-2} \text{s}^{-1}$ at the CO_2 compensation point (Laisk and Sumberg, 1994). This clear example helps to explain why in the NADPH-ME type C_4 plants like sorghum the photorespiration rate actually is low even at very low external CO_2 concentrations. Since alternative ATP consumptions are neglected, the overall C_4 energetics at the CO_2 compensation point is close to that of Fig. 14.1, where the C_4 cycle donates CO_2 to Rubisco in the absence of overcycling and photorespiration. In Fig. 14.6, however, we have assumed an additional ATP is consumed in the mesophyll as a consequence of photorespiration (compare Figs. 14.1 and 14.6). Note the energetics in the BS cells in Fig. 14.6 during photorespiration with the consumption of 3 RuBP is the same as that in Fig. 14.1 in the absence of photorespiration (3 NADPH imported and 6 ATP generated photochemically), whereas

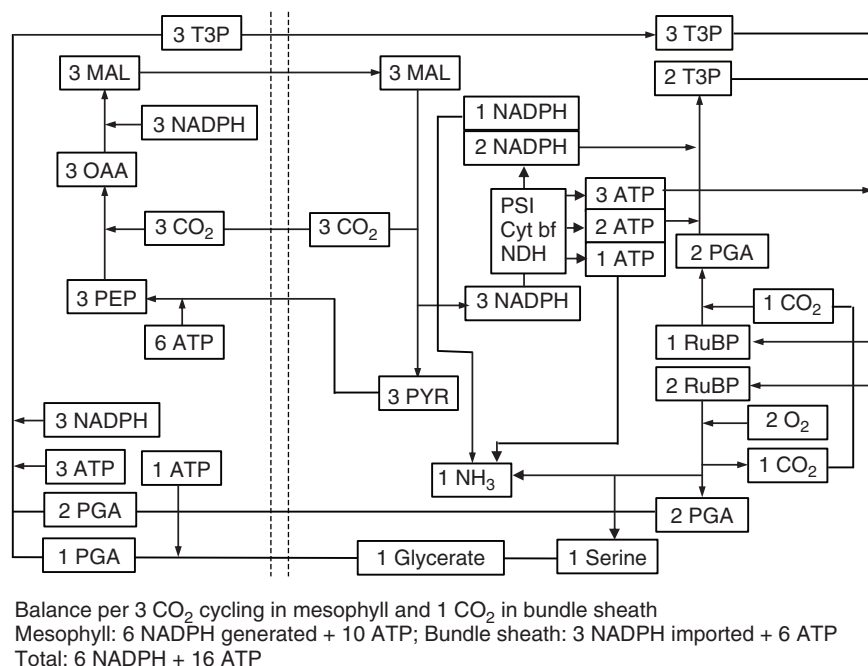


Fig. 14.6. Compartmentation of energy-consuming reactions for C₄ photosynthesis in NADP-ME type species at CO₂ compensation point. Balance is shown per 3 CO₂ cycling between BS and mesophyll; at that time 1 CO₂ is cycling between photorespiration and CO₂ fixation in BS

the mesophyll cells (MC) consume one additional ATP in conversion of glycerate to 3 PGA.

The above example demonstrates how alternative ATP consumption is not the only means of concentrating CO₂ in BS cells of NADP-ME type species. The other reason is consumption of part of the RuBP, the CO₂ acceptor, by photorespiration, which is a common feature of all forms of C₄ photosynthesis. This mechanism, associated with the occurrence of photorespiratory CO₂ evolution, is best demonstrated in the numeric experiment, where the stoichiometry in BS is fixed at 2 ATP/NADPH, and assuming all of the ATP is available to the C₃ cycle (eliminating the alternative ATP consumption for starch synthesis), and with O₂ level set to zero, preventing photorespiration. Under these conditions as discussed earlier, no overcycling occurs (Fig. 14.7a, the leftmost data points), CO₂ is not concentrated in the BS cells (CO₂ = 2 μM when O₂ = 0, A_m = A_b, the condition illustrated in Fig. 14.1) and the rate of photosynthesis is limited to only 10 μmol CO₂ m⁻² s⁻¹. Increasing O₂ causes a simultaneous increase in C_b and photorespiration R_p. Under this condition, the CO₂

concentrating mechanism is based on RuBP oxygenation: the calculated CO₂ concentration in BS cells, C_b, increases to over 50 μM with increasing O₂ concentration (with A_b reaching maximum rates at about 4% O₂ in the gas phase), until the effects of increasing overcycling and increasing R_p become mutually compensated. At higher concentrations, O₂ has a slight negative effect on C₄ photosynthesis, due mainly to increasing energetic losses to support overcycling. With increasing O₂ concentration the requirement for ATP and NADPH per net CO₂ fixed increases. Thus, photorespiration has a direct effect on the concentrating mechanism by alternative RuBP consumption (instead of, but equivalent to, alternative ATP consumption by other processes), as well as generating some CO₂ in the BS compartment.

Figure 14.7b illustrates the effect of O₂ on C₄ photosynthesis with starch synthesis engaged as an alternative ATP consumer. This results in slightly less than 2 ATP/NADPH available for utilization in the C₃ cycle. In this case, in the absence of O₂, there is some CO₂ concentrated in the BS (about 40 μM), which indicates CO₂ overcycling is caused by ATP deficiency in the

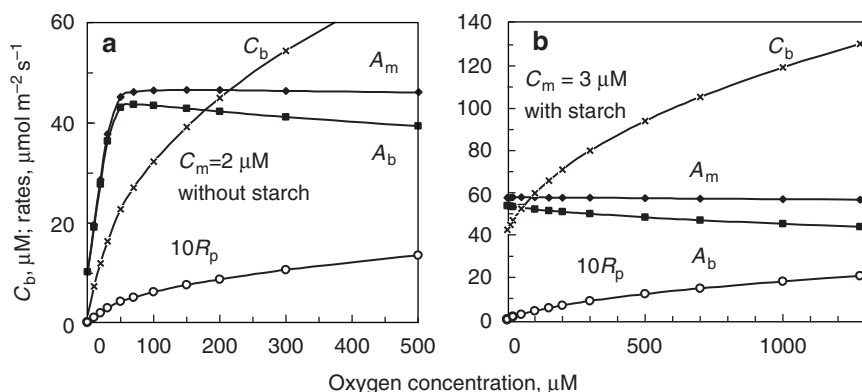


Fig. 14.7. Calculated O₂ dependencies of CO₂ concentration in bundle sheath C_b , net CO₂ assimilation rate in bundle sheath A_b , CO₂ fixation rate in mesophyll, A_m , and rate of CO₂ generation by photorespiration in BS cells (R_p x factor of 10). O₂ levels were varied from 100% (1,280 μM) to zero (21% = 270 μM , calculated for 23°C). Starch synthesis was disabled (panel a) and enabled (panel b); the CO₂ concentration in mesophyll, C_m , is given in panels, PFD = 1,600 $\mu\text{mol quanta m}^{-2} \text{s}^{-1}$ (Laik and Edwards, 2000)

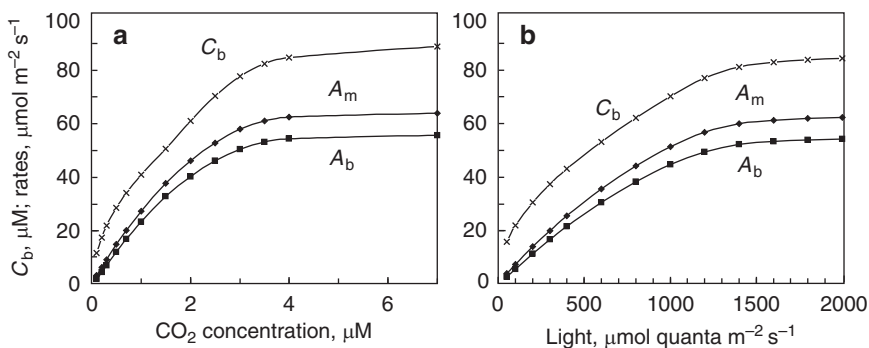


Fig. 14.8. Calculated CO₂ dependencies (panel a) and light dependencies (panel b) of CO₂ concentration in bundle sheath, C_b , net CO₂ assimilation rate in bundle sheath, A_b , and CO₂ fixation rate in mesophyll, A_m (Laik and Edwards, 2000)

absence of RuBP oxygenation. With increasing O₂, there is a large rise in C_b and in overcycling, which is due to the increase in RuBP oxygenation. However, with increasing O₂, there is only a gradual decline in CO₂ fixation, indicating that O₂, a competitor for RuBP, is rising slightly faster in BS than the other competitor, CO₂.

D. CO₂ and Light Responses: Connection of C₄ and C₃ Cycles

With either increasing CO₂ or increasing light (Fig. 14.8), the calculated CO₂ concentration in BS cells reaches values up to 80 μM . At this C_b , the calculated fraction of overcycling is 0.13. The fraction of overcycling remains almost constant with decreasing light or decreasing CO₂ until light levels become low, in agreement with exper-

imental analyses using carbon isotope fractionation (Henderson et al., 1992).

A difference from C₃ photosynthesis is that the C₄ cycle is not self-regenerative, but its metabolite pools are slowly equilibrated with the metabolite pools of the C₃ cycle. A slow response of C₄ photosynthesis to increased external CO₂ concentration, different from the response in C₃ plants, was the primary evidence that C₄ photosynthesis is intrinsically CO₂ saturated in its C₃ part even though its C₄ part may externally be CO₂ limited. It has been proposed that this occurs through regulation of the pool size of C₄ cycle metabolites due to the chemical equilibration between PEP of the C₄ cycle, and PGA of the C₃ cycle, via an enolase–phosphoglyceromutase link (Laik and Edwards, 1997). With this connection of the two cycles in the model, the calculated

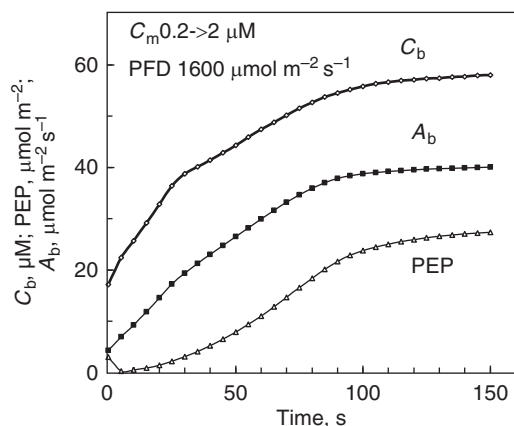


Fig. 14.9. Modeled transients of C_4 photosynthesis from low to high CO_2 (Laisk and Edwards, 2000)

transients in response to a sudden increase in CO_2 concentration are similar to measured transients: a faster initial response is followed by the slower linearly increasing phase (Fig. 14.9). The transient in C_b follows the same pattern as that in A_b , although the C_3 cycle is CO_2 saturated (ATP/NADPH limited) over this range of C_b values. The level of PEP, which is initially very low at the beginning of the transient, increases in parallel with the linear phase of the A_b transient. The length of the transient, about 100 s, fits well with the experimental data (Laisk and Edwards, 1997).

V. Knowns and Unknowns in Photosynthesis

The models for C_3 (Chapter 13) and C_4 photosynthesis (this chapter) may be considered quantitative theory of leaf-level photosynthesis. As any theory, it can test the adequacy of our present knowledge and predict novel findings. When theoretical (simulated) results agree with integral experiments, it provides confidence in our understanding of photosynthesis (here we use the term “integral” for leaf-level experiments by analogy to responses obtained by integration of the model differential equations). Discrepancies between integral experiments and model responses indicate deficiencies in understanding, either faulty experimental results, or inadequate schemes are incorporated in the model. Rearrangements in the model structure resulting in better agreement with integral experiments, even though not yet

proven by differential (e.g. at the cellular/plastidic or molecular-level) experiments, may be considered theoretical predictions. In this sense, the biology of photosynthesis has obtained a completed internal theoretical structure as in “exact sciences”, e.g. in astrophysics, where the internal processes of stars are analyzed on the basis of integral measurements of light emitted from their surface. In contrast to star models, in some parts of the photosynthesis model the detailed information at the plastid and molecular level considerably exceeds that which is included in the model (although in other parts the molecular information may be missing, e.g. the function of NDH dehydrogenase). In most cases it is an intuitive (logical) decision as to how the surplus molecular level information is approximated (considered integrally) in differential equations describing the partial processes. If the integral model responses are correct against experiments, one may believe the intuitive integration of details was made correctly. Here we evaluate some of these aspects of the photosynthetic models described in Chapters 13 and 14.

A. Photosystem II

Photosystem II is one of the best studied parts of photosynthesis. The notion that excitation and electron transport processes in PS II are so fast that they are not limiting the actual photosynthetic rates is correctly integrated into the models. Averaging the variable kinetics of different S-states on the donor side and the two-electron gating at Q_B on the acceptor side did not cause significant distortions in the calculated electron transport rates (but see e.g. Chapter 6 for the importance of S-states). Although the whole antenna is considered homogeneous in the model (neglecting it being composed of several light-harvesting complexes and the core complex), the assumption of excitation equilibration between the whole antenna and the reaction center rather well reproduces the millisecond kinetics of fluorescence responses (considering that this time interval is characteristic to electron transport through the whole chain). Neglecting the excitonic connectivity between individual PS IIs and between PS II and PS I in the model did not contradict the integral fluorescence measurements, indicating that the excitonic connectivity between

the antennae of different PS II may not be as significant as is sometimes believed. Since state transitions occur at very low light, the preset constant antenna cross-sections corresponded to the stabilized states. The model indicates the 810 nm signal is a very sensitive indicator of antenna balancing between the photosystems at low light; so, further modeling the mechanism of state transitions in parallel with measurements of 810 nm transmittance would be a challenge.

Modeling of the “energy dependent” qE component of NPQ as being dependent on luminal pH indicates that our basic understanding of the pH dependent qE mechanism is correct. Importantly, the luminal pH value generated by the electron-coupled H⁺ translocation supporting ATP synthesis driving CO₂ assimilation is indeed the same pH that controls qE. The light dependence of F_m is well simulated, assuming two-proton equilibrium between the luminal protons and the protonated quenching site. Thus, the role of luminal pH as the driver of qE is well understood, although molecular rearrangements in the Chl antenna controlling the life-time of excitation are still a subject of investigations (Ruban et al., 2007). However, the time kinetics of qE are not mechanistically reproduced by the model. Evidently, the assumption that proton-motive force (pmf) is entirely based on H⁺ concentration needs revision. The model does not yet consider that mostly the electric field component of pmf is generated immediately after illumination, which slowly relaxes due to the movement of counter ions, leading to a relatively slow decrease in luminal pH (Cruz et al., 2001) – a possible mechanism for the temporal kinetics of qE.

B. Cytochrome b₆f and Interphotosystem Electron Transport

In the thylakoid membrane, protein concentration is critically high, to the extent that protein crowding may restrict PQ diffusion due to percolation (Tremmel, 2003). In the model we neglected the problem, assuming PQ diffusion is still very fast compared to the whole-chain electron transport time. The modeled light response of fluorescence yield did not contradict this assumption, indicating that there is no extraordinarily high PS II acceptor side reduction during high rates

of photosynthesis, as would be expected if PQ diffusion were rate-limiting. Diffusion of PC has shown to be partially rate-limiting during unphysiologically fast (uncoupled, to methyl viologen) electron transport (Kirchhoff et al., 2004). However, the problem is not significant under physiological conditions in leaves, where only a small part (10–20%) of PC remains unoxidized due to diffusional restrictions under saturation pulses supporting the fastest possible electron transport (Laisk et al., 2007; Oja et al., 2008). Therefore, none of the diffusible electron carriers is critically rate-limiting even during the fastest steady-state photosynthesis; rather, Cyt b₆f is the true rate-limiting enzyme complex in the interphotosystem electron transport chain.

The complex kinetics of the obligatory Q-cycle (Sacksteder et al., 2000) were approximated by the kinetic equation of a single enzyme oxidizing PQH₂ and reducing PC⁺, characterized by its V_m and K_m values. The maximum intrinsic turnover of Cyt b₆f is significantly faster than necessary for maximum steady-state photosynthesis, but its actual turnover is down-regulated in concert with the consumption of protons for ATP synthesis (Laisk and Oja, 1994; Laisk et al., 2005). This “photosynthetic control” of Cyt b₆f turnover was modeled by setting the equilibrium constant of the electron transfer to be dependent on thermodynamic proton back-pressure (equivalent to considering protons as reaction substrates, but assuming the protonation/deprotonation rate constants are very fast). This integrated picture adequately describes steady-state electron transport, but problems occur in the level of photosynthetic control of Cyt b₆f turnover. The steady-state 810 nm signal was not well reproduced (Fig. 13.2 of Chapter 13), but this problem could be caused by inadequate modeling of cyclic electron transport as well. However, the modeled post-illumination transients of the 810 nm signal, T_{810} , clearly differed from the measured curves (Laisk et al., 2006). Proton back-pressure significantly reduces the reaction rate when the reaction product, PC, is relatively reduced (high level of product), but not much when PC is highly oxidized (product absent). As a result, the modeled post-illumination T_{810} transients become curvilinear, but their initial slope is only slightly down-regulated by proton back-pressure (Laisk et al., 2006). In contrast, the

initial slope of experimental curves, as measured at completely oxidized PC, clearly varies with the photosynthetic control (Laisk and Oja, 1994; Laisk et al., 2005). These differences indicate the possibility of proton channeling between individual Cyt b_6f and ATP synthases (Dilley, 1991), eventually resulting in kinetics where the rate of electron transport through any individual Cyt b_6f complex is directly equal to the rate of ATP hydrolysis in CRC. However, there still must be a common pool of free protons in the lumen space rather slowly equilibrated with the proton channels to ATP synthase, controlling NPQ.

The inadequate understanding of the control of Cyt b_6f turnover by ATP hydrolysis is only one side of the coin. The present inadequate understanding of *in vivo* control of Cyt b_6f turnover is best demonstrated during photosynthetic oscillations. Comparison of the calculated and measured phase trajectories (Fig. 13.6, Chapter 13), demonstrates that a regulatory function is missing in the model. This “missing link” may be the regulation of Cyt b_6f directly by PS I acceptor side reduction, as suggested by Johnson (2003). The mechanism of this redox control is not known; however, physical complexing and decomplexing of Cyt b_6f with PS I (Zhang et al., 2001), as well as the movement of Cyt b_6f between the grana and stroma thylakoids (Vallon et al., 1991), may be involved.

C. ATP Synthase

This complex molecular machine was modeled as an integrated single enzyme characterized by its V_m and K_m values, but considering the equilibrium constant depends on the transmembrane proton gradient, as suggested by Mitchell (1966). No special control of proton conductivity of the ATP synthase, as has been proposed by Kanazawa and Kramer (2002), was involved. If the ATP synthase is not considered isolated, but kinetically directly linked to CRC, then the adjustments of ADP and phosphate concentrations to light intensity and CO_2 and O_2 concentrations will kinetically control proton translocation as reaction substrates. The modeling shows that, during photosynthesis, ATP synthase is operating not far from the chemical equilibrium between ADP, P_i , ATP and pmf , under which condition its

kinetic properties are of secondary importance. The absence of light control of ATPase activity in the model does not significantly distort the light responses from those of experiments (though the dark inactivation of ATP synthase may be important in modeling the chloroplast metabolism in the dark).

A basic problem in understanding photosynthesis is how the stoichiometric balance is adjusted between synthesis of NADPH and ATP. Provided the requirement of ATP synthase is $12H^+/3ATP$ (Rumberg et al., 1990), the basic requirement of CRC is satisfied by the $12H^+/2NADPH$ stoichiometry of linear electron flow. Only a small ATP deficiency may develop due to its consumption in starch synthesis and other secondary metabolism. Discovery of 14 subunits III in the ring structure of the CF_0 of spinach ATP synthase (Seelert et al., 2000, 2003; Scheuring et al., 2001) raised the question whether the actual requirement could be $14H^+/3ATP$. In this case a proton deficiency of at least 17% must be covered by additional H^+ -coupled electron flow, such as cyclic electron flow around PS I or linear electron flow to alternative acceptors other than CO_2 (Noctor and Foyer, 2000; Avenson et al., 2005). In our C_3 and C_4 models, using a stoichiometry of $12H^+/3ATP$, and considering fixation of CO_2 and consumption in photorespiration are major requirements for energy in the chloroplast, there was generally a good fit of simulations to experimental photosynthetic responses. Small extra (alternative) ATP requirements for starch and protein synthesis could be covered by electron transport to alternative acceptors, mainly for nitrite reduction. Most importantly, oscillations with the right period were reproduced without any adjustments of pool sizes or reaction rates in the feedback chain. When a ratio of $14H^+/3ATP$ was assumed, the required rates of N reduction became unrealistically high, the experimentally verified equality of the flux ratio of $O_2/CO_2 \sim 1.0$ was violated, oscillations could not be reproduced, and, for stability, the model required fast alternative electron flow and/or H^+ -coupled cyclic electron transport, which was in conflict with experimental results with potato (Laisk et al., 2007). Therefore, either the number of CF_0 subunits is 12 in chloroplastic ATP synthase in potato, and not 14 as measured in spinach chloroplasts (Seelert et al., 2003), or

the number of patterns identified as CF₀ subunits on the atomic force micrographs by Seelert et al. does not determine the number of protons required per turn of the rotor.

This modeling indicates the importance of controlling the photochemical production of assimilatory power within the required stoichiometry with the reducing power, and how detrimental small shifts in the ratio can be to performance of photosynthesis. For example, the typical ETR is about $200 \mu\text{mol e}^- \text{m}^{-2} \text{s}^{-1}$ during light-saturated photosynthesis, requiring an accompanying synthesis of $150 \mu\text{mol ATP m}^{-2} \text{s}^{-1}$ to support CO₂ fixation in the CRC. If the stoichiometry is violated, e.g. by decreasing the ATP/NADPH ratio by 0.1%, $0.2 \mu\text{mol e}^- \text{m}^{-2} \text{s}^{-1}$ would remain unutilized in CRC and begin to accumulate at the acceptor side of PS I. Typically, the density of PS I is somewhat less than $2 \mu\text{mol m}^{-2}$ leaf area. If the unaccepted electrons accumulate right on the PS I acceptor side, it would take only 10 s to block photosynthesis (exponential time constant). If a total pool of redox-equilibrated compounds of $20 \mu\text{mol e}^- \text{m}^{-2}$ accommodates the unaccepted electrons, the time of closure will be extended to 100 s. This example of the time range is typical for photosynthetic transients, such as dark-light induction and the related oscillations. It is evident that such small stoichiometry violations must be under constant feedback control, as suggested in the C₃ model, but are extremely difficult to measure, requiring special equipment and precise calibration procedures (Laisk et al., 2002, 2007; Oja et al., 2003, 2007).

D. Photosystem I

This complex is the hub of the photosynthetic machinery. Understanding processes controlling the donation of electrons to the donor side, and branching of electrons between different routes on the acceptor side, is a key to understanding photosynthesis.

Electron flow through PS I is controlled simultaneously from its donor and acceptor side. At the donor side Cyt b₆f controls the rate of PQH₂ oxidation, as well as CET is probably circulating via Cyt b₆f. If these two rates together are slower than the potential of ETR through PS I, the donor pigment P700 becomes partially oxidized, regulating the actual ETR through PS I to be

equal to the rate of electron supply. On the other hand, if the donor side electron flow exceeds the capacity of the acceptor side chain to deliver electrons to CRC plus CET and alternative pathways, some PS I become closed on their acceptor side. The term “PS I acceptor side closure”, while being in use for some time (Klughammer and Schreiber, 1994), is not easy to understand. There is a sequence of very low-potential electron carriers on the PS I acceptor side between the primary electron acceptor and Fd – the central reduced compound which accumulates and signals availability of reducing power for photosynthesis. Only from the lowest-potential primary acceptors (quinone and Chl) the back-reaction to P700⁺ is sufficiently fast to compete with electron donation from PC, when the latter is reduced and docked at PS I (Golbeck, 1987). Our modeling has shown that PC may become considerably oxidized even at very low PFDs, as it is dependent on excitation partitioning between the photosystems, a situation that could facilitate the back-reaction. Nevertheless, the known rate constant for the back-reaction directly from Fd⁻ or the FeS carriers is still too slow and, even if it occurs, it must be distinguished from cyclic electron flow (see below). For direct back-reaction, a very high reduction of Fd is required in order to “close” PS I by reducing the primary acceptors and cause a back-reaction from them. Contrary to this theory, in reality PS I becomes partially closed even when Fd is only partially reduced (Klughammer and Schreiber, 1994; Laisk et al., 2005). In the model, we simulated this situation by setting a “false” E_m , rather close to the E_m of Fd, for the carrier that is able to close PS I (conditionally denoted FeS in the model). In this way we approximated the possible electron channeling on the PS I acceptor side. Such modeling assumes, Fd is not a freely diffusing pool (at least not all Fd), but every PS I is equipped with a channeled chain of carriers from the primary acceptors to Fd and FNR. Only by this assumption did it become possible to reproduce a gradual decrease of photosynthesis with a gradual increase in reduction of Fd (see also Laisk, 1993).

In the C₄ model for NADP-ME type C₄ plants, strict control of the stoichiometry of synthesis of NADPH and ATP is required in BS chloroplasts. This was achieved by assuming electron channeling, through complexing of malic enzyme

with NDH, and/or with FNR, NADPH and GAP dehydrogenase forming a complex with channeling of electrons to reduce BPGA. The formation of enzyme complexes which channel metabolites and electrons has been a hot topic for some time (Keleti, 1990; Süss et al., 1995; Anderson et al., 2005). Only by experimental evidence for complexes through structural studies, combined with modeling of kinetic differences between diffusion versus channeling systems, will new vistas be opened.

Mainstream linear electron flow passes through ferredoxin-NADP reductase, FNR, dropping over a large redox potential difference. Since normally the chloroplast NADP system is not highly reduced (Gerst et al., 1994), the FNR reaction is significantly out of equilibrium. Not much is known about the regulation of this enzyme, except its dark inactivation (Talts et al., 2007) and peculiar kinetics with respect to NADPH (Cassan et al., 2005). The simple mechanism of inactivation of FNR by NADPH, which is accomplished in the model by setting a relatively low $K_m(\text{NADPH})$ value (high inhibitory affinity of NADPH), was sufficient to prevent the NADP system from overreduction at high light and low CO_2 concentrations; even so, Fd becomes significantly reduced. Further kinetic studies of FNR will help to better understand this important electron transfer step.

As already noted above, ferredoxin is the control center of the photosynthetic machinery. In the model, thiol groups of light-activated CRC enzymes are reversibly redox-equilibrated with the ferredoxin-thioredoxin system, resulting in the symmetrical temporal kinetics of activation and inactivation. In reality, activation is fast, but inactivation is slow, indicating that the two processes are controlled by different redox reactions. The fast enzyme activation, as well as the calculated fast regeneration of CRC intermediates, does not agree with the relatively slow dark-light activation of photosynthesis (Laisk et al., 2006). Since the measured induction rate is faster in the presence of O_2 (Laisk and Oja, 1998), the process is evidently controlled by regeneration of ATP facilitated by the Mehler reaction, rather than by regeneration of CRC pools or enzyme activation.

Measurement of the rate of Mehler type oxygen reduction during photosynthesis has been a difficult task (Ruuska et al., 2000). A recent new

approach, based on the speed of P700 reduction following removal of O_2 (Laisk et al., 2007; see also Section C above), showed that the rate of the Mehler reaction is only a fraction of a per cent of the linear flow under CO_2 and light saturating conditions, at 21% O_2 . The process was modeled as a first-order reaction between Fd^- and O_2 occurring at a very slow rate, but sufficient to induce a small positive response of photosynthesis to increasing O_2 concentration in C_3 plants under high CO_2 and light, as was first observed many years ago (Viil et al., 1972, 1977).

E. Cyclic Electron Flow

Another ongoing problem is related to PS I cyclic electron flow, which involves branching off from Fd^- and donating electrons back to PS I donor side ("cycling around cyclic", summarized by Ulrich Schreiber 1988, personal communication). Since the initial work of D. Arnon (Arnon et al., 1958; Arnon, 1959; Arnon and Chain, 1975, 1979), it has been a common belief that electrons can cycle around PS I, generate *pmf* and photophosphorylate ADP, along with the occurrence of linear electron flow. Experimental evidence about the existence of cyclic photophosphorylation is based on the measurements of P/O ($=\text{ATP}/\text{O}_2$) ratios in isolated thylakoids and chloroplasts, mainly based on the fact that the P/O ratio is low when electrons are flowing to methyl viologen, but increases when NADP (or O_2) is the acceptor, causing higher reduction of Fd (Hosler and Yocum, 1985, 1987). It has been common dogma to classify electron transport as non-cyclic and cyclic, emphasizing an essential role of cyclic photophosphorylation in photosynthesis (e.g. to make up any deficit of ATP from linear electron flow in C_3 plants, to protect against photoinhibition, and to function in PS II deficient chloroplasts in some C_4 plants). However, in these early works no cycling of electrons around PS I was measured and the obtained P/O ratios could indicate variable contribution of the Q-cycle under those extreme experimental conditions (methyl viologen) as well. The actual cycling of electrons around PS I was indicated by the 810 nm signal, showing faster post-illumination re-reduction of P700 than possible by the linear flow (Clarke

and Johnson, 2001; Golding and Johnson, 2003; Golding et al., 2004). This reinforced the trust in cyclic phosphorylation as a universal mean for correcting any stoichiometry differences between ATP and NADPH during photosynthesis (Kramer et al., 2004). However, after the 810 nm signal was quantitatively calibrated, it became evident that the cyclic rate was very slow during light-limited photosynthesis, but became very fast during light-saturated photosynthesis (Laisk et al., 2005, 2007). The most conflicting result was the occurrence of fast cyclic electron flow under far-red light, where photosynthetic ATP consumption was negligible (Talts et al., 2007). Recently we showed fast cycling of electrons around PS I (up to $40\text{ e}^- \text{ s}^{-1}$ per PS I) under intense far-red light, when linear electron flow was blocked to less than $5\text{ e}^- \text{ s}^{-1}$ per PS I by very low CO₂ and O₂ concentrations (A. Laisk and E. Talts, 2008, unpublished). These results, showing largely different ratios between the cyclic and linear flow suggested CET cannot be functional in adjusting the ATP/NADPH ratio by photosynthetic phosphorylation. Rather, the fast cycling of electrons around PS I either is uncoupled from proton transport and ATP synthesis, having a photoprotective nature (Laisk et al., 2007) or a regulated mechanism short-circuiting the proton gradient must be postulated. If cyclic flow is not phosphorylating, the definition of the energy-dissipating PS I cycle closely approaches the term charge recombination. Therefore, the mechanistic basis for such fast uncoupled electron transport from PS I acceptor side to the donor side is not yet clear. An attempt to model it as charge recombination resulted in strong dependence of the recombination rate on the presence of P700⁺, in disagreement with experiments, and indicating a preceding lower-potential electron carrier is the likely electron acceptor. The assumption of a first-order reaction cycling electrons from Fd⁻ to PC⁺ (as well as to Cyt f) also was not perfect, because the modeled cyclic rate became already too fast at low PFDs, causing a significantly higher reduction of P700 and PC than observed experimentally. Considering that experimentally the kinetics of electron cycling are impossible to distinguish from the kinetics of linear electron flow through Cyt b₆f, a possible pathway involving a kind of reversal of the Q-cycle may be $\text{Fd} \rightarrow \text{the novel Cyt } c_1 \rightarrow \text{Cyt } b_h \rightarrow \text{Cyt } b_l \rightarrow \text{Rieske}$

$\text{FeS} \rightarrow \text{Cyt } f \rightarrow \text{PC} \rightarrow \text{P700}$. This pathway can function only when PQH₂ oxidation is restricted by high H⁺ back-pressure, so that Rieske FeS is available for the back-reaction from Cyt b_h, in accordance with the increased cycling rates at light saturation of photosynthesis. However, an alternative explanation for the presence of disproportionately fast cyclic rates would be if proton leakage is regulated as an overflow valve, stabilizing the maximum ΔpH at a certain level. Then the cyclic flow might still be coupled with proton translocation. Thus, elucidating the mechanistic basis for the energy-dissipating PS I cycle (or overflow type control of proton leakage) is a necessary next step in understanding electron transport pathways of photosynthesis. Since most studies on CET have been performed on C₃ plants, its occurrence, how it responds to changes in rates of photosynthesis, and its potential contribution to the high ATP requirements, remains to be investigated in C₄ plants.

F. The C₃ Cycle of Carbon Assimilation

The kinetics of the unique enzyme Rubisco is probably one of the best-understood parts of photosynthesis. Models based on the competition between the substrates CO₂ and O₂ (Laisk, 1970; Farquhar et al., 1980; Von Caemmerer and Farquhar, 1981) have found the widest application, however, attempts to predict leaf photosynthetic rate on the basis of Rubisco content have been unsuccessful. The average k_{cat} value of a Rubisco reaction site can vary from 1.5 to at least $4\text{--}5\text{ s}^{-1}$ in leaves, indicating that, the higher the Rubisco content, the lower its average activation state (Eichelmann and Laisk, 1999; Eichelmann et al., 2008). Mechanisms, and factors, controlling Rubisco activation are poorly understood, although results from some models of Rubisco activation (Von Caemmerer, 2000; Chapter 9 of this book by Susanne Von Caemmerer, Graham Farquhar and Joseph Berry), have potential for incorporation into metabolic models of photosynthesis.

With the exception of Rubisco, only one general equation (Eq. 13.44, Chapter 13) has been applied to describe the overall kinetics of the remaining 12 enzymatic steps in the C₃ cycle, which have different catalytic properties and

reaction mechanisms. In cells, enzyme concentrations are usually high and metabolite channeling may occur (noted in Section D), altering the kinetics. If metabolic channeling is demonstrated, it would be a fascinating challenge for modeling. However, the relatively high concentration of substrates and products during photosynthesis significantly linearizes the kinetic responses of single enzymes, hiding details of the enzymatic mechanism. Therefore, even more important than the kinetic details of enzymes are the feedback and feedforward loops controlling the outflow of carbon from the CRC, such as control of activation of starch synthesis by the PGA/ P_i ratio, and the fine control of sucrose synthesis by inactivation of the cytosolic FBPase by F2,6BP. The mathematical formulations applied currently for such regulation may be insufficient. For example, the mathematics applied to describe control of the activation state of sucrose phosphate synthetase neglects the time dependent kinetics of protein dephosphorylation/phosphorylation controlling the activity of the enzyme (Huber et al., 1991), which will be most important when the oscillatory transients are modeled.

G. C₄ plant CO₂ Concentrating Mechanisms

Among C₄ plants there are three biochemical types of C₄ cycles, NADP-ME, NAD-ME and PEP-CK. This chapter describes the first C₄ metabolic model for the NADP-ME type, which includes all of the enzymatic steps of the C₄ cycle, C₃ cycle, sucrose and starch biosynthesis. The basic idea of the model is based on experimental evidence that the C₄ cycle is CO₂ saturated (limited by energetic cofactors) at all external CO₂ concentrations (Laisk and Edwards, 1997), in accordance with evidence that photorespiration is slow at all CO₂ concentrations down to strictly limiting values (Laisk and Edwards, 1998). These facts suggested that energetic cofactors NADPH and ATP are available in BS (where PS II activity is absent) in strict stoichiometry with imported CO₂. It is generally accepted that NADPH is imported into BS in 1:1 stoichiometry with CO₂ via MAL oxidation by the malic enzyme. The present model indicates

there must be tight control of ATP production in BS chloroplasts relative to the rate of generation of NADPH by NADP-ME. However, the availability of ATP from cyclic photophosphorylation in BS has been considered to be unlimited. Long before evidence that cyclic electron flow can become uncoupled from H⁺ translocation (Section E above), we suggested that uncontrolled cyclic phosphorylation cannot function in BS of NADP-ME type C₄ species. Rather the rate of production of ATP may be regulated by the interaction of NADPH with the NDH complex. One proposed function of NDH is to keep cyclic electron flow charged with electrons, the level of which could be controlled by availability of NADPH generated from NADP-ME (Ivanov et al., 2007). Strict control is achieved in the current model by having the electrons pass through the transport chain from NADPH generated by NADP-ME → NDH → PQ → Cyt b₆f → PS I → Fd → NADPH → BPGA only once, supporting the synthesis of exactly 2 ATP per 2 e⁻ that are necessary for the phosphorylation of one PGA and one Ru5P, to complete the energy requirement in the CRC in BS. Since 2e⁻ transport through Cyt b₆f is coupled with translocation of 4 H⁺, in cooperation with the mesophyll (enough for one ATP), we suggested that the electrons are donated from NADPH to PQ via NADPH dehydrogenase (NDH), an analog of the mitochondrial Complex I enzyme, where electron transport is coupled with the translocation of 4H⁺/NADPH, sufficient for the synthesis of the other necessary ATP (Laisk and Edwards, 2000). This was a bold hypothesis, as only very slow NDH activity had been shown in C₃ plants at that time and there was no question of function of cyclic photophosphorylation. If a central role of NDH (or a similarly functioning enzyme) in C₄ photosynthesis is found, it would be a nice example of modeling predicting function in the biology of photosynthesis.

Regardless of the mechanism, cyclic or linear, fine control of the ATP/NADPH ratio is required. This current modeling of NADP-ME type C₄ photosynthesis shows that the critical ATP/NADPH ratio to support the C₃ cycle in BS chloroplast is within a narrow range around 2.0. Several possible mechanisms have been proposed as to how BS chloroplasts can maintain

this ratio. These include a NDH dependent cyclic flow, linear electron flow from MAL to NADPH to PQ to PS I, and an antimycin A sensitive ferredoxin–plastoquinone reductase-dependent CEF with NDH contributing to control the redox poise (Takabayashi et al., 2005; Ivanov et al., 2007). It is known that expression of the plastid-NDH is higher in BS than in mesophyll chloroplasts of NADP-ME type species, sorghum (Kubicki et al., 1996) and maize (Takabayashi et al., 2005), which suggests NDH has a role in photochemical production of ATP in BS chloroplasts. A recent detailed analysis (Majeran et al., 2008) reports a 1,000 kDa BS specific NDH complex in maize, with associated proteins of unknown function (a complex altogether containing more than 15 proteins). The authors speculate that this novel complex possibly functions for inorganic carbon concentration – an independent conclusion based on structural evidence.

In NAD-ME and PEP-CK plants there is photochemical production of reducing power in BS chloroplasts, so function is not dependent on delivery of reductive power from the C₄ cycle, as in the NADP-ME plants. These subtypes also have more photorespiration under limiting CO₂ than NADP-ME type species (Furbank and Badger, 1982; Laisk and Edwards, 1998; Kiirats et al., 2002). Interestingly, in NAD-ME type plants, the NDH complex is suggested to be higher in mesophyll chloroplasts (which have a high demand for ATP relative to NADPH in synthesis of aspartate) than in BS chloroplasts (Takabayashi et al., 2005). Despite there being such large biochemical and structural differences among C₄ taxa (Edwards and Voznesenskaya, in press) the fraction of overcycling among the C₄ species examined is astonishingly similar, about 20% (Henderson et al., 1992) or 20–40% (Kubasek et al., 2007). This may be associated with a similar control of the relative capacities of the C₄ and C₃ cycle (e.g. PEPC/Rubisco ratio), with C₄ pathway overcycling driven in part by RuBP oxygenase activity, and with the effectiveness of concentrating CO₂ in BS cells dependent on diffusive resistance to CO₂ loss (controlled in different ways among C₄ species). More comparative experimental and modeling studies are needed to understand common versus unique features of the CO₂ concentrating mechanisms among C₄ species.

Acknowledgments

This work was supported by Targeted Financing Theme SF0180045s08 from Estonian Ministry of Education and Science and Grants 6607 and 6611 from Estonian Science Foundation, and by NSF Grant IBN-0641232.

References

- Anderson LE, Gatla N and Carol AA (2005) Enzyme co-localization in pea chloroplasts: glyceraldehyde-3-P dehydrogenase, triose-P isomerase, aldolase and seduheptulose biphosphatase. *Photosynth Res.* 83: 317–328
- Arnon DI (1959) Conversion of light into chemical energy in photosynthesis. *Nature* 184: 10–21
- Arnon DI and Chain RK (1975) Regulation of ferredoxin-catalyzed photosynthetic phosphorylation. *Proc Natl Acad Sci USA* 72: 4961–4965
- Arnon DI and Chain RK (1979) Regulatory electron transport pathways in cyclic photophosphorylation. *FEBS Lett* 102: 133–138
- Arnon DI, Whatley FR and Allen MB (1958) Assimilatory power in photosynthesis. *Science* 127: 1026–1034
- Avenson TJ, Kanazawa A, Cruz JA, Takizawa K, Ettinger WE and Kramer DM (2005) Integrating the proton circuit into photosynthesis: progress and challenges. *Plant Cell Environ* 28: 97–109
- Berry J and Farquhar GD (1978) The CO₂ concentration function of C₄ photosynthesis: a biochemical model. In: Hall D, Coombs J and Goodwin T (eds) *Proceedings of the 4th International Congress on Photosynthesis*, pp 119–131. Biochemical Society, London
- Campbell WJ and Ogren WL (1990) Electron transport through photosystem I stimulates light activation of ribulose biphosphate carboxylase/oxygenase (Rubisco) by rubisco activase. *Plant Physiol* 94: 479–484
- Campbell WJ and Ogren WL (1992) Light activation of Rubisco by Rubisco activase and thylakoid membranes. *Plant Cell Physiol* 33: 751–756
- Canvin DT, Berry JA, Badger MR, Fock H and Osmond B (1980) Oxygen exchange in leaves in the light. *Plant Physiol* 66: 302–307
- Cassan N, Lagouette B and Setif P (2005) Ferredoxin-NADP⁺ reductase. Kinetics of electron transfer, transient intermediates, and catalytic activities studied by flash-absorption spectroscopy with isolated photosystem I and ferredoxin. *J Biol Chem* 280: 25960–25972
- Clarke JE and Johnson GN (2001) In vivo temperature dependence of cyclic and pseudocyclic electron transport in barley. *Planta* 212: 808–816
- Collatz GJ, Ribas-Carbo M and Berry JA (1992) Coupled photosynthesis-stomatal conductance model for leaves of C₄ plants. *Aust J Plant Physiol* 19: 519–538

- Cruz JA, Sacksteder CA, Kanazawa A and Kramer DM (2001) Contribution of electric field ($\Delta\psi$) to steady-state transthylakoid proton motive force (pmf) in vitro and in vivo. Control of pmf parsing into $\Delta\psi$ and ΔpH by ionic strength. *Biochemistry* 40: 1226–1237
- Cseh Z, Vianelli A, Rajagopal S, Krumova S, Kovacs L, Papp E, Barzda V, Jennings R and Garab G (2005) Thermo-optically induced reorganizations in the main light harvesting antenna of plants. I. Non-Arrhenius type temperature dependence and linear light-intensity dependencies. *Photosynth Res* 86: 263–273
- Dilley RA (1991) Energy coupling in chloroplasts: a calcium-gated switch controls proton fluxes between localized and delocalized proton gradients. *Current Topics in Bioenergetics* 16: 265–317
- Doncaster HD and Leegood RC (1987) Regulation of phosphoenolpyruvate carboxylase activity in maize leaves. *Plant Physiol* 84: 82–87
- Edwards GE (1986) Carbon fixation and partitioning in the leaf. In: Shannon JC, Knievel DP and Boyer CD (eds) *Regulation of Carbon and Nitrogen Reduction and Utilization in Maize*, pp 51–65. Waverly Press, Baltimore, MD
- Edwards GE and Ku MSB (1987) The biochemistry of C_3 - C_4 intermediates. In: Hatch MD and Boardman NK (eds) *The Biochemistry of Plants*, pp 275–325. Academic, New York
- Edwards GE and Voznesenskaya E (2009) C_4 photosynthesis: Kranz forms and single-cell C_4 in terrestrial plants. In: Raghavendra A and Sage RF (eds) *Photosynthesis and Related CO_2 Concentrating Mechanisms*. Advances in Photosynthesis and Respiration. Springer, Dordrecht, in press
- Edwards GE and Walker DA (1983) C_3 , C_4 : Mechanisms, and Cellular and Environmental Regulation, of Photosynthesis. Blackwell, Oxford/London
- Eichelmann H and Laisk A (1999) Ribulose-1,5-bisphosphate carboxylase/oxygenase content, assimilatory charge and mesophyll conductance in leaves. *Plant Physiol* 119: 179–189
- Eichelmann H, Talts E, Oja V, Rasulov B, Padu E and Laisk A (2008) Rubisco activity is related to photosystem I in leaves. In: Allen JF, Gantt E, Golbeck JH and Osmond B (eds) *Photosynthesis. Energy from the Sun: 14th International Congress on Photosynthesis*, pp 853–856. Springer, Dordrecht, The Netherlands
- Farquhar GD, Von Caemmerer S and Berry JA (1980) A biochemical model of photosynthetic CO_2 assimilation in leaves of C_3 species. *Planta* 149: 78–90
- Furbank RT and Badger MR (1982) Photosynthetic oxygen exchange in attached leaves of C_4 monocotyledons. *Aust J Plant Physiol* 9: 553–558
- Furbank RT, Stitt M and Foyer CH (1985) Intercellular compartmentation of sucrose synthesis in leaves of *Zea mays* L. *Planta* 164: 172–178
- Furbank RT, Jenkins CLD and Hatch MD (1989) CO_2 concentrating mechanism of C_4 photosynthesis. *Plant Physiol* 91: 1364–1371
- Gao Y and Woo KC (1996) Regulation of phosphoenolpyruvate carboxylase in *Zea mays* by protein phosphorylation and metabolites and their roles in photosynthesis. *Aust J Plant Physiol* 23: 25–32
- Gerst U, Schönknecht G and Heber U (1994) ATP and NADPH as the driving force of carbon reduction in leaves in relation to thylakoid energization by light. *Planta* 193: 421–429
- Golbeck JH (1987) Structure, function and organization of the photosystem I reaction center complex. *Biochim Biophys Acta* 895: 167–204
- Golding AJ and Johnson GN (2003) Down-regulation of linear and activation of cyclic electron transport during drought. *Planta* 218: 107–114
- Golding AJ, Finazzi G and Johnson GN (2004) Reduction of the thylakoid electron transport chain by stromal reductants – evidence for activation of cyclic electron transport upon dark adaptation under drought. *Planta* 220: 356–363
- Hatch MD (1987) C_4 photosynthesis: A unique blend of modified biochemistry, anatomy and ultrastructure. *Biochim Biophys Acta* 895: 81–106
- He D and Edwards G (1996) Estimation of diffusive resistance of bundle sheath cells to CO_2 from modeling of C_4 photosynthesis. *Photosynth Res* 49: 195–208
- Henderson SA, Von Caemmerer S and Farquhar GD (1992) Short-term measurements of carbon isotope discrimination in several C_4 species. *Aust J Plant Physiol* 19: 263–285
- Hosler JP and Yocum CF (1985) Evidence for two cyclic photophosphorylation reactions concurrent with ferredoxin-catalyzed non-cyclic electron transport. *Biochim Biophys Acta* 808: 21–31
- Hosler JP and Yocum CF (1987) Regulation of cyclic photophosphorylation during ferredoxin-mediated electron transport. Effect of DCMU and the NADPH/NADP⁺ ratio. *Plant Physiol* 83: 965–969
- Huber JL, Hite DRC, Outlaw WH Jr and Huber SC (1991) Inactivation of highly activated spinach leaf sucrose-phosphate synthase by dephosphorylation. *Plant Physiol* 95: 291–297
- Ivanov B, Asada K and Edwards GE (2007) Analysis of donors of electrons to photosystem I and cyclic electron flow by redox kinetics of 700 in chloroplasts of isolated bundle sheath strands of maize. *Photosynth Res* 92: 65–74
- Jiao JA and Chollet R (1988) Light/dark regulation of maize leaf phosphoenolpyruvate carboxylase by *in vivo* phosphorylation. *Arch Biochem Biophys* 261: 409–417
- Johnson G (2003) Thiol regulation of the thylakoid electron transport chain – a missing link in the regulation of photosynthesis. *Biochemistry* 42: 3040–3044
- Kanai R and Edwards EE (1999) The biochemistry of C_4 photosynthesis. In: Sage RF and Monson RK (eds) *C_4 Plant Biology*, pp 49–87. Academic Press, New York

- Kanazawa A and Kramer DM (2002) *In vivo* modulation of nonphotochemical exciton quenching (NPQ) by regulation of the chloroplast ATP synthase. *Proc Natl Acad Sci USA* 99: 12789–12794
- Keleti T (1990) Coupled reactions and channelling: their role in the control of metabolism. In: Cornish-Bowden A and Cárdenas ML (eds) *Control of Metabolic Processes*, pp 259–270. Plenum Press, New York
- Kiirats O, Lea PJ, Franceschi VR and Edwards GE (2002) Bundle sheath diffusive resistance to CO₂ and effectiveness of C₄ photosynthesis and refixation of photorespired CO₂ in a C₄ cycle mutant and wild-type *Amaranthus edulis*. *Plant Physiol* 130: 964–976
- Kirchhoff H, Schöttler MA and Maurer JWE (2004) Plastocyanin redox kinetics in spinach chloroplasts: evidence for disequilibrium in the high potential chain. *Biochim Biophys Acta* 1659: 63–72
- Klughammer C and Schreiber U (1994) An improved method, using saturating light pulses, for the determination of photosystem I quantum yield via P700⁺ - absorbance changes at 830 nm. *Planta* 192: 261–268
- Kramer DM, Avenson TJ and Edwards GE (2004) Dynamic flexibility in the light reactions of photosynthesis governed by both electron and proton transfer reactions. *Trends Plant Sci* 9: 349–357
- Ku MSB and Edwards GE (1975) Photosynthesis in mesophyll protoplasts and bundle sheath cells of various type of C₄ plants. IV. Enzymes of respiratory metabolism and energy utilizing enzymes of photosynthetic pathways. *Z. Pflanzenphysiol* 77: 16–32
- Kubasek J, Setlik J, Dwyer S and Santrucek J (2007) Light and temperature alter carbon isotope discrimination and estimated bundle sheath leakiness in C₄ grasses and dicots. *Photosynth Res* 91: 47–58
- Kubicki A, Funk E, Westhoff P and Steinmüller K (1996) Differential expression of plastome-encoded *ndh* genes in mesophyll and bundle sheath chloroplasts of the C₄ plant *Sorghum bicolor* indicates that the complex I-homologous NAD(P)H-plastoquinone oxidoreductase is involved in cyclic electron transport. *Planta* 199: 276–281
- Laisk A (1970) A model of leaf photosynthesis and photorespiration. In: Shetlik I (ed) *Prediction and Measurement of Photosynthetic Productivity*, pp 295–306. PUDOC, Wageningen
- Laisk A (1993) Mathematical modeling of free-pool and channeled electron transport in photosynthesis: evidence for a functional supercomplex around photosystem I. *Proc R Soc Lond B* 251: 243–251
- Laisk A and Edwards GE (1997) CO₂ and temperature-related induction of photosynthesis in C₄ plants: an approach to the hierarchy of rate-limiting processes. *Aust J Plant Physiol* 24: 505–516
- Laisk A and Edwards GE (1998) Oxygen and electron flow in C₄ photosynthesis: Mehler reaction, photorespiration and CO₂ concentration in bundle sheath. *Planta* 205: 632–645
- Laisk A and Edwards GE (2000) A mathematical model of C₄ photosynthesis: The mechanism of concentrating CO₂ in NADP-malic enzyme type species. *Photosynth Res* 66: 199–224
- Laisk A and Oja V (1994) Range of the photosynthetic control of postillumination P700 reduction rate in sunflower leaves. *Photosynth Res* 39: 39–50
- Laisk A and Oja V (1998) *Dynamic Gas Exchange of Leaf Photosynthesis. Measurement and Interpretation*. CSIRO, Collingwood, Australia
- Laisk A and Sumberg A (1994) Partitioning of the leaf CO₂ exchange into components using CO₂ exchange and fluorescence measurements. *Plant Physiol* 106: 689–695
- Laisk A, Oja V, Rasulov B, Rämme H, Eichelmann H, Kasparova I, Pettai H, Padu E and Vapaavuori E (2002) A computer-operated routine of gas exchange and optical measurements to diagnose photosynthetic apparatus in leaves. *Plant Cell Env* 25: 923–943
- Laisk A, Eichelmann H, Oja V and Peterson RB (2005) Control of cytochrome b₆f at low and high light intensity and cyclic electron transport in leaves. *Biochim Biophys Acta* 1708: 79–90
- Laisk A, Eichelmann H and Oja V (2006) C₃ photosynthesis *in silico*. *Photosynth Res* 90: 45–66
- Laisk A, Eichelmann H, Oja V, Talts E and Scheibe R (2007) Rates and roles of cyclic and alternative electron flow in potato leaves. *Plant Cell Physiol* 48: 1575–1588
- Leegood RC and Von Caemmerer S (1989) Some relationships between contents of photosynthetic intermediates and the rate of photosynthetic carbon assimilation in leaves of *Zea mays* L. *Planta* 178: 258–266
- Mahler HR and Cordes EH (1966) *Biological Chemistry*. Harper & Row, New York
- Majeran W, Zybaïlov B, Ytterberg AJ, Dunsmore J, Sun Q and Van Wijk KJ (2008) Consequences of C₄ differentiation for chloroplast membrane proteomes in maize mesophyll and bundle sheath cells. *Mol Cell Proteomics* 7: 1609–1638
- Mitchell P (1966) Chemiosmotic coupling in oxidative and photosynthetic phosphorylation. *Biol Rev* 41: 445–502
- Monson RK, Edwards GE and Ku MSB (1984) C₃-C₄ intermediate photosynthesis in plants. *Bioscience* 34: 563–574
- Noctor G and Foyer CH (2000) Homeostasis of adenylate status during photosynthesis in a fluctuating environment. *J Exp Bot* 51: 347–356
- Oja V, Eichelmann H, Peterson RB, Rasulov B and Laisk A (2003) Deciphering the 820 nm signal: redox state of donor side and quantum yield of photosystem I in leaves. *Photosynth Res* 78: 1–15
- Oja V, Eichelmann H and Laisk A (2007) Calibration of simultaneous measurements of photosynthetic carbon dioxide uptake and oxygen evolution in leaves. *Plant Cell Physiol* 48: 198–203
- Oja V, Eichelmann H and Laisk A (2008) Equilibrium or disequilibrium? A dual-wavelength investigation of photosystem I donors. In: Allen JF, Gantt E, Golbeck JH and

- Osmond B (eds) Photosynthesis. Energy from the Sun: 14th International Congress on Photosynthesis, pp 687–690. Springer, Dordrecht, The Netherlands
- Peisker M (1979) Conditions for low and oxygen-independent CO₂ compensation concentrations in C₄ plants as derived from a simple model. *Photosynthetica* 13: 198–207
- Ruban AV, Berera R, Iliaia C, Van Stokkum IHM, Kennis JTM, Pascal AA, Van Amerongen H, Bruno R, Horton P and Van Grondelle R (2007) Identification of a mechanism of photoprotective energy dissipation in higher plants. *Nature* 450: 575–578
- Rumberg B, Schubert K, Strelow F and Tran-Anh T (1990) The H⁺/ATP coupling ratio at the H⁺-ATP-synthase of spinach chloroplasts is four. In: Baltscheffsky M (ed) Current Research in Photosynthesis, Vol. III, pp 125–128. Kluwer, Dordrecht, The Netherlands
- Ruuska SA, Badger MR, Andrews TJ and Von Caemmerer S (2000) Photosynthetic electron sinks in transgenic tobacco with reduced amounts of rubisco: little evidence for significant Mehler reaction. *J Exp Bot* 51: 357–368
- Sacksteder CA, Kanazawa A, Jacoby ME and Kramer DM (2000) The proton to electron stoichiometry of steady-state photosynthesis in living plants: a proton-pumping Q cycle is continuously engaged. *Proc Natl Acad Sci USA* 97: 14283–14288
- Sage RF (2004) The evolution of C₄ photosynthesis. *New Phytol* 161: 341–370
- Scheuring S, Fotiadis D, Möller C, Müller SA, Engel A and Müller DJ (2001) Single proteins observed by atomic force microscopy. *Single Mol* 2: 59–67
- Seelert H, Poetsch A, Dencher NA, Engel A, Stahlberg H and Müller DJ (2000) Proton powered turbine of a plant motor. *Nature* 405: 418–419
- Seelert H, Dencher NA and Müller DJ (2003) Fourteen protomers compose the oligomer II of the proton-rotor in spinach chloroplast ATP synthase. *J Mol Biol* 333: 337–344
- Stitt M and Heldt HW (1985) Intercellular metabolite distribution and properties of the cytosolic fructosebisphosphatase in leaves of *Zea mays* L. *Planta* 164: 179–188
- Sumberg A and Laisk A (1995) Measurement of the CO₂/O₂ specificity of Rubisco in leaves. In: Mathis P (ed) Photosynthesis: From Light to Biosphere, Vol. V, pp 615–618. Kluwer, Dordrecht/Boston, MA/London
- Süss K-H, Prokhorenko I and Adler K (1995) In situ association of calvin cycle enzymes, ribulose-1,5-bisphosphate carboxylase/oxygenase activase, ferredoxin-NADP⁺ reductase, and nitrite reductase with thylacoid and pyrenoid membranes of *Chlamydomonas reinhardtii* chloroplasts as revealed by immunoelectron microscopy. *Plant Physiol* 107: 1387–1397
- Takabayashi A, Kishine M, Asada K, Endo T and Sato F (2005) Differential use of two cyclic electron flows around photosystem I for driving CO₂-concentration mechanism in C₄ photosynthesis. *Proc Natl Acad Sci USA* 102: 16898–16903
- Talts E, Oja V, Rämme H, Rasulov B, Anijalg A and Laisk A (2007) Dark inactivation of ferredoxin-NADP reductase and cyclic electron flow under far-red light in sunflower leaves. *Photosynth Res* 94: 109–120
- Tremmel IG, Kirchhoff H, Weis E and Farquhar GD (2003) Dependence of plastoquinol diffusion on the shape, size, and density of integral thylakoid proteins. *Biochim Biophys Acta* 1607: 97–109
- Usuda H (1987) Change in levels of intermediates of the C₄ cycle and reductive pentose phosphate pathway under various light intensities in maize leaves. *Plant Physiol* 84: 549–554
- Vallon O, Bulte L, Dainese P, Olive J, Bassi R and Wollman F-A (1991) Lateral redistribution of cytochrome b6/f complexes along thylakoid membranes upon state transitions. *Proc Natl Acad Sci USA* 88: 8262–8266
- Viil J, Laisk A, Oja V and Pärnik T (1972) Positive influence of oxygen on photosynthesis. *Doklady AN SSSR (Proc Acad Sci USSR)* 204 (5): 1269–1271 (in Russian)
- Viil J, Laisk A, Oja V and Pärnik T (1977) Enhancement of photosynthesis caused by oxygen under saturating irradiance and high CO₂ concentrations. *Photosynthetica* 11 (3): 251–259
- Von Caemmerer S (2000) Biochemical Models of Leaf Photosynthesis. CSIRO Publ, Collingwood, Australia
- Von Caemmerer S and Farquhar GD (1981) Some relationships between the biochemistry of photosynthesis and the gas exchange of leaves. *Planta* 153: 376–387
- Von Caemmerer S and Furbank RT (1999) Modeling C₄ photosynthesis. In: Sage RF and Monson RK (eds) C₄ Plant Biology, pp 173–211. Academic, San Diego, CA/London/Boston, MA/New York/Sydney/Tokyo/Toronto
- Weiner H, Burnell JN, Woodrow IE, Heldt HW and Hatch MD (1988) Metabolite diffusion into bundle sheath cells from C₄ Plants. *Plant Physiol* 88: 815–822
- Winter H, Robinson DG and Heldt HW (1993) Subcellular volumes and metabolite concentrations in barley leaves. *Planta* 191: 180–190
- Winter H, Robinson DG and Heldt HW (1994) Subcellular volumes and metabolite concentrations in spinach leaves. *Planta* 193: 530–535
- Zhang H, Whitelegge JP and Cramer WA (2001) Ferredoxin: NADP⁺ oxidoreductase is a subunit of the chloroplast cytochrome b6f complex. *J Biol Chem* 276: 38159–38165

Chapter 15

Flux Control Analysis of the Rate of Photosynthetic CO₂ Assimilation

Ian E. Woodrow*

School of Botany, The University of Melbourne, VIC 3010, Australia

Summary.....	349
I. Introduction.....	350
II. Flux Control Coefficients: Theory and Challenges.....	352
III. Reversible Reactions Can Be Flux Limiting.....	352
A. Aldolase.....	353
B. Transketolase.....	354
IV. Small Control Coefficients Are Hard to Detect.....	354
A. Glyceraldehyde 3-Phosphate Dehydrogenase.....	354
B. Phosphoribulokinase.....	355
C. Triose Phosphate/Phosphate Translocator.....	355
D. Fructose 1,6-Bisphosphatase.....	356
E. Carbonic Anhydrase.....	356
F. Rubisco Activase.....	356
V. Enzymes with Higher Control Coefficients.....	356
A. Sedoheptulose 1,7-Bisphosphatase.....	356
B. Ribulose 1,5-Bisphosphate Carboxylase/Oxygenase.....	357
VI. Photosynthetic Electron Transport.....	358
VII. Concluding Remarks.....	358
Acknowledgments.....	359
References.....	359

Summary

Metabolic flux control analysis offers an opportunity to understand how fluxes are determined and thus how they can be increased. Enzymes are assigned a control coefficient (usually between zero and one) which is a measure of the degree to which the flux is sensitive to small changes in enzyme concentration. This chapter examines research on the application of control analysis to the photosynthetic system of C₃ plants, specifically the net rate of CO₂ fixation. Control coefficients have been measured for a number of the enzymes, typically by reducing the concentration of a target enzyme in transgenic plants then comparing their flux and enzyme concentrations to those of the wild type. There have been surprisingly many difficulties with this approach. Firstly, many transgenic plants have markedly lower enzyme concentrations than the wild type, so it has been difficult to make accurate estimations of the enzyme-flux relationship in the vicinity of the wild type value. Second, natural variation, compounded by variation due to a lack of precision in measurements, has often required a very large number of

* Author for correspondence, e-mail: iewood@unimelb.edu.au

replicates in order to detect significant values. Many studies have not used sufficient replication. Third, confounding variables, such as ontogenetic variation and untargeted changes in the concentration of other enzymes, have not always been identified and taken into account. As a consequence of these challenges, there are few studies in which control coefficients have been detected with a high degree of certainty. This situation is set to improve, however, with the use of transgenic plants with both an increased and decreased target enzyme concentration. Several such studies have now been published, and in two cases, estimates of the control coefficients have been markedly improved.

I. Introduction

Photosynthesis is the driver of biomass acquisition in plants, which is closely coupled to fitness related attributes such as size and seed production. Given this connection, it is logical that natural selection has operated on the photosynthetic system to gain the maximum output for the minimum input of limiting resources (e.g. nitrogen from which the enzymes are constructed). Such maximization is indeed a complex and shifting target given the complex variability – long and short term – of environmental factors that impact both directly and indirectly on the photosynthetic system. At the whole plant level, resources are allocated to create a certain amount of leaf material, and this material can be spread over a greater or lesser area, i.e., a higher or lower leaf area ratio (LAR) for a given leaf weight ratio. The advantage of a high LAR is increased light capture and photosynthesis, but this is constrained e.g. by an increased rate of water loss and susceptibility to herbivory. At the leaf level, resources are allocated to the various pathways of carbon metabolism (i.e. photosynthesis, respiration etc.) such that carbon can be exported to sustain respiration in non-photosynthetic tissues and growth. The advantage of high relative investment in photosynthesis is constrained inter alia by the need to maintain sufficiently high maintenance respiration rates.

Abbreviations: A_{sat} – light saturated rate of net CO₂ assimilation; C_i – intercellular CO₂ concentration; C_n^J – control coefficient of enzyme n with respect to flux J ; CA – carbonic anhydrase; GAPDH – glyceraldehyde phosphate dehydrogenase; FBPase – fructose 1,6-bisphosphatase; LAR – leaf area ratio; FNR – NADP⁺-dependent ferredoxin oxidoreductase; PRK – phosphoribulokinase; Rubisco – ribulose 1,5-bisphosphate carboxylase/oxygenase; SBPase – sedoheptulose 1,7-bisphosphatase; TPT – triose phosphate/phosphate translocator

Nevertheless, consistent with this central role in plant growth and fitness, photosynthesis in most plants receives the single largest allocation of protein resources (measured as nitrogen) of all of the metabolic pathways, and the CO₂ fixing enzyme, ribulose bisphosphate carboxylase/oxygenase (Rubisco), receives the largest allocation of N of all of the catalysts.

Experimental assessment of whether the photosynthetic system (Fig. 15.1) yields the maximum output (carbon skeletons) for the minimum input of resources (mainly N, but other inputs could be considered) has proved a considerable experimental challenge for which there is still no satisfactory answer. An early step in attempting to understand the optimisation of photosynthesis was the application of metabolic flux control theory (Kacser and Burns, 1973) to analysis of the rate of photosynthesis. Such flux control analysis did not explicitly address the issue of optimisation; rather it sought to quantify the degree to which individual enzymes control the rate of photosynthesis with the implicit assumption that in an optimised system with a complex network of regulatory feedbacks, flux control is shared amongst most if not all of the catalysts. The first analyses (Woodrow, 1986; Pettersson and Ryde-Pettersson, 1988) used models that were parameterised by measurements of both substrate concentrations and kinetic constants to estimate the flux control coefficients – the sensitivity of the flux to changes in enzyme concentration. These models showed that indeed flux control was shared amongst many enzymes, but at high light intensities, control was largely in the hands of Rubisco. The models also emphasised the role of CO₂ delivery to Rubisco; significant control could reside with all of the resistances to CO₂ transfer to the stroma: the boundary layer, the stomata, and aspects of the internal architecture of leaves (Woodrow et al., 1990).

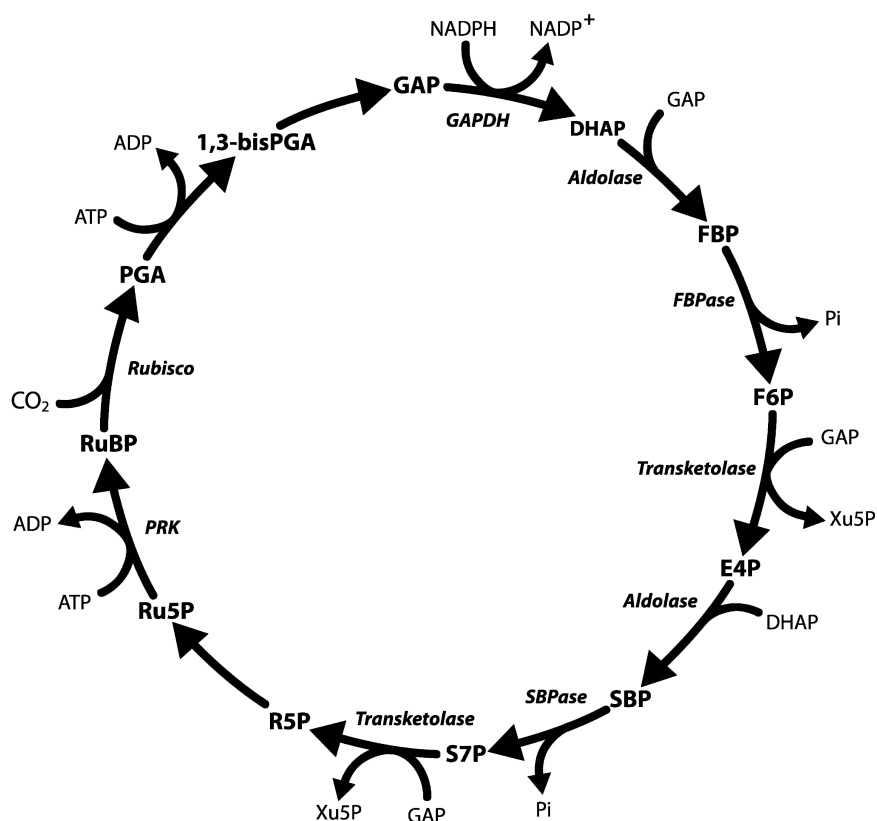


Fig. 15.1. Scheme of the Calvin Cycle, showing the enzymes (labelled on the inner side of the circle) for which flux control analysis has been undertaken. Note that the stoichiometry of the Rubisco catalysed reaction is not included (i.e. 2 PGA molecules produced per carboxylation) and not all of the reactions are listed (i.e. processing of Xu5P and carbon export from the cycle). Abbreviations for the intermediate compounds are as follows: PGA, 3-phosphoglycerate; 1,3-bisPGA, 1,3-bisphosphoglycerate; GAP, glyceraldehyde 3-phosphate; DHAP, dihydroxyacetone 3-phosphate; Pi, inorganic phosphate; FBP, fructose 1,6-bisphosphate; F6P, fructose 6-phosphate; E4P, erythrose 4-phosphate; Xu5P, xylulose 5-phosphate; SBP, sedoheptulose 1,7-bisphosphate; S7P, sedoheptulose 7-phosphate; R5P, ribose 5-phosphate; Ru5P, ribulose 5-phosphate; RuBP, ribulose 1,5-bisphosphate

The advent of genetic engineering offered the opportunity to refine flux control analysis and to investigate optimisation by titrating the effects of changes in resource allocation one enzyme at a time. Until recently, such titrations generally involved reductions in enzyme concentration but increasingly we are seeing enhancements (e.g. Wu et al., 2007). Despite the initial excitement, enzyme titrations have not yielded results that are markedly better than the initial modelling results. The reasons for this have largely involved uncontrolled variables in the flux experiments, the difficulty of making small changes in enzyme concentration, and the difficulty of measuring the flux with sufficient accuracy. Put simply, in order to measure the effect of a change in enzyme

concentration on a flux at least two individual plants must be compared under the assumption that the only variable is the concentration of the target enzyme. Moreover, the difference in target enzyme concentration needs to be relatively small, which demands very accurate measurement of the flux. These have proved extremely difficult demands to meet given the limitations of equipment and the range of variables that can be introduced into experiments by varying ontogenetic effects, genetic background and growth conditions. Under such conditions, highly replicated and rigorously analysed experiments are mandatory (Small, 1993; Thomas and Fell, 1994; Cornish-Bowden and Hofmeyr, 1994; Pettersson, 1996), but this has not generally been the case.

This chapter examines research involving photosynthetic CO₂ fixation in C₃ plants and the titration of enzyme concentrations using transgenic plants. An emphasis is placed on identifying cases where we can be relatively certain that non-zero control coefficients have been detected.

II. Flux Control Coefficients: Theory and Challenges

The flux control coefficient for enzyme n with respect to flux is defined as

$$C_n^J = \frac{\partial J}{\partial [E_n]} \frac{[E_n]}{J}, \quad (15.1)$$

which is the relative change of the flux J per (infinitesimal) relative change in enzyme concentration $[E_n]$. The flux control coefficient is thus a dimensionless number, usually between 0 and 1. A flux control coefficient of zero indicates that the flux is insensitive to changes in the activity of that enzyme, and a coefficient of unity indicates that relative changes in enzyme activity effect equal relative changes in flux (Kacser and Burns, 1973; Heinrich and Rapoport, 1974). It is also noteworthy that flux control coefficients for a defined system sum to unity, but this will not be fully applicable to the photosynthetic system because some enzymes (most notably Rubisco) have active site concentrations that are comparable to their substrate concentrations (Woodrow and Mott, 1993).

There are two key points about control coefficients that are important to consider when appraising the experimental data on flux control analysis of the photosynthetic system. First, they are extremely difficult to measure because of the experimental challenges attached to estimating the slope of the flux versus $[E]$ relationship at the $[E]$ of interest (usually the wild type $[E]$ value). The simplest and most accurate way to estimate this slope and thus the control coefficient would be to measure the flux in a leaf, then to apply a highly specific inhibitor of an enzyme and re-measure the flux (Small, 1993). In this way, the only variable would be enzyme activity. If the flux could be measured very accurately and the change in enzyme activity were relatively small, then a good estimate of the flux control coefficient could be made. Such an approach has

apparently only been used for one enzyme in the Calvin-Benson cycle – Rubisco (Woodrow and Mott, 1988). In this case, the inhibitor was O₂ – which inhibits the carboxylase activity of Rubisco but promotes the oxygenase activity – and the assumption was that other effects on electron transport and respiration did not confound the control coefficient estimate. Otherwise, all of the experimental studies of flux control and photosynthesis have involved transgenic plants in which the concentration of a targeted enzyme was titrated, usually downwards. Such approaches are very difficult to adapt for estimation of especially relatively small flux (Table 15.1) control coefficients, firstly because the concentration of the targeted enzyme is not the only variable (there can be secondary effects on other enzyme concentrations, for example), and secondly because most transgenic plants show a marked difference in enzyme concentration to the wild type. Thus, assumptions have to be made about the relationship between flux and enzyme concentration before estimates of the flux control coefficient can be made (Thomas and Fell, 1994; Pettersson, 1996). Overall, very few studies have rigorously come to terms with these limitations.

III. Reversible Reactions Can Be Flux Limiting

There is a view amongst researchers in flux control analysis that enzymes catalysing the “reversible reactions” of photosynthesis such, as transketolase and aldolase, should not be flux limiting. This is an incorrect view (Kacser and Burns, 1973). Consider a simple metabolic pathway comprising two enzyme-catalysed reactions (Fig. 15.2): the first is a reversible reaction catalysed by E_1 and the second a largely irreversible reaction catalysed by E_2 . Let the rate equations for the two reactions be

$$v_1 = k_1[S_1] - k_{-1}[S_2] \quad (15.2)$$

and

$$v_2 = k_2[S_2], \quad (15.3)$$

where k_1 and k_{-1} are the rate constants for the forward and reverse reactions catalysed by E_1 , k_2 is the rate constant for the reaction catalysed by

Table 15.1. Enzymes of the photosynthetic system whose flux control coefficients have been analysed using transgenic plants

Enzyme	Transgenic plant	Over-expression ^a	Control coefficient ^b	Key reference
Rubisco	Tobacco/rice	Yes	0.2–0.6	Quick et al. (1992)
Seduheptulose biphosphatase	Tobacco	Yes	<0.2	Lefebvre et al. (2005)
Fd/NADP oxidoreductase	Tobacco	No	1.0	Hajirezaei et al. (2002)
Cytochrome b ₆ f	Tobacco	No	Small	Price et al. (1998)
Transketolase	Tobacco	No	Small	Henkes et al. (2001)
Phosphate translocator	Tobacco	Yes	<0.1	Häusler et al. (2000)
Aldolase	Potato	No	Small	Haake et al. (1998)
Rubisco activase	Tobacco/arabidopsis	Yes	Small	Hammond et al. (1998)
Carbonic anhydrase	Tobacco	No	<0.05	Price et al. (1994)
Phosphoribulo-kinase	Tobacco	No	Small	Paul et al. (1995)
Fructose biphosphatase	Potato	No	Small	Kossman et al. (1994)
GAP-dehydrogenase	Tobacco	No	Small	Price et al. (1995a)

^aIndicates studies in which transgenic plants with more than wild type enzyme activity have been examined

^bEstimated control coefficient with respect to the rate of CO₂ assimilation under growth conditions. “small” indicates that the experimental data does not decisively estimate a control coefficient that is significantly greater than zero

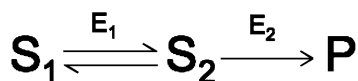


Fig. 15.2. Simple metabolic pathway in which flux control is shared by two enzymes. The first enzyme (E_1) catalyses a reversible reaction involving the interconversion of substrates S_1 and S_2 . The second enzyme (E_2) catalyses the formation of product (P) from S_2

E_2 , and S_1 and S_2 are the substrates for the reactions catalysed by E_1 and E_2 , respectively. The first noteworthy point about this system is that both E_1 and E_2 have positive control coefficients given as follows:

$$C_1^J = 1 - \frac{k_{-1}S_2}{k_1S_1} \quad (15.4)$$

and

$$C_2^J = \frac{k_{-1}S_2}{k_1S_1}. \quad (15.5)$$

This means that $C_1^J = 0$ when the reaction is at equilibrium (i.e. $k_1[S_1] = k_{-1}[S_2]$), which is not possible when the flux $J > 0$, and $C_1^J = 0.2$, for example, when the rate of the reverse reaction is 80% that of the forward reaction. Clearly there is no reason to assume that enzymes catalysing reactions that are appreciably reversible must have control coefficients of zero.

A. Aldolase

With this theory in mind, it is noteworthy that of the two flux control studies of enzymes catalysing reactions close to equilibrium (i.e. aldolase and transketolase), both have estimated relatively high control coefficients. In the first study of potato plastid aldolase, antisense plants with varying amounts of enzyme were examined for the rate of photosynthesis under growth and high light conditions, and for a range of enzyme and metabolite concentrations (Haake et al., 1998). An approximately hyperbolic relationship between aldolase concentration and net CO₂ assimilation rate was found up to the wild type concentration. It was estimated from the curve that the control coefficient was 0.24 under ambient conditions and somewhat higher under saturating light and CO₂. In a follow up study (Haake et al., 1999), plants were grown under different environmental conditions, including two light regimes (70 and 390 μmol photons m⁻² s⁻¹). Flux control coefficients were measured under ambient conditions and values of 0.15 and 0.21 were estimated for the low and high light conditions, respectively.

While there is strong evidence from these studies that marked reductions in aldolase effect significant reductions in CO₂ assimilation rate under growth conditions, there is less evidence that the flux control coefficients of aldolase in the wild type are as high, or even significantly different from zero. The first reason for this is that there

were no estimates of flux in antisense plants with aldolase concentrations close to that of the wild type. The highest concentration in antisense plants was actually some 65% of wild type. Thus, estimation of the slope of the flux versus enzyme concentration plot at wild type concentration is dependent upon curve fitting based largely upon the relatively low aldolase concentrations and the assumption that the curve is hyperbolic, a point acknowledged by the investigators (Haake et al., 1998). A rigorous assessment of the error in the slope estimate would probably have highlighted the uncertainty attached to the flux control estimate (Pettersson, 1996); it is highly likely that the probability of detection of a slope greater than zero is relatively low. Moreover, the authors found significant variation in other enzyme concentrations in the antisense plants including SBPase and FBPase. This variation may have accounted for at least some of the flux variation recorded, especially in view of the strong evidence for a measurable and positive control coefficient for SBPase (see below), and it may have caused deviation from any hyperbolic relationship between enzyme concentration and flux.

B. Transketolase

The study of antisense tobacco with reduced levels of transketolase produced stronger evidence for a finite flux control coefficient, particularly under saturating light and CO₂ conditions where an approximately linear relationship between CO₂ assimilation rate and enzyme concentration was observed (Henkes et al., 2001). Under lower irradiances, however, the same problems outlined above for aldolase also applied, and there is little evidence that the authors detected a slope of the CO₂ assimilation rate versus enzyme concentration curve that was significantly greater than zero – i.e. that transketolase has an appreciable and positive control coefficient. One of other problems with this study is that the plants were grown in a glasshouse with some additional lighting with no record of the integrated average light conditions. The authors note that on some sunny days, the light intensity reached 600 $\mu\text{mol photons m}^{-2} \text{s}^{-1}$. Under similar conditions, the authors apparently detected a significant difference between CO₂ assimilation rate in the wild type and antisense plants with some 60% of the

wild type level, but again the estimation of the control coefficient relies on assumptions about the shape of the relationship between flux and transketolase concentration. If it is hyperbolic, then it is likely that transketolase has a positive flux control coefficient in these plants for at least part of the day.

IV. Small Control Coefficients Are Hard to Detect

Structural appraisal of the photosynthetic system shows that the feedback connections are extensive enough, such that all enzymes should have a finite control coefficient. Nevertheless, as noted above, detecting small values potentially requires massive replication and thoughtful modelling in order to fit curves to the flux versus enzyme concentration graph. There are several studies of transgenic plants in which statistical power was clearly lacking and the authors have concluded that the control coefficient was either zero or close to zero.

A. Glyceraldehyde 3-Phosphate Dehydrogenase

Price et al. (1995a) produced transgenic tobacco plants with a relatively wide range of glyceraldehyde 3-phosphate dehydrogenase (GAPDH) concentrations, including some very close to those of the wild type. Plants were grown in a glasshouse with a peak irradiance of about 900 $\mu\text{mol photons m}^{-2} \text{s}^{-1}$. Even when CO₂ assimilation rates were measured at 1, 500 $\mu\text{mol photons m}^{-2} \text{s}^{-1}$, a roughly hyperbolic relationship between flux (i.e. A_{sat}) and GAPDH concentration was found. This hyperbolic model ($r^2 = 0.78$; $p < 0.0001$; Fig. 15.3a) could have been used to calculate a control coefficient of about 0.17, but this would have been misleading and the authors made no such attempt. A modified hyperbolic model provided a better fit to the data ($r^2 = 0.84$; $p < 0.0001$; Fig. 15.3b), and this curve predicts a much smaller control coefficient at the mean wild type concentration. It is clear, however, that between about 40% and 100% of the wild type GAPDH concentration a linear model, which would tend to over-estimate the control coefficient, has a slope that is not significantly different

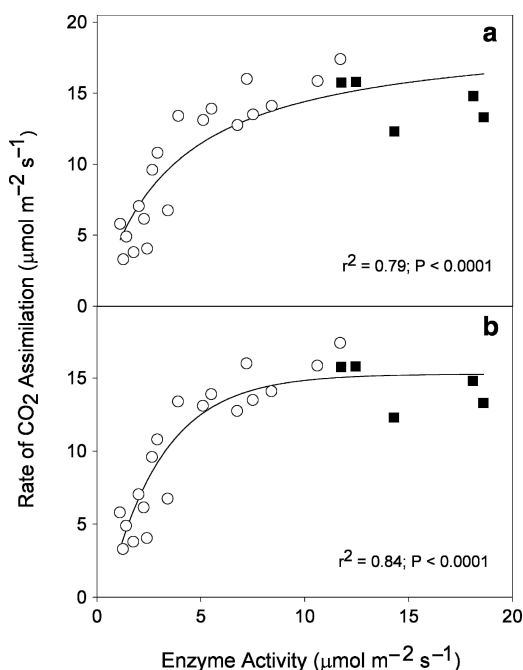


Fig. 15.3. Typical data set showing the relationship between the net rate of CO_2 assimilation and the concentration of an enzyme. The data are adapted from Price et al. (1995a) in which the concentration (measured as activity) of glyceraldehyde 3-phosphate dehydrogenase was varied in transgenic tobacco plants. Both the flux and enzyme concentration was expressed in $\mu\text{mol m}^{-2} \text{s}^{-1}$. The wild type values ($n = 5$) are indicated by the closed squares and the transgenic plant values are indicated by the open circles. (a) A rectangular hyperbola was used to model the data and a significant correlation was detected ($r^2 = 0.79$; $P < 0.0001$). The slope of the graph at the mean wild type enzyme concentration was estimated from the graph equation, which was then used to calculate a control coefficient of 0.17. (b) A modified hyperbola was used to model the data and a significant correlation was detected ($r^2 = 0.84$; $P < 0.0001$). The slope of the graph at the mean wild type enzyme concentration was estimated from the graph equation, which was then used to calculate a control coefficient of close to zero

from zero ($r^2 = 0.026$; $p = 0.56$; Fig. 15.4). Thus, calculation of the GAPDH control coefficient will require much greater experimental replication or quite a different experimental approach.

B. Phosphoribulokinase

Estimates of the control coefficient of phosphoribulokinase (PRK) with respect to the CO_2 fixation rate have also not been successful due to a lack of statistical power. Paul et al. (1995)

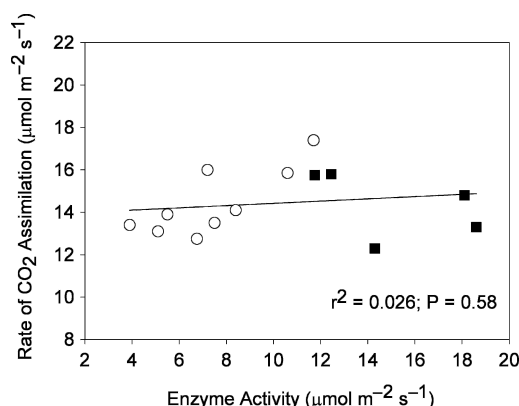


Fig. 15.4. Relationship between the net rate of CO_2 assimilation and the concentration of an enzyme in the vicinity of the wild type concentration. The data are a subset of those presented in Fig. 15.3. A first order polynomial was used to model the data. A slope that was different from zero was not detected ($r^2 = 0.026$; $P = 0.58$); thus, a non-zero control coefficient was not detected

grew transgenic tobacco plants at an irradiance of $300 \mu\text{mol photons m}^{-2} \text{s}^{-1}$. Plants with a range of PRK activities from about 7–100% of the wild type value were measured under growth conditions and, similar to GAPDH, an approximately hyperbolic relationship between flux and PRK concentration was measured. The authors concluded that the control coefficient was zero because there was no evidence of a positive slope over the range of 20–100% of the wild type PRK concentration. A higher control coefficient of some 0.25 was calculated, however, when plants were measured at saturating irradiances of over $800 \mu\text{mol photons m}^{-2} \text{s}^{-1}$ (Paul et al., 2000). In this case, the authors did not use a hyperbolic model to fit the data; rather they applied a linear model to all but the lowest PRK data points. Such an approach almost certainly over-estimates the control coefficient (Small and Kacser, 1993), and the use of a hyperbolic model would have resulted in a much lower estimate. Moreover, given the high degree of scatter in the data in the vicinity of the wild type PRK concentration, it is debatable whether a non-zero control coefficient has been detected.

C. Triose Phosphate/Phosphate Translocator

Häusler et al. (2000) used transgenic tobacco plants with both decreased and increased activities of the chloroplast triose phosphate/phosphate

translocator (TPT), ranging from 30% to 240% of the wild type value. Relatively high concentrations of the TPT were formed by over-expressing a TPT gene from *Flavaria trinervia* (FtTPT). This study had a sizeable advantage over previous flux control studies: estimation of the slope of the flux versus enzyme concentration curve involved data both above and below the enzyme concentration of the wild type level, which reduces the likelihood of overestimation of the control coefficient. Häusler et al. (2000) found that under ambient conditions there was a small (but perhaps not statistically significant) effect of TPT activity on the rate of CO₂ assimilation. Nevertheless, a convincing estimate of a control coefficient of about 0.3 was made for plants under saturating light and CO₂. This excellent analysis emphasises the utility of both under- and over-expressing the target enzyme in flux control analyses.

D. Fructose 1,6-Bisphosphatase

Flux control by chloroplast fructose 1,6-bisphosphatase (FBPase) has not been explicitly examined. Some information can, however, be gleaned from the study of Kossman et al. (1994) in which transgenic potato plants with reduced amounts of FBPase were examined for various parameters including the CO₂ assimilation rate. The plants were grown in a glasshouse at about 250 $\mu\text{mol photons m}^{-2} \text{ s}^{-1}$ but measurements were made on leaf disks at relatively high CO₂. The authors found a reduction in the O₂ evolution rate, at both saturating and sub-saturating irradiances, when FBPase was reduced to some 35% of the wild type level. It is, however, impossible to estimate the control coefficient under growth conditions from these data. It seems unlikely that a non zero control coefficient could have been detected.

E. Carbonic Anhydrase

Carbonic anhydrase (CA) is thought to enhance the rate of photosynthesis by catalysing the rapid equilibration of inorganic carbon species across the stroma and thus increasing the supply of CO₂ to Rubisco (Cowan, 1986). Price et al. (1994) used transgenic tobacco plants with markedly reduced amounts of chloroplast CA to measure the role of this enzyme in enhancing the CO₂ assimilation rate. This is a notable study because

it highlights the importance of accurate measurements of flux and the need for high degrees of replication in order to detect small effects. The authors found that when CA activity was reduced to about 2% of the wild type level, no significant reduction in A_{sat} could be detected. However, they did detect a significant difference in the stable carbon isotope composition of leaves, which was equated with a 15 μbar difference in CO₂ partial pressure at the site of carboxylation, and a 4.4% difference in A_{sat} . Based on these estimates, the CA control coefficient is apparently very small, somewhere between zero and 0.044.

F. Rubisco Activase

Rubisco activase plays a role in regulating the rate of photosynthesis by promoting the activation of Rubisco (Portis, 2003). Studies using transgenic tobacco plants failed to detect a significant reduction in the rate of CO₂ assimilation in response to small changes in activase concentration (Jiang et al., 1994; Hammond et al., 1998). In fact, Jiang et al. (1994) did not record an effect on photosynthesis under growth conditions until activase was reduced by two- to threefold. These authors did, however, estimate a small effect of activase on photosynthesis under light saturation and calculated a control coefficient of about 0.28. As with other studies (see Figs. 15.3 and 15.4), this estimate relied on certain assumptions about the relationship between flux and enzyme concentration. Interestingly, recent work involving over-expression of the large isoform of activase in rice also showed an increase in A_{sat} in plants with greater than the wild type level of activase (Wu et al., 2007).

V. Enzymes with Higher Control Coefficients

A. Sedoheptulose 1,7-Bisphosphatase

The relationship between the rate of photosynthesis and the concentration of sedoheptulose 1,7-bisphosphatase (SBPase) has been relatively well studied using tobacco plants in which enzyme concentration has been both reduced and enhanced. Overall, evidence indicates that the light saturated rate of CO₂ assimilation A_{sat} is

sensitive to SBPase activity, although the magnitude of the control coefficient is less certain. The first study of plants with reduced SBPase (Harrison et al., 1998) showed a strong correlation between A_{sat} and SBPase, but these results were confounded to some degree by variation in stomatal conductance and intercellular CO_2 concentration C_i . In fact, C_i titrations of the flux apparently revealed little if any sensitivity of A_{sat} to SBPase activity in the neighbourhood of the wild type concentration at constant C_i . Further analysis of these transgenic plants by Raines et al. (2000) yielded a control coefficient estimate of about 0.3 for SBPase with respect to A_{sat} , but, as in previous cases, this estimate is highly dependant upon the model used to fit the data (see Figs. 15.3 and 15.4).

Another potentially important confounding variable, not just in SBPase studies but all studies, was uncovered when Ölçer et al. (2001) examined the relationship between A_{sat} and SBPase in leaves of different ages. They found that leaf age and position on a plant could markedly confound experimental results because the SBPase control coefficient was different for all leaf classes; they estimated a range of -0.2 to about 0.5 for the youngest to oldest fully expanded leaves. As noted above, however, these estimates depended markedly upon the statistical model used in the analyses as there were few data points in the vicinity of the wild type enzyme concentration.

Evidence for a control coefficient greater than zero for SBPase has, however, been strengthened following research on plants with enhanced levels of this enzyme. This work has effectively allowed examination of variation in CO_2 assimilation rate on both sides of the wild type enzyme concentration, which has allowed a slope to be calculated with greater precision. Miyagawa et al. (2001) enhanced the activities of both SBPase and FBPase by introducing a cyanobacterial SBPase/FBPase into the chloroplast. The transformed plants show an increase in A_{sat} of some 20% in response to a doubling of SBPase activity, which equates to a control coefficient of about 0.2 if the contribution of the rise in FBPase activity (50–100% rise) is ignored. The CO_2 assimilation rate was also sensitive to SBPase overexpression at the growth irradiance ($400 \mu\text{mol photons m}^{-2} \text{s}^{-1}$). Subsequent research (Tamoi et al., 2006) separated the

effects of the two bisphosphatases by enhancing the activity of each one separately. These results showed a significant rise in A_{sat} of some 25% in response to increases in SBPase of between 60% and 330%. A smaller but significant rise in A_{sat} of 15% was observed in response to a 130% rise in FBPase. Curiously, the CO_2 assimilation rate was apparently sensitive to both FBPase and SBPase activity at all irradiances, including subsaturating values.

One of the possible uncontrolled variables in these studies of the effects of enzyme enhancement was that of leaf ontogeny. Because plants with enhanced enzyme levels grew faster and because between treatments, leaves of the same age were sampled, there would have been an ontogenetic effect confounding the control coefficient estimates. The higher growth rates indicate, however, that the control coefficients were still greater than zero. To overcome this problem, Lefebvre et al. (2005) increased the SBPase activity in tobacco by overexpression of an Arabidopsis cDNA in tobacco plants. They measured whole plant photosynthesis (although the plants were the same age) and found that A_{sat} was sensitive to SBPase activity and that the response was consistent with a control coefficient of about 0.2.

B. Ribulose 1,5-Bisphosphate Carboxylase/Oxygenase

The evidence that Rubisco plays a major role in determining the rate of photosynthesis was established well before the application of transgenic plant systems to this question (review by Woodrow and Mott, 1988). One of the many compelling pieces of evidence for the flux limiting role of Rubisco is the sensitivity of photosynthesis to CO_2 and O_2 concentration changes, which can be assumed to largely reflect the sensitivity of photosynthesis to changes in Rubisco activity. This assumption, together with the Rubisco kinetic constants for the two gasses, was used by Woodrow and Mott (1988) to make the first estimation of the flux control coefficient of Rubisco (in soybeans) over a spectrum of light intensities. A range from zero in the dark to about 0.7 under saturating light was estimated. As discussed previously, these gas titration methods have advantages over approaches involving

transgenic plants because different plants do not have to be compared.

The numerous studies of Rubisco variation in transgenic plants (reviews by Stitt and Schultze, 1994; Stitt and Sonnewald, 1995; Raines, 2003), which have almost exclusively involved reductions in Rubisco concentration, have been in broad agreement with these control coefficient estimates based on gas titrations, although in some studies the control coefficient under growth conditions has been surprisingly low. For example, when tobacco plants were grown under an irradiance of $300 \mu\text{mol photons m}^{-2} \text{s}^{-1}$, a relatively low control coefficient of about 0.1–0.2 was estimated under the same conditions, although the statistical certainty of these relatively low estimates was not assessed (Quick et al., 1992). Interestingly, the plants used in these experiments were grown under nutrient saturation for growth, but the Rubisco control coefficient rose when nitrogen supply was reduced (Quick et al., 1992). This work highlights the interesting idea that under high nitrogen conditions, the allocation of nitrogen amongst the enzymes of photosynthesis may not be optimised in terms of the photosynthetic flux and that other unidentified constraints may be operating. For example, Rubisco could be acting as an effective nitrogen store, which could push down its flux control coefficient.

A recent study of rice attempted to refine our picture of Rubisco's role in limiting the rate of CO_2 fixation. Suzuki et al. (2007) transformed rice plants with the *rbcs* sense gene, which resulted in an increase in Rubisco concentration of some 30% on a leaf area basis. Curiously, the authors failed to detect a significant effect on A_{sat} , even at low CO_2 . They concluded that Rubisco activity must have been down regulated in a compensatory manner, even under Rubisco limited conditions.

VI. Photosynthetic Electron Transport

There have been relatively few studies in which transgenic plants have been used to assess the role of components of the electron transport chain in limiting the rate of CO_2 assimilation. In one study (Price et al., 1995b, 1998), transgenic tobacco plants were produced with reduced amounts of

the Reiske FeS protein of the cytochrome b_6f complex. A range of protein concentrations were measured in the transgenic plants (5% to 80% of the wild type level), and parallel variation in the concentration of other components of the complex was also found. Interestingly, Price et al. (1995b) measured an approximately linear relationship between A_{sat} and the concentration of the Rieske FeS protein (which would yield a control coefficient of 1.0, but in the follow up paper (Price et al., 1998) the relationship was less clear. In this study, significant variation in the wild type A_{sat} and Rieske FeS concentrations makes it impossible to calculate a control coefficient with any certainty, and the results are consistent with a relatively small coefficient (see example in Figs. 15.3 and 15.4).

A high control coefficient was also estimated for NADP^+ -dependent ferredoxin oxidoreductase (FNR) in transgenic tobacco (Hajirezaei et al., 2002). In relatively well replicated experiments, there were highly significant (linear) correlations between FNR concentration and both A_{sat} and the CO_2 assimilation rate at a sub-saturating irradiance. Moreover, using a hyperbolic model, the authors estimated control coefficients of close to unity for both conditions. In view of the summation theorem (Kacser and Burns, 1973) and the sizeable estimates of control coefficients for other enzymes (including some in the electron transport system identified using inhibitors, e.g. Kirchhoff et al., 2000), this estimate of a high control coefficient for FNR is not logical. It seems that experimental errors and confounding variables (e.g. uncontrolled variation in the concentrations of other enzymes) may be playing a considerable role in this study.

VII. Concluding Remarks

Since its first application to photosynthesis in 1980s, metabolic flux control analysis has transformed the way we view the regulation of the photosynthetic flux. Rather than emphasising single limiting factors, the analysis has provided a holistic framework in which the contribution of all of the enzymes to the determination of flux can be considered. This is becoming increasingly important, for example, in efforts to increase photosynthetic rates using genetic engineering.

Nevertheless, our understanding of how the rate of photosynthesis is determined is still far from complete. Under saturating irradiances, there is good evidence that photosynthesis is largely limited by the amount of Rubisco and the capacity of the stomata (and other resistances to CO₂ transfer) to deliver CO₂ to the site of carboxylation. SBPase, together with other enzymes such as the TPT, may also have a small role in flux determination under these conditions. The picture becomes less clear, however, under growth and lower irradiances. The role of Rubisco diminishes under these conditions, but how flux control is allocated amongst the other components of the Calvin-Benson Cycle and electron transport system remains to be determined.

Experimental design will need to be improved in order to answer this question. Research to-date has been handicapped by the presence of uncontrolled, confounding variables, both within wild type reference plants and transgenic plants, and the difficulty of measuring fluxes and enzyme concentrations accurately. In order to measure control coefficients with appropriate confidence, highly replicated experiments, preferably involving both relatively low and high enzyme concentrations obtained by under- and over-expression and careful control of many experimental variables, are necessary. Such studies are relatively rare.

Acknowledgments

The author thanks those colleagues who were influential in developing ideas about flux control in the photosynthetic system: Joe Berry, Keith Mott, Tim Ball and Graham Farquhar. Some of this work was supported by funding from the Australian Research Council.

References

- Cornish-Bowden A and Hofmeyr JHS (1994) Determination of control coefficients in intact metabolic systems. *Biochem J* 298: 367–375
- Cowan IR (1986) Economics of carbon fixation in higher plants. In: Givnish, TJ (ed) *On the Economy of Plant Form and Function*, pp 133–170. Cambridge University Press, Cambridge
- Haake V, Zrenner R, Sonnewald U and Stitt M (1998) A moderate decrease of plastid aldolase activity inhibits photosynthesis, alters the levels of sugars and starch, and inhibits growth of potato plants. *Plant J* 14: 147–157
- Haake V, Geiger M, Walch-Liu P, Engels C, Zrenner R and Stitt M (1999) Changes in aldolase activity in wild-type potato plants are important for acclimation to growth irradiance and carbon dioxide concentration, because plastid aldolase exerts control over the ambient rate of photosynthesis across a range of growth conditions. *Plant J* 17: 479–489
- Hajirezaei MR, Peisker M, Tschiersch H, Palatnik JF, Valle EM, Carrillo N and Sonnewald U (2002) Small changes in the activity of NADP⁺-dependent ferredoxin oxidoreductase lead to impaired plant growth and restrict photosynthetic activity in transgenic tobacco plants. *Plant J* 29: 281–293
- Hammond ET, Andrews TJ, Mott KA and Woodrow IE (1998) Regulation of Rubisco activation in antisense plants of tobacco containing reduced levels of Rubisco activase. *Plant J* 14: 101–110
- Harrison EP, Willingham NM, Lloyd JC and Raines CA (1998) Reduced sedoheptulose-1,7-bisphosphatase levels in transgenic tobacco lead to decreased photosynthetic capacity and altered carbohydrate accumulation. *Planta* 204: 27–36
- Häusler RE, Schlieben NH and Flügge UI (2000) Control of carbon partitioning and photosynthesis by the triose phosphate/phosphate translocator in transgenic tobacco plants (*Nicotiana tabacum*). II. Assessment of control coefficients of the triose phosphate/phosphate translocator. *Planta* 210: 383–390
- Heinrich R and Rapoport TA (1974) A linear steady state treatment of enzymatic chains. *Eur J Biochem* 42: 89–95
- Henkes S, Sonnewald U, Badur R, Flachmann R and Stitt M (2001) A small decrease of plastid transketolase activity in antisense tobacco transformants has dramatic effects on photosynthesis and phenylpropanoid metabolism. *Plant Cell* 13: 535–551
- Jiang C-Z, Quick WP, Aired R, Kliebenstein D, Rodermel SR (1994) Antisense inhibition of Rubisco activase expression. *Plant J* 5: 787–98
- Kacser H and Burns JA (1973) The control of flux. *Symp Soc Exp Biol* 27: 65–104
- Kirschhoff H, Horstmann S and Weis E (2000) Control of the photosynthetic electron transport by PQ diffusion microdomains in thylakoids of higher plants. *Biochim Biophys Acta* 1459: 148–168
- Kossmann J, Sonnewald U and Willmitzer L (1994) Reduction of the chloroplastic fructose 1,6-bisphosphatase in transgenic potato plants impairs photosynthesis and plant growth. *Plant J* 6: 637–650
- Lefebvre S, Lawson T, Zakhleniuk OV, Lloyd JC and Raines CA (2005) Increased sedoheptulose-1,7-bisphosphatase activity in transgenic tobacco plants stimulates photosynthesis and growth from an early stage in development. *Plant Physiol* 138: 451–460

- Miyagawa Y, Tamoi M, and Shigeoka S (2001) Overexpression of a cyanobacterial fructose-1,6-/sedoheptulose-1,7-bisphosphatase in tobacco enhances photosynthesis and growth. *Nature Biotech* 19: 965–969
- Ölçer H, Lloyd JC, and Raines CA (2001) Photosynthetic capacity is differentially affected by reductions in sedoheptulose-1,7-bisphosphatase activity during leaf development in transgenic tobacco plants. *Plant Physiol* 125: 982–989
- Paul MJ, Knight JS, Habash D, Parry MAJ, Lawlor DW, Barnes SA, Loynes A and Gray JC (1995) Reduction in phosphoribulokinase activity by antisense RNA reduces CO₂ assimilation and growth in low irradiance. *Plant J* 7: 535–542
- Paul MJ, Driscoll SP, Andralojc PJ, Knight JS, Gray JC and Lawlor DW (2000) Decrease of phosphoribulokinase activity by antisense RNA in transgenic tobacco: definition of the light environment under which phosphoribulokinase is not in large excess. *Planta* 211: 112–119
- Pettersson G (1996) Errors associated with experimental determinations of enzyme flux control coefficients. *J Theor Biol* 179: 191–197
- Pettersson G and Ryde-Pettersson U (1988) A mathematical model of the Calvin photosynthesis cycle. *Eur J Biochem* 175: 661–672
- Portis AR Jr (2003) Rubisco activase – Rubisco's catalytic chaperone. *Photosynth Res* 75: 11–27
- Price GD, Von Caemmerer S, Evans JR, Yu JW, Lloyd J, Oja V, Kell P, Harrison K, Gallagher A and Badger MR (1994) Specific reduction of chloroplast carbonic anhydrase activity by antisense RNA in transgenic tobacco plants has a minor effect on photosynthetic CO₂ assimilation. *Planta* 193: 331–340
- Price GD, Evans JR, Von Caemmerer S, Yu JW and Badger MR (1995a) Specific reduction of chloroplast glyceraldehyde 3-phosphate dehydrogenase activity by antisense RNA reduces CO₂ assimilation via a reduction in ribulose biphosphate regeneration in transgenic tobacco plants. *Planta* 195: 369–378
- Price GD, Yu JW, Von Caemmerer S, Evans JR, Chow WS, Anderson JM, Hurry V and Badger MR (1995b) Chloroplast cytochrome b(6)/f and ATP synthase complexes in tobacco – transformation with antisense RNA against nuclear encoded transcripts for the Rieske FeS and ATP-delta polypeptides. *Aust J Plant Physiol* 22: 285–297
- Price GD, Von Caemmerer S, Evans JR, Siebke K, Anderson JM and Badger MR (1998) Photosynthesis is strongly reduced by antisense suppression of chloroplastic cytochrome bf complex in transgenic tobacco. *Aust J Plant Physiol* 25: 445–452
- Quick WP, Fichtner K, Schulze E-D, Wendler R, Leegood RC, Mooney H, Rodermeil SR, Bogorad L and Stitt M (1992) Decreased ribulose-1,5-bisphosphate carboxylase/oxygenase in transgenic tobacco transformed with “antisense” rbcS. IV. Impact on photosynthesis and plant growth altered nitrogen supply. *Planta* 188: 522–531
- Raines CA (2003) The Calvin cycle revisited. *Photosynth Res* 75: 1–10
- Raines CA, Harrison EP, Ölçer H and Lloyd JC (2000) Investigating the role of the thiol-regulated enzyme sedoheptulose-1,7-bisphosphatase in the control of photosynthesis. *Physiol Plant* 110: 303–308
- Small JR (1993) Flux control coefficients determined by inhibitor titration: the design and analysis of experiments to reduce errors. *Biochem J* 296: 423–433
- Small JR and Kacser H (1993) Responses of metabolic systems to large changes in enzyme activities and effectors. 1. The linear treatment of unbranched chains. *Eur J Biochem* 213: 613–624
- Stitt M and Schultze E-D (1994) Does Rubisco control the rate of photosynthesis and plant growth? An exercise in molecular ecophysiology. *Plant Cell Environ* 17: 465–487
- Stitt M and Sonnewald U (1995) Regulation of metabolism in transgenic plants. *Annu Rev Plant Physiol Plant Mol Biol* 46: 341–368
- Suzuki Y, Ohkubo M, Hatakeyama H, Ohashi K, Yoshizawa R, Kojima S, Hayakawa T, Yamaya T, Mae T and Makino A (2007) Increased Rubisco content in transgenic rice transformed with the ‘sense’ rbcS gene. *Plant Cell Physiol* 48: 626–637
- Tamoi M, Nagaoka M, Miyagawa Y and Shigeoka S (2006) Contribution of fructose-1,6-bisphosphatase and sedoheptulose-1,7-bisphosphatase to the photosynthetic rate and carbon flow in the Calvin cycle in transgenic plants. *Plant Cell Physiol* 47: 380–390
- Thomas S and Fell DA (1994) Metabolic control analysis – sensitivity of control coefficients to experimentally determined variables. *J Theor Biol* 167: 175–200
- Woodrow IE (1986) Control of the rate of photosynthetic carbon dioxide fixation. *Biochim Biophys Acta* 851: 181–192
- Woodrow IE and Berry JA (1988) Enzymatic regulation of photosynthetic CO₂ fixation in C₃ plants. *Annu Rev Plant Physiol Plant Mol Biol* 39: 533–594
- Woodrow IE and Mott KA (1988) A quantitative assessment of the degree to which RuBP carboxylase/oxygenase limits the steady state rate of photosynthesis during sun-shade acclimation of *Helianthus annuus*. *Aust J Plant Physiol* 15: 253–262
- Woodrow IE and Mott KA (1993) Modelling C₃ photosynthesis: a sensitivity analysis of the photosynthetic carbon reduction cycle. *Planta* 191: 421–432
- Woodrow IE, Ball JT and Berry JA (1990) Control of photosynthetic carbon dioxide fixation by the boundary layer, stomata and ribulose 1,5-bisphosphate carboxylase/oxygenase. *Plant Cell Environ* 13: 339–347
- Wu HR, Li LB, Jing YX and Kuang TY (2007) Over- and antisense expressions of the large isoform of ribulose-1,5-bisphosphate carboxylase/oxygenase activase gene in *Oryza sativa* affect the photosynthetic capacity. *Photosynthetica* 45: 194–201

Chapter 16

Packing the Photosynthetic Machinery: From Leaf to Canopy¹

Ülo Niinemets*

*Institute of Agricultural and Environmental Sciences, Estonian University of Life Sciences,
Kreutzwaldi 1, Tartu 51014, Estonia*

Niels P.R. Anten

*Department of Plant Ecology, Utrecht University, P.O. Box 80084, 3508 TB, Utrecht,
The Netherlands*

Summary.....	364
I. Introduction.....	364
A. Plant Canopies as Highly Variable Systems.....	364
B. Basic Problem of Scaling in Canopies.....	365
II. Inherent Differences in Microenvironment and Photosynthetic Potentials	
Within the Canopy.....	367
A. Environmental Variation Within Plant Canopies.....	367
1. Gradients in Light Availability.....	367
2. Simulation of Canopy Light Environment.....	369
3. Co-variations among Environmental Drivers in Plant Canopies.....	371
B. Light-dependent Modifications in Leaf Structure, Chemistry and Function.....	373
1. General Framework to Evaluate Photosynthetic Acclimation.....	373
2. Importance of Within-canopy Gradients in Nitrogen and Leaf Dry Mass per Unit Area.....	373
3. Role of Within-leaf Nitrogen Partitioning.....	375
4. Mechanisms of Within-canopy Acclimation of Photosynthetic Potentials.....	377
C. Light-dependent Modifications in Foliage Inclination Angle Distributions and Spatial Clumping.....	378
D. Modifications to Interacting Environmental Drivers.....	378
III. Scaling Photosynthesis from Leaves to Canopy.....	379
A. Predictive Integration Models.....	379
1. Early Models with Empirical Parameterization of Photosynthesis.....	379
2. Models Including Process-based Parameterization of Photosynthesis.....	380
3. Further Advancements in Predictive Integration Models.....	380
B. Optimization Algorithms.....	381
1. Optimal Distribution of Foliar Nitrogen and Foliar Dry Mass Within the Canopy.....	381
2. Optimal Canopy Leaf Area Index and Leaf Angle Distribution.....	383
3. Difficulties with Simple Optimization Models.....	383
C. Evolutionarily Stable Distributions of Limiting Resources and Structural Traits.....	385
1. Evolutionarily Stable Nitrogen and Leaf Area Distributions.....	385
2. Evolutionarily Stable Leaf Angle and Plant Height.....	386
3. Evolutionarily Stable Strategies and Canopy Models.....	386
D. Whole-canopy Level Integration Approaches: Big Leaf Models.....	388
IV. Concluding Remarks.....	389
Acknowledgments.....	389
References.....	390

¹ Dedicated to the memory of Professor Olevi Kull (22.06.1955–31.01.2007)

* Author for correspondence, e-mail: ylo.niinemets@emu.ee

Summary

Plant canopies are characterized by extensive and interacting gradients in light, temperature, humidity and wind. As every leaf in the canopy is exposed to unique combinations of environmental variables and has distinctive suite of structural and physiological traits, modeling canopy photosynthesis is a challenging endeavor. Due to the highly non-linear response of photosynthesis to light, temperature and humidity, whole canopy photosynthesis cannot be derived from the average values of light and temperature, but complex models simulating both temporal and spatial variability in environmental drivers and photosynthetic potentials are needed to estimate canopy photosynthesis. Two fundamentally different classes of canopy models have been developed. Predictive integration algorithms that describe the actual spatial distribution of foliage elements and photosynthetic capacity have the objective to simulate whole-stand carbon uptake and other canopy processes as closely as possible. Recent advances in these models have led to complex three-dimensional (3D) models that are capable of simulating radiation interception in discontinuous canopies considering complex radiative transfer phenomena such as penumbra and light scattering. A large number of parameters needed is the disadvantage of these explicit integration algorithms. Alternatively, optimization models predict total canopy leaf area and foliage photosynthetic potentials from the assumption of maximization of canopy photosynthesis by the optimal use of available nitrogen or foliage biomass. Significantly smaller number of parameters is needed for these models as the spatial distributions of foliage and photosynthetic characteristics are determined by assumptions about optimality. However, the simple optimization models considering only light as the key environmental factor and assuming that plant canopy consists of identical individual non-competing plants result in a significant bias between simulated and measured photosynthesis profiles within the canopy, limiting the use of such models in practical scaling applications. Recently developed models considering competition between different individuals have yielded better correspondence between the data and predictions, suggesting that optimization models have a large potential for predictive purposes. More information of the functioning of plant canopies, in particular of the response of plants to multiple environmental stresses in the canopies as well as competitive interactions is still needed to define “right” optimization functions and to correctly simulate photosynthetic productivity in highly heterogeneous canopy environment.

I. Introduction

A. Plant Canopies as Highly Variable Systems

Prediction of whole plant and whole stand integrated photosynthetic production is the final goal of research linking photosynthesis to plant productivity. However, scaling from single leaf photosynthetic performance to whole canopy integrated response is associated with inherent complexities because of variations in environment and foliage physiology and structure. Plant canopies exhibit extensive within-canopy variation in light availability, often more than 50-fold between canopy top and bottom (e.g. Pearcy, 2007). Light intensity also strongly varies during the day, between the days and during the season, further augmenting the strongly dynamic nature of leaf light environment. In addition

to light availability, gradients in several other environmental factors accompany light gradients in plant canopies (e.g. Niinemets and Valladares, 2004 for a review). For instance, air and leaf temperatures increase with increasing height in the canopy due to greater amount of penetrating solar energy (Chiariello, 1984; Eliáš et al., 1989; Sharkey et al., 1996). Inherent co-variation between the environmental drivers in plant canopies implies complex multivariate influences on foliage function, and suggests that predictions of canopy photosynthetic performance need to be linked to detailed simulations of canopy micrometeorology (e.g. Baldocchi et al., 2002).

In addition to strong environmental variation, foliage photosynthetic potentials are not constant for all leaves within the canopy. Photosynthetic capacity increases dramatically with increasing light availability from the bottom

to the top of plant canopies (e.g. Kull, 2002; Anten, 2005; Niinemets, 2007 for reviews). The structure of leaves and shoots also changes as plants acclimate to various light availabilities in the canopy, thereby altering foliage light harvesting efficiency, but also the light transmission by different foliage layers (Cescatti and Zorer, 2003; Cescatti and Niinemets, 2004). There is also evidence of variable shapes of temperature response curves of photosynthetic potentials and mitochondrial respiration rates (Niinemets et al., 1999; Griffin et al., 2002;

Bauerle et al., 2007), reflecting physiological adjustment to within-canopy temperature gradient. This high variability in foliage structure and physiological potentials further underscores the complex nature of plant canopies, and has important implications for scaling from single leaf photosynthetic activities to predict whole canopy photosynthetic productivity.

B. Basic Problem of Scaling in Canopies

Because of extreme complexity in environment, foliage physiology and structure, it is tempting to use simplified algorithms that use average micrometeorological conditions and average leaf photosynthetic characteristics in scaling from a leaf to canopy. However, leaf photosynthesis responds non-linearly to key environmental drivers – light, temperature and air humidity (Fig. 16.1) – and use of averages results in major integration errors (Smolander and Lappi, 1985; de Pury and Farquhar, 1997). For example, net assimilation rate, A , depends on quantum flux density, Q , according to a non-linear hyperbolic relationship. For any two values of quantum flux density, Q_1 and Q_2 , the use of the average $\bar{Q} = (Q_1 + Q_2)/2$ overestimates the true average photosynthesis rate, $\bar{A} = [A_1(Q_1) + A_2(Q_2)]/2 < A(\bar{Q})$ (Fig. 16.1a). Analogously, A responds to temperature, T , according to a non-linear relationship with an optimum, and use of an average of any two leaf temperatures results in overestimation of leaf carbon gain both below, $\bar{A} < A(\bar{T}_{1,2})$, and above, $\bar{A}' < A(\bar{T}_{2,3})$, the optimum temperature (Fig. 16.1b). The situation is similar with the photosynthetic response to water vapor deficit (v). Integration error in this case results from modifications of stomatal openness by v and from changes in A due to differences in intercellular CO_2 concentration (Fig. 16.1c).

Simulations of daily leaf photosynthesis using measured light and temperatures at various canopy locations (Fig. 16.2a, c) and realistic estimates of foliage photosynthetic potentials suggest a major integration error of 1.3–1.6-fold overestimation in daily photosynthesis if average daily Q and T values are used in the predictions (Fig. 16.2b, d). The integration error is expected to be larger in environments with greater fluctuations in environmental conditions. In the lower

Abbreviations: A – leaf net assimilation rate; A_C – canopy assimilation rate; A_D – daily leaf assimilation rate; A_g – gross leaf assimilation rate; A_{\max} – light-saturated assimilation rate (photosynthetic capacity); $A_0 - A_{\max}$ of the leaves in the top of the canopy; C_B – chlorophyll binding, the ratio of chlorophyll to nitrogen invested in light harvesting; C_i – intercellular CO_2 concentration; f_Q – fraction of light absorbed by canopy; F_B – fraction of leaf nitrogen in rate limiting proteins of photosynthetic electron transport; F_L – fraction of leaf nitrogen in light harvesting; F_R – fraction of leaf nitrogen in Rubisco; FR – far-red light; g_s – stomatal conductance; h – canopy depth; J – rate of photosynthetic electron transport; J_{\max} – capacity for photosynthetic electron transport; $J_{mc} - J_{\max}$ per unit cytochrome f protein; K – extinction coefficient for light; K_n – scaling exponent for the reduction of nitrogen content with L_C ; L – leaf area index; L_C – cumulative leaf area index; L_{ev} – evolutionarily stable leaf area index; L_{opt} – optimal leaf area index; M_A – leaf dry mass per unit area; N_A – leaf nitrogen content per unit area; N_b – “non-photosynthetic” nitrogen content; N_M – leaf nitrogen content per dry mass; $N_0 - N_A$ of the topmost leaves in the canopy; N_P – photosynthetic nitrogen content; P – probability of beam penetration; Q – photosynthetic quantum flux density; Q_{int} – seasonal average daily integrated Q ; $Q_O - Q$ above the canopy; q_R – relative quantum flux density; R/FR – red/far-red light ratio; R_D – non-photorespiratory respiration rate continuing in light; R_n – dark respiration rate at night; RuBP – Ribulose 1,5-bisphosphate; T – leaf temperature; V_{cmax} – maximum carboxylase activity of ribulose 1,5-bisphosphate carboxylase/oxygenase (Rubisco); $V_{cr} - V_{cmax}$ per unit Rubisco protein; W_c – potential carboxylation rate limited by Rubisco; W_j – potential carboxylation rate limited by electron transport; α_A – quantum yield of photosynthesis for an absorbed light; α_I – that for incident light; β – relative contribution of given plant to total canopy leaf area index; Γ^* – photosynthetic CO_2 compensation point in the absence of R_D ; θ – solar zenith angle; λ – lagrangian multiplier; v – water vapor deficit; ξ – leaf absorptance; Ω – spatial clumping index; χ_A – leaf chlorophyll content per unit area

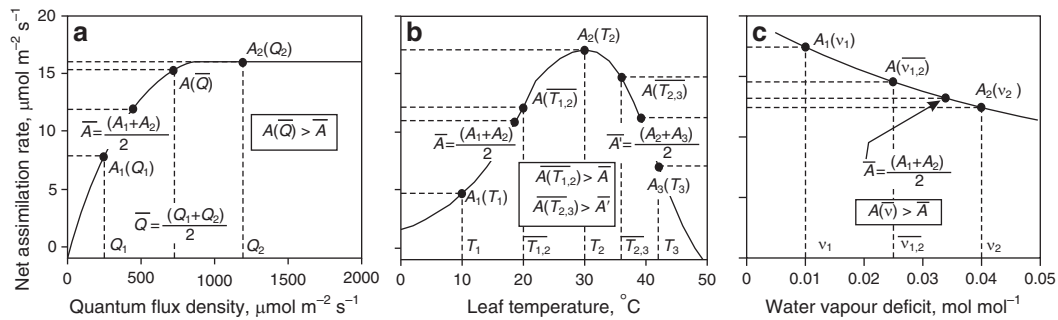


Fig. 16.1. Illustration of the problem of integration of photosynthesis using average values of quantum flux density (Q ; a), temperature (T ; b) and water vapor deficit (v ; c). Due to non-linearity of photosynthetic responses, the average of any two simulated photosynthesis rates (\bar{A}) is lower than the value predicted using the average light (\bar{Q}), temperature (\bar{T}) or humidity (\bar{v}). These simulations were conducted with the Farquhar et al. (1980) steady-state photosynthesis model. Light dependence of photosynthetic electron transport, J , was simulated according to a non-rectangular hyperbola with the curvature factor set to 0.85, leaf absorptance to 0.85, and fixing the quantum yield of CO_2 -saturated photosynthetic electron transport for an incident light at $0.248 \text{ mol mol}^{-1}$. We used a value of maximum carboxylase activity of Rubisco (V_{cmax}) of $50 \mu\text{mol m}^{-2} \text{s}^{-1}$, while the capacity for photosynthetic electron transport (J_{max} , $\mu\text{mol e}^{-} \text{m}^{-2} \text{s}^{-1}$) was set at $2.5V_{\text{cmax}}$ $\text{mol e}^{-}/\text{mol CO}_2$. The non-photorespiratory respiration rate continuing in the light was set at $0.02V_{\text{cmax}}$. These are typical values for upper canopy leaves in temperate deciduous species (Niinemets et al., 1998). For the temperature response, the temperature dependence of V_{cmax} (Niinemets and Tenhunen, 1997 for details) was also used for J_{max} , as the temperature responses of these partial processes of photosynthesis are highly coordinated (Medlyn et al., 2002). In the simulations in (a) and (b), the intercellular CO_2 mole fraction (C_i) was set at $281 \mu\text{mol mol}^{-1}$, corresponding to an ambient (C_a) CO_2 mole fraction of $375 \mu\text{mol mol}^{-1}$ and a C_i/C_a ratio of 0.75. In (c), dependence of stomatal conductance for CO_2 (g_s) on vapor pressure deficit (v) was simulated according to an hyperbolic relationship $g_s = g_{s,\text{max}}/(v:f) + g_{s,\text{min}}$, with $g_{s,\text{max}}$ of $300 \text{ mmol m}^{-2} \text{s}^{-1}$, $g_{s,\text{min}}$ $10 \text{ mmol m}^{-2} \text{s}^{-1}$ and f (sensitivity of stomata to v) of 110 mol mol^{-1} . Net assimilation rate and C_i were derived iteratively for a given g_s .

canopy, direct irradiance characterized by high peak intensities comprises about a half or more of the total light intercepted by the leaves, creating highly dynamic light field alternating with periods of low diffuse irradiance (Baldocchi and Collineau, 1994; Palva et al., 2001). Thus, light fluctuates more strongly in the lower than in the upper canopy (Palva et al., 2001) and the integration error is expected to be particularly large in the lower canopy (Fig. 16.2b vs. d). Overall, these simulations demonstrate that high spatial and temporal resolution of canopy micrometeorological data is required to scale up the photosynthetic production from leaf to canopy over the day, days and season(s).

Non-uniform distribution of foliage assimilation potentials within the canopies constitutes another challenge in scaling up photosynthetic fluxes. Studies demonstrate that the assumption of a constant average assimilation capacity for all leaves in the canopy results in significant error of whole canopy photosynthesis (e.g. Hirose and Werger, 1987a; Gutschick and Wiegel, 1988; Baldocchi and Harley, 1995). Thus, the scaling models need to consider both within-canopy spa-

tial and temporal variation in microclimate as well as spatial variation in foliage assimilation potentials.

In the current review, we first provide an overview of canopy micrometeorology. Second, we explore how leaves acclimate to within-canopy environmental gradients. Third, we critically review how canopy models have considered the complexities of plant photosynthetic responses to light and temperature. We distinguish between predictive integration models and optimization models as possible alternatives for scaling up the carbon and water fluxes. The first set of models describes the light environment and foliage photosynthesis in very detailed manner and can provide the highest accuracy of predicted fluxes, however, these models often require extensive parameterization. As an alternative, optimization models predict profiles of leaf area and photosynthesis assuming that canopy production is maximized for a given resource investment in leaves. The assumption of optimality significantly reduces the parameterization effort, but there is increasing evidence that most plant canopies do not satisfy the criteria for simple

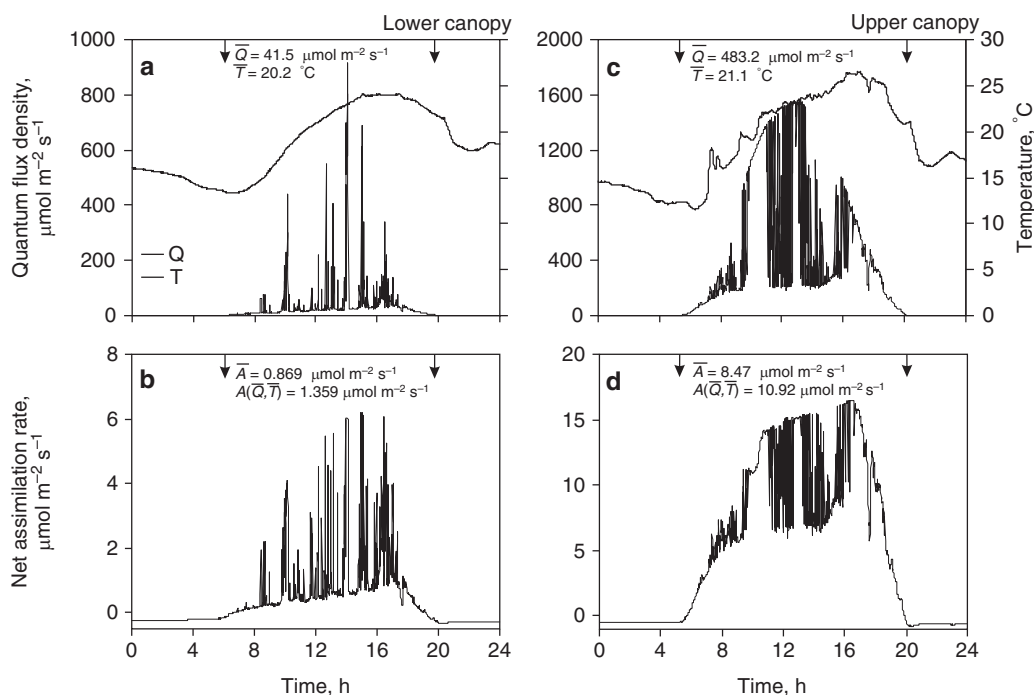


Fig. 16.2. Diurnal variation in quantum flux density, Q , and air temperature, T , in the lower (a) and upper canopy (c) of a mixed deciduous temperate forest at Järvselja, Estonia ($58^{\circ}22' \text{ N}$, $27^{\circ}20' \text{ E}$) on Aug. 24, 1995 (Niinemets and Kull, unpublished data) and simulated net assimilation rate in lower (b) and upper canopy (d). The simulations of net assimilation rate were conducted using the same parameterization for upper canopy (d) as in Fig. 16.1. For the lower canopy (b), V_{cmax} was reduced by a factor of 2.5 compared with the upper canopy (Niinemets et al., 2004b for within-canopy variation in leaf photosynthetic potentials). The daily average net assimilation rate, \bar{A} , was calculated for the light period ($Q > 3 \mu\text{mol quanta m}^{-2} \text{s}^{-1}$) denoted by arrows (between 6:02–19:50 h for the lower and 5:23–20:10 h for the upper canopy). Net assimilation rates corresponding to daily average temperature (\bar{T}) and quantum flux density (\bar{Q}), $A(\bar{Q}, \bar{T})$, were also calculated

optimization (Anten, 2005). The reasons for deviation of actual canopies from theoretical optima are analyzed and alternatives for efficient parameterization of canopy models are suggested.

II. Inherent Differences in Microenvironment and Photosynthetic Potentials Within the Canopy

A. Environmental Variation Within Plant Canopies

1. Gradients in Light Availability

Light is the most variable environmental driver in plant canopies. Natural closed plant canopies sustain high leaf area indices (L , foliage area per ground area) commonly more than $3\text{--}5 \text{ m}^2 \text{ m}^{-2}$ in grass and broad-leaved forest canopies, and

more than $10 \text{ m}^2 \text{ m}^{-2}$ in canopies of shade-tolerant conifers (Asner et al., 1998; Cescatti and Niinemets, 2004, Fig. 16.3a) and in evergreen tropical rainforests (Kitajima et al., 2005). These high leaf area indices make the exposure of all the foliage to full sunlight impossible due to the unavoidable shading within the canopy. Typically, light availabilities differ 20–50-fold between canopy top and bottom in closed plant stands (Lieffers et al., 1999, Fig. 16.3a), but more than 100-fold in some extremely dense tropical rainforests (Valladares, 2003; Kitajima et al., 2005). Even in stands with discontinuous vegetation cover, such as free-standing trees in open woodlands, leaf area density (leaf area per unit crown volume of individual trees) reaches high values, resulting in a significant light gradient within the canopy (crown) of each individual vegetation component (Bégué et al., 1994; Asner and Wessman, 1997).

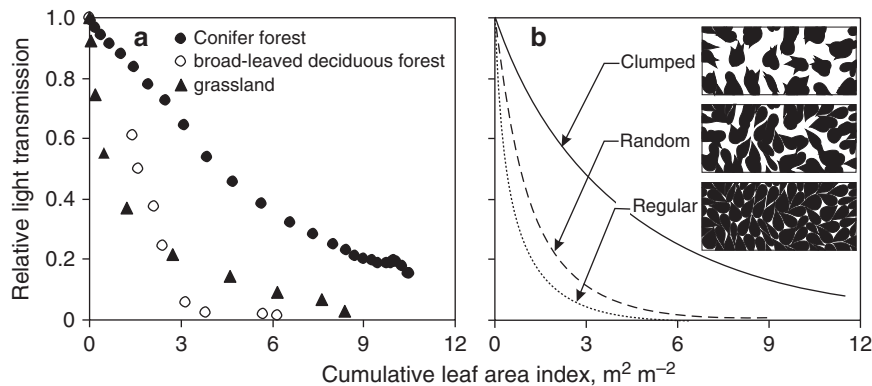


Fig. 16.3. Sample relationships of canopy light transmittance vs. cumulative leaf area index, L_C ; (a) in the canopies of mixed temperate conifer forest dominated by *Abies concolor*, *Calocedrus decurrens*, *Pinus lambertiana*, *Pinus ponderosa* and *Pseudotsuga menziesii* (Gersonde et al., 2004), broad-leaved temperate deciduous forest dominated by *Acer saccharum* (Ellsworth and Reich, 1993), and mixed temperate grassland dominated by a series of grass (*Agrostis canina*, *Calamagrostis canescens*, *Carex disticha*) and forb (*Achillea ptarmica*, *Caltha palustris*, *Veronica scutellata*) species (Fliervoet and Werger, 1984), and theoretical light transmission vs. L_C (b) for hypothetical canopies with clumped, random and regular foliage dispersion. For the temperate conifer forest, the projected leaf area (S_p) was multiplied by 1.1 to obtain the projection area (half of the total surface area, S_H , (Niinemets et al., 2002). In the simulations, leaf angular distribution was spherical, and light transmission at given L_C was integrated over the entire sky hemisphere using the theory of light penetration in non-random media (see Nilson, 1971; Cescatti and Niinemets, 2004 for details of light models). A Markov model with a clumping coefficient $\Omega_0 = 0.3$ was used for the clumped canopy (Eq. 16.1). Light transmission in a regular canopy was simulated by a positive binomial model with the parameter Δ_L (the thickness of a structurally independent leaf layer) set at 1. The values of Δ_L increase with increasing the degree of regularity and $\Delta_L \rightarrow 0$ for a random dispersion. In the insets in (b) that illustrate the concept of foliage dispersion, the number of leaves is equal in all boxes

The way light transmission varies with canopy depth is a function of the distribution of leaf area along the canopy height, as well as of foliage inclination angle and spatial aggregation (Cescatti and Niinemets, 2004 for a review). Differences in foliage inclination angle distributions (characterized by so-called G -function) alter overall canopy transmittance and the way it varies with solar inclination angle, while differences in spatial aggregation (clumping) alter canopy light transmittance independently of solar angle. In the simplest case, for a vertically and horizontally homogeneous canopy, the probability for beam penetration at any given solar zenith angle (θ) and L is given as follows (Nilson, 1971, so-called Markov model):

$$P(\theta) = e^{\frac{-G(\theta) \Omega L}{\cos \theta}}, \quad (16.1)$$

where $G/\cos \theta$ is the extinction coefficient (K). The spatial clumping index $\Omega = 1$ for canopies with randomly dispersed foliage, $1 > \Omega \geq 0$ for aggregated canopies and $\Omega > 1$ for regularly dispersed canopies (Nilson, 1971, Fig. 16.3b). All else being equal, canopies with regular dispersion

intercept more and canopies with aggregated dispersion less light than the canopies with random dispersion (Fig. 16.3b). As random, and particularly regular, dispersions result in very steep light gradients, such that the lowermost foliage may have insufficient light for positive net photosynthesis (Fig. 16.3a), canopies with large L (e.g. in conifers) are typically strongly aggregated (Baldocchi et al., 1985; Cescatti, 1998; Cescatti and Niinemets, 2004; Niinemets et al., 2004a, Fig. 16.3a). Clumped foliage dispersion is also common in open discontinuous canopies (Asner and Wessman, 1997; Cescatti and Niinemets, 2004).

Natural canopies are often composed of multiple species with species-specific foliage inclination angle distributions and spatial aggregations. Because G and Ω are not constant with L in mixed stands, light profiles within such canopies are generally more complex than the profiles in monotypic canopies (e.g. Fig. 16.3a vs. Anten and Hirose, 1999, 2003). Furthermore, the G and Ω functions can vary as the result of acclimation to long-term changes of

irradiance in the canopy (Section II.C below, Stenberg et al., 1999; Cescatti and Zorer, 2003; Niinemets et al., 2006b). Thus, interspecific differences in foliage characteristics combined with species-specific acclimation responses result in very versatile within-canopy light gradients in natural communities.

Because the light pathlengths through the canopy are longer, lower canopy leaves receive relatively less light than the upper canopy leaves in the morning and evening, i.e. the day is effectively shorter in the lower canopy than in the upper canopy. This is especially so at higher latitudes where solar zenith angles are greater than at low latitudes. This has important implications for the distribution of periods with positive and negative carbon balance. For example, since the majority of light compensation points of photosynthesis are between Q of 3 and $10 \mu\text{mol quanta m}^{-2} \text{s}^{-1}$ (Craine and Reich, 2005), in a temperate deciduous forest the part of the day with positive carbon balance was about 4 h less in the bottom than in the top of the canopy (threshold $Q > 3 \mu\text{mol quanta m}^{-2} \text{s}^{-1}$) or even 7 h for the threshold $Q > 10 \mu\text{mol m}^{-2} \text{s}^{-1}$ (Fig. 16.4).

Because foliage absorbs light selectively, light quality also varies significantly within the canopy. In particular, the penetrating solar radiation becomes depleted by blue and red wavebands and enriched by green and far-red wavebands. The modified red/far-red ratio has important consequences for plant morphogenesis and can play a role in canopy development and in filling gaps by foliage (Casal and Smith, 1989; Gilbert et al., 1995), but the photomorphogenetic importance of light quality differs between the species (Pons and de Jong-van Berkel, 2004; Section II.B.4). Differences in light quality can also significantly modify the efficiency of light use in photosynthesis (McCree, 1972; Evans, 1987), in particular, the partitioning of light between photosystems I and II (Liu et al., 1993; Murchie and Horton, 1998).

2. Simulation of Canopy Light Environment

As the use of average light leads to strong overestimation of carbon gain (Fig. 16.1), calculation of light distribution in the canopy forms a core of any scaling up model. One-dimensional (1D) canopy light interception models introduced

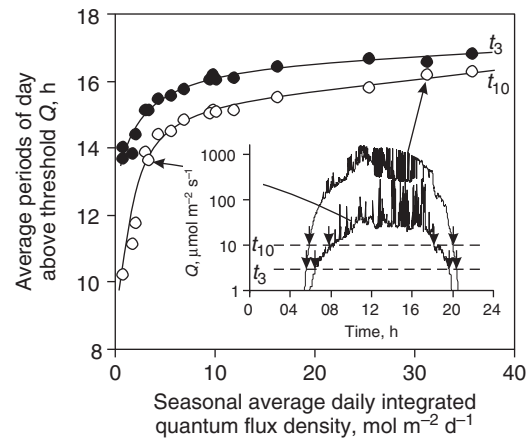


Fig. 16.4. Average periods of day with instantaneous quantum flux density $Q \geq 3 \mu\text{mol quanta m}^{-2} \text{s}^{-1}$ (t_3) and $Q \geq 10 \mu\text{mol quanta m}^{-2} \text{s}^{-1}$ (t_{10}) in relation to within-canopy gradient in seasonal average integrated quantum flux density (Q_{int}) in Järvelja broad-leaved deciduous forest ($58^\circ 22' \text{ N}$, $27^\circ 20' \text{ E}$) for 1995 growing season (Niinemets, unpublished data). The inset demonstrates representative daily time-courses of Q measured on Aug. 31, 1995 at canopy heights of 13 m ($Q_{\text{int}} = 1.82 \text{ mol quanta m}^{-2} \text{ day}^{-1}$, denoted by an arrow) and 18 m ($Q_{\text{int}} = 31.4 \text{ mol quanta m}^{-2} \text{ day}^{-1}$). The scale of Q is log-transformed to better visualize the onsets of threshold Q . The threshold Q values of 3 and $10 \mu\text{mol m}^{-2} \text{s}^{-1}$ correspond to the range of compensation Q , above which leaf carbon balance becomes positive in temperate deciduous broad-leaved trees (Craine and Reich, 2005)

by Monsi and Saeki (1953) are based on turbid medium analogy (Lambert-Beer law). These models assume that the canopy is composed of randomly distributed infinitesimally small leaf elements. In the simplest case, light transmission through the canopies of various depth h is predicted assuming optically black leaves and a certain light extinction coefficient K that depends on foliage inclination angle distribution, and assuming uniform leaf area density in the canopy (L/h , Fig. 16.5). Description of various spatial distributions of L in the canopy requires at least two more parameters (e.g. using Weibull function Mori and Hagihara, 1991; Niinemets, 1996), while consideration of foliage spatial clumping (Ω , Eq. 16.1) requires at least one more parameter. Relaxing the assumption of optically black leaves, i.e. accounting for scattered light, requires information of leaf reflectance and transmittance at any given wavelength and parameterization of an appropriate reflectance distribution function (Schaeppman-Strub et al., 2006). An assumption







Dimension	Number of parameters	Visualization
1	2	
1	4	
1	5	
2	4-7	
3	2n-3n	
3	∞	

Fig. 16.5. Illustration of the hierarchy of radiation transfer models in canopy. The number of parameters required to simulate light within the canopy increases with relaxing the assumptions on canopy structure and addition of levels of complexity. For a given total leaf area index L , one-dimensional models assuming uniform distribution of foliage require only two parameters – light extinction coefficient, K , and canopy height, h , (L/h describing the uniform distribution of leaf area within the canopy). Parameterization of actual leaf area distributions requires at least two more parameters, while accounting for foliage clumping requires at least one additional parameter. In the two-dimensional hedgerow models the distance between rows and row orientation are needed. Three-dimensional (3D) models require estimation of leaf area density, extinction coefficient and clumping at a series of canopy locations, the parameterization effort depending on the number of canopy locations chosen and the efficiency with which canopy and non-canopy regions can be separated. As a further advancement of 3D models, models describing the location of every foliage element in the canopy and simulating light environment by Monte Carlo ray-tracing techniques have been developed. However, the number of parameters required for such models is practically infinite (e.g. North, 1996)

that leaf reflectance and transmittance are equal and light is scattered equally upwards and downwards makes the calculation of scattered fluxes relatively simple (Goudriaan, 1977). Such a simplified consideration of scattered fluxes has been used in several recent canopy model analyses (Anten and Hirose, 1998; Anten et al., 2004; Aan et al., 2006).

Because, under clear day conditions, there are leaves in each canopy layer that are exposed to direct light with high intensity (“sunlit” foliage)

and those that are not (“shaded” foliage), derivation of mean irradiance for each canopy layer will again result in the integration problem in calculating photosynthesis in any given layer. This problem was remedied by separating between sunlit and shaded foliage classes in every canopy layer, resulting in correct integration of canopy photosynthetic fluxes (Duncan et al., 1967). The scheme of Duncan et al. (1967) was further improved by including simple expressions for leaf angular distributions and for scattered light fluxes (Goudriaan, 1977). Because of the apparent ease of parameterization and inclusion of most of the fundamental radiative transfer characteristics, these 1D models are still widely used to estimate canopy light profiles and integrating photosynthetic fluxes (e.g. Anten et al., 2004; Aan et al., 2006). For relatively homogenous herbaceous stands (Anten, 1997; Hikosaka et al., 1999b) or early successional forest stands (Selaya et al., 2007), these 1D models can provide good predictions of canopy light environment.

In reality, many plant stands exhibit strong vertical and horizontal heterogeneity due to significant variation in plant height, non-homogeneous plant dispersal in stand, local differences in leaf area index and species composition. In non-homogeneous stands, application of 1D models is not justified. Two-dimensional (2D) models developed for hedgerow orchards describe plant stand as regularly dispersed rows of light-absorbing canopy and non-absorbing empty rows (row models). The distance between the rows and row orientation determine the beam path-length in the canopy. Thus, for such 2D models, at least two more parameters are needed – distance between and azimuth angle of canopy rows (Jackson and Palmer, 1972; Jackson, 1980). However, such models can only be used when the rows are unidirectional and regularly spaced, e.g. as in orchard or grain crops.

In further development of light interception models, three-dimensional (3D) models were introduced, considering the heterogeneous spatial distribution of foliage (Myneni, 1991; Ryel, 1993). In these 3D models, the parameterization effort is dependent on the number of individual canopy volume elements (voxels) selected in the three-dimensional space. For every voxel, leaf area density and basic radiative

transfer characteristics are needed (Fig. 16.5). Heavy computing requirements and parameterization difficulties have initially limited the use of simple 3D models (Falge et al., 1997). In more effective 3D computing algorithms, the crown shape of every tree and leaf area distribution within the crown are described, thereby effectively discriminating between canopy and non-canopy space and significantly reducing the computing load (e.g. Cescatti, 1997a).

Probably, the most accurate snapshot of canopy light environment can be achieved by 3D Monte Carlo ray-tracing models that simulate the exact locations of every canopy element (Pearcy and Yang, 1996; Casella and Sinoquet, 2003; Sinoquet et al., 2005). Such models constitute a promising tool for the quantitative analysis of light interception by complex foliage geometry (Sinoquet et al., 1998; Valladares and Pearcy, 1998). In addition, phenomena that are difficult to simulate using statistical light interception models, such as penumbra (half-shade between “sunlit” and “shaded” leaf classes) and bidirectional reflectance, can be numerically evaluated using ray tracing techniques (Cescatti and Niinemets, 2004). Due to the vast amount of geometric information required, parameterization of such models is often not feasible and practical, especially given that the geometry is subject to change as plants move in wind and during growth. Nevertheless, plant stands can be constructed of flexible “virtual plants” (Godin, 2000; Godin and Sinoquet, 2005) or the ray-tracing models can be parameterized on the basis of allometric relationships and canopy hemispherical photographs (Casella and Sinoquet, 2003). This way the importance of specific plant architectural features on canopy radiative transfer characteristics can be studied in extensive computer-generated plant stands.

Already in early stages of light model development, it has been realized that there is a trade off between the precision and generality of light models (Cowan, 1968). More complicated mechanistic models can be used to simulate canopy carbon gain at higher spatial and temporal resolution, but these models also rely more heavily on input data, and their parameterization may become overtly laborious. Complicated 3D models are usually applied in studies attempting to analyze photosynthesis at the level of

individual plant element (shoot, branch) or individual plant. They are especially useful for quantification of consequences of architectural plant traits (e.g., branching pattern) on light interception and carbon gain (Ackerly and Bazzaz, 1995; Pearcy et al., 2004; Valladares and Niinemets, 2007). Simple 1D models on the other hand can be more useful when the objective is to quantitatively assess ecosystem carbon gain over large areas with relatively homogenous vegetation (Section III.D), e.g. to gain insight into vegetation responses to environmental conditions, including plant responses to global change (e.g. Haxeltine and Prentice, 1996; Pan et al., 1998; Arneth et al., 2007).

3. Co-variations among Environmental Drivers in Plant Canopies

In addition to light, multiple other environmental factors vary with height in plant canopies. Day-time temperatures increase and night-time temperatures decrease with increasing height in the canopy (Baldocchi et al., 2002; Niinemets and Valladares, 2004; Fig. 16.6a). While the difference in average air temperatures between canopy top and bottom may be on the order of 2–4°C (Fig. 16.6a), the differences can be significantly larger during certain periods of day (Eliáš et al., 1989; Niinemets and Valladares, 2004). Furthermore, temperatures of sun-exposed leaves may exceed ambient air temperature by more than 10°C (Hamerlynck and Knapp, 1994; Singsaas et al., 1999; Valladares and Niinemets, 2007), especially when latent heat loss via transpiration is curbed due to stomatal closure in water-stressed leaves.

Given that foliage dark respiration rates increase exponentially with temperature (Atkin et al., 2005 for a review), differences in the night-time temperature can importantly modify the carbon balance of foliage in different canopy locations. Longer night period (Fig. 16.4) combined with higher night-time temperatures may cause the leaves in the lower canopy to use a relatively larger proportion of their daily photosynthesis for maintenance respiration than the leaves in the upper canopy.

Air relative humidity is generally also lower in the upper canopy (Chiariello, 1984; Niinemets and Valladares, 2004; Fig. 16.6a inset). This in

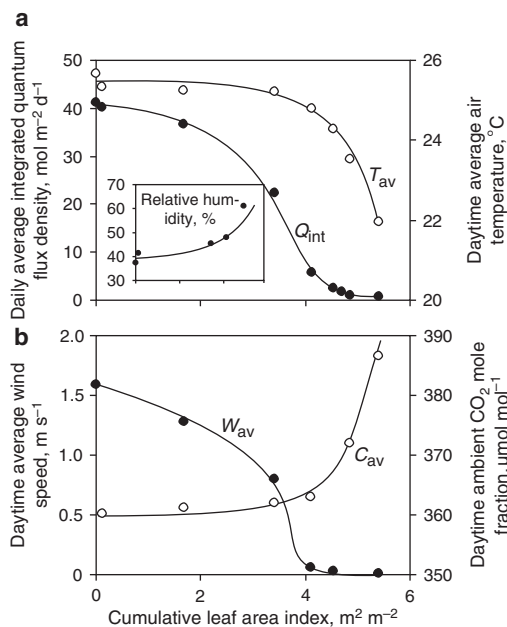


Fig. 16.6. Within-canopy variation in average integrated quantum flux density (Q_{int}), average temperature (T_{av}), average day-time wind speed (W_{av}) and average day-time CO_2 concentration (C_{av}) in a mixed deciduous broad-leaved forest dominated by *Acer campestre*, *Carpinus betulus*, *Quercus cerris* and *Q. petraea* at Báb, Slovakia (48°10'N 17°53'E). Data (Eliáš et al., 1989) were recalculated using daily time-courses and measured canopy profiles in July. CO_2 concentration measurements in 1987 were adjusted to current climates (2007, <http://cdiac.ornl.gov>) using an offset of $31.2 \mu\text{mol mol}^{-1}$.

combination with greater solar radiation input and higher leaf temperatures implies that the evaporative demand increases with height in the canopy. During periods of limited soil water availability, such differences in evaporative demand can result in stronger reductions in stomatal conductance and in intercellular CO_2 concentrations in upper canopy leaves. Overall, photosynthesis in the upper canopy is more strongly limited by CO_2 due to higher quantum flux densities that lead to greater assimilation sink and stronger drawdown of CO_2 concentration in leaf intercellular air space (Francey et al., 1985; Hanba et al., 1997), enhanced by relatively stronger reduction of stomatal conductance in the upper canopy (Aasamaa et al., 2004; Niinemets et al., 2004c).

As soil respiration is releasing CO_2 and photosynthetic activity of bottom leaves is low, average day-time CO_2 concentrations decrease

with increasing height in the canopy (Buchmann et al., 1996; Fig. 16.6b). Given that light-saturated assimilation rates respond nearly linearly to CO_2 concentrations at the current ambient CO_2 , this gradient can significantly add to the severe CO_2 limitations of photosynthesis in the upper canopy. On the other hand, the elevation of CO_2 in the lower parts of the canopy stimulates photosynthesis of shaded leaves through its effect on quantum yield (DeLucia and Thomas, 2000; Sefcik et al., 2006).

Average wind speed and air turbulence increase with increasing height in the canopy as well (Grantz and Vaughn, 1999; Marcolla et al., 2003; Fig. 16.6b). Greater turbulence results in higher boundary layer conductance for CO_2 , water vapor and heat exchange. While the higher boundary layer conductance increases transpiration rate, the increased heat exchange counteracts the rise, reducing transpiration via lowering leaf temperature. Thus, the net effect of enhanced turbulence on leaf transpiration depends on the induced modifications in all components of leaf energy balance (convection, latent energy loss, solar radiation absorption, thermal radiation emission and absorption), and can be quantitatively assessed by iteratively solving the leaf energy balance (Gates, 1980). Although enhanced turbulence tends to reduce leaf temperature, the overall hazard of leaf heat stress is still larger in the upper canopy. Apart from the direct effects on leaf energy balance, enhanced wind speed also implies stronger mechanical stress. Leaf loss through wind damage has been shown to be greater in the upper than in the lower canopy (Yasumura et al., 2002). Coping with such mechanical stresses may require relatively higher biomass investments in mechanical support compared to the photosynthetic machinery.

This evidence indicates that within-canopy variation in a series of environmental drivers interacts with the variation in light. Such climatic differences are not considered in simple scaling up models that consider only within-canopy variation in light. More complex soil-vegetation-atmosphere-transfer (SVAT) models can be employed to predict the canopy profiles of key environmental variables (e.g. Katul and Albertson, 1999; Baldocchi et al., 2002; Marcolla et al., 2003). SVAT models have huge potential for analysis and simulation of the effects

of interactive environmental drivers on canopy photosynthetic productivity.

B. Light-dependent Modifications in Leaf Structure, Chemistry and Function

1. General Framework to Evaluate Photosynthetic Acclimation

Plant leaves have a large capacity for acclimation to within-canopy light gradient. As the result of this acclimation, foliage photosynthetic potentials increase with increasing light availability in the canopy (Fig. 16.7), thereby enhancing photosynthetic production in higher light (e.g. classical studies by Hirose and Werger, 1987a; Gutschick and Wiegel, 1988). Depending on plant functional type, foliage photosynthetic capacity (light-saturated assimilation rate, A_{\max}) varies between 2 and 20-fold from the canopy top to bottom (Fig. 16.7). What is responsible for this large within-canopy variation in A_{\max} ? To separate the sources of variation in photosynthetic capacity, it is germane to distinguish between the component processes of A_{\max} – the capacity for the light reactions and photosynthetic electron transport, and the capacity for the dark reactions, mainly limited by the carboxylase activity of ribulose 1,5-bisphosphate (RuBP) carboxylase/oxygenase, Rubisco (Farquhar et al., 1980). According to this steady-state photosynthesis model, foliage net assimilation rate, A , is given as the minimum of the two potential RuBP carboxylation rates, W_c that denotes Rubisco-limited and W_j that denotes electron-transport limited carboxylation rate:

$$A = \left(1 - \frac{\Gamma^*}{C_i}\right) \min(W_c, W_j) - R_D, \quad (16.2)$$

where R_D is the rate of non-photorespiratory respiration in light and Γ^* is the hypothetical CO_2 compensation point of photosynthesis in the absence of R_D , and C_i is the intercellular CO_2 concentration. The Rubisco $V_{c\max}$ determines the maximum value of W_c , while the capacity for photosynthetic electron transport, J_{\max} , the maximum value of W_j .

Both the maximum rates, $V_{c\max}$ and J_{\max} , can be expressed via the abundance and specific chemical activities of rate-limiting proteins per unit leaf area. $V_{c\max}$ per unit leaf area is given as (Niinemets and Tenhunen, 1997)

$$V_{c\max} = 6.25 V_{cr} M_A F_R N_M, \quad (16.3)$$

where V_{cr} is the specific activity, i.e. the maximum rate of RuBP carboxylation per unit Rubisco protein ($V_{cr} = 20.5 \mu\text{mol g}^{-1} \text{s}^{-1}$ at 25°C , Jordan and Ogren, 1984), M_A is leaf dry mass per unit area, F_R is the fraction of leaf nitrogen in Rubisco, N_M is leaf nitrogen content per dry mass. J_{\max} is given as

$$J_{\max} = 8.06 J_{mc} M_A F_B N_M, \quad (16.4)$$

where J_{mc} is the capacity for photosynthetic electron transport per unit cytochrome *f* ($J_{mc} = 156 \text{ mol e}^- (\text{mol cyt } f)^{-1} \text{ s}^{-1}$ at 25°C), and F_B is the fraction of leaf nitrogen in bioenergetics, i.e. in the rate-limiting proteins of NADPH and ATP production in chloroplasts (Niinemets and Tenhunen, 1997). The scaling coefficients 6.25 and 8.06 depend on the stoichiometry of rate-limiting proteins and nitrogen content of proteins.

Equations (16.3) and (16.4) demonstrate that foliage photosynthetic potentials per unit leaf area may vary because of differences in nitrogen partitioning in photosynthetic machinery (F_R and F_B), nitrogen concentration of foliage (N_M) and leaf structure (M_A). All else being equal, increases in M_A result in larger $V_{c\max}$ and J_{\max} because of accumulation of nitrogen and photosynthetic proteins per unit leaf area. Nitrogen content per unit area, $N_A = N_M M_A$, and analogously, $V_{c\max}$ and J_{\max} per unit area are equal to M_A times $V_{c\max}$ and J_{\max} per unit dry mass. Thus, different combinations of structural and chemical traits can result in similar foliage photosynthetic potentials.

2. Importance of Within-canopy Gradients in Nitrogen and Leaf Dry Mass per Unit Area

Relevance of various structural and chemical traits for within-canopy variation in photosynthetic potentials differs among plant functional types. In herbaceous species, and in woody species with continuous foliage development and senescence throughout the season, such as fast-growing *Salix* species, foliage is generally formed in high irradiance and becomes gradually overtopped and shaded by younger foliage. In such canopies, M_A is relatively invariable (ca. 1.3-fold variation in Fig. 16.7a, see also for analogous patterns Hirose et al., 1988; Kull et al., 1998).

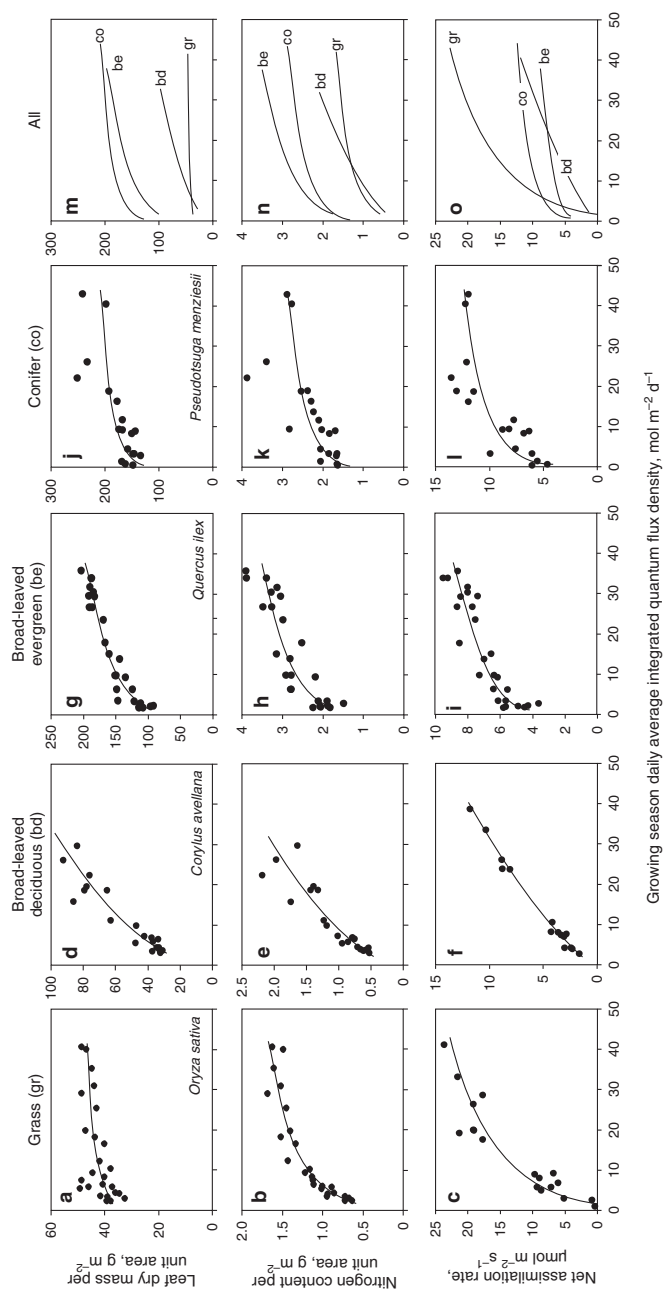


Fig. 16.7. Influence of within-canopy variation in integrated quantum flux density, Q_{int} , on leaf structure, chemistry and photosynthetic capacity. Leaf dry mass per unit area (M_A ; a, d, g, j, m), leaf nitrogen content per area (N_A ; b, e, h, k, n) and light-saturated net assimilation rate (A_{max} ; c, f, i, l, o) in relation to Q_{int} in representative canopies of annual grass (a–c, data from Anten et al., 2004, ambient CO_2 -grown non-fertilized plants), broad-leaved deciduous (d–f, data from Niinemets et al., 1998), broad-leaved evergreen (g–i, data from Niinemets et al., 2006a) and conifer trees (j–l, data from Bond et al., 1999) canopies. Relationships on a common scale are also shown (m–o). Data are expressed on the basis of projected leaf area. In all species, except the conifer, A_{max} was standardized to common intercellular CO_2 mole fraction of $245 \mu\text{mol mol}^{-1}$, leaf temperature of 25°C , and incident quantum flux density of $1,500 \mu\text{mol quanta m}^{-2} \text{s}^{-1}$ using Farquhar et al. (1980) photosynthesis model (parameters derived in the original publications). For the conifer species, A_{max} corresponds to light-saturated assimilation rates measured at ambient CO_2 mole fraction of $360 \mu\text{mol mol}^{-1}$ at constant leaf cuvette temperature of 25°C . The statistical relationships are fitted by non-linear regressions and are all significant at $P < 0.001$. The fraction of variance explained (r^2) is larger than 0.8, except for M_A in grass species (a, $r^2 = 0.39$) and for all three variables in the conifer species (j–l, $r^2 = 0.49$ – 0.67)

This apparent constancy in M_A is because M_A is mostly determined by the light at which the leaves are formed (Brooks et al., 1994; Anten et al., 1998; Yamashita et al., 2002; Niinemets et al., 2004b, 2006a). In these species, the within-canopy gradient in leaf nitrogen content per area is mainly achieved by nitrogen reallocation from older shaded leaves to younger exposed foliage (Hirose et al., 1988; Hikosaka et al., 1993). For instance, there is 2.2-fold variation in N_M and 2.6-fold variation in N_A in the canopy of annual grass species *Oryza sativa* (Fig. 16.7b). Nitrogen reallocation in canopies with short-lived foliage is often associated with senescence of shaded foliage (Hikosaka et al., 1993; Ono et al., 2001; Weaver and Amasino, 2001; Hikosaka, 2005), explaining very low rates of light-saturated photosynthesis in lowermost canopy positions (Fig. 16.7c).

By contrast, in most temperate deciduous trees, all leaves are formed at about the same time as a single flush, and the leaves are maintained through the entire growing season. As the result, light conditions remain similar during most of the leaf life span (Niinemets et al., 2004b). Adjustment of M_A to light environment during leaf growth and development is the primary determinant of the within-canopy variation in N_A and A_{\max} per area (Fig. 16.7d–f), while N_M and A_{\max} per dry mass are less variable in such canopies (Kull, 2002; Meir et al., 2002; Niinemets, 2007; Fig. 16.7d–f). In conifers with complex three-dimensional shape of leaf cross-section, leaf dry mass per unit projected area ($M_{A,P}$) is equal to dry mass per unit total area ($M_{A,T}$) times total to projected surface area ratio ($M_{A,P} = S_T/S_P M_{A,T}$). This is relevant as S_T/S_P typically increases with light availability in the canopy, amplifying the effect of light on biomass accumulation per unit projected area (e.g. Niinemets et al., 2007a).

Canopy profiles of N_A and A_{\max} of current-year foliage of evergreen broad-leaved trees and conifers are also mainly driven by variation in M_A (Fig. 16.7g–i). However, older foliage of broad-leaved evergreens and evergreen conifers becomes gradually shaded by newly formed foliage. As M_A of these shaded leaves is acclimated to its former higher light environment, M_A of older leaves is weakly correlated with leaf current light environment (Niinemets et al., 2006a; Wright et al., 2006). In fact, significant

re-acclimation to modified leaf light environment can occur within the older leaves of evergreen species, such that A_{\max} of older leaves scales better with leaf current than with previous light environment. Such a re-acclimation is mainly associated with modifications in nitrogen partitioning among components of foliage photosynthetic machinery (Brooks et al., 1994; Niinemets et al., 2006a).

3. Role of Within-leaf Nitrogen Partitioning

As A_{\max} varies commonly between 5–20-fold in herbaceous canopies, variation in N_A alone is not enough to explain the variability in A_{\max} (e.g. Pons and de Jong-van Berkel, 2004; Fig. 16.7c). In fact, the large within-canopy variation in A_{\max} suggests that foliage nitrogen partitioning, F_R and F_B (Eqs. 16.3, 16.4), also significantly varies within the canopy. To understand the economics of foliar nitrogen distribution, it is further important to consider that a significant part of photosynthetic nitrogen is invested in light harvesting pigment-binding proteins. Modifications in the fraction of nitrogen in pigment-binding complexes (F_L) alter leaf chlorophyll content per unit area (χ_A) (Niinemets and Tenhunen, 1997):

$$\chi_A = N_M M_A F_L C_B, \quad (16.5)$$

where C_B , mmol Chl (g N)^{−1} – the ratio of chlorophyll to nitrogen invested in chlorophyll and its binding proteins – depends on the stoichiometry of chlorophyll-binding proteins engaged in light harvesting. C_B is typically around 2.1–2.5 mmol g^{−1} (Niinemets and Tenhunen, 1997; Niinemets et al. 1998). Changes in χ_A in turn alter leaf absorptance ξ . An empirical relationship has been derived between ξ and χ_A for a wide range of species (Evans, 1993b):

$$\xi = \frac{\chi_A}{\chi_A + 0.076}, \quad (16.6)$$

where 0.076 is an empirical constant and χ_A is in mmol m^{−2}. Differences in leaf anatomy seem to exert only a moderate effect on leaf absorptance, but Eq. (16.6) cannot be used for species with waxy or hairy leaves (Evans and Poorter, 2001). While the maximum quantum yield of photosynthesis on an absorbed light basis, α_A , is very

conservative among C_3 species (Ehleringer and Björkman, 1977), the quantum yield for an incident quantum flux density, α_I , is directly dependent on $\xi(\alpha_I = \alpha_A \xi)$. Thus, modifications in the fraction of N in light harvesting alter leaf light use efficiency and thereby strongly affect photosynthesis at low to moderate light (Eq. 16.5).

An important ecological question is whether N partitioning among photosynthetic compounds is optimal, i.e. whether N is distributed among the photosynthetic proteins in a way that maximizes leaf photosynthesis at a given leaf light environment. The total nitrogen invested in photosynthetic machinery per unit leaf area N_P is given as

$$N_P = N_A(F_R + F_B + F_L). \quad (16.7)$$

Photosynthesis is maximized for a given N_P if A cannot be increased by any redistribution of nitrogen between F_R , F_B and F_L . In practice, this condition means that the potential carboxylation rates (Eq. 16.2), $W_c(V_{cmax}, C_i)$ and $W_j(J_{max}, \alpha_I, Q, C_i)$ are equal and there is no excess capacity in either light or dark reactions of photosynthesis. Solving Eqs. (16.2–16.7) for optimal nitrogen partitioning at the current ambient CO_2 concentration demonstrates that optimal F_L increases with decreasing Q to enhance light capture and harvesting efficiency (Fig. 16.8a). The optimal fraction of N in

Rubisco increases strongly with increasing Q , to meet the requirement for faster photosynthesis. Optimal partitioning of N to electron transport F_B also increases initially with Q but then levels off with further increases in Q . This apparent plateau in F_B results from the circumstance that at current ambient CO_2 concentrations, photosynthesis at high light is more sensitive to changes in Rubisco activity than to changes in electron transport capacity (Fig. 16.8a).

In practice, due to alterations in solar inclination angle and heterogeneous distribution of gap fraction in the canopy, plant leaves are exposed both to high and low light during the day. Thus, the leaves partitioning N optimally for low light are non-optimal at high light and vice versa (Fig. 16.8b). Due to the high cost of protein turnover and unpredictability of weather conditions, full optimality in leaf nitrogen partitioning is not possible. Nevertheless, the optimality-based predictions on foliar nitrogen partitioning among the components of photosynthetic apparatus qualitatively hold true. Allocation of N to light harvesting increases with enhanced shading (Evans, 1993a; Hikosaka and Terashima, 1996; Niinemets and Tenhunen, 1997; Fig. 16.8c). According to these studies, a major fraction, 0.3–0.6 of total leaf nitrogen, is invested in light harvesting in low light. There is also

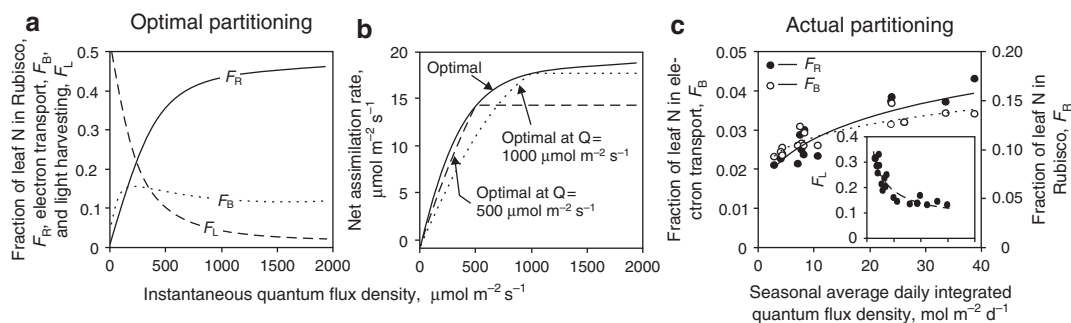


Fig. 16.8. Variation of (a) optimal leaf N partitioning between the components of leaf photosynthetic machinery with instantaneous quantum flux density, Q , and (b) simulated light response curves of net assimilation rate for the optimal N partitioning depicted in (a) and for N partitioning that is optimal for $Q = 500$ and $Q = 1,000 \mu\text{mol quanta m}^{-2} \text{s}^{-1}$, and (c) observed N partitioning in relation to within-canopy gradient in irradiance in temperate deciduous broad-leaved species *Corylus avellana* (data from Niinemets et al., 1998). Foliage N partitioning is considered optimal, if any redistribution of N between the components of photosynthetic machinery cannot yield higher photosynthesis at current environmental conditions. The optimality condition implies that the limiting processes in the Farquhar et al. (1980) model, RuBP carboxylation (limited by Rubisco activity, W_c) and RuBP regeneration (limited by light harvesting and/or electron transport, W_j) are equal. In the simulations (a) and (b), the fraction of nitrogen in photosynthetic machinery was fixed at 0.6, leaf temperature was kept at 25°C , intercellular CO_2 concentration was held at $275 \mu\text{mol mol}^{-1}$, the curvature of the non-rectangular light response function was set at 0.85, and the values of V_{cmax} , J_{max} and the initial quantum yield of photosynthetic electron transport were calculated according to Eqs. (16.3–16.7). In (c), the data were fitted by non-linear regressions ($r^2 > 0.8$ for all)

evidence of significant increase of F_R and F_B with increasing light availability (Hikosaka and Terashima, 1996; Grassi and Bagnaresi, 2001; Fig. 16.8c). Light-dependent modifications in F_R and F_B are specially significant in herbaceous species, where alterations in nitrogen partitioning are responsible for a major part of the A_{\max} gradient observed (Hikosaka and Terashima, 1996; Fig. 16.7a). In woody species, in evergreens in particular, light-dependent modifications in F_R and F_B are moderate, and in some cases F_R and F_B have been found to be essentially constant along the light gradient (Niinemets, 1998; Evans and Poorter, 2001; Niinemets et al., 2006a). Analysis of light-acclimation across a large number of species suggested that modifications of M_A and associated alterations in total nitrogen content per area are generally more important determinants of light-dependent changes in A_{\max} than nitrogen partitioning within the leaves (Evans and Poorter, 2001).

4. Mechanisms of Within-canopy Acclimation of Photosynthetic Potentials

The phenomenon of within-canopy photosynthetic acclimation is extensively documented, but the acclimation mechanisms, in particular how the plants sense the light climate and what triggers the acclimation, are still not well known. Large number of studies have proposed that changes in the red (660 nm)/far-red (730 nm) ratio of light (R/FR) constitute the primary signal in light acclimation (Smith, 1995; Murchie and Horton, 1997; Van Hinsberg, 1997). As plant foliage more strongly absorbs red than far-red light, a decrease in R/FR is an almost unmistakable indication of shading by leaves positioned higher in the canopy (Smith, 1982). While changes in light quality play an important role in many photomorphogenic modifications, like stem elongation and foraging for light (Smith, 1982), flowering (Myster, 1999) and seed germination (Ahola and Leinonen, 1999), the evidence of light quality effects on N allocation and photosynthesis is equivocal. Enrichment by FR light stimulates leaf senescence and N remobilization in several herb species (Guiamet et al., 1989; Skinner and Simmons, 1993; Rousseaux et al., 1996, 2000). This effect may be responsible for redistribution of nitrogen within the herbaceous canopies

(Fig. 16.7a–c). However, in other species, similar N gradients can develop under neutral shading (constant R/FR ratio, e.g., Hikosaka et al., 1994). The overall effect of light quality on leaf morphology and photosynthetic capacity seems to be moderate in tree species with long-living foliage (Kwesiga and Grace, 1986; Kwesiga et al., 1986; Lei and Lechowicz, 1998 for experimental evidence; Pons and de Jong-van Berkel, 2004; Terashima et al., 2005 for a review). As an alternative explanation, it has been suggested that development of thicker leaves in the upper canopy is mediated through the abundance of sugars produced during photosynthesis (Kull and Kruijt, 1999; Yano and Terashima, 2001; Terashima et al., 2005). In tree species with determinate growth, leaf primordia are formed in the previous growing season, and high-light formed buds have already more mesophyll layers than the buds formed under low light (Eschrich et al., 1989; Kimura et al., 1998; Uemura et al., 2000). As thicker leaf primordia contribute to higher rates of photosynthesis and sugar production in developing leaves, this finding is in general agreement with the “sugar gradient” hypothesis for formation of within-canopy gradients in photosynthetic capacity (Niinemets et al., 2004b).

It has also been postulated that modifications in photosynthetic capacity result from differences in concentration of cytokinins during leaf growth and development (Pons et al., 2001). Cytokinins play an important role in delaying leaf senescence (Stoddart and Thomas, 1982). They are transported from roots by the transpiration stream and can therefore be distributed among leaves in proportion to the amount of evaporated water. As the transpiration rate is roughly proportional to the amount of absorbed solar energy, cytokinin distribution in the canopy should approximately match the light gradient (Pons and Bergkotte, 1996). This hypothesis is supported by experimental evidence that a reduction in transpiration rate induces responses similar to shading, such as decreases in chlorophyll *a/b* ratio, reductions in photosynthetic capacity (Pons and Bergkotte, 1996; Pons et al., 2001) and curbed expression of *rbcS* gene that encodes the small subunit of Rubisco (Boonman et al., 2007). Application of a synthetic cytokinin benzyl adenine reversed these

effects (Boonman et al., 2007). However, partial shading of a variety of mutant plants of *Arabidopsis thaliana* deficient in either cytokinin-, photoreceptor-, or sugar-mediated signal transduction pathway resulted in shade acclimation patterns similar to those observed in wild type *A. thaliana* (Boonman, 2006). This evidence collectively indicates that shade acclimation involves multiple independent mechanisms.

C. Light-dependent Modifications in Foliage Inclination Angle Distributions and Spatial Clumping

Apart from within-canopy alterations in A_{\max} and modifications in light harvesting efficiency of single leaves that result from changes in M_A and N_A , there are further important modifications in leaf light harvesting efficiency due to within-canopy variation in foliage orientation and spatial aggregation. Leaf inclination angles are generally more vertical at higher light, reducing the interception of excessive solar irradiance in midday, while allowing light to penetrate to deeper canopy layers (e.g. Valladares and Niinemets, 2007 for a review). In contrast, more horizontal foliage inclination angles are highly beneficial in understory environments, where most of light enters from low zenith angles (e.g. Muraoka et al., 1998). For example, in a tall grass canopy, smaller species occupying the lower canopy had more horizontal leaves than upper canopy dominants (Anten and Hirose, 1999). 30% of the difference in light capture by upper and lower canopy species was due to differences in foliage orientation (Anten and Hirose, 1999). Because light-dependent foliage orientation results in more uniform distribution of light within the canopy, this acclimation pattern improves whole canopy photosynthesis (Gutschick and Wiegel, 1988; Cescatti and Niinemets, 2004). However, a significant variation in foliage inclination angles within the canopy also implies that the light extinction coefficient (K , Eq. 16.1) actually varies with canopy depth, complicating prediction of within canopy light environment.

Plant foliage is generally also more strongly aggregated at higher light availability, especially in species with small leaves such as needle-leaved conifers (Cescatti and Zorer, 2003; Niinemets

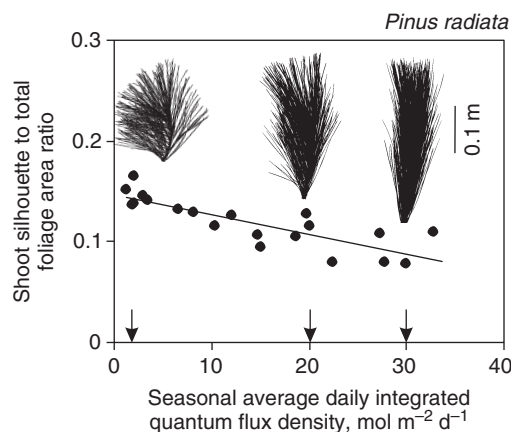


Fig. 16.9. Shoot silhouette to total area ratio (S_S) in relation to average daily integrated quantum flux density Q_{int} in the evergreen conifer *Pinus radiata* (modified from Niinemets et al., 2006b). Variation in S_S primarily results from alterations in foliage spatial aggregation (clumping, Fig. 16.3 for definition). Representative shoot silhouettes are also shown for Q_{int} values of 1.87, 20.1 and 30.0 mol quanta $\text{m}^{-2} \text{day}^{-1}$ (denoted by arrows)

et al., 2006b; Fig. 16.9), but foliage can also be significantly aggregated in broad-leaved species (Niinemets et al., 2005). Shoots with clumped foliage harvest light significantly less efficiently than shoots with randomly dispersed foliage (Fig. 16.3b). However, for shoots situated in high radiation field that exceeds the saturation point of photosynthesis, such clumping should not necessarily reduce daily photosynthesis, but allows concentration of photosynthetic biomass to higher light where photosynthetic gains are the largest. Less clumped foliage in low light (Fig. 16.9), in turn, implies greater foliage light harvesting efficiency and more efficient use of limiting light availabilities. Thus, within-canopy variation in foliage aggregation is another important structural acclimation response that makes the distribution of light throughout the canopy more uniform, and thereby increases whole canopy carbon gain (Cescatti, 1998; Cescatti and Niinemets, 2004).

D. Modifications to Interacting Environmental Drivers

Complex interactions between multiple environmental drivers in plant canopies (Section II.A.3.) constitute a challenge for the plants. In particular, higher temperatures and lower humidities imply

that foliage can sustain higher heat and water stress in the upper canopy. Understanding plant response to multiple stresses is important as the possible interactive effects cannot be predicted from single factor analyses (Valladares et al., 1997).

There is evidence that heat resistance of photosynthetic electron transport is higher in leaves exposed to higher light (Niinemets et al., 1999; Griffin et al., 2002; Bauerle et al., 2007). The shape of the temperature response curve of J_{\max} varies across the canopy such that the optimum temperature for J_{\max} scales positively with light availability. In addition, the shape of mitochondrial respiration rate also varies within the canopy (Griffin et al., 2002). The greater heat resistance of photosynthetic apparatus in leaves at higher light is possibly associated with the higher concentration of sugars (Niinemets and Kull, 1998) that enhance the stability of thylakoid membranes (e.g. Hüve et al., 2006). Accumulation of neutral osmotica such as sugars also protects photosynthetic apparatus against water stress (Kaiser, 1987). Thus, accumulation of sugars provides an important mechanism for simultaneous acclimation to drought and heat stress in the upper canopy.

Photosynthetic acclimation to temperature can also be achieved by modifications in membrane fluidity through changes in membrane lipid composition (Logue et al., 2000; Davy de Virville et al., 2002) and accumulation of xanthophyll zeaxanthin (Tardy and Havaux, 1997; Havaux, 1998). Accumulation of zeaxanthin in leaves at higher light is commonly observed and this response is mainly believed to help the plants to cope with excess excitation energy (Demmig-Adams and Adams, 2006 for a review). Possible involvement of zeaxanthin in thermal stability of membranes provides an additional exciting example of simultaneous acclimation to interacting light and heat stresses.

As the temperature response curves of dark reactions (V_{\max}) and light-reactions of photosynthesis (J_{\max}) are different and the Rubisco-limited rate of carboxylation W_c (Eq. 16.2) is more sensitive to temperature than the RuBP-limited rate of carboxylation W_j , modification of nitrogen partitioning between the proteins controlling dark and light reactions of photosynthesis can also alter the temperature optimum for pho-

tosynthesis (Hikosaka, 1997; Hikosaka et al., 1999a). Thus, enhanced investment of nitrogen in Rubisco not only increases light-saturated photosynthesis rate (Fig. 16.8), but is also expected to increase the optimum temperature of photosynthesis. Thus, actual within-leaf nitrogen partitioning patterns may reflect concurrent adjustment to both within-canopy light and temperature gradients.

These data demonstrate that interacting environmental characteristics can importantly affect plant carbon gain (Valladares et al., 1997, 2002; Niinemets and Valladares, 2004), but the overall understanding of plant responses to several environmental stresses simultaneously is still fragmentary and more research on interacting stresses is clearly needed. Nevertheless, the evidence outlined indicates that there are several mechanisms by which plants can acclimate to coexisting environmental stresses within the canopies.

III. Scaling Photosynthesis from Leaves to Canopy

A. Predictive Integration Models

1. Early Models with Empirical Parameterization of Photosynthesis

Predictive integration models (1D multilayer models or 3D voxel-based models) were developed to scale up the information of leaf-level photosynthesis to whole stand level. The main objective of such models has been to simulate and predict the whole-stand carbon uptake and other canopy processes as closely as possible. Among other applications, such models form the basis of crop growth models that are commonly used in farm management and regional planning (see Van Ittersum et al., 2003).

Scaling up photosynthesis from leaf to canopy requires understanding of the distribution of foliage and photosynthetic potentials within the canopy and information of temporal and spatial variation in environmental conditions within the canopy. Early integration models were 1D models that divided the canopy between a series of independent layers, calculated quantum flux density in every layer on the basis of

Lambert-Beer's law and the rate of net assimilation on the basis of light-response curve of photosynthesis (e.g. Saeki, 1959). These models were further improved by including sunlit and shaded leaf area fractions (Duncan et al., 1967) and leaf photosynthetic response to temperature (Hozumi et al., 1972; Woledge and Leafe, 1976) whereas leaf temperature was derived from leaf energy balance (Allen et al., 1964; Jarvis, 1980; Oechel, 1985).

2. Models Including Process-based Parameterization of Photosynthesis

The early models based on empirical dependencies of photosynthesis on light and temperature were unable to predict the photosynthetic responses to altered intercellular CO₂ concentrations, e.g. in water-stressed leaves. (Tenhunen et al. (1976, 1977) developed a semi-mechanistic model of C₃ leaf photosynthesis for scaling-up purposes. This model included the CO₂ and temperature responses of photosynthesis on the basis of enzyme kinetics. The proposed temperature response is basically used in all later leaf and canopy models (e.g. Farquhar et al., 1980; Harley and Baldocchi, 1995; Medlyn et al., 2002). A more advanced process-based leaf photosynthesis model that is currently most widely used in scaling up from leaf to canopy, landscape and biome scale was developed by Farquhar et al. for C₃ plants (1980, Eq. 16.2) and (Collatz et al., 1992) for C₄ species.

To be useful for prediction of photosynthesis in field conditions, the Farquhar et al. (1980) model must be coupled with a model that predicts stomatal conductance. The empirical model of Ball et al. (1987) linking stomatal conductance to humidity, CO₂ concentration and photosynthesis using only one empirical stomatal sensitivity parameter is frequently employed to calculate internal CO₂ concentration and net assimilation rates (e.g. Tenhunen et al., 1990; Baldocchi, 1994; Baldocchi and Harley, 1995; Harley and Baldocchi, 1995). The difficulty with the Ball et al. (1987) model is that the empirical stomatal sensitivity parameter varies with soil water availability (Tenhunen et al., 1990; Sala and Tenhunen, 1996), but may even vary during a day (Mencuccini et al., 2000; Moriana et al., 2002), complicating the model

parameterization. Alternatively, optimization models that maximize carbon gain for given water use can be employed (Cowan, 1982; Hari et al., 1999; Hari et al., 2000). The overall advantage of coupling stomatal conductance to photosynthesis is that no separate description of the variation of conductance along the canopy is needed.

3. Further Advancements in Predictive Integration Models

While the variation in foliage photosynthetic potentials with canopy depth was included in some early photosynthesis models (e.g. Tooming, 1967), in most successive scaling-up models, the photosynthetic capacity was considered constant for all leaves in the canopy until recently (Tenhunen et al., 1990; Baldocchi and Harley, 1995; Harley and Baldocchi, 1995; Falge et al., 1996). As more and more information becomes available, different photosynthetic capacities are currently assigned to leaves in different canopy locations (Baldocchi and Harley, 1995; Baldocchi and Amthor, 2001; Baldocchi and Wilson, 2001; Medlyn, 2004), thereby significantly improving the estimates of canopy carbon gain.

In addition to the major progress in consideration of physiological processes, SVAT models predicting the profiles of all environmental drivers in the canopy are increasingly being used (Katul and Albertson, 1999; Baldocchi et al., 2002; Marcolla et al., 2003). Simple 1D descriptions are progressively being replaced by 3D canopy models (Ryel et al., 1993; Falge et al., 1996; Sinoquet and Le Roux, 2000; Sinoquet et al., 2001; Cescatti and Niinemets, 2004). While in the 1D models photosynthetic capacity is constant for all leaves in a given canopy layer, parameterization of 3D models is much more complicated as both leaf area density and photosynthetic capacity are needed for every 3D element, voxel. However, strong correlations between photosynthetic characteristics and long-term leaf light environment (II.B) can be employed to parameterize leaf physiology in such canopy models (Sinoquet and Le Roux, 2000; Sinoquet et al., 2001). Fixing first the canopy architecture, light environment can be predicted for every voxel. Using this information,

foliage photosynthetic potentials are calculated for canopy elements using the regressions with average leaf light environment (e.g. Sinoquet and Le Roux, 2000; Fig. 16.7).

The progress in canopy models is facilitated by overall consensus in canopy modeling scientific community that any improvement in description of environmental characteristics and foliage physiological characteristics improves the estimates of canopy carbon gain (Baldocchi and Amthor, 2001; Bacour et al., 2002; Larocque, 2002). With more effective parameterization routines, e.g. such as predictive relationships between foliage physiology and light environment, the parameterization of more complex models becomes more feasible. However, the more detailed models inevitably become less general and less flexible with increasing the number of parameters, limiting their practical use (Cowan, 1968). A parameterized canopy model is basically a snapshot of the continuously changing canopy architecture at certain fixed time. The dynamic aspects can be considered by including growth processes in the models (e.g. Sterck et al., 2005; Sterck and Schieving, 2007). An alternative to further complicating the models can be the use of optimization principles assuming that the canopy is constructed in a way that maximizes its carbon gain in a given environment.

B. Optimization Algorithms

1. Optimal Distribution of Foliar Nitrogen and Foliar Dry Mass Within the Canopy

Optimization algorithms rely on economic analogies, for canopy models predicting that plants are maximizing profit (carbon gain) with the given availability of limiting resources (nitrogen, light). So far, optimization theory in canopy models has mainly served to analyze the adaptive significance of foliage acclimation and resource distributions in dense stands, and has rarely been used for scaling-up purposes. However, the optimization theory provides an implicit theoretical framework to scale up from leaf to plant, and as such can be a useful platform for construction of general scaling-up models. For this, the mechanisms leading to certain structural and physiological patterns should be understood, i.e. the “true” optimality condition(s) should be defined.

Optimization models postulate that leaf characteristics should vary in the canopy in a way that maximizes the whole plant or stand carbon gain. As a large part of nitrogen is present in photosynthetic proteins, N is often a limiting element in soil, and its uptake from soil and assimilation by plant requires a substantial amount of energy (Gutschick, 1981; Field and Mooney, 1986; Chapin et al., 1987). Thus, maximizing canopy photosynthesis per unit N can have adaptive significance. As N invested in rate-limiting photosynthetic proteins is more effectively used at higher light, Field (1983) suggested that N should be reallocated from shaded older leaves in the lower canopy to younger exposed leaves in the upper canopy to maximize daily canopy photosynthesis. The whole canopy photosynthesis is maximized with respect to nitrogen use when N is distributed among the leaves so that any further reallocation of N between the leaves cannot increase the canopy carbon gain. On the basis of mass-based leaf N content (N_M), this optimality criterion is given as (Field, 1983):

$$\frac{\partial A_D}{\partial N_M} = \lambda_1, \quad (16.8)$$

where A_D is daily leaf carbon gain and λ_1 is a Lagrangian multiplier (Field, 1983). Lagrangian multipliers are widely used in nonlinear constrained optimization, for instance, in economics in maximizing profit with a given limited resource (Silberberg, 1974). The meaning of λ in such an optimization is the marginal value of the limiting resource, i.e. how much the output is changing with a given change in resource availability. In canopy optimization according to Eq. (16.1), λ_1 is the marginal value of nitrogen, and thus, λ_1 depends on total canopy nitrogen (Field, 1983).

However, in canopies consisting of leaves of similar age, such as broad-leaved deciduous temperate forests, N_M is often invariable (e.g. Ellsworth and Reich, 1993; Kull and Niinemets, 1993; and references in 16.II.B.2), while nitrogen contents per area (N_A) vary due to light-dependent modifications in leaf dry mass per unit area (M_A). In dense vegetation, plants can increase their photosynthesis by maintaining higher N_A and M_A in upper illuminated leaves relative to lower shaded parts of the canopy

(Tooming, 1967; Mooney and Gulmon, 1979). Thus, canopy photosynthesis can also be maximized by varying the degree of stacking of foliar mass per unit area (Gutschick and Wiegel, 1988):

$$\frac{\partial A_D}{\partial M_A} = \lambda_2, \quad (16.9)$$

where λ_2 depends on total foliage biomass in the canopy. Combining the effects of light on M_A and reallocation of N from shaded senescent leaves, most current optimization models are based on N_A (Farquhar, 1989):

$$\frac{\partial A_D}{\partial N_A} = \lambda_3. \quad (16.10)$$

As A_D increases with increasing quantum flux density, while the change in A_D is progressively decreasing with increasing N_A , $\partial A_D / \partial N_A$ is an increasing function of light and a decreasing function of N_A . Thus, Eq. (16.10) predicts that N_A should decline from the top towards the bottom of the canopy. However, this equation does not define the specific form of the optimal N distribution.

Hirose and Werger (1987b) explicitly assumed that both within-canopy N and light distributions decline exponentially with canopy depth. The steepness of the decline of N_A was characterized by scaling exponent K_n , analogous to the extinction coefficient for light, and the optimal N distribution was solved iteratively as the K_n value maximizing canopy photosynthesis (Hirose and Werger, 1987b). The optimal K_n values for herbaceous stands of *Solidago altissima* increased with increasing canopy leaf area index and steepness of the within-canopy light gradient. These results suggested that the optimal N distribution should follow the light distribution in the canopy.

It was further analytically demonstrated that if leaf photosynthetic capacity (A_{\max}) and respiration rate (R_D) are increasing linear functions of N_A , the optimal distribution of A_{\max} should match the light distribution (Farquhar, 1989; Anten et al., 1995b; Sands, 1995a):

$$A_{\max} = A_0 \frac{Q}{Q_0}, \quad (16.11)$$

where Q/Q_0 is the relative light intensity, and A_0 is the photosynthetic capacity of the highest most illuminated leaves in the canopy. From

Eqs. (16.10) and (16.11), the optimal N distribution in the canopy can be defined as:

$$N_A = N_b + N_0 \frac{Q}{Q_0} = N_b + N_0 e^{KL_c}, \quad (16.12)$$

where K is the extinction coefficient for light, N_b is the amount of leaf N not associated with photosynthesis (“non-photosynthetic” N) and N_0 is N_A of leaves at the top of the canopy (Anten et al., 1995b). In accordance with these predictions, non-uniform N distribution patterns have been observed in a whole range of plant stands including herbaceous mono- and dicotyledonous species, deciduous and evergreen broad-leaved trees and evergreen conifers (Fig. 16.7). In all cases, the optimal within-canopy distribution in N resulted in considerable increases in estimated carbon gain as compared to the uniform N distribution, ranging from 6% in the broad-leaved evergreen *Nothofagus fusca* (Hollinger, 1996) to 30% in the herbaceous legume *Glycine max* (Anten et al., 1995b). Experimental observations also confirmed the general prediction that plant stands with steeper light gradients – either due to higher leaf area, more horizontal foliage or lower foliage clumping – also have steeper N gradients (Hirose et al., 1988; Anten et al., 1995b). However, actual N_A always declined less steeply with increasing canopy depth relative to the predicted theoretical optimum distribution. As the result, canopy photosynthetic rates calculated for the actual distributions were 4–15% lower than the predicted maxima for optimum N distributions (Anten et al., 2000 for a review).

“Coordinated” leaf nitrogen distribution (Chen et al., 1993) is another way of optimization of canopy photosynthesis. The “coordination” theory of N distribution postulates that leaf nitrogen is distributed in the canopy such that dark (limited by V_{\max} , Eq. 16.3) and light (limited by J_{\max} , Eq. 16.4) reactions of photosynthesis limit daily photosynthesis to a similar degree. Chen et al. (1993) assumed linear correlations of V_{\max} and J_{\max} on N_A , and the resulting within-canopy distribution of “coordinated” N_A was generally similar to the optimal distribution as described by Eq. (16.12). The model assumed that the dependencies of V_{\max} and J_{\max} on N_A are quantitatively different from each other, i.e. J_{\max}/V_{\max} ratio was predicted to depend on N_A .

Available data, however, indicate that J_{\max}/V_{\max} ratio is essentially constant within the canopy (Niinemets, 1998; Grassi et al., 2001), suggesting that “coordinated” N distribution often little differs from the optimal N distribution (Eq. 16.12).

2. Optimal Canopy Leaf Area Index and Leaf Angle Distribution

Canopy photosynthesis is not only affected by the distribution of photosynthetic compounds within and among leaves, but also by the amount, orientation and dispersion of foliage. If photosynthesis were only limited by light availability, canopy carbon gain could be increased by adding new leaves until the daily light compensation point of lowermost leaves has been achieved (Monsi and Saeki, 1953). Beyond this optimum L , a further increase of L reduces canopy carbon gain as the carbon balance of additional leaves in lower canopy becomes negative. From this reasoning, it was predicted that the optimal L should increase with light availability (Saeki, 1960; Monsi et al., 1973).

In dense stands with large L , canopy carbon gain is also enhanced by more vertically inclined and more strongly aggregated foliage (Cescatti, 1997b; Cescatti and Niinemets, 2004). This is because such architectural modifications result in greater light penetration to deeper canopy layers, allowing the plants to support a larger number of leaf layers with positive carbon balance. In canopies with vertical leaves, light is also more evenly distributed among the leaves in the canopy. Because of the non-linear hyperbolic relationship between photosynthesis and light, the more uniform light distribution increases whole canopy carbon gain. This simple analysis suggests that optimal L is larger in canopies with more vertical and/or more strongly aggregated leaves. Available data support this assumption (Duncan, 1971; Monsi et al., 1973; Winter and Ohlrogge, 1973; Sonohat et al., 2002; Cescatti and Niinemets, 2004; Gersonde et al., 2004).

Soil nutrient availability can importantly alter the optimal L (Anten, 2005). There is a general increase of L with increasing soil N availability (Linder, 1987; Hinckley et al., 1992; Albaugh et al., 1998), indicating that in natural conditions, leaf area growth is usually strongly limited by the availability of nutrients, especially nitrogen. For a fixed total amount of nitrogen in the canopy,

an increase in L does not only imply increased light capture, but also a reduction in N_A and associated A_{\max} . Considering this, it is possible to show that there is an optimal L , at which canopy photosynthesis is maximized for a given amount of total canopy N (Anten et al., 1995a). In this work it was further shown that for a given amount of canopy N, leaf area production should increase and N_A decrease with increasing leaf photosynthetic nitrogen use efficiency A_{\max}/N_A , and that leaf production should be lower and N_A higher in stands with horizontal relative to stands with vertical leaves. These qualitative predictions were in good agreement with observations, and there was a strong correlation between predicted and actual values of optimal L and mean leaf N contents. This approach has further been successfully used to predict the effects of elevated CO_2 on L at different soil nitrogen availabilities (Hirose et al., 1996, 1997; Anten et al., 2004).

3. Difficulties with Simple Optimization Models

While simple optimization models predict a direct proportionality between A_{\max} , N_A , M_A and light availability (Eq. 16.11), these traits often scale with light in a non-linear manner (Fig. 16.7). In the case of quasi-linear scaling, N_A , M_A and A_{\max} vs. light relationships have generally a positive y-intercept at zero light. Both curvilinearity and significant y-intercepts suggest that the within-canopy distributions of these characteristics are less steep than the predicted optimal distributions (Meir et al., 2002; Niinemets et al., 2004b; Niinemets and Valladares, 2004).

Similar discrepancies between optimal and actual L and foliage angular distributions have also been observed. While observed and predicted values of L were strongly correlated, the observed values of L were consistently larger than the optimal values (Schieving and Poorter, 1999; Anten, 2002; Fig. 16.10). Although more vertical foliage is beneficial for carbon gain in dense stands, many plant species have horizontal rather than vertical leaves under such conditions (Hikosaka and Hirose, 1997; Kitajima et al., 2005), suggesting that these canopies are “non-optimal”.

Several explanations have been offered for the apparent non-optimality of plant canopies. The first line of argument is that optimization is too anthropocentric. Why should plants

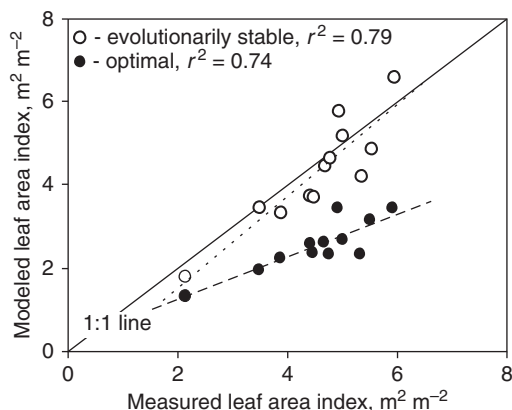


Fig. 16.10. Modeled and measured leaf area index (L) for 12 herbaceous plant stands (modified from Anten, 2002). Predictions were made using either simple optimization ("optimal", filled symbols, dashed line) or competitive optimization ("evolutionarily stable", open symbols, dotted line). In the competitive situation, plants increase leaf area in order to shade out the competitors; as a result, L maximizing carbon gain of an individual in a given stand ("evolutionarily stable" L) is larger than L maximizing whole stand carbon gain ("optimal" L). The following stands were studied: *Amaranthus cruentus*, *Oryza sativa*, *Sorghum bicolor* (all three species at both high and low N availability), and *Glycine max* (data from Anten et al., 1995a), *Leersia hexandra*, *Hymenachne amplexicaulis*, *Paspalum fasciculatum* and a dense and an open stand of *Hyparrhenia rufa* (data from Anten et al., 1998). *A. cruentus*, *S. bicolor*, *H. rufa* and *P. fasciculatum* are C_4 species, others are C_3 species

follow our conception of what is most effective (Kull and Jarvis, 1995; Kull, 2002)? Indeed, the idea of maximizing the output for a limited amount of resources invested was borrowed from economics. When extrapolating this concept to plants, one should not make an a priori assumption that the plants must be optimal (Anten, 2005). The second line of reasoning is that there are shortcomings in the models used to predict the trait values. If all missing details of the photosynthetic system were described and all costs and benefits accounted for, the models would make much better predictions, an example being the separate optimization of light and dark reactions of photosynthesis ("coordinated" N distribution, Chen et al., 1993). Badeck (1995) further showed that simple optimization based on A_{\max} alone (Eq. 16.11) breaks apart if leaf photosynthetic properties (convexity of the light response curve and/or initial quantum yield) vary within the canopy. Changes in these parameters may be related to changes in leaf optics that are

likely due to modified leaf architecture and distribution of photosynthetic resources within the leaves. This leads to "optimal distribution" of photosynthetic capacity that is different from that predicted by Eq. 16.12 (Badeck, 1995).

In addition, environmental variation in canopies does not only involve light but a suite of other factors, including temperature, humidity and windiness (16.11.4.3). These different factors interactively affect leaf photosynthesis and their presence could partly explain the deviations between observations and optimal profiles of foliage traits predicted on the basis of light variation alone (Niinemets and Valladares, 2004). There are trade-offs between light and nitrogen use efficiency, and maximization of photosynthetic nitrogen use efficiency does not simultaneously optimize light use efficiency (Niinemets and Tenhunen, 1997; Hirose and Bazzaz, 1998). So, plants may not be able to optimize the use of both resources simultaneously. The balance between these two processes is obviously different in different species. Shade tolerant species tend to be more "optimal" in terms of light use, intolerant species in terms of nitrogen use (Kull and Tulva, 2002). A similar line of reasoning can be used for the tradeoff between water and nitrogen use efficiencies (Field et al., 1983). Buckley et al. (2002) have constructed a canopy model that simultaneously optimizes nitrogen and water use.

There are also inherent structural constraints in adjusting to high and low light. High light adjustment is limited by intrinsic inefficiencies of very thick leaves that result from low light penetration and high internal diffusion resistances to CO_2 (Enríquez et al., 1996; Niinemets and Sack, 2006). Low light adjustment is limited by biomechanical constraints associated with leaf mechanical stability and positioning. Leaves can not float in air by themselves and need to be supported by stems, branches and petioles. To maintain a prostrate structure capable of intercepting light, the leaf lamina needs to have a certain degree of rigidity (Niinemets and Fleck, 2002; Niinemets et al., 2007b). As certain amount of structural tissue is needed for leaf self-support and further tissue is needed for positive photosynthesis, leaves will always have a certain minimum M_A (Meir et al., 2002). Thus, full proportionality between N_A , M_A and light is principally not

possible. In agreement with this, M_A was constrained to have a maximum and minimum values in the optimization model of Gutschick and Wiegel (1988).

Acclimation to environment is also costly in terms of protein turnover (Noguchi et al., 2001; Hachiya et al., 2007 for estimates of energy cost of protein turnover). Light conditions strongly fluctuate between days and during the season, and there is evidence of plant adjustment to day-to-day fluctuations in light conditions (Demmig-Adams et al., 1989; Naidu and DeLucia, 1997; Logan et al., 1998; Niinemets et al., 2003). However, as fluctuations between days are unpredictable, the benefits of very rapid acclimation may be small due to high protein cost during frequent changes in the light environment. Thus, plants may be suboptimally adjusted to any given light environment to maximize the cost (protein turnover)/benefit (carbon gain) ratio under fluctuating light conditions.

In mature leaves, acclimation may be limited by anatomical constraints on re-acclimation (Oguchi et al., 2005). This may be relevant when there are long-term modifications in light conditions, for instance, due to gap formation in the canopy or enhanced shading of older foliage by younger leaves. Anatomical limitations can be especially important in herbaceous rapidly expanding canopies, in woody continuously growing canopies, e.g. willow and poplar stands and in evergreen species. Data do show that older foliage of woody evergreens is not “optimal” for their current light environment (Brooks et al., 1994; Niinemets et al., 2006a). Including all such constraints on full optimality in the models may significantly improve the predictions.

Finally, inaccurate predictions of optimization models can also result from the basic assumption that there is no competition between individual plants in the canopy. The optimal performance of entire stand and that of a population of individual plants (evolutionarily stable strategy) can differ significantly.

C. Evolutionarily Stable Distributions of Limiting Resources and Structural Traits

The optimization models discussed so far consider the trait values optimal if whole canopy

carbon gain is maximized. The implicit assumption of such an optimization is that the optimal trait values of an individual plant are independent of those of its neighbors (Parker and Maynard-Smith, 1990). In dense vegetation, however, plants strongly influence each other's resource availability, and competitive, individual-based optimization would be a more realistic approach.

1. Evolutionarily Stable Nitrogen and Leaf Area Distributions

Competitive optimization based on game theory (Maynard-Smith, 1974) has been used to explain why within-canopy profiles of N_A and M_A are less steep than predicted by the whole-canopy optimization approaches. As M_A affects light capturing capacity of a plant through the amount of foliar area produced for given biomass, as well as the nitrogen content ($N_A = M_A N_M$), Schieving and Poorter (1999) used a competitive optimization to analyze M_A distribution of plants in a stand. They asked whether a monospecific stand can be invaded by mutant plants that are the same in every respect as the resident population except for a different M_A distribution. Their analysis demonstrated that a plant stand with both optimal N_A distribution and L can successfully be invaded by a mutant that has a lower M_A . This is because the individuals with lower M_A produce more leaf area for given total foliage mass, capture more light, shade the neighbors with higher M_A and increase their share of total canopy carbon gain. Although the carbon gain of the whole stand is reduced relative to the maximum because of overall higher shading, the key of mutants' success is to shade and reduce the carbon gain of the neighbors more than mutants' own carbon gain (so-called “cheating” strategy). The evolutionarily stable stand – the one that cannot be invaded by other mutants – was shown to have a larger L , a more uniform N distribution and lower productivity than the optimal stand (Schieving and Poorter, 1999; Fig. 16.11). With somewhat different assumptions, Anten and Hirose (2001) and Anten (2002) obtained similar results. They further demonstrated that the evolutionarily stable L and associated average N_A were in better agreement with the actual observations than the estimates based on the simple optimization (Fig. 16.10), though the accuracy of

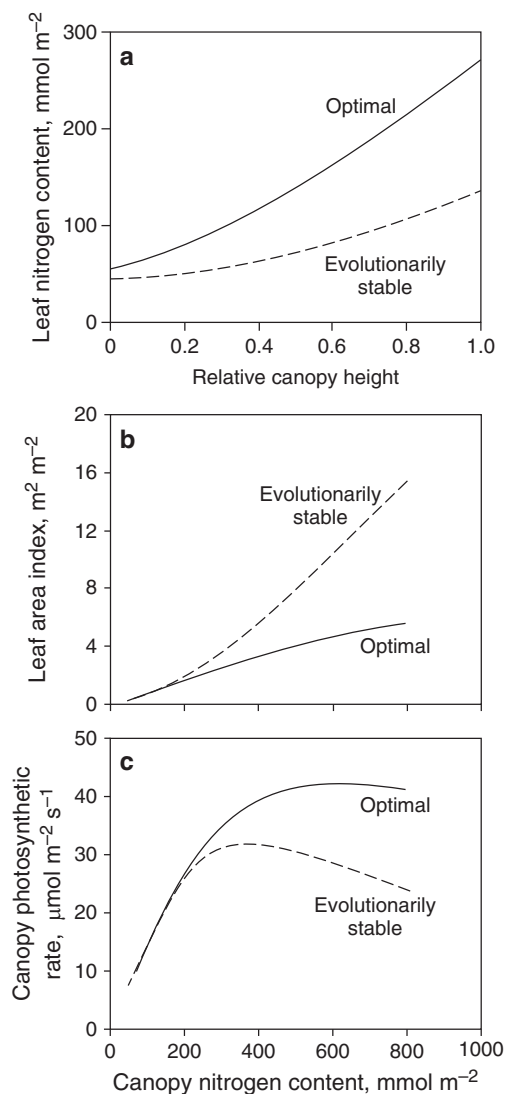


Fig. 16.11. Simulated leaf nitrogen content, N_A , as a function of height in the canopy (a), leaf area index, L , (b) and canopy assimilation rate, A_C , (c) as functions of total canopy nitrogen. The simulations were conducted for optimal and evolutionarily stable (competitive) situations (modified from Schieving and Poorter, 1999). The optimal scenario assumes no competition between the plants within the stand, and therefore, optimal L that maximizes A_C (L_{opt}) is the same for the stand and each individual in the stand. The evolutionarily stable scenario is based on game theory and assumes competition between the individuals in the stand. Competing plants increase their L beyond L_{opt} as this results in shading of neighbors and in greater carbon gain of the individual with larger L than in neighbors with lower L . In evolutionarily stable stand, none of the individuals can increase its own carbon gain by further increases in L (evolutionarily stable leaf area index, L_{ev}). While L is larger in the evolutionarily stable stand, A_C is smaller due to greater shading and N_A is lower due to distribution of the given amount of nitrogen over a larger leaf area

the predictions depended on the assumed strength of plant-to-plant interactions in the evolutionarily stable stand.

2. Evolutionarily Stable Leaf Angle and Plant Height

Simple optimization models predict that on productive sites supporting a large L , whole-stand canopy photosynthesis is maximized by vertically inclined leaves. Competitive optimization provides an explanation for the existence of dense stands with horizontal foliage inclination. A mutant positioning leaves horizontally captures more light and can invade a stand with vertical leaves by shading and thereby reducing the carbon gain of neighbors more than its own carbon gain (Hikosaka and Hirose, 1997). Therefore, evolutionarily stable stands that cannot be invaded by mutants with different inclination angles tend to have horizontal leaves.

In a similar manner, game theory has been used to explain differences in stand height. As less biomass is needed in support structures, short plant stature is optimal for carbon gain (e.g., current selection for short-stature orchard trees). However, such an optimal stand is vulnerable to invasion by taller competitors that are able to shade out the shorter neighbors. Thus, evolutionarily stable stands are taller than the optimal stands (Givnish, 1982; Iwasa et al., 1984; Pronk et al., 2007).

3. Evolutionarily Stable Strategies and Canopy Models

Plants consistently overinvest in resource harvesting, e.g. in leaves and stem height. These “non-optimal” investment patterns have profound consequences for interpreting the adaptive significance of given plant trait values and for estimation of the productivity of plant stands (Anten, 2005). Competitive optimization models tend to predict better within-canopy variation in photosynthetic traits and associated canopy photosynthesis than simple optimization models. Thus, these models provide a more sophisticated, yet still simple, theoretical framework to scale from leaf traits to whole-stand productivity (Anten, 2002), and they have potential as a predictive tool to understand canopy responses

to globally changing environment. However, currently the competitive optimization models face a number of difficulties that limit their practical applicability.

The first limitation is that the predicted values are very sensitive to the assumptions on how plants interact and compete with each other. The distinction between simple and competitive optimization in canopy modeling comes down to the assumed degree of interaction between neighbor plants. In the simple optimization, this interaction is disregarded, and the positive effects of increases in leaf area on photosynthesis readily become limited by self-shading. By contrast, in the competitive optimization, the target plant only constitutes a part of the total canopy leaf area. If this plant increases its leaf area at the constant leaf area of its neighbors, self-shading increases less, while the plant will capture a greater fraction of light. Due to this mechanism, individual plants can increase their carbon gain by increasing their leaf area even if the leaf area of population is greater than optimal (Anten and Hirose, 2001). However, this benefit depends on the extent to which the shading experienced by a plant is determined by the plant itself and by its neighbors (Hikosaka and Hirose, 1997; Anten, 2002). Evolutionarily stable L decreases, while stand photosynthesis increases with the extent to which plants determine their own light climate. This interaction can be quantitatively described by the relative contribution of given plant to total canopy leaf area index ($0 < \beta < 1$, β decreasing with increasing the degree of interaction, Fig. 16.12).

The degree to which plants influence each other's light availability is hard to estimate, and it is also expected to be variable. In stands with very broad canopies such as large trees, the interaction is likely to be small. By contrast, in stands of herbaceous plants with relatively narrow canopies, the interaction is anticipated to be larger (Hikosaka and Hirose, 1997). Especially high degree of interaction may be observed in plants carrying leaves on long internodes or long petioles as such architectural features result in extensive spread of leaves in space and in intermixing of foliage of neighboring plants (Takenaka, 1994; Hikosaka et al., 2001). Few actual estimates of the degree of interaction are available. In a stand of herbaceous annual

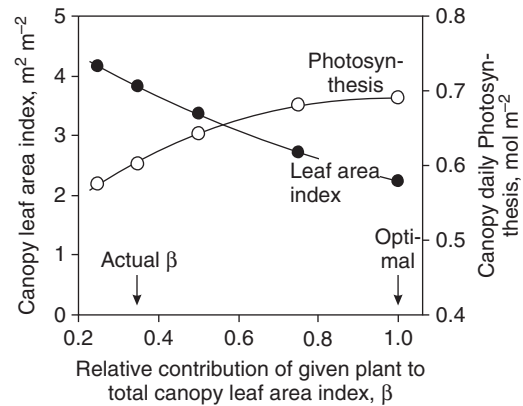


Fig. 16.12. Dependence of canopy leaf area index that maximizes canopy photosynthesis (filled symbols) and the maximum canopy photosynthesis achieved (open symbols) on the ratio of leaf area index of a given individual plant to total stand leaf area index (β) (modified from Anten, 2002). β characterizes the degree of interaction between the neighboring plants. $\beta = 1$ (no interaction) corresponds to the simple optimization, while $\beta < 1$, corresponds to various evolutionarily stable strategies. The data denoted as “actual β ” corresponds to measurements of L and canopy photosynthesis in Venezuelan savanna grass *Hymenachne amplexicaulis* (Anten et al., 1998)

Xanthium canadense, a value of β of 0.3 was estimated (Hikosaka et al., 2001). In an extensive comparison between actual and evolutionarily stable L , $\beta = 0.5$ provided the best match between actual and predicted L (Anten, 2002; Fig. 16.10).

The competitive optimization models also include a number of other important simplifications that may affect their predictive ability. They assume that all plants in the population, except the mutant, are identical. In reality, most plant stands are composed of several species and even in monospecific stands, plants usually differ from each other both genetically and phenotypically. These complications call for reconsideration of the types of evolutionary games that are considered in these models (Anten, 2005; Vermeulen et al., 2008). These models also do not consider the 3D heterogeneity of plant canopies and non-random dispersion of foliage area. In clumped canopies, light penetrates much deeper into the canopies and average irradiance on leaf surface is higher. Thus, the apparent overinvestment in leaf area is not so clearly evident in clumped canopies.

D. Whole-canopy Level Integration Approaches: Big Leaf Models

As outlined in 16.III.A.1, detailed predictive 1D multi-layered or 3D voxel-based canopy models can simulate canopy photosynthesis with a great degree of accuracy, at least for relatively homogeneous stands such as crops (e.g. Baldocchi and Amthor, 2001; Müller and Diepenbrock, 2006). An important drawback of these models is that they require a large amount of data for parameterization. A simpler approach may be needed for simulation of carbon gain over large land areas as in global biogeochemical studies (Tans et al., 1990; Sellers et al., 1992). As a possible solution to this problem, so-called 'big leaf' models were developed (Sellers et al., 1992; Amthor, 1994; Lloyd et al., 1995; Kull, 2002). The term 'big leaf' refers to the fact that the light response curve of whole canopy photosynthesis is similar to that of an individual leaf. The major assumption of the big leaf models is that canopy assimilation rate can be calculated using the parameter values of the topmost leaves in the canopy. Box 16.1 gives a simplified version of this to illustrate the concept that canopy photosynthesis (A_C) in big leaf models is proportional to the photosynthesis of the upper canopy leaves (A_0) and the fraction of light absorbed by the canopy (f_Q , $0 < f_Q < 1$):

$$A_C \sim A_0 f_Q. \quad (16.13)$$

The parameters required, f_Q and the photosynthetic characteristics of the leaves in the top of the canopy, can be determined by means of remote sensing techniques, in combination with some knowledge of photosynthetic physiology of given species (Sellers et al., 1992; Gamon et al., 1995; Hanan et al., 1995; North, 2002).

The big leaf models make two further assumptions (Box 16.1): within a homogeneous layer, all leaves receive the same average light intensity, and the within-canopy N distribution is optimal, such that the photosynthetic capacity scales with light distribution (Eq. 16.11). As for the assumption of homogeneous light environment, this can lead to a considerable overestimation of canopy photosynthesis due to the curvilinear light response of photosynthesis (Figs. 16.1 and 16.2). The big-leaf models overcome this problem by using various empirical coefficients

that reduce the overestimation of canopy photosynthesis (Sellers et al., 1992; Amthor, 1994; Lloyd et al., 1995). As these correction factors are purely empirical, prediction of required corrections for various light availabilities or different stand leaf area indices is difficult, if not impossible (de Pury and Farquhar, 1997, 1999). De Pury and Farquhar (1997) introduced the concept of sunlit and shaded foliage (Duncan et al., 1967; see 16.III.A) into the big leaf models. Thus, the canopy was composed of two big leaves, a 'sunlit big leaf' and a 'shaded big leaf'. The estimates of canopy photosynthesis of a *Triticum aestivum* canopy made with this model were in good agreement with those made with a more complicated layered model. The model has further been advanced by including energy balance and stomatal traits (Dai et al., 2004). Still, as discussed in 16.II.A.2, the assumption that there are only two light classes ignores penumbral effects. This may lead to underestimation of canopy photosynthesis, especially in canopies with small leaf elements such as conifer stands (Ryel et al., 2001; Cescatti and Niinemets, 2004).

The assumption of optimal distribution of N within the canopy employed in big leaf models leads to underestimation of canopy photosynthesis, because real patterns of N distribution and the associated distributions of A_{\max} are less steep than the optimal distribution (16.III.B.3). An overestimation of within-canopy decline in A_{\max} can lead to at least 12% underestimation of canopy carbon gain (Fig. 16.13). On the other hand, simply assuming that all leaves have A_{\max} equal to that of the topmost leaves can lead to 15–20% overestimation of canopy carbon gain (Fig. 16.13). For a series of herbaceous stands, Anten (1997) found that the scaling exponent of N distribution (K_n) was strongly correlated with the extinction coefficient for light (K) and that on average, $K_n = 0.4K$, giving the following distribution function for photosynthetic capacity in the canopy:

$$A_{\max} = A_0 \left(\frac{Q}{Q_0} \right)^{0.4}. \quad (16.14)$$

Such an empirical correction significantly reduces the error in estimation of whole canopy photosynthesis (Fig. 16.13).

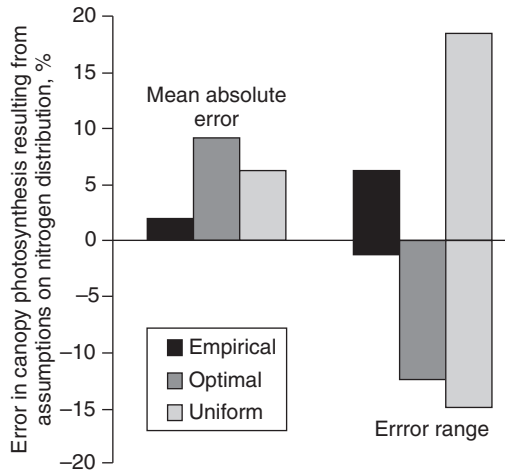


Fig. 16.13. The mean absolute error and the error range in estimating canopy photosynthesis assuming that within-canopy nitrogen distribution is either uniform or optimal, and using an empirical within-canopy nitrogen distribution. For a uniform distribution, nitrogen content of every leaf in the canopy is equal to that of the uppermost leaf, while for the optimal distribution, leaf N content decreases in proportion with relative light availability from canopy top to bottom (Eq. 16.11). For the empirical function used, nitrogen content is a power function of light (Eq. 16.14). Errors in canopy photosynthesis were calculated relative to the measured nitrogen distributions. Calculations were made for the same herbaceous stands as in Fig. 16.10 ($n = 12$)

Overall, big leaf models provide a simple framework that can be potentially used to predict carbon balance over large areas. However, currently these models contain unrealistic assumptions that require inclusion of several fudge factors. With further development of optimization models, big leaf models are expected to more realistically simulate canopy carbon gain.

IV. Concluding Remarks

Huge progress has been made in describing canopy light environment and foliage physiological potentials, and in developing simulation models of canopy photosynthesis. The developments in canopy models have been both towards more detailed 1D multilayered and 3D voxel-based integration models and more advanced optimization models. In the light of this progress, the crucial question in current canopy modeling research is how complicated/realistic should be the models? More detailed models tend to be

more realistic and give more accurate predictions, as canopy micro-environment and foliage physiology are described in a more detailed manner. Accuracy is especially critical for models used for management decisions or policy-making such as models describing yield of crops as a function of certain management practices. However, the more detailed the models, the larger set of input data they require. As many canopy models are used to make estimates of carbon exchange over large areas, heavy reliance on parameterization information can become logistically and financially problematic, rendering the use of such models impractical. Analytical understanding of more complicated models also becomes increasingly difficult. This can be problematic when models are used to advance the conceptual understanding of plant performance in their natural environment. Optimization models including big leaf models, provide an alternative way to understand canopy functioning. However, to employ these models for predictive purposes, further work is clearly needed to reduce the need for empirical correction factors. Use of competitive optimization, inclusion of interactions between environmental drivers in the canopy, and the structural and physiological limitations on acclimation may result in significant improvement of optimization models.

Acknowledgments

The work of Ü. N. on photosynthesis is funded by the Estonian Ministry of Education and Science (grant SF1090065s07), and the Estonian Academy of Sciences. This chapter was written when Ü. N. was holding F.C. Donders Chair at Utrecht University.

Box 16.1 A simple big leaf model

For simplicity, we approximate the response of leaf photosynthesis to light by a rectangular hyperbola and simulate only gross leaf assimilation rate (A_g):

$$A_g = \frac{A_{\max} \alpha_I Q}{(A_{\max} + \alpha_I Q)}, \quad (16.B1)$$

where Q is the incident instantaneous quantum flux density, α_I is the quantum yield for an incident light (initial slope of the light response curve), and A_{\max} is the photosynthetic capacity (light-saturated photosynthetic rate). Such simplifications are not made in current predictive big leaf models (see the main text), but we apply them here to highlight the major concepts. Following Beer's law, Q at any depth in the canopy is given as:

$$Q = Q_0 e^{-KL_C}, \quad (16.B2)$$

where Q_0 is the above-canopy quantum flux density, L_C is the cumulative leaf area index above a given leaf in the vegetation, and K is the extinction coefficient for light. Defining relative quantum flux density, q_R , as Q/Q_0 , Q is:

$$Q = Q_0 q_R. \quad (16.B3)$$

We further assume that the quantum yield, α_I , is constant, while A_{\max} at any height in the canopy scales linearly with q_R in the canopy:

$$A_{\max} = A_0 q_R, \quad (16.B4)$$

where A_0 is the photosynthetic capacity of uppermost leaves. Combining Eqs. (16.B3) and (16.B4), and substituting into Eq. (16.B1) gives:

$$A_g = \frac{A_0 \alpha_I Q_0}{A_0 + \alpha_I Q_0} q_R. \quad (16.B5)$$

In this equation, only q_R varies with the depth in the canopy, everything else is constant (Anten et al., 1995b; Sands, 1995a, b).

Canopy photosynthetic rate, A_C , is obtained by integrating leaf photosynthetic rate (A_g) over total canopy leaf area index L :

$$A_C = \int_0^L A_g dL_C. \quad (16.B6)$$

Replacing A_g from Eq.(16.B5), we get:

$$A_C = \int_0^L \frac{A_0 \alpha_I Q_0}{A_0 + \alpha_I Q_0} q_R dL_C. \quad (16.B7)$$

Since $\frac{A_0 \alpha_I Q_0}{A_0 + \alpha_I Q_0}$ is independent of L_C , we can rewrite Eq. (16.B7) as:

$$A_C = \frac{A_0 \alpha_I Q_0}{A_0 + \alpha_I Q_0} \int_0^L q_R dL_C, \quad (16.B8)$$

Further considering that $q_R = e^{-KL_C}$, the solution of Eq. (16.B8) is given as:

$$A_C = \frac{A_0 \alpha_I Q_0}{A_0 + \alpha_I Q_0} \frac{(1 - e^{-KL})}{K}. \quad (16.B9)$$

The quantity $(1 - e^{-KL})$ is equal to the fraction of light intercepted by the canopy (f_Q) (sensu Sellers et al., 1992). Comparing Eqs. (16.B1) and (16.B9) it is evident that canopy photosynthesis is proportional to the photosynthetic rate per unit area of the uppermost leaves in the canopy multiplied by f_Q .

References

- Aan A, Hallik L and Kull O (2006) Photon flux partitioning among species along a productivity gradient of an herbaceous plant community. *J Ecol* 94: 1143–1155
- Aasamaa K, Söber A, Hartung W and Niinemets Ü (2004) Drought acclimation of two deciduous tree species of different layers in a temperate forest canopy. *Trees* 18: 93–101
- Ackerly DD and Bazzaz FA (1995) Seedling crown orientation and interception of diffuse radiation in tropical forest gaps. *Ecology* 76: 1134–1146
- Ahola V and Leinonen K (1999) Responses of *Betula pendula*, *Picea abies*, and *Pinus sylvestris* seeds to red/far-red ratios as affected by moist chilling and germination temperature. *Can J Forest Res* 29: 1709–1717
- Albaugh TJ, Allen HL, Dougherty PM, Kress LW and King JS (1998) Leaf area and above- and belowground growth responses of loblolly pine to nutrient and water additions. *Forest Sci* 44: 317–328
- Allen LH, Yocum CS and Lemon ER (1964) Photosynthesis under field conditions. VII. Radiant energy exchanges within a corn crop canopy and implications in water use efficiency. *Agron J* 56: 253–259
- Amthor JS (1994) Scaling CO_2 -photosynthesis relationships from the leaf to the canopy. *Photosynth Res* 39: 321–350
- Anten NPR (1997) Modelling canopy photosynthesis using parameters determined from simple non-destructive measurements. *Ecol Res* 12: 77–88
- Anten NPR (2002) Evolutionarily stable leaf area production in plant populations. *J Theor Biol* 217: 15–32

- Anten NPR (2005) Optimal photosynthetic characteristics of individual plants in vegetation stands and implications for species coexistence. *Ann Bot* 95: 495–506
- Anten NPR and Hirose T (1998) Biomass allocation and light partitioning among dominant and subordinate individuals in *Xanthium canadense* stands. *Ann Bot* 82: 665–673
- Anten NPR and Hirose T (1999) Interspecific differences in above-ground growth patterns result in spatial and temporal partitioning of light among species in a tall-grass meadow. *J Ecol* 87: 583–597
- Anten NPR and Hirose T (2001) Limitations on photosynthesis of competing individuals in stands and the consequences for canopy structure. *Oecologia* 129: 186–196
- Anten NPR and Hirose T (2003) Shoot structure, leaf physiology, and daily carbon gain of plant species in a tallgrass meadow. *Ecology* 84: 955–968
- Anten NPR, Schieving F, Medina E, Werger MJA and Schuffelen P (1995a) Optimal leaf area indices in C_3 and C_4 mono- and dicotyledonous species at low and high nitrogen availability. *Physiol Plant* 95: 541–550
- Anten NPR, Schieving F and Werger MJA (1995b) Patterns of light and nitrogen distribution in relation to whole canopy carbon gain in C_3 and C_4 mono- and dicotyledonous species. *Oecologia* 101: 504–513
- Anten NPR, Werger MJA and Medina E (1998) Nitrogen distribution and leaf area indices in relation to photosynthetic nitrogen use efficiency in savanna grasses. *Plant Ecol* 138: 63–75
- Anten NPR, Hikosaka K and Hirose T (2000) Nitrogen utilization and the photosynthetic system. In: Marshall B and Roberts J (eds) *Leaf Development and Canopy Growth*, pp 171–203. Sheffield Academic Press, Sheffield
- Anten NPR, Hirose T, Onoda Y, Kinugasa T, Kim HY, Okada M and Kobayashi K (2004) Elevated CO_2 and nitrogen availability have interactive effects on canopy carbon gain in rice. *New Phytol* 161: 459–471
- Arneth A, Niinemets Ü, Pressley S, Bäck J, Hari P, Karl T, Noe S, Prentice IC, Serça D, Hickler T, Wolf A and Smith B (2007) Process-based estimates of terrestrial ecosystem isoprene emissions: incorporating the effects of a direct CO_2 -isoprene interaction. *Atm Chem Phys* 7: 31–53
- Asner GP and Wessman CA (1997) Scaling PAR absorption from the leaf to landscape level in spatially heterogeneous ecosystems. *Ecol Modell* 103: 81–97
- Asner GP, Wessman CA and Archer S (1998) Scale dependence of absorption of photosynthetically active radiation in terrestrial ecosystems. *Ecol Appl* 8: 1003–1021
- Atkin OK, Bruhn D, Hurry VM and Tjoelker M (2005) The hot and the cold: unravelling the variable response of plant respiration to temperature. *Evans review no. 2. Funct Plant Biol* 32: 87–105
- Bacour C, Jacquemoud S, Tourbier Y, Dechambre M and Frangi JP (2002) Design and analysis of numerical experiments to compare four canopy reflectance models. *Remote Sens Environ* 79: 72–83
- Badeck F-W (1995) Intra-leaf gradient of assimilation rate and optimal allocation of canopy nitrogen: a model on the implications of the use of homogeneous assimilation functions. *Aust J Plant Physiol* 22: 425–439
- Baldocchi D (1994) An analytical solution for coupled leaf photosynthesis and stomatal conductance models. *Tree Physiol* 14: 1069–1079
- Baldocchi DD and Amthor JS (2001) Canopy photosynthesis: history, measurements, and models. In: Mooney HA, Saugier B and Roy J (eds) *Terrestrial Global Productivity: Past, Present, and Future*, pp 9–31. Academic, San Diego, CA
- Baldocchi D and Collineau S (1994) The physical nature of solar radiation in heterogeneous canopies: spatial and temporal attributes. In: Caldwell MM and Pearcy RW (eds) *Exploitation of Environmental Heterogeneity by Plants: Ecophysiological Processes Above- and Below-ground*, Physiological Ecology. A series of Monographs, Texts and Treatises, pp 21–71. Academic, San Diego, CA
- Baldocchi DD and Harley PC (1995) Scaling carbon dioxide and water vapour exchange from leaf to canopy in a deciduous forest. II. Model testing and application. *Plant Cell Environ* 18: 1157–1173
- Baldocchi DD and Wilson KB (2001) Modeling CO_2 and water vapor exchange of a temperate broadleaved forest across hourly to decadal time scales. *Ecol Modell* 142: 155–184
- Baldocchi DD, Hutchison BA, Matt DR and McMillen RT (1985) Canopy radiative transfer models for spherical and known leaf inclination angle distributions: a test in an oak-hickory forest. *J Appl Ecol* 22: 539–555
- Baldocchi DD, Wilson KB and Gu L (2002) How the environment, canopy structure and canopy physiological functioning influence carbon, water and energy fluxes of a temperate broad-leaved deciduous forest - an assessment with the biophysical model CANOAK. *Tree Physiol* 22: 1065–1077
- Ball JT, Woodrow IE and Berry JA (1987) A model predicting stomatal conductance and its contribution to the control of photosynthesis under different environmental conditions. In: Biggens J (ed) *Progress in Photosynthesis Research, Proceedings of the VII International Photosynthesis Congress*, vol IV, pp 221–224. Martinus Nijhoff, Dordrecht
- Bauerle WL, Bowden JD and Wang GG (2007) The influence of temperature on within-canopy acclimation and variation in leaf photosynthesis: spatial acclimation to microclimate gradients among climatically divergent *Acer rubrum* L. genotypes. *J Exp Bot* 58: 3285–3298
- Bégué A, Hanan NP and Prince SD (1994) Radiative transfer in shrub savanna sites in Niger: preliminary results from HAPEX-Sahel. 2. Photosynthetically active radiation interception of the woody layer. *Agric Forest Meteorol* 69: 247–266
- Bond BJ, Farnsworth BT, Coulombe RA and Winner WE (1999) Foliage physiology and biochemistry in response

- to light gradients in conifers with varying shade tolerance. *Oecologia* 120: 183–192
- Boonman A (2006) Plant Acclimation to the Light Gradient in Canopies; Functional Significance and Regulation by Cytokinin. Ph.D. thesis, Department of Biology, Utrecht University
- Boonman A, Prinsen E, Gilmer F, Schurr U, Peeters AJM, Voesenek LACJ and Pons TL (2007) Cytokinin import rate as a signal for photosynthetic acclimation to canopy light gradients. *Plant Physiol* 143: 1841–1852
- Brooks JR, Hinckley TM and Sprugel DG (1994) Acclimation responses of mature *Abies amabilis* sun foliage to shading. *Oecologia* 100: 316–324
- Buchmann N, Kao W-Y and Ehleringer JR (1996) Carbon dioxide concentrations within forest canopies - variation with time, stand structure, and vegetation type. *Glob Change Biol* 2: 421–432
- Buckley TN, Farquhar GD and Miller JM (2002) The mathematics of linked optimisation for water and nitrogen use in a canopy. *Silva Fenn* 36: 639–669
- Casal JJ and Smith H (1989) The function, action and adaptive significance of phytochrome in light-grown plants. *Plant Cell Environ* 12: 855–862
- Casella E and Sinoquet H (2003) A method for describing the canopy architecture of coppice poplar with allometric relationships. *Tree Physiol* 23: 1153–1170
- Cescatti A (1997a) Modelling the radiative transfer in discontinuous canopies of asymmetric crowns. I. Model structure and algorithms. *Ecol Modell* 101: 263–274
- Cescatti A (1997b) Modelling the radiative transfer in discontinuous canopies of asymmetric crowns. II. Model testing and application in a Norway spruce stand. *Ecol Modell* 101: 275–284
- Cescatti A (1998) Effects of needle clumping in shoots and crowns on the radiative regime of a Norway spruce canopy. *Ann Sci For* 55: 89–102
- Cescatti A and Niinemets Ü (2004) Sunlight capture. Leaf to landscape. In: Smith WK, Vogelmann TC and Chritchley C (eds) *Photosynthetic Adaptation. Chloroplast to Landscape*, Ecological Studies, 178, pp 42–85. Springer, Berlin
- Cescatti A and Zorer R (2003) Structural acclimation and radiation regime of silver fir (*Abies alba* Mill.) shoots along a light gradient. *Plant Cell Environ* 26: 429–442
- Chapin FS, III, Bloom AJ, Field CB and Waring RH (1987) Plant responses to multiple environmental factors. *Bio-Science* 37: 49–57
- Chen J-L, Reynolds JF, Harley PC and Tenhunen JD (1993) Coordination theory of leaf nitrogen distribution in a canopy. *Oecologia* 93: 63–69
- Chiariello N (1984) Leaf energy balance in the wet lowland tropics. In: Medina E, Mooney HA, Vásquez-Yanes C and Mooney HA (eds) *Physiological Ecology of Plants of the Wet Tropics*. Proc Intl Symp in Oxatepec and Los Tuxtlas, Mexico, June 29 to July 6, 1983, Tasks for Vegetation Science, 12, pp 85–98. Dr. W. Junk Publishers, The Hague
- Collatz GJ, Ribas-Carbo M and Berry JA (1992) Coupled photosynthesis-stomatal conductance model for leaves of C₄ plants. *Aust J Plant Physiol* 19: 519–538
- Cowan IR (1968) The interception and absorption of radiation in plant stands. *J Appl Ecol* 5: 367–379
- Cowan IR (1982) Regulation of water use in relation to carbon gain in higher plants. In: Lange OL, Nobel PS and Osmond CB (eds) *Physiological Plant Ecology*, vol II, *Encyclopedia of Plant Physiology*, 12B, pp 589–613. Springer, Berlin
- Craine JM and Reich PB (2005) Leaf-level light compensation points in shade-tolerant woody seedlings. *New Phytol* 166: 710–713
- Dai Y-J, Dickinson RE and Wang YP (2004) A two-big-leaf model for canopy temperature, photosynthesis, and stomatal conductance. *J Climate* 17: 2281–2299
- Davy de Virville J, Cantrel C, Bousquet AL, Hoffelt M, Tenreiro AM, Vaz Pinto V, Arrabaça JD, Caiveau O, Moreau F and Zachowski A (2002) Homeoviscous and functional adaptations of mitochondrial membranes to growth temperature in soybean seedlings. *Plant Cell Environ* 25: 1289–1297
- de Pury DGG and Farquhar GD (1997) Simple scaling of photosynthesis from leaves to canopies without the errors of big-leaf models. *Plant Cell Environ* 20: 537–557
- de Pury DGG and Farquhar GD (1999) A commentary on the use of a sun/shade model to scale from the leaf to a canopy. *Agric Forest Meteorol* 95: 257–260
- DeLucia EH and Thomas RB (2000) Photosynthetic responses to CO₂ enrichment of four hardwood species in a forest understory. *Oecologia* 122: 11–19
- Demmig-Adams B and Adams WW, III (2006) Photoprotection in an ecological context: the remarkable complexity of thermal energy dissipation: Tansley review. *New Phytol* 172: 11–21
- Demmig-Adams B, Winter K, Winkelmann E, Krüger A and Czygan FC (1989) Photosynthetic characteristics and the ratios of chlorophyll, β-carotene, and the components of the xanthophyll cycle upon a sudden increase in growth light regime in several plant species. *Bot Acta* 102: 319–325
- Duncan WG (1971) Leaf angles, leaf area and canopy photosynthesis. *Crop Sci* 11: 482–485
- Duncan WG, Loomis RS, Williams WA and Hanau R (1967) A model for simulating photosynthesis in plant communities. *Hilgardia* 38: 181–205
- Ehleringer J and Björkman O (1977) Quantum yields for CO₂ uptake in C₃ and C₄ plants. Dependence on temperature, CO₂ and O₂ concentration. *Plant Physiol* 59: 86–90
- Eliáš P, Kratochvílová I, Janoush D, Marek M and Masarovichová E (1989) Stand microclimate and physiological activity of tree leaves in an oak-hornbeam forest. I. Stand microclimate. *Trees* 4: 227–233
- Ellsworth DS and Reich PB (1993) Canopy structure and vertical patterns of photosynthesis and related leaf traits in a deciduous forest. *Oecologia* 96: 169–178

- Enríquez S, Duarte CM, Sand-Jensen K and Nielsen SL (1996) Broad-scale comparison of photosynthetic rates across phototrophic organisms. *Oecologia* 108: 197–206
- Eschrich W, Burchardt R and Essiamah S (1989) The induction of sun and shade leaves of the European beech (*Fagus sylvatica* L.): anatomical studies. *Trees* 3: 1–10
- Evans JR (1987) The dependence of quantum yield on wavelength and growth irradiance. *Aust J Plant Physiol* 14: 69–79
- Evans JR (1993a) Photosynthetic acclimation and nitrogen partitioning within a lucerne canopy. I. Canopy characteristics. *Aust J Plant Physiol* 20: 55–67
- Evans JR (1993b) Photosynthetic acclimation and nitrogen partitioning within a lucerne canopy. II. Stability through time and comparison with a theoretical optimum. *Aust J Plant Physiol* 20: 69–82
- Evans JR and Poorter H (2001) Photosynthetic acclimation of plants to growth irradiance: the relative importance of specific leaf area and nitrogen partitioning in maximizing carbon gain. *Plant Cell Environ* 24: 755–767
- Falge E, Graber W, Siegwolf R and Tenhunen JD (1996) A model of the gas exchange response of *Picea abies* to habitat conditions. *Trees* 10: 277–287
- Falge E, Ryel RJ, Alsheimer M and Tenhunen JD (1997) Effects of stand structure and physiology on forest gas exchange: a simulation study for Norway spruce. *Trees* 11: 436–448
- Farquhar GD (1989) Models of integrated photosynthesis of cells and leaves. *Phil Trans R Soc Lond Ser B-Biol Sci* 323: 357–367
- Farquhar GD, Von Caemmerer S and Berry JA (1980) A biochemical model of photosynthetic CO₂ assimilation in leaves of C₃ species. *Planta* 149: 78–90
- Field C (1983) Allocating leaf nitrogen for the maximization of carbon gain: Leaf age as a control on the allocation program. *Oecologia* 56: 341–347
- Field C and Mooney HA (1986) The photosynthesis - nitrogen relationship in wild plants. In: Givnish TJ (ed) *On the Economy of Plant Form and Function*. Proceedings of the Sixth Maria Moors Cabot Symposium, “Evolutionary Constraints on Primary Productivity: Adaptive Patterns of Energy Capture in Plants”, Harvard Forest, August 1983, pp 25–55. Cambridge University Press, Cambridge
- Field C, Merino J and Mooney HA (1983) Compromises between water-use efficiency and nitrogen-use efficiency in five species of California evergreens. *Oecologia* 60: 384–389
- Fliervoet LM, Werger JA (1984) Canopy structure and microclimate of two wet grassland communities. *New Phytol* 96: 115–130
- Francey RJ, Gifford RM, Sharkey TD and Weir B (1985) Physiological influences on carbon isotope discrimination in huon pine (*Lagarostrobos franklinii*). *Oecologia* 66: 211–218
- Gamon JA, Field CB, Goulden ML, Griffin KL, Hartley AE, Joel G, Peñuelas J and Valentini R (1995) Relationships between NDVI, canopy structure, and photosynthesis in three Californian vegetation types. *Ecol Appl* 5: 28–41
- Gates DM (1980) *Biophysical Ecology*. Springer, New York
- Gersonde R, Battles JJ and O’Hara KL (2004) Characterizing the light environment in Sierra Nevada mixed-conifer forests using a spatially explicit light model. *Can J Forest Res* 34: 1332–1342
- Gilbert IR, Seavers GP, Jarvis PG and Smith H (1995) Photomorphogenesis and canopy dynamics. Phytochrome-mediated proximity perception accounts for the growth dynamics of canopies of *Populus trichocarpa* x *deltoides* ‘Beaupré’. *Plant Cell Environ* 18: 475–497
- Givnish TJ (1982) On the adaptive significance of leaf height in forest herbs. *Am Nat* 120: 353–381
- Godin C (2000) Representing and encoding plant architecture: A review. *Ann Forest Sci* 57: 413–438
- Godin C and Sinoquet H (2005) Functional-structural plant modelling. *New Phytol* 166: 705–708
- Goudriaan J (1977) *Crop Micrometeorology: A Simulation Study*. PUDOC, Wageningen, The Netherlands
- Grantz DA and Vaughn DL (1999) Vertical profiles of boundary layer conductance and wind speed in a cotton canopy measured with heated brass surrogate leaves. *Agric Forest Meteorol* 97: 187–197
- Grassi G and Bagnaresi U (2001) Foliar morphological and physiological plasticity in *Picea abies* and *Abies alba* saplings along a natural light gradient. *Tree Physiol* 21: 959–967
- Grassi G, Colom RR and Minotta G (2001) Effects of nutrient supply on photosynthetic acclimation and photoinhibition of one-year-old foliage of *Picea abies*. *Physiol Plant* 111: 245–254
- Griffin KL, Turnbull MH and Murthy R (2002) Canopy position affects the temperature response of leaf respiration in *Populus deltoides*. *New Phytol* 154: 609–619
- Guamet JJ, Willemoes JG and Montaldi ER (1989) Modulation of progressive leaf senescence by the red:far-red ratio of incident light. *Bot Gaz* 150: 148–151
- Gutschick VP (1981) Evolved strategies in nitrogen acquisition by plants. *Am Nat* 118: 607–637
- Gutschick VP and Wiegel FW (1988) Optimizing the canopy photosynthetic rate by patterns of investment in specific leaf mass. *Am Nat* 132: 67–86
- Hachiya T, Terashima I and Noguchi K (2007) Increase in respiratory cost at high growth temperature is attributed to high protein turnover cost in *Petunia x hybrida* petals. *Plant Cell Environ* 30: 1269–1283
- Hamerlynck EP and Knapp AK (1994) Leaf-level responses to light and temperature in two co-occurring *Quercus* (*Fagaceae*) species: implications for tree distribution patterns. *Forest Ecol Manage* 68: 149–159
- Hanan NP, Prince SD and Bégue A (1995) Estimation of absorbed photosynthetically active radiation and

- vegetation net production efficiency using satellite data. *Agric Forest Meteorol* 76: 259–276
- Hanba YT, Mori S, Lei TT, Koike T and Wada E (1997) Variations in leaf $\delta^{13}\text{C}$ along a vertical profile of irradiance in a temperate Japanese forest. *Oecologia* 110: 253–261
- Hari P, Mäkelä A, Berninger F and Pohja T (1999) Field evidence for the optimality hypothesis of gas exchange in plants. *Aust J Plant Physiol* 26: 239–244
- Hari P, Mäkelä A and Pohja T (2000) Surprising implications of the optimality hypothesis of stomatal regulation gain support in a field test. *Aust J Plant Physiol* 27: 77–80
- Harley PC and Baldocchi DD (1995) Scaling carbon dioxide and water vapour exchange from leaf to canopy in a deciduous forest. I. Leaf model parametrization. *Plant Cell Environ* 18: 1146–1156
- Havaux M (1998) Carotenoids as membrane stabilizers in chloroplasts. *Trends Plant Sci* 3: 147–151
- Haxeltine A and Prentice IC (1996) BIOME3: an equilibrium terrestrial biosphere model based on ecophysiological constraints, resource availability, and competition among plant functional types. *Glob Biogeochem Cycle* 10: 693–709
- Hikosaka K (1997) Modelling optimal temperature acclimation of the photosynthetic apparatus in C_3 plants with respect to nitrogen use. *Ann Bot* 80: 721–730
- Hikosaka K (2005) Leaf canopy as a dynamic system: ecophysiology and optimality in leaf turnover. *Ann Bot* 95: 521–533
- Hikosaka K and Hirose T (1997) Leaf angle as a strategy for light competition: optimal and evolutionary stable light extinction coefficient within a leaf canopy. *Écoscience* 4: 501–507
- Hikosaka K and Terashima I (1996) Nitrogen partitioning among photosynthetic components and its consequence in sun and shade plants. *Funct Ecol* 10: 335–343
- Hikosaka K, Okada K, Terashima I and Katoh S (1993) Acclimation and senescence of leaves: their roles in canopy photosynthesis. In: Yamamoto HY and Smith CM (eds) *Photosynthetic Responses to the Environment*, pp 1–13. American Society of Plant Physiologists, Madison, WI
- Hikosaka K, Terashima I and Katoh S (1994) Effects of leaf age, nitrogen nutrition and photon flux density on the distribution of nitrogen among leaves of a vine (*Ipomoea tricolor* Cav.) grown horizontally to avoid mutual shading of leaves. *Oecologia* 97: 451–457
- Hikosaka K, Murakami A and Hirose T (1999a) Balancing carboxylation and regeneration of ribulose-1,5-bisphosphate in leaf photosynthesis: temperature acclimation of an evergreen tree, *Quercus myrsinaefolia*. *Plant Cell Environ* 22: 841–849
- Hikosaka K, Sudoh S and Hirose T (1999b) Light acquisition and use by individuals competing in a dense stand of an annual herb, *Xanthium canadense*. *Oecologia* 118: 388–396
- Hikosaka K, Nagashima H, Harada Y and Hirose T (2001) A simple formulation of interaction between individuals competing for light in a monospecific stand. *Funct Ecol* 15: 642–646
- Hinckley TM, Friend AL and Mitchell AK (1992) Response at the foliar, tree, and stand levels to nitrogen fertilization: a physiological perspective. In: Chappell HN, Weetman GF and Miller RE (eds) *Forest Fertilization: Sustaining and Improving Nutrition and Growth of Western Forests*. Institute of Forest Resources Contribution, No. 73, pp 82–89. University of Washington, Seattle, WA
- Hirose T and Bazzaz FA (1998) Trade-off between light- and nitrogen-use efficiency in canopy photosynthesis. *Ann Bot* 82: 195–202
- Hirose T and Werger MJA (1987a) Maximizing daily canopy photosynthesis with respect to the leaf nitrogen allocation pattern in the canopy. *Oecologia* 72: 520–526
- Hirose T and Werger MJA (1987b) Nitrogen use efficiency in instantaneous and daily photosynthesis of leaves in the canopy of a *Solidago altissima* stand. *Physiol Plant* 70: 215–222
- Hirose T, Werger MJA, Pons TL and Van Rheenen JWA (1988) Canopy structure and leaf nitrogen distribution in a stand of *Lysimachia vulgaris* L. as influenced by stand density. *Oecologia* 77: 145–150
- Hirose T, Ackerly DD, Traw MB and Bazzaz FA (1996) Effects of CO_2 elevation on canopy development in the stands of two co-occurring annuals. *Oecologia* 108: 215–223
- Hirose T, Ackerly DD, Traw MB, Ramseier D and Bazzaz FA (1997) CO_2 elevation, canopy photosynthesis, and optimal leaf area index. *Ecology* 78: 2339–2350
- Hollinger DY (1996) Optimality and nitrogen allocation in a tree canopy. *Tree Physiol* 16: 627–634
- Hozumi K, Kiritani H and Nishioka M (1972) Estimation of canopy photosynthesis and its seasonal change in a warm-temperate evergreen oak forest at Minamata (Japan). *Photosynthetica* 6: 158–168
- Hüve K, Bichele I, Tobias M and Niinemets Ü (2006) Heat sensitivity of photosynthetic electron transport varies during the day due to changes in sugars and osmotic potential. *Plant Cell Environ* 29: 212–228
- Iwasa Y, Cohen D and Leon JA (1984) Tree height and crown shape, as results of competitive games. *J Theor Biol* 112: 279–297
- Jackson JE (1980) Light interception and utilization by orchard systems. *Hortic Rev* 2: 208–267
- Jackson JE and Palmer JW (1972) Interception of light by model hedgerow orchards in relation to latitude, time of year and hedgerow configuration and orientation. *J Appl Ecol* 9: 341–357
- Jarvis PG (1980) Stomatal conductance, gaseous exchange and transpiration. In: Grace J, Ford ED and Jarvis PG (eds) *Plants and Their Atmospheric Environment*. The 21st Symposium of the British Ecological Society, Edinburgh

- 26–30 March 1979, pp 175–204. Blackwell Scientific, Oxford
- Jordan DB and Ogren WL (1984) The CO_2/O_2 specificity of ribulose 1,5-bisphosphate carboxylase/oxygenase. Dependence on ribulosebisphosphate concentration, pH and temperature. *Planta* 161: 308–313
- Kaiser WM (1987) Effects of water deficit on photosynthetic capacity. *Physiol Plant* 71: 142–149
- Katul GG and Albertson JD (1999) Modeling CO_2 sources, sinks, and fluxes within a forest canopy. *J Geophys Res* 104: 6081–6091
- Kimura K, Ishida A, Uemura A, Matsumoto Y and Terashima I (1998) Effects of current-year and previous-year PPFDs on shoot gross morphology and leaf properties in *Fagus japonica*. *Tree Physiol* 18: 459–466
- Kitajima K, Mulkey SS and Wright J (2005) Variation in crown light utilization characteristics among tropical canopy trees. *Ann Bot* 95: 525–547
- Kull O (2002) Acclimation of photosynthesis in canopies: models and limitations. *Oecologia* 133: 267–279
- Kull O and Jarvis PG (1995) The role of nitrogen in a simple scheme to scale up photosynthesis from leaf to canopy. *Plant Cell Environ* 18: 1174–1182
- Kull O and Kruijt B (1999) Acclimation of photosynthesis to light: a mechanistic approach. *Funct Ecol* 13: 24–36
- Kull O and Niinemets Ü (1993) Variation in leaf morphology and nitrogen concentration in *Betula pendula* Roth., *Corylus avellana* L. and *Lonicera xylosteum* L. *Tree Physiol* 12: 311–318
- Kull O and Tulva I (2002) Shoot structure and growth along a vertical profile within a *Populus-Tilia* canopy. *Tree Physiol* 22: 1167–1175
- Kull O, Koppel A and Noormets A (1998) Seasonal changes in leaf nitrogen pools in two *Salix* species. *Tree Physiol* 18: 45–51
- Kwesiga F and Grace J (1986) The role of the red/far-red ratio in the response of tropical tree seedlings to shade. *Ann Bot* 57: 283–290
- Kwesiga FR, Grace J and Sandford AP (1986) Some photosynthetic characteristics of tropical timber trees as affected by the light regime during growth. *Ann Bot* 58: 23–32
- Larocque GR (2002) Coupling a detailed photosynthetic model with foliage distribution and light attenuation functions to compute daily gross photosynthesis in sugar maple (*Acer saccharum* Marsh.) stands. *Ecol Modell* 148: 213–232
- Lei TT and Lechowicz MJ (1998) Diverse responses of maple saplings to forest light regimes. *Ann Bot* 82: 9–19
- Lieffers VJ, Messier C, Stadt KJ, Gendron F and Comeau PG (1999) Predicting and managing light in the understory of boreal forests. *Can J Forest Res* 29: 796–811
- Linder S (1987) Responses to water and nutrients in coniferous ecosystems. In: Schulze ED, Zwölfer H, Golley F, Lange OL, Olson JS and Remmert H (eds) *Potentials and Limitations of Ecosystem Analysis*, Ecological Studies, 61, pp 180–202. Springer, Berlin
- Liu L-X, Chow WS and Anderson JM (1993) Light quality during growth of *Tradescantia albiflora* regulates photosystem stoichiometry, photosynthetic function and susceptibility to photoinhibition. *Physiol Plant* 89: 854–860
- Lloyd J, Grace J, Miranda AC, Meir P, Wong SC, Miranda HS, Wright IR, Hash JHC and McIntyre J (1995) A simple calibrated model of Amazon rainforest productivity based on leaf biochemical properties. *Plant Cell Environ* 18: 1129–1145
- Logan BA, Demmig-Adams B and Adams WW III (1998) Antioxidants and xanthophyll cycle-dependent energy dissipation in *Cucurbita pepo* L. and *Vinca major* L. upon a sudden increase in growth PPFD in the field. *J Exp Bot* 49: 1881–1888
- Logue JA, De Vries AL, Fodor E and Cossins AR (2000) Lipid compositional correlates of temperature-adaptive interspecific differences in membrane physical structure. *J Exp Biol* 203: 2105–2115
- Marcolla B, Pitacco A and Cescatti A (2003) Canopy architecture and turbulence structure in a coniferous forest. *Bound-Layer Meteorol* 108: 39–59
- Maynard-Smith J (1974) The theory of games and the evolution of animal conflicts. *J Theor Biol* 47: 209–221
- McCree KJ (1972) The action spectrum, absorptance and quantum yield of photosynthesis in crop plants. *Agric Meteorol* 9: 191–216
- Medlyn BE (2004) A MAESTRO retrospective. In: Mencuccini M, Grace JC, Moncrieff J and McNaughton K (eds) *Forests at the Land-Atmosphere Interface*, pp 105–121. CAB International, Wallingford, UK
- Medlyn BE, Dreyer E, Ellsworth D, Forstreuter M, Harley PC, Kirschbaum MUF, Le Roux X, Montpied P, Strassmeyer J, Walcroft A, Wang K and Loustau D (2002) Temperature response of parameters of a biochemically based model of photosynthesis. II. A review of experimental data. *Plant Cell Environ* 25: 1167–1179
- Meir P, Kruijt B, Broadmeadow M, Barbosa E, Kull O, Carswell F, Nobre A and Jarvis PG (2002) Acclimation of photosynthetic capacity to irradiance in tree canopies in relation to leaf nitrogen concentration and leaf mass per unit area. *Plant Cell Environ* 25: 343–357
- Mencuccini M, Mambelli S and Comstock J (2000) Stomatal responsiveness to leaf water status in common bean (*Phaseolus vulgaris* L.) is a function of time of day. *Plant Cell Environ* 23: 1109–1118
- Monsi M and Saeki T (1953) Über den Lichtfaktor in den Pflanzengesellschaften und seine Bedeutung für die Stoffproduktion. *Jpn J Bot* 14: 22–52
- Monsi M, Uchijima Z and Oikawa T (1973) Structure of foliage canopies and photosynthesis. *Annu Rev Ecol Syst* 4: 301–327
- Mooney HA and Gulmon SL (1979) Environmental and evolutionary constraints on the photosynthetic characteristics of higher plants. In: Solbrig OT, Jain S, Johnson GB and Raven PH (eds) *Topics in Plant Population Biology*, pp 316–337. Columbia University Press, New York

- Mori S and Hagihara A (1991) Crown profile of foliage area characterized with the Weibull distribution in a hinoki (*Chamaecyparis obtusa*) stand. *Trees* 5: 149–152
- Moriana A, Villalobos FJ and Fereres E (2002) Stomatal and photosynthetic responses of olive (*Olea europaea* L.) leaves to water deficits. *Plant Cell Environ* 25: 395–405
- Müller J and Diepenbrock W (2006) Measurement and modelling of gas exchange of leaves and pods of oilseed rape. *Agric Forest Meteorol* 139: 307–322
- Muraoka H, Takenaka A, Tang Y, Koizumi H and Washitani I (1998) Flexible leaf orientations of *Arisaema heterophyllum* maximize light capture in a forest understorey and avoid excess irradiance at a deforested site. *Ann Bot* 82: 297–307
- Murchie EH and Horton P (1997) Acclimation of photosynthesis to irradiance and spectral quality in British plant species: chlorophyll content, photosynthetic capacity and habitat preference. *Plant Cell Environ* 20: 438–448
- Murchie EH and Horton P (1998) Contrasting patterns of photosynthetic acclimation to the light environment are dependent on the differential expression of the responses to altered irradiance and spectral quality. *Plant Cell Environ* 21: 139–148
- Myneni RB (1991) Modelling radiative transfer and photosynthesis in three-dimensional vegetation canopies. *Agric Forest Meteorol* 55: 323–344
- Myster J (1999) The effects of temperature alterations, irradiance level, photoperiod, and day extension light quality on morphogenesis, growth, and flowering of *Begonia x hiemalis* Fotsch. *Gartenbauwissenschaft* 64: 206–213
- Naidu SL and DeLucia EH (1997) Acclimation of shade-developed leaves on saplings exposed to late-season canopy gaps. *Tree Physiol* 17: 367–376
- Niinemets Ü (1996) Changes in foliage distribution with tree size and relative irradiance: differences between the saplings of *Acer platanoides* and *Quercus robur*. *Ecol Res* 11: 269–281
- Niinemets Ü (1998) Adjustment of foliage structure and function to a canopy light gradient in two co-existing deciduous trees. Variability in leaf inclination angles in relation to petiole morphology. *Trees* 12: 446–451
- Niinemets Ü (2007) Photosynthesis and resource distribution through plant canopies. *Plant Cell Environ* 30: 1052–1071
- Niinemets Ü and Fleck S (2002) Petiole mechanics, leaf inclination, morphology, and investment in support in relation to light availability in the canopy of *Liriodendron tulipifera*. *Oecologia* 132: 21–33
- Niinemets Ü and Kull O (1998) Stoichiometry of foliar carbon constituents varies along light gradients in temperate woody canopies: implications for foliage morphological plasticity. *Tree Physiol* 18: 467–479
- Niinemets Ü and Sack L (2006) Structural determinants of leaf light-harvesting capacity and photosynthetic potentials. In: Esser K, Lüttge UE, Beyschlag W and Murata J (eds) *Progress in Botany*, vol. 67, pp 385–419. Springer, Berlin
- Niinemets Ü and Tenhunen JD (1997) A model separating leaf structural and physiological effects on carbon gain along light gradients for the shade-tolerant species *Acer saccharum*. *Plant Cell Environ* 20: 845–866
- Niinemets Ü and Valladares F (2004) Photosynthetic acclimation to simultaneous and interacting environmental stresses along natural light gradients: optimality and constraints. *Plant Biol* 6: 254–268
- Niinemets Ü, Kull O and Tenhunen JD (1998) An analysis of light effects on foliar morphology, physiology, and light interception in temperate deciduous woody species of contrasting shade tolerance. *Tree Physiol* 18: 681–696
- Niinemets Ü, Oja V and Kull O (1999) Shape of leaf photosynthetic electron transport versus temperature response curve is not constant along canopy light gradients in temperate deciduous trees. *Plant Cell Environ* 22: 1497–1514
- Niinemets Ü, Ellsworth DS, Lukjanova A and Tobias M (2002) Dependence of needle architecture and chemical composition on canopy light availability in three North American *Pinus* species with contrasting needle length. *Tree Physiol* 22: 747–761
- Niinemets Ü, Kollist H, García-Plazaola JI and Becerril JM (2003) Do the capacity and kinetics for modification of xanthophyll cycle pool size depend on growth irradiance in temperate trees? *Plant Cell Environ* 26: 1787–1801
- Niinemets Ü, Al Afas N, Cescatti A, Pellis A and Ceulemans R (2004a) Petiole length and biomass investment in support modify light interception efficiency in dense poplar plantations. *Tree Physiol* 24: 141–154
- Niinemets Ü, Kull O and Tenhunen JD (2004b) Within canopy variation in the rate of development of photosynthetic capacity is proportional to integrated quantum flux density in temperate deciduous trees. *Plant Cell Environ* 27: 293–313
- Niinemets Ü, Sonninen E and Tobias M (2004c) Canopy gradients in leaf intercellular CO₂ mole fractions revisited: interactions between leaf irradiance and water stress need consideration. *Plant Cell Environ* 27: 569–583
- Niinemets Ü, Sparrow A and Cescatti A (2005) Light capture efficiency decreases with increasing tree age and size in the southern hemisphere gymnosperm *Agathis australis*. *Trees* 19: 177–190
- Niinemets Ü, Cescatti A, Rodeghiero M and Tosens T (2006a) Complex adjustments of photosynthetic capacity and internal mesophyll conductance to current and previous light availabilities and leaf age in Mediterranean evergreen species *Quercus ilex*. *Plant Cell Environ* 29: 1159–1178
- Niinemets Ü, Tobias M, Cescatti A and Sparrow AD (2006b) Size-dependent variation in shoot light-harvesting efficiency in shade-intolerant conifers. *Int J Plant Sci* 167: 19–32
- Niinemets Ü, Lukjanova A, Turnbull MH and Sparrow AD (2007a) Plasticity in mesophyll volume fraction modulates light-acclimation in needle photosynthesis in two pines. *Tree Physiol* 27: 1137–1151

- Niinemets Ü, Portsmouth A, Tena D, Tobias M, Matesanz S and Valladares F (2007b) Do we underestimate the importance of leaf size in plant economics? Disproportionate scaling of support costs within the spectrum of leaf physiognomy. *Ann Bot* 100: 283–303
- Nilson T (1971) A theoretical analysis of the frequency of gaps in plant stands. *Agric Meteorol* 8: 25–38
- Noguchi K, Go C-S, Miyazawa S-I, Terashima I, Ueda S and Yoshinari T (2001) Costs of protein turnover and carbohydrate export in leaves of sun and shade species. *Aust J Plant Physiol* 28: 37–47
- North PRJ (1996) Three-dimensional forest light interaction model using a Monte Carlo method. *IEEE Trans Geosci Remote Sensing* 34: 946–955
- North PRJ (2002) Estimation of fAPAR, LAI, and vegetation fractional cover from ATSR-2 imagery. *Remote Sens Environ* 80: 114–121
- Oechel WC (1985) A proposed model of the diurnal patterns of photosynthesis, transpiration and energy balance in the plant canopy. In: Kruger FJ, Miller PM, Miller J and Oechel WC (eds) *Simulation Modelling of Fynbos Ecosystems: Systems Analysis and Conceptual Models*, South African National Scientific Programmes Report, 105, pp 78–80. Foundation for Research Development Council for Scientific and Industrial Research, Pretoria
- Oguchi R, Hikosaka K and Hirose T (2005) Leaf anatomy as a constraint for photosynthetic acclimation: differential responses in leaf anatomy to increasing growth irradiance among three deciduous trees. *Plant Cell Environ* 28: 916–927
- Ono K, Nishi Y, Watanabe A and Terashima I (2001) Possible mechanisms of adaptive leaf senescence. *Plant Biol* 3: 234–243
- Palva L, Markkanen T, Siivola E, Garam E, Linnavuo M, Nevas S, Manoochehri F, Palmroth S, Rajala K, Ruotoistenmäki H, Vuorivirta T, Seppälä I, Vesala T, Hari P and Sepponen R (2001) Tree scale distributed multipoint measuring system of photosynthetically active radiation. *Agric Forest Meteorol* 106: 71–80
- Pan Y, Melillo JM, McGuire AD, Kicklighter DW, Pitelka LF, Hibbard K, Pierce LL, Running SW, Ojima DS, Parton WJ, Schimel DS, Borchers J, Neilson R, Fisher HH, Kittel TGF, Rossenbloom NA, Fox S, Haxeltine A, Prentice IC, Sitch S, Janetos A, McKeown R, Nemani R, Painter T, Rizzo B, Smith T and Woodward FI (1998) Modeled responses of terrestrial ecosystems to elevated atmospheric CO₂: A comparison of simulations by the biogeochemistry models of the vegetation/ecosystem modeling and analysis project (VEMAP). *Oecologia* 114: 389–404
- Parker GA and Maynard-Smith J (1990) Optimality theory in evolutionary biology. *Nature* 348: 27–33
- Pearcy RW (2007) Responses of plants to heterogeneous light environments. In: Pugnaire FI and Valladares F (eds) *Handbook of Functional Plant Ecology*, 2nd edn, pp 213–257. CRC Press, Boca Raton, FL
- Pearcy RW and Yang W (1996) A three-dimensional crown architecture model for assessment of light capture and carbon gain by understory plants. *Oecologia* 108: 1–12
- Pearcy RW, Valladares F, Wright SJ and Lasso de Paulis E (2004) A functional analysis of the crown architecture of tropical forest *Psychotria* species: Do species vary in light capture efficiency and consequently in carbon gain and growth? *Oecologia* 139: 163–177
- Pons TL and Anten NPR (2004) Is plasticity in partitioning of photosynthetic resources between and within leaves important for whole-plant carbon gain in canopies? *Funct Ecol* 18: 802–811
- Pons TL and Bergkotte M (1996) Nitrogen allocation in response to partial shading of a plant: possible mechanisms. *Physiol Plant* 98: 571–577
- Pons TL, Jordi W and Kuiper D (2001) Acclimation of plants to light gradients in leaf canopies: Evidence for a possible role for cytokinins transported in the transpiration stream. *J Exp Bot* 52: 1563–1574
- Pons TL and de Jong-van Berkel Y (2004) Species-specific variation in the importance of the spectral quality gradient in canopies as a signal for photosynthetic resource partitioning. *Ann Bot* 94: 725–732
- Pronk TE, Schieving F, Anten NPR and Werger MJA (2007) Plants that differ in height investment can coexist if they are distributing non-uniformly within an area. *Ecological Complexity* 4: 182–191
- Rousseaux MC, Hall AJ and Sánchez RA (1996) Far-red enrichment and photosynthetically active radiation level influence leaf senescence in field-grown sunflower. *Physiol Plant* 96: 217–224
- Rousseaux MC, Hall AJ and Sánchez RA (2000) Basal leaf senescence in a sunflower (*Helianthus annuus*) canopy: responses to increased R:FR ratio. *Physiol Plant* 110: 477–482
- Ryel RJ (1993) Light Relations in Tussock Grasses as Assessed with a New Three-Dimensional Canopy Photosynthesis Model. Structure and Function of Foliage Organization of a Growth Form Prevalent in Environments Characterized by Stress. Ph.D. Dissertation, Julius-Maximilians-Universität Würzburg
- Ryel RJ, Beyschlag W and Caldwell MM (1993) Foliage orientation and carbon gain in two tussock grasses as assessed with a new whole-plant gas-exchange model. *Funct Ecol* 7: 115–124
- Ryel RJ, Falge E, Joss U, Geyer R and Tenhunen JD (2001) Penumbra and foliage distribution effects on *Pinus sylvestris* canopy gas exchange. *Theor Appl Climatol* 68: 109–124
- Saeki T (1959) Variation of photosynthetic activity with aging of leaves and total photosynthesis in a plant community. *Bot Mag Tokyo* 72: 404–408
- Saeki T (1960) Interrelationships between leaf amount, light distribution and total photosynthesis in a plant community. *Bot Mag Tokyo* 73: 55–63

- Sala A and Tenhunen JD (1996) Simulations of canopy net photosynthesis and transpiration in *Quercus ilex* L. Under the influence of seasonal drought. *Agric Forest Meteorol* 78: 203–222
- Sands PJ (1995a) Modelling canopy production. I. Optimal distribution of photosynthetic resources. *Aust J Plant Physiol* 22: 593–601
- Sands PJ (1995b) Modelling canopy production. II. From single-leaf photosynthetic parameters to daily canopy photosynthesis. *Aust J Plant Physiol* 22: 603–614
- Schaepman-Strub G, Schaepman ME, Painter TH, Dangel S and Martonchik JV (2006) Reflectance quantities in optical remote sensing - definitions and case studies. *Remote Sens Environ* 103: 27–42
- Schieving F and Poorter H (1999) Carbon gain in a multispecies canopy: the role of specific leaf area and photosynthetic nitrogen-use efficiency in the tragedy of the commons. *New Phytol* 143: 201–211
- Sefcik LT, Zak DR and Ellsworth DS (2006) Photosynthetic responses to understory shade and elevated carbon dioxide concentration in four northern hardwood tree species. *Tree Physiol* 26: 1589–1599
- Selaya NG, Anten NPR, Oomen RJ, Matthies M and Werger MJA (2007) Above-ground biomass investments and light interception of tropical forest trees and lianas early in succession. *Ann Bot* 99: 141–151
- Sellers PJ, Berry JA, Collatz GJ, Field CB and Hall FG (1992) Canopy reflectance, photosynthesis, and transpiration. III. A reanalysis using improved leaf models and a new canopy integration scheme. *Remote Sens Environ* 42: 187–216
- Sharkey TD, Singsaas EL, Vanderveer PJ and Geron C (1996) Field measurements of isoprene emission from trees in response to temperature and light. *Tree Physiol* 16: 649–654
- Silberberg E (1974) A revision of comparative statics methodology in economics, or, how to do comparative statics on the back of an envelope. *J Econ Theory* 7: 159–172
- Singsaas EL, Laporte MM, Shi J-Z, Monson RK, Bowling DR, Johnson K, Lerdau M, Jasentuliyana A and Sharkey TD (1999) Kinetics of leaf temperature fluctuation affect isoprene emission from red oak (*Quercus rubra*) leaves. *Tree Physiol* 19: 917–924
- Sinoquet H and Le Roux X (2000) Short term interactions between tree foliage and the aerial environment: An overview of modelling approaches available for tree structure-function models. *Ann Forest Sci* 57: 477–496
- Sinoquet H, Thanisawanyangkura S, Mabrouk H and Kasemsap P (1998) Characterization of the light environment in canopies using 3D digitising and image processing. *Ann Bot* 82: 203–212
- Sinoquet H, Le Roux X, Adam B, Ameglio T and Daudet FA (2001) RATP: a model for simulating the spatial distribution of radiation absorption, transpiration and photosynthesis within canopies: Application to an isolated tree crown. *Plant Cell Environ* 24: 395–406
- Sinoquet H, Sonohat G, Phattaralerphong J and Godin C (2005) Foliage randomness and light interception in 3D digitized trees: An analysis of 3D discretization of the canopy. *Plant Cell Environ* 29: 1158–1170
- Skinner RH and Simmons SR (1993) Modulation of leaf elongation, tiller appearance and tiller senescence in spring barley by far-red light. *Plant Cell Environ* 16: 555–562
- Smith H (1982) Light quality, photoperception, and plant strategy. *Annu Rev Plant Physiol* 33: 481–518
- Smith H (1995) Physiological and ecological function within the phytochrome family. *Annu Rev Plant Physiol Plant Mol Biol* 46: 289–315
- Smolander H and Lappi J (1985) Integration of a nonlinear function in a changing environment: Estimating photosynthesis using mean and variance of radiation. *Agric Forest Meteorol* 34: 83–91
- Sonohat G, Sinoquet H, Varlet-Grancher C, Rakocovic M, Jacquet A, Simon JC and Adam B (2002) Leaf dispersion and light partitioning in three-dimensionally digitized tall fescue-white clover mixtures. *Plant Cell Environ* 25: 529–538
- Stenberg P, Kangas T, Smolander H and Linder S (1999) Shoot structure, canopy openness, and light interception in Norway spruce. *Plant Cell Environ* 22: 1133–1142
- Sterck FJ and Schieving F (2007) 3-D growth patterns of trees: effects of carbon economy, meristem activity, and selection. *Ecol Monogr* 77: 405–420
- Sterck FJ, Schieving F, Lemmens A and Pons TL (2005) Performance of trees in forest canopies: explorations with a bottom-up functional-structural plant growth model. *New Phytol* 166: 827–843
- Stoddart L and Thomas H (1982) Leaf senescence. In: Boulter D and Parthier B (eds) *Encyclopedia of Plant Physiology*, New series, vol 14A, pp 135–151. Springer, Berlin
- Takenaka A (1994) Effects of leaf blade narrowness and petiole length on the light capture efficiency of a shoot. *Ecol Res* 9: 109–114
- Tans PP, Fung IY and Takahashi T (1990) Observational constraints on the global CO₂ budget. *Science* 247: 1431–1438
- Tardy F and Havaux M (1997) Thylakoid membrane fluidity and thermostability during the operation of the xanthophyll cycle in higher-plant chloroplasts. *Biochim Biophys Acta - Biomembr* 1330: 179–193
- Tenhunen JD, Yocum CS and Gates DM (1976) Development of a photosynthesis model with an emphasis on ecological applications. I. Theory. *Oecologia* 26: 89–100
- Tenhunen JD, Weber JA, Filipek LH and Gates DM (1977) Development of a photosynthesis model with an emphasis on ecological applications. III. Carbon dioxide and oxygen dependence. *Oecologia* 30: 189–207

- Tenhunen JD, Sala Serra A, Harley PC, Dougherty RL and Reynolds JF (1990) Factors influencing carbon fixation and water use by mediterranean sclerophyll shrubs during summer drought. *Oecologia* 82: 381–393
- Terashima I, Araya T, Miyazawa S-I, Sone K and Yano S (2005) Construction and maintenance of the optimal photosynthetic systems of the leaf, herbaceous plant and tree: an eco-developmental treatise. *Ann Bot* 95: 507–519
- Tooming H (1967) Mathematical model of plant photosynthesis considering adaptation. *Photosynthetica* 1: 233–240
- Uemura A, Ishida A, Nakano T, Terashima I, Tanabe H and Matsumoto Y (2000) Acclimation of leaf characteristics of *Fagus* species to previous-year and current-year solar irradiances. *Tree Physiol* 20: 945–951
- Valladares F (2003) Light heterogeneity and plants: from ecophysiology to species coexistence and biodiversity. In: Esser K, Lüttge U, Beyschlag W and Hellwig F (eds) *Progress in Botany*, vol 64, pp 439–471. Springer, Berlin
- Valladares F and Niinemets Ü (2007) The architecture of plant crowns: from design rules to light capture and performance. In: Pugnaire FI and Valladares F (eds) *Handbook of Functional Plant Ecology*, 2nd edn, pp 101–149. CRC Press, Boca Raton, FL
- Valladares F and Pearcy RW (1997) Interactions between water stress, sun-shade acclimation, heat tolerance and photoinhibition in the sclerophyll *Heteromeles arbutifolia*. *Plant Cell Environ* 20: 25–36
- Valladares F and Pearcy RW (1998) The functional ecology of shoot architecture in sun and shade plants of *Heteromeles arbutifolia* M. Roem., a Californian chaparral shrub. *Oecologia* 114: 1–10
- Valladares F and Pearcy RW (2002) Drought can be more critical in the shade than in the sun: A field study of carbon gain and photo-inhibition in a Californian shrub during a dry El Niño year. *Plant Cell Environ* 25: 749–759
- Van Hinsberg A (1997) Morphological variation in *Plantago lanceolata* L.: effects of light quality and growth regulators on sun and shade populations. *J Evol Biol* 10: 687–701
- Van Ittersum MK, Leffelaar PA, Van Keulen H, Kropff MJ, Bastiaans L and Goudriaan J (2003) On approaches and applications of the Wageningen crop models. *Eur J Agron* 18: 201–234
- Vermeulen PJ, Anten NPR, Schieving F, Werger MJA and During HJ (2008) Height convergence in response to neighbour growth: genotypic differences in the stoloniferous plant *Potentilla reptans*. *New Phytol* 177: 688–697
- Weaver LM and Amasino RM (2001) Senescence is induced in individually darkened *Arabidopsis* leaves, but inhibited in whole darkened plants. *Plant Physiol* 127: 876–886
- Winter SR and Ohlrogge AJ (1973) Leaf angle, leaf area, and corn (*Zea mays* L.) yield. *Agron J* 65: 395–397
- Woledge J and Leafe EL (1976) Single leaf and canopy photosynthesis in a ryegrass sward. *Ann Bot* 40: 773–783
- Wright IJ, Leishman MR, Read C and Westoby M (2006) Gradients of light availability and leaf traits with leaf age and canopy position in 28 Australian shrubs and trees. *Funct Plant Biology* 33: 406–419
- Yamashita N, Koike N and Ishida A (2002) Leaf ontogenetic dependence of light acclimation in invasive and native subtropical trees of different successional status. *Plant Cell Environ* 25: 1341–1356
- Yano S and Terashima I (2001) Separate localization of light signal perception for sun or shade type chloroplast and palisade tissue differentiation in *Chenopodium album*. *Plant Cell Physiol* 42: 1303–1310
- Yasumura Y, Hikosaka K, Matsui K and Hirose T (2002) Leaf-level nitrogen-use efficiency of canopy and understorey species in a beech forest. *Funct Ecol* 16: 826–834

Chapter 17

Can Increase in Rubisco Specificity Increase Carbon Gain by Whole Canopy? A Modeling Analysis

Xin-Guang Zhu*

Partner Institute of Computational Biology, Chinese Academy of Sciences-Max Planck
Society of Germany, Yue Yang Road 320, Shanghai 200031, China

Stephen P. Long

Department of Plant Biology, University of Illinois at Urbana Champaign, Edgar R. Madigan
Laboratory, 1201 W. Gregory Drive, Urbana, IL 61801, USA

Summary.....	401
I. Introduction.....	402
II. Theory and Model Description.....	404
A. The Inverse Relationship between k_C and τ	404
B. Leaf Photosynthesis.....	405
C. Canopy Microclimate.....	406
D. Canopy Photosynthesis.....	406
III. The Impact of the Inverse Relationship on Leaf and Canopy Level Photosynthesis.....	407
IV. Current Efforts of Engineering Rubisco for Higher Photosynthesis.....	410
V. Why Has Evolution Failed to Select the Optimal Rubisco?.....	412
VI. Concluding Remarks.....	413
Acknowledgments.....	413
References.....	413

Summary

Genetic modification of Ribulose bis-phosphate carboxylase-oxygenase (Rubisco) to increase the specificity for CO_2 relative to O_2 (τ) would decrease photorespiration and in principle should increase crop productivity. When the kinetic properties of Rubisco from different photosynthetic organisms are compared, it appears that Rubiscos with higher τ generally have lower maximum catalytic rates of carboxylation per active site (k_C). Given this inverse relationship, we explored whether increasing τ results in increased leaf and canopy photosynthesis. A steady-state biochemical model of leaf photosynthesis was coupled to a canopy biophysical microclimate model and used in this chapter. C_3 photosynthetic CO_2 uptake rate (A) is either limited by Rubisco or by the rate of regeneration of ribulose-1,5-bisphosphate (RuBP). The latter is mainly determined by the rate of whole chain electron transport (J). Thus, if J is limiting, an increase in τ will increase net CO_2 uptake because more products of the electron transport chain will be partitioned away from photorespiration into photosynthetic CO_2 fixation. The effect of an increase in τ on Rubisco-limited photosynthesis depends on k_C , but differently dependent on the concentration of CO_2 . Assuming a strict inverse relationship between k_C and τ , theoretical simulations

* Author for correspondence, e-mail: zhuxinguang@picb.ac.cn

showed that a decrease, not an increase, in τ increases Rubisco-limited (light-saturated) photosynthesis at the current atmospheric CO_2 concentration. Crop canopies have both sunlit and shaded leaves. In addition, during a diurnal period light levels are high at midday and low at dawn and dusk. As a result, both light-limited and light-saturated photosynthesis contribute to total crop carbon gain. For canopies, the present average τ found in C_3 terrestrial plants is supra-optimal for the present ambient atmospheric CO_2 concentration of $370 \mu\text{mol mol}^{-1}$, but would be optimal for a CO_2 concentration of around $200 \mu\text{mol mol}^{-1}$, a value close to the average of the last 400,000 years. Replacing the Rubisco of terrestrial C_3 plants with one with a lower, but optimal τ would increase canopy carbon gain by 3%. Because there are Rubiscos with significant deviations from the average inverse relationship between k_C and τ , we also used the canopy model to compare the rates of canopy photosynthesis for several such Rubiscos. These simulations suggested that very substantial increases ($>25\%$) in crop carbon gain could result if specific Rubiscos deviating either towards a higher τ or higher k_C can be expressed in C_3 plants.

I. Introduction

Ribulose biphosphate carboxylase/oxygenase (Rubisco; EC 4.1.1.39) is the most abundant protein in leaf. The catalytic efficiency of Rubisco has a critical role in the rate of photosynthetic CO_2 uptake, as well as water and nitrogen use efficiency of plants (Long et al., 2006a). Much effort has been, and continue to be placed in understanding catalysis by Rubisco – both how it evolved and how to engineer it for higher efficiency by mutation or replacement with foreign forms (Spreitzer and Salvucci, 2002; Parry et al., 2003; Spreitzer et al., 2005; Raines, 2006). In this chapter we extend the previous work (Zhu et al., 2004a; Long et al., 2006a) with a modeling approach to identifying ‘better’ Rubisco for higher productivity, providing updates on recent advances in Rubisco engineering.

Rubisco is a bifunctional enzyme. It catalyzes the addition of CO_2 to ribulose-1,5-bisphosphate (RuBP) through the photosynthetic carbon reduction cycle (PCRC) to produce two molecules of 3-phosphoglycerate (3-PGA), which are then metabolized to triose phosphate. It also catalyzes the oxygenation of RuBP by O_2 to produce one molecule of 3-PGA and one molecule of 2-phosphoglycolate. The latter is metabo-

lized through the photosynthetic carbon oxidation pathway (PCOP) releasing one CO_2 for every two oxygenations. PCOP serves to recycle 75% of the carbon entering 2-phosphoglycolate through RuBP oxygenation. CO_2 and O_2 compete for the same active sites of Rubisco. Although PCOP provides precursors for various metabolic pathways, these are dispensable since plants can be grown successfully at saturating CO_2 concentrations, where little or no photorespiration occurs (Spreitzer, 1999). Photorespiration in C_3 crops is estimated to decrease productivity by over 30% at the current atmospheric CO_2 concentration (Ogren, 1984; Long, 1998). While the benefit of decreasing photorespiration as a means to increase crop yields was once questioned (Evans, 1993), C_3 crops grown under elevated CO_2 show highly significant and substantial gains in yield (Kimball, 1983; Long, 1998; Long et al., 2004; Ainsworth and Long, 2005). In greenhouse and chamber environments these yield increases may be close to the theoretical increase in leaf photosynthesis (Long et al., 2006b; Ainsworth et al., 2008). Competitive inhibition of carboxylation by O_2 , the release of CO_2 by the PCOP pathway and the energetic cost of recycling the carbon diverted to this pathway all contribute to the reduction in C_3 crop productivity (Long, 1991). Theoretically, inhibition of PCOP reactions downstream of Rubisco, but before the glycine decarboxylase, will decrease photorespiratory CO_2 release. However, any restriction here will prevent recycling of carbon back to the PCRC. Decreasing the activity of glycine decarboxylase also proved to be an inappropriate solution for decreasing photorespiratory CO_2 release. Photosynthesis in

Abbreviations: LAI – leaf area index; PCOP – photosynthetic carbon oxidation pathway; PCRC – photosynthetic carbon reduction cycle; A – photosynthetic CO_2 fixation rate; J – electron transport rate; k_C , k_O – catalytic constants of Rubisco site for CO_2 and O_2 , respectively; K_C , K_O – Michaelis – Menten constants of Rubisco for CO_2 and O_2 , respectively; $\tau_{\text{CO}_2/\text{O}_2}$ – specificity of Rubisco

Arabidopsis with deficient glycine decarboxylase activity was irreversibly inhibited in normal air (Somerville and Ogren, 1982; Somerville and Somerville, 1983). Similarly the host-selective toxin victorin, which severely inhibits glycine decarboxylase activity, caused symptoms typical of Victoria blight disease on susceptible plants (Douce and Heldt, 2000). Therefore, the only feasible means to eliminate photorespiration and increase net photosynthesis for field-grown crops is via modification of Rubisco to prevent the initial reaction of the pathway, RuBP oxygenation or, as in C_4 species, increasing the CO_2 concentration at Rubisco active sites to competitively inhibit the oxygenation reaction. Decreasing photorespiratory CO_2 loss by increasing the specificity of Rubisco for CO_2 relative to O_2 is an obvious target.

The specificity of Rubisco for CO_2 relative to O_2 (τ), was first defined by Jordan and Ogren (1981) as:

$$\tau = \frac{k_C K_O}{k_O K_C},$$

where k_C and k_O are the catalytic constants, i.e. numbers of carboxylations and oxygenations respectively that one active site of Rubisco may catalyze per second. K_C and K_O are the Michaelis–Menten constants of Rubisco for CO_2 and O_2 respectively. Although Rubisco is a highly conserved protein within C_3 terrestrial plants, τ shows great variation when the full diversity of photosynthetic organisms are considered (Jordan and Ogren, 1981; Tabita, 1999; Tcherkez et al., 2006). When measured at 25°C, terrestrial C_3 plants show an average τ of 92.5; cyanobacteria and green algae generally have a lower τ of about 50–60, while a few marine red algae may have a τ above 100 (Tabita, 1999; Tcherkez et al., 2006). The existence of different τ in Rubisco from different organisms, especially the existence of high τ in marine non-green algae, raises the possibility of transforming C_3 crop plants to express these forms of Rubisco with a higher τ , so decreasing photorespiration. So far, efforts to increase Rubisco-limited photosynthetic rate by increasing τ via directed mutagenesis have had little success (Chene et al., 1992; Romanova et al., 1997; Madgwick et al., 1998; Ramage et al., 1998; Whitney and Andrews,

2001; Houtz and Portis, 2003; Whitney and Sharwood, 2007), though exciting progress has been made (Whitney and Sharwood, 2007). Most mutants exhibit a lower τ than the wild-type from which they were obtained from (Bainbridge et al., 1995; Parry et al., 2003). Comparison of the kinetic properties of Rubisco from different photosynthetic bacteria, green algae and land plants suggests an inverse relationship between τ and k_C (Bainbridge et al., 1995; Spreitzer and Salvucci, 2002; Zhu et al., 2004a; Tcherkez et al., 2006). This correlation suggests τ might only be increased via genetic engineering of the protein at the expense of a decrease in k_C and vice versa – higher k_C is at the cost of lower specificity. Slower catalysis could be overcome by expressing more Rubisco in the photosynthetic cell, however, Rubisco already represents about 50% of leaf soluble protein in C_3 crop leaves and calculations of volumes suggest there may not be physical capacity to add more (Pyke and Leech, 1987).

What is the implication for photosynthesis at the leaf and canopy level if we assume that τ can be increased only at the expense of k_C ? It has been pointed out that τ , by itself, does not necessarily confer higher Rubisco-limited photosynthesis if k_C is too low or K_C is too high (Whitney et al., 2001; Spreitzer and Salvucci, 2002). Furthermore, extrapolating conclusions based on leaf photosynthesis models to the crop canopy level is complicated by the fact that net carbon uptake in a canopy will be the result of a combination of photosynthesis by both sunlit leaves and shaded leaves. Photosynthesis in these two kinds of leaves responds differently to changes in k_C and τ . How can the impacts of these opposing effects be evaluated at the canopy level – the level at which crop production in the field setting will be determined?

The widely validated C_3 biochemical model of Farquhar et al. (1980) predicts the steady-state rate of leaf photosynthetic CO_2 uptake (A) for given conditions of light, temperature and CO_2 concentration. It assumes that for any given set of conditions A is limited by either the activity of Rubisco or the rate of regeneration of RuBP, which is in turn limited by the rate of whole chain electron transport (J). Changes in τ and k_C affect RuBP-limited and Rubisco-limited photosynthesis differently. An increase in τ will increase RuBP-limited photosynthesis because a lower

oxygenase activity diverts less of the limiting flow of electrons to PCOP. Rubisco-limited photosynthesis however depends on changes in both, k_C and τ . Increasing τ without a change in k_C will increase Rubisco-limited photosynthesis because there is less inhibition of carboxylation by oxygen and less CO_2 released by the PCOP cycle. An increase in τ together with a decrease in k_C (following the inverse relationship) will influence Rubisco-limited photosynthesis in a complex manner depending on the relative changes in k_C and τ . At low light, A is limited by J , but at high light it is more likely to be limited by Rubisco. For a crop canopy with multiple layers of leaves, total CO_2 uptake results from a combination of both RuBP-limited and Rubisco-limited photosynthesis. Because photorespiratory loss decreases with rising CO_2 , the benefit of increasing τ at the expense of k_C also depends on the atmospheric CO_2 concentration. By integrating the steady-state biochemical model of leaf photosynthesis (Farquhar et al., 1980) into a canopy microclimate model (Norman, 1980; Forseth and Norman, 1991), these combined effects can be assessed. Here the previously described modeling approach (Zhu et al., 2004a) is used to examine how increasing τ affects crop photosynthesis for current and past CO_2 concentrations, assuming that (i) τ and k_C have a fixed inverse relationship and (ii) Rubisco content per unit leaf area keeps constant at a level typical of sun leaves in non-stressed mature C_3 crops. Because some naturally occurring forms of Rubisco appear to deviate substantially from the average inverse relationship between τ and k_C , we also assessed hypothetical values to C_3 crop canopy photosynthesis, substituting the average form of Rubisco with forms from other photosynthetic organisms, including C_4 plants and algae. We also explore whether there would be benefit in expressing different forms of Rubisco in shade versus sun leaves with crop canopy.

II. Theory and Model Description

A. The Inverse Relationship between k_C and τ

First, we quantified the apparent inverse relationship between τ and k_C based on literature estimates for both values at 25°C from different

photosynthetic organisms (Jordan and Ogren, 1981, 1984; Jordan and Chollet, 1985; Parry et al., 1989; Read and Tabita, 1994; Bainbridge et al., 1995; Horken and Tabita, 1999; Tcherkez et al., 2006) (Fig. 17.1). Where values were obtained at temperatures other than 25°C , estimates were corrected to 25°C following the parameters and equations of Bernacchi et al. (2001). Ignoring mutant forms of Rubisco, the least-square best-fit inverse relationship of τ and k_C was determined (Fig. 17.1). This relationship was approximated by Eq. (17.1) and assumed in the subsequent simulations unless otherwise noted:

$$k_C = \left(\frac{e^{5.16}}{\tau} \right)^{\frac{1}{0.69}} \quad (r^2 = 0.89), \quad (17.1)$$

where k_C (s^{-1}) is the maximum rate of carboxylation per active site of Rubisco (2.5 for the control). The specificity factor τ is bound with k_C via Eq. (17.2):

$$\tau = \frac{k_C K_O}{k_O K_C}, \quad (17.2)$$

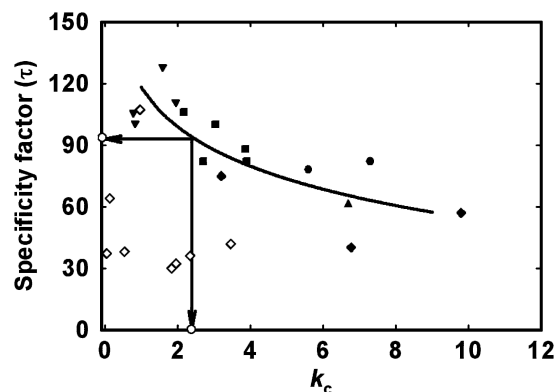


Fig. 17.1. The CO_2/O_2 specificity (τ) versus catalytic rate per active site (k_C) for Rubisco from different photosynthetic organisms. Values are for wild type (closed symbols) and mutated forms (open symbols) from Jordan and Ogren (1981), Jordan and Ogren (1984), Jordan and Chollet (1985), Parry et al. (1989), Bainbridge et al. (1995), Read and Tabita (1994), Horken and Tabita (1999), Tcherkez et al. (2006). ■ C_3 plants; ● C_4 plants; ▲ green algae; ▼ non-green algae; ◆ prokaryotes; empty diamond, mutant. The least-square best-fit inverse relationship (—) between τ and k_C for the wild-type forms of Rubiscos was an exponential (Eq. 17.1). The arrows point to the τ (92.5) and k_C (2.5) of a hypothetical 'average' C_3 crop Rubisco, used for the subsequent simulations (adapted from Zhu et al., 2004a)

where k_O (s^{-1}) is the maximum rate of oxygenation per active site of Rubisco, K_C ($\mu\text{mol mol}^{-1}$) is Rubisco Michaelis–Menten constant for CO_2 (460 for the control); K_O (mmol mol^{-1}) is Rubisco Michaelis–Menten constant for O_2 (330 for the control). The Rubisco maximum rate $V_{C_{\max}}$ is calculated via the Rubisco content, M :

$$V_{C_{\max}} = k_C M. \quad (17.3)$$

B. Leaf Photosynthesis

Prediction of the leaf-level photosynthetic rate was based on the mechanistic steady-state biochemical model of Farquhar et al. (1980) as modified by Von Caemmerer (2000), which has been widely used and validated across a large range of terrestrial C_3 plants (Von Caemmerer and Farquhar, 1981; Long, 1985; Harley, 1992; Farquhar et al., 2001). Equations (17.4–17.7) were used to predict the leaf photosynthetic rate of CO_2 uptake:

$$A = \left(1 - \frac{\Gamma^*}{C_i}\right) \min(W_C, W_J) - R_d, \quad (17.4)$$

$$\text{where } \Gamma^* = \frac{0.5 O_i}{\tau}, \quad (17.5)$$

Rubisco-limited rate is:

$$W_C = \frac{V_{C_{\max}} C_i}{C_i + K_C(1 + O_i/K_O)}, \quad (17.6)$$

and electron transport limited rate is:

$$W_J = \frac{J C_i}{4.5 C_i + 10.5 \Gamma^*}. \quad (17.7)$$

In these equations A ($\mu\text{mol CO}_2 \text{ m}^{-2} \text{ s}^{-1}$) is net photosynthetic CO_2 uptake rate and R_d is dark respiration rate in the light (assumed to be zero); the value of intercellular CO_2 concentration (C_i) is assumed to be 70% of the ambient CO_2 concentration (C_a) (Eq. 17.8):

$$C_i = 0.7 C_a. \quad (17.8)$$

Although O_2 concentration (mmol mol^{-1}) should be expected to mirror the absolute gradient in CO_2 concentration (about 100 ppm higher within the leaf in full sunlight relative to the background of 21% O_2), this difference is assumed to be insignificant and the intercellular O_2 concentra-

tion is considered to equal the external ambient concentration:

$$O_i = O_a. \quad (17.9)$$

The following Eqs. (17.10, 17.11) were used to predict the potential rate of electron transport governing the RuBP-limited rate of photosynthesis (Evans and Farquhar, 1991):

$$J = \frac{I_2 + J_{\max} - \sqrt{(I_2 + J_{\max})^2 - 4\Theta I_2 J_{\max}}}{2\Theta}, \quad (17.10)$$

$$I_2 = I_0 (1 - s)(1 - r)/2, \quad (17.11)$$

where J ($\mu\text{mol e}^- \text{ m}^{-2} \text{ s}^{-1}$) is the potential rate of whole chain electron transport through PS II for a given I_2 (the latter being photon flux density absorbed by PS II) and J_{\max} is the maximum (light saturated) J , assumed to be 250 or 180 $\mu\text{mol e}^- \text{ m}^{-2} \text{ s}^{-1}$; Θ is convexity factor for the non-rectangular hyperbolic response of electron transport through PS II to photon flux (assumed to be 0.7). In Eq. (17.11) r is the fraction of light reflected and transmitted (assumed to be 0.23); s is spectral imbalance, indicating the percentage of light energy that can not be used in photochemistry (assumed to be 0.25).

The amounts and properties of Rubisco estimated for non-stressed mature C_3 crop leaves were used in the simulation (Wullschleger, 1993). The kinetic constants (K_O and K_C) were those of Bernacchi et al. (2001). The values of τ and k_C for the average C_3 leaf were set to 92.5 and 2.5 respectively, which were obtained by calculating the τ corresponding to the average k_C of terrestrial C_3 plants following the inverse relationship shown in Fig. 17.1. Variation in τ around this C_3 average was simulated by changing K_O and K_C simultaneously, each contributing to a half of the change in τ . For this, the effect of an arbitrary variable m (%) change on K_C and K_O was predicted as

$$\Delta(K_O) = \sqrt{1 + m/100} - 1, \quad (17.12)$$

$$\Delta(K_C) = \frac{1 - \sqrt{1 + m/100}}{\sqrt{1 + m/100}}, \quad (17.13)$$

where m represents the percent changes in τ . In addition, k_C was predicted from τ as defined in

Fig. 17.1 (Eq. 17.1). Variation in k_C was bound with $V_{C_{\max}}$ as

$$V_{C_{\max}} = Mk_C,$$

where M is the concentration of Rubisco active sites per unit leaf area, assumed to be $26 \mu\text{mol m}^{-2}$, calculated from the average $V_{C_{\max}}$ from 109 studies of C_3 plant species (Wullschleger, 1993). A fixed ratio of k_O to k_C of 0.3 was assumed at 25°C (Bernacchi et al., 2001). Leaf temperature was kept constant at 25°C throughout the simulations except for data presented below in Fig. 17.4d.

C. Canopy Microclimate

To estimate canopy photosynthesis, we used the sunlit/shaded model in WIMOVAC, a program integrating the widely used biochemical model of Farquhar et al. (1980) on the background of the biophysical model of canopy microclimate of Norman (1980), as described in detail previously (Humphries and Long, 1995). In brief, following Forseth and Norman (1993) the sunlit/shaded model treats the leaves of the canopy as two populations – those sunlit and those shaded at any given time. Without going into detailed simulation of the temporal and spatial heterogeneity of light inside the canopy (Zhu et al., 2004b), this division of leaves into sunlit and shaded classes has already shown a substantial improvement in prediction over models which simply assumed an exponential decline in light through canopy layers (Norman, 1980). The diffuse, direct, and scattered light conditions at sunlit and shaded leaves were simulated using the equations of this canopy microclimate model (Eqs. 17.14–17.24).

$$F_{\text{sun}} = (1 - e^{-\kappa F / \cos \theta}) \cos \theta / \kappa, \quad (17.14)$$

$$F_{\text{shade}} = F - F_{\text{sun}}, \quad (17.15)$$

where F is total Leaf Area Index (LAI), and subscripts indicate the sunlit and shaded LAI, $\text{m}^2 \text{m}^{-2}$, θ is solar zenith angle and κ is dimensionless foliar absorption coefficient. The latter is calculated from an empirical relationship

$$\kappa = \frac{(x^2 + \tan^2 \theta)^{0.5} \cos \theta}{x + 1.744(x + 1.882)^{-0.733}}, \quad (17.16)$$

where x is the ratio of horizontal/vertical projected area of leaves in a canopy (assumed to

be 1). The solar zenith angle is related to geographic coordinates:

$$\cos \theta = \sin \Omega \sin \delta + \cos \Omega \cos \delta \cos 15 (t - t_{\text{sn}}), \quad (17.17)$$

$$\delta = -23.5 \cos \left[\frac{360 (D_j + 10)}{365} \right], \quad (17.18)$$

where $\Omega (^\circ)$ is latitude (calculations done for $\Omega = 44^\circ$) and δ is solar declination ($^\circ$); t (h) is time of a day, t_{sn} (h) is time of solar noon and D_j is day of the year (200 in calculations). The following radiation parameters were calculated from the solar constant considering Earth-Sun geometry and atmospheric transmittance:

$$I_{\text{dir}} = I_s \alpha^{[(p/p_0)/\cos \theta]}, \quad (17.19)$$

$$I_{\text{diff}} = 0.5 I_s \left(1 - \alpha^{[(p/p_0)/\cos \theta]} \right) \cos \theta, \quad (17.20)$$

$$I_{\text{shade}} = I_{\text{diff}} \cdot e^{(-0.5 F^{0.7})} + I_{\text{scat}}, \quad (17.21)$$

$$I_{\text{scat}} = 0.07 I_{\text{dir}} (1.1 - 0.1 F) e^{-\cos \theta}, \quad (17.22)$$

$$I_{\text{sun}} = I_{\text{dir}} \cos \lambda / \cos \theta + I_{\text{shade}}, \quad (17.23)$$

$$\lambda = \cos^{-1} \kappa, \quad (17.24)$$

where I_s is solar constant, i.e. the photon flux density in a plane perpendicular to the solar beam above the atmosphere ($2,600 \mu\text{mol quanta m}^{-2} \text{s}^{-1}$ of photosynthetically active radiation); I_{dir} is that of direct radiation, I_{diff} is that of the sky diffuse radiation, I_{shade} is mean I for shaded leaves within a canopy, I_{sun} is mean I for sunlit leaves within a canopy; I_{scat} is photon flux density of scattered radiation within the canopy, all I (except solar constant) in $\mu\text{mol quanta m}^{-2} \text{s}^{-1}$ on horizontal plane. Parameter λ is angle between leaf surface and the direct-beam solar radiation; α is atmospheric transmittance (assumed to be 0.85), corrected for the declination of the atmospheric pressure from the standard (p/p_0).

D. Canopy Photosynthesis

The above-calculated photon flux densities were in turn used to calculate photosynthesis for sunlit

and shaded leaves separately and dynamically (Eq. 17.25):

$$A_c = f(I_{\text{sun}}, T_a, C_i, O_i) F_{\text{sun}} + f(I_{\text{shade}}, T_a, C_i, O_i) F_{\text{shade}}, \quad (17.25)$$

where A_c ($\mu\text{mol m}^{-2} \text{s}^{-1}$) is now canopy carbon uptake per meter square of ground area per second and f indicates A as a function of these variables as described in Eqs. (17.1–17.11). The daily total canopy CO_2 uptake (A'_c) is then calculated as the summation of the photosynthetic CO_2 uptake for all the leaves throughout the whole day (Eq. 17.26):

$$A'_c = \int_0^{t=24} A_c dt, \quad (17.26)$$

where A'_c ($\text{mmol m}^{-2} \text{day}^{-1}$) is A_c integrated over the course of 1 day. The canopy temperatures were maintained at a constant 25°C . K_O , K_C and $V_{C_{\text{max}}}$ were as given in the leaf photosynthesis model. The Rubisco content of the leaves was as given in the leaf photosynthesis model, kept constant throughout the simulations.

III. The Impact of the Inverse Relationship on Leaf and Canopy Level Photosynthesis

Equation (17.1) effectively described the inverse inter-relationship between k_C and τ (Fig. 17.1). Using this inverse relationship, we calculated k_C from τ . At each CO_2 concentration the light-saturated rate of CO_2 uptake, A_{sat} , was calculated for a range of τ (from 40 to 160). The optimal τ for any given CO_2 concentration was assumed to be that at which A_{sat} was maximal. Figure 17.2 shows that the optimal τ for A_{sat} declines exponentially with increasing CO_2 concentration. The τ of 92.5 – the average for terrestrial C_3 plants – would be optimal for a CO_2 concentration of about $150 \mu\text{mol mol}^{-1}$, but supra-optimal at the current atmospheric concentration of $370 \mu\text{mol mol}^{-1}$ (Fig. 17.2). Furthermore, simulations showed that, at the current CO_2 concentration, a decrease in τ from the current 92.5–65, corresponding to an increase in k_C from 2.5–4.1, would increase A_{sat} by 12%.

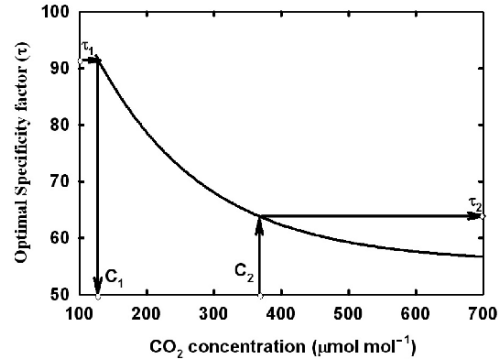


Fig. 17.2. Assuming a fixed number of active sites per unit leaf area and the dependence of k_C on τ of Fig. 17.1, the line shows the τ that will give the highest light-saturated rate of leaf photosynthetic CO_2 uptake (A_{sat}) for any given atmospheric CO_2 concentration. The average τ for terrestrial C_3 crop plants (92.5) is indicated (τ_1) together with the interpolated atmospheric CO_2 concentration (C_1) at which it would yield the maximum A_{sat} . Point τ_2 is the specificity that would yield the highest A_{sat} at the current CO_2 concentration of the atmosphere (C_2). At C_2 , decrease in τ from the current average (τ_1) to the optimum for current CO_2 concentration (τ_2) can increase light-saturated leaf photosynthetic carbon uptake by 12% (adapted from Zhu et al., 2004a)

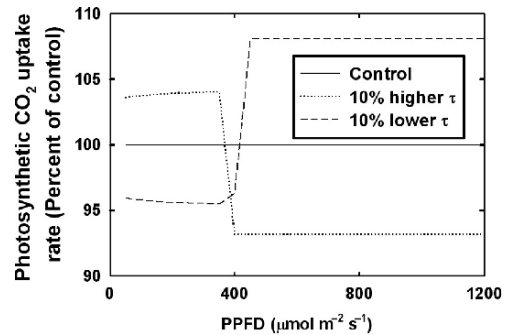


Fig. 17.3. The relative effects of a 10% increase and of a 10% decrease in τ on net photosynthetic CO_2 uptake as a function of photon flux. Calculations assume the dependence of k_C on τ of Fig. 17.1. The control is the average τ (92.5) and average k_C (2.5 CO_2 per active site per second) for terrestrial C_3 vascular plants. — control; 10% higher τ ; --- 10% lower τ (adapted from Zhu et al., 2004a)

However, photosynthesis of leaves in real canopies can be not only light-saturated, but also light-limited. The light-limited photosynthesis is in fact RuBP-limited while light-saturated photosynthesis is commonly Rubisco-limited. The effect of varying τ at different light levels on single leaves is shown in Fig. 17.3. Leaves with a simulated 10% higher τ exhibited higher light-limited photosynthesis and lower light-saturated

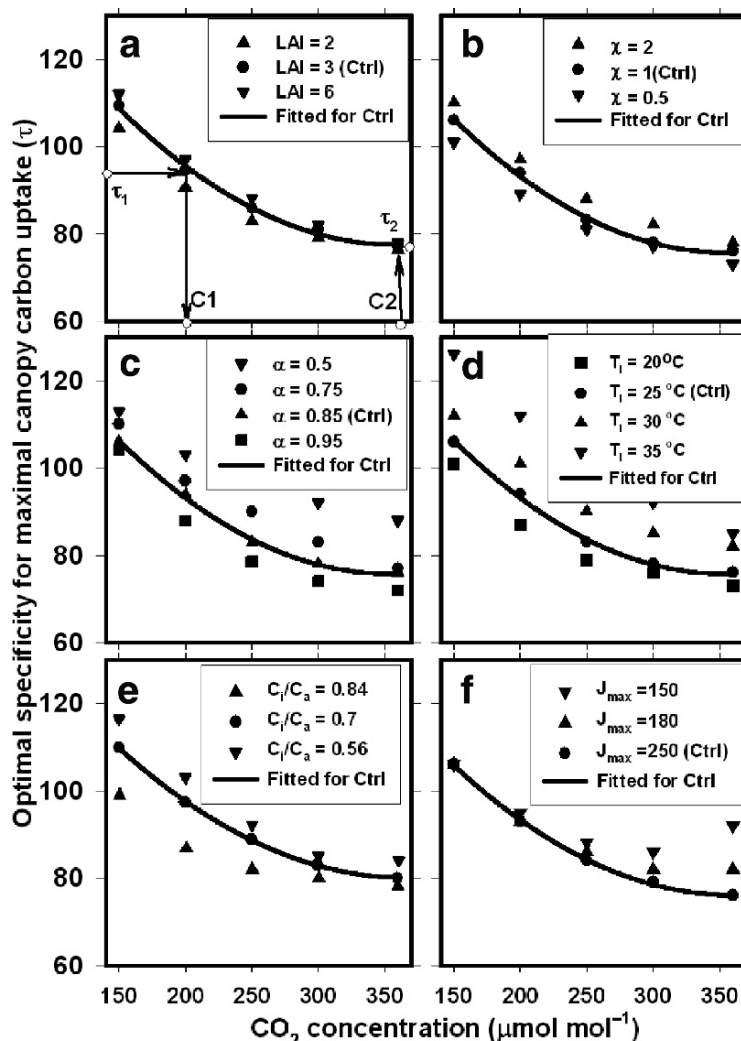


Fig. 17.4. Conditions are the same as in the legend of Fig. 17.2, but showing the τ that results in the greatest daily total canopy carbon gain (A'_c) at any given CO_2 concentration. The prediction uses sun–earth geometry to determine solar angles and incident photon flux, to predict light at different points within the canopy. The control is for the 200th day of the year, and assumes a day with clear sky, a constant leaf temperature of 25°C , a maximum rate of electron transport supporting ribulose-1,5 bisphosphate regeneration (J_{\max}) of $250 \mu\text{mol e}^- \text{m}^{-2} \text{s}^{-1}$, a leaf area index 3 and a random inclination of foliage. As in Fig. 17.2, the atmospheric CO_2 concentration (C_1) at which the average specificity of C_3 crops (τ_1) would be optimal for maximizing A'_c and the specificity (τ_2) that would be optimal for maximizing A'_c in the current atmosphere (C_2) are also indicated in panel (a). For each individual simulation, control parameters were used except for the tested parameters that were varied. The six parameters varied in the simulations are LAI (a), the ratio of horizontal/vertical projected leaf area χ (b), atmospheric transmittance α (c), canopy temperature (d), the ratio of C_i/C_a (e) and J_{\max} (f). In panel (c) the values of τ at different temperatures were all converted to τ at 25°C for easy comparison. The percentage increase of canopy carbon uptake by decreasing τ from τ_1 to τ_2 at C_2 is 3.1% in panel (a) (adapted from Zhu et al., 2004a)

photosynthesis compared to those with unaltered τ . Similarly, leaves containing a Rubisco with 10% lower τ (and therefore higher k_C) exhibited higher light-saturated photosynthesis and lower light-limited photosynthesis compared to the control.

Since variation in CO_2 concentration does not affect the opposing influence of increasing τ on light-saturated and light-limited photosynthesis equally, it results in a different optimal τ for canopy photosynthesis at each CO_2 concentration. Assuming J_{\max} of $250 \mu\text{mol quanta m}^{-2} \text{s}^{-1}$,

a canopy of LAI = 3 with random angles of leaf orientation and inclination (i.e. a ratio of the horizontal/vertical projected leaf area, χ , of unity – a good approximation to many C_3 crop canopies, Forseth and Norman, 1993), simulations showed that at 44°N latitude on the 200th day of the year, the current τ is higher than that which would be optimal for achieving maximal canopy photosynthesis at the current atmospheric CO_2 concentration (Fig. 17.4a). The optimal τ ($\tau_2 = 78$; Fig. 17.4a) for maximizing the daily integral of canopy CO_2 uptake (A'_c) for current CO_2 concentration (point C_2 in Fig. 17.4a), fell significantly below the current average of 92.5 (τ_1). The τ of 92.5 would be optimal for an atmospheric CO_2 concentration of about 220 $\mu mol\ mol^{-1}$ (Fig. 17.4a).

In the above simulations, LAI was assumed to be constant. In reality, LAI of canopies constantly change during crop growth and development. Because LAI influences the light conditions inside canopy (Eqs. 17.14, 17.15, 17.21), canopies with different LAI will have different optimal τ under each CO_2 concentration. To test the validity of the conclusions obtained using an LAI of 3, we also assessed sensitivity to change in LAI. We used an LAI of 2 to represent a canopy at the early stage of development and an LAI of 6 to represent a fully closed canopy. Simulations showed that alteration of LAI does not change the trend, i.e. the optimal τ decreases with increasing CO_2 concentration (Fig. 17.4a). Similarly, several other factors also influence the ratio between Rubisco- and RuBP-limited photosynthesis in canopy. These factors include χ , atmospheric transmittance (α), temperature and J_{max} . The parameters α and χ influence light conditions inside canopy (Eq. 17.16). Temperature differentially influences the processes or enzymes underlying RuBP-limited photosynthesis and Rubisco-limited photosynthesis (Bernacchi et al., 2001, 2003; Long and Bernacchi, 2003) which correspondingly causes a change in the ratio between them. CO_2 concentration and J_{max} also influence the RuBP- and Rubisco-limited photosynthesis differently (Eqs. 17.6, 17.7, 17.10). We conducted sensitivity analysis for each factor (Fig. 17.4). Overall, the general trend that optimal τ decreases with increasing CO_2 concentration was followed, except under low J_{max} .

It is remarkable that even with large changes in LAI, χ , α , temperature and the ratio of C_i/C_a , the CO_2 dependence of the optimal τ changes little (Fig. 17.4a–e). This pattern broke down only when J_{max} was lowered by 40% (to 150 $\mu mol\ e^{-}\ m^{-2}\ s^{-1}$). Here the optimal τ for canopy carbon uptake first decreases, then increases with increase in the CO_2 concentration (Fig. 17.4f). This is because a higher proportion of canopy photosynthesis is RuBP-limited under lower J_{max} , and the gain due to high τ outweighs the loss due to lower k_C . However, as noted earlier for well fertilized C_3 crops, a J_{max} of 150 $\mu mol\ e^{-}\ m^{-2}\ s^{-1}$ would be rather low (Wullschlegel, 1993).

If Rubisco was modified to a τ that would maximize A'_c , the increase in A'_c is greater in canopies with properties favoring Rubisco-limited photosynthesis (higher J_{max} , lower V_{cmax} , lower LAI, lower χ , higher atmospheric transmittance, and lower ratio of C_i/C_a) compared to those favoring RuBP-limited photosynthesis. This result suggests that modifying τ to its optimum would be particularly beneficial to plants in semi-arid regions where plants generally show low stomatal conductance (Gomes et al., 2002) and low LAI, which could result in greater contribution of carbon uptake from light saturated photosynthesis. As a consequence of these two factors, a high proportion of canopy photosynthesis would be Rubisco-limited in semi-arid regions. Therefore, improved ability to assimilate CO_2 at low C_i by optimizing τ would also allow increased efficiency of water use, which can be a competitive advantage in these regions. As shown in leaf photosynthesis, optimizing τ and k_C can increase A'_c by up to 12% when all leaves are light-saturated and Rubisco-limited, e.g. during early crop growth prior to canopy closure.

Increase in carboxylation rate (increase in k_C) will only benefit V_{cmax} -limited assimilation. If J_{max} is decreased so is the proportion of photosynthesis over a diurnal cycle that is V_{cmax} -limited. How much would variation in J_{max} influence the optimal τ and A'_c ? Compared to the optimal τ of 78 for current CO_2 concentration at a J_{max} of 250 $\mu mol\ e^{-}\ m^{-2}\ s^{-1}$, the optimal τ for the J_{max} of 180 $\mu mol\ e^{-}\ m^{-2}\ s^{-1}$ is slightly higher, at 83 ($k_C = 2.9$; Fig. 17.4f and Table 17.1). The gain in canopy photosynthesis that would be achieved by using a Rubisco with

Table 17.1. Specificity (τ) found to be optimal for a canopy of Leaf Area Index (LAI) = 3 and random inclination of foliage elements on a clear summer day at latitude 44° assuming two different capacities for whole chain electron transport (J_{\max}). The increases in the daily integral of canopy photosynthesis that would result from substituting such an optimal Rubisco into the canopy, relative to the current average form ($\tau = 92.5$). The proportion of the daily integral of canopy carbon gain (A'_c) that would be obtained under Rubisco-limited conditions is also given. The atmospheric CO_2 concentration at which the current Rubisco would yield the highest A'_c for the two values of J_{\max} is also calculated (adapted from Zhu et al., 2004a)

	J_{\max} ($\mu\text{mol e}^- \text{m}^{-2} \text{s}^{-1}$)	
	180	250
Predicted optimal τ for current atmospheric (CO_2)	83	78
Predicted percent increase in A'_c that would be achieved by substituting the optimal τ under current (CO_2)	1.7%	3.1%
Predicted increase in A'_c with the optimal τ under current (CO_2)	15 $\text{mmol m}^{-2} \text{day}^{-1}$	30 $\text{mmol m}^{-2} \text{day}^{-1}$
The percent of A'_c that is Rubisco-limited for the corresponding optimal Rubisco	52%	61%
The predicted optimal atmospheric (CO_2) ($\mu\text{mol mol}^{-1}$) for current τ	200	220

an optimal τ for this J_{\max} is also smaller (Table 17.1, Fig. 17.4f). As stated earlier, this difference can be explained by the fact that at the higher J_{\max} (of $250 \mu\text{mol m}^{-2} \text{s}^{-1}$), 61% of A'_c is attributed to Rubisco-limited photosynthesis, but only 52% for the lower J_{\max} (Table 17.1). Therefore, the lower the J_{\max}/V_{Cmax} ratio in a leaf or canopy, the less important k_C is, since a smaller proportion of plant carbon is fixed by Rubisco-limited photosynthesis (Table 17.1). The J_{\max} value of $250 \mu\text{mol e}^- \text{m}^{-2} \text{s}^{-1}$ used in these simulations is high, but in line with values reported for C_3 crops grown under high nitrogen and high light (Farage et al., 1998; Bunce, 2000). Decreasing J_{\max} by 28% (from 250 to $180 \mu\text{mol m}^{-2} \text{s}^{-1}$) roughly halved the advantage of selecting a Rubisco optimized for canopy carbon gain (Table 17.1). The benefit of replacing current Rubisco with a form with a higher k_C and correspondingly lower τ will in part depend on the amount of Rubisco relative to the capacity for regeneration of RuBP. Although a close positive correlation between these two capacities is apparent in surveys of C_3 species (Wulfschleger, 1993), over twofold variation in the ratio of these two capacities is found within crops (Bunce, 2000) and linkage can also be varied by altering *rbcS* expression (Harrison et al., 2001).

In all the canopy level simulations, we assumed $26 \mu\text{mol}$ Rubisco active sites per meter square leaf area, as estimated from V_{Cmax} and k_C of Rubisco (Wulfschleger, 1993). Rubisco content varies between species and leaves within a

canopy, and even in mature leaves transferred from low to high growth irradiances (Sims and Pearcy, 1992; Frak et al., 2001; Oguchi et al., 2003). Theoretically, decreasing k_C with increasing τ could be compensated for by simply increasing the amount of Rubisco. As noted earlier, Rubisco typically accounts for about 50% of leaf soluble protein, and there may be little or no physical capacity to add more (Pyke and Leech, 1987). At such a high concentration, Rubisco is already expensive in terms of the amount of nitrogen and energy it represents. Increasing Rubisco to compensate for a lower k_C may result in a proportional decrease in efficiency of nitrogen use, an undesirable trait in crop plants.

IV. Current Efforts of Engineering Rubisco for Higher Photosynthesis

Figure 17.1 indicates that there are Rubiscos with considerable deviation from the average inverse relationship between τ and k_C assumed in the simulations above. For example, Rubiscos from some non-green algae have been reported with a significantly greater τ than that of C_3 crops, yet apparently with a similar or higher k_C (Whitney et al., 2001c) while C_4 forms of Rubisco generally appear to have adapted to the high CO_2 environment by increasing k_C at the expense of K_C with little change in τ (Sage, 2002). Other important observations with respect to the potential

Table 17.2. Estimates of the daily canopy carbon gain (A'_c), as in Table 17.1 and Fig. 17.4, assuming the hypothetical replacement of the 'average' form of Rubisco from C_3 crop species with Rubiscos from other species. Reported values for k_C and K_C of these species (Jordan and Ogren, 1984; Seeman et al., 1984; Whitney et al., 2001) were used to calculate K_O using Eq. (17.2) and assuming a fixed ratio of k_O to k_C of 0.3 at 25°C (Bernacchi et al., 2001). The Farquhar et al. (1980) model uses intercellular CO_2 concentration C_i . Since K_C was reported as the CO_2 concentration around Rubisco in solution (C_c), mesophyll conductance was used to adjust this reported value to K_C expressed as intercellular CO_2 concentration (adapted from Zhu et al., 2004a)

Species	A'_c (mmol m ⁻² day ⁻¹)	A'_c (%)	A_{sat} (μmol m ⁻² s ⁻¹)
Current 'average' C_3 crop			
$k_C = 2.5$, $\tau = 92.5$	1,040	100	14.9
Tobacco			
$k_C = 3.4$, $\tau = 82$	1,170	111.4	19.1
<i>Zea mays</i>			
$k_C = 5.6$, $\tau = 78$	1,180	111.9	19.8
<i>Amaranthus edulis</i>			
$k_C = 7.3$, $\tau = 82$	1,250	117.1	28.3
<i>Griffithsia monilis</i>			
$k_C = 2.6$, $\tau = 167$	1,430	127	21.5
<i>Phaeodactylum tricornutum</i>			
$k_C = 3.4$, $\tau = 113$	965	92.3	12.5
<i>A. edulis</i> /current	1,360	131	28.3

for increasing crop photosynthesis are that (i) among higher plants, k_C and K_C vary far more than τ , especially in comparisons of C_3 and C_4 species (Yeoh et al., 1981; Seeman et al., 1984) and (ii) non-green algal Rubiscos possess very high τ that may not be compromised by a very low K_C (Whitney et al., 2001c). Table 17.2 shows the predicted effects of hypothetically substituting the 'average' C_3 terrestrial Rubisco used in the preceding simulations with Rubisco from different organisms. Compared to the average C_3 crop used in the previous simulations, the tobacco Rubisco parameters result in an 11.4% increase in A'_c . Thus, the lower than average τ (82) is more than compensated for by the higher k_C (3.4) of the tobacco Rubisco. Of the two C_4 Rubiscos examined, Rubisco from *Amaranthus edulis* substantially increased A'_c compared to the crop C_3 Rubisco forms due to its high k_C , with maintenance of a sufficiently low K_C . Rubisco from a non-green alga, *Griffithsia monilis*, which has a higher τ but maintains a similar k_C and K_C to tobacco (Whitney et al., 2001c), would increase A'_c by 27% (Table 17.2). Most C_3 annual crop canopies form leaves at the top of the canopy so that they start life in high light and then become progressively shaded as new leaves form above. Shading is sensed in plant leaves by the balance of red/far-red light via the phytochrome system (Gilbert et al., 2001). This suggests a possibility

where plants trigger the replacement of a high k_C Rubisco with a high τ form as the leaf acclimates to shade. We simulated such a scenario where a form of Rubisco with a high k_C (*A. edulis*) was expressed in the sunlit leaves and another form with high τ (current C_3 average) in the shade leaves; this increased A'_c by 31% (Table 17.2) (Long et al., 2006a).

How far are we from realizing these suggested increases? Engineering Rubisco in higher plants is challenging because of the different locations of the large (L) plastid encoded and small (S) nuclear encoded subunits of Rubisco and the complex mechanism coordinating the expression, post-translational modifications and assembly of both L and S subunits into the hexadecamer (L_8S_8) of the functional enzyme within the chloroplast stroma (Whitney and Andrews, 2001a; Whitney et al., 2001; Houtz and Portis, 2003). Given this difficulty, can Rubisco from foreign organisms be used to support plant autotrophic growth at all? Replacing Rubisco in tobacco with the simple homodimeric form of the enzyme from the α -proteobacterium *Rhodospirillum rubrum*, which has no small subunits and no special assembly requirements, produced plants which were autotrophic and reproductive, though requiring CO_2 supplementation. This established that the activity of Rubisco from a very different phylogeny can be integrated into chloroplast

photosynthetic metabolism without prohibitive problems (Whitney and Andrews, 2001b). So far, successful transformation of the higher-plant plastome with sequences coding the non-green algal Rubisco has not been achieved. Rubiscos from non-green algae are expressed abundantly but not assembled in tobacco chloroplasts (Whitney et al., 2001) possibly due to problems in either folding or assembling these evolutionarily different forms of Rubisco. On the other hand, tobacco (*Nicotiana tabacum*) plants have been successfully transformed with plastid DNA that contained the Rubisco large subunit (*rbcL*) gene from either sunflower (*Helianthus annuus*) or the cyanobacterium *Synechococcus* PCC6301, along with a selectable marker. Three stable lines of transformants with altered *rbcL* genes were generated with two lines containing Rubisco (with the L subunit from sunflower, or a chimeric sunflower/tobacco large subunit from homologous recombination) with catalytic activities, which demonstrated the feasibility of using a binary system. In a binary system, different forms of the *rbcL* gene are constructed in a bacterial host and then introduced into a vector for homologous recombination in transformed chloroplasts to produce an active chimeric enzyme in vivo (Kanevski et al., 1999). The catalytic activities of the hybrid enzymes, however, were only around 25% of the wildtype Rubisco (Kanevski et al., 1999). Compared to the genetic manipulation of L subunit, the means for engineering the S subunit (either native or foreign) has remained an elusive challenge because multiple copies of Rubisco small subunit gene exist in plant nuclei, which make targeted mutagenic or placement strategies difficult. One potential way to get around the difficulty of simultaneous expression of the L and S Rubisco subunits is to use fusion proteins, as demonstrated recently by the success of linking the L and S subunits of *Synechococcus* PCC6301 Rubisco to generate correctly assembled Rubisco in *E. coli* with catalytic capacity similar to wildtype *Synechococcus* (Whitney and Sharwood, 2007). However, fused tobacco L and S peptides did not assemble in *E. coli* (Whitney and Sharwood, 2007) possibly due to chaperonin incompatibility (Gatenby, 1984; Kettleborough et al., 1990). Studies to assess the applicability of this linking strategy to assemble functional Rubisco complexes of higher plant Rubisco L and

S subunits in chloroplasts are warranted. In brief, great advances were made in engineering higher plant Rubisco in the last decade. It is foreseeable that engineering optimal Rubisco for higher productivity might be achievable within a decade.

V. Why Has Evolution Failed to Select the Optimal Rubisco?

Why evolution has failed to select a Rubisco that is optimal for canopy photosynthetic uptake? There are a few potential reasons.

1. Our simulation suggests that Rubisco of current C_3 plants would be optimal for an atmospheric CO_2 concentration of about $200 \mu\text{mol mol}^{-1}$ (Table 17.1, Fig. 17.4a–f). This falls in the range of the atmospheric CO_2 concentrations over the last 450,000 years, which fluctuated between 180 and $290 \mu\text{mol mol}^{-1}$ as detected from the Vostok ice core (Barnola et al., 1999). The current Rubisco found in C_3 crops might be a result of evolutionary optimization to the low CO_2 and high O_2 concentrations over the past 450,000 years. The unprecedented rapid increase in CO_2 concentration since the Industrial Revolution may have far exceeded the speed of potential Rubisco evolution. On this same line, the concentration of enzymes in the photorespiratory pathway of existing C_3 plants are much higher than the theoretical optimal concentrations for current atmospheric conditions (Zhu et al., 2007), also suggesting that the evolution of plant metabolism lags behind the rapid change of atmospheric CO_2 concentration.
2. Evolution selects for fecundity, not productivity. From purely a productivity perspective, Rubisco without any oxygenation reaction will be most desired. Although RuBP oxygenation is not needed under ideal growth conditions since plants grow perfectly well under extremely high CO_2 concentrations, photorespiration could be critical for survival of plants under some stress conditions, e.g. high light and low CO_2 in drought and hot summers. Under such stress conditions, plants with photorespiration could gain a better chance of survival because photorespiration allows dissipation of excess energy even when stomata are closed.
3. Another potential reason that Rubisco is not optimal for photosynthesis might be related to inherent physical constraints of the enzyme. The repeated

evolution of C_4 photosynthesis from C_3 photosynthesis – despite the complexities of the Kranz structure (Dengler and Nelson, 1999; Sage, 1999, 2004) and partitioning of enzymes and transporters (Leegood, 1999) to avoid photorespiration – suggest that land plants may have met an evolutionary barrier: the “best” achievable structure of higher plant Rubisco for high CO_2 affinity with an adequate k_C might have already been obtained (Long, 1998). The rationale is that if it were possible to significantly increase τ without decreasing k_C , evolution would have already found a route, rather than evolving the complex Kranz structure and using the C_4 pathway for concentrating CO_2 .

VI. Concluding Remarks

In conclusion, this chapter describes the rationale behind the efforts of studying the mechanisms, evolution, and engineering of Rubisco. In particular, we examined the rationale of current efforts to increase photosynthetic rate by increasing τ . We demonstrated that if higher τ can only be achieved at the expense of k_C , then an increase in τ will in fact result in decreased daily canopy carbon gain for the current atmospheric CO_2 concentration, not the usually assumed increase. In shade environments or leaves with a low J_{max}/V_{Cmax} , increasing τ can increase the total canopy carbon gain for the current CO_2 concentration. The optimal τ reflects a balance between the Rubisco-limited photosynthesis and RuBP-limited photosynthesis. The simulations here also show that crop carbon gain could be increased substantially by substituting the existing average C_3 crop Rubisco with those from other photosynthetic organisms. Specifically, substituting the average existing C_3 crop Rubisco with the *Griffithsia monilis* Rubisco (a non-green alga) could increase carbon gain by more than 25% without any increase in the amount of Rubisco (and therefore nitrogen) per unit leaf area. Substituting with the Rubisco from *Amaranthus edulis* would increase carbon gain by 17%.

Selective expression of a Rubisco with a high k_C at the top of the canopy and Rubisco with a high τ in the lower canopy would increase canopy photosynthesis even more. Significant advances have been made in the transgenic expression of foreign Rubiscos in higher plants. It is foreseen-

able that engineering optimal Rubisco for higher productivity using an existing Rubisco might be achievable within a decade.

Acknowledgments

The authors thank support from the National Science Foundation Grant IBN 04-17126.

References

- Ainsworth EA and Long SP (2005) What have we learned from 15 years of free-air CO_2 enrichment (FACE)? A meta-analytic review of the responses of photosynthesis, canopy. *New Phytol* 165: 351–371
- Ainsworth EA, Rogers A and Leakey ADB (2008) Targets for crop biotechnology in a future high CO_2 and high O_3 World. *Plant Physiol* 147: 13–19
- Bainbridge G, Madgwick PJ, Parmar S, Mitchell R, Paul M, Pitts J, Keys AJ and Parry MAJ (1995) Engineering Rubisco to change its catalytic properties. *J Expt Bot* 46: 1269–1276
- Barnola JM, Raynaud D, Lorius C and Barkov NI (1999) Historical CO_2 record from the Vostok ice core. In: *Trends: A Compendium of Data on Global Change. Carbon dioxide Information Analysis Center. Oak Ridge National laboratory, Department of Energy, Oak Ridge, TN*
- Bernacchi CJ, Singsaas EL, Pimentel C, Portis JAR and Long SP (2001) Improved temperature response functions for models of Rubisco-limited photosynthesis. *Plant Cell Environ* 24: 253–259
- Bernacchi CJ, Pimentel C and Long SP (2003) *In vivo* temperature response functions of parameters required to model RuBP-limited photosynthesis. *Plant Cell Environ* 26: 1419–1430
- Bunce JA (2000) Contrasting effects of carbon dioxide and irradiance on the acclimation of photosynthesis in developing soybean leaves. *Photosynthetica* 38: 83–89
- Chene P, Day AG and Fersht AR (1992) Mutation of asparagine 111 of Rubisco from *Rhodospirillum rubrum* alters the carboxylase/oxygenase specificity. *J Mol Biol* 225: 891–896
- Dengler NG and Nelson T (1999) Leaf structure and development in C_4 photosynthesis. In: Sage RF and Monson RK (eds) *C4 Plant Biology*, pp 133–172, Academic Press, San Diego, CA
- Douce R and Heldt HW (2000) Photorespiration. In: Leegood RC, Sharkey TD and Von Caemmerer S (eds) *Photosynthesis: Physiology and Metabolism*, pp 115–136. Kluwer (now Springer), Dordrecht

- Evans JH and Farquhar GD (1991) Modelling canopy photosynthesis from the biochemistry of C_3 chloroplast. In: Boote KJ and Loomis RS (eds) *Modelling Crop Photosynthesis – From Biochemistry to Canopy*, pp 1–15. Crop Science Society of America, Madison, WI
- Evans LT (1993) *Crop Evolution, Adaptation and Yield*. Cambridge University Press, Cambridge
- Farage PK, McKee IF and Long SP (1998) Does a low nitrogen supply necessarily lead to acclimation of photosynthesis to elevated CO_2 ? *Plant Physiol* 118: 573–580
- Farquhar GD, Von Caemmerer S and Berry JA (1980) A biochemical model of photosynthetic CO_2 assimilation in leaves of C_3 species. *Planta* 149: 78–90
- Farquhar GD, Von Caemmerer S and Berry JA (2001) Models of photosynthesis. *Plant Physiol* 125: 42–45
- Forseth IN and Norman JM (1991) Modeling of solar irradiance, leaf energy budget, and canopy photosynthesis. In: Hall DO, Scurlock JMO, Bolhar-Nordenkamp RC, Leegood RC and Long SP (eds) *Photosynthesis and Productivity Research in a Changing Environment*, pp 207–219. Chapman & Hall, London
- Forseth IN and Norman JM (1993) Modelling of solar irradiance, leaf energy budget, and canopy photosynthesis. In: Hall DO, Scurlock JMO, Bolhar-Nordenkamp RC, Leegood RC and Long SP (eds) *Techniques in Photosynthesis and Productivity Research for a Changing Environment*, pp 129–167. Chapman & Hall, London
- Frak E, Le Roux X, Millard P, Dreyer E, Jaouen G, Saint-Joanis B and Wendler R (2001) Changes in total leaf nitrogen and partitioning, of leaf nitrogen drive photosynthetic acclimation to light in fully developed walnut leaves. *Plant Cell Environ* 24: 1279–1288
- Gatenby AA (1984) The properties of the large subunit of maize ribulose biphosphate carboxylase-oxygenase synthesized in *Escherichia Coli*. *Eur J Biochem* 144: 361–366
- Gilbert IR, Jarvis PG and Smith H (2001) Proximity signal and shade avoidance differences between early and late successional trees. *Nature* 411: 792–795
- Gomes FP, Mielke MS and de Almeida AAF (2002) Leaf gas exchange of green dwarf coconut (*Cocos nucifera* L. var. nana) in two contrasting environments of the Brazilian north-east region. *J Hortic Sci Biotech* 77: 766–772
- Harley PC (1992) Modeling photosynthesis of cotton in elevated CO_2 . *Plant Cell Environ* 15: 271–282
- Harrison EP, Olcer H, Lloyd JC, Long SP and Raines CA (2001) Small decreases in SBPase cause a linear decline in the apparent RuBP regeneration rate, but do not affect Rubisco carboxylation capacity. *J Exp Bot* 52: 1779–1784
- Horken KM and Tabita FR (1999) Closely related form I ribulose biphosphate carboxylase/oxygenase molecules that possess different CO_2/O_2 substrate specificities. *Arch Biochem Biophys* 361: 183–194
- Houtz RL, Portis AR (2003) The life of ribulose 1,5-bisphosphate carboxylase/oxygenase - Posttranslational facts and mysteries. *Arch Biochem Biophys* 414: 150–158
- Humphries SW and Long SP (1995) WIMOVAC: A software package for modelling the dynamics of plant leaf and canopy photosynthesis. *Comput Appl Biosci* 11: 361–371
- Jordan DB and Chollet R (1985) Subunit dissociation and reconstitution of ribulose-1,5-bisphosphate carboxylase from *Chromatium vinosum*. *Arch Biochem Biophys* 236: 487–496
- Jordan DB and Ogren WL (1981) Species variation in the specificity of ribulose biphosphate carboxylase/oxygenase. *Nature* 291: 513–515
- Jordan DB and Ogren WL (1984) The carbon dioxide/oxygen specificity of ribulose-1,5-bisphosphate carboxylase/oxygenase. *Planta* 161: 308–313
- Kanevski I, Maliga P, Rhoades DF and Gutteridge S (1999) Plastome engineering of ribulose-1,5-bisphosphate carboxylase/oxygenase in tobacco to form a sunflower large subunit and tobacco small subunit hybrid. *Plant Physiol* 119: 133–141
- Kettleborough CA, Parry MAJ, Keys AJ and Phillips AL (1990) Chimeras of the Rubisco large subunit from wheat and anacystis do not assemble into active enzyme in *Escherichia coli*. *J Exp Bot* 41: 1287–1292
- Kimball BA (1983) Carbon dioxide and agricultural yield - An assemblage and analysis of 430 prior observations. *Agronomy J* 75: 779–788
- Leegood RC (1999) The regulation of C_4 pathway. In: Sage RF and Monson RK (eds) *C_4 Plant Biology*, pp 89–131. Academic Press, San Diego, CA
- Long SP (1985) Leaf gas exchange. In: Barber J and Baker NR (eds) *Photosynthetic Mechanistic Mechanisms and the Environment*, pp 453–500. Elsevier, London
- Long SP (1991) Modification of the response of photosynthetic productivity to rising temperature by atmospheric CO_2 concentrations: Has its importance been underestimated? *Plant Cell Environ* 14: 729–739
- Long SP (1998) Rubisco, the key to improved crop production for a world population of more than eight billion people? In: Waterlow JC and Riley R (eds) *Feeding the World Population-Rank Prize Symposium*, pp 124–136. Oxford University Press, Cary, NC
- Long SP and Bernacchi CJ (2003) Gas exchange measurements, what can they tell us about the underlying limitations to photosynthesis? Procedures and sources of error. *J Exp Bot* 54: 2393–2401
- Long SP, Ainsworth EA, Rogers A and Ort DR (2004) Rising atmospheric carbon dioxide: Plants FACE their future. *Annu Rev Plant Biol* 55: 591–628
- Long SP, Zhu XG, Naidu SL and Ort DR (2006a) Can improvement in photosynthesis increase crop yields? *Plant Cell Environ* 29: 315–330
- Long SP, Ainsworth EA, Leakey ADB, Nosberger J and Ort DR (2006b) Food for thought: Lower-than-expected crop yield stimulation with rising CO_2 concentrations. *Science* 312: 1918–1921

- Madgwick PJ, Parmar S and Parry MAJ (1998) Effect of mutations of residue 340 in the large subunit polypeptide of rubisco from *Anacystis nidulans*. *Eur J Biochem* 253: 476–479
- Norman JM (1980) Interfacing leaf and canopy light interception models. In: Hesketh JD and Jones JW (eds) *Predicting Photosynthesis for Ecosystem Models*, Vol. 2, pp 49–67. CRC Press, Boca Raton, FL
- Ogren WL (1984) Photorespiration, pathway, regulation & modification. *Annu Rev Plant Physiol* 35: 415–442
- Oguchi R, Hikosaka K and Hirose T (2003) Does the photosynthetic light-acclimation need change in leaf anatomy? *Plant Cell Environ* 26: 505–512
- Parry MAJ, Keys AJ and Gutteridge S (1989) Variation in the specificity factor of C₃ higher plant Rubiscos determined by the total consumption of RuBP. *J Exp Bot* 40: 317–320
- Parry MAJ, Andralojc PJ, Mitchell RAC, Madgwick PJ and Keys AJ (2003) Manipulation of Rubisco: The amount, activity, function and regulation. *J Exp Bot* 54: 1321–1333
- Pyke KA and Leech RM (1987) The control of chloroplast number in wheat mesophyll cells. *Planta* 170: 416–420
- Raines CA (2006) Transgenic approaches to manipulate the environmental responses of the C₃ carbon fixation cycle. *Plant Cell Environ* 29: 331–339
- Ramage RT, Read BA and Tabita FR (1998) Alteration of the alpha helix region of cyanobacterial ribulose 1,5-bisphosphate carboxylase/oxygenase to reflect sequences found in high substrate specificity enzymes. *Arch Biochem Biophys* 349: 81–88
- Read BA and Tabita FR (1994) High substrate specificity factor ribulose bisphosphate carboxylase/oxygenase from eukaryotic marine algae and properties of recombinant cyanobacterial rubisco containing “algal” residue modifications. *Arch Biochem Biophys* 312: 210–218
- Romanova AK, Cheng ZQ and McFadden BA (1997) Activity and carboxylation specificity factor of mutant ribulose 1,5-bisphosphate carboxylase/oxygenase from *Anacystis nidulans*. *Biochem Mol Biol Int* 42: 299–307
- Sage RF (1999) Why C₄ photosynthesis? In Sage RF and Monson RK (eds) *C₄ Plant Biology*, pp 3–14. Academic Press, San Diego, CA
- Sage RF (2002) Variation in the k_{cat} of Rubisco in C₃ and C₄ plants and some implications for photosynthetic performance at high and low temperature. *J Exp Bot* 53: 609–620
- Sage RF (2004) The evolution of C-4 photosynthesis. *New Phytol* 161: 341–370
- Seeman JR, Badger MR and Berry JA (1984) Variations in the specificity activity of ribulose-1,5-bisphosphate carboxylase between species utilizing differing photosynthetic pathways. *Plant Physiol* 74: 791–794
- Sims DA and Pearcy RW (1992) Response of leaf anatomy and photosynthetic capacity in *Alocasia-Macrorrhiza* (Araceae) to a transfer from low to high light. *Am J Bot* 79: 449–455
- Somerville CR and Ogren WL (1982) Mutants of the cruciferous plant *Arabidopsis thaliana* lacking glycine decarboxylase activity. *Biochem J* 202: 373–380
- Somerville SC and Somerville CR (1983) Effects of oxygen and carbon dioxide on photorespiratory flux determined from glycine accumulation in a mutant of *Arabidopsis thaliana*. *J Exp Bot* 34: 415–424
- Spreitzer RJ (1999) Questions about the complexity of chloroplast ribulose-1,5-bisphosphate carboxylase/oxygenase. *Photosynth Res* 60: 29–42
- Spreitzer RJ and Salvucci ME (2002) RUBISCO: Structure, regulatory interactions, and possibilities for a better enzyme. *Annu Rev Plant Biol* 53: 449–475
- Spreitzer RJ, Peddi SR and Satagopan S (2005) Phylogenetic engineering at an interface between large and small subunits imparts land-plant kinetic properties to algal Rubisco. *Proc Natl Acad Sci USA* 102: 17225–17230
- Tabita FR (1999) Microbial ribulose 1,5-bisphosphate carboxylase/oxygenase: A different perspective. *Photosynth Res* 60: 1–28
- Tcherkez GGB, Farquhar GD and Andrews TJ (2006) Despite slow catalysis and confused substrate specificity, all ribulose bisphosphate carboxylases may be nearly perfectly optimized. *Proc Natl Acad Sci USA* 103: 7246–7251
- Von Caemmerer S (2000) *Biochemical Models of Leaf Photosynthesis*. CSIRO Publishing, Collingwood, Australia
- Von Caemmerer S and Farquhar GD (1981) Some relationships between the biochemistry of photosynthesis and the gas exchange of leaves. *Planta* 153: 376–387
- Whitney SM and Andrews TJ (2001a) The gene for the ribulose-1,5-bisphosphate carboxylase/oxygenase (Rubisco) small subunit relocated to the plastid genome of tobacco directs the synthesis of small subunits that assemble into Rubisco. *Plant Cell* 13: 193–205
- Whitney SM and Andrews TJ (2001b) Plastome-encoded bacterial ribulose-1,5-bisphosphate carboxylase/oxygenase (RubisCO) supports photosynthesis and growth in tobacco. *Proc Natl Acad Sci USA* 98: 14738–14743
- Whitney SM and Sharwood RE (2007) Linked Rubisco subunits can assemble into functional oligomers without impeding catalytic performance. *J Biol Chem* 282: 3809–3818
- Whitney SM, Baldett P, Hudson GS and Andrews TJ (2001) Form I Rubiscos from non-green algae are expressed abundantly but not assembled in tobacco chloroplasts. *Plant J* 26: 535–547
- Wullschlegel SD (1993) Biochemical limitations to carbon assimilation in C₃ plants - A retrospective analysis of the A/C_i curves from 109 species. *J Exp Bot* 44: 907–920
- Yeoh H-H, Badger MR and Watson L (1981) Variations in kinetic properties of ribulose-1,5-bisphosphate carboxylases among plants. *Plant Physiol* 67: 1151–1155

Zhu X-G, Portis Jr. AR and Long SP (2004a) Would transformation of C₃ crop plants with foreign Rubisco increase productivity? A computational analysis extrapolating from kinetic properties to canopy photosynthesis. *Plant Cell Environ* 27: 155–165

Zhu X-G, Ort DR, Whitmarsh J and Long SP (2004b) The slow reversibility of photosystem II thermal energy dissipation on transfer from high to low light

may cause large losses in carbon gain by crop canopies. A theoretical analysis. *J Exp Bot* 55: 1167–1175

Zhu X-G, de Sturler E and Long SP (2007) Optimizing the distribution of resources between enzymes of carbon metabolism can dramatically increase photosynthetic rate: A numerical simulation using an evolutionary algorithm. *Plant Physiol* 145: 513–526

Chapter 18

Role of Photosynthetic Induction for Daily and Annual Carbon Gains of Leaves and Plant Canopies

Manfred Küppers* and Michael Pfiz

*Institut für Botanik und Botanischer Garten, Universität Hohenheim, Garbenstraße 30,
70599 Stuttgart, Germany*

Summary.....	417
I. Introduction.....	418
II. Representation of Plant Architecture by Digital Reconstruction.....	418
A. Measurements of Plant Segments for Digital Crown Reconstruction.....	419
III. The Dynamic Light Environment.....	419
A. Measurements of Incident Light.....	421
B. Modeling the Light Environment via Hemispherical Photography.....	424
C. Example of the Light Climate from a Tropical Rainforest.....	426
IV. Models of Dynamic Photosynthesis.....	427
A. Physiological Models.....	427
B. Empirical Models.....	427
C. Number of Parameters Required.....	428
V. Calculation of Crown Carbon Acquisition.....	429
A. Steady-state Versus Dynamic Photosynthesis at the Leaf Level.....	429
B. Scaling from Leaf to Crown.....	429
C. Scaling from Day to Year.....	430
VI. Annual Carbon Gains from Steady-state and Dynamic Photosynthesis Simulations.....	431
A. An Indirect Evaluation of the Two Approaches: Carbon Allocation Based on Carbon Gain Either from Steady-state or Dynamic Simulations.....	432
B. The Dynamic Approach Is Plausible.....	434
C. A Biological Application: Relative Allocation Between Leaves, Supportive and Below-ground Plant Parts.....	435
VII. Concluding Remarks.....	436
Acknowledgments.....	436
References.....	436

Summary

Although quite a body of literature exists on carbon gains by plant canopies, the methodology for determination of crown carbon balances of individual plants is very limited. Similarly, little is known about the role of induction for photosynthesis of individual crowns in dynamic light. Therefore, six woody species (pioneers on completely open, mid-successionals on partly closed and late-successionals in the deep shade of a fully closed premontane tropical rainforest) were analyzed in detail concerning daily and annual leaf as well as canopy carbon gains – using, first, a standard steady-state and, second, an

* Author for correspondence, e-mail: kupperts@uni-hohenheim.de

empirical dynamic model of net photosynthesis adequate to handle the effects of lightflecks. For establishing carbon gains of young trees their crown architectures have been monitored over 2 years and precisely reconstructed. Light was monitored above the forest canopy, and, via hemispherical photography, adjusted to each individual plant site. An example is given of necessary steps to calculate crown carbon gain from that of leaf with a steady-state and a dynamic model, results from the two approaches are compared and an example of a biological application is presented. Observed biomass increments of all individuals showed plausible agreement when the dynamic photosynthesis model as carbon input to growth was used. The steady state approach resulted in strong, unrealistic overestimations, ranging from 30% (on open sites) to 650% (in the shaded understorey). We conclude that dynamic photosynthesis models are quantitatively sufficient to determine exact crown carbon gains and to differentiate plant carbon economies of shade tolerant and intolerant species in dynamic light.

I. Introduction

Exact knowledge of carbon gain is needed e.g. to estimate carbon sinks at the plant, stand and landscape level, either in the context of scientific questions or as information in decision making. Nearly all simulations of leaf, crown and stand carbon gain are based on steady-state photosynthesis (Farquhar and Von Caemmerer, 1982; Küppers and Schulze, 1985; Caldwell et al., 1986; Pearcy and Yang, 1996; de Pury and Farquhar, 1997; Niinemets and Tenhunen, 1997). However, evidence increases that steady-state simulations of canopy carbon gain are strongly overestimated if the dynamic time scales of light changes are ignored (Chazdon and Pearcy, 1986; Pfitsch and Pearcy, 1989; Jarvis 1995; Pearcy et al., 1997; Valladares et al., 1997; Yanhong et al., 1997; Stegemann et al., 1999; Naumburg et al., 2001; Naramoto et al., 2001; Timm et al., 2004).

Depending on its exposition in space and its position on the plant every single leaf of a tree crown is differently affected by the environment. For sun leaves in the outer canopy light may be allowing for photosynthesis close to a steady state, but already in a leaf layer 5–20 cm inwards from the canopy surface, light becomes highly dynamic (Percy et al., 1994; Küppers

et al., 1996, 1997). Presumably most leaves, but certainly those completely covered by vegetation, are exposed to dynamic light, mainly generated by shading from upper leaves and their movements in wind (Roden and Pearcy, 1993; Marcolla et al., 2003). Therefore, we are interested how the dynamic changes in leaf photosynthesis are carried over to the whole crown.

Very few studies have tried to address this problem (Percy and Yang, 1996). Timm et al. (2004) performed up-scaling of carbon gain from leaf to crown on tree saplings growing in the understorey of a perhumid tropical forest; here, most environmental factors except light were constant and seasonality was of minor significance, so that up-scaling from daily to annual carbon gain was also possible. This up-scaling required the accurate description of plant architecture and leaf position within the tree crowns, specification of the dynamic light environment for every leaf, the implementation of a dynamic photosynthesis model on the leaf level, and finally, deduction and evaluation of crown carbon gain.

II. Representation of Plant Architecture by Digital Reconstruction

Whenever it is the aim to quantify total plant carbon gain from photosynthesis, description of the crown or canopy arrangement in space is unavoidable (Norman, 1980; Tenhunen et al., 1980; Barnes et al., 1990; Beyschlag et al., 1992; Nobel et al., 1993; Whitehead et al., 2004), up to the counting of leaves in defined sun/shade positions and age classes (Cremer, 1975; Schulze et al., 1977; Pook, 1984; Küppers BIL, 1999).

Abbreviations: $A(I, P)$ – net photosynthetic rate depending on irradiance and induction; $P(I, t)$ – photosynthetic induction depending on irradiance and time; PPFD – photosynthetic photon flux density; R – mitochondrial respiration rate in the light (<0); RuBP – ribulose 1,5-bisphosphate; Rubisco – ribulose 1,5-bisphosphate carboxylase – oxygenase; Φ – maximum quantum yield

Plant architecture can be recorded either by manually measuring size and orientation of plant organs or by various methods of processing two-dimensional images to three-dimensional objects (rev. Godin, 2000). The first approach allows to distinguish age classes (Pook, 1984; Wilson et al., 2001) and accounts for special features e.g. such as feeding damage. The second approach is the practical solution for large canopies (over 100,000 leaves), allowing for the calculation of statistical parameters, such as distribution of leaf size, angle, clustering etc. This information can be used to simulate light distribution within plant stands (e.g. Cescatti, 1997). However, investigations into small canopies allow treating each leaf individually at high accuracy. Therefore, Timm et al. (2004) employed tropical tree saplings – exhibiting a maximum of 200–250 leaves – of which growth and exact leaf exposition were monitored and digitally reconstructed without the need of destructive sampling; their approach, based on Pearcy and Yang (1996), will be in focus here.

A. Measurements of Plant Segments for Digital Crown Reconstruction

The approach of Pearcy and Yang (1996) is very powerful in order to reconstruct small plant individuals. However, it requires numerous measurements on individual segments, such as length, diameter and orientation of axes in space, position of nodes and petioles, size of leaf blades as well as classification of typical leaf shapes (Fig. 18.1), but the resulting digital reconstructions are highly accurate and can hardly be distinguished from photographs (Figs. 18.2 and 18.3). They allow looking at and into crowns from all directions, so that leaf overlapping becomes fully evident (Fig. 18.3). For small individuals repetitive reconstructions allow to monitor growth in terms of architecture, leaf population and biomass. They enable to link leaves with crown and plant carbon gain, furthermore with plant growth and carbon allocation.

Canopies are not static, irrespective of whether plants are deciduous or evergreen (Pook, 1984) and they often undergo astonishingly high changes in leaf area index even in closed evergreen forests (Küppers et al., 2008). Their changes may be environmentally driven or part of

a plant inherent process, or both, such as during rapid growth of shade-intolerant pioneers which frequently shed their leaves once those become shaded (Figs. 18.4 and 18.5). Such processes can be documented applying the procedure of Pearcy and Yang (1996) and Pearcy et al. (2005), and plants can be compared in their development without harvesting.

III. The Dynamic Light Environment

On the way to simulate crown photosynthesis the problem arises of modeling “phylloclimate” (Chelle, 2005) around each leaf. This includes leaf temperature across a leaf blade in patchy light, vapor pressure gradients during fast changes in leaf temperature and, most important, light itself. In the canopy the average steady-state light field can be treated statistically in analogy to the Lambert-Beer’s extinction law – as is the classical approach based on leaf area indices (Monsi and Saeki, 1953; Larcher, 2003; Whitehead and Walcroft, 2005). However, we know that different light dynamics result in different carbon gains and growth rates, although the daily sums of irradiance may be identical (Küppers et al., 1988; Ackerly and Bazzaz, 1995; Leakey et al., 2003).

For studying transient responses of leaf gas exchange to dynamic radiation it is important to define the terms *lightfleck* and *sunfleck*, which are typical for such light. Sunflecks have a spatial and a temporal component. Smith et al. (1989) classify sunflecks in terms of gap geometry, talking about *sun gaps*, where direct sun radiation dominates on clear days, *sun patches*, where a direct beam is at the centre, and *sunflecks* where light is slightly less in the centre than in a full beam and lasts less than one minute. This definition causes problems in practical use, for in a closed understorey much of the time where light is dynamic it may not be from direct beams but from diffuse light (compare Fig. 18.6a with 18.6b). To account for this we prefer the term *lightfleck* which includes all changes in light above certain thresholds irrespective of whether it is direct or diffuse. Unfortunately, these thresholds depend on the decision of the analyzing scientist and cannot be fully objectified, as demonstrated in Fig. 18.7. All these thresholds have to be exceeded simultaneously, only then a change in light is counted as

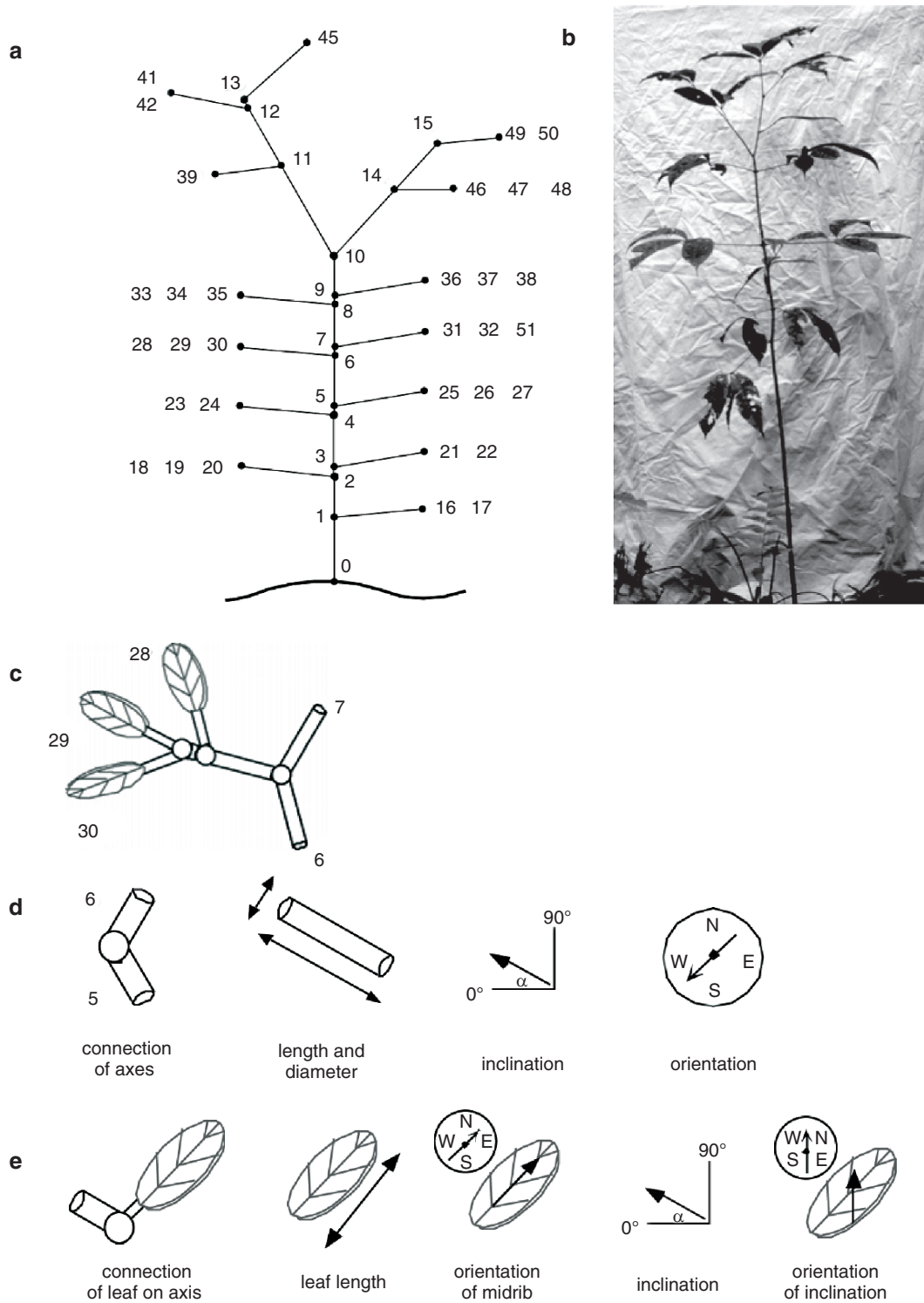


Fig. 18.1. Segmentation of a *Billia colombiana* plant for measurements and reconstruction. (a) Numbering of nodes and leaves; (b) photograph of the plant at its natural site; (c) connections between leaves and axes; (d) measurements made on axes; (e) measurements made on leaves (from Timm et al., 2004)

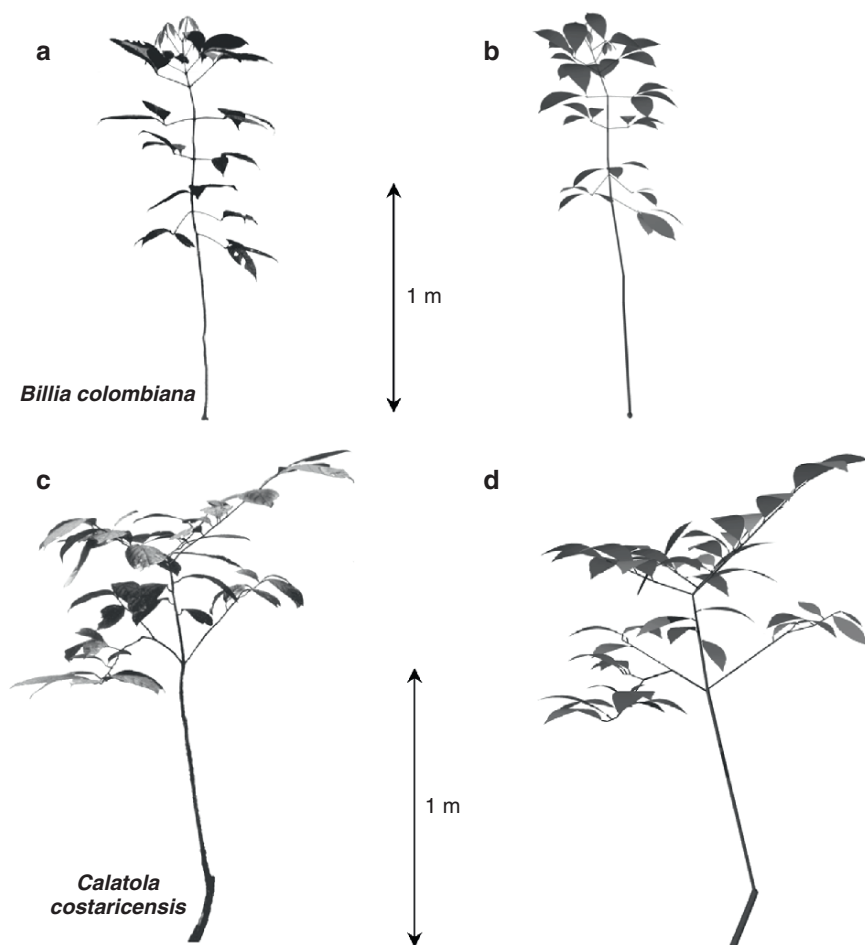


Fig. 18.2. Comparisons of photographs and digitally reconstructed canopies. (a) Photograph of a *Billia colombiana* plant; (b) reconstruction of this plant individual; (c) photograph of a *Calatola costaricensis* plant; (d) reconstruction of this plant individual (from Timm et al., 2004)

a lightfleck: one concerns the step in irradiance both in absolute terms and relative to the background of dim light (Fig. 18.7a), another the rate of change in light during increase and decrease (Fig. 18.7b) and a third the duration of the high light event (Fig. 18.7c; for details see Stegmann 1999, pp 28–29). Applying these steps the number of lightflecks could be determined for the daily light courses in Fig. 18.6.

Exact, detailed description of the dynamic light environment is presumably the most challenging task in the calculations of crown photosynthesis. There are two basic ways to obtain the necessary information: either to continuously measure incident light for representative leaves, or to model radiation three-dimensionally in a time scale of seconds to minutes. Nevertheless, both methods

distinguish lightflecks from diffuse background radiation, and they can be combined to reduce technical and simulation efforts.

A. Measurements of Incident Light

Lightflecks can be tiny and may generate significant light heterogeneity even across a single leaf. Therefore, it may be necessary to have several light sensors installed on one leaf. For example, Küppers et al. (1997) and Chelle (2005) attached light sensors directly to leaf blades. In these measurements special care was taken on low-weight and flexible wiring. Carefully and adequately installed sensors can record changes in light even in response to small changes in leaf orientation

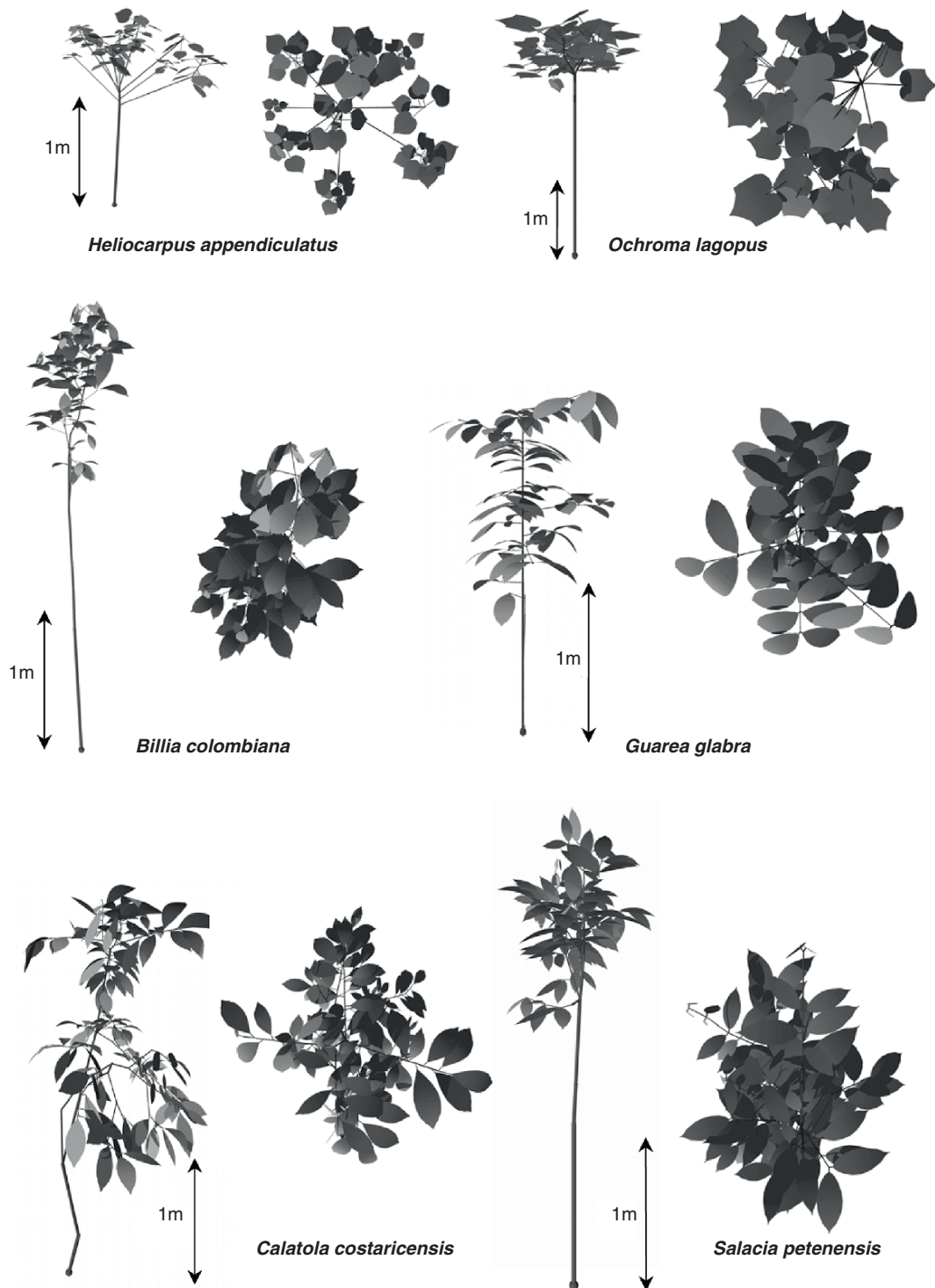


Fig. 18.3. View at digitally reconstructed crowns of different species from side and from above, leaf overlapping is clearly evident (from Stegemann, 1999; Timm et al., 2004)

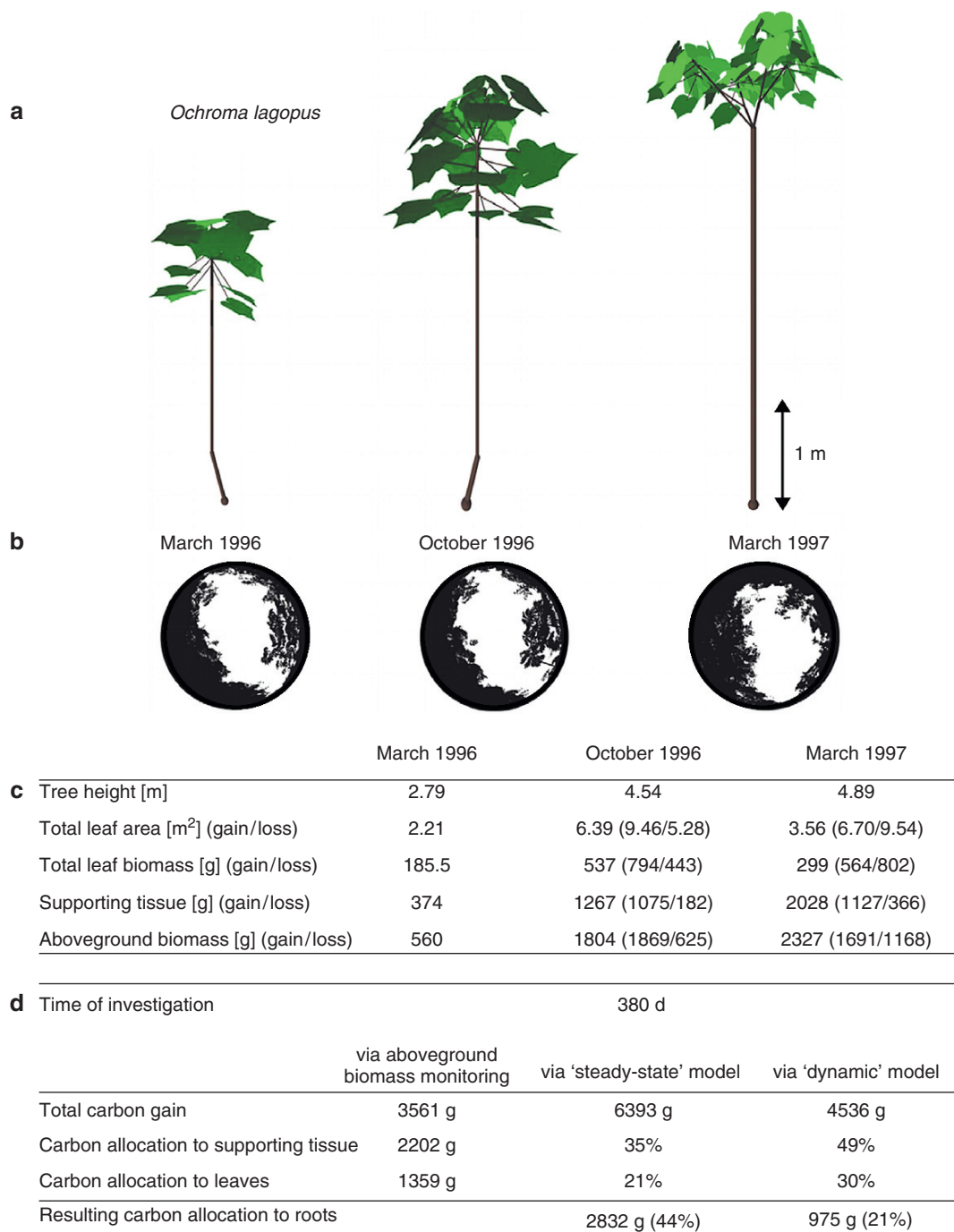


Fig. 18.4. Development of an individual of the shade-intolerant pioneer *Ochroma lagopus* from an open site and deduction of its annual carbon allocation. Light green leaf area: sun exposed, dark green: (self-)shaded (from Timm et al., 2004). **(a)** Above-ground architectural development as reconstructed via the method described in Fig. 18.1; **(b)** change in the individual's light environment as indicated by hemispherical photography immediately above its uppermost leaves; **(c)** growth and biomass parameters of the respective individual; **(d)** deduction of annual assimilate flux balances (carbon allocation) as percentage of total annual crown carbon gain, either via a steady-state or a dynamic photosynthesis model. Carbon gain and allocation of biomass are given in equivalents of dry matter (CH₂O)_n. See also Color Plates, Fig. 2

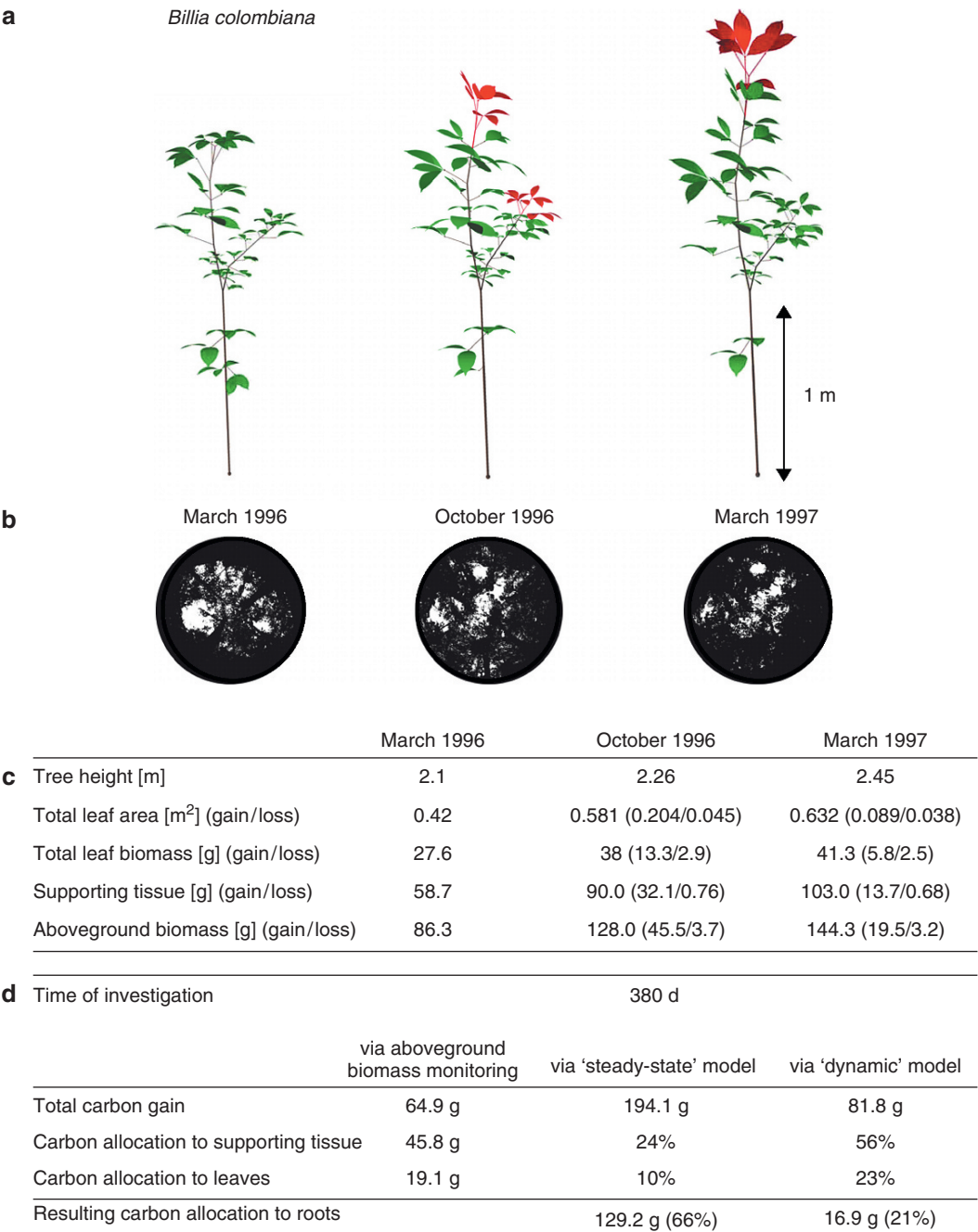


Fig. 18.5. The same as Fig. 18.4, but for an individual of the mid- to late-successional shade-tolerant *Billia colombiana* below a closed canopy. Red leaf area: newly developed (from Timm et al., 2004). See also Color Plates, Fig. 3

caused by wind or rain. However, technology for such installations has not yet become commercially available, probably because maintenance costs are high and shading of leaves by sensors might decrease carbon assimilation.

B. Modeling the Light Environment via Hemispherical Photography

When light environments have to be compared across the crowns of several plant individuals it is

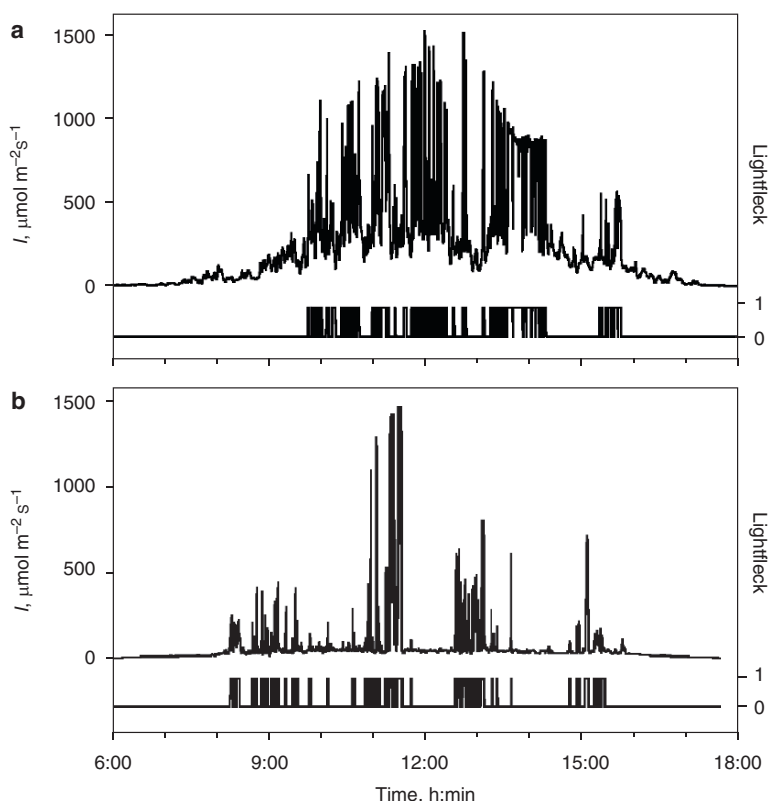


Fig. 18.6. Diurnal course of photosynthetic active radiation (I_i , $\mu\text{mol quanta m}^{-2} \text{s}^{-1}$, upper curve) at a recently closed gap above a plant's crown. Lightfleck events are indicated in the lower part of the graph. Site: Costa Rica, pre-montane rain forest; (a) upper canopy, number of lightflecks 87 (calculation see Fig. 18.7); (b) closed understorey, number of lightflecks 82, but of much lower step size compared to (a) (from Stegemann, 1999)

practically impossible to position vast amounts of light sensors in each crown. In order to get around these technical problems, mathematical modeling (simulation) can be combined with hemispherical photography and the employment of a few light sensors. Hemispherical photography characterizes the static light distribution (Anderson, 1964; Rich, 1990; Cescatti, 2007) for it takes into account, first, the geographic position of the plant to calculate the daily solar tracks and, second, the shape of gaps above individual crowns or leaves. Light sensors measure the dynamics in light in the crowns as well as effects of cloud cover above the canopy. Moreover, the combined approach can now be linked with models of plant architecture (Fig. 18.8) so that finally daily courses of

dynamic light can be simulated for each leaf in an individual's crown. However, the exact temporal simulation of lightflecks and dim light phases still remain problematic (Marquardt, 1999).

Stegemann (1999, pp 48–52) and Timm et al. (2004) performed the following steps to model dynamic light in addition to direct measurements. (1) Diurnal courses of incident light were recorded in 1-min steps above the forest canopy over 2 years; (2) light was measured in the forest canopy just above an individual plant's uppermost leaves; (3) for all plant crowns light penetration and absorption was deduced with respect to temporal courses and daily amounts (Percy and Yang, 1996). From the last step net photosynthesis could be calculated.

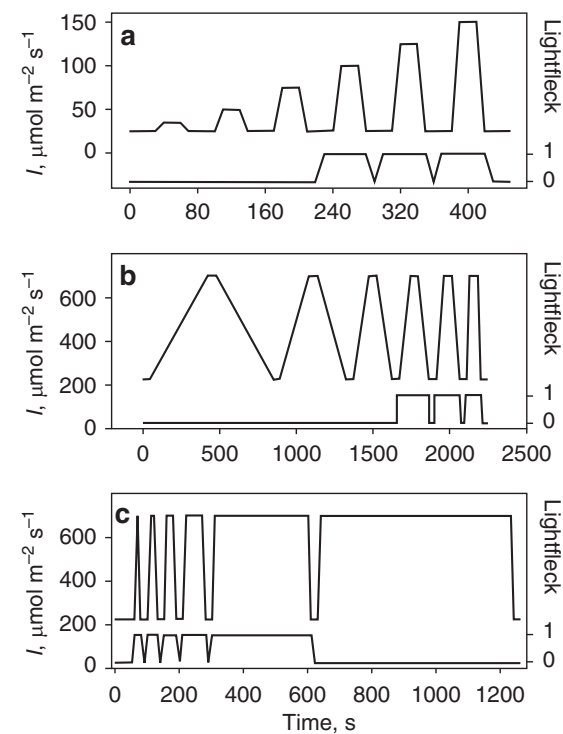


Fig. 18.7. Recognizing and counting of lightflecks and the effects of thresholds: the upper part of respective graph indicates a schematic time course of light, lower part the counting of lightflecks: (a) threshold of “step in irradiance”, (b) threshold of “rate of change”, (c) threshold of “duration of high light event” (modified after Stegemann, 1999)

C. Example of the Light Climate from a Tropical Rainforest

According to Baldocchi and Collineau (1994) tropical rainforests show severe light gradients in their upper layers, where already 60% of the incoming light is absorbed. These forests can support twice as much leaf area as temperate forests because high sun angles and tree crown shapes allow enough sunflecks to penetrate gaps and to support multiple storied canopies. Thus, they are ideal to demonstrate the importance of dynamic light for actual carbon gains.

Figure 18.6 shows typical daily courses of light for the same sunny day, one in a closing gap, the other in the closed understorey of a mature forest canopy. Dim light backgrounds differ strongly, amounting about $200 \mu\text{mol quanta m}^{-2} \text{s}^{-1}$ in the first (Fig. 18.6a) and about $20 \mu\text{mol quanta m}^{-2} \text{s}^{-1}$ in the second (Fig. 18.6b), but they are in both cases frequently interrupted by lightflecks. In the understorey most lightfleck peaks do not reach maximum possible values, since in some cases they are generated by strong changes in diffuse rather than direct radiation. The number of lightflecks is higher in the closing gap indicating very high light dynamics all over the day. In the tropical understorey most lightflecks are short in time (one third are shorter than 2 s) and exhibit relatively low peaks (Fig. 18.6). However,

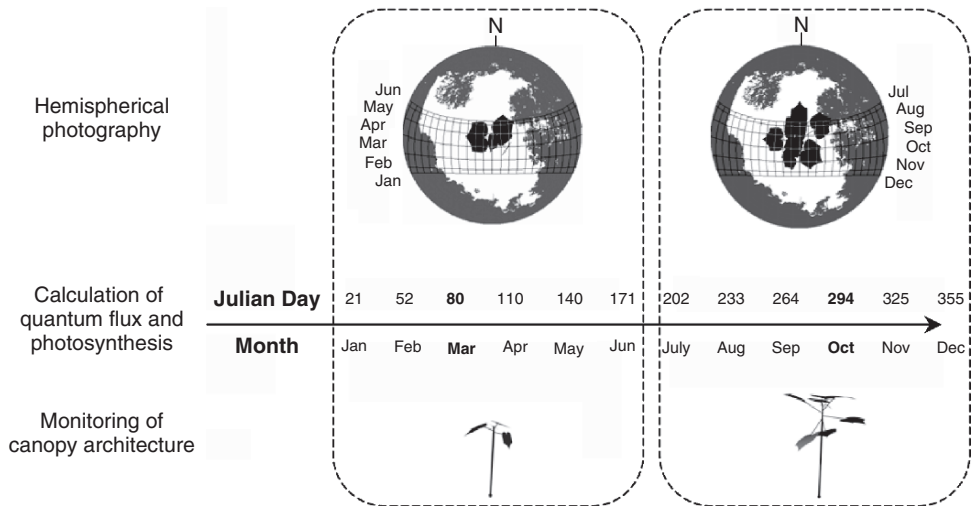


Fig. 18.8. Determination of daily and annual incident radiation at a particular plant site and in relation to an individual’s architecture. On the bold-faced Julian days, plant architecture and hemispherical photographs were updated in the calculations for the period within the dotted frame (from Timm et al., 2004)

according to Pearcy et al. (1994) and Küppers et al. (1996) most daylight is contributed by rare lightflecks of very high peaks (Fig. 18.6a), lasting about 1–5 min. This is in the time scale where photosynthetic induction becomes strongly affected.

IV. Models of Dynamic Photosynthesis

Physiological models of leaf gas exchange appear to be an easy solution to estimate crown photosynthesis. These models transfer knowledge from laboratory research to field ecology, providing causality for the observations and refining sub-models of various aspects. However, these models require deeper species-specific knowledge of leaf properties concerning e.g. anatomical arrangement and adaptation of chloroplasts (Terashima et al., 1988), the underlying biochemistry and diffusion processes (Section A below), and they may demand for special experiments in order to obtain the parameters needed. Empirical models greatly avoid this, and for a low number of factors they can be easily parameterized even under field conditions. Such models have reasonable predictive power, allowing also for comparative studies. But this is bought dearly by low expandability and low or no analytical power concerning the underlying processes, so that every further factor considered may exponentially increase the number of required measurements.

Biochemical models are ample (Part IV, Chapter 9 of this book), and over the past decades their quality of predictions has much improved, although they may be based only on crude mathematical descriptions of key biochemical processes (Kirschbaum et al., 1988, 1998; Gross et al., 1991; Pearcy et al., 1997). However, for intensive use in the field their parameterization is still problematic for they need a high number of biochemical and gas exchange analyses.

A. Physiological Models

In the physiological context, the interface between leaf environment and photosynthesis is controlled by light activation of the different stages of CO₂-assimilation. Pearcy et al. (1997) considered light activation of Rubisco and RuBP regeneration in variable light as main components transiently limiting carbon fixation under ambi-

ent conditions – even more important than stomatal limitations (Kirschbaum and Pearcy, 1988a; Allen and Pearcy, 2000; Tang and Liang, 2000; Portes et al., 2006). Pearcy et al. (1997) connected the appropriate carbon pools with the activities of Rubisco and RuBP regeneration chain, carbon supply to the Calvin-Benson cycle being determined by light-dependent stomatal conductance (Gross et al., 1991; Kirschbaum et al., 1998). Their model is of high power for the analysis and prediction of leaf gas exchange, metabolite pools, stomatal movements, effects of photorespiration, oxygen release and consumption, overall (Rubisco and RuBP-regeneration) induction states and the effects of light- and “darkflecks” on carbon gain (Kirschbaum et al., 1998). However, for the process of up-scaling from leaf to canopy this model is unnecessarily complicated, as this was not the original intention it was developed for. Other, even more biochemically oriented models, run into the same disadvantage.

B. Empirical Models

Therefore, a simpler empirical model was developed by Stegemann et al. (1999) taking account of changes in induction states of photosynthesis. In this context *induction* P does neither refer to the physiological induction process in the mesophyll nor to stomatal effects separately, but to the overall relative induction *state* ($0 \leq P \leq 1$). Stomatal responses are assumed (and have indeed been found) small and/or sufficiently synchronized with the photosynthetic apparatus so that their contribution on P is of minor significance (Valladares et al., 1997; Allen and Pearcy, 2000; Tang and Liang, 2000). The model consists of two sections; in one of them photosynthetic induction $P(I, t)$ is described as a function of light at the leaf's location and of time, in the other net photosynthesis A is determined from incident photon irradiance I as an instantaneous response, considering the momentary induction state, $P(I, t)$. This photosynthetic induction is mainly determined by the so-called “slow phase induction” (e.g. Rubisco activation, Kirschbaum and Pearcy, 1988b; Pearcy et al., 1994) and here defined as

$$P(I, t) = \frac{A_{\max}(P) - R}{A_{\max}(P_{\max}) - R}, \quad (18.1)$$

where $A_{\max}(P)$ refers to the light saturated net photosynthesis at a given induction ($P < 1$), and $A_{\max}(P_{\max})$ to the maximum (light saturated) net photosynthesis at full induction $P_{\max} = 1$. $A_{\max}(P_{\max})$ is the true “photosynthetic capacity” in the steady state at ambient CO_2 -concentration. To calculate CO_2 -assimilation close to “gross” photosynthesis (but neglecting photorespiration), mitochondrial respiration rate in the light ($R < 0$) is set constant. In this definition it is inherently assumed that the ratio of carboxylation to oxygenation of Rubisco is constant at all irradiances.

The logical sequence is the following: an “instantaneous” light response curve is defined as

$$A(I, P) = R + P(I, t)$$

$$[A_{\max}(P_{\max}) - R](1 - e^{-\phi I}) \quad (18.2)$$

neither including dynamic changes in the pools of intermediates nor the slower regulatory changes from enzyme activation. The light response is approximated by an exponential expression with the constant ϕ defining the maximum quantum yield, while the maximum rate is $A_{\max}(P_{\max}) - R$. However, this steady-state light response is modified according to the present induction state ($0 \leq P(I, t) \leq 1$), depending on time t and light intensity I , proportionally influencing the whole light response curve.

The time course of induction $P(I, t)$ is solved by integrating the differential equation

$$\frac{dP(I, t)}{dt} = \kappa [P_{\text{eq}}(I) - P(I, t)], \quad (18.3)$$

stating that at any light intensity I the induction state exponentially approaches a light-dependent “equilibrium” value $P_{\text{eq}}(I)$ with a rate constant κ . This equilibrium $P_{\text{eq}}(I)$ is assumed to be also exponentially dependent on light intensity (Fig. 18.9a),

$$P_{\text{eq}}(I) = 1 - e^{-\omega I}. \quad (18.4)$$

Substituting Eq. (18.4) into Eq. (18.3) we obtain the differential equation numerically integrated to find $P(I, t)$ at any t and I values:

$$\Delta P = \kappa[(1 - e^{-\omega I}) - P(I, t)]\Delta t. \quad (18.5)$$

This integrated $P(I, t)$ is used to calibrate the light response curve of Eq. (18.2).

In the canopy, for the same photon irradiance, a leaf exhibits different rates of net photo-

synthesis depending on its induction state. Eq. (18.2) inherently describes a variable light compensation point as well as a variable quantum yield in the linear part of the response curve (Fig. 18.9b). Recent studies have shown that generally this is in accordance with observations (Timm et al., 2002), however, in experiments with complete darkness the key enzymes of the Calvin-Benson cycle lose activity almost completely (Kirschbaum et al., 2004, 2005), while in the natural situation of the understorey there is still sufficient light ($> 5 \mu\text{mol quanta m}^{-2} \text{s}^{-1}$) to maintain the activity high enough for a full quantum yield at low light. Potentially this model could be extended to take into account these recent observations of Kirschbaum et al. by introducing a variable factor ϕ depending on induction. Their findings demonstrate the need for the definition of $P(I, t)$ as given in Eq. (18.1) using the light saturated net photosynthesis in all cases rather than actual net photosynthesis, since at low light in the so-called “quantum yield region” the same $A(I, P)$ can be observed despite different momentary induction $P(I, t)$.

The model simulates dynamic leaf gas exchange at a reasonable accuracy despite an uncertainty in physiology; it was tested against direct measurements under identical light dynamics in the laboratory, in the field at open sites (canopy gaps) and in the deeply shaded understorey using fast responding leaf gas exchange systems (Stegemann, 1999; Stegemann et al., 1999; Timm et al., 2002).

C. Number of Parameters Required

Comparing the number of parameters required to run a biochemical (29 input parameters, Kirschbaum et al., 1998) and an empirical model of dynamic photosynthesis (six input parameters, Stegemann et al., 1999) the latter has advantages, however, at the cost of loss of information on the biochemical processes involved. For both approaches it is essential to distinguish parameters varying within a crown (e.g. accounting for sun/shade acclimation) and others that are sufficiently constant among different leaves. The simpler empirical model still provides high accuracy, saving the time of calculations and for determining parameters; therefore, further steps in Section V are based on the empirical model.

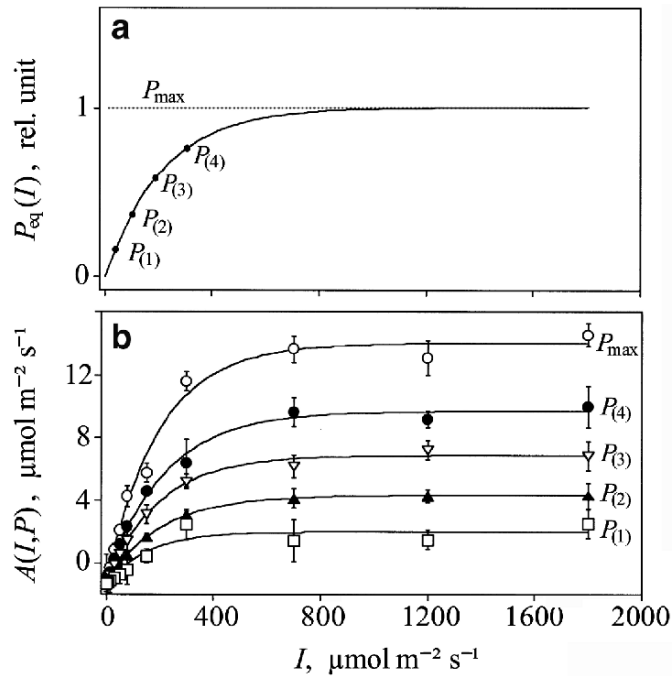


Fig. 18.9. Schematic light response curves of (a) equilibrium induction $P_{eq}(I)$ to a constant incident irradiance (I) as given by Eq. (18.4); (b) measured (data points) and calculated (lines) “quasi steady state” light response curves of net photosynthesis $A(I, P)$ as dependent on different levels of induction $P_{eq}(I)$ (from Stegmann et al., 1999)

V. Calculation of Crown Carbon Acquisition

A. Steady-state Versus Dynamic Photosynthesis at the Leaf Level

It is well established that steady state models neglecting changes in photosynthetic induction overestimate leaf carbon gain. Percy et al. (1994) and Schulte et al. (2003) observed an overestimation of 20–30%. Figure 18.10 gives an example of true and modeled carbon gains using either a steady-state photosynthesis approach (Fig. 18.10b) or the above described empirical dynamic model (Fig. 18.10c). As long as induction is high (Fig. 18.10d) simulated as well as measured photosynthesis responses agree well in both approaches (in the example at the beginning of the time course). Induction declines as soon as low light interrupts the initial high light phase, so that for the steady-state approach measured and modeled responses diverge (middle of time course). The difference is at maximum at the lowest induction.

Figure 18.11 shows how the deviation between simulated and measured carbon gain increases the more the assumption of full induction becomes deficient (up to 60%, in the extreme up to 180%). Then the steady-state approach runs into a systematic error (Fig. 18.11d–f) while the error for the dynamic model remains small and at random at all observed induction states (Fig. 18.11a–c). In natural dynamic light regimes (e.g. Fig. 18.6) induction rarely exceeds 80%, frequently (in dim light phases) it falls to 40% or lower. Percy et al. (1994) give similar values for Rubisco induction.

B. Scaling from Leaf to Crown

Direct measurements of crown carbon gain are difficult to perform because canopy chambers are costly and unavoidably generate their inherent “glass-house effects”, such as higher air humidity, elevated temperature and strong ventilation (Gold and Caldwell, 1990; Medhurst et al., 2006). Since such measurements are almost impossible to do simultaneously for several individual

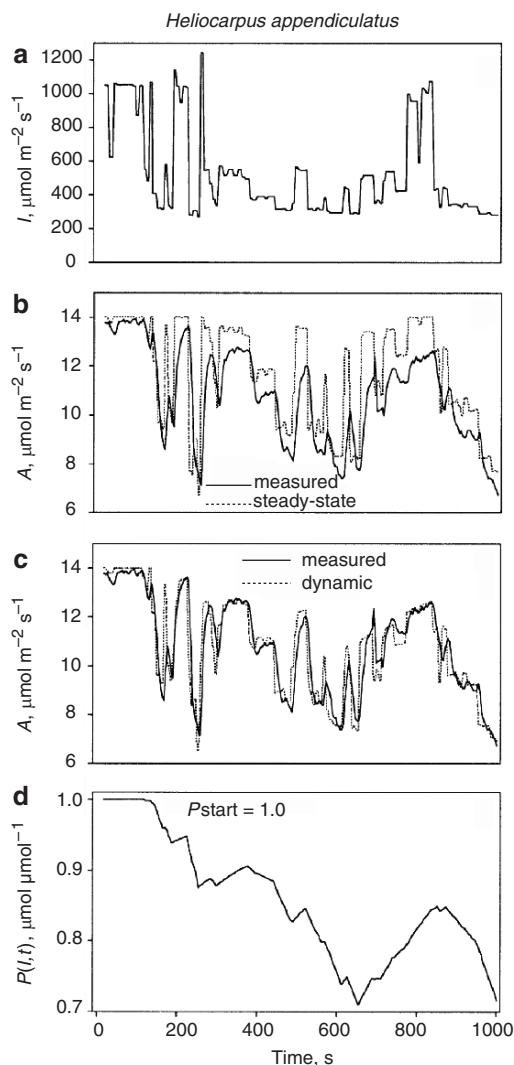


Fig. 18.10. Comparison of the response of net photosynthesis (A) for a given time course of dynamic light (I , panel a), either modeled via a steady state approach (b) or the dynamic approach (c) Photosynthetic induction calculated via the dynamic model is presented in (d) (from Stegemann et al., 1999)

plants, simulation models of net photosynthesis have been frequently applied, integrating the carbon gain from leaf to plant (Norman, 1980; Tenhunen et al., 1980; Caldwell et al., 1986; Beyschlag et al., 1992; Leuning et al., 1995; Whitehead et al., 2004). The models, however, have been tested in environments where induction processes did not play a major role, or where “mean” light response curves of net photosynthesis – inherently containing changes in induction –

have been derived from measured diurnal courses of leaf gas exchange.

Here, in order to scale from leaf to crown, the following steps were performed for each individual leaf of 28 plants (Timm, 1999; Timm et al., 2004). (1) To account for changes in cloud cover diurnal courses of incident light were recorded above the forest canopy in one-second steps; (2) light below the forest canopy, just above an individual plant’s uppermost leaves was also recorded; (3) temporal courses and daily integrals of light penetrating into crowns were deduced for each plant following the approach described in Section III.B; (4) the plant’s architecture was subsequently entered into the routine “Y-Plant” (Percy and Yang, 1996) to yield diurnal courses of light for each of its leaves; (5) the latter information was then used to simulate net photosynthesis on the leaf level according to Section IV.B; (6) up-scaling to the crown was performed by summing up the carbon gains over all individual leaves in the crown (Fig. 18.12).

C. Scaling from Day to Year

In the classic approaches leaf gas exchange was monitored over extended periods (Schulze, 1970; Mooney, 1972; Küstle und Mitscherlich, 1975; Fuchs et al., 1977; Linder and Lohammar, 1981; Küppers, 1984; Caldwell et al., 1986; Matyssek and Schulze, 1987; Oren and Zimmermann, 1989; Kellomäki and Wang, 1997; Küppers, 1999; Körner et al., 2005; Medhurst et al., 2006), so that scaling from day to year could be performed by summing up all daily carbon balances. These approaches were expensive and required technical maintenance of equipment all year round.

It is similarly difficult to simulate net photosynthesis for every day and each leaf even in small plant crowns. Assume a plant with 150 leaves in its crown; this would afford $150 \times 365 = 54,750$ runs, and for a total of 28 plants about 1.5 million simulations! In order to reduce this effort, Timm et al. (2004) simulated net photosynthesis for typical weather conditions. They categorized cloudy days (average PPFD $< 15 \text{ mol photons m}^{-2} \text{ day}^{-1}$), days of variable cloudiness ($15\text{--}30 \text{ mol photons m}^{-2} \text{ day}^{-1}$) and sunny days ($> 30 \text{ mol photons m}^{-2} \text{ day}^{-1}$) from all year

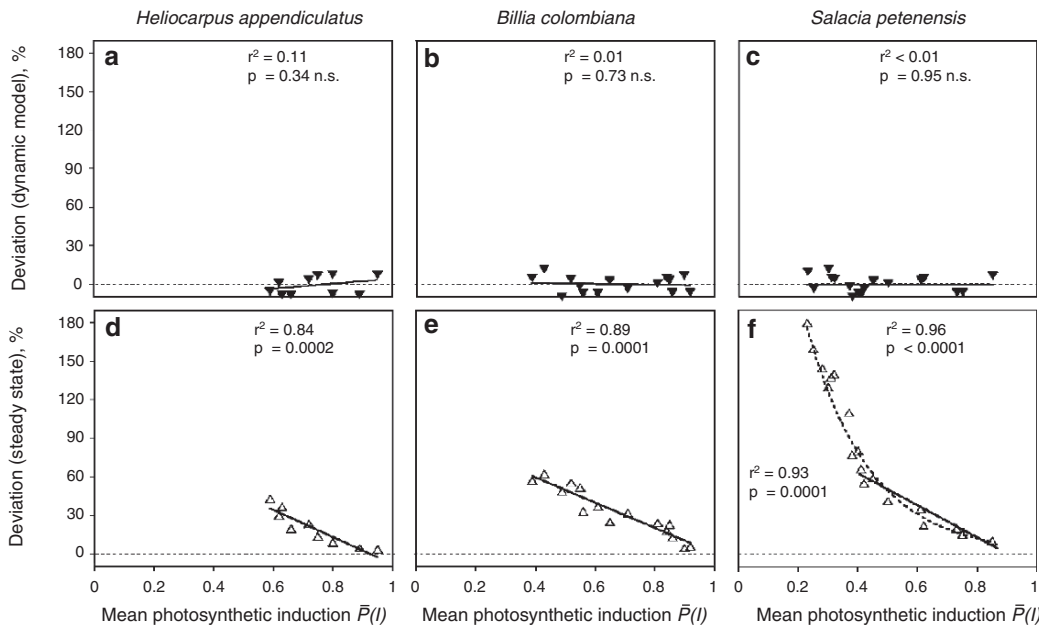


Fig. 18.11. Deviations of modeled from measured total carbon gains (at leaf level) as a function of mean photosynthetic induction $\bar{P}(I, t)$ either for the dynamic photosynthesis model (a–c) or the steady state model (d–f). Mean photosynthetic induction $\bar{P}(I, t)$ is calculated over time spans similar to Fig. 18.10. (a) and (d) for an open gap site, (b) and (e) from a recently closed gap in mid succession, (c) and (f) from the understorey of a closed forest (from Stegemann, 1999)

round monitoring of light. In order to scale up to annual carbon gains, diurnal simulations were run once a month for these three typical weather conditions, taking half-annual changes in plant architecture into account (Figs. 18.4, 18.5 and 18.8). Total daily carbon gains were weighted with respect to frequency of weather conditions (here 58.9% cloudy, 35.6% variable, 5.5% sunny). Crown respiration at night was calculated via total leaf area, a measured mean leaf respiration rate and the length of the nightly dark period.

VI. Annual Carbon Gains from Steady-state and Dynamic Photosynthesis Simulations

To our knowledge no other study has been published – except Timm et al. (2004) – in which the outcomes of simulations of *annual* crown carbon gains are compared for steady-state and dynamic models. The two different approaches are summarized in the flow chart of Fig. 18.13. For comparison, a factor f (≤ 1) was calculated as the quotient between annual crown carbon gains

from the dynamic approach divided by the gain from steady-state approach (for identical light conditions and identical plant architectures).

In order to illustrate the effects of the two approaches we choose the example of a neotropical mountane forest in Costa Rica as published by Stegemann et al. (1999) and Timm et al. (2004). Here the shade intolerant pioneers *Heliocarpus appendiculatus* and *Ochroma lagopus* were examined in the open or in wide gaps (Fig. 18.4), the mid-successional species *Guarea glabra* and *Billia colombiana* in intermediate shade situations of recently closed gaps full of lightflecks (Fig. 18.5 and 18.6a) and the shade-tolerant, late successional species *Calatola costaricensis* and *Salacia petenensis* in the deeply shaded understorey of a closed, mature canopy (Fig. 18.6b). Large deviations in annual crown carbon gains were found. In case of the pioneer *Ochroma* (Fig. 18.4) in a wide gap the overestimation amounted 30–41% ($f = 0.70 - 0.73$), whereas in the late-successional species it rose up to 103–258% ($f = 0.28 - 0.49$). In the mid-successional situation just after gap closure the highest light dynamics could be observed as

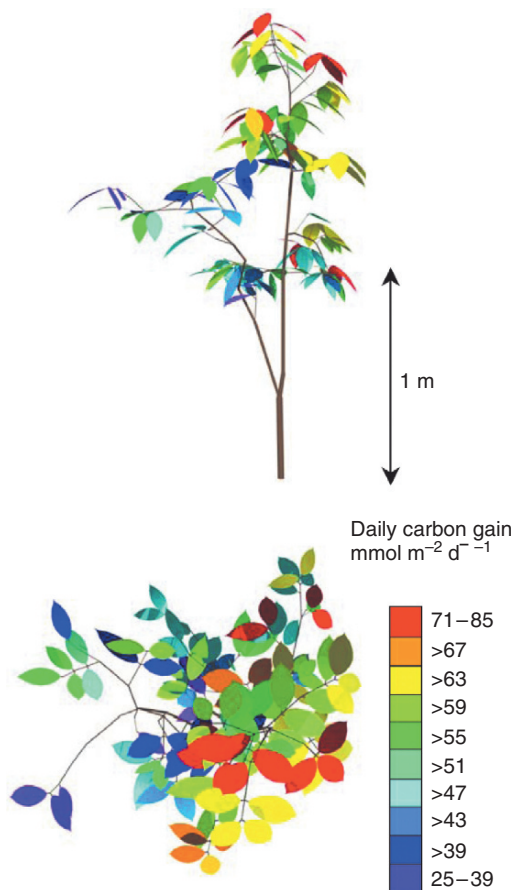


Fig. 18.12. Daily carbon balance of each individual leaf in the crown of a *Salacia petenensis* plant. Crown carbon gain was determined by summing up the individual balances. In the mean over 380 days carbon gain amounted to 426 mg day^{-1} (from Timm et al., 2004). See also Color Plates, Fig. 4

indicated by the highest percentage of time where light was irradiated in lightflecks (Table 18.1). This resulted in the strongest overestimation by the steady state model, amounting 653% (*Guarea*, $f = 0.13$). The smaller deviations at the gap sites are simply a consequence of the generally higher light levels, allowing for generally higher photosynthetic induction (Table 18.1, Fig. 18.14a). Indeed, the site- and species-specific mean f and the percentage of lightflecks of the selected day, taken as a measure of light dynamics, are linearly correlated (Fig. 18.14b; $p = 0.014$, $r^2 = 0.813$).

A. An Indirect Evaluation of the Two Approaches: Carbon Allocation Based on Carbon Gain either from Steady-state or Dynamic Simulations

Direct testing of the two modeling approaches would require all year round monitoring of total crown carbon gains on many individuals, which is only possible at major efforts in equipment and manpower. However, linking modeled crown carbon gains with real plant growth allows for an indirect test of plausibility of the two approaches. This can be achieved from measurements on an individual's total annual dry matter increment above ground and balancing it with the amount of available carbohydrates acquired from (modeled) crown photosynthesis.

The above-ground dry matter increment in stem, twigs and leaf material of an individual plant must be balanced by crown carbon gain in order to allow for growth over extended periods. Calculating the amount of CO_2 which must be assimilated to match the respective dry matter increment of an organ or plant part gives the fraction of total annual carbon gain allocated to that organ. Summing up over all above-ground increments in dry matter (e.g. from reconstruction of crowns, Figs. 18.4 and 18.5) leaves a certain amount of carbon gain available for below-ground allocation to root growth, root respiration and exudation (Linder and Axelsson, 1982; Küppers, 1982, 1985; Matyssek, 1985; Oren and Zimmermann, 1989). Here a plausibility check can be done.

For this, daily net carbon gain is converted into dry matter according to Küppers (1982), Larcher (2003) and Timm et al. (2004). In the first example (Fig. 18.4c, d) an individual of the pioneer *Ochroma* ($f = 0.71$, see section above) invested the total of $1,869 + 1,691 = 3,561 \text{ g}$ into its biomass. Both modeling approaches match these requirements, for resulting total carbon gains amounted to $6,393 \text{ g}$ (steady-state) or $4,536 \text{ g}$ (dynamic) and are larger than the observed above-ground biomass increments. From this an allocation to the root of $(6,393 - 3,561)100/6,393 = 44\%$ results for the steady-state and 21% for the dynamic model, respectively. In the second example from a mid-successional gap situation (*Billia*, Fig. 18.5d), modeled crown carbon gains differed much more

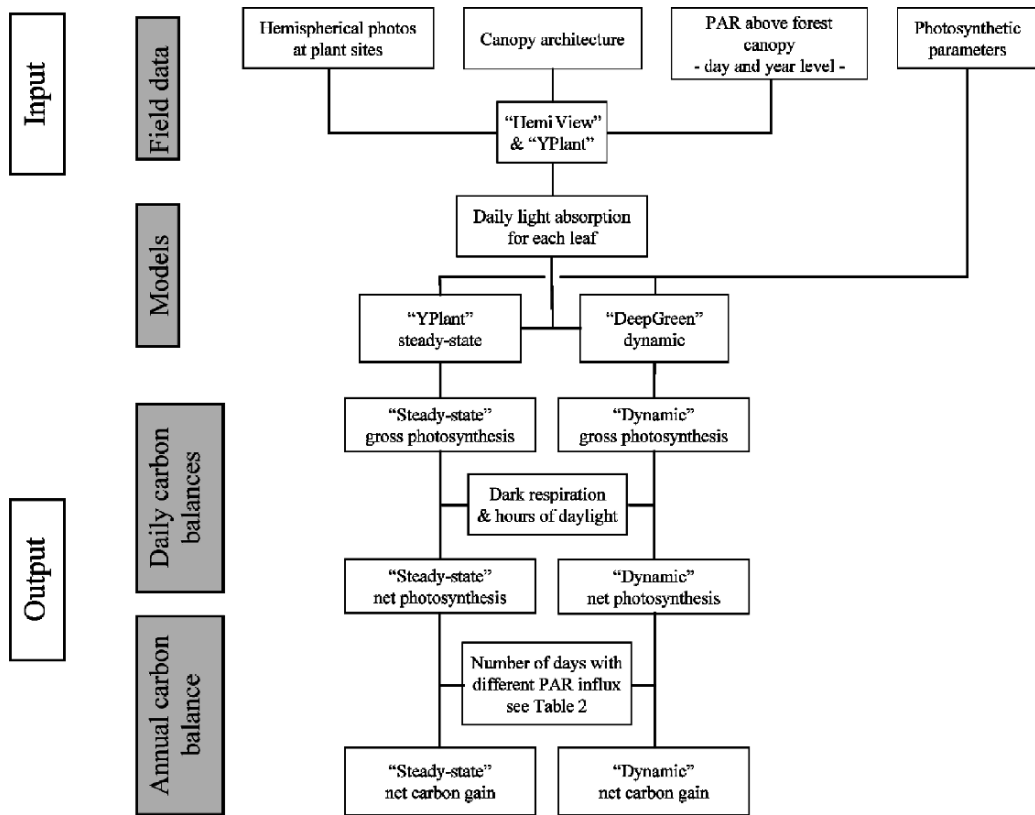


Fig. 18.13. Flow chart for the determination of annual crown carbon gain of each individual plant, either via a steady state or a dynamic photosynthesis model (“Y-Plant” after Percy and Yang, 1996; “HemiView” after Rich, 1990; “DeepGreen” from Stegemann et al., 1999). In both approaches crown architecture and light are identical

Table 18.1. Comparison of modeled annual carbon balances via the steady-state and the dynamic approach results a factor f (for definition see text). Especially for the mid-successional trees the overestimation by the first approach is large (very small f). Obviously, dynamics of light (here indicated as percentage of light in lightflecks) rather than absolute amounts of radiation are related to f , whereas other photosynthetic characteristics (light compensation point, photosynthetic capacity) clearly depend on the amount of light (not shown) (Timm et al., 2004)

	Gap		Mid-successional		Late-successional	
	<i>Heliocarpus appendiculatus</i> (n = 5)	<i>Ochroma lagopus</i> (n = 5)	<i>Guarea glabra</i> (n = 3)	<i>Billia colombiana</i> (n = 5)	<i>Calatola costaricensis</i> (n = 5)	<i>Salacia petenensis</i> (n = 5)
PAR in lightflecks (<5 min) on a sunny day (% of time in daylight)	19	15	78	73	62	67
Mean annual crown induction P_{crown}	0.64 ± 0.04	0.50 ± 0.05	0.37 ± 0.02	0.48 ± 0.06	0.47 ± 0.06	0.41 ± 0.03
f = annual carbon gain, dynamic/steady state	$0.50 - 0.62$	$0.70 - 0.73$	$0.13 - 0.25$	$0.37 - 0.42$	$0.36 - 0.38$	$0.28 - 0.49$

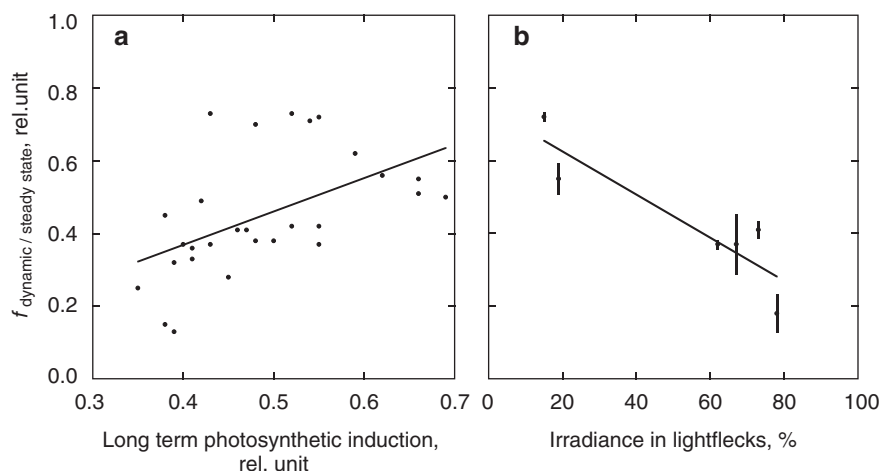


Fig. 18.14. Factor f (the quotient between annual crown carbon gains from the dynamic approach divided by the result of the steady-state approach) as a function of mean annual crown induction for each plant individual from the series in Table 18.1 (a) and as a function of the percentage of lightflecks on a sunny day (b) (calculated from data of Stegemann, 1999)

(in relative terms; $f = 0.42$) between steady-state and dynamic approach. This resulted a root allocation of 66% (steady-state) and 21% (dynamic), respectively. This way the allocation was determined for all 28 investigated individual plants (Table 18.2).

For carbon investment into roots, the allocation percentages obtained from the steady-state approach give a range of 44–90% and are – without exception – much higher than the same allocation percentages obtained from the dynamic model (7–43%; Table 18.2). Difference between the two approaches is the more pronounced the lower the mean induction state of photosynthesis (e.g. *Guarea* and *Salacia*, Table 18.1 and Fig. 18.14a).

B. The Dynamic Approach Is Plausible

The question arises, which of the given ranges are more reliable. One direct indication comes from leaf gas exchange measurements, where the steady-state approach resulted in a clear overestimation of carbon gain (Fig. 18.10; Percy et al., 1994). Another comes from the knowledge on root/shoot ratios: saplings and young trees generally exhibit root/shoot dry matter ratios around 0.25/0.75 (Chalmers and Van den Ende, 1975; Wartinger et al., 1990; Schulze, 1994; Heilmeyer et al., 1997) with a declining (but not increasing!) value with plant age when more and more carbon becomes accumulated in the stem (Givnish, 1988).

In the shade environment (e.g. that of *Guarea*, *Billia*, *Calatola* and *Salacia*), this ratio is known to become even lower (Givnish, 1988; Olff et al., 1990; Bazzaz and Grace, 1997; Lei and Lechowicz, 1998). However, since nearly all of the partitioning studies looked into standing crop dry matter allocation rather than into the true allocational investments via assimilate flux balances as we have done here, those numbers from the literature may differ from our flux based allocation values. Flux balances are of similar percentages as dry matter partitioning when accumulation or storage is of a small and constant fraction (see especially Chalmers and Van den Ende, 1975; Heilmeyer et al., 1997). Nevertheless, most information – whether dry matter or flux based – show that carbon investment into roots, especially in shade plants, is generally lower (<23–30%, Chalmers and Van den Ende, 1975; Wartinger et al., 1990; Heilmeyer et al., 1997) than the numbers obtained here from the steady-state approach (44–90%; Table 18.2). We conclude that the steady-state approach results in a strong overestimation of carbon investment into below-ground functions, both in relative and absolute terms, and, consequentially, underestimates relative investments into above-ground components.

Table 18.2. Comparison of ranges (in percentage of annual crown carbon gain) of allocation to leaves, supportive structures and roots for the six species from a secondary forest succession (after Timm et al., 2004)

		Leaves		Supporting tissues		Roots	
		Steady state	Dynamic	Steady state	Dynamic	Steady state	Dynamic
<i>Heliocarpus</i>	Range	13 – 25	24 – 41	17 – 31	31 – 61	51 – 65	15 – 31
<i>appendiculatus</i>	Mean	18.0 ± 5.2	32.5 ± 7.3	23.5 ± 6.1	42.9 ± 12.1	58.5 ± 5.3	24.6 ± 6.7
<i>Ochroma</i>	Range	21 – 28	30 – 38	26 – 34	36 – 49	44 – 50	22 – 29
<i>lagopus</i>	Mean	24.5 ± 2.4	34.2 ± 3.0	28.6 ± 3.6	40.0 ± 5.2	46.9 ± 2.3	25.8 ± 2.8
<i>Guarea</i>	Range	5 – 9	18 – 61	2 – 16	13 – 64	79 – 90	19 – 26
<i>glabra</i>	Mean	6.1 ± 2.6	38.2 ± 21.6	7.8 ± 7.4	38.8 ± 25.4	86.1 ± 5.8	23.0 ± 3.9
<i>Billia</i>	Range	8 – 17	20 – 41	13 – 24	31 – 56	67 – 76	21 – 43
<i>colombiana</i>	Mean	11.1 ± 3.3	27.4 ± 7.9	17.3 ± 4.1	42.6 ± 9.8	71.6 ± 3.6	30.0 ± 8.4
<i>Calatola</i>	Range	4 – 11	10 – 29	17 – 23	46 – 62	71 – 75	21 – 34
<i>costaricensis</i>	Mean	6.8 ± 3.1	18.2 ± 8.5	20.5 ± 2.5	55.0 ± 6.1	72.7 ± 1.3	26.8 ± 4.6
<i>Salacia</i>	Range	0 – 12	0 – 24	20 – 34	44 – 80	54 – 78	7 – 42
<i>petenensis</i>	Mean	3.6 ± 5.3	7.6 ± 9.9	24.8 ± 5.5	69.3 ± 15.0	71.5 ± 9.9	23.1 ± 2.8

C. A Biological Application: Relative Allocation Between Leaves, Supportive and Below-ground Plant Parts

Here we present a biological example of carbon allocation and carbon use by individual plants enrolled in the competitive situation of a successional sequence. For the reasons given in the previous section we consider only data in Table 18.2 obtained from the dynamic modeling approach as the reliable.

It appears to be astonishing that most species, whether from open sites or the understorey, invest a mean of ca. 25% into their roots (Table 18.2, Timm et al., 2004, their Fig. 18.9). It has been suggested that roots – for physiological reasons – demand this fraction for their normal functioning irrespective of the plant's ecological niche (Schulze, 1982, 1994; Brouwer, 1983; Küppers, 1994). Even more amazing is the observation that most carbon is invested into supportive structures in those plants that grow in the deeply shaded understorey, like *Calatola* and *Salacia*, although they have the smallest absolute amounts of carbon available. Most likely, such species must invest into long-lasting, “high quality” structures (e.g. their dry wood density is 0.5 g cm^{-3} versus 0.18 g cm^{-3} in the pioneers; Timm, 1999) in order to be able to gradually – in the far future at a higher plant age – reach the canopy. In fact, their organs have the maximum observed longevity (leaves last 5 years; Timm et al., 2004), so that

long-term costs (Bloom et al. 1985) for replacement of organs by new ones are much less than in pioneers like *Heliocarpus* and *Ochroma*: the pioneers replace their sun leaves by a new cohort already after 150 days (Fig. 18.4), for growing in the open they can afford for this high turnover rate. Their pioneer niche obviously enforces this behavior since otherwise self-shading might produce photosynthetically less effective crown sections resulting in lower carbon and, thus, slower height gain, taking part of the competitive characteristics from the pioneer. Vice versa, shade tolerant late successional cannot afford high turnover rates for lack of carbon. They must build long-lasting tissues and structures.

However, the percentages of allocation to a certain organ may fluctuate enormously within the same species, even in neighboring plants (Table 18.2). For example, in some of the *Salacia* plants from the understorey no leaf production was observed over more than a year (Timm, 1999), obviously because other demands were more important than increasing the photosynthetic tissue. In the given case it was the growth of new axes before new leaves could be built. Indeed, maximum variability was observed in allocation to supportive structures (e.g. Küppers, 1985; Timm et al., 2004), because here a plant has the best chances to adapt to the actual environmental situation without endangering its nutrient and water supply via roots or carbon supply via leaves.

VII. Concluding Remarks

Modeling of photosynthesis serves either for a better mechanistic, molecular and physiological understanding of the photosynthetic process itself or it quantitatively predicts the amounts of carbon gained, which is needed to understand and interpret plant growth and competition or to evaluate carbon budgets on a landscape scale.

Almost all photosynthesis models used in scaling up from leaf to globe (Ehleringer and Field, 1993) are based on steady-state photosynthesis, while accurate tests are still very rare (Aber et al., 1996) and often with low temporal resolution. Probably most leaves world-wide do not regularly experience conditions allowing for steady states in photosynthesis, neither in grass steppes nor in forests (Küppers et al., 1996, 1997) nor in deserts (Schulze and Hall, 1982). When tests of steady-state models are reported to be successful (Tenhunen et al., 1980; Küppers and Schulze, 1985; Wang and Jarvis, 1990; Aber et al., 1996) we should rather ask why they were successful in the given case than to extend the result for every situation.

Model comparisons on the leaf level clearly show that there is a need for a better link between the dynamics of light in canopies and the dynamic responses of plant CO₂-assimilation (Chazdon and Pearcy, 1986; Pfitsch and Pearcy, 1989; Gross et al., 1991; Küppers and Schneider, 1993; Poorter and Oberbauer, 1993; Barradas and Jones, 1996; Küppers et al., 1997; Yanhong et al., 1997; Pearcy et al., 1997; Kirschbaum et al., 1998; Stegemann et al., 1999; Naumburg et al., 2001; Naramoto et al., 2001; Timm et al., 2002; Schulte et al., 2003; Fig. 18.10). The temporal induction strongly controls the photosynthetic capacity (Küppers et al., 1986; Chazdon and Pearcy, 1991; Stegemann et al., 1999) and, possibly, the quantum yield of photosynthesis (Timm et al., 2002; Kirschbaum et al., 2004, 2005). Stomatal response to light during induction has in some cases been successfully modeled (Kirschbaum et al., 1988) but it still is a matter of concern. In well-watered plants it appears to be mainly the biochemical limitation controlling the induction state (Küppers and Schneider, 1993; Allen and Pearcy, 2000), based mainly on the slower Rubisco induction and the

faster induction of the Calvin cycle (Kirschbaum and Pearcy, 1988b), but the role of stomata in the induction of photosynthesis increases at increasing water limitation (Portes et al., 2006). Here, our knowledge is still very limited. Similarly, temperature effects (Küppers and Schneider, 1993) are not yet sufficiently studied.

Acknowledgments

We would like to thank Hans-Christoph Timm for providing some original data from his field work. Field work in Costa Rica was supported by DFG (Ku 592/11-1 and 11-2).

References

- Aber JD, Reich PB and Goulden ML (1996) Extrapolating leaf CO₂ exchange to the canopy: A generalized model of forest photosynthesis compared with measurements by eddy correlation. *Oecologia* 106: 257–265
- Ackerly DD and Bazzaz FA (1995) Leaf dynamics, self-shading and carbon gain in seedlings of a tropical pioneer tree. *Oecologia* 101: 289–298
- Allen MT and Pearcy RW (2000) Stomatal behavior and photosynthetic performance under dynamic light regimes in a seasonally dry tropical rain forest. *Oecologia* 122: 470–478
- Anderson MC (1964) Light relations of terrestrial plant communities and their measurement. *Biol Rev* 39: 425–86
- Baldocchi D and Collineau S (1994) The physical nature of solar radiation in heterogeneous canopies: spatial and temporal attributes. In: Caldwell MM and Pearcy RW (eds) *Exploitation of Environmental Heterogeneity by Plants*, pp 21–71. Academic, San Diego, CA
- Barnes PW, Beyschlag W, Ryel R, Flint SD and Caldwell MM (1990) Plant competition for light analyzed with a multispecies canopy model III. Influence of canopy structure in mixtures and monocultures of wheat and wild oat. *Oecologia* 82: 560–566
- Barradas VL, Jones HG (1996) Responses of CO₂ assimilation to changes in irradiance: laboratory and field data and a model for beans (*Phaseolus vulgaris* L.). *J Exp Bot* 47: 639–645
- Bazzaz F and Grace J (eds) (1997) *Plant Resource Allocation*. Academic Press, San Diego
- Beyschlag W, Ryel RJ, Ullmann I (1992) Experimental and modelling studies of competition for light in roadside grasses. *Bot Acta* 105: 285–291
- Bloom AJ, Chapin III FS and Mooney HA (1985) Resource limitation in plants – an economic analogy. *Annu Rev Ecol Syst* 16: 363–392

- Brouwer R (1983) Functional equilibrium: Sense or non-sense? *Neth J Agric Sci* 41: 207–248
- Caldwell MM, Meister HP, Tenhunen JD and Lange OL (1986) Canopy structure, light microclimate and leaf gas exchange of *Quercus coccifera* L. in a Portuguese macchia: measurements in different canopy layers and simulations with a canopy model. *Trees* 1: 25–41
- Chalmers DJ and Van den Ende B (1975) Productivity of peach trees: factors affecting dry-weight distribution during tree growth. *Ann Bot* 39: 423–432
- Chazdon RL and Pearcy RW (1986) Photosynthetic responses to light variation in rainforest species. I. Induction under constant and fluctuating light conditions. *Oecologia* 69: 517–523
- Chazdon RL and Pearcy RW (1991) The importance of sunflecks for forest understorey plants. *Bioscience* 41: 760–766
- Cescatti A (1997) Modelling the radiative transfer in discontinuous canopies of asymmetric crowns. I. Model structure and algorithms. *Ecol Modell* 101: 263–274
- Cescatti A (2007) Indirect estimates of canopy gap fraction based on the linear conversion of hemispherical photographs. *Methodology and comparison with standard thresholding techniques*. *Agric Forest Meteorol* 143: 1–12
- Chelle M (2005) Phylloclimate or the climate perceived by individual plant organs: What is it? How to model it? What for? *New Phytol* 166: 781–790
- Cremer KW (1975) Temperature and other climatic influences on shoot development and growth of *Eucalyptus regnans*. *Aust J Bot* 23: 27–44
- De Pury DGG and Farquhar GD (1997) Simple scaling of photosynthesis from leaves to canopies without the errors of big-leaf models. *Plant Cell Environ* 20: 537–557
- Ehleringer JR and Field CB (1993) *Scaling Physiological Process: Leaf to Globe*. Academic, New York
- Farquhar GD and Von Caemmerer S (1982) Modelling of photosynthetic response to environmental conditions. In: Lange OL, Nobel PS, Osmond CB and Ziegler H (eds) *Physiological Plant Ecology II: Water Relations and Carbon Assimilation*. *Encyclopedia of Plant Physiology*, New Series Vol. 12B, pp 549–587. Springer, Berlin
- Farquhar GD, Von Caemmerer S and Berry JA (2001) Models of photosynthesis. *Plant Physiol* 125: 42–45
- Fuchs M, Schulze E-D and Fuchs MI (1977) Spatial distribution of photosynthetic capacity and performance in a mountain spruce forest of Northern Germany. II. Climatic control of carbon dioxide uptake. *Oecologia* 29: 329–340
- Givnish TJ (1988) Adaptation to sun and shade: a whole-plant perspective. *Aust J Plant Physiol* 15: 63–92
- Godin C (2000) Representing and encoding plant architecture: A review. *Ann For Sci* 57: 413–438
- Gold WG and Caldwell MM (1990) The effects of the spatial pattern of defoliation on regrowth of a tussock grass. III. Photosynthesis, canopy structure and light interception. *Oecologia* 82: 12–17
- Gross LJ, Kirschbaum MUF and Pearcy RW (1991) A dynamic model of photosynthesis in varying light taking account of stomatal conductance, C₃-cycle intermediates, photorespiration and Rubisco activation. *Plant Cell Environ* 14: 881–893
- Heilmeyer H, Erhard M and Schulze E-D (1997) Biomass allocation and water use under arid conditions. In: Bazzaz F and Grace J (eds) *Plant Resource Allocation*, pp 93–111. Academic, San Diego, CA
- Jarvis PG (1995) Scaling processes and problems. *Plant Cell Environ* 18: 1079–1089
- Kellomäki S and Wang KY (1997) Photosynthetic responses of Scots pine to elevated CO₂ and nitrogen supply: results of a branch-in-bag experiment. *Tree Physiol* 17: 231–240
- Kirschbaum MUF and Pearcy RW (1988a) Gas exchange analysis of the relative importance of stomatal and biochemical factors in photosynthetic induction in *Alocasia macrorrhiza*. *Plant Physiol* 86: 782–785
- Kirschbaum MUF and Pearcy RW (1988b) Gas exchange analysis of the fast phase of photosynthetic induction in *Alocasia macrorrhiza*. *Plant Physiol* 87: 818–821
- Kirschbaum MUF, Gross LJ and Pearcy RW (1988) Observed and modelled stomatal responses to dynamic light environments in the shade plant *Alocasia macrorrhiza*. *Plant Cell Environ* 11: 111–121
- Kirschbaum MUF, Küppers M, Schneider H, Giersch C and Noe S (1998) Modelling photosynthesis in fluctuating light with inclusion of stomatal conductance, biochemical activation and pools of key photosynthetic intermediates. *Planta* 204: 16–26
- Kirschbaum MUF, Ohlemacher C and Küppers M (2004) Loss of quantum yield in extremely low light. *Planta* 218: 1046–1053
- Kirschbaum MUF, Oja V and Laisk A (2005) The quantum yield of CO₂ fixation is reduced for several minutes after prior exposure to darkness. Exploration of the underlying causes. *Plant Biol* 7: 58–66
- Körner C, Ashhoff R, Bignucolo O, Hättenschwiler S, Keel SG, Peláez-Riedl S, Pepin S, Siegwold RTW and Zotz G (2005) Carbon flux and growth in mature deciduous forest trees exposed to elevated CO₂. *Science* 309: 1360–1362
- Künstle E, Mitscherlich G (1975) Photosynthese, Transpiration und Atmung in einem Mischbestand im Schwarzwald: I. Photosynthese. *Allg Forst Jagdz* 146: 45–63
- Küppers BIL (1999) *Ecophysiological Field Studies on Gas Exchange and Nitrogen Relations in Snow Gum, Alpine Ash and Associated Acacias – From Leaf to Canopy*. Doctoral Thesis, University of Darmstadt, Cuvillier, Göttingen
- Küppers M (1982) *Kohlenstoffhaushalt, Wasserhaushalt, Wachstum und Wuchsform von Holzgewächsen im Konkurrenzgefüge eines Heckenstandortes*. Doctoral Thesis, University of Bayreuth
- Küppers M (1984) Carbon relations and competition between woody species in a Central European hedgerow. III. Carbon and water balance on the leaf level. *Oecologia* 65: 94–100

- Küppers M (1985) Carbon relations and competition between woody species in a Central European hedgerow. IV. Growth form and partitioning. *Oecologia* 66: 343–352
- Küppers M (1994) Canopy gaps: Competitive light interception and economic space filling – a matter of whole plant allocation. In: Caldwell MM and Pearcy RW (eds) *Exploitation of Environmental Heterogeneity by Plants: Ecophysiological Processes Above and Below Ground*, pp 111–144. Academic, San Diego, CA
- Küppers M and Schneider H (1993) Leaf gas exchange of beech (*Fagus sylvatica* L.) seedlings in lightflecks: effects of fleck length and leaf temperature in leaves grown in deep and partial shade. *Trees* 7: 160–168
- Küppers M and Schulze E-D (1985) An empirical model of net photosynthesis and leaf conductance for the simulation of diurnal courses of CO₂ and H₂O exchange. *Aust J Plant Physiol* 12: 513–526
- Küppers M, Wheeler AM, Küppers BIL, Kirschbaum MUF and Farquhar GD (1986) Carbon fixation in eucalypts in the field – analysis of diurnal variations in photosynthetic capacity. *Oecologia* 70: 273–282
- Küppers M, Koch G and Mooney HA (1988) Compensating effects to growth of changes in dry matter allocation in response to variation in photosynthetic characteristics induced by photoperiod, light and nitrogen. In: Evans JR, Von Caemmerer S and Adams WW (eds) *Ecology of Photosynthesis in Sun and Shade* pp 287–298. CSIRO, Melbourne (Aust J Plant Physiol 15)
- Küppers M, Timm H, Orth F, Stegemann J, Stöber R, Schneider H, Paliwal K, Karunaichamy KSTK and Ortiz R (1996) Effects of light environment and successional status on lightfleck use by understory trees of temperate and tropical forests. *Tree Physiol* 16: 69–80
- Küppers M, Giersch C, Schneider H and Kirschbaum MUF (1997) Leaf gas exchange in light- and sunflecks: response patterns and simulations. In: Rennenberg H, Eschrich W and Ziegler H (eds) *Trees – Contribution to Modern Tree Physiology*, pp 77–96. Backhuys Publishers, Leiden
- Küppers M, Motzer T, Schmitt D, Ohlemacher C, Zimmermann R, Horna V, Küppers BIL and Mette T (2008) Stand structure, transpiration responses in trees and vines and stand transpiration of different forest types within the mountain rainforest. In: Beck E, Bendix J, Kottke I, Makeschin F and Mosandl R (eds) *Ecol Stud* 198. Gradients in a Tropical Mountain Ecosystem of Ecuador, pp 243–258. Springer, Berlin/Heidelberg
- Larcher W (2003) *Physiological Plant Ecology*, Springer, New York
- Leakey ADB, Press MC and Scholes JD (2003) Patterns of dynamic irradiance affect the photosynthetic capacity and growth of dipterocarp tree seedlings. *Oecologia* 135: 184–193
- Lei TT and Lechowicz MJ (1998) Diverse responses of maple saplings to forest light regimes. *Ann Bot* 82: 9–19
- Leuning R, Kelliher FM, de Pury DGG and Schulze E-D (1995) Leaf nitrogen, photosynthesis, conductance and transpiration: scaling from leaves to canopies. *Plant Cell Environ* 18: 1183–2000
- Linder S and Axelsson B (1982) Changes in C uptake and allocation patterns as a result of irrigation and fertilization in a young *Pinus sylvestris* stand. In: Waring RH (ed) *C Uptake and Allocation in Subalpine Ecosystems as a Key to Management*, pp 38–44. IUFRO Workshop, Oregon State University, Corvallis
- Linder S and Lohammar T (1981) Amount and quality of information on CO₂ exchange required for estimating annual carbon balance of coniferous trees. *Stud For Suec* 160: 73–87
- Marcolla B, Pitacco A and Cescatti A (2003) Canopy architecture and turbulence structure in a coniferous forest. *Boundary-Layer Meteorology* 108: 39–59
- Marquardt I, 1999. Untersuchungen zum Lichtklima unter Verwendung hemisphärischer Fotos – mit besonderer Berücksichtigung von sechs Baumarten unterschiedlicher sukzSSIONALER Stellung in einem tropischen Regenwald in Costa Rica. Diploma thesis, University of Halle/Saale, Germany
- Matyssek R (1985) Der Kohlenstoff-, Wasser- und Nährstoffhaushalt der wechselgrünen und immergrünen Koniferen, Lärche, Fichte, Kiefer. Doctoral Thesis, University of Bayreuth
- Matyssek R and Schulze E-D (1987) Heterosis in hybrid larch (*Larix decidua* x *leptolepis*) II. Growth characteristics. *Trees* 1: 225–231
- Medhurst J, Parsby J, Linder S, Wallin G, Ceschia E and Slaney M (2006) A whole-tree chamber system for examining tree-level physiological responses of field-grown trees to environmental variation and climate change. *Plant Cell Environ* 29: 1853–1869
- Monsi M and Saeki T (1953) Über den Lichtfaktor in den Pflanzengesellschaften und seine Bedeutung für die Stoffproduktion. *Jpn J Bot* 14: 22–52
- Mooney H (1972) The carbon balance of plants. *Annu Rev Ecol Sys* 3: 315–346
- Naramoto M, Han Q and Kakubari Y (2001) The influence of previous irradiance on photosynthetic induction in three species grown in the gap and understory of a *Fagus crenata* forest. *Photosynthetica* 39: 545–552
- Naumburg E, Ellsworth DS and Pearcy RW (2001) Crown carbon gain and elevated CO₂ responses of understory saplings with differing allometry and architecture. *Funct Ecol* 15: 263–273
- Niinimets Ü and Tenhunen JL (1997) A model separating leaf structural and physiological effects on carbon gain along light gradients for the shade-tolerant species *Acer saccharum*. *Plant Cell Environ* 20: 845–866
- Nobel PS, Forseth IN and Long SP (1993) Canopy structure and light interception. In: Hall DO, Scurlock JMO,

- Bolhar-Nordenkamp HR, Leegood RC and Long SP (eds) Photosynthesis and Production in a Changing Environment, pp 79–90. Chapman & Hall, London
- Norman J (1980) Interfacing leaf and canopy light interception models. In: Hesketh JD and Jones JW (eds) Predicting Photosynthesis for Ecosystem Models, pp 49–68. CRC Press, Boca Raton, FL
- Oloff H, Van Andel J and Bakker JP (1990) Biomass and shoot/root allocation of five species from a grassland succession series at different combinations of light and nutrient supply. *Funct Ecol* 4: 193–200
- Oren R and Zimmermann R (1989) CO₂-assimilation and the carbon balance of a healthy and a declining *Picea abies* (L.) Karst. stand. In: Schulze E-D, Lange OL and Oren R (eds) Air Pollution and Forest Decline. A Study on Spruce (*Picea abies*) on Acid Soils. *Ecol Stud* 77, pp 352–369. Springer, Berlin
- Pearcy RW and Yang W (1996) A three-dimensional crown architecture model for assessment of light capture and carbon gain by understory plants. *Oecologia* 108: 1–12
- Pearcy RW, Chazdon RL, Gross LJ and Mott KA (1994) Photosynthetic utilization of sunflecks, a temporally patchy resource on a time scale of seconds to minutes. In: Caldwell MM and Pearcy RW (eds) Exploitation of Environmental Heterogeneity by Plants: Ecophysiological Processes Above and Below Ground, pp 175–208. Academic, San Diego, CA
- Pearcy RW, Gross LJ and He D (1997) An improved dynamic model of photosynthesis for estimation of carbon gain in sunfleck light regimes. *Plant Cell Environ* 20: 411–424
- Pearcy RW, Muraoka H and Valladares F (2005) Crown architecture in sun and shade environments: assessing function and trade-offs with a three-dimensional simulation model. *New Phytol* 166: 791–800
- Pfitsch WA and Pearcy RW (1989) Steady-state and dynamic photosynthetic response of *Adenocaulon bicolor* (Asteraceae) in its redwood forest habitat. *Oecologia* 80: 471–476
- Pook EW (1984) Canopy dynamics of *Eucalyptus maculata* Hook. I. Distribution and dynamics of leaf populations. *Aust J Bot* 32: 387–403
- Poorter L and Oberbauer SF (1993) Photosynthetic induction responses of two rainforest tree species in relation to light environment. *Oecologia* 96: 193–199
- Portes MT, Alves TH and Souza GM (2006) Water deficit affects photosynthetic induction in *Bauhinia forficata* Link (Fabaceae) and *Esenbeckia leiocarpa* Engl. (Rutaceae) growing in understory and gap conditions. *Braz J Plant Physiol* 18: 491–502
- Rich PM (1990) Characterizing plant canopies with hemispherical photographs. *Rem Sens Rev* 5: 13–29
- Roden JS and Pearcy RW (1993) Photosynthetic gas exchange response of poplars to steady-state and dynamic light environments. *Oecologia* 93: 208–214
- Schulte M, Offer C and Hansen U (2003) Induction of CO₂-gas exchange and electron transport: comparison of dynamic and steady-state responses in *Fagus sylvatica* leaves. *Trees* 17: 153–163
- Schulze E-D (1970) Der CO₂-Gaswechsel der Buche (*Fagus sylvatica* L.) in Abhängigkeit von den Klimafaktoren im Freiland. *Flora* 159: 177–232
- Schulze E-D (1982) Plant life forms as related to plant carbon, water and nutrient relations. In: Lange OL, Nobel PS, Osmond CB and Ziegler H (eds) Encyclopedia of Plant Physiology. Physiological Plant Ecology 12B. Water Relations and Photosynthetic Productivity, pp 615–676. Springer, Berlin/Heidelberg
- Schulze E-D (ed) (1994) Flux Control in Biological Systems. From Enzymes to Populations and Ecosystems. Academic, San Diego, CA
- Schulze E-D and Hall AE (1982) Stomatal control of water loss. In: Lange OL, Nobel PS, Osmond CB and Ziegler H (eds) Encyclopedia of Plant Physiology. Physiological Plant Ecology 12B. Water Relations and Photosynthetic Productivity, pp 181–230. Springer, Berlin/Heidelberg
- Schulze E-D, Fuchs MI and Fuchs M (1977) Spatial distribution of photosynthetic capacity and performance in a mountain spruce forest of northern Germany. I. Biomass distribution and daily CO₂ uptake in different crown layers. *Oecologia* 29: 43–61
- Smith WK, Knapp AK and Reiners W A (1989) Penumbral effects on sunlight penetration in plant communities. *Ecology* 70: 1603–1609
- Stegemann J (1999) Kohlenstoffökonomie neotropischer Baumarten. I. Plastizität der dynamischen CO₂-Assimilation auf Blatt- und Kronenebene. Doctoral thesis, University of Hohenheim
- Stegemann J, Timm H-C and Küppers M (1999) Simulation of photosynthetic plasticity in response to highly fluctuating light: an empirical model integrating dynamic photosynthetic induction and capacity. *Trees* 14: 145–160
- Tang Y and Liang N (2000) Characterization of the photosynthetic induction response in a *Populus* species with stomata barely responding to light changes. *Tree Physiol* 20: 969–976
- Tenhunen JD, Meyer A, Lange OL and Gates DM (1980) Development of a photosynthesis model with an emphasis on ecological applications. V. Test of the applicability of a steady-state model to description of net photosynthesis of *Prunus armeniaca* under field conditions. *Oecologia* 45: 147–155
- Terashima I, Wong SC, Osmond CB and Farquhar GD (1988) Characterisation of non-uniform photosynthesis induced by abscisic acid in leaves having different mesophyll anatomies. *Plant Cell Physiol* 29: 385–394
- Timm H-C (1999) Kohlenstoffökonomie neotropischer Baumarten. II. Strategien der Kohlenstoffallokation und Monitoring der Kronenarchitektur. Doctoral Thesis, University of Hohenheim

- Timm H, Stegemann J and Küppers M (2002) Photosynthetic induction strongly affects the light compensation point of net photosynthesis and coincidentally the apparent quantum yield. *Trees* 16: 47–62
- Timm H-C, Küppers M and Stegemann J (2004) Non-destructive analysis of architectural growth, dry matter increment and assimilate allocation in pioneer, mid- and late successional tropical tree saplings: consequences of using steady-state and dynamic photosynthesis models. *Ecotropica* 10: 101–121
- Valladares F, Allen MT and Pearcy RW (1997) Photosynthetic responses to dynamic light under field conditions in six tropical rainforest shrubs occurring along a light gradient. *Oecologia* 111: 505–514
- Wang YP and Jarvis PG (1990) Description and validation of an array model: MAESTRO. *Agric For Meteorol* 51: 257–280
- Wartinger A, Heilmeier H, Hartung W and Schulze E-D (1990) Daily and seasonal courses of leaf conductance and abscisic acid in the xylem sap of almond trees (*Prunus dulcis* M.) under desert conditions. *New Phytol* 116: 581–587
- Whitehead D and Walcroft AS (2005) Forest and shrubland canopy carbon uptake in relation to foliage nitrogen concentration and leaf area index: a modelling analysis. *Ann For Sci* 62: 525–535
- Whitehead D, Walcroft AS, Griffin KL, Tissue DT, Turnbull MT, Engel V, Brown KJ and Schuster WSF (2004) Scaling carbon uptake from leaves to canopies: insights from two forests with contrasting properties. In: Mencuccini M, Grace J, Moncrieff J and McNaughton KG (eds) *Forests at the Land-Atmosphere Interface*, pp 231–254. CABI Publishing, Wallingford, UK
- Wilson KB, Baldocchi DD and Hanson PJ (2001) Leaf age affects the seasonal pattern of photosynthetic capacity and net ecosystem exchange of carbon in a deciduous forest. *Plant Cell Environ* 24: 571–583
- Yanhong T, Hiroshi K, Satoh M and Izumi W (1997) Characteristics of transient photosynthesis in *Quercus serrata* under lightfleck and constant light regimes. *Oecologia* 100: 487–500

Chapter 19

Photosynthesis Within Large-Scale Ecosystem Models

Stephan A. Pietsch and Hubert Hasenauer*

Institute of Silviculture

Department of Forest and Soil Sciences, University of Natural Resources and Applied Life Sciences, Peter-Jordan-st. 82, A-1190 Vienna, Austria

Summary.....	441
I. Introduction.....	442
II. Biogeochemical Cycles.....	443
A. Carbon Cycle.....	443
B. Nitrogen Cycle.....	444
C. Water Cycle.....	444
D. Energy Cycle.....	445
E. Interactions Between Cycles.....	445
III. Models of Biogeochemical Cycles.....	446
A. Model Algorithm.....	446
B. Modeled Processes.....	447
1. Photosynthesis.....	447
2. Ground Water Infiltration.....	447
3. Mortality.....	449
C. Model Parameters.....	449
D. Model Drivers.....	450
E. Temporal Model Resolution.....	451
IV. Model Application.....	452
A. Application Procedure.....	452
B. Sensitivity.....	453
C. Validation.....	453
D. Dynamic Model Behavior.....	454
V. Examples of Model Application.....	456
A. Application to Virgin Forests.....	456
B. Assessing Ecosystem Specific Model Parameters.....	458
C. Assessing Model Dynamics.....	459
VI. Concluding Remarks.....	461
Acknowledgments.....	462
References.....	462

Summary

In large scale ecosystem models photosynthesis interacts with other ecosystem processes such as transpiration, evaporation, soil hydrology, assimilate allocation, growth and maintenance respiration, biomass mortality, heterotrophic respiration, decomposition, mineralization, and nutrient leaching and

* Author for correspondence, e-mail: hubert.hasenauer@boku.ac.at

volatilization. These processes are of biological, physicochemical and hydro-geological nature and are summarized under the term biogeochemistry. This chapter explains the relations among photosynthesis and the biogeochemical cycles of carbon, nitrogen, water and energy and describes how these complex cycles are integrated in a modeling environment by outlining: (i) the model algorithm, (ii) the mechanistic detail of the implementation of processes such as photosynthesis, groundwater infiltration and biomass mortality, (iii) the role of model parameters, (iv) the properties of model drivers and (v) the constraints provided by the temporal resolution of the model implementation. Emphasis is laid on the single steps of model application, from model initialization and the consideration of historical land use and land use change to the simulation of a current ecosystem. Tests of model sensitivity and the necessity of model validation versus field observations are explained. Besides statistic validation procedures, which provide accuracy and precision of model predictions, methods from higher mathematics are introduced to analyze model dynamics. These methods allow the distinction between stable and unstable model behavior. In scenario simulations such as climate change impact studies no observations are available to assess the accuracy and precision of model predictions and model stability becomes the key criterion to judge the predictive value of model outputs. If model dynamics remain stable then model predictions remain valid, if, however, model dynamics become unstable then the interpretation of model results is meaningless. Next, examples of model application are provided dealing with (i) virgin forest conditions unaffected by direct human impact, (ii) model calibration and validation for production forests, where human impact affected species composition and site quality and (iii) the assessment of model dynamics and how the results of such analyses may be interpreted. Concluding remarks emphasize the central position of photosynthesis, the importance of field observations for model validation and the key role of assessing model dynamics in scenario studies.

I. Introduction

Large scale ecosystem models describe the fluxes of carbon, nitrogen, water and energy within ecosystems. Photosynthesis and related processes are central as they transform inorganic carbon into carbohydrates, thus providing the organic backbone for structural and functional molecules of living organisms. In large scale ecosystem models other processes such as allocation of assimilates for growth of

shoots and roots, growth and maintenance respiration, phenological biomass turnover, mortality, decomposition, mineralization, denitrification, evapotranspiration, soil water outflow and flooding, surface reflectance or heat transfer must be considered in order to capture the growth and decay following mortality within these ecosystems. These processes are of biological, physicochemical, and hydro-geological nature and may be summarized by the term biogeochemistry. All of these processes directly or indirectly depend on photosynthesis (Fig. 19.1).

Within ecosystem models, all processes must be addressed at a similar level of detail in order to ensure a balanced representation of reality (Waring and Running, 1998). Differences in the level of detail and/or temporal and spatial resolution may lead to biased and inconsistent predictions, given that a single modeled process may dominate the system in such instances. For example, a well balanced approach has to prevail between the treatments of photosynthesis and transpiration so that the trade-off between the carbon gain and water loss, influenced by stomatal conductance, is properly addressed. Stomatal conductance and transpiration are affected by

Abbreviations: GPP—gross primary production: net plant C uptake from photosynthesis (kg C m^{-2}); LAI—leaf area index: leaf area per m^2 ground area ($\text{m}^2 \text{ m}^{-2}$); NEE—net ecosystem exchange: rate of C sequestration within an ecosystem (kg C m^{-2}); NPP—net primary production: GPP minus plant respiration (kg C m^{-2}); PHAR—photosynthetically active radiation: part of the solar radiation that is utilized for photosynthesis (W m^{-2}); R_h —heterotrophic respiration: C release during decomposition processes (kg C m^{-2}); Rubisco—Ribulose 1,5-bisphosphate carboxylase/oxygenase; PEP—phosphoenol pyruvate; VPD—vapor pressure deficit: difference between the partial pressure of atmospheric water vapor at 100% relative humidity and the partial pressure of atmospheric water vapor at actual relative humidity (Pa)

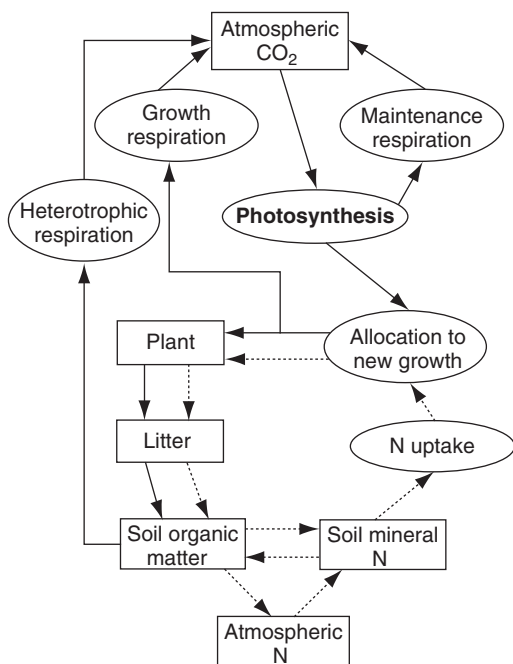


Fig. 19.1. Simplified schematic of the fluxes (arrows), state variables (boxes) and processes (ellipses) considered in large scale ecosystem models. Solid lines indicate carbon fluxes, dotted lines indicate nitrogen fluxes, water and energy pools and fluxes were left out for clarity (Thornton et al., 2002, modified)

issues of soil hydrology. The trade-off between soil moisture and litter decomposition affects mineral nitrogen release. Soil mineral nitrogen content constrains plant growth and affects the leaf area available for radiation absorption. Radiation absorption provides the energetic source and determines the carbon assimilation potential of photosynthesis.

In the previous chapters of this book, photosynthesis is modeled with a high level of detail. Conceptually, this would require that the other processes, such as transpiration, groundwater infiltration, biomass turnover or decomposition, must be treated in a comparable detail. This increases computation time, and as such, data handling ability may become the limiting factor in large scale model applications. Another difficulty may be the comparison of model output to field observations, since field observations are usually not available at the same level of detail as modeled processes.

The purpose of this chapter is to demonstrate how complex large scale ecosystem models may

be applied and tested versus field observations. This chapter will (i) give a description of the biogeochemical cycles in order to address the mass and energy balance, (ii) describe the structural features of the models and (iii) explain the steps of model application.

II. Biogeochemical Cycles

Biogeochemical cycles (BGC) describe the transformation of energy and matter within ecosystems (Waring and Running, 1998). Using solar short wave radiation (photosynthetically active) and inorganic matter, autotrophic processes produce organic matter charged with internal chemical energy. At the end of the cycle, heterotrophic decay releases long wave radiation (heat) and inorganic matter. Carbon, nitrogen, water and energy are considered as the key components within the modeling environment.

A. Carbon Cycle

The carbon source for photosynthesis is provided by CO₂, whose concentration within the leaves depends on the atmospheric concentration and stomatal conductance. The rate of photosynthesis depends on the amount of the primary carbon fixing enzyme (ribulose 1,5-bisphosphate carboxylase/oxygenase, Rubisco, in C₃ plants and phosphoenol pyruvate, PEP, carboxylase in C₄ and CAM plants). The reaction rate is calculated using enzyme kinetics, leaf temperature, absorbed radiation and photosynthetic electron transport rate according to different models (e.g. for C₃, de Pury and Farquhar, 1997; for C₄, Laisk and Edwards, 2000). Leaf Area Index (LAI, m² leaf area per m² ground area) is calculated from carbon allocated to leaves multiplied by the specific leaf area (m² leaf area per kg leaf carbon). LAI controls canopy radiation absorption, which provides the energetic source for photosynthetic carbon fixation.

Gross Primary Production (GPP) is the rate of photosynthesis minus the leaf maintenance respiration during daytime (R_{md}) which is calculated as a function of leaf nitrogen concentration (Ryan, 1991) and daytime length. Net Primary Production (NPP) is based on GPP minus autotrophic respiration (R_a). The latter

includes the maintenance respiration of (i) leaves during nighttime, (ii) all other tissues during the whole day and (iii) growth respiration (R_g), which is a function of the amount of carbon allocated to different plant structural compartments (Penning de Vries, 1974). NPP is partitioned into the leaves, roots and stems as a function of dynamic allocation patterns, considering possible limitations in the availability of, and the competition for, nitrogen.

Net Ecosystem Carbon Exchange (NEE) provides the balance between NPP and heterotrophic respiration (R_h). R_h depends on the decomposition activity, which is regulated by soil temperature and soil moisture, as well as the amount of decomposition material. The ecosystem acts as a carbon sink when the amount of carbon released via R_h is lower than NPP. The ecosystem acts as a net carbon source when R_h exceeds NPP due to high amounts of decomposable material and/or high decomposition activity. The amount of decomposable material is governed by the mortality rate of vegetation biomass. Mortality thereby links living biomass with litter and soil organic matter and influences the total ecosystem carbon content.

B. Nitrogen Cycle

Nitrogen (N) sources include deposition, nitrogen fixation and decomposition fluxes. Plant uptake, microbial immobilization and volatile and leaching losses are nitrogen sinks. Plant N demand is determined by NPP. The immobilization demand is calculated from the decomposition rate and depends on the amount of decomposable material. Decomposition rates of litter and soil carbon pools change with soil temperature (Lloyd and Taylor, 1994) and soil moisture (Andren and Paustian, 1987). These factors determine the magnitude of N mineralization from decomposition and influence the heterotrophic respiration.

A small portion of N is released into the atmosphere during mineralization by denitrification. Nitrogen may percolate down to groundwater or it may be released into the atmosphere via denitrification, when soil mineral nitrogen content exceeds the sum of microbial and plant nitrogen demand. If the sum of microbial and plant nitrogen demand is equal to the amount of available

soil mineral nitrogen, no denitrification occurs (Aber, 1992).

Plants and microorganisms compete for soil mineral nitrogen when the amount of available soil mineral nitrogen is lower than the demand. While plant demand depends on NPP, microbial demand depends on (i) the amount of material available for decomposition and (ii) the decomposition rate, which depends on the temperature and soil moisture (Andren and Paustian, 1987; Lloyd and Taylor, 1994). The availability of mineral N and the sum of plant and microbial N demand defines a supply/demand ratio, which is used for the allocation of N available for uptake by plants and microorganisms.

C. Water Cycle

Water enters terrestrial ecosystems from (i) the atmosphere by rainfall, (ii) the snowpack by melting, (iii) lateral inflows like flooding, and (iv) the ground water table by soil water recharge. Rainfall is partially intercepted by the canopy. If the amount of rainfall exceeds the potential canopy interception, it is routed to the soil water pool. Water is released from a snow pack and adds to the soil water pool, if the energy input from temperature and radiation exceeds the energy of melting. Lateral water inflow occurs when water input from rainfall or snowmelt exceeds the capacity of standard water discharge routes, e.g. brooks and rivers.

The upper limit for soil water content is the soil porosity, which equals the total volume of soil pores. Ground water recharge, of the soil volume accessible by plants, occurs only if the soil water content falls below the field capacity. Field capacity is equal to the soil water content when the gravitational force is equal to the retention force of soil water potential and is lower than soil water saturation. Below the field capacity, the upward pressure of the soil water potential exceeds the downward pressure from gravitation. The amount of ground water ascent is defined by the net upward force and the soil hydraulic conductivity, which depend on soil texture and soil water content (Pietsch et al., 2003).

Water leaves the ecosystem by plant transpiration, soil evaporation, snow sublimation and soil water outflow. Plant transpiration depends on the atmospheric vapor pressure deficit, leaf

temperature and water potential, and stomatal conductance to water vapor. Stomatal conductance is regulated by the leaf water potential, atmospheric vapor pressure deficit and temperature. Additionally, canopy transpiration depends on the wind speed. Evaporation of soil water is governed by the atmospheric vapor pressure deficit and the temperature. Sublimation of snow water is determined by the radiation energy input. Soil water outflow includes all water, which is above soil water saturation and a proportion of soil water above field capacity (Chang, 2003).

D. Energy Cycle

Energy enters ecosystems as solar radiation and sensible heat of atmospheric temperature. A portion of solar radiation is reflected by plant surfaces, whereas another part is absorbed by leaves and other plant organs. The remaining radiation is transmitted to the snow pack or bare soil, where another proportion is reflected and the rest is absorbed. The sum of reflected radiation is due to the ecosystem type, vegetation cover, snow cover and the soil type; it is called the albedo. In addition to the energy loss via the albedo effect, energy also leaves the ecosystem as latent heat during processes such as snow sublimation, transpiration and evaporation of water intercepted by the canopy or water stored in the soil. Radiation absorption by leaves and the temperature of the surrounding air, determine the leaf temperature. This affects the enzyme activity of carbon assimilation. The mean air temperature over longer durations of time (days, weeks) determines soil temperature, which, in turn, affects the activity of decomposition enzymes. Air temperature also affects stomatal conductance and regulates the water vapor flux density and the energy loss due to latent heat transfer between vegetation and the atmosphere.

E. Interactions Between Cycles

As is evident from the description of the carbon, nitrogen, water and energy cycles, none of them can be calculated as a single, linear, causal relationship. Among these cycles, multiple interactions exist and have to be considered within modeling in order to mimic nature as closely as possible. Conceptually, these interactions are

organized as feedback loops, making the modeled ecosystem behave in a strongly nonlinear fashion.

An important trade-off exists between photosynthetic carbon gain and transpiration water loss. Carbon availability for photosynthesis depends on the partial pressure of atmospheric CO₂ and the stomatal conductance. The partial pressure of atmospheric CO₂ is a physical function of elevation. Stomatal conductance is driven by an atmospheric vapor pressure deficit and the leaf water potential. Leaf water potential depends upon soil water potential, and it is derived from the texture of the soil and the soil water content. Soil water content is influenced by water input via precipitation and results from the amount of rainfall, which is not intercepted by the canopy. Canopy size depends on the amount of carbon allocated to leaves and it is regulated by the amount of carbon which is assimilated via photosynthesis (Pietsch and Hasenauer, 2005b).

Next, there is the trade-off between photosynthetic carbon gain and nitrogen availability. Carbon assimilated by photosynthesis is incorporated into structural and functional biomolecules which exhibit a certain N/C-ratio. Wood has a low N/C-ratio and thus has a low demand of nitrogen per unit carbon. Leaves have a high N/C-ratio due to their high content of enzymatic proteins. The carbon fixing protein Rubisco may account for up to 30% of nitrogen in the leaves alone (Evans, 1989). Nitrogen availability constrains photosynthetic carbon fixation.

Another example is biomass turnover and mortality, which follow seasonal and plant life-time cycles. Both influence the litter availability for decomposition at a certain time of the season or at a certain time during the plant life cycle. The more biomass is available for decomposition, the higher is the microbial nitrogen demand, which lowers the amount of nitrogen for plant uptake. Decomposition enhances ecosystem nitrogen loss due to denitrification-induced volatile nitrogen release. Low availability of nitrogen for plant uptake particularly affects leaf growth due to the high N/C ratio of leaves and their resulting high demand for nitrogen per carbon assimilated via photosynthesis. A decreased growth rate of leaves means less radiation is intercepted by the leaves and a resulting lower rate of photosynthetic carbon assimilation is observed. Less carbon assimilation leads to a lower plant nitrogen demand.

Nitrogen released from enhanced decomposition will gradually increase soil mineral nitrogen content and cause volatile and leaching losses of mineral nitrogen. With time the amount of decomposable biomass will decrease and microbial nitrogen demand will decline. More nitrogen will be available for plant uptake at the start of the next season or new plant life cycle and plant growth is favored. Biomass is built up until turnover or mortality occurs, and the amount of decomposable material increases again (Pietsch and Hasenauer, 2006).

Decomposition activity depends on soil moisture and temperature. When plant growth is limited by low nitrogen availability, canopy size is reduced and less radiation and precipitation is intercepted by plant surfaces. This increases the soil temperature and moisture, which both enhance decomposition. This may increase N-leaching as well as soil evaporation depending on the precipitation regime. Soil evaporation decreases soil moisture, which, in turn, regulates decomposition activity (Merganicova et al., 2005).

These four examples illustrate the multiple feedback processes among the cycles of water and carbon, carbon and nitrogen, nitrogen demand of decomposers and plants and their link to the energy cycle. All together the biogeochemical cycles resemble a complex network of feedback loops. None of the cycles can be modeled without considering the others.

III. Models of Biogeochemical Cycles

Within large-scale BGC modeling, an ecosystem is viewed as a set of ecosystem compartments (the atmosphere, leaves, stems, roots, litter, soil) carrying water, carbon and nitrogen pools as well as energy. The sizes of the pools define the state of an ecosystem. Changes in state depend on the fluxes of energy and matter amongst the pools. These fluxes govern the energy and matter balance within a given ecosystem. Pools as well as fluxes are restricted by the interactions among the cycles of energy and matter (Section II.E). This section describes (i) the general model algorithm, (ii) the technical implementation of a few processes governing the fluxes of energy and matter, (iii) the model parameters

defining the interactions among the pools and fluxes, (iv) the dynamic and static input variables driving/constraining flux dynamics among the pools and (v) the constraints provided by the temporal resolution of models.

A. Model Algorithm

Similar to nature, the present state of an ecosystem is determined by its state in the past and the forces driving the changes from the past to the present state. In large scale ecosystem models this classical recursion is addressed as follows: after each simulated time step the sizes of the different pools are changed by the fluxes. Hence, the size of a pool depends on its present state and the balance between influx and efflux. The general production formula may be expressed as follows:

$$\Theta_{T_{n+1}} = f(\Theta_{T_n}, \varphi_{T_n}, \alpha, \sigma), \quad (19.1)$$

where $\Theta_{T_{n+1}}$ is the set of pool sizes at time T_{n+1} , Θ_{T_n} is the set of pool sizes one recursion step earlier, φ_{T_n} is the set of model drivers at time T_n (which induce the fluxes among the pools and thereby cause the changes from Θ_{T_n} to $\Theta_{T_{n+1}}$), α is the model parameter set encapsulating specific properties of the modeled ecosystem, σ is the set of physical site properties, and f is the functional algorithm of the model implementation.

The modeled state of an ecosystem at a time T_{n+1} depends on its state at time T_n , and so forth:

$$\Theta_{T_0} \rightarrow \Theta_{T_1} \rightarrow \dots \rightarrow \Theta_{T_{n-1}} \rightarrow \Theta_{T_n} \rightarrow \Theta_{T_{n+1}}. \quad (19.2)$$

Accordingly any Θ_{T_n} relies on the values of state at time T_0 , i.e. the initial conditions. In some situations the initial conditions may be available from previous measurements, e.g. sites of long-term research. In general the information about the initial conditions is either missing or incomplete. While e.g. the age of forest stand may be known (or determined on site from increment cores) the state of the plot before stand establishment is often unknown. It may have been a virgin forest, a coppice forest used for fuel wood which in turn may have been degraded due to extensive litter raking, or it may also have previously been an abandoned meadow, pasture or a piece of arable land.

B. Modeled Processes

1. Photosynthesis

The equations for calculating photosynthetic carbon assimilation are based on the work of Kuehn and McFadden (1969), Woodrow and Berry (1980), Farquhar et al. (1980), Wullschlegel (1993) and de Pury and Farquhar (1997). Net photosynthetic carbon assimilation at the leaf level is given by the equation:

$$A = \min(A_v, A_j) - R_{ml}, \quad (19.3)$$

where A_v is the Rubisco limited rate of photosynthesis, A_j is the electron transport limited rate of photosynthesis and R_{ml} is the leaf maintenance respiration. A_v is calculated using

$$A_v = \frac{V_{max} \cdot (P_C - \Gamma)}{P_C + K_C \cdot (1 + \frac{P_O}{K_O})}, \quad (19.4)$$

where V_{max} is the Rubisco maximum rate per unit leaf area, P_C is the partial pressure of CO_2 within the leaf, Γ is the CO_2 compensation point of photosynthesis, K_C is the Michaelis-Menten constant of Rubisco for CO_2 , P_O is the partial pressure of O_2 and K_O is the Michaelis-Menten constant of Rubisco for O_2 . V_{max} is defined as:

$$V_{max} = \frac{N_l \cdot N_{IR} \cdot Act_R}{N_R}, \quad (19.5)$$

whereby N_l is the leaf N content per unit leaf area, N_{IR} is the proportion of leaf N contained in Rubisco, N_R is the fraction of N in Rubisco and Act_R is the Rubisco activity. Act_R is calculated from the Rubisco activity at $25^\circ C$ (Act_{R25}), the Q_{10} for Rubisco activity (Q_{10R}) and temperature (t):

$$Act_R = Act_{R25} \cdot Q_{10R}^{\frac{t-25}{10}} \text{ if } t > 15^\circ C, \quad (19.6)$$

$$Act_R = Act_{R25} \cdot Q_{10R}^{\frac{t-15}{10}} \text{ if } t \leq 15^\circ C. \quad (19.7)$$

The Michaelis-Menten constants K_O and K_C also exhibit temperature dependence and are

calculated from their respective values at $25^\circ C$ (K_{O25} , K_{C25}) and the respective Q_{10} -values

$$K_O = K_{O25} \cdot Q_{10O}^{\frac{t-25}{10}}, \quad (19.8)$$

$$K_C = K_{C25} \cdot Q_{10C}^{\frac{t-25}{10}} \text{ if } t > 15^\circ C, \quad (19.9)$$

$$K_C = K_{C25} \cdot Q_{10C}^{\frac{t-15}{10}} \text{ if } t \leq 15^\circ C. \quad (19.10)$$

The CO_2 compensation point (Γ) is calculated under the assumption that the ratio of maximal oxygenase and carboxylase activity of Rubisco equals 0.21 (Wullschlegel, 1993):

$$\Gamma = \frac{0.21 \cdot P_O \cdot K_C}{2 \cdot K_O}. \quad (19.11)$$

The electron transport-limited rate of photosynthesis A_j is calculated as

$$A_j = \frac{J \cdot (P_C - \Gamma)}{4.5 \cdot P_C + 10.5 \cdot \Gamma}. \quad (19.12)$$

Here J is the rate of electron transport per unit leaf area and is given by

$$J = J_{max} + PHAR \cdot \frac{p_{abs}}{ppe} - \sqrt{\frac{(-J_{max} - PHAR \cdot \frac{p_{abs}}{ppe})^2 - 4 \cdot 0.7 \cdot J_{max} \cdot \frac{p_{abs}}{ppe}}{2 \cdot 0.7}}, \quad (19.13)$$

where J_{max} is the potential rate of electron transport defined as

$$J_{max} = 2.1 \cdot V_{max}. \quad (19.14)$$

PHAR is photosynthetically active radiation, p_{abs} is the leaf absorption coefficient defining the fraction of PHAR effectively absorbed by the leaves and ppe is the amount of photons absorbed by photosystem II per electron transported.

2. Ground Water Infiltration

Infiltration of ground water may be calculated based on the deviation of soil water potential from water potential at field capacity, which equals the amount of energy available for water ascent (Pietsch et al., 2003). Soil water potential consists of two different forces, which counter-act on vertical ground water movement. The first,

gravitation, acts downwards, and the second, soil matric potential, which is given by the deviation from the matric potential at field capacity, is directed upwards. The sum of both forces drives water infiltration from the ground water table into the rooting zone. The amount of water ascent per day depends on soil hydraulic conductivity. The calculation (see Pietsch, 2003) starts from the deviation of water potential from field capacity ($\Delta\Psi$) given by

$$\Delta\Psi = \frac{\mu_{fc} - \mu_{act}}{\overline{V}_w}, \quad (19.15)$$

whereby μ_{fc} is the chemical potential of soil water at field capacity, μ_{act} is the chemical potential of soil water at the actual water content and \overline{V}_w is the partial molal volume of water which is always close to $1.8 \times 10^{-5} \text{ m}^3 \text{ mol}^{-1}$. Since water has no net charge, the electrical term of the chemical potential can be neglected, thus leaving μ_{fc} and μ_{act} as

$$\mu_{fc} = \mu^* - \overline{V}_w \Pi_{fc} + \overline{V}_w P_{fc} + mgh_1, \quad (19.16)$$

$$\mu_{act} = \mu^* - \overline{V}_w \Pi_{act} + \overline{V}_w P_{act} + mgh_2, \quad (19.17)$$

where μ^* is the arbitrary reference potential, Π_{fc} and Π_{act} are the matric potential at field capacity and actual soil water content, P_{fc} and P_{act} are the hydrostatic pressure difference between atmosphere and soil water content at field capacity and at actual soil water content, m is the molar mass of water, g is the rate of gravitational acceleration and h_1 and h_2 are the potential heights of soil water, which will be explained in Eq. (19.21).

The soil matric potential is calculated from soil texture data using an equation fitted by Brooks and Corey (1964) in a simplified form as used by Clapp and Hornberger (1978),

$$\Pi_{act} = \Pi_{sat} \cdot \left(\frac{\Theta_{act}}{\Theta_{sat}} \right)^{-b}, \quad (19.18)$$

with Π_{act} and Π_{sat} as the matric potential, Θ_{act} and Θ_{sat} as the volumetric water content at actual and saturation soil water content, respectively, and b the slope of the retention curve (see Cosby et al., 1984).

By substituting Eqs. (19.16) and (19.17) into Eq. (19.15) the reference potential and the hydrostatic pressure terms are cancelled out, thereby

explicitly excluding differences in hydrostatic pressure as possible cause of water ascent. This leaves Eq. (19.15) in the form

$$\Delta\Psi = \frac{\overline{V}_w(-\Pi_{fc} + \Pi_{act}) + mg(h_1 - h_2)}{\overline{V}_w}. \quad (19.19)$$

Since mass equals density multiplied by volume, the partial molal volume can be removed and Eq. (19.19) can be rewritten as

$$\Delta\Psi = (-\Pi_{fc} + \Pi_{act}) + \rho_w g(h_1 - h_2), \quad (19.20)$$

where ρ_w is the density of soil water and is set to $1,000 \text{ kg m}^{-3}$, as an approximation over the possible temperature range of soil water ($1,000$ at 4°C and less than 0.5% deviation between -30 and $+30^\circ\text{C}$).

When calculating the gravitational force, the difference in potential soil water height needs to be defined. The potential height is the increase in potential energy in accordance with vertical water ascent, which occurs when the soil water content is below field capacity. The calculation is based on the deviation of the actual soil water content from the soil water content at field capacity. Soil water mass is converted into soil water volume using the approximation for ρ_w given above, which changes the units from $[\text{kg m}^{-2}]$ to $[\text{m}^3 \text{ m}^{-2}]$ or simply $[\text{m}]$. The division of this number by the porosity at field capacity gives the potential height of soil water. Formally $h_1 - h_2$ is then defined by

$$(h_1 - h_2) = \frac{sw_{fc} - sw_{act}}{1000 \cdot \Theta_{fc}}, \quad (19.21)$$

where sw_{act} and sw_{fc} are the actual soil water content and the soil water content at field capacity $[\text{m}]$, respectively, and Θ_{fc} is the volumetric water content at field capacity, which equals the non drainable porosity. The actual amount of ground water (gw_{in}) entering the rooting zone per unit time is given by

$$gw_{in} = K \cdot \Delta\Psi \quad (19.22)$$

with $\Delta\Psi$ indicating the overall force acting on ground water as defined in Eqs. (19.20) and (19.21) and where K is the soil hydraulic conductivity coefficient, calculated from the soil texture and actual soil water content according to Saxton et al. (1986):

$$K = 2.778 \cdot 10^{-6}$$

$$\cdot \exp \left(a_0 + a_1 \cdot \%s + \frac{a_2 + a_3 \cdot \%s + a_4 \cdot \%c + a_5 \cdot \%c^2}{\Theta_{\text{act}}} \right), \quad (19.23)$$

whereby $\%s$ and $\%c$ give the percentages of sand and clay, a_0 – a_5 are the coefficients calculated via multiple nonlinear regression techniques (see Saxton et al., 1986), and Θ_{act} is the actual volumetric water content.

3. Mortality

Studies on the temporal development of mortality rates in production forests revealed that mortality rate follows a U- or J-shape versus stand age (see e.g. Harcomb, 1987; Peterken, 1996; Lorimer et al., 2001; Monserud and Sterba, 2001). Under undisturbed conditions mortality rate decreases from regeneration via juvenescence and reaches a minimum during the optimum phase of ecosystem development. Mortality increases again, towards the old growth and breakdown stages. Under undisturbed conditions, the U-shaped development of mortality can be assumed (Pietsch and Hasenauer, 2006). Since the death of old biomass-rich individuals creates space for regeneration, the two ends of the “U” – shape will overlap. Hence, a trajectory consisting of two individually scaled half-ellipses can be used to describe the temporal evolution of the mortality rate (Fig. 19.2). Formally, both ellipses are given by

$$\frac{(x - c_x)^2}{a^2} + \frac{(y - c_y)^2}{b^2} = 1, \quad (19.24)$$

where c_x , c_y are the x- and y coordinates of the centre of the respective ellipse, a and b are the two semi-axes, x is time and y is the mortality rate. Solving this quadratic equation for y gives

$$y = c_y \pm \frac{b}{a} \sqrt{a^2 - x^2 + 2xc_x - c_x^2}. \quad (19.25)$$

The semi-axes a , b and the center coordinates c_x , c_y of the ellipse can be expressed as

$$a = c_x = \frac{T}{2}, \quad (19.26)$$

$$b = \frac{mort_{\text{max}} - mort_{\text{min}}}{2}, \quad (19.27)$$

$$c_y = b + mort_{\text{min}} = \frac{mort_{\text{max}} + mort_{\text{min}}}{2}, \quad (19.28)$$

where T is the length of the low or high mortality phase, and $mort_{\text{max}}$ and $mort_{\text{min}}$ are the maximum and minimum mortality rates. Substituting the Eqs. (19.26), (19.27) and (19.28) into Eq. (19.25) results in

$$y = \frac{mort_{\text{max}} + mort_{\text{min}}}{2} \pm \frac{mort_{\text{max}} - mort_{\text{min}}}{T} \cdot \sqrt{T \cdot x - x^2}. \quad (19.29)$$

In Eq. (19.29) the first right hand term is the mean annual mortality rate. The second right hand term governs the changes along the mortality cycle. Subtraction gives the trajectory of the low mortality phase and addition gives the trajectory of the high mortality phase (Fig. 19.2). The parameters $mort_{\text{max}}$, $mort_{\text{min}}$ and T vary by species and site and climate conditions and may be set for each stand separately or generalized for a watershed or region.

C. Model Parameters

The parameters of complex large-scale ecosystem models define key properties of the modeled ecosystem. Model parameters include (i) allometric parameters, regulating the allocation of carbon assimilated via photosynthesis to the different root and shoot compartments, (ii) turnover and mortality parameters, describing the portions of the plant pools that are either replaced each year or removed through plant death, (iii) N/C

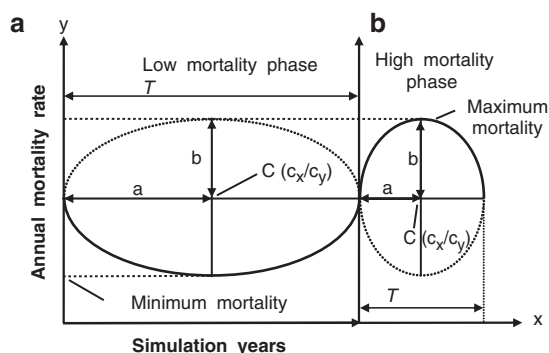


Fig. 19.2. The trajectory of mortality (bold line) along the lower half (a) and upper half (b) of two individual ellipses. The x and y axes denote time and mortality rate, respectively. $C(c_x/c_y)$ are the coordinates of the centers of the ellipses, a and b are the two half-axes, T is the length of each mortality cycle along the half-ellipses (Pietsch and Hasenauer, 2006)

ratios, which define nutrient requirements for new growth, photosynthetic capacity, plant respiration rates and litter quality, (iv) percentages of lignin, shielded and unshielded cellulose, and labile material in fine roots, leaves and dead wood, controlling litter recalcitrance and influencing decomposition rates, (v) morphological parameters, which define the distribution of LAI at the leaf and canopy level, (vi) single parameters that define water interception, canopy radiation absorption and the time span of transfer growth and litter fall, as proportions of the growing season and (vii) ecophysiological parameters, controlling rates and limitations of leaf conductance for water and carbon dioxide. Ecophysiological parameters are a special case because they follow fast dynamics and their values have to be chosen according to the temporal resolution of the model implementation (see Section III.E).

According to the type of model application, the values of the parameters reflect either general plant functional types (biomes) such as evergreen needle leaf (ENF), deciduous needle leaf (DNF), deciduous broadleaf (DBF), evergreen broadleaf (EBF), C_3 grass, etc. or they represent specific ecosystems dominated by a single species (e.g. beech or spruce forests, etc.) or an ecosystem specific assembly of species (e.g. arid grasslands, temperate pastures and meadows or tropical savannas). The restriction to certain biomes is logical for assessing the fluxes of energy, water, carbon and nitrogen on a continental or global scale. If the same information is required at the

regional to local scale, specific ecosystem parameters may be needed and useful. This is especially important in large parts of Europe where historic land use as well as a silvicultural management practices strongly have affected the species distribution and the structure of central European forests (Spiecker et al., 2004). Different species have different impacts on site quality due to species-specific differences in litter production, chemistry and decomposition rates contributing to the quantity of nutrients cycled between vegetation and soil (Schlesinger, 1997; Finzi and Schlesinger, 2002).

For Central Europe, parameter sets exist for grasslands, meadows and pastures (Pietsch and Hasenauer, 2003) and the major forest types like Common beech, Sessile/pedunculate oak, European larch, Cembran pine, Scots pine and Norway spruce forests, the latter represented by two different parameter sets to cover the different ecophysiology of highland and lowland spruce variants (Pietsch et al., 2005). An example for biome specific parameter sets is given in White et al. (2000).

D. Model Drivers

Model drivers may be distinguished as (i) static, (ii) slow or (iii) rapidly changing variables. Static input variables are elevation, slope and aspect as well as soil depth and soil texture. Static model drivers are site-specific properties that do not change during a simulation. Soil depth and soil texture determine the soil water outflow, retention and evaporation and influence plant water uptake. If not measured they may be interpolated from surrounding sites using Kriging techniques (Petritsch and Hasenauer, 2007). Slope and aspect define the exposition that is important for solar radiation input. Elevation determines the atmospheric pressure and thereby influences the partial pressures of atmospheric CO_2 and water vapor. A lower partial pressure of CO_2 decreases the amount of external CO_2 -molecules and hence the thermodynamic gradient between intracellular CO_2 and external atmospheric CO_2 , i.e. the driving force for CO_2 uptake. Exactly the opposite is evident for H_2O because the transport of water moves in the opposite direction as CO_2 . While the intracellular amount of water will always be close to 56 mol l^{-1} , the amount of

external atmospheric water molecules is reduced under lower atmospheric pressures. Slope aspect and elevation may be known from on site determination, or it may be taken from digital elevation maps.

Slow dynamic model drivers change from year to year. A typical example is the nitrogen deposition rate, which depends on regional topography, wind direction and the precipitation regime. The levels of this parameter have increased substantially since pre-industrial times. Historical nitrogen deposition is published by Holland et al. (1999), or for Central Europe by Ulrich and Williot (1993). Present day nitrogen deposition data for Central Europe is available from regional interpolations using data from permanent field stations (e.g. Schneider, 1998). Another slow model driver is the increase in atmospheric CO₂ concentration, which is a global property and does not change from plot to plot. Historical records of atmospheric CO₂-concentration are available from ice core measurements (Petit et al., 1997, 1999; Etheridge et al., 1996) and from measurements in recent decades (Keeling et al., 1989).

Model inputs with fast dynamics are meteorological variables, such as temperature, precipitation, radiation and vapor pressure deficit, which change within less than a daily time step. These data may be available from measurements, or may be extrapolated from the nearest climate station (Thornton et al., 2000). Another option is provided by interpolation of data from multiple climate stations using Gaussian filters (Hasenauer et al., 2003) or Kriging methods (Petritsch and Hasenauer, 2007). Sometimes meteorological input data is generated using statistical methods, such as the Markov chain approach (Richardson and Wright, 1984; Racsko et al., 1991; Semenov et al., 1998) or dynamic methods such as atmospheric circulation models (Tiedtke, 1989; Collins et al., 2002).

E. Temporal Model Resolution

Model drivers induce fluxes amongst the pools by changing the size of each pool. The length of the time step of the recursion defines the temporal resolution within the model. For large scale models it may range from one second (ORCHIDEE,

Krinner et al., 2005) to one month (TEM, Melillo et al., 1993), typically it is one day (LPJ, Sitch et al., 2003; Biome-BGC, Thornton, 1998; MC1, Bachelet et al., 2001). Regardless of the chosen time step the model drivers with fast dynamics have to be adapted to fit the time step. For meteorological drivers this adaptation is achieved by averaging the values over the time step that is implemented in the model. For a daily time step e.g., day time air temperature (t_{day}), which affects leaf temperature during photosynthesis, may be estimated from the daily minimum and maximum air temperature (t_{min} , t_{max}) as

$$t_{\text{day}} = 0.45 \cdot \left(t_{\text{max}} - \frac{t_{\text{min}} - t_{\text{max}}}{2} \right) + \frac{t_{\text{min}} - t_{\text{max}}}{2}. \quad (19.30)$$

Other meteorological model drivers may be fitted to a daily time step by averaging the values over the length of the daylight period. The length of the daylight period may be calculated from daily earth-sun geometry and the position on earth (Carbone, 2007). The amount of daily photosynthetic carbon assimilation is then calculated using t_{day} in Eqs. (19.6)–(19.10) for Rubisco limited photosynthesis or mean daytime radiation in Eq. (19.13) for electron transport limited photosynthesis. The minimum of both (see Eq. 19.3) is then multiplied with the length of the daylight period in order to give an estimate for photosynthetic carbon assimilation over the modeled time step (e.g. 1 day). Note that the average output value of nonlinear functions (e.g. photosynthesis rate) may not match the output value achieved by using average values of variables (e.g. for radiation or temperature) in nonlinear equations. For a daily time step, the calculated value may be lower or higher versus the average output value of the non linear function. It is important to check that the averaging procedure does not lead to differences in the mean values of the nonlinear function if calculated over multiple simulation steps (see e.g. Fig. 19.8).

A similar averaging approach is applied to the ecophysiological parameters controlling stomatal conductance (g) to water vapor and CO₂. Stomatal conductance has an upper limit (g_{max}) which is down-regulated to actual stomatal conductance (g_{act}) by environmental factors, such as leaf water

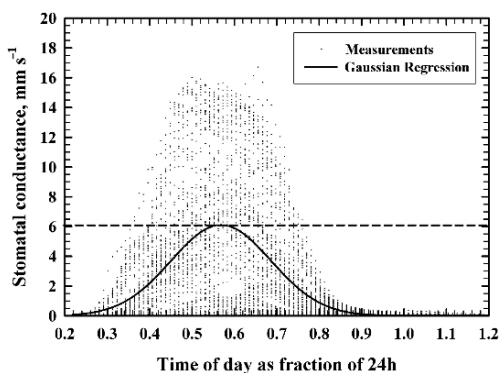


Fig. 19.3. Stomatal conductance of Common beech in Kreisbach, Austria. Measurements were performed every 15 min throughout the growing season 1999. The maximum of the daily average stomatal conductance used in a model with a daily time step results from the peak of a Gaussian regression as indicated by the dashed line. For Common beech the value of the maximum of daily average stomatal conductance equals 6 mm s^{-1} .

potential (Ψ), previous minimum air temperature, daytime vapor pressure deficit (vpd) and radiation (PHAR):

$$g_{\text{act}} = g_{\text{max}} \cdot m_{\text{tmin}} \cdot m_{\text{vpd}} \cdot m_{\Psi} \cdot m_{\text{PHAR}} \quad (19.31)$$

The variables m_x are multipliers with values between 0 and 1, which are used to reduce g_{max} to g_{act} . Since radiation and vapor pressure deficit are mean values for a given time step the parameter g_{max} also needs to be averaged for the time step. Fig. 19.3 illustrates this averaging step for daily g_{max} of Common beech as previously outlined.

IV. Model Application

In this section the principles of model application within different spatial and temporal scales will be presented as follows: (i) precursor modeling steps to model a current ecosystem's behavior, (ii) tests for model sensitivity, (iii) how a large scale ecosystem modeling may be validated, and (iv) how model dynamics may be assessed.

A. Application Procedure

Model applications often begin with the assumption that undisturbed conditions exist as they would within a virgin ecosystem (Pietsch and Hasenauer, 2002). This initial state assumes that human management activities are absent and

the ecosystem has had sufficient time to reach its dynamic equilibrium. In models the virgin ecosystem conditions are achieved by so called self initialization procedures. During self initialization the model is run until the running average of each model output approach steady state. The time scale for averaging is the length of one complete mortality cycle. In model implementations, the possibly infinite time needed to reach the steady state is shortcut by comparing the averages of soil carbon content. Soil carbon content is the last among the pools reach a steady state, and self initialization is terminated when the average soil carbon content differs by less than 0.5 g C m^{-2} between two successive mortality cycles.

The results of the self initialization procedure need to be corrected for possible degradation effects due to changes in land use and ecosystem management (Pietsch and Hasenauer, 2002). Conceptually, this step is essential, as historic land management may have led to a decline in nutrient status and soil fertility (Mayer and Ott, 1991; Ott et al., 1997). Therefore, scenarios of historical land use are assumed, and simulated, as part of the model initialization process (Pietsch et al., 2005) prior to the actual simulation run. A typical historical land use scenario for Central Europe is the assumption that repeated clear cuts have occurred at intervals of 20 (coppice systems), 100 (Norway spruce ecosystems) or 200 years (Cembra pine ecosystems). Fig. 19.4 depicts the conceptual outline and the corresponding modeling steps.

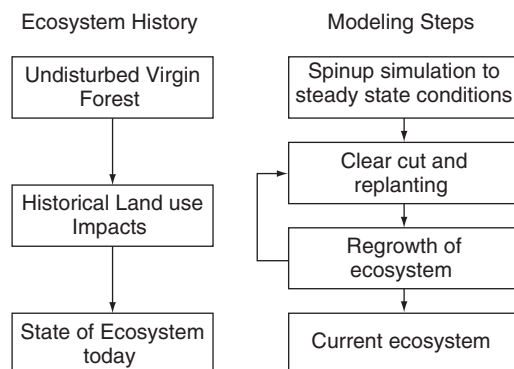


Fig. 19.4. The historical development of a typical ecosystem in Central Europe from undisturbed virgin forest conditions, via intensive historical land use to the state of the ecosystem today, and the modeling steps mimicking this development (Pietsch et al., 2005)

B. Sensitivity

The sensitivity of a large scale ecosystem model is a property, which describes the range of model predictions caused by variations in model parameters and model drivers. It may be assessed by a partial, full or complete sensitivity analysis.

In the partial sensitivity analysis single model parameters are tested, for example, by comparing with field observations. The resulting relative variation of model outputs (e.g. NPP, LAI, biomass carbon storage, etc.) is then related to the relative variation of the chosen input parameter. An evident constraint of this approach is that the sensitivity of the model with respect to a single parameter varies depending on the values of other parameters and site and climate conditions. For example, in tropical forests, generally stocking on deep clayey soils and frequent rainfall throughout the year, the parameters determining stomatal conductance (soil water potential and atmospheric VPD) have a low impact on the stomatal conductance and on the model performance. In forests stocking on shallow sandy soils with extended periods without rainfall, stomatal conductance and other model outputs will be highly sensitive to these parameters. In alpine forest ecosystems, the low minimum temperatures may become the key controlling parameter for stomatal conductance (Pietsch and Hasenauer, 2005b). Model sensitivity to this parameter may mask the sensitivity to soil water potential or VPD; therefore, partial sensitivity analysis is a useful tool when (i) the ecosystem type is well defined, (ii) the range of site conditions is known and (iii) the temporal variation in model drivers can be estimated. Partial sensitivity analysis may also be used in estimating the parameters of processes added to the model algorithm. This assumes that all other parameters are defined or derived from previously validated model runs. In such cases, new parameters are varied along a grid of reasonable values in order to select the values with the best fit compared to real observations (Pietsch and Hasenauer, 2006).

Full sensitivity analysis uses sets of randomly selected model parameters. Each set of parameters is used for model simulations across the estimated range in site and climate conditions using Monte Carlo methods. Full sensitivity analysis is

useful if the ecosystem is poorly defined. It may be used to assess the type of ecosystem which occurs under certain site-specific and climatic conditions. This approach may be considered as an optimization procedure; however, the results have to be interpreted carefully since nonlinear systems such as ecosystem models may exhibit several solutions. Note that not all ecosystems which could occur under given site and climate conditions, are the result of evolutionary, human and/or random impacts and constraints.

Complete sensitivity analysis is done by varying model parameters, site conditions and model drivers. This approach is the most thorough test of model sensitivity and allows one to theoretically explore which ecosystems may emerge under certain physical, site-specific and climate constraints.

C. Validation

A large-scale ecosystem model together with its parameters resemble a formalized, scientific hypothesis of observable real-world phenomena. Since the work of Popper (1935) it has become widely accepted that scientific hypotheses must be falsifiable. A hypothesis that cannot be falsified by observations is a belief, and as such it is not a scientific result. With respect to large scale ecosystem models, falsification is accomplished by comparing predictions versus field observations and error assessment.

Model errors have several reasons. Firstly, ecosystem models always represent an abstraction and simplification of reality; they can not take all ecosystem processes into consideration. Secondly, the temporal resolution of the model (see Section III.E) may vary between one second (ORCHIDEE, Krinner et al., 2005), 1 day (LPJ, Sitch et al., 2003; Biome-BGC, Thornton, 1998; MC1, Bachelet et al., 2001) and one month (TEM, Melillo et al., 1995). Additionally, the accuracy of field observations contributes to model errors. All instruments and methods exhibit uncertainties in measurement. Lastly, the lack of complete information about the status of an ecosystem when model application begins (see Section III.A) is likely one of the most important uncertainties in model application.

Within model validation, criteria are necessary to help with the assessment of the accuracy,

precision and bias of predictions. Model accuracy is described by the mean error and is calculated as the difference between the mean of predictions and the mean of observations. Precision is the variation of the errors versus the mean error. A model is biased if the predicted mean is significantly different from the observed mean. One option to determine model error ranges and their limits is to calculate the confidence, prediction and tolerance intervals of predictions as described by Reynolds (1984). The confidence interval CI for the mean of the differences can be used to evaluate discrepancies between the observed and estimated mean. The prediction interval PI can be interpreted as the range of the differences among predictions versus observations. The tolerance interval TI provides the limit that contains a specified portion (e.g. 95%) of the distribution of the differences when the model is used repeatedly. This type of error assessment requires normal distribution of model errors.

D. Dynamic Model Behavior

Large-scale ecosystem models describe the dynamics of physical, chemical and biological processes within ecosystems. Classical methods of model validation (see Section IV.C) capture static aspects of the model but fail to assess model dynamics. Like ecosystems themselves, ecosystem models may exhibit stable, instable or chaotic dynamics (Pietsch and Hasenauer, 2005a, 2006). The assessment of the type of prevailing model behavior may be done using methods from ergodic theory (Eckmann and Ruelle, 1985). The word ergodic is a combination of the Greek words for work (ergon) and path (odos) and was first used in statistical mechanics, when Boltzmann (1877) used probability to define entropy. Later, Poincaré (1982) studied the stability of the dynamics of planetary orbits and found that consecutive orbits differed in length and shape (see Fig. 19.5a), i.e. where not periodic but quasi-periodic. The most important finding by Poincaré was that the behavior of a dynamic system may be analyzed by (i) inserting a single plane orthogonal to the flow of the trajectories (Fig. 19.5b), and (ii) by looking at the return of the system's trajectory within the plane after traveling a full quasi period (Fig. 19.5c).

He suggested that the orbital dynamics are stable when the intersection points stay within a limited area of the plane and that the orbital dynamics have to be considered as unstable if they leave this area. This approach to analyze dynamic systems is called a Poincaré map, which contains all the information to characterize the dynamics of the system, but only provides a one dimensional time series (Ruelle, 1995). Ruelle (1978) proposed that the Poincaré map provides the contour or silhouette of the space attracting the system and suggested that if one looks at this silhouette from different directions a multidimensional picture of system behavior will emerge. He reached this effect by grouping consecutive points of the Poincaré map in n -tuples, i.e. ordered sets of pairs (2-tuples), triplets (3-tuples), etc. The mathematical proof of Ruelle's assumption was provided by Takens (1981). The n -tuples created using the Ruelle-Takens transformation may be drawn in an n -dimensional graph depicting the full dynamics of the system, where n denotes the degrees of freedom of the system and is equal to the number of dynamic system drivers minus one. Such graphs are called attractors and provide an opportunity to visually distinguish between stable and unstable dynamics.

The Poincaré map and the Ruelle-Takens transformation may also be applied to the outputs of large scale ecosystem models, because the models are driven by daily weather values which resemble climate. Climate is a quasi periodic system (Broer et al., 2002), because it is similar from year to year, but always a little different in the temperature and precipitation profiles which is responsible for the different lengths of successive growing seasons. The quasi periodicity of model inputs is transferred to the model outputs. For model outputs the length of one quasi period may be determined as the time span between the start of the growing season to the start of the next growing season. Fig. 19.5d provides an example of an attractor reconstructed from modeled NPP of 22 Cembran pine stands from the time of planting (between 1748 and 1932) up to the year 1998. The attractor is embedded in a three-dimensional graph because three out of seven dynamic model drivers (minimum temperature, maximum temperature, precipitation, PHAR, VPD, CO₂ concentration and nitrogen deposition; see Section III.D) are calculated from the others: PHAR

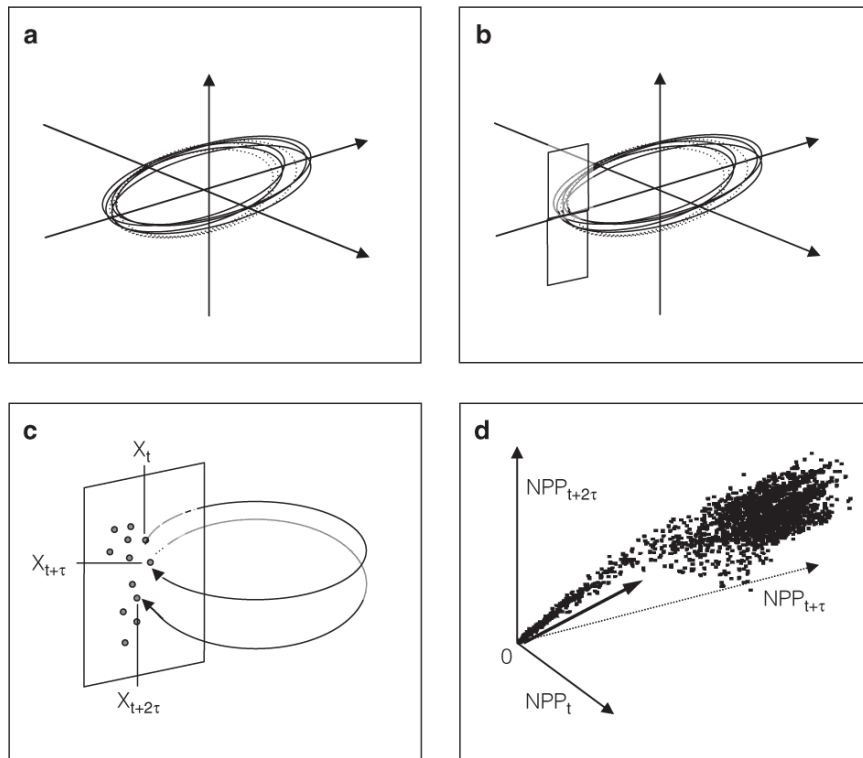


Fig. 19.5. a: Quasi periodic motion of a planet in space. The cycle length τ varies among the individual turns. *b:* Placing a plane at one position of the orbit and plotting the points in the plane. *c:* The points where the systems trajectories cross the plane give the Poincaré map of the system, i.e. the series of points $X_t, X_{t+\tau}, X_{t+2\tau}, \dots$. The points of the Poincaré map can be seen as a one dimensional time series. *d:* A Ruelle-Takens transformation groups consecutive points of the Poincaré map into an ordered sets of n -tuples $\{(X_t, X_{t+\tau}, \dots, X_{t+n\tau}), (X_{t+\tau}, X_{t+2\tau}, \dots, X_{t+(n+1)\tau}), \dots\}$ representing the attractor of system behavior. The attractor shown here was reconstructed from NPP predictions for 22 Cembran pine plots planted between 1,748 and 1,932 close to Murau, Austria. The attractor was embedded in a three-dimensional system since the simulation was run with four independent model drivers resulting in three degrees of freedom (see text). The time of planting (lowest NPP values) resembles the source of the NPP attractor. The arrow indicates the direction of stand development over time. The attraction basin enlarges at higher NPP values when canopy closure increases the competition for resources (Pietsch and Hasenauer, 2005a)

and VPD are calculated from (i) minimum and (ii) maximum temperature and (iii) precipitation (Hasenauer et al., 2003) and the increase in nitrogen deposition is derived from (iv) the increase in CO_2 concentration. This results in four independent model drivers, three degrees of freedom or a three-dimensional system for embedding the attractor. A detailed description for the application of this attractor reconstruction procedure is given in Pietsch and Hasenauer (2005a).

Typical examples of ecosystem and ecosystem model behavior are sources, sinks, limit cycles, saddles or riddled basins. Large-scale ecosystem models are stable when the attractor configuration is a source, a sink or a limit cycle. In such situations model behavior is fully

deterministic. Model behavior is unstable when saddle-like attractor configurations occur, as the model becomes very sensitive to small variations in early conditions of simulation and diverging final results cannot be predicted, but must be explained only after the simulation run. Examples of such model behavior come from studies on lake eutrophication in which the ecosystem exhibits a sudden shift from standard dynamics to algal blooms (Scheffer et al., 2001). Such model behavior is called post-deterministic. Model behavior must be classified as chaotic when retrospective explanation of diverging model results is not possible due to statistically indistinguishable earlier conditions. In such cases model application is meaningless.

V. Examples of Model Application

This section presents three modeling examples referring to the application procedures outlined in Section IV. The first example will deal with virgin forest conditions, the second example will address the necessity of ecosystem specific parameter choice for model validation and the third example will demonstrate the assessment of model dynamics.

A. Application to Virgin Forests

Among real world ecosystems, virgin forests resemble the best approximation of natural conditions. Natural conditions refers to (i) the absence of human exploitation of forest resources such as timber, litter, fruits, resin or water and (ii) the absence of silvopastoral-, pathogen- or game-management practices. Here we present a model application example of the central European virgin forest reserve Rothwald, a first-category IUCN wilderness area with a documented absence of logging and forest management for more than 700 years (Pietsch and Hasenauer, 2006). Rothwald is one of the last virgin forest areas in the Alps and covers approximately 250 ha of unmanaged forest with different successional stages from regeneration to optimal and breakdown phases. In virgin forests such as Rothwald a mosaic of different stages shifts over time, but the abundance of all stages remains constant if the region is large enough (Heinselman, 1973). The 'mosaic cycle' concept of ecosystems (Remmert, 1991) assumes the maintenance of an overall steady state at the landscape level with local disequilibria due to vegetation dynamics. Rothwald resembles such a mosaic cycle and provides an excellent test case for the accuracy of the self-initialization procedure of complex large scale ecosystem models.

We first collected data on stem, soil and necromass carbon and nitrogen content from 18 permanent field plots across all successional stages. Next, we ran standard model self-initialization using a constant annual mortality rate of living biomass. Model predictions for the 18 sites, on average exhibited an overestimation of ecosystem carbon content of up to 400% (Pietsch and Hasenauer, 2006). The inconsistency of model results was due to the assumption of constant mortality. When mortality is kept

constant, the ecosystem remains a net carbon sink until a steady state is established at ecosystem carbon saturation; however, in the real world an ecosystem exhibits a life cycle from regeneration via juvenescence to optimal growth, old growth and breakdown. During the early phases of an ecosystem's life cycle concurrence among individuals is high, which results in the death of individuals not fit enough to survive the competition with stronger individuals. In such situations mortality is high and the number of individuals declines. This competition induced mortality rate decreases until the trees reach the physiologic limitation of their life cycle. The remaining big trees die and biomass mortality is high. The open space will then be covered by regeneration and the next successional cycle begins.

Based on these successional principles a dynamic mortality routine as outlined in Fig. 19.2 may be used. For estimating the parameters of minimum and maximum annual mortality rate of vegetation biomass partial sensitivity analyses were used by testing minimum annual mortality rates between 0.5% and 2.5% and maximum annual mortality rates between 0.5% and 15%. The results of this calibration procedure were 0.9% minimum and 6% maximum annual mortality rate (Pietsch and Hasenauer, 2006), and using these settings the model delivered unbiased results for the mosaic cycle represented by the virgin forest reserve Rothwald (Fig. 19.6).

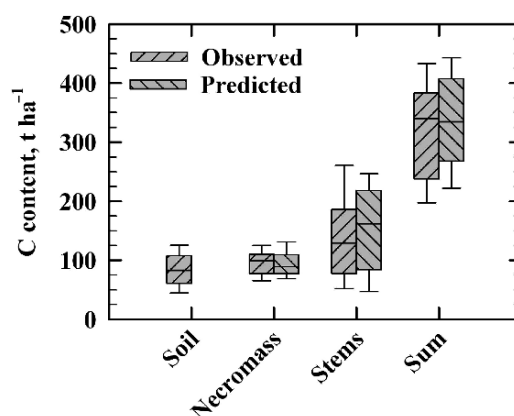


Fig. 19.6. Predicted compared to observed C content of soil, necromass, stems and their sum using the dynamic mortality model during self-initialization for the virgin forest reserve Rothwald in Austria. The boxes represent the 25% and 75% percentiles and the whiskers show the 10% and 90% percentiles of predictions and observations (Pietsch and Hasenauer, 2006)

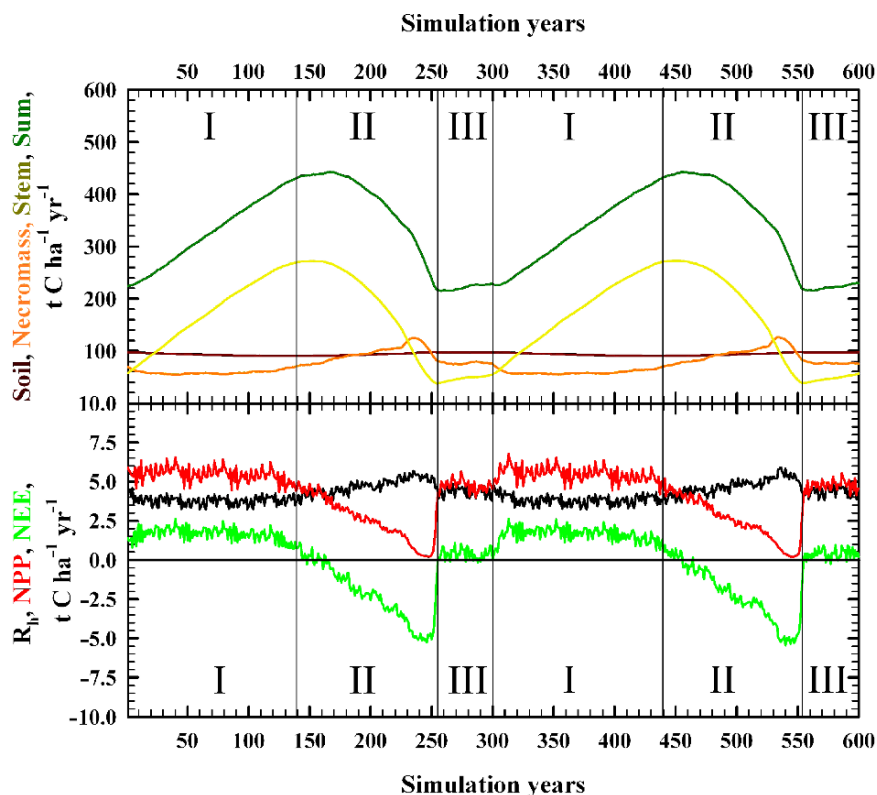


Fig. 19.7. Modeled pools and fluxes for the virgin forest reserve Rothwald using model parameters for Common beech forests. Upper graph: Comparison of the temporal development of modeled soil, necromass, stem and total ecosystem carbon content for 600 simulation years at landscape level steady state. Lower graph: Corresponding annual C fluxes from heterotrophic respiration (R_h), net primary production (NPP) and net ecosystem exchange (NEE). I – optimum phase; II – breakdown/regeneration phase; III – juvenescence (Pietsch and Hasenauer, 2006). See also Color Plates, Fig. 5

Ecosystems exhibit periods in which they act as a net carbon sink (optimum phase), as carbon neutral (stationary phases with no net carbon exchange – old growth, juvenescence) and as a net carbon source (breakdown, regeneration). Such source-sink transitions are a part of natural ecosystem dynamics and they restrict complex large scale ecosystem models to the steady state at the landscape level. Fig. 19.7 presents an example of the development of carbon pools and ecosystem fluxes for two life cycles of one of the plots in the virgin forest Rothwald.

Figure 19.7 shows the simulation of the carbon dynamics of a virgin forest including periods in which the system acts as a C-source and a C-sink. The amount of carbon assimilated during the optimum phase of growth is released during breakdown and

regeneration phases. Over the complete life cycle of the virgin forest the net rate of carbon sequestration equals zero. This is an important result given that virgin forests are considered as the optimal stage of ecosystem carbon storage and are often seen as the reference for managed forests!

Although the goal of this study was to test and adjust the self initialization procedure as it is used within large scale ecosystem modeling, we demonstrated also the C sink and C source behavior of old growth forests. Regular timber extraction helps to keep a forest in the optimum phase of growth and at a high level of net ecosystem carbon sequestration via photosynthetic carbon assimilation. This is an issue of increasing importance in the context of climate change and mitigation measures.

B. Assessing Ecosystem Specific Model Parameters

Applications of ecosystem models at the continental or global scale use parameter sets capturing broad ecophysiological characteristics of plant functional types or biomes, such as evergreen needle leaf forests, deciduous broadleaf forests, temperate grasslands, tropical savannas, etc. One constraint of this approach is that in Europe as well as in many other parts of the world, historic land use and ecosystem management practices strongly affected ecosystem structure and species composition (Spiecker et al., 2004). Additionally, plant functional types restrict the integration of species-specific growth responses induced by forest management practices (e.g. tending, thinning, etc.). Such interventions change the biomass density within the forest and the growth of the remaining biomass

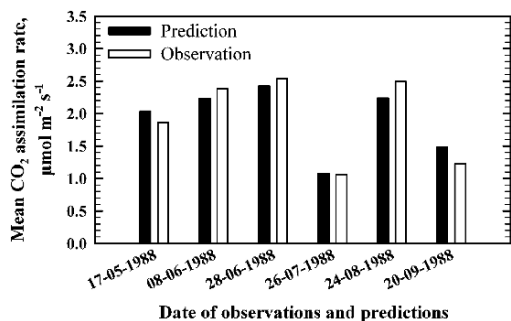


Fig. 19.8. Predicted and observed carbon assimilation rates of shade leaves of Common beech in Hochbuch, Vienna Woods, Austria. Assimilation rate is given on a m² leaf area basis. Observed values reflect the mean value of half-hourly measurements taken during the daylight period of the respective day (Pietsch and Hasenauer, 2002)

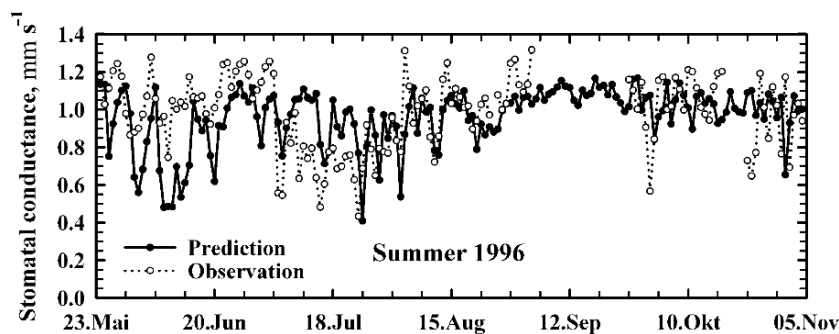


Fig. 19.9. Predicted and observed daily mean stomatal conductance of Cembran pine on Mt. Patscherkofel, Austria, during the summer 1996 (Pietsch and Hasenauer, 2005b)

is strongly sensitive to tree species (Assmann, 1970).

Within large scale ecosystem models, the type of ecosystem is defined by model parameters. Accordingly, a tree species may be defined by obtaining species-specific model parameters from the literature and/or from in-depth research sites. This information allows a “tuning” or “calibration” process for a given tree species. Typical examples of field observations and model predictions by tree species are given for daily mean CO₂ assimilation (Fig. 19.8), stomatal conductance (Fig. 19.9), transpiration and soil water content (Fig. 19.10). In our efforts to produce a species specific BGC model we established parameter sets for Common beech (*Fagus sylvatica*), pedunculate/sessile oak (*Quercus robur/petraea* agg.), European larch (*Larix decidua*), Scots pine (*Pinus sylvestris*), Cembran pine (*Pinus cembra*) and Norway spruce (*Picea abies*) forest ecosystems in central Europe. For Norway spruce, two different parameter sets were necessary to cover the physiological differences between highland (>1,000 m a.s.l.) and lowland (<1,000 m a.s.l.) variants. For details and the full set of parameters by species we refer to Pietsch et al. (2005).

Once such parameter set is established with data from intensive research plots in combination with published literature, the species specific model performance needs to be tested across the growing conditions of a species. The key is that the parameters defined using limited data need to produce unbiased and consistent results in large scale applications. Available data for this type of validation typically come from forest inventories (Fig. 19.11).

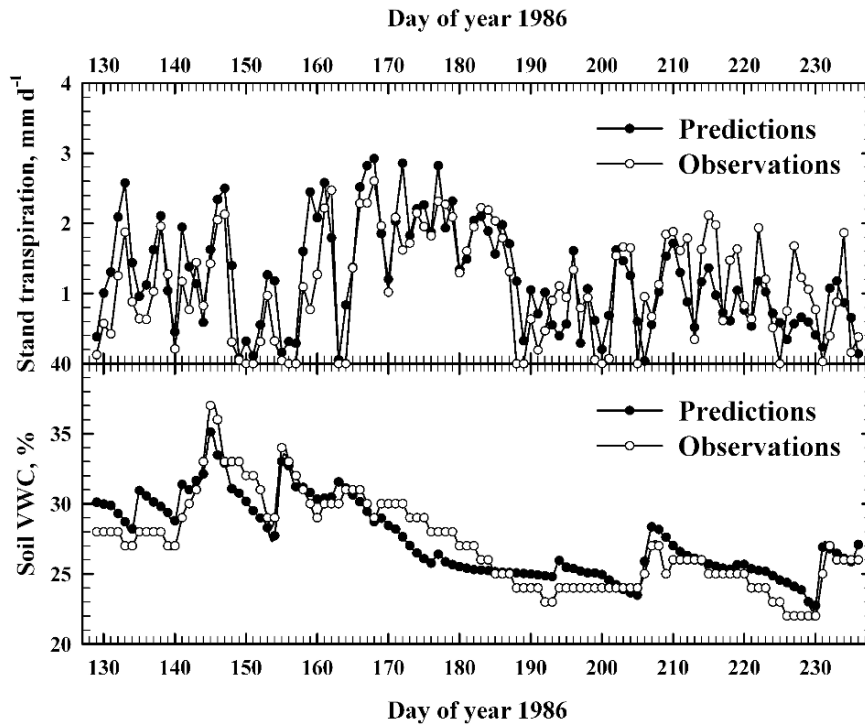


Fig. 19.10. Predicted and observed daily stand transpiration and soil volumetric water content (VWC) of a Norway spruce stand in Zebrakovsky creek, Czech Republic (Pietsch and Hasenauer, 2002)

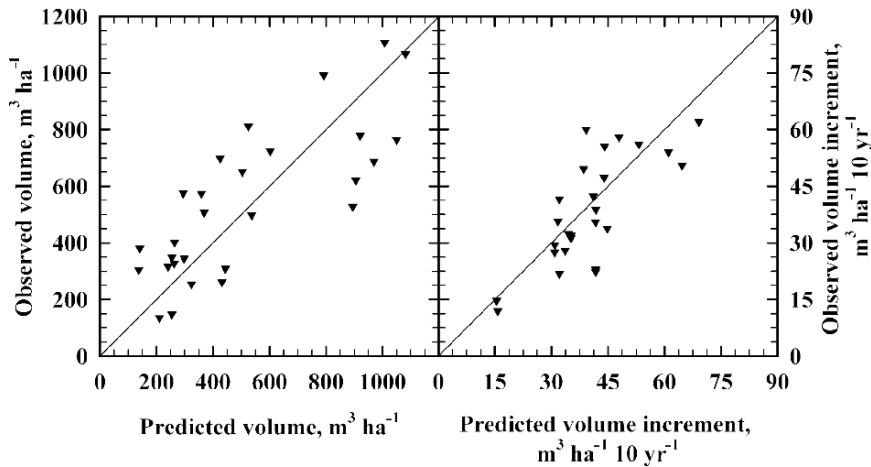


Fig. 19.11. Predicted and observed volume (*left*) and 10-year volume increment for 24 lowland stands of Norway spruce in Austria (Pietsch et al., 2005)

C. Assessing Model Dynamics

Model dynamics such as real world ecosystem dynamics may exhibit stable and unstable phases. The attractor represents system dynamics (see

Section IV.D). This section presents an example of stable ecosystem model behavior and explains the importance of analyzing the attractor of model dynamics. For an example of unstable model behavior we refer to Pietsch and Hasenauer (2005a).

The attractor shown in Fig. 19.12a represents the dynamics of modeled Net Ecosystem carbon Exchange (NEE) of the virgin forest successional cycle (optimum, old growth, breakdown, regeneration and adolescence phases) using the site conditions of 18 established research plots. Fig. 19.12b shows the same for one single plot and one development cycle in order to demonstrate that the attractor represents a limit cycle (i.e. a stable configuration of ecosystem model behavior). The attractor of NEE is embedded in a two dimensional graph, since in this application (i) VPD and (ii) PHAR were calculated from temperature and precipitation (Hasenauer et al., 2003) and (iii) CO₂-concentration and N-deposition were kept constant throughout the simulation. This reduced the number of seven independent dynamic model drivers to three, i.e. daily minimum temperature, maximum temperature and precipitation. Three independent model drivers result in two degrees of freedom and a two dimensional attractor of model dynamics (see Section IV.D).

In the attractor of virgin forest dynamics, there are regions with high and low visitation frequency as indicated by the density of the points of the attractor (Fig. 19.12a). The density of the attracting space reflects the amount of information needed to describe the state of the system. Referring to Fig. 19.12b the following gives an ecological interpretation of the attractor densities for the different phases of the virgin forest development cycle.

- (i) Regeneration: During regeneration, the open canopy space becomes occupied by new plants and the C source strength of the ecosystem declines. The competition for light and nutrients is low and little information is required to predict the development of the ecosystem.
- (ii) Adolescence: With adolescence, the ecosystem achieves canopy closure and enters a stationary phase with small fluctuations between C sink and C source. The competition for light becomes important and individual tree competition is evident. More information is required to understand which individuals will survive and which will die.
- (iii) Optimum: When the ecosystem enters the optimum phase it becomes a net C sink. The individuals that survived adolescence grow at different rates and small differences in nutrient or light availability are important for the competitive situation of a tree within the stand. The amount of information needed to predict the performance of individual trees is at its maximum. At the peak of the optimum phase, C sink strength is at its maximum and the most successful individuals dominate the ecosystem. The amount of information needed to predict ecosystem performance starts to decrease.
- (iv) Old Growth: The maintenance costs of the accumulated biomass increase during the old growth phase. In years with unfavorable climate conditions single individuals die due a negative individual carbon balance. The ecosystem enters another stationary phase with small fluctuations between carbon sink and carbon source.

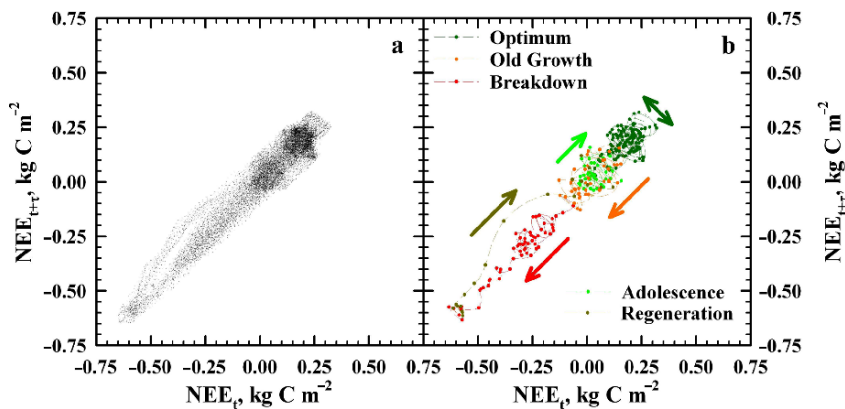


Fig. 19.12. Attractor of modeled NEE for the successional cycle evident within the virgin forest reserve Rothwald. **a:** NEE-Attractor for the virgin forest successional cycle reconstructed from model results using site and climate conditions of 18 research plots. **b:** Attractor reconstructed for one single plot and one successional cycle. Arrows indicate the trends of model behavior during different phases of the successional cycle. (S.A. Pietsch, unpublished) See also Color Plates, Fig. 6

The amount of information needed to describe the system increases compared to the optimum phase.

- (v) Breakdown: During this phase individuals collapse under the maintenance costs of their biomass and the ecosystem becomes a net C source. This process accelerates with time and less information is needed to predict ecosystem behavior. This is evident from the decreasing attractor density towards the peak of C source strength.

A visual analysis of the attractor reconstructed from an ecosystem level process (NEE) provides information on the individuals constituting the ecosystem. This is an important result showing that a process resulting from the sum of the behavior of individuals also contains information on the individuals. This information is of practical value for the determination of sample size in field studies. If an ecosystem is in phase with high attractor density, then a higher number of samples will be needed to gather the amount of information necessary to understand dynamics of the ecosystem. If the ecosystem is in a phase with low attractor density, then a smaller sample size will be necessary to understand the dynamics of the ecosystem. Ergodic theory provides a link between the process-based description of an ecosystem and the statistical description of the individuals residing within this ecosystem.

VI. Concluding Remarks

Large-scale ecosystem models describe the transformation of energy and matter within an ecosystem. Among the processes determining the fluxes of energy and matter, photosynthesis has the central role and is the key of the interactions between the carbon, water, nitrogen and energy cycle. Photosynthesis interacts with the water cycle by the trade-off between carbon uptake and water loss across leaf stomata. Photosynthesis is linked to the nitrogen cycle by the high proportion of leaf nitrogen allocated to the carbon fixing enzymes Rubisco and PEP-Carboxylase. The energy cycle is influenced by photosynthesis via solar short-wave radiation absorption, which fuels photosynthetic electron transport rate.

Complex large scale ecosystem models link photosynthesis with processes of plant growth and decay. In this context the models serve as diagnostic tools to assess and understand observed ecosystem carbon, water and nutrient dynamics. Comparisons of model predictions on states and fluxes with field observations are essential for testing the formal implementation of ecosystem processes. This is paramount for ensuring a realistic representation of reality over time periods, starting from days to seasons (Figs. 19.8–19.10, Section V.B.) and continuing to complete ecosystem life cycles (Fig. 19.6, Section V.A).

Model validations require independent observations covering the full variation range of ecosystem development stages. Data should include different site and climate conditions across the ecosystems distribution range. Validation is the key step in assessing the error component of model applications (i.e. the accuracy and precision of model predictions; see Section IV.C). Validation allows the comparison of prediction uncertainty with observed variation. When prediction uncertainty exceeds observed variation, an expert guess may be more accurate than a model application.

Validations of complex large-scale ecosystem models form the backbone for any scenario analyses. After rigorous model validation, one final important question remains: How reliable are model predictions beyond the range of conditions prevalent during the validation process?

A possible solution to this problem may be an analysis of model dynamics using methods from ergodic theory (Section IV.D) If the model dynamics remain stable under a given scenario (e.g. climate change), then model predictions may be considered as feasible.

Currently, we understand the major relations among ecosystem processes ranging from photosynthesis to decomposition. The implementation of the processes in a formal model allows us to mimic nature and to determine the accuracy and precision of model predictions. For the future, we will have to investigate the relationship between model dynamics and real world ecosystem dynamics (Sections IV.D and V.C). Such understanding may enable us to evaluate the quality of model predictions on future ecosystem behavior as it may develop with changing climate.

Acknowledgments

This research was funded by the Austrian Science Foundation (FWF) project number P20660-B16 (Ergodic theories within Ecosystem Modeling), the Austrian Federal Ministry of Science and Education (BMWF), the Austrian Federal Ministry of Agriculture, Forestry, Environment and Water Management (BMLFUW) and the Austrian Federal Ministry of Transport, Innovation and Technology (BMVIT). We thank Agu Laisk for helpful comments on the chapter.

References

- Aber JD (1992) Nitrogen cycling and nitrogen saturation in temperate forest ecosystems. *Trends Ecol Evol* 7: 220–22
- Andren O and Paustian K (1987) Barley straw decomposition in the field: a comparison of models. *Ecol* 68: 1190–1200
- Assmann E (1970) *The Principles of Forest Yield Study*. Pergamon Press, Oxford
- Bachelet D, Lenihan J, Daly C, Neilson R, Ojima D and Parton W (2001) MC1: a dynamic vegetation model for estimating the distribution of vegetation and associated ecosystem fluxes of carbon, nutrients, and water. USDA Forest Service, Pacific Northwest Station, Gen Tech Rep PNW-GTR-508
- Boltzmann, L (1877) Über die Beziehung zwischen dem zweiten Hauptsatze der mechanischen Wärmetheorie und der Wahrscheinlichkeitsrechnung respektive den Sätzen über das Wärmegleichgewicht. *Wiener Berichte* 76: 373–435
- Broer H, Simó C and Vitolo R (2002) Bifurcations and strange attractors in the Lorenz-84 climate model with seasonal forcing. *Nonlinearity* 15: 1205–1267
- Brooks RH and Corey AT (1964) Hydraulic properties of porous media. *Hydrology Papers* 3, Colorado State University, Fort Collins, CO
- Carbone G (2007) *Exercises in Weather and Climate*, 6th ed, Prentice-Hall, Upper Saddle River, NJ
- Chang M (2003) *Forest Hydrology: An Introduction to Water and Forests*. CRC Press LLC, Boca Raton, FL
- Clapp RB and Hornberger GM (1978) Empirical equations for some soil hydraulic properties. *Water Resource Res* 14: 601–604
- Collins WJ, Derwent RG, Johnson CE and Stevenson DS (2002) A comparison of two schemes for the convective transport of chemical species in a Lagrangian global chemistry model. *Quart J Royal Meteor Soc* 128: 991–1009
- Cosby BJ, Hornberger GM, Clapp RB and Ginn TR (1984) A statistical exploration of the relationships of soil moisture characteristics to the physical properties of soils. *Water Resource Res* 20: 682–690
- de Pury DGG and Farquhar GD (1997) Simple scaling of photosynthesis from leaves to canopies without the errors of big-leaf models. *Plant Cell Environ* 20: 537–557
- Eckmann J-P and Ruelle D (1985) Ergodic theory of chaos and strange attractors. *Rev Modern Phys* 57: 617–656
- Etheridge DM, Steele LP, Langenfelds RL, Francey RJ, Barnola J-M and Morgan VI (1996) Natural and anthropogenic changes in atmospheric CO₂ over the last 1000 years from air in Antarctic ice and firn. *J Geophys Res* 101: 4115–4128
- Evans JR (1989) Photosynthesis and nitrogen relationships in leaves of C₃ plants. *Oecologia* 78: 9–19
- Farquhar G, Von Caemmerer S and Berry J (1980) A biochemical model of photosynthetic CO₂ fixation in leaves of C₃ species. *Planta* 149: 78–90
- Finzi A and Schlesinger WH (2002) Species control variation in litter decomposition in a pine forest exposed to elevated CO₂. *Global Change Biol* 8: 1217–1229
- Harcomb PA (1987) Tree life tables: Simple birth, growth and death data encapsulate life histories and ecological roles. *Bioscience* 37: 557–568
- Hasenauer H, MerganiĀlová K, Petritsch R, Pietsch SA and Thornton PE (2003) Validating daily climate interpolations over complex terrain in Austria. *Agric Forest Meteorol* 119: 87–107
- Heinselman ML (1973) Fire in the virgin forests of the boundary waters canoe area, Minnesota. *Quaternary Res* 3: 329–382
- Holland EA, Dentener FJ, Braswell BH and Sulzman JM (1999) Contemporary and pre-industrial global nitrogen budgets. *Biogeochem* 46: 7–43
- Keeling CD, Bacastow RB, Carter AF, Piper SC, Whorf TP, Heimann M, Mook WG and Roeloffzen H (1989). A three-dimensional model of atmospheric CO₂ transport based on observed winds: 1. Analysis of observational data. In: Peterson DH (ed) *Aspects of Climate Variability in the Pacific and the Western Americas*. *Geophys Monogr* 55: 165–235
- Krinner G, Viovy N, de Noblet-Ducoudré N, Ogée J, Polcher J, Friedlingstein P, Ciais P, Sitch S and Prentice C (2005) A dynamic global vegetation model for studies of the coupled atmosphere-biosphere system. *Global Biogeochem Cycles* 19: GB1015
- Kuehn GD and McFadden BA (1969) Ribulose 1,5-diphosphate carboxylase from *Hydrogenomonas eutropha* and *Hydrogenomonas facilis*. I. Purification, metallic ion requirements, inhibition, and kinetic constants. *Biochemistry* 8: 2394–2402
- Laisk A and Edwards GE (2000) A mathematical model of C₄ photosynthesis: The mechanism of concentrating CO₂ in NADP-malic enzyme type species. *Photosynth Res* 66: 199–224

- Lloyd J and Taylor JA (1994) On the temperature dependence of soil respiration. *Funct Ecol* 8: 315–323
- Lorimer CG, Dahir SE and Nordheim EV (2001) Tree mortality rates and longevity in mature and old growth hemlock hardwood forests. *J Ecol* 89: 960–971
- Mayer H and Ott E (1991) *Gebirgswaldbau-Schutzwaldpflege*. Fischer Verlag, Stuttgart
- Melillo JM, McGuire AD, Kicklighter DW, Moore III B, Vorosmarty CJ and Schloss AL (1993) Global climate change and terrestrial net primary production. *Nature* 363: 234–240
- Melillo JM, Kicklighter DW, McGuire AD, Peterjohn WT and Newkirk KM (1995) Global change and its effects on soil organic carbon stocks. In: Zepp RG and Sonntag Ch (eds) *Role of Nonliving Organic Matter in the Earth's Carbon Cycle*, pp 175–189. Wiley, Chichester
- Merganičova K, Pietsch SA and Hasenauer H (2005) Modeling the impacts of different harvesting regimes on the growth of Norway spruce stands. *Forest Ecol Manag* 207: 37–57
- Monserud RA and Sterba H (2001) Modeling individual tree mortality for Austrian tree species. *Forest Ecol Manag* 113: 109–123
- Ott E, Frehner M, Frey H-U and Löscher P (1997) *Gebirgswälder-Ein Praxisorientierter Leitfaden für Standortgerechte Waldbehandlung*. Paul Haupt Verlag, Bern
- Penning de Vries FWT (1974) Substrate utilization and respiration in relation to growth and maintenance in higher plants. *Netherlands J Agric Sci* 22: 40–44
- Peterken GF (1996) *Natural Woodland: Ecology and Conservation in Northern Temperate Regions*. Cambridge University Press, Cambridge
- Petit JR, Basile I, Leruyet A, Raynaud D, Lorius C, Jouzel J, Stievenard M, Lipenkov VY, Barkov NI, Kudryashov BB, Davis M, Saltzman E and Kotlyakov V (1997) Four climate cycles in Vostok ice core. *Nature* 387: 359–360
- Petit JR, Jouzel J, Raynaud D, Barkov NI, Barnola J-M, Basile I, Bender M, Chappellaz J, Davis M, Delayque G, Delmotte M, Kotlyakov VM, Legrand M, Lipenkov VY, Lorius C, Pépin L, Ritz C, Saltzman E and Stievenard M (1999) Climate and atmospheric history of the past 420,000 years from the Vostok ice core, Antarctica. *Nature* 399: 429–436
- Petrtsch R and Hasenauer H (2007) Interpolating input parameters for large scale ecosystem models. *Aust J Forest Sci* 124: 135–151
- Pietsch SA and Hasenauer H (2002) Using mechanistic modeling within forest ecosystem restoration. *Forest Ecol Manag* 159: 111–131
- Pietsch SA and Hasenauer H (2003) *Stoffkreislaufmodellierung im Grasland: Machbarkeitsstudie für die Adaptierung eines biogeochemisch mechanistischen Modells*. Inst. of Forest Growth Research, Vienna
- Pietsch SA and Hasenauer H (2005a) Using ergodic theory to assess the performance of ecosystem models. *Tree Physiol* 25: 825–837
- Pietsch SA and Hasenauer H (2005b) Modeling Cembra pine forest ecosystems in Austria. *Aust J Forest Sci* 122: 37–54
- Pietsch SA and Hasenauer H (2006) Evaluating the self-initialization procedure of large scale ecosystem models. *Global Change Biol* 12: 1658–1669
- Pietsch SA, Hasenauer H, Kučera J and Čermák J (2003) Modeling effects of hydrological changes on the carbon and nitrogen balance of oak in floodplains. *Tree Physiol* 23: 735–746
- Pietsch SA, Hasenauer H and Thornton PE (2005) BGC-Model parameter sets for central European forest stands. *Forest Ecol Manag* 211: 264–295
- Poincaré H (1892) *Les Méthodes Nouvelles de la Mécanique Céleste*. Vol. 1: *Solutions Périodiques, Non-Existence des Méthodes Uniformes, Solutions Asymptotiques*. Gauthier-Villars, Paris
- Popper KR (1935) *Logik der Forschung. Zur Erkenntnistheorie der Modernen Wissenschaft*. Julius Springer, Wien
- Racsko P, Szeidl L and Semenov MA (1991) A serial approach to local stochastic weather models. *Ecol Modell* 57: 27–41
- Remmert H (1991) *The Mosaic Cycle Concept of Ecosystems*. Ecological Studies 85. Springer, Berlin
- Reynolds MR Jr (1984) Estimating the error in model predictions. *Forest Sci* 30: 454–469
- Richardson CW and Wright DA (1984) *WGEN: A Model for Generating Daily Weather Variables*. US Department of Agriculture, Agricultural Research Service, ARS-8
- Ruelle D (1978) Sensitive dependence on initial condition and turbulent behaviour of dynamical systems. *Ann NY Acad Sci* 316: 408–416
- Ruelle D (1995) *Turbulence, strange attractors and chaos*. World Scientific Series on Non-linear Science, Series A Vol 16, World Scientific Press, Singapore
- Ryan MG (1991) Effects of climate change on plant respiration. *Ecol Applicat* 1: 157–167
- Saxton KE, Rawls WJ, Romberger JS and Papendick RI (1986) Estimating generalized soil-water characteristics from texture. *Soil Sci Soc Am J* 50: 1031–1036
- Scheffer M, Carpenter S, Foley JA, Folke C and Walker B (2001) Catastrophic shifts in ecosystems. *Nature* 413: 591–596
- Schlesinger WH (1997) *Biogeochemistry: An Analysis of Global Change*, 2nd ed, Academic, San Diego, CA
- Schneider J (1998) *Kartierung der nassen Deposition in Österreich*. Umweltbundesamt Wien
- Semenov MA, Brooks RJ, Barrow EM and Richardson CW (1998) Comparison of WGEN and LARS-WG stochastic weather generators for diverse climates. *Clim Res* 10: 95–107
- Sitch S, Smith B, Prentice IC, Arneth A, Bondeau A, Cramer W, Kaplan JO, Levis S, Lucht W, Sykes MT, Thonicke K and Venevsky S (2003) Evaluation of ecosystem dynamics, plant geography and terrestrial carbon cycling in the LPJ dynamic global vegetation model. *Global Change Biol* 9: 161–185

- Spiecker H, Hanse J, Klimo E, Skovsgaard, JP, Sterba H, Von Teuffel K (2004) Norway spruce conversion – options and consequences. European Forest Institute Research Report. S. Brill Academic, Leiden/Boston/Köln
- Takens F (1981) Detecting strange attractors in turbulence. In: Rand D and Young L-S (eds) *Dynamical Systems and Turbulence*, pp 366–381. Springer, Berlin
- Thornton PE (1998) Description of a Numerical Simulation Model for Predicting the Dynamics of Energy, Water, Carbon and Nitrogen in a Terrestrial Ecosystem. Ph.D.-thesis. University of Montana, Missoula, MT
- Thornton PE, Hasenauer H and White MA (2000) Simultaneous estimation of daily solar radiation and humidity from observed temperature and precipitation: An application over complex terrain in Austria. *Agric Forest Meteorol* 104: 255–271
- Tiedtke M (1989) A comprehensive mass flux scheme for cumulus parameterization in large-scale models. *Monthly Weather Rev.* 117: 1779–1800
- Ulrich E and Williot B (1993) *Les Dépôts Atmosphériques en France de 1850 à 1990, Dépôts en Milieu Rural et en Forêt, Dépôts dans les Zones Industrialisées et Urbaines*. Imprimerie de l'Office National des Forêts, Paris
- Waring RH and Running SW (1998) *Forest Ecosystems: Analysis at Multiple Scales*, 2nd ed, Academic, San Diego, CA
- White MA, Thornton PE, Running SW and Nemani RR (2000) Parameterization and sensitivity analysis of the BIOME-BGC terrestrial ecosystem model: Net primary production controls. *Earth Interactions Paper* 4–003. <http://EarthInteractions.org>
- Woodrow IE and Berry JA (1980) Enzymatic regulation of photosynthetic CO₂ fixation in C₃ plants. *Annu Rev Plant Physiol Plant Mol Biol* 39: 533–594
- Wullschlegel SD (1993) Biochemical limitations to carbon assimilation in C₃ plants – A retrospective analysis of the A/C_i curves from 109 species. *J Exp Bot* 44: 907–920

Chapter 20

Photosynthesis in Global-Scale Models

Andrew D. Friend*

*Department of Geography, University of Cambridge, Downing Place, Cambridge CB2 3EN,
UK*

Richard J. Geider

*Department of Biological Sciences, University of Essex, Wivenhoe Park, Colchester
CO4 3SQ, UK*

Michael J. Behrenfeld

*Department of Botany and Plant Pathology, Oregon State University, Cordley Hall,
2082, Corvallis, OR 97331, USA*

Christopher J. Still

*Department of Geography and Institute for Computational Earth System Science,
University of California Santa Barbara, Santa Barbara, CA 93106, USA*

Summary.....	466
I. Introduction.....	467
A. Terrestrial Photosynthesis.....	467
B. Marine Photosynthesis.....	468
C. Coastal Photosynthesis.....	468
II. Description of Model Approaches.....	469
A. Terrestrial Models.....	469
1. CO ₂ Fixation.....	469
2. Photosynthetic Capacity.....	471
3. Environmental Forcing.....	473
B. Marine Models.....	474
1. Photosynthetic Capacity.....	474
2. Bio-optical Algorithms.....	475
3. Biogeochemical Models.....	478
4. Environmental Forcing.....	479
III. Global Simulation.....	480
A. Terrestrial Photosynthesis.....	480
1. CO ₂ Fixation.....	480
2. Photosynthetic Capacity.....	481
3. Environmental Forcing.....	482

* Author for correspondence, e-mail: adf10@cam.ac.uk

B. Marine Photosynthesis	483
1. Underwater Light Field.....	484
2. Phytoplankton Carbon, Chlorophyll, and Net Primary Production.....	484
C. Global Simulation Results	485
IV. Concluding Remarks	486
A. Future Challenges.....	486
1. Terrestrial Systems.....	486
2. Marine Systems.....	487
Acknowledgments.....	488
References.....	488

Summary

Photosynthesis models are now routinely used in many types of global investigations. Much of this work is driven by global environmental change concerns, with global models seen as key tools with which to synthesize current understanding, explain paleoclimatic variability in global biogeochemistry and ecology, and forecast ecosystem responses to climate change and increasing atmospheric CO₂ levels. We discuss the approaches used to model terrestrial and marine photosynthesis at the global scale. Models in both realms fall into two equivalent categories, one empirical and one mechanistic. Within each category there are many similarities between terrestrial and marine models. Most empirical approaches estimate the distribution of photosynthetic capacity (chlorophyll in the oceans, LAI on land) from space and apply a photosynthetic light-use efficiency approach to obtain an estimate of carbon uptake. Mechanistic approaches attempt to simulate the distribution of capacity itself, as well as the rate of photosynthesis, and are thus capable of projecting terrestrial and marine carbon fluxes into the future and distant past.

A completely new state-of-the-art global combined simulation of terrestrial and marine production is presented. Terrestrial photosynthesis is calculated using a mechanistic approach that treats the within-leaf light gradient, among other improvements over previous methods. Marine production utilizes a new approach that treats spatial and temporal variation in phytoplankton chlorophyll to C ratio. Mean contemporary annual net primary productivity is estimated to be 107.3 Pg C year⁻¹, with 51.1% coming from land and 48.9% from the oceans.

Improvements in prognostic modeling of global photosynthesis will come about through attention to the same issues in both terrestrial and marine environments. These primarily concern high quality validation data at scales appropriate to test global models and the development of methodologies to deal with the variety of physiological and phenological types. In addition, attention needs to be given to both the potential importance of phenotypic plasticity and better mechanistic approaches for the prediction of photosynthetic capacity distribution in space and time. Dialogue between modelers, experimental physiologists, and ecologists needs to improve. Without this there is a very real danger that global models will assume a shared acceptance of an *in silico* reality that bears only superficial resemblance to that *in vivo*.

Abbreviations: AOD – atmospheric optical depth; APAR – absorbed PAR; AVHRR – advanced very high resolution radiometer; CASA – Carnegie Ames Stanford approach; CbPM – carbon-based production model; *Chl* – chlorophyll *a* concentration; *Chl a* – chlorophyll *a*; *C_{phyto}* – ocean carbon concentration; DGOM – dynamic green ocean model; DGVM – dynamic global vegetation model; *E₀* – incident PAR at the sea surface; *f_{PAR}* – fraction of PAR; GCM – global climate model; GPP – gross primary production; LAI – leaf area index; LUE – light use efficiency; MLD – mixed layer depth; MODIS – moderate-resolution imaging spectro-

radiometer; NDVI – normalized difference vegetation index; NIR – near infrared; NOAA – National Oceanic and Atmospheric Administration; NPP – net primary production; *P^{Chl}* – chlorophyll *a*-specific photosynthesis rate; *P(z, t)* – depth and time resolved net carbon fixation rate per unit volume; PAR – photosynthetically active radiation; Rubisco – ribulose 1,5-bisphosphate carboxylase/oxygenase; RuBP – ribulose 1,5-bisphosphate; SeaWiFS – sea-viewing wide field-of-view sensor; *SLA* – specific leaf area

I. Introduction

All food and fiber on which humanity depends has its origin in the capture of atmospheric CO₂ by photosynthesis, and so quantifying present and future global spatial and temporal distributions of this essential process is a key scientific objective. Recent increases in computing power, together with the production of key global datasets, have allowed many researchers to develop methodologies for modeling photosynthesis at the global scale in both the terrestrial (Melillo et al., 1993; Potter et al., 1993; Warnent et al., 1994; Prince and Goward, 1995; VEMAP Members, 1995; Foley et al., 1996; Hunt et al., 1996; Kaduk and Heimann, 1996; Sellers et al., 1996a; Brovkin et al., 1997; Post et al., 1997; Dickinson et al., 1998; Xiao et al., 1998; Cox et al., 2000; Friend and White, 2000; McGuire et al., 2001; Bonan et al., 2003; Sitch et al., 2003; Running et al., 2004; Woodward and Lomas, 2004; Friend and Kiang, 2005; Krinner et al., 2005; Sato et al., 2007) and marine (Morel, 1991; Longhurst et al., 1995; Behrenfeld and Falkowski, 1997a; Behrenfeld et al., 2005; Carr et al., 2006) environments. These efforts have been driven by three ambitious research objectives: (i) synthesis of our understanding of the current ecological and biogeochemical state of terrestrial and oceanic environments (e.g. the distribution of ecosystem production and structure on land and the distribution of nutrients, dissolved oxygen, and marine biota in the oceans); (ii) accounting for paleoclimatic variability in global biogeochemistry and ecology; and (iii) forecasting the responses of ecosystems to climate change and altered anthropogenic nutrient loading (including CO₂), and their feedbacks on global biogeochemistry and climate. Models provide an efficient means to integrate and test our knowledge, especially at large spatial scales.

Contemporary concerns regarding global environmental change have provided the motivation for much of the modeling described in this chapter. Understanding controls on plant production across environmental gradients up to the global scale is a prerequisite for the development of capabilities for predicting the impacts of future environmental change on Earth's ecosystems. In addition to the need to predict impacts, the current interest in the contemporary behavior of the global carbon cycle (driven largely by awareness

of the potential consequences of rising concentrations of anthropogenic greenhouse gases for global climate) is responsible for a widening interest in global plant production models. However, attribution of observed atmospheric CO₂ concentrations and their variability in space and time is far from straightforward. In particular, it is currently not possible to unequivocally identify the process or processes responsible for the uptake of the major part of the $\approx 57\%$ of anthropogenic CO₂ emissions that does not remain in the atmosphere on an annual timescale, or explain why the efficiency of these natural carbon sinks appears to have been decreasing since 2000 (Canadell et al., 2007). Photosynthesis is the primary driver of the contemporary global carbon cycle and, therefore, understanding the dynamics of atmospheric CO₂, and hence future climate, requires a detailed understanding of the global distribution of photosynthesis and how it responds to environmental forcings. Clearly respiration is the other key to determining surface-atmosphere CO₂ fluxes, and the reader is referred to Trumbore (2006) and Amthor (2000) for the terrestrial perspective on this complex subject, and to Geider (1992) and Laws et al. (2000b) for a marine perspective on phytoplankton respiration. Recent marine perspectives on community respiration are given by Williams et al. (2004) and Riser and Johnson (2008).

Researchers have approached the challenges of modeling terrestrial and marine photosynthesis separately; we also briefly consider coastal ecosystems.

A. Terrestrial Photosynthesis

Most models of terrestrial vegetation have a photosynthesis-centric approach, treating plant growth as the carbon balance of photosynthesis, respiration, and litter turnover, with ecosystem dynamics resulting from the relative growth (or productivity) of different physiologies and/or individuals. Photosynthesis and radiation algorithms tend to be the most sophisticated and best understood components of these models, partly because of the relative ease of measuring canopy processes and partly because of the almost universal adoption of the leaf-level, mechanistic model of photosynthesis developed by Graham Farquhar, Susanne von Caemmerer, and Joseph

Berry almost 30 years ago (Farquhar et al., 1980; Chapter 9 of this book by Susanne von Caemmerer, Graham Farquhar and Joseph Berry).

Global-scale models of terrestrial photosynthesis are now an important component of global climate models (GCMs) because of the importance of vegetation processes for soil moisture dynamics and the partitioning of surface energy, processes increasingly shown to be important for the physical climate system (Pitman, 2003). Stomatal conductance algorithms in GCMs are usually based on a representation of photosynthesis (e.g. Randall et al., 1996; Friend and Kiang, 2005), and a few GCMs now predict vegetation growth, and hence surface characteristics, from carbon balance (e.g. Betts et al., 1997; Bonan et al., 2003). An increasing number of GCMs also include a treatment of the global carbon cycle, allowing diagnosis of atmospheric CO₂ concentrations from anthropogenic emissions and net natural surface fluxes. This has led to predictions of future feedbacks between climate and atmospheric CO₂ (Fung et al., 2005; Friedlingstein et al., 2006). However, the outcomes of such model experiments depend critically on the modeled responses of photosynthesis and respiration to temperature and rising atmospheric CO₂, processes poorly constrained in current models.

B. Marine Photosynthesis

Models of marine photosynthesis fall into two broad categories. First, bio-optical algorithms calculate net primary production (NPP) from satellite remote sensing observations of ocean color, sea surface temperature, and solar radiation incident upon the sea surface (Behrenfeld et al., 1997a, b; Carr et al., 2006). These algorithms are used to document the seasonal, interannual, and spatial variability of NPP in the ocean (Behrenfeld et al., 2006; Polovina et al., 2008). Second, dynamic models of plankton ecology and ocean biogeochemistry simulate the present state of the ocean carbon cycle by embedding descriptions of chemical, biogeochemical, and ecological processes within an ocean general circulation model (Doney et al., 2003). These models are used to assess the effects of changes in external forcing on ocean ecosystems and the ocean carbon cycle (Orr et al., 2005; Moore et al., 2006a), to simulate the evolution of the ocean carbon

cycle on glacial/interglacial time scales, and to project the ocean carbon cycle into the future (Le Quéré et al., 2005; Schmittner et al., 2008). Accuracy in hindcasting the carbon cycle into the past and forecasting the carbon cycle into the future relies on accurate descriptions of ocean physics, chemistry, ecology, and biogeochemistry (Doney et al., 2003). Primary productivity estimates obtained from these two approaches are largely independent. One point of intersection between the bio-optical algorithms and biogeochemical models is the surface ocean chlorophyll *a* (Chl *a*) field. Satellite derived Chl *a* can be exploited in different ways in the two approaches. The Chl *a* field is an input to bio-optical calculations, whereas it is used in validating biogeochemical models. In addition, assimilation of the Chl *a* field can be used to improve the output of biogeochemical models (Gregg, 2008).

C. Coastal Photosynthesis

Our discussion of marine photosynthesis in this chapter focuses on the phytoplankton, comprising the drifting microscopic algae and cyanobacteria, which account for about 90 percent of marine NPP (Duarte and Cebrián, 1996; Field et al., 1998). None-the-less, we acknowledge the importance of the coastal zone to NPP and the carbon cycle. The coastal zone receives inputs of organic matter and nutrients from terrestrial sources and exchanges organic matter and nutrients with the ocean (Gattuso et al., 1998). The coastal zone includes estuaries, intertidal habitats, shallow water subtidal vegetated habitats, and coral reefs. These habitats are relatively small in spatial extent (Duarte and Cebrián, 1996; Borge et al., 2005), but include a wide range of distinct plant functional groups such as mangroves, salt marsh grasses, seagrasses, benthic microalgae, macroalgae, and endosymbiotic algae within corals. Estimates that these plants contribute about 10% of global marine NPP are obtained by extrapolation from local studies to the global scale on the basis of estimates of the area occupied by these different habitats (Duarte and Cebrián, 1996; Field et al., 1998). As a consequence, NPP of the subtidal benthic communities is poorly quantified. A step towards improving estimates of the contribution of these communities to NPP on a global

scale was taken by Gattuso et al. (2006), who used SeaWiFS imagery to define the surface area of the sea bed where there is sufficient light to support net community production.

II. Description of Model Approaches

Global-scale models of photosynthesis have to confront three major challenges: characterization of the dependency of CO₂ uptake on forcings, the distribution of capacity (i.e. the amounts of Rubisco and light-harvesting machinery) in space and time, and the environmental forcing itself. A wide range of approaches has been used for all three, depending on the intended application and often the background of the researchers. Approaches to the dependency of terrestrial CO₂ uptake on forcings can be classified as either “top-down” or “bottom-up” (the terms refer to strategies of model development: either from the whole to the parts or from the parts to the whole). Marine bio-optical NPP algorithms are similar to the “top-down” terrestrial models, treating NPP as the product of capacity (e.g. Chl *a* concentration) and Chl *a*-specific photosynthesis, which is related to environmental forcing (Field et al., 1998). However, unlike in terrestrial models, marine photosynthesis is rarely treated separately from growth because of the rapid turnover of the phytoplankton.

A. Terrestrial Models

1. CO₂ Fixation

a. “Top-down” Approaches

The most widely used “top-down” approach to modeling terrestrial photosynthesis has its heritage in the ideas of Monteith (1972), who found a linear relationship between absorbed solar radiation and dry matter production of well-watered herbaceous vegetation. A maximum potential efficiency of conversion of energy in the form of radiation to fixed energy in the form of dry matter is assumed, and then scaled depending on the influence of various environmental factors such as temperature and atmospheric vapor pressure deficit (e.g. Running et al., 2004). This

approach assumes a linear relationship between total canopy absorbed radiation and photosynthesis, and so can be used with satellite-based measurements of absorbed solar radiation to estimate the global distribution of photosynthesis (e.g. Prince and Goward, 1995). One such photosynthesis product is derived from the MODIS instrument at 8 day intervals, and has global coverage at 1 km resolution (Zhao et al., 2005).

Light-use efficiency (LUE), or the conversion efficiency between absorbed photosynthetically active radiation (APAR) and plant growth, is often given in units of g C (MJ APAR)⁻¹. Canopy LUE is determined by many biological and biophysical factors in addition to the maximum quantum yield of photosynthesis, including maximum light-saturated photosynthetic rates, the fraction of photosynthesis consumed by autotrophic respiration, and the diffuse fraction of irradiance (Monteith, 1972, 1977; Prince, 1991; Potter et al., 1993; Field et al., 1998; Ruimy et al., 1999; Running and Hunt, 1993; Goetz and Prince, 1998; Gower et al., 1999; Choudhury, 2001; Running et al., 2004; Jenkins et al., 2007). The widely used CASA carbon cycle model (Potter et al., 1993; Field et al., 1995, 1998; Randerson et al., 1997, 2005) predicts NPP, or gross primary production (GPP) minus autotrophic respiration, as: $NPP = LUE \times APAR$, where $LUE = \varepsilon^* \times T \times W$. LUE is modeled in CASA as departing from a theoretical universal optimum (ε^*) due to climatic variations given by stress scalar terms for temperature (*T*) and moisture (*W*) (Potter et al., 1993; Lobell et al., 2002). Spatial and temporal variations in APAR are prescribed from surface irradiance and the fraction of incident photosynthetically active radiation (f_{PAR}) absorbed by vegetation, derived from satellite observations (Potter et al., 1993; Field et al., 1998; Ruimy et al., 1999).

The model of Sato et al. (2007) uses a rather more complex “top-down” approach than the standard LUE algorithm. Leaf-level photosynthesis is calculated as a simple saturating function of incident PAR, with an initial slope of 0.05 mol CO₂ (mol quanta)⁻¹ for C₃ plants. This initial slope is assumed to vary with air temperature and intercellular CO₂ concentration in C₃ leaves, and leaf-level photosynthesis is integrated across 10 cm deep layers within individual tree crowns. Kaduk and Heimann (1996) employ a

similar method to calculate daily canopy light-dependent photosynthesis, but include a canopy-depth dependency for the leaf-level maximum rate and apply linear empirical functions of mean daily temperature, drought stress, and atmospheric CO_2 to the canopy rate; they assume an LUE of $0.07 \text{ mol CO}_2 (\text{mol quanta})^{-1}$.

The “TEM” model (Xiao et al., 1998) also uses a “top-down” approach to modeling photosynthesis. Monthly GPP at a given location is calculated as a multiplicative function of responses to incident PAR, leaf area, temperature, atmospheric CO_2 , water availability, and nitrogen availability.

b. “Bottom-up” Approaches

C₃ Photosynthesis

“Bottom-up” approaches to modeling environmental regulation of C_3 terrestrial photosynthesis in global models are usually based on the biochemical approach of Farquhar et al. (1980). Instantaneous leaf-level photosynthesis is calculated as the net rate of Rubisco-catalyzed RuBP carboxylation. For a given mean intercellular CO_2 concentration, net carboxylation in all leaf chloroplasts is assumed to be limited either by the Rubisco content and its turnover rate or by the rate of production of RuBP. The latter is limited either by the amount of light absorbed or by the potential rate of electron transport. At high rates of photosynthesis, triose phosphate utilization is sometimes assumed to become limiting (Sharkey, 1985; Harley et al., 1992).

Farquhar et al. (1980) concluded that despite the mechanistic principles of their model, its application requires empirical specification of key parameters. These include Rubisco carboxylase capacity, electron transport capacity, and their respective temperature responses. The situation is challenging as the parameters specifying photosynthetic capacity vary by two orders of magnitude among different species and growth conditions (Wullschlegel, 1993). In response, parameter estimation techniques have been developed that utilize observations such as ecosystem CO_2 fluxes measured with the eddy-covariance technique (Knorr and Kattge, 2005; Friend et al., 2007; Wang et al., 2007).

A further concern is that insight gained from the Farquhar et al. (1980) model can be compromised by empirical treatments of the interaction between limiting processes (Rubisco and electron transport) and regulation of electron transport by absorbed light (Badeck, 1995; Kull and Kruijt, 1998). These problems can be overcome by an explicit treatment of the light gradient within leaves. Such an approach not only obviates the need for these empirical functions, but also provides a framework for the mechanistic treatment of the relationship between photosynthesis and leaf nitrogen content (Kull and Kruijt, 1998; Friend, 2001; Friend and Kiang, 2005). Details of this methodology are elaborated below in Section III.

C₄ Photosynthesis

The photosynthetic pathway composition (C_3/C_4 fraction) is a fundamental physiological and ecological distinction in tropical and subtropical savannas, as well as many temperate grasslands (e.g. in the North American Great Plains). C_4 plants have higher photosynthetic rates at high temperatures and under high light (Collatz et al., 1992; Long, 1999) and higher water-use efficiency than do comparable C_3 plants (Pearcy and Ehleringer, 1984; Farquhar et al., 1989; Sage and Monson, 1999). The lower nitrogen requirement of C_4 plants (due to reduced Rubisco content and lack of photorespiratory enzymes) results in a higher photosynthetic nitrogen use efficiency, or the ratio of photosynthesis to leaf nitrogen content.

These functional differences can have important implications for biosphere-atmosphere exchanges of carbon, water, and energy. For example, C_4 plants typically partition more net radiation to sensible heat than latent heat compared to comparable C_3 plants operating under identical conditions. This partitioning has important implications for surface temperature and humidity at regional scales (Sellers et al., 1992).

A hallmark of C_4 plants is their dominance in high light and high temperature grassland and savanna environments (Long, 1999; Sage et al., 1999). The C_4 pathway concentrates CO_2 around the Rubisco enzyme, effectively eliminating the wasteful process of photorespiration, but at the expense of additional energy. This expense

is less critical when solar radiation is abundant, which also raises leaf temperatures and photorespiration in C_3 plants. As a result, photosynthesis in unstressed C_4 leaves does not saturate at high light, unlike the characteristic saturation for most C_3 plants (Collatz et al., 1991, 1992). Canopy models show that under identical conditions C_3 plants are often light saturated while C_4 plants remain light limited under almost all light levels and temperatures (C.J. Still, unpublished). This is supported by eddy flux studies that have examined canopy light responses for different ecosystems (Ruimy et al., 1995; Waring et al., 1995; Gu et al., 2002; Turner et al., 2003; Schwalm et al., 2006; Jenkins et al., 2007). For example, Turner et al. (2003) studied the relationship between gross primary production (GPP) and APAR in a cross-biome comparison. The C_4 -dominated tallgrass prairie displayed a nearly linear relationship between GPP and APAR, unlike other biomes that exhibited more typical light saturation (i.e., a hyperbolic relationship between these variables).

C_4 plants will likely respond quite differently than C_3 plants to the suite of anthropogenic global changes being imposed on the Earth system, and this will strongly influence C_3/C_4 distributions and carbon fluxes. In addition to the well-known differences imposed by rising atmospheric CO_2 on photosynthesis (Poorter, 1993; Wand et al., 1999; Morgan et al., 2007), warmer temperatures favor C_4 grasses, while higher CO_2 favors C_3 grasses (Collatz et al., 1998). Changes in the timing of precipitation will be also important, with more cool-season rain typically favoring C_3 grasses and more warm-season rain favoring C_4 grasses. Also, C_3 and C_4 grasses exhibit different responses to nitrogen, with deposition generally favoring C_3 grasses (Wedin and Tilman, 1996a,b; Collins et al., 1998; Brown, 1999). Because of these differences, it is essential to capture spatial and temporal variations in photosynthetic pathway when modeling global photosynthesis and its responses to environmental forcings.

The C_3 photosynthesis model of Farquhar et al. (1980) has been adapted for C_4 physiology by Collatz et al. (1992), who simplified the biochemical-intercellular transport model of Berry and Farquhar (1978) to capture the CO_2 concentration mechanism of C_4 plants. In this model, carboxylation is limited by either

light, CO_2 concentration in the mesophyll cells, or Rubisco catalytic activity. Most mechanistic treatments of C_4 photosynthesis in global models utilize this approach (e.g. Sellers et al., 1996a).

2. Photosynthetic Capacity

It is helpful to separate local terrestrial photosynthetic capacity into two components, foliage area and the amount of photosynthetic machinery per unit foliage area. Foliage area is usually quantified as a “leaf area index” (LAI). LAI is the mean, one-sided foliage area per unit ground area, and in global models is typically followed for each vegetation type within each land surface pixel. Models without dynamic nutrient cycles prescribe photosynthetic capacity per unit foliage area from a look-up table of values per biome or vegetation type (e.g. Sellers et al., 1996b; White et al., 2000), or assume unlimited N supply and optimal distribution of N over foliage layers (e.g. the “LPJ” model of Sitch et al., 2003). Foliage area can be prescribed from satellite measurements (Randerson et al., 1997), modeled prognostically (Friend and White, 2000; Sitch et al., 2003; Krinner et al., 2005), or constrained by assimilating measurements into a prognostic model (Demarty et al., 2007).

Global satellite measurements of LAI at 4 km resolution have been derived from the AVHRR sensor, flying on the NOAA series of polar-orbiting satellites since 1978. This instrument was designed purely for operational meteorological applications, but two of the bands have found increasing use since the early 1980s for monitoring vegetation type and condition (Tucker et al., 1985). These two bands are in the visible and near infrared (NIR) frequencies, with green leaves having a higher reflectance of NIR wavelengths and strong absorption of red light by chlorophyll. A normalized difference vegetation index (NDVI) is derived as the ratio of the difference between the measured NIR and visible reflectances and their sum. This index increases with LAI and much work has been undertaken to determine its relationship with vegetation state (Justice et al., 1985; Myneni et al., 1997) and rates of photosynthesis (Nemani et al., 2003; Slayback et al., 2003).

More recently, instruments have been launched into space specifically to monitor terrestrial

vegetation activity. The resulting data are used to calculate indices similar to NDVI, but additional wavebands have been included to enable estimates of the effects of atmospheric properties on individual measurements. A number of these products are now available (Morisette et al., 2006), with the most widely used coming from NASA's Moderate Resolution Imaging Spectroradiometer (MODIS) instrument, which has been used to produce a global 1 km LAI product every 8 days since early 2000 (<http://cliveg.bu.edu/modismisr/laifpar/laifpar.html>).

Despite their many advantages, all global satellite-based measurements of LAI suffer from problems of saturation and contamination. Particular problems therefore occur in monitoring moist tropical ecosystems. Problems are also evident where changes in background reflectivity contaminate the measurements, such as snow cover. For all these reasons, and for prediction of vegetation activity in the more distant past and in the future, it is essential to develop mechanistic predictive capabilities for LAI. In this role, satellite-based measurements function for model parameterization and validation. However, our current understanding of the complex environmental and biological controls on leaf area display across different species and vegetation types has not allowed the development of a general model of vegetation growth dynamics. LAI has been predicted using fixed C allocation coefficients (Potter et al., 1993; Kucharik et al., 2000), dynamic C allocation and turnover in response to cold and stress factors (Dickinson et al., 1998), and prescribed allometric relationships (Sitch et al., 2003). Other approaches use optimality criteria, such as maximizing NPP with respect to light and soil water (Woodward et al., 1995; Kaduk and Heimann, 1996), maximizing LAI given soil moisture constraints (Neilson, 1995), or assuming a functional balance between access to light, water, CO₂, and soil nutrients (e.g. Friedlingstein et al., 1999). Semi-mechanistic approaches have also been developed, such as following the annual C balance of leaves at the base of the crown (Friend et al., 1997).

All of these methods, to a greater or lesser extent, do well in predicting global relationships among the distribution of mean and maximum LAI and major drivers such as soil moisture and temperature. However, it is unclear if these

parameterizations will also hold in the future, when increasing atmospheric CO₂ and changed nutrient relations will interact strongly with climate, hydrological, and species changes and so likely have significant impacts on foliage area and activity. Improved predictive ability for global models will come from knowledge concerning the physiology of allocation in individual plants, followed by calibration using high quality *in situ* and satellite data at the scales of interest.

Leaf phenology refers to the science of the annual cycle of leaf area display. Both the spatial pattern of mean behavior and local inter-annual variability are key components of terrestrial ecosystem models. Timing of leaf display has been the subject of rather more analysis than absolute values of LAI, particularly in temperate forests. However, modeling vegetation-specific phenology at large spatial scales remains a significant challenge (Botta et al., 2000; Kucharik et al., 2006; Kathuroju et al., 2007). Local, species-specific empirical parameterizations of inter-annual variability are well characterized for temperate deciduous forest ecosystems, but their applicability at scales necessary for global simulations is doubtful (Kathuroju et al., 2007). There is clearly a conceptual problem in applying local inter-annual parameterizations to explain mean spatial variability.

Botta et al. (2000) parameterized biome-specific empirical phenological models at the global scale using AVHRR measurements scaled to a 0.5° resolution. Leaf onset is predicted either from a temperature sum (with an influence from the number of chilling days for cool deciduous broadleaf forests) or soil moisture (with a biome-specific time delay from some critical moisture value), depending on the biome type. This approach works well for mean dates in temperature-controlled regions, but is less effective for water-controlled regions such as tropical grasslands and savannas because of greater spatial heterogeneity and data problems. Improvements should result from the development of mechanistic models of grassland growth dynamics.

As mentioned previously, photosynthetic capacity per unit of foliage area in global models of photosynthesis is often prescribed using fixed values for different vegetation types. However, growth conditions can have a large influence

on capacity (Wullschlegel, 1993), and so some global models now include an interactive N cycle with prognostic foliage N (Friend and White, 2000; Woodward and Lomas, 2004; Thornton and Zimmerman, 2007). Foliage N is then related to photosynthetic capacity through assumed relationships with Rubisco and chlorophyll concentrations. A problem that remains largely unaddressed, however, is that specific leaf area (SLA), and hence the relationships between LAI, foliage C and N contents, and photosynthetic capacity, is highly variable among species, and even within species under different growth conditions (Knops and Reinhart, 2000). Global models almost all assume a fixed value for each vegetation type, although some recent efforts have been made to make SLA a dynamic variable, at least within canopies (Thornton and Zimmerman, 2007).

Foliage N is thought to limit photosynthesis in many terrestrial ecosystems (Field and Mooney, 1986), although there is evidence that P may be more important than N within the tropics (Vitousek, 1984) due to the highly weathered state and high sorption capacity of many moist tropical forest soils (Lloyd et al., 2001). Although tropical foliar P levels are often limiting, the importance of P for future responses of tropical rainforests to environmental change is unclear given the possibility of desorption of phosphate ions from their fixation sites in response to increased rates of plant uptake (Lloyd et al., 2001). We are not aware of any global photosynthesis/ecosystem model that contains an explicit P cycle (cf. Parton et al., 2005).

It is not clear how best to formulate plant N dynamics in global models. Friend et al. (1997) calculate allocation of N to foliage as a function of total plant N content, with fixed relative C:N ratios among foliage, stem, and fine roots. N is taken up using a function related to the plant N status, fine root mass, and soil mineral N concentration. More sophisticated allocation schemes are being developed in which foliage N dynamics are controlled by the local transpiration rate, as indicated by experimental results (Pons and Bergkotte, 1996), a methodology that has interesting implications for the mechanistic modeling of soil moisture effects on LAI and phenology.

The local foliage N content accounts for only part of the relation between nutrient availability

and plant photosynthetic capacity. Experimental evidence indicates that in most species studied, N supply actually has a greater influence on leaf area than on capacity per unit leaf area. For example, Taub (2002) measured a 37% increase in mean leaf mass in response to fertilization across 17 C₃ grass species, whereas mean growth rate per unit leaf area increased by only 12%. Studies such as this demonstrate that allocation shifts in response to nutrient supply need to be carefully included in global models.

3. Environmental Forcing

Global-scale models of terrestrial photosynthesis generally treat the supply of CO₂ to the chloroplasts much more simply than controls on photosynthesis itself. Most approaches explicitly consider stomatal conductance and leaf and/or canopy boundary layer conductance. However, the complexity of stomatal behavior is typically avoided by assuming that stomata act to maintain the intercellular air space concentration of CO₂ (C_i) at some specified ratio to the external concentration (C_a), thereby allowing calculation of stomatal conductance directly from the rate of net photosynthesis (A_n). This ratio is assumed fixed as light, temperature, and CO₂ concentration vary, with different values for C₃ and C₄ leaves. However, changing hydrological factors such as the leaf-to-air humidity gradient and soil moisture content change C_i/C_a, and this dependency can be included. Compelling evidence for the conservative nature of C_i/C_a was provided by Wong et al. (1979). However, a complication for practical applications is that A_n depends on C_i, requiring an iterative modeling process to obtain and equilibrium value of C_i under any given set of forcing conditions.

A frequently used parameterization of leaf-level stomatal conductance (g_{sc}), derived by Ball et al. (1987) from their own observations and subsequently modified by Leuning (1995), is:

$$g_{sc} = g_0 + \frac{a_1 A_n}{(C_s - \Gamma) \cdot \left(1 + \frac{D_s}{D_0}\right)}, \quad (20.1)$$

where D_s and C_s are the leaf surface vapor pressure deficit and CO₂ concentration, respectively, g₀ is conductance as A_n → 0 when light → 0, Γ is the CO₂ compensation point for

net photosynthesis, D_0 is the value of D_s that reduces $g_{sc} - g_0$ by 50%, and a_1 represents the slope of the relationship between conductance and net photosynthesis. It is well known that stomata close at low soil moisture contents, but it is not clear how this behavior should be combined with Eq. (20.1), resulting in a range of different, albeit simple, approaches. A fundamental issue is whether stomata respond directly to soil moisture, or through changes in photosynthetic capacity, as seems likely after sufficient time for adjustments (Wong et al., 1979). The “SiB2” model of Sellers et al. (1996a) and the Dynamic Global Vegetation Model (DGVM) of Krinner et al. (2005) reduce photosynthetic capacity under soil moisture stress, and then use the Ball et al. (1987) formulation for stomatal conductance, thereby simultaneously reducing photosynthesis and stomatal conductance.

Methodologies for calculation of atmospheric forcing and surface energy and water balances vary greatly depending on the model timestep, whether or not the aim is to explore climate feedbacks, and the general interests of the researchers. Weather generators are frequently employed to introduce daily weather variability given long-term mean-monthly climate (Friend, 1998). Sometimes these are extended to sub-daily timesteps. There is great variation in the detail with which the canopy boundary layer is treated, ranging from no explicit treatment (Sitch et al., 2003), to simple treatment of a canopy boundary layer (Woodward and Lomas, 2004), and full coupling to GCMs (Foley et al., 1998; Friend and Kiang, 2005). The level of detail used to treat atmospheric processes tends to be replicated for below-ground hydrology and surface energy balance.

Many global photosynthesis models use the so-called “big-leaf” hypothesis for the scaling of leaf-level photosynthesis (and stomatal conductance) to the canopy, despite significant doubts as its validity (Friend, 2001; Chapter 16 of this book by Ülo Niinemets and Niels P. R. Anten). More realistic approaches consider vertical gradients in photosynthetic capacity and radiation environment, including direct and diffuse irradiance and sun and shade leaves (Bonan et al., 2003). It is perhaps surprising that the radiation environment is frequently modeled in a somewhat *ad hoc* fashion, with little justification given for the level of

detail chosen and frequently no use of observations to constrain the approach, particularly with respect to different canopy geometries. Nevertheless, strong evidence exists that correctly simulating the canopy radiation environment is critical for accurate simulation of canopy photosynthesis (Friend, 2001; Baldocchi and Wilson, 2001).

B. Marine Models

1. Photosynthetic Capacity

Primary productivity in the sea is driven by a combination of physical, chemical, and biological factors. The most important is the biomass of phytoplankton, which is analogous to the “photosynthetic capacity” as defined in the previous section on terrestrial photosynthesis. Chlorophyll *a* is the most commonly used index of phytoplankton biomass because it is specific to the phytoplankton, and can be readily measured by a variety of methods on different space and time scales. In addition to spectrophotometric and fluorimetric determinations on samples extracted in polar solvents (Jeffrey et al., 1997), these methods include *in situ* sensing of chlorophyll fluorescence (Falkowski and Kiefer, 1985) and remote sensing of ocean color (O’Reilly et al., 1998; Morel et al., 2007).

Global distributions of chlorophyll concentration are available from several sensors including CZCS in the 1980s, and more recently SeaWiFS, MODIS-Aqua, and MERIS (Antoine et al., 2005; Morel et al., 2007). Chlorophyll *a* concentrations derived using these sensors agree over a wide range ($0.1\text{--}3\text{ mg m}^{-3}$), but diverge at the low Chl *a* concentrations ($<0.1\text{ mg m}^{-3}$) characteristic of the oligotrophic open ocean regions (Morel et al., 2007). Satellite estimates compare favorably with surface observations on discrete samples (Gregg and Casey, 2004), especially when issues regarding the validity of these “truth” observations are taken into account (Marrari et al., 2006). However, sampling errors may bias estimates of monthly and annual mean Chl *a* concentrations (Gregg and Casey, 2007b). Overestimates were inferred for regions that are poorly sampled due to low sun angle or high cloud cover (Gregg and Casey, 2007b). These are the times/locations when/where phytoplankton

growth is reduced (and thus Chl *a* concentrations are low) because incident light is low.

Satellite measurements of ocean color provide estimates of Chl *a* concentration for the upper 20% of the euphotic zone. However, the Chl *a* profile often shows vertical structure with a subsurface maximum that lies at depths where photosynthesis is limited by light. Surface observations of Chl *a* can be extrapolated to the entire euphotic zone based on typical vertical profiles of Chl *a* obtained from a climatology of *in situ* observations (Sathyendranath et al., 1995), or from empirically derived relationships between surface Chl *a* and the subsurface vertical distributions (Uitz et al., 2006).

The Chl *a* concentration can be reduced when incident light is low and/or nutrients are limiting. The light environment experienced by phytoplankton depends on the vertical attenuation of light and the mixed layer depth (MLD). In the clearest ocean waters, net photosynthesis can occur to depths of about 150 m. However, as Chl *a* concentration increases, light penetration decreases (Morel and Maritorena, 2001). At a concentration of $1 \text{ mg Chl } a \text{ m}^{-3}$, the photic zone depth declines to about 25 m, whereas at 10 mg m^{-3} Chl *a*, the photic zone is only about 10 m deep (Morel and Maritorena, 2001).

The MLD can vary from about 10 to >500 m. Phytoplankton are redistributed within the mixed layer by turbulence on time scales <1 day. During seasons when incident solar radiation is low and the surface layer is deeply mixed, light limits marine photosynthesis. At mid- and high-latitudes in winter the Chl *a* concentration typically drops to about 0.1 mg m^{-3} (Ward and Waniek, 2007). In temperate and polar regions during winter, the combination of low Chl *a* and low incident light limit primary production. Light limitation may be exacerbated by low Fe availability leading to Fe-light co-limitation (Boyd et al., 2001). During spring, Chl *a* concentration increases as incident solar radiation increases and the mixed layer shoals, consistent with critical depth theory (Follows and Dutkiewicz, 2001).

In the tropics, and in temperate latitudes during summer, the mixed layer typically lies within the euphotic zone and inorganic nutrients are limiting. In these oligotrophic waters, Chl *a* concentration drops below 0.1 mg m^{-3} . Nutrient limitation can be described either in terms of

Liebig-type limitation of yield (e.g. of Chl *a* concentration) or Blackman-type limitation of growth rate (Cullen et al., 1992). Both types of limitation operate in the sea. Liebig-type limitation may impose a greater constraint on primary productivity because, at a given incident photon flux density, primary productivity is proportional to phytoplankton biomass, and Liebig-type nutrient availability sets an upper limit to biomass. Blackman-type limitation of growth rate may be superimposed on Liebig-type limitation of biomass to further reduce primary productivity. For example, the upper limit on phytoplankton biomass may be set by the N upwelled from deep waters, but CO_2 and/or Fe may limit the rate at which inorganic N is converted into biomass (Moore et al., 2006b), and/or affect the composition of the phytoplankton assemblage (Tortell et al., 2002). Finally, co-limitation may act in several ways to limit the growth rate and/or affect the community structure of the phytoplankton (Arrigo, 2005).

2. Bio-optical Algorithms

An index of the light utilization efficiency, widely used in marine systems, is defined in Eq. (20.2). This efficiency, designated Ψ , is obtained by dividing the time- and depth-integrated primary productivity by the product of the depth-integrated Chl *a* concentration and the time-integrated photon flux incident upon the sea surface (Falkowski and Raven, 2007):

$$\Psi = \frac{\int_{\text{dawn}}^{\text{dusk}} \int_0^{Z_c} \text{NPP}(z, t) dz dt}{\int_0^{Z_c} \text{Chl}(z) dz \cdot \int_{\text{dawn}}^{\text{dusk}} E_0 dt} \quad (20.2)$$

In this equation, $\text{NPP}(z, t)$ is the net carbon fixation rate, $\text{Chl}(z)$ is the Chl *a* concentration, and E_0 is the incident PAR. The integration in time (t) is from dawn to dusk, and the integration over depth (designated z) is from the surface ($z = 0$) to the bottom of the euphotic zone ($z = z_c$). Ψ can be considered to be the product of the water-column-averaged optical cross-section and the water-column-averaged quantum efficiency of photosynthesis (Falkowski and Raven, 2007). Where the value of Ψ is known, Eq. (20.2) can be rearranged to calculate the daily water column integral NPP from the Chl *a* concentration and the incident PAR. Based on a review of the

data available at the time, Platt (1986) suggested that Ψ varied by about $\pm 40\%$ around a typical value of $0.48 \text{ g C (mol photons)}^{-1} \text{ m}^2 (\text{g Chl } a)^{-1}$. More recently, based on more comprehensive coverage of the global ocean, Falkowski and Raven (2007) showed that Ψ varies much more widely (from <0.1 – 1.5).

To obtain more accurate estimates of marine primary production, oceanographers employ bio-optical remote sensing algorithms. These algorithms can be classified into four categories depending on whether the algorithm resolves the depth, time, and/or wavelength dependencies of photosynthetic rate (Behrenfeld and Falkowski, 1997b). Central to bio-optical algorithms is treatment of NPP as the product of the Chl *a* concentration $Chl(z, t)$, g m^{-3} , and the Chl *a*-specific net photosynthesis rate P^{Chl} , $\text{g C (g Chl } a)^{-1} \text{ h}^{-1}$:

$$\text{NPP}(z, t) = Chl(z, t) \cdot P^{\text{Chl}}(z, t). \quad (20.3)$$

There are two basic approaches to parameterizing the light dependence of P^{Chl} (Sathyendranath and Platt, 2007). First, P^{Chl} can be specified as a function of PAR (Sathyendranath and Platt, 1989). In this case, the photosynthesis light curve is parameterized in terms of the light-saturated photosynthesis rate and the light-limited initial slope. These models are often resolved spectrally because the initial slope scales with the Chl *a*-specific light absorption coefficient, which varies with wavelength. A third parameter may be employed to describe the inhibition of photosynthesis at supraoptimal PAR. In the second approach, primary productivity is calculated from the product of the rate of light absorption and the quantum efficiency of photosynthesis (Morel, 1991). In this case, both the maximum quantum efficiency and the dependence of quantum efficiency on the rate of light absorption are specified. Provided that compatible mathematical formulations are chosen for the photosynthesis versus PAR and quantum yield versus PAR curves, these approaches are equivalent (Geider, 1990; Morel et al., 1996; Sathyendranath and Platt, 2007).

The coupling of photosynthesis to light and the effects of phytoplankton on the attenuation of light in water vary markedly with the wavelength of PAR. Phytoplankton dominate

the variable component of light attenuation in open ocean waters where the concentrations of colored dissolved organic matter and suspended particulate matter are low (Morel and Maritorena, 2001). Phytoplankton cells absorb a variable proportion (typically <10 – 70%) of the incident photons (Stramski and Mobley, 1997), and variations in cell size and cellular Chl *a* content lead to systematic variations in the Chl *a*-specific light absorption coefficient (Bricaud et al., 2004; 2007). In addition, the composition of photosynthetic pigments varies widely, and this variability affects the shape of the light absorption spectrum and thus NPP in the light-limited regions of the photosynthesis-PAR response curve (Sathyendranath and Platt, 2007). This spectral variability may affect competition for light in nature (Wood, 1985; Stomp et al., 2007). These are compelling reasons for including spectral dependencies in bio-optical algorithms (Morel et al., 1996; Behrenfeld, 1997b; Smyth et al., 2005; Sathyendranath and Platt, 2007).

The effects of temperature, photoacclimation, and nutrient limitation can be introduced by specifying how these variables affect the parameters of the photosynthesis-PAR relationships. For example, the light-saturated rate increases with temperature and declines in response to nutrient limitation or light limitation. Although sea surface temperature can be estimated directly using satellite remote sensing, the effects of these limitations must be obtained indirectly. Nutrient concentrations (N, P, Si) can be inferred from their correlation with temperature, although such correlations are site specific (Kamykowski et al., 2002; Switzer et al., 2003). The effect of light limitation can be parameterized in terms of the optical depth and incident PAR. Although we have a general understanding of how phytoplankton photosynthesis responds to these environmental variables based on laboratory studies (Geider et al., 1998), it is difficult to use this information directly in bio-optical algorithms. Instead, we rely on empirical relationships developed using ship-based observations. Perhaps the biggest obstacle to accounting for the effects of environmental variables on the parameters of the photosynthesis-PAR relationship is under-sampling in the world ocean (Banse and Postel, 2003; Carr et al., 2006).

There have been several round-robin comparisons of the performance of bio-optical algorithms of pelagic primary productivity. The most recent of these (Carr et al., 2006) found that global estimates of annual marine primary productivity varied by a factor of two amongst the 24 bio-optical models examined. A common set of input data consisted of sea surface Chl *a* concentrations, sea surface temperature, incident PAR, and MLD. The algorithms varied in complexity. The simplest algorithm estimated NPP directly from Chl *a* concentration without considering any of the other input variables. The most complicated algorithms included depth resolution of Chl *a* concentration and spectral resolution of PAR. The major limitations in the application of bio-optical algorithms identified were gaps in the observations of phytoplankton photosynthesis across the full range of conditions encountered in the ocean (Carr et al., 2006).

The Chl *a*-specific net photosynthesis rate (P^{Chl}), although commonly reported by oceanographers (MacIntyre et al., 2002) and commonly employed in bio-optical algorithms, is a poor index of phytoplankton growth. This is because there is taxonomic and phenotypic plasticity in the ratio of Chl *a*-to-biomass (Geider et al., 1998; Behrenfeld et al., 2005). For many applications, the carbon-specific rate of photosynthesis is more informative. Carbon-specific photosynthesis has units of inverse time and can be related to the specific growth rate (μ with units h^{-1}), provided that growth and net photosynthesis are measured on the same time scale. μ is related to P^{Chl} (with units of $\text{g C (g Chl } a)^{-1} \text{ h}^{-1}$) as follows:

$$\mu = \theta \cdot P^{\text{Chl}}, \quad (20.4)$$

where θ is the Chl *a*-to-carbon ratio in $\text{g Chl } a (\text{g C})^{-1}$.

Recently, bio-optical algorithms have been developed to estimate carbon-specific photosynthesis from satellite data (Behrenfeld et al., 2005; Westberry et al., 2008). These models also provide estimates of the carbon-to-Chl *a* ratio of the phytoplankton, which can be used as an index of the degree of light acclimation and nutrient limitation. This approach predicted a similar global marine NPP to other bio-optical approaches. However, the distributions of NPP in space and time differed significantly between the

Chl *a*-based and carbon-based algorithms (Westberry et al., 2008). This approach is used to obtain a new estimate of marine primary production in Section III.B.

Most bio-optical algorithms calculate NPP as the product of a capacity (e.g. the Chl *a* concentration) and a “conversion efficiency” (e.g. P^{Chl}), as in Eq. (20.3). However, it is not necessary to explicitly separate “capacity” from “conversion efficiency”, because NPP can be expressed as:

$$\begin{aligned} \text{NPP}(z, t) \\ = f[\text{Chl}(z, t), N(z), T(z), E(z), \dots], \end{aligned} \quad (20.5)$$

where z is the depth, $N(z)$ is the concentration of a limiting nutrient “ N ” at depth z , $T(z)$ the temperature at depth z , $E(z)$ is the photon flux density at depth z , etc. (Huot et al., 2007). In Eq. (20.5), remotely sensed Chl *a* serves directly as a predictor of NPP, together with other variables inferred from satellite remote sensing and/or climatologies (Huot et al., 2007). One can take this approach a step further by employing a biomass-independent algorithm that uses estimates of inherent optical properties rather than Chl *a* in the calculation of NPP (Sathyendranath and Platt, 2007).

Processes other than photosynthesis are important in determining marine NPP and the role of marine ecosystems in the carbon cycle. These processes include export production, calcification, and nitrogen fixation.

On land, atmospheric carbon in CO_2 can be sequestered in biomass and/or soil organic matter. These two compartments are in intimate contact with the atmosphere. In the oceans, phytoplankton sequester atmospheric carbon by facilitating its transport to the deep ocean, thus removing it from intimate contact with the atmosphere. This biologically driven vertical transport of carbon is referred to as the “biological pump” (Sigman and Haug, 2003). The biological pump consists of uptake of CO_2 and nutrients by phytoplankton near the sea surface (typically $<150 \text{ m}$ deep), sinking of particulate organic matter to below the permanent thermocline ($>1,000 \text{ m}$ deep), and remineralisation of organic matter to CO_2 and nutrients in the deep ocean or burial of organic carbon in the sediments (Sigman and Haug, 2003). Primary production removed from

the surface water by the biological pump is referred to as export production. Export production can be calculated from bio-optical algorithms of NPP by including further parameterizations describing the relationship between NPP and particle sinking (Dunne et al., 2007), which may be related to food-web structure (Laws et al., 2000a). For the ocean as a whole, export production accounts for about 20% of NPP (Laws et al., 2000a; Dunne et al., 2007).

Many marine organisms have calcium carbonate shells or scales. Amongst the important groups of planktonic calcifiers are coccolithophorids, foraminifera, and pteropods. Calcification removes inorganic carbon from the ocean, but increases the partial pressure of CO_2 (p_{CO_2}). This is evident from the stoichiometric equation for the precipitation of calcium carbonate: $\text{Ca}^{2+} + 2 \text{HCO}_3^- \leftrightarrow \text{CaCO}_3 + \text{CO}_2 + 2\text{H}^+$. This increase of p_{CO_2} due to calcification partially offsets the ability of the ocean biota to sequester atmospheric CO_2 by the biological pump. However, CaCO_3 acts as ballast, which accelerates the sinking of organic matter, potentially increasing export production. Recently, algorithms for the remote sensing of suspended calcium carbonate concentration (Balch et al., 2005) and the rate of calcification (Balch et al., 2007) have been developed and applied.

Nitrogen fixation provides up to 50% of the key limiting resource of fixed nitrogen in large parts of the oligotrophic open ocean. This new nitrogen allows increased phytoplankton biomass and primary productivity. Blooms of the colonial diazotroph *Trichodesmium* appear to be superimposed on a low background rate of N_2 fixation. These blooms are considered to make a major contribution to oceanic N_2 fixation (Capone et al., 2005). Recently, algorithms for detecting *Trichodesmium* blooms from water-leaving radiance have been developed (Westberry and Siegel, 2006). The spatial patterns of *Trichodesmium* blooms retrieved by these algorithms are largely consistent with previously reported blooms (Westberry and Siegel, 2006), with putative *Trichodesmium* blooms found most often in the eastern tropical Pacific and the Arabian Sea. The nitrogen cycle is closely coupled to the carbon cycle in marine systems, and increased understanding of the sources and sinks of fixed

nitrogen (Deutsch et al., 2007; Duce et al., 2008) will continue to inform models of marine NPP and export production.

3. Biogeochemical Models

Whereas the NPP of phytoplankton can be obtained from bio-optical algorithms, investigations of the response of the marine carbon cycle to climate change employ biogeochemical models. Biogeochemical models examine the coupling of plankton dynamics to ocean physics. Unlike terrestrial vegetation, which is rooted in place, the oceans are a dynamic fluid. Phytoplankton are suspended in the water column and drift with the currents. The nutrients that phytoplankton need to grow and the grazers that feed on the phytoplankton also drift with the currents. To account for these effects, models of ocean ecosystems are embedded within physical models of ocean circulation and mixing (e.g. Ocean General Circulation Models). At any point in the ocean, the rate of change of phytoplankton biomass is determined by the physical processes of advection and diffusion, and the ecological processes of production (e.g. photosynthesis and nutrient uptake), consumption (e.g. grazing), and dissipation (e.g. respiration and excretion) (Doney et al., 2003).

Current models of plankton ecology and biogeochemistry can be traced to the seminal work of Fasham et al. (1990). These authors embedded an ecological model, which represented the state-of-the-art understanding of plankton processes in the late 1980s, within a simple physical model of the annual cycle of incident solar radiation, MLD, vertical exchange, and vertical nutrient fluxes at one location in the Sargasso Sea near Bermuda. Inorganic nitrogen and light were the only limiting factors in the ecological model. The model included two inorganic forms of nitrogen (nitrate and ammonium) and five ecological components (phytoplankton, zooplankton, bacterioplankton, dissolved organic nitrogen, and detritus). Models derived from Fasham et al. (1990) are sometimes referred to as NPZD models, indicating that they describe the dynamics of inorganic Nutrients, Phytoplankton, Zooplankton, and Detritus. NPZD models have been embedded within 3D ocean GCMs to study ocean plankton dynamics

and plankton biogeochemistry at the basin scale (Sarmiento et al., 1993) and ocean scale (Popova et al., 2006a, b).

NPZD models were developed to examine the effects of changes in physical forcing (primarily seasonal variability of MLD) on seasonal and spatial variability of chlorophyll concentration (Fasham et al., 1990). These models lack taxonomic resolution, and Chl *a* is used to represent the biomass of all phytoplankton groups. More recently, dynamic green ocean models (DGOMs) have been developed to study the feedbacks between climate and the ocean microbiota (Le Quéré et al., 2005; Hood et al., 2006; Gregg and Casey, 2007a). The most sophisticated of these DGOMs include several phytoplankton functional groups and several interacting element cycles. Typically, two of the functional groups are defined taxonomically, namely the diatoms and the diazotrophs (which use N₂ as a nitrogen source), and two of the functional groups are defined by cell size, namely the picophytoplankton (0.2–2 μm nominal diameter) and nanophytoplankton (2–20 μm diameter). DGOMs may also include calcifying organisms (coccolithophorids and foraminifera in the open ocean) as functional groups because of the importance of calcification in the marine carbon cycle (Orr et al., 2005). The element cycles included in the models are those of C, N, P, Fe, and Si. Of these five elements, N, P, Fe, or Si can limit phytoplankton growth rate and yield.

The model of Moore et al. (2004) illustrates the importance of including different functional groups in models of upper ocean biogeochemistry. Diazotrophs accounted for about 0.5% of primary production, but fixed enough N₂ to provide the N source that supported about 10% of primary production and 8% of export production (Moore et al., 2004). In this work, diatoms disproportionately contributed to export production, but CaCO₃ from the coccolithophores was the key driver of the export flux to the deep ocean. Unfortunately, different DGOMs may yield widely different assessments of the contributions of key functional groups, including diatoms and coccolithophores, to NPP (Gregg and Casey, 2007a), indicating that a consensus model has yet to be achieved.

4. Environmental Forcing

Models of ocean biogeochemistry typically divide the ocean into a set of vertical divisions within a latitude/longitude grid (Doney et al., 2003). The output of the biogeochemical models is affected by the sizes of the boxes in the grid and the physical oceanographic model within which the biogeochemical model is embedded (Berline et al., 2007). The spatial resolution of the physical model, both in the vertical and in the horizontal, affects the fidelity of the physical model in representing ocean circulation and mixing. The fidelity of the physical model is also affected by temporal resolution, especially with respect to the ability of the model to represent vertical mixing near the sea surface. Errors in the physical model will lead to errors in nutrient fluxes and the light environment, and thus affect the output of the biogeochemical model (Berline et al., 2007; Najjar et al., 2007).

A recurrent problem in plankton biogeochemical models is underestimation of primary productivity in the oligotrophic subtropical gyres relative to observations (McGillicuddy et al., 1998; Berline et al., 2007). The problem applies not only to NPP in models, but also to accounting for export production (McGillicuddy et al., 1998). Although underestimation of the rate of nitrogen fixation may account for some of the discrepancy, it is also clear that inclusion of mesoscale processes, which were neglected in course resolution (>2°) models, is necessary to obtain accurate nutrient budgets.

Mesoscale eddies (50–100 km diameter) play an important role in transporting heat, salinity, momentum, and nutrients in the ocean. Mesoscale eddies increase nutrient supply and thus primary production in the nutrient-impooverished subtropical ocean (McGillicuddy et al., 1998, 2007). If the perturbation in nutrient supply is sufficient to change the structure of the open ocean food web, then the operation of the biological pump may also be affected (Laws et al., 2000a; Brix et al., 2006). Associated with eddies are sub-mesoscale (5–10 km wide) features. Nutrient transport associated with these features may be as important as that attributed to the mesoscale eddies (Lapeyre and Klein, 2006;

McGillicuddy et al., 2007). With increases in computing power, the latitudinal and longitudinal resolution of GCMs has increased from $>2^\circ$ to $<0.1^\circ$ (McGillicuddy et al., 2003), providing enough spatial resolution to represent important mesoscale oceanographic features.

Vertical mixing and stratification have long been known to play significant roles in plankton ecology and ocean biogeochemistry (Platt et al., 2003; Popova et al., 2006b). MLD is affected by seasonal periodicity (e.g. solar radiation and wind patterns), long-term fluctuations in the climate system (e.g. ENSO and other teleconnections), episodic events (e.g. storms), and the diel cycle of solar radiation. MLD in turn affects the entrainment of nutrients from deep waters to the photic zone, the detrainment of organisms and organic matter from the photic zone to the deep ocean, and the light environment encountered by phytoplankton (Platt et al., 2003). Phytoplankton biomass and productivity respond primarily to variability in mixing and nutrient fluxes, and survival of zooplankton through the winter also depends on the extent of mixing (Popova et al., 2006b).

Most biogeochemical models used to describe the current state of the ocean employ a time step of one day, whereas models designed to examine the evolution of the ocean carbon cycle on time scales of 100–1,000 years employ longer time steps, typically a month. In a recent study, Popova et al. (2006b) examined how the time step, which ranged from 6 h to 1 month, affected the simulation of NPP and new production in a global ocean biogeochemical model. Diel variability of MLD (Woods and Onken, 1982) appeared to be particularly important in controlling the performance of the biogeochemical model (Popova et al., 2006b). The mixed layer shoals during the day as solar radiation heats the surface waters, trapping plankton near the surface. MLD increases at night as loss of heat from the sea surface leads to convective mixing, redistributing the plankton into deeper waters and transporting nutrients to the surface.

Physical forcing refers not only to ocean circulation and MLD, which are affected by incident solar radiation, but also to the input of nutrients to the sea surface. Inorganic and organic nitrogen, phosphorus, and trace elements are deposited to the surface ocean in wet and

dry deposition from the atmosphere (Jickells et al., 2005; Duce et al., 2008). In particular, with the recognition that Fe is a limiting nutrient for NPP in about 1/3 of the ocean, designated as High-Nitrate/Low-Chlorophyll (HNLC) regions (de Baar et al., 2005), and that Fe may limit N_2 fixation in oligotrophic ocean regions that account for most of the rest of ocean surface area (Falkowski, 1997), the deposition of Fe-containing aerosols has been recognized to play an important role in ocean carbon cycle (Moore et al., 2006b; Moore and Doney, 2007). The aeolian supply of nutrients can be specified from dust deposition fields derived from atmospheric transport models such as GOCART (Ginoux et al., 2001), and assumptions regarding the N, P, and Fe content and solubility in the atmospheric aerosols.

III. Global Simulation

A simulation is presented here to illustrate the state-of-the-art of modeling photosynthesis at the global scale. Mean annual terrestrial and marine fields of the recent historical period are combined to give a global picture. The first such combined assessment was published by Field et al. (1998); the simulation presented here is designed to be an update to this. The terrestrial simulation uses the mechanistic biochemical model described by Friend and Kiang (2005), with some modifications, and the marine simulation uses the bio-optic “Carbon-based Primary Model” (CbPM) model of Westberry et al. (2008).

A. Terrestrial Photosynthesis

1. CO_2 Fixation

Foliage-level C_3 photosynthesis is modeled using the approach of Kull and Kruijt (1998) as implemented by Friend (2001) and Friend and Kiang (2005), but with some improvements (e.g. improved handling of numerical roots when solving for the intercellular air space CO_2 concentration). Kull and Kruijt (1998) took as their starting point the model of Farquhar et al. (1980) and added a treatment of light extinction over chloroplasts to separate regions of the leaf that are light-saturated or light-limited. Photosynthesis in

the light-saturated region is taken as the minimum of the electron transport capacity- and Rubisco-limited rates. Under many conditions, light extinction over the light-saturated chloroplasts causes the rate of CO₂ fixation in deeper chloroplasts to be limited by the rate of light harvesting. Photosynthesis in this region is a linear function of the total amount of light absorbed by light-limited chloroplasts and the intrinsic quantum efficiency. All three rates are expressed on an N basis, enabling straightforward scaling to the leaf and canopy levels. Kull and Kruijt (1998) showed that if the chlorophyll to N ratio is assumed constant throughout the leaf, then the following analytical solution can be derived:

$$A = \left(1 - \frac{\Gamma^*}{C_i}\right) \cdot [m_{\text{sat}}N_{\text{sat}} + \alpha m_1 I_a], \quad (20.6)$$

where A is total leaf photosynthesis, Γ^* is the CO₂ partial pressure for the compensation of oxygenation and carboxylation reactions, C_i is the partial pressure of CO₂ in the intercellular air space, m_{sat} is the N-normalized rate of light-saturated carboxylation (i.e., the minimum of the electron transport capacity- and Rubisco-limited rates), N_{sat} is the cumulative N at which limitation by light harvesting occurs, α is the intrinsic quantum efficiency, m_1 is the ratio of the CO₂-controlled RuBP supply-limited carboxylation rate to its theoretical maximum, and I_a is the amount of light absorbed by light harvesting-limited chloroplasts. A single extinction coefficient is used to calculate light absorption over chloroplasts, and N_{sat} is calculated from m_{sat} , total leaf N, and total absorbed light.

This approach has been shown to perform substantially better than the traditional implementation of the Farquhar et al. (1980) model for a wide range of forest canopies (S. Zaehle and A.D. Friend, unpublished).

The approach of Kull and Kruijt (1998) was adapted for C₄ physiology, with the same overall approach of separation of light-saturated and light-limited regions. However, bundle-sheath chloroplast CO₂ is assumed to be 7,800 Pa – as calculated from the full intercellular (ICT) transport model of Collatz et al. (1992) under peak photosynthetic rates – and an additional potential limitation to light-saturated photosynthesis from the CO₂ concentrating mechanism is

included. This is parameterized as a linear dependence on the CO₂ concentration in the intercellular spaces of the mesophyll (after Eq. 4A of Collatz et al., 1992), with a $Q_{10} = 2$ temperature dependence and a linear scaling factor relating the PEPcase rate constant for CO₂ to foliar photosynthetic N content (calibrated using the ICT model to be 3.2 mol CO₂ (mol N)⁻¹ s⁻¹). In addition, the fractional RuBP quantum requirement for the production of RuBP in the bundle-sheaths is assumed to be 0.6 (Berry and Farquhar, 1978).

2. Photosynthetic Capacity

Terrestrial vegetation is classed into seven generalized plant types (GPTs), and each is assigned typical parameter values related to its foliage physiology (Table 20.1). These values were derived from the literature (see legend to Table 20.1) and *in situ* measurements at representative sites compiled in the FLUXNET database of eddy-covariance CO₂ flux sites (Friend and Kiang, 2005). The natural variation in these parameters between species and growth conditions within each GPT is very wide, particularly for specific leaf area and foliar N content. Nevertheless, the use of typical values addresses the overall broad regional behavior of vegetation for global-scale studies. More local assessments would require greater precision in biological (and physical) parameterization.

Each terrestrial 1/4° pixel is assigned a dominant GPT using the Loveland et al. (2000) land cover database with the SiB classification system. This is an AVHRR-based product, and dominant cover types were each assigned to dominant GPTs using the mapping given in Table 20.2.

Mean-monthly LAI is prescribed from observations made by the MODIS instrument and available through the Department of Geography, Boston University (<http://cliveg.bu.edu/>; Yang et al., 2006). A complication arose from misalignment between the original 1/4° dataset (MOD15_BU) and the actual distribution of land area, particularly in Oceania, necessitating adjustments by eye to the original grid. A mean-monthly LAI climatology was then created from the original February 2000–December 2006 data. These data are used to prescribe monthly LAI in the global photosynthesis simulations without temporal interpolation.

Table 20.1. Parameter values assigned to the different generalized plant types (GPTs) used in the global terrestrial simulations. GPT codes are: NLEV = needleleaf evergreen, BREV = broadleaf evergreen, NLCD = needleleaf cold deciduous, BRCD = broadleaf cold deciduous, C3GR = C₃ herbaceous, and C4GR = C₄ grass. Specific leaf areas (*SLAs*) come from Bond-Lamberty and Gower (2007) (moss: mean of min and max measurements); White et al. (2000) (NLEV, NLCD, BRCD, C3GR); McWilliam et al. (1993) (BREV; mean assuming 0.5 kg [C] kg [DM]⁻¹); and the value for C4GR is assumed equal to that for C3GR. *N* (foliar N content as percentage of dry mass) taken from Liu et al. (2007) (moss), White et al. (2000) (NLEV, NLCD, BRCD, C3GR), Martínez-Sánchez et al. (2003), assuming SLA used here (BREV), and calibrated against CO₂ flux data from Hanan et al. (2005) (C4GR). *f_N* is relative photosynthetic capacity per unit foliar N, calibrated from eddy-covariance flux data as described by Friend and Kiang (2005) (NLEV, BREV, BRCD, C3GR); C4GR *f_N* is calibrated against CO₂ flux data from Hanan et al. (2005); moss *f_N* is set to the default value in the original Kull and Kruijt (1998) model; NLCD *f_N* is set to the value for BRCD. Minimum foliar surface conductance to water, *g_{min}*, is assumed infinite for moss (very thin cuticle); other values come from Vostrál et al. (2002) (NLEV, assumed the same for NLCD); and the rest are calibrated from latent heat flux data (Friend and Kiang 2005; Hanan et al., 2005)

GPT	<i>SLA</i> m ² kg [C] ⁻¹	<i>N</i> % [DM]	<i>f_N</i> fraction	<i>g_{min}</i> mm s ⁻¹	<i>g_{max}</i> mm s ⁻¹
Moss	61	2.6	1	∞	∞
NLEV	8.2	1.1	0.9	0.04	6
BREV	18	1.8	1.1	0.1	5
NLCD	22	1.7	1.5	0.04	6
BRCD	32	1.8	1.5	0.06	6
C3GR	27	1.8	1.3	0.06	6
C4GR	27	1	2	0.06	15

Table 20.2. Mapping of SiB land cover type (Loveland et al., 2000) to dominant generalized plant types (GPTs) for use in the global terrestrial simulation

Simple Biosphere (SiB) Classification	Dominant GPT
Water Bodies	Missing
Evergreen broadleaf trees	Broadleaf evergreen (BREV)
Broadleaf deciduous trees	Broadleaf cold deciduous (BRCD)
Deciduous and evergreen trees	Needleleaf evergreen (NLEV)
Evergreen needleleaf trees	Needleleaf evergreen (NLEV)
Deciduous needleleaf trees	Needleleaf cold deciduous (NLCD)
Ground cover with trees and shrubs	C ₄ grass (C4GR)
Groundcover only	C ₄ grass (C4GR)
Broadleaf shrubs with perennial ground cover	Broadleaf evergreen (BREV)
Broadleaf shrubs with bare soil	Broadleaf evergreen (BREV)
Groundcover with dwarf trees and shrubs	Broadleaf evergreen (BREV)
Bare soil	Bare
Agriculture or C ₃ grassland	C ₃ herbaceous (C3GR)
Persistent wetland	Moss
Ice cap and glacier	Missing
Missing data	Missing

LAI × mean N content (Table 20.1) gives total canopy N in each pixel for each month. Foliar N is distributed over horizontal canopy layers using a simple exponential decline with canopy depth, fitted to data collected in a high canopy N tropical rainforest (Carswell et al., 2000). The ratio of chlorophyll to foliar N is assumed to increase with depth, with a relationship fitted to the data of Kull and Kruijt (1998). These relationships are described fully by Friend and Kiang (2005).

3. Environmental Forcing

The biochemical model is driven by the intercellular partial pressures of CO₂ and O₂, leaf temperature, and the flux of photosynthetically active photons penetrating the leaf. Leaf photosynthesis is integrated across sun and shade foliage in horizontal layers with thicknesses of 0.5 LAI units at a 30 min timestep to give canopy photosynthesis. Intercellular O₂ is assumed constant at 20.9 kPa,

but CO_2 is calculated from the balance of fixation in chloroplasts, respiration from mitochondria, and diffusion through the stomatal pores (permeable epidermis in the case of moss). A unique numerical solution for the mean intercellular CO_2 is obtained for the entire canopy on each timestep. Canopy stomatal conductance is calculated using the semi-empirical model described by Friend and Kiang (2005). This includes empirical responses to soil water potential, intercellular CO_2 partial pressure, intercellular to free air specific humidity gradient, and the potential rate of canopy photosynthesis under conditions of saturating CO_2 (Friend and Kiang, 2005). An effect of mean canopy height is also included, but for the simulations shown here mean canopy height is fixed at 0.5 m to avoid the need for a global canopy height dataset. Soil water potential in each soil layer is calculated from relative water content as in Friend (1995).

Foliar mitochondrial respiration is required to balance the CO_2 flux, and is calculated as a function of canopy N and temperature. The temperature response for C_3 leaves is taken from Bernacchi et al. (2001), and the response for C_4 leaves is taken from Collatz et al. (1992). N dependence of respiration is calibrated from eddy-covariance sites with different linear relationships for C_3 and C_4 physiologies.

Incoming direct and diffuse PAR is distributed over canopy layers using the scheme of Spitters et al. (1986), as implemented by Friend (2001). Canopy temperature, boundary layer transfer coefficients, and soil moisture are calculated using the land surface scheme of the NASA Goddard Institute for Space Studies global climate model II (Hansen et al., 1983), with the coefficient for CO_2 transfer assumed to equal that for sensible heat. Two soil layers are used, 0.1 and 2 m depth, and the spatial distribution of field capacity in each is calculated by aggregating the IGBP-DIS 5' dataset to $1/4^\circ$ (Global Soil Data Task Group, 2000). Canopy temperature is assumed to equal the temperature of the upper soil layer, and the intercellular specific humidity is assumed saturated at that temperature. Potential soil evaporation uses a soil surface resistance calculated from the relative moisture content of the upper soil layer and relative humidity at the soil surface calculate from its soil water potential

(Xue et al., 1996), and is reduced as a negative exponential function of LAI. Canopy transpiration is subtracted from the soil layer with the highest relative water content, with all plant types assumed to have access to both layers.

Atmospheric forcing at 10 m above canopy top is created using a weather generator parameterized with mean-monthly fraction of wet days, precipitation per wet day, 24-h maximum and minimum temperatures, 24-h shortwave radiation, and water vapor pressure. These values are derived from the 10' CRU CL 2.0 1961–1990 mean climatology (New et al., 2002), and aggregated to $1/4^\circ$. 24-h shortwave radiation is calculated from relative sunshine duration using the mean global parameterization of Friend (1998).

The weather generator described by Friend (1998) generates daily precipitation, minimum and maximum temperatures, total shortwave irradiance, and mean water vapor partial pressure. Mean daily atmospheric optical depth (AOD) is calculated from the generated daily shortwave and potential daily shortwave with no atmosphere. AOD is then assumed constant during the day and used with sun angle to estimate $1/2$ -hr values of direct and diffuse PAR using the relationships given by Spitters et al. (1986), assuming a fixed ratio of PAR to total shortwave. Atmospheric pressure, wind speed, and atmospheric CO_2 concentration are assumed constant (viz. 101325 Pa, 2 m s^{-1} , 14.1 mmol m^{-3}). Daily precipitation is spread evenly across sub-daily timesteps. A linear regression is calculated for each day between the temperature extremes and shortwave radiation. This relationship is then used to calculate air temperature at each timestep, from which water vapor mixing ratio is derived from the generated mean daily water vapor pressure. Downward longwave irradiance is parameterized as a function of cloud cover fraction and air temperature using the formulation of Pirazzini et al. (1998), with clear-sky emissivity set to 0.69, and cloud cover fraction assumed fixed at 0.8.

B. Marine Photosynthesis

Water-column integrated global ocean net primary production (NPP) was calculated using the *Carbon-based Production Model* (CbPM) as described by Westberry et al. (2008), with only

minor modifications to input data sets. The CbPM is a depth-resolved, spectral model that is unique among ocean NPP algorithms in two significant respects. First, the CbPM calculates NPP as the product of phytoplankton biomass (carbon concentration, C_{phyto}) and growth rate, μ (i.e., $\text{NPP} = \mu \times C_{\text{phyto}}$), where C_{phyto} is derived from satellite particulate backscattering coefficients (b_{bp}) and μ is derived from the ratio of satellite chlorophyll and C_{phyto} concentrations. Thus, both phytoplankton biomass and physiological variability are derived directly from remotely sensed ocean properties. This contrasts with traditional chlorophyll-based algorithms where $\text{NPP} = \text{Chl} \times P^{\text{Chl}}$ and empirical, field-based relationships are applied to describe variability in P^{Chl} . The second innovation of the CbPM is that information on surface mixing depth, depth of the nutricline, and physiological responses to light- and nutrient-conditions are used to iteratively evolve distributions of chlorophyll, light, and NPP through the water column for each satellite pixel. This approach contrasts with earlier treatments where empirical Gaussian functions based on surface chlorophyll concentration are used to describe depth-variations in chlorophyll, that are then applied to estimate water-column light- and NPP distributions.

A complete description of the CbPM approach is provided by Westberry et al. (2008), while here only a brief overview is given. Additional information on the CbPM, model code, and global products can be found on the Ocean Productivity Website at: <http://science.oregonstate.edu/ocean.productivity/>.

1. Underwater Light Field

Global, gridded 8-day fields of cloud-corrected PAR ($\text{Ein m}^{-2} \text{ day}^{-1}$) incident at the sea surface and diffuse attenuation coefficients at 490 nm, $K_d(490)$, (m^{-1}), were obtained from the OceanColor Web (<http://oceancolor.gsfc.nasa.gov>) and based on Sea-viewing Wide Field-of-view Sensor (SeaWiFS) measurements between September 1997 and July 2007 (spatial resolution of $\sim 18 \text{ km}$ at the equator). PAR was decomposed spectrally using constant fractions estimated from an atmospheric radiative transfer model

(Ricchiazzi et al., 1998; Westberry et al., 2008). Spectral diffuse attenuation coefficients for the visible waveband, $K_d(\lambda)$, were calculated from $K_d(490)$ using the model of Austin and Petzold (1986). Combining these spectral irradiance and attenuation estimates permits the differential propagation of light with depth and yields an accurate characterization of the underwater light environment.

In the CbPM, $K_d(\lambda)$ is assumed to be constant within the mixed layer. Below this surface layer, chlorophyll concentration varies with depth in response to changing light and nutrient conditions (see below), which consequently alters $K_d(\lambda)$. This feedback between physiological acclimation and light attenuation is captured by iteratively propagating light through the water column (Westberry et al., 2008). For these calculations, MLD was obtained from the Ocean Productivity Website and defined as the depth at which density is 0.125 kg m^{-3} greater than the density at 10 m.

2. Phytoplankton Carbon, Chlorophyll, and Net Primary Production

Global, gridded 8-day fields of SeaWiFS normalized water leaving radiances, $n\text{Lw}(\lambda)$, were obtained from the OceanColor Web and inverted using a non-linear minimization method that solves for three unknown quantities: Chl , b_{bp} , and absorption by colored dissolved matter (a_{cdm}) (Maritorena et al., 2002). Variations in b_{bp} reflect changes in particle abundance and can be related to phytoplankton carbon (C_{phyto}) because (1) the particle size spectrum in the open ocean is highly conserved, (2) phytoplankton contribute directly and significantly to b_{bp} , and (3) the concentration of individual components of the particle assemblage covaries with phytoplankton abundance (Behrenfeld and Boss, 2003, 2006; Westberry et al., 2008). In the CbPM, mixed layer C_{phyto} is calculated as:

$$C_{\text{phyto}} = 13,000 \cdot (b_{\text{bp}} - b_{\text{bpNAP}}), \quad (20.7)$$

where b_{bpNAP} is a correction for background scattering from non-algal particles (0.00035 m^{-1} , from Westberry et al., 2008). Below the mixed layer, the vertical profile of C_{phyto} is assumed uniform and equal to the surface value up to a depth where growth rate (see below) equals

a constant and low background loss rate (0.1 day^{-1}), after which C_{phyto} decreases smoothly with depth (Westberry et al., 2008).

Chlorophyll concentration is a function of both phytoplankton biomass and physiological variability in intracellular pigmentation (i.e., $Chl:C$ ratio). Under nutrient-replete conditions, $Chl:C$ is a strong function of growth irradiance (I_g) and can be characterized as a decreasing exponential function of I_g . In the mixed layer, I_g is the median daily PAR for the mixing depth. Phytoplankton growth rates in the mixed layer are first described as a saturating function of I_g and then adjusted downward to account for nutrient stress effects. This adjustment is made using the difference between satellite-derived $Chl:C$ and the anticipated nutrient-replete $Chl:C$ value for the given mixed layer I_g value (Westberry et al., 2008).

Below the mixed layer, an iterative scheme is employed for calculating the vertical distribution of phytoplankton Chl and μ . With each vertical increment, the phytoplankton community acclimates to the slightly lower light level of its depth horizon by increasing intracellular pigmentation ($Chl:C$), with μ responding accordingly. This photoacclimation response is similar to that employed for the mixed layer, but is also influenced by the vertical distribution of nutrients. Specifically, depth-dependent relaxation from surface nutrient stress enhances growth rates for a given I_g (thus, increased $Chl:C$). This nutrient effect is characterized according to distance from the nitracline, where nitracline depths are provided from monthly climatological nutrient fields reported in the World Ocean Atlas (Conkright et al., 2002; Westberry et al., 2008). The vertical nutrient gradient thus allows chlorophyll concentration to increase more rapidly from the surface to the nitracline than would otherwise occur from photoacclimation alone. Below the nitracline, phytoplankton are assumed to be nutrient replete, such that continued depth-dependent changes in chlorophyll are due only to changes in light and C_{phyto} . Once this iterative process is complete, NPP at each depth (z) is calculated as:

$$\text{NPP}(z) = \mu(z) \cdot C_{\text{phyto}}(z) \quad (20.8)$$

and then integrated over the water column to achieve an areal NPP estimate ($\text{mg C m}^{-2} \text{ day}^{-1}$) for each satellite pixel.

C. Global Simulation Results

Global fields of NPP were obtained by combining the terrestrial and marine simulation results, with terrestrial NPP estimated simply as 50% of GPP. This ratio is commonly observed and is consistent with theoretical considerations (Dewar, 1996). In any case, greater complexity in modeling autotrophic respiration introduces uncertainties relative to the better-constrained photosynthesis model components due to the lack of fundamental information concerning how respiration and the processes it supports are physiologically controlled (e.g. Trumbore, 2006).

Figure 20.1 shows mean annual NPP. Global NPP is $107.3 \text{ Pg C year}^{-1}$, with $54.8 \text{ Pg C year}^{-1}$ on land and $52.5 \text{ Pg C year}^{-1}$ in the oceans. Field et al. (1998) estimated $56.4 \text{ Pg C year}^{-1}$ on land and $48.5 \text{ Pg C year}^{-1}$ in the oceans, with the latter including a 1 Pg C year^{-1} contribution from macroalgae, not considered here. Differences with our simulation could be due to the time period and/or the methods. As expected, the general patterns are similar to those found in other studies, such as Field et al. (1998). However, compared to this work, boreal forest NPP is around 50% higher (at 50° N) in these new simulations, whereas tropical forest NPP is lower by $\approx 40\%$ (e.g. at -10° S). The greatest differences for ocean NPP are in the southern Ocean, where the new model estimates fluxes $\approx 50\%$ below those of Field et al. (1998). These lower values are compensated by higher NPP towards the equator (e.g. $\approx 40\%$ higher at 0° N). Further work will be necessary to determine the source of these large differences, but are likely linked to improved treatment of leaf-level photosynthesis on land and of spatial and taxonomic physiological variability in the ocean. Establishing the accuracy of these simulations will need to utilize a combination of tower, sea surface, and atmospheric CO_2 concentration measurements (Friend et al., 2007).

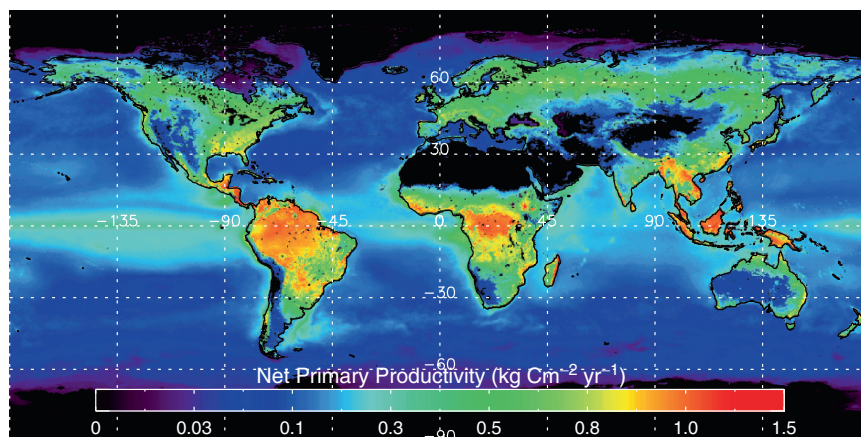


Fig. 20.1. Mean annual net primary productivity (NPP) simulated by Hybrid6.5 (land) and the CbPM (ocean) for the period 2000–2007. Total mean annual NPP is $107.3 \text{ Pg C year}^{-1}$, with 51.1% coming from land and 48.9% from the oceans. Land pixels simulated with $1/4^\circ$ resolution and ocean pixels with $1/12^\circ$ resolution. Land leaf area dynamics prescribed from MODIS satellite retrievals, ocean production calculated using data from the SeaWiFS instrument. Full simulation details are given in the text. See also Color Plates, Fig. 7

IV. Concluding Remarks

It is interesting to note that terrestrial and marine approaches to modelling primary production both fall into two equivalent categories, one essentially empirical (using remote sensing) and one mechanistic. Both “top-down” approaches rely on remote-sensing of the distribution of photosynthetic capacity (Chl *a* and carbon in the sea, LAI on land), and in most cases use a linear scaling with absorbed light. “Bottom-up” approaches are built using understanding of the environmental controls on capacity, and have the potential to evaluate photosynthesis outside of the period of the satellite record, using DGOMs in the case of the sea and DGVMs on land. The following section gives an overview of the issues that need to be addressed in the future to increase our confidence in this second class of model.

A. Future Challenges

1. Terrestrial Systems

Prognostic global simulations of future terrestrial photosynthesis will continue to play a major role in studies of future potential impacts of, and feedbacks on, global environmental change. However, validation of existing approaches remains a major problem. We lack key datasets for

testing canopy-scale simulations of photosynthesis, partly due to the small number of sites with measurement towers and partly due to inherent methodological problems resulting in missing data and difficulty in separating photosynthesis from net ecosystem exchange. High quality datasets need to be assembled to allow precise evaluation of models, including identification of potential sources of bias such as hydrological feedbacks, canopy temperatures, and physiological attributes. It is frustrating that data constraints mean that model evaluations fail to separate bias in physics from bias in physiology. Datasets need to be assembled that contain the full range of necessary ancillary information, such as canopy nitrogen contents, temperatures, soil moisture, radiation profiles, and site history.

Current models are also poorly constrained with respect to controls on spatial and temporal variation in capacity (i.e. leaf area and nitrogen content), contributions of physiological diversity, and the potential for physiologies, populations, and species mixes to adapt to environmental change. Future projections will depend critically on how well capacity and ecosystem changes are modeled. However, most models currently treat these processes very simply, if at all. Aggregation of species into a few functional types makes parameterization easier, but it is likely that the system response to changing climate

and atmospheric CO₂ cannot be fully captured by a few fixed physiological types. The potential effects of physiological adjustment (phenotypic plasticity), competition between individuals and species with variable physiologies, and evolution need to be evaluated. These are the mechanisms whereby organisms and ecosystems maintain their viability in the face of environmental change. Identification of trade-offs between key physiological traits will make the problem of parameterization of a large number of plant types substantially easier. All these developments will require close collaborations among experimentalists and modelers.

2. Marine Systems

Development and application of ocean biogeochemical models are driven by the desire to understand how the ocean carbon cycle has responded to climate change in the past (glacial to interglacial) and how it will respond to global warming in the future. By necessity, the parameterization of biogeochemistry included in an ocean GCM must be highly simplified when compared with reality, and there will always be a tradeoff between realism and tractability. A major step forward in ocean biogeochemical models was subdividing generic phytoplankton used in early NPZD models into a small number of phytoplankton functional types used in DGOMs. However, even DGOMs employ a small number of trophic interactions, a limited amount of metabolic diversity (genotypes present), and typically neglect physiological plasticity (phenotypic response) (Hood et al., 2007). Increasing the number of phytoplankton types has raised important problems including how to validate model performance (Anderson, 2005) and how to specify parameter values (Friedrichs et al., 2007). The data needed to validate multi-group biogeochemical models may not be available, and more complex ecological models do not necessarily perform better at accounting for the variability that is seen in the existing datasets than simpler models with much more highly aggregated ecology (Anderson, 2005). Data assimilation, typically using an adjoint method, can improve estimates of parameter values (Friedrichs et al., 2007). However, the predictive skill of a tuned model depends critically upon the availability of appropriate datasets

for parameter estimation and model validation (Friedrichs et al., 2007). The lack of appropriate data for calibrating bio-optical NPP algorithms has also been emphasized (Carr et al., 2006; Sathyendranath and Platt, 2007). It is likely that parameter estimation and model validation will be improved with increased use of the expanding range of products that can be retrieved from satellite observations. These include initial attempts to map pelagic calcium carbonate production (Balch et al., 2007), *Trichodesmium* blooms (Westberry and Siegel, 2006), and phytoplankton groups (Alvain et al., 2005, 2008).

Another important issue, which has not received equal attention, is how much physiological detail to include for each functional type (Flynn, 2005, 2006; Hood et al., 2007). It can be argued that the simple parameterizations of phytoplankton physiology, such as the Monod equation for limitation of growth rate by the concentration of a single limiting nutrient, need to be replaced by models that include more sophisticated treatments of the interactions amongst limiting factors and physiological acclimation (Flynn, 2005; Hood et al., 2007). Alternatively, better parameterizations of phytoplankton functional types may arise by explicitly modeling the costs and benefits of trade-offs amongst functional traits (Litchman et al., 2007) and by conducting competition experiments *in silico* in ocean GCMs (Follows et al., 2007).

New processes may need to be included in the parameterizations of phytoplankton functional types. One significant difference between marine and terrestrial models is that marine models ignore CO₂ limitation. The historical reason for this is that dissolved inorganic carbon (DIC) in seawater is not a limiting factor in the sense of Liebig's Law of the Minimum. However, the potential for CO₂ limitation of marine phytoplankton photosynthesis in the sense of Blackman's Law arises because CO₂ accounts for only about 1% of the DIC in seawater (Wolf-Gladrow et al., 1999). Although CO₂ limitation is suppressed in many algae and cyanobacteria by biophysical CO₂ concentration mechanisms (Giordano et al., 2005), reductions of growth rate with reductions of pCO₂ below ambient levels have been reported for some diatoms (Riebesell et al., 1993). There is also evidence that CO₂ availability affects competition within the phytoplankton community (Tortell

et al., 2002). Perhaps the most significant recent finding is that N_2 fixation and growth of *Trichodesmium* is sensitive to the increases in pCO_2 that are expected to occur over the next 100 years (Hutchins et al., 2007).

In light of our rapidly increasing knowledge of the diversity of marine microbes afforded by genomic approaches, Hood et al. (2007) have concluded that “traditional modeling tools ... to simulate marine-ecosystem dynamics and biogeochemical cycles will be insufficient to allow an informed synthesis of this information...”. They suggest increased use of overarching ecological theories based on thermodynamic constraints or concepts of resilience, continued development and application of physiological models, increased use of simulations of natural selection, and increased use of individual-based models to study microbial interactions. Some of these approaches can be employed within ocean GCMs, whereas others can be used to develop new parameterizations of the role of microbes in ocean biogeochemistry. However, increasing model complexity in this way will compound concerns with respect to obtaining the appropriate data for model validation.

New functional types may need to be included in models. For example, anoxygenic photoheterotrophic bacteria (Kolber et al., 2001) have been shown to be abundant and active in oligotrophic waters, which account for about 60% of the open ocean surface area (Koblizek et al., 2007; Lami et al., 2007). These organisms contain bacteriochlorophyll and have a similar photosynthetic efficiency and spectral light utilization to oxygenic phytoplankton. However, they rely on an organic carbon source, instead of water, as an electron donor. Bacteriochlorophyll is present at concentrations considerably lower than Chl *a* (Lami et al., 2007), so it is unlikely that anoxygenic photosynthesis makes a major direct contribution to marine primary production, although these photoheterotrophic bacteria may be important in other ways (Kolber et al., 2001).

Acknowledgments

ADF acknowledges the support of the Centre National de la Recherche Scientifique (France) and the European Commission through Contract

Number MRTN-CT-2004-512464 (GREENCYCLES Marie Curie Research Training Network). ADF also wishes to thank Sönke Zaehle for numerous stimulating discussions on modeling primary productivity. MJB acknowledges support from the National Aeronautics and Space Administration (USA) and wishes to thank Robert O'Malley and Toby Westberry for ocean modeling contributions to this work. RJG's work on modeling marine photosynthesis is supported by the UK Natural Environment Research Council MARQUEST initiative. CJS acknowledges the support of the NASA New Investigator Program.

References

- Alvain S, Moulin C, Dandonneau Y and Bréon FM (2005) Remote sensing of phytoplankton groups in case 1 waters from global SeaWiFS imagery. *Deep-Sea Res Pt I* 52: 1989–2004
- Alvain S, Moulin C, Dandonneau Y and Loisel H (2008) Seasonal distribution and succession of dominant phytoplankton groups in the global ocean: a satellite view. *Global Biogeochem Cy* 22: GB3001
- Amthor JS (2000) The McCree-de Wit-Penning de Vries-Thornley respiration paradigms: 30 years later. *Ann Bot-London* 86: 1–20
- Anderson TR (2005) Plankton functional type modelling: running before we can walk? *J Plankton Res* 27: 1073–1081
- Antoine D, Morel A, Gordon HR, Banzon VF and Evans RH (2005) Bridging ocean color observations of the 1980s and 2000s in search of long-term trends. *J Geophys Res* 110: C06009
- Arrigo KR (2005) Marine microorganisms and global nutrient cycles. *Nature* 437: 349–355
- Austin RW and Petzold TJ (1986) Spectral dependence of the diffuse attenuation coefficient of light in ocean waters. *Opt Eng* 25: 473–479
- Badeck F-W (1995) Intra-leaf gradient of assimilation rate and optimal allocation of canopy nitrogen: a model on the implications of the use of homogeneous assimilation functions. *Aust J Plant Physiol* 22: 425–439
- Balch WM, Gordon HR, Bowler BC, Drapeau DT and Booth ES (2005) Calcium carbonate measurements in the surface global ocean based on Moderate-Resolution Imaging Spectroradiometer data. *J Geophys Res* 110: C07001
- Balch W, Drapeau D, Bowler B and Booth E (2007) Prediction of pelagic calcification rates using satellite measurements. *Deep-Sea Res Pt II* 54: 478–495
- Baldocchi DD and Wilson KB (2001) Modeling CO_2 and water vapor exchange of a temperate broadleaved forest across to decadal time series. *Ecol Modell* 142: 155–184

- Ball JT, Woodrow IE and Berry JA (1987) A model predicting stomatal conductance and its contribution to the control of photosynthesis under different environmental conditions. In: Biggins J (ed) *Progress in Photosynthesis Research*, Vol IV, pp. 221–224. Martinus Nijhoff, Dordrecht, The Netherlands
- Banse K and Postel JR (2003) On using pigment-normalized, light-saturated carbon uptake with satellite-derived pigment for estimating column photosynthesis. *Global Biogeochem Cy* 17: 1079
- Behrenfeld MJ and Boss E (2003) The beam attenuation to chlorophyll ratio: an optical index of phytoplankton photoacclimation in the surface ocean? *Deep-Sea Res Pt I* 50: 1537–1549
- Behrenfeld MJ and Boss E (2006) Beam attenuation and chlorophyll concentration as alternative optical indices of phytoplankton biomass. *J Mar Res* 64: 431–451
- Behrenfeld MJ and Falkowski PG (1997a) Photosynthetic rates derived from satellite-based chlorophyll concentration. *Limnol Oceanogr* 41: 1–20
- Behrenfeld MJ and Falkowski PG (1997b) A consumer's guide to phytoplankton primary productivity models. *Limnol Oceanogr* 42: 1479–1491
- Behrenfeld MJ, Bale AJ, Kolber ZS, Aiken J and Falkowski PG (1996) Confirmation of iron limitation of phytoplankton photosynthesis in the equatorial Pacific Ocean. *Nature* 383: 508–511
- Behrenfeld MJ, Boss E, Siegel DA and Shea DM (2005) Carbon-based ocean productivity and phytoplankton physiology from space. *Global Biogeochem Cy* 19: GB1006
- Berline L, Brankart JM, Brasseur P, Ourmieres Y and Verron J (2007) Improving the physics of a coupled physical-biogeochemical model of the North Atlantic through data assimilation: Impact on the ecosystem. *J Marine Syst* 64: 153–172
- Bernacchi CJ, Singas EL, Pimentel C, Portis Jr AR and Long SP (2001) Improved temperature response functions for models of Rubisco-limited photosynthesis. *Plant Cell Environ* 24: 253–259
- Berry JA and Farquhar GD (1978) The CO₂ concentration function of C₄ photosynthesis: a biochemical model. In: Hall D, Coombs J and Goodwin T (eds) *Proceedings of the 4th International Congress on Photosynthesis*, pp. 119–131. Biochemical Society, London
- Betts RA, Cox PM, Lee SE and Woodward FI (1997) Contrasting physiological and structural vegetation feedbacks in climate change simulations. *Nature* 387: 796–799
- Bonan GB, Levis S, Sitch S, Vertenstein M and Oleson KW (2003) A dynamic global vegetation model for use with climate models: Concepts and description of simulated vegetation dynamics. *Global Change Biol* 9: 1543–1566
- Bond-Lamberty B and Gower S (2007) Estimation of stand-level leaf area for boreal bryophytes. *Oecologia* 157: 584–592
- Borges AV, Delille B and Frankignoulle M (2005) Budgeting sinks and sources of CO₂ in the coastal ocean: Diversity of ecosystem counts. *Geophys Res Lett* 32: L1460
- Botta A, Viovy N, Ciais P, Friedlingstein P and Monfray P (2000) A global prognostic scheme of leaf onset using satellite data. *Global Change Biol* 6: 709–725
- Boyd PW, Crossley AC, DiTullio GR, Griffiths FB, Hutchins DA, Queguiner B, Sedwick PN and Trull TW (2001) Control of phytoplankton growth by iron supply and irradiance in the subantarctic Southern Ocean: Experimental results from the SAZ Project. *J Geophys Res* 106: 31573–31583
- Bricaud A, Claustre H, Ras J and Oubelkheir K (2004) Natural variability of phytoplanktonic absorption in oceanic waters: Influence of the size structure of algal populations. *J Geophys Res* 109: C11010
- Bricaud A, Mejia C, Blondeau-Patissier D, Claustre H, Crepon M and Thiria S (2007) Retrieval of pigment concentrations and size structure of algal populations from their absorption spectra using multilayered perceptrons. *Appl Optics* 46: 1251–1260
- Brix H, Gruber N, Karl DM and Bates NR (2006) On the relationships between primary, net community, and export production in subtropical gyres. *Deep-Sea Res Pt II* 53: 698–717
- Brovkina V, Ganopolski A and Svirezhev Y (1997) A continuous climate-vegetation classification for use in climate-biosphere studies. *Ecol Modell* 101: 251–261
- Brown RH (1999) Agronomic implications of C₄ photosynthesis. In: Sage RF and Monson RK (eds) *C₄ Plant Biology*, pp. 473–507. Academic, San Diego, CA
- Canadell JG, Le Quéré C, Raupach MR, Field CB, Buitenhuis ET, Ciais P, Conway TJ, Gillett NP, Houghton RA and Marland G (2007) Contributions to accelerating atmospheric CO₂ growth from economic activity, carbon intensity, and efficiency of natural sinks. *Proc Natl Acad Sci USA* 104: 18866–18870
- Capone CG, Burns JA, Montoya JP, Subramaniam A, Mahaffey C, Gunderson T, Michaels AF and Carpenter EJ (2005) Nitrogen fixation by *Trichodesmium* spp.: An important source of new nitrogen to the tropical and subtropical North Atlantic Ocean. *Global Biogeochem Cy* 19: GB2024
- Carr M-E, Friedrichs MAM, Schmeltz M, Aita MN, Barber R, Behrenfeld M, Bidigare R, Buitenhuis ET, Campbell J, Ciotti A, Dierssen H, Dowell M, Dunne J, Esaias W, Gentili B, Gregg W, Groom S, Hoepffner N, Ishizaka J, Kameda T, Le Quéré C, Lohrenz S, Marra J, Mélin F, Moore K, Morel A, Reddy TE, Ryan J, Scardi M, Smyth T, Turpie K, Tilstone G, Waters K and Yamanaka Y (2006) A comparison of global estimates of marine primary production from ocean color. *Deep-Sea Res Pt II* 53: 741–770
- Carswell FE, Meir P, Wandelli EV, Bonates LCM, Kruijt B, Barbosa EM, Nobre AD, Grace J and Jarvis PG (2000) Photosynthetic capacity in a central Amazonian rain forest. *Tree Physiol* 20: 179–186

- Choudhury BJ (2001) Estimating gross photosynthesis using satellite and ancillary data: approach and preliminary results. *Remote Sens Environ* 75: 1–25
- Collatz GJ, Ball JT, Griwet C and Berry JA (1991) Physiological and environmental regulation of stomatal conductance, photosynthesis and transpiration: A model that includes a laminar boundary layer. *Agr Forest Meteorol* 54: 107–136
- Collatz GJ, Ribas-Carbo M and Berry JA (1992) Coupled photosynthesis-stomatal conductance model for leaves of C_4 plants. *Aust J Plant Physiol* 19: 519–538
- Collatz GJ, Berry JA and Clark JS (1998) Effects of climate and atmospheric CO_2 partial pressure on the global distribution of C_4 grasses: Present, past, and future. *Oecologia* 114: 441–454
- Collins SL, Knapp AK, Briggs JM, Blair JM and Steinauer EM (1998) Modulation of diversity by grazing and mowing in native tallgrass prairie. *Science* 280: 745–747
- Conkright ME, Garcia HE, O'Brien TD, Locarnini RA, Boyer TP, Stephens C and Antonov JJ (2002) World Ocean Atlas 2001. Volume 4: Nutrients. Levitus S (ed) NOAA Atlas NESDID 52, US Government Printing Office, Washington, DC de Baar HJW, Boyd PW, Coale KH, Landry MR, Tsuda A, Assmy P, Bakker DCE, Bozec Y, Barber RT, Brzezinski MA, Buesseler KO, Boye M, Croot PL, Gervais F, Gorbunov MY, Harrison PJ, Hiscock WT, Laan P, Lancelot C, Law CS, Levasseur M, Marchetti A, Millero FJ, Nishioka J, Nojiri Y, Van Oijen T, Riebesell U, Rijkkenberg MJA, Saito H, Takeda S, Timmermans KR, Veldhuis MJW, Waite AM and Wong C-S (2005) Synthesis of iron fertilization experiments: From the Iron Age in the Age of Enlightenment. *J Geophys Res* 110, C09S16
- Cox PM, Betts RA, Jones CD, Spall SA and Totterdell IJ (2000) Acceleration of global warming due to carbon-cycle feedbacks in a coupled climate model. *Nature* 408: 184–187
- Cullen JJ, Yang X and MacIntyre HL (1992) Nutrient limitation of marine photosynthesis. In: Falkowski PG and Woodhead AV (eds) *Primary Productivity and Biogeochemical Cycles in the Sea*, pp 69–88. Plenum Press, New York
- Demarty J, Chevallier F, Friend AD, Viovy N, Piao S and Ciais P (2007) Assimilation of global MODIS leaf area index retrievals within a terrestrial biosphere model. *Geophys Res Lett* 34: L15402
- Deutsch C, Sarmiento JL, Sigman DM, Gruber N and Dunne JP (2007) Spatial coupling of nitrogen inputs and losses in the ocean. *Nature* 445: 163–167
- Dewar RC (1996) The correlation between plant growth and intercepted radiation: An interpretation in terms of optimal plant nitrogen content. *Ann Bot-London* 78: 125–136
- Dickinson RE, Shaikh M, Bryant R and Graumlich L (1998) Interactive canopies for a climate model. *J Climate* 11: 2823–2836
- Doney SC, Keith LK and Moore JK (2003) Global Ocean Carbon Cycle Modeling. In: Fasham MFR (ed) *Ocean Biogeochemistry: The Role of the Ocean Carbon Cycle in Global Change*, pp 217–238. Springer, Berlin/Heidelberg/New York
- Duarte CM and Cebrián J (1996) The fate of marine autotrophic production. *Limnol Oceanogr* 41: 1758–1766
- Duce RA, LaRoche J, Altieri K, Arrigo KR, Baker AR, Capone DG, Cornell S, Dentener F, Galloway J, Ganeshram RS, Geider RJ, Jickells T, Kuypers MM, Langlois R, Liss PS, Liu SM, Middelburg JJ, Moore CM, Nickovic S, Oschlies A, Pedersen T, Prospero J, Schlitzer R, Seitzinger S, Sorensen LL, Uematsu M, Ulloa O, Voss M, Ward B and Zamora L (2008) Impacts of atmospheric anthropogenic nitrogen on the open ocean. *Science* 320: 893–897
- Dunne JP, Sarmiento JL and Gnanadesikan A (2007) A synthesis of global particle export from the surface ocean and cycling through the ocean interior and on the seafloor. *Global Biogeochem Cy* 21: GB4006
- Falkowski PG (1997) Evolution of the nitrogen cycle and its influence on the biological sequestration of CO_2 in the ocean. *Nature* 387: 272–275
- Falkowski PG and Kiefer DA (1985) Chlorophyll a fluorescence in phytoplankton: relationship to photosynthesis and biomass. *J Plankton Res* 7: 715–731
- Falkowski PG and Raven JA (2007) *Aquatic Photosynthesis*. 2nd Edition. Princeton University Press, Princeton, NJ
- Farquhar GD, Von Caemmerer S and Berry JA (1980) A biochemical model of photosynthetic CO_2 assimilation in leaves of C_3 species. *Planta* 149: 78–90
- Farquhar GD, Ehleringer JR and Hubick KT (1989) Carbon isotope discrimination and photosynthesis. *Annu Rev Plant Phys* 40: 503–537
- Fasham MJR, Ducklow HW and McKelvie SM (1990) A nitrogen-based model of plankton dynamics in the oceanic mixed layer. *J Mar Res* 48: 591–639
- Field C and Mooney HA (1986) The photosynthesis-nitrogen relationship in wild plants. In: Givnish TJ (ed) *On the Economy of Plant Form and Function*, pp. 25–55. Cambridge University Press, Cambridge, UK
- Field CB, Randerson JT and Malmström CM (1995) Global net primary production: Combining ecology and remote sensing. *Remote Sens Environ* 51: 74–88
- Field CB, Behrenfeld MJ, Randerson JT and Falkowski P (1998) Primary production of the biosphere: Integrating terrestrial and oceanic components. *Science* 281: 237–240
- Flynn KJ (2005) Castles built on sand: Dysfunctionality in plankton models and the inadequacy of dialogue between biologists and modellers. *J Plankton Res* 27: 1205–1210
- Flynn KJ (2006) Reply to Horisons Article 'Plankton functional type modeling: Running before we can walk' Anderson (2005): II Putting trophic functionality into plankton functional types. *J Plankton Res* 28: 873–875
- Foley JA, Prentice IC, Ramankutty N, Levis S, Pollard D, Sitch S and Haxeltine A (1996) An integrated biosphere model and land surface processes, terrestrial carbon bal-

- ance, and vegetation dynamics. *Global Biogeochem Cy* 10: 603–628
- Foley JA, Levis S, Prentice IC, Pollard D and Thompson SL (1998) Coupling dynamic models of climate and vegetation. *Global Change Biol* 4: 561–579
- Follows M and Dutkiewicz S (2001) Meteorological modulation of the North Atlantic spring bloom. *Deep-Sea Res Pt II* 49: 321–344
- Follows MJ, Dutkiewicz S, Scott Grant S and Chisholm SW (2007) Emergent biogeography of microbial communities in a model ocean. *Science* 315: 1843–1846
- Friedlingstein P, Joel G, Field CB and Fung IY (1999) Toward an allocation scheme for global terrestrial carbon models. *Global Change Biol* 5: 755–770
- Friedlingstein P, Bopp L, Rayner P, Cox P, Betts R, Jones C, Von Bloh W, Brovkin V, Cadule P, Doney S, Eby M, Matthews HD, Weaver AJ, Fung I, John J, Bala G, Joos F, Strassmann K, Kato T, Kawamiya M, Yoshikawa C, Knorr W, Lindsay K, Matthews HD, Raddatz T, Reick C, Roeckner E, Schnitzler K-G, Schnur R and Zeng N (2006) Climate-carbon cycle feedback analysis: Results from the C⁴MIP model intercomparison. *J Climate* 19: 3337–3353
- Friedrichs MAM, Dusenberry JA, Anderson LA, Armstrong RA, Chai F, Christian JR, Doney SC, Dunne J, Fujii M, Hood R, McGillicuddy DJ, Moore JK, Schartau M, Spitz YH and Wiggert JD (2007) Assessment of skill and portability in regional marine biogeochemical models: Role of multiple planktonic groups. *J Geophys Res* 112: C08001
- Friend AD (1995) PGEM: An integrated model of leaf photosynthesis, transpiration, and conductance. *Ecol Modell* 77: 233–255
- Friend AD (1998) Parameterisation of a global daily weather generator for terrestrial ecosystem modeling. *Ecol Modell* 109: 121–140
- Friend AD (2001) Modelling canopy CO₂ fluxes: Are ‘big-leaf’ simplifications justified? *Global Ecol Biogeogr* 10: 603–619
- Friend AD and Kiang NY (2005) Land surface model development for the GISS GCM: Effects of improved canopy physiology on simulated climate. *J Climate* 18: 2883–2902
- Friend AD and White A (2000) Evaluation and analysis of a dynamic terrestrial ecosystem model under pre-industrial conditions at the global scale. *Global Biogeochem Cy* 14: 1173–1190
- Friend AD, Stevens AK, Knox RG and Cannell MGR (1997) A process-based, terrestrial biosphere model of ecosystem dynamics (Hybrid v3.0). *Ecol Modell* 95: 249–287
- Friend AD, Arneth A, Kiang NY, Lomas M, Ogée J, Rödenbeck C, Running SW, Santaren J-D, Sitch S, Viovy N, Woodward FI and Zaehle S (2007) FLUXNET and modelling the global carbon cycle. *Global Change Biol* 13: 610–633
- Fung IY, Doney SC, Lindsay K and John J (2005) Evolution of carbon sinks in a changing climate. *Proc Natl Acad Sci USA* 102: 11201–11206
- Gattuso JP, Frankignoulle M and Wollast R (1998) Carbon and carbonate metabolism in coastal aquatic ecosystems. *Annu Rev Ecol Syst* 29: 405–434
- Gattuso JP, Gentili B, Duarte CM, Kleypas JA, Middelburg JJ and Antoine D (2006) Light availability in the coastal ocean: Impact on the distribution of benthic photosynthetic organisms and their contribution to primary production. *Biogeochemistry* 3: 489–513
- Geider RJ (1990) The relationship between steady state phytoplankton growth and photosynthesis. *Limnol Oceanogr* 35: 971–972
- Geider RJ (1992) Respiration: Taxation without representation. In: Falkowski PG and Woodhead AV (eds) *Primary Productivity and Biogeochemical Cycles in the Sea*, pp 333–360. Plenum Press, New York
- Geider RJ, MacIntyre HL and Kana TM (1998) A dynamic regulatory model of phytoplankton acclimation to light, nutrients and temperature. *Limnol Oceanogr* 43: 679–694
- Ginoux M, Chin I, Tegen J, Prospero M, Holben B, Dubovik O and Lin SJ (2001) Sources and distributions of dust aerosols simulated with the GOCART model. *J Geophys Res* 106: 20255–20273
- Giordano M, Beardall J and Raven JA (2005) CO₂ concentrating mechanisms in algae: Mechanisms, environmental modulation, and evolution. *Annu Rev Plant Biol* 56: 99–131
- Global Soil Data Task Group (2000) *Global Gridded Surfaces of Selected Soil Characteristics (IGBP-DIS). [Global Gridded Surfaces of Selected Soil Characteristics (International Geosphere-Biosphere Programme - Data and Information System)]*. Data set. Available on-line [<http://www.daac.ornl.gov>] from Oak Ridge National Laboratory Distributed Active Archive Center, Oak Ridge, Tennessee, U.S.A.
- Goetz SJ and Prince SD (1998) Variability in carbon exchange and light utilization among boreal forest stands: Implications for remote sensing of net primary production. *Can J Forest Res* 28: 37–389
- Gower ST, Kucharik CJ and Norman JM (1999) Direct and indirect estimation of leaf area index, f_{apar}, and net primary production of terrestrial ecosystems. *Remote Sens Environ* 70: 29–51
- Gregg WW (2008) Assimilation of SeaWiFS ocean chlorophyll data into a three-dimensional global ocean model. *J Marine Syst* 69: 205–225
- Gregg WW and Casey NW (2004). Global and regional evaluation of the SeaWiFS chlorophyll data set. *Remote Sens Environ* 93: 463–479
- Gregg WW and Casey NW (2007a) Modeling coccolithophores in the global oceans. *Deep-Sea Res Pt II* 54: 447–477
- Gregg WW and Casey NW (2007b) Sampling biases in MODIS and SeaWiFS ocean chlorophyll data. *Remote Sens Environ* 111: 25–35

- Gu L, Baldocchi D, Verma SB, Black TA, Vesala T, Falge EM and Dowty PR (2002) Advantages of diffuse radiation for terrestrial ecosystem productivity. *J Geophys Res* 107: NO. D6, 4050
- Hanan NP, Berry JA, Verma SB, Walter-Shea EA, Suyker AE, Burba GG and Denning AS (2005) Testing a model of CO₂, water and energy exchange in Great Plains tall-grass prairie and wheat ecosystems. *Agr Forest Meteorol* 131: 162–179
- Hansen J, Russell G, Rind D, Stone P, Lacis A, Lebedeff S, Ruedy R and Travis L (1983) Efficient three-dimensional global models for climate change studies: Models I and II. *Mon Weather Rev* 111: 609–662
- Harley PC, Thomas RB, Reynolds JF and Strain BR (1992) Modelling photosynthesis of cotton grown in elevated CO₂. *Plant Cell Environ* 15: 271–282
- Hood RR, Laws EA, Armstrong RA, Bates NR, Brown CW, Carlson CA, Chai F, Doney SC, Falkowski PG, Feely RA, Friedrichs MAM, Landry MR, Keith Moore J, Nelson D, M, Richardson TL, Salihoglu B, Schartau M, Toole DA and Wiggert JD (2006) Pelagic functional group modeling: Progress, challenges and prospects. *Deep-Sea Res Pt II* 53: 459–512
- Hood RR, Laws EA, Follows MJ and Siegel DA (2007) Modeling and prediction of marine microbial populations in the genomic era. *Oceanography* 20: 155–167
- Hunt Jr ER, Piper SC, Nemani R, Keeling CD, Otto RD and Running SW (1996) Global net carbon exchange and intra-annual atmospheric CO₂ concentrations predicted by an ecosystem process model and three-dimensional atmospheric transport model. *Global Biogeochem Cy* 10: 431–456
- Huot Y, Babin M, Bruyant F, Grob C, Twardowski MS and Claustre H (2007) Relationship between photosynthetic parameters and different proxies of phytoplankton biomass in the subtropical ocean. *Biogeosciences* 4: 853–868
- Hutchins DA, Fu FX, Zhang Y, Warner ME, Feng Y, Portune K, Bernhardt PW and Mulholland MR (2007) CO₂ control of *Trichodesmium* N₂ fixation, photosynthesis, growth rates, and elemental ratios: Implications for past, present, and future ocean biogeochemistry. *Limnol Oceanogr* 52: 1293–1304
- Jeffrey SW, Mantoura RFC and Wright SW (1997) *Phytoplankton Pigments in Oceanography: Guidelines to Modern Methods*. UNESCO, Paris, France
- Jenkins JP, Richardson AD, Braswell BH, Ollinger SV, Hollinger DY and Smith M-L (2007) Refining light-use efficiency calculations for a deciduous forest canopy using simultaneous tower-based carbon flux and radiometric measurements. *Agr Forest Meteorol* 143: 64–79
- Jickells TD, An ZS, Andersen KK, Baker AR, Bergametti G, Brooks N, Cao JJ, Boyd PW, Duce RA, Hunter KA, Kawahata H, Kubilay N, LaRoche J, Liss PS, Mahowald N, Prospero JM, Ridgwell AJ, Tegen I and Torres R (2005) Global iron connections between desert dust, ocean biogeochemistry, and climate. *Science* 308: 67–71
- Justice CO, Townshend JRG, Holben BN and Tucker CJ (1985) Phenology of global vegetation using meteorological satellite data. *Int J Remote Sens* 8: 1271–1318
- Kaduk J and Heimann M (1996) A prognostic phenology scheme for global terrestrial carbon cycle models. *Climate Res* 6: 1–19
- Kamykowski D, Zentara SJ, Morrison JM and Switzer AC (2002) Dynamic global patterns of nitrate, phosphate, silicate, and iron availability and phytoplankton community composition from remote sensing data. *Global Biogeochem Cy* 16: NO. 4, 1077
- Kathuroju N, White MA, Symanzik J, Schwartz MD, Powell JA and Nemani RR (2007) On the use of the advanced very high resolution radiometer for development of prognostic land surface phenology models. *Ecol Modell* 201: 144–156
- Knops JMH and Reinhart K (2000) Specific leaf area along a nitrogen fertilization gradient. *Am Midl Nat* 144: 265–272
- Knorr W and Kattge J (2005) Inversion of terrestrial ecosystem model parameter values against eddy covariance measurements by Monte Carlo sampling. *Global Change Biol* 11: 1333–1351
- Koblizek M, Masin M, Ras J, Poulton AJ and Prášil O (2007) Rapid growth rates of aerobic anoxygenic phototrophs in the ocean. *Environ Microbiol* 9: 2401–2406
- Kolber ZS, Plumley FG, Lang AS, Beatty JT, Blankenship RE, VanDover CL, Vetriani C, Koblizek M, Rathgeber C and Falkowski PG (2001) Contribution of aerobic photoheterotrophic bacteria to the carbon cycle in the ocean. *Science* 292: 2492–2495
- Krinner G, Viovy N, de Noblet-Ducoudré N, Ogée J, Polcher J, Friedlingstein P, Ciais P, Sitch S and Prentice IC (2005) A dynamic global vegetation model for studies of the coupled atmosphere-biosphere system. *Global Biogeochem Cy* 19: GB1015
- Kucharik CJ, Foley JA, Delire C, Fisher VA, Coe MT, Linters JD, Young-Molling C and Ramankutty N (2000) Testing the performance of a Dynamic Global Ecosystem Model: Water balance, carbon balance, and vegetation structure. *Global Biogeochem Cy* 14: 795–825
- Kucharik CJ, Barford CC, El Maayar M, Wofsy SC, Monson RK and Baldocchi DD (2006) A multiyear evaluation of a Dynamic Global Vegetation Model at three Ameriflux forest sites: Vegetation structure, phenology, soil temperature, and CO₂ and H₂O vapor exchange. *Ecol Modell* 196: 1–31
- Kull O and Kruijt B (1998) Leaf photosynthetic light response: A mechanistic model for scaling photosynthesis to leaves and canopies. *Funct Ecol* 12: 767–777
- Lami R, Cottrell MT, Ras J, Ulloa O, Obernosterer I, Claustre H, Kirchman DL and Lebaron P (2007) High abundances of aerobic anoxygenic photosynthetic bacteria in the South Pacific Ocean. *Appl Environ Microbiol* 73: 4198–4205

- Lapeyre G and Klein P (2006) Impact of the small-scale elongated filaments on the oceanic vertical pump. *J Mar Res* 64: 835–851
- Laws EA, Falkowski PG, Smith WO, Ducklow H and McCarthy JJ (2000a) Temperature effects on export production in the open ocean. *Global Biogeochem Cy* 14: 1231–1246
- Laws EA, Landry MR, Barber RT, Campbell L, Dickson ML and Marra J (2000b) Carbon cycling in primary production bottle incubations: Inferences from grazing experiments and photosynthetic studies using C-14 and O-18 in the Arabian Sea. *Deep-Sea Res Pt II* 47: 1339–1352
- Le Quéré C, Harrison SP, Prentice IC, Buitenhuis ET, Aumont O, Bopp L, Claustre H, Cotrim Da Cunha L, Geider R, Giraud X, Klaas C, Kohfeld KE, Legendre L, Manizza M, Platt T, Rivkin RB, Sathyendranath S, Uitz J, Watson AJ and Wolf-Gladrow D (2005) Ecosystem dynamics based on plankton functional types for global ocean biogeochemistry models. *Global Change Biol* 11: 2016–2040
- Leuning R (1995) A critical appraisal of a coupled stomatal-photosynthesis model for C₃ plants. *Plant Cell Environ* 18: 339–355
- Litchman E, Klausmeier CA, Schofield OM and Falkowski PG (2007) The role of functional traits and trade-offs in structuring phytoplankton communities: Scaling from cellular to ecosystem level. *Ecol Lett* 10: 1170–1181
- Liu X-Y, Xiao H-Y, Liu C-Q and Li Y-Y (2007) $\delta^{13}\text{C}$ and $\delta^{15}\text{N}$ of moss *Haplocadium microphyllum* (Hedw.) Broth. for indicating growing environment variation and canopy retention on atmospheric nitrogen deposition. *Atmos Environ* 41: 4897–4907
- Lloyd J, Bird MI, Veenendaal E and Kruijt B (2001) Should phosphorus availability be constraining moist tropical forest responses to increasing CO₂ concentrations? In: Schulze E-D, Harrison SP, Heimann M, Holland EA, Lloyd J, Prentice IC and Schimel D (eds) *Global Biogeochemical Cycles in the Climate System*, pp 96–114. Academic, San Diego, CA, USA
- Lobell BD, Hicke JA, Asner GP, Field CB, Tucker CJ and Los O (2002) Satellite estimates of productivity and light use efficiency in United States agriculture, 1982–98. *Global Change Biol* 8: 722–735
- Long SP (1999) Environmental responses. In: Sage RF and Monson RK (eds) *C₄ Plant Biology*, pp. 215–249. Academic, San Diego, CA
- Longhurst A, Sathyendranath S, Platt T and Caverhill C (1995) An estimate of global primary production in the ocean from satellite radiometer data. *J Plankton Res* 17: 1245–1271
- Loveland TR, Reed BC, Brown JF, Ohlen DO, Zhu Z, Yang L and Merchant JW (2000) Development of a global land cover characteristics database and IGBP DISCover from 1 km AVHRR data. *Int J Remote Sens* 21: 1303–1330
- MacIntyre HL, Kana TM, Anning T and Geider RJ (2002) Photoacclimation of photosynthesis irradiance response curves and photosynthetic pigments in microalgae and cyanobacteria. *J Phycol* 38: 17–38
- Maritorena S, DA Siegel and AR Peterson (2002) Optimization of a semianalytical ocean color model for global-scale applications. *Appl Optics* 41: 2705–2714
- Marrari M, Hu CM and Daly K (2006) Validation of SeaWiFS chlorophyll a concentrations in the Southern Ocean: A revisit. *Remote Sens Environ* 105: 367–375
- Martínez-Sánchez JL (2003) Nitrogen and phosphorus resorption in trees of a neotropical rain forest. *J Trop Ecol* 19: 465–468
- McGillicuddy DJ, Robinson AR, Siegel DA, Jannasch HW, Johnson R, Dickey T, McNeil J, Michaels AF and Knap AH (1998) Influence of mesoscale eddies on new production in the Sargasso Sea. *Nature* 394: 263–266
- McGillicuddy Jr DJ, Anderson LA, Doney SC and Maltrud ME (2003) Eddy-driven sources and sinks of nutrients in the upper ocean: Results from a 0.1 degrees resolution model of the North Atlantic. *Global Biogeochem Cy* 17: NO. 2, 1035
- McGillicuddy Jr DJ, Anderson LA, Bates NR, Bibby T, Buesseler KO, Carlson CA, Davis CS, Ewart C, Falkowski PG, Goldthwait SA, Hansell DA, Jenkins WJ, Johnson R, Kosnyrev VK, Ledwell JR, Li QP, Siegel DA and Steinberg DK (2007) Eddy/wind interactions stimulate extraordinary mid-ocean plankton blooms. *Science* 316: 1021–1026
- McGuire AD, Sitch S, Clein JS, Dargaville R, Esser G, Foley J, Heimann M, Joos F, Kaplan J, Kicklighter DW, Meier RA, Melillo JM, Moore B, Prentice IC, Ramankutty N, Reichenau T, Schloss A, Tian H, Williams LJ and Wittenberg U (2001) Carbon balance of the terrestrial biosphere in the twentieth century: Analyses of CO₂, climate and land use effects with four process-based ecosystem models. *Global Biogeochem Cy* 15: 183–206
- McWilliam A-LC, Roberts JM, Cabral OMR, Leita, MVBR, de Costa, ACL, Maitelli, GT and Zamparoni CAGP (1993) Leaf area index and above-ground biomass of *terra firme* rain forest and adjacent clearing in Amazonia. *Funct Ecol* 7: 310–317
- Melillo JM, McGuire AD, Kicklighter DW, Moore B, Vorosmarty CJ and Schloss AL (1993) Global climate change and terrestrial net primary production. *Nature* 363: 234–240
- Monteith JL (1972) Solar radiation and productivity in tropical ecosystems. *J Appl Ecol* 9: 747–766
- Monteith JL (1977) Climate efficiency of crop production in Britain. *Philos Trans R Soc B* 281: 277–294
- Moore JK and Doney SC (2007) Iron availability limits the ocean nitrogen inventory stabilizing feedbacks between marine denitrification and nitrogen fixation. *Global Biogeochem Cy* 21: GB2001

- Moore JK, Doney SC and Lindsay K (2004) Upper ocean ecosystem dynamics and iron cycling in a global three-dimensional model. *Global Biogeochem Cy* 18: GB4028
- Moore JK, Doney SC, Lindsay K, Mahowald N and Michaels AF (2006a) Nitrogen fixation amplifies the ocean biogeochemical response to decadal timescale variations in mineral dust deposition. *Tellus B* 58: 560–572
- Moore CM, Mills MM, Milne A, Langlois R, Achterberg EP, Lochte K, Geider RJ and La Roche J (2006b) Iron supply limits primary productivity during spring bloom development in the central North Atlantic. *Global Change Biol* 12: 626–634
- Morel A (1991) Light and marine photosynthesis: A spectral model with geochemical and climatological implications. *Prog Oceanogr* 26: 263–306
- Morel A and Maritorena S (2001) Bio-optical properties of oceanic waters: A reappraisal. *J Geophys Res* 106: 7163–7180
- Morel A, Antoine D, Babin M and Dandonneau Y (1996) Measured and modeled primary production in the northeast Atlantic (EUMELI JGOFS program): The impact of natural variations in photosynthetic parameters on model predictive skill. *Deep-Sea Res Pt I* 43: 1273–1304
- Morel A, Huot Y, Gentili B, Werdell PJ, Hooker SB and Franz BA (2007) Examining the consistency of products derived from various ocean color sensors in open ocean (Case 1) waters in the perspective of a multi-sensor approach. *Remote Sens Environ* 111: 69–88
- Morgan JA, Milchunas DG, LeCain DR, West M and Mosier AR (2007) Carbon dioxide enrichment alters plant community structure and accelerates shrub growth in the shortgrass steppe. *Proc Natl Acad Sci USA* 104: 14724–14729
- Morisette JT, Baret F, Privette JL, Myneni RB, Nickeson JE, Garrigues S, Shabanov NV, Weiss M, Fernandes RA, Leblanc SG, Kalacska M, Sanchez-Azofeifa GA, Chubey M, Rivard B, Stenberg P, Rautiainen M, Voipio P, Manninen T, Pilant AN, Lewis TE, Iames JS, Colombo R, Meroni M, Busetto L, Cohen WB, Turner DP, Warner ED, Petersen GW, Seufert G and Cook R (2006) Validation of global moderate-resolution LAI products: A framework proposed within the CEOS land product validation subgroup. *IEEE T Geosci Remote* 44: 1804–1817
- Myneni RB, Keeling CD, Tucker CJ, Asrar G and Nemani RR (1997) Increased plant growth in the northern high latitudes from 1981–1991. *Nature* 386: 698–702
- Najjar RG, Jin X, Louanchi F, Aumont O, Caldeira K, Doney SC, Dutay JC, Follows M, Gruber N, Joos F, Lindsay K, Maier-Reimer E, Matear RJ, Matsumoto K, Monfray P, Mouchet A, Orr JC, Plattner GK, Sarmiento JL, Schlitzer R, Slater RD, Weirig MF, Yamanaka Y and Yool A (2007) Impact of circulation on export production, dissolved organic matter, and dissolved oxygen in the ocean: Results from Phase II of the Ocean Carbon-cycle Model Intercomparison Project (OCMIP-2). *Global Biogeochem Cy* 21: GB3007
- Neilson RP (1995) A model for predicting continental-scale vegetation distribution and water balance. *Ecol Appl* 5: 362–385
- Nemani RR, Keeling CD, Hashimoto H, Jolly WM, Piper SC, Tucker CJ, Myneni RB and Running SW (2003) Climate-driven increases in global terrestrial net primary production from 1982 to 1999. *Science* 300: 1560–1563
- New M, Lister D, Hulme M and Makin I (2002) High-resolution data set of surface climate over global land areas. *Climate Res* 21: 1–25
- O'Reilly JE, Maritorena S, Mitchell BG, Siegel DA, Carder KL, Garver SA, Kahru M and McClain C (1998) Ocean color chlorophyll algorithms for SeaWiFS. *J Geophys Res* 103: 24937–24953
- Orr JC, Fabry VJ, Aumont O, Bopp L, Doney SC, Feely RA, Gnanadesikan A, Gruber N, Ishida A, Joos F, Key RM, Lindsay K, Maier-Reimer E, Matear R, Monfray P, Mouchet A, Najjar RG, Plattner GK, Rodgers KB, Sabine CL, Sarmiento JL, Schlitzer R, Slater RD, Totterdell IJ, Weirig MF, Yamanaka Y and Yool A (2005) Anthropogenic ocean acidification over the twenty-first century and its impact on calcifying organisms. *Nature* 437: 681–686
- Parton WJ, Neff J and Vitousek PM (2005) Modelling Phosphorus, Carbon and Nitrogen Dynamics in Terrestrial Ecosystems. In: Turner BL, Frossard E and Baldwin DS (eds) *Organic Phosphorus in the Environment*, pp. 325–334. CAB International, Oxfordshire
- Pearcy RW and Ehleringer J (1984) Comparative eco-physiology of C₃ and C₄ plants. *Plant Cell Environ* 7: 1–13
- Pirazzini R, Nardino M, Orsini A, Calzolari F, Georgiadis T and Levizzani V (1998) Parameterization of the downward longwave radiation from clear and cloudy skies at Ny Ålesund (Svalbard). Conference Presentation to the International Radiation Symposium (IRS), 24–29 July, 2000, St. Petersburg, Russia. PDF: <http://www.bo.ibimet.cnr.it/fileadmin/ibimet/repository/acta13.pdf>
- Pitman AJ (2003) The evolution of, and revolution in, land surface schemes designed for climate models. *Int J Climatol* 23: 479–510
- Platt T (1986) Primary production of the ocean water column as a function of surface light intensity: Algorithms for remote sensing. *Deep-Sea Res* 33: 149–163
- Platt T, Broomhead DS, Sathyendranath S, Edwards AM and Murphy EJ (2003) Phytoplankton biomass and residual nitrate in the pelagic ecosystem. *Proc R Soc A* 459: 1063–1073
- Polovina JJ, Howell EA and Abecassis M (2008) Ocean's least productive waters are expanding. *Geophys Res Lett* 35: L03618
- Pons TL and Bergkotte M (1996) Nitrogen allocation in response to partial shading of a plant: Possible mechanisms. *Physiol Plantarum* 98: 571–577

- Poorter H (1993) Interspecific variation in the growth response of plants to an elevated ambient CO₂ concentration. *Vegetatio* 104–105: 77–97
- Popova EE, Coward AC, Nurser GA, de Cuevas B, Fasham MJR and Anderson TR (2006a) Mechanisms controlling primary production in a global ecosystem model. I: Validation of the biological simulation. *Ocean Science* 2: 249–266
- Popova EE, Coward AC, Nurser GA, de Cuevas B and Anderson TR (2006b) Mechanisms controlling primary production in a global ecosystem model. II: The role of upper ocean short-term periodic and episodic events. *Ocean Science* 2: 267–279
- Post WM, King AW and Wulfschleger SD (1997) Historical variations in terrestrial biospheric carbon storage. *Global Biogeochem Cy* 11: 99–109
- Potter CS, Randerson JT, Field CB, Matson PA, Vitousek PM, Mooney HA, Klooster SA (1993) Terrestrial ecosystem production: A process model based on global satellite and surface data. *Global Biogeochem Cy* 7: 811–841
- Prince SD (1991) A model of regional primary production for use with coarse resolution satellite data. *Int J Remote Sens* 12: 1313–1330
- Prince SD and Goward SN (1995) Global primary production: A remote sensing approach. *J Biogeogr* 22: 815–835
- Randall DA, Dazlich DA, Zhang C, Denning AS, Sellers PJ, Tucker CJ, Bounoua L, Berry JA, Collatz GJ, Field CB, Los SO, Justice CO and Fung I (1996) A revised land surface parameterization (SiB2) for atmospheric GCMs. Part III: The greening of the Colorado State University General Circulation Model. *J Climate* 9: 738–763
- Randerson JT, Thompson MV, Conway TJ, Fung IY and Field CB (1997) The contribution of terrestrial sources and sinks to trends in the seasonal cycle of atmospheric carbon dioxide. *Global Biogeochem Cy* 11: 535–560
- Randerson JT, Van der Werf GR, Collatz GJ, Giglio L, Still CJ, Kasibhatla P, Miller JB, White JWC, DeFries RS and Kasischke ES (2005) Fire emissions from C₃ and C₄ vegetation and their influence on interannual variability of atmospheric CO₂ and $\delta^{13}\text{C}$. *Global Biogeochem Cy* 19: GB2019
- Ricchiazzi P, Yang SR, Gautier C and Sowle D (1998) SBDART: A research and teaching software tool for plane-parallel radiative transfer in the Earth's atmosphere. *B Am Meteorol Soc* 79: 2101–2114
- Riebesell U, Wolf-Gladrow DA and Smetacek V (1993) Carbon dioxide limitation of marine phytoplankton growth rates. *Nature* 361: 249–263
- Riser SC and Johnson KS (2008) Net production of oxygen in the subtropical ocean. *Nature* 451: 323–325
- Ruimy A, Jarvis PG, Baldocchi DD and Saugier B (1995) CO₂ fluxes over plant canopies and solar radiation: A review. *Adv Ecol Res* 26: 1–68
- Ruimy A, Kergoat L and Bondeau A (1999) Comparing global models of terrestrial net primary productivity (NPP): Analysis of differences in light absorption and light-use efficiency. *Global Change Biol* 5: 56–64
- Running SW and Hunt Jr ER (1993) Generalization of a forest ecosystem process model for other biomes, BIOME-BGC, and an application for global-scale models. In: Ehleringer JR and Field CB (eds) *Scaling physiological processes: Leaf to globe*, pp. 141–158. Academic, San Diego, CA
- Running SW, Nemani RR, Heinsch FA, Zhao M, Reeves M and Hashimoto H (2004) A continuous satellite-derived measure of global terrestrial primary production. *BioScience* 54: 547–560
- Sage RF and Monson RK (1999) *C₄ Plant Biology*. Academic, San Diego, CA
- Sage RF, Wedin DA and Li M (1999) *The Biogeography of C₄ Photosynthesis: Patterns and Controlling Factors*. Academic, New York
- Sarmiento JL, Slater RD, Fasham MJR, Ducklow HW, Toggweiler JR and Evans GT (1993) A seasonal three dimensional ecosystem model of nitrogen cycling in the North Atlantic euphotic zone. *Global Biogeochem Cy* 7: 417–450
- Sathyendranath S and Platt T (1989) Remote sensing of ocean chlorophyll: Consequence of non-uniform pigment profile. *Appl Optics* 28: 490–495
- Sathyendranath S and Platt T (2007) Spectral effects in bio-optical control on the ocean system. *Oceanologia* 49: 5–39
- Sathyendranath S, Longhurst AR, Caverhill CM and Platt T (1995) Regionally and seasonally differentiated primary production in the North Atlantic. *Deep-Sea Res Pt I* 42: 1773–1802
- Sato H, Itoh A and Kohyama T (2007) SEIB-DGVM: A new Dynamic Global Vegetation Model using a spatially explicit individual-based approach. *Ecol Model* 200: 279–307
- Schmittner A, Oschlies A, Matthews HD and Galbraith ED (2008) Future changes in climate, ocean circulation, ecosystems, and biogeochemical cycling simulated for a business-as-usual CO₂ emission scenario until year 4000 AD. *Global Biogeochem Cy* 22: GB1013
- Schwalm CR, Black TA, Amiro BD, Arain MA, Barr AG, Bourque CP-A, Dunn AL, Flanagan LB, Giasson M-A, Lafleur PM, Margolis HA, McCaughey JH, Orchansky AL and Wofsy SC (2006) Photosynthetic light use efficiency of three biomes across an east-west continental-scale transect in Canada. *Agr Forest Meteorol* 140: 269–286
- Sellers PJ, Hall FG, Asrar G, Strebel DE and Murphy RE (1992) An overview of the First International Satellite Land Surface Climatology Project (ISLSCP) Field Experiment (FIFE). *J Geophys Res* 97(D17): 18345–18371
- Sellers PJ, Randall DA, Collatz GJ, Berry JA, Field CB, Dazlich DA, Zhang C, Collelo GD and Bounoua L

- (1996a) A revised land surface parameterization (SiB2) for atmospheric GCMs. Part I: Model formulation. *J Climate* 9: 676–705
- Sellers PJ, Los SO, Tucker CJ, Justice CO, Dazlich DA, Collatz GJ and Randall DA (1996b) A revised land surface parameterization (SiB2) for atmospheric GCMs. Part II: The generation of global fields of terrestrial biophysical parameters from satellite data. *J Climate* 9: 706–737
- Sharkey TD (1985) Photosynthesis in intact leaves of C₃ plants: Physics, physiology and rate limitations. *Bot Rev* 51: 53–105
- Sigman DM and Haug GH (2003) The biological pump in the past. In: Elderfield H (ed) *Treatise on Geochemistry* Volume 6, pp 491–528. Elsevier, Amsterdam
- Sitch S, Smith B, Prentice IC, Arneth A, Bondeau A, Cramer W, Kaplan JO, Levis S, Lucht W, Sykes MT, Thonicke K and Venevsky S (2003) Evaluation of ecosystem dynamics, plant geography and terrestrial carbon cycling in the LPJ dynamic global vegetation model. *Global Change Biol* 9: 161–185
- Slayback DA, Pinzon JE, Los SO and Tucker CJ (2003) Northern hemisphere photosynthetic trends 1982–1999. *Global Change Biol* 9: 1–15
- Smyth TJ, Tilstone GH and Groom SB (2005) Integration of radiative transfer into satellite models of ocean primary production. *J Geophys Res* 110: C10014
- Spitters, CJT, Toussaint, HAJM and Goudriaan, J (1986) Separating the diffuse and direct component of global radiation and its implications for modelling canopy photosynthesis. Part I. Components of incoming radiation. *Agr Forest Meteorol* 38: 217–229
- Stomp M, Huisman J, Voros L, Pick FR, Laamanen M, Haverkamp T and Stal LJ (2007) Colourful coexistence of red and green picocyanobacteria in lakes and seas. *Ecol Lett* 10: 290–298
- Stramski D and Mobley CD (1997) Effects of microbial particles on oceanic optics: A database of single-particle optical properties. *Limnol Oceanogr* 42: 538–549
- Switzer AC, Kamykowski D and Zentara SJ (2003) Mapping nitrate in the global ocean using remotely sensed sea surface temperature. *J Geophys Res* 108: NO. C8, 3280
- Taub DR (2002) Analysis of interspecific variation in plant growth responses to nitrogen. *Can J Bot* 80: 34–41
- Thornton PE and Zimmerman NE (2007) An improved canopy integration scheme for a land surface model with prognostic canopy structure. *J Climate* 20: 3902–3923
- Thornton PE, Lamarque J-F, Rosenbloom NA and Mahowald NM (2007) Influence of carbon-nitrogen cycle coupling on land model response to CO₂ fertilization and climate variability. *Global Biogeochem Cy* 21: GB4018
- Tortell PD, DiTullio GR, Sigman DM and Morel FMM (2002) CO₂ effects on taxonomic composition and nutrient utilization in an Equatorial Pacific phytoplankton assemblage. *Mar Ecol-Prog Ser* 236: 37–43
- Trumbore S (2006) Carbon respired by terrestrial ecosystems - recent progress and challenges. *Global Change Biol* 12: 141–153
- Tucker CJ, Townshend JRG and Goff TE (1985) African land cover classification using satellite data. *Science* 227: 369–375
- Turner DP, Urbanski S, Bremer D, Wofsy SC, Meyers T, Gower ST and Gregory M (2003) A cross-biome comparison of daily light use efficiency for gross primary production. *Global Change Biol* 9: 383–395
- Uitz J, Claustre H, Morel A and Hooker S (2006) Vertical distribution of phytoplankton communities in open ocean: An assessment based on surface chlorophyll. *J Geophys Res* 111: C08005
- VEMAP Members (Melillo JM, Borchers J, Chaney J, Fisher H, Fox S, Haxeltine A, Janetos A, Kicklighter DW, Kittel TGF, McGuire AD, McKeown R, Neilson R, Nemani R, Ojima DS, Painter T, Pan Y, Parton WJ, Pierce L, Pitelka L, Prentice C, Rizzo B, Rosenbloom NA, Running S, Schimel DS, Sitch S, Smith T and Woodward, I) (1995) Vegetation/ecosystem modeling and analysis project: Comparing biogeography and biogeochemistry models in a continental-scale study of terrestrial ecosystem responses to climate change and CO₂ doubling. *Global Biogeochem Cy* 9: 407–437
- Vitousek P (1984) Litterfall, nutrient cycling and nutrient limitation in tropical forests. *Ecology* 65: 285–298
- Vostral CB, Boyce RL and Friedland AJ (2002) Winter water relations of New England conifers and factors influencing their upper elevational limits. I. Measurements. *Tree Physiol* 22: 793–800
- Ward SJE, Midgley GF, Jones MH and Curtis PS (1999) Responses of wild C₄ and C₃ grass (Poaceae) species to elevated atmospheric CO₂ concentration: A meta-analytic test of current theories and perceptions. *Global Change Biol* 5: 723–741
- Wang YP, Baldocchi D, Leuning R, Falge E and Vesala T (2007) Estimating parameters in a land-surface model by applying nonlinear inversion to eddy covariance flux measurements from eight fluxnet sites. *Global Change Biol* 13: 652–670
- Ward BA and Wanick JJ (2007) Phytoplankton growth conditions during autumn and winter in the Irminger Sea, North Atlantic. *Mar Ecol-Prog Ser* 334: 47–61
- Waring RH, Law BE, Goulden ML, Bassow SL, McCreight RW, Wofsy SC and Bazzaz FA (1995) Scaling gross ecosystem production at Harvard Forest with remote sensing: A comparison of estimates from a constrained quantum-use efficiency model and eddy correlation. *Plant Cell Environ* 18: 1201–1213
- Warnant P, François L, Strivay D and Gérard J-C (1994) CARAIB: A global model of terrestrial biological productivity. *Global Biogeochem Cy* 8: 255–270

- Wedin DA and Tilman D (1996a) Influence of nitrogen loading and species composition on the carbon balance of grasslands. *Science* 274: 1720–1723
- Wedin DA and Tilman D (1996b) Spatial and temporal distribution of *Trichodesmium* blooms in the world's oceans. *Global Biogeochem Cy* 20: GB4016
- Westberry T, Behrenfeld MJ, Siegel DA and Boss E (2008) Carbon-based primary productivity modeling with vertically resolved photoacclimation. *Global Biogeochem Cy* 22: GB2024
- White MA, Thornton PE, Running SW and Nemani RR (2000) Parameterization and sensitivity analysis of the BIOME-BGC terrestrial ecosystem model: Net primary production controls. *Earth Interactions* 4: 1–85
- Williams PJL, Morris PJ and Karl DM (2004) Net community production and metabolic balance at the oligotrophic ocean site, Station ALOHA. *Deep-Sea Res Pt I* 51: 1563–1578
- Wolf-Gladrow DA, Riebesell U, Burkhardt S and Jelle B (1999) Direct effects of CO₂ concentration on growth and isotopic composition of marine phytoplankton. *Tellus B* 51: 461–476
- Wong SC, Cowan IR and Farquhar GD (1979) Stomatal conductance correlates with photosynthesis capacity. *Nature* 282: 424–426
- Wood AM (1985) Adaptation of photosynthetic apparatus of marine ultraplankton to natural light fields. *Nature* 316: 253–255
- Woods JD and Onken R (1982) Diurnal variation and primary production in the ocean - preliminary results of a Lagrangian ensemble model. *J Plankton Res* 4: 735–756
- Woodward FI and Lomas MR (2004) Vegetation dynamics - simulating responses to climatic change. *Biol Rev* 79: 643–670
- Woodward FI, Smith TM and Emanuel WR (1995) A global land primary productivity and phytogeography model. *Global Biogeochem Cy* 9: 471–490
- Wullschlegel SD (1993) Biochemical limitations to carbon assimilation in C₃ plants - a retrospective analysis of the A/C_i curves from 109 species. *J Exp Bot* 44: 907–920
- Xiao X, Melillo JM, Kicklighter DW, McGuire AD, Prinn RG, Wang C, Stone PH and Sokolov A (1998) Transient climate change and net ecosystem production of the terrestrial biosphere. *Global Biogeochem Cy* 12: 345–360
- Xue Y, Sellers PJ, Kinter JL and Shukla J (1991) A simplified biosphere model for global climate studies. *J Climate* 4: 345–364
- Yang W, Huang D, Tan B, Stoeve JC, Shabanov NV, Knyazikhin Y, Nemani RR and Myneni RB (2006) Analysis of leaf area index and fraction of PAR absorbed by vegetation products from the Terra MODIS sensor: 2000–2005. *IEEE T Geosci Remote* 44: 1829–1842
- Zhao M, Heinsch FA, Nemani RR and Running SW (2005) Improvement of the MODIS terrestrial gross and net primary production global data set. *Remote Sens Environ* 95: 164–176

- A**
- Absorption spectra, 46, 56–58, 60, 64, 68, 72–74, 476
 - Acceptor side quenching, 132, 145
 - Activation, 86, 89, 109–114, 146, 165, 210, 211, 216–219, 221, 224, 235–237, 242, 262, 269, 275, 276, 279, 280, 283, 285, 290, 296, 308, 309, 314, 330, 331, 342–344, 356, 428
 - energy, 216, 217, 237, 242
 - Adenosine triphosphate (ATP), 20, 21, 87, 107, 109, 111, 113, 114, 152, 159, 162, 211, 213, 214, 218, 219, 233, 238, 239, 247–255, 260, 263, 268, 269, 280, 281, 283, 296, 299–302, 307, 308, 310, 311, 313, 314, 318, 319, 324–331, 334–336, 338–345, 373
 - Albedo, 283, 445
 - Alternative electron flow, 250, 256, 257–259, 264, 267, 301, 302, 308, 315, 329, 334, 340
 - Antenna aggregates, 59, 64, 66, 68, 70, 72, 76, 77
 - Apparent equilibrium constant, 97, 178, 186–194, 196–199, 203
 - Arrhenius equations, 232, 237
 - Assimilation potentials, 366, 443
 - Assimilatory power, 325, 326, 341
 - Atmospheric vapor pressure deficit, 444, 445, 469
 - ATP synthase, 109, 111, 113, 126, 154, 162, 164, 165, 252, 253, 300, 301, 307, 311, 340
 - Attractor (model dynamics), 196, 454, 455, 459–461
- B**
- Back-reaction, 180, 341
 - Balanced truncation, 24
 - Big-leaf hypothesis, 474
 - BioModels Database, 5
 - Blackman type models (limitation), 278, 284, 475
 - Bleaching, 12, 46, 47, 60, 73
 - Boundary layer (conductance), 222, 232, 240, 308, 350, 372, 473, 474, 483
 - Bra vectors, 61
 - Brownian diffusion (dynamics), 152, 153, 166–168, 171
 - Buffer capacity, 162
 - Bundle sheath, 263, 324–326, 328, 329, 332, 334–337, 481
- C**
- CO₂ dissolution, 241
 - C₄ cycle (pathway), 324–327, 330, 331, 334, 335, 337, 344, 345, 413, 470
 - C₄ plants, 93, 281, 324–327, 329, 330, 334, 335, 341–344, 404, 470, 471
 - Calcification, 477–479
 - Calvin-Benson-Bassham carbon reduction cycle (CRC), 17, 19–21, 108, 119–112, 114, 171, 233, 239, 240, 247, 253, 255, 267, 276, 281, 283–285, 296, 300–302, 307, 308, 310, 311, 313, 314, 316, 318, 324, 331, 340–342, 344, 352, 359, 427, 428
 - Canopy, 221, 223, 224, 232, 243, 363–390, 401–413, 417–436, 443–446, 450, 455, 460, 467, 469–471, 473, 474, 481–483, 486
 - Carbamylation, 216, 218, 219, 279, 280, 283, 284, 290
 - Carbon assimilation, 232, 234, 235, 239, 265, 297, 319, 343, 424, 443, 445, 447, 449, 451, 457, 458
 - balance, 369, 371, 383, 389, 417, 420, 432, 433, 460, 467, 468
 - dynamics, 457
 - investment, 434
 - reduction, 210, 276, 443, 467–469, 477–480, 487
 - Carbonic anhydrase, 241, 330, 350, 353, 356
 - Carboxylation, 211–213, 216, 219, 220, 223, 232–234, 236, 237, 242, 243, 248–252, 254, 268, 269, 276, 277, 279–283, 285–287, 290, 291, 297, 302, 308, 313, 316, 325, 334, 351, 356, 359, 365, 373, 376, 401, 402, 404, 409, 438, 470, 471, 481
 - Catalytic cycle, 154, 157, 158, 307
 - turnover rate, 216
 - CellML (Markup Language), 5, 6
 - Channeling, 178, 330, 331, 340–342, 344
 - Charge separation, 22, 27, 33–50, 56, 86, 87, 89, 93–97, 101, 126, 127, 129, 152, 158–160, 162, 179, 181, 182, 187, 189, 190, 254, 257, 259, 304
 - Charge transfer (CT) states, 34, 35, 39, 40, 47–50
 - Chemical equilibration, 337, 340
 - potential, 180, 300, 448
 - Chlorophyll (Chl) *a* fluorescence, 18, 20, 21, 85–114, 125–146, 153, 163, 164, 220, 223, 224, 248, 296, 303, 474
 - concentration, 473, 474, 479, 484, 485
 - binding proteins, 375
 - Chromophores, 34, 50, 60, 73, 312
 - Closed (state of a) reaction center, 95, 97, 98, 129, 145, 158
 - CO₂ assimilation rate, 150, 210, 211, 213–216, 218–224, 233, 253, 256, 287, 289, 290, 305, 335, 337, 353, 354, 356–358
 - compensation point, 211, 221, 232, 234, 242, 248, 249, 325, 327, 335, 336, 365, 373, 447, 473
 - partial pressures, 211, 213, 215, 219–221, 248, 249, 256, 264, 267, 268, 287, 356, 481, 483
 - response curve, 213, 218, 220, 234, 287, 296, 317
 - transfer conductance, 219, 220
 - Compartments, 6–8, 10–13, 27, 152–154, 161, 162, 166, 167, 181, 189, 297, 298, 302, 303, 311, 327, 331, 336, 444, 446, 449, 477
 - Complementary area, 100
 - Comprehensive Model Space (CMS), 18–25, 27, 28, 318, 319
 - Computational singular perturbation, 25
 - Connectivity (parameter), 18, 86, 91, 92, 100–103, 105, 128, 132, 135, 144, 190–192, 197, 297, 338
 - Control analysis, 92, 115, 349–359
 - Coordination theory, 382
 - Core complexes, 34, 35, 40, 50, 58, 196–198, 338
 - LH2 complex, 55, 58, 59
 - Coupling energies, 55, 56, 59–61, 63, 64, 70
 - Couplings (between energy states), 35, 36, 39, 41, 44, 57, 61, 64, 72, 76, 77
 - Crop yields, 402
 - Crowding, 196, 339
 - Cyclic electron flow (transfer, transport) 10, 107–110, 112, 114, 159, 162, 165, 167–170, 179, 247, 248, 259, 260, 263, 265, 299–301, 302, 306, 313, 324, 339, 340–344
 - photophosphorylation, 326, 334, 335, 342, 344
 - Cytochrome b₆f complex, 159
- D**
- Dark adaptation, 87, 88, 92, 96, 97, 102, 103, 107, 109, 111, 112, 126–130, 132–137, 139–145, 158, 202, 256, 265, 305
 - respiration, 269, 313, 314, 365, 371, 405

Databases

- BioModels Database, 5
- JWS Online, 5
- Day respiration, 211, 212, 249
- De-localization, 57
- Diagonal disorder, 60–63, 68, 71, 72
- Diffusion, 12–14, 156, 162, 166, 168, 169, 171, 178, 179, 181, 183, 192, 195, 196, 199–203, 211, 215, 220–222, 224, 232, 240, 249, 256, 257, 266, 298, 299, 305, 306, 308, 319, 328, 329, 331, 339, 342, 427, 478, 483
 - resistance, 220, 257, 296, 308, 312, 331, 335, 384
- Dimensionality reduction, 18, 21, 24
- Disorders (dynamic), 34, 35, 43–45, 48, 56, 57, 59–64, 66, 68, 71, 72, 76, 77, 195
- Domain size, 195, 197, 198, 200, 201
- Donor side quenching, 127–132, 135, 143–145
- Dwell time, 200, 201

E

- Ecosystem dynamics, 457, 459, 461, 467, 468
 - management, 452, 458
- Electric field, 86, 91, 96, 97, 102, 156, 161, 165, 300, 339
- Electrochemical (transmembrane) potential, 12, 86, 90, 96, 105, 108, 126, 161, 145, 152–154, 159, 164
- Electrogenic steps, 160
- Electron transfer, 34, 35, 44, 47–49, 56, 126, 131, 154–156, 158–161, 164, 165, 168, 169, 177–203, 298, 301, 304, 306, 307, 314, 339, 342
 - transport (chain), 86, 87, 89, 90, 92–97, 100, 102–115, 126, 128, 152–156, 159–163, 166–171, 210, 211, 213–221, 223, 224, 232–234, 238–240, 243, 247–269, 283, 285, 286, 296–299, 301, 302, 305, 307, 308, 310, 313–319, 324–331, 338–340, 343, 344, 352, 358, 359, 365, 366, 373, 376, 401–403, 405, 408, 410, 443, 447, 451, 461, 470
 - transport limited rate, 213–215, 220, 221, 248, 405, 447
 - trapping, 127–131, 134, 135, 138, 140, 145
- Electronically excited state, 34, 64
- Electron-phonon coupling, 40, 41, 73
- Energetic connectivity, 86, 92, 100–102, 105
- Energy transfer, 22, 35–38, 40–42, 44, 49, 50, 58, 59, 67, 68, 71, 77, 90, 95, 132, 144, 145, 301
- Enthalphy, 217
- Entropy, 179, 189, 217, 237, 454
- Environmental forcing, 467, 469, 471, 473, 479, 482
 - gradients, 366, 467
- Equilibrium constant, 96, 97, 139, 159, 162, 178
- Ergodic theory, 454, 461
- Excitation, 22, 27, 33–36, 38–44, 47–50, 55–77, 86, 87, 89, 90, 92–94, 98–101, 103, 107, 109, 110, 113, 114, 126–131, 133–146, 158, 159, 166, 180, 190, 247, 253, 257, 260, 261, 264, 265, 297, 299–301, 303–305, 312, 329, 338, 339, 341, 379
- Exciton, 34–50, 55–77, 126, 130, 256
 - lattice coupling, 55, 56, 65, 67–69, 73
 - phonon coupling, 36, 41, 60, 63–68, 72–75, 77
- Excitonic polaron, 56, 64–71, 76, 77
- eXtensible Markup Language (XML), 5, 14, 19

F

- Feedback loops, 14, 445, 446
- Flash fluorescence induction, 86, 89, 90
 - train, 134
- Fluctuations, 44, 57, 60, 98, 168, 195, 196, 312, 365, 385, 460, 480

- Fluorescence anisotropy, 62, 63, 70, 71
 - emission, 18, 19, 21, 25, 27, 56, 60, 71, 75, 87, 90, 93, 95, 98, 113, 256
 - induction, 19, 86, 89, 111, 126–128, 132, 137–142, 144–146, 152–154, 160, 163, 165, 166, 171, 312, 314
 - line narrowing, 34, 36, 37, 47, 56, 59, 64, 73–75
 - oscillations, 111
 - rise (FLR), 86, 87, 90–92, 97, 100, 102, 130, 136, 137, 146
 - (FL) spectrum, 63, 64, 66, 71–74, 77
 - transient (induction, FLI), 25, 26, 36, 37, 44, 45, 47, 85–115, 137, 153, 156, 160, 163, 166
- Flux control (coefficients), 350, 352–254, 357, 358
- Foliar N, 375, 376, 381, 473, 481, 482
- Foliar P, 473
- Förster theory, 38, 39, 50
- Free energy, 96, 177, 179–181, 184, 188, 189, 297, 300, 308
- Frenkel exciton, 56, 57, 59–64, 66, 68–71, 76, 77

G

- Gaussian distribution, 60, 68
- GENESIS, 5
- G-function, 368
- Global climate model (GCM), 466, 468, 474, 478, 480, 483, 487, 488
- Grana stacks (area), 113, 166, 169, 198, 199
- Gross Primary Production (GPP), 442, 443, 466, 469–471, 485
- Ground water, 442–444, 447, 448

H

- Hamiltonian, 35, 60, 61, 64–66, 76
- Heat dissipation, 27, 87, 95, 98, 103
 - engine, 179
- Heterogeneity, 41, 56, 57, 70, 90–92, 100, 101, 103, 105, 107, 112, 115, 126, 138, 143, 169, 171, 195, 196, 198, 199, 203, 223, 298, 370, 387, 406, 421, 472
- Heterogeneous systems, 128, 130, 142, 153, 170, 203
- Heterotrophic decay, 443
- Homogeneous broadening, 34, 36, 57
- Huang-Rhys factor, 37, 71–76
- Human management, 452

I

- Inactivation, 11, 219, 340, 342, 344
- Inclination angles, 368, 369, 376, 378, 386
- Induction curves, 127, 128, 132, 136–142, 144, 146, 152–154, 163–166, 171, 314
- Inhomogeneous (line) broadening, 34, 57
- Initial conditions, 9–12, 27, 67, 99, 100, 190, 192, 446
- Interaction energy, 35–37
- Intercellular air space, 221, 240, 372, 473, 480, 481
- Intercellular CO₂ partial pressure, 219, 20, 249, 256, 264, 268, 483

J

- JWS Online, 5

K

- Kautsky effect, 19, 87
- Ket vectors, 61
- Kinetic approach, 153, 171
 - equilibrium, 94, 105, 108, 110
- Kok model, 86, 94, 95, 106

L

- Lagrangian multiplier, 65, 365, 381
- Lambert-Beer law, 110, 369, 380, 419
- Land management, 452

Latent heat, 371, 445, 470, 482
 LD (Linear Dichroism) spectra, 43, 46
 Leaf Area Index (LAI), 365, 367, 368, 370, 372, 382–384, 386–388, 390, 402, 406, 408–410, 419, 442, 443, 450, 453, 466, 471–473, 481–483, 486
 Leakage, 107, 162, 164, 269, 307, 324, 325, 328, 329, 335, 343
 Liebig-type limitation, 475
 Light compensation points, 369, 383, 428, 433
 gradients, 90, 103, 115, 364, 367–369, 373, 377, 382, 426, 466, 470
 reactions, 21, 126
 Lightfleck, 418, 419, 421, 425–427, 431–434
 Light-harvesting (complex, LHC), 20, 33–50, 56–58, 86, 94, 98, 105, 106, 108, 113, 114, 152, 190, 168, 250, 338, 365, 375, 376, 378, 469, 481
 Linear electron transport (LET), 113, 247, 248, 250–252, 254–257, 259–263, 299
 Line-narrowed fluorescence (FLN), 34, 36, 37, 47, 56, 59, 64, 69, 70, 73–75
 Liquid state model, 178
 Litter, 443–446, 450, 456, 467
 Localization length, 37, 38, 65–68
 Lumenal pH, 21, 109, 113, 300, 305, 313, 339
 Lumping (of reactions in models), 21, 25, 26

M

Maintenance respiration, 317, 350, 371, 441–444, 447
 Markov model, 368
 Markovian process, 192
 Mass action approach (law), 152, 153, 154, 156, 161
 Master equation approach, 153–155
 Maximum fluorescence, F_M , 86–89, 92, 93, 98, 100–102, 104, 106, 112, 113, 126, 130, 132–135, 137, 152, 254, 256, 258, 259, 262, 265, 304, 305, 312, 313, 339
 Mesophyll diffusion resistance, 257, 308
 Metabolite pools, 334, 337, 427
 Michaelis constant, 232, 234, 237, 276, 289
 Michaelis-Menten curve, 277–281, 284, 287, 290
 Microdomains, 166
 Mineralization, 441, 442, 444
 Minimum fluorescence, F_0 , 68, 86–88, 93, 102–104, 106, 126, 127, 129, 130, 132, 133, 138, 140–144, 152, 152, 256, 304, 305, 312
 Minimum Information Requested In the Annotation of biochemical Models (MIRIAM), 4, 6–9, 18, 19, 21, 26, 28
 Mobile carriers, 152, 153, 156, 161, 166–168, 170, 177–179, 181, 199, 201, 202
 Model accuracy, 233–235, 454
 description formats, 5
 reduction, 24, 25, 28, 99, 105
 Modeling environments, 3, 4, 9, 13, 442, 443
 scene, 167, 169, 170
 Monopartite model, 94
 Monte Carlo (method), 370, 371, 453
 Mortality, 441, 442, 444–446, 449, 450, 452, 456
 Mosaic cycle, 456
 Multi(ple) turnover, 89, 90, 126, 127, 129, 130, 132, 136, 202
 Multiparticle models, 153, 162, 170, 171
 Multi-PSB (Phonon Side Band), 73, 74

N

NADPH dehydrogenase (NDH), 296, 299, 301, 306, 310, 311, 324, 326, 327, 330, 331, 334, 338, 342, 344, 345
 Net CO₂ assimilation rate, 211, 222, 305, 335, 337, 350, 353
 Net Primary Production (NPP), 442–444, 453–455, 457, 466, 468, 469, 472, 483–487, 475–480

NEURON, 5

Nitrite reduction, 251, 252, 295, 296, 301, 302, 310, 312, 316, 318, 329, 340
 Nitrogen assimilation, 257, 265, 268, 318
 content, 249, 258, 264, 318, 319, 365, 373–375, 377, 381, 383, 385, 386, 389, 443, 444, 446, 447, 456, 470, 473, 481, 482, 486
 partitioning, 373, 375–377, 379
 requirement, 470
 Non-photochemical fluorescence (FL) quenching, 22, 86, 98, 112, 129, 141, 165, 256, 297, 298, 303, 305, 312, 329
 Non-photosynthetic absorption, 262, 264, 334
 pigments, 257, 261–264
 Non-radiative recombination, 130, 157
 Non-rectangular hyperbola, 215, 366
 Normal law, 61
 Normalized difference vegetable index (NDVI), 466, 471, 472
 Nuclear modes, 34, 36

O

Ocean carbon cycle, 468, 480, 487
 OD (Optical Density) spectra, 36, 42, 46, 47
 OJDIP (O-J-I-P) fluorescence induction curves, 86, 89–92, 94, 103–107, 109, 111, 114, 126–128, 136–141, 144, 153, 154, 156, 163, 314
 Open-source libraries, 6
 Optimal distribution, 381–384, 388, 389, 471
 Optimization models (principles), 364, 366, 380–383, 385–387, 389
 Oscillations, 89, 106, 111, 114, 115, 133, 145, 296, 314–316, 340, 341
 Overcycling, 324, 325, 327–329, 335–337, 345
 Oxygen evolving complex (OEC), 23, 86, 87, 91, 92, 94, 95, 99, 101, 103, 105, 108, 126–130, 136, 144, 152, 154, 156, 158, 159, 164, 165, 297–299, 304
 Oxygenation, 212, 213, 216, 232–236, 242, 243, 250, 254, 268, 278, 281, 282, 285, 287, 308, 324, 325, 336, 337, 402, 403, 405, 412, 428, 481

P

Partial pressure of atmospheric CO₂, 445
 Partitioning of excitation, 264, 312
 Penumbra, 364, 371, 388
 PEP carboxylase (PEPC), 325, 329, 330, 443, 461
 Percolation, 196, 339
 Peripheral LH2 complex, 55, 58, 59
 Phonons, 34–41, 44, 46–48, 56, 57, 60, 63–69, 71–77
 Photoacclimation, 476, 485
 Photochemical phase, 89, 90, 97, 126, 145
 quenching, 126, 130
 Photoreaction center, 152, 154
 Photorespiration, 210–212, 223, 232–234, 236, 247, 248, 250, 252, 253, 255, 257, 264, 266–269, 276, 281, 296, 301, 310, 324, 325, 327–329, 335–337, 340, 344, 345, 401–403, 412, 413, 427, 428, 470, 471
 Photosynthetic capacity, 216, 241, 364, 365, 373, 374, 377, 380, 382, 384, 388, 390, 428, 433, 436, 450, 466, 470–474, 481, 482, 486
 induction, 114, 417–436
 potentials, 364, 365, 367, 373, 377, 379–381
 production, 364, 366, 373
 Photosystem I (PS I), 18, 20, 33, 35, 40, 41, 50, 86, 88–93, 102–104, 106–112, 114, 115, 126, 137, 146, 151–156, 159–171, 178, 179, 188, 198, 199, 247–249, 251–154, 256, 259–261, 263–266, 269, 276, 280, 283, 296–299, 301–303, 305, 306, 312–316, 324, 326, 327, 329–331, 334, 338, 340–345

Photosystem II (PS II), 18–25, 27, 28, 34, 35, 43, 44, 46–50, 86–94, 96–111, 114, 115, 126–128, 130, 132, 133, 144, 145, 151–166, 168, 170, 178, 180, 188, 192, 195, 198, 199, 215, 223, 224, 248–254, 256–261, 263–266, 268, 269, 276, 283, 296–299, 301–307, 312–314, 324, 326, 329, 334, 338, 339, 342, 344, 405, 419, 447

Phylloclimate, 419

Phytoplankton, 109, 466–469, 474–480, 484, 485, 487, 488

Picosecond time-resolved measurements, 60

Pigment proteins, 34–36, 56, 57, 76, 264

Pixel, 471, 481, 482, 484–486

Plant canopies, 223, 364–367, 371, 378, 383, 387, 417–436

Plastocyanin diffusion, 298, 305

Plastoquinol, 97, 159, 160, 164, 165

Plastoquinone, 86, 88, 90, 108, 159, 160, 306

Poincaré map, 454, 455

Poisson distribution (process), 11, 188, 190, 192, 193, 194, 197, 198

Polaronic model of excitons, 64

Protein turnover, 376, 385

Proton fluxes, 154, 164, 256

Proton gradient, 87, 107, 111, 161, 162, 306, 307, 329, 340, 343

 pump, 126, 137, 160, 177, 179–192, 189

 slip, 253, 268, 300, 307, 311

 transport, 86, 128, 154, 160–162, 195, 295, 306, 310, 324, 343

PS I fluorescence, 93

Pseudocyclic electron flow, 247–252, 263, 266

Pseudo-PSB (Phonon Side Band), 73, 74

Pump and probe technique, 86, 90

Q

Q-cycle, 137, 159, 160, 161, 247–255, 262, 268, 269, 299, 306, 307, 311, 324, 327, 339, 342, 343

Q_B non-reducing PS II centers, 90, 100, 103, 104, 107, 134, 135

q_E type quenching, 86, 98, 112–114, 339

Quantum yield, 87, 180, 188, 221, 223, 224, 232, 238, 247, 248, 255, 257–259, 262–265, 297, 312, 334, 335, 365, 366, 372, 375, 376, 384, 390, 418, 428, 436, 469, 476

Quasi-steady state (QSSA), 18, 21, 25, 104, 301, 429

Quenching (quencher), 21, 22, 86, 87, 90, 93, 98, 101, 102, 104–107, 112, 126–136, 138, 141–145, 157, 165, 250, 256, 296–298, 300, 303, 305, 312, 329, 339

Quinone, 18, 22, 23, 86, 87, 98, 105, 108, 126, 127, 152, 155, 157, 158, 164, 165, 178, 180, 187, 189, 195–203, 296, 341

 domains, 195, 196, 198, 200, 201, 203

R

Radiation, 179, 180, 223, 253, 276–278, 281–285, 287–289, 364, 369, 370, 372, 378, 406, 419, 421, 425, 426, 433, 442–447, 449–452, 461, 466–471, 474, 475, 478, 480, 483, 486

Radiative deactivation, 98

Radical pair, 22, 48, 49, 86, 94, 101, 104, 127, 129

 recombination, 127, 129, 130, 145

Reaction centers (RC), 22, 25, 34, 40, 44, 46, 47, 56–59, 86, 87, 90, 97, 98, 104, 113, 126–146, 152–155, 158–160, 164, 166, 169, 177–181, 187–190, 193, 195–197, 200–203, 256, 261, 265, 297, 303, 338

 compartments, 153

Real phonon sideband (Real-PSB), 73, 74

Recombination reactions, 101, 179

Red states, 40, 41

Redfield theory, 34, 35, 38–41, 43, 49

Redox equilibrium, 188, 199, 298, 301, 305

Redox-controlled enzymes, 300

Reducing power, 252, 281, 302, 311, 325, 326, 334, 341, 345

Remote sensing, 388, 468, 474, 476–478, 486

Reorganization (energy), 34, 36, 39, 40, 44, 47, 48, 65, 66, 69, 70, 72, 74, 77, 96

Resonant (exciton) coupling energy, 55, 70, 431

Resonant interactions, 59, 66

Respiration (rate), 178, 199, 201, 211, 212, 221, 232, 234, 236, 241, 242, 249, 268, 269, 308, 313, 314, 316–318, 350, 352, 365, 366, 371–373, 379, 382, 405, 418, 428, 431, 432, 441

Reversible radical pair (RRP) model, 86, 94, 96, 101, 104

Rubisco, 18, 20, 210–213, 215, 216, 218–221, 223, 224, 232–240, 242, 243, 248, 249, 255–257, 266, 275–291, 296–298, 300, 307, 308, 311–313, 324, 325, 327, 330–335, 343, 345, 350–353, 356–359, 365, 373, 376, 377, 379, 401–413, 418, 427–429, 436, 442, 443, 445, 447, 451, 461, 466, 469–471, 473, 481

 activase, 218, 219, 235, 236, 279, 280, 283, 284, 290, 353, 356

 activation state, 211, 218, 219, 221, 236, 285, 296, 331

 -limited photosynthesis (rate), 23, 210, 215, 220, 221, 224, 234, 235, 237, 239, 242, 285, 401–405, 407, 409, 410, 413, 451, 481

 sites, 218, 235, 280, 290, 402

RuBP regeneration (limited photosynthesis), 210, 213–215, 217, 218, 223, 224, 232, 233, 235, 237–240, 247, 248, 250, 253, 276, 282, 284–287, 289–291, 325, 39, 376, 377, 403, 409

Ruelle-Takens transformation, 454, 455

S

Schrödinger equation, 65

Secondary metabolism, 328, 340

Self initialization, 452, 456, 457

Self-trapped excitons, 56, 64, 66, 67, 69–71, 74, 76, 77

Semantic encoding, 6

Semi closed state, 98, 135

Shpol'skii effect, 58

Simulation platforms, 5

Single molecule fluorescence, 62

Single turnover, 17, 89, 98, 127–130, 132–134, 187, 192, 194, 199, 203, 303

Singlet state, 87

Site energies, 34–36, 40–42, 44, 46–49, 60, 61, 65, 67, 72

Soil carbon pools, 444

 hydraulic conductivity, 444, 448

 matric potential, 448

 moisture, 443, 444, 446, 468, 472–474, 483, 486

 water content, 444, 445, 448, 458

Solar radiation, 369, 372, 406, 442, 445, 450, 468, 469, 471, 475, 478, 480

Solid state model, 178

Spatial heterogeneity, 56, 171, 406, 472

Specificity, 179, 212, 216, 232, 242, 248, 249, 256, 276, 282, 401–404, 407, 408, 410

Spectral hole burning, 36, 41, 59, 60, 62–64, 69, 72–75

 inhomogeneity, 57

Spillover, 114, 297

S-state (transitions), 22, 23, 25, 73, 87, 91, 94–96, 103–108, 110, 113, 126, 127, 129, 158, 164, 165, 264, 298, 304, 338

Standard free energy, 96, 180, 300

 potentials, 180, 181, 183, 184, 191, 195

Starch synthesis, 108, 110, 268, 296, 297, 300, 302, 308, 310, 311, 318, 319, 335–337, 340, 344

Stark signal (spectrum), 36, 38, 46–48
 State transitions, 113, 114, 261, 264, 339
 variables, 18, 20, 25, 27, 99, 101, 110, 111, 297, 298, 301, 305, 443
 Static disorders, 68, 72, 76
 Stoichiometry, 6, 91, 109, 163, 189, 192, 194, 197, 198, 203, 212, 214, 247–269, 299, 319, 325–330, 334–336, 340, 341, 343, 344, 351, 373, 375
 Stomatal conductance, 219, 222, 232, 240, 267, 357, 365, 366, 372, 380, 409, 427, 442, 443, 445, 451–453, 458, 468, 473, 474, 483
 Stromal area, 166, 169
 Structural disorder, 60, 61
 Successional cycle, 456
 Sucrose synthesis, 108, 110, 297, 300, 308–310, 312, 326, 344
 Sun gaps, 409
 patches, 419
 flecks, 419, 426
 Supercomplex, 34, 177, 178, 180, 189–195, 198, 200–202
 Superradiance enhancement factor, 66–68
 Systems Biology Markup Language (SBML), 3–9, 11–14, 18, 19, 21, 26, 27
 Systems Biology Ontology (SBO), 4, 6, 7, 18
T
 Transient absorption (TA) spectra, 41–43, 49
 Temperature, 18, 36, 37, 40, 44–47, 49, 64, 65, 73, 88, 89, 92, 93, 95, 101, 156, 161, 166, 168, 179, 210, 213, 214, 216–222, 224, 232–243, 269, 275, 276, 280, 286, 305, 308, 335, 364–367, 371, 372, 374, 376, 389, 380, 384, 403, 406, 408, 409, 419, 429, 436, 443–448, 451, 452, 454, 455, 460, 468–470, 472, 473, 476, 477, 481–483
 gradients, 365, 379
 response, 217, 220, 224, 233–239, 241, 242, 365, 366, 379, 380, 470, 483
 Thermal phase, 89, 90, 97, 115, 145

Three-dimensional lattice, 64, 66
 Three-state trapping model, *see* TST model
 Time step, 312, 446, 451, 452, 480
 Triosephosphate utilization limited photosynthesis, 240, 289
 Transition dipole, 36, 39, 59–63, 69, 71, 72
 Transition energies, 34–36, 40, 42, 44, 59, 60, 68, 71, 72
 Transmembrane potential, 152, 154, 156, 161, 165
 proton gradient, 87, 107, 161, 162, 340
 Transpiration, 221, 222, 371, 372, 377, 441–445, 458, 473, 483
 Triose transport limitation, 223, 232
 Triplet state, 46, 47, 87
 TST model (TSTM), 98, 103, 104, 126, 127, 129, 140, 145
 Two-dimensional lattices, 64, 66
 Two-electron gate (TEG) model, 85, 86, 93–95, 103–106

U

Unified Modeling Language (UML), 4, 5

V

Vapor pressure, 217, 240, 366, 419, 442, 444, 445, 451, 452, 469, 473, 483
 Variable fluorescence, 86, 87, 91–93, 98, 100, 115, 126–128, 130–138, 141, 143, 145, 146, 164
 Vibrational modes, 35, 76
 Virtual Cell, 3, 4, 9–11, 14
 Voxels, 370, 379, 380, 388

W

Water content, 444, 445, 448, 449, 458, 459, 483
 field capacity, 448
 potential, 222, 444, 445, 447, 448, 453, 483
 Water-water cycle, 248, 249, 251, 252, 306

Z

Zero-phonon (holes), 34, 48, 56, 63, 66, 69